

Proceedings book; 19th Internatioal foundrymen conference: Humans - Valuable Resource for Foundry Industry Development

Edited book / Urednička knjiga

Publication status / Verzija rada: **Published version / Objavljena verzija rada (izdavačev PDF)**

Publication year / Godina izdavanja: **2021**

Permanent link / Trajna poveznica: <https://urn.nsk.hr/urn:nbn:hr:115:446762>

Rights / Prava: [In copyright](#) / [Zaštićeno autorskim pravom.](#)

Download date / Datum preuzimanja: **2025-01-13**



SVEUČILIŠTE U ZAGREBU
METALURŠKI FAKULTET
UNIVERSITY OF ZAGREB
FACULTY OF METALLURGY

Repository / Repozitorij:

[Repository of Faculty of Metallurgy University of Zagreb - Repository of Faculty of Metallurgy University of Zagreb](#)



University of Zagreb
Faculty of Metallurgy
Sisak, Croatia



University of Ljubljana
Faculty of Natural Sciences and Engineering
Ljubljana, Slovenia



University North
Koprivnica, Croatia



Technical University of Košice
Faculty of Materials, Metallurgy and Recycling
Košice, Slovakia



University of Split
Faculty of Chemistry and Technology
Split, Croatia



ELKEM AS
Norway



PROCEEDINGS BOOK

19th INTERNATIONAL FOUNDRYMEN CONFERENCE

Humans - Valuable Resource for Foundry Industry Development



Split, June 16th – 18th, 2021

ORGANIZERS

University of Zagreb Faculty of Metallurgy, Sisak, Croatia

University of Ljubljana Faculty of Natural Sciences and Engineering, Ljubljana, Slovenia

University North, Koprivnica, Croatia

Technical University of Košice Faculty of Materials, Metallurgy and Recycling, Košice, Slovakia

University of Split Faculty of Chemistry and Technology, Split, Croatia

ELKEM ASA, Oslo, Norway

PROCEEDINGS BOOK**19th INTERNATIONAL FOUNDRYMEN CONFERENCE**

Humans - Valuable Resource for Foundry Industry Development

EDITORS

Natalija Dolić, Zdenka Zovko Brodarac, Sandra Brajčinović

TECHNICAL EDITOR

Sandra Brajčinović

PUBLISHER

University of Zagreb

Faculty of Metallurgy

Aleja narodnih heroja 3

44000 Sisak

Croatia

PRINT

InfOmArt Zagreb d.o.o.

Nikole Tesle 10

44000 Sisak

Croatia

ISSUE

200 copies

ISBN

978-953-7082-39-0

-A CIP record is available in computer catalogue of the National and University Library in Zagreb under the number 001103309

PREFACE

Knowledge is becoming an increasingly important resource for economic development. The Republic of Croatia is facing the challenges of the world economy, with the aim to meet certain requirements in shaping the education system. Ensuring the quality assurance of the education system is just one of the requirements set up as a continuous mission of University of Zagreb Faculty of Metallurgy and other co-organizers from the high-education. As the level of education of the population affects the progress of the economy, it is extremely important for the Republic of Croatia to increase the ratio of highly educated persons. In recent years, the ratio of the highly educated population of the Republic of Croatia has been growing, but in comparison with Europe, Croatia is still lagging behind. In order to increase the share of highly educated persons, it is necessary to invest in the quality of education, both in higher education and in secondary and primary education. This would increase awareness of the importance of education, which would ultimately result in an increase in the ratio of **highly educated and competent professionals**.

Metal industry as a base branch represents an important factor contributing to the economic potential of each country. Current market development as well as technical and economic objective, the production of high-quality, low-cost and environmentally friendly casting, requires application of recent and advanced materials, as well as production technologies, followed and supported by understanding of production process. The metal industry has been recognized as a “driving subdivision” of economy development.

Until the recession and deepening of the economic crisis in Croatia, companies operated stably, focused on streamlining production, investing in technology and employee’s education, increasing product quality and productivity, developing innovation and fighting for the market. The recession and economic crisis have slowed the strengthening of this economic activity. In order to overcome and mitigate the negative results caused by falling orders and reduced production, companies have developed new production programs and sought new customers and markets in order to maintain good positions within their market niches. Taking into account the growing need of large (global) producers for small series products, it is assumed that it will build a network of suppliers in which Croatian producers can be included. Small quantities are sufficient to employ their production capacities, and with a skilled workforce and new market opportunities, the growth of existing companies is expected, as well as the establishment of new ones. By investing in modern equipment and production certification, metal producers indicate a desire for growth. The main features of Croatian industry are stable product quality and reliability in accordance with EU standards, while on the other hand it is important to invest in available professional workforce, targeted support of scientific institutions, good production infrastructure with emphasis on modern technologies and transport links to the world.

Despite the recognizability and importance of the profession, the profession is underestimated by the amount of the average net monthly salary per employee in legal entities. The gross value added of the product is also indicative. Since the Croatian market is too small for significant production growth, companies in the observed activity primarily direct their production capacities to EU countries, which also means increasing the level of productivity of assets and labor. Competitiveness can be based exclusively on modern technology, efficient production processes but also on a highly skilled workforce. All this requires investment in infrastructure and educational study programs that should strive to acquire primarily practical knowledge and skills with an emphasis on the development and application of modern materials and technologies, in order to change this status of the Republic of Croatia.

Therefore, the motto of the **19th International Foundrymen Conference** is focused to the **HUMANS** as a **valuable resource for foundry industry development**. Human resources have an unavoidable role in scientific, technological and practical aspects concerning research, development and application of casting technology with the common perspective – increase of competitiveness.

Special attention will be focused towards the competitiveness ability of foundries, improvement of materials features and casting technologies, environmental protection as well as subjects connected to the application of castings.

During this Conference 49 papers will be presented in hybrid mode (online and in situ) due to pandemic of COVID-19 virus. In this Conference scientists from 14 countries (Australia, Austria, Bosnia and Herzegovina, Croatia, Czech Republic, India, Kosovo, Poland, Romania, Spain, Serbia, Slovenia, Slovakia, United States of America) recognized the importance to be a part of this scientific event. Book of Abstracts of the 19th International Foundrymen Conference includes summaries of the papers. The Proceedings book consists of papers *in extenso* published in electronic format (USB). Full length papers have undergone the international review procedure, done by eminent experts from corresponding fields, but have not undergone linguistic proof reading. Sequence of papers in Proceedings book has been done by category of papers in following order: plenary lectures, invited lectures, oral and poster presentation, and inside the category alphabetically by the first author's surname.

Within the Conference Student section is organized. This is an opportunity for industry to meet and recruit human resources as a main potential for business development. Coexistence of material science and sustainable technology in economic growth represent a knowledge transfer between small and medium enterprises' (SMEs'), industry and higher education institutions. Higher education at the Faculty of Metallurgy (HEI), conceived through the program and the learning outcomes, is based, inter alia, on promoting students' scientific and research work on applied topics, enabling ambitious and creative young people to become independent problem solvers, developing and supporting their curiosity, analytics and communication: **Graduates like the labour market needs!**

This occasion represents an opportunity to discuss and increase the mutual collaboration between HEIs' and industry with the aim of information exchange related to advanced experience in foundry processes and technologies, gaining the new experience in presentation and / or teaching methods and techniques within lifelong learning process.

The organizers of the Conference would like to thank all participants, reviewers, sponsors, auspices, media coverage and all those who have contributed to this Conference in any way.

President of Organizing Board



Prof. Zdenka Zovko Brodarac, PhD



Sisak, photo by Barbara Tubić Bulat



Split, photo by Zvonimir Dadić

LETTER OF SUPPORT

President of the Republic of Croatia
Zoran Milanović

UNDER THE PATRONAGE

Ministry of Science and Education of the Republic of Croatia
Ministry of Economy and Sustainable Development
University of Zagreb
Mittel Europäische Giesserei Initiative (MEGI)
Chamber of Commerce of Republic of Croatia
Croatian Business Angels Network
City of Sisak
City of Split

SPONSORED BY

GOLDEN SPONSOR

COMET d.o.o., Novi Marof (HR)
LABTIM ADRIA d.o.o., Sesvete (HR)

BRONZE SPONSOR

Kontroltest International d.o.o., Zagreb (HR)
EDC d.o.o., Zagreb (HR)
IDEF d.o.o., Zagreb (HR)
Tvornica gline Kutina d.o.o., Kutina (HR)
MECAS ESI s.r.o., Plzen (CZ) & TC LIVARSTVO Ltd, Ljubljana (SI)
LTH Metalni lijev d.o.o., Benkovac (HR)
Labeko d.o.o., Zagreb (HR)

MEDIA COVERAGE

IRT 3000
Foundry Lexicon
Foundry Planet

SUPPORTING ASSOCIATION AND COMPANIES

Croatian Foundry Association
Slovenian Foundry Association

ORGANIZING COMMITTEE

Zdenka Zovko Brodarac, President, University of Zagreb Faculty of Metallurgy, Sisak, Croatia

Natalija Dolić, Vice President, University of Zagreb Faculty of Metallurgy, Sisak, Croatia

Sandra Brajčinović, University of Zagreb Faculty of Metallurgy, Sisak, Croatia

Damijan Cerinski, University of Zagreb Faculty of Metallurgy, Sisak, Croatia

Franjo Kozina, University of Zagreb Faculty of Metallurgy, Sisak, Croatia

Ladislav Lazić, University of Zagreb Faculty of Metallurgy, Sisak, Croatia

Barbara Tubić Bulat, University of Zagreb Faculty of Metallurgy, Sisak, Croatia

Mitja Petrič, University of Ljubljana Faculty of Natural Sciences and Engineering, Ljubljana, Slovenia

Maja Vončina, University of Ljubljana Faculty of Natural Sciences and Engineering, Ljubljana, Slovenia

Vlado Tropša, University North, Koprivnica, Croatia

Sanja Šolić, University North, Koprivnica, Croatia

Iveta Vasková, Technical University of Košice Faculty of Materials, Metallurgy and Recycling, Košice, Slovakia

Maroš Halama, Technical University of Košice Faculty of Materials, Metallurgy and Recycling, Košice, Slovakia

Ladislav Vrsalović, University of Split Faculty of Chemistry and Technology Split, Croatia

Sandra Svilović, University of Split Faculty of Chemistry and Technology Split, Croatia

Gordana Gojsević Marić, ELKEM ASA, Oslo, Norway

LOCAL ORGANIZING COMMITTEE

Dražan Jozić, University of Split Faculty of Chemistry and Technology, Split, Croatia

Antonija Čelan, University of Split Faculty of Chemistry and Technology, Split, Croatia

Mario Nikola Mužek, University of Split Faculty of Chemistry and Technology, Split, Croatia

Ivana Smoljko, University of Split Faculty of Chemistry and Technology, Split, Croatia

Nikša Čatipović, University of Split Faculty of Electrical Engineering, Mechanical Engineering and Naval Architecture, Split, Croatia

Zvonimir Dadić, University of Split Faculty of Electrical Engineering, Mechanical Engineering and Naval Architecture, Split, Croatia

Jure Krolo, University of Split Faculty of Electrical Engineering, Mechanical Engineering and Naval Architecture, Split, Croatia

Mario Podrug, University of Split University Department for Health Studies, Split, Croatia

PROGRAM COMMITTEE

Hasan Avdušinović (BA)	Zoran Kožuh (HR)
Branko Bauer (HR)	Vladimir Krutiš (CZ)
Anita Begić Hadžipašić (HR)	Ladislav Lazić (HR)
Ana Beroš (BA)	Dragan Manasijević (RS)
Jaka Burja (SI)	Srećko Manasijević (RS)
Peter Cvahte (SI)	Branislav Marković (RS)
Lidija Ćurković (HR)	Miloš Matvija (SK)
Attila Diószegi (SE)	Jožef Medved (SI)
Mile Djurdjević (AT)	Primož Mrvar (SI)
Natalija Dolić (HR)	Daniel Novoselović (HR)
Regina Fuchs-Godec (SI)	Milena Premović (RS)
Almaida Gigović-Gekić (BA)	Karlo T. Raić (RS)
Stanisław Gil (PL)	Vera Rede (HR)
Zoran Grubač (HR)	Stoja Rešković (HR)
Maros Halama (SK)	Iulian Riposan (RO)
Dario Iljkić (HR)	Zdravko Schauerl (HR)
Ivana Ivanić (HR)	Peter Schumacher (AT)
Igor Jerković (HR)	Božo Smoljan (HR)
Dražan Jozić (HR)	Tahir Sofilić (HR)
Željko Kamberović (RS)	Miroslav Sokić (RS)
Sebastjan Kastelic (SI)	Sanja Šolić (HR)
Varužan Kervorkijan (SI)	Nada Štrbac (RS)
Ivica Kladarić (HR)	Ladislav Vrsalović (HR)
Borut Kosec (SI)	Zdenka Zovko Brodarac (HR)
Dražan Kozak (HR)	Irena Žmak (HR)

REVIEW COMMITTEE

Vesna Alar (HR)	Ladislav Lukáč (SK)
Hasan Avdušinović (BA)	Dragan Manasijević (RS)
Branko Bauer (HR)	Marija Mihailović (RS)
Anita Begić Hadžipašić (HR)	Aleksandra Mitovski (RS)
Vladimir Bermanec (HR)	Primož Mrvar (SI)
Ivan Brnardić (HR)	Daniel Novoselović (HR)
Damijan Cerinski (HR)	Vesna Ocelić Bulatović (HR)
Vesna Conić (RS)	Helena Otmačić Ćurković (HR)
Natalija Dolić (HR)	Mitja Petrič (SI)
Regina Fuchs-Godec (SI)	Zora Pilić (BA)
Ivica Garašić (HR)	Milena Premović (RS)
Veselinka Grudić (ME)	Jasna Prlic Kardum (HR)
Senka Gudić (HR)	Žarko Radović (ME)
Dario Iljkić (HR)	Sam Ramrattan (USA)
Marica Ivanković (HR)	Vera Rede (HR)
Svetlana Ivanov (RS)	Massimo Rogante (IT)
Jelena Jakić (HR)	Zdravko Schauerl (HR)
Ivan Jandrlić (HR)	Aleksandar Sedmak (RS)
Jaroslav Jerc (SK)	Ljerka Slokar Benić (HR)
Sebastjan Kastelic (SI)	Božo Smoljan (HR)
Witold Kazimierz Krajewski (PL)	Ivana Smoljko (HR)
Ján Kizek (SK)	Davor Stanić (HR)
Ivica Kladarić (HR)	Ivan Stojanović (HR)
Borut Kosec (SI)	Jovica Stojanović (RS)
Stjepan Kožuh (HR)	Josip Stojšić (HR)
Zoran Kožuh (HR)	Nada Štrbac (RS)
Marijana Kraljić Roković (HR)	Iveta Vaskova (SK)
Jure Krolo (HR)	Tatjana Volkov-Husović (RS)
Sandra Kučina Softić (HR)	Maja Vončina (SI)
Stanislav Kurajica (HR)	Ladislav Vrsalović (HR)
Darko Landek (HR)	Nediljka Vukojević Medvidović (HR)
Martina Lovrenić Jugović (HR)	Zdenka Zovko Brodarac (HR)

CONTENTS

Denisa Anca, Mihai Chisamera, Stelian Stan, Iulian Riposan SOLIDIFICATION PATTERN OF HIGH-Si DUCTILE IRON CASTINGS IN THE PRESENCE OF MOULD COATINGS WITH S OR O CONTENT AND WITH OR WITHOUT PROTECTIVE AGENTS FOR THEIR DIFFUSION INTO THE IRON MELT	1
Luka Čadež MORE THEN A MANUFACTURER – BRODOSPLIT	2
Doru M. Stefanescu, Gorka Alonso, Ramon Suarez NUCLEATION AND CRYSTALLIZATION OF SPHEROIDAL GRAPHITE IN CAST IRON	3
Hasan Avdušinović, Almaida Gigović-Gekić, Šehzudin Dervišić INFLUENCE OF ELEVATED WORKING TEMPERATURES ON MECHANICAL PROPERTIES OF AUSTEMPERED DUCTILE IRON	4
Dario Iljkić, Sunčana Smokvina Hanza, Božo Smoljan, Loreta Pomenić, Lovro Štic, Lovro Liverić LOAD CAPACITY AND CORROSION BEHAVIOR OF QUENCHED AND TEMPERED STEEL 42CrMo4 AND CAST STEEL GS-42CrMo4	16
Sonja Jozić SEMI-SOLID METAL PROCESSING; CHALLENGES AND INOVATIONS	26
Varužan Kevorkijan MICROSTRUCTURE AND FORMABILITY DEVELOPMENT IN Al STRIP CASTING FOR QUALITY-DEMANDING FOIL PRODUCTION	42
Dražan Kozak, Katarina Monkova, Darko Damjanović, Marina Franulović, Jerzy Józwik, Katarina Pisačić EXPERIMENTAL AND NUMERICAL ANALYSIS OF PRINTED LATTICE STRUCTURE	51
Vladimír Krutiš, Václav Káňa, Marek Dostál, Jarmil Cileček EFFICIENT METHOD OF MANUFACTURING DEMANDING PROTOTYPE CASTINGS USING INVESTMENT CASTING TECHNOLOGY	66
Dragan Manasijević, Ljubiša Balanović, Ivana Marković, Milan Gorgievski, Uroš Stamenković, Kristina Božinović STRUCTURAL AND THERMAL PROPERTIES OF THE Sn–Zn ALLOYS	75

Jožef Medved, Maja Vončina, Stanislav Kores, Matej Mesarič PRINCIPLE OF TITANIUM DIOXIDE REDUCTION IN LIQUID ALUMINIUM	93
Primož Mrvar, Milan Terčelj, Mitja Petrič, Danijel Mitrović, Goran Kugler DAMAGE ANALYSIS OF COMPACTED GRAPHITE CAST IRON	101
Iveta Vasková, Petra Delimanová, Martina Hrubovčáková, Marianna Bartošová BENTONITE – ECOLOGICAL BINDING MATERIAL OF FIRST GENERATION AND ITS USING IN FOUNDRY	109
Irena Žmak, Ida Mujkić DEMAND, SUPPLY, ENERGY CONSUMPTION AND SUSTAINABILITY OF PRIMARY AND SECONDARY COPPER PRODUCTION	119
Branko Bauer, Ivana Mihalic Pokopec, Marko Šaban EFFECT OF HIGH SILICON CONTENT ON THE PROPERTIES OF DUCTILE IRON CASTINGS	130
Dipak Ghosh MODERN ALPHASET (APNB)-REFINED FORMULATIONS WITH BETTER UNDERSTANDING OF CHEMISTRY	141
Almaida Gigović-Gekić, Hasan Avdušinović, Amna Hodžić, Dejana Kasapović INFLUENCE OF ANNEALING OF AUSTENITIC STAINLESS STEELS ON PITTING CORROSION RESISTANCE	163
Karlo Jurković, Sebastjan Kastelic, Primož Mrvar, Branko Bauer APPLICATION OF COMPUTER SIMULATION FOR VERTICAL CENTRIFUGAL CASTING	171
Jure Krolo, Ivana Dumanić, Sonja Jozić, Branimir Lela INFLUENCE OF SEMI-SOLID METAL PROCESSING AND ARTIFICIAL AGING ON MICROSTRUCTURE AND HARDNESS OF THE AISi9Cu3(Fe)	186
Vladimir Krutiš, Martin Madaj, Vlastimil Kolda CO-DESIGN IN CASTING - A WAY TO ACHIEVE OPTIMAL DESIGN AND PRODUCTION OF CASTINGS	194
Ladislav Lazić, Martina Lovrenić-Jugović, Lorena Mrkobrada, Željko Grubišić, Damijan Cerinski POSSIBILITY OF ENERGY EFFICIENCY IMPROVING OF THE MELTING FURNACE IN SECONDARY ALUMINIUM PRODUCTION	208
Mitja Petrič, Bastri Zeka, Tilen Balaško, Primož Mrvar, Boštjan Markoli PRODUCTION AND CASTING OF AISi7MgLi ALLOY	216

Barbara Tubić Bulat, Zdenka Zovko Brodarac, Primož Mrvar INFLUENCE OF SOLIDIFICATION AND PROCESSING PARAMETERS ON NODULAR CAST IRON MICROSTRUCTURE - AN OVERVIEW	226
Anita Bašić, Mario Nikola Mužek, Marija Ćosić, Sandra Svilović THE COPPER ADSORPTION ON ZEOLITE NaX - THE IMPELLER LOCATION IMPACT	237
Sandra Brajčinović, Anita Begić Hadžipašić CORROSION RESISTANCE OF CEMENTING STEEL X19NiCrMo4 IN MEDIUM OF 5% NaOH AND 5% H ₂ SO ₄	249
Sandra Brajčinović, Anita Begić Hadžipašić, Franjo Kozina INHIBITORY EFFECT OF COMMERCIAL INHIBITOR VCI 379/611 ON CORROSION BEHAVIOR OF X153CrMoV12 TOOL STEEL FOR COLD WORK	260
Anđela Čović, Pero Dabić, Damir Barbir ACTIVITY ASSESSMENT OF PHOTSENSITIVE DYES ANTHOCYANIN, RHODAMINE B, RUTHENIUM N3 AND RHODAMINE B+ANTHOCYANIN MIXTURE FOR APPLICATION IN SOLAR CELLS	269
Ivana Gabelica, Lidija Ćurković, Vilko Mandić, Mihone Kerolli Mustafa PREPARATION AND CHARACTERIZATION OF POROUS ALUMINA CERAMICS USING WASTE COFFEE GROUNDS (WCG)	282
Ivana Gabelica, Lidija Ćurković, Ivana Panžić RAPID MICROWAVE-ASSISTED SYNTHESIS OF Fe ₃ O ₄ /SiO ₂ /TiO ₂ CORE-SHELL NANOCOMPOSITE	289
Stanisław Gil, Wojciech Bialik, Bolesław Machulec, Agnieszka Tomaszewska, Sławomir Kozłowski IMPACT OF FeSi FERROALLOY CASTING CONDITIONS ON THEIR STRUCTURE AND GRAIN SIZE AFTER CRUSHING PROCESS	296
Peter Hajduch, Mile B. Đurđević, Srećko Manasijević IMPROVING THE MICROSTRUCTURE AND MECHANICAL PROPERTIES OF EN AC 43200 CAST ALUMINUM ALLOY MODIFIED WITH ZIRCONIUM	303
Ivan Jandrlić, Franjo Kozina, Tin Brlić, Milica Vučenović INFLUENCE OF COLD REDUCTION ON THE STRUCTURE AND HARDNESS OF COLD DRAWN COPPER WIRE	314
Angela Kapitanović, Lana Brkić, Helena Pintarić, Dajana Mikić, Helena Otmačić Ćurković PREPARATION AND CHARACTERIZATION OF ARTIFICIAL PATINA ON BRONZE	325

Sebastjan Kastelic, Almir Mahmutović, Matic Žbontar, Primož Mrvar, Mitja Petrič	338
MAKING PROTOTYPE CASTING USING 3D PRINTING AND INVESTMENT CASTING	
Franjo Kozina, Zdenka Zovko Brodarac, Ivan Jandrić, Renato Jagustović	345
ANALYSIS OF THE CRACK FORMATION IN ASIS M2 HIGH-SPEED TOOL STEEL DURING UTILIZATION	
Stjepan Kožuh, Ivana Ivanić, Semir Oraščanin, Aleš Nagode, Ladislav Vrsalović	362
MICROSTRUCTURE AND MICROHARDNESS OF Cu-Al-Mn-Zr ALLOYS BEFORE AND AFTER HEAT TREATMENT	
Stjepan Kožuh, Domagoj Kovačević, Ivana Ivanić, Borut Kosec, Mirko Gojić	372
CHARACTERIZATION OF WELDED DUPLEX STAINLESS STEEL AFTER ANNEALING	
Filipa Krželj, Irena Žmak, Milan Vukšić, Lidija Ćurković	383
RHEOLOGICAL PROPERTIES OF WATER-BASED ALUMINA SUSPENSIONS IN RECYCLING WASTE ALUMINA POWDER	
Darko Landek, Lidija Ćurković, Ivana Gabelica	391
SIMULATION MODEL OF CONVENTIONAL SOLID STATE SINTERING OF Al ₂ O ₃ CERAMICS	
Vaso Manojlović, Željko Kamberović, Miroslav Sokić, Branislav Marković, Milorad Gavrilovski, Slobodan Radosavljević	403
IMPACT OF MOULD POWDER ON PHYSICOCHEMICAL PROPERTIES OF SLAG IN THE CONTINUOUS CASTING PROCESS	
Daniel Novoselović, Štefanija Klarić, Francois Botha, Saša Gojković	410
POSSIBILITIES OF ONLINE LABORATORY PRACTICALS IN TEACHING OF CASTING COURSES	
Daniel Novoselović, Štefanija Klarić, Josip Cumin, Saša Štrbac	421
DETERMINATION OF RESIDUAL STRESSES IN STRESS LATTICE WITH SIMULATION SOFTWARE	
Katarina Pantović Spajić, Branislav Marković, Miroslav Sokić, Mladen Bugarić, Gvozden Jovanović, Vaso Manojlović, Ksenija Stojanović	435
CHEMICAL LEACHING OF SUBBITUMINOUS COAL FROM THE BOGOVINA - EAST FIELD (BOGOVINA BASIN, SERBIA) USING HYDROCHLORIC ACID	

Anamarija Stoilova Pavasovic, Frano Barbir PRELIMINARY STUDY ON TEMPERATURE DISTRIBUTION PATTERNS IN PEM FUEL CELLS	441
Ivan Stojanović, Ivan Cindrić, Lara Janković, Daniela Rakela Ristevski EVALUATION OF INFRARED DRIED SOLVENT-BORNE COATINGS	452
Ivan Stojanović, Anna Poropat TESTING OF ANTICORROSIVE PROPERTIES OF ELECTROSTATIC POWDER COATING ON DIFFERENT TYPES OF ELECTRIC RESISTANCE WELDS	462
Zrinka Švagelj, Vera Rede, Ivana Gabelica, Lidija Čurković EFFECT OF BINDER ADDITION ON THE RHEOLOGICAL BEHAVIOUR OF ALUMINA SUSPENSIONS	475
Ladislav Vrsalović, Senka Gudić, Verena Šučurović, Ivana Ivanić, Stjepan Kožuh, Mirko Gojić, Borut Kosec CORROSION STUDY OF CuAlNi ALLOY IN STIRRED H ₂ SO ₄ SOLUTION	482
Nediljka Vukojević Medvidović, Ladislav Vrsalović, Teo Ugrina, Ivona Jukić ELECTROCOAGULATION AUGMENTED WITH NATURAL ZEOLITE – THE NEW HYBRID PROCESS FOR TREATMENT OF LEACHATE FROM COMPOSTING OF BIOWASTE	489



19th INTERNATIONAL FOUNDRYMEN CONFERENCE
Humans - Valuable Resource for Foundry Industry Development

Split, June 16th-18th, 2021

<https://ifc.simet.hr/>

SOLIDIFICATION PATTERN OF HIGH-Si DUCTILE IRON CASTINGS IN THE PRESENCE OF MOULD COATINGS WITH S OR O CONTENT AND WITH OR WITHOUT PROTECTIVE AGENTS FOR THEIR DIFFUSION INTO THE IRON MELT

Denisa Anca, Mihai Chisamera, Stelian Stan, Iulian Riposan*

Politehnica University of Bucharest, Bucharest, Romania

Plenary lecture

Subject review

Abstract

The main objective of the present paper is to evaluate by thermal (cooling curve) analysis the solidification pattern and the occurrence of the layer of degenerate graphite at the surface of ductile iron castings (3.15%Si, typically as 450-18 grade, ISO 1563/2011), with and without mould coating, including S or O, and different agents (carbonic material, iron powder) to blocking their diffusion into the iron melt. The obtained cast samples [standard ceramic cup] are used for structure evaluation [metal matrix and graphite parameters], in the superficial layer and the casting body.

It is found that the mould coating materials influence not only the parameters of the solidification cooling curves, during eutectic reaction and up to the end of solidification, but also the occurrence and the thickness of the un-desired skin layer, in the same or in an opposite way. Despite that the used ceramic mould is not able to supply active agents for nodularising elements consumption into the iron melt, a surface layer at different graphite morphologies comparing to the casting body is present, but at a large range of thickness, from 50 up to 200 μm . Higher level of skin thickness as metal matrix evaluation comparing to the graphite phase evaluation is present in all of the experimented variants.

Sulphur presence in the mould coating will promote higher skin thickness comparing to oxygen [up to 50% by oxygen and 2.5-3.3 times for sulphur action], despite than in the casting body the graphite nodularity limited decreased (from 85% up to 82-83% level). Carbonic material or iron powder supplementary addition decreases these un-desired effects, but the solidification undercooling comparing to the equilibrium system is prominently increased. It is found that carbonic material is more efficient to limit oxygen and iron powder to limit sulphur negative effects on the casting skin thickness.

Keywords: *thermal analysis, solidification cooling curves, eutectic undercooling, ductile cast iron, mould coating, sulphur, oxygen, degenerated graphite surface layer, structure*

*Corresponding author (e-mail address): iulian.riposan@upb.ro



**Solidification Pattern of High - Si DI
Castings in the Presence of Mould
Coatings with S or O Content & with or
without Protective Agents for their
Diffusion into the Iron Melt**

Denisa ANCA, Mihai CHISAMERA, Stelian STAN, Iulian RIPOSAN

POLITEHNICA University of Bucharest, Bucharest, ROMANIA

**The main objective of the present paper
Is to evaluate the Solidification Pattern &
the Occurrence of Graphite Degeneration:**

- **in the surface layer of relatively High Si Ductile Iron**
 - 3.15%Si, typically as 450-18 grade, ISO 1563/2011,
 - solidified in ceramic mould without **S**-contribution,
- **as influence of mould coating**
 - with & without **S** or **O**-content, *and*
 - with or without supplementary addition
 - iron powder / carbonic material
 - to delay the **S** or **O** diffusion from the coating into the iron melt

OUTLINE

- **INTRODUCTION**

- *High Si-Ductile Cast Irons

- *Casting Skin Formation in Mg-treated Cast Irons

- **EXPERIMENTAL PROCEDURE**

- *Un-coated & coated moulds / O or S bearing / Fe-powder or Carbonic Material

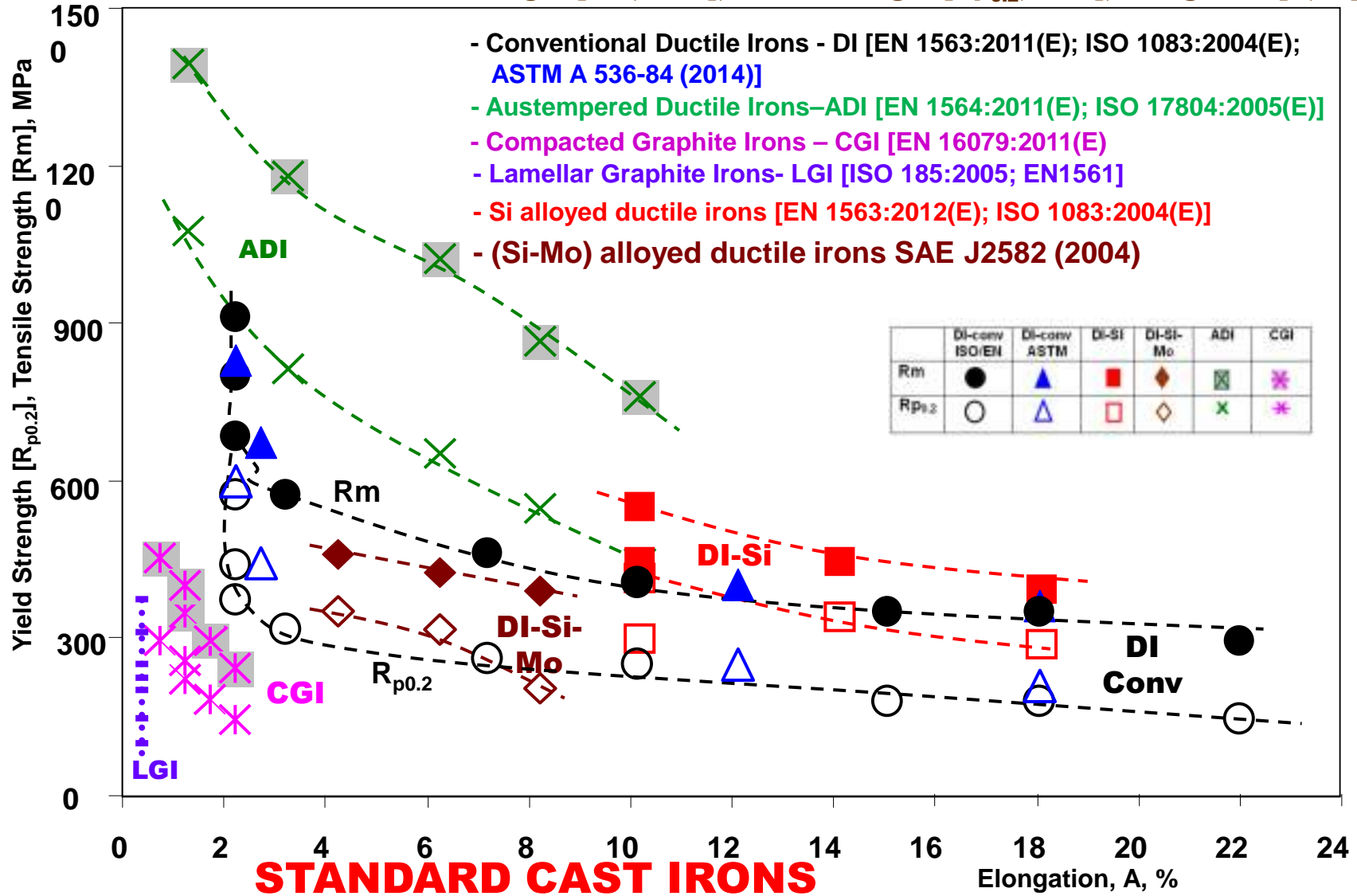
- **RESULTS**

- *Cooling Curves and Structure Analyses Results

- **CONCLUSIONS**

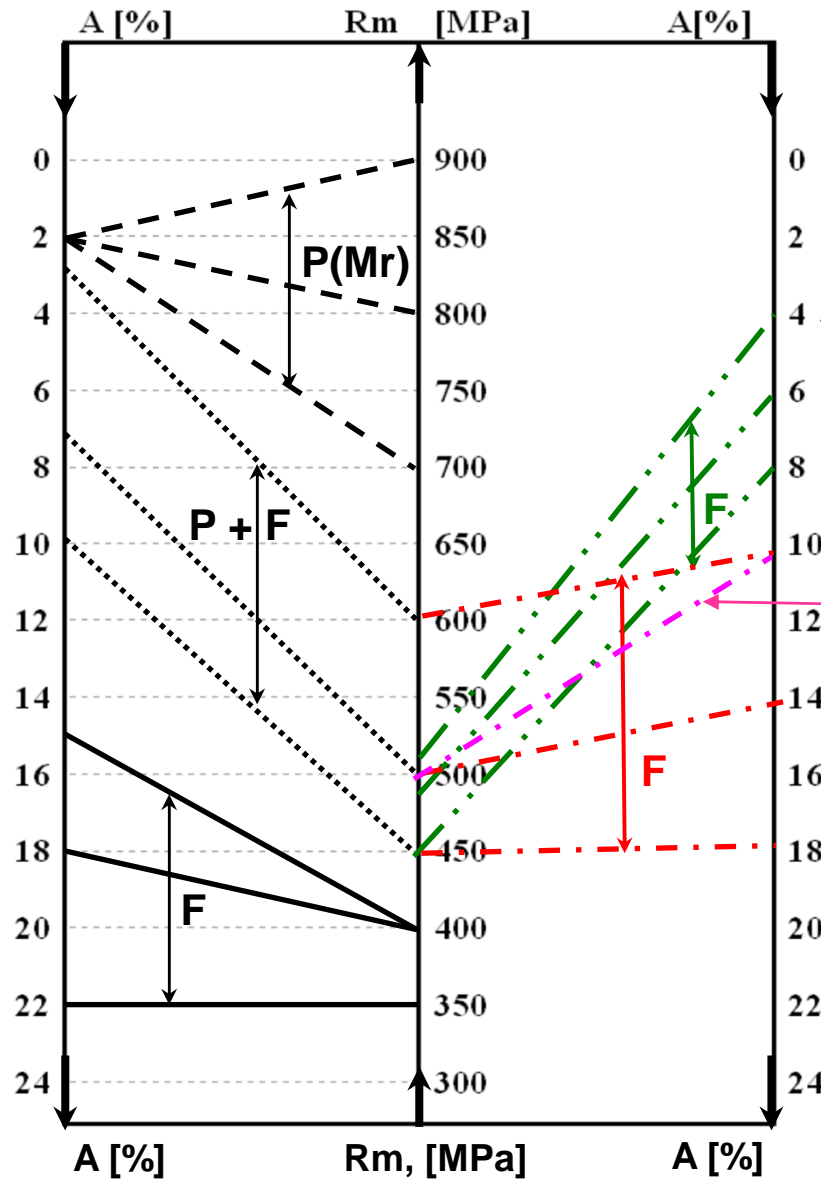
Si & Si-Mo DI – High Performance Materials

Minimal values of Tensile Strength [R_m, MPa], Yield Strength [R_{p0.2}, MPa], Elongation [A, %]



Si & Si-Mo Alloyed Ductile Cast Irons – High Performance Materials

Conventional
Ductile Irons
ISO 1083 [2004]
ISO 1563 [2011]
[P / P + F / F]



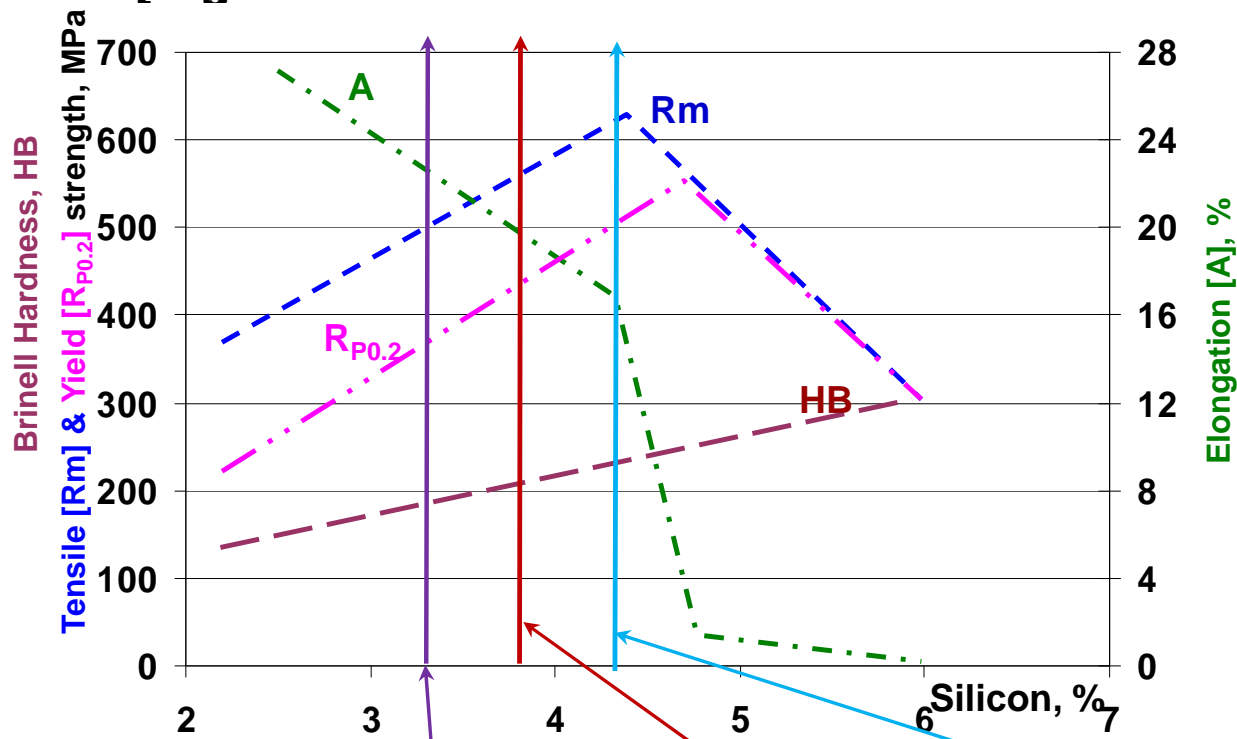
Si / Si - Mo
alloyed
Ductile Irons
[Ferritic]

$\% Mo$
SAEJ 2582 [2004]
[Si - Mo]

$\% Si$
[Si] ISO 1083 [2004]
[Si] ISO 1563 [2011]

Silicon influence on the mechanical properties of ductile cast irons

[High-Si Ferritic Ductile Cast Irons ISO 1563 / 2011 Grades]



Standard grades: 3.2%Si (450-18); 3.8%Si (500-14); 4.3%Si (600-10) - ISO 1563/2011

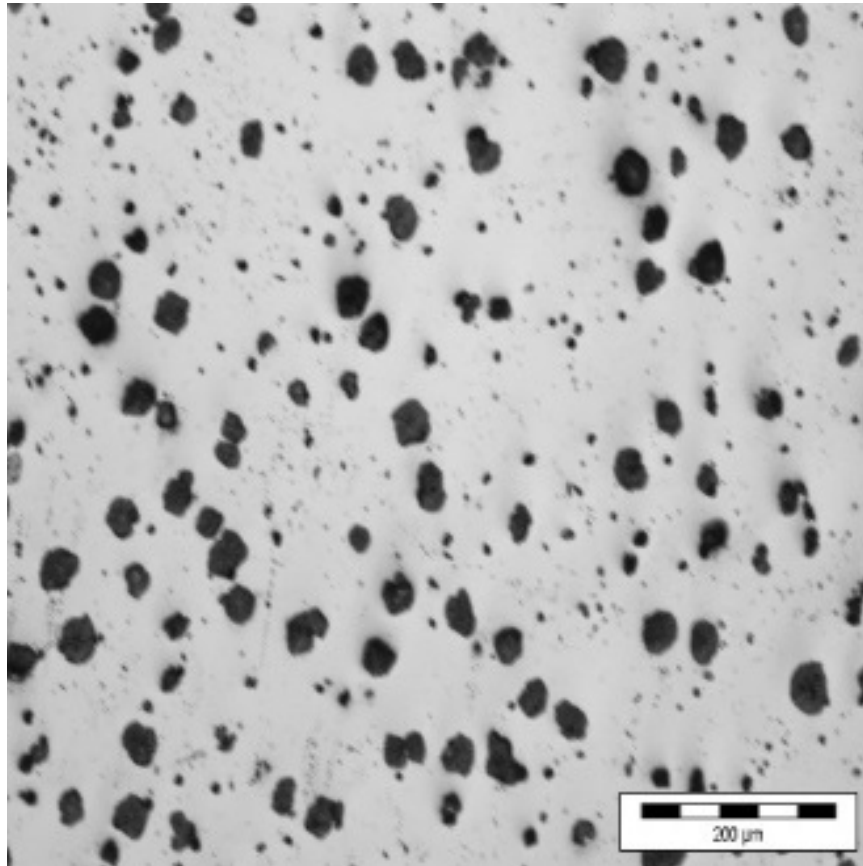
*Typical Si content:

- To reach the maximum: **Tensile Strength [4.2 - 4.4%Si]; (+128 MPa) / %Si**
Yield Strength [4.6 - 4.8%Si]; (+ 118 MPa) / %Si
- Elongation [E] decreasing: (- 5% E / %Si) < 4.3%Si; (- 30% E) / %Si, 4.3 up to 4.8%Si
- Continue hardness [HB] increasing: (+ 45 HB) / %Si, for 2.5 – 6%Si [150 to 310 HB]

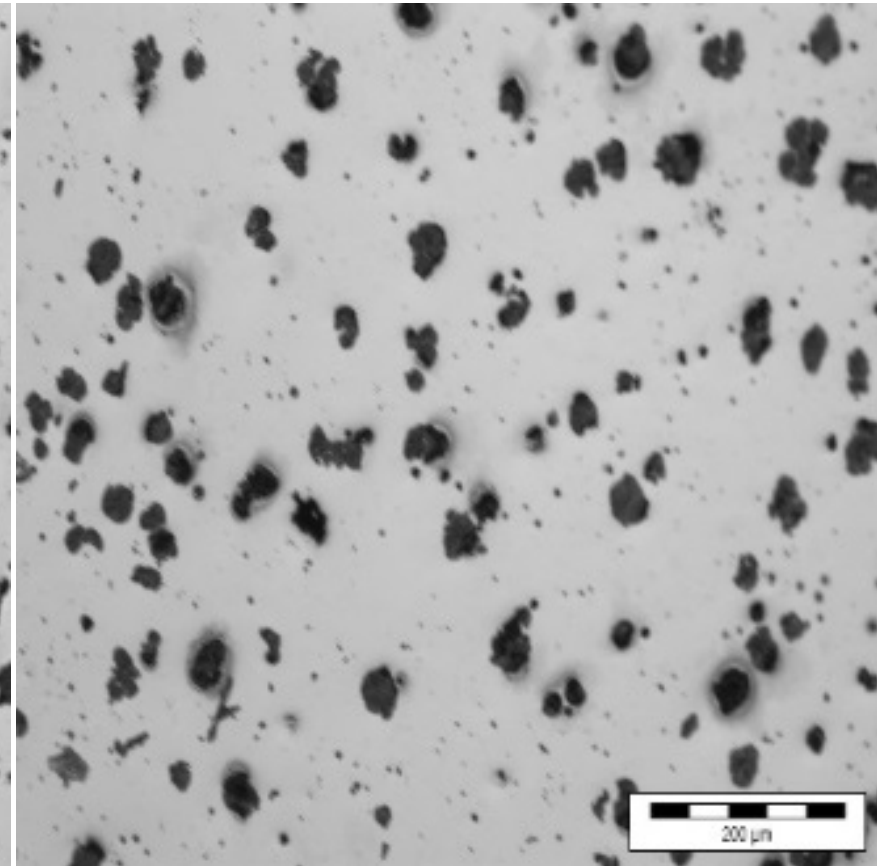
[Stets, W., Loblich, H., Gassner, G., Schumacher, P., 2013 Keith Millis Symp. Ductile Iron, Nashville, TN, 283-292]

TYPICAL OBTAINED GRAPHITE PHASE

2.5%Si



4.1%Si



[S. Stan, I. Riposan, M. Chisamera, I. Stan, 73rd WFC, Krakow, Poland, 2018; JMEP, 2019, 28(1), 278 – 286; 122nd AFS Congr., 2018, Fort Worth, TX, USA (THE BEST PAPER AWARD)]

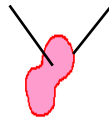
- **Graphite nodularity negative affected by Si content**

- **it decreases**, but remains at the accepted level for general applications [ISO 945]
 - **it would be insufficient** to be accepted as high performance ductile cast irons

- **High Si & Si-Mo DI: nodularity must be carefully considered**

- by including a minim. limit of the accepted **Sphericity Shape Factor [SSF]**
- **graphite real perimeter** / instead of **maximum Feret**, such as in ISO 945 [**RSF**]

$$\text{SSF} = 4 \cdot \pi \cdot A_G / P_G^2 \text{ versus } \text{RSF} = 4 \cdot A_G / \pi \cdot F_{\max}^2$$



- higher the minim. imposed **SSF**, higher difference between 2.5%Si and 4%Si DI

- **More experiments are necessary to find a specific**

- inoculant to improve graphite phase quality**

- **to increase graphite particles compactness [higher SSF level]**
- **to avoid Chunky Graphite formation [Si – specific effect]**

[S. Stan, I. Riposan, M. Chisamera, I. Stan, 73rd WFC, Krakow, Poland, 2018; JMEP, 2019, 28(1), 278 – 286; 122nd AFS Congr., 2018, Fort Worth, TX, USA (THE BEST PAPER AWARD)]

* **Chunky graphite sensitivity: Si - influencing element [Si, Ni, Ca, Ce]**

* **Effect of Si and Ni on the chunky graphite in heavy castings (micro / macro analysis):**

- chunky graphite present only at high Si and Ni content and not at lower content
- higher Si, a strong influence on chunky graphite formation, especially in castings with a slow cooling rate
- Ni promotes chunky graphite, but only in the thermal center of the casting (lowest cooling rate)
- the elongation was severely limited when chunky graphite appeared in the microstructure

[Bauer, B., Mihalic Pokopec, I., Petric, M., Mrvar, P. SPCI-XI, 2017, Sweden; Mater. Sci. Forum, 2018, 925, 70-77]

* **Chunky graphite - known defect in high Si-DI, commonly counteracted using Ce / Sb**

[Larrañaga P., Asenjo I., Sertucha J., Suarez, R., Ferrer, I., Lacaze, J. Metallurg. & Mater. Trans. A, 2009, 40, 654-661]

* **In particular, Bi-containing inoculants have proved successful in Si alloyed DI**

[Stets W., Loblich H., Gassner G., Schumacher P. 2013 Keith Millis Symp. On DI, 2013, Nashville, TN, USA, 283-292]

[Dommaaschk, C. WFO Technical Forum, 2017, Gauteng, South Africa, Session 11, Plenary, Paper No. 2]

* **It was found that the pre-condition to achieve optimized properties are well shaped graphite nodules, achievable with:**

- special inoculation techniques, *adjusted to* the high Si content *and* the solidification rate [time].

For Si – DI it is more important that an appropriate inoculation technique is chosen, because the high Si content may cause differing graphite shapes.

[Stets W., Loblich H., Gassner G., Schumacher P. 2013 Keith Millis Symp. On DI, 2013, Nashville, TN, USA, 283-292]

Ceramic moulds used in foundry are usually coated:

***To control metal-mould chemical interaction (casting surface roughness)**

***Coating influences the solidification characteristics of the casting body**

***Coating influences graphite degeneration in the casting surface layer [skin]**

- **Mg-treated cast irons**

- **will favour skin, in the presence of available S or O, to diffuse into the surface layer**

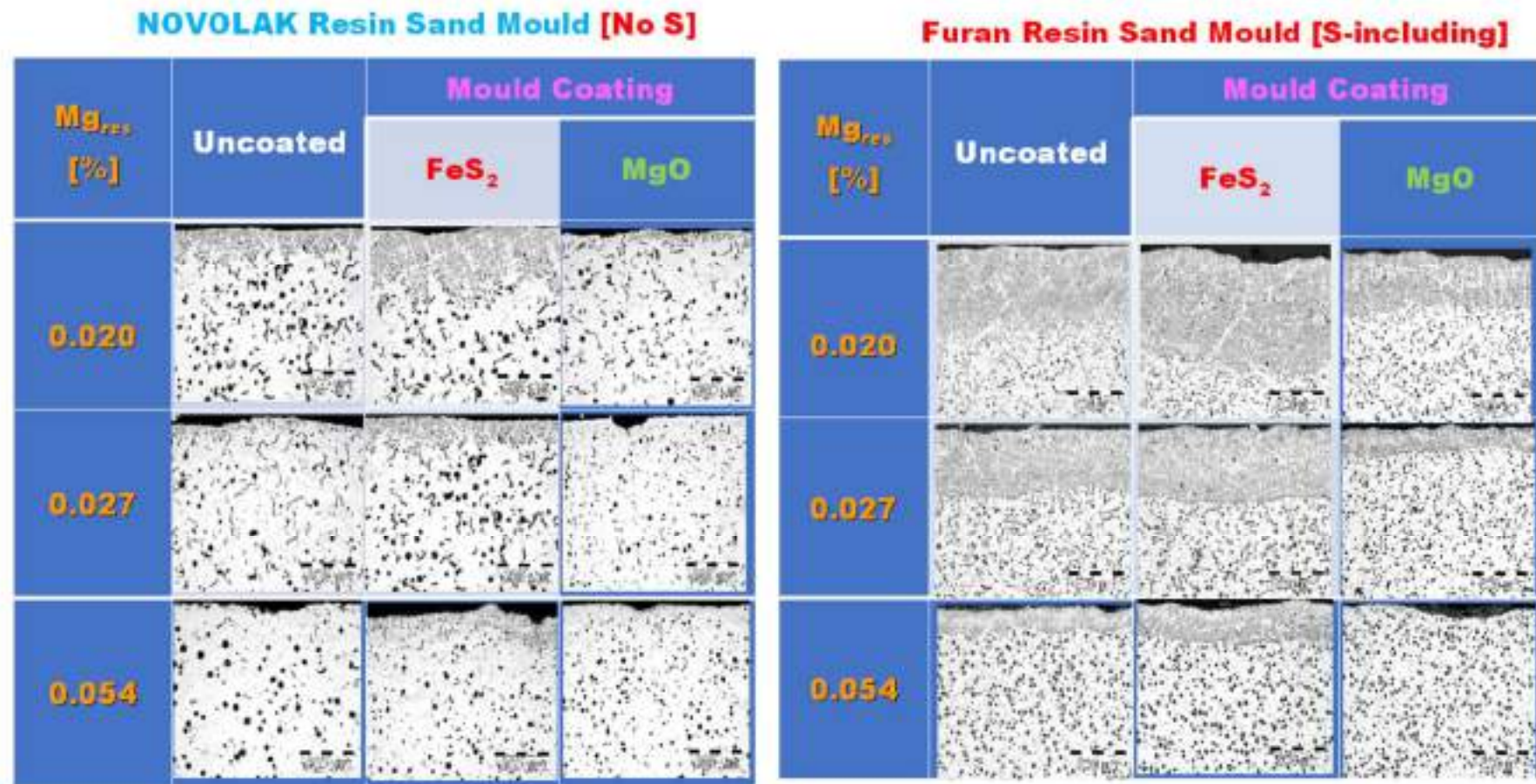
- **contrary, inorganic materials expected to act as desulphurization items (Al_2O_3 , CaCO_3 , Basic slag, CaF_2 , Talc, Mg), are favourable for skin thickness decreasing**

***The surface layer with degenerated graphite causes stress raisers in the casting, similar to a notch,**

- **so all the properties are reduced, especially the fatigue limit and impact resistance**

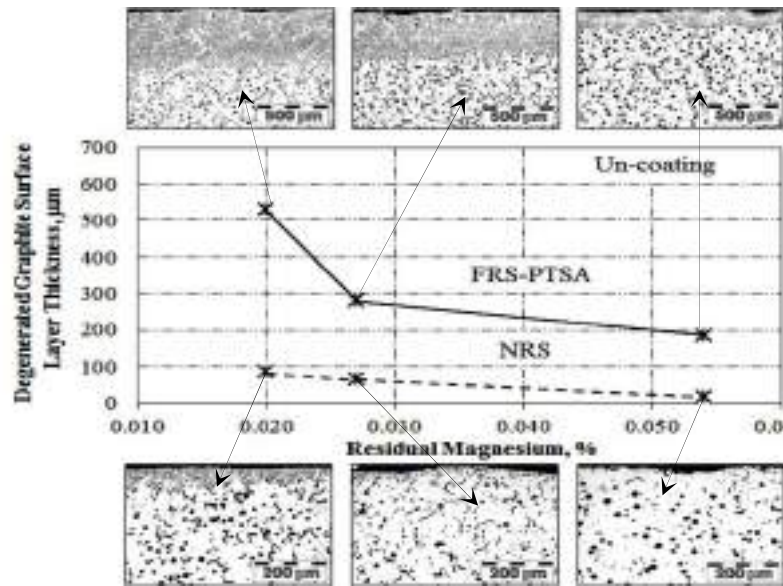
GRAPHITE DEGENERATION IN THE SURFACE LAYER OF CASTINGS

Mg_{res} – Mould Type [with / without S] – Mould Coating [with S / with Desulphurizer]

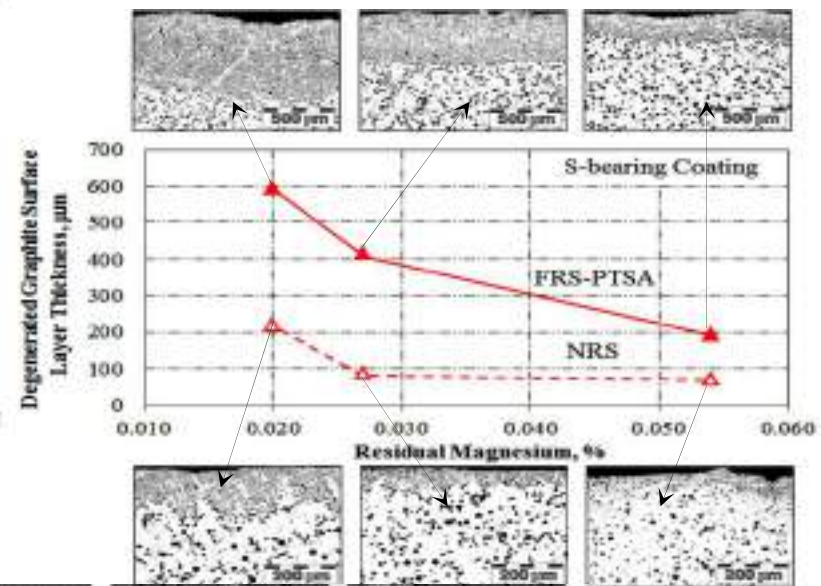


[N. Ivan, M. Chisamera, I.Riposan, ISIJ International, 2012, 52 (10), 1848–1855]

Un-coating



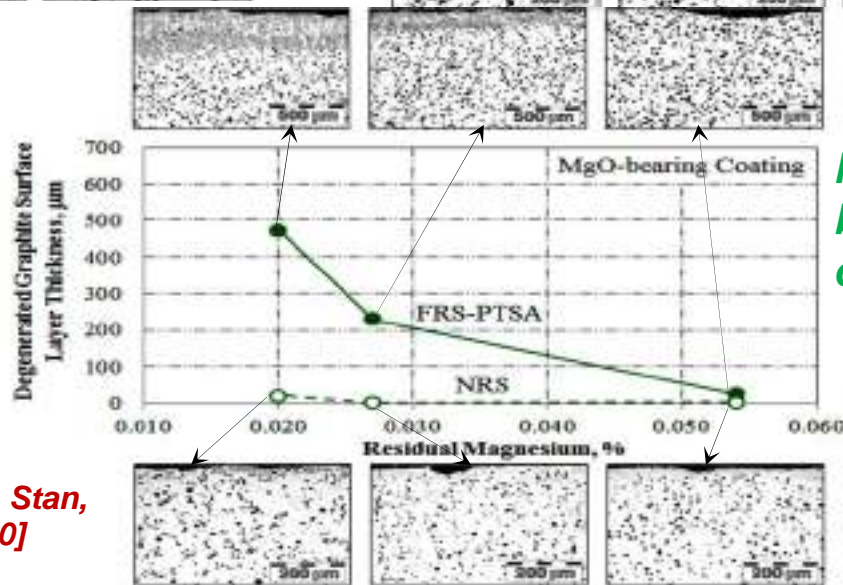
S - bearing coating



FRS-PTSA: Furan resin sand – P-Toluol Sulphonic Acid
[S-bearing mould]

NRS: (Novolak) Phenol - formaldehyde resin coated Sand (Croning process)
[No S-bearing mould]

[N. Ivan, M. Chisamera, I.Riposan, S. Stan, AFS Transactions, 2013, 121, 379-390]



MgO – bearing coating

Experimental Procedure Parameters & Characteristics

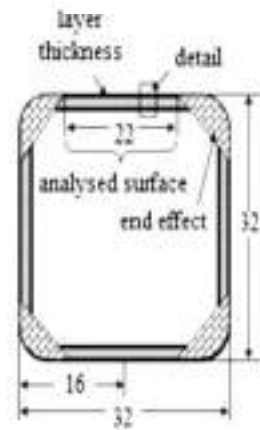
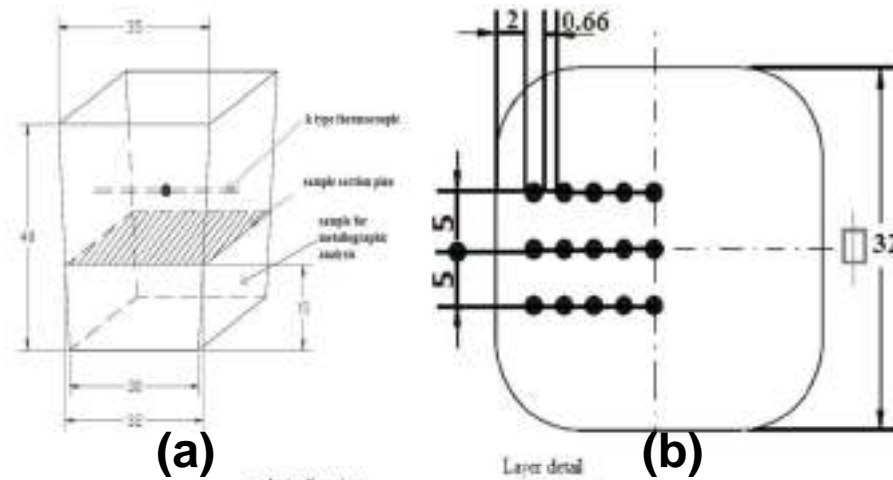
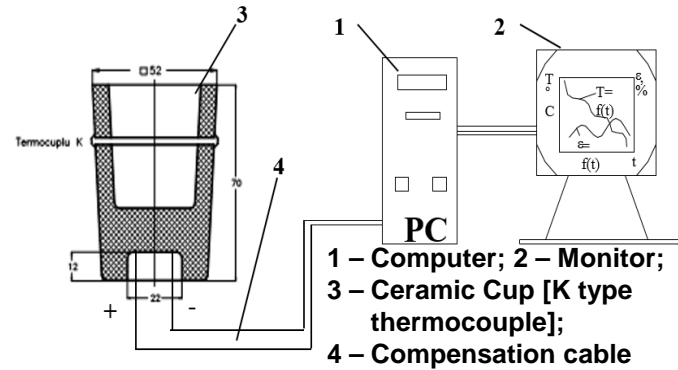
1 - Melting **2 - Nodularization** **3 - Inoculation** **4 - Casting**

No	Characteristics
1	Coreless Induction Furnace, graphite crucible, 10kg, 8000 Hz; Pig iron, cast iron scrap, recarburiser; 1565°C superheating, 10 minutes
2	Tundish Cover technique, 10 kg ladle, 1500°C temperature treatment; 2.0wt.% FeSiCaMgRE [wt.%,: 8.2Mg, 1.87Ca, 1.1RE, 0.85Al, 46.0Si, bal Fe]
3	Transfer Tundish Cover to Pouring Ladle, in stream inoculation; 0.8wt.% FeSiCaBaAl [wt.%,: 1.0Ca, 1.0Ba, 1.1Al, 75Si, bal Fe]
4	Standard Ceramic cup [Novolak resin sand], thermal analysis [7.3 mm cooling modulus; 33/37 x 40 mm size; 0.35kg]; - Typical thermo-physical properties: 1487 W S ^{1/2} /m ² K thermal diffusivity, 1280 J/kg K specific heat, 1.08 W/m K thermal conductivity & 1600 kg/m ³ density; - 1350°C pouring temperature

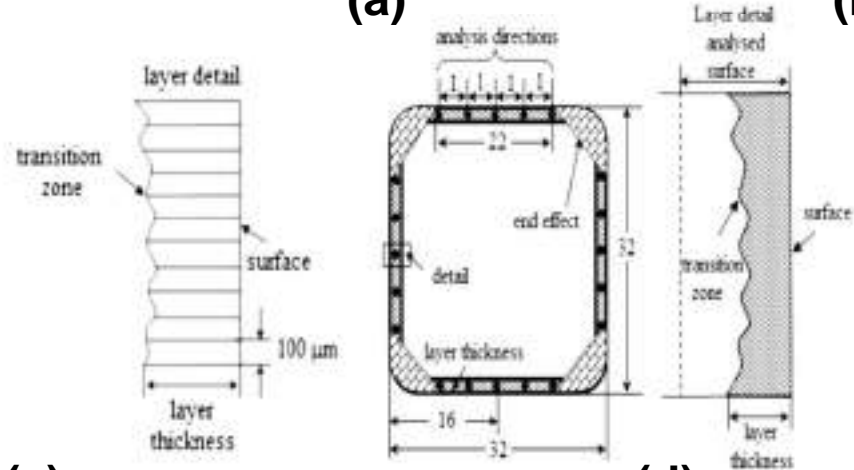
Three experimental variants are recorded:

- (a) **Un-coated mould**, without **O** or **S** available to diffuse into the iron melt, as reference variant
- (b) **Coated mould**, including **O** (Fe_2O_3 bearing coating) or **S** (FeS_2 bearing coating), as potential sources of these active elements to react with iron melt, before solidification, at least in the superficial layer
- (c) **Supplementary addition** of other substances [**carbonyl material-MC** or **iron powder-Fe**] on the previous Fe_2O_3 or FeS_2 bearing coatings, as potential blockage of **O** or **S** diffusion into the melt

Metallographic sample drawn (a) Analysis points on the sample section (b)



(c)



(d)

Layer thickness (c)

Layer structure parameters (d)

RESULTS

Chemical composition of Mg-treated and inoculated cast iron

Chemical composition, wt.%						Carbon Equivalent,* %	Antinodulizing Factor**	Pearlitic Factor***
C	Si	Mn	P	S	Mg	CE	K	Px
3.65	3.15	0.1	0.013	0.004	0.049	4.6	0.72	-0.22

Minor elements (wt.%): 0.08Cr, 0.05Mo, 0.072Ni, 0.002Al, 0.02Cu, 0.016V, 0.004W, less than 0.002Pb and Bi, less than 0.005Sn, Sb, As, Sb, Ti.

***CE** = %C + 0.3(%Si + %P) + 0.4(%S) – 0.027(%Mn).

****K** = 4.4 (%Ti) + 2.0 (%As) + 2.4 (%Sn) + 5.0 (%Sb) + 290 (%Pb) + 370 (%Bi) + 1.6 (%Al).¹⁴

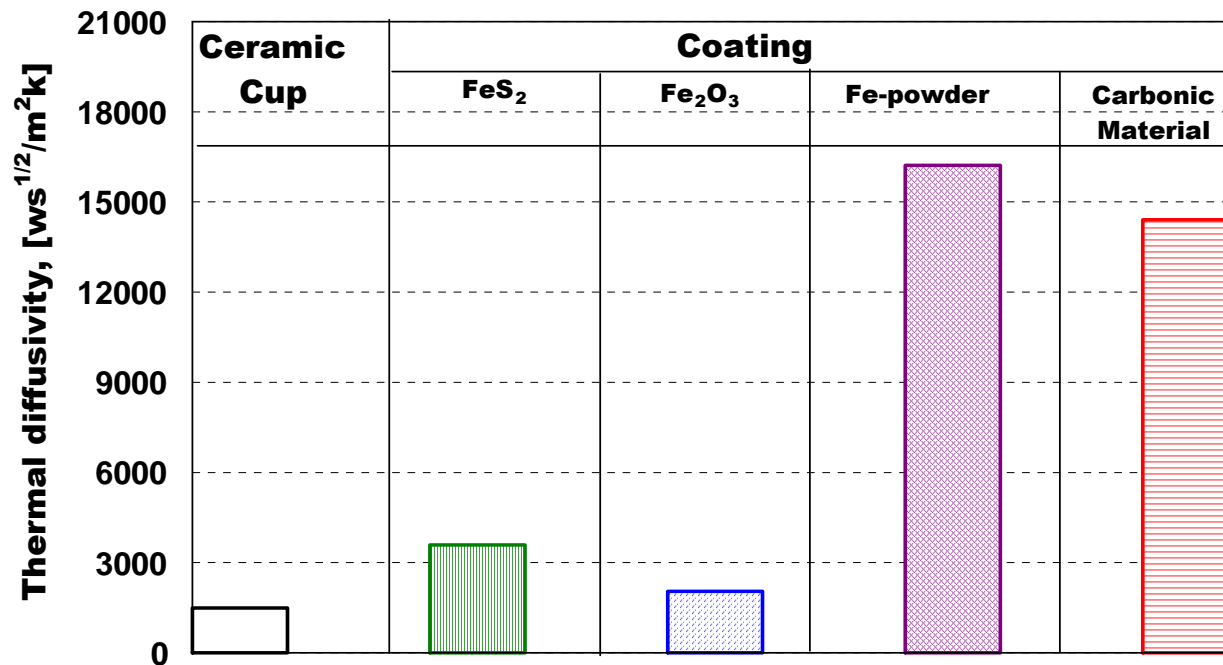
*****Px** = 3 (%Mn) – 2.65 (%Si - 2) + 7.75 (%Cu) + 90 (%Sn) + 357 (%Pb) + 333 (%Bi) + 20.1 (%As) + 9.60Cr + 71.7 (%Sb).¹⁴

COOLING CURVE ANALYSIS

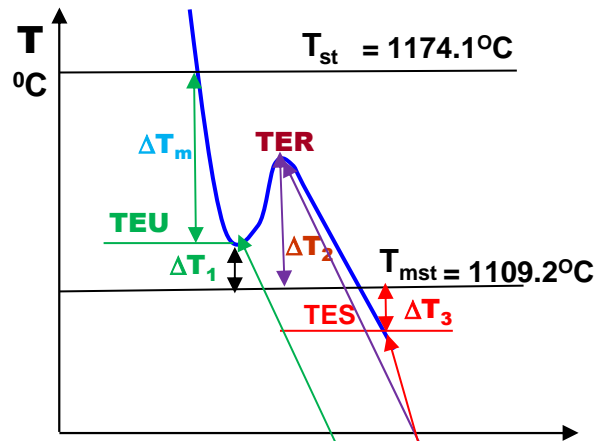
The solidification parameters, identified by thermal (cooling curve) analysis are influenced by two important factors:

- (a) thermal - physical properties of the applied mould coatings to determine the solidification cooling rate *and*
- (b) the presence of active materials in the coating composition, according to their capacity to diffuse into the iron melt their self, or depending on their capacity to block the diffusion of other substances, such as **O** or **S**

THERMAL DIFFUSIVITY [W S^{1/2} / m² K]



COOLING CURVE ANALYSIS



Un-Coating - REFERENCE

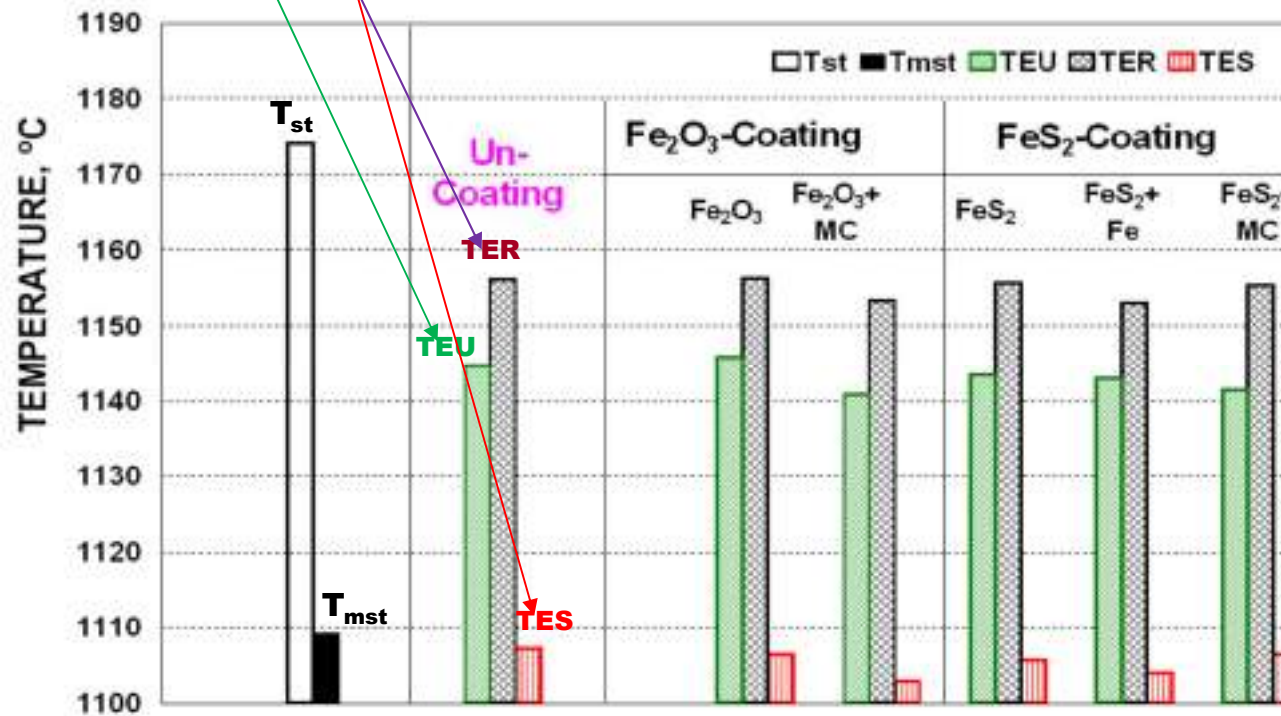
Fe₂O₃: TEU >, TER ≈, TES <

Fe₂O₃ + MC: TEU <<, TER <<, TES <<

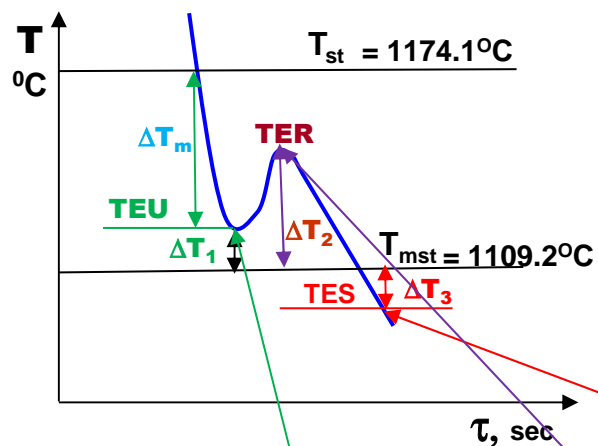
FeS₂: TEU <, TER ≈, TES <

FeS₂ + MC: TEU <<, TER <, TES <

FeS₂ + Fe: TEU <<, TER <, TES <<



COOLING CURVE ANALYSIS



Un-Coating [UC] - REFERENCE

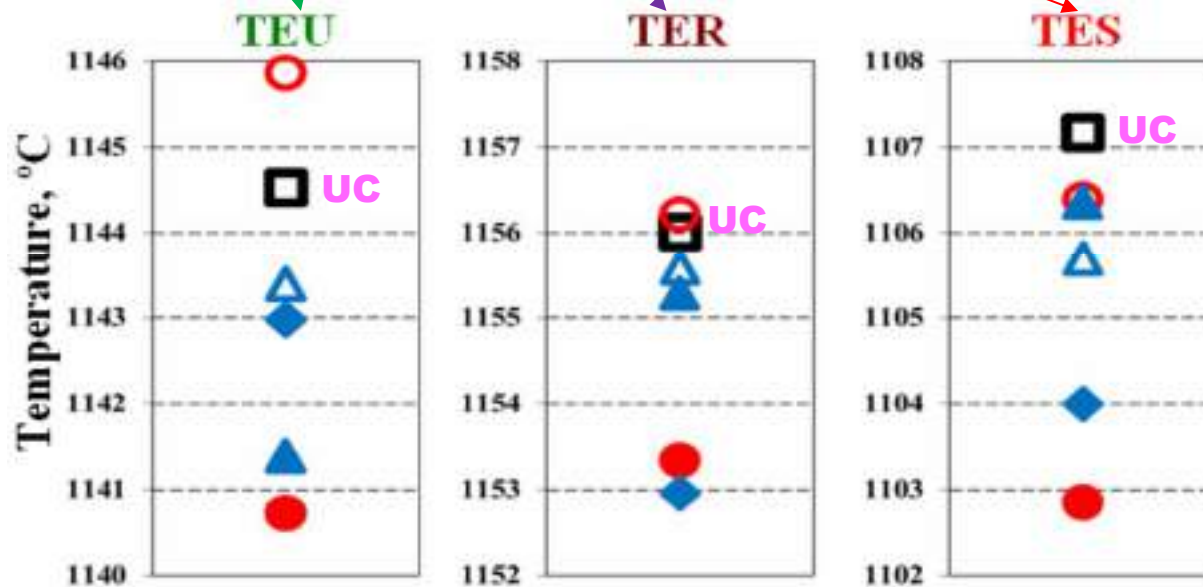
Fe_2O_3 : **TEU** >, **TER** \approx , **TES** <

$\text{Fe}_2\text{O}_3 + \text{MC}$: **TEU** <<, **TEU** <<, **TES** <<

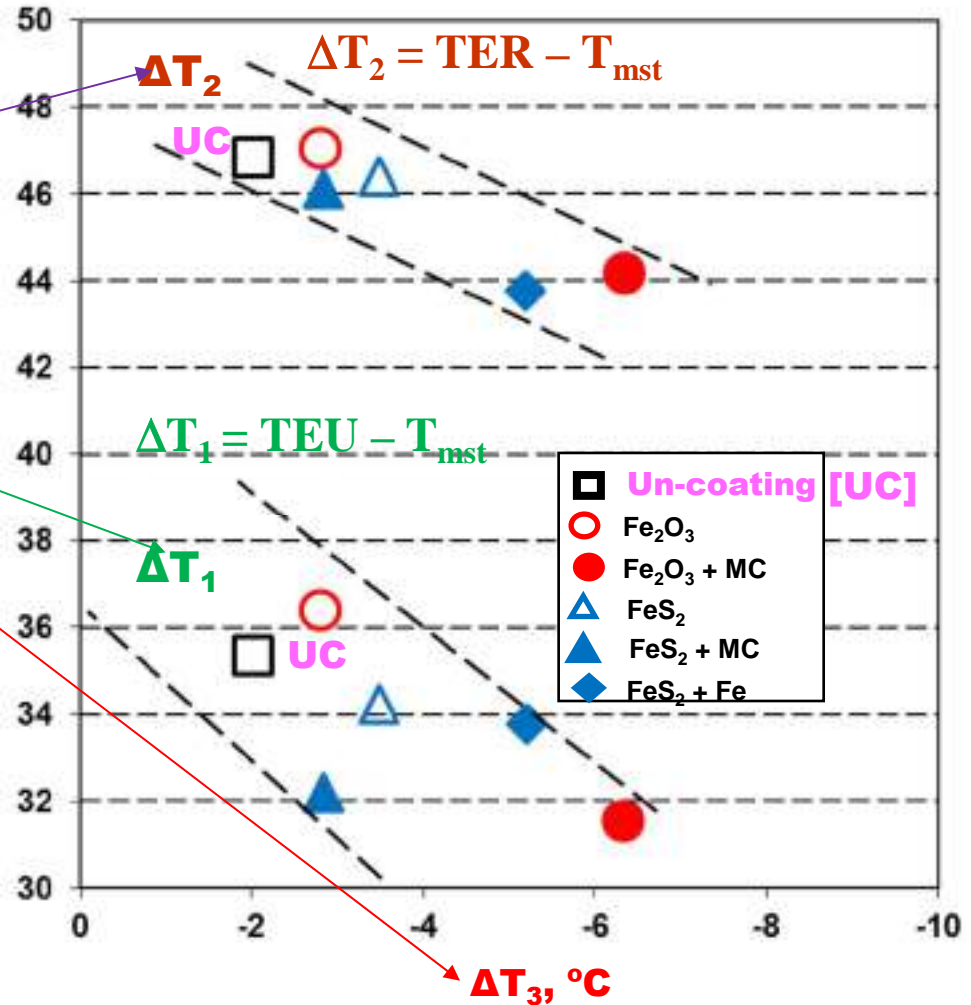
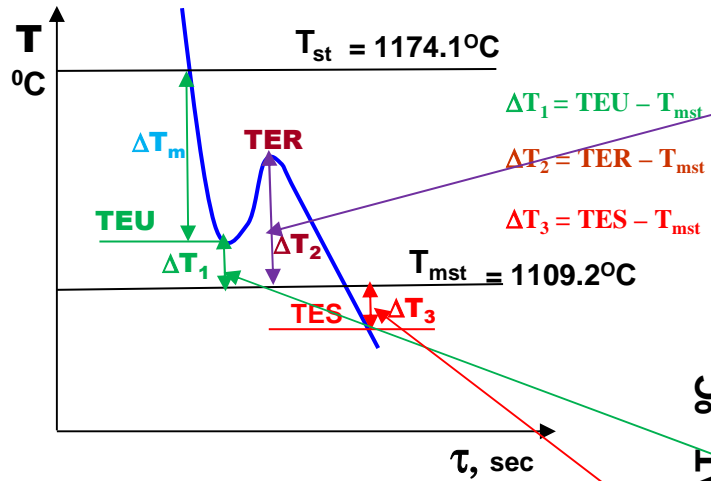
FeS_2 : **TEU** <, **TER** \approx , **TES** <

$\text{FeS}_2 + \text{MC}$: **TEU** <<, **TER** <, **TES** <

$\text{FeS}_2 + \text{Fe}$: **TEU** <<, **TER** <, **TES** <<



COOLING CURVE ANALYSIS



Un-Coating [UC] - REFERENCE

Fe₂O₃: $\Delta T_1 >$, $\Delta T_2 \approx$, $\Delta T_3 <$

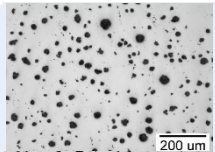
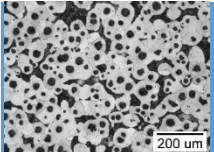
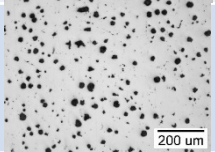
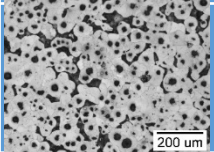
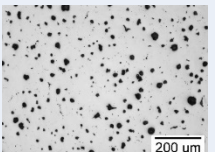
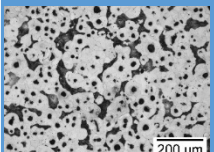
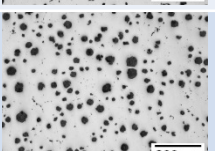
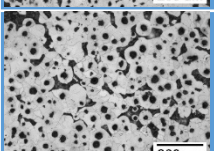
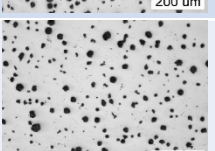
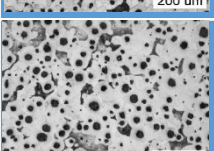
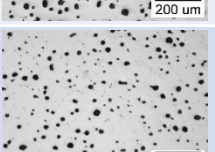
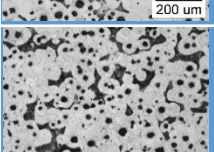
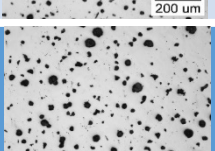
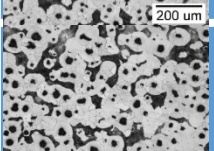
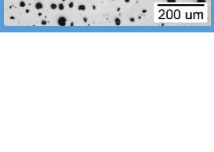
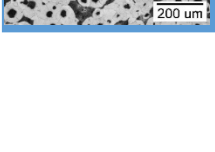
Fe₂O₃ + MC: $\Delta T_1 \ll$, $\Delta T_2 \ll$, $\Delta T_3 \ll$

FeS₂: $\Delta T_1 <$, $\Delta T_2 <$, $\Delta T_3 <$

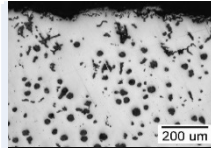
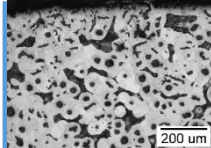
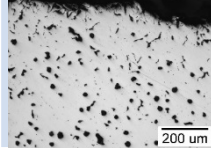
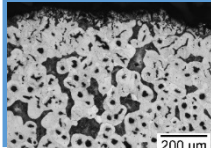
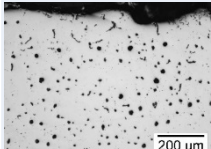
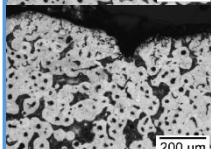
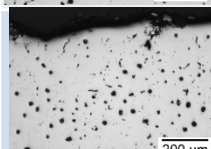
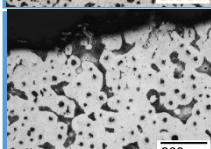
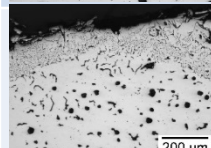
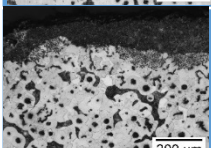
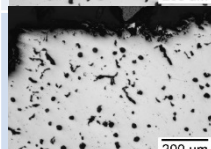
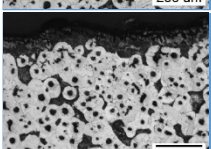
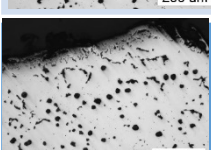
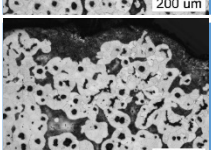
FeS₂ + MC: $\Delta T_1 \ll$, $\Delta T_2 <$, $\Delta T_3 \ll$

FeS₂ + Fe: $\Delta T_1 \ll$, $\Delta T_2 <$, $\Delta T_3 \ll$

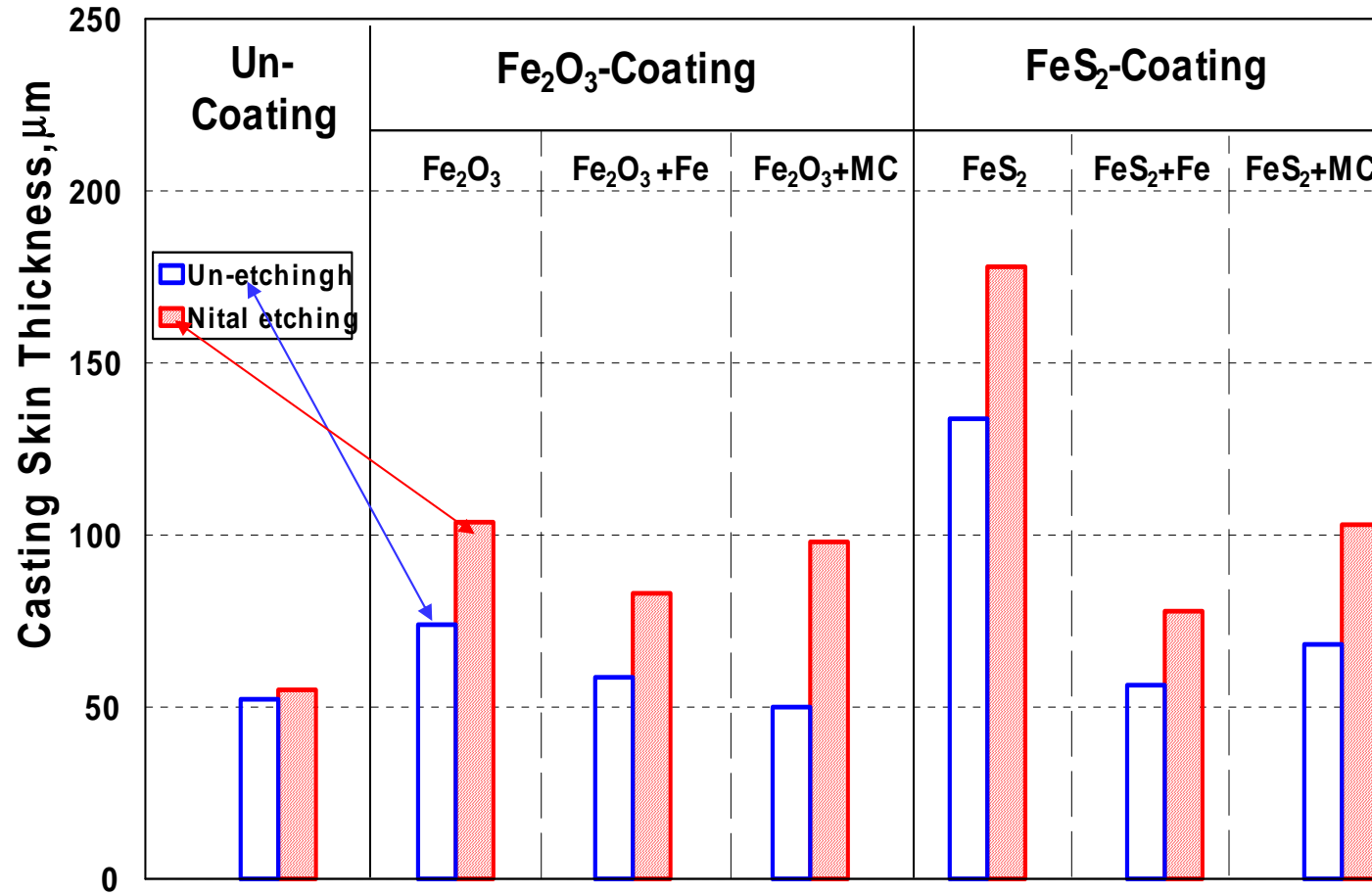
Structure characteristics in the casting body

S / O Source Coating	Protective Coating	Samples	
		Un-etching	Nital etched
Un-Coating [UC]	Un-Coating [UC]		
	-		
Oxygen (Fe ₂ O ₃ -bearing coating)	Fe-powder coating		
	MC-powder coating		
	-		
Sulphur (FeS ₂ -bearing coating)	Fe-powder coating		
	MC-powder coating		
	-		

Structure in the casting surface layer (skin)

S / O Source Coating	Protective Coating	Samples	
		Un-etching	Nital etched
Un-Coating [UC]	Un-Coating [UC]		
Oxygen (Fe_2O_3 -bearing coating)	-		
	Fe-powder coating		
	MC-powder coating		
Sulphur (FeS_2 -bearing coating)	-		
	Fe-powder coating		
	MC-powder coating		

Graphite degenerated surface layer (casting skin) thickness



CONCLUSIONS

- **The lowest eutectic temperature (TEU)**

- increased by O-bearing coating,
- decreased by S-bearing coating,
- MC or Fe-powder supplementary addition leads to TEU-decreasing for both O & S bearing coatings application.

- **The highest (recalescence) eutectic temperature TER**

- practically not affected by O and S-bearing coatings,
- MC visibly decreases TER for O-bearing coating, but only at limited level for S-bearing coating,
- Fe-bearing coating visibly decreases TER for S-bearing coating

- **The temperature at the end of solidification TES**

- at a lower level for all of the tested mould coating variants, comparing to the un-coated mould solidification,
- supplementary MC or Fe-powder addition much more decrease TES

- **Graphite nodularity inside of the castings**
 - O or S bearing coating limited negative effect: from 85% up to 82-83%
 - application of MC or Fe-powder on the previous O or S bearing coating:
 - favours the graphite nodularity increasing up to 83.5-84%.
 - better results are obtained by
 - MC addition on the O-bearing coating *and*
 - Fe-powder on the S-bearing coating.
- **Surface layer at different graphite morphologies**
 - despite that the ceramic mould is not able to supply active agents for nodularising elements consumption into the iron melt
 - at a large range of thickness, from 50 up to 200 μ m.
 - higher level of skin thickness as metal matrix evaluation comparing to the graphite phase evaluation

- **The lowest thickness of the surface layer (skin) is obtained without mould coating**
 - while O or S included in the mould coating increase the casting skin thickness, but at different power:
 - up to 50% by **Oxygen** and 2.5-3.3 times for **Sulphur** action,
 - despite that in the casting body the graphite nodularity limited decreases
- **Supplementary substance addition, to block O or S diffusion from mould coating into the iron melt:**
 - is efficient as the skin thickness decreases,
 - for both O and S-bearing coating application,
 - for both MC or Fe-powder bearing coating application on the O or S-bearing coating

- **Despite that the mould coatings influence the solidification pattern by two ways:**

- by their thermal-physical properties (solidification cooling rate), *and*
- as possible sources for active substances, able to diffuse into the iron melt, to affect structure characteristics,

The casting skin formation appears to be attributed mainly to the second influencing factor

- **The negative role of **O** and especially of **S** in graphite degeneration in the surface casting layer**

- could be counteract by addition of materials able to block the diffusion of these elements into the iron melt
- it was found that Carbonic Material is more efficient to limit Oxygen & Fe-powder to limit Sulphur negative effects

Make Good Iron Castings !!!

THANK YOU



19th INTERNATIONAL FOUNDRYMEN CONFERENCE
Humans - Valuable Resource for Foundry Industry Development
Split, June 16th-18th, 2021
<https://ifc.simet.hr/>

MORE THEN A MANUFACTURER - BRODOSPLIT

Luka Čadež*

BRODOSPLIT d.d., Croatia

Plenary lecture
Subject review

Abstract

Progress of process of informatization and digitalization in Brodosplit in last five years is based on employment of young people who are ready to accept challenges and who can quickly accept any kind of software. Their contribution enabled implementation of new 3D software and consequently new way in making of drawings for production, beginning of integration process between new 3D software and legacy IT system that encompasses all the business processes, as well as automatization of certain tasks. Thanks to such an approach, production efficiency has been increased, particularly in technological process of pre-outfitting that has direct impact on significant savings in shipbuilding production.

Keywords: *informatization, digitalization, employment, implementation, integration, automatization, production, pre-outfitting*

*Corresponding author (e-mail address): luka.cadez@brodosplit.hr



19th INTERNATIONAL FOUNDRYMEN CONFERENCE
Humans - Valuable Resource for Foundry Industry Development

Split, June 16th-18th, 2021

<https://ifc.simet.hr/>

NUCLEATION AND CRYSTALLIZATION OF SPHEROIDAL GRAPHITE IN CAST IRON

Doru M. Stefanescu^{1*}, Gorka Alonso², Ramon Suarez³

¹ The Ohio State University, Columbus, OH and The University of Alabama, Tuscaloosa, Alabama, USA

² IK4-Azterlan, Durango, Spain

³ IK4-Azterlan and Veigalan Estudio 2010, Durango, Spain

Plenary lecture

Subject review

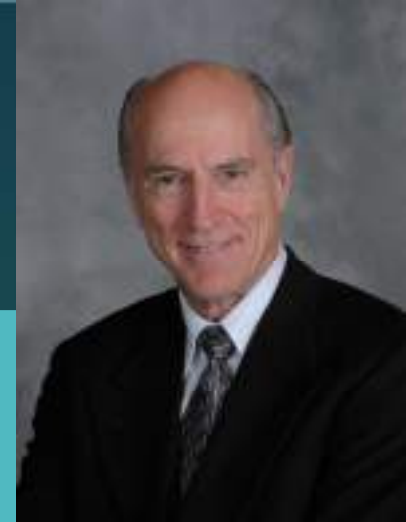
Abstract

The last decade has witnessed significant research efforts directed to the understanding of nucleation and crystallization of graphite and associated solidification phenomena, driven in part by the ever-growing interest in the use of spheroidal graphite cast iron in the manufacture of large castings such as wind turbine parts. These applications raised new challenges to the production of sound castings, mostly because of the exceedingly long solidification times imposed by the size of the castings. These solidification conditions resulted in many instances in graphite degeneration with subsequent decrease of mechanical properties. Obviously, the subject of graphite nucleation and crystallization in cast iron is still in need of additional answers. Over the years, many reviews of the subject have been published. The goal of this paper is to provide an update on the advances achieved in comprehending the mechanisms that govern the nucleation and crystallization of spheroidal graphite and related imperfect morphologies from iron-carbon-silicon melts. In this analysis, we examine not only the crystallization of graphite in cast iron, but also that of metamorphic graphite (natural graphite formed through transformation by heat, pressure, or other natural actions), and of other materials with similar lattice structure and crystallization morphologies.

Keywords: *spheroidal graphite, graphite nucleation, graphite crystallization, graphene, metamorphic graphite*

*Corresponding author (e-mail address): stefanescu.1@osu.edu

Nucleation and Crystallization of Spheroidal Graphite in Cast Iron



PROF. DORU MICHAEL STEFANESCU



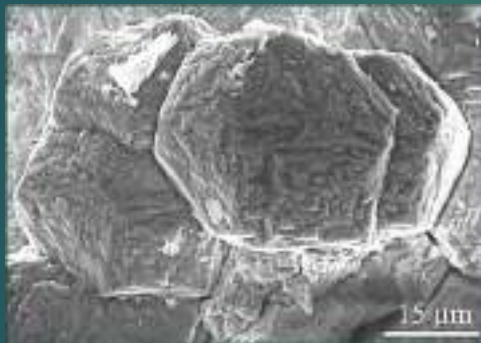
Outline

- ▶ **Introduction**
- ▶ **Background and some basic concepts**
- ▶ **Nucleation of graphite**
 - During solidification
 - During solid-state transformation
- ▶ **Growth of graphite during solidification**
- ▶ **Solid-state growth of graphite**
- ▶ **Conclusions**



Introduction

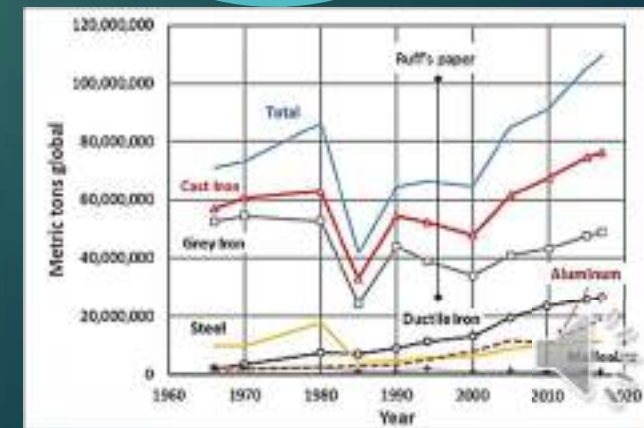
- ▶ Primitive people worked with meteoric iron long before learning to extract it from iron ore
- ▶ They were probably aware that meteoric iron contains sometimes graphite (Fig.), but were ignorant of its effects on iron



SEM image of graphite octahedrons from an iron meteorite

- ▶ Attempts to produce spheroidal graphite (SG) iron:
 - ▶ 1938: **Carl Adey** produced graphite nodules by fast solidification of Fe with 0.04%S; no addition of spheroidizing elements
 - ▶ 1943: **Keith Millis** made a ladle addition of Mg to cast iron through a Cu-Mg alloy and produced SG
 - ▶ 1948: patents by **Millis** and **Morrogh** (Ce alloy)
- ▶ The new material, *ductile iron*, experienced an explosive expansion in industry

SG iron and aluminum are the only casting materials that have experienced continuous global growth since 1965



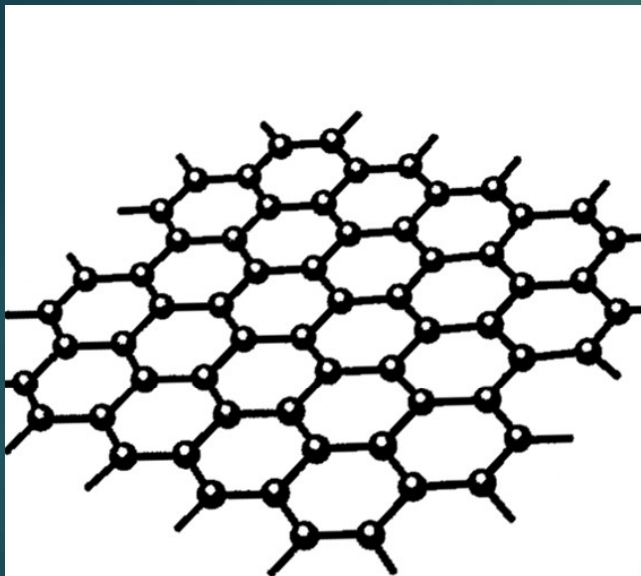
Outline

- ▶ **Introduction**
- ▶ **Background and some basic concepts**
- ▶ **Nucleation of graphite**
 - During solidification
 - During the solid-state transformation
- ▶ **Growth of graphite during solidification**
- ▶ **Solid-state growth of graphite**
- ▶ **Conclusions**

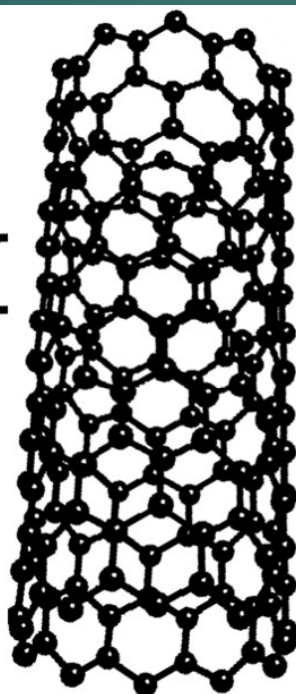


Growth of hexagonal crystals

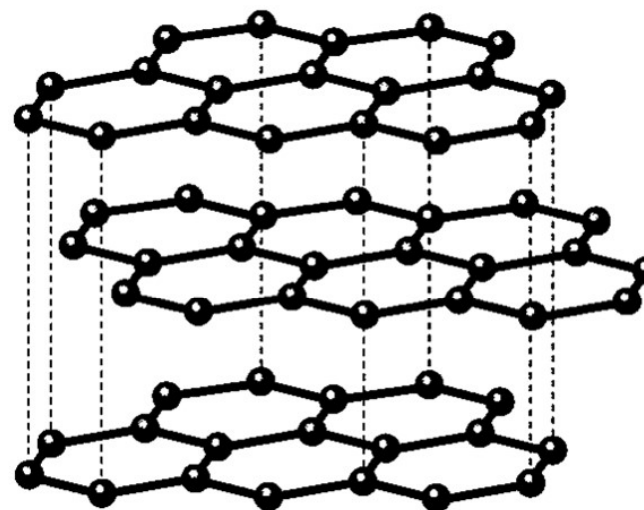
The crystal lattice of graphite - Allotropes of carbon



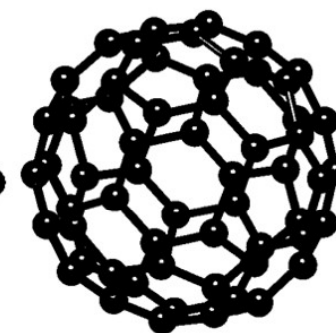
2-D graphene



1-D carbon nanotube



3-D graphite



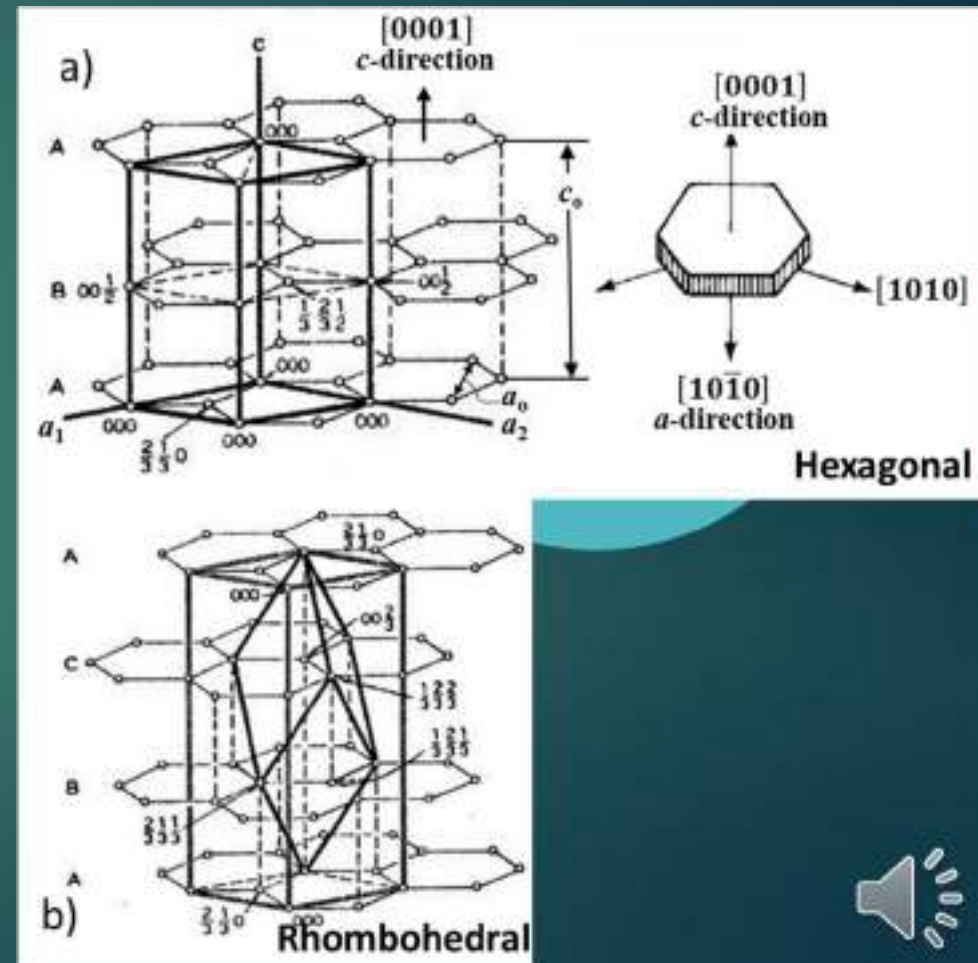
0-D fullerene



Growth of hexagonal crystals

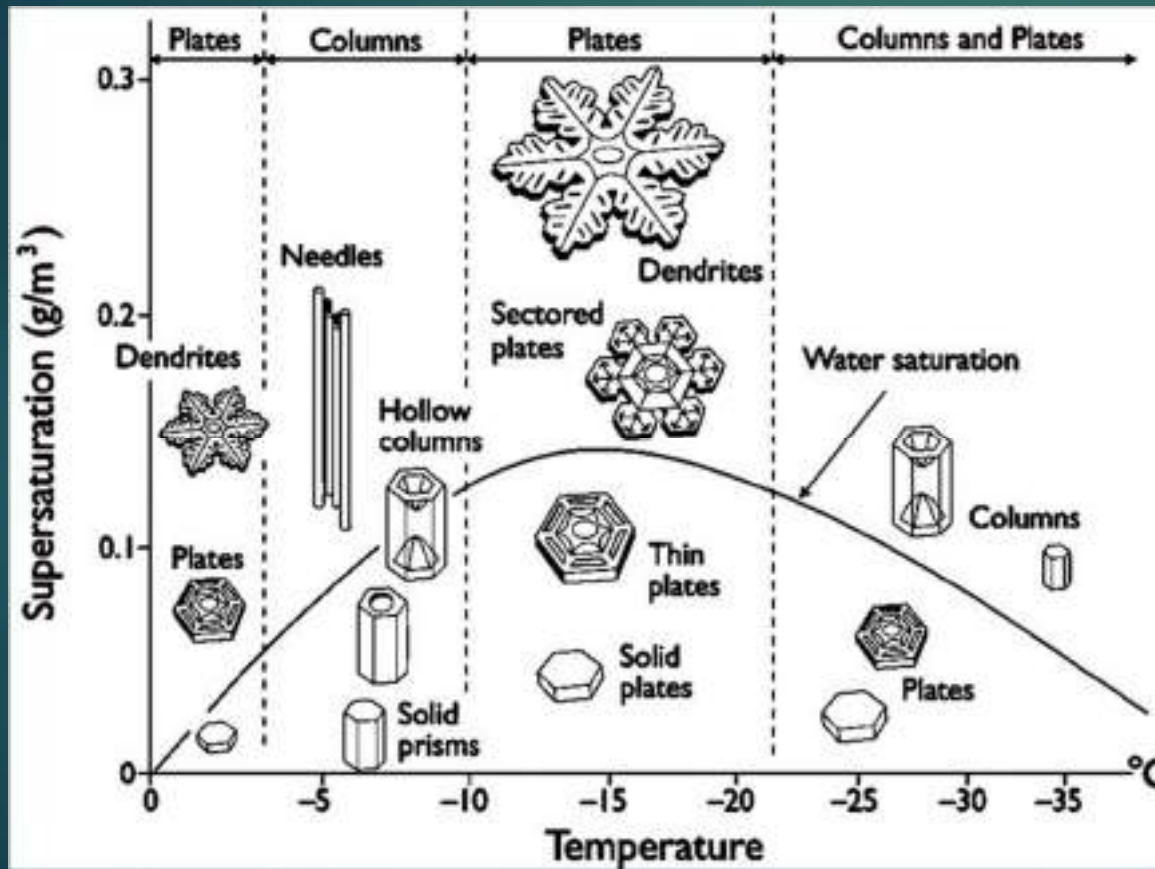
The crystal lattice of graphite – Preferred growth habit

- ▶ The prism plane is a high energy plane at which impurities absorb preferentially.
- ▶ Atoms added easily in the *a*-direction, but with lower probability in the *c*-direction → the preferred growth habit for graphite is in the *a*-direction, producing a sheet.
- ▶ This explains graphite flakes found in natural graphite and graphite lamellae in gray cast iron.
- ▶ In Ni-C, Co-C and Fe-C alloys, SG can be produced, where the graphite aggregate appears to grow in the *c*-direction. This departure from the Bravais' rule and the Gibbs-Wulff theorem has been a topic that continues to stimulate research.



Growth of hexagonal crystals

Ice crystals

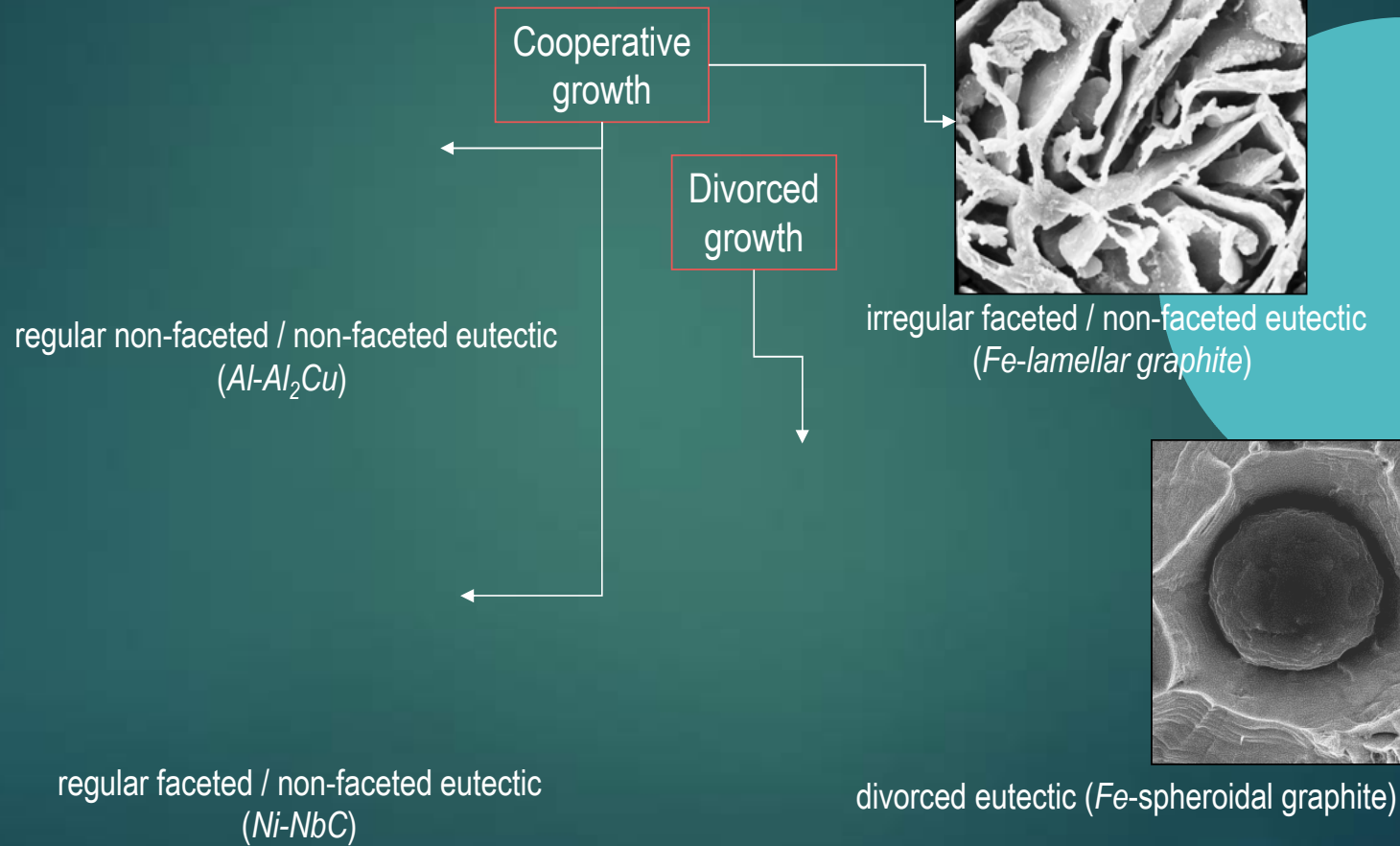


Nakaya 1954



Eutectic Solidification

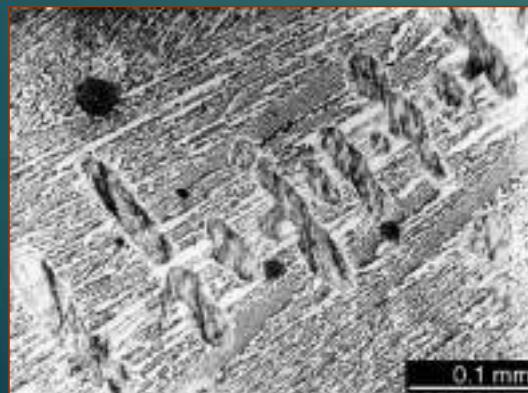
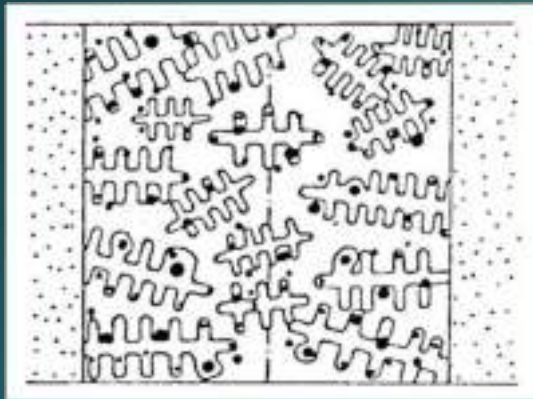
Types of eutectics



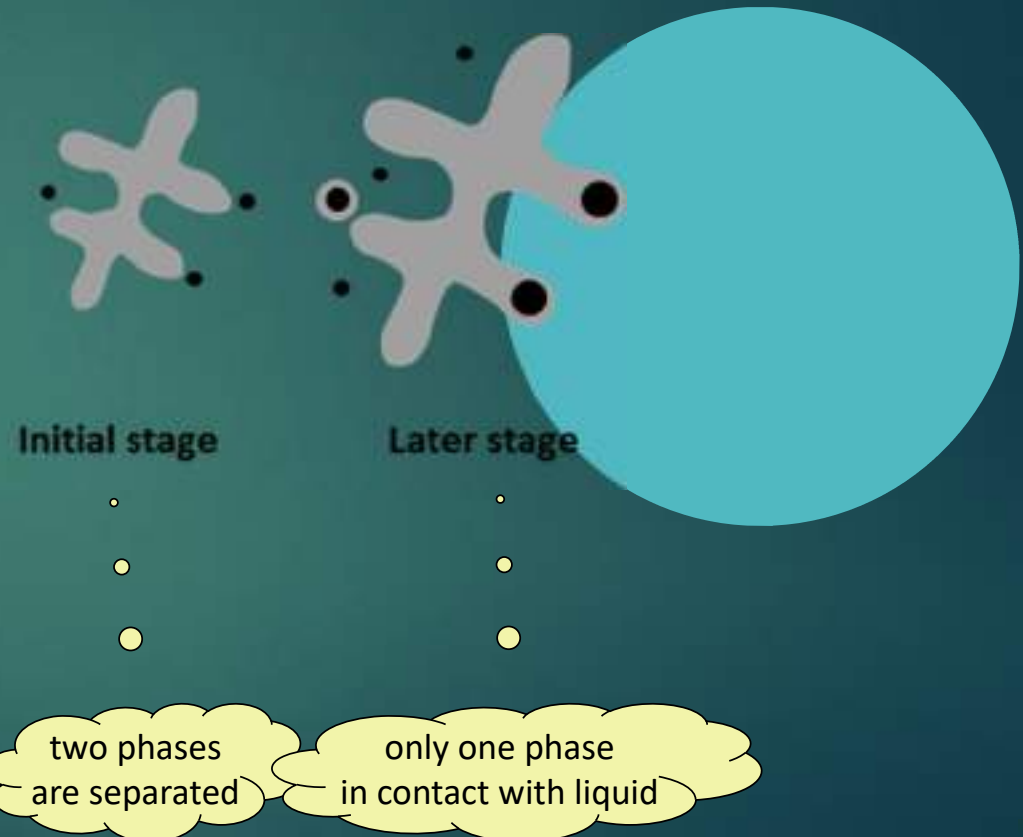
Eutectic Solidification

The divorced spheroidal graphite/austenite eutectic

Ellerbrok/Engler 1981

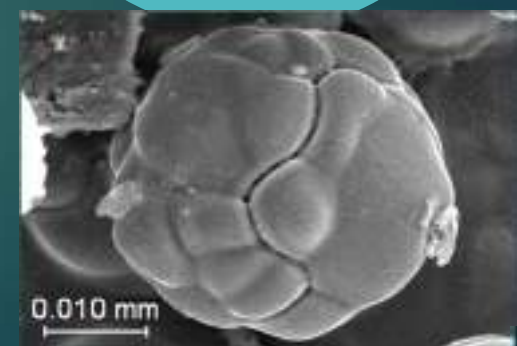
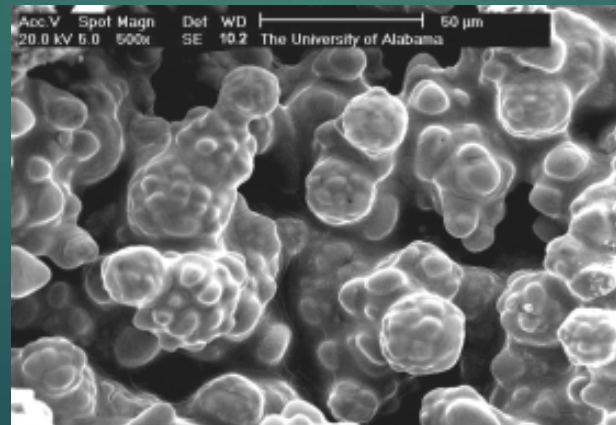
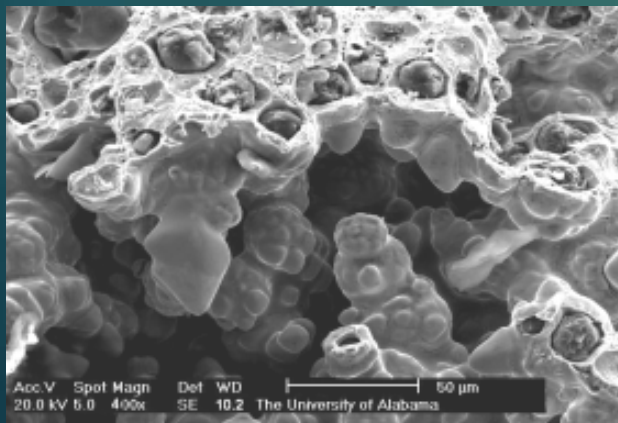
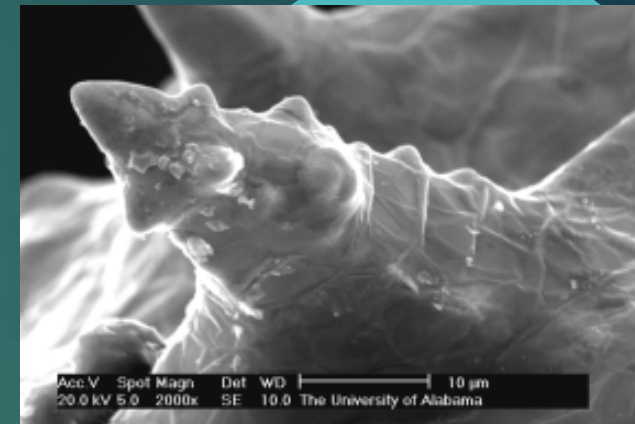
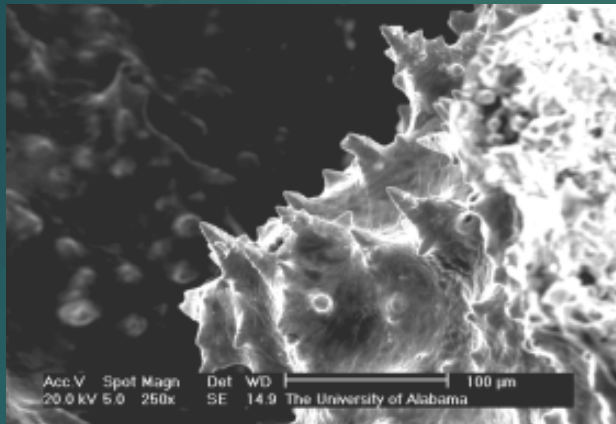


Fredriksson et al. 2005



Eutectic Solidification of Cast Iron

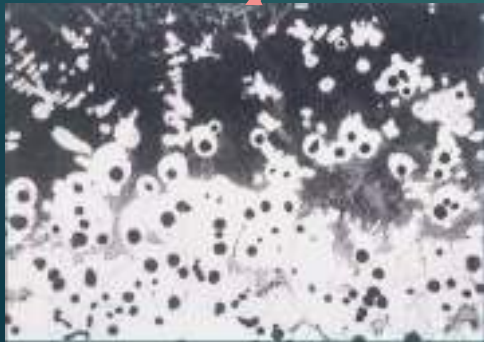
Spheroidal graphite/austenite - *Interrupted solidification (porosity)*



Eutectic Solidification of Cast Iron

Directional solidification – *Effect of solute and growth rate*

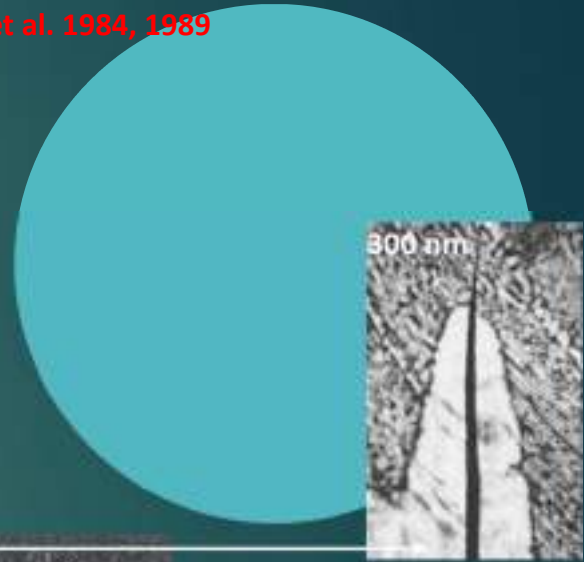
Stefanescu et al. 1984, 1989



5.0 $\mu\text{m/s}$



1.2 $\mu\text{m/s}$



300 nm

1 mm

Li, Liu, Loper 1990



Crystal growth mechanisms relevant to graphite

Investigative methods

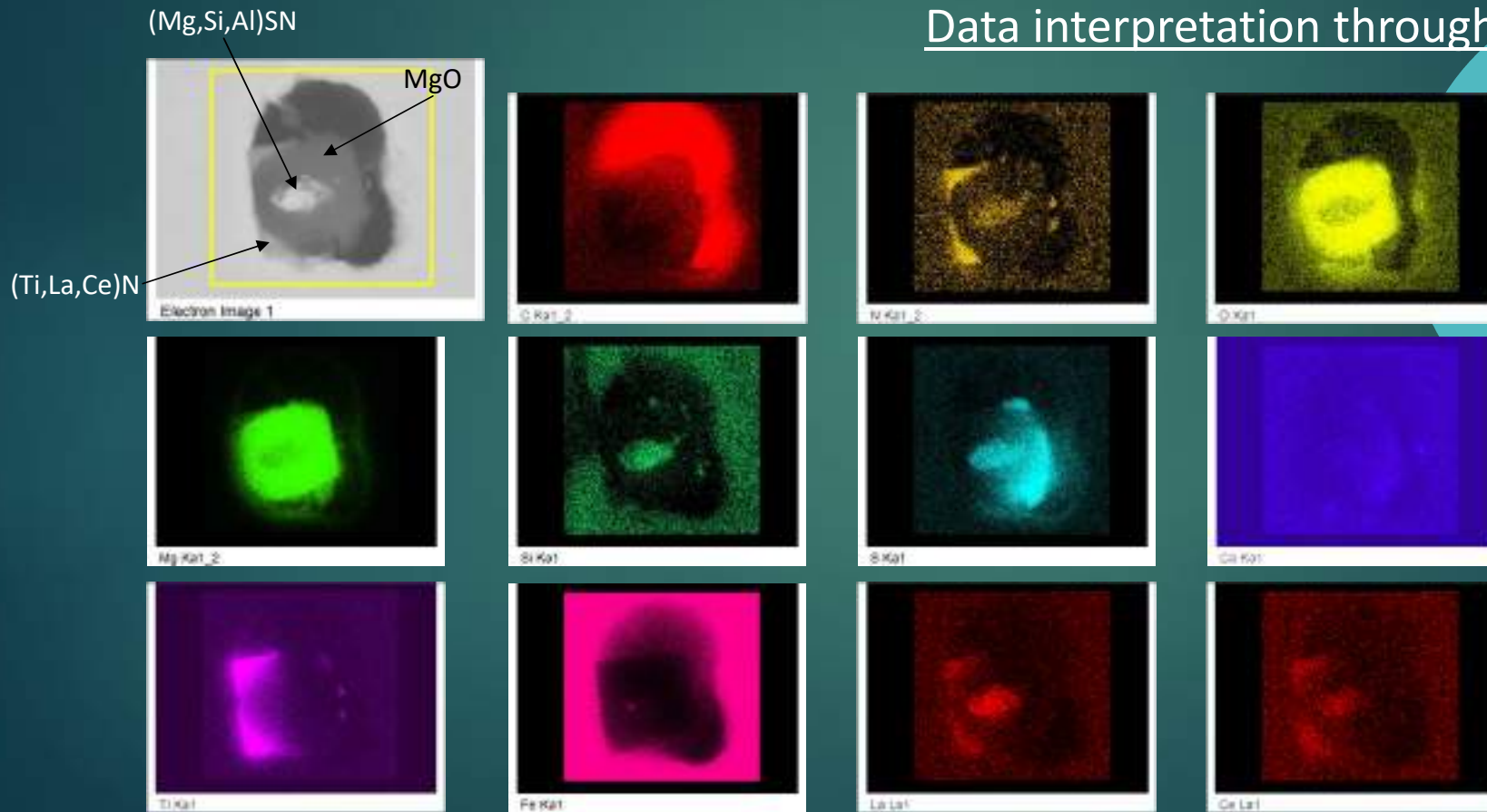
- ▶ Length scale of interest:
 - Nano-scale for atomic attachment and aggregation
 - Micro-scale for aggregation
- ▶ Sample preparation:
 - Room temperature samples – show final product
 - Quenched from the liquid or mushy zone – may reveal intermediate stages of growth
- ▶ Instrumentation
 - Optical microscopy
 - SEM + deep etching: best for assessing overall morphology formation
 - Energy-Dispersive X-ray Spectroscopy (EDX): for composition
 - TEM: the method of choice for examining attachment mechanisms



Crystal growth mechanisms relevant to graphite

Investigative methods - EDX

Data interpretation through mapping

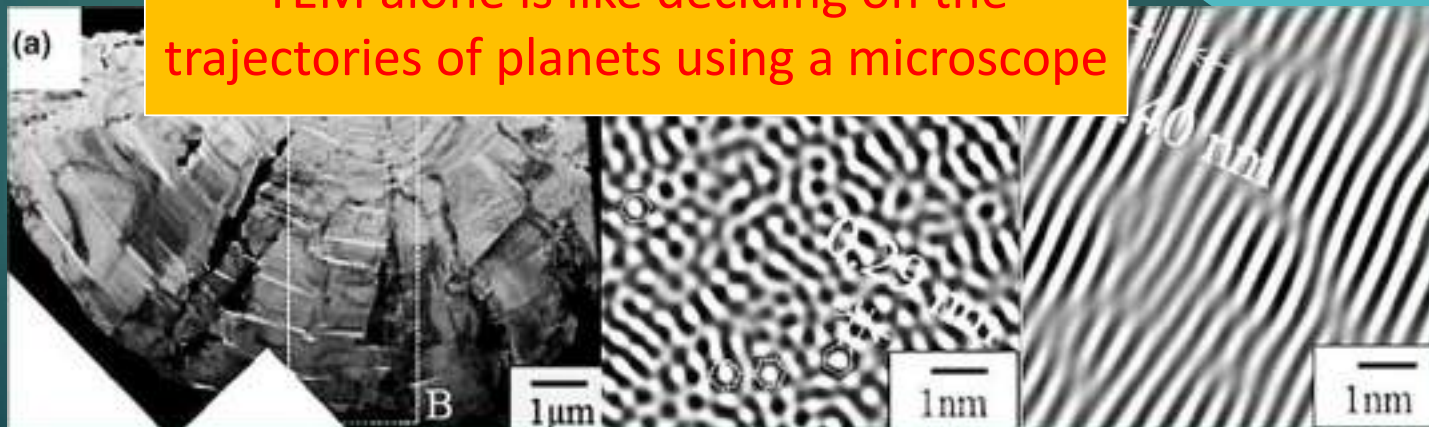
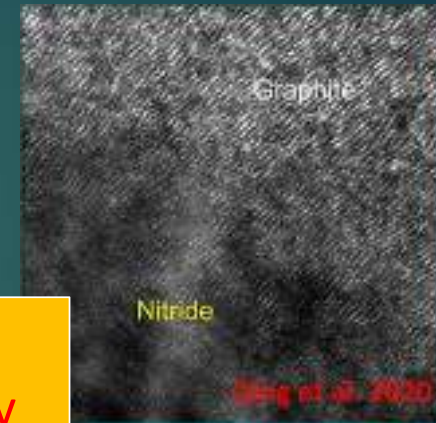


Crystal growth mechanisms relevant to graphite

Investigative methods - TEM

- ▶ Semi-coherent interface between graphite lattice and nucleus crystal (Mg–Al–Si nitride)
- ▶ Graphite lattice near the nucleus shows high curvature and high density of crystallographic defects
- ▶ a) columnar growth with
b) amorphous central
intermediate region H

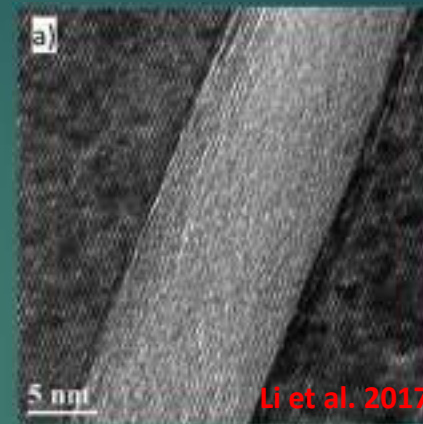
Deriving conclusions on micro-scale graphite growth in metallic solution by TEM alone is like deciding on the trajectories of planets using a microscope



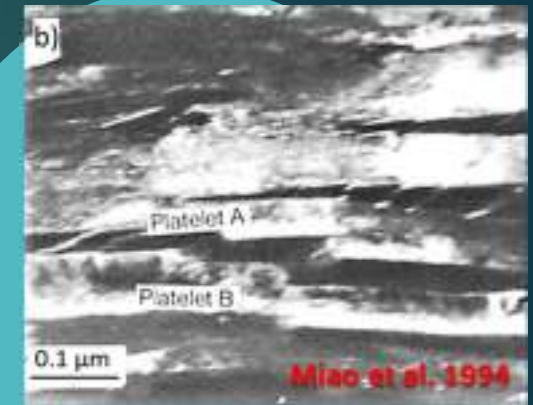
Crystal growth mechanisms relevant to graphite

The building blocks

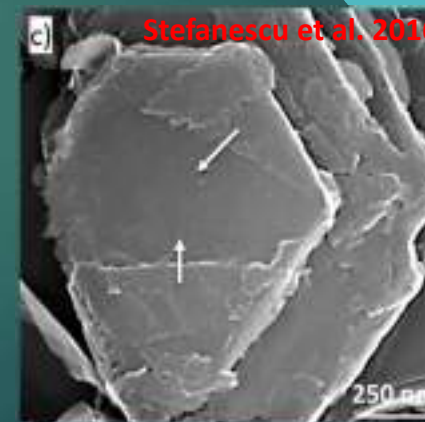
- ▶ Growth of a graphite crystal starts with the formation of 2-D graphene sheets that develop in the *a*-direction.
- ▶ Crystallization of graphite from Fe-C melts begins with the stacking of the graphene sheets in the *c*-direction into hexagonal faceted graphite platelets that are the basic building blocks of the graphite aggregates.
- ▶ To produce graphite aggregates, the platelets must thicken and aggregate.



platelets in steel



platelets in SG iron



aggregation of platelets
in CG iron



Crystal growth mechanisms relevant to graphite

Atomic attachment - *Mechanisms for lateral growth*

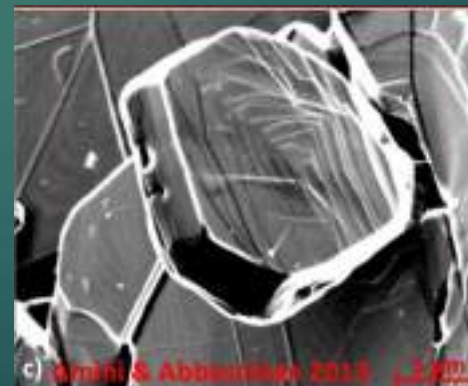
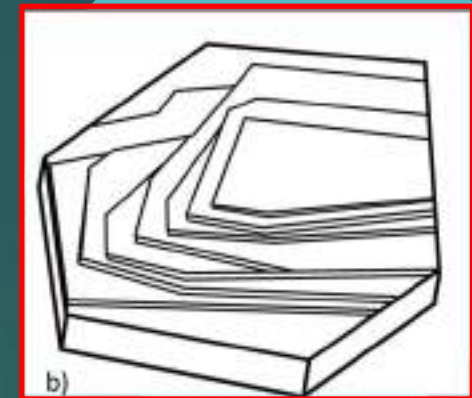
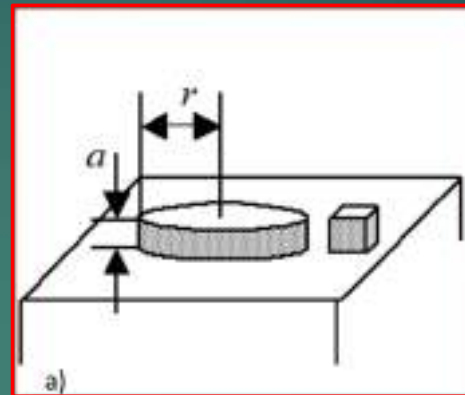
- ▶ The operating growth mechanism of a crystal is a function of the nature of the interface and of the driving force (undercooling, supersaturation)
- ▶ For atomically rough (non-faceted) interfaces, such as dendritic austenite, the interface advances through continuous growth; requires small driving forces
- ▶ For atomically smooth (faceted) interfaces crystals, such as graphite or ice, the interface advances through lateral growth
 - ▶ two-dimensional (2-D) nucleation of a new layer - requires larger driving forces
 - ▶ defect-controlled growth -requires lower driving force
- ▶ Thickening of the platelets occurs through layer growth in the *c-direction*



Crystal growth mechanisms relevant to graphite

Atomic attachment - *Two-dimensional (2-D) nucleation*

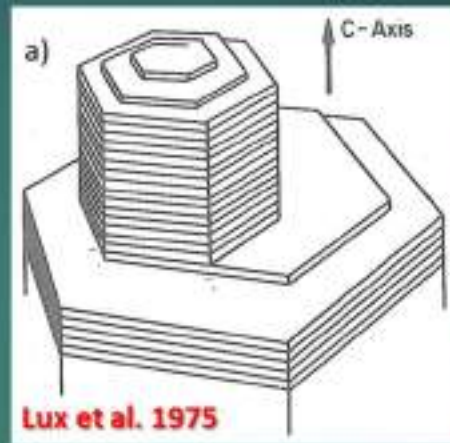
- ▶ 2-D nucleation (Fig. a) is slow and could not explain graphite thickening during graphite growth - poly-nucleation (PNG), was considered.
- ▶ PNG: many 2-D nuclei form on the surface of a growing crystal, and on top of the already growing islands (Fig. b). It has been shown to occur on graphite plates in a Ni-C alloy (Fig. c).
- ▶ There is no experimental evidence that demonstrates that this mechanism contributes to SG growth.



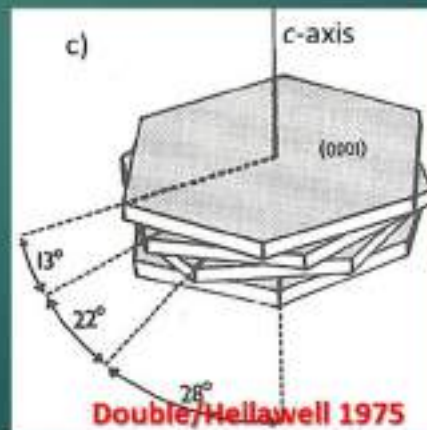
Crystal growth mechanisms relevant to graphite

Atomic attachment - Defect-controlled growth

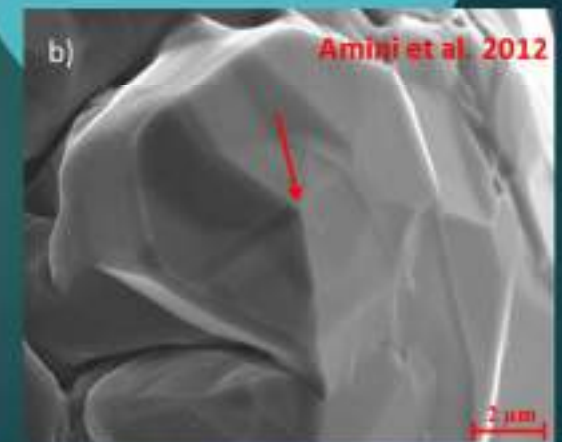
- ▶ growth occurs from steps on the graphite layers related to screw dislocations and twisted boundaries defects **Frank 1949**
- ▶ basal plane and non-basal dislocations on single crystal flakes of natural graphite **Delavignette/Amelinckx 1962**
- ▶ more recently - spiral growth for pyrolytic graphite spheres, and for both lamellar and compacted graphite



Spiral growth by screw dislocation



Growth from step at twist boundary



Spiral growth in graphite from Ni-C alloy

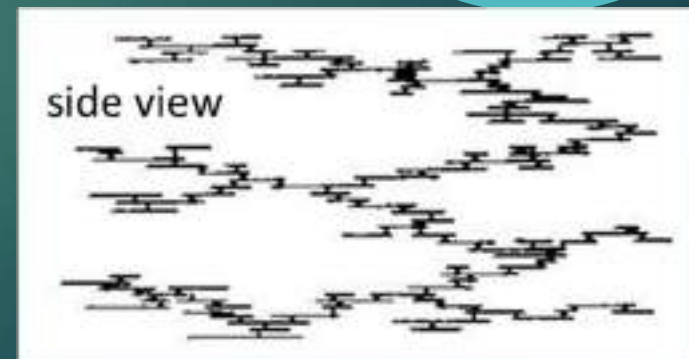
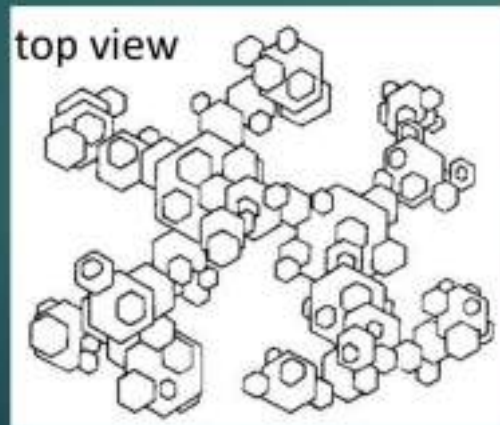


Crystal growth mechanisms relevant to graphite

Aggregation of graphite platelets – *Foliated crystals*

WHAT ARE FOLIATED CRYSTALS?

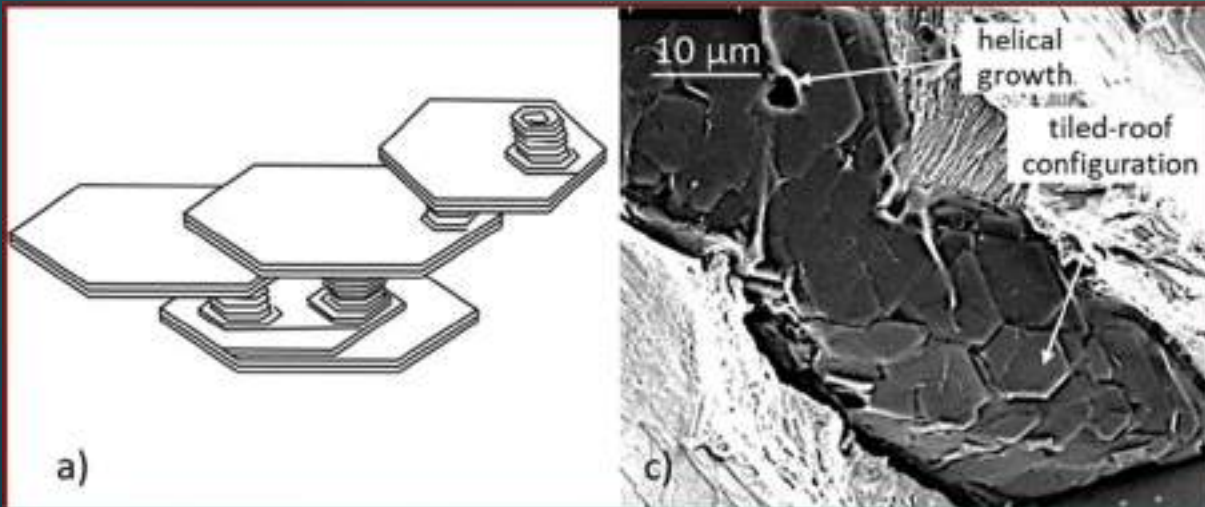
- ▶ foliated crystals/dendrites: assemblies of thin plates separated by solvent impurity layers **Saratovkin 1959, Flemings 1974**
- ▶ the concept was used to explain graphite growth in cast iron and the entrapment of iron between the foliated graphite plates **Saratovkin 1959, Roviglione/Hermida 2004, Stefanescu et al. 2016**



Crystal growth mechanisms relevant to graphite

Aggregation of graphite platelets – *Foliated crystals*

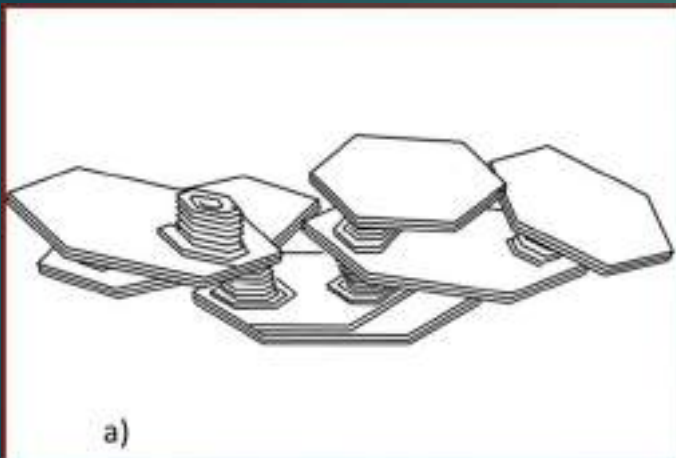
- ▶ At low constitutional undercooling or supersaturation, Gr grows in the *a*-direction as hexagonal faceted foliated plates (Fig. a)
- ▶ When crystals grow parallel to one another tiled-roof configurations result (Fig. c)
- ▶ Foliated growth found also for Al_3Ti crystals in Al-Ti alloys and Si crystals in Al-Si alloys (Fig. b)



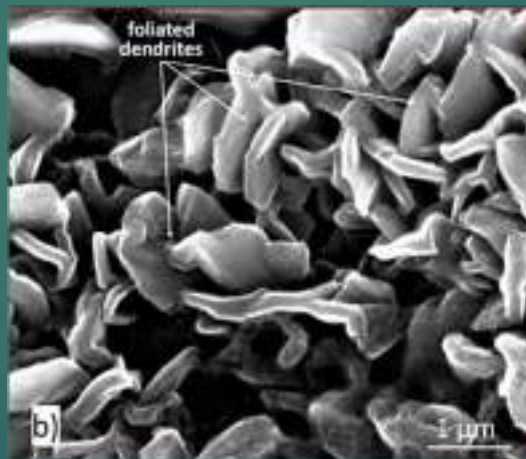
Crystal growth mechanisms relevant to graphite

Aggregation of graphite platelets – *Foliated crystals*

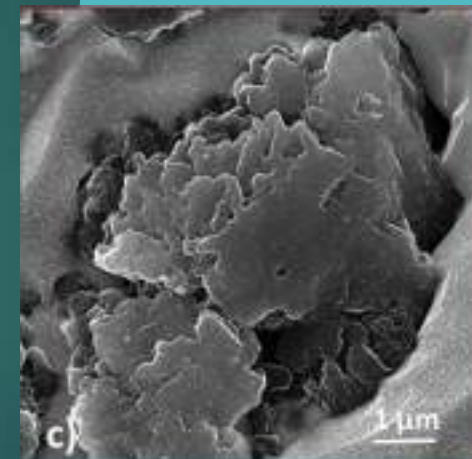
If the overall growth of the foliated crystal is less organized (Fig. a), dendritic structures are produced



a)
foliated dendrites in 0.18% Ti
lamellar graphite iron



b)
foliated dendrites in 0.18% Ti
lamellar graphite iron



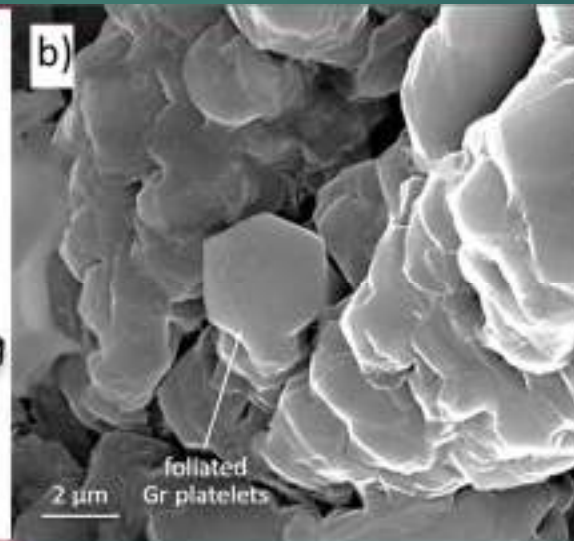
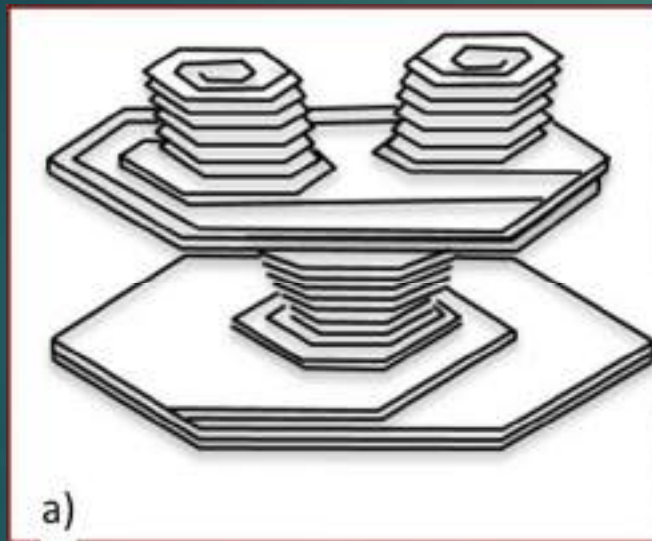
c)
foliated dendrites
in chunky graphite



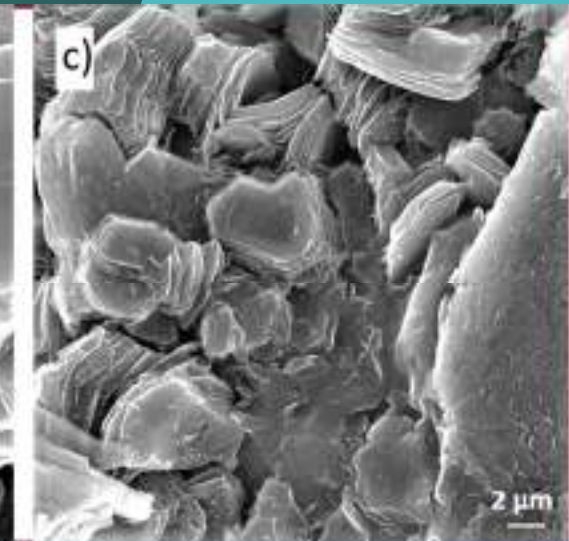
Crystal growth mechanisms relevant to graphite

Aggregation of graphite platelets – *Foliated crystals*

Stacking of the crystals in the [0001] *c-direction* generates columns



stacking of foliated hexagonal platelets in the *c-direction* in CG iron



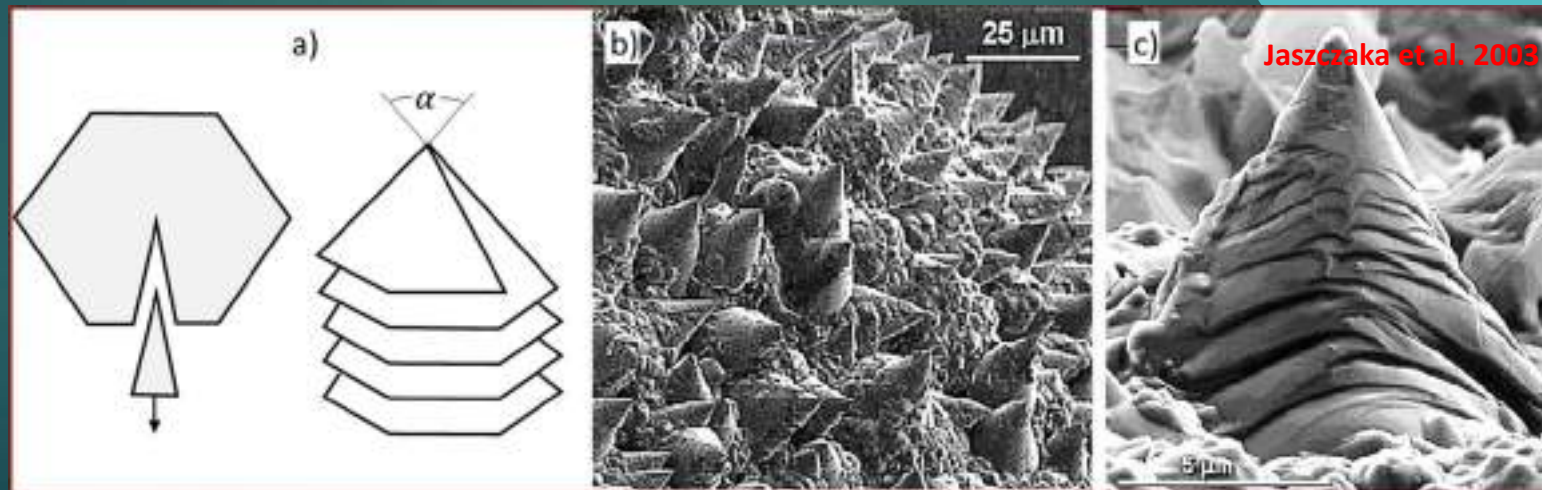
growth of blocky graphite from foliated platelets in 0.01% Sb CG iron



Crystal growth mechanisms relevant to graphite

Aggregation of graphite platelets – *Disclinations/micro-spiral growth*

- ▶ Disclinations are line defects corresponding to “adding” or “subtracting” an angle around a line
- ▶ Positive wedge disclination mechanism - the initial graphite layer adopts a dome-shaped configuration by introducing a 5-fold carbon ring in the 6-fold carbon network. Successive sheets rotate over previous ones, producing a micro-spiral cone around a “disclination” with a 5-fold carbon ring core **Amelinckx et al. (1992)**



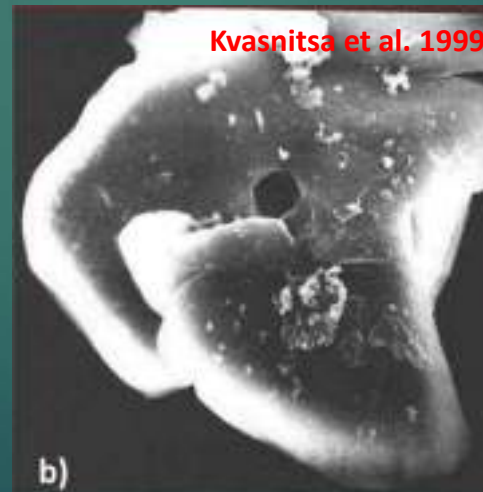
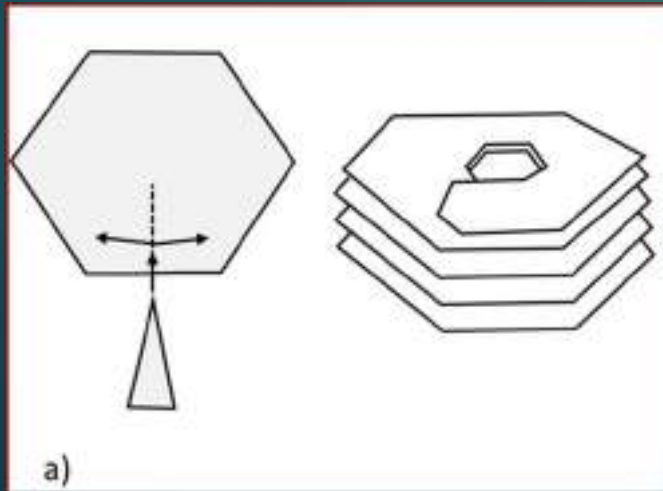
graphite cones on a quasi-spherical metamorphic graphite



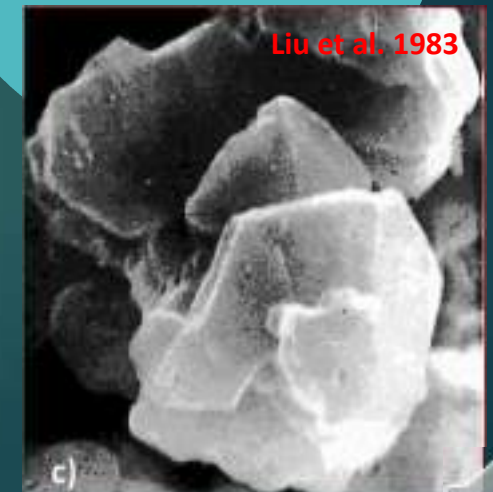
Crystal growth mechanisms relevant to graphite

Aggregation of graphite platelets – *Disclinations/helical growth*

- ▶ Negative wedge disclination mechanism - when inserting a wedge into the basic hexagon (Fig. a)
- ▶ It explains macro-spiral (helical) growth
 - in metamorphic graphite - upward spiraling with hexagonal cavities in the middle of the aggregate (Fig. b)
 - in chunky graphite (Fig. c)



overlapping segments and hexagonal hole
in metamorphic graphite



chunky graphite in cast iron

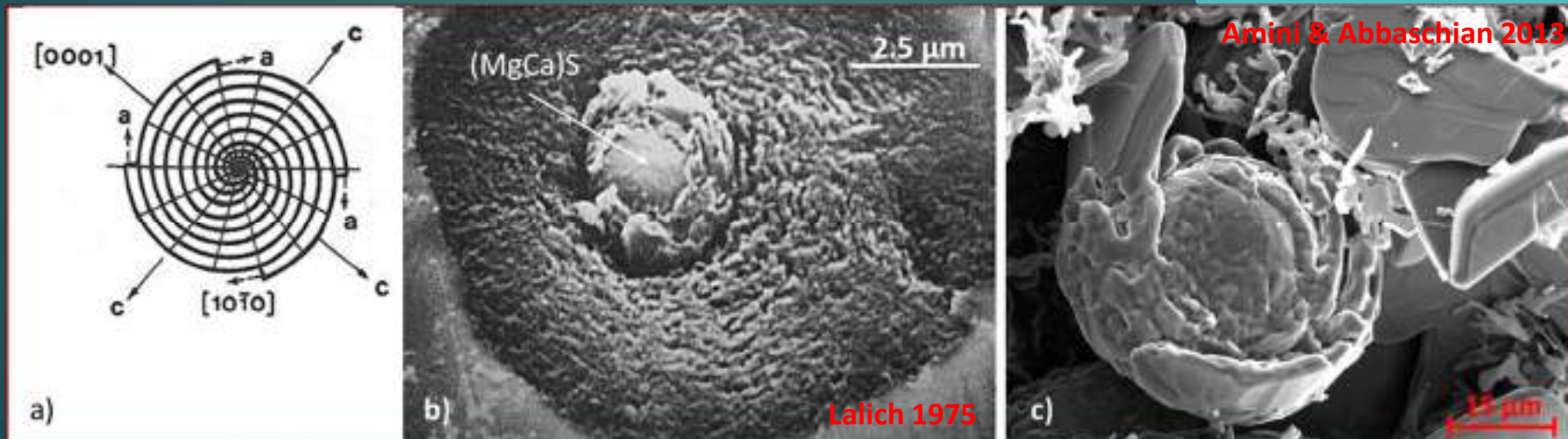
Crystal growth mechanisms relevant to graphite

Aggregation of graphite platelets – *Curved-circumferential growth*

- ▶ Curved-circumferential growth mechanism - bending of graphite platelets growing in the α -direction can occur by the movement of steps around the surface of spheroids (Fig. a)

Sadocha/ Gruzlesky (1975)

- ▶ This mechanism explains SG in high-purity Fe-C-Si alloys without Mg or Ce additions



circumferential growth in cast iron
around a (MgCa)S nucleus

circumferential growth in a Ni-C alloy



Crystal growth mechanisms relevant to graphite

Aggregation of graphite platelets – *Hopper crystals*

- ▶ Hopper crystals belong to the family of skeletal crystals which develop when atoms are added more rapidly to the edges and corners of a growing crystal than to the centers of crystal faces, resulting in either branched dendritic habit, or hollow stepped depressions (hoppers)
- ▶ Hopper crystals are found in many materials, such as ice, halite, bismuth, galena, gold and quartz



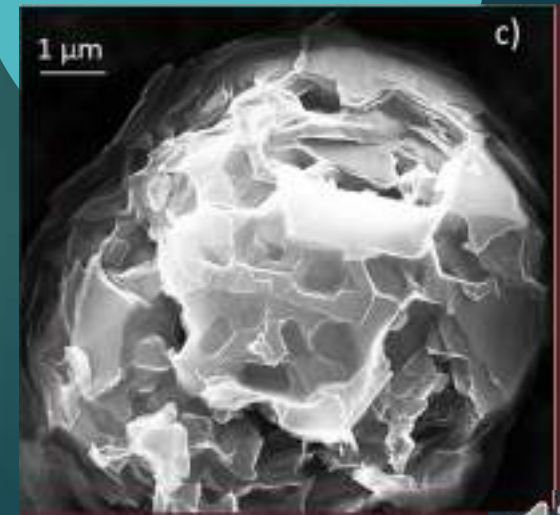
hopper crystal in a β - Si_3N_4 crystal



hopper crystal in ice



dendritic/hopper crystal in salt



quasi-spheroidal graphite
hopper crystal in malleable iron

Crystals growth mechanisms relevant to graphite

Crystallographic considerations

- ▶ Crystallographic compatibility implies that the substrate must have a coherent or semicoherent interface with the solid to be nucleated
- ▶ **Turnbull/Vonnegut 1952** - crystallographic compatibility measured through linear disregistry

$$\delta = (a_n - a_s)/a_s$$

a_s and a_n are the interatomic spacing along shared low-index crystal directions in the solid nucleus and the nucleant

- ▶ A planar disregistry of 5.9% was considered to be indicative of a highly effective nucleant, and one of 11.2% moderately effective

- ▶ **Bramfitt 1970** - planar disregistry that included the angular difference between the crystallographic directions within the plane

$$\delta_{(hkl)_n}^{(hkl)_s} = \sum_{i=1}^3 \frac{|(d_{[uvw]_s}^i \cos\theta) - d_{[uvw]_n}^i|}{3 \cdot d_{[uvw]_n}^i} 100$$

$(hkl)_s$ is a low-index plane of the substrate, $[uvw]_s$ is a low-index direction in $(hkl)_s$, $(hkl)_n$ is a low-index plane in the nucleated solid, $[uvw]_n$ is a low-index direction in $(hkl)_n$, $d_{[uvw]_n}$ is the interatomic spacing along $[uvw]_n$, $d_{[uvw]_s}$ is the interatomic spacing along $[uvw]_s$, and θ is the angle between $[uvw]_s$ and the $[uvw]_n$

- ▶ Highly effective inoculants have low disregistry, typically <12.



Outline

- ▶ **Introduction**
- ▶ **Background and some basic concepts**
- ▶ **Nucleation of graphite**
 - ▶ During solidification
 - ▶ During the solid-state transformation
- ▶ **Growth of graphite during solidification**
- ▶ **Solid-state growth of graphite**
- ▶ **Conclusions**



Nucleation of Graphite during Solidification

Homogeneous Nucleation

Supporting arguments

- ▶ graphite grows from small size crystalline graphite already present in the melt **Boyles (1947)**
- ▶ short-range order regions in melts with >3.5% C are carbon clusters containing approximately 15 atoms. C_n or $(Fe_3C)_n$ clusters (or molecules) that exist in dynamic equilibrium in molten Fe-C alloys may serve as nuclei for graphite **Steeb/Maier 1974**
- ▶ no impurities in the center of spheroids in Mg-free iron produced in vacuum furnace implies homogeneous nucleation of SG **Dhindaw/Verhoeven 1980**
- ▶ in low-C gray irons, graphite nucleates at the austenite/liquid interface without the presence of any foreign inclusions **Stefanescu et al. 2016**
- ▶ after the dissolution of FeSi in liquid iron, SiC crystals could form in the diffusion zone around the dissolving particles; the local supersaturation of C and Si in the melt after SiC dissolution, may provide the necessary driving force for homogeneous nucleation of graphite **Fredriksson 1984**



Nucleation of Graphite during Solidification

Heterogeneous nucleation - *Nucleation on oxides*

Oxides have been identified in the nuclei of SG by many investigators:

- ▶ MgO, SiO₂ **Heine/ Loper 1966, Poyet/Ponchon 1969**
- ▶ Mg, Al, Si, Ti oxides **Jacobs et al. 1974**
- ▶ CeO₂ and Fe₂O₃ with some MgO; no silicates **Francis 1979**
- ▶ 2-stage nucleation on CaO, with subsequent formation of Ca-silicate and silica on the oxide **Gad/Bennett 1984**



Nucleation of Graphite during Solidification

Nucleation on oxides – *Thermodynamic hierarchy*

- ▶ Established by the standard free energy of formation from pure elements
- ▶ Double and complex oxides have lower free energy than single oxides → higher probability of formation
- ▶ Consequence → single oxides are only seldom found as nuclei for SG
- ▶ The reaction energy in solution is defined by element activity; could be significantly different from that of pure elements
- ▶ Ca reactions with S could be more favorable than oxide formation in cast iron; thus, the hierarchy may be considerably different for cast iron melts

Single Oxides	Melting Temp., °C	ΔG, kJ/mol	Double Oxides	Melting Temp., °C	ΔG, kJ/mol	Complex Oxides	ΔG, kJ/mol
Al ₂ O ₃	2072	-1210	5CaO·4TiO ₂	-	-5470	2MgO·2CaO·14Al ₂ O ₃	-26,200
Ti ₂ O ₃	-	-1120	3CaO·2SiO ₂	-	-2960	3CaO·Al ₂ O ₃ ·3SiO ₂	-4850
Y ₂ O ₃	-	-988 ^{c)}	2TiO ₂ ·ZrO ₂	-	-2190	2MgO·CaO·2SiO ₂	-3980
CaO	2927 ^{a)}	-960 ^{b)}	Al ₂ O ₃ ·SiO ₂	-	-1860	2CaO·FeO·SiO ₂	-3700
SrO	2665 ^{a)}	-892 ^{b)}	2MgO·SiO ₂	1898 ^{a)}	-1570	-	-
MgO	2832 ^{a)}	-858 ^{b)}	SrO·SiO ₂	1580 ^{a)}	-1186 ^{a)}	-	-
ZrO ₂	-	-821 ^{b)}	BaO·SiO ₂	1605 ^{a)}	-1180 ^{a)}	-	-
BaO	2013 ^{a)}	-812 ^{b)}	MgO·SiO ₂	1577 ^{a)}	1110	-	-
TiO	1843 ^{b)}	-811 ^{b)}	2FeO·SiO ₂	-	-1010	-	-
SiO ₂	-	-649	MgO·2TiO ₂	-	-1820	-	-
MnO	-	-553 ^{b)}	FeO·2TiO ₂	-	-1550	-	-
Fe ₃ O ₄	-	-320 ^{b)}	Al ₂ O ₃ ·SiO ₂	-	-1860	-	-



Nucleation of Graphite during Solidification

Nucleation on sulfides

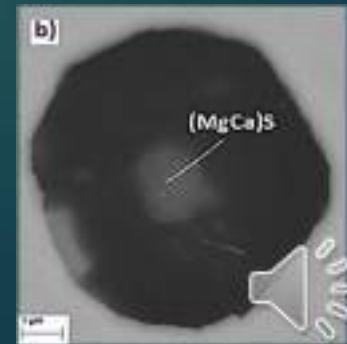
- ▶ Nuclei for LG and SG are complex oxides and sulfides, including MgS, CeS and LaS
Warrick 1966
- ▶ Later work on sulfides:
 - MgS **Stransky/Rek , Mercier et al., Lalich/Hitchings , Nieswaag/Zuithoff , Jacobs et al.**
 - CaS **Nieswaag/Zuithoff , Jacobs et al.**
 - SrS **Jacobs et al.**
 - in laboratory melts, nuclei were primarily Mg, Ca or RE sulfides, while in cupola irons they were complex mixtures of sulfides and silicates **Lalich/Hitchings**
- ▶ First two-stage nucleation theory of double-layered (cored) nucleation **Jacobs et al. (1974)**
 - ❖ SG nucleates on duplex sulfide-oxide inclusions; a core made of (Ca-Mg)S or (Ca-Mg-Sr)S, and an outer shell of complex (Mg-Al-Si-Ti)S
- ▶ Two-stage theory, but in a different sequence: MgO core with (MgCa)S shell
Igarashi/Okada 1998



Nucleation of Graphite during Solidification

Nucleation on sulfides

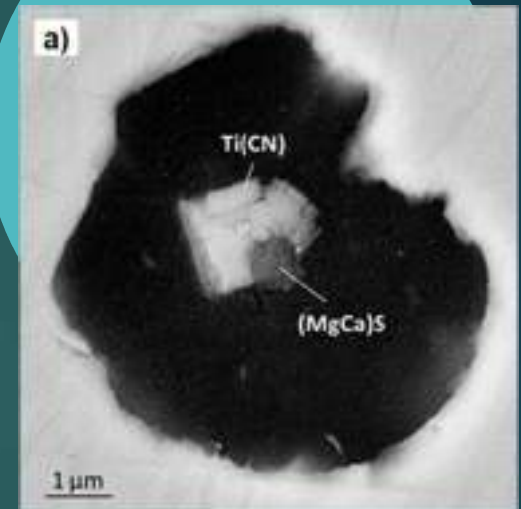
- ▶ MnS or complex (MnX)S compounds which have low crystallographic misfit with graphite and have a core of complex Al-Ca-Mg oxide, are nucleants for lamellar graphite **Naro & Wallace 1978, Riposan et al. 2003, Moumeni et al. 2013**
- ▶ However, MnS was never found in the center of graphite nodules, thus, it is not a nucleant for SG.
- ▶ Oxides have lower energy of formation than the sulfides. However, as the free energy values are close, and the iron melts are chemically nonhomogeneous, it is not necessary that the formation of oxides during cooling precedes that of sulfides.
- ▶ It is possible that oxides and sulfides form simultaneously at various locations in the melt, as sulfides have been found as one-stage nucleants for SG (Fig.)



Nucleation of Graphite during Solidification

Nucleation on nitrides – *TiN* and *Ti(CN)*

- ▶ Zr, Ti and Al nitrides have lower energy of formation than sulfides
- ▶ TiC rarely appears as a nucleant, but Ti(CN) frequently does. Planar registry calculations → TiN has better crystallographic compatibility with graphite than TiC ($\delta = 1.11$ compared to $\delta = 2.69$) **Alonso et al. 2019**
- ▶ As TiN also has a lower energy of formation than TiC, and as N is always present in cast iron, Ti(CN) is a more probable inclusion to act as nucleant than TiC alone
- ▶ In most cases, the titanium carbonitride was found to nucleate on sulfides (Fig.) or oxides **Stefanescu et al. 2019**



Nucleation of Graphite during Solidification

Nucleation on nitrides - $(Mg-Si-Al)N$

- ▶ First reported $(Mg-Si)N$ as nuclei for SG **Mercier et al. 1969**
- ▶ Complex $(Mg-Si-Al)N$ are SG nuclei even though there is no obvious crystallographic similarity between the two **Igarashi/Okada 1998, Solberg/Onsoien 2001, Nakae/Igarashi 2002**
- ▶ Thermodynamic and disregistry calculations confirm the capability of these nitrides to serve as nuclei for spheroidal graphite (Fig.) **Stefanescu et al. 2019**



Stefanescu et al. 2019

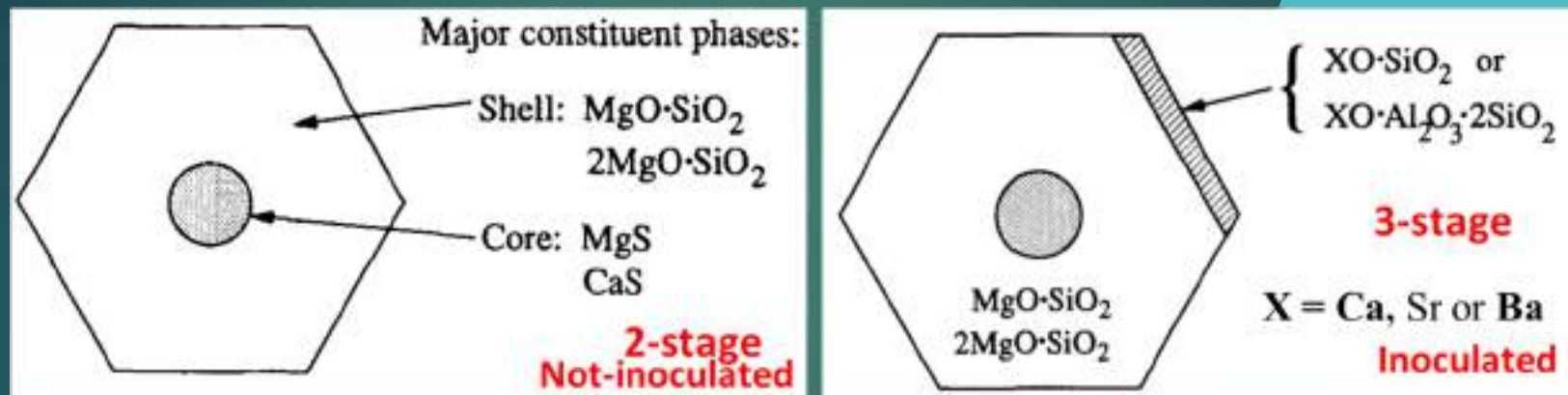


Nucleation of Graphite during Solidification

Nucleation on complex compounds

- ▶ The silicate theory - the first 3-stage nucleation theory

Skaland et al. 1993



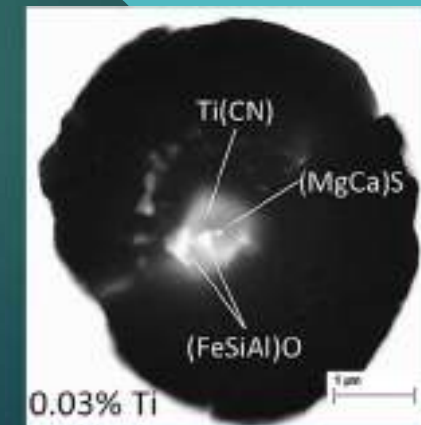
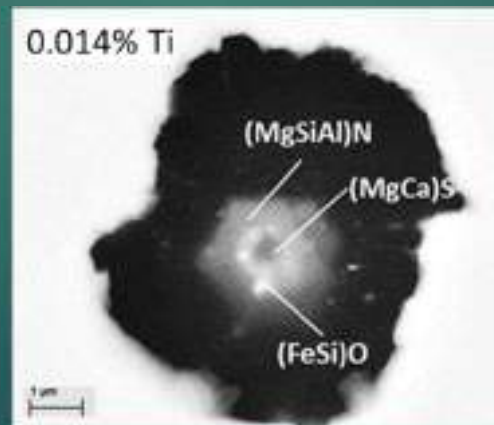
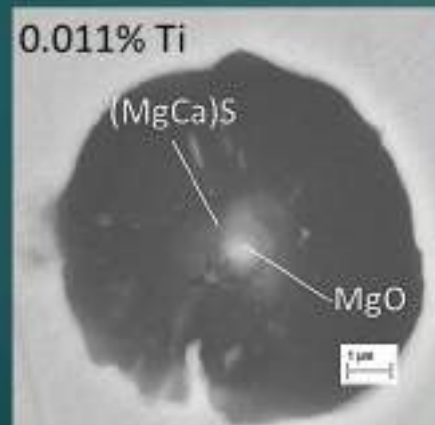
- ▶ Discrepancy between **Skaland et al.** silicate theory (epitaxial growth mechanism of graphite on silicates with an (MgCa)S core) and other experimental reports (nuclei are Mg or MgCa sulfides with an MgO core or attachment)
- ▶ Reason: **Skaland** used a base melt with very low sulfur (0.0036%S) **Nakae/Igarashi 2002**



Nucleation of Graphite during Solidification

Nucleation on complex compounds – *Effect of %Ti*

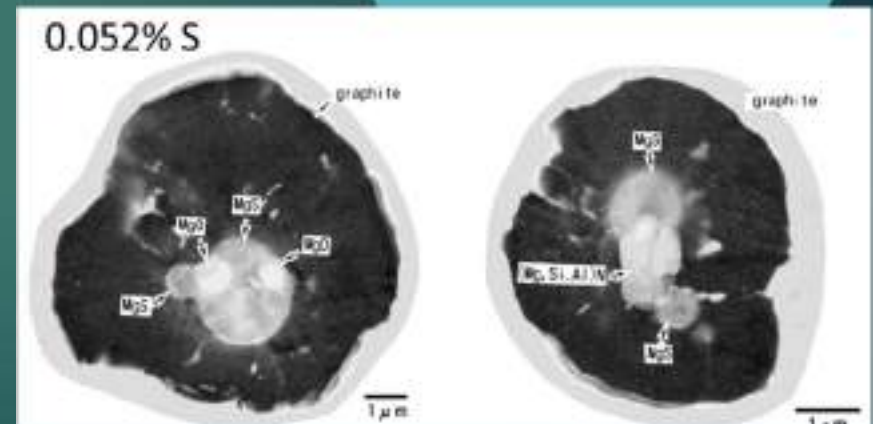
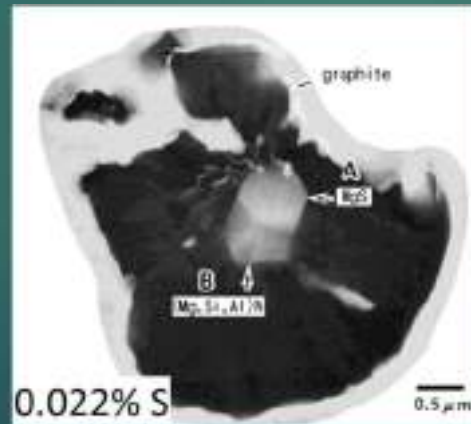
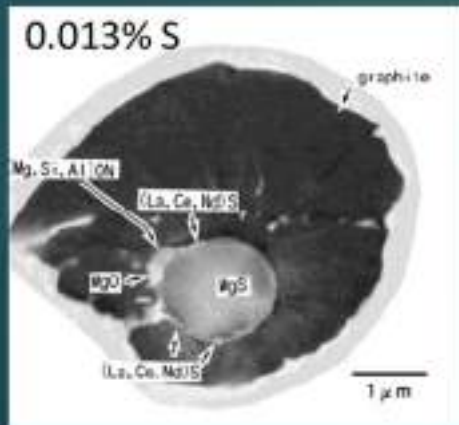
- ▶ $Ti \leq 0.011\%$ $MgO \rightarrow (MgCa)S$ or $MgO \rightarrow (MgCa)S \rightarrow (MgSiAl)N$
- ▶ $Ti = 0.014\%$ $MgO \rightarrow (MgCa)(OS)$ or $(MgCa)S \rightarrow (MgSiAl)N$
- ▶ $0.02\% \leq Ti \leq 0.03\%$ $(MgCa)S$ or $(MgCa)(OS) \rightarrow Ti(CN)$ or/and $(MgSiAl)N$
- ▶ $Ti = 0.036\%$ $(MgCa)S$ or $(MgCa)(OS) \rightarrow Ti(CN)$



Nucleation of Graphite during Solidification

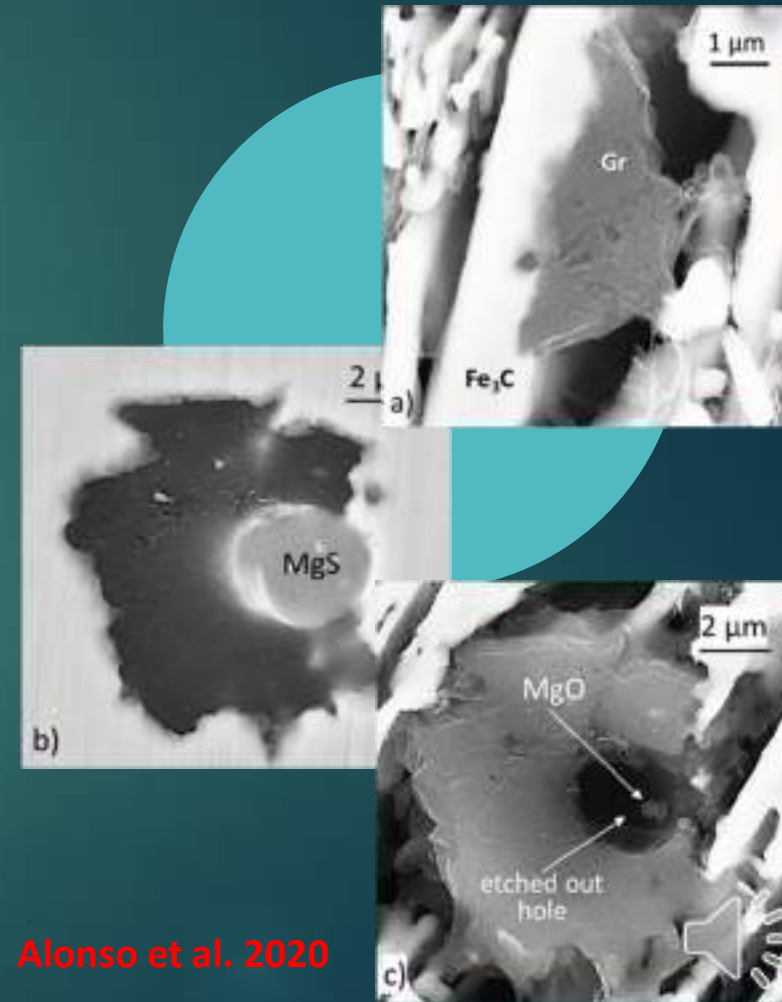
Nucleation on complex compounds – *Effect of %S*

- ▶ In irons free of Ti, (MgSiAl)N was found in most samples
- ▶ At S > 0.013%, MgS with an oxide core is most frequent
- ▶ Lanthanides and Ce sulfides may partially cover the MgS
- ▶ Common sequential nucleation *oxide* → *sulfide* → *nitride*



Nucleation of graphite during solid-state transformation – *Annealed (malleable) iron*

- ▶ In the absence of Mg, nucleation occurs on the pre-existing iron carbide plates (Fig. a)
- ▶ In a limited number of cases, sequential nucleation $\text{MgO} \rightarrow \text{MgS}$ was observed on residual oxides/sulfides coming from the charge materials that included SG iron returns (Fig. b,c)
- ▶ Additions as low as 0.017% Mg induced significant nucleation in the liquid with the formation of new Mg or complex Mg sulfide and oxide inclusions, on which most nucleation occurred during subsequent annealing



Alonso et al. 2020

Outline

- ▶ Introduction
- ▶ Background and some basic concepts
- ▶ Nucleation of graphite
 - ▶ During solidification
 - ▶ During the solid-state transformation
- ▶ Growth of graphite during solidification
- ▶ Solid-state growth of graphite
- ▶ Conclusions



Growth of graphite during solidification

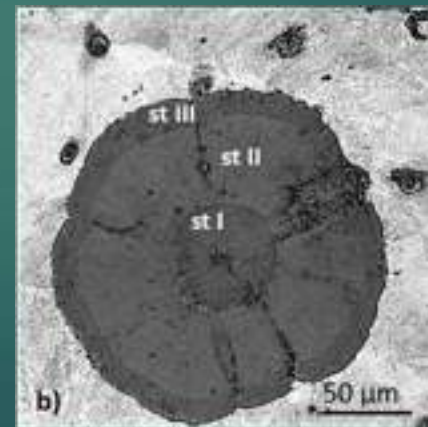
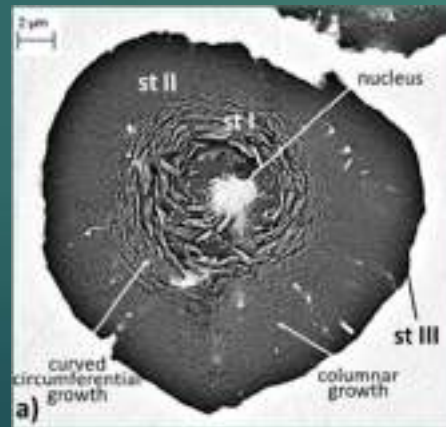
- ▶ Industrial cast irons exhibit a large variety of graphite morphologies:
 - “standard” shapes: lamellar (LG), compacted (CG), spheroidal (SG), and temper or aggregated graphite (in malleable iron)
 - “degenerated” morphology: such as spiky, exploded, or chunky graphite
- ▶ This wide variation in shape and crystallography is a consequence of the chemical complexity of the iron melts, and the transitory nature of nucleation, local segregation and cooling rate during solidification
- ▶ Room temperature graphite morphology in cast Fe-C alloys is the result of crystallization from the liquid, initially controlled by attachment kinetics, and then by crystallization and growth in the austenite, pearlite or ferrite, controlled by carbon diffusion.



Growth of graphite during solidification

Growth of spheroidal graphite – *Growth stages*

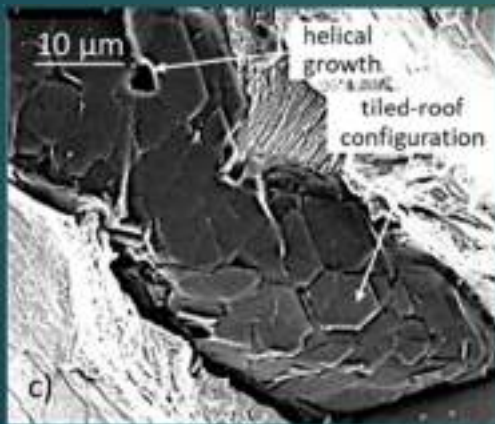
- ▶ The graphite spheroid is the product of several growth stages:
 - curved circumferential growth in contact with the liquid (stage I)
 - columnar-layer growth through an austenite shell during the eutectic reaction (stage II)
 - growth during the solid-solid transformation (stage III).
- ▶ However, in many instances, graphite spheroids with only 1 or 2 stages are found.



Growth of graphite during solidification

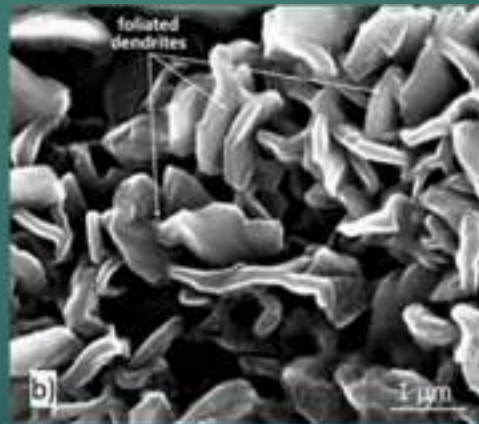
Growth of spheroidal graphite – *Current understanding*

At low undercooling and supersaturation graphite grows in the general *a*-direction as large plates made of hexagonal faceted platelets distributed in a tiled-roof configuration (Fig. c).



lamellar graphite

As the driving force increases, graphite platelets begin stacking in the *c*-direction forming foliated dendrites (Fig. b).



compacted graphite

Upon further increase in undercooling and supersaturation following additions of graphite compacting elements (e.g., Mg, Ce) or higher cooling rate, foliated graphite platelets stack increasingly along the *c*-direction, producing polyhedral blocks (Fig. c).



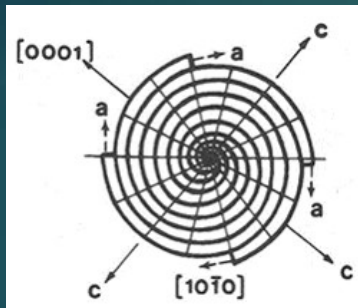
compacted graphite



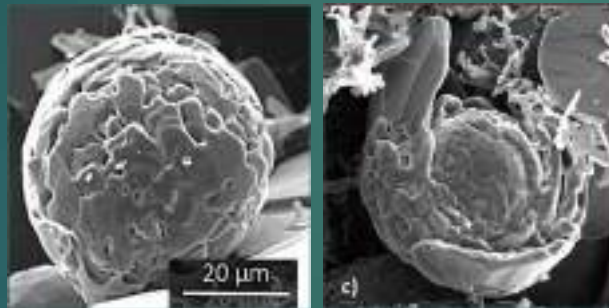
Growth of graphite during solidification

Growth of spheroidal graphite – Stage I

- ▶ The growth in the early stages of solidification (stage-I) is consistently explained by the curved-circumferential crystal growth mechanism



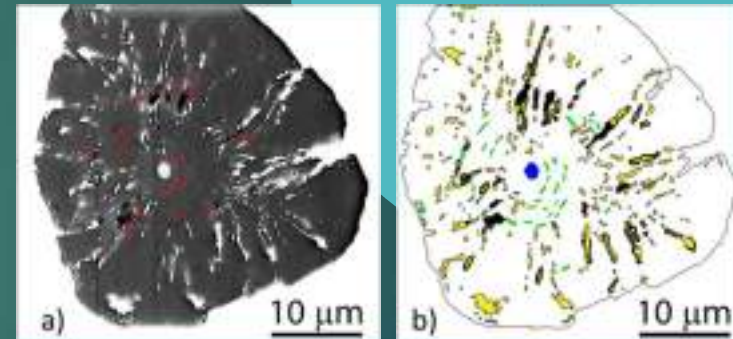
Sadocha/Gruzleski 1975



Amini/Abbaschian 2013

- ▶ It is supported by plasma, thermal or chemical etching micrographs on Fe-C-Si and Ni-C alloys.

- ▶ High-resolution focused ion beam (FIB) 3D tomography confirmed the existence of 2 stages through the observation of concentric voids in the central region (circumferential growth) and radially oriented voids in the outside region (sector growth)



Ghassemali et al. 2019

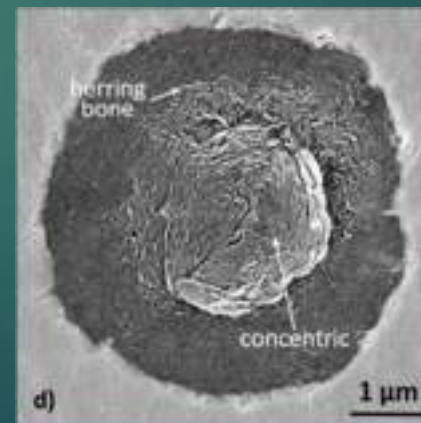
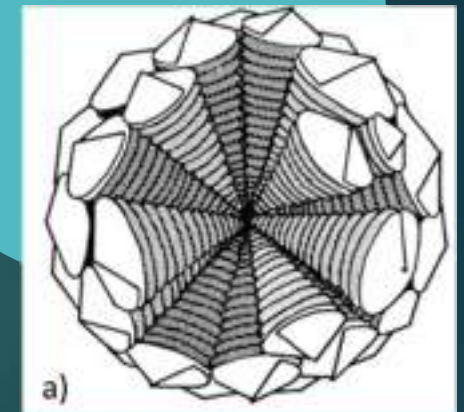
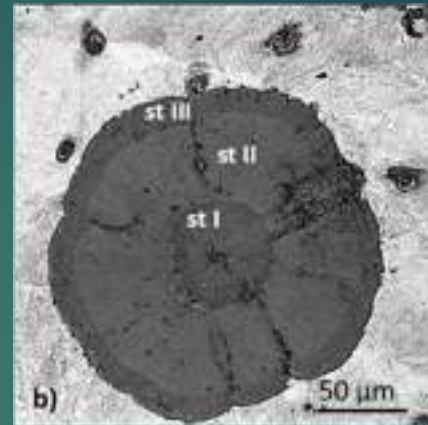
- ▶ The curved platelets are not always in direct contact along the planes (Fig c); thus, a curved-circumferential foliated dendrite growth can also be envisioned



Growth of graphite during solidification

Growth of spheroidal graphite – Stage II

- ▶ For stage II, the images in Fig. b suggest a radial growth of cylindrical columns or of conical sectors, similar to the pyramidal sectors found in ice and silicon crystals.
- ▶ The cone-helix model postulated by **Double and Hellowell 1974**, based on positive wedge disclination, explains this type of growth (Fig. a)
 - It explains the *herring-bone* appearance of graphite platelets in some spheroids (Fig. b)
 - It is consistent with the observation that the growing ends of whiskers produced through carbon pyrolysis assumed a conical shape



Growth of graphite during solidification

Growth of spheroidal graphite – Stage II and cylindrical columns

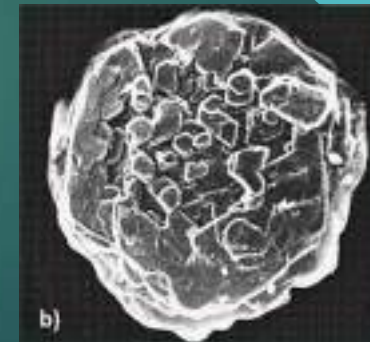
- ▶ Neither the curved circumferential growth, nor the con-helix model can explain the growth of cylindrical columns observed in ice crystals, Al-Si alloys, metamorphic graphite (*Fig.*), Ni-C alloys (*Fig. e*) and in Fe-C-Si alloys
- ▶ Apparent nucleation of new crystals found on polyhedral ice plates and on metamorphic graphite (*Fig. b*) may point to the possibility that poly-nucleation may explain the growth of such shapes.
- ▶ Alternatively, as the platelets of the column present clear separations, they could be the result of foliated crystal stacking through foliated growth.



metamorphic graphite



Ni-C alloys



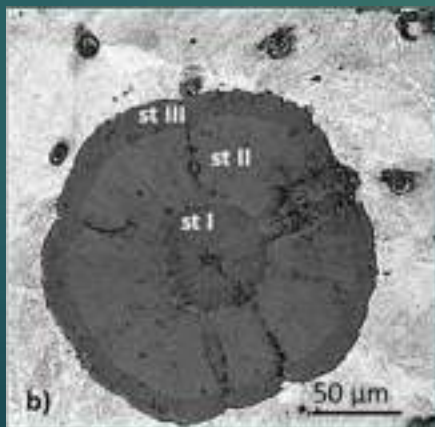
metamorphic graphite



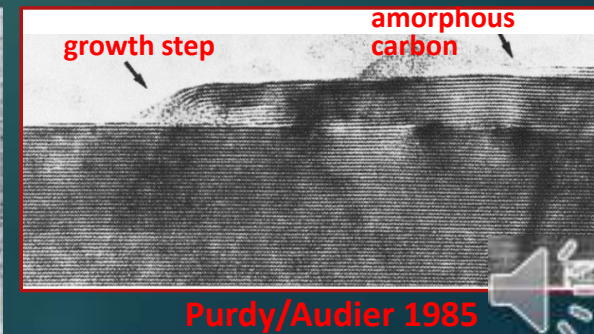
Growth of graphite during solidification

Growth of spheroidal graphite – *Stage III*

- ▶ The decreased carbon solubility in the austenite with lower temperature produces carbon atoms migration to the growing graphite - stage-III graphite growth.
- ▶ High diffusion rates may result in recrystallization of carbon, and thus, in the morphing of stage-III microstructure into the conical sector structure of stage-II



- ▶ Examples of crystallization of amorphous carbon to form spheroids are also found for processes unrelated to metal casting, such as heating of amorphous carbon in an electronic beam.
- ▶ Crystallization of the amorphous carbon can occur at all stages of solidification. It may thicken the existing platelets or grow new platelets. It may fill the spaces between the columnar crystals or not.



Growth of graphite during solidification

Growth of spheroidal graphite – *Early theories*

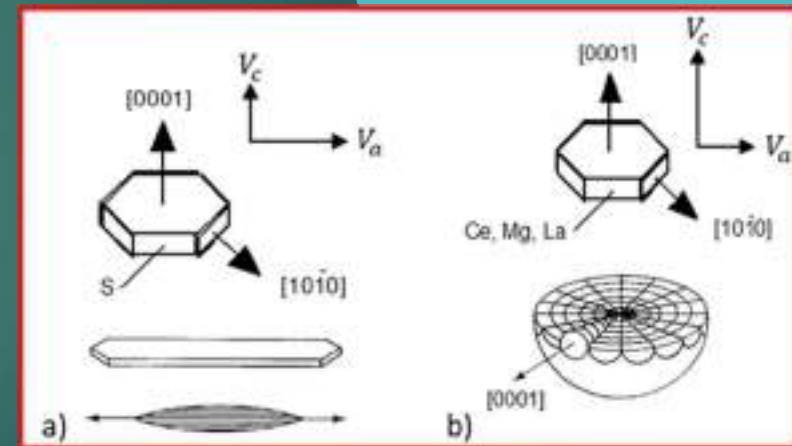
Morrogh 1955

Twisted graphite crystals radiating from a common center



Herfurth 1965

Interplay between the growth velocity of the basal face (0001) and the prism face ($10\bar{1}0$) of the graphite crystal



Growth of graphite during solidification

Growth of spheroidal graphite – *Early theories*

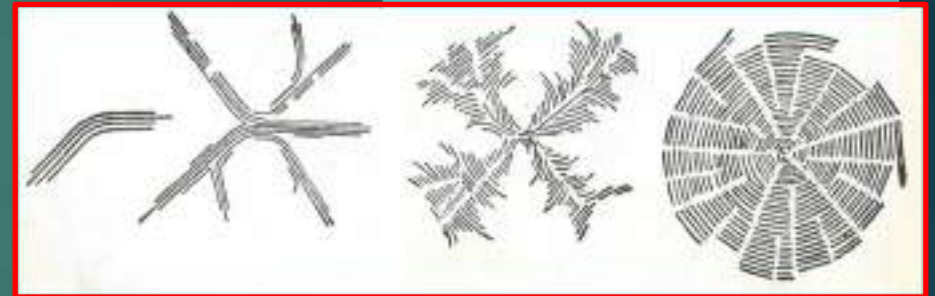
Vertman & Samarin 1969

Splitting of graphite platelets because of adsorption of Mg



Bunin et al. 1969

Branching of LG to form SG

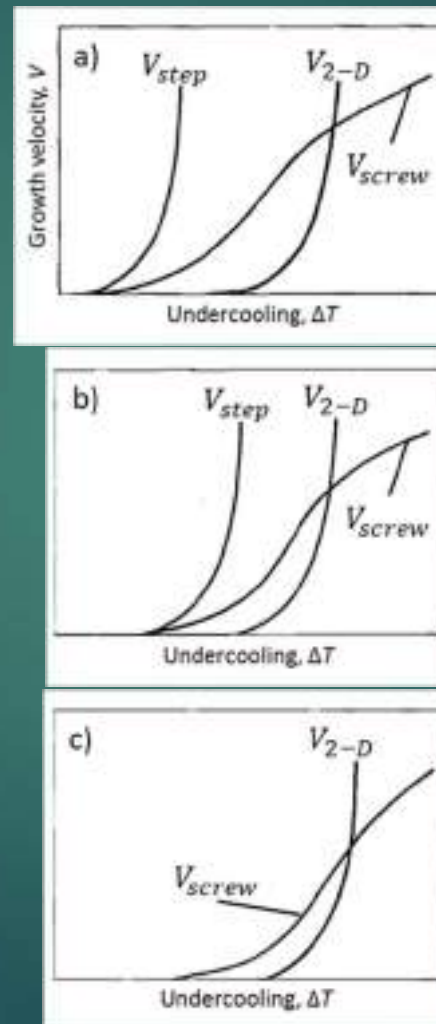


Growth of graphite during solidification

Growth of spheroidal graphite

defect growth of graphite - growth occurs from steps on the graphite layers **Minkoff/Lux 1975**

- ▶ *2-D nucleation or step at twisted boundary*- mechanisms governed by exponential laws; apply to the prism surfaces of graphite
- ▶ *spiral growth of screw dislocations* - governed by a parabolic law and applies to the basal surfaces



When surface-active impurities (e.g. S) are present in the melt, (Fig. a), the curve for growth on the step of a defect boundary, V_{step} , is at a lower undercooling than those for growth by 2-D nucleation, V_{2-D} , or by screw dislocation, V_{screw} . Thus, defect boundary growth is dominant.

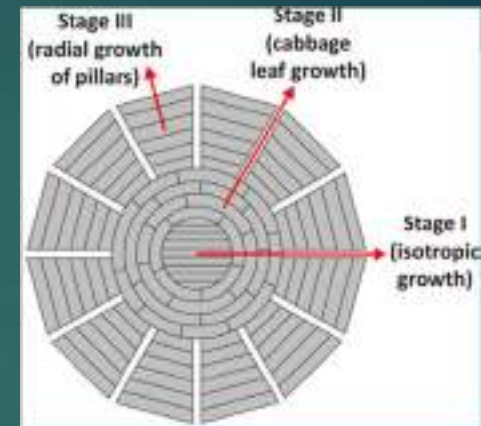
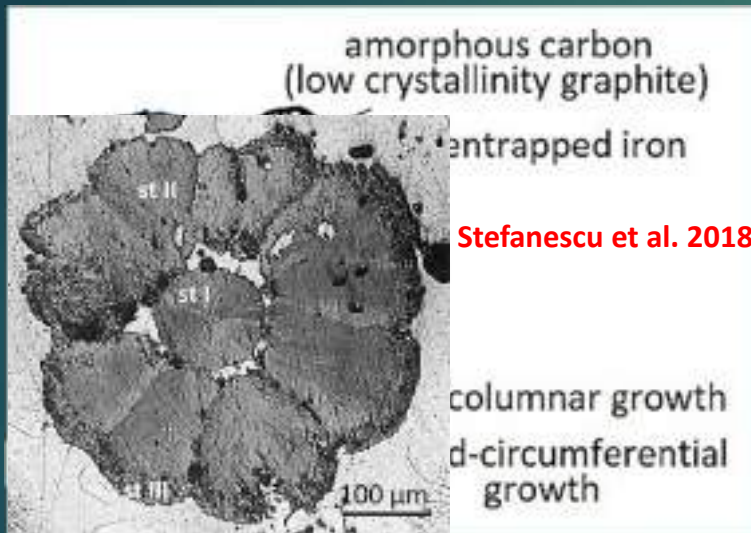
In a pure melt or at high cooling rate, the growth velocity curves are displaced to higher undercooling (Fig. b). This allows growth through screw dislocations. SG forms

Impurities react with the surface-active elements and neutralize growth on twist boundary, leaving only the curves for V_{2-D} and V_{screw} displaced to greater undercooling (Fig. c)



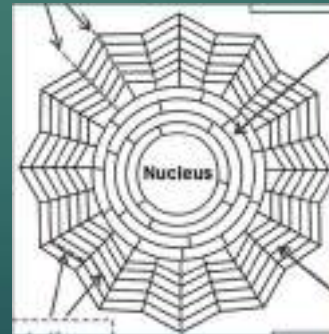
Growth of graphite during solidification

Growth of spheroidal graphite - *Recent models*



Amini/Abbaschian 2013

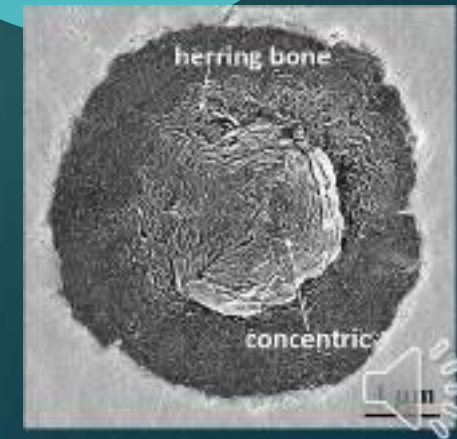
tilt/twinning
boundaries



circumferential growth
of curved graphene layers

radial growth
of conical structures

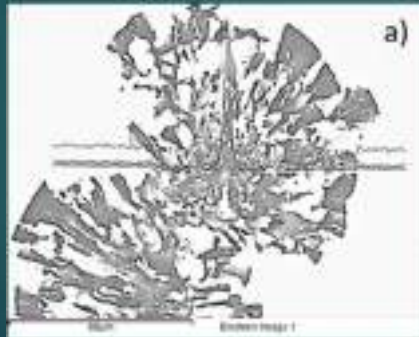
Qing et al. 2017



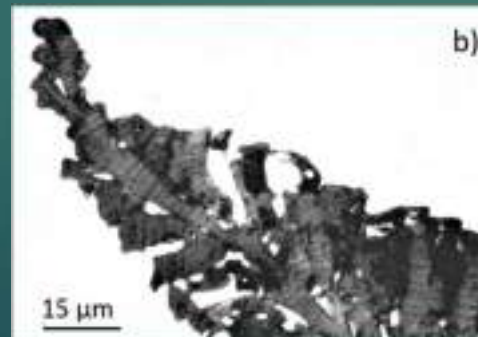
Growth of graphite during solidification

Growth of degenerated graphite

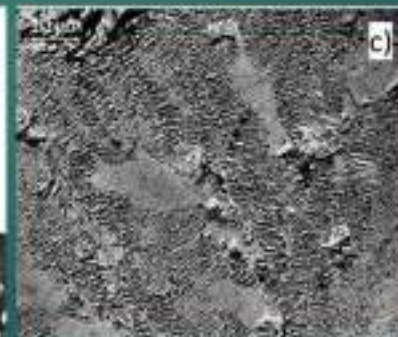
- ▶ Graphite degeneration may start with the separation of the conical graphite columns (Fig.)
- ▶ Many forms of degenerated graphite: dendritic, exploded, chunky, and spiky.
- ▶ Graphite dendrites were observed in Sb containing CG irons (Fig. a) and in slow-cooling Ce-treated SG irons (Fig. b).
- ▶ Unlike the common stem-dendrites in LG iron that grow along the *a*-direction, the dendrites in Mg or Ce-treated irons are stacked in the *c*-direction (Fig. c).



Stefanescu et al. 2016



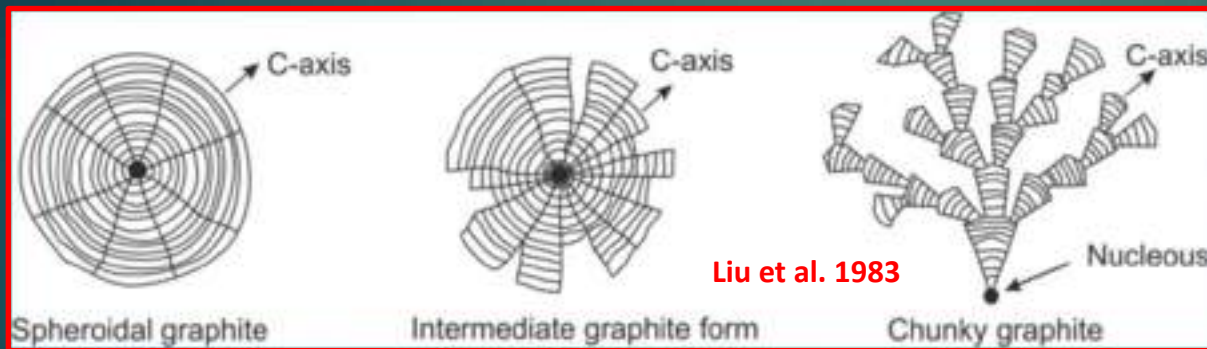
Hamasumi 1965



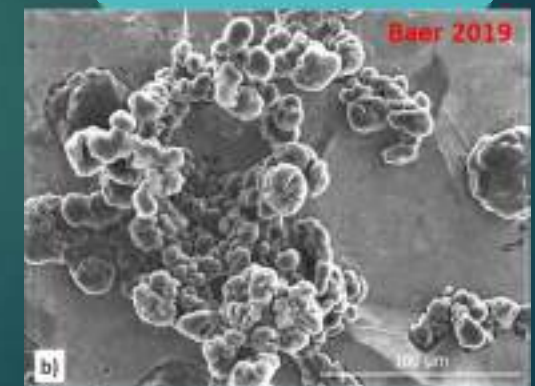
Growth of graphite during solidification

Growth of chunky graphite (CHG)

- ▶ The schematic representation in the Fig. captures two important elements of the morphology of CHG, the radial growth and the interconnection of various segments.



Interconnected CHG



Chain-linked graphite spheres

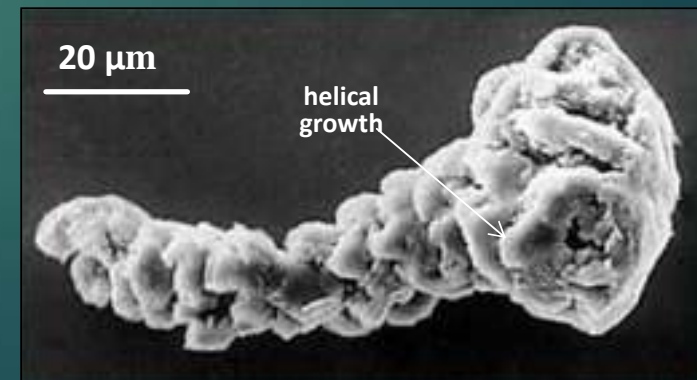
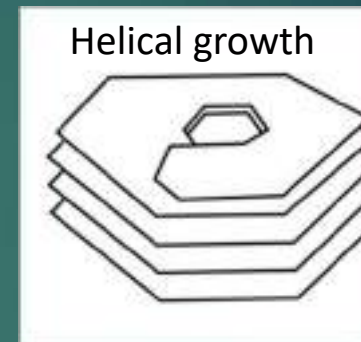
- ▶ Interconnection is always seen, but radial growth is not always present.
- ▶ However, Baer 2019 concluded that chunky graphite in these materials exhibits the same microstructural features as typical for conventional ferritic SG irons.



Growth of graphite during solidification

Growth of chunky graphite (CHG)

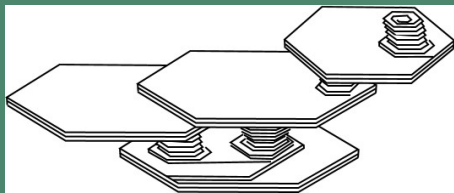
- ▶ TEM images of dendritic and CHG graphite show that the aggregate is made of graphite layers stacked in the *c-direction*
- ▶ Hexagonal blocks obtained by ultrasonic vibration breaking of CHG aggregates exhibited parallel graphite platelets; conclusions: **Itofuji/Uchikawa 1990**
 - ▶ no spiral growth
 - ▶ the basic substructure of CG, SG and CHG is the same; they grow through the same mechanism,
- ▶ This idea also supported by **Lacaze et al.** based on TEM work
- ▶ However, the helical growth of chunky graphite has been documented.



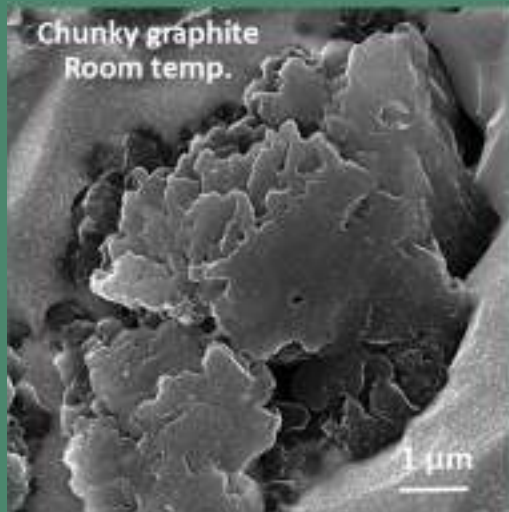
Growth of graphite during solidification

Growth of chunky graphite (CHG)

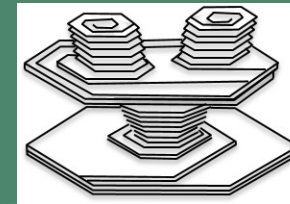
Foliated dendrites



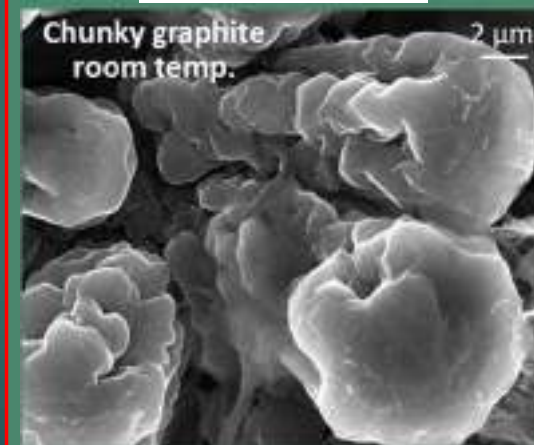
Chunky graphite
Room temp.



Foliated crystals stack into
clusters of polyhedral blocks



Chunky graphite
room temp.



Growth of graphite during solidification

Growth of graphite – *Lamellar-to-spheroidal transition*

- ▶ In Mg-treated irons graphite growth takes place through a multitude of mechanisms as a function of the local conditions (undercooling, supersatation) at the solidifying interface
- ▶ Schematic representations of graphite growth can give a general idea of the transitions from lamellar to spheroidal graphite
- ▶ The difference between the schematics in the figs. is in the proposed mechanisms for the LG-to-SG transition:
 - **Bunin** – branching of graphite lamellae
 - **Stefanescu** – stacking of graphite platelets



Bunin et al. 1969

Branching of LG to form SG



(a) tiled-roof lamellar graphite; (b) curly, lamellar and compacted graphite; (c) chunky and degenerated spheroidal graphite; (d) spheroidal graphite



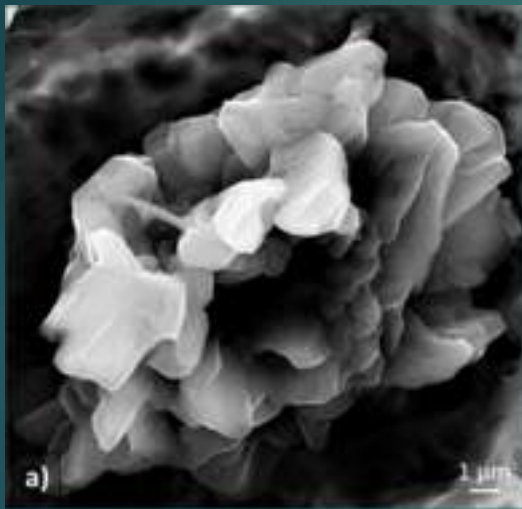
Outline

- ▶ Introduction
- ▶ Background and some basic concepts
- ▶ Nucleation of graphite
 - ▶ During solidification
 - ▶ During the solid-state transformation
- ▶ Growth of graphite during solidification
- ▶ Solid-state growth of graphite
- ▶ Conclusions

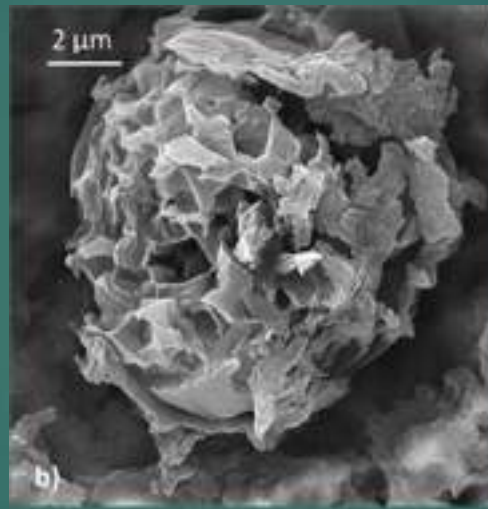


Solid-state growth of graphite

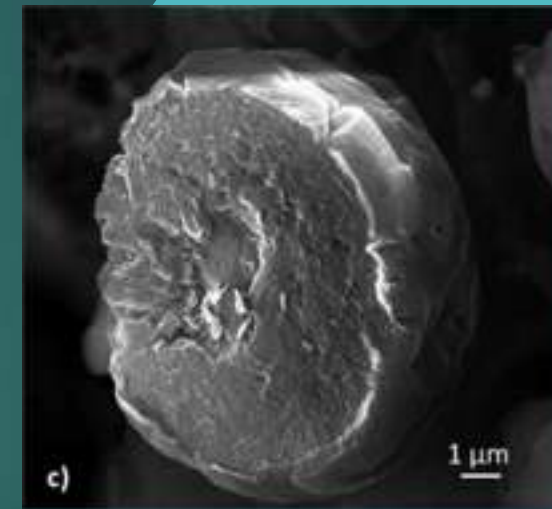
Annealed iron - *Effect of %Mg*



a)
irregular graphite in
no Mg iron



b)
skeletal-hopper graphite in
0.017% Mg iron

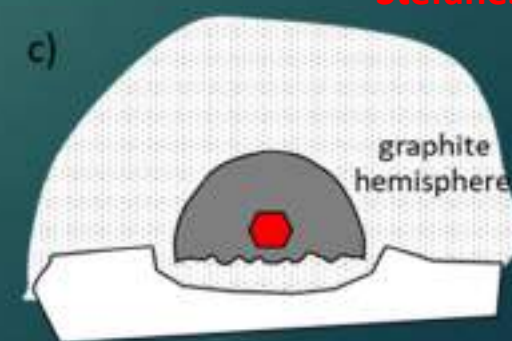
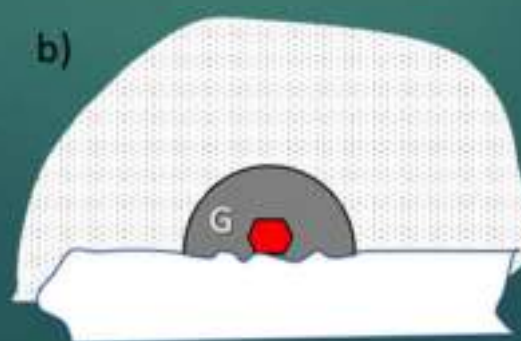
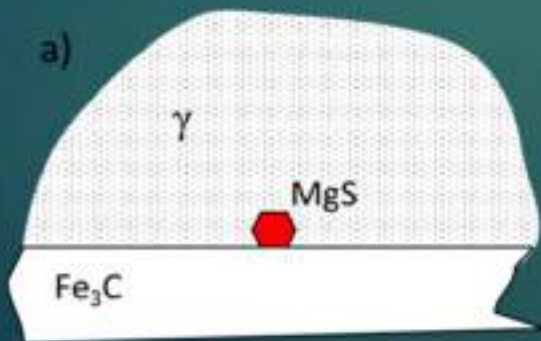
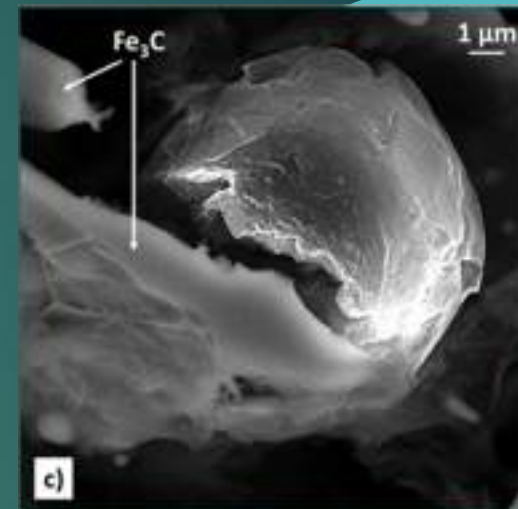
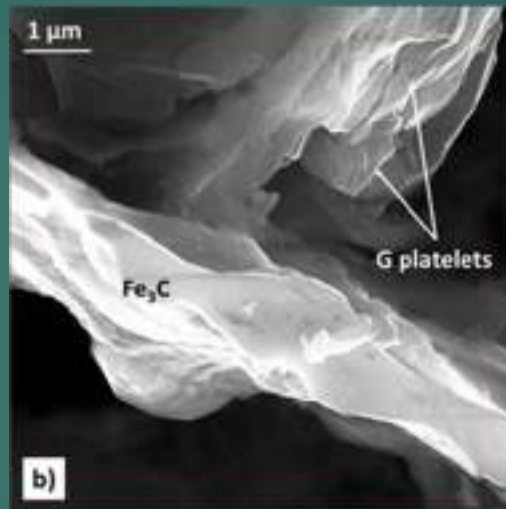
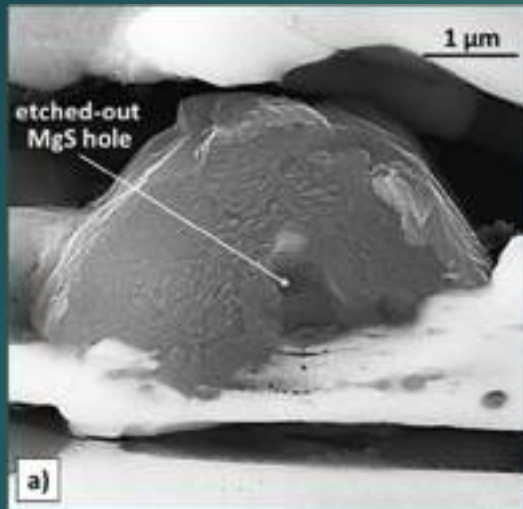


c)
hemispherical graphite in
0.047% Mg iron



Solid-state growth of graphite

Annealed iron – Graphite hemispheres in 0.047%Mg iron



Stefanescu et al. 2020



Conclusions

- ▶ Both nucleation and growth of spheroidal graphite are complex phenomena controlled by thermodynamics, attachment kinetics, melt supersaturation and undercooling
- ▶ These phenomena are controlled in practice by technology factors such as melt chemistry, inoculation, cooling rate, furnace atmosphere etc.
- ▶ The abundance of experimental and theoretical information available to the researcher can be conducive to a variety of conclusions
- ▶ It is best to leave this conclusions to the creative minds of the scientist that have listened to this talk





www.researchgate.net/profile/Doru_Stefanescu2/publications





19th INTERNATIONAL FOUNDRYMEN CONFERENCE

Humans - Valuable Resource for Foundry Industry Development

Split, June 16th-18th, 2021

<https://ifc.simet.hr/>

INFLUENCE OF ELEVATED WORKING TEMPERATURES ON MECHANICAL PROPERTIES OF AUSTEMPERED DUCTILE IRON

Hasan Avdušinović^{1*}, Almaida Gigović-Gekić¹, Šehzudin Dervišić²

¹ University of Zenica Faculty of Metallurgy and Technology, Zenica, Bosnia and Herzegovina

² University Džemal Bijedić Mostar Doctoral Study Politehnica, Mostar, Bosnia and Herzegovina

Invited lecture

Original scientific paper

Abstract

Austempered Ductile Iron (ADI) is a class of ductile iron subjected to a specific heat treatment process (austenitization and austempering). The heat treatment gives to that type of Ductile Iron excellent mechanical properties. The high mechanical properties (tensile strength, hardness and impact energy) of ADI are the result of its unique ausferrite microstructure. In this paper an example of influence of elevated operating temperatures on the mechanical properties of the ADI samples is presented. Mechanical properties of the additionally treated ADI samples were changed due to decomposition of the ausferrite microstructure especially in the temperature region higher than 450 °C. The ADI samples were additionally heat treated at 250 °C, 350 °C, 450 °C, 500 °C, 600 °C, and 700 °C for two hours respectively and correlation between applied temperature and mechanical properties due to decomposition of the ausferrite microstructure were investigated.

Keywords: *austempering, ausferrite microstructure decomposition, isothermal treatment, tensile strength, mathematical modeling*

*Corresponding author (e-mail address): hasan.avdusinovic@unze.ba

INTRODUCTION

Austempered Ductile Iron (ADI) is the most prominent achievement so far in cast iron metallurgy. The relatively simple heat treatment, low cost and very interesting combination of strength properties, toughness and wear resistance, make it so attractive material for many applications. Mechanical properties of ADI can vary over a wide range of values depending on the parameters selected in the manufacturing process [1, 2]. Mechanical performance values are defined by certain standards such as American ASTM A897/897M or European EN 1564 [3,4]. There have been extensive interests in the processing and development of ADI during last two decades and extensive research efforts are still underway. This is a type of cast iron that ideally fits between the properties of gray and

steel cast iron, combining strength and ductility, and in a very short time has found wide application. Heat treatment technology for obtaining ADI involves austenitization in the temperature range 850 – 920 °C, followed by tempering in the temperature range 260–420 °C (Figure 1.).

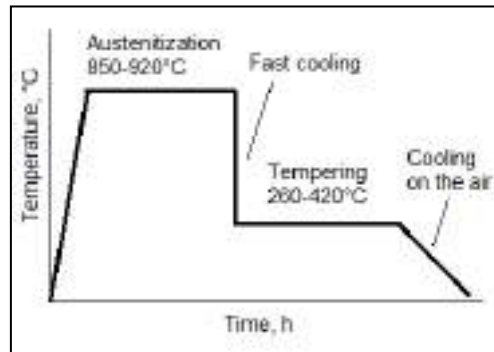


Figure 1. Austempering process

During tempering two stage transformations process can be seen. In the first stage, austenite (γ) transforms into ferrite (α) and carbon enriched austenite (γ_{HC}), Equation (1).



If the heat treated material is held at austempering temperature for too long it will undergo a second stage transformation process. During the second stage, the carbon enriched austenite (γ_{HC}) further transforms into ferrite (α) and carbide (ϵ), Equation (2) [5].



In this case heat treated material will contain a large amount of carbide and this makes the material very brittle. Therefore reaction presented with Equation (2) is undesirable and has to be avoided.

Factors affecting mechanical properties of the ADI castings are:

- Chemical composition and alloying elements,
- Temperature and time of austenitization,
- Temperature and time of austempering,
- Casting design and cooling rate.

The base material for the production of Austempered Ductile Iron is ductile cast iron. Ductile cast iron is a type of cast iron with spherical graphite. The ductile form of graphite is most commonly achieved by the addition of magnesium to molten iron, whereby the morphology and amount of nodules are primarily regulated by the addition of inoculants before the crystallization process. Quality ductile cast iron is considered to have a nodularity greater than 90 %, while ASTM A897M-06 recommends a minimum nodularity of 80 % and a number of nodules of 100/mm² for the ADI castings production. Liquid metal production involves melting the input material and preparing the melt. The quality of the liquid metal depends on the quality of the charged material, control of the melting process, melt

preparation, nodulation, and inoculation. Sorelmetal, steel scrap and return (circular) material are most commonly used to produce high-quality ductile cast iron. In addition to the basic materials for the preparation of ductile cast iron, additives are used, if necessary FeSi, FeMn, FeMo, and CaC₂, SiC carbides. The purpose of the additive addition is to obtain the prescribed chemical composition in mass% according to ASTM A897M-06 for ductile iron [5]. Table 1 shows the recommended chemical composition of ductile iron in mass% according to ASTM A897M-06.

Table 1. Recommended chemical composition of ductile iron in mass % (ASTM A897M-06)

%C	%Si	%Mn	%S	%P	%Mg
3.60±0.2	2.50±0.2	0.35±0.05	0.02 max	0.04 max	(%Sx0.76)+0.025±0.0025

For the production process of austempered ductile iron, it is necessary to have good quality casting (whitout visible and hidden defects) known chemical composition, whit properly conducted inoculation in order to reduce the risk of possible segregation. ADI material has a 10% lower specific density than steel, as well as lower production costs of up to 50% compared to steel forgings, so it is increasingly being used as a replacement for parts made of forged or cast steel. The most influential parameter affecting the mechanical properties of ADI materials is the tempering temperature. Transformation at higher tempering temperatures (330 do 400 °C) achieves high ductility and toughness, but less tensile strength and hardness. However, transformation at lower tempering temperatures (250 do 330°C) achieves high tensile strength, hardness and abrasion resistance, and less toughness. The mechanical properties depend on the final microstructure, which at higher temperatures of austempering contains a higher amount of residual austenite, haveing higher toughness, while at lower temperatures a finer microstructure is present (nice aciculare ferrite needles) with less retained austenite, haveing higher strength and hardness [6]. The mechanical characteristics of ADI materials according to ASTM standard A897/897M and European standard EN1564 are shown in Tables 2 and 3.

Table 2. Mechanical properties according to ASTM standard A897/897M

No.	Tensile strength (MPa)	Elongation (%)	Impact energy (MPa)	Hardness (HB)
1	850	10	100	269-321
2	1050	7	80	302-363
3	1200	4	60	341-444
4	1400	1	35	366-477
5	1600	N/A	N/A	444-555

Table. 3. Mechanical characteristics according to EN 1564

Class	Tensile strength (MPa)	Rp _{0.2} (MPa)	Elongation (%)	Hardness (HB)
800	800	500	8	260-320
1000	1000	700	5	300-360
1200	1200	850	2	340-440
1400	1400	1100	1	380-480

MATERIALS AND METHODS

Testing material

Ductile cast iron of conventional composition was used in the present investigation as a base material for ADI production. The detailed chemical composition of the base material is presented in Table 4.

Table 4. Chemical composition of ductile cast iron (%)

C	Si	S	P	Mn	Mg	Cu	Ni
3.2	2.67	0.007	0.0424	0.291	0.0487	0.0461	0.0598

The microstructure of the ductile cast iron is shown in Figure 2.

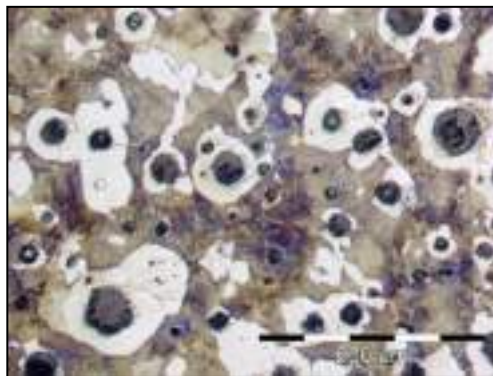


Figure 2. Microstructure of ductile cast iron (200x, Nital)

Ductile cast iron was cast in the form of U blocks. From these U blocks tensile test samples according BAS EN 6892-1/17 [7] and impact energy samples according ASTM A897/897M were prepared. Hardness testing according BAS EN 6507-1/2007 were carried out on impact energy samples [8]. A schematic draw of tensile test sample and impact energy sample used for investigation are shown in the Figures 3 and 4.

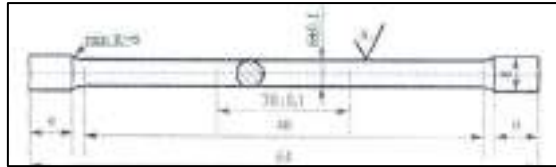


Figure 3. Tensile test specimen(measures in mm)

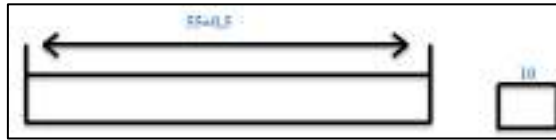


Figure 4. Impact energy specimen (measures in mm)

Heat treatment for ADI production

Heat treatment process for ADI samples production was conducted according heat treatment diagram presented on Figure 5.

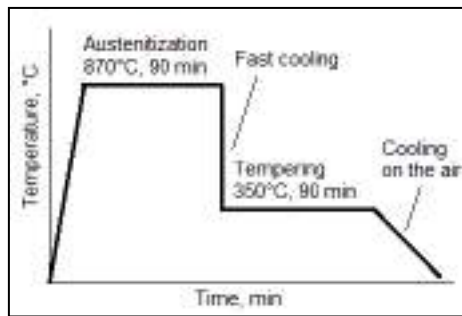


Figure 5. Heat treatment diagram for ADI sample production

Heat treatment for ADI samples production finished at Faculty of Metallurgy and Technology (Laboratory for metallography and heat treatment). For austenitization laboratory furnace without protective atmosphere and for tempering KNO_3 salt bath was used. To confirm quality of the heat treatment parameters and the used equipment trial test of two sets of sample were heat treated (two tensile test samples and six impact energy test samples). Microstructure of the ADI sample is presented on the figure 6 and mechanical properties of the ADI samples are presented in Tables 5, 6, and 7.

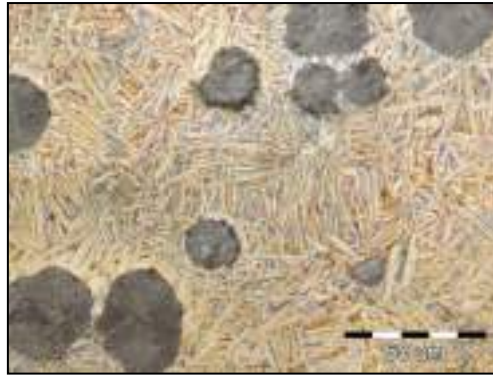


Figure 6. Microstructure of the ADI sample (500x, Murakami)

Table 5. Tensile strength of the ADI samples

No.	Diameter (mm)	Surface (mm ²)	Tensile strength (N/mm ²)
1	6.02	28.45	1102
2	6.02	28.45	1108

Table 6. Impact energy of the ADI samples

No.	Length (mm)	Width (mm)	Height (mm)	Values (J)
1	55.15	9.95	10.03	140
2	55.20	9.96	10.04	165
3	55.15	10.02	10.02	129
4	55.10	10.04	10.03	160
5	55.10	10.05	10.02	141
6	55.20	10.01	10.03	162

Table 7. Hardness of the ADI samples

No.	1	2	3	4	5	Average
Values (HB)	228	230	230	235	238	232

Ausferritic microstructure presented on the Figure 6, and mechanical properties of the treated samples, after trial test, presented in the Tables 5, 6, and 7 indicate that the heat treatment parameters were correct for continuation of the experimental procedure.

For testing influence of the elevated operating temperatures to mechanical properties of the ADI additional six sets of sample were prepared and treated according heat treatment diagram presented on Figure 5. Each of prepared six sets consists of 12 samples (3-tensile test samples and 9-impact energy samples).

Additional heat treatment of ADI samples

To test influence of the elevated working temperatures on mechanical properties of ADI each of already prepared six sets of ADI samples was reheated to different temperature and

hold for two hours and than cooled on the air to room temperature. The diagram of additional heat treatment of ADI samples is presented on Figure 7.

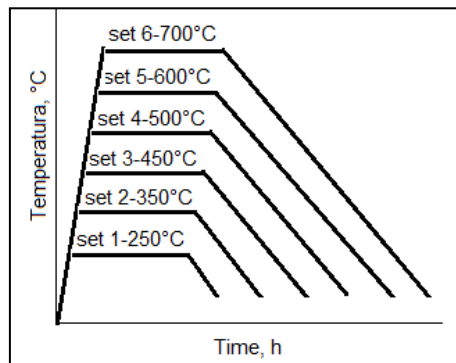


Figure 7. Additional heat treatment of the ADI samples

After additional heat treatment mechanical properties investigation of the treated samples were conducted. The same set of properties were investigated for all samples (volume fraction of the retained austenite, tensile strength, impact energy, and hardness). All mechanical property testing were conducted at Institute 'Kemal Kapetanovic' in Zenica using calibrated equipment according above mentioned standards. For investigation of volume fraction of retained austenite in the re-heated ADI samples Feritiscop was used.

RESULTS AND DISCUSSION

Results of the mechanical properties investigation

After additionally heat treatments of the prepered sets of samples all samples were tested and results are presented in Tabel 8.

Tabele 8. Average propertiy values of the additionally heat treated samples

Property	Set 1	Set 2	Set 3	Set 4	Set 5	Set 6
Volume fraction of the retained austenite, (%)	35.35	35.85	19.25	13.95	9.25	0.75
Tensile strength, (N/mm ²)	1104	1135	1145	1082	914	567
Impact mpact energy, (J)	153	140	56	63	88	121
Hardness, (HB)	229	210	246	233	121	154

Average values of the investigated properties of the additionally treated samples are presented on the Figures 8 to 11.

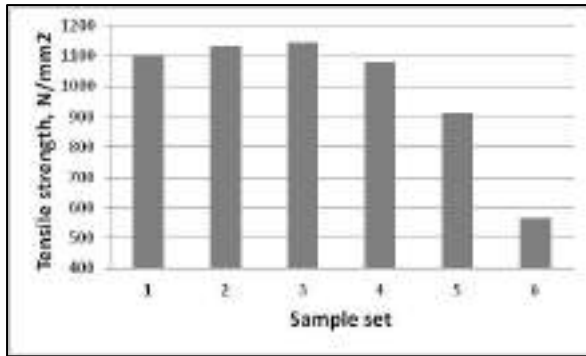


Figure 8. Tensile strength of the samples

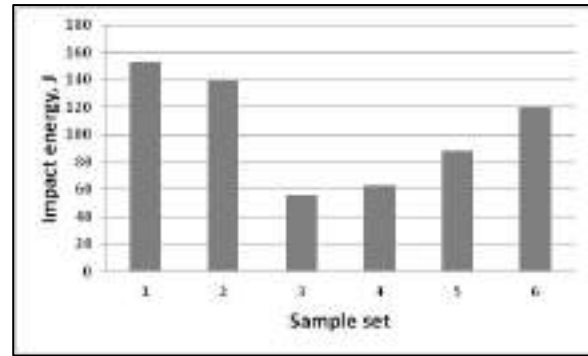


Figure 9. Impact energy of the samples

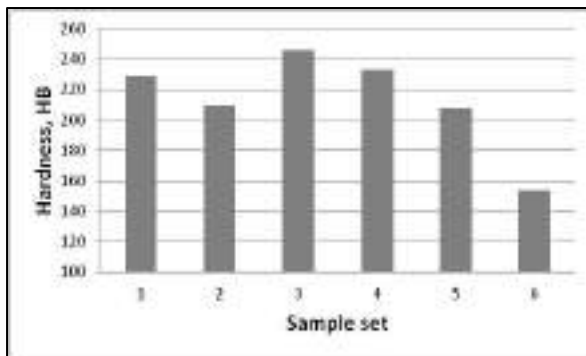


Figure 10. Hardness of the samples

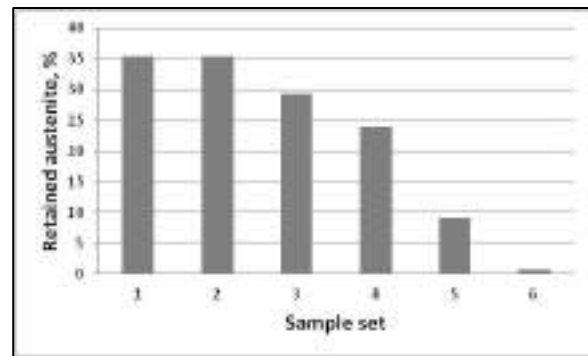


Figure 11. Volume fraction of retained austenite

Mathematical models on mechanical properties, temperature and volume fraction of retained austenite

Preliminary analysis of the obtained results showed a clear dependence of the tensile strength of the treated material on the temperature and the degree of transformation of the initial microstructure, i.e. the transformation of retained austenite. Having in mind the existing dependence, the next step of processing and analysis of the results was done with the aim of formulating a mathematical model of the dependence of the obtained parameters. The influence of temperature (x_1) and the volume fraction of retained austenite (x_2) on the mechanical properties (Y) were analyzed using certain regression model. The values of the variables x_1 , x_2 and Y used for calculation are given in Table 8.

The analysis of the existing dependence was performed using linear regression model (note: the model is linear if the regression function is linear in unknown parameters). The proposed model (first order model with interaction with ε representing measurement error) is presented by Equation 3 [9].

$$Y = \beta_0 + \beta_1 x_1 + \beta_2 x_2 + \beta_3 x_1 x_2 + \varepsilon \quad (3)$$

The higher order models are meaningless to consider because the number of parameters (6 or more) is equal/higher than the sample size ($n=6$). Such models would fit the data perfectly, which does not mean that it would be useful for reliably predicting the value of a dependent variable. Using a model with too many parameters arise the problem of so-called

over fitting [10]. One of the common indicators of model adequacy is the coefficient of determination R^2 . However, the problem with the coefficient of determination is that it can be inflated by too many predictors in relation to the sample size. Therefore, it is more reliable to use the adjusted coefficient of determination (R^2_a) that takes into account the size of the model (i.e. the number of parameters). For this reason, and given the small size of the sample in the observed case ($n = 6$), additional caution is required when validating the adopted model. The results of regression analysis for proposed model are presented in Table 9. The basic data of regression analysis for proposed model are summarised and presented in Tables 10 and 11.

Table 9. Evaluation results for the proposed model

Regression Statistics		ANOVA					
Multiple R	0.999497		df	SS	MS	F	Signific.F
R Square	0.998994	Regression	3	250954.1	83651.37	661,971	0.001509
Adjusted R Square	0.997485	Residual	2	252.7342	126.3671		
Standard Error	11,24131	Total	5	251206.8			
Observations	6						
	Coefficients	St. Error	t Stat	P-value	Lower 95%	Upper 95%	
Intercept	2132,428	88.08181	24,2096	0.001702	1753,442	2511,413	
X_1	-2.25029	0.129321	-17.4009	0.003286	-2.80671	-1.69387	
X_2	-31.9632	1,811137	-17.6482	0.003195	-39.7559	-24.1706	
X_1X_2	0.074769	0.002945	25,390 6	0.001548	0.062099	0.087439	

Table 10. Results of analysis of variance for proposed model

Variable included	Regression sum of squares	Residual sum of squares	Determination coefficient R^2 (adjusted)	Determination coefficient R^2	Standard error
X_1, X_2, X_1X_2	250954.1	126.3671	0.997485	0.999497	11.24131

Table 11. Linear regression coefficients for proposed model

Variable included	b_0	b_1	b_2	b_3
X_1, X_2, X_1X_2	2132.428	-2.25029	-31.9632	0.074769

In order to be able to talk about the adequacy of the proposed models, it is necessary to meet some standard assumptions (errors are normally distributed and uncorrelated, with zero mean and constant variance). An informal check of the model assumptions can be made by observing certain diagnostic plots - residual plots and normal q-q plots presented in Figures 12 and 13. It should be said that with such a small sample, it is difficult to note a deviation from the assumptions. With the mentioned caution due to the small sample, based on these plots cannot be concluded that the standard assumptions were violated.

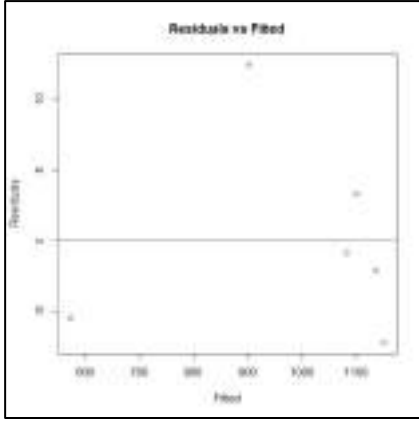


Figure 12. Residuals plot for the model

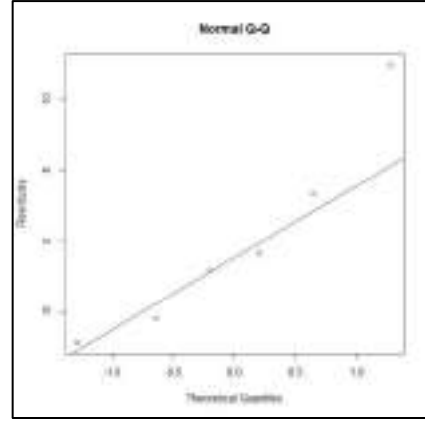


Figure 13. Normal q-q plot for the model

The results in Table 9 suggest that model is adequate. The adjusted coefficient of determination is high (0.997485). A very small p-value suggests that there is a significant linear relationship between the dependent variable (tensile strength) and at least one predictor. In addition, high t-value in Table 9 (i.e. small p-values) further suggests that all predictors (x_1 , x_2 , x_1x_2) contribute significantly to the model.

Therefore, a regression equation is proposed to estimate the tensile strength (y) as a function of temperature (x_1) and the volume fraction of residual austenite (x_2) as follows:

$$Rm = 2132 - 2.250x_1 - 31.96x_2 + 0.0748x_1x_2 \quad (4)$$

The presence of multicollinearity (a high degree of linear dependence of variables x_1 , and x_2) can cause instability in the estimation of regression coefficients. Variance inflation factors (VIF) can serve as a measure of the presence of multicollinearity . They are defined as:

$$VIF_j = \frac{1}{1-R_j^2}, \quad j = 1,2,3, \quad (5)$$

Where R_j^2 is coefficient of determination obtained by regression of j-predictor with respect to the remaining predictors. In proposed model VIF's values are quite high: $VIF_1 = 17.70$, $VIF_2 = 26.09$ and $VIF_3 = 5.54$.

VIF values greater than 10 are a signal for a possible multicollinearity problem [10]. However, by looking at the values of t-statistics for individual coefficients, it can be concluded that they are not overly inflated by the high values of VIF's. In addition, multicollinearity does not reduce the predictive power or reliability of the model as a whole, at least within the sample data set; it only affects calculations regarding individual predictors [10]. As an additional confirmation that multicollinearity does not strongly affect the stability in the observed case, it is possible to check what the results of the assessment look like by dropping the first data:

$$y = 1926 - 1.969x_1 - 32.55x_2 + 0.0849x_2 \quad (6)$$

It can be observed that the regression parameter estimates did not change dramatically compared to those obtained using the whole sample. Similar (stable) estimates are also obtained by dropping one of the remaining data.

Finally, although by various criteria proposed model seems to be the adequate, it is necessary to try to provide a larger sample in order to obtain more reliable estimates of the parameters and possibly confirm the validity of the model. With a larger sample, it would be possible to gain a better insight into the actual presence of the multicollinearity and possibly take some remedial measures against its effects.

The methodology for obtaining the mathematical model of the dependence of hardness and impact energy of the tested specimens on the temperature and the amount of residual austenite was made according to the steps explained for the tensile strength model, so in order not to repeat the whole procedure, adequate model was selected and shown by Equations (7) and (8).

$$HB = 550 - 0.564x_1 - 0.812x_2 + 0.012x_1x_2, R^2_{adj} = 0.969 \quad (7)$$

$$KV = -241.321 + 0.524x_1 + 12.06x_2 - 0.019x_1x_2, R^2_{adj} = 0.95 \quad (8)$$

CONCLUSIONS

- Additional re-heating of the ADI samples strongly affects the mechanical properties of the samples
- Tensile strength decreases as the reheating temperature increases. Noticeable decrease of the tensile strength starts at the temperatures above 450°C
- Impact energy of the tested samples strongly depend of the reheating temperatures. The lowest impact energy was recorded on the sample set three (450°C)
- Hardness of the tested sample, also, depend on the reheating temperature. The highest hardness was recorded on the samples with lowest impact energy
- Obtained results showed a clear dependence of the mechanical properties of the treated material on the reheating temperature and the degree of transformation of the initial microstructure, i.e. the transformation of retained austenite
- The proposed models are adequate - the adjusted coefficients of determination are very high (0.99, 0.97 and 0.95)
- The presence of multicollinearity (a high degree of linear correlation between predictors) can cause instability in the estimation of regression coefficients.
- Recommendation is to provide a larger sample in order to obtain more reliable estimates of the parameters for additional validity of the models

Acknowledgements

This work was supported by the Federal Ministry of Education and Science of Federation of Bosnia and Herzegovina and company „Pobjeda“ Tešanj-Turbe Foundry.

REFERENCES

- [1] P. Sellamuthu, D. G. Harris Samuel, D. Dinakaran, V. P. Premkumar, Z. Li, S. Seetharaman, Austempered Ductile Iron (ADI): Influence of austempering temperature on microstructure, Mechanical and Wear Properties and Energy Consumption, *Metals* 2018, 8, 53; doi:10.3390/met8010053.
- [2] A. Krzynska, Searching for Better Properties of ADI, *Archives of Foundry Engineering* Volume 13 , Special Issue 1/2013, pp. 91-96.
- [3] ASTM A897/897M, Standard Specification for Austempered Ductile Iron
- [4] EN 1564:1997 E, Founding, Austempered Ductile Iron
- [5] D. M. Stefanescu, *Cast Iron Science and Technology*, ASM International, 2017., <http://doi.org/10.31399/asm.hb.v01a.9781627081795>.
- [6] J. R. Keough, *Austempered Ductile Iron*, Ductile Iron Society, Strongsville, Ohio, USA, 1998.
- [7] BAS EN 6892-1/17, *Metallic Materials-Part 1. Method of testing at room temperature*
- [8] BAS EN 6507-1/18 *Metallic Materials-Hardness testing at room temperature*
- [9] S. Ekinović, *Metode statističke analize u microsoft EXCEL-u*, Zenica, 2008.
- [10] S. Chattarjee, A. S. Hadi, B. Price, *Regression Analysis by Example (Third ed.)* John Wiley and sons, ISBN 978-0-471-31946-7-2000.



19th INTERNATIONAL FOUNDRYMEN CONFERENCE
Humans - Valuable Resource for Foundry Industry Development
Split, June 16th-18th, 2021
<https://ifc.simet.hr/>

**LOAD CAPACITY AND CORROSION BEHAVIOR OF QUENCHED AND TEMPERED
STEEL 42CrMo4 AND CAST STEEL GS-42CrMo4**

**Dario Iljkić^{1*}, Sunčana Smokvina Hanza¹, Božo Smoljan², Loreta Pomenić³, Lovro Štic¹,
Lovro Liverić¹**

¹ University of Rijeka Faculty of Engineering, Rijeka, Croatia

² University North University Center Koprivnica, Koprivnica, Croatia

³ Juraj Dobrila University of Pula, Pula, Croatia

Invited lecture
Original scientific paper

Abstract

In this research the load capacity and corrosion behavior of quenched and tempered steel 42CrMo4 and cast steel GS-42CrMo4 was investigated. Load capacity and corrosion behavior of steel and cast steel depend on processing history. The influence of processing parameters on load capacity, i.e. strength and toughness was investigated by using the 2^{5-2} factor experiment. It was found out that yield strength is insensitive on differences between applied manufacturing processes, but by application of hot working (plastic deformation above recrystallization temperature) and with proper pouring temperature the Charpy-V notch toughness is increased. Also, Charpy-V notch toughness is increased by interactive effect of the proper cooling rate during the casting and hot working. Corrosion behavior was evaluated by electrochemical measurements in 3.5 % aqueous solution of sodium chloride, NaCl. It was found out that by application of hot working the corrosion resistance is increased. Microstructure analysis shows that hot working leads to refining of microstructure and thus increasing load capacity and corrosion resistance of steel. It was found out that ASTM grain size number of prior austenite was equal to N.6-N.7 for steel processed by hot working, and N.4-N.5 for cast steel processed without hot working.

Keywords: *load capacity, corrosion, steel, quenching, tempering*

*Corresponding author (e-mail address): darioi@riteh.hr

INTRODUCTION

Load capacity and corrosion behavior are very important characteristics of steel in his exploitation. Load capacity depends on yield strength and toughness, i.e., fracture resistance and on deformation resistance. Microstructure, as well as load capacity and corrosion behavior differences of quenched and tempered steel and cast steel arise from different

processing history. Basic processes in steel production are melting and pouring, hot forming, and adequate heat treatment processes.

Good proportion between yield strength and toughness as well as corrosion behavior of quenched and tempered steel arises from fine dispersion of ferrite-cementite mixture. Load capacity and corrosion behavior of quenched and tempered steel are higher if the grain size of previous austenite is finer [1, 2]. Moreover, due to refinement of previous austenite grain size the hardenability of steel can be less. Due to less hardenability of steel the bainite and fine pearlite can be formed except martensite after the quenching [3, 4]. Load capacity and corrosion behavior of quenched and tempered steel are better if as-quenched microstructure consists of homogenous martensite.

Mechanical properties of quenched and tempered steel castings with typical as-cast microstructure depend on properties of metal matrix, but they are less than mechanical properties of quenched and tempered steel with same chemical composition [5].

The aim of this research is to investigate the differences in load capacity and corrosion behavior of quenched and tempered steel 42CrMo4 and cast steel GS-42CrMo4. It is known that the load capacity and corrosion behavior of steel and cast steel depend on pouring temperature, cooling rate during the casting, as well as, application of hot working, normalization, and homogenization [6]. In order to determine the influence of such part of manufacturing process on the load capacity of investigated steel and cast steel, an investigation based on the factor experiment was done. In order to determine corrosion behavior difference between steel and cast steel, corrosion properties of these samples were evaluated by electrochemical methods.

EXPERIMENTAL SECTION

Using the factor experiment 2⁵⁻², influence of pouring temperature, cooling rate during the casting, application of hot working, normalization, homogenization on yield strength and Charpy-V notch toughness of quenched and tempered steel 42CrMo4 and cast steel GS-42CrMo4 was done (Table 1). The first step in preparation of factor experiment was casting of steel specimens for different treatments. Chemical composition of steel specimens used in different treatments are shown in Table 2. Prescribed chemical composition of steel 42CrMo4 is shown in Table 3. All specimens in factor experiment was quenched from 850 °C/50 min/oil with H-value equal to 0.35 and tempered at 570 °C/50 min/air. Mechanical properties of prepared steel specimens in factor experiment were examined by tensile test in accordance to EN 10002 and Charpy-V notch test in accordance to EN 10045 standard.

Corrosion behavior of quenched and tempered steel 42CrMo4 and cast steel GS-42CrMo4 in factor experiment was determined for steel specimens prepared by treatment 1 and treatment 5. Steel specimen prepared by treatment 1 represents a cast steel, while steel specimen prepared by treatment 5 represents steel. Corrosion behavior were determined by electrochemical measurements on PARSTAT 2263 Potentiostat/Galvanostat using "PowerSuite" and "PowerCORR" software. Specimens prepared as working electrodes for electrochemical measurements were with surface area of 1 cm². Working electrodes were prepared for measurements by manual grinding with sandpapers of 500, 800, 1200, 2400 grit and then polished with diamond paste of 1 μm particle size. Before each change of sandpaper and after polishing, the samples were degreased with ethanol, washed with

distilled water and dried in a stream of warm air. Measurements were performed in aqueous solution with 3.5 wt. % NaCl at room temperature (25 ± 2 °C). Saturated calomel electrode was used as the reference electrode, and two graphite electrodes as counter electrodes. Saturated calomel electrode was placed near working electrode by using Luggin capillary. For better understanding of mechanical properties and electrochemical measurements results of quenched and tempered steel 42CrMo4 and cast steel GS-42CrMo4, metallographic examination of specimens treated by treatment 1 and 5 was done. In preparation of metallographic samples, specimens were etched in nital (ethanol solution with 2 wt.% HNO₃) and picric-hydrochloric acid (5 cm³ HCl, 1 g picric acid, 100 cm³ ethanol).

Table 1. Factors for the factor experiment 2⁵⁻²

Treatment	Pouring temperature/°C (X ₁)	Die temperature/°C (X ₂)	Hot working (X ₃)	Normalization (X ₄)	Homogenization (X ₅)
1	1514	105	no	yes	yes
2	1590	105	no	no	no
3	1514	20	no	no	yes
4	1590	20	no	yes	no
5	1514	105	yes	yes	no
6	1590	105	yes	no	yes
7	1514	20	yes	no	no
8	1590	20	yes	yes	yes

Table 2. Chemical composition of steel GS-42CrMo4 specimens used in different treatments

Treatment	Weight percent/%									
	C	Si	Mn	P	S	Cr	Cu	Mo	Ni	V
1, 3, 5, 7	0.44	0.15	0.63	0.013	0.026	1.19	0.19	0.23	0.18	0.17
2, 4, 6, 8	0.43	0.15	0.63	0.010	0.023	1.20	0.19	0.23	0.16	0.14

Table 3. Prescribed chemical composition of steel 42CrMo4: EN 10083-3:2006

Steel	Weight percent/%						
	C	Si	Mn	P	S	Cr	Mo
EN 42CrMo4	0.38-0.45	≤0.40	0.60-0.90	≤0.025	≤0.030	0.90-1.20	0.15-0.30

RESULTS AND DISCUSSION

Load capacity

Results of factor experiment 2⁵⁻² application for yield strength and Charpy-V notch toughness are shown in Table 4 and 5.

Table 4. Factor experiment 2^{5-2} for yield strength

Treatment	X_1	X_2	X_3	X_4 X_1X_2	X_5 X_1X_3	X_2X_3	$X_1X_2X_3$	Yield strength, $R_{p0.2}$ /MPa		
								I	II	Average
1	-1	-1	-1	1	1	1	-1	1102	1108	1105
2	1	-1	-1	-1	-1	1	1	1110	1128	1119
3	-1	1	-1	-1	1	-1	1	1136	1096	1116
4	1	1	-1	1	-1	-1	-1	1088	1120	1104
5	-1	-1	1	1	-1	-1	1	1070	1060	1065
6	1	-1	1	-1	1	-1	-1	1029	1122	1075.5
7	-1	1	1	-1	-1	1	-1	1086	1126	1106
8	1	1	1	1	1	1	1	1138	1118	1128
E_x	8.63	22.38	-17.38	-3.63	7.63	24.38	9.38	$S_p^2=858.31$		
Q_x	297.56	2002.56	1207.56	52.56	232.5	2376.56	351.56	$F_{tab}(99\%)=11.26$		
F	0.35	2.33	1.41	0.06	0.27	2.77	0.41			

E_x - average factor effect; F - Fisher's variable; F_{tab} - table value of Fisher's variable; Q_x - sums of squares of average factor or interaction effect; S_p^2 - estimator of variance into treatments.

Table 5. Factor experiment 2^{5-2} Charpy-V notch toughness

Treatment	X_1	X_2	X_3	X_4 X_1X_2	X_5 X_1X_3	X_2X_3	$X_1X_2X_3$	Charpy-V notch toughness, KV/J				
								I	II	III	IV	Average
1	-1	-1	-1	1	1	1	-1	20	24	23	24	22.75
2	1	-1	-1	-1	-1	1	1	14	15	14	14	14.25
3	-1	1	-1	-1	1	-1	1	23	24	25	24	24
4	1	1	-1	1	-1	-1	-1	25	26	18	18	21.75
5	-1	-1	1	1	-1	-1	1	48	49	50	47	48.5
6	1	-1	1	-1	1	-1	-1	41	37	44	37	39.75
7	-1	1	1	-1	-1	1	-1	46	44	49	40	44.75
8	1	1	1	1	1	1	1	40	38	37	40	38.75
E_x	-6.38	1.00	22.25	2.25	-1.00	-3.38	-0.88	$S_p^2=6.65$				
Q_x	325.13	8.00	3960.50	40.50	8.00	91.13	6.13	$F_{tab}(99\%)=7.82$				
F	48.92	1.20	595.94	6.09	1.20	13.71	0.92					

E_x - average factor effect; F - Fisher's variable; F_{tab} - table value of Fisher's variable; Q_x - sums of squares of average factor or interaction effect; S_p^2 - estimator of variance into treatments.

On the base of the factor experiment results it was found out that yield strength is insensitive on differences between applied manufacturing processes, but by application of hot working and with proper pouring temperature the Charpy-V notch toughness is

increased. Also, Charpy-V notch toughness is increased by interactive effect of the proper cooling rate during the casting and hot working application.

The relation between Charpy-V notch toughness results and pouring temperature, ϑ_p , hot working application and temperature of die, ϑ_d was established by regression analysis [5]:

$$KV = 35.065 - 0.084x_1 + 8.508x_3 + 0.040x_{23} \quad (1)$$

Hot working is applying in steel production and for steel factor x_3 is equal to one and for production of cast steel is equal to minus one. Including concrete values for other factors difference from optimal pouring temperature, $\Delta\vartheta_p$, and interaction of temperature of die, ϑ_d and hot working application, Equation 1 can be written as:

$$KV_S = 43.573 - 0.084\Delta\vartheta_p + 0.040\vartheta_d \quad (2)$$

$$KV_{CS} = 26.557 - 0.084\Delta\vartheta_p - 0.040\vartheta_d \quad (3)$$

where KV_S/J is Charpy-V notch toughness of steel, KV_{CS}/J is Charpy-V notch toughness of cast steel, $\Delta\vartheta_p/^\circ C$ is difference from optimal temperature of pouring, and $\vartheta_d/^\circ C$ is temperature of die during the pouring.

Maximal Charpy-V notch toughness of steel and cast steel can be obtained by temperature of die during the pouring equal to 105 °C and by difference from optimal temperature of pouring equal to 0 °C. Charpy-V notch toughness of steel 42CrMo4 and cast steel GS-42CrMo4 can be expressed by:

$$KV_S = KV_{S_{max}} [1 - 0.00176\Delta\vartheta_p - 0.000837(105 - \vartheta_d)] \quad (4)$$

$$KV_{CS} = KV_{S_{max}} [0.644 - 0.00176\Delta\vartheta_p - 0.000837(105 + \vartheta_d)] \quad (5)$$

where $KV_{S_{max}}/J$ is maximal Charpy-V notch toughness of steel and cast steel.

Since Charpy-U notch toughness, KU is related to hardness HV [7,8], and Charpy-V notch toughness, KV is related to Charpy-U notch toughness, KU [9] it can be found out that Charpy-V notch toughness, KV for steel manufactured by casting from optimal temperature of pouring and by optimal temperature of die during the pouring is equal to:

$$KV_{S_{max}} = 264.26 - (1.129 - 0.554S)HV \quad KV \leq 80 \text{ J} \quad (6)$$

$$KV_{S_{max}} = 442.84 - (2.201 - 1.082S)HV \quad KV > 80 \text{ J} \quad (7)$$

Corrosion behavior

Electrochemical measurements of quenched and tempered steel 42CrMo4 and cast steel GS-42CrMo4 prepared by treatment 1 and 5 started with stabilization of potential in aqueous solution with 3.5 wt. % NaCl at open circuit potential for a period of 1 h. Open circuit potential E_{ocp} measurements for quenched and tempered steel and cast steel specimens are

shown in Figure 1. Quenched and tempered cast steel specimen shows negative value of initial potential, and that potential is nearly the same during the time which means that specimen is corrosion-active. Time dependence of open circuit potential for steel specimen is substantially different. Quenched and tempered steel specimen started with positive value of initial potential, and that potential decreases during the 250 s. After 250 s potential rises to time of 500 s when specimen starts to showing tendency of passivation. Further over time potential decreases to the negative values, and at the end steel specimen becomes corrosion-active. At the time of ~2800 s potential of both samples becomes equalized.

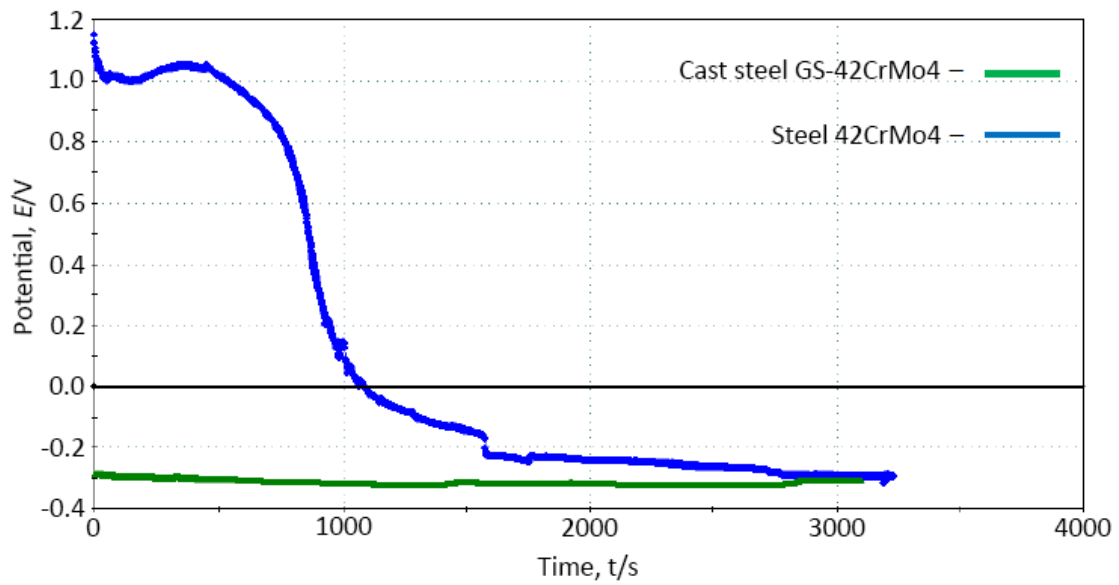


Figure 1. Variation of the open circuit potentials with time for the quenched and tempered steel 42CrMo4 and cast steel GS-42CrMo4 specimens in aqueous solution with 3.5 wt. % NaCl

After the stabilization of open circuit potential, Tafel extrapolation method was conducted by recording polarization curves of the quenched and tempered steel and cast steel 42CrMo4 specimens in the range of -250 mV from corrosion potential to +450 mV from corrosion potential at scan rate 0.5 mVs^{-1} . Tafel extrapolation curves for quenched and tempered steel and cast steel specimens are shown in Figure 2. Corrosion parameters obtained by Tafel extrapolation method of quenched and tempered steel and cast steel specimens are shown in Table 6.

Table 6. Corrosion parameters obtained by Tafel extrapolation method of the quenched and tempered steel 42CrMo4 and cast steel GS-42CrMo4 specimens in aqueous solution with 3.5 wt.% NaCl

Specimen	$\beta_A/\text{mV}\cdot\text{dec}^{-1}$	$\beta_C/\text{mV}\cdot\text{dec}^{-1}$	$E_{\text{corr}}/\text{mV}$	$j_{\text{corr}}/\mu\text{A}\cdot\text{cm}^{-2}$	$v_{\text{corr}}/\text{mm}\cdot\text{py}$
Cast steel	38.291	-247.408	-109.597	$3.828\cdot 10^{-1}$	$0.0428\cdot 10^{-1}$
Steel	627.037	-783.031	-382.499	$2.952\cdot 10^{-1}$	$0.0329\cdot 10^{-3}$

From Table 6 is visible that corrosion potential E_{corr} of the steel specimen has more negative value than cast steel specimen. However, corrosion current density j_{corr} of steel specimen is much lower than that of steel casting which indicates that corrosion of steel casting is higher than corrosion of steel. Moreover, corrosion rate v_{corr} obtained by Tafel extrapolation

method of steel specimen is much lower than that of cast steel. It can be concluded that steel specimen is more resistant to corrosion in aqueous solution with 3.5 wt. % NaCl than steel casting specimen.

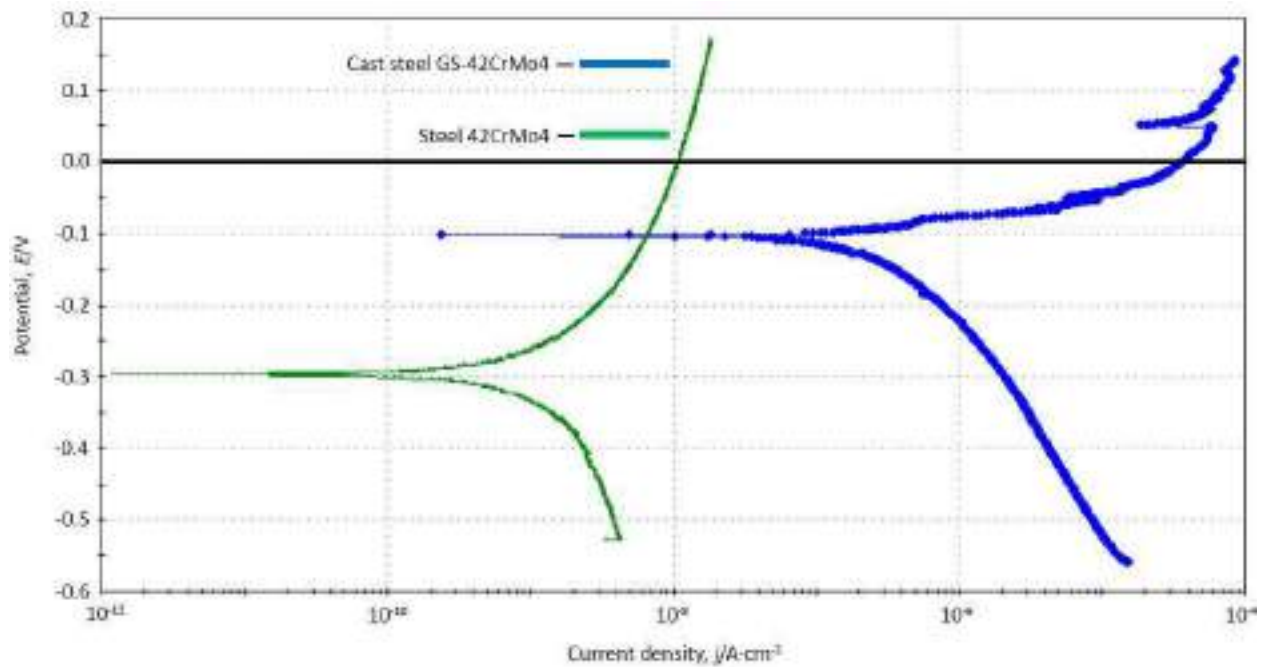


Figure 2. Tafel extrapolation curves for the quenched and tempered steel 42CrMo4 and cast steel GS-42CrMo4 specimens in aqueous solution with 3.5 wt. % NaCl

Figure 3 shows the quenched and tempered steel 42CrMo4 and cast steel GS-42CrMo4 specimens after electrochemical measurements of corrosion behavior in aqueous solution with 3.5 wt.% NaCl. From Figure 3 is visible that corrosion process in cast steel specimen is much more intense than in steel specimen.

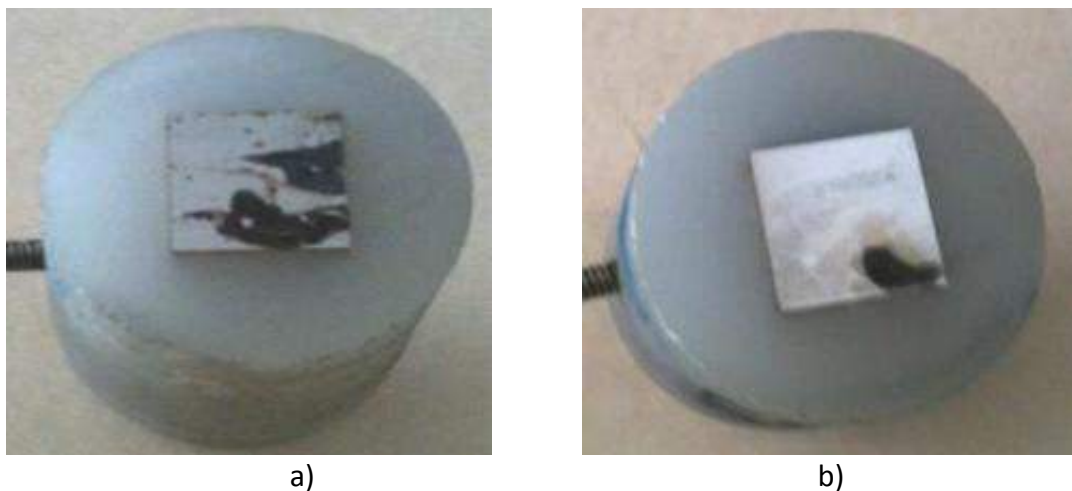


Figure 3. The quenched and tempered specimens after electrochemical measurements of corrosion behavior in aqueous solution with 3.5 wt.% NaCl, a) cast steel GS-42CrMo4, b) steel 42CrMo4

Better load capacity and corrosion resistance of quenched and tempered steel in comparison to quenched and tempered cast steel arise from finer microstructure steel. Figure 4 shows the microstructure of quenched and tempered cast steel GS-42CrMo4 prepared by treatment 1. From Figure 4a is visible that microstructure of quenched and tempered cast steel consists of tempered martensite. From Figure 4b is visible that ASTM number of prior austenite grain size of quenched and tempered cast steel is equal to N.4-N.5. Figure 5 shows the microstructure of quenched and tempered steel 42CrMo4 prepared by treatment 5. From Figure 5a is visible that microstructure of quenched and tempered steel consists of tempered martensite. From Figure 5b is visible that ASTM number of prior austenite grain size of quenched and tempered steel is equal to N.6-N.7.

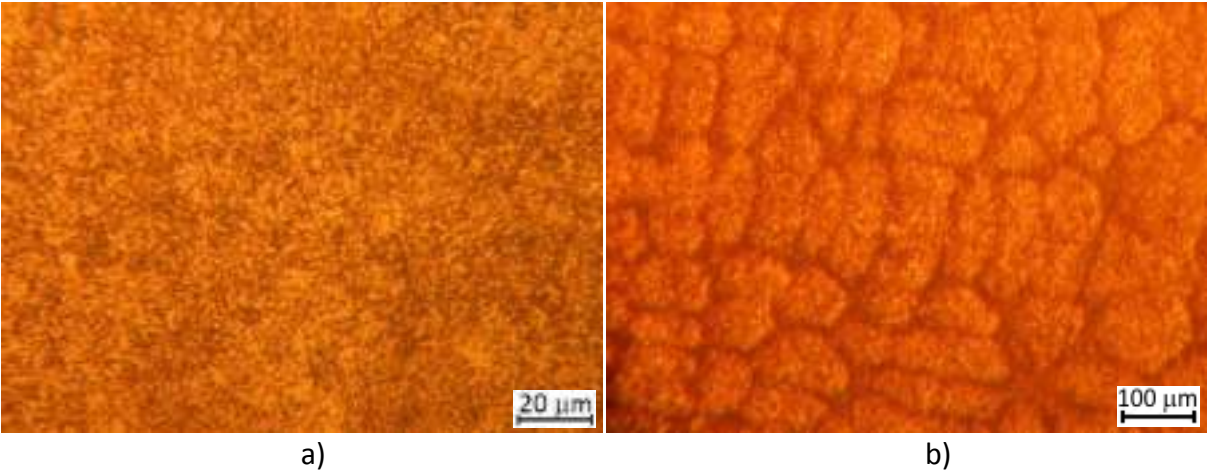


Figure 4. Microstructure of quenched and tempered cast steel GS-42CrMo4 prepared by treatment 1, a) tempered martensite; nital; 500:1, b) prior austenite grain size; picric acid; 500:1

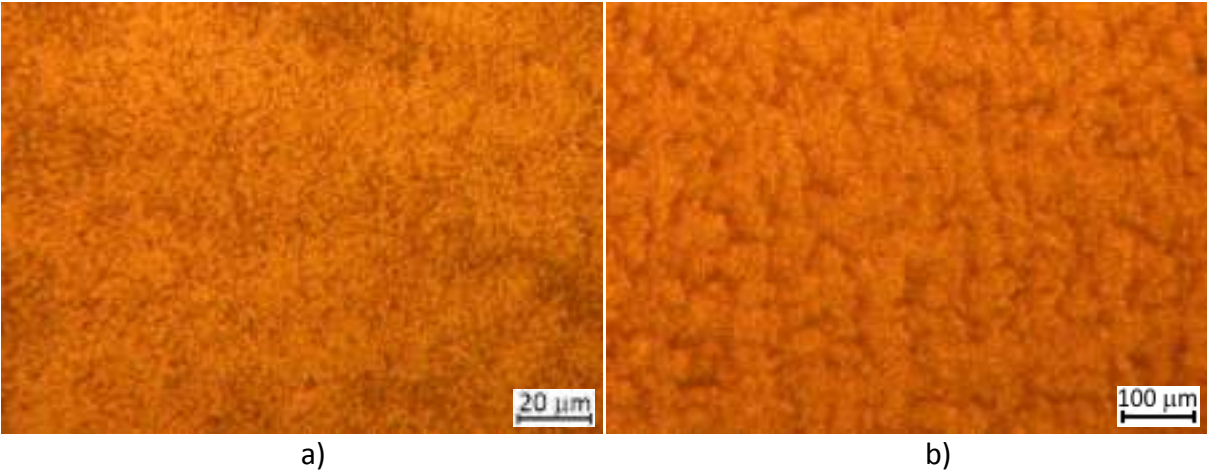


Figure 5. Microstructure of quenched and tempered steel 42CrMo4 prepared by treatment 5, a) tempered martensite; nital; 500:1, b) prior austenite grain size; picric-hydrochloric acid; 500:1

CONCLUSIONS

Since load capacity of steel directly depends on toughness and yield strength, these two mechanical properties of steel 42CrMo4 and cast steel GS-42CrMo4 were investigated. During the experimental work based on the 2^{5-2} factor experiment results, yield strength was constant and equal to standard values of quenched and tempered steel, independently on investigated parameters of casting, hot working, homogenization and normalization. Also, it was found out that by application of hot working and with proper pouring temperature the Charpy-V notch toughness is increased. Charpy-V notch toughness is increased by interactive effect of the proper cooling rate during the casting and hot working. Furthermore, new relations between the Charpy-V notch toughness, and hardness of quenched and tempered steel and cast steel was established.

Difference of corrosion behavior of quenched and tempered cast steel GS-42CrMo4 and quenched and tempered steel 42CrMo4 in 3.5 % aqueous NaCl solution, shows the influence of microstructural modifications during the processing of steel. Better corrosion resistance of quenched and tempered steel 42CrMo4 is attributed to the hot working which is applied in processing of steel. This process result with fine spherical shaped grains instead coarse-grained structure formed by casting, and the pores, gas bubbles and micropores, which originate from the casting process at high temperatures, are welded and the material becomes more compact. It can be concluded that hot working increases corrosion resistance of steel in comparison to the cast steel. To investigate the influence of individual microconstituents on the corrosion properties of the tested steel, further research should be continued.

Acknowledgements

This work has been supported in part by Croatian Science Foundation under the project IP-2020-02-5764 and in part by the University of Rijeka under the project number uniri tehnic-18-116.

REFERENCES

- [1] B. Smoljan, An analysis of combined cyclic heat treatment performance, *Journal of Materials Processing Technology*, 155-156(2004), pp. 1704-1707.
- [2] S. Smokvina Hanza, L. Štic, L. Liverić, V. Špada, Corrosion behaviour of tempered 42CrMo4 steel, *Materiali in tehnologije / Materials and technology*, 55(2021)3, pp.91-97.
- [3] S. Mahajan, et al., Grain refinement of steel cyclic rapid heating, *Metallography*, 6(1973), pp. 337-345.
- [4] G. E. Totten, *Steel Heat Treatment: Metallurgy and Technologies*, Boca Raton: CRC Press, Taylor & Francis Group, 2007.
- [5] D. Iljkić, A contribution to the development of the mechanical properties prediction of quenched and tempered steel and cast steel, *Doctoral Thesis, Department of Materials Science and Engineering, Faculty of Engineering, University of Rijeka, 2010 (in Croatian)*

- [6] J. Campbell, Castings, Oxford, United Kingdom: Butterworth Heinemann, 2003.
- [7] E. J. Pavlina, C. J. Van Tyne, Correlation of Yield Strength and Tensile Strength with Hardness for Steels, Journal of Materials Engineering and Performance, 17(2008)6, pp. 888-893.
- [8] E. Just, Verguten-Werkstoffbeeinflussung durch Harten und Anlassen, VDI-Ber., 256(1976), pp. 125-140 (in German)
- [9] Impact Toughness Testing, In section: Impact Toughness Testing and Fracture Mechanics, ASM Handbook-Volume 8: Mechanical Testing and Evaluation, Material Park, OH: ASM International, 2000.



19th INTERNATIONAL FOUNDRYMEN CONFERENCE
Humans - Valuable Resource for Foundry Industry Development
Split, June 16th-18th, 2021
<https://ifc.simet.hr/>

SEMI-SOLID METAL PROCESSING; CHALLENGES AND INOVATIONS

Sonja Jozić*

University of Split Faculty of Mechanical Engineering and Naval Architecture, Split, Croatia

Invited lecture
Subject review

Abstract

Semi-solid metal (SSM) processing is novel melt treatment and alloy manipulation dealing with semi-solid slurries. SSM could be considered as an effective alternative to classical casting and forging manufacturing processes. In the absence of shear forces, the semi-solid slug is similar to a solid, while applying of shear forces the viscosity is greatly reduced, and the material flows like a liquid. Currently, this process strives to be industrially successful, generating different products with high quality parts in various industrial sectors. Since its establishment until today, numerous technologies around the world have been developed and implemented in order to produce the correct globular microstructure. The main objective of this paper is to classify currently available innovative technologies and to provide a comprehensive overview of possible mechanisms that result in better product quality and lower costs, taking into account the many challenges related with this new technology.

Keywords: *semi-solid processing, thixoforming, globular microstructure*

*Corresponding author (e-mail address): sjozic@fesb.hr

INTRODUCTION

Semi-solid metal processing could be an effective alternative to classical casting and forging processes. This technology is a simple manufacturing process for components of different shapes. It is mostly performed in one step, providing well structural integrity and good mechanical properties. Semi-solid metal processing has already been established as a sustainable production method, but it is still in intensive research and development process. This paper describes the properties of semi-solid processing, together with historical and technical background, industrial application as well as examples of commercialization. Semi-solid metal (SSM) processing is an advanced technology used to produce high quality and low cost parts [1]. The procedure is nowadays applied in various branches of industry and represents an improved replacement by conventional forming technologies, such as casting and forging processes. It uses thixotropy of semi-solid metals and offers means for

the production of complex shapes that are significantly higher quality than part obtained by casting process. As a result, SSM appeared as a new production scheme for the production of complex components of aluminum and magnesium alloys. SSM processing enables the production of a globular microstructure instead of a dendritic one which is normally achieved by conventional processing technique.

This technology is applying for alloy treatment in the area between solidus and liquidus temperature. The interval between these two temperatures represents the space in which the metal alloy is in a slurry state. The slurry, a mixture of liquid and solid phase, is prepared in a variety ways, including direct or indirect mechanical stirring, chemical processing of molten metal and manipulation with casting temperature. All those methods are based on inducing shear forces in the molten metal to allow powerfull mixing of the mixture and on the correct temperature gradient which will ultimately result in a homogeneous microstructure and fine distribution of solids in the liquid. Mixing breaks down the primary dendrites. The lower pouring temperature directly affects the nucleation and growth of the primary crystals. Nucleation controls the size of the resulting grains, and growth affects grain morphology and the distribution of alloying elements within the matrix.

Semi-solid metal processing is based on thixotropic behavior of different alloys in the semi-solid state. A material that has thixotropic properties at rest (without the action of forces) behaves as if it were in a solid state, and becomes liquid by the action of forces. By the force action, the bond between the globules breaks down, the viscosity decreases and the material flows out as a liquid. Processes based on thixotropic behaviour (ie. the viscosity depends on time and shear stress) have advantages over conventional processes such as die casting where the flow of molten metal is turbulent [2].

Semi-solid metal processing dates back to the early 1970s, when Flemings et al, at MIT, studied the flow behavior of thin/led alloys in the semi-solid state [2]. He and his collaborators studied the solidification behavior of molten metal under conditions in which they form a suspension of globular primary solid particles in a liquid metal melt. This is then achieved by stirring the slurry while cooling to the desired temperature. Initial findings clearly showed that, in such conditions, the viscosity of the metal in the semi-solid state depends on the solid fraction, the shear rate, and the history of time. Although this behavior can be expected for two-phase emulsions, it was a fairly new discovery for metal systems, which would normally show a dendritic microstructure.

The intensive efforts in science and industry to empower semi-solid metal processing are encouraged by the significant technological potential which these innovative technologies can provide [2]:

Compared to conventional casting, the high viscosity value of the semi-solid metal prevents the occurrence of turbulence during mould filling and reduces component defects that could occur due to air trapping. Another advantage is that due to the high solids fraction of about 40 % during mould filling, the volume loss during complete solidification is reduced, leading to reduced shrinkage porosity. Furthermore, the low gas content results in a microstructure suitable for heat treatment. This is enormously important for the serial production of aluminum alloy components in the automotive industry. Decreasing of the semi-solid metal process temperature can lead to a increase in tool life compared to conventional die casting.

Compared to conventional forging, SSM processing is characterized by a reduced forming load and the possibility of producing complex geometric components, which cannot be produced by forging. Replacing forging with semi-solid processing will offer economic benefits if components with added value can be produced. This can be achieved by

increased geometric complexity, weight savings when replacing steel with aluminum alloy or the production of composite components. Additional benefits may arise if some finishing or joining can be avoided.

The advantages of semi-solid processing are due to the behavior of thixotropic slurries during mould filling. This is related to the microstructure of these slurries. The slurries generally consist of solid, non-dendritic, almost globular primary particles immersed in a liquid matrix. This will be discussed in more detail below.

MICROSTRUCTURE OF SEMI-SOLID ALLOYS

The main advantage of semi-solid technology is related to the flow properties of the metal in the form of a slurry, which, in the semi-solid state, is non-Newtonian and exhibits shear thinning behavior [2]. The viscosity of a semi-solid metal is higher than when the metal is in a liquid state with a reduced risk of turbulence [3], which is common for high-pressure die casting [3, 4].

Under the influence of shear forces acting on the semi-solid metal when poured into the mould, the viscosity decreases and the metal slurry very well fills the mould cavity, completely in a quiet manner [5]. As a result, the semi-solid cast parts have almost no gas porosity at all.

The production of structural elements with good mechanical properties is possible due to the low or even non-existent porosity of the material. Advantages such as good dimensional tolerances, high production rates, high surface quality, complex almost near-shaped parts and thin parts which do not require any machining [6] place SSM machining far above high pressure die casting.

Since the discovery of this method [7], a quite lot of research has been conducted around the world. The research is based on the development of new and alternative methods of raw material production for different alloys that are suitable for SSM processing. Today, a large number of different techniques for the production of semi-solid processing are known. The main difference is in the percentage of liquid/solid fraction as a variant of production.

There are two main semi-solid casting processes: thixo-casting and rheo-casting [8].

By rheo-casting process a blank is initially heated to the temperature above the liquidus temperature, then cooled up to the semi-solid phase in which the globular microstructure achieves. Suspension with solid fraction of usually between 10 % and 30 % [9], is transferred directly to the shot sleeve for the purposes of injection into the die.

By thixocasting process, blanks, which have almost globular or rosette similar microstructure, are heated up in the semi-solid region to the corresponding solid fractions (typically between 50 % and 60 % [6]), and then were placed in a modified sleeve to be injected into the die [3].

SSM methods can be classified according to the initial step of which is used for preparation of semi-solid materials, i.e., from a liquid, controlled solidification of a solid state, severe plastic deformation and recrystallization [8].

The basic idea is to obtain a raw material with the microstructure of a solid, globular phase surrounded by a liquid phase. As already mentioned, when shear stress is applied, the globular solid particles move easily next to each other, reducing the viscosity and forcing the material to behave like a liquid. On the other hand, if shear stress is applied to the dendritic

microstructure, the liquid phase remains trapped between the dendritic arms thus preventing their free movement, ultimately increasing the viscosity of the alloy [10]. In experiments performed by Spencer et al. on the Sn - Pb15 alloy [7] it was shown that the constant shearing action causes the formation of a non-dendritic microstructure, which is a characteristic of semi-solid alloy. By further shearing during cooling, it is also possible to obtain spheroidal particles, usually with some trapped liquid. Some authors have reported that high shear rate and slow cooling rate can accelerate the formation of globular particles instead of rosettes [11]. One of the first proposed mechanisms is shown in Figure 1.

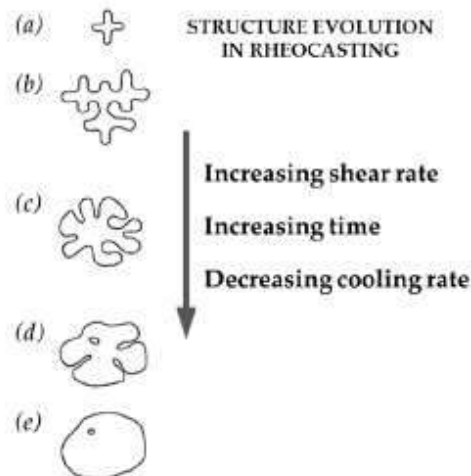


Figure 1. Schematic illustration of evolution of structure during solidification with vigorous agitation: (a) initial dendritic fragment; (b) dendritic growth; (c) rosette; (d) ripened rosette; (e) spheroid [2]

Numerous explanations can be found in the literature on how dendritic transforms into globular morphology, such as ripening, shear, bending, and abrasion with other growing crystals, dendritic fragmentation, remelting, and growth control mechanisms [2]. It has been observed that the dendritic arms are plastically bent under the shear force created by stirring the melt. Plastic bending introduces large misalignments into the dendritic arms in the form of "geometrically necessary dislocations". Such dislocations, if randomly distributed, would have a high elastic energy that can be reduced by dislocation migration to create a grain boundary. At high temperatures, these dislocations rearrange, causing, under certain conditions, the separation of dendritic branches [3, 5], as shown in Figure 2.

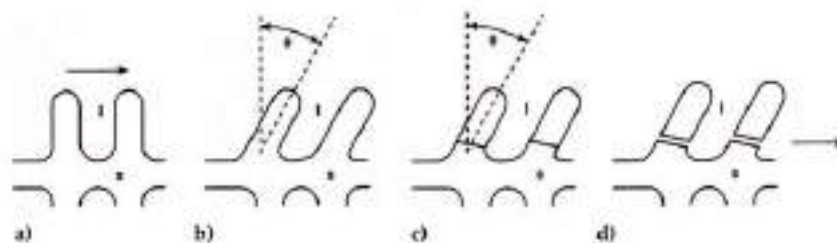


Figure 2. Dendrite arm fragmentation mechanism; (a) un-deformed dendrite, (b) after bending, (c) reorganization of the lattice bending to give grain boundaries, (d) fragmentation through wetting of grain boundary by liquid metal [3]

The size of the globules is usually determined by their mean diameters. It should be large enough to form a solid network of solid phase and, at the same time, small enough that the mixture can flow unhindered into the mould cavity. It starts from that the minimum wall thickness of the casting, produced by SSM technology, should not be less than 30 times the grain radius [2]. The optimal primary particle size for SSM technologies is less than 100 μm, [12]. It is very difficult to determine the grain size, the newer method used is microtomography shown in Figure 3.

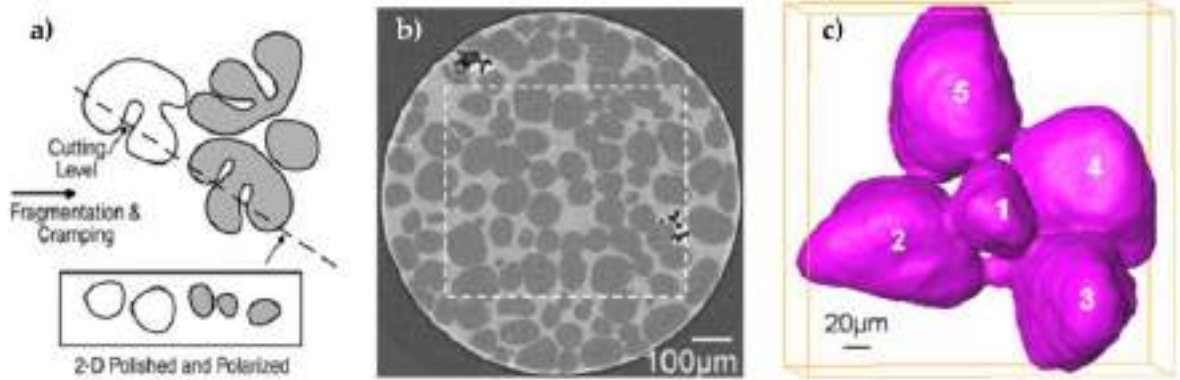


Figure 3. Schematic representation of 2D analysis, b) 3D image processing with 2D slice, c) volume representation on the acquired tomography data [13]

The shape factor is a parameter that describes the circularity of a crystal grain. Parameter values are within the interval between zero and one. A value of zero indicates an irregular crystal grain shape. The closer the shape factor value is to one, the closer the crystal grains are to the circular shape. A value of one indicates a perfectly circular crystal grain. The shape factor is calculated according to the expression:

$$SF = \frac{\sum_i \frac{N^4 \cdot \pi \cdot A}{P^2}}{N} \tag{1}$$

where N is number of globules, P - circumference of globule [μm], A - surface of the globule [μm²]. For laminar die filling the shape factor should preferably be one. In SSM processing every value above 0.6 is considered to be appropriate.

The entrapped liquid is a special characteristic of the thixocasting process. This liquid, as shown in Figure 4, does not contribute to the sliding of the globules during processing. That means that the liquid fraction is lower than the theoretical one and that the viscosity increases during die filling due to a sponge effect that can be induced [11].

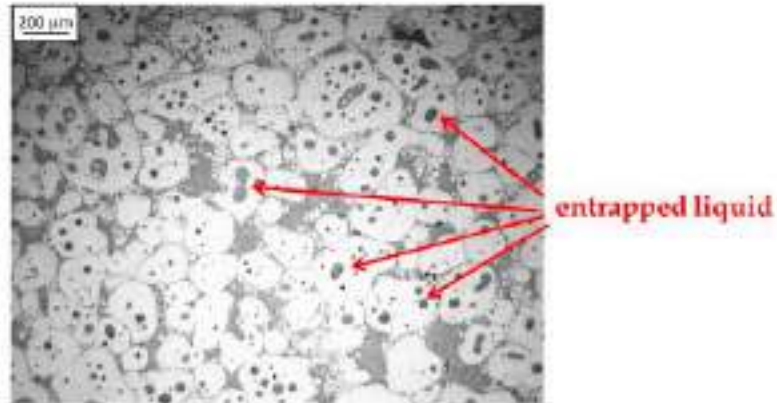


Figure 4. Thixocasting microstructure with entrapped liquid in globules [5]

The amount of entrapped liquid can be estimated by image analysis of 2D polished section areas, however, as in the case of the shape factor and globule size, defects can be introduced when some of the entrapped liquid islands appear to be isolated, even though they are connected to the liquid phase at deeper levels [5].

INDUSTRIAL APPLICATIONS OF SEMI-SOLID CASTINGS

The next goal is to present the industrial applications of semi-solid metal processing and strategies necessary for the wider commercialization as well. Over the last three decades, a many of technologies have been developed, mostly in the laboratory environment, to take advantage of the unique behavior of semi-solid slurries. Despite many advantages, although there have been many successful commercial applications of semi-solid cast aluminum parts, the process has not yet achieved the widespread commercial application as it was conceived during its early days.

In today's manufacturing business world, the fact that the rate of change is very fast cannot be avoided. In addition to conventional incremental innovations, radical innovations have become very important and are used as a source of competitive advantage in the global market [6].

The development of semi-solid metal processing is an example of the full range of experiences involved in transforming a "research idea" into a successful "commercial product" [6].

After a series of failed attempts to directly exploit the technology in the U.S., the original patents for MIT technology were eventually licensed to the International Telephone and Telegraph Corporation (ITT Corp.) in the late 1970s. The philosophy was to keep strict secrecy around all semi-solid processing developments. However, by around 1985, ITT Teves, a subsidiary of ITT Corporation and a leading manufacturer of brake systems, established a semi-solid production facility in northern Germany, sparking interest in a number of European manufacturers. As a result, in the late 1980s, a number of European manufacturers began to develop their own independent approaches for raw material production and parts design.

Buehler, Europe's leading manufacturer of casting press, began promoting its real-time controlled machines as suitable for semi-solid processing. Buehler and their partner at the time, developed an electromagnetic mixing system and a horizontal continuous caster, for

raw material production. Similarly, Pechiney, in France (today a subsidiary of Alcan Aluminum) began its work on a vertical continuous wheel, for raw materials, using a combination of radial and longitudinal electromagnetic mixers. Also in Italy, Magnetti Marelli has developed a convective slug heating system in combination with IdraPress machines for the production of automotive fuel rails [14]. Among the European manufacturers, the most prominent proponent of semi-solid processing was Buehler, who took the opportunity to increase the sales of their horizontal die casting machines. By the mid 1990s, Buehler had installed more than 40 machines to produce SSM parts worldwide [6]. Stampal S.p.A. in Turin, it invested in Buehler machines, and Fiat participated in the process of subsidizing the research and development of some parts of its Punto, Panda, and Alfa Romeo models (see Figure 5).



Figure 5. Parts produced by Stampal S.p.A. for various automotive manufacturers using the MHD (magneto hydrodynamic stirring) feedstock route [14]

At the end of the 1990s, Ube, Japanese die casting machine manufacturer has entered the market with new rheocasting process. Semi-solid metal processing has become an accepted way of producing components from aluminum and magnesium alloys. Since thixoforming is a relatively “new process,” it had to be established by exploiting alloys that were already available. As a result, widely tested alloys of aluminum and silicon A356, A357 and A357 have been selected for the materials, on which the process can show its full potential. The total production of aluminum castings is about 1,500,000 m in North America and Europe and 1,000,000 m in Japan. However, thixoforming represents only about 1 %, figure

6, of the total in this huge market where permanent moulding and die casting processes are still overwhelmingly dominant [25].

SSM products have better properties than their die-cast counterparts due to the reduced gate velocities used in SSM, which resulted in uniform die filling as shown in 7.

In order for this procedure to become competitive and widely applicable, it is necessary to overcome the constraints in the activities such as dynamic application for load-bearing parts (fatigue properties), in the development of alloys - expansion of the existing portfolio of thixoformable alloys (better mechanical properties) and in material recycling.

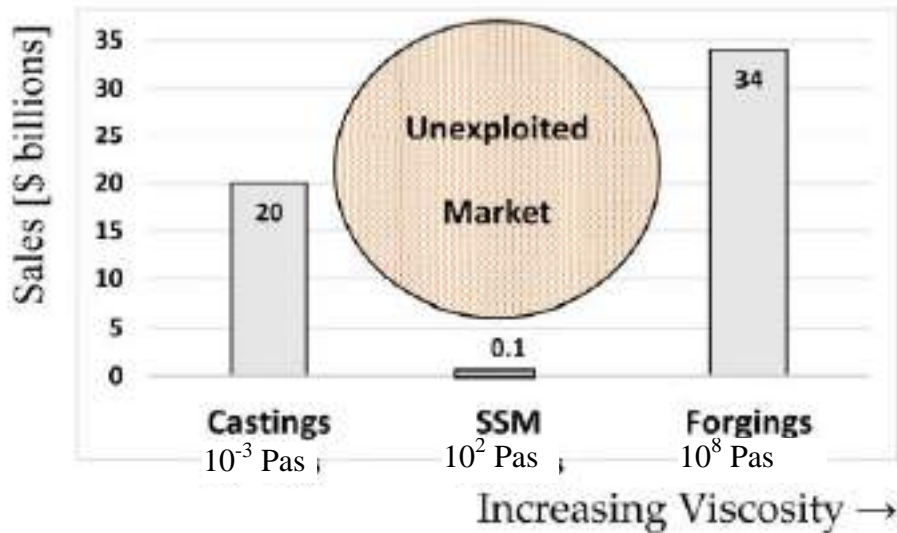


Figure 6. Semi-solid market annual US sales, end of 20th century [25]

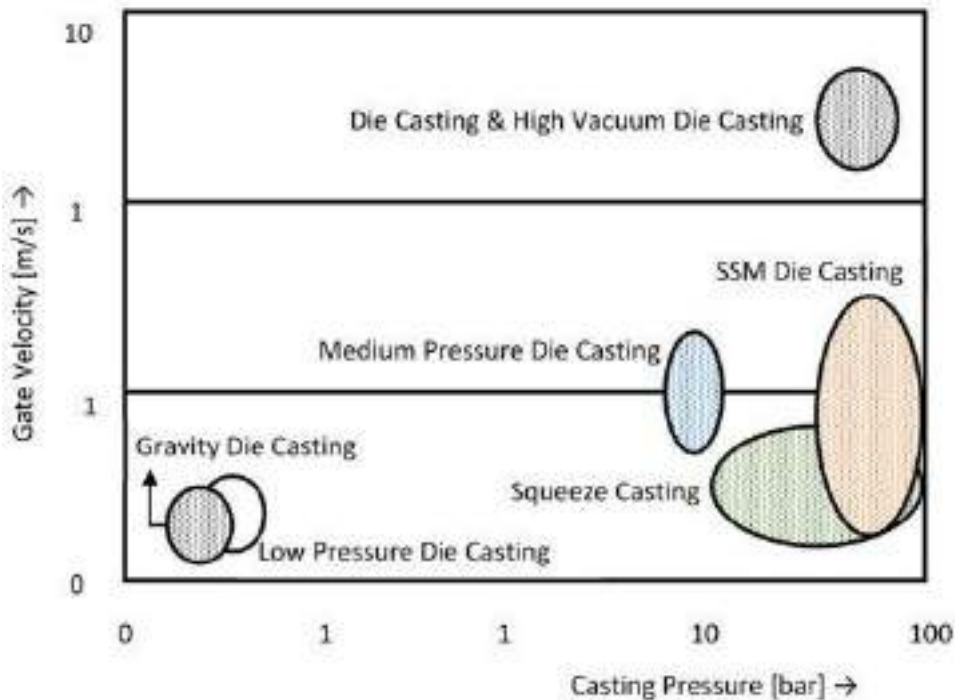


Figure 7. Relation between casting pressure and velocity of the metal at the gate [25]

CURRENT STATE OF SEMI-SOLID METAL PROCESSING

The methodologies used to achieve the required non-dendritic, near-spheroidal microstructures suitable for SSM feedstocks were critical to the success of commercialization or otherwise of this group of processes. Over the years, at the research and development level, different procedures have been developed, with different levels of success, to obtain these required near spheroidal microstructures [23]. In commercial SSM applications the following routes have been used to obtain raw materials:

(a) Continuous casting with magneto-hydrodynamic (MHD) stirring of the melt during solidification [14, 6].

(b) Semi Solid Rheocasting (SSR), where a cold spinning 'finger' is inserted into the melt acting as a source of nucleation [15, 16].

(c) Gas Induced Semi Solid Rheocasting (GISS) [17, 18], where the nucleation is induced by fine

bubbles of argon gas introduced into the melt by a perforated graphite rod.

(d) Through the SEED (Swirled Enthalpy Equilibration Device) process [19, 20], where a high fraction solid slurry is obtained as liquid metal is cooled into the semi-solid temperature range.

(e) Thixomoulding, an injection moulding technology that uses magnesium pellets or chips that has been successfully producing commercial parts over the past four decades [21, 22].

The SSR, GISS and SEED processes enable on-site recycling and thus significant potential savings. The MHD process usually requires a raw material supplier and does not provide on-site recycling, and provides better product quality thanks to greater raw material quality consistency. Thixomoulding uses magnesium pellets heated and sheared in a plastic extrusion setup. It is a commercially successful process, with millions of components produced each year for the car and consumer products / electronics markets (computers, VCRs, mobile phone accessories, sporting goods) [23].

Compared with high pressure die casting, SSM processing gives a number of advantages to the final products, such as fine, uniform and almost no porosity of the microstructure, the ability of heat treatment after processing to improve the mechanical properties, reduce energy consumption and reduce thermal shock, and thus longer mould life, due to the lower thermal content of the semi-solid material. Higher melting alloys, such as hypereutectic aluminum-silicon alloys with a very high silicon content (25 % to 40 %), super alloys or non-casting steels, can still be processed by SSM methods.

Disadvantages of the thixoforming process can cause a poor response in the industry. The most well-known shortcoming of thixoforming was the special requirement for a feedstock billet which could increase production costs. Waste from the forming process cannot be recycled. The important points in thixoforming were viscosity and solid fraction. Both depend on temperature control, so precise technical control required highly technical personnel. Although SSM processing has been conducted in a research light for 40 years, continuous research in thixoforming is necessary to support the development of new components [27].

Identifying traces and deficiencies of thixoforming will lead to deeper research, which will improve thixoforming in many aspects.

However, although the process potential is clearly seen and has had numerous attempts at full commercialization throughout its long history, it has been successfully exploited in a

limited number of cases [24], using mostly conventional AlSi7Mg type aluminum alloys (A356 and 357).

TOOL TECHNOLOGIES FOR SEMI-SOLID METALS PROCESSING

Reducing production costs by decreasing of number of forming steps, reducing forming forces and improving product quality is achievable by using innovative semi-solid metal processing. SSM processing is currently most widely used in light metals and presents a direct competition with highly sophisticated conventional casting technologies, such as high pressure die casting (HPDC). Though the benefits of thixoforming are much more visible in the processing of ferrous metals, economically in terms of a sizeable market and technically due to the higher capacity construction, the transition to high-melting alloys is still underrepresented.

The lack of appropriate tools and dies that meet the requirements of the process, is one of the main shortcomings for the industrial application of thixoforming processes.

Tool and material systems used in semi-solid metal processes are subject to severe deformations if applied in steel thixoforming, resulting in a deviation in the shape accuracy of manufactured components because of the tool wear and thus short tool life.

The reason for this lies in the complex profile of the loads acting on the tool during the semi-solid metalworking.

Four main load categories can be distinguished:

- (i) mechanical, (ii) thermal, (iii) chemical and (iv) tribological influences (Figure 8).

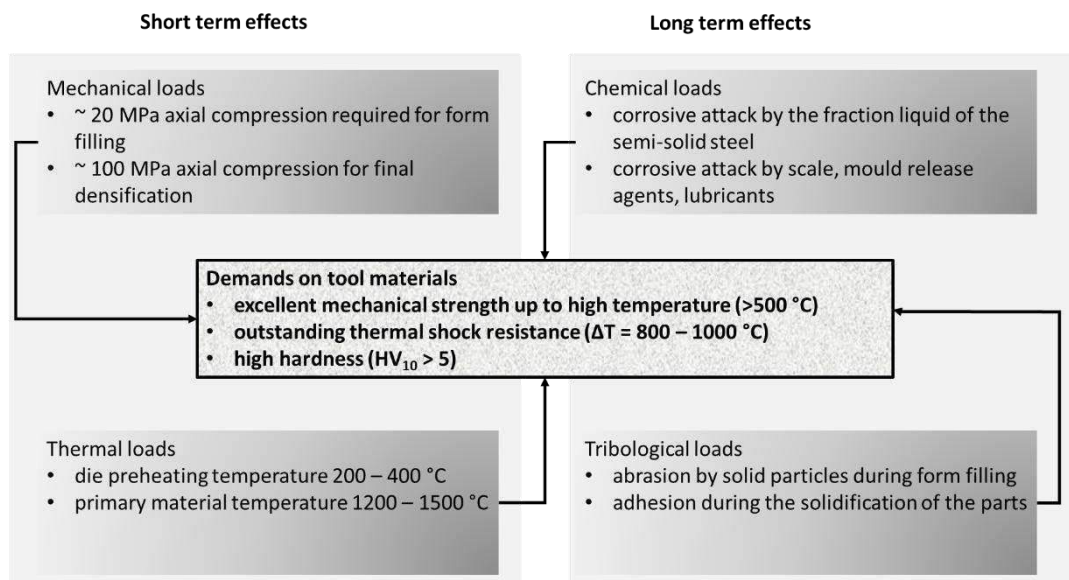


Figure 8. Load profile acting on steel thixoforming dies and resulting demands on tool materials [2]

Mechanical loads include the forming pressure required to fill the die, as well as the final thickening pressure to eliminate porosity in the working parts. While the die pressure is relatively low at approximately 25 MPa according to the literature, the compressive pressure values are diverse in the literature and range from 50 MPa to 1500 MPa [1, 2]. The

preheated primary material in contact with the die and the amount of heat transferred from the semi-solid slurry to the die during filling and solidification of the die, thermally loads the die. The die temperature is directly dependent on the working alloy, which is usually for the steel in the range of 1200 °C to 1500 °C. Therefore, severe heat shocks occurring on the die in each thixoforming cycle.

The surface of the die is chemically affected mainly by the liquid fraction of the semi-solid slurry during the filling of the die. Residual stresses on the preheated primary material strongly affect the chemical interaction between the die and the metal during filling. In order to avoid the oxides inclusion in the casting it is recommended to use a protective atmosphere. Solid particles from the semi-solid slurry cause abrasive damage to the die during material flow and by the ejection of the solidified part.

Mechanical and thermal loads are classified as short-term effects. In contrast, chemical and tribological loads result in surface degradation during steady-state operation, hence they are classified as long-term effects, [1, 2].

The presence of these influences results in an extremely complex die load, compared to the die load for the classical forging and casting method. Contrary to initial expectations resulting from light metal thixoforming, a reduction in process temperatures compared to conventional casting processes (sand casting and gravity casting in permanent moulds) will not reduce the requirements for tool materials.

The solution is not a simple transfer of state-of-the-art tool solutions applied in conventional metal forming processes, but to develop custom tool systems mandatory for semi-solid processing of high melting alloys. Figure 9, schematically shows die temperatures during cyclic thixoforming without any temperature control.

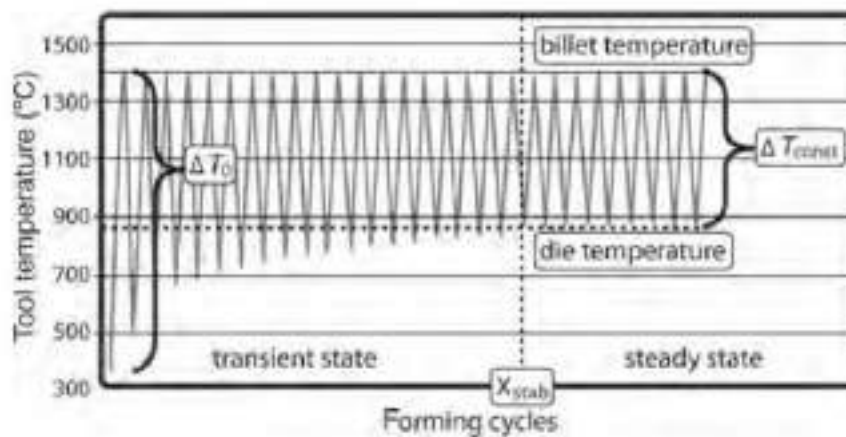


Figure 9. Schematic temperature evolution in steel thixoforming dies during sequenced processing in thixoforging and thixocasting without active temperature control [2]

Starting from the usual die preheating temperature of 350 °C, a temperature close to the working material temperature, for example 1400 °C, is very fast established on the die surface. During the dwell time, after one cycle (forming and ejecting the part), the die temperature drops to value above the preheating temperature until the next cycle begins. During the continuous forming average, the lowest die temperature is constantly increased until a stable state is reached. Thereafter, the temperature of the die changes from the lower to the upper stable limit. There are two phases on the time axis: transition state characterized by severe thermal shocks and a steady state with reduced thermal shocks,

although the average die temperature during operation is significantly higher than in the transition state.

The process carried out in this way would require die systems that can operate at high temperatures, while demonstrating outstanding thermal shock resistance. The upper thermal limit depends on the working alloy, the only parameter that affects the conditions of the thermal process is the temperature of the die. To minimize the transition state, the die temperature can be corrected by heating / cooling devices to a predefined value.

The resulting die temperatures relative to the cycle time are shown in Figure 10. The mean die temperature is reduced compared to the first performance, and the thermal shocks are quite high. Therefore, it is required a die materials with excellent thermal shock resistance, whereas the demands on high temperature stability are decreased.

An alternative solution would be to increase the preheating temperatures of the mould to more than 1000 °C. With this solution, heat shocks on the die are reduced, but die materials that are stable at high temperatures are required (Figure 11).

However, the change in die preheating temperature reflects on the choice of die material and the whole process as well.

Decreased die temperatures lead to fast solidification of the semi-solid slurry in the die cavity, thus reducing the maximum flow length and increasing the minimum wall thickness. Therefore, this process layout is appropriate for the production of workpieces in bulk, compact geometry by gradual forming, ie thixoforging and thixocasting. Due to the short cycle time, the productivity of this process layout is quite high.

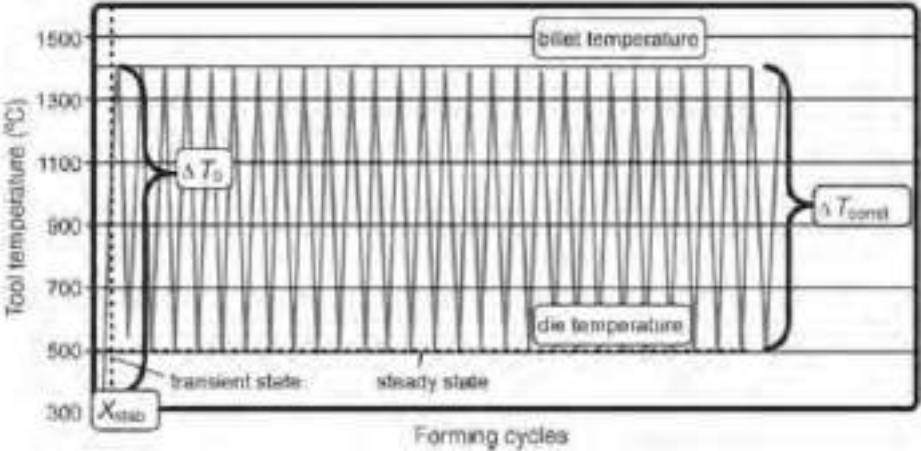


Figure 10. Schematic temperature evolution of steel thixoforging dies during sequenced processing in thixoforging and thixocasting with active cooling of the dies [2]

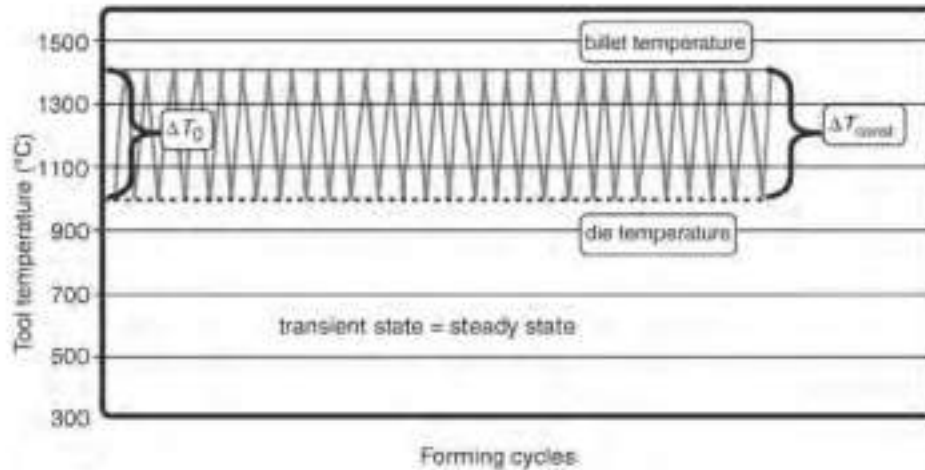


Figure 11. Schematic temperature evolution of steel thixoforming dies during sequenced processing in thixoforging and thixocasting using self-heating tools at high operating temperatures [2]

On the other hand, increased die temperatures lead to slower solidification and allow the production of thin-walled parts with increased flow length and reduced minimum wall thickness. However, the productivity of this process layout is reduced compared to the previous concept.

The ceramic materials, used to make the dies, have an advantage over steel, with respect to the requirements for processing of semi-solid steels. Thanks to the ionic / covalent bond, they have a high hardness, are thermochemically stable and resistant to corrosion against solid and molten metals. But therefore fracture toughness and heat resistance are weak compared to metallic materials. These constraints can be overcome by using hybrid tools, namely by applying ceramic coatings of different thicknesses to metal substrates by thermal spraying technique or by physical / chemical vapour deposition (PVD / CVD). With tools designed in this way, the substrate withstands mechanical loads, and the coating withstands corrosion and tribological loads. The thin layers deposited by the vapor deposition represent a thermal barrier, so thermal shock is not crucial for the coating, but the substrate must also withstand them. Thermal spray coatings, greater thickness and defined porosity, protect the substrate from thermal loads. The porosity strictly reduces the load-bearing capacity of these coatings, which must then be adjusted to mechanical loads. Recent research has shown that hot isostatic pressing can reduce porosity [4].

An example of this hybrid concept is given in Figure 12, showing a thixoforging tool with a flat, physical vapour deposition (PVD)-coated upper swage, a plasma-enhanced chemical vapour deposition (PECVD)-coated liner and a bulk ceramic punch mounted on a steel plunger. Conversely, the demands on die materials to be applied in the concept of hot tools operating at temperatures higher than 1000 °C, regarding high temperature strength and chemical stability in oxidizing atmospheres, are met exclusively by ceramic materials.

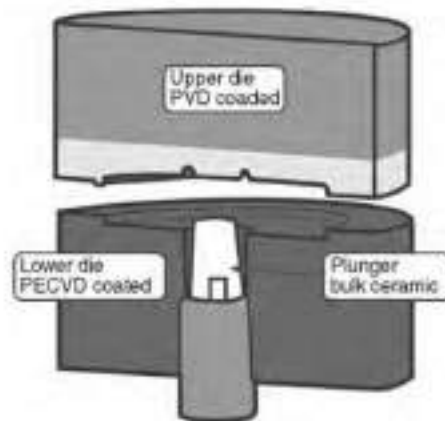


Figure 12. Hybrid tool concept [2]

A test strategy (Figure 13) was established by Meyer-Rau [26] according to the load profile in order to examine the qualification of the different die materials and coating systems for the semi-solid processing of steels. Based on fundamental characterization methods typically applied for coatings and bulk ceramics, the resistance against thermomechanical, chemical and tribological loads was subsequently examined in model tests, which were custom-developed to reproduce the specific attack on dies during steel thixoforming separately.

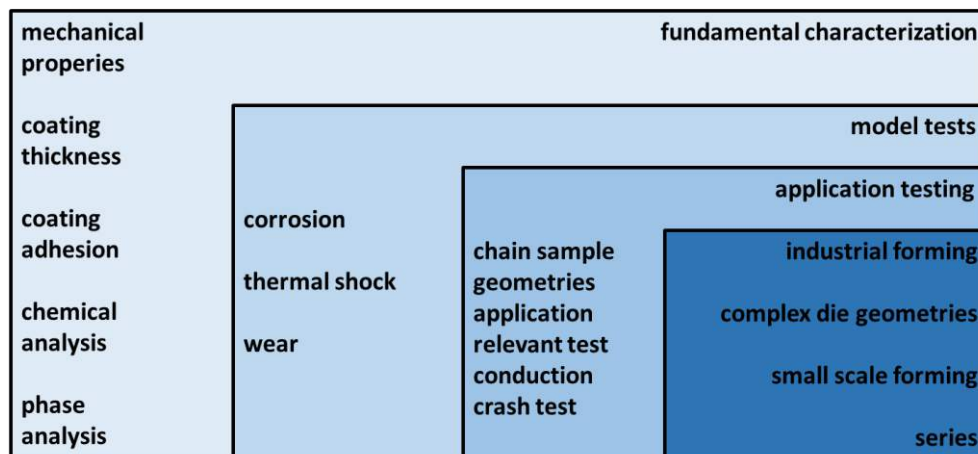


Figure 13. Testing strategy for evaluation and qualification of potential tool materials and systems [26]

CONCLUSION

The world around us is changing very fast and provides us with many challenges, but equally many opportunities. Two important areas, where engineers and scientists can solve this problem in both, the short and long term, are: better use of resources and more efficient use of energy. Semi-solid metal alloy casting appears to have met a number of objectives as it can provide the industry with a production methodology for mass production, better performance, with reduced energy consumption and increased efficiency.

Because of its near net-shape capabilities, SSM processing does not need extra machining processes. Thanks to the microstructure associated with the process and the corresponding rheological advantages, the process yields products with better mechanical properties than traditional ones, because the flow of metal into the mould cavity is uniform and porosity and shrinkage are significantly reduced or eliminated.

In this process, the energy consumption is lower due to the fact that the metal is never completely in a liquid state. Certain product design features can now be combined into complex near-net shape designs that require fewer post-production operations before final use.

In order for production technology to be commercially viable and ultimately successful, it should provide: better quality, better design, cost reduction, weight reduction, or a combination of all of these. From the above review of the current status of industrial SSM processing, it is obvious that meets all these requirements, and therefore needs to ensure its commercial future. The fact that a number of manufacturers, mostly in China, have chosen to believe in this process supports the expectation that SSM processing will eventually become an acceptable 'conventional' manufacturing process.

REFERENCES

- [1] Z. Fan, Semisolid metal processing, *International Materials Reviews*, 47(2002)2, pp. 49-85.
- [2] G. Hirt, R. Kopp - Thixoforming Semi-solid metal processing-wiley (2009)
- [3] S. Nafisi, R. Ghomashchi, *Semi-solid processing of aluminum alloys*, Springer International Publishing, Switzerland, 2016.
- [4] M. C. Flemings, Solidification Processing, *Materials Transactions*, 46(2005)5, pp. 895-900.
- [5] A. Pola, M. Tocci, P. Kapranos, Microstructure and properties of semi-solid aluminum alloys: A Literature Review, *Metals* 2018, 8, 181; doi:10.3390/met8030181
- [6] H. Kirkwood, M. Suery, P. Kapranos, H. V. Atkinson, K. P. Young, *Semi-solid processing of alloys*, Springer Series in Materials Science, Berlin Heidelberg, 2010.
- [7] D.B. Spencer, R. Mehrabian, M. C. Flemings, Rheological behavior of Sn-15 pct Pb in the crystallization range. *Metall. Trans.* 3(1972), 1925-1932.
- [8] G. Hirt, R. Kopp, *Thixoforming, Semi-solid metal processing*, Wiley-VCH, Verlag GmbH & Co. KGaA, Weinheim, Germany, 2008.
- [9] S. Midson, Rheocasting processes for semi-solid casting of aluminum alloys, *Die Cast. Eng.* 50(2006), pp. 48-51.
- [10] M. N. Mohammed, M. Z. Omar, M. S. Salleh, K. S. Alhawari, P. Kapranos, Semisolid metal processing techniques for nondendritic feedstock production, *Sci. World J*, 2013(2013), 752175.
- [11] M. N. Mohammed, M. Z. Omar, M. S. Salleh, K. S. Alhawari, and P. Kapranos, Semisolid Metal Processing Techniques for Nondendritic Feedstock Production, *The Scientific World Journal*, Volume 2013, Article ID 752175, p. 16.
- [12] D. Apelian, Semi-solid processing routes and microstructure evolution, In *Proceedings of the Seventh International Conference titled Advanced Semi-Solid Processing of Alloys and Composites*, Tsukuba, Japan, 24–28 September 2002, pp. 25-30.

- [13] N. Limodin, L. Salvo, M. Suéry, M. DiMichiel, In situ investigation by X-ray tomography of the overall and local microstructural changes occurring during partial remelting of an Al–15.8 wt.% Cu alloy. *Acta Mater.* 55(2007), pp. 3177-3191.
- [14] K. P. Young, D. E. Taylor, H. P. Cheskis, W. G. Watson, Process and apparatus for continuous slurry casting. U.S. Patent 4,482,012, 1 June 1982.
- [15] J. A. Yurko, M. C. Flemings, A. Martinez, Semisolid rheocasting (SSR)-Increasing the capabilities of Die casting. *J. Die Cast Eng.* 48(2004), pp. 50–52.
- [16] J. A. Yurko, R. W. Brower, R. A. Martinez, M. C. Flemings, P. Bertelli, Process and Apparatus for Preparing a Metal Alloy. U.S. Patent 6918427, 19 July 2005.
- [17] J. Wannasin, S. Junudom, T. Rattanochaikul, M. C. Flemings, Development of the gas induced semi-solid metal process for aluminum die casting applications, *Solid State Phenom.* 2008, 141–143, 97-102.
- [18] J. Wannasin, M. C. Flemings, Process for preparing molten metals for casting at a low to zero superheat temperature, WO Patent PCT/TH2014/000025, 2014, Accessible on Internet: <http://www.gissco.com/GISS-process>, (10. 04. 2021).
- [19] D. Doutre, J. Langlais, S. Roy, The seed process for semi-solid forming, In Proceedings of the 8th International Conference on Semi-Solid Processing of Alloys and Composites (S2P '04), Limassol, Cyprus, 21–23 September 2004, pp. 397-408.
- [20] D. Doutre, G. Hay, P. Wales, Semisolid concentration processing of metallic alloys. U.S. Patent 6,428,636 B2, 6 August 2002.
- [21] R. Decker, S. LeBeau, B. Wilson, J. Reagan, N. Moskovich, B. Bronfin, Thixomolding at 25 years, *Solid State Phenom.* 256(2016), pp. 3-8.
- [22] J. Mihelich, R. F. Decker, Apparatus for processing corrosive molten metals, U.S. Patent 5,711,366A, 27 January 1998.
- [23] P. Kapranos, Current State of Semi-Solid Net-Shape Die Casting, *Metals* 2019, 9, 1301; doi:10.3390/met9121301.
- [24] P. Kapranos, Semi-solid metal processing-A process looking for a market, *Solid State Phenom.* (2008)1-8, pp. 141-143.
- [25] R. Barbucci, E. Armenia, V. Quagliariello, The fate of thixotropy in hydrogels, January 2017 In book: *Hydrogels Design, Synthesis & Application in Drug Delivery & Regenerative Medicine* Publisher: CRC Press, Taylor & Francis Group, Editors: Singh
- [26] S. Meyer-Rau, R. Telle, Testing strategies for corrosive interactions of ceramics with semi-solid and molten metal alloys, *Journal of the European Ceramic Society*, 25(2005), pp. 1049-1055.
- [27] N. H. Husain, A. H. Ahmad, M. M. Rashidi, An overview of thixoforming process, 4th International Conference on Mechanical Engineering Research (ICMER2017) IOP Publishing IOP Conf. Series: Materials Science and Engineering 257(2017)012053 doi:10.1088/1757-899X/257/1/012053.



19th INTERNATIONAL FOUNDRYMEN CONFERENCE
Humans - Valuable Resource for Foundry Industry Development
Split, June 16th-18th, 2021
<https://ifc.simet.hr/>

**MICROSTRUCTURE AND FORMABILITY DEVELOPMENT IN Al STRIP CASTING
FOR QUALITY - DEMANDING FOIL PRODUCTION**

Varužan Kevorkijan *

Impol Aluminium Industry, Slovenska Bistrica, Slovenia

Invited lecture
Original scientific paper

Abstract

In comparison with hot-rolled strip, continuous cast strip is a cost-effective raw material for foil production, but different in terms of microstructure, phase composition, formability, and other technological characteristics. Due to the very rapid solidification of molten metal in a continuous thin strip, the microstructure consists of a strongly supersaturated aluminum solid solution and an increased fraction of fine particles of intermetallic phases, precipitated in Al crystal grains. This reduces cast-strip formability. Also, the cast strip's surface is oxidized and contaminated with graphite, which is an additional difficulty.

To produce strip from technical aluminum (group AA 1XXX) and alloys of the Al-Fe type (group AA 8xxx) it was necessary to change the casting parameters as well, as the parameters for further strip processing, which differ from conventional roll-casting procedures. Continuous cast strip is primarily intended for insulation, converter, and household foils of different widths. The principal foil characteristics, prescribed by EN standards, are the mechanical characteristics, surface quality, porosity, and thermostability.

The research work was focused on achieving the listed characteristics by changing the alloy composition and the conditions of transformation of continuous cast strip into the foil. A suitable thermomechanical treatment changes the distribution of alloy elements in the existing microstructural phases and thereby also their effect on static recrystallization, thereby affecting the surface quality and the mechanical characteristics of the foil.

In this study, the optimum composition and the process parameters of continuous casting that make it possible to use the strip as raw material for producing sheets and insulation, converter, and household foils of standard quality are presented.

Keywords: *the continuous casting of Al strips, production of foil stock and foils, tailoring of microstructure, composition, and formability of strips*

*Corresponding author (e-mail address): varuzan.kevorkijan@impol.si

INTRODUCTION

Converting, household and insulation foils are medium to high added-value products if manufactured from in-house raw material [1, 2]. The basic challenges that manufacturers wish to deal with are mastering new technology, use of continuous cast strips for making high-quality foil, and broadening their marketing possibilities with final products of new quality.

For that purpose, it was essential (i) to develop and master new knowledge in the field of developing cast strip properties (roughness, oxide impurities, etc.); to modify the chemical composition of alloys for continuous casting and unify various alloys into a few suitable for continuous casting, without affecting the properties of final products, which is very challenging in terms of technology; (iii) to develop the microstructure, phase composition, and formability of cast strip as well as final products (firstly 8-10 μm gauge insulating, converter, and household foils); and (iv) to continue the development of new products/applications from cast strips.

The introduction of continuous casting of thin aluminum strips based on AA 1050 and AA 8011 causes a fundamental change in the microstructure and therefore physical and chemical properties of the material when compared to conventional working of DC or semi-continuous cast slabs [3-7].

During water-cooled rolling, due to the increased speed of crystallization, and simultaneous hot rolling in a semi-solid state, the solid solution is strongly supersaturated, and non-equilibrium intermetallic phases Al_mFe and $\text{Al}_x\text{Fe}_y\text{Si}_y$ are precipitated. The composition, distribution, size, shape, and fraction of the microstructural constituents have a crucial effect on the formability of these alloys and the final quality of the foil. The presence of fine-grain equilibrium oxide in the metal at the strip surface, the size and orientation of solidification grains, and the central segregations all affect grain size and microporosity [3-5]. Relaxation processes are slower, because of the shorter free path for dislocation sliding during cold working, caused by the greater number of precipitates in the continuous cast alloys.

Understanding how the interrelationship between important alloying as well as trace elements (**Si, Fe, Mn, Cr, Zn, Ti**) in aluminum space lattice affects their solubility makes it possible to change and optimize the chemical composition of aluminum alloys 1050 and 8011, achieving in that way the standard and comparable quality of foil stock suitable for further downstream processing.

The project objective was to understand the processes and determine the evolution of microstructure of rapidly solidifying aluminum alloys (1050 and 8011) cast in new caster, to enable faster development and implementation of new alloys to expand the range of products made from continuous cast thin strip. By knowing the effect of continuous casting process parameters, by optimizing and unifying alloys, and understanding thermomechanical processes we can expect to be able to change sufficiently the microstructure, the chemical composition of the existing phases, and thereby the technological properties and quality level of foil made from continuous cast strip in such a way as to get a favorable response in the market. The new knowledge gained about the material will furthermore serve as a basis

for describing foil properties and their comparison with foil made from hot-rolled strips manufactured from conventional semi- continuously cast slabs.

EXPERIMENTAL PROCEDURES

The R and D activities are made of two main parts:

- Strip production on the twin-roll Jumbo C3 caster, and
- Foil production from caster strip

Strip production on twin roll caster

The activities were divided into **four phases**, each phase corresponding to one of the casting widths (1050, 1150, 1600, and 1700 mm). Each phase covers: casting parameter definition, developing casting operator ability and autonomy to produce under stable casting conditions, improving cast strip geometry (longitudinal gauge variations over the coil length below +/- 2 %, longitudinal gauge variations over one roll revolution below +/-1%, cross profile between 0 and 1%, tilting between two edges limited to 1%), and improving cast strip surface quality, taking into account the feedback from the rolling mill regarding the end products (foil production).

Casting parameters were defined for various widths, alloys and roll cambers, as specified in Table 1.

Table 1. Various alloys, roll cambers and strip widths used for determining casting parameters

	Width (mm)			
	1050	1150	1600	1700
Alloys	AA 1050 AA 1200 AA 8011 AA 8079	AA 1200 AA 8011	AA 1050 AA 1200 AA 8011 AA 8079	AA 1200 AA 8011
Roll camber (mm)	0.3	0.3	0.5	0.5

Foil production from caster strip

For the whole foil production program (final gauge from 0.006 to 0.100 mm), some representative final thickness and widths were chosen. The suitability of the technological procedures for all foils in the thickness range from 0.006 to 0.100 mm was assessed based on the approval of the technology and process for foil production and the approval of quality by customers for the chosen representative final thickness and width. The approval of caster strip quality and technology process for foil production was also performed for all chosen widths using alloys AA 1050, AA 1200, AA 8011 and AA 8079.

RESULTS AND DISCUSSION

Definition of casting parameters

Casting parameters established for each particular alloy, casting width, and roll camber, are listed in Table 2.

Table 2. Casting parameters for selected strips used in this study

	AA 1050	AA 1200	AA 8011	AA 8079
Cast width (mm)	1750	1750	1750	1650
Cast gauge (mm)	6	6	6	6
Launder temperature (°C)	750	750	750	750
Alpur temperature (°C)	735-740	730-735	730-735	735-740
Grain refiner addition (kg/t)	2.0-2.2	3	3	1.0-1.2
CFF temperature setpoint (°C)	720-725	720-725	720-725	720-30
Roll speed (m/min)	1.00-1.10	1.00-1.10	1.00-1.10	1.10-1.20
Strip speed (m/min)	1.15-1.25	1.15-1.25	1.15-1.25	1.25-1.35
Productivity (t/h/m)	1.10-1.25	1.11-1.25	1.11-1.22	1.22-1.32
Total productivity after trimming (t/h)	1.75-2.00	1.90-2.12	1.89-2.07	1.95-2.11

As-cast microstructure of strips

The as-cast microstructure of strips was monitored in the longitudinal and the transverse cross-section at the mid-width (Fig. 1) as well as at the mid-thickness (Fig. 2) of the coils AA 1200. It has been shown that selected casting parameters result in the production of a cast strip of good quality, with especially: very fine microstructure, typical of strip casting at 6 mm with adequate grain refiner addition, small centerline segregation, similar to that in the cast strip of competitors, no hard phases (that could lead to porosity problems), and no surface segregations.

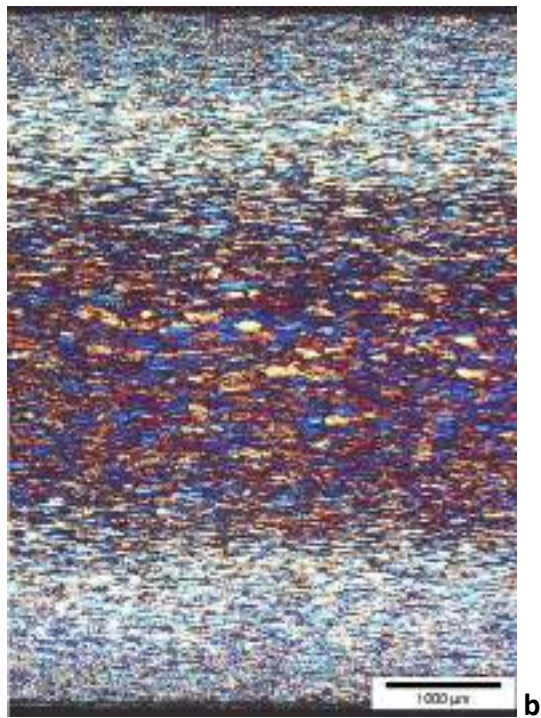
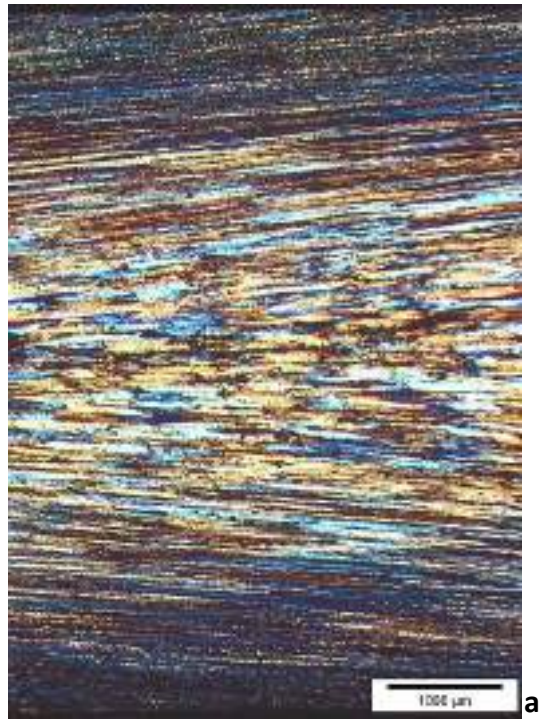


Figure 1. As-cast microstructure observation: (a) in the longitudinal and (b) in the transverse cross-section at the mid-width of the AA 1200 coil

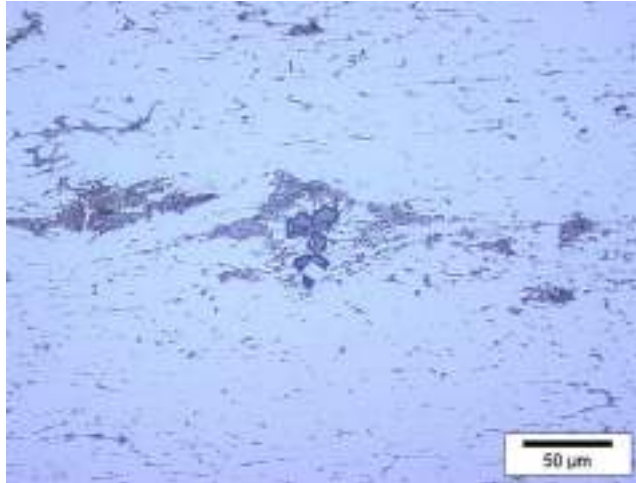


Figure 2. As-cast microstructure at the mid-thickness of the coil AA 1200

Foil production

Fabrication schedules through to the 8-9 μm gauge have been developed for the downstream processing of strips of AA 1050, AA 1200, AA 8011, AA 8079, and AA 8006 alloys. These schedules were field-tested during industrial trials at a rolling mill, where foils are produced from both hot rolled foil stock and as-cast strips.

The key improvements leading to the successful further downstream processing of the foil stock to the converting, household, and insulation foils of standard quality, are:

- Correction of the Fe/Si ratio, and
- Process modification.

The following process modification was proposed for the AA 1200:

- as cast 6 mm,
- rolling down to 3 mm,
- program homogenization at 560-580 $^{\circ}\text{C}$ for 6 h,
- rolling down to 0.6 mm,
- annealing at 320-330 $^{\circ}\text{C}$ for 3 h,
- rolling down to the final gauge 8-9 μm .

For the AA 8011 two different process modifications were applied:

A)

- as cast 6 mm,
- rolling to 0,6 mm,
- annealing at 280-290 $^{\circ}\text{C}$ for 3 h,
- rolling down to the final gauge of 8-9 μm .

B)

- as cast 6 mm,
- rolling down to 3 mm,
- program homogenization at 560-580 °C for 3 h,
- rolling down to 0,6 mm,
- annealing at 290-300 °C for 3 h,
- rolling down to the final gauges 8-9 µm.

The following three downstream processing routes were applied resulting in thin gauge foils:

1st and 2nd tests: standard downstream processing route:

- Cold rolling down to 0.6 mm,
- Intermediate annealing at 0.6 mm (metal temperature 400 °C for 1 hour),
- Foil rolling down to final gauge.

3rd test: standard downstream processing route and one processing route with homogenization:

- Cold rolling down to 3.2 mm (one pass),
- Homogenization (metal temperature 550 °C during 8 to 10 hours),
- Cold rolling down to 0.6 mm,
- Intermediate annealing at 0.6 mm (metal temperature 400 °C for 1 hour),
- Foil rolling down to final gauge.

Trials with AA 1050 alloy for insulation foil products (final gauge 70 µm)

The same downstream processing route down to 70 µm was used in all trials. The main results are:

- 1st trial: non-proper strip surface aspect with longitudinal lines,
- 2nd trial: acceptable strip surface aspect, similar to hot-rolled material,
- 3rd trial: acceptable strip surface aspect, similar to hot-rolled material.

It has been determined that the poor surface aspect obtained with the coils of 1st trial was mainly due to a large grain size at the as-cast state because of not enough grain refiner (large feathery grains were observed at the strip mid-thickness). This was solved during the 2nd and especially the 3rd trial by increasing the grain refiner rate from 1 to 1.6 kg/t-3 kg/t.

Trials with AA 1200 and AA 8011 alloys for foil products (final gauge 8 µm):

The surface quality of the mat side at the final gauge was the most important parameter to be controlled. A correlation between the surface aspect of the mat side and the grain size of the foil was found. A similar correlation was established in the strip (cold-rolled down to 0.6 mm), after intermediate annealing.

The results obtained could be summarized as follows:

Regarding AA 1200 alloy, the foil with Fe/Si ratio 1:1 from the 2nd trial the grain size was small both, at the final gauge and after intermediate annealing (without any large surface grains). The grain size was, however, slightly larger than in the foil from reference caster material. The foil with Fe/Si ratio 2:1 from the 2nd trial has larger grains at the final gauge and large surface grains are observed after intermediate annealing. The foil with Fe/Si ratio 2:1 from the 1st trial has numerous large grains both at the final gauge and after intermediate annealing.

In the case of AA 8011 alloy, the foil from the 2nd trial has a slightly larger grain size at the final gauge than the foil from the 1st trial. The material from the 2nd trial also has a few large surface grains after intermediate annealing.

It was found that the Fe/Si ratio 1:1 for foils made from AA 1200 alloy gave a better surface quality of the final product. Also, the increased grain-refining rate was the key to the improved mat-side surface aspect in the 2nd and 3rd trials.

Taking into account the foils from AA 8011 alloy, the slightly lower mat-side quality of the 2nd and 3rd trials compared to the 1st trial may be due to the higher casting speed. A possible explanation is that casting speed is affecting the solidification front, the segregation regime of the alloying elements, and therefore the distribution of the recrystallization nuclei.

Suitability of caster material for foil downstream processing

Isolation foil (70 μm): Alloy 1050 is suitable for the production of isolation foil, using a standard processing route (without homogenization). The quality obtained (especially surface aspect) is comparable to hot-rolled material

Technical foil: Alloy 1050 is suitable for the production of technical foil, using a standard processing route (without homogenization)

Household foil (10 μm): Alloy 8011 processed through standard route (no homogenization) is suitable for the production of household foil

Converter foil (8 to 10 μm): Alloys 1200* and 8011 processed through a route with homogenizing are suitable for the production of converter foil. Homogenization is giving the good mat-side quality needed for converter foil

Blister foil (about 20 μm): For this specific case, thermostability is a key property. For alloys 1200 and 8011 processed through the standard route (without homogenization), thermostability is within the specifications. Depending on the surface quality requirements, a specific processing route will probably have to be defined for this foil product

Porosity (general comment for all foils): Porosity from caster material is usually at a low level, well within the specifications, except in some cases. A sufficient proportion of ingots must always be used in the furnace charge (at least 50 to 70 %) and filtration could be increased.

CONCLUSIONS

Complete casting parameters from strip production on the caster were defined and approved for alloys: AA 1050, AA 1200, AA 8011, AA 8079.

Various strip downstream processing routes for foil stock and foil production were tested on the level of industrial trials.

Based on this, several process modifications were introduced resulting in significant quality improvements of the as-cast strip, foil stock, and foils.

Insulation, converter, and household foils of standard quality in gauge between 8-70 μm were produced and foil production technology for these target products was successfully implemented.

REFERENCES

- [1] CRU Aluminium Research Group, Continuous casting of aluminum sheet, CRUInternational Ltd., London, 2000.
- [2] B. Taraglio and C. Romanowski, Thin gauge/high-speed roll casting technology for foil production, Light Metals 1995, (J. Evans), TMS, 1995, Warrendale, Pennsylvania, USA, p. 1165.
- [3] O. Daaland, A. B. Espedal, M. L. Nedreberg, I. Alvestad, Thin gauge twin-roll casting, process capabilities and product quality, Light Metals 1997, (R. Huglen), TMS, 1997, Warrendale, Pennsylvania, USA, pp. 745.
- [4] M. Gupta, D. P. Cook, J. Sahai, Strip casting of aluminum using twin roll casters, in C. E. Eckert (ed.), Light Metals 1999, (C. E. Eckert), TMS, 1999, Warrendale, Pennsylvania, USA, pp. 925.
- [5] S. Ertan, M. Dundar, Y. Birol, K. Sariogly, E. Ozden, A. S. Akkurt, G. Yildizbayrak, S. Hamer, C. Romanowski, The effect of casting parameters on twin-roll cast strip microstructure, Light Metals 2000, (R. D. Peterson), TMS, Warrendale, Pennsylvania, USA, 2000, p. 667.
- [6] C. A. Santos, J. A. Spim Jr., A. Garcia, Modelling of solidification in twin-roll strip casting, J. Mater. Process. Technol., 102(2000), p. 33.
- [7] D. S. Kim, W. S. Kim, A. V. Kuznetsov, Analysis of coupled turbulent flow and solidification in the wedge-shaped pool with different nozzles during twin-roll strip casting, Numerical Heat Transfer, A, 41(2002), 1.



19th INTERNATIONAL FOUNDRYMEN CONFERENCE
Humans - Valuable Resource for Foundry Industry Development

Split, June 16th-18th, 2021

<https://ifc.simet.hr/>

**EXPERIMENTAL AND NUMERICAL ANALYSIS OF
PRINTED LATTICE STRUCTURE**

Dražan Kozak^{1*}, Katarina Monkova^{2,3}, Darko Damjanović¹, Marina Franulović⁴, Jerzy Józwiak⁵, Katarina Pisačić⁶

¹ University of Slavonski Brod Mechanical Engineering Faculty in Slavonski Brod, Slavonski Brod, Croatia

² Technical University in Košice Faculty of Manufacturing Technologies with the seat in Prešov, Prešov, Slovakia

³ Tomas Bata University in Zlin Faculty of Technology, Zlin, Czech Republic

⁴ University of Rijeka Faculty of Engineering, Rijeka, Croatia

⁵ Lublin University of Technology Faculty of Mechanical Engineering, Lublin, Poland

⁶ University North, Varaždin, Croatia

Invited lecture

Original scientific paper

Abstract

Additive manufacturing techniques enable produced components with extremely complex, not only external shapes, but also with the internal structures in their cores. One of these structures are lattice structures. Mechanical characteristics of such a 3D printed lattice structure depend firstly on the material from which it is made. Further, it also strongly depends on the topology of the structure itself. By varying of topology of a lattice structure, the physical response of such a structure can be significantly different and accordingly it can be easily adopted for a specific case.

This research deals with the originally designed 3D printed lattice structure, which is analysed both experimentally and numerically by uniaxial compression test. The samples were made from ABSplus - P430 Ivory plastic by FDM technique without the use of supporting material. The produced lattice specimens were subjected to a full range (up to failure) compression tests on the Zwick 1456 testing machine equipped with TestExpert software to process the measured data. The force-displacement diagram has been recorded during the testing. It was simulated also by finite element method to determine the stresses, displacements and reaction force obtained on upper plate, as well. The mesh sensitivity study was performed to check the mesh convergence.

Keywords: *3D printing, ABS plastic, lattice structure, finite element analysis, force-displacement, compression test*

*Corresponding author (e-mail address): dkozak@unisb.hr

INTRODUCTION

Some of the main reasons for using porous materials is noise absorption and mass reduction which results in improved mechanical characteristics and decrease in material consumption. Noise is considered unwanted in everyday life and engineering practice, so it is eliminated usually in two ways, with the active noise reduction systems [1] and passive absorbers. For passive absorption resonant and porous absorption materials are used [2]. Porous materials are classified as materials of low specific density with a range of physical, mechanical, thermo-electrical and acoustic properties. Their mechanical properties depend on material and topology of the structure, including geometry and relative density, or so-called "volume ratio" V_r . Volume ratio expresses percentage ratio of the volume of solid phase to the total volume, as follows:

$$V_r = \frac{\text{Volume of solid phase}}{\text{Total volume}} \cdot 100 [\%] \quad (1)$$

Not all materials that contain pores are considered as porous materials. Pores and fractures that are results of errors in casting and welding procedures will have negative impact on the performance of machine parts and it is aimed to reduce their occurrence. Materials that are called porous have two main characteristics: they must contain a lot of pores and pores contributing to the improvement of material performance [3]. Porous materials can be classified in several ways, one way is by the origin of material, as it is found in nature or manmade. Natural porous materials are wood, sponge and felt. Researchers have tested natural materials and found them to be good sound absorbers [4-7]. Manmade materials are usually more predictable, and it is usually easier to simulate their properties numerically. Second classification of porous materials is by pore size, so there are microporous materials with the pore size less than 2 nm, mesoporous with the pore size of 2 to 50 nm and macroporous with the pore size larger than 50 nm [8]. Another classification is according to geometry as shown in Figure 1.

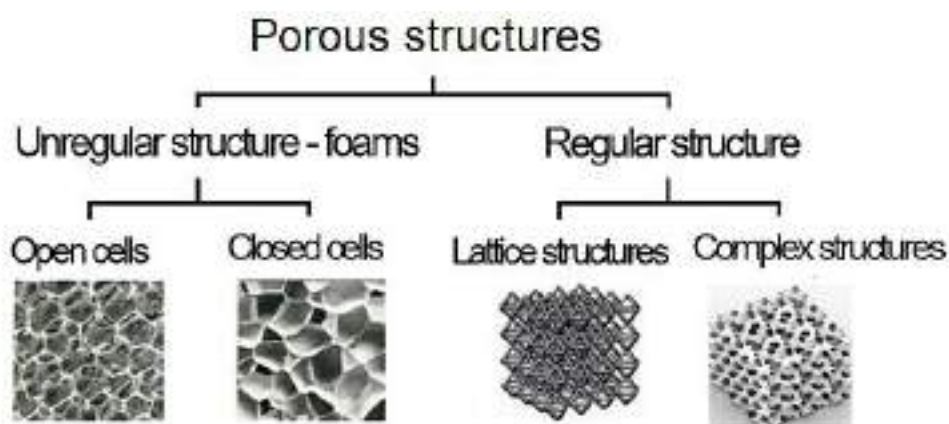


Figure 1. Classification of porous structures according to the geometry

Recently, materials with the large pores and regular structures are manufactured by additive technologies and they are often called lattice structures (LS) and cellular lattice structures (LSC) [9]. The advantage of regular cellular lattice structures comparing to irregular ones is

better control of mechanical properties. Main characteristic of lattice structures is connecting points of the structure by straight beams with various cross sections. Structures with complex shape surfaces are usually described by mathematical formula such as Schoen gyroid structure:

$$\sin\left(\frac{2\pi}{L}x\right)\cos\left(\frac{2\pi}{L}y\right)+\sin\left(\frac{2\pi}{L}y\right)\cos\left(\frac{2\pi}{L}z\right)+\sin\left(\frac{2\pi}{L}z\right)\cos\left(\frac{2\pi}{L}x\right)-t=0 \quad (2)$$

where L stands for the size of the basic cell parameter and t is decisive factor of the cross-section strut.

Common techniques for producing lattice structured parts are 3D printing, FDM (Fused Deposition Modelling), SLM (Selective Laser Melting), SLS (Selective Laser Sintering), SHS (Selective Heat Sintering), Polymer Printing/Jetting and that [10-12]. In the recent years FDM has become widely available partially due to the low price of additive materials such as ABS (Acrylonitrile Butadiene Styrene), wax filament, HDPE (High-density Polyethylene) and others. Zieliński et.al. [13] investigated various additive manufacturing (AM) techniques to find if AM is appropriate technology for producing porous samples used for noise reduction. The authors [13] used one pore and four pores open porous structures and have found AM useful for producing specimens for good noise reduction.

The usage of body-centered cubic (BCC) cells in lattice structures (LS) is explored in several articles. The article [14] explores the effect of a strut length and orientation on elastic mechanical characteristics of modified (BCC) lattice structures (LS). The researchers performed finite element analysis on two sets of models. The first set has 13 models having fixed strut length with the strut angle varying from 40 to 100 with the step 5. In the second set the strut length is varied but kept constant across a model, with the same strut angle variation, while one model in each set has the angle 70,53° which is also the angle of the reference model. The reference model was printed by the FDM 3D printer using an ABS filament and tested experimentally under compression. The results show that the specimen with the strut angle of 100° has the highest modulus, while the highest strain energy absorption and specific stiffness, but the least weight has the model with the strut angle of 40°.

The researchers [15] regard lattice structures as excellent candidates for use in lightweight energy absorbing applications, such as crush protection. They investigate differences between BCC and a reinforced variant called BCC_z. The mechanical anisotropy of structures was explored by applying a compressive load in two orthogonal directions. They examined functionally graded lattice which had a density gradient along one orthogonal direction. The results showed increase in energy absorption in the BCC_z graded structure comparing to non-graded version.

Design of a new lattice structure in the article [16] has been considered to fall into same category as defining a new material due to its unique properties. Using Metal additive manufacturing (MAM) technology many obstacles in creating new and innovative structures has been removed. The authors introduced a new circular cell based LS, they produced specimens with three wall thicknesses to compare them with BCC LS with equivalent strut diameters.

Beside strength and stiffness of the plastic LS, other mechanical properties of LS have also been researched, such as e.g., damping [17], as well as properties of various other AM materials such as Ti-6AL-4V [18]. Since producing parts by SLS or SLM technology has

limitations in size and rather high price, researchers explore other technologies such as Wire Arc Additive Manufacturing (WAAM) [19] for structures to remain high efficiency but at lower costs.

Since LS have complex geometry, the numerical simulations run on LS have long computing time and researchers investigate simplification procedures to decrease computing cost. Authors [20] propose a beam element to replace a lattice structure. In the article [21] researchers offer reduced order model lattice-type structure design which improves on approximation schemes used in [22-26] using component-wise reduced order modeling to make solution of an ordinary FEM model of a lattice efficient enough for the many-query context of design optimization.

Image-to-analysis framework is applied to efficiently evaluate the bending behavior of AM produced LS in [27]. Authors used the Finite Cell Method (FCM) to perform a three-dimensional numerical analysis of the three-point bending test of a lattice structure and compare the designed to manufactured properties. They undertook a comprehensive study on the use of dimensionally reduced beam models to the prediction of the bending behavior of lattice beams and validate classical and strain gradient beam theories applied in combination with the FCM.

MATERIALS AND METHODS

This work will showcase behavior of the sample quasi-statically loaded by means of experimental testing and numerical analysis. The investigated structures have BCC basic cell, which is patterned in three directions, the 3D model was produced in PTC Creo 6. The size of the sample is 60 x 70 x 80 mm, with the basic cell size $a = 10$ mm, volume ratio $V_r = 69,5$ % and the diameter of the beam cross section $\phi_d = 4$ mm, as shown in the Figure 2, a) (basic cell) and 2, b) (whole sample model).

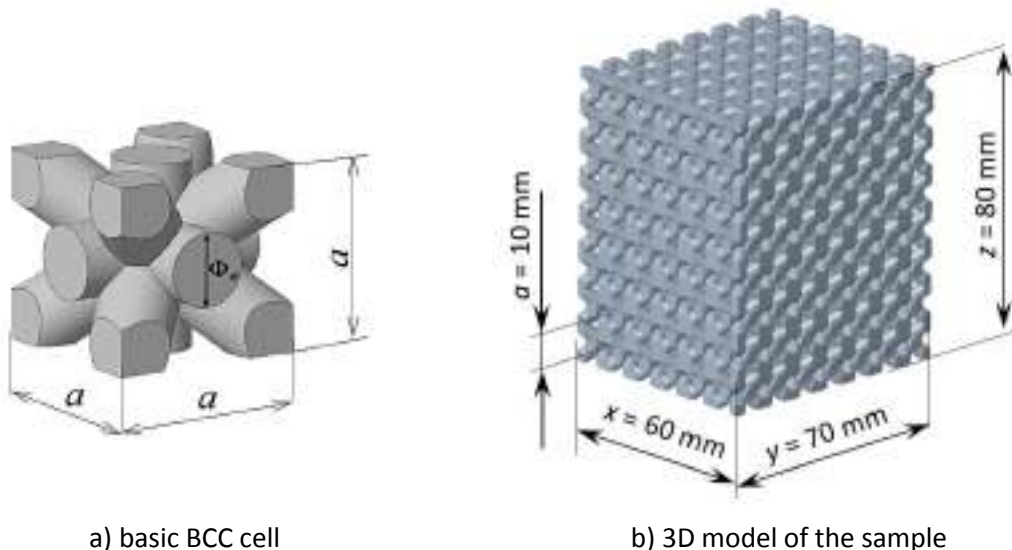


Figure 2. Geometry of the sample [27]

Figure 3 shows real sample which was produced of the material ABSplus filament – specifically P430 Ivory plastics (Ivory is the color), that is a durable thermoplastic material suitable to produce functional prototypes as well as for household use-end products [28].

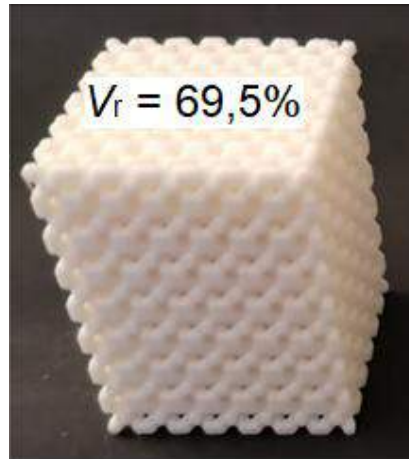


Figure 3. Considered specimen with $V_r = 69,5\%$

Preliminary tests were aimed at verifying the material properties declared by the manufacturer of the ABSplus filament. Both experimental test and numerical analysis were run on the sample of ABS filament. For experimental analysis tensile test machine CS 225 was used, it is shown in Figure 4. Tests were carried out at the ambient temperature $20\text{ }^\circ\text{C}$ and relative humidity 52% . Totally five samples of length 10 mm and diameter $1,75\text{ mm}$ of the ABSplus filament were tested and an average value of maximal limit strength R_m was calculated.



Figure 4. Tensile test equipment

Numerical analysis was done in CAD/CAM system PTC CREO 6.0, Figure 5.



Figure 5. Numerical results for compression stress at ultimate strength R_m

The results of preliminary test are summarized in the Table 1 and show that strength at maximal stress corresponded to the producer datasheet. It should be noted here that for FEM analysis, Poisson's ratio with value $\nu = 0,394$ has been used.

Table 1. Results of preliminary tests

<i>Mechanical property</i>	<i>Experimental analysis</i>	<i>Producer</i>	<i>Numerical analysis</i>
<i>Compression ultimate strength R_m, MPa</i>	45,18	43	43,49
<i>Young's modulus E, MPa</i>	2194,86	2140	-

In this research FDM was used to produce the samples. Sample was printed with 3D printer Prusa i3 Mk2, model shown in Figure 6.



Figure 6. Image of 3D printer Prusa i3 Mk2S [29]

Fused Deposition Modelling is one of the common techniques for 3D printing of plastics. As a rule, an FDM 3D printer comprises an extruder, a nozzle, a print chamber, and a filament feeding system. After accessing the feeding system, the material gets guided to the extruder where it is then melted. Then, the nozzle extrudes a melted filament onto the build plate of a print chamber, creating a 3D printed model.

The following conditions were used for the porous samples producing:

- material: ABSplus Ivory
- diameter of the filament: ϕ 1,75 mm
- melting temperature of the filament: 300 °C
- temperature of the internal printer environment: 75 °C
- temperature of the base: 100 °C

- layer thickness: 0,25 mm.

The building direction during 3D-printing corresponded to the z-axis and samples were printed using no supports.

The main purpose of compression testing in this research was to determine the behavior and response of the lattice structure under compressive loading. Uniaxial quasi-static compression tests over the entire range (up to failure) were performed according to the ISO 844 standard at an ambient temperature of 22 °C controlling the displacement at 0,1 mm/s. The measured data for force and displacement were recorded.

The test setup is shown in Figure 7, a) – the test machine with control unit b) specimen positioned between plates.



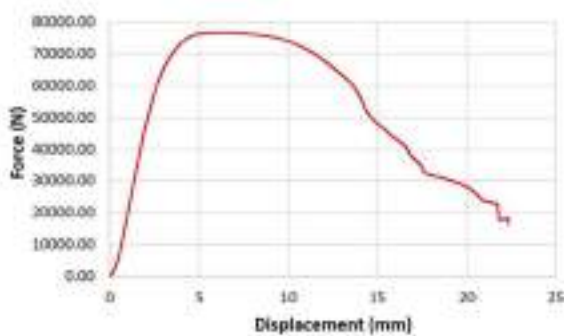
a) testing machine



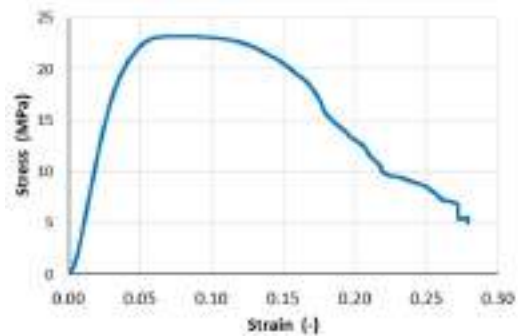
b) specimen between plates

Figure 7. Experimental set up

Some of the obtained curves are shown in Figures 8, a) and 8, b).



a) Force - displacement



b) Stress - strain

Figure 8. Examples of compression test results

NUMERICAL ANALYSIS

Numerical methods, like Finite element method (FEM) are used for in-depth analysis of components and structures. Due to the complexity of LS geometry, as shown in Figure 9., the finite element analysis seems very suitable.

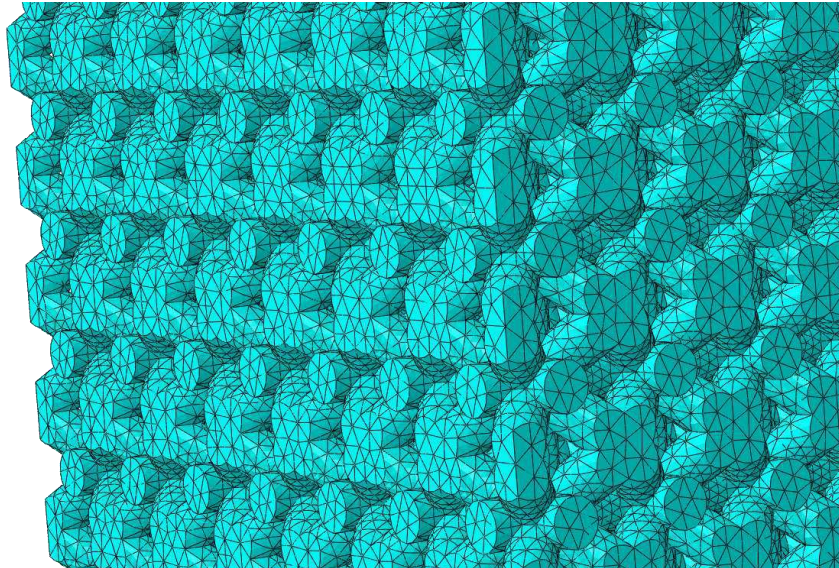
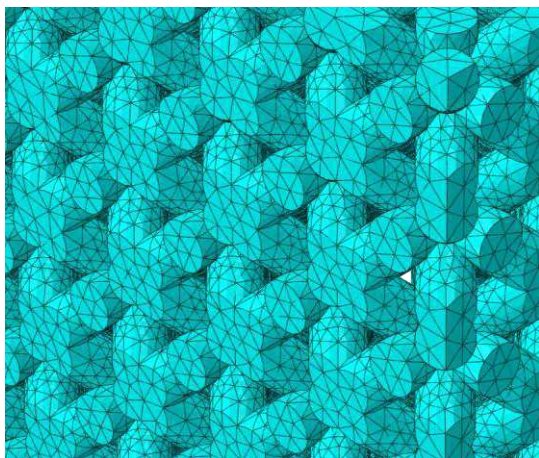
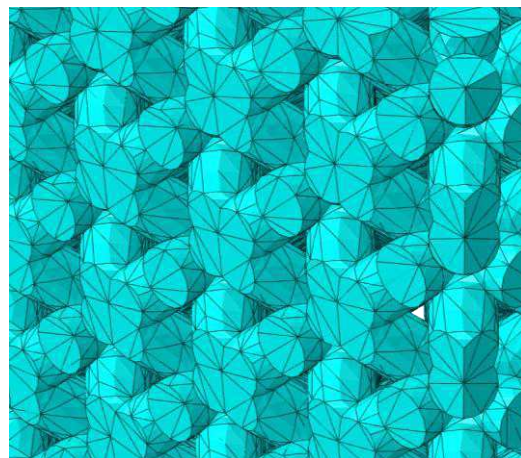


Figure 9. Finite element mesh of a BCC LS

In [21-27], as explained in more detail in the introduction, several procedures of FEM analysis of such structures are presented. Most methods have not so good approach in comparison to using straightforward FEM. The main aim of this research is to develop fast and reliable procedure for numerical analysis of LS. To do that, first important step is to perform a mesh sensitivity study to determine the convergence of the mesh and conclude which finite element mesh is appropriate to get reliable results. For this study elements sized 2, 4, 6, 8, 10, 12, 14 mm are compared. Figure 10. shows the look of the mesh with a) 2 mm size and b) 14 mm size.



a) element size 2 mm



b) element size 14 mm

Figure 10. Various size elements

For material model used in FEM analysis elastic-plastic material is used. Linear elastic parameters are shown in Table 1, while the plastic part of the material model is presented in Figure 11.

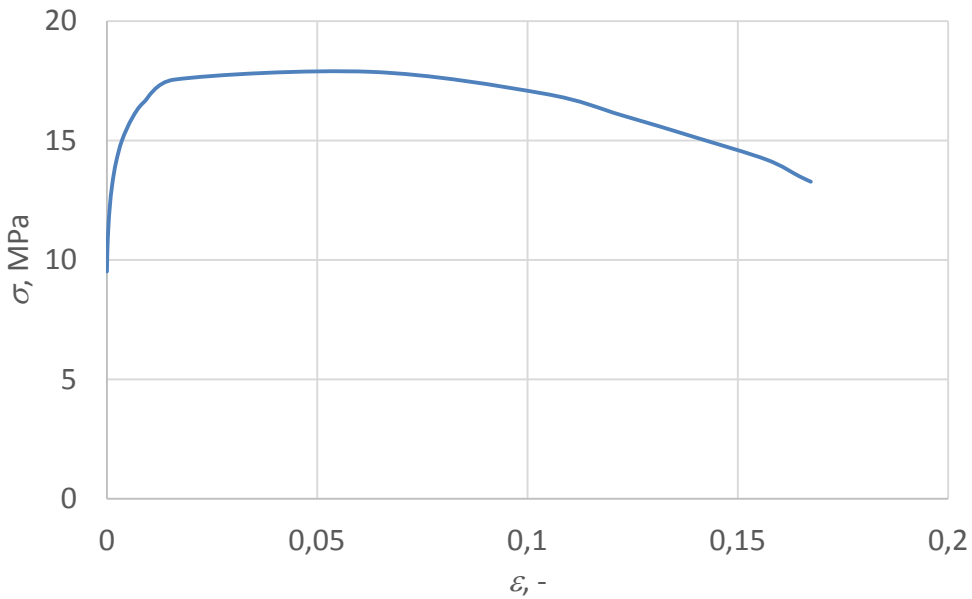


Figure 11. Plastic part of material model

For all models, the results of maximal principal stress, reaction force obtained on upper plate and CPU time are extracted. To get results most comparable to the experimental data, simulation is set up in a way so that the specimen is placed between two rigid plates, while the displacement of the upper plate is controlled.

The simulation is set that way so that force can be obtained at the upper plate which is loading plate thus is possible to obtain force-displacement curve to compare it with experimentally obtained one. Boundary conditions are shown in the Figure 12 and explained in the further text.

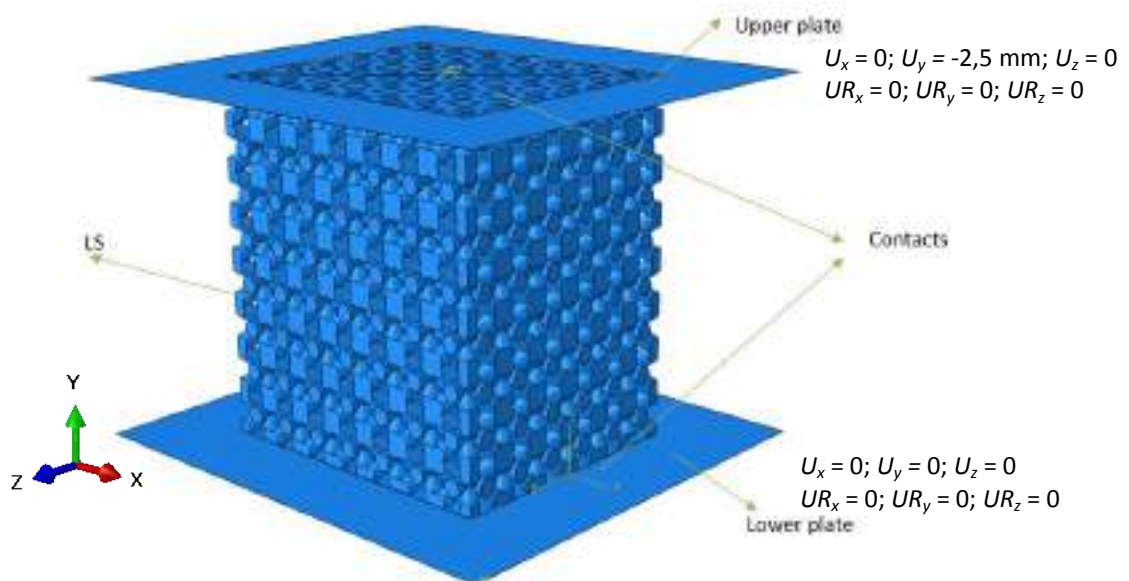


Figure 12. Finite element model setup and boundary conditions

LS is modelled as a 3D deformable model with elastic-plastic material model.

Upper plate is modelled as a rigid surface, where $U_x = 0$; $U_y = -2,5$ mm; $U_z = 0$, $UR_x = 0$; $UR_y = 0$; $UR_z = 0$. Lower plate is modelled as well as a rigid surface, where $U_x = 0$; $U_y = 0$; $U_z = 0$, $UR_x = 0$; $UR_y = 0$; $UR_z = 0$.

Contact between plates is set so that it is considering normal and tangential behavior of the model. Contact in normal direction is set as a hard contact with separation after the contact, while contact in tangential direction is set using the penalty formulation with friction coefficient of 0,2.

PRELIMINARY RESULTS AND DISCUSSION

As mentioned, several various mesh sizes are used for mesh sensitivity study. Table 2 shows statistics of mesh for each element size.

Table 2. Number of elements in relation of element size

Element size, mm	Number of elements, -
2	2287751
4	2269436
6	1651838
8	1124910
10	910395
12	722255
14	699920

Diagrams in Figures 13 and 14 show the convergence of results for maximal principal stress and reaction force on upper plate, while diagram in Figure 15 shows the CPU time versus number of elements.

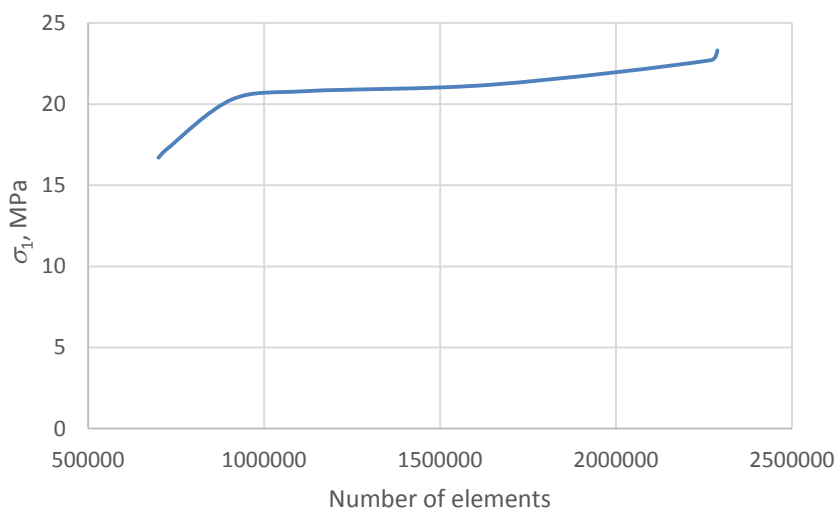


Figure 13. Convergence of maximal principal stress

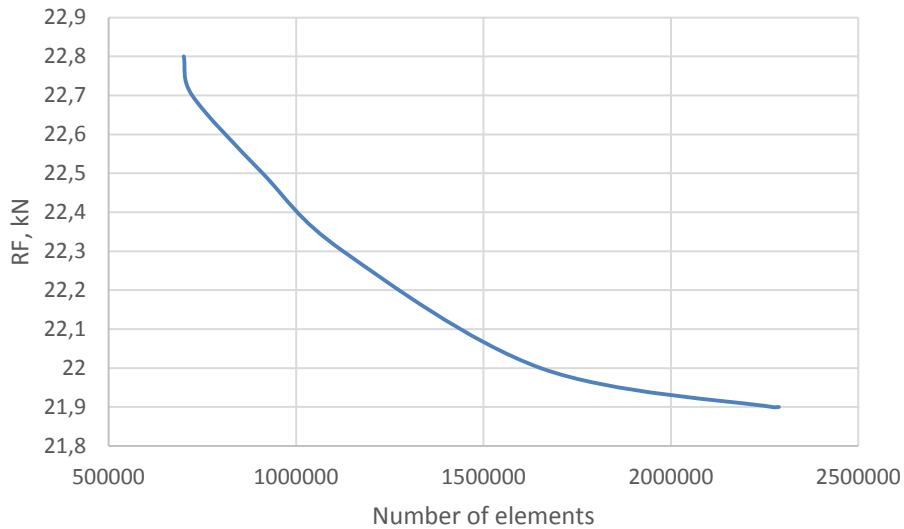


Figure 14. Convergence of reaction force RF on upper plate

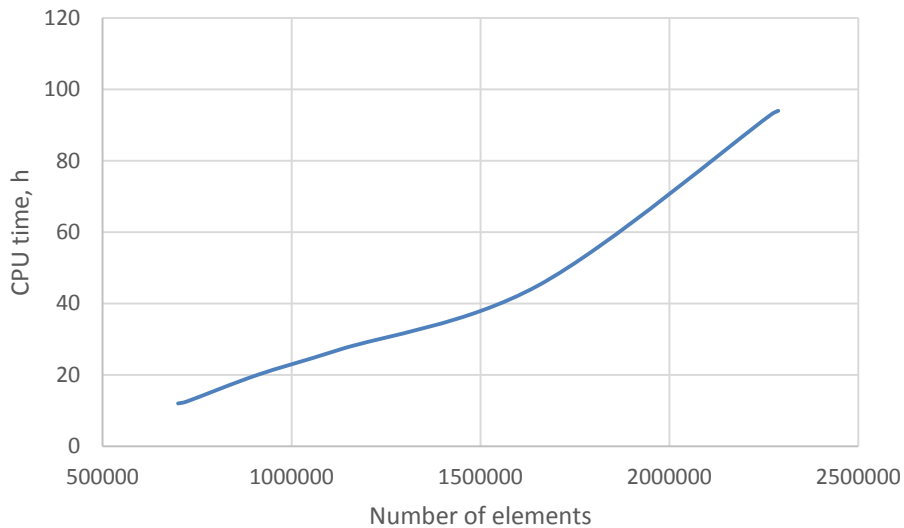


Figure 15. CPU time in relation of number of elements

As expected, stresses are highly depended on element size, and with this preliminary convergence study it can be concluded that mesh size of 6 mm gain reliable results for reasonable time. Further, reaction force RF is not so depended on number of elements. It can be seen in Figure 14 that for element size of 14 mm RF = 22.8 kN, while for element size of 2 mm RF = 21.9 kN, difference being less than 1 kN. Regarding CPU time, for element size 2 mm CPU time is 94 h, while for element size 14 mm CPU time is 12 hours. For chosen element size of 6 mm CPU time is 45 hours.

Hereafter, results for max principal stress and displacements are shown. It should be noted that those are preliminary results, since some deviations in relation to experimental results and numerical model are still present, so the material model should be improved.

Figure 16 shows displacements distribution for displacement of upper plate of 2.5 mm in negative y direction. Figure 17 shows effective von Mises stress, and maximal principal stress distribution for displacement of upper plate of 2.5 mm.

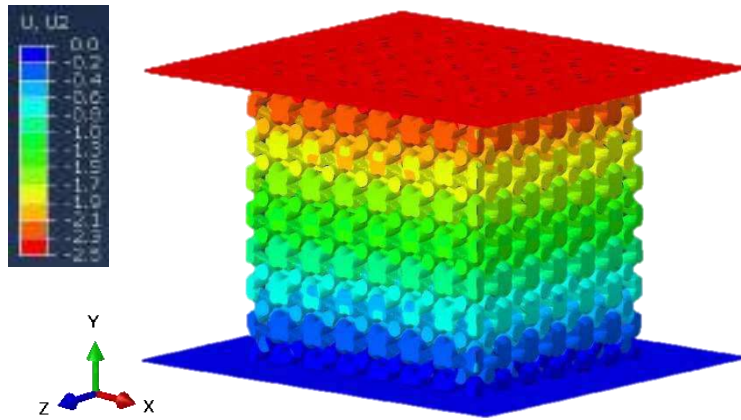


Figure 16. Displacements along y direction for displacement of upper plate of -2.5 mm

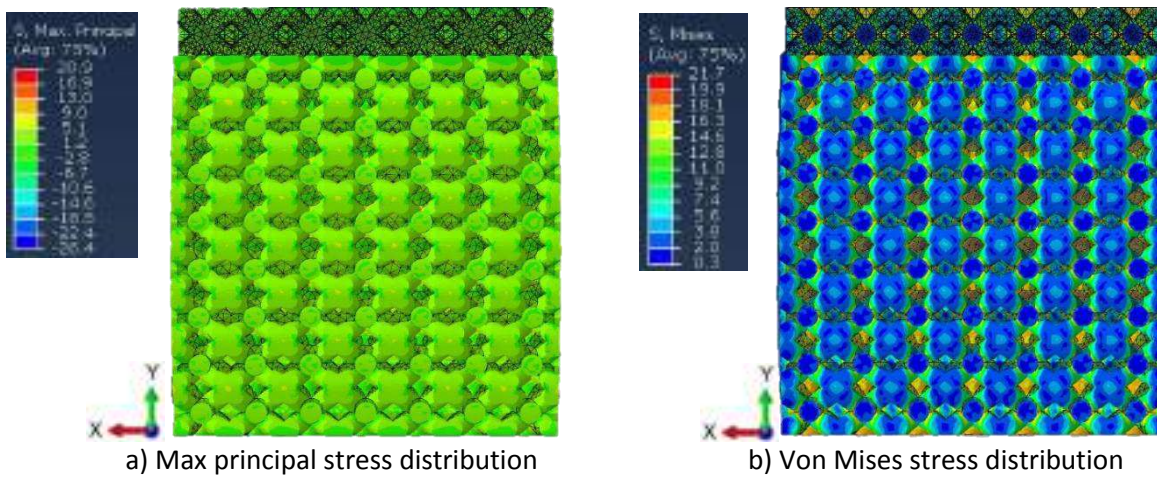


Figure 17. Maximal principal stress distribution and von Mises effective stress distribution for the displacement of upper plate of -2.5 mm

CONCLUSIONS

Firstly, from results of preliminary tests, it can be concluded that the maximal strength stress of the ABS filament used in sample production, corresponds to the product declaration. Secondly, the research is aiming to compare experimental and numerical analysis of a simple lattice structure loaded quasi-statically by compression. Only some preliminary results are presented here, but the final aim is to make fast and reliable numerical procedure as the basis for simulations of the behaviour of more complex structures embedded in the kernel of real components.

To have reliable results, simulations are performed previously with the aim to get the convergence of the mesh. Mesh study was run using finite element sizes of 2, 6, 8, 10, 12 and 14 mm and the resulting stresses, reaction forces on upper plate displacement and CPU time have been considered and compared to determine which element size is best choice in means of reliable results and reasonable computational cost.

The LS are computationally demanding, and further research would be beneficial, for example simulating one-unit cell of the same lattice geometry then model with 8 unit cells,

27 unit cells etc. The question such a research would answer is if the model with less cells could be representative of a large scale model and if simplifications could be possible to reduce computational cost.

Acknowledgements

This work has been supported by Croatian Science Foundation under the project number IP-2019-04-3607, and by the Ministry of Education, Science, Research, and Sport of the Slovak Republic through the project APVV-19-0550.

REFERENCES

- [1] J. Jiang, Y. Li, Review of active noise control techniques with emphasis on sound quality enhancement, *Applied Acoustics*, Volume 136, 2018, pp. 139-148.
- [2] L. Cao, Q. Fu, Y. Si, B. Ding, J. Yu, Porous materials for sound absorption, *Composites Communications*, 10(2018), pp. 25-35.
- [3] P. S. Liu, G. F. Chen, *Porous materials processing and applications*, Butterworth-Heinemann, Oxford 2014.
- [4] C. Wassilieff, Sound absorption of wood-based materials *Appl. Acoust.* 48(1996)4, pp. 339-356.
- [5] H. Kolya, C. Kang, Hygrothermal treated paulownia hardwood reveals enhanced sound absorption coefficient: An effective and facile approach, *Applied Acoustics*, 2020, 107758.
- [6] C. Meriç, H. Erol, A. Özkan, On the sound absorption performance of a felt sound absorber, *Applied Acoustics*, 114(2016), pp. 275-280.
- [7] W. Yang, Y. Li, Sound absorption performance of natural fibers and their composites, *Sci. China Technol. Sci.* 55(2012), pp. 2278-2283.
- [8] J. Mikšić, *Porozni materijali, završni rad*, Sveučilište Josipa Jurja Strossmayera u Osijeku, Odjel za kemiju, Osijek 2017.
- [9] Y. Wang, L. Zhang, S. Daynes, H. Zhang, S. Feih, M. Y. Wang, Design of graded lattice structure with optimized mesostructures for additive manufacturing, *Materials & Design*, 142(2018), pp. 114-123.
- [10] X. Zhang, Z. Qu, H. Wang, *Engineering Acoustic Metamaterials for Sound Absorption: From Uniform to Gradient Structures*, *iScience*, 23(2020)5
- [11] N. Gao, H. Hou, Sound absorption characteristic of micro-helix metamaterial by 3D printing, *Theoretical and Applied Mechanics Letters*, 8(2018)2, pp. 63-67.
- [12] T. Dupont, P. Leclaire, R. Panneton, O. Umnova, A microstructure material design for low frequency sound absorption, *Applied Acoustics*, 136(2018), pp. 86-93.
- [13] T. G. Zieliński, K. C. Opiela, P. Pawłowski, N. Dauchez, T. Boutin, J. Kennedy, D. Trimble, H. Rice, D. Van Damme, G. Hannema, R. Wróbel, S. Kim, S. G. Mosanenzadeh, N. X. Fang, J. Yang, B. B. de La Hossieraye, M. C. J. Hornikx, E. Salze, M. Galland, R. Boonen, A. C. de Sousa, E. Deckers, M. Gaborit, J. Groby, Reproducibility of sound-absorbing periodic porous materials using additive manufacturing technologies: Round robin study, *Additive Manufacturing*, Volume 36, 2020.

- [14] Abdulhadi HS, Mian A. Effect of strut length and orientation on elastic mechanical response of modified body-centered cubic lattice structures. *Proceedings of the Institution of Mechanical Engineers, Part L: Journal of Materials: Design and Applications*. 2019;233(11):2219-2233.
- [15] I. Maskery, A. Hussey, A. Panesar, A. Aremu, C. Tuck, I. Ashcroft, R. Hague, An investigation into reinforced and functionally graded lattice structures. *Journal of Cellular Plastics*. 2017;53(2):151-165.
- [16] Z. Alomar, F. Concli, Compressive behavior assessment of a newly developed circular cell-based lattice structure, *Materials & Design*, Volume 205, 2021, 109716.
- [17] F. Scalzo, G. Totis, E. Vaglio, M. Sortino, Experimental study on the high-damping properties of metallic lattice structures obtained from SLM, *Precision Engineering*, 71(2021), pp. 63-77.
- [18] M. Doroszko, A. Falkowska, A. Seweryn, Image-based numerical modeling of the tensile deformation behavior and mechanical properties of additive manufactured Ti-6Al-4V diamond lattice structures, *Materials Science and Engineering: A*, 2021, 141362.
- [19] Z. Yu, D. Ding, Z. Pan, H. Li, Q. Lu, X. Fang, A strut-based process planning method for wire arc additive manufacturing of lattice structures, *Journal of Manufacturing Processes*, 65(2021), pp. 283-298.
- [20] F. Liu, L. Wang, D. Jin, X. Liu, P. Lu, Equivalent Beam Model for Spatial Repetitive Lattice Structures with Hysteretic Nonlinear Joints, *International Journal of Mechanical Sciences*, 200(2021), p. 106449.
- [21] S. McBane, Y. Choi, Component-wise reduced order model lattice-type structure design, *Computer Methods in Applied Mechanics and Engineering*, 381(2021), p. 113813.
- [22] D. B. P. Huynh, D. J. Knezevic, A. T. Patera, A static condensation reduced basis element method: Complex problems, *Computer Methods in Applied Mechanics and Engineering*, 259(2013), pp. 197-216.
- [23] K. Smetana, A new certification framework for the port reduced static condensation reduced basis element method, *Computer Methods in Applied Mechanics and Engineering*, 283(2015), pp. 352-383.
- [24] D. A. White, W. J. Arrighi, J. Kudo, S. E. Watts, Multiscale topology optimization using neural network surrogate models, *Computer Methods in Applied Mechanics and Engineering*, 346(2019), pp. 1118-1135.
- [25] Z. Wu, L. Xia, S. Wang, T. Shi, Topology optimization of hierarchical lattice structures with substructuring, *Computer Methods in Applied Mechanics and Engineering*, 345(2019), pp. 602-617.
- [26] Y. Choi, G. Boncoraglio, S. Anderson, D. Amsallem, C. Farhat, Gradient-based constrained optimization using a database of linear reduced-order models, *Journal of Computational Physics*, 423(2020), p. 109787
- [27] N. Korshunova, G. Alaimo, S.B. Hosseini, M. Carraturo, A. Reali, J. Niiranen, F. Auricchio, E. Rank, S. Kollmannsberger, Bending behavior of octet-truss lattice structures: Modelling options, numerical characterization and experimental validation, *Materials & Design*, 205(2021), p. 109693.
- [28] K. Monkova, M. Vasina, M. Zaludek, P. P. Monka, J. Tkac, Mechanical vibration damping and compression properties of a lattice structure, *Materials* 2021, 14, 1502.
- [29] ABSplus-P430, Accessible on internet: <https://www.3d-prototyp.com/uploads/Materialdatenblaetter/ABSplus-P430.pdf>, (14.05.2021.)

[30] Original Prusa i3 MK2 release!, Accessible on internet:
https://blog.prusaprinters.org/original-prusa-i3-mk2-release_4332/, (17.5.2021.)



19th INTERNATIONAL FOUNDRYMEN CONFERENCE
Humans - Valuable Resource for Foundry Industry Development

Split, June 16th-18th, 2021

<https://ifc.simet.hr/>

**EFFICIENT METHOD OF MANUFACTURING DEMANDING PROTOTYPE
CASTINGS USING INVESTMENT CASTING TECHNOLOGY**

Vladimír Krutiš^{1*}, Václav Káňa¹, Marek Dostál², Jarmil Cileček³

¹ Brno University of Technology Faculty of Mechanical Engineering, Institute of Manufacturing Technology, Brno, Czech Republic

² Brno University of Technology Institute of Machine and Industrial Design, Brno, Czech Republic

³ AluCAST s.r.o., Tupesy, Czech Republic

Invited lecture

Original scientific paper

Abstract

Recently, the shapes of the castings have been designed to meet at least the basic requirements of the construction technology. It is the adaptation of the part construction to the production method to ensure efficient and quality production. The construction technology was focused on the model partition with respect to the pre-selected production technology focused on the elimination of hot spots by an ideal connection and wall transition to the elimination of foundry defects. For these reasons, the shapes of the castings were rather conservative, to meet the requirements for functionality and production technology. The development of new optimization methods in the 3D design such as topological optimization or generative design and the development of 3D printing methods have shifted the design of part shapes to an area that previously only belonged to artistic castings. Investment casting technology is trying to meet these new challenges. The speed of model preparation using 3D printing has advanced this technology considerably, especially when it comes to prototyping production. Connection with virtual manufacturing using numerical simulations then creates a field to produce castings on the first attempt. Rapid prototyping also includes Cyclone technology, which shortens the preparation of a ceramic shell from a few days to a few hours. This article deals with the interconnection of several different approaches and methods for casting production, where the main requirement is the time of delivery of the first prototype.

Keywords: *ceramic mold, additive manufacturing, numerical simulation*

*Corresponding author (e-mail address): krutis@fme.vutbr.cz

INTRODUCTION

Serially produced castings as well as first prototype ones are in increasing demand by the customers. The prototype castings are expected to be of maximum quality with prompt delivery while preserving the comprehensiveness of the requested part. For this reason, a foundry needs to adopt fast-prototyping technologies to meet the new challenges and technologies. Advances of the 3D-printing open up space for foundry technology as well. However, the application of such new methods entails the command of further technological processes necessary for the numerical simulation and design of a technology to manufacture a prototype at the first attempt and, possibly, without faults. The achievement of the above goals is conditioned not only by using the right production technology, but by having a grip on the planning and management of all the projects as well. At present, investment casting is among the favoured technologies for the manufacturing of prototypes. This is given by its variability and potential to produce very sophisticated shapes. It can be very well coupled with 3D printing to form what is called a hybrid technology [1].

PROJECT CALL

The project was initiated based on the requirements of a Formula Student team of designers who had been trying to change the production technology replacing a welding by a casting, to create a new a concept for the formula dubbed Dragon 9. A great challenge and a critical project parameter at the same time was the deadline as the castings had to be delivered within one month. For this reason, the project management was focussed on simultaneous engineering. This approach involves maximum cooperation between designers and technologists using all virtual engineering tools available. For this project, a method was designed involving elements of virtual prototyping, virtual manufacturing, additive technologies, and rapid prototyping using special equipment to produce ceramic shells.

The project's aim was to develop and manufacture a steering wheel holder from the material $AlSi7Mg0.3$, which, for the previous formula version, was manufactured as the assembly of a steel welding and an aluminium workpiece - Figure 1. The requirements for the development of the workpiece were the following:

- Reduced holder weight
- Increased stiffness
- Shorter manufacturing time



Figure 1. Change of the manufacturing technology for the steering wheel holder (welding->casting)

CASTING DESIGN

The casting design is the result of topological optimisation to find the optimal distribution of material in the design space. This method replaces the traditional approach of manual redesign or parametric optimisation. The advantages it brings include independence of the design size. During the optimisation process, material is taken away from the total volume while observing previously set limitations such as:

- the outer boundaries of a part
- limited strength of a part
- preserving the interconnecting regions [2]

This part was topologically optimised by the ANSYS Workbench 18.1 program for the below boundary conditions:

- a torque of 20 Nm
- 700 N suspended on the steering wheel
- a pressure of 150 N on steering-wheel side
- a pressure of 200 N on both steering-wheel sides

Figure 2 shows the input model for topological optimisation, so-called working space, in which the part to be optimised must be placed. From this space, 70% of the material has been removed based on the calculation. The result of the topological optimisation can be seen in the middle while the final CAD model is on the right.

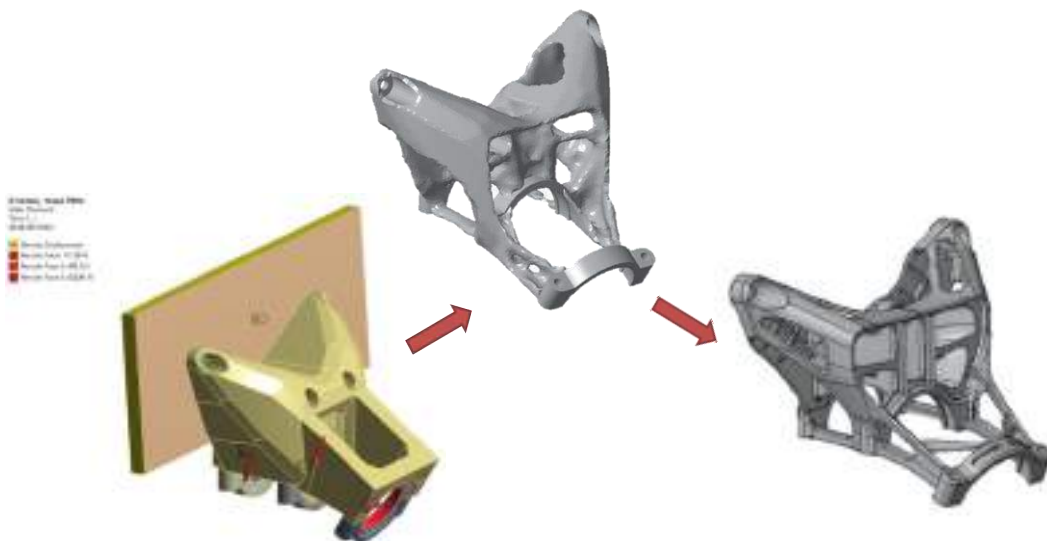


Figure 2. Topological optimisation of the casting shape

A typical topological optimisation may take up to tens of hours depending on the optimisation quality required. To achieve the best possible results, the optimisation should take place in several steps each one removing only a small amount of the material. This means that the calculation must be performed repeatedly, at each stage using as input the output of the previous optimisation step. In this particular case, only one iteration was used with the calculation taking about 10 hours. Next a CAD design was processed including a complete set of drawings for the part manufactured. The outer size of the casting is

approximately 140 by 100 by 80 mm with an average casting wall thickness of 2 mm and radii of 1 mm. To check the adequacy of the design, the holder was subjected to FEM analyses (Figure 3) and their results were then used for further optimisation to reduce the weight. The forces required for such a load had been determined from the reactions in the bearings on the steering column. All FEM analyses were carried out by the Ansys Workbench 18.1 programme.

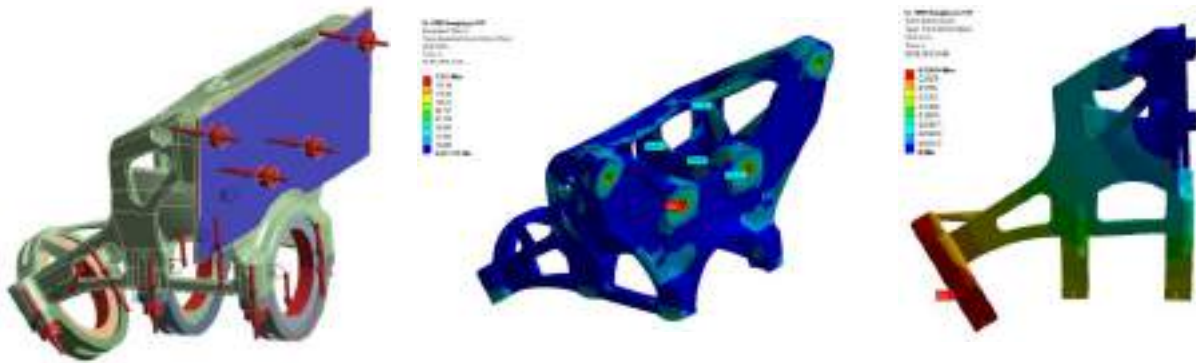


Figure 3. FEM analyses of holder load

As a result of this new concept of the steering column attachment, 164 g (50%) of material have been saved with the holder stiffness improving by 47 %. After the optimisation, the holder now weighs 169 g.

TECHNOLOGY ANALYSES

Another indispensable part of virtual engineering is virtual manufacturing (VM). The CAE methods along with optimisation methods transfer the manufacturing into a virtual space in which the technology chosen may be subjected to any test to enable casting at the first attempt.

To eliminate casting defects in the manufacturing of the holder, numerical analyses were done by the ProCAST program to verify and optimise the process parameters, the functioning of the gating system, the solidification of the casting and the cooling down of the shell – Fig. 4.

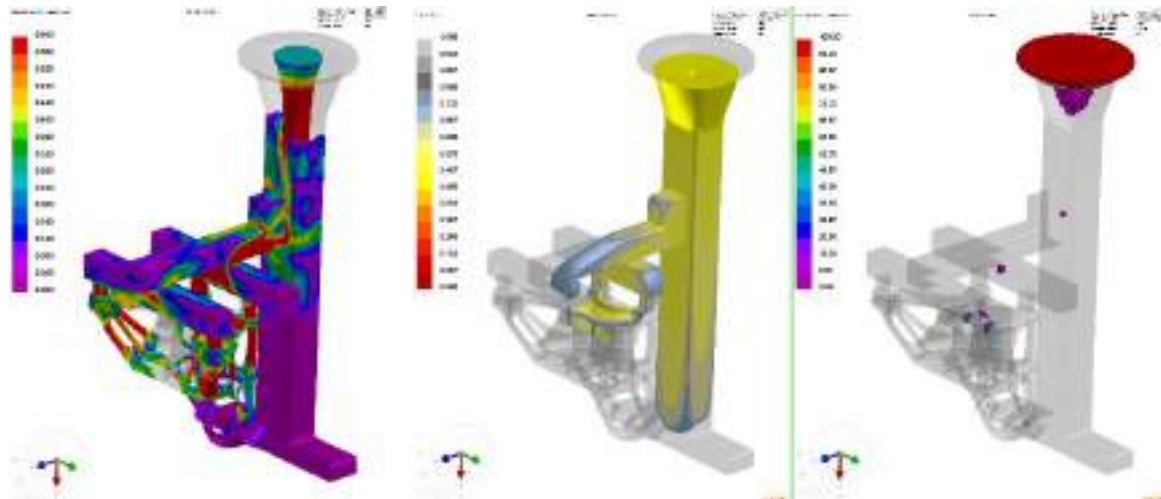


Figure 4. Simulated filling and hardening of the casting

ADDITIVE MANUFACTURING OF THE MODEL

Additive manufacturing and its options have been developing at a breath-taking pace. In the investment casting technology, its application can be mostly found in the creation of models, but direct printing of a ceramic mould or of ceramic blades is also possible. Two model printing technologies were used in the project. The first one was material jetting printing (MJP), which can be used to directly print the wax models. The printer used was ProJet MJP 2500 IC with wax being VisiJet® M2 iCast RealWax™. The other one was binder printing (BJ) on the printer VX1000 using the material PMMA with a wax finish of the model. Figure 5 shows models printed by the two methods. The finish of both models was of a very good quality; however, no detailed assessment and comparison were made of the surface roughness and quality. Without any additional finishing, the models were then immediately wrapped in ceramic suspension.



a) VisiJet® material

b) PMMA material

Figure 5. 3D printed holder models

The casting models for the investment casting technology must meet a number of requirements. In addition to the surface finish, minimum quantity of ash matter after melting, and low thermal expansivity, exact size is another important aspect. A model manufactured using classical waxes and matrix mould is always subject to some contraction. In printed models, this contraction is normally not taken into consideration. Only the shrinkage of the cast material or the change of size of the shell is entered. Therefore, both models manufactured were scanned in the ATOS Core system and, subsequently matched with the original data – Figure 6.

The assessment of the size tolerances implies that the model made from VisiJet® showed a maximum deviation from the CAD data of up to 0.4 mm while, with the PMMA material, it was up to 0.25 mm and only for the model part that had to be repaired due to a crack caused by the transport of the model.

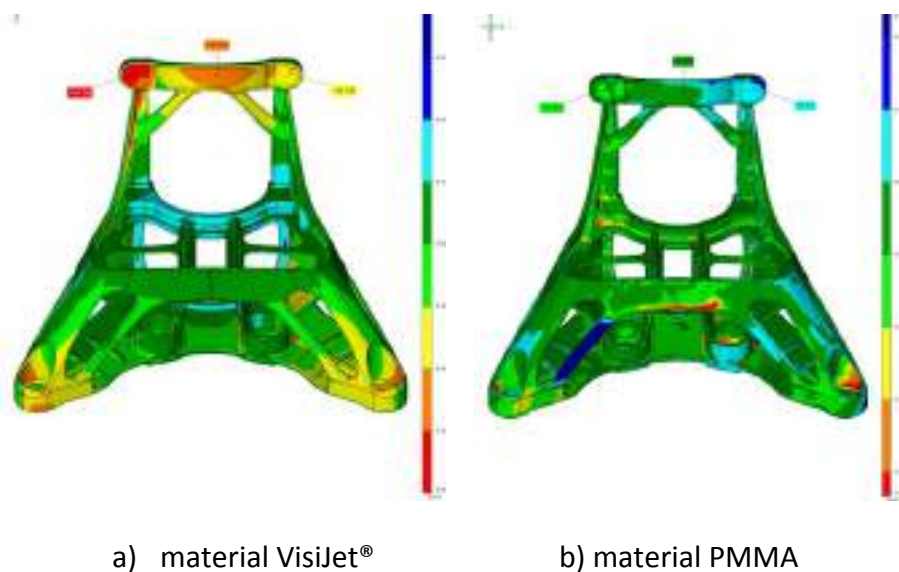


Figure 6. Graphical assessment of the size tolerances for VisiJet® and PMMA

RAPID PROTOTYPING OF THE CERAMIC SHELL

Two procedures were used to manufacture the shell. The first one (Method A) was based on the classical manufacture of the shell by AluCAST, s.r.o. As the primary shell layer, ceramic slurry was used of the PrimeCoat binder, Zirkon (-200) powder, and Molochite (50-80) calcined clay. The reinforcing layers were formed by the same binder but with Molochite powder and Molochite (16-30) calcined clay.



Figure 7. Preparation of the cluster and manufacture of the ceramic shell

The second one (Method B) was based on the Cyclon device – Fig. 7, used for rapid manufacture of prototypes. Using this device, the manufacture of shells can take just hours rather than days. The drying system uses fast and turbulent air flow that carries away humidity. Infrared light outbalances the down-cooling keeping the temperature stable at ± 1 ° C. A mirror inside the chamber reflects infrared light to be evenly distributed over all shell parts. Continual rotation of the cluster guarantees very mild and even drying, which is also supported by the pre-dried air accelerating the entire process [3]. For the manufacture of the shell, ceramic slurry was used based on the PrimeCoat binder and fused-silica SiO₂ (-200mesh). Zircon sand was used as the first stucco and, with mullit (30-80) used for next layers. The below Table 1 compares the times needed to manufacture the shell by both methods.

Table 1. Comparison of shell manufacturing times

	Nb. of Layers	Drying time		Total time of shell manufacture
Method A	6	Layers 1-3	12 hours	4 days
		Layers 4-6	24 hours	
Method B	8*	Layers 1-3	20 min	4 hours
		Layers 3-8	30 min	

* Different numbers of layers are due to the different materials of the ceramic suspension and different grain sizes of the stucco.

Once the ceramic shell was finished, the wax was de-melted, and the printed models fired. After the first degree in an autoclave, next firing followed in an annealing furnace at a temperature of 800°C. After the shell was cooled down, the model was cleansed to clear the shell of all the remnants of the model used, particularly of the residual ash matter. As mentioned above, the Cyclone device is especially designed for rapid prototyping and used for single-part production where the shells are manufactured within hours. However, both the above methods can be assigned to the Rapid Prototyping category.

PROTOTYPE PRODUCTION

The shells were cast at AluCAST s.r.o. from a pouring temperature of 720°C. A shell was first tempered to 750°C. This temperature was higher than the usual shell temperature for Al castings to ensure the metal filling all the thin profiles as only one part was being manufactured that had to be cast at the first try. The pouring time was 5 sec. The casting then underwent the T6 heat treatment. As it had to meet particularly mechanical requirements, tensile tests were carried out for additionally cast testing samples.



Figure 8. Final casting shape after sand blasting

To verify the size precision, the casting was scanned and matched with CAD data. The maximal deviations of the casting size were less than 0.8 mm – Figure 8.

CONCLUSION

The present project has shown benefits from open cooperation between designers and technologists on a steering-wheel holder project. This cooperation style fits the concept which is being called simultaneous engineering. In order to meet the deadline of the casting delivery, several different tools and methods were used of rapid prototyping. Figure 9 represent an approximate workflow used for the design and manufacture of the casting. The casting was successfully tested during the Spring part of the Formula Student races with the BUT team coming in fifth in a world-wide competition of designer teams.

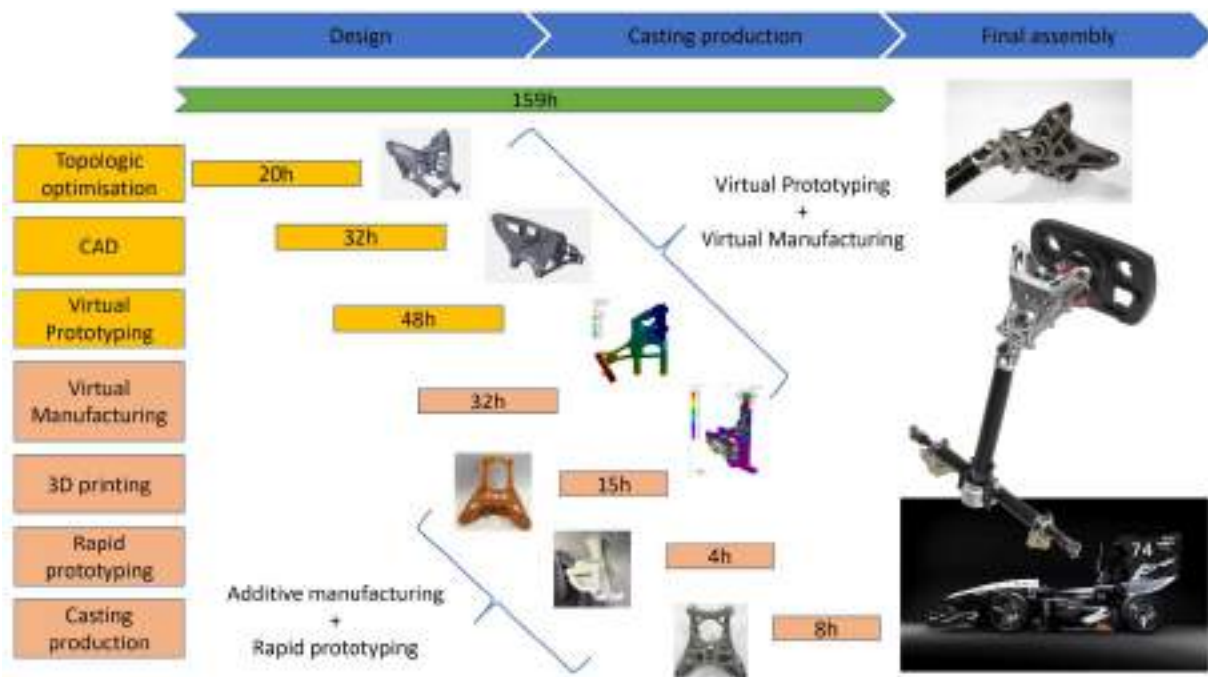


Figure 9. The workflow of the casting design and manufacture (only the actual times are listed for an operation)

Acknowledgements

This work was supported by the specific research project of BUT FME Brno, no FSI-S-19-5981 Research on rapid prototyping using investment casting technology.

REFERENCES

- [1] P. Kumar, I. P. S. Ahuja, and R. Singh, A framework for developing a hybrid investment casting process, *Asian Review of Mechanical Engineering*, ISSN 2249 - 6289 2(2013)2, pp. 49-55.
- [2] J. Starek, Topologic optimisation, Accessible on Internet: <https://www.svsfem.cz/blog/topologicka-optimalizace-pomaha-snizit-hmotnost-automobilu>
- [3] M. Kügelgen, From 7 days to 7 hours – Investment casting parts within the shortest time, 68th WFC - World Foundry Congress7th, 2008, pp. 147-151.



19th INTERNATIONAL FOUNDRYMEN CONFERENCE
Humans - Valuable Resource for Foundry Industry Development

Split, June 16th-18th, 2021

<https://ifc.simet.hr/>

STRUCTURAL AND THERMAL PROPERTIES OF THE Sn–Zn ALLOYS

**Dragan Manasijević^{*}, Ljubiša Balanović, Ivana Marković, Milan Gorgievski,
Uroš Stamenković, Kristina Božinović**

University of Belgrade Technical Faculty in Bor, Bor, Serbia

Invited lecture
Original scientific paper

Abstract

Four hypereutectic Sn-Zn alloys with 69.5, 48.3, 28.1 and 14.1 at.% of Zn were produced by mixing and melting of pure metals Sn and Zn followed by cooling in air to room temperature. Microstructure and chemical compositions of prepared samples were analyzed by using scanning electron microscopy (SEM) with energy dispersive X-ray spectrometry (EDS). It was found that morphology of primary (Zn) phase changes from rounded and equiaxed dendritic structure to plate-like grains and finally to needle-like shape of grains with decreasing Zn content. Formation of characteristic broken-lamellar type of eutectic microstructure was observed in all investigated alloys. Melting behavior of the alloys was studied using differential scanning calorimetry (DSC). Phase transition temperatures and corresponding heat effects were experimentally determined and compared with the results of thermodynamic and phase equilibria calculations using the CALPHAD (CALculation of PHase Diagrams) method and optimized thermodynamic parameters from literature. Thermal diffusivity of the studied alloys was measured using xenon flash method in the temperature range from 25 to 150 °C. Based on the measured values of thermal diffusivity and calculated specific heat capacity data, thermal conductivities of the solid alloys were obtained. It was found that thermal conductivity decreases monotonously with increasing temperature and Sn content. The results of thermal conductivity measurements were compared with literature data and with the data obtained from the Wiedemann-Franz law and measured electrical conductivities.

Keywords: Sn–Zn alloys, solder, microstructure, thermal conductivity

*Corresponding author (e-mail address): dmanasijevic@tfbor.bg.ac.rs

INTRODUCTION

Metals Sn and Zn and their alloys have found application in various industrial fields [1-5]. These alloys are especially important in soldering processes [4-6]. Thanks to its good characteristics such as low melting point, excellent mechanical properties and low cost, the Sn–9 mass% Zn eutectic solder alloy has been extensively studied and considered as a prospective substitute for Sn–Pb solders [4-9]. Also, Sn–Zn alloys with high content of Zn

have been proposed as suitable high-temperature lead free solders [6]. However, poor oxidation resistance and wetting properties of the Sn–Zn alloys have significantly limited their practical usage [4-9]. Beside in lead-free soldering, Sn–Zn alloys are of large importance in steel coating industry [1] and they represent highly promising anodes for lithium-ion batteries [3].

Phase relations in the Sn-Zn system are well known. Thermodynamic modeling of the Sn–Zn binary system was performed by several authors [10, 11]. Fig. 1 shows the phase diagram of the Sn-Zn system calculated by using optimized thermodynamic parameters from the COST 531 lead-free solders database [12].

According to the phase diagram shown in Fig. 1, Sn and Zn form a eutectic phase diagram. The eutectic temperature is 198.6 °C and eutectic composition 13.5 at% Zn (7.9 mass% Zn). Solubility of Zn in Sn is very limited and solubility of Sn in Zn is negligible.

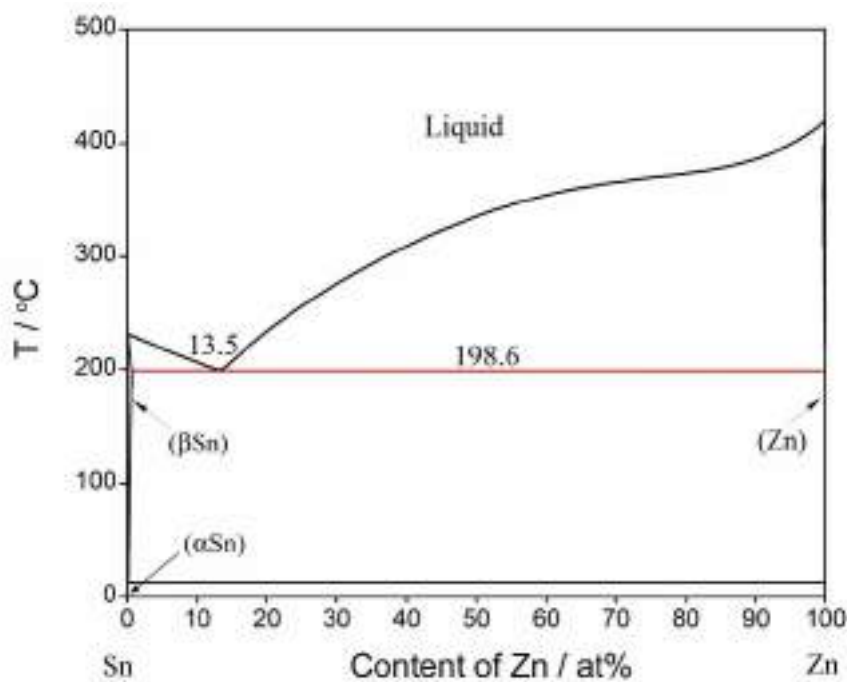


Figure 1. Phase diagram of the Sn-Zn system calculated by using optimized thermodynamic parameters from [12]

Beside microstructure and mechanical characteristics of the material, thermal properties such as thermal conductivity and specific heat capacity are of crucial importance for solder selection and the development of soldering process. The most of the fabrication processes are modelled mathematically before they are implemented in a production. The accuracy of such modeling strongly depends on knowing the values of the thermophysical properties of the materials involved, which are used as necessary inputs for every model. Thermal conductivity represents the most important thermal property involved in models of thermal expansion and heat transfer and the knowledge of the thermal conductivity of solders can result in a better controlled soldering process.

So far, electrical and thermal conductivities of the Sn-Zn alloys were studied by few groups of authors. Ari et al. [2] investigated temperature dependence of electrical resistivity of solid Sn-Zn alloys for two compositions (1 and 8.9 mass% Zn), while Matsugi et al. [8] studied five compositions (1, 9, 20, 50, and 80 mass% Zn). Both author groups have found that electrical

resistivity of alloys increases monotonously with the increasing temperature. Also, at constant temperature, electrical resistivity decreases with the increasing concentration of Zn.

Experimental investigations of thermal conductivity for the solid Sn–Zn alloys were carried out by Matsugi et al. [8], Meydaneri et al. [13], and for the liquid Sn–Zn alloys by Plevachuk et al. [9]. Matsugi et al. [8] have found that thermal conductivity of Sn-Zn solid alloys decreases monotonously with increasing temperature and Sn concentration. They expressed the thermal conductivity of each alloy as a function of temperature and composition [8].

It is known that cooling rate has a significant effect on the microstructure and properties of the Sn-Zn alloys [7]. Hence, the main objective of the present study is to examine correlations between microstructure, melting behavior, thermal and electrical conductivities of the air-cooled hypereutectic Sn-Zn alloys in a wide composition range. For this purpose, microstructure characterization of prepared samples was carried out using the SEM-EDS method. Phase transition temperatures and their heat effects were measured using DSC technique and the obtained results were compared with the results of thermodynamic calculations. Thermal conductivity variations with temperature and composition were experimentally studied by using the xenon flash method and electrical conductivity variation with composition at room temperature was experimentally determined.

MATERIALS AND METHODS

Sample preparation

The hypereutectic Sn-Zn alloys with 69.5, 48.3, 28.1 and 14.1 at.% of Zn were prepared by mixing and melting pieces of pure Sn (99.99 %) and Zn (99.99 %) in evacuated quartz tubes. Samples were heated at 500 °C for 20 min. The melts were stirred for adequate homogenization and cooled in air by removing tubes from the furnace. The total masses of the prepared samples were about 4 g.

Microstructure analysis

Microstructure analysis was carried out using scanning electron microscopy (SEM) with energy dispersive X-ray spectrometry (EDS). Grinding of the samples was done using silicon carbide grinding papers. Final polishing was achieved using micropolish with 0.5 μm Al_2O_3 slurry. No chemical etching was required because the distribution of the phases was revealed clearly due to differential polishing effects. Microstructure observations and chemical analysis of the studied alloys samples were done by using the TESCAN VEGA3 scanning electron microscope equipped with the energy dispersive spectrometer (Oxford Instruments X-act). All SEM images of the microstructures were taken on the polished surfaces of the studied alloys samples in backscattered electron mode with the accelerating voltage of 20 kV. A standard sample for quant optimization of the EDS detector (Oxford Instruments X-act) was the high purity copper (99.9999 %).

Differential scanning calorimetry measurements

Phase transition temperatures and their heat effects were measured by a simultaneous thermal analyzer SDT Q600 (TA Instruments). The instrument was calibrated by measuring the melting points and the heat of melting of a known mass of standard materials (pure metals: In and Zn). The samples with masses of about 50 mg were placed in alumina crucibles, and DSC heating curves were recorded in the temperature range from 25 to 500 °C under a protective flowing Ar atmosphere with a heating rate of 5 °Cmin⁻¹. Empty alumina crucible was used as a reference material.

Determination of thermal diffusivity and thermal conductivity

Thermal diffusivity and thermal conductivity of the studied samples were investigated using the flash method first described by Parker et al. [14]. Front face of a thin disk specimen is irradiated by a short energy pulse from a heat source such as laser or xenon lamp, depending of a used method i.e. laser-flash or xenon-flash method, and the temperature of the rear face is continuously recorded as a function of time. Determination of thermal diffusivity is based on following equation:

$$\alpha = \frac{1.37L^2}{\pi^2 t_{1/2}} = 0.1388 \frac{L^2}{t_{1/2}} \quad (1)$$

where L represents the thickness of the sample and $t_{1/2}$ is the half-rise time, defined as the time interval required for the rear face temperature to reach half of the maximal temperature value. Thermal diffusivity was measured by using Discovery Xenon Flash (DXF-500) instrument over a range of temperatures from 25 to 150 °C. For the thermal diffusivity measurements, the samples were cut into cylinders with 3 mm thickness (12.6 mm in diameter and 3 mm thick with plane-parallel ground end faces). Then, they were placed in a vacuum furnace and heated with the constant heating rate to a measurement temperature. When the furnace reached the required temperature the front surface of the specimen was heated by an energy pulse from the xenon-lamp. Temperatures of the rear face of the samples were monitored using the nitrogen-cooled IR detector (InSb sensor) [15, 16]. Each experimental point is an average of three measurements.

The relationship between thermal diffusivity and thermal conductivity is given as:

$$\lambda = \alpha \cdot \rho \cdot Cp \quad (2)$$

where λ is thermal conductivity (Wm⁻¹K⁻¹), α is thermal diffusivity (m²s⁻¹), ρ is density (kgm⁻³), and Cp is specific heat capacity (Jkg⁻¹K⁻¹).

The densities of the studied alloys at room temperature were measured by indirect Archimedean method [17]. The density of a solid can be obtained according to the following equation:

$$\rho = \frac{A}{A - B} \rho_0 \quad (3)$$

where ρ is density of the sample (kgm⁻³), A is weight of sample in air, B is weight of sample in

liquid and ρ_0 is density of liquid (distilled water was used with the density $\rho_0 = 0.99679 \text{ kgm}^{-3}$). Densities were measured by using a density determination kit linked to the electronic balance (Mettler Toledo instrument). Corresponding densities at higher temperatures were obtained using the measured density values at room temperature and thermal expansion coefficients for the Sn–Zn alloys from Lee et al. [6]. The specific heat capacities were calculated using the CALPHAD method and optimized thermodynamic parameters from the thermodynamic database [12].

Electrical conductivity measurements

Electrical conductivity was measured using the Foerster SIGMATEST 2.069 instrument. This device uses eddy currents for measuring the electrical conductivity of non-magnetic materials. Before each measuring the conductivity tester was calibrated with two standard plates with the electrical conductivity of 8.4 MSm^{-1} and 58.05 MSm^{-1} .

RESULTS AND DISCUSSION

Microstructure analysis

Microstructure and chemical analysis of the alloy samples were carried out using SEM-EDS. The conducted chemical analysis using EDS has provided insight into overall compositions, compositions of primary (Zn) phase and (Sn)+(Zn) eutectic. First, overall compositions of the alloy samples were determined by analyzing an as large as possible part of their surface. Based on the EDS results overall compositions of the investigated alloys are determined to be Sn–69.5Zn, Sn–48.3Zn, Sn–28.1Zn, and Sn–14.1Zn (in at%). The phase compositions were obtained by examining the surface of the same phase at different parts of the sample (at least five different positions of the same phase are examined per phase). The results of chemical analysis obtained by application of EDS analysis are shown in Table 1. There is negligible solubility of Sn in the (Zn) phase. SEM images of alloys microstructures, recorded under the low and high magnifications, are shown in Figs. 2a and 2b for the Sn–69.5Zn alloy, Figs. 3a and 3b for the Sn–48.3Zn alloy, Figs. 4a and 4b for the Sn–28.1Zn alloy, and Figs. 5a and 5b for the Sn–14.1Zn alloy.

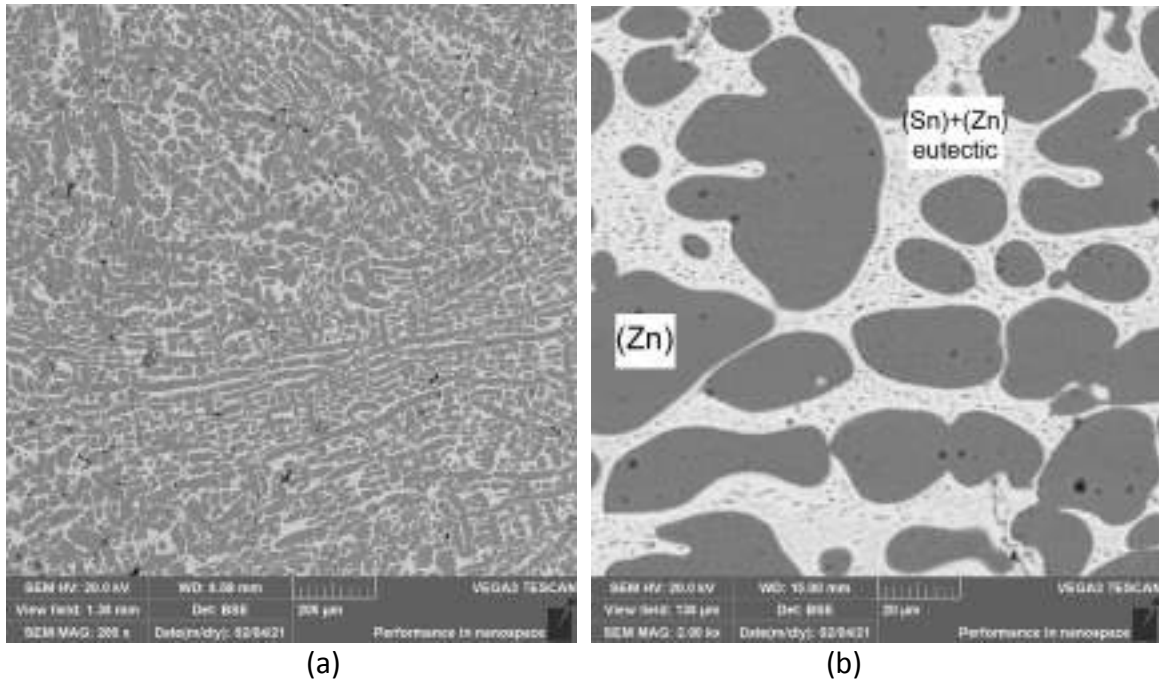


Figure 2. SEM images of the Sn–69.5Zn alloy: (a) low magnification; (b) high magnification

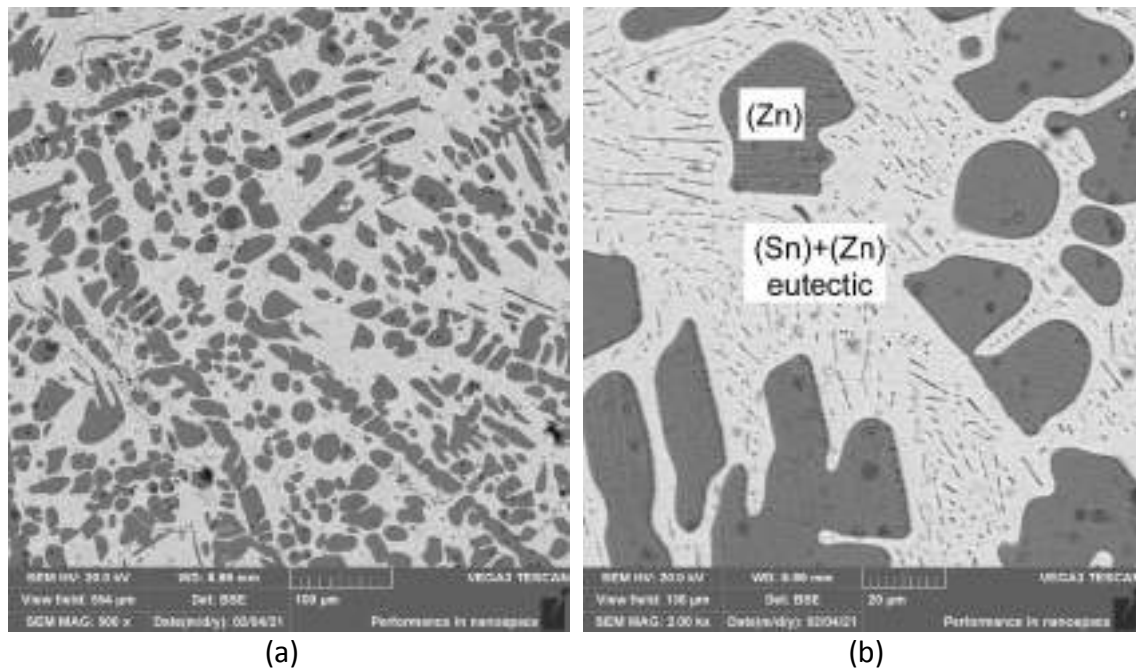


Figure 3. SEM images of the Sn–48.3Zn alloy: (a) low magnification; (b) high magnification

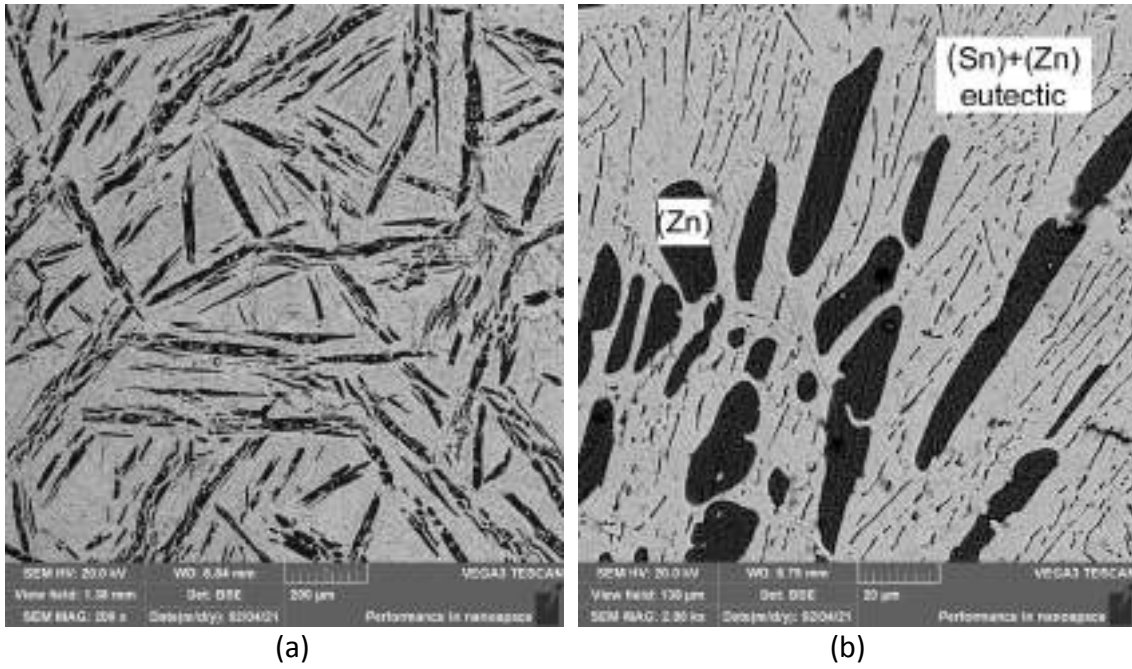


Figure 4. SEM images of Sn–28.1Zn alloy: (a) low magnification; (b) high magnification

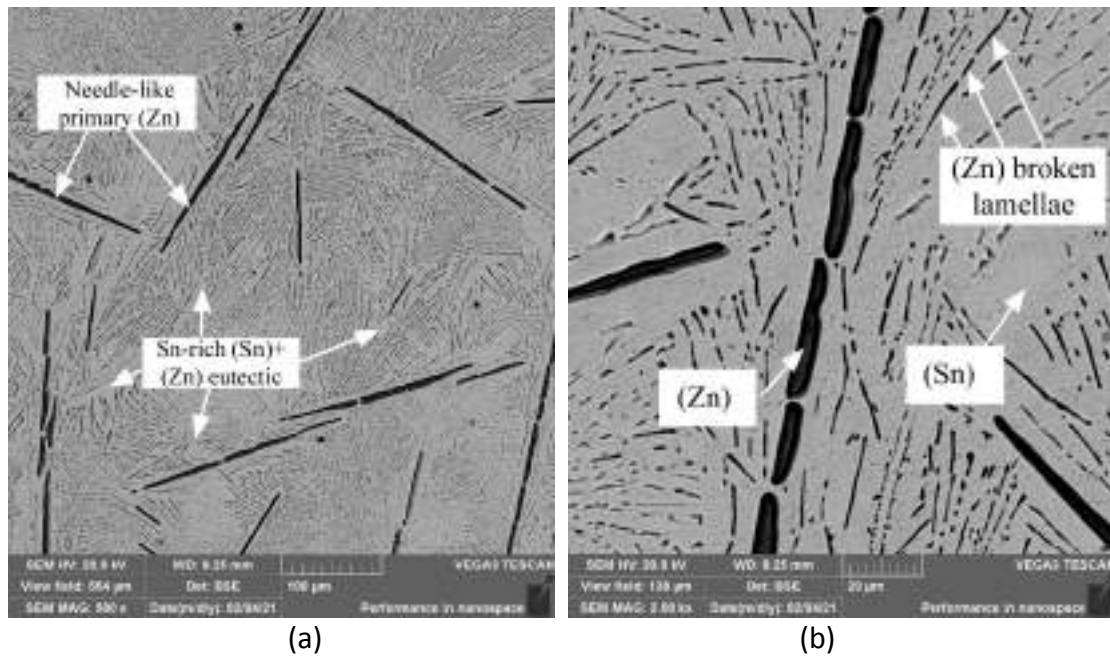


Figure 5. SEM images of the Sn–14.1Zn alloy: (a) low magnification; (b) high magnification

As can be seen from Figs. 2-5, the microstructures of all four studied hypereutectic Zn-Sn alloys are formed by the primary (Zn) dendrites (dark phase) surrounded by the (Sn)+(Zn) eutectic mixture (bright regions). Dendrites of the (Zn) primary phase are randomly oriented. As the Zn content decreases, the fraction of the primary (Zn) phase decreases and that of the (Sn)+(Zn) eutectic increases. The morphology of the (Zn) primary phase changes with decreasing Zn content from the rounded and equiaxed grain structure to plate-like shape and finally to needle-like shape in the near-eutectic Sn–14.1Zn alloy. The details of the eutectic structure can be seen under the large magnification. The Sn-Zn eutectic has a

broken-lamellar type eutectic structure in all investigated samples. It consists of tiny, discontinued, faceted lamellae of Zn and the nonfaceting Sn phase in the matrix (indicated in Fig.5b).

Table 1. Experimentally determined compositions of co-existing phases using EDS analysis

Experimental composition of the sample / at%	Microstructure	Identified phases and microconstituents	Composition / at%	
			Sn	Zn
Sn–69.5Zn	Rounded and equiaxed primary (Zn) dendrites with eutectic (Sn)+(Zn) in the inter-dendritic regions	(Zn)	-	100
		(Sn)+(Zn) eutectic	88.2±1.2	11.8±0.6
Sn–48.3Zn	Rounded and equiaxed primary (Zn) grains surrounded by the (Sn)+(Zn) eutectic	(Zn)	-	100
		(Sn)+(Zn) eutectic	89.1±1.2	10.9±0.9
Sn–28.1Zn	Plate-like primary (Zn) grains in the eutectic (Sn)+(Zn) base	(Zn)	-	100
		(Sn)+(Zn) eutectic	88.4±1.0	11.6±0.6
Sn–14.1Zn	Needle-like primary (Zn) grains in the eutectic (Sn)+(Zn) base	(Zn)	-	100
		(Sn)+(Zn) eutectic	88.5±1.2	11.5±0.8

Melting behavior

DSC analysis was conducted in order to measure the phase transition temperatures and related heat effects of the studied Sn-Zn alloys. The examination of the obtained results was done according to the literature recommendations [18]. The onset temperature of the first DSC peak during heating was used to determine the temperature of the invariant eutectic reaction, and the peak temperature of the second thermal effect was selected as the liquidus temperature. DSC heating runs were repeated totally three times. The results of the second and third measurements showed better mutual consistency and they were used for the determination of phase transition temperatures. Examples of DSC heating curves for the investigated Sn–Zn alloys are shown in Fig. 6(a)-(d).

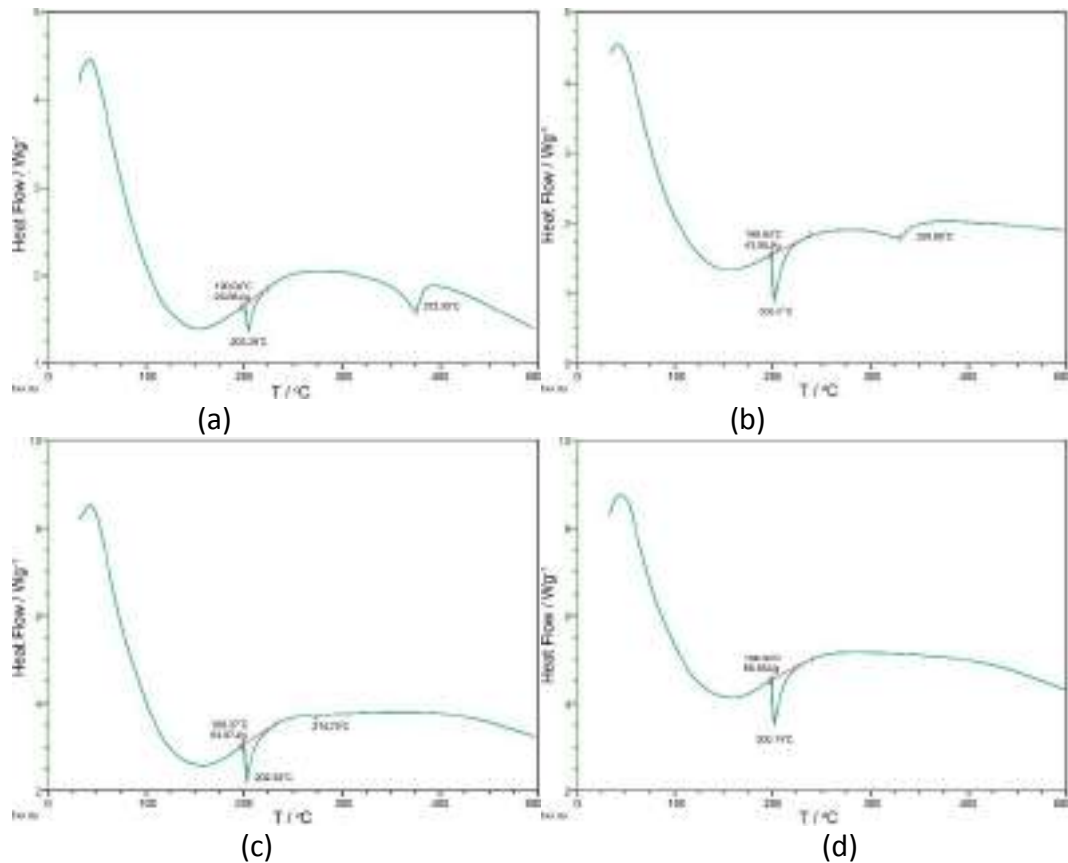


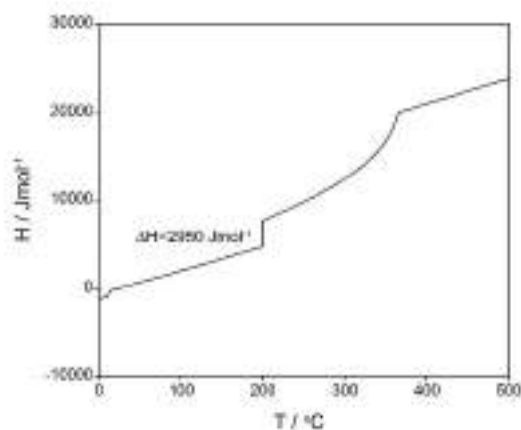
Figure 6. DSC heating curves: (a) Sn–69.5Zn alloy; (b) Sn–48.3Zn alloy; (c) Sn–28.1Zn alloy; (d) Sn–14.1Zn alloy

It can be noticed that DSC heating curves for all four investigated alloys possess a sharp endothermic peak at nearly constant temperature related to the eutectic reaction: $(\text{Sn}) + (\text{Zn}) \rightarrow \text{liquid}$. The temperature of eutectic reaction denotes the start of the melting i.e. alloy solidus temperature. The average measured onset temperature of the eutectic peak is 198.8 °C, which is in excellent agreement with the value of the eutectic temperature according to the phase diagram of the Sn–Zn system (198.6 °C) presented in Fig. 1. DSC heating curves for the Sn–69.5Zn, Sn–48.3Zn and Sn–28.1Zn alloys include additional DSC peak at higher temperature related to the end of melting of (Zn) primary phase. These peaks represent liquidus temperatures of the alloys. It can be noticed that liquidus temperature decreases with decreasing Zn concentration. Only one DSC peak, related to the eutectic reaction, is identified in the case of the near-eutectic Sn–14.1Zn sample. The probable reasons are the proximity of eutectic and liquidus temperatures for this alloy and the small heat effect related to the liquidus phase transition. The results of DSC analysis are presented in Table 2. The uncertainties of phase transition temperatures and their heat effects were evaluated from repeated DSC measurements. Phase transition temperatures and heat effects of eutectic reaction obtained by DSC technique were compared with the corresponding temperatures and enthalpy changes calculated by using the CALPHAD method [19] and optimized thermodynamic parameters from [12]. The comparison between experimental results and results of thermodynamic calculation is also shown in Table 2.

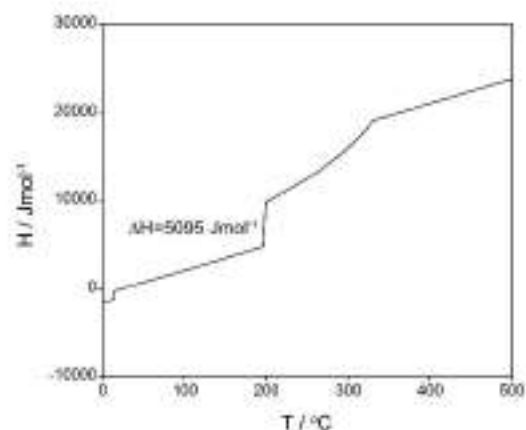
Table 2. Comparison between the results of DSC measurements and thermodynamic calculation for the Sn–Zn alloys

Alloy composition / at%	Temperature of eutectic reaction from DSC / °C	Calculated temperature of eutectic reaction / °C	Heat of eutectic reaction from DSC / Jg ⁻¹ ₁	Calculated enthalpy change for eutectic reaction / Jg ⁻¹	Liquidus temperature from DSC / °C	Calculated liquidus temperature / °C
Sn–69.5Zn	199.0±0.1	198.6	26.7±0.1	36.1	372.9±1.2	364.7
Sn–48.3Zn	198.6±0.1	198.6	44.0±0.1	54.8	339.9±0.8	331.0
Sn–28.1Zn	199.3±0.1	198.6	55.0±0.2	67.9	274.8±0.5	268.5
Sn–14.1Zn	198.4±0.1	198.6	68.6±0.2	75.2	-	202.4

In this work, optimized thermodynamic parameters were taken from [12] and Pandat software [20] was used for the calculations of enthalpy and specific heat capacity. Fig. 7 shows calculated dependence of enthalpy vs. temperature for the investigated alloys. It can be noticed that enthalpies of the Sn-Zn alloys increase with temperature increasing. The gradual increase is interrupted at the temperatures that correspond to the phase transformations. At low temperature there is a change from (α Sn) to (β Sn) allotrope. At the eutectic temperature (198.6 °C) there is pronounced rise in enthalpy, caused by the occurrence of the eutectic reaction. Calculated enthalpy changes of the eutectic reaction for the studied Sn-Zn alloys are to some extent larger than related heat changes measured using DSC (see Table 2). The experimentally determined heat of eutectic reaction for the near-eutectic Sn–14.1 at% Zn is equal to 68.6 J/g, which is close to the value reported by Sahin and Karakurt [7] (73.1 Jg⁻¹ for the Sn-8.8 mass% Zn alloy) and published value of 71.2 Jg⁻¹ for the Sn-8.0 mass% Zn alloy [21]. At liquidus temperatures of hypereutectic Sn-Zn alloys, there is characteristic bend on the enthalpy curves which corresponds to the end of the melting of primary (Zn) phase.



(a)



(b)

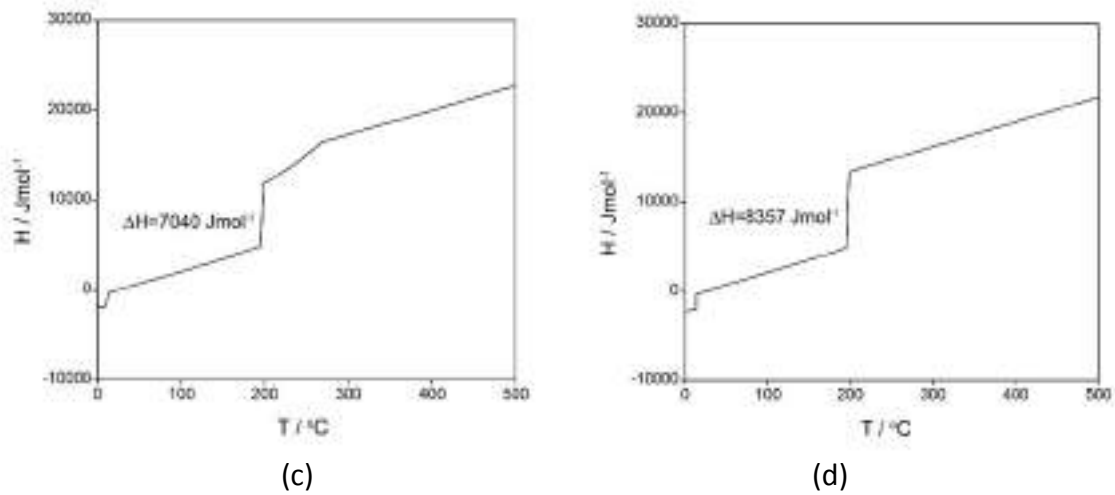


Figure 7. Temperature dependence of enthalpy calculated by using optimized thermodynamic parameters from [12]: (a) Sn–69.5Zn alloy; (b) Sn–48.3Zn alloy; (c) Sn–28.1Zn alloy; (d) Sn–14.1Zn alloy

Thermal conductivity

The values of thermal properties for pure constitutive metals Sn and Zn are given in the reference literature [22]. They are presented in Table 3 for comparison. It can be seen that Zn has higher melting point, latent heat of fusion, specific heat capacity and thermal conductivity than Sn. In contrast, Sn has higher density than Zn.

Table 3. Thermophysical properties of the pure metals Sn and Zn [22]

Metal	Melting point / °C	Latent heat of fusion / Jg ⁻¹	Density / gcm ⁻³	Specific heat capacity / J/g ⁻¹ K ⁻¹	Thermal conductivity / Wm ⁻¹ K ⁻¹
Sn	231.9	59.6	7.298 at 25 °C	0.205 at 25 °C	62.8 at 0 °C
Zn	420.0	100.9	7.133 at 25 °C	0.382 at 20 °C	113.0 at 25 °C

Thermal conductivity can be obtained using the density, thermal diffusivity and specific heat capacity data for the investigated material (Eq. 2). In this study, thermal conductivity of solid Sn–Zn alloys has been investigated in the temperature range from 25 to 150 °C using the flash method. The flash technique directly measures thermal diffusivity [14]. The uncertainty for the thermal diffusivity measurements is $\pm 3\%$ [14,23]. It includes deviation of experimental points, error of the measuring instrument and error in the measurement of sample thickness according to Eq. (1).

Alloys densities were determined by using buoyancy method based on the Archimedes' principle. The obtained results with calculated uncertainties are shown in Table 4.

Table 4. Density measured according to Archimedes' principle

Alloy	Density / gcm ⁻³
Pure Zn	7.13±0.05
Sn-69.5Zn	7.20±0.06
Sn-48.3Zn	7.24±0.07
Sn-28.1Zn	7.26±0.07
Sn-14.1Zn	7.27±0.06
Pure Sn	7.30±0.07

The density of the Sn-Zn alloys increases with the increasing Sn content. The measured densities for the pure Sn and Zn are in very good agreement with the literature values [17, 22] and thus confirm the adequate accuracy of the applied method. The measured density of the Sn-14.1% Zn alloy is also in accordance with the density of the Sn-9 mass% Zn alloy reported in [17]. Densities of studied alloys at higher temperatures (Table 5) were calculated using the measured values at room temperature and the coefficients of thermal expansion (CTE) reported by Lee et al. [6].

The specific heat capacities of the alloys with studied compositions in the temperature range from 25 to 150 °C were calculated using the CALPHAD approach and optimized parameters from the thermodynamic database [12]. The obtained results are shown in Table 5. Accuracy of the calculated specific heat capacity values (estimated to be ± 5%) was assessed based on comparison with the reported experimental specific heat capacity data for the Sn-9 mass% Zn eutectic alloy [21,24].

The overall uncertainty of thermal conductivity, $\delta \lambda$ ($\pm 6\%$) was evaluated using estimated uncertainties for density, thermal diffusivity and specific heat capacity by the following equation:

$$\delta \lambda^2 = \delta \alpha^2 + \delta \rho^2 + \delta C_p^2 \quad (4)$$

where $\delta \alpha$, $\delta \rho$, δC_p are the percentage uncertainties of thermal diffusivity, density and specific heat capacity.

The obtained values of density, thermal diffusivity, specific heat capacity and thermal conductivity for the solid Sn-Zn alloys investigated in the temperature range from 25 to 150 °C are given in Table 5.

From Table 5 it can be noticed that, for all investigated alloys, specific heat capacity increases while density, thermal diffusivity and thermal conductivity gradually decrease with increasing temperature.

Table 5. Density, specific heat capacity, thermal diffusivity, and thermal conductivity of the investigated Sn–Zn alloys in the temperature range 25–150 °C

Alloy / at.%	Temperature / °C	Density / gcm^{-3}	Specific heat capacity, C_p / $\text{Jg}^{-1}\text{K}^{-1}$	Thermal diffusivity / mm^2s^{-1}	Thermal conductivity / $\text{Wm}^{-1}\text{K}^{-1}$
Sn–69.5Zn	25	7.20	0.317	41.19±1.24	94.01±5.64
	50	7.18	0.320	40.11±1.20	92.16±5.53
	100	7.15	0.327	38.38±1.15	89.73±5.38
	150	7.11	0.335	36.75±1.10	87.53±5.25
Sn–48.3Zn	25	7.24	0.282	40.78±1.22	83.26±5.00
	50	7.22	0.285	39.78±1.19	81.86±4.91
	100	7.19	0.293	37.41±1.12	78.81±4.73
	150	7.16	0.301	36.03±1.08	77.65±4.66
Sn–28.1Zn	25	7.26	0.256	37.32±1.12	69.36±4.16
	50	7.24	0.258	36.90±1.11	68.93±4.14
	100	7.21	0.267	34.73±1.04	66.86±4.01
	150	7.18	0.275	32.85±0.99	64.86±3.89
Sn–14.1Zn	25	7.27	0.244	34.87±1.05	61.86±3.71
	50	7.25	0.248	33.64±1.01	60.48±3.63
	100	7.22	0.256	31.77±0.95	58.72±3.52
	150	7.19	0.264	29.63±0.89	56.24±3.37

Thermal conductivities of the studied alloys, obtained in the current study, are plotted in Fig. 8 as functions of temperature. The results show that thermal conductivity decreases with increasing temperature and Sn content. Based on their own experimental results, Matsugi et al. [8] have derived following equation for prediction of thermal conductivity for the solid Sn–Zn alloys as a function of temperature and composition:

$$\lambda = (0.0273Zn - 0.0982)T + 38.183Zn + 98.24 \quad (5)$$

The results obtained by applying the Eq. (5) are attached to the Figure 8 in the form of lines for comparison. It can be seen that there is good agreement between two sets of data for the Sn–69.5Zn and Sn–48.3Zn alloys, as well as for the Sn–28.1Zn alloy at higher temperatures. In the case of the Sn–14.1Zn alloy, thermal conductivities obtained by xenon flash method are considerably lower than values calculated from Eq. (5).

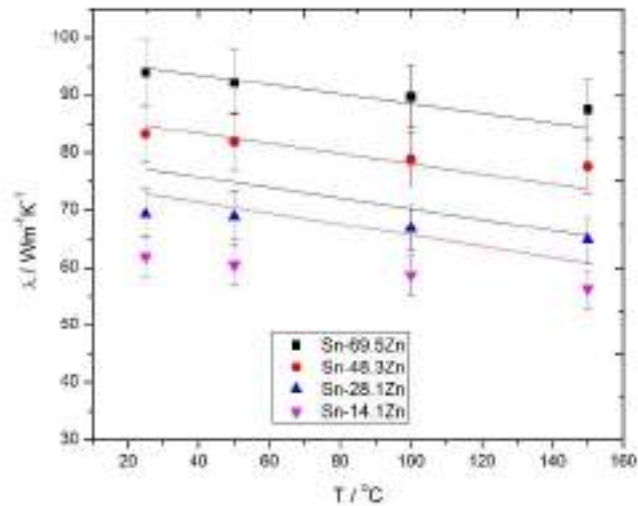


Figure 8. The variation of thermal conductivity with temperature for the solid Sn-Zn alloys. The lines represent corresponding values calculated using the equation from [8]

Fig. 9 shows compositional dependence of the electrical conductivity for the studied Sn-Zn alloys measured at 25 °C. As in the case of thermal conductivity, electrical conductivity of the investigated alloys increases with increasing Zn content.

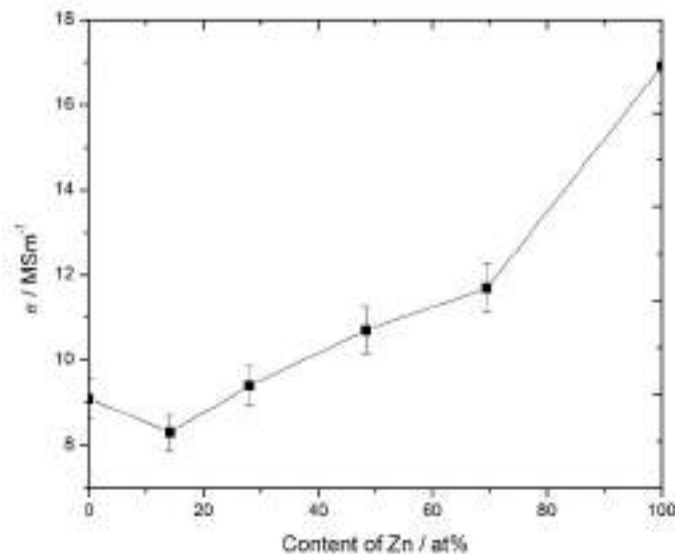


Figure 9. Electrical conductivity variation with composition for the air cooled Sn-Zn alloys at 25 °C

As seen from Figs. 8 and 9, thermal and electrical conductivities are the lowest for the near-eutectic Sn-14.1Zn alloy. The reason could be eutectic microstructure in the Sn-14.1% Zn alloy (Figs. 5a and 5b). It was shown that the phase dispersion in eutectic composition is much higher than that in the hypo- and hypereutectic compositions. The amount of phase boundaries in the near-eutectic alloy is substantially larger than those of hypereutectic alloys [25]. Large fraction of the primary (Zn) phase in hypereutectic alloys reduces the phase boundaries. Since they are the main scattering centers, the conductivity of alloy with near eutectic composition should be lower. The obtained electrical conductivity of the Sn-14.1Zn

alloy from the present study is in good agreement with the electrical conductivity values for the eutectic Sn–9 mass% Zn alloy obtained by Matsugi et al. [8], Plevachuk et al. [9], and Gancarz et al. [26]. Electrical conductivity of Sn-Zn alloys at room temperature increases with increasing the concentration of Zn as the metal with higher conductivity than Sn, but it is also influenced by the microstructure of an alloy, fractions of co-existing phases, their morphologies and the amounts of phase boundaries. Measured electrical conductivities of the studied alloys were used as an input for the estimation of corresponding thermal conductivities using the Wiedemann–Franz law.

The thermal conductivity (λ) of a metal alloy is linked with the electrical conductivity (σ) by the well-known Wiedemann–Franz law:

$$\frac{\lambda}{\sigma} = LT \tag{6}$$

where L is the Lorenz number and T is the absolute temperature. L was regarded to be the constant with theoretical value of $2.44 \times 10^{-8} \text{ W}\Omega\text{K}^{-2}$ in all metal alloys without considering its material and temperature dependence [27].

The obtained results are presented in Fig. 10. It can be noticed that thermal conductivities of the Sn–69.5Zn and Sn–48.3Zn alloys, obtained from the Wiedemann–Franz relation, are to some extent lower than experimentally determined values. For the Sn–28.1Zn and Sn–14.1Zn alloys there is an excellent agreement between two results. The validity of the Wiedemann-Franz relation for the Sn-Zn alloys indicates that electrons are the dominant carriers of heat energy.

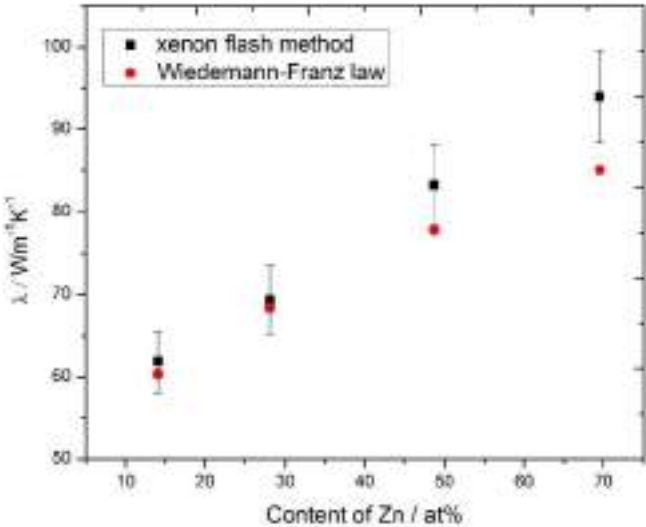


Figure 10. Comparison between thermal conductivities at 25 °C obtained using xenon flash method and calculated using Wiedemann–Franz relation based on the measured electrical conductivities

CONCLUSIONS

In this work, the microstructure, melting behavior, thermal diffusivity, specific heat, density, and thermal conductivity of solid Sn–Zn binary alloys were obtained and systematically investigated.

The main conclusions of the present study may be summarized as follows:

- a) The microstructure of all studied alloys includes grains of the primary (Zn) phase in the eutectic matrix. The morphology of the (Zn) primary phase changes with decreasing Zn concentration from the equiaxed and rounded grain structure to plate-like shape and finally to needle-like shape in the near-eutectic Sn–14.1Zn alloy. The Sn–Zn eutectic is characterized by a broken-lamellar type eutectic structure which consists of discontinued, faceted lamellae of Zn phase and the nonfaceting Sn phase in the matrix.
- b) Experimentally obtained temperature of eutectic reaction is equal to 198.8 °C, which is in excellent agreement with the value of eutectic temperature according to the phase diagram of the Sn–Zn system (198.6 °C). The heat of melting of the near-eutectic Sn–14.1Zn alloy measured by DSC technique is equal to 68.6 Jg⁻¹.
- c) The specific heat capacity of the solid Sn–Zn alloys monotonically increases with increasing temperature and Zn content. The density of the solid Sn–Zn alloys decreases with increasing Zn content and temperature.
- d) The thermal conductivity of the solid Sn–Zn alloys is mainly determined by both alloy composition and temperature. Thermal conductivity monotonically decreases with increasing temperature and Sn content and it is the lowest for the near-eutectic Sn–14.1Zn alloy. The composition and temperature dependences of thermal diffusivity and thermal conductivity are similar.
- e) The reasonable agreement between experimentally obtained thermal conductivity and results deduced from Wiedemann-Franz relation for the Sn-Zn alloys indicates that electrons are the dominant carriers of thermal conduction.

Acknowledgements

The research presented in this paper was done with the financial support of the Ministry of Education, Science and Technological Development of the Republic of Serbia, within the funding of the scientific research work at the University of Belgrade, Technical Faculty in Bor, according to the contract with registration number 451-03-9/2021-14/ 200131.

REFERENCES

- [1] V. L. Scheiber, C. M. Méndez, C. E. Schvezov, A. E. Ares, *The Minerals, Metals & Materials Society*, ed by TMS 2014: 143rd Annual Meeting & Exhibition, Springer, Cham. 2014.
- [2] M. Ari, B. Saatçi, M. Gündüz, M. Payveren, S. Durmuş, *Thermo-electrical characterization of Sn–Zn alloys*, *Mater. Charact.* 59(2008)6, pp. 757-763.
- [3] B. T. Heligman, K. J. Kreder, A. Manthiram, *Zn-Sn interdigitated eutectic alloy anodes with high volumetric capacity for lithium-ion batteries*, *Joule*. 3(2019), pp. 1051-1063.

- [4] A. A. El-Daly, A. E. Hammad, Elastic properties and thermal behavior of Sn–Zn based lead-free solder alloys, *J. Alloy. Compd.* 505 2(2010), pp. 793-800.
- [5] S. Liu, S. Xue, P. Xue, D. Luo, Present status of Sn–Zn lead-free solders bearing alloying elements, *J. Mater. Sci - Mater. El.* 26(2015), pp. 4389-4411.
- [6] J. E. Lee, K. S. Kim, K. Suganuma, M. Inoue, G. Izuta, Thermal properties and phase stability of Zn-Sn and Zn-In alloys as high temperature lead-free solder, *Mater. Trans.* 48(2007)3, pp. 584-593.
- [7] M. Şahin, F. Karakurt, The effect of the solidification rate on the physical properties of the Sn-Zn eutectic alloy, *Physica B.* 545(2018), pp. 48-54.
- [8] K. Matsugi, G. Sasaki, O. Yanagisawa, Y. Kumagai, K. Fujii, Electrical and thermal characteristics of Pb-Free Sn-Zn Alloys for an AC-Low Voltage Fuse Element, *Mater. Trans.* 48(2007)5, pp. 1105-1112.
- [9] Y. Plevachuk, V. Sklyarchuk, P. Svec, D. Janickovic, E. Illekova, A. Yakymovych, Thermophysical structure-sensitive properties of Tin–Zinc alloys, *J. Mater. Sci. - Mater. El.* 28(2017), pp. 750-759.
- [10] B. J. Lee, Thermodynamic assessments of the Sn-Zn and In-Zn binary systems, *Calphad* 20(1996), pp. 471-480.
- [11] S. G. Fries, H. L. Lukas, System Sn–Zn, in: I. Ansara, A. T. Dinsdale, M. H. Rand (Eds.), COST 507, in: *Thermochemical Data base for Light Metal Alloys*, 21998, p. 288.
- [12] A. Kroupa, A. T. Dinsdale, A. Watson, J. Vrestal, J. Vízdal, A. Zemanova, The development of the COST 531 lead-free solders thermodynamic database, *JOM* 59 (2007), pp. 20-25.
- [13] F. Meydaneri, B. Saatçi, M. Gündüz, M. Özdemir, Determination of thermal conductivities of Sn–Zn lead-free solder alloys with radial heat flow and Bridgman-type apparatus, *Continuum Mech. Therm.* 25(2013), pp. 691-704.
- [14] W. J. Parker, R. J. Jenkins, C. P. Butler, G. L. Abbott, Flash method of determining thermal diffusivity, Heat Capacity, and Thermal Conductivity, *J. Appl. Phys.* 32(1961) pp. 1679-1684.
- [15] D. Manasijević, L. Balanović, I. Marković, D. Minić, M. Premović, A. Đorđević, M. Gorgievski, U. Stamenković, Study of thermal properties and microstructure of the Ag–Ge alloys, *J. Therm. Anal. Calorim.* (2021), <https://doi.org/10.1007/s10973-021-10664-y>
- [16] D. Manasijević, L. Balanović, I. Marković, M. Gorgievski, U. Stamenković, D. Minić, M. Premović, N. Štrbac, Phase transformations and thermal conductivity of the In-Ag alloys, *Metallurgical and Materials Engineering* 26(2020)3, pp. 239-251.
- [17] L. Wang, A. P. Xian, Density measurement of Sn-40Pb, Sn-57Bi, and Sn-9Zn by indirect Archimedean method, *J. Electron. Mater.* 34(2005), pp. 1414-1419.
- [18] W. J. Boettinger, U. R. Kattner, K. W. Moon, J. H. Perepezko, In: *Methods for Phase Diagram Determination*, ed. By J.C. Zhao, Elsevier Science, Amsterdam, 2007. p. 151.
- [19] H. L. Lukas, S. G. Fries, B. Sundman, *Computational Thermodynamics: the Calphad Method*, Cambridge University Press, Cambridge, 2007.
- [20] W. Cao, S. L. Chen, F. Zhang, K. Wu, Y. Yang, Y. A. Chang, R. Schmid-Fetzer, W. A. Oates, PANDAT software with PanEngine, PanOptimizer and PanPrecipitation for multi-component phase diagram calculation and materials property simulation, *Calphad* 33(2009), pp. 328-342.

- [21] Indium Corp, Indalloy® 201 Sn-Zn Solder Alloy, Accessible on Internet: <http://www.matweb.com/search/DataSheet.aspx?MatGUID=376d716c9b7e45a9922c4c939fd6900a&ckck=1>, (21.04.2021.)
- [22] ASM Handbook, Volume 2: Properties and Selection: Nonferrous Alloys and Special-Purpose Materials, ASM International, Materials Park, 1990.
- [23] C. Zhang, Y. Du, S. Liu, Y. Liu, B. Sundman, Thermal conductivity of Al–Cu–Mg–Si alloys: Experimental measurement and CALPHAD modeling, *Thermochim. Acta* 635(2016), pp. 8-16.
- [24] J. K. Wu, K. L. Lin, B. Salam, Specific Heat Capacities of Sn-Zn-Based Solders and Sn-Ag-Cu Solders Measured Using Differential Scanning Calorimetry, *J. Electron. Mater.* 38(2009), pp. 227-230.
- [25] H. M. Chen, Q. Wang, D. L. Geng, H. P. Wang, Specific heat, thermal diffusivity, and thermal conductivity of Ag–Si alloys within a wide temperature range of 293-823 K, *J. Phys. Chem. Solids* 153(2021), p. 109997.
- [26] T. Gancarz, P. Fima, J. Pstrus, Thermal Expansion, Electrical Resistivity, and Spreading Area of Sn-Zn-In Alloys, *J. Mater. Eng. Perform.*, 23(2014), pp. 1524-1529.
- [27] Y. Huang, X. Zhou, J. Du, Thermal Conductivity and Mechanical Properties of the Mg–Zn–Sb Ternary Alloys, *Met. Mater. Int.*, 2020.



19th INTERNATIONAL FOUNDRYMEN CONFERENCE
Humans - Valuable Resource for Foundry Industry Development
Split, June 16th-18th, 2021
<https://ifc.simet.hr/>

PRINCIPLE OF TITANIUM DIOXIDE REDUCTION IN LIQUID ALUMINIUM

Jožef Medved^{1*}, Maja Vončina¹, Stanislav Kores², Matej Mesarič²

¹ University of Ljubljana Faculty of Natural Sciences and Engineering, Ljubljana, Slovenia

² TALUM d.d., Kidričevo, Slovenia

Invited lecture
Original scientific paper

Abstract

Titanium dioxide is the most widely used white pigment and is present as a base in majority of paints used in the painting of aluminium tubes and cans. When remelting secondary aluminium painted with paint based on titanium dioxide, it is necessary to know the effects of different melting parameters. In the case of reduction of titanium dioxide in liquid aluminium, the acceptable limit of titanium in the melt could be exceeded. The aim of this investigation was to determine the influence of parameters and conditions of melt treatment, and how they effect on possible reduction of titanium dioxide in liquid aluminium. A series of samples were prepared to which the melt treatment conditions, the temperature and holding time of the melt were changed, and the certain amount of titanium dioxide powder was added. Based on simple thermal analysis, cooling curves and characteristic temperatures were plotted, chemical composition was analysed, differential scanning calorimetry, XRD analysis of slag, optical microscopy was performed, and inclusions were analysed by scanning electron microscope and EDS analysis. Since there was no change in the chemical composition of any sample during the preparation of the first series of samples, and no reduction in titanium dioxide, an XRD analysis of the slag was performed, whereas its presence was investigated. The same happened with a series of samples made with the recycling process, where the presence of titanium dioxide in slag by XRD analysis was proved and no reduction was confirmed. It turned out that under none of the implemented conditions there was no reduction of titanium dioxide in liquid aluminium and consequently introduction of titanium into the melt.

Keywords: *titanium dioxide, aluminothermic reduction, titanium, recycling of aluminium*

*Corresponding author (e-mail address): jozef.medved@omm.ntf.uni-lj.si

INTRODUCTION

Titanium dioxide is the most widely used white pigment and is present as a base in majority of paints used in the painting of aluminium tubes and cans. Due to its properties, the pigment of titanium dioxide has become the most important and most frequently used pigment in the last fifty years, as more than 90 wt. % of its global consumption is

represented by the production of pigments and paints [1]. It is used in two qualities, as a pigment or as a nanomaterial. In pigment form, it is used for paints as it sheds visible light and is consequently opaque. This requires particles about half the wavelength of light. Titanium dioxide as a nanomaterial is transparent and absorbs more ultraviolet light, so it is used for sunscreens. The particles must be smaller than 100 nm to achieve the desired properties. Ultrafine titanium dioxide is also used in vehicle catalysts as it reduces nitrogen oxide emissions. One of the areas of application of titanium dioxide paints is also the industry of aluminium packaging, which in recent years has tended to increase the use of secondary raw materials. Titanium is found in commercially pure aluminium in proportions between 10 ppm and 100 ppm, and it is often necessary to add it in the manufacture of alloys, as it acts as an α -Al grain refiner, which has a favourable effect on mechanical and processing properties. As its share in alloys is limited to prevent the formation of various titanium phases, care must be taken in the manufacture of alloys, especially in recycling processes. When remelting secondary raw materials painted with titanium dioxide-based coatings, it is therefore necessary to know the effects of different melting parameters, as in the case of reduction of titanium dioxide in liquid aluminium the permissible limit of titanium in the melt could be exceeded.

It was found that the melting of secondary aluminium with addition of titanium dioxide contaminates the melt with titanium. When comparing the values of the Gibbs free energy of formation of aluminium and titanium oxide, Al_2O_3 has a lower free energy than TiO_2 , which means that this oxide is more stable. Due to the negative value of Gibbs free energy for the reaction:



one might expect TiO_2 to be reduced by aluminium. The free energy of that reaction is $\Delta G^\circ_{(1276\text{K})} = -402,2 \text{ kJ}$ [1,2,3].

At aluminium melt processing temperatures, titanium remains dissolved in the melt until its proportion is less than 0.15 wt. %. From a metallurgical point of view, this reaction results in the introduction of titanium into the melt and the oxidation of aluminium to Al_2O_3 , which is excreted in the slag and represents losses. In larger quantities of titanium dioxide, when the proportion exceeds 0.15 wt. % Ti in the melt, parallel reactions begin to take place, leading to the formation of the Al_3Ti and Al_2O_3 phases in the slag.

In Figure 1 the influence of the melting temperature on the input of titanium into the melt can be seen. The reaction rate increases with increasing temperature. At temperatures below 800 °C, the reaction rate is relatively low, so the reduction of TiO_2 should not take place. From this can be concluded that the introduction of titanium into the melt can be avoided by melting temperature below 800 °C [2].

The purpose of this work was to investigate the influence of parameters and conditions of melt processing and how they affect the possible reduction of titanium dioxide in liquid aluminium and thus the introduction of titanium into the melt. Two series of samples were prepared, namely one series, where titanium dioxide was added to the melt in the form of powder, and one series, where the preparation of samples took place according to the recycling process. The aim of the investigation was to determine the conditions under which the reduction of titanium dioxide occurs.

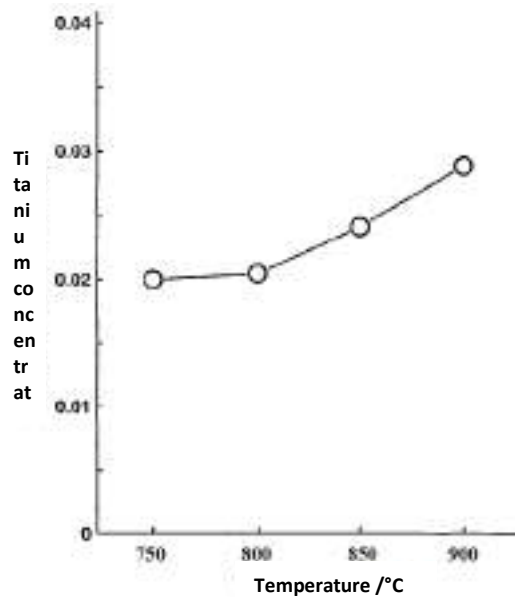


Figure 1. Influence of melting temperature on titanium input [2]

MATERIALS AND METHODS

A series of 18 samples in a resistive electric furnace were prepared. Aluminium of 99.99% purity and ground rutile pigment TiO_2 of RC8 type (Cinkarna Celje, d.d.) were used to make the samples. The production parameters and the method of marking the samples are given in Table 1.

Table 1. The production parameters

Desired concentration of Ti in the melt [wt. %]	Reduction temperature [°C]	Reduction time [min]
A – 0.03	750	5
B – 0.1	900	30
C – 0.5		60

The casting temperature of all samples was 750 °C, the casting took place in a Croning measuring cell, where the course of solidification of the samples was recorded with a thermocouple type K (Ni-NiCr) and an adapted measuring system. Figure 2 shows an induction furnace and a measuring system for recording the solidification of the samples.

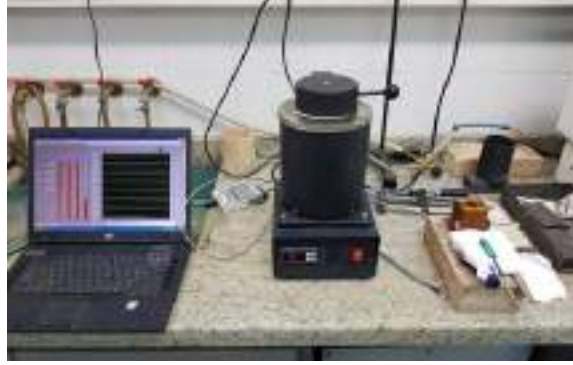


Figure 2. Induction furnace and measuring system for recording the solidification process

RESULTS AND DISCUSSION

Table 2 shows the chemical composition of all samples. The titanium content in all samples was only 0.0003 wt. %. Thus, no increase in the titanium content was detected in the chemical composition, as the Ti content is the same as in the base material.

Table 2. Chemical composition of samples

wt. %/ Sample	Al	Ti	Si	Fe	wt. %/ Sample	Al	Ti	Si	Fe
A199.99	99.994	0.0003	0.0002	0.0002	B900-5	99.952	0.0003	0.0003	0.0017
A750-5	99.993	0.0003	0.0001	0.0012	B900-30	99.992	0.0003	0.0001	0.0009
A750-30	99.994	0.0003	0.0001	0.0008	B900-60	99.991	0.0003	0.0001	0.0019
A750-60	99.994	0.0003	0.0001	0.0009	C750-5	99.993	0.0003	0.0001	0.0007
A900-5	99.992	0.0003	0.0001	0.0014	C750-30	99.987	0.0003	0.0001	0.0015
A900-30	99.993	0.0003	0.0001	0.0009	C750-60	99.993	0.0003	0.0001	0.0013
A900-60	99.993	0.0003	0.0002	0.0008	C900-5	99.987	0.0003	0.0001	0.0027
B750-5	99.993	0.0003	0.0001	0.0009	C900-30	99.988	0.0003	0.0001	0.0011
B750-30	99.993	0.0003	0.0001	0.0008	C900-60	99.992	0.0003	0.0001	0.0017
B750-60	99.994	0.0003	0.0001	0.0008					

Since the solidification of alloys does not proceed in equilibrium in practice, a Scheil diagram of nonequilibrium solidification in Thermo-Calc 2020 was drawn. The database used was TCAL6. The calculation assumes that the solidification of α -Al crystals starts at 660,4 °C and ends at 660,2 °C.

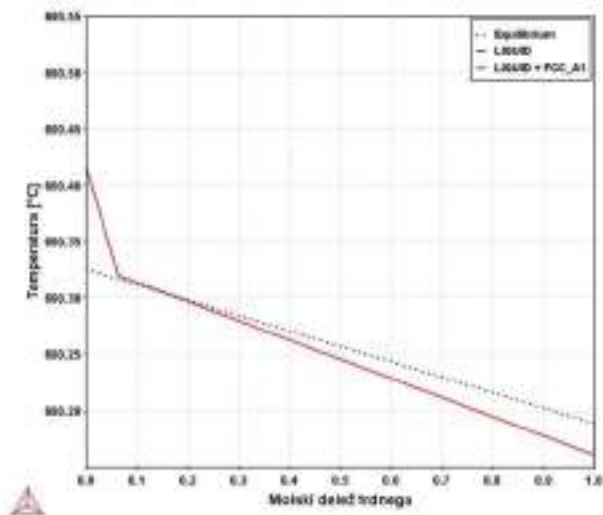


Figure 3. Scheil diagram of nonequilibrium solidification of samples

Figure 4 shows a comparison of the heating and cooling curves for samples C750-60 and C900-60, which have the same amount of added titanium dioxide and the longest holding time (60 min). The heating and cooling curves are very similar, and the differences between enthalpies and temperatures are very small. At 643.7 °C (C750-60) or 641.5 °C (C900-60) the eutectic (α -Al + $\text{Al}_{13}\text{Fe}_4$) melts and at 651.8 °C (C750-60) or 652.2 °C (C900-60) the primary α -Al mixed crystals continues to melt. On the cooling curve, the solidification of α -Al crystals starts at 648.2 °C (C750-60) or 647.2 °C (C900-60).

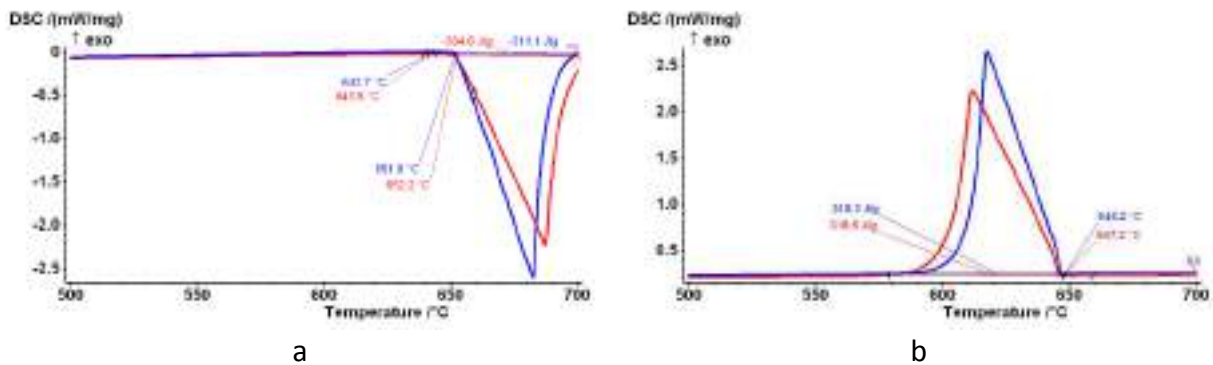


Figure 4. Comparison of heating (a) and cooling (b) DSC curves, C750-60 (blue) and C900-60 (red)

Figure 5 shows the diffractogram of sample C93 (C900-30). The peaks appearing in the diffractogram belong to aluminium, aluminium oxide (Al_2O_3), and aluminium carbide (Al_4C_3), which results from melting in a graphite crucible at high temperatures. Due to the presence of aluminium carbide, the slag is slightly darker than in other samples. No titanium dioxide was detected in the slag, most likely due to the small added proportion during sample preparation and below the detection limit.

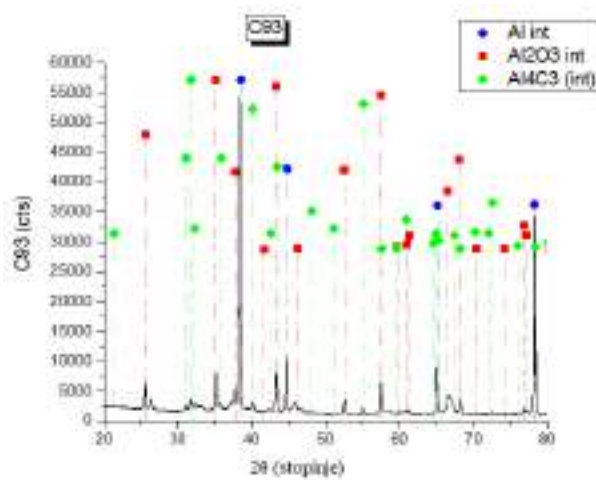
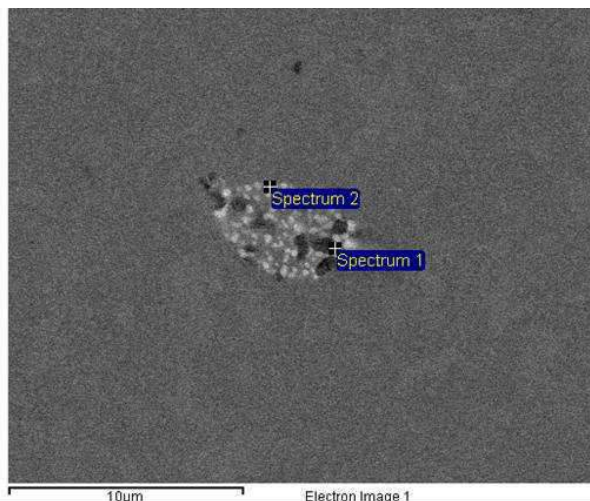


Figure 5. XRD analysis of sample C900-30

Figure 6 shows the microstructure (SEM) and microanalysis (EDS) of the inclusion in sample C750-5. According to its chemical composition, it is alumina, whereas also iron is present.



wt. %	Al	Ti	O	Si	Fe
Sp 1	79.2	0.0	16.6	0.2	4.0
Sp 2	91.0	0.0	2.3	0.0	6.7

Figure 6. Microstructure (SEM) and microanalysis (EDS) of sample C750-5

Figure 7 shows the microstructure and microanalysis of slag from sample 950-5. EDS analysis was made at 7 sites. The analysis in point 2 shows the presence of aluminium, oxygen, titanium, and iron, so it is difficult to determine which compound it is. The analysis in points 3 and 4 is most likely titanium dioxide particles, as the titanium content is just over 50 wt. %, and the titanium dioxide molecule contains about 59 wt. % Ti. Due to the point analysis, which is not completely accurate, as the immediate surroundings were most likely also analyzed, which is why the analysis showed some aluminium and iron in addition to oxygen. The analysis in point 5 in terms of composition indicates the Al_3Fe ($Al_{13}Fe_4$) phase. The analysis showed 37 wt. % of Fe, and the Al_3Fe phase contains about 40 wt. % of Fe, which is slightly less due to the presence of oxygen in the environment. Point 6 is the area analysis. Based on the results of the analysis, the presence of aluminium and titanium oxides, and most likely also the Al_3Fe phase, was assumed in this area. The analysis in point 7 according to the chemical analysis again indicates the Al_3Fe phase. Point 8 represents the area of aluminium, and a small proportion of oxygen, most likely due to oxide cuticle.

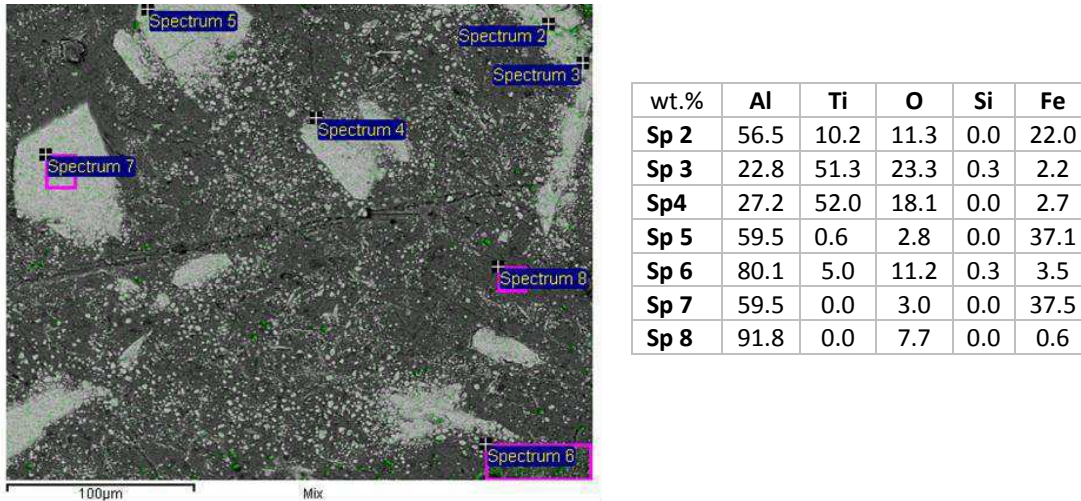


Figure 7. Microstructure (SEM) and microanalysis (EDS) of sample 950-5

CONCLUSIONS

The aim of the study was to determine the conditions under which the reduction of titanium dioxide in liquid aluminium takes place. Samples with different proportions of titanium dioxide additive and different melting temperatures were prepared. From the investigations performed, following conclusions can be made:

- Melting at temperatures of 750 °C and 900 °C, different melt holding times and different proportions of titanium dioxide addition did not show a change in the chemical composition in aluminium alloy, which means that under the mentioned conditions there was no reduction of titanium dioxide.
- DSC analysis, according to the course of the cooling curves, confirms the solidification of the eutectic (α -Al + $Al_{13}Fe_4$) in samples made at 750 °C and 900 °C. The differences between the temperatures and enthalpies of the samples prepared at 750 °C and 900 °C are very small. DSC analysis of samples made after the recycling process is almost the same, as their chemical composition is also almost the same.
- The microstructure of all samples consists of primary mixed crystals of α -Al and eutectic (α -Al + $Al_{13}Fe_4$). The proportion of eutectic in samples prepared at 750 °C and 900 °C is so small that it cannot be detected by optical microscopy, but solidification of the eutectic is shown by DSC analysis.
- XRD analysis of the slag sample from a series of samples made at 750 °C and 900 °C did not show the presence of titanium dioxide, most likely due to the insufficient amount added during melting, which was below the detection limit.
- EDS analysis of slag from sample 950-5 confirmed the presence of titanium dioxide particles. The surface distribution analysis shows an uneven distribution of titanium. EDS analysis of the inclusions in the samples does not show the presence of titanium in any of them but indicates alumina and iron phases.

Acknowledgements

The work was co-financed by the Republic of Slovenia, the Ministry of Education, Science and Sport, and the European Regional Development Fund. The work was carried out in the framework of the project Modelling of thermomechanical processing of The aluminium alloys for high quality products (MARTIN, Grant No.: OP20.03531).

REFERENCES

- [1] TDMA – Titanium Dioxide Manufacturers Association, Accessible on Internet: <https://tdma.info>, (15.02.2020.)
- [2] S. Capuzzi, G. Timelli, Preparation and melting of scrap in aluminium recycling: A review, *Metals – Open Access Metallurgy Journal*, 8(2018)4, p. 15.
- [3] K. Oosumi, Influence of paint on recycling of Aluminium used beverage cans, *Proceedings of the Symposium K: Environment Conscious Materials of the 3rd IUMRS International Conference on Advanced Materials*, 1994., pp. 197-200.
- [4] M. Hosseinpouri, S. A. Mirmonsef, M. Soltanieh, Production of Al-Ti master alloys by aluminothermic reduction technique, *Canadian Metallurgical Quarterly*, 46(2007)2 pp. 139-14.



19th INTERNATIONAL FOUNDRYMEN CONFERENCE

Humans - Valuable Resource for Foundry Industry Development

Split, June 16th-18th, 2021

<https://ifc.simet.hr/>

DAMAGE ANALYSIS OF COMPACTED GRAPHITE CAST IRON

Primož Mrvar*, Milan Terčelj, Mitja Petrič, Danijel Mitrović, Goran Kugler

University of Ljubljana Faculty of Natural Sciences and Engineering, Ljubljana, Slovenia

Invited lecture
Original scientific paper

Abstract

Thermal fatigue testing of SiMoCr CGI (compacted graphite cast iron) cast alloy was performed with nitrided and non-nitrided samples, where cracks were evaluated at 400 / 600 °C and with following number of thermal cycles repetition: 1000, 2000 and 4000. Samples were cyclic inductive heated to set temperature and rapidly cooled with water stream through the bore in the sample. After the test, all the samples were sectioned where cross section was evaluated in detail. All cracks and their lengths were measured and statistically evaluated at 10 mm size measuring area.

Quantitative evaluation of cracks showed correlation between increased crack length and increased temperature and number of thermal cycles. Nitrided samples showed higher surface cohesion, further resulting with less smaller cracks in the surface area. Despite mentioned observation, total length of the cracks was higher on the nitrided samples.

Keywords: thermal fatigue testing, damage analysis, CGI

*Corresponding author (e-mail address): primoz.mrvar@omm.ntf.uni-lj.si

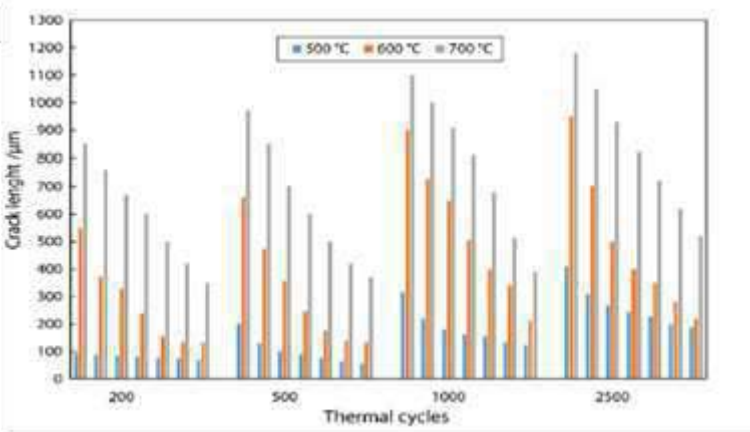
INTRODUCTION

Thermal fatigue properties of the material are important for various reasons. They can describe the material resistance to withstand cyclic thermal load and can be further in use to study surface protection treatments such as nitriding. Knowledge of thermal fatigue material behavior could be used for better determination of the material application, where cyclic thermal loadings are essential.

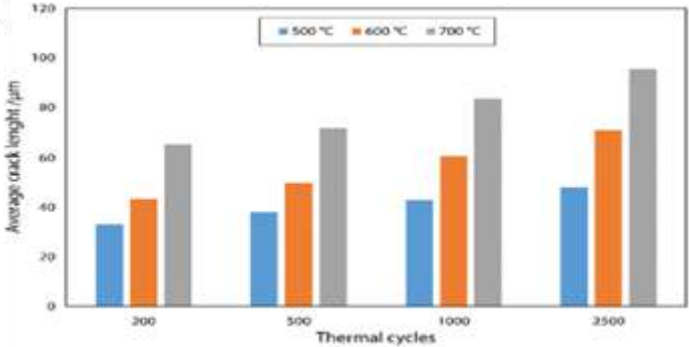
In this study, newly, developed material SiMoCr CGI was subjected to a thermal fatigue testing where samples were divided into: a) nitrided and b) non-nitrided / raw specimens. Mentioned material is at the moment in a testing stage and has a potential to become a cost-effective alternative for hot work tool steels (H13) used for cold-chamber HPDC application as a shoot sleeve [1].

Thermal fatigue of the hot working tool and roller steels with thermomechanical simulator was already investigated by several research groups [2, 3] where clear correlations were found. Crack lengths were increasing as expected with applied temperature and thermal cycle number, Figure 1.

In papers [4-7] cast iron fatigue testing at elevated temperatures was done with similar conclusions drawn.



(a) average crack length



(b) crack length

Figure 1. Quantitative analysis of thermal fatigue cracks (Fe-1.7C-11.3Cr-1.9Ni-1.2Mo) dependent on the maximum test temperature and number of thermal cycles [2, 3]

MATERIALS AND METHODS

Thermal fatigue testing and test conditions

Samples for thermal fatigue testing were obtained from shot sleeve used for cold-chamber High Pressure Die Casting machine (HPDC) after it was subjected to industrial environment. Shot sleeve was gravity casted in green sand molds without of cores and was made of newly developed variation of Compacted Graphite Cast Iron (SiMoCr CGI).

Thermal fatigue tests were carried out at 400 °C and 600 °C for various cycles: 1000, 2000 and 4000 cycles respectively, Table 1. For the purpose of the study, cracks on the inner bore of the sample were investigated where crack lengths were measured on a 10 mm large area.

Table 1. Thermal fatigue testing plan, test conditions

Temp. [°C]	Nitrided sample		Non-nitrided sample	
		400	600	400
No. of cycles	1000	1000	1000	1000
	2000	2000	2000	2000
	4000	4000	4000	4000

For thermal fatigue testing, thermo-mechanical simulator Gleeble 1500D was used. Specimen shape is schematically presented in Figure 2. Temperature was closely monitored with a K-type thermocouple, attached in the middle of the working area. Cyclic cooling of the specimen was performed with a water input, where cooling and heating cycle was computer controlled according to defined program (Figure 3).

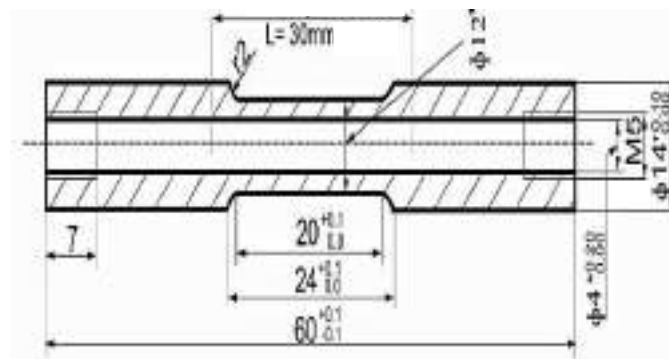


Figure 2. Specimen for thermal fatigue testing



(a)



(b)

Figure 3. Testing cell (a) with K-type surface welded thermocouple (b)

After thermal fatigue testing, samples were sectioned with EDM (electrical discharge machining) process according to the Figure 4, where sample for further analyses are denoted.



Figure 4. EDM sectioned specimen after thermal fatigue testing and a section used for further analyses

For crack evaluation analysis, middle part was taken in consideration where measuring surface for the validation of each specimen was limited to 10 mm in length, (Figure 5). Within this length, all longitudinal cracks were observed and measured with a use of an optical and SEM microscope and their corresponding software. Large data library of visible cracks (>3500 measurements) was gathered and further statistically analyzed.

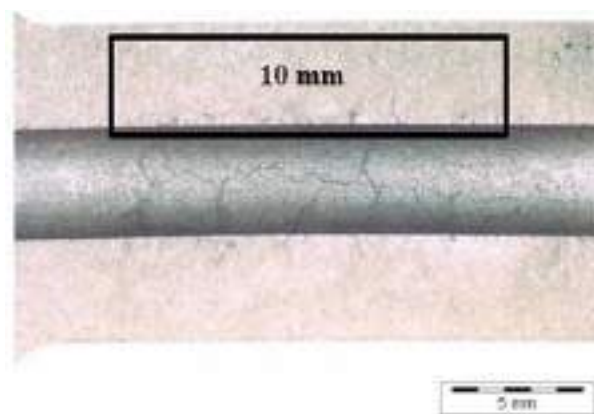


Figure 5. Crack validation area, 10 mm length around the center of the specimen

Metallographic observation and crack evaluation

Metallographic observation was performed with optical microscope Olympus BX61. Crack lengths were measured with corresponding software and all results gathered in an excel table.

Crack evaluation

Cracks were statistically evaluated via statistical software JPM 14.0. Chemical composition of investigated SiMoCr CGI alloy, obtained with spark optical spectroscopy is presented in Table 2.

Method for crack evaluation is presented on a macrograph in Figure 5. For one test condition/sample many consequent micrographs were taken on the 10 mm validation specimen length (Figure6).

Table 2. Chemical composition of SiMoCr CGI alloy [wt. %]

C	Si	Mn	S	Cr	Cu	Mo	Sn	Mg	Fe
3.02	4.72	0.293	0.005	0.176	0.055	0.529	0.019	0.023	Bal.

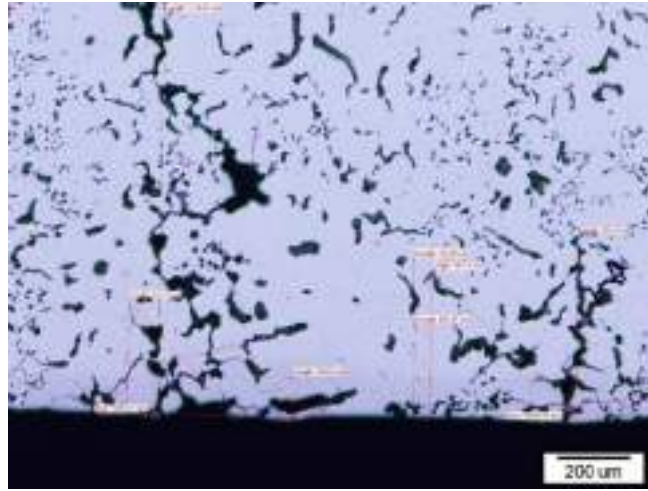


Figure 6. Method for crack length evaluation

RESULTS AND DISCUSSION

Figure 7 is presenting optical analysis of non-nitrided samples, subjected to a thermal fatigue experiment for 1000 cycles and 400 °C/600 °C. Notable deterioration of surface material soundness can be observed on 600 °C sample.



(a)



(b)

Figure 7. Optical micrograph of thermal fatigue sample for 1000 cycles experiment and 400 °C (a) and 600 °C (b), both non-nitrided

Further, SEM micrographs of nitrided samples can be observed in Figure 8. Clear evidence of surface quality improvement and material cohesion can be noticed, even at elevated temperatures, such as 600 °C.

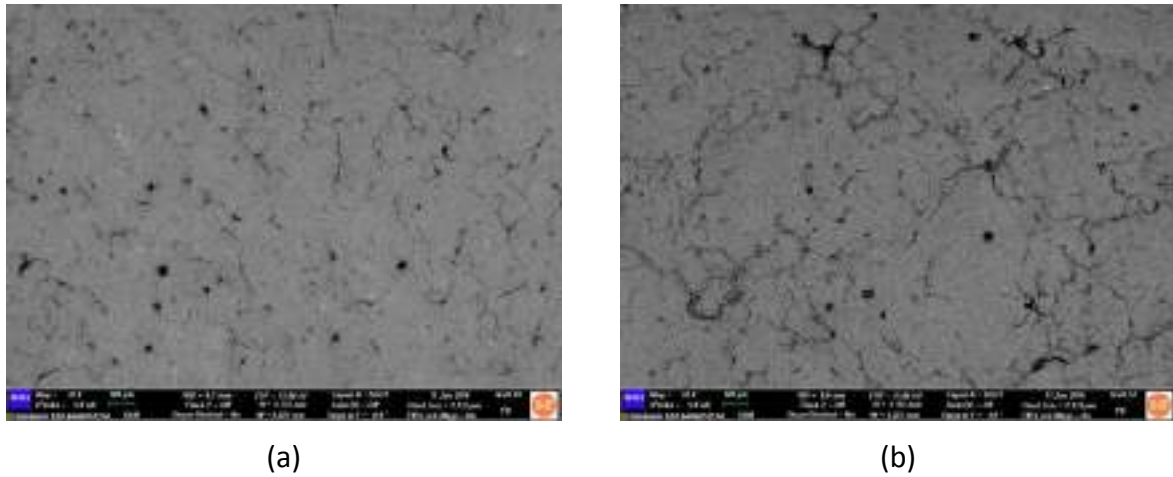


Figure 8. SEM micrograph of thermal fatigue sample for 1000 cycles experiment and 400 °C (a) and 600 °C (b), both nitrided

Over 3500 cracks on tested specimens were counted, statistically evaluated and graphs plotted.

Figure 9 is presenting mean values of all measured cracks on samples subjected to a testing procedure. Samples were divided into nitrided and non-nitrided. No. 0 denote in graphs condition for non-nitrided and No. 1 for nitrided samples. Contrary to what is known from high temperature fatigue testing of hot work tool steels, SiMoCr CGI alloy is showing different trend, where nitrided samples have experienced larger mean crack length values. Observed results can be due to presence of relatively large graphite particles integrated into the metal matrix of SiMoCr CGI, which act as a stress initiator. With a presence of hard surface nitride layer, which can cause, during applied stresses, that crack can easily propagate into the more ductile bulk of the investigated material. It has to be noted that nitride layer does not form full coherent layer on the surface, where graphite particles are completely exposed to the surface.

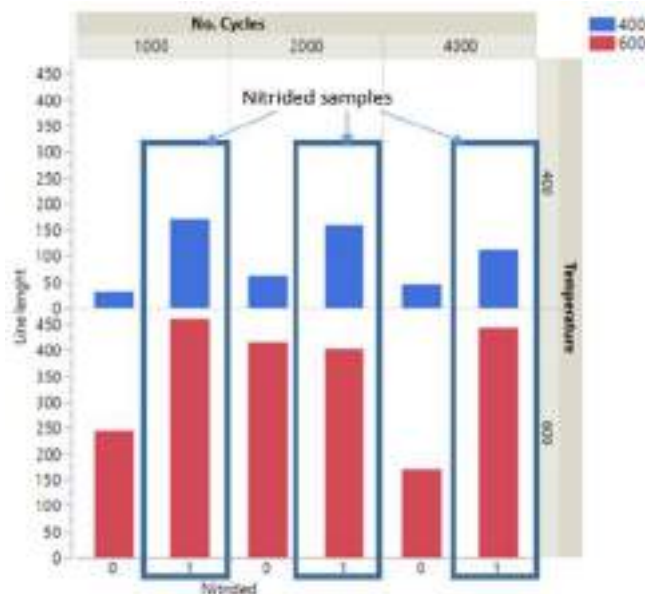


Figure 9. Average crack length (mean values) of SiMoCr CGI subjected to the testing plan

More detailed statistical evaluation was performed of all crack distribution analysis where results are presented in Figure 10. Here, clear difference is observed between nitrided and non-nitrided samples. On non-nitrided samples there is a large area with small length cracks present while with nitrided samples, cracks are larger. Focusing only on surface situation, it is due to hard nitriding layer remaining more macro cohesive.

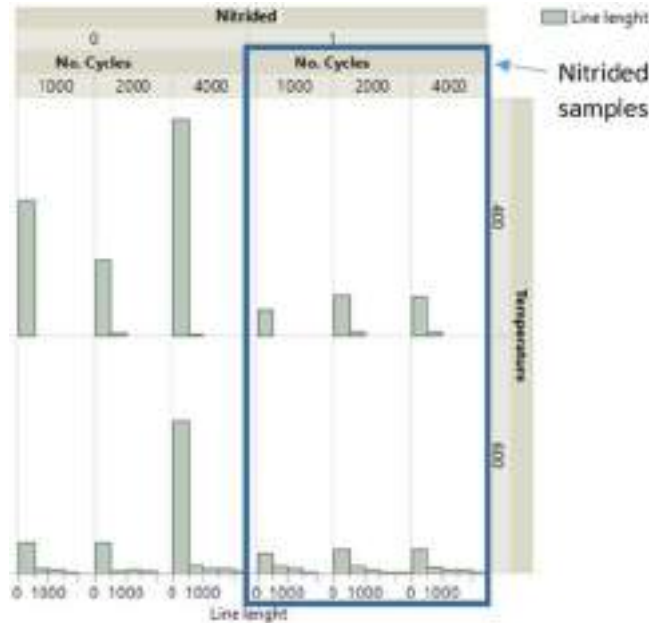


Figure 10. Crack length distribution SiMoCr CGI subjected to a testing plan

CONCLUSIONS

From obtained study, following conclusions could be drawn:

- Mean values of crack lengths after thermal fatigue testing of nitride SiMoCr CGI material are larger compared to non nitride SiMoCr CGI material.
- Nitrided SiMoCr CGI samples after thermal fatigue testing resulted with less shorter cracks (surface more adhesive due to nitride protection), however there were more larger cracks present (crack can easily penetrate to the more ductile bulk).
- Cracks are propagating according to expectations where the length is increasing with higher temperature and cycle loading.
- The initiation of cracks is predominately focused at sharp shaped spots on graphite particles, which are further, due to applied thermal and mechanical stress, becoming interconnected and are resulting with a macro cracks.

Due to large data obtained with the thermal fatigue testing more detail studies with complete micrographs presentations are going to be presented in future papers.

REFERENCES

- [1] R. Helenius, O. Lohne, Inter Heat Transfer to the Die Wall During High Pressure Die Casting of Two Aluminium Alloys, Part 1", IJMC April 2015, 9(2015)2, pp 51–59.

- [2] D. Bombač, M. Gintalas, G. Kugler, M. Terčelj, Thermal fatigue behavior of Fe-1.7C-11.3Cr-1.9Ni-1.2Mo roller steel in temperature range 500–700 °C, *Int. J. Fatigue*, 121(2019), pp. 98-111.
- [3] M. Terčelj, M. Fazarinc, G. Kugler, Testing of thermal fatigue resistance of tools and rolls for hot working, *Mater. Geoenviron.*, 64(2017)3, pp. 161-168.
- [4] G. Byeong-choon, L. Choong-hwan, Thermal fatigue of cast iron brake disk materials, *J. Mech. Sci. Technol.*, 26(2012)6, pp. 1719-1724.
- [5] Y. Misaka, K. Kawasaki, J. Komotori, M. Shimizu, Fatigue Strength of Ferritic Ductile Cast Iron Hardened by Super Induction Heating and Quenching, *Mater. Trans.*, 45(2004)9, pp. 2930-2935.
- [6] M. Pevec, G. Oder, I. Potrč, M. Šraml, Elevated temperature low cycle fatigue of grey cast iron used for automotive brake discs, *Eng. Fail. Anal.*, 42(2014), pp. 221-230.
- [7] H. Morihito, Features on thermal fatigue of ferrite matrix ductile cast iron, in: *Low Cycle Fatigue and Elasto-Plastic Behaviour of Materials*, 1st Edition, Elsevier Science, Amsterdam, 1998.



19th INTERNATIONAL FOUNDRYMEN CONFERENCE
Humans - Valuable Resource for Foundry Industry Development

Split, June 16th-18th, 2021

<https://ifc.simet.hr/>

**BENTONITE – ECOLOGICAL BINDING MATERIAL OF FIRST GENERATION
AND ITS USING IN FOUNDRY**

Iveta Vasková^{*}, Petra Delimanová, Martina Hrubovčáková, Marianna Bartošová

Technical University of Košice Faculty of Materials Metallurgy and Recycling, Košice, Slovakia

Invited lecture
Preliminary work

Abstract

Bentonite is an off-white montmorillonite clay formed from altered volcanic ash. It has a sheet-silicate structure and is especially notable for the way in which it absorbs and loses water and for its base-exchange properties. Sodic bentonite can absorb up to 10 times its own weight in water and can swell to 18 times its dry volume. Thus, it can be applied where its colloidal properties can be exploited. Bentonite has a wide variety of uses including foundry, animal feed, drilling mud, absorbent, industrial, and specialty uses. About 70 % of the world's known supply of Western or sodium-type bentonite occurs in the state of Wyoming (notably in the Mowry Formation), with additional significant deposits elsewhere in the Western United States. Volcanoes of the Yellowstone area of Wyoming were active for long periods in the early Cretaceous (c.100 million years) and deposited ash layers of a few centimeters up to 15 m thick into nearby shallow seas. The ash weathered with time, forming the bentonite. Early uses of bentonite in the 1800s, included lubricant for wagon wheels, sealant for log cabin roofs, and soap. Modern uses are highly variable. In foundry or metal casting, bentonite is mixed with sand to make the molds. The bentonite forms a pliable bond with the sand grains, so the mixture holds its shape well. Bentonite also absorbs excess moisture and oils. Some recent research has shown that the base-exchange properties of bentonite allow it to help remove certain toxins and ammonia. It also reduces feed flow through the intestines so that nutrient uptake is improved, indirectly aiding such factors as milk production, wool growth, and the quality and production of eggs. The aim of this paper is to explore the complex physical – chemical characteristics of bentonite of slovak provenance and to compare with non-slovak, which is considered as European highest quality standard in foundry and to compare from the point of foundry application. These characteristics of raw material have direct relationship with technological properties of bentonite sand mixtures and mainly with the quality of castings poured into these mixtures. To compare technological properties of bentonite forming mixtures with use of various clay types point of view application in foundry industry.

Keywords: *moulding mixture, opening material, inorganic binding system, clay binder*

*Corresponding author (e-mail address): iveta.vaskova@tuke.sk

INTRODUCTION

Bentonite clays, their composition structure and properties influence the properties of moulding mixtures, which influences also inner quality of castings. The quality of bentonites, their availability and price determine the performance and profitability of foundries. Even in Slovakia there is an effort to use the products of Slovak origin. The aim of presented work, which resulted from practical requirement, is to examine the properties of slovak bentonite and its suitability for usage for foundry purposes and compare them with selected bentonite, which is a high quality standard.

Bentonite is a clay foundry binder, which contains at least 75 % of montmorillonitic mineral. The rest are other aluminosilicates, mainly kaolinite, illit, glauconite, chlorite, vermiculite, silica, anatas and others [1]. Furthermore, fragments of earlier rocks occur as quartzite, sandstone, decalcified clays and volcanic glass. All mentioned minerals and rocks, which may occur in bentonite, are considered as pollutants, they negatively affect the technological properties, which depend on the presence of montmorillonite [2]. Therefore bentonites from different locations significantly differ from each other and only 30 % of world production is used for foundry purposes.

Clay binders are the most common foundry binders. They are usually contained in natural sands and are used in clean state to join washed sands and sometimes also artificial opening materials [3].

In praxis, the clay minerals are applied for their valuable properties, resulting primarily from the fine structure, significant degree of dispersion, cation exchange capacity (CEC), etc. this leads to significant technological properties such as plasticity, swelling, severity, the absorption capacity for gases, vapour, solutions, refractoriness and others [4].

MATERIALS AND METHODS

The work was focused on two types of bentonite clays, from which non-slovak bentonite was marked A, which is considered as quality standard in foundry. The second examined clay binder was bentonite of the slovak location – in the paper marked as B.

Basic characteristics of examined bentonites are given in Tab. 1.

Table 1. Basic characteristics of supplied clays

Characteristic	A	B
Status of raw material	After grinding	After grinding
Colour	Pearl - white	Eburnean
Moisture [%]	8.01	4.45
Loss of ignition - LOI [%]	10.42	8.9
Color after anealing	Yellow honey	Bloody orange

Also other physical-chemical characteristics were set:

- specific surface

- comprehensive chemical analysis
- X-ray analysis, focused on montmorillonite content
- content of active bentonite
- pH and electrical conductivity of the suspension
- differential thermal analysis (DTA, TG)

Also some pictures of structure of individual samples were taken using a microscope SEM Olympus OLS 300 LEXT and Nikon SMZ 15000.

The BET method was used to measure the size of the specific surface, which is most suitable for the measurement of powders with high specific surface area, mainly fine. It is based on the adsorption of gases on the surface of powder elements. Tab. 2 shows the measured values of specific surface of given bentonite samples.

Table 2. Surface of powder of bentonites A, B

Sample of bentonit	Surface of powder [m ² /g]
A	50.2162
B	46.6077

According to the BET method there are no big differences in the size of specific surfaces, slightly higher specific surface was measured in bentonite A. The higher specific surface is probably related to the higher quality of connective capabilities of bentonite that affect the technological properties of bentonite moulding mixtures.

With chemical analysis we do not determine mineralogical composition of clays or their technological properties, but it is valuable complement to the evaluation of clay binders. The object of attention are so called harmful oxides, mainly alkali oxides (Na₂O and K₂O) and alkaline earth metals (CaO and MgO). This alkaline oxides react at higher temperatures with silica to form silicate flux, thus reduce refractoriness.

Tab. 3 shows the results of chemical analysis of bentonite A and B. From comparison of results is seen the higher content of SiO₂ and lower content of Al₂O₃ in bentonite sample B. The consequence of this is significant difference in the ratio of SiO₂ to Al₂O₃, namely A = 3.23 and sample B = 4.85. The different value probably indicates a different montmorillonite ratio to other minerals in bentonite. Based on the higher ratio of SiO₂ to Al₂O₃ in bentonite B, we can conclude that it contains more impurities containing SiO₂. From genetic point of view this means, the higher is this ratio, the more SiO₂ is in bentonite and given montmorillonite was created during the conversion of acidic vulcanoclastics rocks. All slovak deposits were created by weathering of acidic vulcanoclastics, unlike for example the locations in northern Czech republic, which were created by weathering of basic rocks.

Table 3. Chemical analysis of bentonites A, B

Sample	SiO ₂	Fe total	CaO	MgO	Fe ₂ O ₃	Al ₂ O ₃	MnO	FeO	Na ₂ O	K ₂ O	SiO ₂ / Al ₂ O ₃
	[%]										
A	59.75	3.90	2.31	6.09	4.08	18.48	0.021	0.431	2.00	1.66	3.23
B	65.92	2.79	2.29	7.15	2.08	13.58	0.085	0.287	1.43	1.66	4.85

Practically, the only objective qualitative and quantitative determination of clay minerals is the X-ray analysis. Diffraction analysis was done and the workplace of Stat Geological Survey of Dionyz Štur (ŠGÚDŠ), Regional Center – Department of Applied Technology of minerals (ATNS), in Košice [5].

Qualitative mineralogical analysis was made from the grist of X-ray samples using diffraction analysis on the device Dron – UM 1 under the following conditions: radiation CuK α , Ni – filter, accelerating voltage 30 kV, current 20 mA, time constant T – 2, aperture 2 – 2 and 2 – 0.5, the shift arm goniometer 2 °/minute. Identification of present mineral phases of X-ray results was done according to conventional ASTM tables using a special program computer technique [5].

Graphical record of X-ray analysis of sample A is shown on Fig. 1 and the record of X-ray analysis of sample B is shown on Fig. 2.

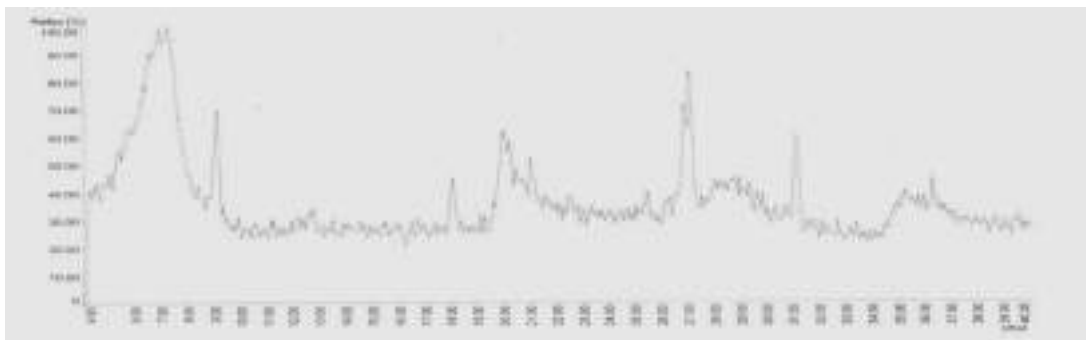


Figure 1. RTG analysis - sample A

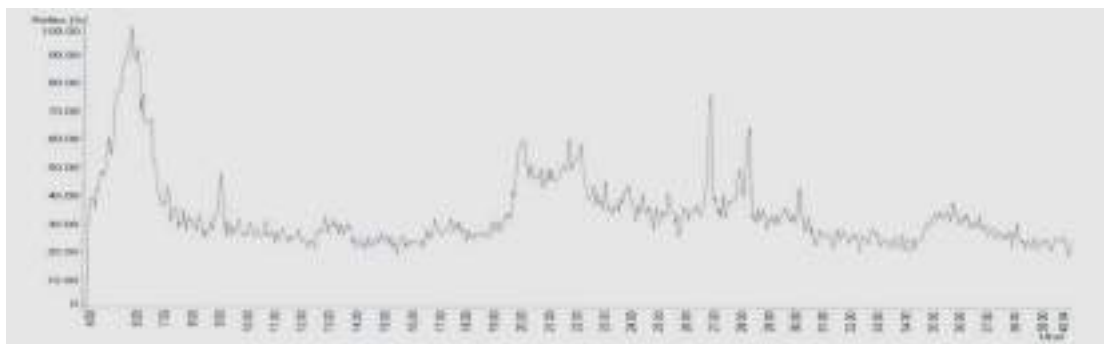


Figure 2. RTG analysis – sample B

With research method – X-ray diffraction analysis has been found the following qualitative mineral composition of the tested samples:

Sample A:

Major minerals (> 15 %): smectite

Secondary minerals (3 to 15%): sericite, plagioclase, quartz, dolomite

Sample B:

Major minerals (> 15 %): smectite, amorphous phase

Secondary minerals (3 to 15 %): cristobalit, plagioclase, quartz

On the basis of ion exchange were achieved the following results:

Sample A: total exchange VKA (mol/kg) – 0.69. The exchange of different ions (mekv/100g): Na – 15.85; Mg – 22.98; Ca – 11.21; K – 1.99. With conversion was determined the content of smectite (montmorillonite) to 75.8 %. By exchange of individual ions it can be assumed that it is natrified calcium – magnesium montmorillonite. Proportional representation of the ion is 82.2 %. This fact highlights the value of basic basal reflex $d = 1.22$ to 1.28 nm determined by X-ray deffraction analysis.

Sample B: total exchange VKA (mol/kg) – 0.35. The exchange of different ions (mekv/100g): Na – 53.3; Mg – 5.88; Ca – 5.00; K – 0.66. With conversion was determined the content of smectite (montmorillonite) to 38.5 %. By exchange of individual ions it can be assumed that it is less natrified calcium – magnesium montmorillonite. Proportional representation of the ions Ca + Mg is 81.3 %. The value of basic basal reflex is $d = 1.47$ to 1.54 nm determined by X-ray diffraction analysis.

The difference in the montmorillonite content is significant, in sample A is nearly twice the value compared to sample B – tab. 4. Higher content of montmorillonite points to higher ability to swelling of binder, resulting in better jacketing of binder at grains of opening material and more technology and foundry characteristics.

Table 4. Montmorillonite content and a adsorption MM in samples A, B

Sample	Montmorillonite content [%]	Adsorption MM [mg/g]
A	75.8	325
B	38.5	210

For evaluation of the active bentonite content (and bentonite in uniform bentonite mixtures) the methylene blue adsorption method (MM) is used. Although the value of adsorption of MM the picture of montmorillonite content in bentonite and moulding compounds, this value cannot be used for predicting the foundry properties of montmorillonite. Foundry properties are determined by interaction of water molecules with the surface of the ground planes and exchangeable cations, as well as of the montmorillonite structure.

MM adsorption reaches higher levels in the bentonite sample A, which corresponds with the observed higher content of montmorillonite with method of X-ray analysis.

Microscopic analysis of clay minerals and other components of clays is very difficult and deadlocked by the high fineness of elements and platelet composition, where between two silicate tetrahedron is gibbsit octahedron. As part of the grid, there is free and grid water. The main component of bentonite A (Fig. 3) is montmorillonite, forming aggregates, well

distributed in the rock, the space between aggregates is filled with amorphous matter. Also appears the weak admixture of organics and probably feldspars in accesoric ammount.

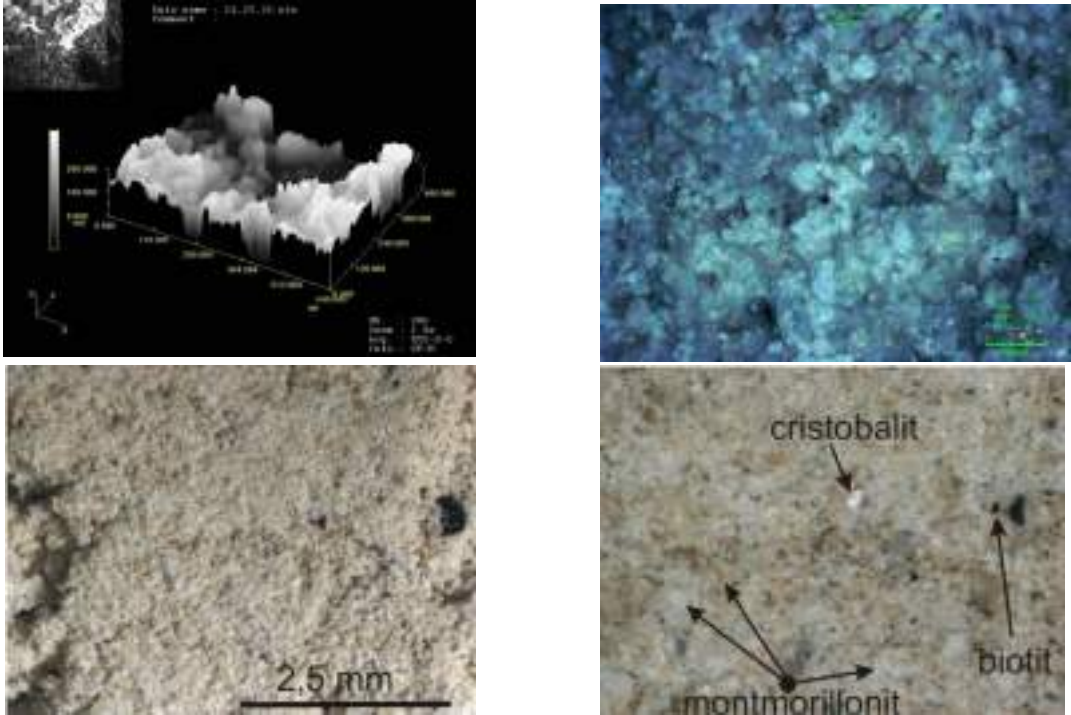


Figure 3. Micrographs of bentonite „A“

In bentonite B (Fig. 4), the montmorillonite is flaky, forming aggregates, the space between aggregates is filled with amorphous matter with very small impurities of Fe (limonite, hematite), quartz is also present and α cristobalit (about 20 volume %). Furthermore, there is mica – biotite (bigger dark grains, it also occurs baueritized , small dark matter is organics and the lightest unit are feldspars, probably part of the grains is already caolitized).

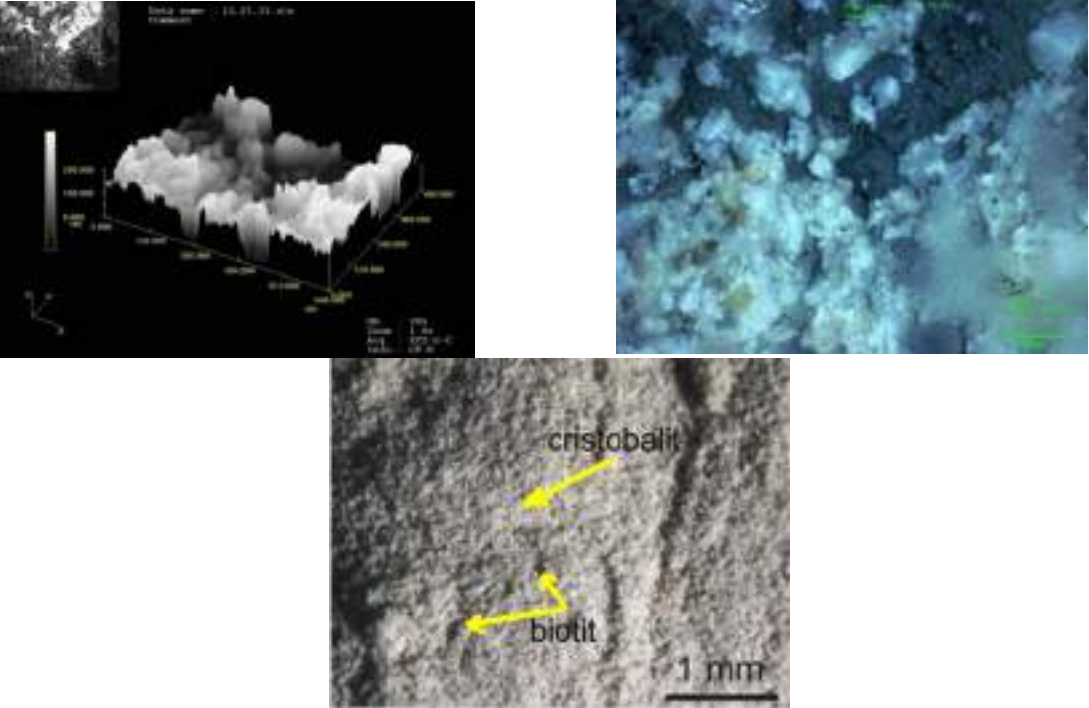


Figure 4. Micrograph of bentonite „B“

Also the thermal analysis of the raw samples was carried out, even when annealed to 550 °C. In bentonite A, the annealing to 550 °C resulted mainly in the total weight loss of TG. This shows, that the temperature is low for a loss of total dehydroxylation. A similar fact has also reflected in the bentonite of slovak provenience. At the temperature 540 °C – 550 °C occurs mild dehydroxylation, almost no loss and next endotherm at 680 – 690 °C is probably caused by decomposition of carbonates, especially MgCO₃.

RESULTS AND DISCUSSION

While the previous tests were realized on pure binder clays A and B, the properties of moulding mixtures were tested on moulding mixtures. The aim of the tests was to compare the basic properties of bentonite mixtures with both types of bentonite, two binders were assessed in a raw state – both in terms of thermostability, annealed at three temperatures – 350, 450 and 550 °C / 1 hour.

For preparation of investigated bentonite moulding mixtures was used the classical laboratory paddle mixer MK 00 (Poland). Investigated moulding mixtures were prepared with the same composition and mixed for 8 minutes:

100 weight % of quartz opening material Š32ŠH, d 50 0.35 mm

8 weight % of bentonite binder – in original and annealed state

x weight % of water – to achieve compactibility 46 – 48 %

For all mixtures were determined, except moisture and compactibility, tensile strength of the raw – the severity, the strength of the graft, tenacity blends based on the ratio of graft strength and compressive strength, tensile condensing zone, breathability and temperature effect of graded exposure to temperature on the properties. All results listed in Tab. 5 are obtained from at least 5 measurements.

Table 5. Measuring average data of bentonite mixtures technological characteristics

Sample	Green strength [kPa]	Shear strength [kPa]	Shear/compressive strength ratio	Permeability [j.p.SI]	Condensation zone strength [kPa]
A	130	33	0.25	73.5	0.52
B	96	27	0.28	71.8	0.38
Difference	- 34	- 6	+ 0.03	- 1.7	- 0.14
%	- 26	- 18	+ 0.12	- 2.3	- 27

Determination of thermal stability of bentonites is important in terms of knowledge of its connective abilities. Part of the three-layer structure of bentonite is molecule (free) water, and mesh (in the form of OH-groups) as part of the crystal grid. Free water is removed at 100 °C, the process is perfectly reversible. At higher temperatures, approximately 400 to 600 °C, tightly bound water is removing, bentonite is irreversibly damaged, is no longer able to bind

water and the degradation occurs. This dehydroxylation temperature varies, depending on the material deposit and determines the thermostability of bentonites.

In order to find and compare the thermal stability of the bentonites, different bentonites samples were annealed at three temperatures graduated after one hour. Comparison of thermal stability of both bentonites covered in the evaluation of technological properties of bentonite mixtures, annealed at temperatures of 350 °C, 450 °C and 550 °C for one hour.

Dependences of the strength of the pressure at raw and strength of the graft on temperature exposure bentonites at different temperatures for both bentonites are shown in Fig. 5.

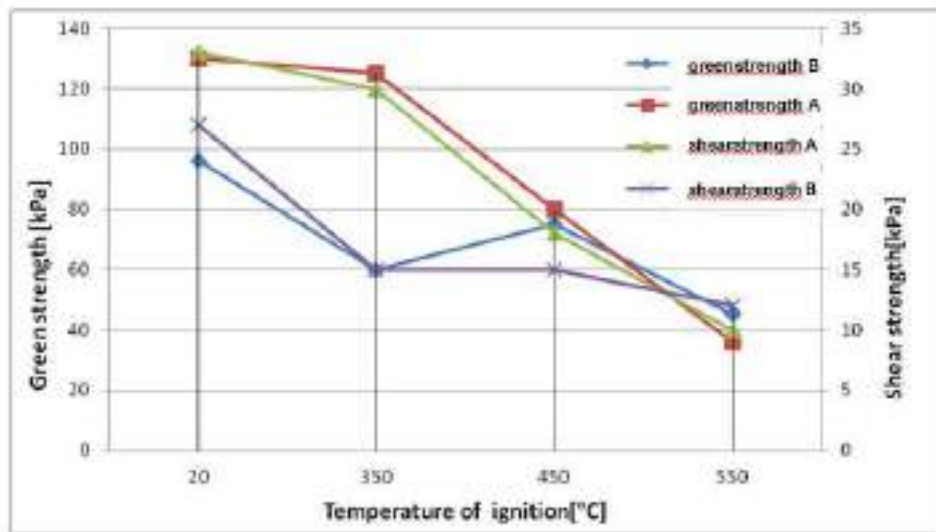


Figure 5. Influence of thermal stability on strength properties of bentonite moulding mixtures

Test of strength in the condensing zone belongs to the most sensitive test for evaluation of bentonite mixtures. In Fig. 6 are given dependences of the strength in condensing zone on the degree of degradation of bentonite after exposure to heat. Generally, a decrease in the strength of the condensation zone in mixtures signals for example imperfect mixing, decrease of moisture, tearing forms during dismantling or higher content of core sand in the mixture. The result is an increased tendency to development of drop send holes and expansion scabs.

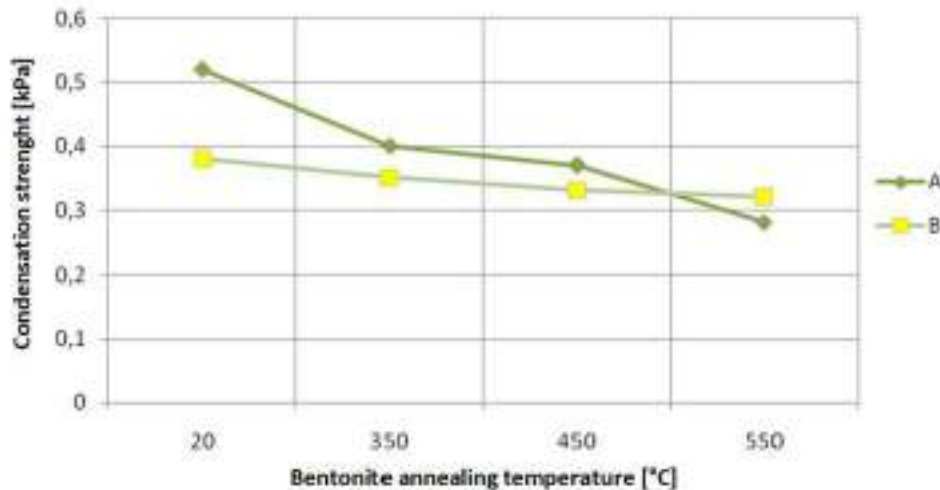


Figure 6. Influence of degradation degree of bentonite after annealing exposure in condensation zone of water

As shown in Fig. 6, to the annealing temperature of 450 °C a mixture of bentonite A has higher values, but when annealed at the temperature 550 °C per hour, bentonite B begins to prevail. This confirms the higher thermal stability of the Slovak bentonite.

CONCLUSIONS

Appropriate physical and chemical characteristics of clay materials are a prerequisite for usage of raw materials in the foundry industry and affect almost all technological characteristics of bentonite mixtures and hence the quality, especially the surface of castings, cast into these forms. These properties can not be affected, are the genesis and the deposit place of material. Measured results, mainly almost double content of montmorillonite in bentonite, indicates a better binding ability of bentonite B and the associated greater strength properties of the bentonite mixture, which is reflected mainly in the economic field.

By evaluation of tests was mainly identified:

- High decrease of severity of mixtures - more for bentonite A (by 72 %) compared with a mixture with bentonite B (by 52 %) and conversely, the strength of the graft decreased significantly in the mixture with bentonite B (by 56 %), also decrease of breathability with bentonite B (by 56 %), compared with A (by 34 %).
- The decrease of strength in the condensation zone of water was more pronounced in mixture with bentonite A (by 46 %) than with bentonite B (by 18 %), at the whole temperature range.
- The resulting severity at the temperature 550 °C is even in a mixture of bentonite A lower than with bentonite B, namely A = 36 kPa and B = 45 kPa (by 25 %).
- Based on the results is the effect of thermal exposure on the properties of moulding mixtures stronger in bentonite A, and this means that bentonite B is thermally stable.

Acknowledgements

„This work was supported by the Slovak Research and Development agency under the contract no. VEGA 1/0498/11“.

REFERENCES

- [1] J. Dehn, S. R. McNutt, The Encyklopedia of Volcanoes, Second Edition, 2015.
- [2] B. Čížek a kol.: Mineralogical Composition And Distribution Of Si, Al, Fe, Mg, and Ca, In The Fine Fractions Of Some Czech And Slovak Bentonites. Geologica carpathica clays, č.1, Slovak Academy of Sciences, Bratislava, 1992.
- [3] P. Jelínek, Bentonitové jíly, struktúra, vlastnosti a použitie jako slévarenská pojiva, 7. Prezentace bentonitových a šamotových výrobků pro slévarenství, Svinčice u Mostů, 2003.
- [4] H. Mäsiar, J. Kasala, N. Kaloforov, Effect of Polyethylene Oxide on Properties of Bentonite Foundry Mixtures, Archives of Foundry Engineering, ISSN 1897-3310, 1(2007), pp. 69-72.
- [5] R. Pastirčák, D. Bolibruchová, Teória zlievania, EDIS, Žilina, 2015.
- [6] J. Derco, RTG difrakčné analýzy vzoriek bentonitov, Štátny geologický ústav Dionýza Štúra, Košice, 2008.
- [7] Z. Klika a kol., Composition, Structure and luminescence of Montmorillonites saturated with Different Aggregates of Methylene Blue, Journal of colloid and interface science, (2007)311.
- [8] I. Vasková, Habilitačná práca, Košice, 2009.



19th INTERNATIONAL FOUNDRYMEN CONFERENCE

Humans - Valuable Resource for Foundry Industry Development

Split, June 16th-18th, 2021

<https://ifc.simet.hr/>

DEMAND, SUPPLY, ENERGY CONSUMPTION AND SUSTAINABILITY OF PRIMARY AND SECONDARY COPPER PRODUCTION

Irena Žmak^{1*}, Ida Mujkić²

¹ University of Zagreb Faculty of Mechanical Engineering and Naval Architecture, Zagreb, Croatia

² Gid Media, Zagreb, Croatia

Invited lecture

Subject review

Abstract

The paper presents a brief overview of the history of copper as the first known metal in human history. Principal properties and chemical compositions of the modern-day copper alloys are described. The methods of primary (i.e. from the ore) and secondary (i.e. from waste) production of copper are discussed. Some countries mine a lot of copper, while the others mostly process the copper ore into copper materials. The growth in value as well as in weight of primary and secondary copper in the last 20 years is presented and analyzed. Several predictive models for future copper production and associated energy consumption have been presented and discussed: for the period up to year 2050 and up to 2100. Current data on end-of-life for copper in different parts of the world and a global average were given, based on which a sustainability level of copper production from the ore in 200, 500, and 1000 years was presented. For the same time periods, the needed global copper resources were estimated based on higher end-of-life recycling rates. Sustainable Development Goals applicable to the production of copper and the use of copper in modern technology is discussed. The Goal that is currently in focus of the world leaders' is Decent Work and Economic Growth, which is also highly applicable to the extractive industry of copper.

Keywords: *copper, production, recycling, sustainability*

*Corresponding author (e-mail address): irena.zmak@fsb.hr

INTRODUCTION

Common public knowledge regards the Copper Age as a distinct period in history when copper was the predominating metal in skillful production of tools weapons. The start of this period has very much varied in the last two centuries, depending on the current findings. Nowadays it is regarded that the first extractive metallurgy began around 5000 BC, when members of the Vinča culture inhabited what is now the town on Belovode in modern day Republic of Serbia [1]. The very concept of the timely determined Copper Age has been

much discussed lately since copper metallurgy was not used in chronologically same periods across Europe. Modern concepts prefer to see copper, and later other metals, just as a technological development stage, which started when copper was smelted, i.e. not strictly determined by a socio-cultural development stage [2].

Around 3000 BS alloying elements started to being added to copper, making yet new materials known as bronze. A well-preserved arsenical copper axe was found besides the 5000 year old mummified body of a man in the Alps, the famous Ötzi, with high concentrations of copper and arsenic, indicating that he himself was a coppersmith [3], [4]. Ancient history was also marked by the discovery of cassiterite, a mineral containing 78.6% tin (Sn), which had to be smelted from the ore, and subsequently added to liquid copper to form the bronze [5]. This invention further enabled the spreading of the use of copper on different civilization as the advanced copper-based weapons meant tribe, or later on civilization, superiority. Contrary to copper resources which were reasonably widespread throughout Europe, tin sources were much more restricted. Similarly, gold resources in Europe were limited to north-western Europe, the Carpathian Mountains, eastern part of Germany and Balkans, Figure 1 [6]. Copper, tin, and gold was later used in ancient Egypt and near East, but it was not superior to Europe at the time. Contrary to favorable European standings of coppersmiths, they were denigrated in ancient Egypt, and described as: “with fingers like a crocodile and a smell like fish excrement” [6]. In the Metal Age, the use of metals brought an added value to its owners, since, contrary to pottery and stone artifacts, they could be remelted when broken or worn.



Figure 1. European sources of copper, tin and gold [6]

The requests for different copper alloys have increased continuously as the industrialization advanced. Different copper alloys were developed with different mechanical properties and chemical resistance as well as with distinct metallurgical properties, Figure 2. Nowadays, different copper alloys are used in different engineering fields: transportation, automotive, IT, power generation and distribution, military, etc. [7].

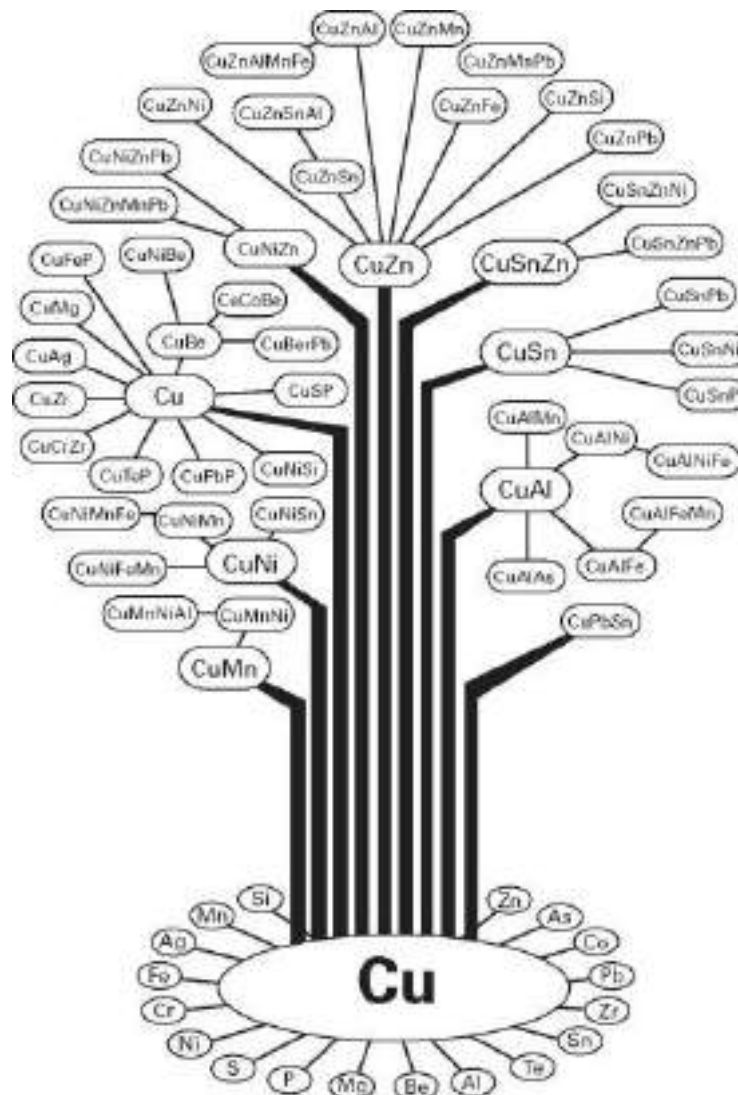


Figure 2. Classification of copper alloys [7]

PRIMARY AND SECONDARY COPPER PRODUCTION

Production of metals involves these main activities: extraction, upgrade, and processing, as shown in Figure 3. All three activities may be applied to primary and secondary metal production. Extraction in primary metal production means that the raw material feedstock is produced from mined virgin mineral ores. In secondary metal production, the term extraction refers to collecting metal waste and scrap. The upgrade activity includes the transformation of these materials into intermediate products: for primary metal production it involves initial ore purification (beneficiation), while for the secondary metal it includes processes like shredding and physical methods of separation. Processing activities include production of finished metal products, either for primary as well as for secondary metals by using different processes of smelting, refining, and re-melting. Oftentimes, these activities are executed at very different locations and/or countries/continents, which may consequently add high transport distance. Primary metal production includes continuous separation and removal of commercially worthless minerals from virgin mineral ore, a

mining process usually called gangue. Gangue processes differ for different metals as well as for different ores used to produce the same metals, e.g. oxidized ores need different processing than sulphide ores of the same element. When copper is produced from sulphide ores, typical processes involved are presented in Figure 4 [8].

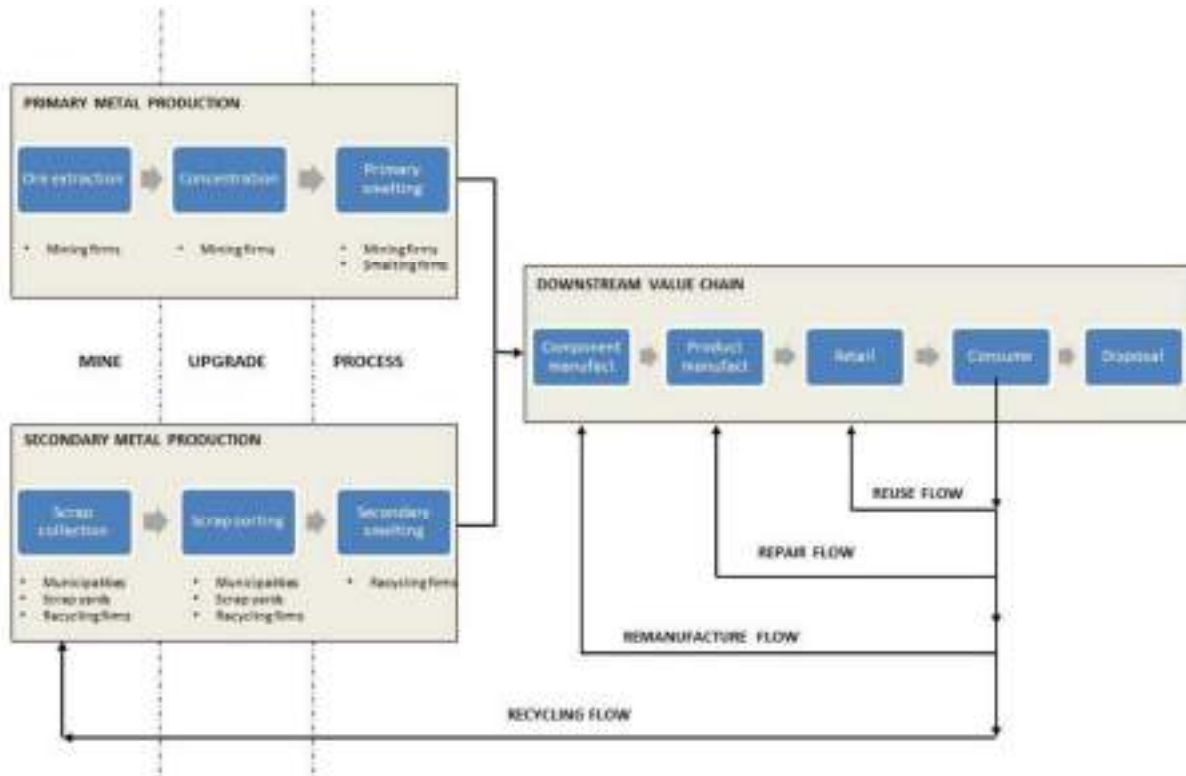


Figure 3. The primary and secondary metal supply chains [8]

During the primary production of metals, the metal component concentration increases continuously along the process of removal of non-metallic materials. Each of these activities inevitably produces wastes, which may have significant environmental impact. Primary metal production results in rock overburden after mining, upgrading produces tailings and processing gives smelting residues. In secondary metal production only the upgrading stage produces recycling residues.

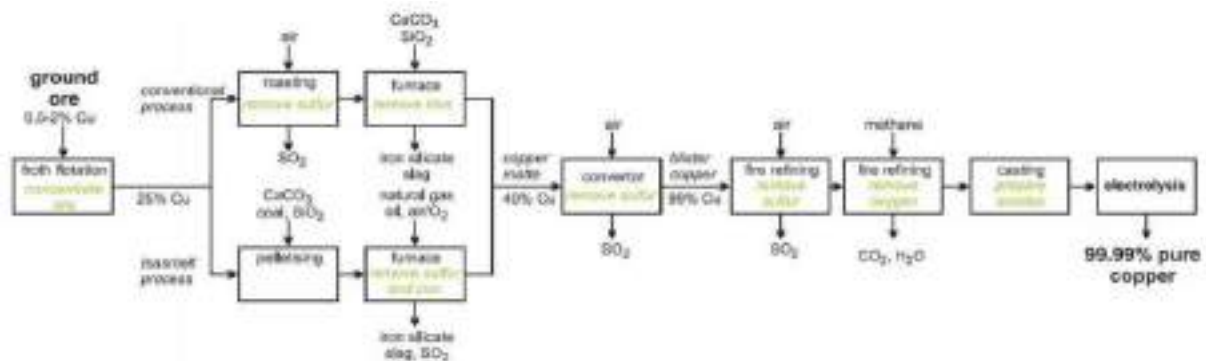


Figure 4. Primary production process for copper in sulphide ore [8]

Some countries are more oriented towards upstream or downstream in the supply chain of different metals, Figure 5. Upstream processes include processes in which materials flow into the organization, while downstream refers to processes in which materials in the form of products are transferred from the product manufacturer to the customers. For example, Cina accounts for 9% of world copper ore mining, while at the same time China produces 25% of world primary copper.

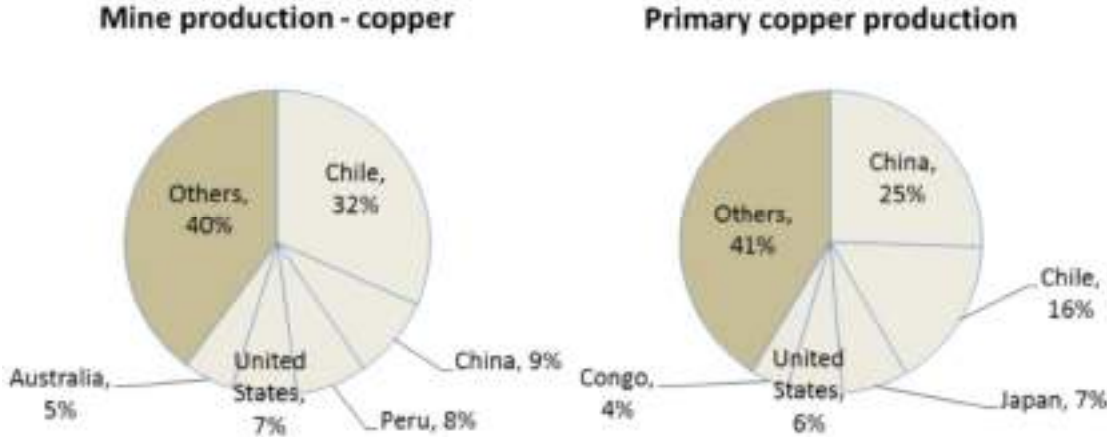


Figure 5. Largest upstream (left) and downstream (right) of copper producers [8]

Over the last two decades the use of upstream primary materials has greatly increased, while at the same time the use of secondary metals has not changed much, considering the weight, Figure 6. The amounts of all primary metals used in 2000 has increased from around 550 Mt to 1700 Mt in 2014, while the secondary metal exports have risen from 60 to 120 Mt. The fraction of secondary metals in current metal supply is visibly decreasing because of the rapid growth of consumption of primary metals in the production of different products.

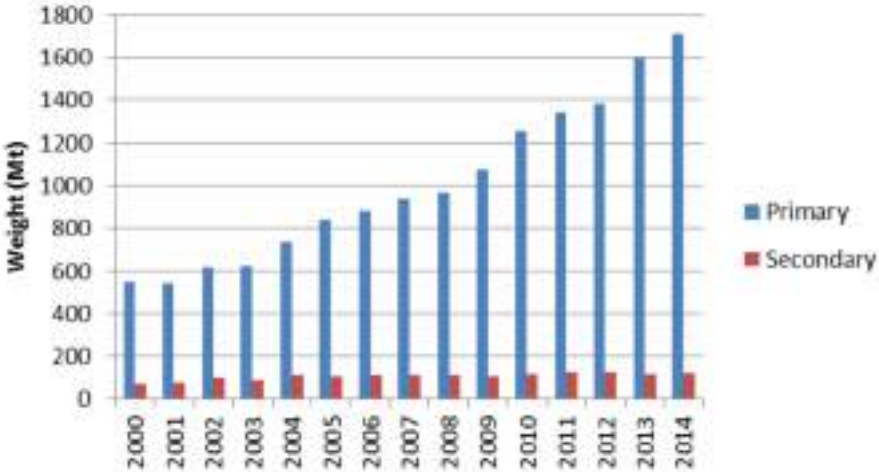


Figure 6. The growth of upstream primary and secondary material exports by weight [8]

Consequently, the export value of primary metals has increased a lot more in the last 20 years than for secondary metals, Figure 7. The nominal value of primary metals exported has increased almost ten times from 2000 to 2011, while the value of exported secondary metals

increased by 5 times. Comparing Figure 6 and Figure 7, it may be concluded that the relative value of secondary metals has significantly increased over the last two decades.

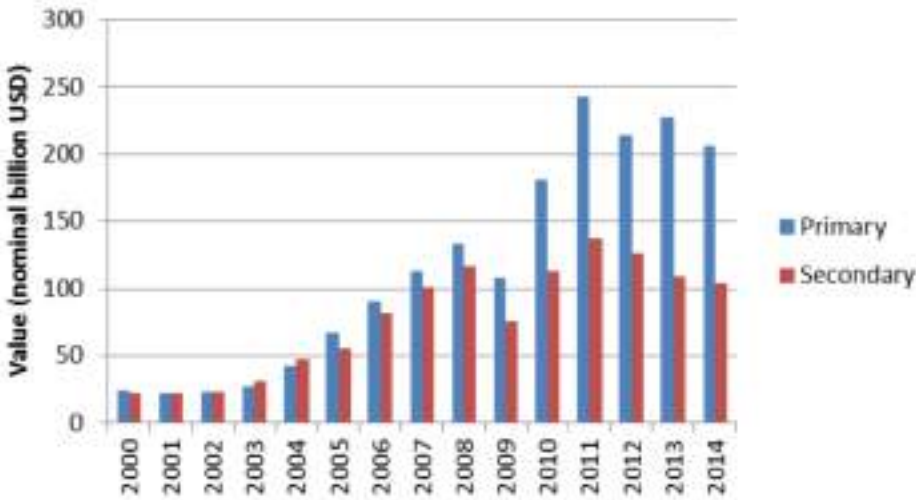


Figure 7. The growth of upstream primary and secondary material exports by nominal value [8]

COPPER DEMAND, SUPPLY AND ENERGY CONSUMPTION FUTURE SCENARIOS

Different scenarios have been developed during the last decades for all exploited resources. Although scenarios may not necessarily present completely accurate calculations, these data are often regarded as important both to the investors, as well as governments. The change in demand and supply of metals depends on several factors, but a general outlook based on current state of the art of industrialized world and population trends, can be assumed. One study developed four scenarios, based on the most important factors: market (M), policy (P), security (S), and equitability (E). Figure 8 shows an increase in predicted total energy needed for the production of copper for 4 scenarios for up to 2050, cumulatively for pyro- and hydrometallurgical processes, which shown more in detail in [9]. Dashed lines show the possible modification of data if improvements in energy efficiency are included in the models.

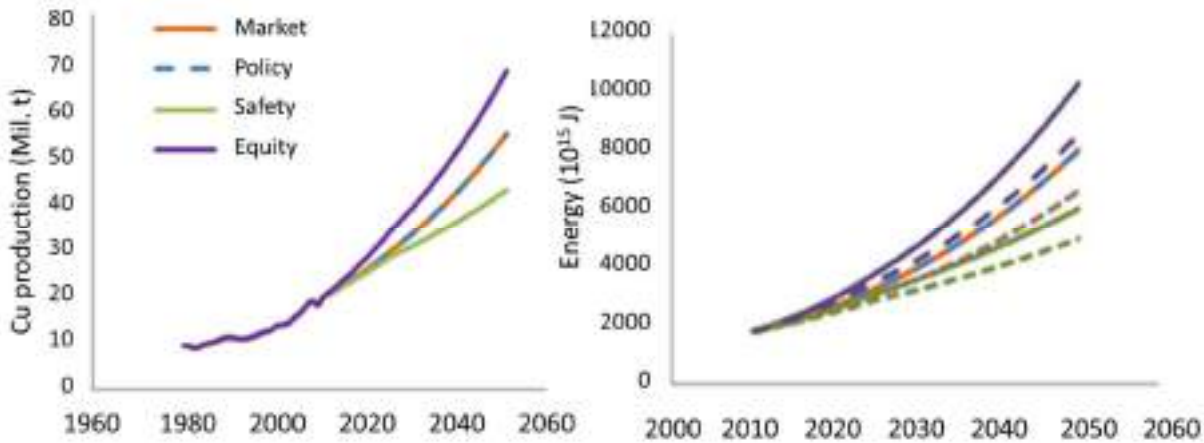


Figure 8. Copper production and required energy up to 2050 vs. model priorities [9]

It is expected that the copper cumulative demand will exceed the reserves according to most scenarios by 2050. Also, it is expected that copper producing countries will not sustain their copper production by 2050, as the required energy for copper production will make between 1 and 2.4 % of all energy demands. The production of other metals which from copper ores is expected to decrease as well if the extraction processes are not improved in their efficiencies [9].

Future scenarios predict that the average copper ore grade will decrease in the following decades based on models of cumulative production, Figure 9. The energy for the primary copper production accounts to 60 % to 90 % of the total energy needed for processing copper ore to copper products. One estimation is that copper mining takes 18%, concentrating 42%, smelting 27 %, refining 7 %, and tailings dams 3 % [9]. In general, the total amount of future energy needed for to primary copper production depends on ore grade, energy efficiency, and the used process, where the later two need to improve significantly in near future to satisfy the growing demands of metal in modern technological societies.

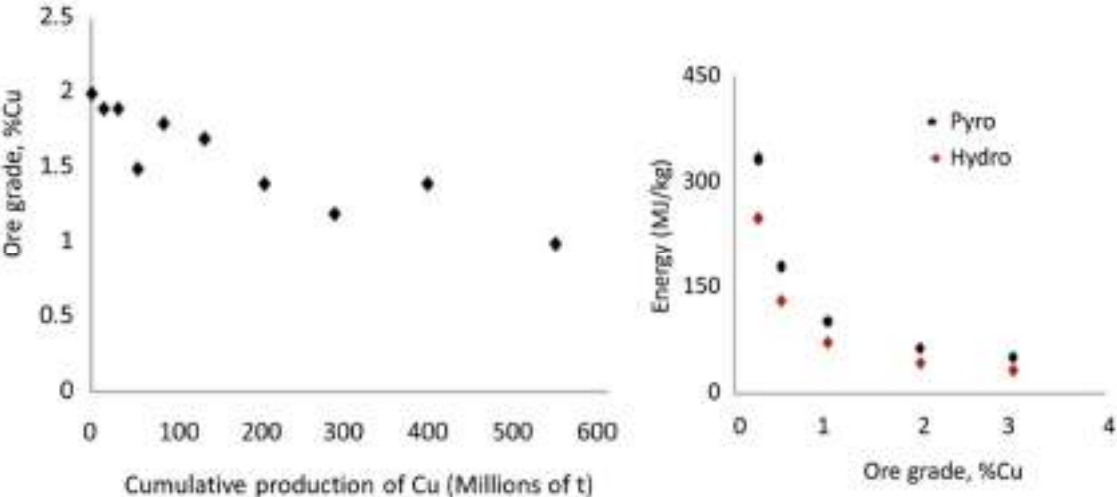


Figure 9. Anticipated decrease of ore grade vs. cumulative production (left). Energy vs. ore grade for pyro- and hydrometallurgy [9]

One other projection study aims to the year 2100 by using the stock dynamics method. There, a strong copper demand growth is expected, as the scenarios included a high share of renewable energy usage. New renewable energy systems are expected to require high amounts of copper, both in the electricity production as well as in the green transport sector, Figure 10 [10].

In all studied scenarios the exhaustion of currently identified copper resources is expected, because of the projected future copper demand increase [10]. As discussed previously, the increasing copper mining influxes the decrease in ore grades. This inevitably leads to increasing the energy use, therefore increasing the environmental impact. Therefore, a transition towards a significantly more circular economy is an imperative, where secondary copper would be much greatly used in the production.

Several other predictive models for global metal demand were calculated for different metals, and aggregated predictions for 2030, 2050, and 2100 were analyzed, Figure 11, where N indicates the total number of studied data points [11].

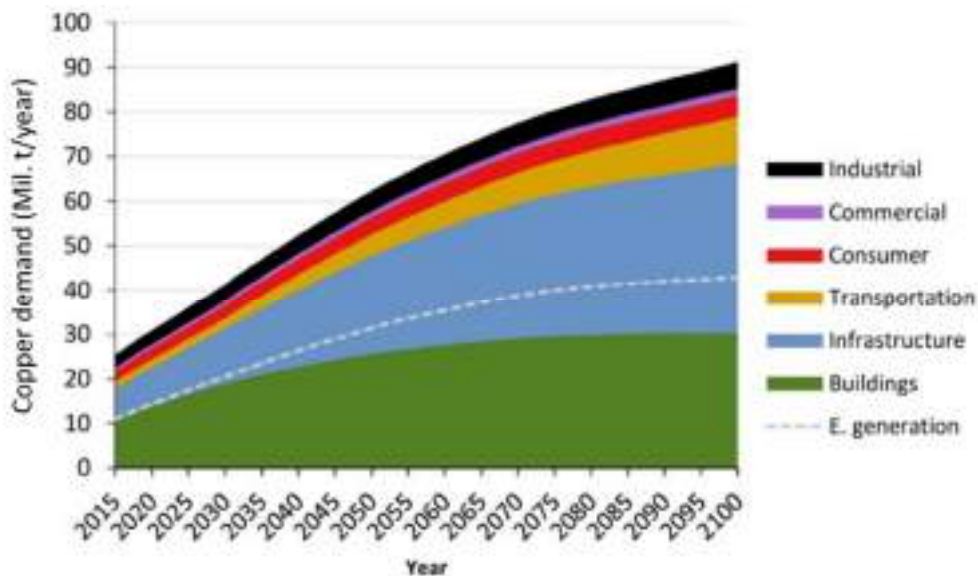


Figure 10. An outlook on the global copper demand up to year 2100 [10]

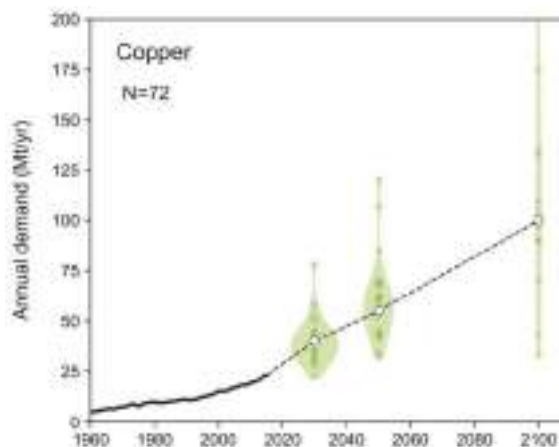


Figure 11. Different predictive models for global copper demand: in 2030, 2050, and 2100. N indicates the number of data points [11]

COPPER SUSTAINABILITY LEVELS FOR END OF LIFE RECYCLING RATES

Estimated copper recycling rates differ greatly across the globe. The recycling rate of copper from end-of-life products in western European countries is approximately between 48 % and 65 %. Around 80 % of copper from end-of-life products is collected for recycling. From this waste around 80 % is recycled to new copper, while the rest of it ends in aluminum or iron recycling processes (about one third) and in landfills or incinerators (two thirds). The Australian end-of-life recycling rate is approximated at 56 % and north American at 45 %. A global end-of-life recycling rate is assumed to be 45 %, which means that more than 50 % of

produced copper ends in landfills or in incinerators. An indicative representation of current end-of-life options of copper containing products on the global level is presented in Figure 12 [12].

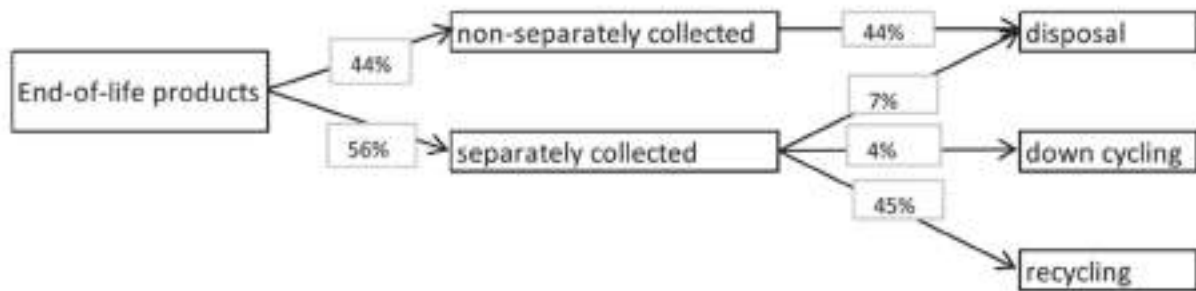


Figure 12. End-of-life of copper containing products on a global level [12]

An estimation based on US Geological Survey from 2018 results in about 10 Gt of global copper resources in the upper three kilometers of the continental part of the planet. Sustainability ambition level is defined as a period of guaranteed, sufficient, and affordable supply of resources. For a sustainability ambition level of 1000 years, required calculated end-of-life recycling rate of copper would need to be 94%, 90% and 56% if estimated global resources were 6 Gt, 10 Gt and 40 Gt, respectively. A maximum copper recycling rate for end-of-life products which may be realistic is up to 85%. For this recycling rate and a sustainability level of 1000 years, 14 Gt of copper resources would be needed, Table 1. with the current recycling copper rate of only 45%, the approximated current copper global resources of 10 Gt would suffice for the next 200 years, Table 1 [12].

Table 1. Minimum amount of needed copper resources (Gt) [12]

Sustainability level (years)	End-of-life recycling rate (%)			
	45	65	75	85
200	10	6	5	3
500	25	16	12	7
1000	49	32	23	14

SUSTAINABLE DEVELOPMENT GOALS RELATED TO COPPER INDUSTRY

In 2015 United Nations adopted the “Transforming our world: the 2030 Agenda for Sustainable Development”, with implementation period up to 2030. The Agenda is a plan of action for people, planet and prosperity [13]. The Agenda is aimed at achieving a balanced and a comprehensive development for improving different aspects of human life on Earth. It consists of 17 Sustainable Development Goals (SDGs), and adjacent 169 Targets. SDGs cover a wide range of challenges and the interrelated economic, social, and environmental aspects of sustainable development.

The goals that are most strongly connected to a sustainable production of primary copper from the ore, as well as a sustainable copper recycling process, are Affordable and Clean Energy (No. 7), Sustainable Cities and Communities (No. 11), Responsible Consumption and

Production (No. 12) and Climate Action (No. 13). Climate action goals are aimed at reducing the carbon-footprint of all the processed which are involved in copper manufacturing industry. Moreover, the responsible consumption and proper purification of water used in different forms of extraction in copper industries is related to Goal No. 6: Clean Water and Sanitation.

Copper is extensively used in new renewable energy production and distribution systems (Goal No. 7), while the increasing manufacture of electrical vehicles contributes to Goal 11: Sustainable Cities and Communities as well as Goal 9: Industry, Innovation and Infrastructure.

In May 2021 the United Nations' Goal of the Month was Goal No. 8: Decent Work and Economic Growth, which is also very much connected to copper extractive industries. On 10 May 2021 António Guterres, UN Secretary-General will hold a roundtable on extractive industries and its potential for improving industrial growth, while supporting sustainable development, and with concern on reducing the developing countries poverty, Figure 13 [14].



Figure 13. United Nations' Sustainable Development Goal of the month, May 2021

CONCLUSIONS

Copper is the oldest metal used by men. Its unique properties have allowed a continuous use of copper through history. Modern day life relies on copper mostly for its excellent electrical conductivity. Good mechanical properties, corrosion resistance, castability and malleability make copper and many of its alloys today a widely used material in many engineering and scientific fields. Due their good recyclability, copper-based materials are environmentally friendly. An improved system of collection of waste copper is needed in order not to endanger the natural resources of copper. By increasing and improving the recycling loops of copper, carbon footprint of primary copper production is reduced, mineral resources are saved, water consumption is lowered, and landscape is preserved. The problem of a more sustainable planet to live on is tackled by United Nations' Sustainable Development Goals, of whom many are strongly connected to the production of both primary and secondary copper. Global leaders from governments, industry, and national organizations work

together through implementation of the Goals on a more sustainable growth and development.

REFERENCES

- [1] M. Radivojevic, J. Kuzmanovic-Cvetkovic, Copper minerals and archaeometallurgical materials from the Vinca culture sites of Belovode and Plocnik: Overview of the evidence and new data, *Starinar*, (2014)64, pp. 7-30.
- [2] M. Pearce, The “Copper Age”- A History of the Concept, *Journal of World Prehistory*, 32(2019)3, pp. 229-250.
- [3] C. Brahic, How Ötzi came to life, *New Scientist*, 239(2018)3190, p. 43.
- [4] D. Festi, D. Brandner, M. Grabner, W. Knierzinger, H. Reschreiter, and K. Kowarik, 3500 years of environmental sustainability in the large-scale alpine mining district of Hallstatt, Austria, *Journal of Archaeological Science: Reports*, 35(2021), p. 102670.
- [5] S. K. Haldar, Minerals and rocks, in *Introduction to Mineralogy and Petrology*, (2020), 2020, pp. 1-51.
- [6] J. M. Coles and A. F. Harding, Eds., *The Bronze Age in Europe: An Introduction to the Prehistory of Europe c.2000-700 B.C.*, Routledge, Reprint, 1.(2016). Abingdon, Oxfordshire, United Kingdom: Routledge, 2016.
- [7] A. Klassert and L. Tikana, Copper and copper-nickel alloys - an overview, *Corrosion behaviour and protection of copper and aluminium alloys in seawater*, (2007), pp. 47-61.
- [8] P. Börkey and A. Mccarthy, Working party on resource productivity and waste: Mapping support for primary and secondary metal production, Accessible on Internet: [https://www.oecd.org/officialdocuments/publicdisplaydocumentpdf/?cote=ENV/EPOC/WPRPW\(2016\)2/FINAL&docLanguage=En](https://www.oecd.org/officialdocuments/publicdisplaydocumentpdf/?cote=ENV/EPOC/WPRPW(2016)2/FINAL&docLanguage=En), (09.05.2021.)
- [9] A. Elshkaki, T. E. Graedel, L. Ciacci, and B. Reck, Copper demand, supply, and associated energy use to 2050, *Global Environmental Change*, 39(2016), pp. 305-315.
- [10] B. W. Schipper, H. C. Lin, M. A. Meloni, K. Wansleben, R. Heijungs, and E. van der Voet, Estimating global copper demand until 2100 with regression and stock dynamics, *Resources, Conservation and Recycling*, 132(2018)November 2017, pp. 28-36.
- [11] T. Watari, K. Nansai, and K. Nakajima, Major metals demand, supply, and environmental impacts to 2100: A critical review, *Resources, Conservation and Recycling*, 164(2021)June 2020, pp. 105-107.
- [12] M. L. C. M. Henckens and E. Worrell, Reviewing the availability of copper and nickel for future generations. The balance between production growth, sustainability and recycling rates, *Journal of Cleaner Production*, 264(2020), pp. 121-460.
- [13] *Transforming our world: the 2030 Agenda for Sustainable Development*, United Nations General Assembly, 2015.
- [14] Goal of the Month Editorial, May 2021: Decent work and economic growth, United Nations Sustainable Development Goals, 2021., Accessible on Internet: <https://www.un.org/sustainabledevelopment/goal-of-the-month/>, (09.05.2021.)



19th INTERNATIONAL FOUNDRYMEN CONFERENCE
Humans - Valuable Resource for Foundry Industry Development

Split, June 16th-18th, 2021

<https://ifc.simet.hr/>

EFFECT OF HIGH SILICON CONTENT ON THE PROPERTIES OF DUCTILE IRON CASTINGS

Branko Bauer^{*}, Ivana Mihalic Pokopec, Marko Šaban

University of Zagreb Faculty of Mechanical Engineering and Naval Architecture, Zagreb, Croatia

Oral presentation

Original scientific paper

Abstract

This paper investigates the influence of silicon content of 3.5 wt.% on the microstructure and mechanical properties of ductile cast iron at different cooling rates. The cast geometry consists of samples with different thickness; cone block with diameter 300 mm and height 350 mm and standard Y2 and Y3 keel-blocks. Microstructure analysis and tensile test were performed on the as-cast materials. Based on the metallographic observations of the present work, it could be concluded that silicon content of 3.5 wt.% has negative effect on spheroidal graphite morphology for this melt and solidification conditions. Tensile test showed that silicon strengthens the ferrite, resulting in an increase in yield and tensile strength, while the elongation decreases. Also, based on the metallographic observations in this investigation, the risk of chunky graphite formation increases with increase in wall thickness, i.e., lowering of the cooling rate. Chunky graphite formation negatively effects on mechanical properties, especially elongation, in cast irons with silicon content higher than 3.5 wt.%.

Keywords: ductile cast iron, high silicon, cooling rate, microstructure, mechanical properties

*Corresponding author (e-mail address): branko.bauer@fsb.hr

INTRODUCTION

Among fully ferritic ductile irons, three new grades EN-GJS-450-18, EN-GJS-500-14 and EN-GJS-600-10 have been introduced in the European Standard EN-1563:2012. These cast iron grades have been defined as “solution strengthened ferritic ductile irons” as they are alloyed with silicon contents in the range 3.2–4.3 wt.%. It has been reported that such high silicon contents promote high nodule count [1–3] and thus favour matrices with very high ferrite fractions. The number of applications of such high silicon ductile iron grades is expected to increase quickly due to a unique combination of tensile strength with high elongation and less variations in mechanical properties. Also, a homogeneous microstructure with single-phase ferritic matrix of high silicon ductile iron grades results in better machinability and low

tool wear compared to conventional ferritic or ferritic-pearlitic ductile irons. This good combination of properties enables reducing the wall thickness of the casting and opens the possibility to replace steel fabricated parts, like forgings or welded structures which can result in huge cost saving and weight saving [4-6]. However, when silicon content is further increased above most common practice, e.g. above 4.2 – 4.3 wt.%, Glavaš et al. [7] and Stets et al. [4] reported that both tensile strength and yield strength rapidly decrease.

On the other hand, the appearance of some graphite degeneration such as chunky graphite has also been related to high silicon contents in ductile irons [1,2,6,8]. Silicon is known as element which has a deleterious effect on the graphite morphology and needs to be counterbalanced during the production of high silicon ductile cast iron. It has been reported that alloys with silicon contents above 2,2 wt.% are related with chunky graphite formation and thus decrease of mechanical properties, especially tensile strength and elongation (common low silicon ductile iron) [8-11]. Also, it was found that in high silicon ductile iron, with silicon content up to 4.0 wt.%, chunky graphite appears frequently even in thinner sections and affects significantly both tensile strength and elongation [6].

The present work investigates the influence of different cooling rates on the graphite morphology and the mechanical properties of ductile cast iron with 3.5 wt.% Si. For this purpose, microstructural investigation as well as mechanical testing were performed.

MATERIALS AND METHODS

Melting and preparation of the base iron for production of high silicon ductile iron melt with 3.5 wt.% Si was carried out in a medium frequency induction furnace with capacity of 5.7 t. The metallic charge consists of 70 % special low-manganese pig iron (Sorelmetal®), 9 % steel scrap, 21 % ductile iron returns, 0.1 % SiC and 0.2 % FeSi, Table 1. For this experiment, 2 tone of remained base iron was used. Targeted silicon content in remain base iron was achieved by the addition of 120 kg/2 t foundry grade FeSi alloy. A check of the melt composition was subsequently made and the melt temperature was then increased to 1510 °C.

Table 1. Metallic charge composition, wt.%

Total	Sorelmetal®	Returns	Steel scrap	SiC	FeSi
5.7 t	70	21	9	0.1	0.2

*Si content: 0.8 wt.% (TA cup, GDOES)

The spheroidising treatment, using the sandwich method process, was carried out by transferring 400 kg of the prepared melt to a sandwich ladle where 1.8 wt. % FeSiMg treatment alloy (44-48 wt.% Si, 3.5-3.8 wt. % Mg, 0.9-1.1 wt.% Ca, 0.5-1.2 wt.% Al, 0.6-0.8 wt.% RE, Fe bal.) and 0.5 wt.% cover alloy (46-50 wt.% Si, 1.8-2.2 wt. % Ba, 0.4-0.6 wt.% Ca, 0.5-1.0 wt.% Al, Fe bal.) have been set at the bottom of the ladle. Simultaneously with spheroidising treatment, inoculation was carried out by adding 0.2 wt.% of Ce based commercial inoculant (70-76 wt.% Si, 1.5-2.0 wt. % Ce, 0.75-1.25 wt.% Al, > 1 wt.% O and S, Fe bal.) in the ladle. The treatment temperature was in the range 1480–1495 °C. The holding time was 3 minutes. After the treatment, the slag was removed from the melt surface and the melt was poured into the moulds. Also, coin sample was taken in order to determine the

chemical composition of treated batch. The pouring temperature was 1380 °C. The pouring time 28 s for cone block and few seconds for keel-blocks.

The cast geometry were standard Y keel-blocks; YII keel- blocks (25 mm) and YIII keel-blocks (50 mm) in accordance with EN 1563:2012 and cone block with diameter of 300 mm and a height of 350 mm, Figure 1. The different thicknesses of Y blocks provided different cooling rates during the solidification. Four standard moulds, two for YII keel-blocks and two for YIII keel-blocks, were produced from chemical bonded sand moulds (furan resin). Cone block was casted separately in sodium silicate bonded sand mould. For this mould, direct pouring process was used where the melt was poured through the feeder. Direct pouring process is the combined use of a feeder sleeve and ceramic foam filter (KALPUR®).

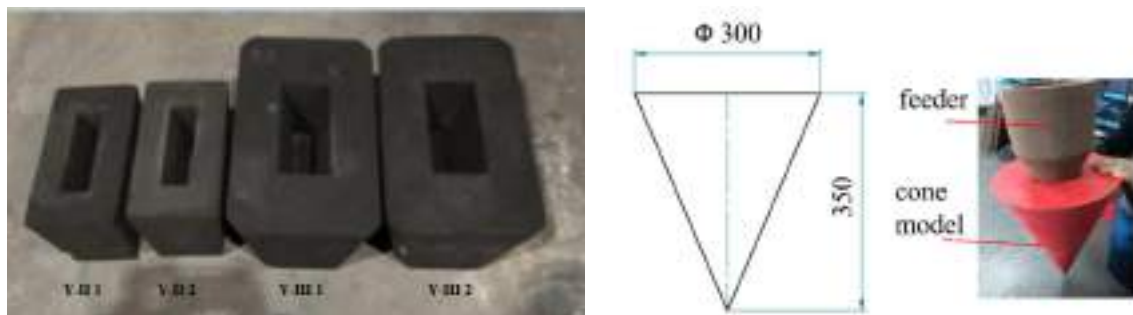


Figure 1. Y keel-block moulds and pattern for cone block

After removing from the moulds, the keel-blocks were cleaned, and test specimens were machined out from the bottom area. Cylindrical specimens with 10 mm gauge diameter for tensile testing were prepared, two from each YII keel-blocks and four from each YIII keel-blocks, Figure 2 a). The dimensions and the shape of the test specimens were in accordance with EN 1563:2012. The tensile test was carried out in accordance with EN ISO 6892-1:2009.

After the tensile testing, samples for the metallographic examinations were taken from the one piece of the tensile specimens (close to rupture), with dimensions $\phi 10 \text{ mm} \times 10 \text{ mm}$. Samples were mechanically polished and then etched by 5 % Nital solution. Microstructure was analysed using an optical microscope (Olympus BX61) with a digital camera and the image analysis system (Analysis® Materials Research Lab).

Coin sample was used for chemical analysis. Carbon and sulphur contents were measured by combustion analysis (ELTRA CS800) while the rest of the analysed elements were determined by the spectrometer (ARL OES Metals Analyzer). The results obtained from this analysis are shown in Table 2., where carbon equivalent values were calculated according to Castro et al. [12]. With eutectic composition assumed at $C_{eq}=4.34 \%$, it could be seen that alloy has hypereutectic composition. It could be observed from Table 2., that the targeted silicon content was not fully achieved.

Table 2. Chemical composition of the cast alloy

C	Si	Mn	S	P	Mg	Co	Cu	Cr	Mo	Ti	C_{eq}
wt. %											
3.51	3.43	0.192	0.013	0.029	0.038	0.016	0.036	0.027	0.0015	0.007	4.48

The cone block was afterwards sectioned along the vertical symmetry plane. One half of the cone block was used for sample preparation for metallographic analysis and other for tensile specimens preparation. Then, one half of the cone block was sectioned along the horizontal symmetry plane 50 mm from the cone base. From the bottom part of the one sectioned cone, a slice of 10 mm thickness was then taken for sample preparation for metallographic analysis, Figure 2b).

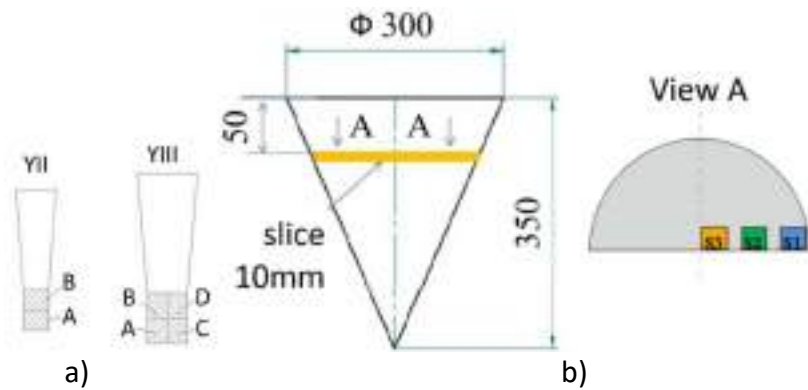


Figure 2. Schematic of sampling; a) tensile test and micrographs on keel-blocks, b) metallographic analysis of cone: S1– cone edge, S2 – mid-way between edge and centre, S3 – cone centre

For the metallographic analysis three samples were prepared, Figure 2 b). The dimensions of sample section were 25 mm × 25 mm. In order to determine the effect of the cooling rate on the graphite morphology, one sample was taken from the thermal centre of casting, S3, where the cooling rate is the lowest, one from the edge where the cooling rate is the highest, S1 and one from the area between these two zones, S2. The metallographic analysis was done by optical microscope (Olympus BX 61) which was equipped with a system for automatic image processing (Analysis® Materials Research Lab) and by SEM/EDS (FE SEM JEOL-JSM-6500 F).

For the tensile test, three samples with 8 mm gauge diameter were taken from the centre of the cone base in the area 0 to 50 mm from the cone base below the feeder. The dimensions and the shape of the test specimens were in accordance with EN 1563:2012. The tensile test was carried out in accordance with EN ISO 6892-1:2009.

RESULTS AND DISCUSSION

Keel-blocks

Figure 3 shows the microstructures of the samples in the polished state, at a magnification of 100x.

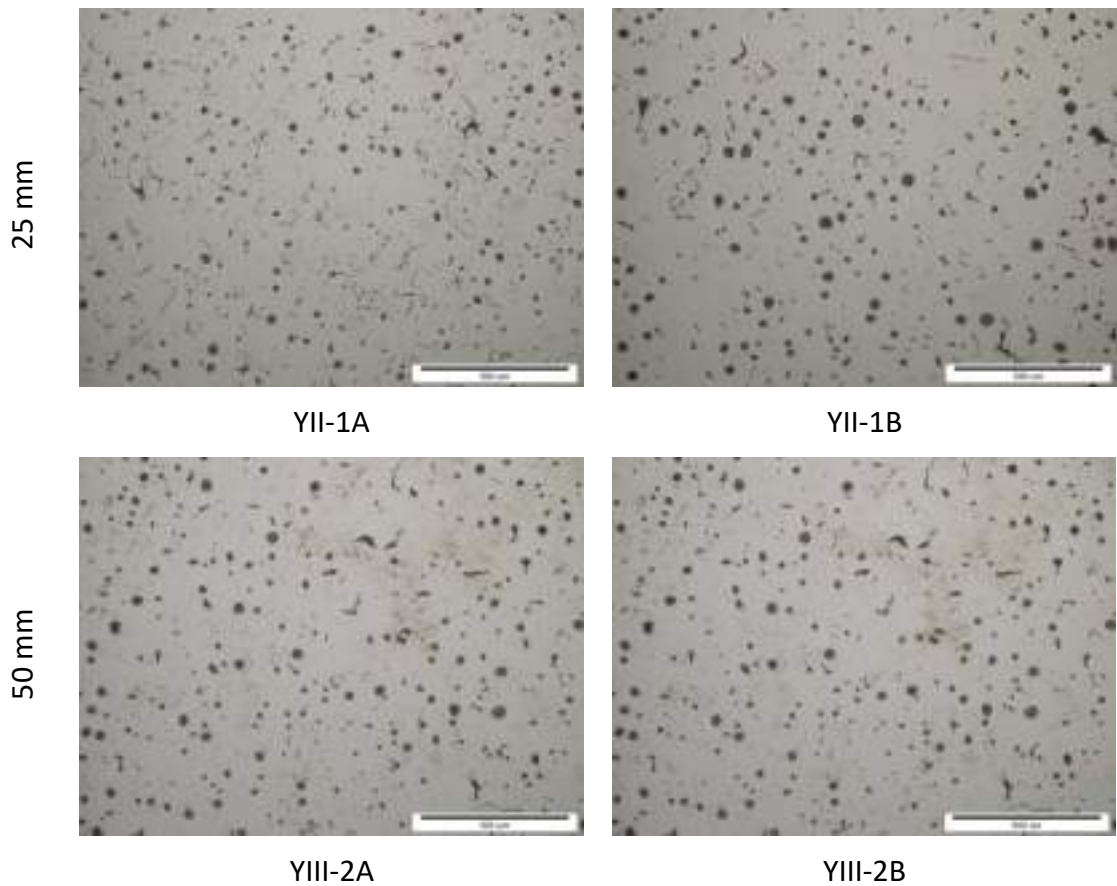


Figure 3. Representative micrographs of the 25 mm and 50 mm keel-blocks; unetched

From the micrographs, it can be seen that carbon was precipitated in the form of graphite in all samples. The precipitated graphite in samples YII-1A and YII-1B is present in vermicular and nodular shape. In samples YIII-2A and YIII-2B, the nodular shape of graphite predominates. Along with nodular graphite, vermicular graphite also appears, but in a smaller proportion. In all samples, the nodules are of regular shape and evenly distributed in the metal matrix. Nodules of equal size predominate and in sample YII-1B they are slightly larger in size compared to other samples. In sample YII-1A, the number of nodules is significantly lower than in other samples and a much higher proportion of vermicular graphite was observed. The reasons for the precipitation of graphite in vermicular shape could be; low residual content of magnesium and/or rare earth elements, high temperatures or long holding time after melt treatment [13, 14] or reaction with mould material.

Figure 4 shows the microstructures of the samples in etched state, at a magnification of 100x.

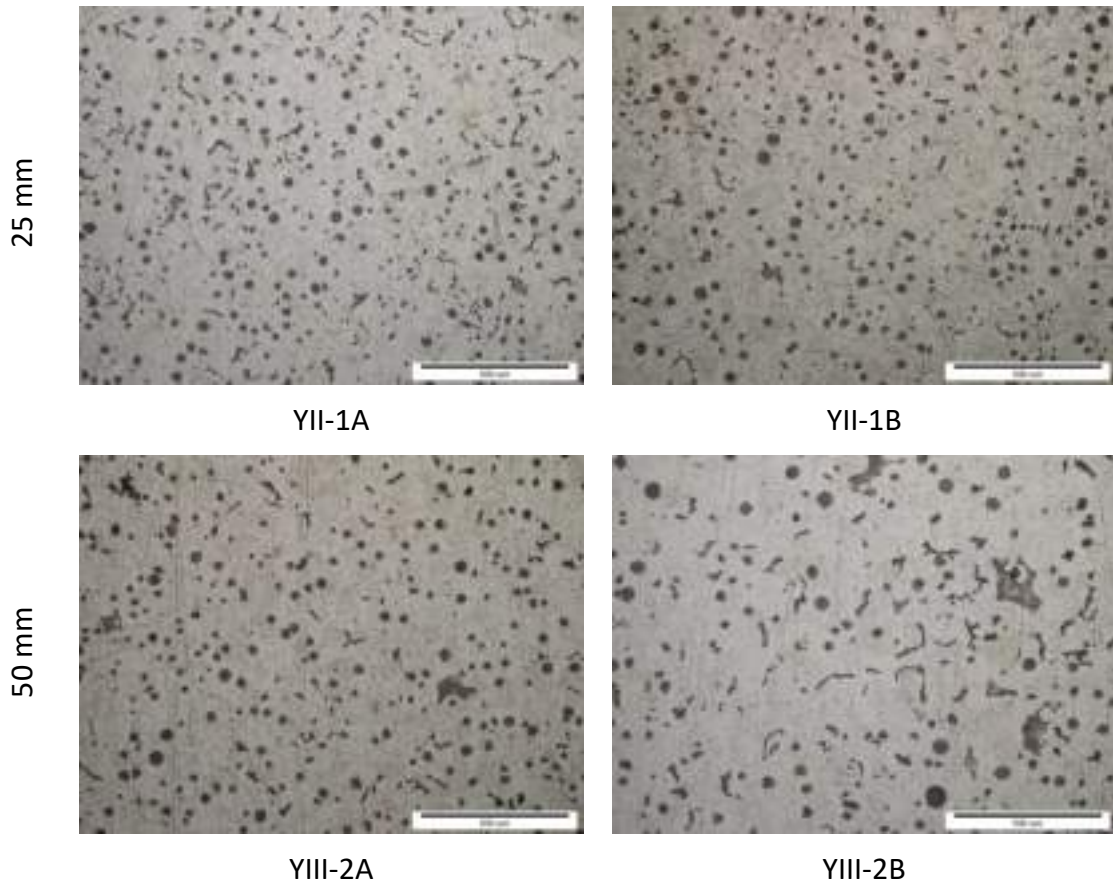


Figure 4. Representative micrographs of the 25 mm and 50 mm keel-blocks; etched

An examination of the microstructures in the etched state shows that the ferrite metal matrix predominates. According to the literature [7], increasing the silicon content in the alloy increases the ferrite content in the metal matrix because silicon is a ferrite promoter. Fully ferritic metal matrix occurs above 3.8 % Si [7].

Table 3 shows the tensile test results together with the $R_{p0.2}/R_m$ ratio for all the specimens.

Table 3. Tensile test results of Y blocks

Sample	R_m N/mm ²	$R_{p0.2}$ N/mm ²	$R_{p0.2}/R_m$	A_5 %	Note	Sampling scheme
YII - 1A	391.36	337.23	0.8617	-	fracture outside L_0	
YII - 1B	494.35	342.42	0.6927	17.42		
YII - 2A	361.25	332.65	0.9208	3.5		
YII - 2B	493.97	351.4	0.7114	15.47		
YIII - 1A	465.58	343.37	0.7375	9.17		
YIII - 1B	474.19	345.45	0.7285	10.92		
YIII - 1C	476.93	350.53	0.7350	10.17		
YIII - 1D	400.64	332.27	0.8293	3.75		
YIII - 2A	455.04	347.21	0.7630	-	fracture outside L_0	
YIII - 2B	479.59	350.24	0.7303	9.83		
YIII - 2C	263.85	259.14	0.9821	1.17		
YIII - 2D	478.08	337.65	0.7063	10.33		

According to the standard HRN EN 1563:2012, the minimum value of tensile strength for this ductile iron grade (EN-GJS-400-15) is 400 N/mm² for wall thickness up to 30 mm (YII block) or 390 N/mm² for wall thickness from 30 mm to 60 mm (YIII block). The diagram in Figure 5 shows that the measured values of tensile strength in most test specimens are above 400 N/mm². Smaller deviations from the standard prescribed value were observed in samples YII-1A and YII-2A, while significant deviation was observed in sample YIII-2C (in this sample the value of tensile strength was only 264 N/mm²). The highest values of tensile strength were measured on samples from Y blocks with a wall thickness of 25 mm, YII-1B and YII-2B, slightly below 500 N/mm². Higher cooling rate increases the tensile strength value in YII-B specimens, while the low nodularity and the appearance of other shapes of graphite in YII-A specimens significantly reduce the tensile strength. A higher cooling rate also increases the tensile strength value when comparing the results of YII and YIII blocks with nodular graphite.

According to the same standard, the minimum value of the yield strength is 250 N/mm². The measured values of the yield strength on all samples are approximately 80 N/mm² above the yield strength indicated in the standard, while for sample YIII-2C the measured value is slightly above the yield strength indicated in the standard, Figure 6. This is the lowest measured value and it amounts to 259 N/mm², which is significantly lower than other measured values (above 330 N/mm²). The influence of cooling rate and different shapes of graphite in the structure on this property was not observed.

From the results it could be seen that the increased silicon content of 3.43% caused an increase in the tensile and yield strength through the strengthening of ferrite. Similar results of the effect of elevated silicon content are visible in [6, 7].

The ratio $R_{p0.2}/R_m$ according to the stated standard for this grade of ductile iron is 0.625, while the ratio of the measured values of the yield strength and tensile strength in this investigation ranges from 0.69 to 0.98. From the results it can be concluded that the increase in silicon content caused an increase of this ratio, Figure 7. Strengthening of ferrite with silicon has a greater effect on yield strength than tensile strength, which in accordance with the literature [6,7].

The minimum value of elongation according to the standard is 15 % for wall thickness up to 30 mm or 14 % for wall thickness up to 60 mm. Higher elongation was measured on samples YII-1B and YII-2B than required in the standard, while on samples YII-1A and YIII-2A fracture occurred outside the L_0 range so that no ductility was measured for these samples. On the remaining samples, the elongation is significantly lower than required in the standard. With the increase of the silicon content ferrite strengthens leading to a decrease in the toughness of the ferrite together with the appearance of graphite shapes other than nodular is reason for the elongation decrease. The effect of increased silicon content on the reduction of elongation is more pronounced in samples with lower cooling rates (samples from YIII blocks).

Deviations in tensile strength values on individual samples may be caused by the presence of a vermicular shape of graphite in a larger proportion in the microstructure. Namely, it is known from the literature that vermicular cast iron has lower tensile strength compared to ductile iron. The same is true for elongation [13].

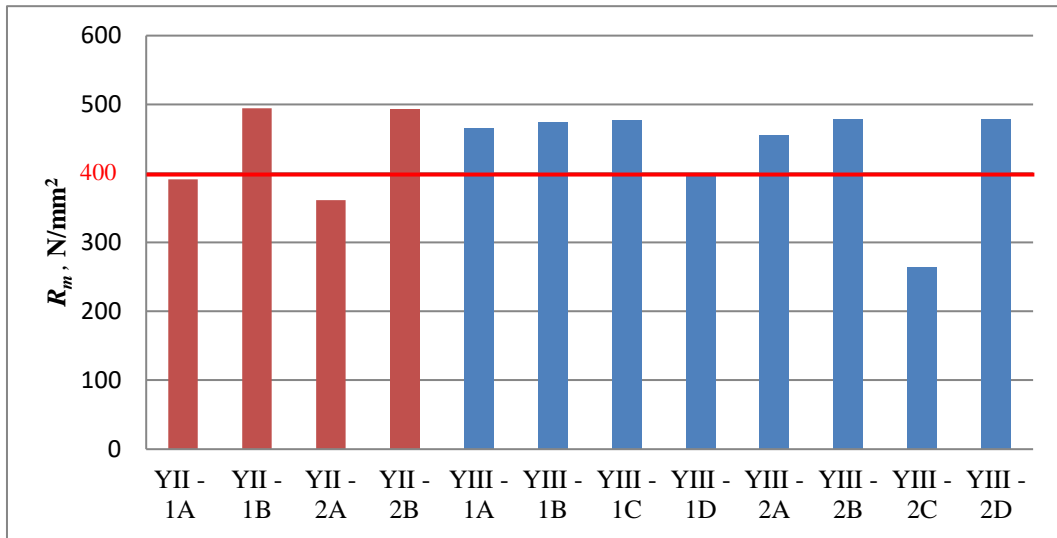


Figure 5. Tensile strength

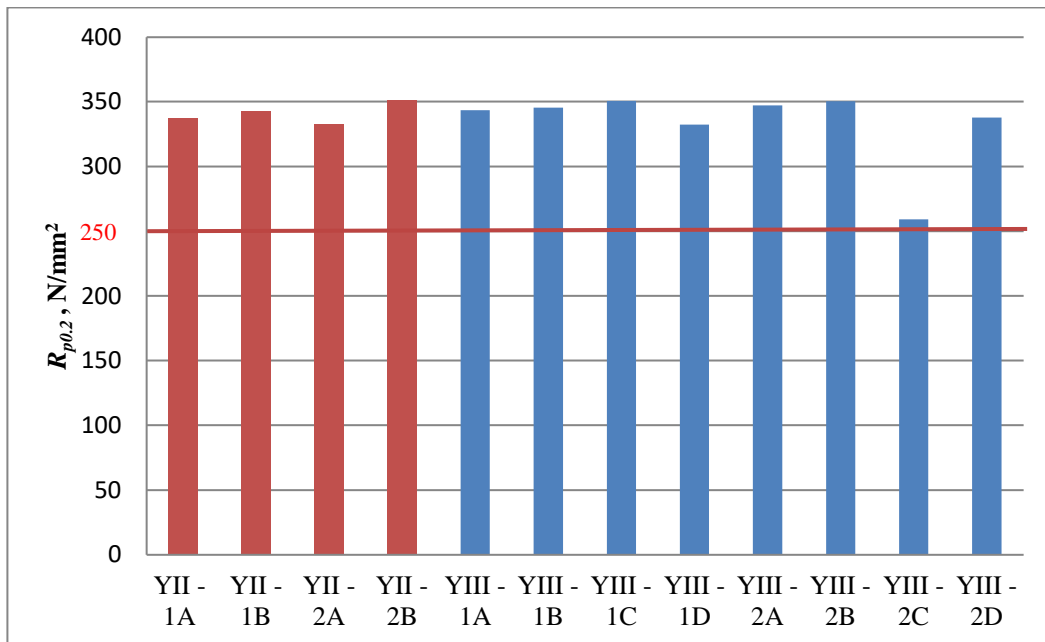


Figure 6. Yield strength

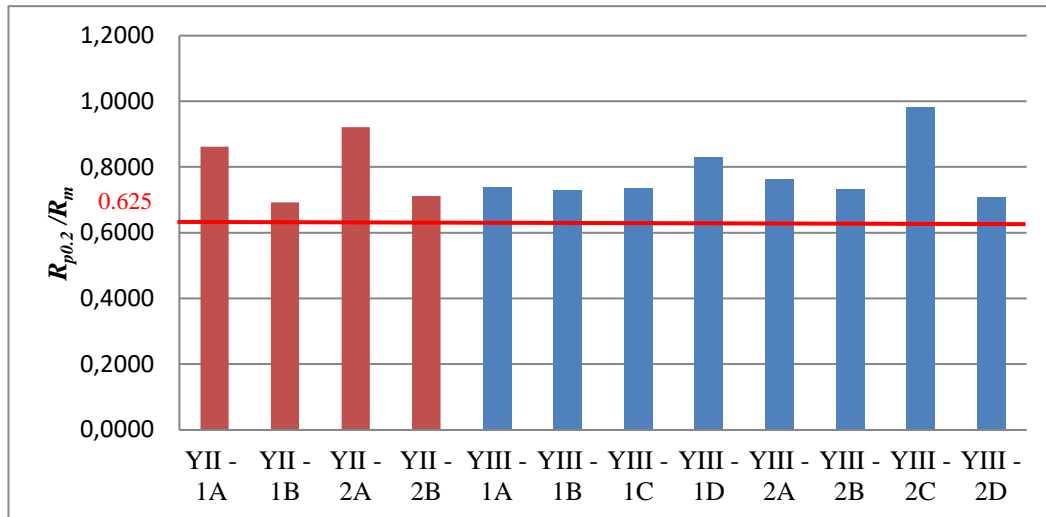


Figure 7. $R_{p0.2}/R_m$ ratio

Cone block

The microstructure of the cone block is shown in Figure 8. From Figure 8 it may be observed that high levels of silicon affect negatively the shape of graphite and nodularity in thick-walled castings. Chunky graphite CHG appeared in a great amount, with only few nodules of regular shape. It can also be seen that CHG surface share increases as the cooling rate decreases. Around the area with CHG there are regular graphite nodules and mostly they are of larger dimensions. The area with CHG is clearly separated from the surrounding area with nodular microstructure. With the occurrence of CHG no other degenerated forms of graphite have been observed. In the etched condition it can be seen that ferritic metal matrix predominates.

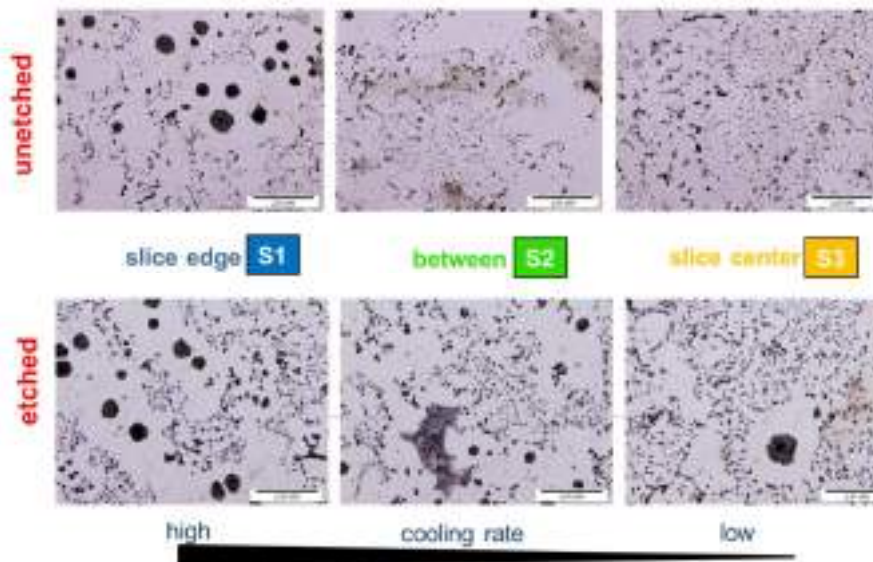


Figure 8. Microstructure of cone block for different cooling rates

CHG appeared in the form of eutectic cells or less often in intercellular form of different dimensions. Here, the size of CHG cells grows parallel to the growth of its amount in the microstructure. It has also been observed that the more CHG the more difficult is to distinguish the eutectic cells (aggregation phenomenon). CHG within the cells appears in the

fine form. Along the outer regions of the cells, the CHG particles are much larger and coarser, which is in accordance with literature [8, 9, 15].

Mechanical properties are shown in Table 4. Tensile strength amounted to approximately 340 N/mm² which is lower than the minimum required value for thick-walled castings EN-GJS-450-18 with 3.2 wt.% Si and EN-GJS-500-14 with 3.8 wt.% Si, 420 N/mm² and 460 N/mm², respectively. The mentioned values from the standard are valid for the wall thickness of 30 mm to 60 mm, whereas for the greater thickness the values are not stipulated by standard and they are agreed between the buyer and the supplier, and even lower values are expected. The occurrence of CHG reduces the tensile strength, which is in accordance with literature. The $R_{p0.2}$ value amounted to approximately 270 N/mm² which is lower than the minimum required for EN-GJS-450-18 and EN-GJS-500-14, 340 N/mm² and 390 N/mm², respectively. The appearance of CHG also reduced $R_{p0.2}$, which is contrary to literature [8-11,15,16]. Elongation is very low, only 1.2 %. Such low values, i.e., when samples have almost no elongation, are in accordance with [15,16].

Table 4. Tensile test results in thermal centre of cone

TRIAL	R_m N/mm ²	$R_{p0.2}$ N/mm ²	A_5 %	Note
1	342	270		fracture outside L_0
2	344	275	1.20	
3	405	276		fracture outside L_0

CONCLUSIONS

Based on the results of this investigation, it can be concluded

- silicon strengthens the ferrite, resulting in an increase in yield strength and tensile strength in high silicon ductile cast iron
- higher silicon content has negative effect on graphite morphology in thick-section cone casting resulting in chunky graphite formation
- higher cooling rate increases tensile strength and elongation, while yield strength is not affected comparing only keel-blocks 25 and 50 mm
- although CHG appeared, there was no significant tensile strength decrease (as it is reported in the literature), which means that positive effect of high silicon content is stronger than negative effect of CHG. The elongation was not positively affected by elevated silicon content in CHG area resulting in low values as expected
- microstructure examination of keel-blocks revealed that graphite precipitated also in vermicular shape having more influence on lowering tensile strength while yield strength was hardly affected.

Acknowledgements

This work was partially supported by the foundry MIV d.d.Varaždin.

REFERENCES

- [1] R. Gonzales-Martinez, U. de la Torre, J. Lacaze, J. Sertucha, Effects of high silicon contents on graphite morphology and room temperatures mechanical properties of as-cast ferritic ductile cast irons. Part 1- Microstructure, *Mater. Sci. Eng. A*, 712(2018), pp. 794-802.
- [2] U. de la Torre, A. Loizaga, J. Lacaze, J. Sertucha, As cast high silicon ductile irons with optimised mechanical properties and remarkable fatigue properties, *Mater. Sci. Technol.*, 30(2014), pp. 1425-143.
- [3] K. A. Kasvayee, E. Ghassemali, I. L. Svenson, J. Olofsson, A. E. W. Jarfons, Characterization and modeling of mechanical behavior of high silicon ductile iron, *Mater. Sci. Eng. A*, 708(2017), pp. 159-170.
- [4] W. Stets, H. Löblich, G. Gassner, P. Schumacher, Solution strengthened ferritic ductile cast iron properties, production and application, *Int. J. Metalcast.*, 8(2014), pp. 35-40.
- [5] P. Hammersberg, K. Hamberg, H. Borgström, J. Lindkvist, L.E. Björkegren, Variation of tensile properties of high silicon ductile iron”, *Mater. Sci. Forum*, 925(2017), pp. 280-287.
- [6] R. Gonzales-Martinez, U. de la Torre, J. Lacaze, J. Sertucha, Effects of high silicon contents on graphite morphology and room temperatures mechanical properties of as-cast ferritic ductile cast irons. Part 2 – Mechanical properties, *Mater. Sci. Eng. A*, 712(2018), pp. 803-811.
- [7] Z. Glavaš, A. Štrkalj, A. Stojaković, The properties of silicon alloyed ferritic ductile irons, *Metalurgija*, 55(2016), pp. 293-296.
- [8] J. Lacaze, L. Magnusson Åberg, J. Sertucha, Review of microstructural features of chunky graphite in ductile cast irons, 2013 Keith Millis Symp. on Ductile Cast Iron, Nashville, USA, 2013, pp. 360-368.
- [9] R. Källbom, K. Hamberg, L. E. Björkegren, Chunky Graphite - Formation and Influence on Mechanical Properties in Ductile Cast Iron”, in: J. Samuelsson, G. Marquis, J. Solin (Eds.), *Competent Design by Castings*, VTT Symposium, Finland, 2005, pp. 63-86.
- [10] P. Ferro, A. Fabrizi, R. Cervo, C. Carollo, Effect of inoculant containing rare earth metals and bismuth on microstructure and mechanical properties of heavy-section near-eutectic ductile iron castings, *J. Mater. Process. Technol.*, 213(2013), pp. 1601-1608.
- [11] H. Löblich, Effect of nucleation condition on the development of chunky graphite in heavy ductile iron castings, *Giessereiforschung*, 58(2006), pp. 2-11.
- [12] M. Castro, M. Herrera, M. M. Cisneros, G. Lesoult, J. Lacaze, Simulation of thermal analysis applied to the description of hypereutectic SG irons, *Int. J. Cast Met. Res.*, 11(1999), pp. 369-374.
- [13] F. Unkić, Z. Glavaš, Lijevanje željeznih metala, Sveučilište u Zagrebu, Metalurški fakultet, Sisak, 2008.
- [14] ..., Common Metallurgical defects in ductile iron. Accessible on internet: www.foundry.elkem.com, (11.01.2019.)
- [15] K. Hartung, O. Knustad, K. Wardenauer, Chunky graphite in ductile cast iron castings- Theories and examples, *Indian Foundry Journal*, 55(2009), pp. 25-29.
- [16] R. Källbom, K. Hamberg, M. Wessen, L.-E. Björkegren: On the solidification sequence of ductile iron castings containing chunky graphite, *Mater. Sci. Eng. A*, 413-414(2005), pp. 346-351.



19th INTERNATIONAL FOUNDRYMEN CONFERENCE
Humans - Valuable Resource for Foundry Industry Development

Split, June 16th-18th, 2021

<https://ifc.simet.hr/>

**MODERN ALPHASET (APNB)-REFINED FORMULATIONS WITH BETTER
UNDERSTANDING OF CHEMISTRY**

Dipak Ghosh*

Forace Polymers Pvt. Ltd, Hardwar, India

Oral presentation
Original scientific paper

Abstract

At present APNB binder, best defined chemistry wise as alkali catalyzed phenol formaldehyde resin in strong aqueous alkaline media, is one of the two most popular self-sets in use in foundries across the World, including India, other one being Furan (FNB). Among many, few basic reasons for rapid growth of this system as sand binder in foundries are friendliness towards workplace environment, compatibility to metals of all chemistry and elimination or drastic reduction in defects in castings related to silica sand expansion at 573 °C. Main variables in formulations of APNB are Phenol: Formaldehyde mole ratio, nature and quantity of alkali used, ratio of two alkalis (NaOH:KOH) if applicable and nonvolatile content. Apart from variation in recipe, there is scope for process variation, for example extent of reaction, sequence of addition of raw materials, reaction temperature, reaction time, parameters to control progress and termination of reaction and likes. Scope of this manuscript is to study eight resin formulations processed with single Phenol: Formaldehyde mole ratio with varying extent of reaction, ratio of two (NaOH and KOH) alkali and sequence of alkali addition for physical properties including initial viscosity and viscosity rise on storage. Also compression strength values of samples made using mixed sand at different stages simulating mold movement for fresh as well as aged resin were studied. Apart from dry compression, which simulate strength of molds during movement till closing, this paper has attempted to test compression strength of samples in hot conditions simulating resistance offered by molds from puncture or deformation during or post pouring (hot strength) till solidification of castings and there after ease of disintegration (retained strength) of molds relating ease of de coring. This method is simple and has been developed by author.

Keywords: *binder, alkali, strength, reclamation, case studies*

*Corresponding author (e-mail address): dghosh@foracepolymers.in

INTRODUCTION

So called Alphaset (APNB) process was introduced in World foundry industry around 1985, as sand binder system for making molds and cores. In India, a country of 5000 foundries, second largest in World with turnover of USD 19 billion and export of USD 3.06 billion [1] trials for this system started in 1986. During last three and half decades, APNB system has been better understood for chemistry of curing, strength development, nature and volume of vapors and gases emitted during mold movement, specific role of NaOH and KOH in formulations and many more. Being resole, resin (binder) undergoes polymerization on its own (heat setting) on storage which is associated with increase in viscosity and reduction in gel time. This system also undergoes controlled polymerization (chemical gelation) in presence of weak organic acids released by hydrolysis of esters of polyhydric alcohols or polybasic acids (hardeners) or both even at ambient temperature. In this 1st stage of curing (without external heat), partial crosslinking of two dimensional chains to three dimensional give strength to molds good enough for stripping, handling and closing. Probable mechanism for crosslinking at this stage is published in a technical paper [2] which once again is shown in Figure 1. APNB undergoes momentary relaxation during metal pouring before gaining further strength (2nd stage of curing) [3]. This unique 2nd stage of curing with heat of molten metal keeps this system ahead of other organic self-sets for producing castings free from defects associated with silica sand expansion, main being veining. APNB, otherwise known as environment friendly system releases formaldehyde gas [4], an eye irritant and potential environment pollutant during curing with esters with probable mechanism as shown in Figure 2. One of the positive features of modern formulations is drastic reduction of formaldehyde concentration in work place by using (N free) chemical scavengers in binder formulations or modifying recipe or both. Another attractive development in recent formulations is increase in storage life of resin. In sand mix, bench life is reduced and strength drops as resin ages. Use of aged resin produces friable molds affecting casting quality. To quantify resin life, individual foundries can generate data and specify limiting viscosity above which bench life of mixed sand and strength of samples are lower and molds are friable. Many foundry men believe KOH based resin formulations produce castings with better quality than NaOH based. But a study [5] way back in 1995 reported reduced hot tear and improved surface finish in castings and longer work life of mixed sand and reduced odor in work place after switching over from K based to Na based binder in a steel foundry. Other difference reported in literature [6] is Na based formulations are more suitable for mechanical reclamation and K based for thermal. According to one more publication [7], Na based alkali gives better quality of mechanically reclaimed (MR) sand with reclaim ability being 60-80%. To conclude, binders containing only Na based formulations are better for foundries practicing mechanical reclamation. As feed sand for thermal reclamation is always mechanically reclaimed, it has to be of high quality for efficient reclamation. Thus it stands, judicious blend of Na and K based formulations are appropriate to foundries practicing thermal reclamation, Na, for achieving good reclamation by mechanical process and K for better reclaim ability by thermal process. Some manufacturers claim they use Li based alkali in place of Na and K for improved performance but author feels it's far from truth. Again, many foundries ask for declaration of % N content in binder. Answer is, this system is free from N, but some manufacturers add N bearing compounds to contain smell of formaldehyde evolved at various stages of mold handling.

In close to 35 years of introduction of APNB, chemistry for synthesis and crosslinking mechanism for APNB have been understood better. Customized resin formulations in combination with suitable esters of specific hydrolysis constant, alone or blend can meet requirements of individual foundries, globally matching wide variations in ambient temperature, sand quality and specific requirements of individual foundries.

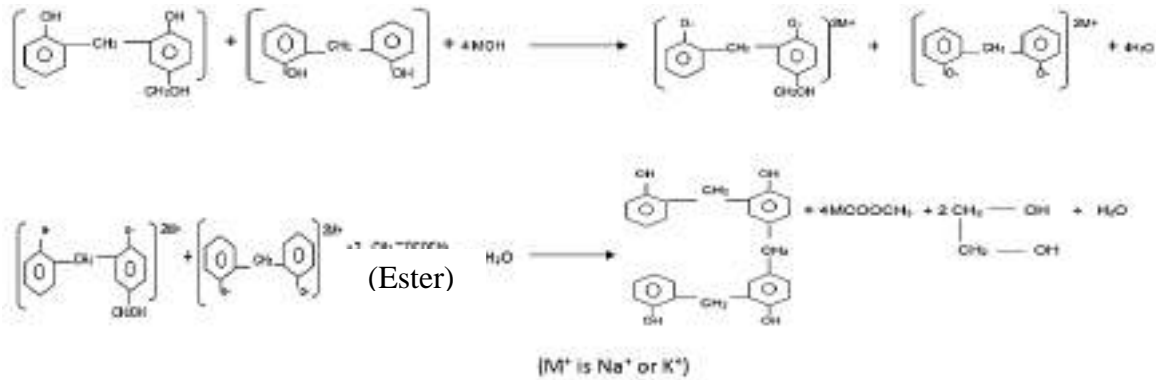


Figure 1. Probable mechanism at 1st stage of curing

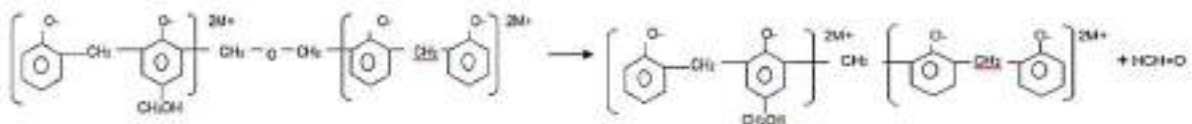


Figure 2. Probable mechanism of release of Formaldehyde (HCHO) during 1st stage of curing

MATERIALS AND METHODS

Resin synthesis

Single mole ratio of Phenol: Formaldehyde was chosen. 2-liter capacity glass vessel with stirring and heating arrangements was charged with hydrated phenol, 37% formalin and first dose of aqueous alkali of particular concentration (NaOH, A-D and KOH, E-H) and mass was held at particular temperature range. In case of A and B, reaction was continued till gel time of mass (base resin, BR-1): aqueous solution of NaOH of particular concentration in particular ratio reached between 5'-30'' to 6'-0'' when tested with GTA (glycerol tri acetate) at 100 (resin solution): 20 (GTA). Resin solution made at this stage (BR1+NaOH solution) was termed A. BR-1 was used to prepare one more solution with KOH (BR1+KOH solution) of same concentration as NaOH in same ratio as A. This solution was termed B. BR1 was cooked further (BR2) till GT of solution of BR2 with NaOH solution of previous concentration in previous ratio with GTA reached between 4'-0'' to 4'-30''. This solution was termed C. Solution of BR2 with KOH solution as NaOH in same concentration in same ratio prepared and termed D. For solutions E-H, reaction was started with KOH solution of same concentration as earlier in same proportions to prepare BR3 and BR4 with GT of 5'-30'' to 6'-0'' and 4'-0''-4'-30'' respectively. A and C are Na-Na, B and D are Na-K, E and G are K-K and F and H are K-Na based.

Table 1. Properties of eight resins

PROPERTIES	A	B	C	D	E	F	G	H
VIS@30°C (CPS)	56	47	66	51	39	44	49	52
Alkali	Na	Na +K	Na	Na+ K	K	K+ Na	K	K+ Na
Molecular weight	Low	Low	High	High	Low	low	High	High
GT 121°C (10 gm), mt-sec	27-0	29-30	24-0	30-0	30-0	27-30	26-30	26-0
Moisture (%)	52.43	52.42	53.01	53.75	55.58	54.12	51.61	54.03
Non-volatile Content (%)	48.74	47.25	49.10	49.35	47.63	47.32	48.06	48.29
Specific Gravity	1.182	1.177	1.183	1.180	1.172	1.184	1.178	1.188
Free Phenol (%), GC	0.47	0.42	0.44	0.43	0.37	0.27	0.41	0.20
Na (%)	5.94	3.21	5.94	3.21	nil	2.73	nil	2.73
K (%)	nil	3.31	nil	3.31	7.18	3.87	7.18	3.87

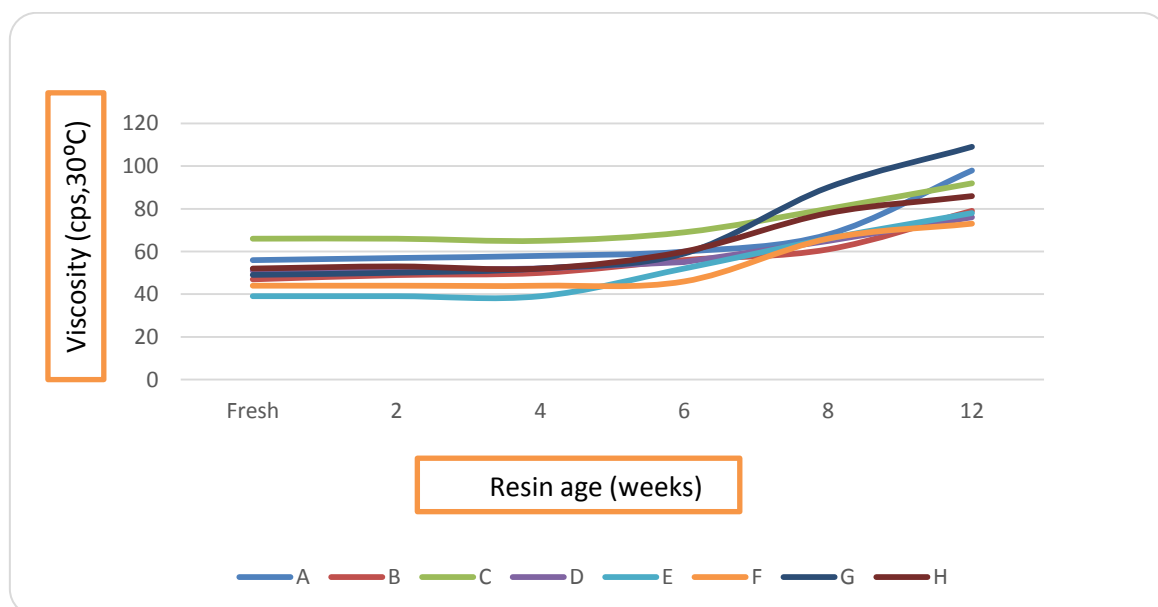


Figure 3. Change in viscosity with resin age

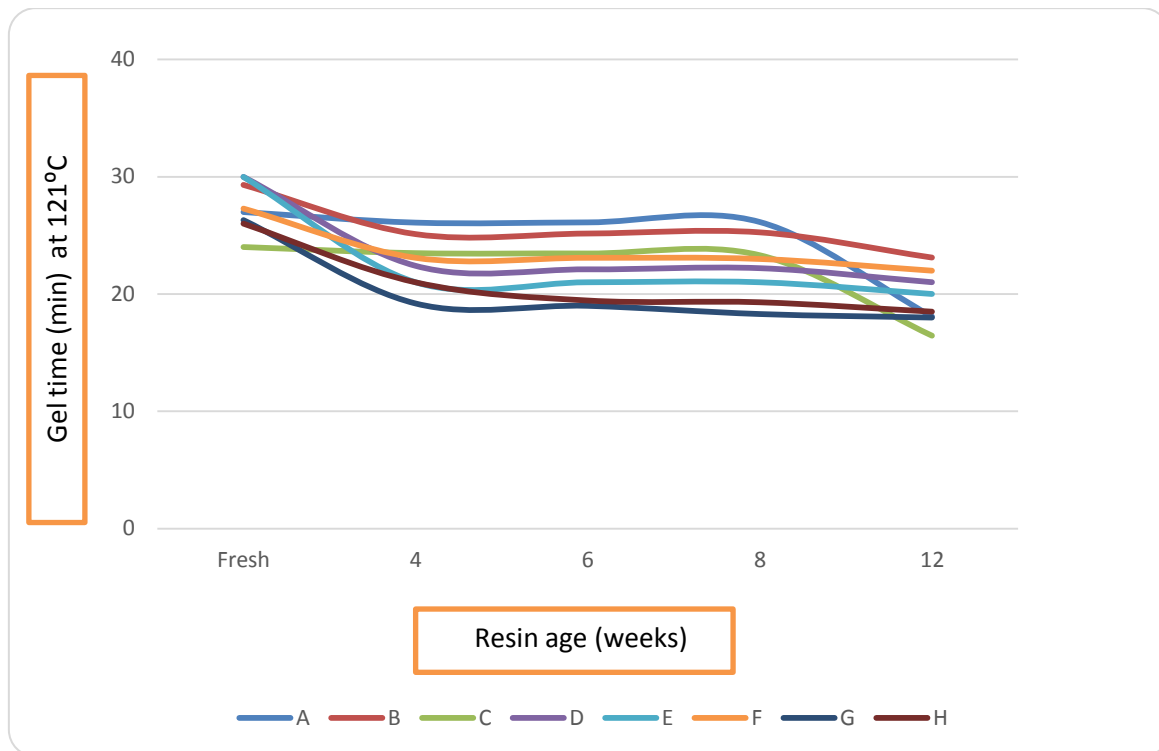


Figure 4. Change in gel time with resin age

Sand test procedure and results

One sand of north Indian origin was chosen. Sieve distribution with respect to % retention and cumulative % retention are exhibited in figs.5 and 6 respectively. Binder addition for all mixes were maintained at 1.6 % by weight of sand and hardener (GTA) 20 % by weight of binder. Mixing was done in laboratory mixer with required dosage of Hardener and Resin with specific cycle. Discharged sand was checked for bench life (BL) manually. Small mixed sand on discharge was kept tightly in a polythene bag. Strip time (ST) was recorded the time it became sufficient hard by feel. Immediate stripped samples were allowed to air dry for 5 minutes, put in oven@120 °C for 5 minutes, cooled to room temperature, applied with thinner based coating and lighted off. Two warm samples were tested for compression. Another two samples were tested for compression when they attained room temperature. Cold samples were soaked in furnace at 450 °C for 5, 10 and 15 minutes and tested for compression in hot (hot strength) as well as cold (retained strength) conditions. Some of these properties are repeated with up to 12 weeks of resin ageing. Many of the sand test properties followed in this paper are unconventional, but author feels, those can be simulated with strength requirements of individual foundries during mold movement (stripping, handling in manipulator, wash degradation, closing, pouring, post pouring and de-coring) to have better control on quality of molds and finally castings.

Further, sand samples, new and reclaimed, mechanical (MR) and thermal (TR) wherever applicable were collected from five foundries and quantitatively analyzed for Na and K contents and also dry compression strength for samples were studied at practical addition level. Studies in this manuscript has conclusively proved that thermally reclaimed sand generated from APNB in many cases lose bonding power on storage depending upon source

of thermal chemical. Further investigation is needed to ascertain parameters of chemical responsible for this phenomenon.

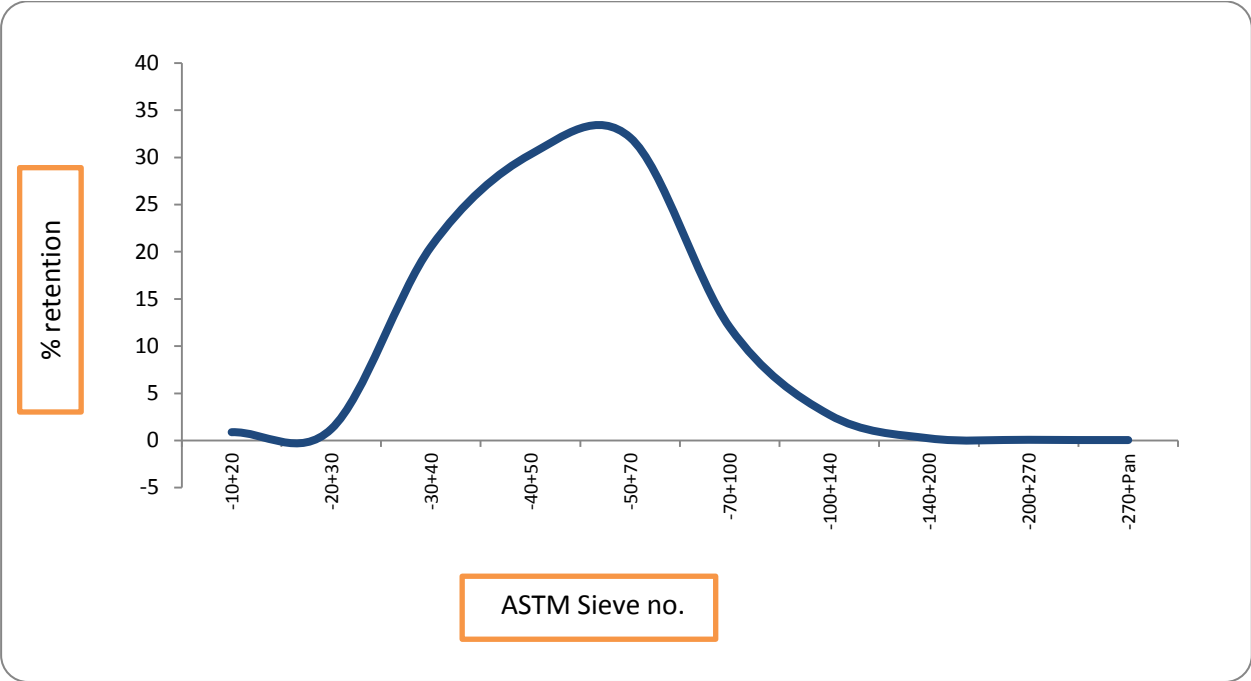


Figure 5. ASTM Sieve no vs % retention of sand used for testing

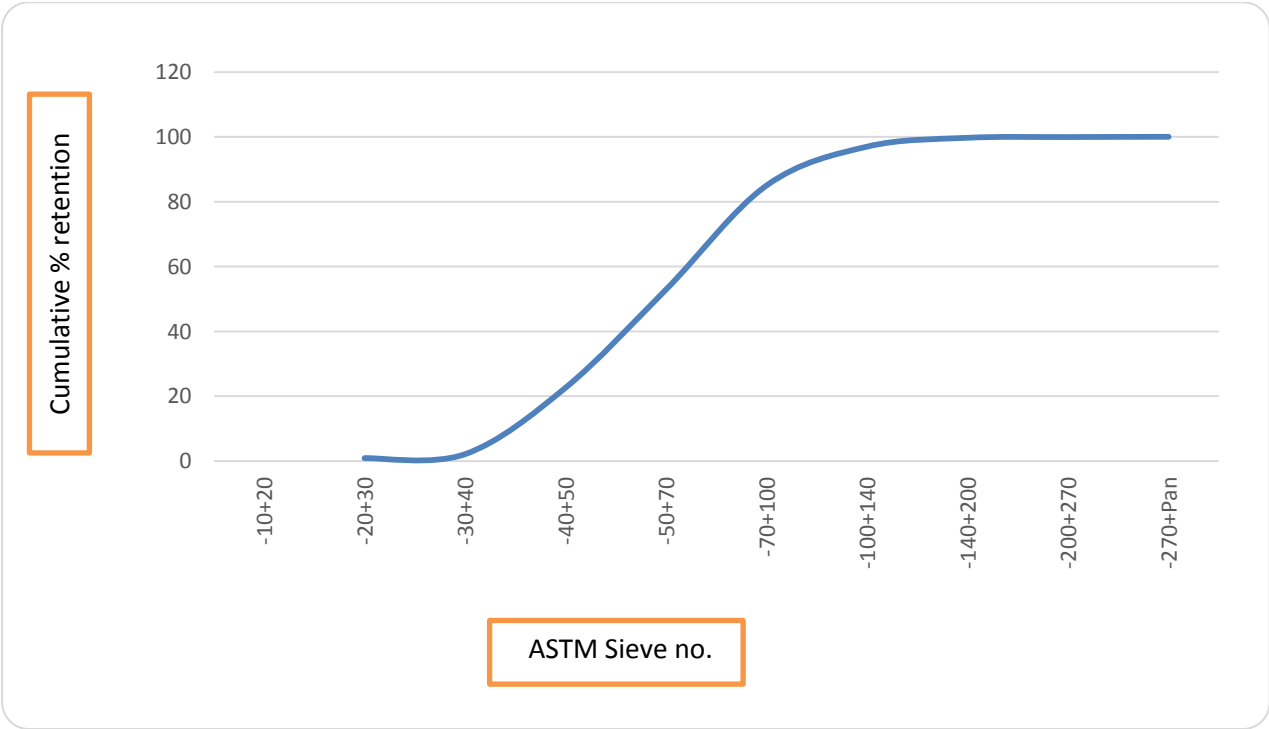


Figure 6. ASTM sieve number vs cumulative % retention

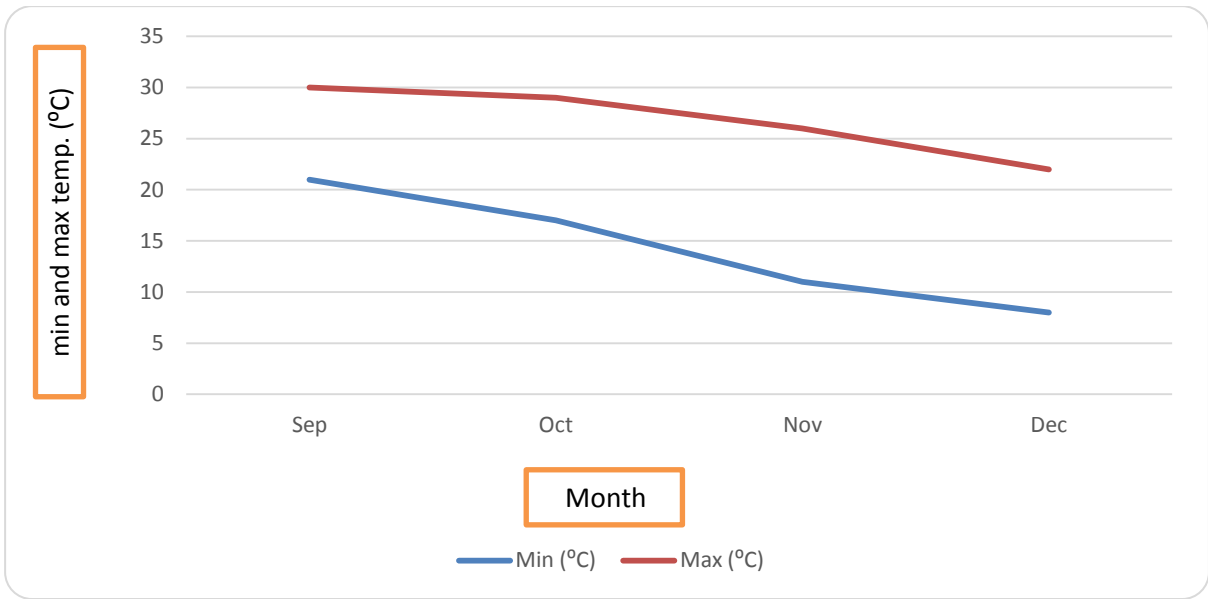


Figure 7. Maximum and minimum temperature during period of experiments

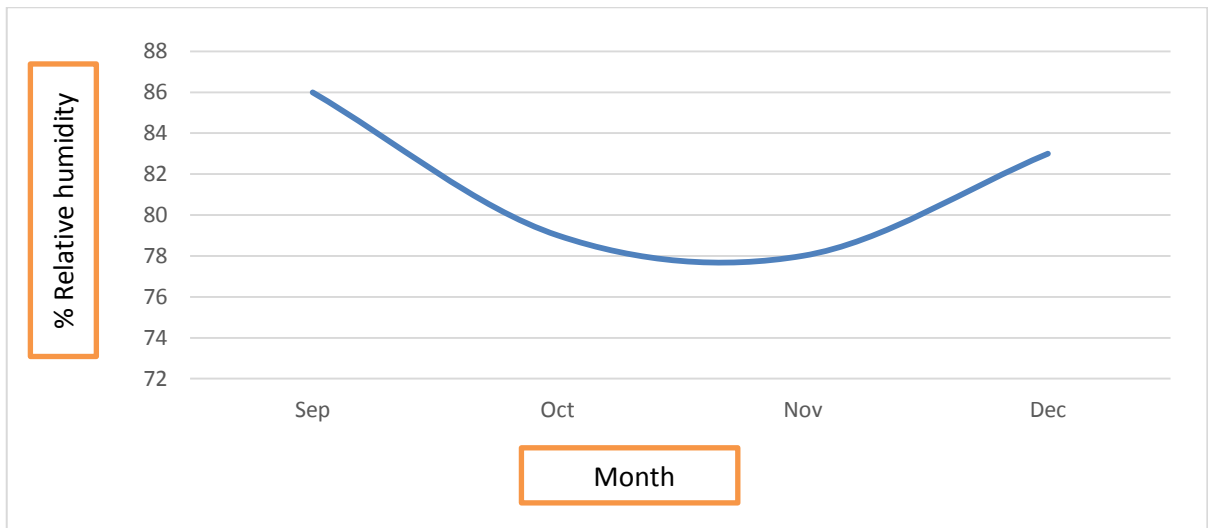


Figure 8. Relative humidity (%) during period of experiments

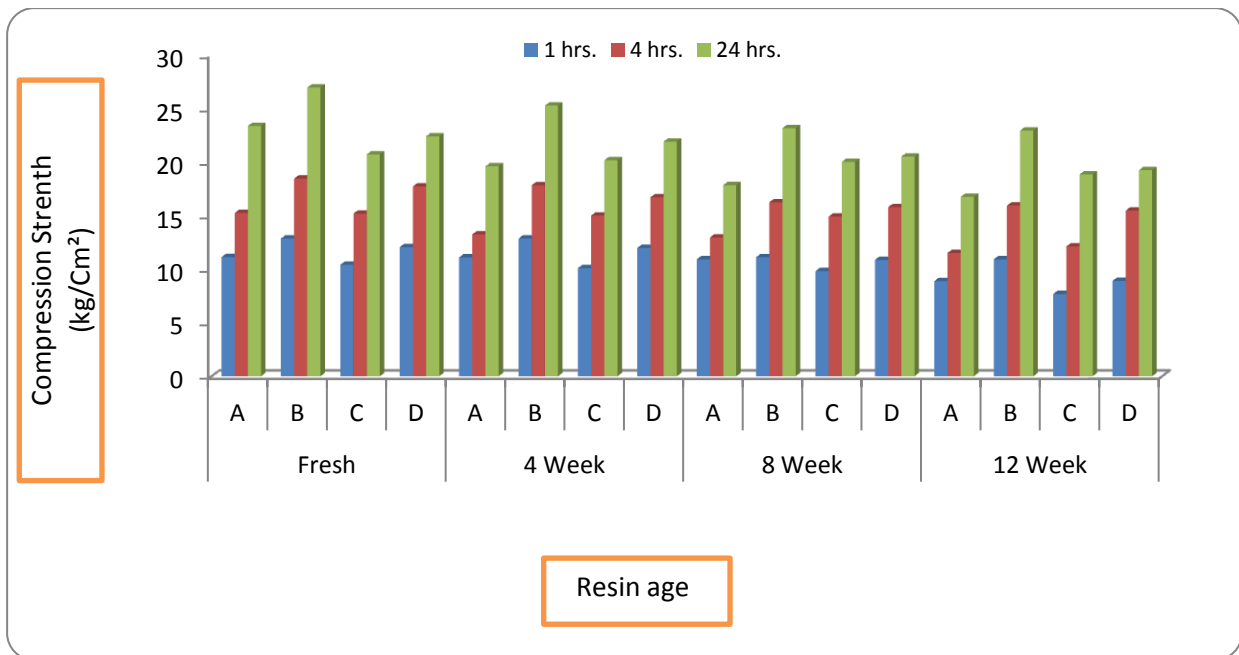


Figure 9. Hourly dry strength of samples made using fresh and aged Resin (A-D)



Figure 10. Hourly dry strength of samples made with fresh and aged Resin (E-H)

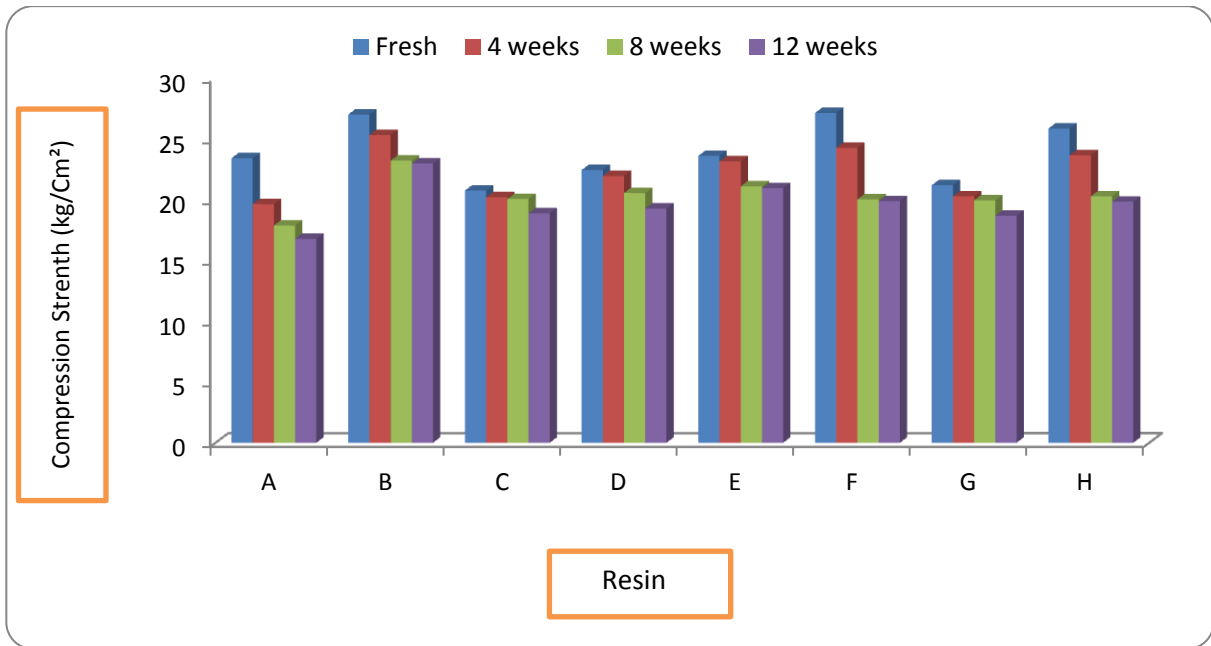


Figure 11. Resin age vs dry compression Strength

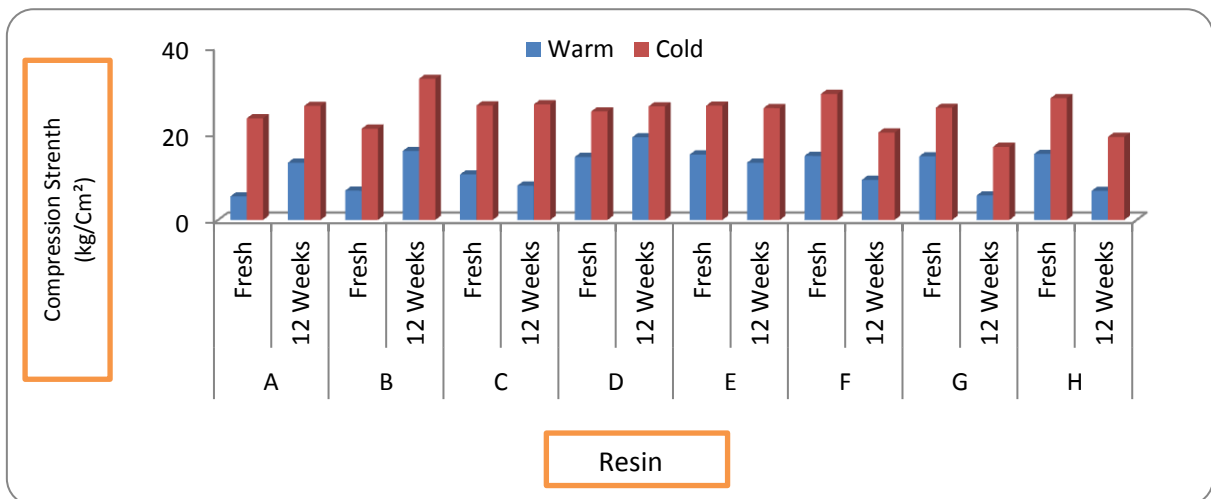


Figure 12. Strength of warm & cold samples after coating & lighting off

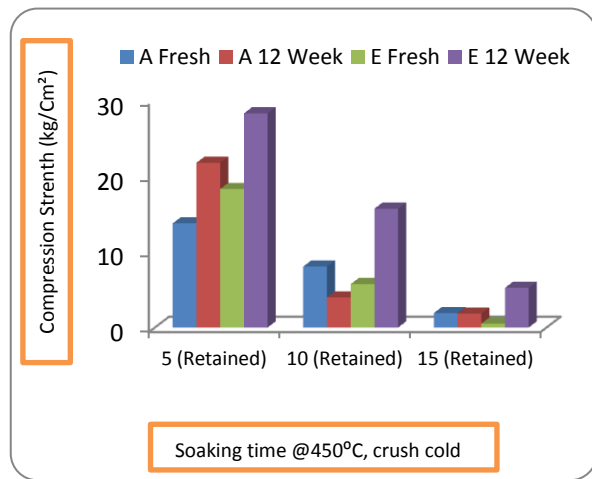
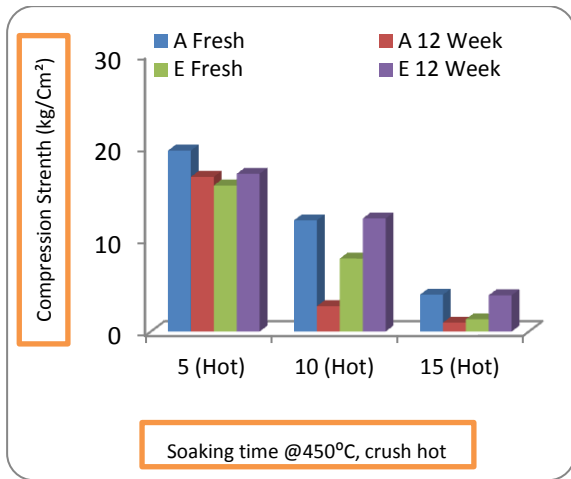


Figure 13. Hot & retained strength of samples made with fresh & 12 weeks aged resin, A & E

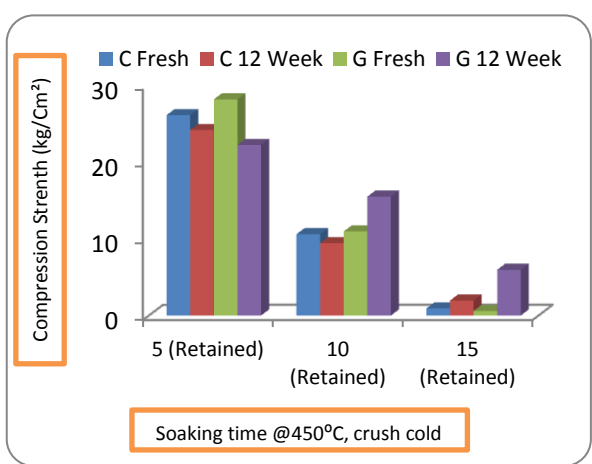
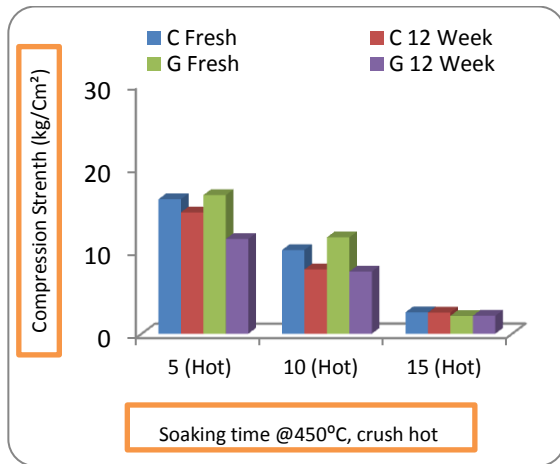


Figure 14. Hot & retained strength of samples made with fresh & 12 weeks aged resin, C & G

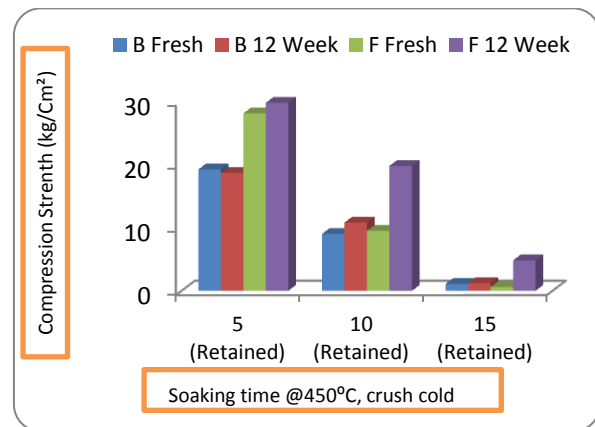
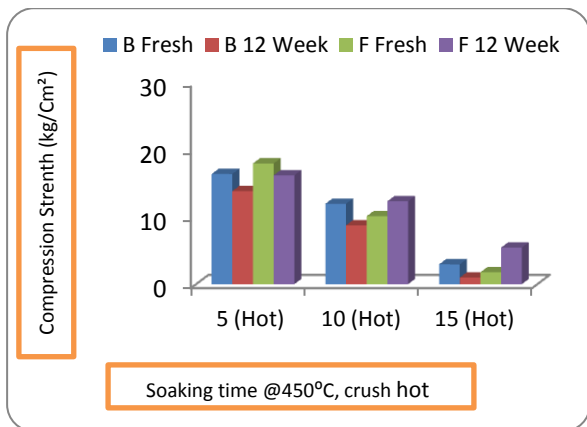


Figure 15. Hot & retained strength of samples made with fresh & 12 weeks aged resin, B & F

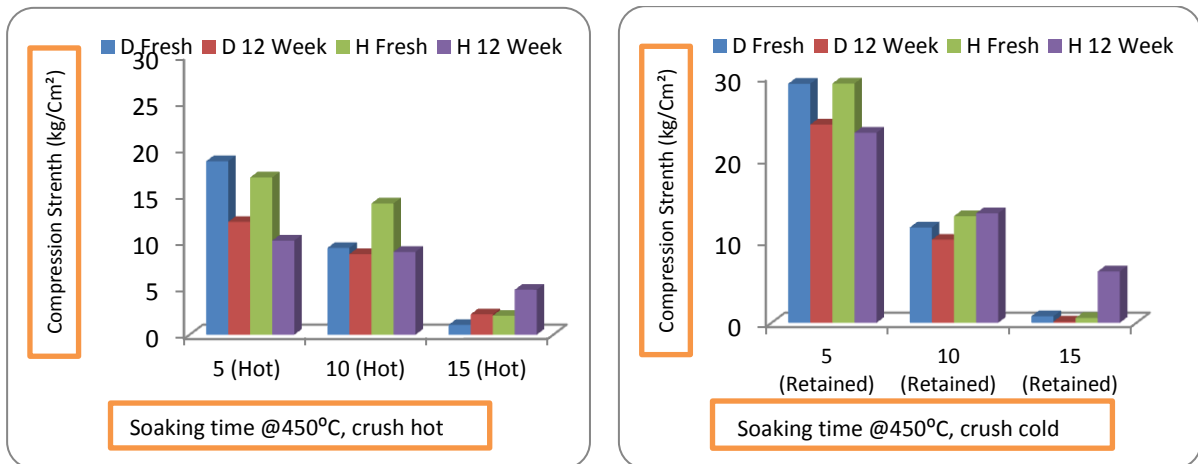


Figure 16. Hot & retained strength of samples made with fresh & 12 weeks aged resin, D & H

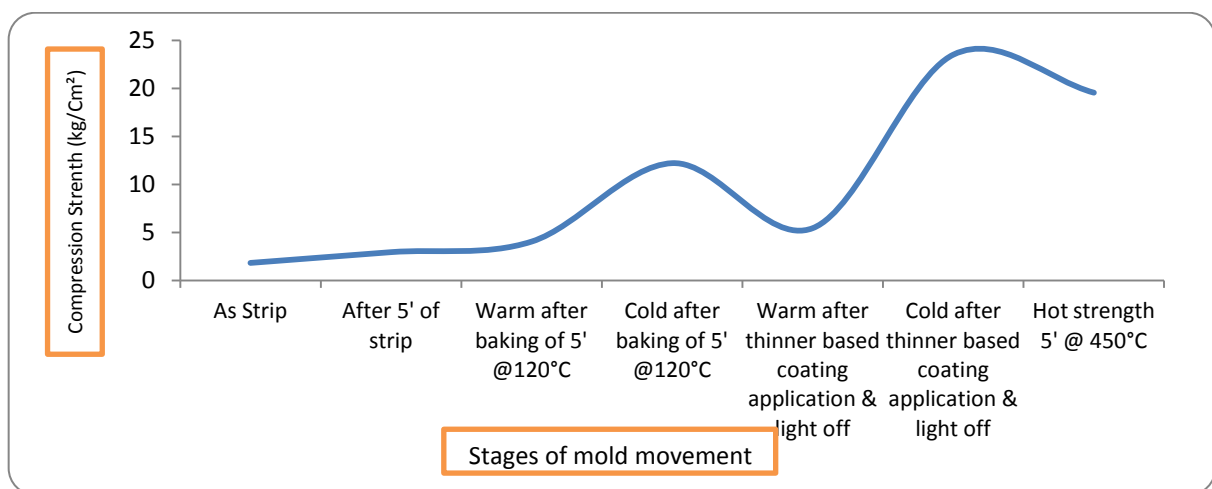


Figure 17. Pattern of compression strength variation at different stages from strip to 5 minutes at furnace (450 °C)

RESULTS AND DISCUSSIONS

Physical & chemical properties of different formulations

1. Formulations using Na based alkali offer more viscosity in fresh resin than K based. Same is trend with mixed alkali also (Table 1)
2. Viscosity of all formulations remains fairly stable over initial period and then rise. Total K based formulations indicate more rate of rise during period of study and prevailing ambient temperature (Fig 3)
3. Gel time (121 °C) of all formulations remain fairly stable over initial period and then decrease. Rate of drop in different formulations are not conclusive (Fig 4)

Sand Mix Properties

1. Dry strength

For comparison of strength during ageing, only 24 hours' values have been studied. In series A-D, B maintains higher strength (24 hrs.) values than others throughout

ageing process (Fig.9). In series E-H, fresh resin F shows higher strength than others but E shows better resistance to deterioration throughout ageing process (Fig.10). Total variation in strength of samples made with fresh resin A-H is close to 20%, B and F being maximum, C and G being minimum (Fig.11). Drop in strength during the period of study varied approximately between 10-28 % in samples made with A-H. A being maximum and E minimum. Samples made using B shows not only consistency in results but also having highest values during period of study. Samples made using fresh samples of C and G show comparatively lower strength but shows maximum resistance to deterioration on ageing. Fresh resins F and H show good strength but drop is more on ageing. Fig.11 shows resin ageing is associated with drop in strength in all cases, of course to different extent. Figs. 11 and 12 shows all samples undergo strength drop in warm condition after application of thinner based wash, ignition and extinction of flame. Lost strength is recovered on cooling.

2. Hot and retained strength

Fig 13.

Figures show comparison of all Na (A) and all K based (E) resins of same molecular weight, fresh and aged for hot and retained strength. Only conclusive observation here is samples made using aged resin E offers maximum resistance to collapse during cooling after soaking in furnace. This phenomenon can be simulated to resistance of molds in cooling line to disintegrate during post solidification.

Fig 14.

This is also comparison between all Na (C) and all K (G) of higher molecular weight than previous one. Here also trend is same. There is no remarkable difference in hot strength between Na and K based but retained strength for K based is more.

Fig 15.

Comparison between B, having almost equal Na and K and F, predominately K, show same trend as previous two.

Fig 16.

D and H with identical formulations of B and F and higher molecular weight also follow more or less same trend as previous ones.

Fig 17.

This fig. shows expected pattern of strength variation in samples simulating stages of mold movement. Excessive softening of mold surface in warm condition (wash degradation) after wash application, ignition and extinction of flame may change geometry of mold surface. Extent of softening is strongly related to components used in coating, both solvent and solid ingredients.

CASE STUDIES

Foundry I (largest castings with Alphaset in India):

Mixer: 60 MT/hr, Reclamation: Mechanical (single attrition), Castings: Steel, molds: boxed, sand weight: 90 MT (one half), liquid metal: 128 MT, finished casting weight: 65 MT, item: turbine.

Addition level in facing (new silica) sand: 1.35:20, backing (MR) sand: 2.35:20, Specs for BL-20 minutes (minimum) in both facing and backing, Specs for 24 hrs. compression $\geq 30 \text{ kg/cm}^2$ for facing and $\geq 25 \text{ kg/cm}^2$ for backing.

Table 3. ROA of one month aged Resin being used by above Foundry

Property	Unit	Value
Viscosity (Brookfield), 30 °C	cps	95
Sp. Gr (30°C)	None	1.24
Gel time @ 121 °C	Mts-Secs	27-15
Nonvolatile content (2 gm, 2 hr, 120 °C, glass Petri dish)	%	55.74
Moisture content	%	52.15
Free phenol ,GC	%	0.12
Na (Flame photometer)	%	1.38
K (Flame photometer)	%	7.15

Table 4. ROA for MR Sand from above Foundry

Parameter	Unit	Value
AFS no	None	40.72
LOI	%	2.08
Na	%	0.039
K	%	0.25

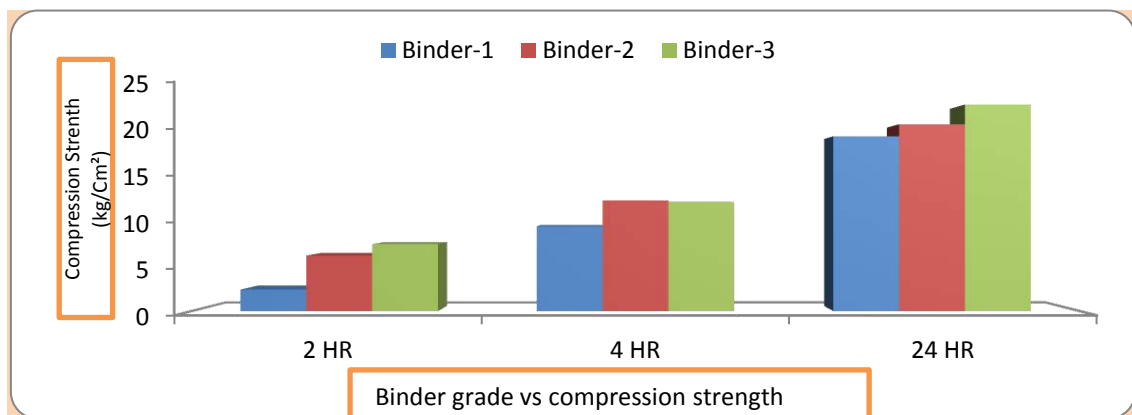


Figure 18. Compression Strength (MR Sand used @ 2.35:20) values of three approved binders in laboratory of Forace Polymers (P) Ltd (Results are lower than specification because of resin ageing, change in testing laboratory or both)

Remarks

1. Specification for strength requirement shows MR Sand offers much lower strength than New Sand at equal addition level in case of APNB.
2. MR Sand (backing) with 20 kg/cm² compression strength is capable of handling pressure of 128 MT of liquid metal.
3. APNB can handle pressure of 128 MT liquid metal in facing (New) sand with compression as low as 30 kg/cm² because of excellent hot strength.

Foundry II (Largest casting in Alphaset, flask less molds):

Mixer: 30 MT/hr, Reclamation: Mechanical (primary followed by secondary), Castings: Steel, Sand weight: 1780 kg (one half), Half mold: 180X140X47 cm, Items: Mn steel and high Cr steel for crushers.

Addition level in facing (new and olivine) as well as backing (MR) 1.6:20. Specs for 1 hr. compression in New Sand is ≥ 10 kg/cm².

Mold making and pouring cycle: Mold filling, stripping in roll over (~45 mts) preheating in IR, flood coating with Mg or Zr thinner based coatings by tilting with help of manipulator, lighting off and passing through hot air oven, approx. 45 mts @ 150-250 °C. Molds are closed and poured within 18-30 hrs. of making. Some castings are cooled for 48-56 hrs. before shifting to knock out chamber. Critical stages:

- BL of mixed sand, particularly MR: Should be ≥ 5 mts
- Strip strength for roll over strip, close to 45 mts: New Sand compression should be ≥ 7.5 kg/cm²
- Handling strength at manipulator for coating application: MR sand ≥ 10 kg/cm²
- Some of the molds should not collapse post pouring and during cooling of castings to prevent leakage of sand during casting movement to avert (a) loss of sand and (b) cleaning of leaked space. Should have good retained strength.

Table 5. ROA of one month aged Resin being used by above Foundry

Property	Unit	Value
Viscosity (Brookfield), 30°C	cps	83
Sp. Gr (30°C)	None	1.205
Gel time @ 121°C	Mts-Secs	25-20
Nonvolatile content (2 gm, 2 hr, 120°C, glass Petri dish)	%	53.08
Moisture content	%	49.82
Free phenol ,GC	%	0.33
Na (Flame photometer)	%	3.99
K (Flame photometer)	%	3.14

Table 6. Properties of Sand

Parameter	Unit	Silica Sand	MR, followed by dynamically reclaimed sand
AFS No.	None	44.64	45.39
L.O.I (%)	%	0.589	1.329
Na (Flame photometer)	%	Not applicable	Not available
K (Flame photometer)	%	Not applicable	Not available

Remarks

1. As stripped strength of $\geq 7.5 \text{ Kg/cm}^2$ is enough for stripping of flask less molds of largest size using APNB in the Country. Maximum strength requirement is at the stage of handling the molds in manipulator for applying flood coating. Same is $\geq 10 \text{ kg/cm}^2$. Manipulator grips both facing new sand & backing MR Sand. Thus MR Sand also should have good strength.
2. In case of boxed molds, it is desired that system should have good hot strength and low retained strength, but in case of flask less molds, retained strength also should be good where cooling cycle of castings is as high as 36 hours in order to prevent leakage of sand from molds on cooling line.

Foundry III (Steel valves), Reclamation MR followed by TR

Supplier for additive for thermal reclamation: B

Produces steel valves in flask less as well as boxed molds. Mold facing TR: New Sand = 85:15, mold backing MR. Addition level 1.3% in facing and 1.6% in backing.

Table 7. Properties of Resin (2 weeks aged)

Property	Unit	Value
Viscosity (Brookfield, 30°C)	Cps	70
Sp. Gr (30°C)	None	1.24
Moisture content	%	49.92
Non-volatile content (2 gm, 2 hr, 120°C, Glass Petri Dish)	%	55.96
Free Phenol% ,GC	%	0.27
Gel Time @121°C	Mts-Secs	28-30
Na (Flame photometer)	%	1.44
K (Flame photometer)	%	7.38

Table 8. Properties of MR and TR Sand (Fresh)

Parameter	Unit	New Sand	MR Sand	TR sand
AFS no	None	40.124	44.025	45.30
LOI	%	0.991	0.993	0.69
Na	%	Not applicable	0.092	0.0189
K	%	Not applicable	0.090	0.045

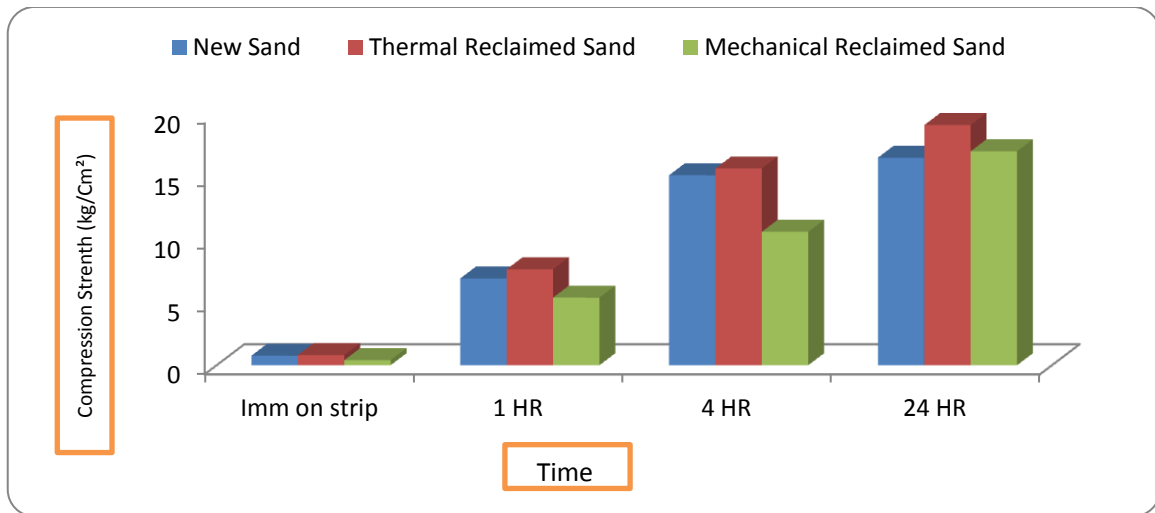


Figure 19. Compression Strength of New & TR Sand (9th day of generation) @1.3:20 & MR Sand @1.6:20 with medium fast catalyst

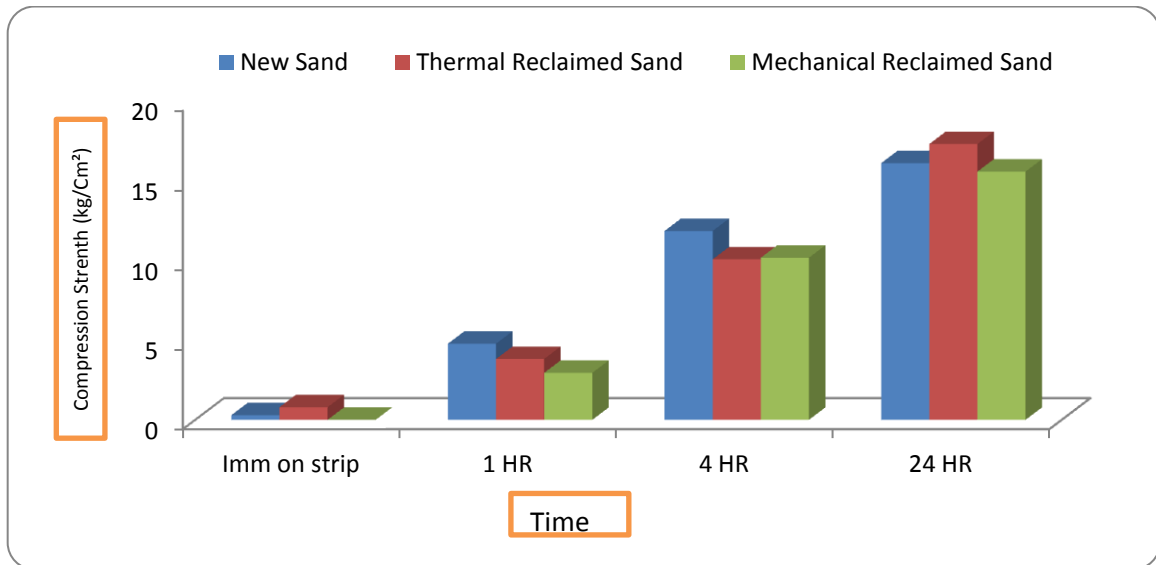


Figure 20. Compression Strength New & TR (after 8 weeks of generation) Sand @1.3:20 & MR Sand @1.6:20 weight of sand with medium fast catalyst

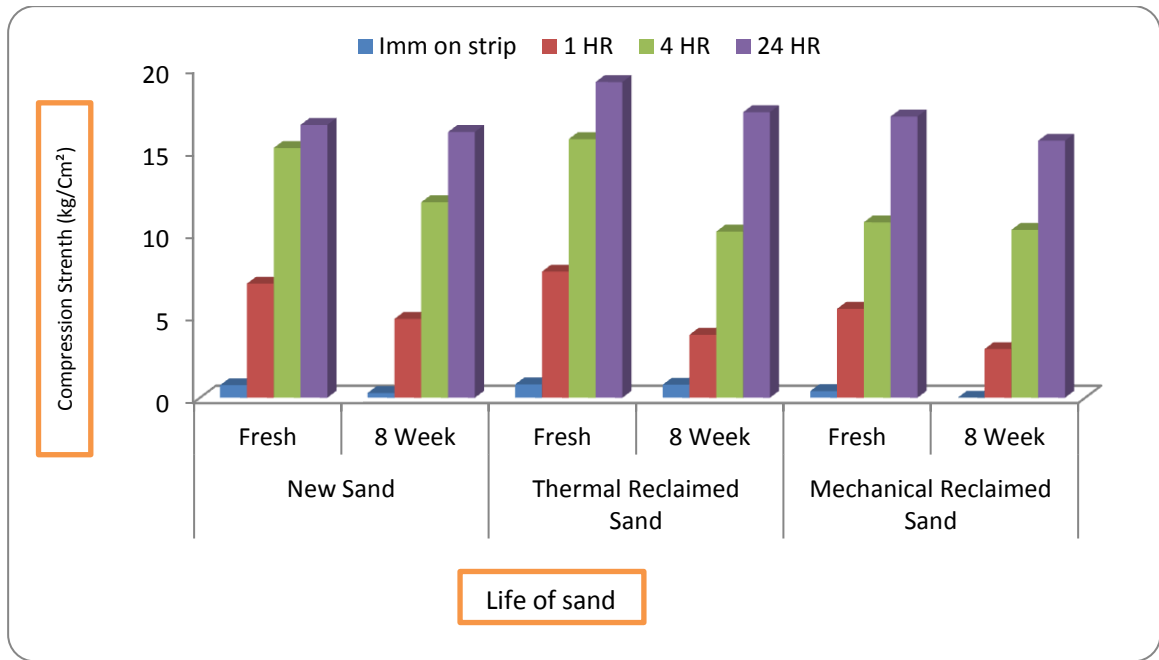


Figure 21. Storage time vs. compression of MR & TR sand with New sand as reference
Life of sand

Remarks

TR sand generated using additive of supplier B is stable

Foundry IV (Steel castings for Railways, in boxed as well as flask less molds)

Supplier for additive for thermal reclamation: A

Addition: 1.2 % by weight of sand

Resin supplier: Two

Table 9. Properties of Resins

Property	Unit	Binder Supplier (X)	Binder Supplier (Y)
Resin age (days)	Days	30	27
Viscosity (Brookfield, 30°C)	Cps	80	105
Sp. Gr (30°C)	None	1.22	1.223
Moisture content	%	47.68	48.78
Non-volatile Content (2 gm, 2 hr, 120°C, Glass Petri Dish)	%	54.82	54.92
Free Phenol, GC	%	0.1	0.11
Gel Time @121°C	Mts-Secs	22-40	20-50
Na (Flame photometer)	%	4.28	8.01
K (Flame photometer)	%	2.7	0.41

Table 10. Properties of MR and TR Sand received on 9th day of generation

Parameter	Unit	MR Sand	TR Sand
AFS no	None	41.8	47.0
LOI	%	1.86	0.58
Na	%	0.20	0.013
K	%	0.034	0.011

Sand mix properties of above sands on 10th day of generation

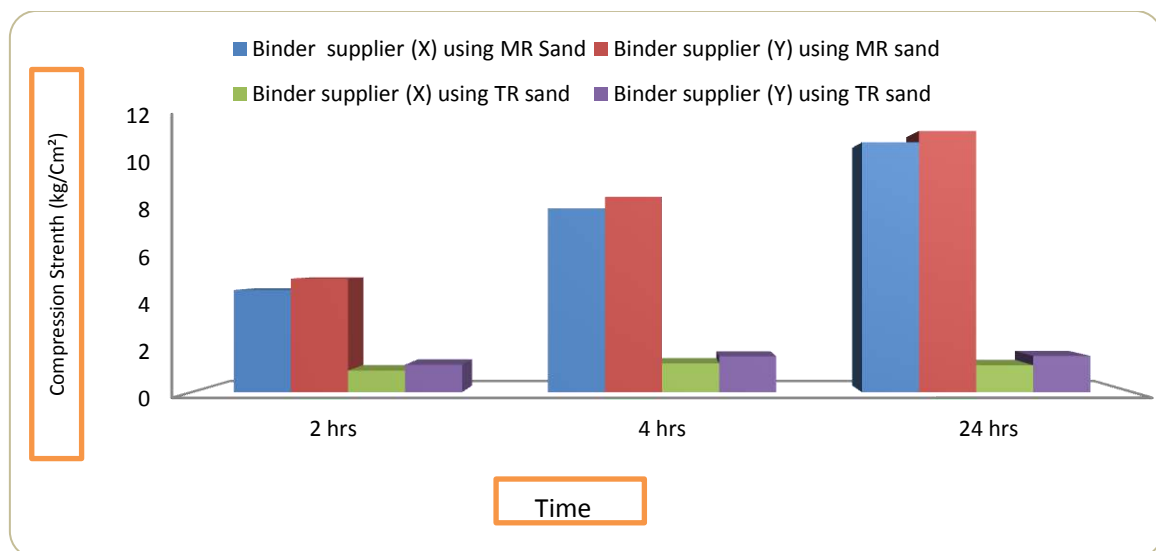


Figure 22. Compression Strength MR & TR Sand used @1.5:20 with medium fast hardener after 8 weeks of generation

Remarks

Example of another steel foundry producing railway castings generating TR sand using additive of supplier A. TR sand has become totally in-active in a period within 10 days of generation.

Foundry V (Producing valve body steel castings up to 10 MT, boxed molds)

Sand: Saudi, one of the best quality available

Reclamation: Mechanical followed by thermal

TR chemical supplier: Originally A then B

History of thermal reclamation:

Systematic experiments were done with variation on parameters like additive doses, chamber temperature, sand flow rate etc. with chemical from supplier A. Experiments were continued with additives for couple of other suppliers. Final solution came when experiments were done with additive of supplier B.

Table 11. ROA of one month aged Resin being used by above Foundry

Property	Unit	Value
Viscosity (Brookfield), 30 °C	cps	55
Sp. Gr (30 °C)	None	1.124
Gel time @ 121 °C	Mts-Secs	28-40
Nonvolatile content (2 gm, 2 hr, 120 °C, glass Petri dish)	%	58.03
Moisture content	%	47.74
Free phenol ,GC	%	0.37
Na (Flame photometer)	%	0.64
K (Flame photometer)	%	8.05

Additive supplier: A

Additive: 1.4 % by weight of sand. Sand mix properties in TR sand @1:21

Table 12. MR Sand (inlet sand in TR chamber) & TR sand (out let from TR chamber) properties

Parameter	Unit	MR Sand (Value)	TR Sand (Value)
AFS no	None	39-42.5	40.51-46.78
ADV	(ml 0.1 N Hcl/100 gm sand)	11.40-12.10	9.90-11.30
LOI	%	1.30-1.50	0.03-0.06%

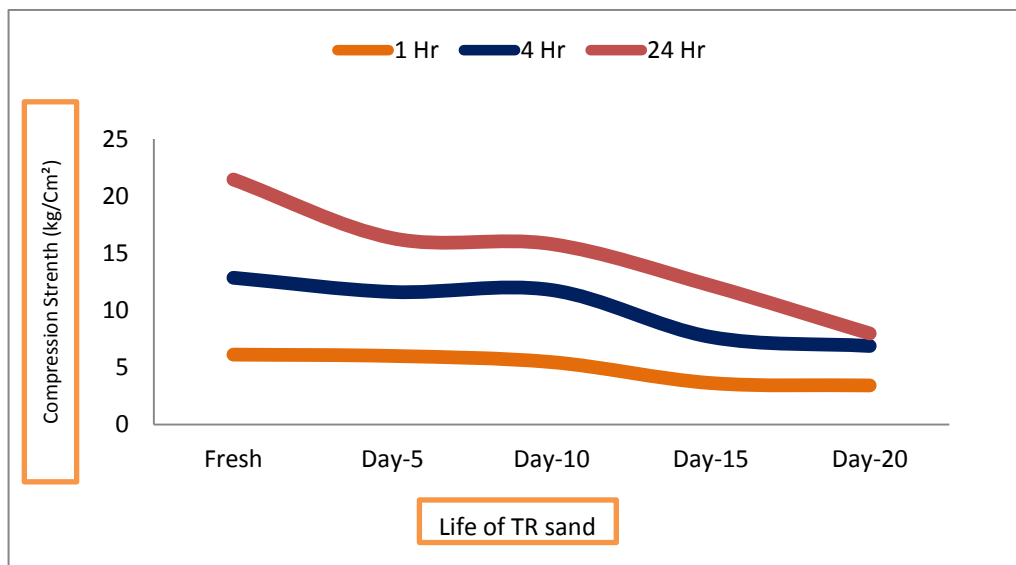


Figure 23. Storage life Vs compression of TR san

RT during period of experiment: 29-30 °C, RH-59-70 % except on 5th day 81 % (data collected from foundry)

Additive supplier: B

Additive used 1.19 % by weight of sand and Sand mix properties in TR sand @1:21

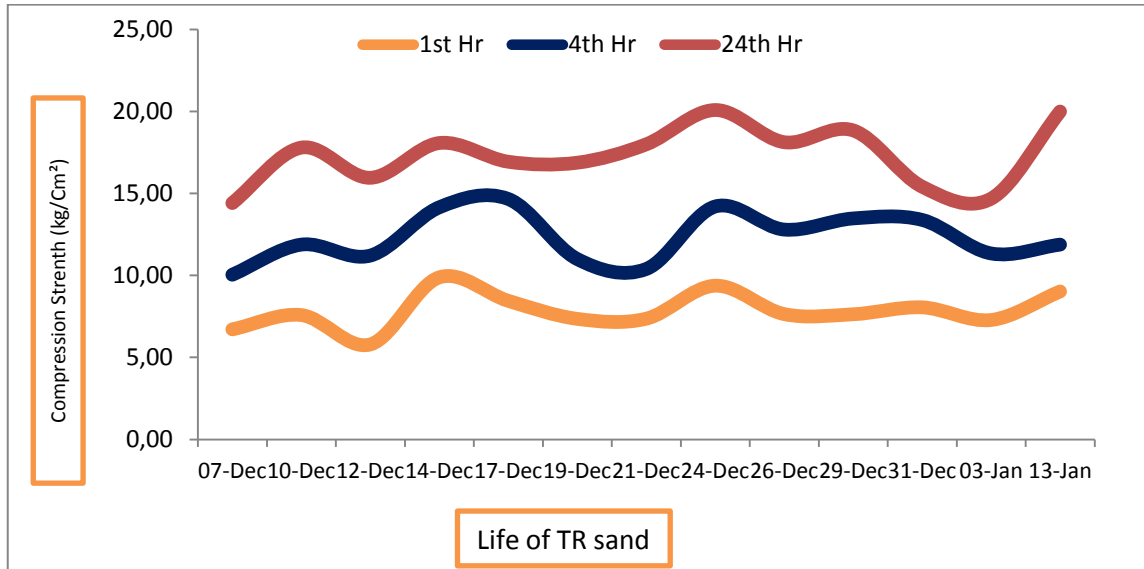


Figure 24. Compression strength of TR sand studied for a period of 5 weeks (data collected from foundry)

Table 13. New, TR & MR Sand properties

Parameter	Unit	New Sand	TR Sand	MR Sand
AFS no	None	48.06	43.35	46.31
LOI	%	0.688	0.390	1.83
Na	%	NA	0.019	0.161
K	%	NA	0.018	0.057

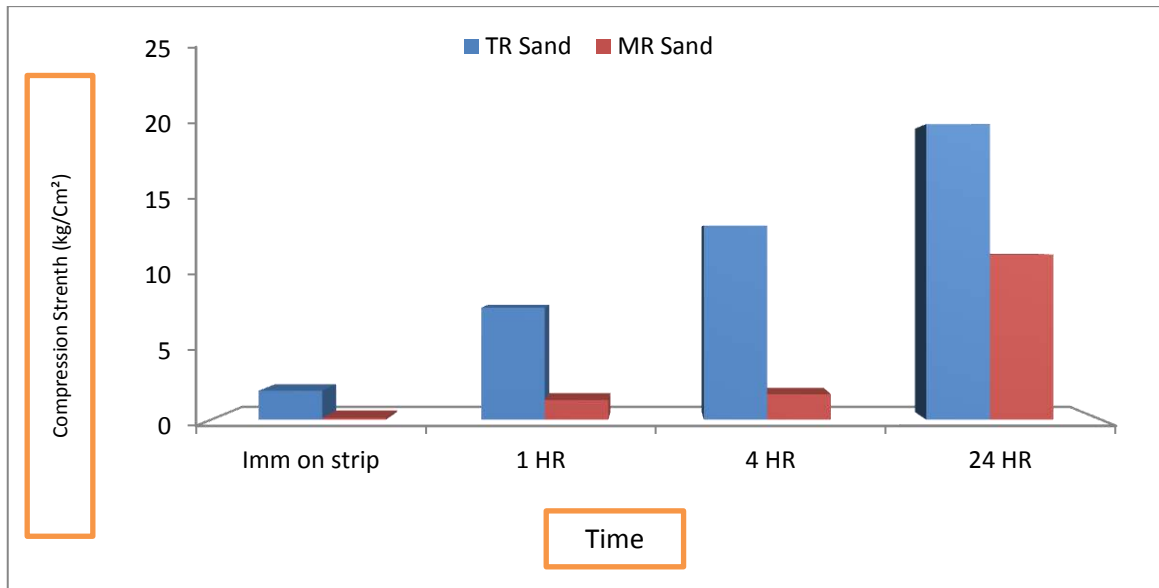


Figure 25. Compression Strength of TR sand (after one month of generation) @1.0:21 & MR Sand @1.2:21 with fast catalyst. RT-10-20 °C, RH- 58-73%

Remarks

1. This foundry uses minimum percentage of binder both in New/TR (1%) and MR (1.2%) Sand. Specification for 24-hour compression are 20 & 11 Kg/Cm² respectively i.e. in case of boxed molds, steel castings can be poured in molds with dry compression of as low as 20 Kg/cm².
2. Most phenomenal observation is that thermal sand generated using additive of supplier A loses stability on storage, right from day 1 to become inert towards reactivity with binder within a period of as low as a week.
TR sand generated using additive of supplier B is stable. Graphs are shown in Figure 24 & Figure 25.

CONCLUSIONS

1. Modern Alphasert is a sand binder system used for making molds and cores in foundries without application of heat or gas is most versatile among self -sets which can meet requirements for foundries pouring castings with varying chemistry and sizes, in boxed and flask less molds, at high as well as low sand temperature
2. With better understanding of chemistry, it has been possible to formulate recipe customized to meet specific requirements of individual customers
3. Two recent developments are reduction of smell of formaldehyde in work place making it more environment friendly than ever before and formulations much more stable than original ones
4. Regarding role of NaOH & KOH in formulations, both are having advantages and disadvantages. KOH based formulations are more effective for thermal reclamation and NaOH based in mechanical.

5. According to one study, in a steel foundry, cracks in castings could be eliminated along with increase in bench life of mixed sand and reduction in smell at work place after switching over from K to Na based formulations.
6. Formulations based on judicious blend of two alkali are more flexible than single alkali
7. It is always advisable to study dry, hot and retained strength requirements of molds from stripping to post pouring and develop customized formulations for individual foundries to get maximum benefits
8. Specifications for dry strength values should be laid down by generating data over a period of time and should be just enough to meet values at different stages of mold handling. It has been found that values as low as 20 Kg/cm² in TR/new sand and 10 Kg/cm² in MR Sand are good enough to produce steel castings weighing 10 MT in boxed molds. Specifying strength requirements more than required unnecessarily increases binder demand which in turn produces more gas and pushes the castings towards vulnerability for defects
9. There is scope for further studies on finding out effect of change of other variables main being P: F mole ratio. over wide range

REFERENCES

- [1] Foundry informatics center (center of excellence of the Institute of Indian Foundry men). (n. d.), Accessible on Internet: <http://foundryinfo-india.org/>, (20.06.2020.)
- [2] D. K. Ghosh, Comparison of molding sand technology between Alphasit (APNB) and Furan (FNB), Archives of Foundry Engineering, 19(2019)4
- [3] N. Murray, Self-set chemical binders: characteristics and influence on casting quality, Metel Asia: June 1998.
- [4] HA-International, LLC-US (2017). International publication number WO 2017/10556 A1 dt 396 22/06/17. International application published under the patent corporation treaty (PCT), 2017.
- [5] W. A. Gorby, WHEMCO and L. W. Markow and D. L. Winters, Borden, Binder behaviours examined, Modern casting, 1995.
- [6] M. Holtzer, Influence of Reclaim addition to the molding sand matrix obtained in the Alphasit technology on the emission of gases-comparison with molding sand with Furfuryl resin, Archives of foundry Engineering, 15(2015)1, pp. 121-125.
- [7] M. Lucarz et al, Comparison of properties of Alkali-Phenolic binders in terms of selection of molding sand for steel castings, Materials 12(2019)22, pp. 3705.



INFLUENCE OF ANNEALING OF AUSTENITIC STAINLESS STEELS ON PITTING CORROSION RESISTANCE

Almaida Gigović-Gekić*, Hasan Avdušinović, Amna Hodžić, Dejana Kasapović

University of Zenica Faculty of Metallurgy and Technology, Zenica, Bosnia and Herzegovina

Oral presentation

Expert work

ABSTRACT

Austenitic stainless steels are mostly used at high temperature and it is very important to know a behavior of these materials at temperature region of application. It is known that during heating of the austenitic stainless steel i.e. with increasing temperature and time of annealing a microstructure is changed. On the first place, there is precipitation of carbides followed by precipitation of secondary phases. Change of microstructure influence on steel properties especially on mechanical properties and corrosion resistance. In this work influence of annealing at 750 °C on the pitting corrosion resistance is presented. Change in microstructure as precipitation of carbides and formation of sigma phase decrease the pitting corrosion resistance.

Keywords: *austenitic stainless steel, pitting corrosion resistance, delta ferrite, carbides, sigma phase*

*Corresponding author (e-mail address): almaida.gigovic-gekic@mtf.unze.ba

INTRODUCTION

Austenitic stainless steel is widely used in almost all industrial sectors (transport, food, chemical, building industry etc.) thanks to good mechanical properties (strength and toughness at elevated and room temperature) and corrosion resistance. This type of stainless steels has different chemical compositions and properties but the common characteristic is the austenite microstructure stable at room temperature. Depending on chemical composition of austenitic steel, the presence of a delta ferrite is possible. The alpha-genic elements (Cr, Si, Ti, Al, Mo, V, Nb and W) stabilize and support the formation of the delta ferrite [1, 2]. The effects of the delta ferrite on the corrosion resistance of the austenitic stainless steels were not clearly understood yet. However, the effect of the delta ferrite on corrosion resistance of the austenitic stainless steel usually were explained with the formation of Cr depleted zone, low concentrations of Cr and Mo in austenite phase, precipitation of a sigma phase and segregation of sulfur or phosphorus along the δ/γ

interface [3]. As mention before the austenitic microstructure with or no the delta ferrite is stable on the room temperature but with heating that microstructure becomes unstable. Because the high temperature application of austenitic stainless steel it is important to study influence of the microstructure on mechanical and corrosion properties of these steels. During annealing or welding these steels, the precipitation of the carbides ($M_{23}C_6$, MC, M_6C and M_7C_3) is the first step followed by precipitation of other intermetallic phases (σ , χ , η , G, R and other phases). Presence of the delta ferrite in austenitic stainless steel helps the precipitation of the secondary phases especially carbides and sigma phases. Precipitation of carbides or sigma phase produces narrow chromium depletion regions usually within the grains or at δ/γ boundary. The chromium-depleted regions are susceptible to preferential corrosion attack because an austenite and the carbides or sigma phase produce galvanic effect i.e. difference between electrochemical potential. There are several techniques for testing of corrosion behavior of the austenitic stainless steels in different media but the most used is the electrochemical technique of cyclic polarization and potentiodynamic measurements in chloride-containing media [3-6].

MATERIALS AND METHODS

The aim of this work is to investigate an influence of the annealing of austenite stainless steel at 750 °C on the pitting corrosion resistance. Two types of samples were used for this testing, the sample with 10,38 % a delta ferrite and sample with 0,1 % delta ferrite. Chemical composition and the delta ferrite content of tested samples are given in Table 1. According to previous research increasing content of delta ferrite increases rate of sigma phase precipitation during annealing at high temperature [7]. Four samples were tested on the pitting corrosion resistance in 10 % $FeCl_3$ solution. Two samples were taken from the rod with 10.38 % delta ferrite. One sample was tested in solution annealed state (1030 °C/60 minutes/water) and second sample was first solution annealed and then annealed at 750 °C for 30 minutes and cooled in air. The aim of this annealing was decomposition of the delta ferrite and precipitation of the sigma phases. The same procedures repeated for the rod with 0.10 % delta ferrite.

Table 1. Chemical composition and the delta ferrite content of tested samples

Sample	Chemical composition, wt %								Delta ferrite, %	
	C	Si	Mn	Cr	Ni	N	P	S	Initial state	Annealed at 750 °C
1692	0.04	4.41	7.4	18.0	8.1	0.183	0.007	0.005	10.38	0.94
1720	0.05	3.9	9.0	16.0	8.7	0.179	0.007	0.006	0.10	0.00

The delta ferrite content was determined using magnetic induction method by Feritscope MP 30E-S probe EGAB 1.3 Fe. Microstructures of initial state of samples are presented in Figure 1 and 2. The metallographic examination was performed on Olympus optical microscope with max. magnification of 1000x. Murakami's (10 g $K_3Fe(CN)_6$, 10 g NaOH and 100 ml H_2O) and Kalling's (100 ml HCl, 5 g $CuCl_2$ and 100 ml C_2H_5OH) reagents were used for etching. Murakami's reagent at room temperature was used for identification of carbides

while heated at 100 °C was used for identification of the delta ferrite and sigma phase. Murakami's reagent at high temperature (90-100 °C) colored the delta ferrite in brown and the sigma phase in blue. Kalling's reagent was used for identification of the delta ferrite. Microstructure of the sample 1692 at room temperature is austenitic with the delta ferrite stringers elongated in the rolling direction. After annealing at 750 °C for 30 minutes, delta ferrite, sigma phase and carbides were present in the austenitic microstructure. From Table 1, it can be seen that the content of delta ferrite decreased after annealing at 750 °C for sample 1692. The delta ferrite decomposed on the carbides, secondary austenite and sigma phase. The carbides precipitation at the austenitic grain boundary was observed too. Microstructure of 1720 sample is austenitic at room temperature but the carbides precipitation at the austenitic grain boundary after annealing at 750 °C for 30 minutes was occurred.

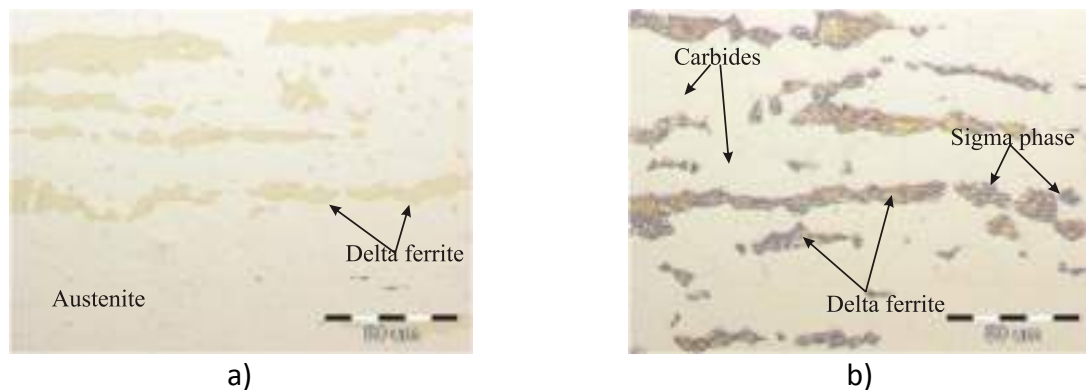


Figure 1. Microstructure of sample 1692: a) solution annealed state and b) annealed at 750 °C for 30 minutes, Murakami's reagent, 500x

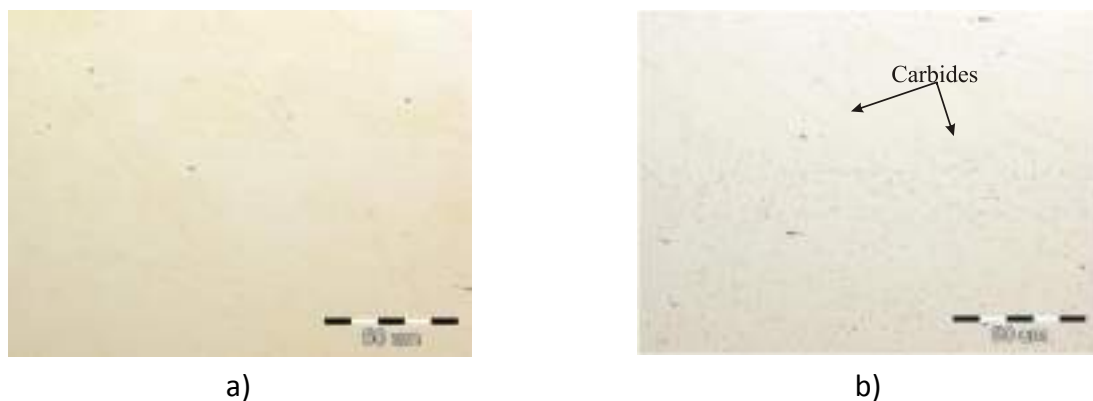


Figure 2. Microstructure of sample 1720: a) solution annealed state and b) annealed at 750 °C for 30 minutes, Murakami's reagent, 500x

Corrosion testings were conducted in the corrosion cell according to Standard ASTM G5, on instrument potentiostat/galvanostat, Princeton Applied Research, model 263A-2, with the software PowerCORR® (Standard, ASTM G5-94). Investigation was performed in 10% FeCl₃ solution. Method of cyclic polarization was used for investigation of pitting corrosion. Tests were performed at room temperature, 20±1 °C. A standard three-electrode corrosion cell was used. The working electrode was austenitic stainless steel (in the initial and annealed

state with different content of the delta ferrite) in the form of a disk who embedded in a holder having an exposed area of $A = 113.1 \text{ mm}^2$. A saturated calomel electrode (SCE) used as the reference electrode with a constant potential (0.2415 V) and as a counter electrode two graphite rods were used. Potential was measured versus the reference electrode. The method of cyclic polarization includes scanning of the potential to a vertex potential and reverses at the current threshold after crossing the vertex potential. Scan rate was 0.5 mV/s in the range of potentials from -0.2 to 0.25 V.

RESULTS AND DISCUSSION

Pitting corrosion of stainless steels is manifested by the rapid growth of current after achieving specific values of anode potential, pitting potential (E_{pitt}). Pitting potential is the potential at which pitting starts and that phenomenon is noticed when the current of the polarization curve suddenly start to rise. Surface of hysteresis loop is generally measure of the intensity of pitting corrosion. Generally, alloys that are susceptible to pitting corrosion exhibit a large hysteresis [8-10]. The results of pitting corrosion tests of investigated samples are given in Figure 3 and Table 2. The pitting potential was measured at the inflection point [11].

Table 2. The values of pitting potential for tested samples

Pitting potential	1692p Initial state	1692z Annealed state	1720p Initial state	1720z Annealed state
$E_{\text{pitt}}, \text{V}$	0.13	0.11	0.07	0.05

From the results presented in Table 2 could be seen that there is no significant difference between results but the samples in the initial state had more positive (higher) pitting potential in regard to the annealed state. According that more negative values (lower) of the pitting potential (E_{pitt}) of the samples in the annealed state indicate a greater tendency to form pits compared to samples in the initial state where the E_{pitt} is somewhat more positive. Sample 1692p showed slightly better resistance to pitting corrosion compared to sample 1720p although having higher delta ferrite contents. The reason for this may be a higher content of chromium because the resistance to pitting corrosion can also be described by a pitting resistance equivalent (PRE) which is often defined as [10]

$$\text{PRE} = \text{Cr} + 3.3\text{Mo} + 16\text{N}, \text{ wt.}\%$$

According to this formula, sample 1692 has a higher PRE number (PRE=20.93) and therefore has greater pitting corrosion resistance.

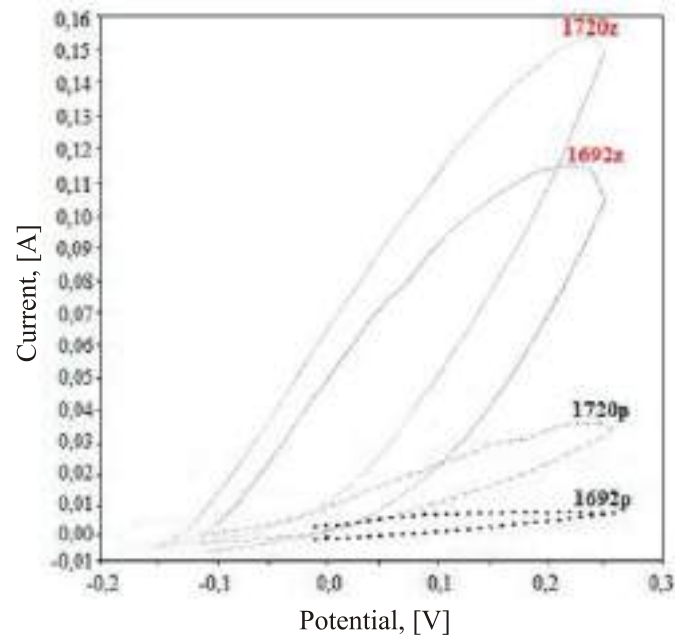


Figure 3. Cyclic polarization curves of samples tested in 10 % FeCl₃ solution

The results in Figure 3, show that sample solution annealed (1692p and 1720p) has smaller surfaces of hysteresis loop compared to sample annealed at 750 °C. It means that samples 1692z and 1720z has more intense pitting corrosion. Analysis of macrostructure and microstructure of samples 1692 and 1720 tested on pitting corrosion is shown in Figure 4-7. Analysis of macrostructure show that the highest concentration of pits was on sample 1692 in annealed state.

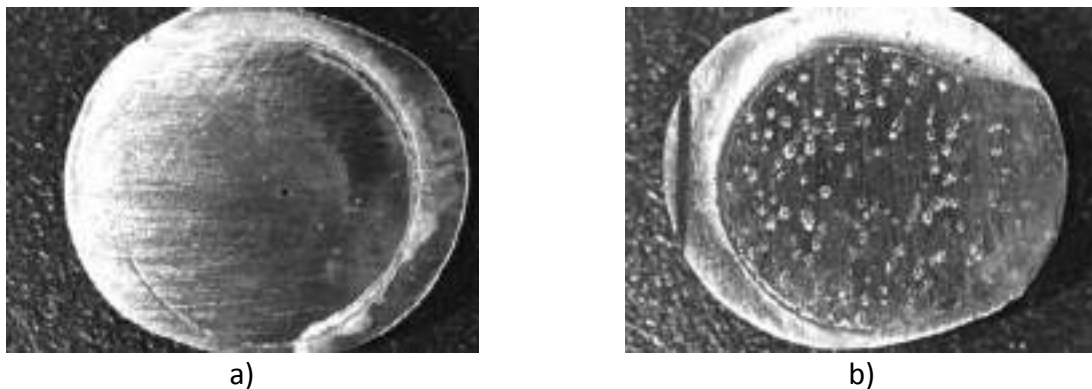


Figure 4. Macrostructure of sample 1692 tested on the pitting corrosion resistance in 10% FeCl₃: a) initial state and b) annealed at 750 °C, 8x

It is known that a thin protective passive film is formed on the surface of austenitic stainless steels consisting of mixed oxides of chromium and iron. This film provide excellent corrosion resistance but under certain condition, particularly in the presence of chloride ions, it could be damaged at weak sites as like as second phases, inclusions, grain boundaries etc. [1, 10]

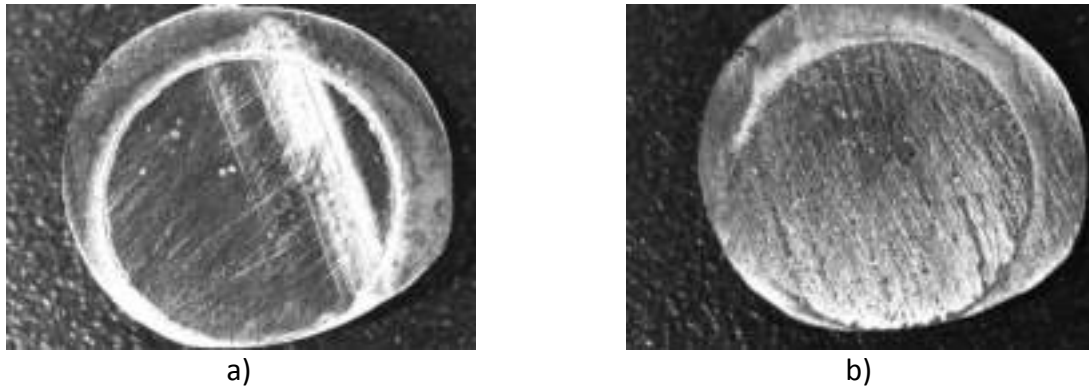


Figure 5. Macrostructure of sample 1720 tested on the pitting corrosion resistance in 10% FeCl_3 : a) initial state and b) annealed at 750 °C, 8x

From the microstructure analysis of 1692 samples (Figure 6) could be seen that the pits were found just on the boundary between austenite and delta ferrite phase as like as on the place of the sigma phases precipitating from the delta ferrite during annealing. Formation of the pits was aided precipitation of carbides on austenite/delta ferrite boundary too.

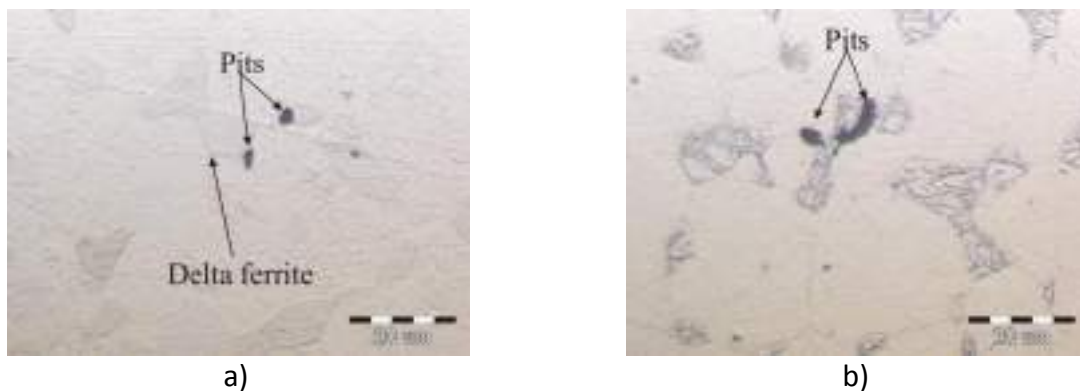


Figure 6. Microstructure of sample 1692 tested on the pitting corrosion resistance in 10% FeCl_3 : a) initial state and b) annealed at 750 °C, Kalling's reagent, 1000x

In the case of sample 1720 (Figure 7), the pits were formed near inclusions in initial state and on the austenite grain boundary in annealed state because precipitation of carbides.

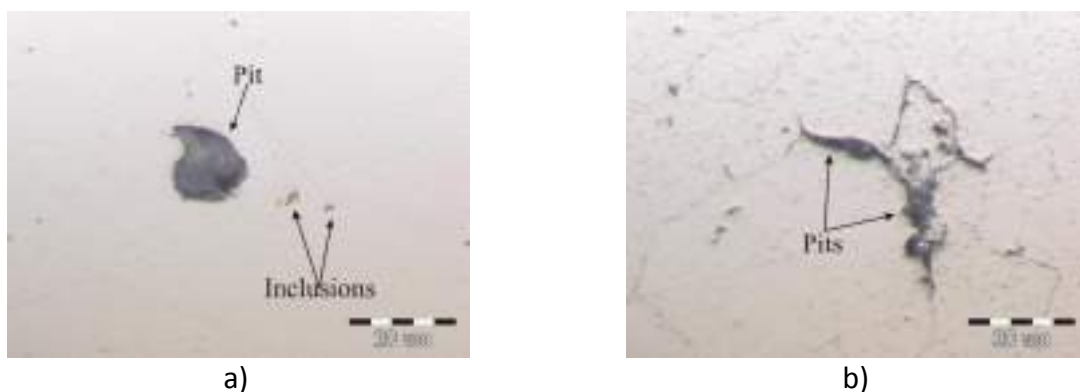


Figure 7. Microstructure of sample 1720 tested on the pitting corrosion resistance in 10% FeCl_3 : a) initial state and b) annealed at 750 °C, Kalling's reagent, 1000x

The main reason for a pitting formation on austenite/delta ferrite, sigma/austenite and austenite/carbide interfaces is the depletion of major alloying elements like chromium in the austenite phase due to the formation of the secondary phases that are rich in these element i.e. formation of a galvanic effect (difference between electrochemical potential) [1, 3-6].

CONCLUSIONS

In this paper the results of influence of austenitic stainless steel annealing at 750 °C for 30 minutes on pitting corrosion in 10% FeCl₃ are presented. From the results it can be concluded that change of initial microstructure during annealing at higher temperature decrease resistance to pitting corrosion of the austenitic stainless steels. The carbides precipitate at the delta ferrite and austenitic grain boundaries. The sigma phase is formed at the delta ferrite. Formations of these phases decrease the pitting corrosion resistance of austenitic stainless steel.

REFERENCES

- [1] H. S. Khatak, B. Raj, Corrosion of austenitic stainless steels mechanism, Mitigation and Monitoring, Narosa Publishing House, New Delhi, 2002.
- [2] A. Gigović-Gekić, M. Oruč, H. Avdušinović, R. Sunulahpašić, Regression analysis of the influence of a chemical composition on the mechanical properties of the steel Nitronic 60, *Materiali in Tehnologije*, 48(2014), pp. 433-437.
- [3] S. Y. Kim, H. S. Kwon, H. Kim, Effect of delta ferrite on corrosion resistance of type 316 stainless steel in acidic chloride solution by micro-droplet cell, Accessible on Internet: www.scientific.net/SSP.124-126.1533, (03.03.2018.)
- [4] A. Kocijan, M. Conradi, The corrosion behaviour of austenitic and duplex stainless steels in artificial body fluids, *Materials and Technology*, 44(2010), pp. 21-24.
- [5] O. Osoba, R. A. Elemuren, I. C. Ekpe, Influence of delta ferrite on corrosion susceptibility of AISI 304 austenitic stainless steel, Accessible on Internet: <https://www.tandfonline.com/doi/full/10.1080/23311916.2016.1150546>, (13.01.2020.)
- [6] S. S. M. Tavares, G. F. Feijo, H. N. Farneze, M. J. R. Sandim, I. R. S. Filho, Influence of microstructure on the corrosion resistance of AISI 317L (UNS S31703), Accessible on Internet: <http://dx.doi.org/10.1590/1980-5373-MR-2016-1107>, (13.01.2020.)
- [7] A. Gigović-Gekić, M. Oruč, S. Muhamedagić, Effect of delta ferrite content on the tensile properties in Nitronic 60 steel at room temperature and 750 °C, *Materials and Technology*, vol. 46(2012), pp. 519-523.
- [8] F. Bikić, D. Mujagić, Investigation of possibility for reducing AISI 303 stainless steel pitting corrosion by microalloying with boron or zirconium, *Bulletin of the Chemists and Technologists of Bosnia and Herzegovina*, 42(2014), pp. 41-46.
- [9] S. Čatić, A. Odošajić, H. Keran, Ispitivanje nehrđajućih čelika na piting koroziju, *Proceedings of International Symposium of MNM 2008, Fakultet za metalurgiju i materijale*, 22-23. 05. 2008, Zenica, BiH, pp. 343-347.
- [10] G. S. Frankel, *ASM Handbook Vol. 13A*, (Editors: D. Cramer, B. S. Covino), ASM International, OH, 2003.

[11] M. Iannuzzi, How to determine pitting and repassivation potentials, Accessible on Internet: www.aboutcorrosion.com/2014/04/13/howto-determine-pitting-and-repassivation-potentials, (21.02.2020.)



19th INTERNATIONAL FOUNDRYMEN CONFERENCE

Humans - Valuable Resource for Foundry Industry Development

Split, June 16th-18th, 2021

<http://www.simet.hr/>

APPLICATION OF COMPUTER SIMULATION FOR VERTICAL CENTRIFUGAL CASTING

Karlo Jurković¹, Sebastjan Kastelic², Primož Mrvar², Branko Bauer^{1*}

¹ University of Zagreb Faculty of Mechanical Engineering and Naval Architecture, Zagreb, Croatia

² University of Ljubljana Faculty of Natural Sciences and Engineering, Ljubljana, Slovenia

Oral presentation

Preliminary work

ABSTRACT

Vertical centrifugal casting is used for casting of tubes where the diameter is larger than the length or it is used for cone shaped castings. Both non-cylindrical and asymmetrical parts can be casted using this process. Short tubes, slide bearings and smaller ring-shaped products are commonly casted. Simulation helps to understand filling and solidification process and casting parameters. A significant problem of vertical centrifugal casting is related to the solidification process. Using simulation software, which is based on the finite element method, it is possible to find optimal parameters and thus reduce the occurrence of defects. Also, using the software leads to significant savings on the production line, the production is more economical with better quality, extended product life and better mechanical and tribological properties of the castings. The main parameters that need to be defined are pouring rate, pouring temperature, mould temperature and rotational speed of the mould.

Simulation of filling and solidification was carried out using ProCAST software to determine influence of parameters on final quality of stainless-steel casted tube. According to the results of simulation, rotational mould speed of 1400 rpm and the pouring temperature of 1510 °C are recommended.

Keywords: *centrifugal casting, casting parameters, numerical simulation, stainless steel, ProCAST software*

*Corresponding author (e-mail address): branko.bauer@fsb.hr

INTRODUCTION

Today, the world is on the edge of a new industrial era based on the fast – evolving technology. As a response to technological changes in the metalworking industry and high customers requirements in the global market, vertical centrifugal castings are gaining application. Vertical centrifugal casting process is used for producing pipes (tubes) or a shapes connected to a pipe such as an elbow, a safe end, or nozzle that are relatively large in

diameter and short in length. The usual maximum length of the casting is two times the outside diameter of the casting. The mould is a cavity for production of a solid casting of the desired shape and size. Vertical axis machines are also used for production of castings of asymmetrical configurations. The gating system of centrifugal castings usually employs a single gate, which combines the function of gate and riser. Centrifugal force greatly magnifies the feeding action of the riser and produces a greater metal density in the casting than would otherwise result [1, 2].

Stainless steel castings have a tremendously wide scope of application resulting from the ability to produce components of both complex shape and of compositions which afford excellent corrosion resistance and high temperature properties. Compared to other casting processes, the advantages of vertical centrifugal casting of stainless steel are: fine grain structure with good mechanical properties, good dimensional stability, excellent weldability and reduced scrap [2].

Centrifugal casting defects mainly relate to the solidification process, so the main aspect is understanding the solidification process in vertical centrifugal casting and identification of optimal parameters. Numerical simulation technology is widely utilized to simulate the temperature field, solidification, segregation, and microstructure evolution during the casting process, so casting has advanced from a non-visible to a visible process. Lu et al. [3] studied the casting defects that appear on the inside surface of a wet-type cylinder liner. The modelling of fluid flow has been examined and the thermal solidification and microstructure evolution behaviour of vertical centrifugal casting have been explored using the ProCAST software. Based on these analyses, the process of vertical centrifugal casting could be optimized. It is expected that the results would help to reduce scrap and improve the quality of product. Mohapatra et al. [4] analysed effect of processing factors on the characteristics of centrifugal casting. The pouring rate, pouring temperature, mould temperature and mould material can be suitably selected and altered in isolation or in combination, to generate a desired thermal gradient in the melt which decides its cooling rate. The cooling rate of the melt has the greatest impact on the grain structure of the casting. Dong et al. [5] studied simulation on filling and solidification of horizontal centrifugal casting Babbitt lining of bimetallic bearing. The simulation results showed that the rotational speed and the pouring rate had effects on the flow behaviour of the metallic melt in the filling process. The cooling method had a significant influence on the solidification rate of each location inside the casting and also on the grains size, which defines the mechanical property of the casting. Ali [6] studied the optimization of centrifugal casting parameters of AlSi alloy by using design of experiments and the response surface methodology. Sen et al. [7] studied flow behaviour in vertical centrifugal casting. Based on the results of cold modelling studies, it has been found that with increase in mould diameter, G force increases which results in formation of fluid cylinder of better dimensional accuracy.

In this paper, the filling and solidification processes of vertical centrifugal casting, Figure 1, were simulated using the technology of computer simulation of casting process in software ProCAST. The effects of centrifugal casting parameters such as, pouring temperature and mould rotational speed were investigated by the simulation analysis.

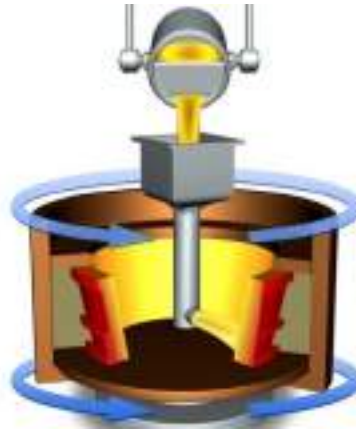


Figure 1. Vertical centrifugal casting process [8]

MATERIALS AND METHODS

The stainless steel tube casting process was simulated for production in vertical centrifugal casting machine. The schematic representation of mould and induction heated ladle is shown in Figure 2. The molten metal is poured from the ladle into the bottom of mould cavity. Due to the influence of centrifugal force, molten metal flows towards the mould wall.

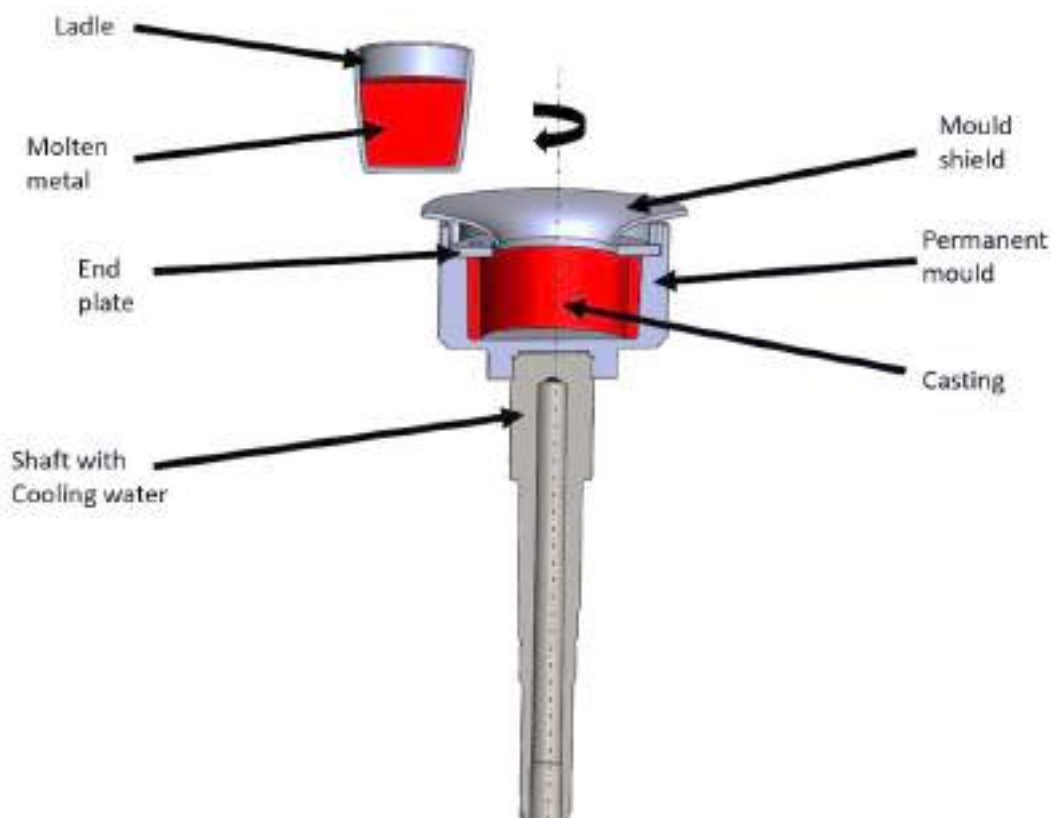


Figure 2. Mould and ladle setup in centrifugal casting machine

The size of the mould determines the outer dimensions of the desired tube while the amount of melt in the ladle determines its thickness. Diameter of the mould amounts to 84

mm and height of the mould amounts to 42 mm. The mass of the molten metal contained in the ladle amounts to 0.56 kg. Casting with an outer diameter of 84 mm, a height of 42 mm and thickness of 7mm was obtained, Figure 3.

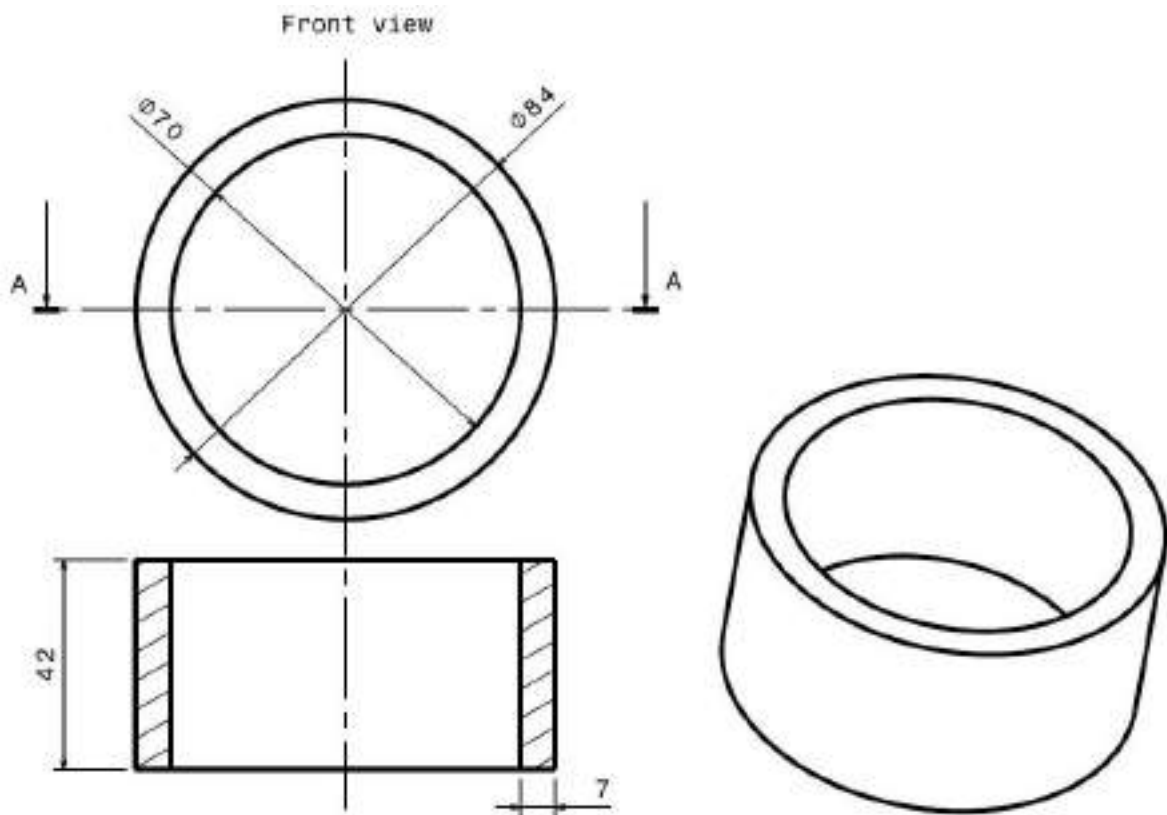


Figure 3. Dimensions of casting

The casting material is austenitic stainless steel EN 1.4581 (GX5CrNiMoNb19-11-2). According to ProCAST database the liquidus temperature amounts to 1442 °C and solidus temperature amounts to 1343 °C. To study the effect of pouring temperature, in this paper pouring temperature was set at 1485 °C and 1510 °C. The molten stainless steel density at 1500 °C amounts to 7100 kg/m³. The mould is made of EN 1.2343 (X37CrMoV5-1) which is equivalent to AISI H11 alloy tool steel for hot working. The coating was not used because the mould filling was primarily investigated. Heat transfer coefficient HTC between liquid metal and the mould was set on 2000 W/m²K. Preheating mould temperature was 400 °C. Cooling was provided through water cooled shaft with water temperature of 25 °C. The shaft is made of duplex stainless steel EN 1.4507 in quenched and tempered condition. The mould temperature field just before casting is shown in Figure 4.

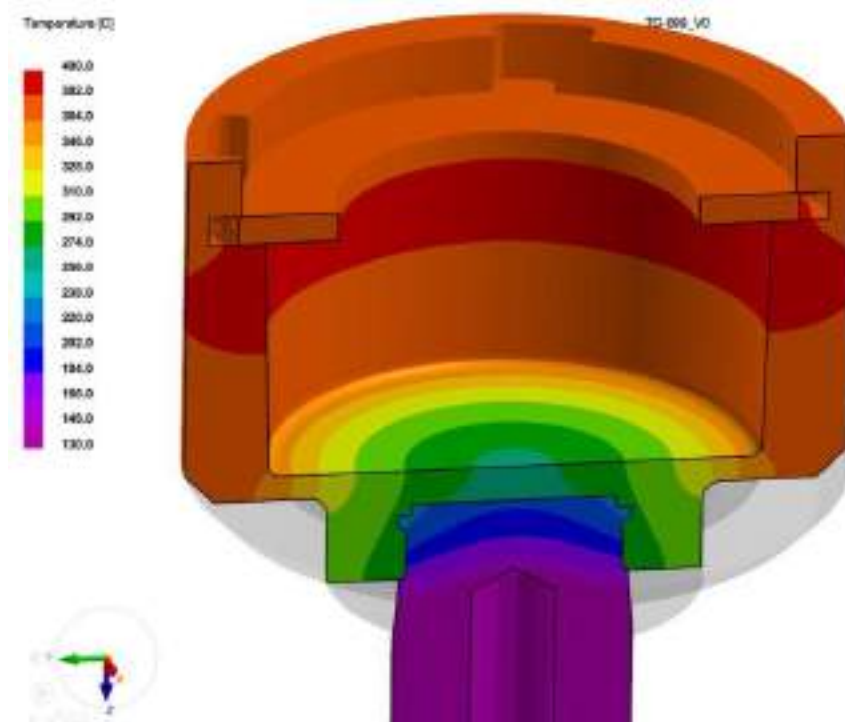


Figure 4. Temperature field of mould before casting

The next parameter is pouring rate (inlet velocity), another description of pouring time. The relationship between the pouring time, the filling limit and the inlet velocity is as follows:

$$Pouring\ time = \frac{Volume \times Filling\ limit\ (\%)}{Area \times Inlet\ velocity} \quad (1)$$

For full filling limit (100%), the pouring time is 1.05 s. Inlet velocity decreases with time as the ladle turns in order to pour the melt. The initial velocity starts with 1.5 m/s and ends with 1.3 m/s. Inlet velocity curve from ProCAST is shown in Figure 5. The diameter of inlet was 8 mm. The melt is poured directly into the centre of mould cavity.

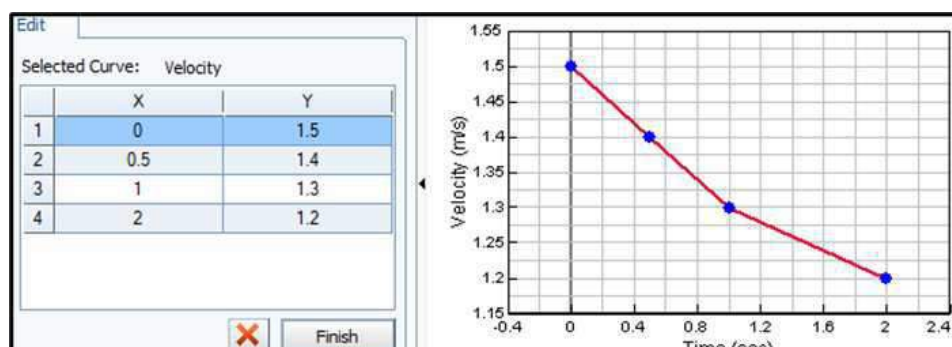


Figure 5. Inlet velocity as a function of time

The most important parameter is the mould rotational speed. It is calculated according to the following formula:

$$n = 264 \sqrt{\frac{h}{r_1^2 - r_2^2}} \quad (2)$$

where n is the mould rotational speed, h is the height of the casting and r_1 is the inner radius at the top of the casting, while r_2 is inner radius (in inches) at the bottom of the casting [1].

Also, it is clearly defined that gravitational force and centrifugal force act on the casting at the same time. The centrifugal force must be higher than the gravitational force. The optimal speed of rotation for vertical centrifugal casting results in a centrifugal force of 75 g (75 times the force of gravity) on the inside diameter. According to the nomograph in reference [1] for casting inside diameter 70 mm at a centrifugal force of 75 g, rotational speed of mould amounts to 1400 rpm. To study the effect of rotational speed, in this paper rotational speed was set at 700, 1000 and 1400 rpm.

The main aim of the experiment is providing a better understanding of the process of filling, solidification, distribution of tensile and compressive stresses and changes caused by: different speeds of rotation of the mould and changes in pouring temperature. In this way, it is possible to obtain more accurate dimensions of the casting, better surface quality and the ability to predict the location of defects.

RESULTS AND DISCUSSION

The filling process and temperature field of casting with mould rotational speed 1400 rpm and pouring temperature 1485 °C is shown in Figure 6.

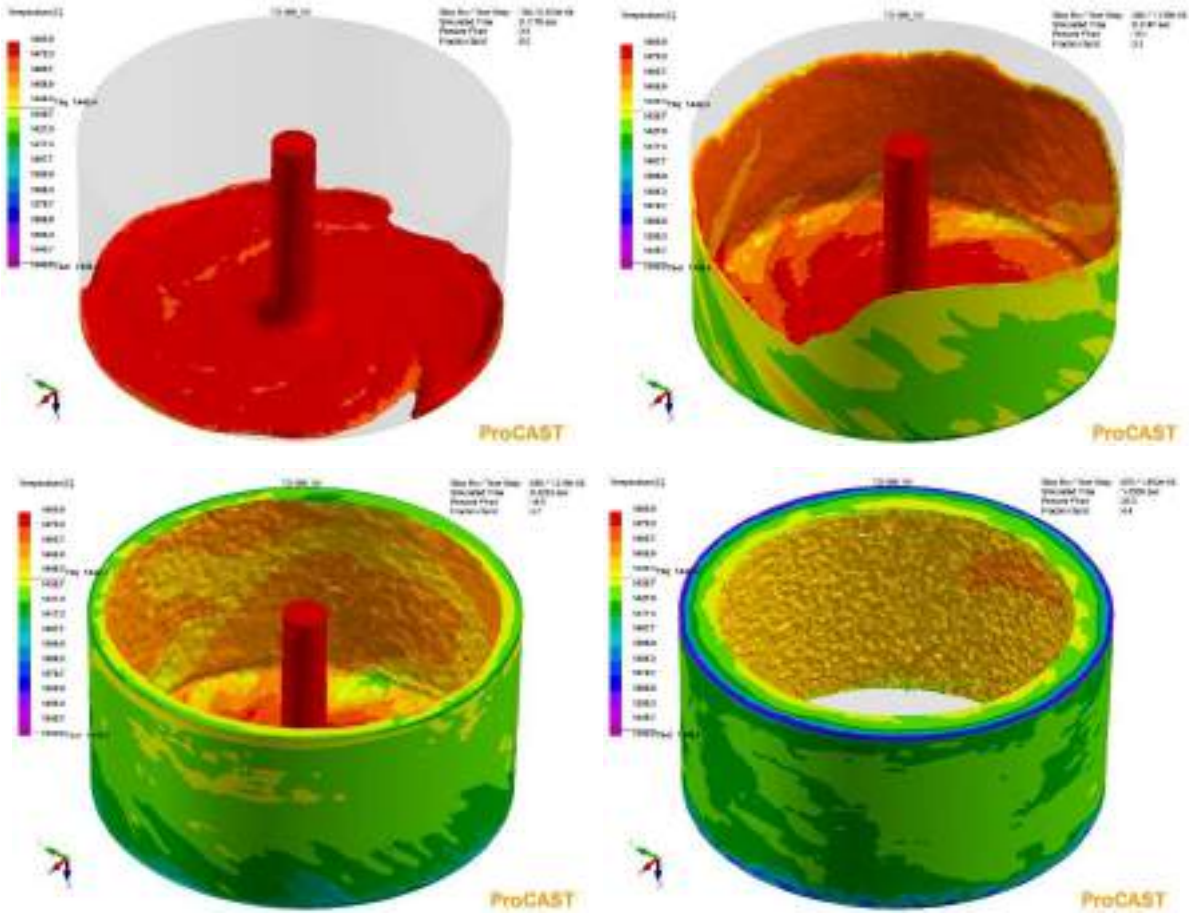


Figure 6. Process of filling at rotational speed 1400 rpm and pouring temperature 1485 °C

At the end of filling, the solidification process has already started along the edges of the tube. The results (Fraction Solid) show that the percentage of solidified material at the end of filling is 4.4%.

The process of solidification starts from the outer edges and continues further towards inner radius and middle of the casting, Figure 7. The solidification takes place evenly and opposite to the direction of heat dissipation. With the given parameters, the solidification time for the casting is 13.5 s, and the solidification direction can be seen in Figure 7.

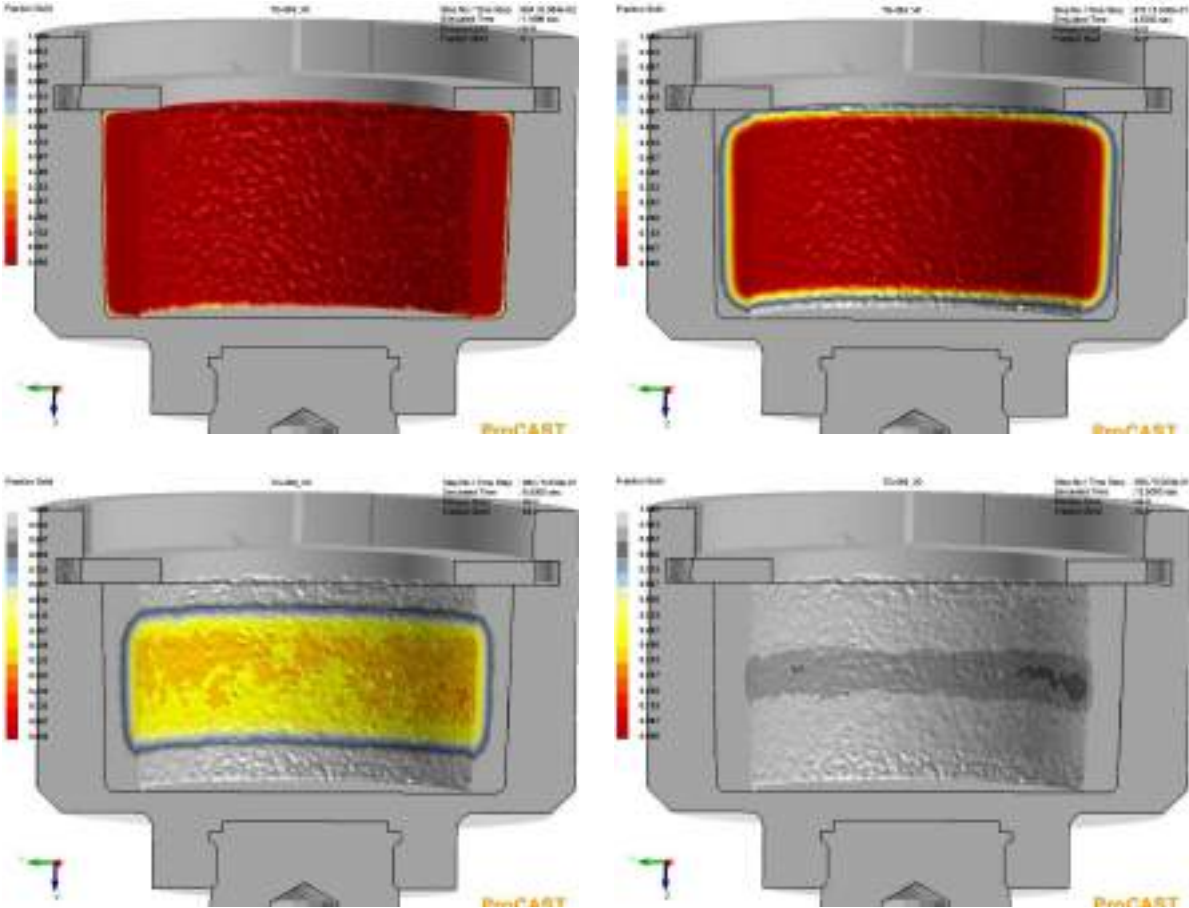


Figure 7. Solidification of the casting

Since the middle of the casting solidifies last i.e. the casting is fed from the middle, the greatest possibility of a casting defects is in that part. Hence, a detailed analysis of surface is recommended in this area.

In order to analyse the effect of rotational speed, after initial experiment with 1400 rpm, two lower rotational speeds were set; 700 and 1000 rpm. The following analysis shows the solidification results at the end of filling as a function of the mould rotational speed. It is noticeable, at different rotational speeds, the simulations show different percentages of solidified material Table 1.

Table 1. Fraction of solidified material at the end of filling as a function of the mould rotational speed

	Mould rotational speed (rpm)	Fraction solid (%)
1.	700	3,3%
2.	1000	2,7%
3.	1400	4,4%

Temperature field of casting at the end of filling and fraction solid (%) at the different mould rotational speeds are shown in Figure 8. It was determined by simulation that at the highest mould rotational speed, fraction solid is highest, 4,4%. That was expected due to higher centrifugal force the pressure on the mould wall was higher and the cooling was faster. At middle rotational speed 1000 rpm fraction solid is lowest what was not expected and need to be further investigated.

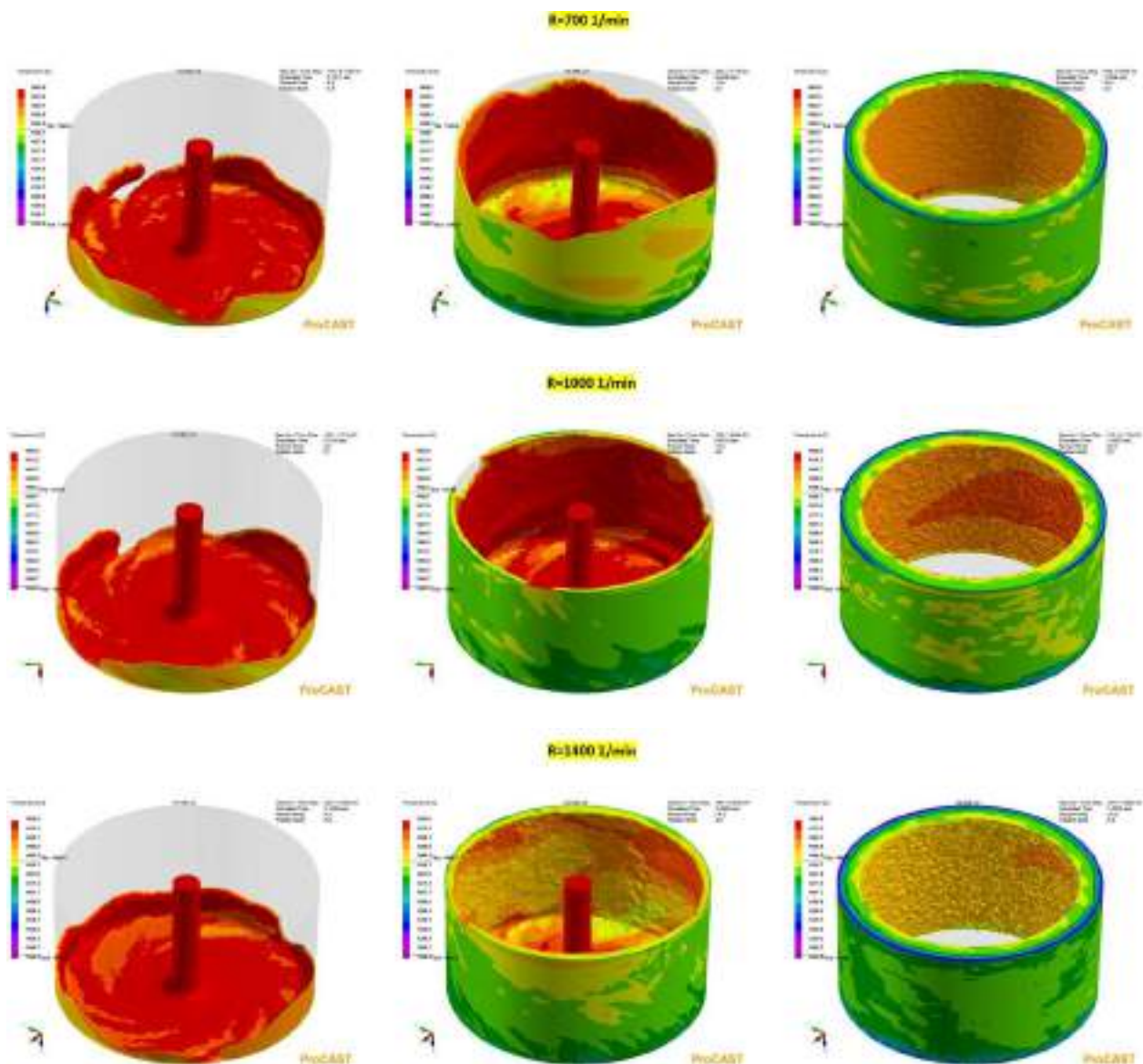


Figure 8. Temperature field and fraction solid (%) at the different mould rotational speeds

Figure 9 shows molten metal velocity along the tube wall at different mould rotational speeds, 0.88 s after pouring start. The melt rises upwards in parallel layers for rotational speed of the mould 1400 rpm. At lower rotational speeds, the wave is formed in bottom part and the flow is not parallel, also, the wall thickness is smaller in the upper part. Analysis of the influence of mould rotational speed is showing that a speed of 1400 rpm is more suitable.

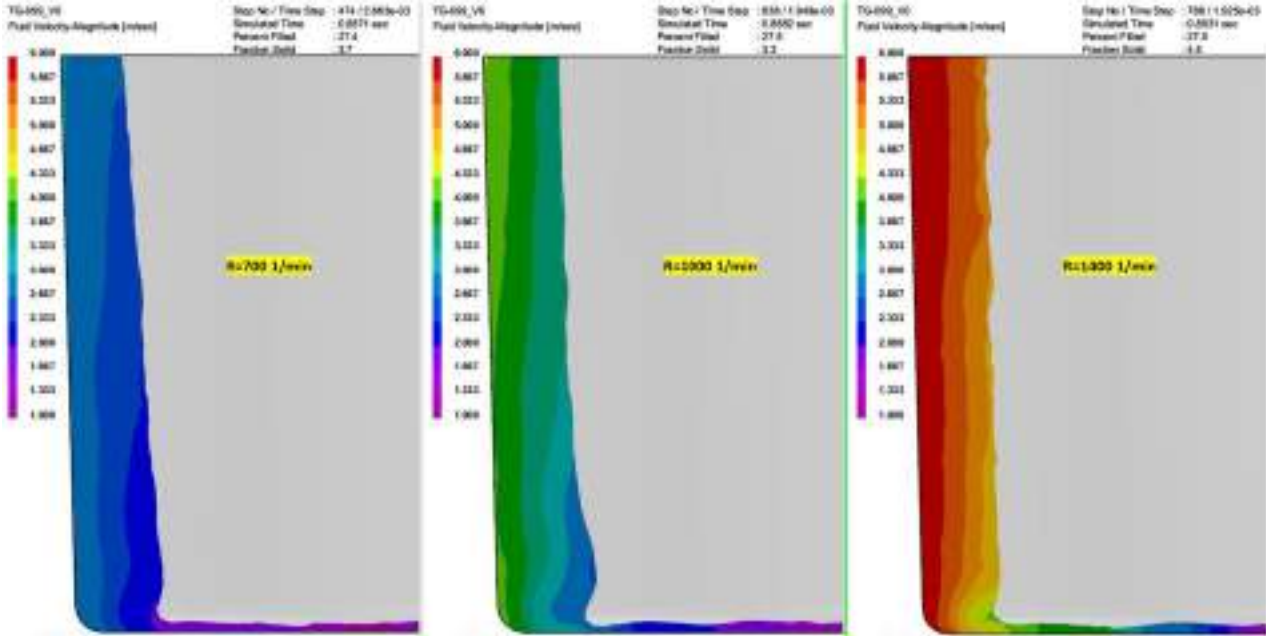


Figure 9. Molten metal velocity along the tube wall at different mould rotational speeds, 0.88 s after pouring start

Figure 10 shows process of filling and temperature field of casting at rotational speed 1400 rpm and pouring temperatures 1485 °C and 1510 °C. The melt with higher pouring temperature has higher viscosity and fills the outer wall of the tube after 0.37 s, while the melt with lower pouring temperature needs 0.45 s. The initial pouring temperature affects also the solidification process. The results (Fraction Solid) show that the percentage of solidified material at the end of filling is 2.8% for higher pouring temperature and 4.2% for lower pouring temperature. Analysis of the influence of pouring temperature is showing that a pouring temperature of 1510 °C is more suitable.

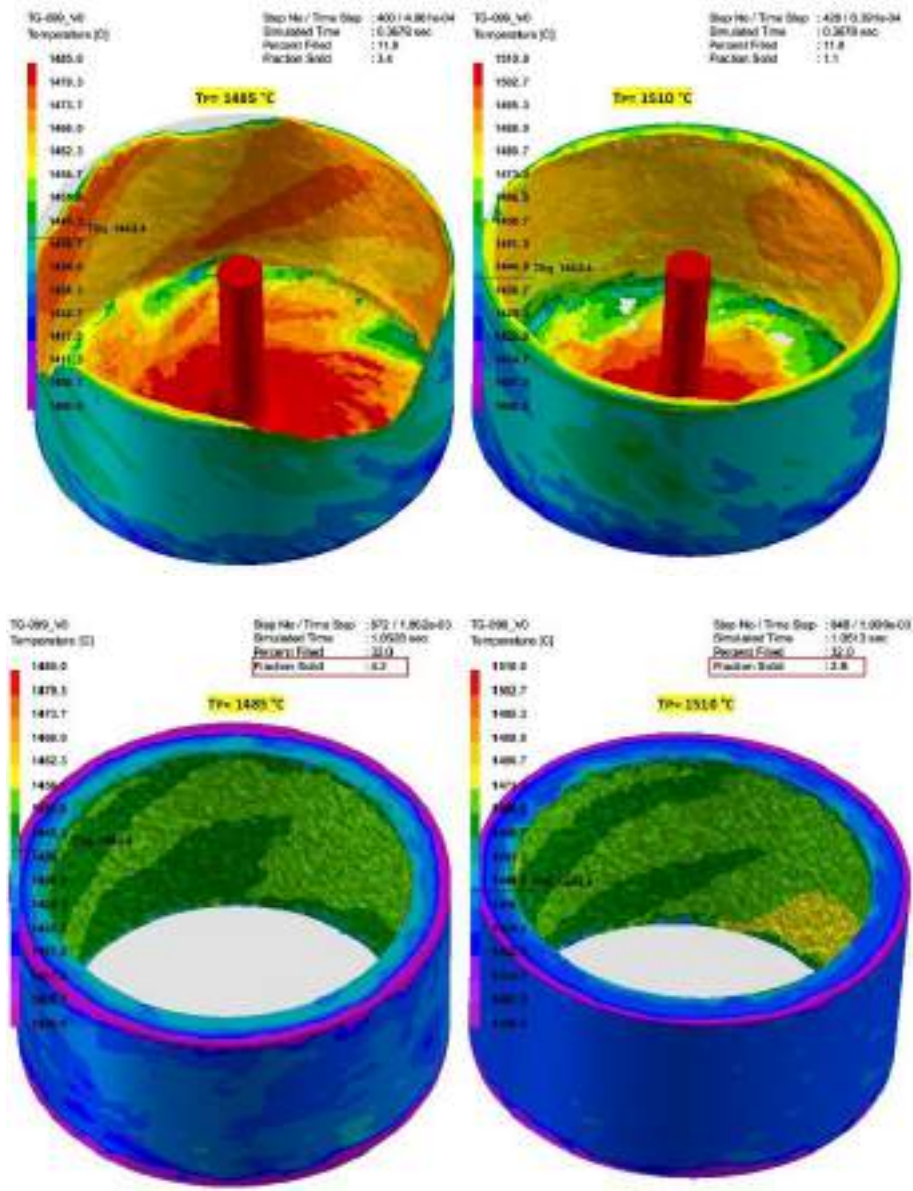
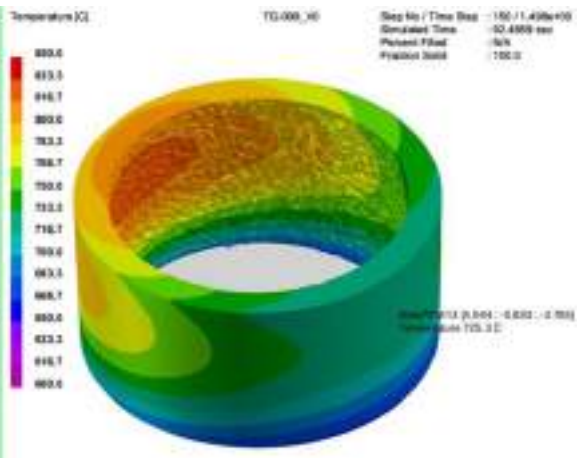
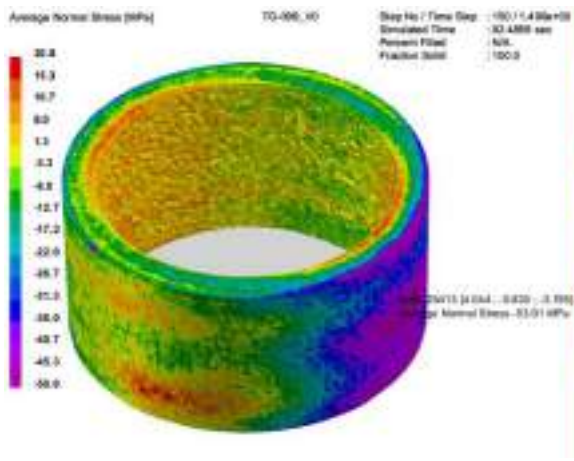
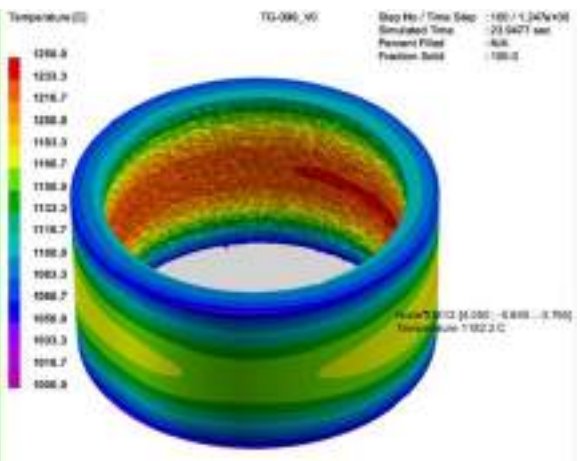
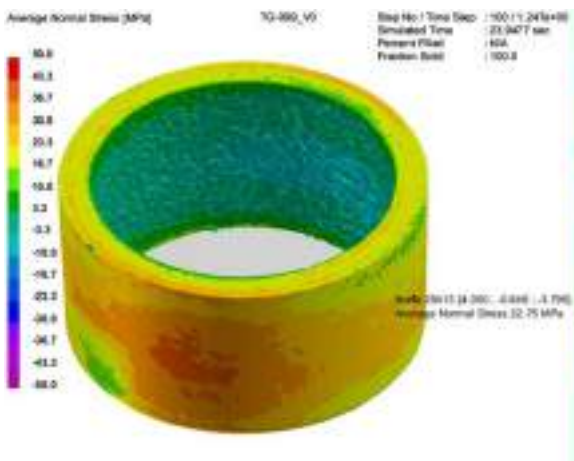
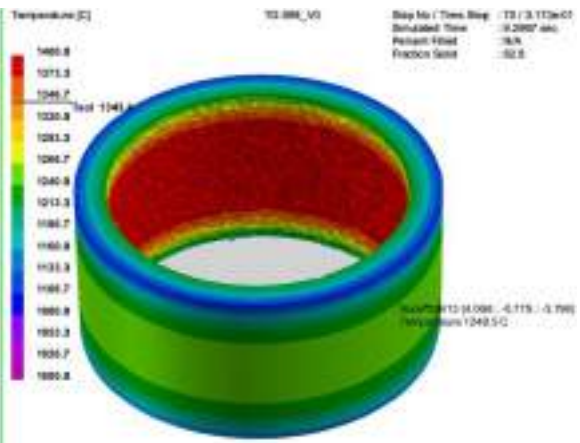
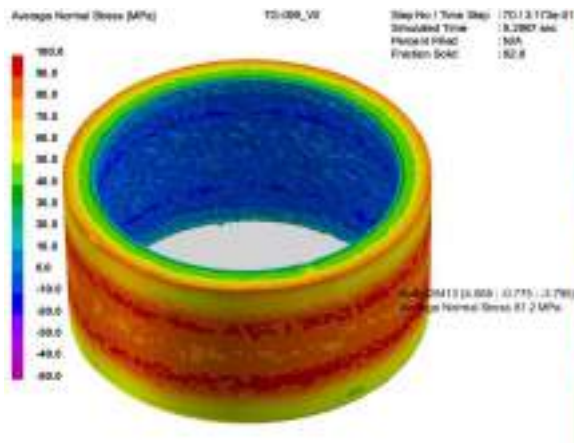


Figure 10. Process of filling at rotational speed 1400 rpm and pouring temperatures 1485 °C and 1510 °C

Figure 11 shows the distribution of average normal tensile and compressive stresses in the tube at the different temperatures i.e. cooling times, Table 2. Rotational speed was 1400 rpm and the pouring temperature amounted to 1485 °C. As the casting cools, the stresses shift from the tensile to the compressive. After 318.6 seconds, the cooling effect of the shaft on the thermal field of the casting is visible, Figure 11.



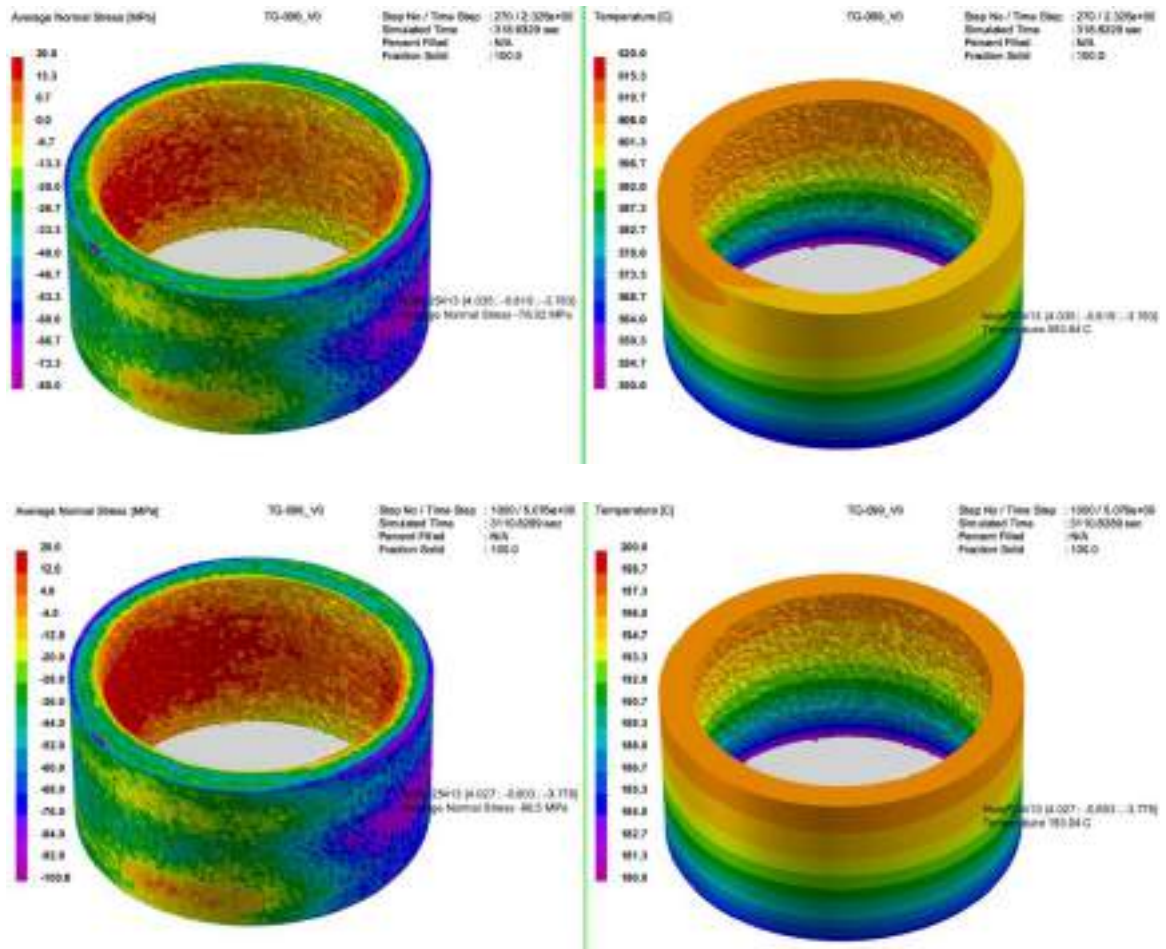


Figure 11. Tensile and compressive stresses at the different temperatures i.e. cooling times, mould rotational speed 1400 rpm, pouring temperature 1485 °C

Table 2. Results of average normal stresses

	Stress (MPa)	Temperature (°C)	Fraction solid (%)	Time (s)
1.	81,2	1248,5	82,8	9,3
2.	22,75	1182,2	100	23,9
3.	-53,91	725,3	100	92,5
4.	-76,02	593,84	100	318,6
5.	-96,5	193,04	100	3110,8

After solidification, the casting contracts away from the mould surface and air gap forms. It also contracts in height. The lengths of the casting along the X and Y directions were measured before solidification and after cooling (52 min after pouring). Deformation along the x-axis amounts to 0.84 mm and along the y-axis 0.83 mm, Figure 12. As a consequence of stress, deviation in the dimensions of the casting is additionally possible.

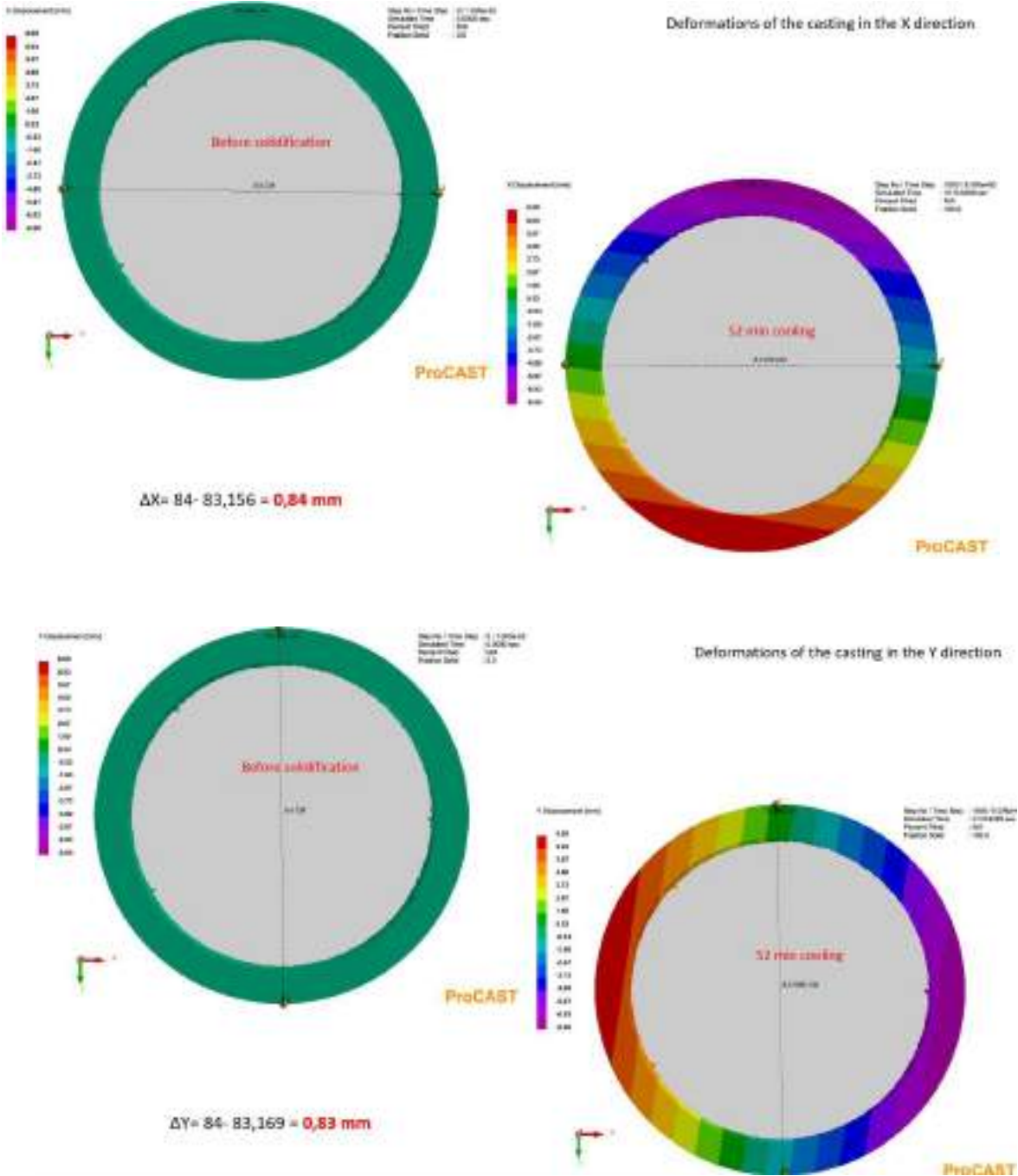


Figure 12. Deformations of the casting in X and Y direction

Using numerical simulations, it is possible to obtain the distribution of microstructure in the casting. Simulation shows dendritic secondary arm spacing distribution DSAS in μm , Figure 13.

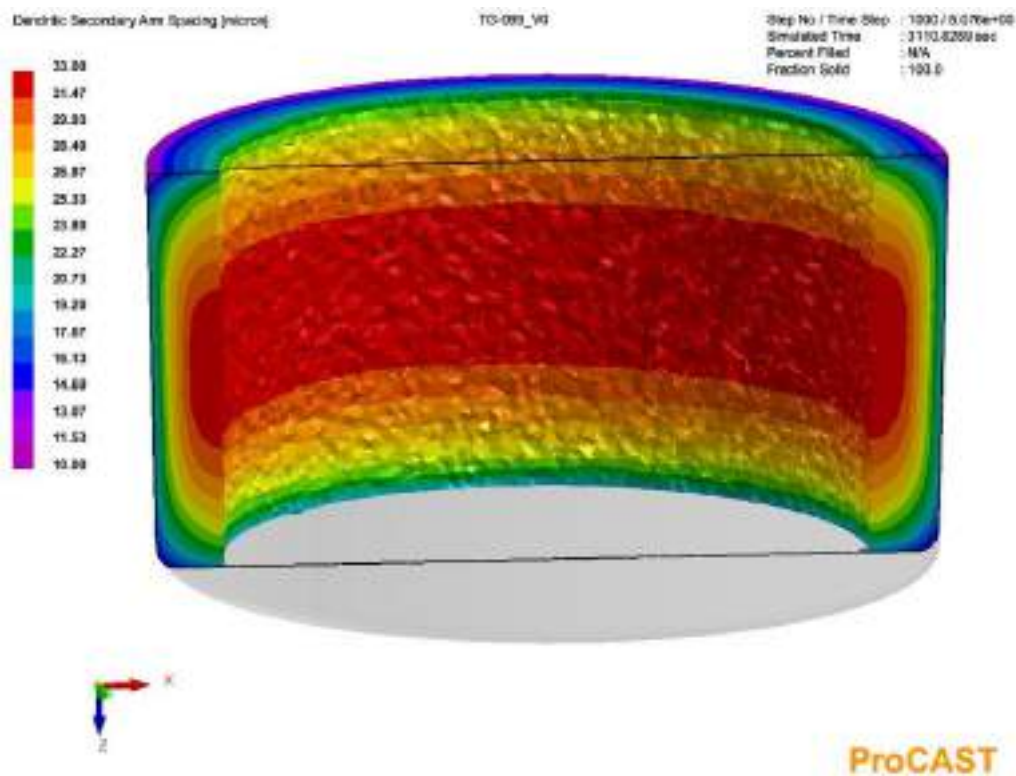


Figure 13. Dendritic secondary arm spacing, microstructure of the casting

Seen from the cross section, the larger grains are located on the inner radius of the casting and their size decreases in the direction towards the outer radius. If the height of the casting is taken into consideration, the largest grains are located in the middle and decrease towards the bottom and top sides of the casting.

Inside the casting the DSAS ranges from 10 to 30 μm , depending on the duration of solidification. DSAS amounts to 10 μm at the edges of the casting where the cooling rate is highest and 30 μm at the place of the last solidification, where cooling rate is lowest. Higher DSAS means coarser grains i.e. lower mechanical properties. On the cross-section in the middle of the casting, DSAS ranges from 22 to 30 μm , which is quite homogeneous.

CONCLUSION

Vertical centrifugal casting is a very complex process that requires a lot of knowledge and skills. If only one small segment is disturbed, the possibility of mistake is high. To prevent this from happening and to reduce defects, numerical simulations are used. With the help of simulations, the flow of the molten metal can be easily predicted and it is clear how the solidification process takes place in the mould cavity.

In the present paper, simulation of filling and solidification was carried out using ProCAST software to determine influence of mould rotational speed and pouring temperature on final quality of casting. Casting of stainless-steel EN 1.4581 tube with an outer diameter of 84

mm, a height of 42 mm and thickness of 7mm was simulated. Effect of rotational speeds of 700 rpm, 1000 rpm and 1400 rpm at pouring temperature of 1485 °C was analysed and effect of pouring temperatures 1485 °C and 1510 °C at 1400 rpm was also analysed. For rotational speed of 1400 rpm and the pouring temperature of 1485 °C deformations, stresses and microstructure were simulated.

According to the results of simulation, rotational speed of 1400 rpm and the pouring temperature of 1510 °C are recommended. As the casting cools, the stresses shift from the tensile to the compressive. Deformation along the x-axis amounts to 0.84 mm and along the y-axis 0.83 mm. On the cross-section in the middle of the casting, microstructure expressed through dendritic secondary arm spacing DSAS ranges from 22 to 30 µm, which is quite homogeneous. Since the inner side in the middle of the casting solidifies last i.e. the casting is fed from the middle, the greatest possibility of a casting defects is in that part. Hence, a detailed analysis of surface is recommended in this area.

Acknowledgements

This research is supported by ESI ERDF - European Regional Development Fund project VARC Vacuum centrifugal casting of rotationally symmetric parts (KK.01.2.1.02.0096) and the company Fripol d.o.o. from Ljubešćica, Croatia.

REFERENCES

- [1] ..., Casting, ASM Handbook, Vol. 15, ASM International, Ohio, 2008.
- [2] C. O. Ruud, A. A. Diaz, M. T. Anderson, Grain structure identification and casting parameters of austenitic stainless steel (CASS) piping, Pacific Northwest National Laboratory, Richland, 2009.
- [3] S.-L. Lu, F.-R. Xiao, S.-J. Zhang, Y.-W. Mao, B. Liao, Simulation study on the centrifugal casting wet-type cylinder liner based on ProCAST, Applied Thermal Engineering, 73(2014)1, pp. 512-521.
- [4] S. Mohapatra, H. Sarangi, U. K. Mohanty, Effect of processing factors on the characteristics of centrifugal casting, Manufacturing Review, 7(2020)26, pp. 1-15.
- [5] Q. Dong, Z. Yin, H. Li, G. Gao, Y. Mao, Simulation study on filling and solidification of horizontal centrifugal casting babbitt lining of bimetallic bearing, International Journal of Metalcasting, 15(2021)1, pp. 119-129.
- [6] S. M. Ali, Optimization of centrifugal casting parameters of AISi Alloy by using the response surface methodology, International Journal of Engineering (IJE), IJE TRANSACTIONS B: Applications, 32(2019)11, pp. 1516-1526.
- [7] S. Sen, S. Reddy, B. K. Muralidhara, P. G. Mukunda, Study of flow behaviour in vertical centrifugal casting, Materials Today Proceedings, 24(2020)2, pp. 1392-1399.
- [8] ..., Review of Centrifugal Casting Methods; Types, Process..., Accessible on Internet: <https://mechanicalbase.com/review-of-centrifugal-casting-methods-types-process/>, (17.3.2021.)



19th INTERNATIONAL FOUNDRYMEN CONFERENCE
Humans - Valuable Resource for Foundry Industry Development

Split, June 16th-18th, 2021

<https://ifc.simet.hr/>

**INFLUENCE OF SEMI-SOLID METAL PROCESSING AND ARTIFICIAL AGING ON
MICROSTRUCTURE AND HARDNESS OF THE AISi9Cu3(Fe)**

Jure Krolo^{*}, Ivana Dumanić, Sonja Jozić, Branimir Lela

University of Split Faculty of Electrical Engineering, Mechanical Engineering and Naval Architecture,
Split, Croatia

Oral presentation

Original scientific paper

Abstract

In order to achieve a uniform, non-dendritic microstructure with less porosity, semi-solid metal processing has been widely used in aluminum production as an alternative to conventional casting methods. In order to successfully perform semi-solid metal processing suitable globular microstructure must be obtained at required semi-solid temperature. In this paper, as cast dendritic structure was severely deformed with equal channel angular pressing and after reheating on suitable semi-solid temperature fine globular microstructure was formed. Influence of holding times at selected semi-solid temperature on globule formation was investigated. Hardness of the obtained microstructure after artificial aging was determined.

Keywords: *semi-solid metal processing, heat treatment, ECAP, microstructure, hardness*

*Corresponding author (e-mail address): jkrolo@fesb.hr

INTRODUCTION

In the last few decades, semi-solid metal (SSM) processing was considered as an alternative to the conventional high pressure die casting (HPDC) in the production of the automotive, aerospace, electronics and other components [1-4]. In SSM starting material is in the form of the slurry consisted of both solid and liquid phase of the selected alloy. Main benefits of the mentioned process are reduced shrinkage compared with HPDC, less (or eliminated) porosity, minimized (or eliminated) solidification shrinkage, prolonged die life due to less thermal shock and lower energy consumption [2-4]. SSM technologies are generally categorized into two groups: rheo-routes and thixo-routes [3]. For both routes in order to successfully perform SSM suitable starting material should have globular microstructure consisted of globular solid α aluminium uniformly dispersed in a low melting matrix phase. Such structure has thixotropic properties, stands still at rest, but with applied pressure flows

readily with laminar flow and higher viscosity than fully melt of the same alloy [1, 4]. Therefore, one of the key steps to perform SSM is to prepare suitable semi-solid starting material with dendrite-free, but globular microstructure. In rheo-routes starting material is prepared directly from liquid phase and then it is injected into a die or a mould for component shaping. Thixo-routes refers to the preparation of the feedstock material, reheating between solidus and liquidus and finally its shaping [3].

The main aim of this research is to use severe plastic deformation process in order to perform thermomechanical treatment route for thixo feedstock preparation. Thermomechanical treatment route is usually based on deformation of the as casted ingot and starting dendritic structure. The second step is reheating of the deformed ingot on suitable semi-solid temperature where fine globular microstructure is formed [2, 3]. Usually used processes to deform casted ingots are rolling and extrusion process, but in this research equal channel angular pressing (ECAP) was employed. ECAP is the process capable to introduce significant plastic deformation into the material, without change of the starting material cross-sectional area. Heavily deformed microstructure than could be easily changed to globular microstructure by heating at the semi-solid range. Several researches have showed that ECAP process is a more capable method for preparation thixo feedstock material with smaller globule sizes compared with more common methods such as casting with electromagnetic stirring (EMS) and grain refining [5, 6]. ECAP is especially recommended for high silicon alloys due to the poor effect of the EMS refinement in terms of grain size and its shape, because in the aluminium-silicon alloys with higher silicon content (> 4 wt.% Si) effect of stirring is not enough or effect of the grain refiner is limited [6, 7]. Few more reports confirmed ECAP as a viable method for preparation of the suitable thixo feedstock with desirable globule sizes below $100 \mu\text{m}$ [3, 8-12]. Most used aluminium alloy for SSM is AlSi7Mg (A 356) due to the wide solidification range [1-3]. The main aim in this work is to produce material with globular structure by ECAP process followed by heating in semi-solid range for AlSi9Cu3(Fe) alloy with high silicon content (8 - 11 wt.% Si).

Furthermore, it is well known that mechanical and fatigue properties of aluminium cast depend on size, distribution, volume and morphology of intermetallic phases and silicon particles [13-20]. When SSM processing is employed, it is possible to change formed phases in the processed AlSi9Cu3(Fe) aluminium alloy in more desirable form than in as cast samples [14]. Usually, formed phases for AlSi9Cu3(Fe) aluminium alloy are primary aluminium, eutectic and polyhedral silicon phases and additionally Fe-rich and Cu-rich intermetallic phases [14, 15]. Few authors emphasized the significant effect of morphology and size of the Fe-rich intermetallic compounds on microstructural and mechanical properties for AlSi9Cu3(Fe) alloy [14, 16]. The iron-containing compounds that form during solidification processes appear in a few shapes and sizes, usually divided into three different morphologies: β -Fe₅AlSi needles, α -Al₁₅(MnFe)₃Si₂ Chinese script (also called α_c - phase) and polyhedral crystals [14, 17]. The β -Fe₅AlSi intermetallic compound usually has needle-like morphology and detrimental effect to mechanical properties of the cast components [14, 17-18].

Irizalp et al. [14] showed that an increase in material strength occurred in the thixoforming process because α -Al₁₅(MnFe)₃Si₂ intermetallic particle solidified as desirable polyhedral-shaped compared with Chinese script shape in gravity casting. Also, the β -Al₅FeSi particle was solidified in the form of a small plate in thixoforming compared with needle shape like in gravity casting. Silicon phase particles were also formed in desirable polyhedral shape. According to Hurtalova et al. plate-like type of morphology of eutectic Si have detrimental

effect on mechanical properties, because Si platelets are hard but brittle and can crack exposing the soft matrix [15]. Another method to change the morphology and distribution of intermetallic phases and silicon particles into more desirable shape is heat treatment [15, 19, 20]. During heat treatment, fragmentation and spheroidization of the silicon phase occur [13, 17]. According to the Hortalova et al. [15] during heat treatment β -Al₅FeSi phase was dissolved into very small needles (difficult to observe), while the skeleton-like α -Al₁₅(MnFe)₃Si₂ phase at 505°C tends to fragmentation and at 515°C or 525°C to spheroidization and segmentation. Cu rich phase gradually dissolved into the surrounding Al matrix with an increase in solution treatment time which is one of the key factors for AlSi9Cu3(Fe) alloy strength improvement [15, 19]. Hardness improvement through the formation of Cu based precipitates (Al₂Cu) during aging can be achieved [15, 20].

An important advantage of the SSM processing is a possibility to perform heat treatment due to the reduced porosity in SSM structures, which is not usual practice for conventional HPDC components due to the possibility of blistering [4]. As described above, both heat treatment and SSM processing have a great influence on the shape and distribution of the phase particles which should have an impact on mechanical properties. Therefore, in this paper, the influence of holding times of AlSi9Cu3(Fe) thixo feedstock at semi-solid temperature on globule formation was investigated. Thixo feedstock was produced by ECAP process. Furthermore, obtained samples were artificially aged in order to investigate hardness of the prepared thixo feedstock with desirable globular microstructure.

MATERIALS AND METHODS

Aluminium AlSi9Cu3(Fe) alloy offers good fluidity, pressure tightness, resistance to hot cracking, good mechanical properties and is used to make various automotive parts such as air brake castings, gear cases and air-cooled cylinder heads. Thus, AlSi9Cu3(Fe) was used for this study. Standard composition of this alloy is shown in Table 1. This study consists of the microstructure and hardness analysis of ECAPed samples reheated at semi-solid temperature.

Table 1. Chemical composition of aluminum alloy AlSi9Cu3(Fe) (Wt.%)

Elements	Fe	Si	Mn	Ni	Cr	Ti	Cu	Pb	Mg	Zn	Sn	Al
Min. - Max. (%)	1,3	8 - 11	0,55	0,55	0,15	0,25	2 - 4	0,35	0,05 – 0,55	1,2	0,15	Bal.

In order to form round samples, as-received ingots were melted at 700 °C in “Demiterm Easy” furnace and poured into the steel die. Before applying the deformation process, it is necessary to use an appropriate heat treatment to AlSi9Cu3(Fe) samples. Due to the as cast material brittle characteristic, in order to reduce the crack appearance during deformation, cylindrical samples with 15 mm in diameter and 100 mm in height were annealed at 350 °C for 5 h to increase ductility. Then, samples were furnace cooled to room temperature. To impose plastic deformation on the samples, ECAP tool was used. ECAP tool used in this study has two equal cross section channels (15,1 mm in diameter) and the inner channel angle of 90 ° and the outer curvature angle of 12 °. Graphite grease was used to reduce friction between the die and samples. Next step was heating ECAPed samples at the semi-solid temperature for 10 min, 15 min and 20 min. According to [2, 4, 21] 50 % of solid fraction is a good selection for thixoforming processes. The semi-solid temperatures were investigated

by Birol et al. [4]. They concluded that a sign of thixoformability occurred at 568 °C and once the temperature exceeded 572 °C slugs were no longer able to sustain their own weight and were deformed too much. Thus, in this research temperature range for reheating at semi-solid range was set to 570 °C ± 3 °C. The temperature of the semi-solid samples was measured by contact thermometer DT 02 and K-type thermocouple probe. The heating rate of the samples was 1,6 °C/s and the samples reached the desired semi-solid temperature after approximately 6 minutes. This time is added to the selected holding times (10 min, 15 min, 20 min) at semi-solid temperature. After that, samples in the semi-solid state were directly cooled in the cold water to freeze microstructure. In order to investigate aging potential, additionally the artificial aging was carried out at 175 °C for 8 h. Due to the quenching step after semisolid heating, preliminary results and potential for energy savings, additional solid solution treatment was omitted from this research. Aging time and temperature were selected according to the previous researchers [4, 18, 19]. However, the final artificial aging parameters were also chosen in accordance with the conventional cycles normally applied in the automotive industry, whereas increasing the productivity and reducing the manufacturing cost is related with shortening the total time [20, 22–24]. To observe microstructure after preparation steps (Figure 1), samples were ground, polished, electropolished (with “Struers LectroPol-5” device) and then etched using hydrofluoric acid (0,5 % HF) in a duration of 10 s at room temperature. Optical microscope “OPTON Axioskop” was used to investigate microstructure. Furthermore, Vickers hardness measurements were performed by using 5 N load and standard Amsler Otto Wolpert D-6700 hardness measurement device. For better understanding, Figure 1 shows the main steps of the process used in this study.

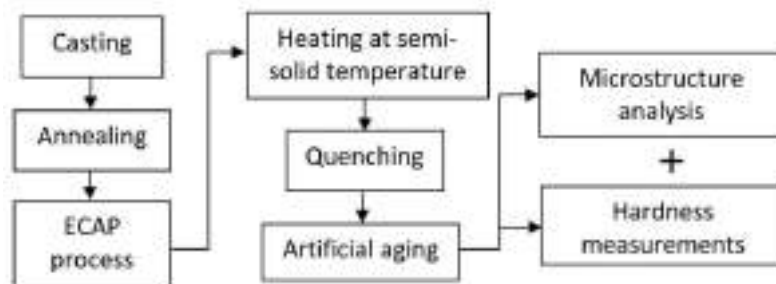


Figure 1. Research methodology steps

RESULTS AND DISCUSSION

As mentioned, ECAP process is used to apply high plastic strain to a solid sample. By this process, as casted dendritic microstructure of AlSi9Cu3(Fe) alloy (Figure 2a) is distorted and bonds are broken (Figure 2b).

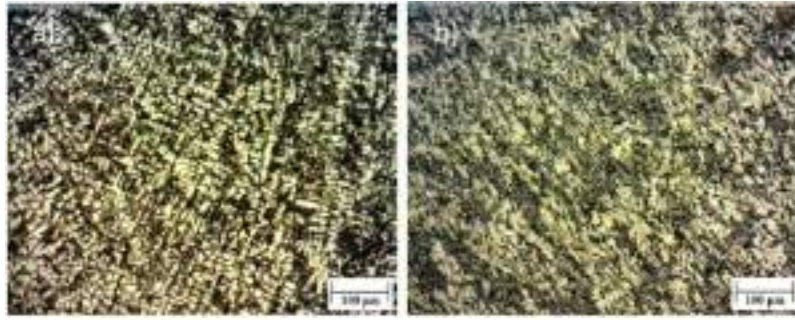


Figure 2. Microstructure of the AlSi9Cu3(Fe) a) as casted b) heavily deformed

During ECAPed samples reheating, created locations of the recrystallization nucleus cause new grains to nucleate within the structure [6]. When the temperature rises to semi-solid range, the high-energy grain boundaries of these new grains are penetrated by liquid, leading to the fragmentation of original grains to small equiaxed grains [25]. This process results in very homogeneous and spherical microstructure. In order to study semi-solid microstructure and globularization of solid particles, reheating (at semi-solid temperature) of ECAPed samples with different holding times was carried out. Figure 3 shows microstructure of deformed samples after different holding times (10 min, 15 min, 20 min) at selected semi-solid temperature. According to Figure 3, reheating changed deformed structure into globular for all observed times. With 10 min holding time, globular solid α – Al matrix (white areas) surrounded with liquid eutectic (black areas) was formed, Figure 3a. Due to relatively higher reheating time (15 min), globular solid α – Al was still preserved with few merged globules, Figure 3b. Coarsening of the globular microstructure is obtained after increase of holding time at 20 min for selected semi-solid temperature, where globules merge is pronounced, but globular microstructure still can be observed, Figure 3c.

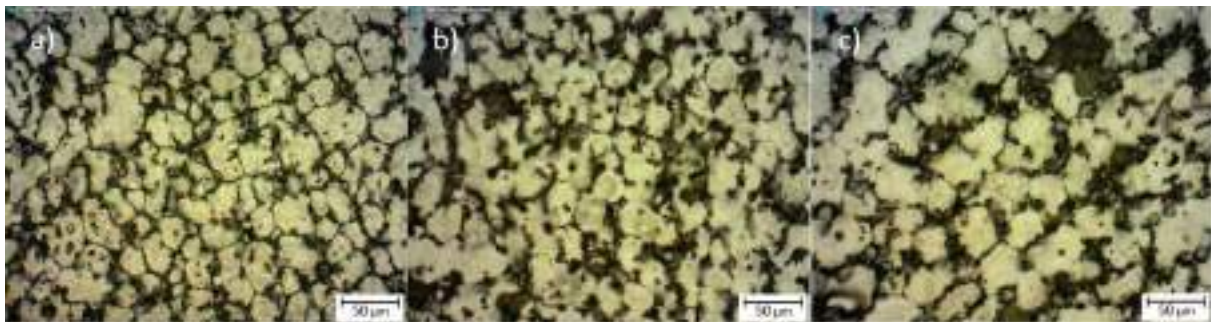


Figure 3. Obtained semi-solid globular microstructure with different holding times: a) 10 min b) 15 min c) 20 min

It is important to mention that desired globules size for thixoforming process is usually under 100 μm [1, 26]. In this research, obtained globule size for 10 min, 15 min and 20 min holding times were 29,3 μm , 33,6 μm and 41,3 μm , respectively, Figure 4. Therefore, it is possible to create thixo feedstock of AlSi9Cu3(Fe) with appropriate, globular, microstructure by ECAP process. Semi solid temperature holding times have a great influence on globule sizes, however, in 10 min time frame, globular, homogeneous, good sized microstructure can be obtained. Due to the globules coarsening and merging phenomena, holding times longer than 20 min for the investigated process are not recommended. Furthermore, according to the EN AC standard [27] usual required hardness of the as casted AlSi9Cu3(Fe) alloy is 80

HBW, while in this research measured value was 100 HV. After artificial aging of samples obtained with 10 min, 15 min and 20 min holding times hardness measurement results were 109,38 HV, 110,5 HV and 94,6 HV, respectively, Figure 4. However, it is important to mention that on all samples after semisolid heating and quenching some blistering and porosity occurred, which was more pronounced for longer holding times on semisolid temperatures. Blisters are generally associated to the expansion of gas porosity, which includes gas from physical entrapment, gas from lubricant decomposition, and gas initially dissolved in the molten metal (e.g., hydrogen) [19]. This is probably the reason for hardness drop for 20 min holding time. In order to perform actual industrial SSM process thixoforming step is still missing and it should contribute to blistering and porosity minimization [2-4]. According to this research, if thixoforming would be performed in cold mould and with additional artificial aging step, obtained samples hardness could be around 37,5 % higher than the minimum hardness of AlSi9Cu3(Fe) according to the EN AC standard or 10 % higher than as gravity casted samples in this research.

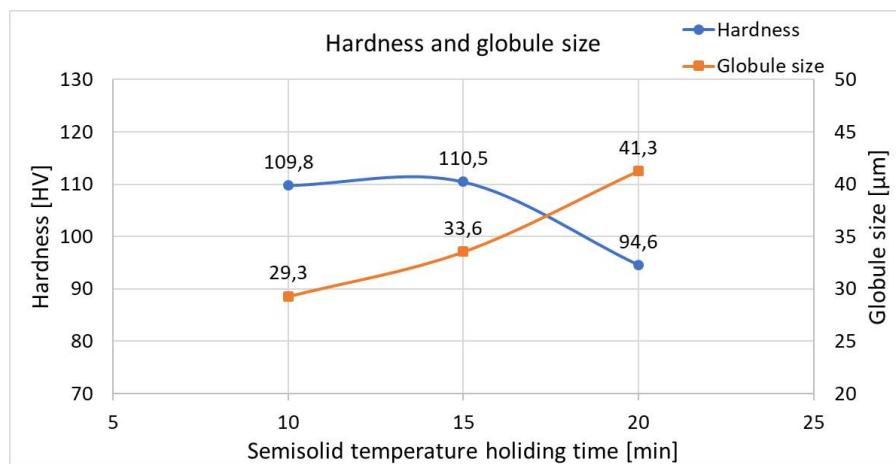


Figure 4. Hardness and globule size of the semi-solid globular microstructure with different holding times: a) 10 min b) 15 min c) 20 min

CONCLUSIONS

According to the results presented in this paper, ECAP process seems suitable for thixo feedstock preparation with homogeneously distributed fine globular microstructure. Suitable holding times after samples reaching required semisolid temperature range were 10 min and 15 min. For longer holding time, globular microstructure tends to coarsen and globules to merge. Furthermore, obtained samples seem to have aging potential and obtained hardness for samples obtained with 10 min and 15 min were around 110 HV which is around 37,5 % higher than the minimum hardness of AlSi9Cu3(Fe) according to the EN AC standard or 10 % higher than as gravity casted samples in this research. For future research it is suggested to prepare thixo feedstock with the process described in this research and to perform thixoforming step in cold mould and to artificially age obtained samples. Benefits of this approach are to omit solid solution heat treatment step for energy savings and to reduce the possibility of blistering which can occur during solid solution.

REFERENCES

- [1] D. H. Kirkwood, M. Suéry, P. Kapranos, H.V. Atkinson, K. P. Young, *Semi-solid processing of alloys*, Springer, Berlin, 2010.
- [2] G. Hirt, R. Kopp, *Thixoforming: Semi-solid metal processing*, John Wiley & Sons, 2009.
- [3] S. Nafisi, R. Ghomashchi, *Semi-Solid Processing of Aluminum Alloys*, Springer International Publishing, 2016. <https://doi.org/10.1007/978-3-319-40335-9>
- [4] Y. Birol, Forming of AlSi8Cu3Fe alloy in the semi-solid state, *Journal of alloys and compounds*, 470(2009)1-2, pp. 183-187.
- [5] K. N. Campo, E. J. Zoqui, Thixoforming of an ECAPed Aluminum A356 Alloy: Microstructure Evolution, Rheological Behavior, and Mechanical Properties, *Metallurgical and Materials Transactions A*, 47(2016)4, pp. 1792-1802.
- [6] L. V. Torres, L. F. Torres, E. J. Zoqui, Electromagnetic stirring versus ECAP: morphological comparison of Al-Si-Cu alloys to make the microstructural refinement for use in SSM processing, *Advances in Materials Science and Engineering*, 2016(2016).
- [7] C. T. W. Proni, L. V. Torres, R Haghayeghi, and E. J. Zoqui, ECAP: an alternative route for producing AlSiCu for use in SSM processing, *Materials Characterization*, 118(2016), pp. 252-262.
- [8] J. L. Fu, H. J. Jiang, K. K. Wang, Influence of processing parameters on microstructural evolution and tensile properties for 7075 Al alloy prepared by an ECAP-based SIMA process, *Acta Metallurgica Sinica*, 31(2018)4, pp. 337-350.
- [9] R. Meshkabadi, G. Faraji, A. Javdani, V. Pouyafar, Combined effects of ECAP and subsequent heating parameters on semi-solid microstructure of 7075 aluminum alloy, *Transactions of Nonferrous Metals Society of China*, 26(2016)12, pp. 3091-3101.
- [10] I. Dumanić, J. Krolo, S. Jozić, B. Lela, D. Bajić, Dražen, P. Ljumović, Influence of the processing route on the microstructure formation at semi-solid temperatures for aluminum alloy A380, *CONFERENCE PROCEEDINGS of the 20th International Conference on Materials*, (S. Šolić, Z. Schauerl, D. Pugar), May, 2019., Vela Luka, Croatia, pp. 137-144.
- [11] M. Aghaie-Khafri and D. Azimi-Yancheshme, The study of an Al-Fe-Si alloy after equal-channel angular pressing (ECAP) and subsequent semisolid heating, *J Miner. Met. Mater Soc. (JOM)*, 64(2012), No. 5, p. 585. <https://doi.org/10.1007/s11837-012-0306-4>
- [12] S. Ashouri, M. Nili-Ahmadabadi, M. Moradi and M. Iranpour, Semi-solid microstructure evolution during reheating of aluminum A356 alloy deformed severely by ECAP, *J. Alloy. Compd.*, 466(2008), No. 1-2, p. 67 <https://doi.org/10.1016/j.jallcom.2007.11.010>
- [13] E. Tillova, M. Chalupova, L. Hurtalova, Evolution of phases in a recycled Al-Si cast alloy during solution treatment, *The Scanning Electron Microscope*, INTECH, 411-438, 2011.
- [14] S. G. Irizalp, N. Saklakoglu, Effect of Fe-rich intermetallics on the microstructure and mechanical properties of thixoformed A380 aluminum alloy, *Engineering Science and Technology, an International Journal*, 17(2014)2, pp. 58-62.
- [15] L. Hurtalova, E. Tillova, M. Chalupova, The Structure Analysis of Secondary (Recycled) AlSi9Cu3 Cast Alloy with and without Heat Treatment, *Engineering Transactions* 61(2013)3, pp. 197-218.
- [16] W. Yang, F. Gao, S. Ji, Formation and sedimentation of Fe-rich intermetallics in Al-Si-Cu-Fe alloy. *Transactions of Nonferrous Metals Society of China*, 25(2015)5, pp. 1704-1714.

- [17] M. Eduarda Farinaa, B. Pedro, C. Raimundo Frick Ferreirab, B. A. Dedavida, Effects of Solidification Rate in the Microstructure of Al-Si5Cu3 Aluminum Cast Alloy, *Materials Research*, 20(2017)2, pp. 273-278.
- [18] G. Timelli, S. Capuzzi, A. Fabrizi, Precipitation of primary Fe-rich compounds in secondary AlSi9Cu3(Fe) alloys, *Journal of Thermal Analysis and Calorimetry*, 123(2016)1, pp. 249-262.
- [19] A. Fabrizi, S. Capuzzi, A. De Mori, G. Timelli, Effect of T6 Heat Treatment on the Microstructure and Hardness of Secondary AlSi9Cu3(Fe) Alloys Produced by Semi-Solid SEED Process, *Metals*, 8(2018)10, pp. 750.
- [20] R. Gecu, S. Acar, A. Kisasoz, K. A. Guler, A. Karaaslan, Microstructural evaluation of T6-treated A380 alloy manufactured by semi-solid metal casting, In ICETI-International Conference on engineering Technology and innovation, March, 2017, Sarajevo, pp. 284-288.
- [21] S. Gencalp, N. Saklakoglu, Semisolid microstructure evolution during cooling slope casting under vibration of A380 aluminum alloy, *Mater. Manuf. Process.*, 25(2010), No. 9, p. 943. <https://doi.org/10.1080/10426911003636944>
- [22] D. L. Zhang, L. H. Zheng, D. H. StJohn, Effect of a short solution treatment time on microstructure and mechanical properties of modified Al-7wt.%Si-0.3wt.%Mg alloy. *J. Light Met.* 2002, 2, 27-36.
- [23] Y. Han, A. M. Samuel, H. W. Doty, S. Valtierra, F. H. Samuel, Optimizing the tensile properties of Al-Si-Cu-Mg 319-type alloys: Role of solution heat treatment. *Mater. Des.* 2014, 58, 426-438.
- [24] E. Tillová, M. Chalupová, L. Kuchariková, J. Belan, Závodská, D. Selection of optimal solution heat treatment of the casting cylinder heads., *MATEC Web Conf.*, 2018, 157, 02053.
- [25] M. Moradi, M. Nili-Ahmadabadi, B. Heidarian, M. Habibi-Parsa, 2008, Study of ECAP processing routes on semi-solid microstructure evolution of A356 alloy. In *Solid State Phenomena*, Vol. 141, Trans Tech Publications, pp. 397-402.
- [26] Y. Birol, 2008, Semisolid processing of near-eutectic and hypereutectic Al-Si-Cu alloys. *Journal of Materials Science*, 43(10), pp. 3577-3581.
- [27] European Steel and Alloy Grades; Grade ENAC-AlSi9Cu3(Fe)(Zn), Accessible on Internet: http://www.steelnumber.com/en/steel_alloy_composition_eu.php?name_id=1249, (20. 02. 2020.)



19th INTERNATIONAL FOUNDRYMEN CONFERENCE
Humans - Valuable Resource for Foundry Industry Development

Split, June 16th-18th, 2021

<https://ifc.simet.hr/>

CO-DESIGN IN CASTING - A WAY TO ACHIEVE OPTIMAL DESIGN AND PRODUCTION OF CASTINGS

Vladimir Krutiš^{1*}, Martin Madaj², Vlastimil Kolda³

¹ Brno University of Technology, Faculty of Mechanical Engineering, Brno, Czech Republic

² Arkance Systems CZ s.r.o., Prague, Czech Republic

³ Mecas ESI, Brno, Czech Republic

Oral presentation

Preliminary work

Abstract

The article deals with optimal "work-flow" from the initial design of an aluminum casting through its optimization using virtual tools up to its own production using so-called hybrid technology. The case study demonstrates the use of new approaches in the design of a machine component using generative design (GD), which is the entry point for the so-called Co-Design - a quick evaluation of the technological design of the structure. Final numerical simulations verify both the suitability of the machine component for the required load, and the technological simulation confirms the ability of manufacturing the designed casting for the chosen foundry technology. In this case, the design was directed to the production of prototypes using a 3D printed model and subsequent production of ceramic shell by rapid prototyping methods.

Keywords: *Co-Design, numerical simulation, rapid prototyping, generative design, virtual manufacturing, investment casting*

*Corresponding author (e-mail address): vko@esi-group.com

INTRODUCTION

The benefits resulting from collaboration between the designer and the technologist in the design of a casting are certainly very familiar not only to many foundries, but also to their customers. The entire theory behind "simultaneous engineering" is based on the idea of dialogue and teamwork of experts who actively participate in the design of the required plans. The combination of know-how and resources should lead to an optimal plan that respects the constructional and material requirements imposed on the part itself and guarantees efficient production whilst minimizing the costs associated with the subsequent modification or change of technology during production. However, this approach requires an understanding of each other's goals and requirements, and in particular a willingness to

work together and learn something new. It also requires an open mind when it comes to investment and the use of virtual tools, which are essential support tools for an effective decision-making process. This multidisciplinary approach has been functioning in the automotive and aerospace industries for many years, but it is certainly possible to apply it in smaller-scale projects.

VIRTUAL PROTOTYPING

Virtual prototyping represents one element of virtual engineering. Virtual prototyping (VP) is a set of methodologies focused on supporting processes in the product development phase. VP involves the use and combination of several tools, which include computer-aided design (CAD), computer-automated design (CAutoD), and computer-aided engineering (CAE) to validate a design before executing a physical prototype. VP in the field of castings is basically a design activity that leads to the optimal design of the shape of castings. Until recently, the shapes of castings were designed to meet at least the basic requirements for the technology behind the design. This involves the adaptation of the design of the part to the method of production and the properties of materials to ensure that production is efficient and of high quality. The technology behind the design was focused on the method of dividing the model with respect to the pre-selected production technology, concentrated on the elimination of hot spots by means of an ideal connection and wall transition and, in many cases, responded to the need for directed solidification with regard to the elimination of foundry defects. For these reasons, the shapes of the castings tended to be conservative, to meet the requirements for functionality and the production technology selected. The development of new optimization methods in 3D design (including cloud solutions), including topological optimization or generative design and the development of 3D printing methods, has shifted the design of component patterns to an area that in the past was purely the domain of artistic castings.

What is generative design?

The term “generative design” (GD) is currently used in many different areas of industry, especially in mechanical engineering and construction, but GD also extends into electrical engineering and other fields [1], [2]. GD represents a different approach to design using the genetic algorithms mentioned in [3], using optimised results that have a high probability of meeting the specified requirements; this would often be very difficult, if not impossible, to achieve using the traditional “manual” design process. In the case of mechanical engineering, it can consist, for example, of a reduction in the number of components used, stiffness or weight; in construction, for example, the use of space, the amount of daylight, or the propagation of sound in rooms. Outputs from generative design can also meet high aesthetic demands. According to [4] and [5], GD is a technology that can create and evaluate thousands of different design variants based on many different specific inputs (max./min. dimensions, weight, material, production method, production cost, etc.) and the required outputs; from this, the constructor/designer can then choose the most suitable alternatives. Generating such many design variants is possible thanks to the relatively massive expansion of cloud systems, where the user does not have to use their own workstation for the calculation but uses the “unlimited” cloud performance. Users may then easily orientate

themselves around the results, and the selection of the most suitable variants is then made possible by means of robust filtering tools.

Generative design or topological optimization?

Unlike topological optimization [6], where the design area is precisely defined and the pattern is created within this area, the initial geometry of the model does not necessarily depend on the input parameters for the generative design. In the context of engineering components, only the “connection” areas must be present, or areas that the design should avoid. At the same time, however, it is possible for the initial geometry of the body to be defined. Topological optimization forms a part of generative design, although the two terms are often confused. A comparison of the area of the generative design plan with topological optimization, supplemented by the optimization of the shape in which the topology is maintained, can be seen in Figure 1. From shape optimization to generative design, the exact initial specification of the optimized/created geometry gradually “disappears”. On the other hand, even in generative design, it is possible to determine relatively precisely boundaries within which the final geometry is to be located.

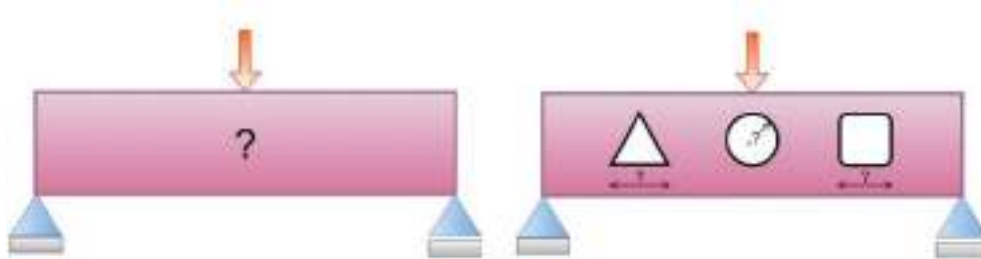


Figure 1. Optimization charts

Traditional vs. generative design process

In the traditional design process, the engineer must directly create the required geometry, based on experience with previous designs and requirements given by the future usage of the product, the material used, planned production method, etc. Each design variant must then be evaluated, and in case of any deficiencies, corrections need to be made to the design. The whole process is then repeated until the product is deemed fit for release for production. Depending on the complexity of the product, this can take many hours of work. By contrast, for generative design, the designer specifies the initial conditions and constraints, and GD then uses evolutionary algorithms to automatically evaluate many tens to thousands of variants to find the best solution. In each step, the design is tested to see if it meets the specified criteria and, based on the test results, changes are applied in the next step to achieve an optimized final version that meets the required criteria. An example of individual design iterations showing strength analysis results can be found in Figure 2. Compared to traditional methods, generative design can create a massively greater number of design variants in a fraction of the time.

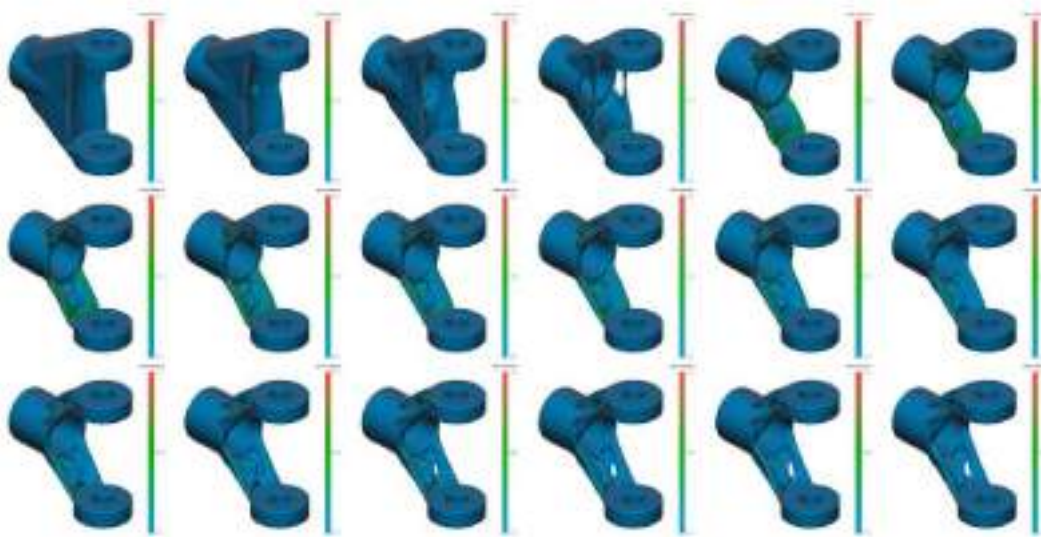


Figure 2. Continuous evaluations of individual GD design iterations

Basic principles of generative design

All design problems are inherently multidimensional, and their solutions must meet several often-conflicting requirements. In order to address such problems, the generative design uses artificial intelligence in the form of metaheuristic, or search algorithms that are more suitable for this activity than artificial neural networks, which first need to learn how the model being assessed works. The generative design algorithm does not, by contrast, must know how the model being assessed works, but can learn how to work with the model. A specific type of search algorithm that is used in generative design are evolutionary/genetic algorithms inspired by Darwin's theory of evolution. By selecting the most suitable candidates, crossbreeding and mutations, the most suitable candidate meeting the entry requirements for the proposal is repeatedly sought. As can be seen from Figure. 2, in most cases the bodies created by generative design have irregular, organic shapes, which can be supplemented by exactly defined geometry resulting from the initial constraint conditions. This brings with it the advantages, for example in the form of optimized weight, stiffness, or non-traditional appearance. On the other hand, problems associated with the need to further use the model for simulations, or the need to add additional geometric elements, may arise. Marinov et al. [7] therefore presented a solution that greatly simplifies the handling of generative design outputs to the point that the manual procedures associated with converting the pattern of the generated body to the boundary representation (B-rep) are completely eliminated, which would thus lead to further extension of the design phase. In this process, the organic parts of the geometry are parameterized and approximated using T-NURCC surfaces, the boundaries of which are then extended into the original "connecting" bodies, and the result is a single closed boundary representation of the solid body. Thanks to the parameterization, the organic shape of the model may then be modified at a later stage at any time. This feature is currently fully integrated with the Autodesk Fusion 360 application, as shown in Figure. 3



Figure 3. Editable output from GD in Fusion 360

Generative design vs. production methods

Certain production specifics can also be associated with the organic pattern of the body. If the initial production conditions are not specified, additive production methods appear to be the most appropriate production methods [4]. Additive production is not limited by the complexity of the pattern, and it is, therefore, possible to achieve the most suitable designs in terms of minimum weight. For this type of production, it is possible to consider, for example, the direction of application of layers of material, or other 3D printing parameters. Generative design tools also make it possible to define more conventional production methods, such as milling or cutting, whilst including the size of the tools as a matter of course. Pressure casting is one of the input conditions for generative design; this considers the minimum wall thickness, the direction of pulling the casting out of the mold, and the size of the bevel. When setting the conditions for machining methods or die casting, more conventional design shapes can be generated that take, to a certain extent, the design technology into account. Of the current foundry methods, hybrid technologies, which address the production of a non-permanent model by 3D printing, are best suited for this method of component design. Here, the method of casting into ceramic shells using a meltable or combustible model is mainly used.

ALUMINIUM HINGE CASE STUDY

The original shape of the component in question

As an example of the possibility of using GD to produce cast parts, an aluminum hinge loaded with the weight of the load over the installed arm was chosen. The selected assembly component is highlighted in red in Figure 4.

A finite element method (FEM) was first performed to determine whether there is the potential for weight saving and optimization of the body topology for a given component. For a given, simplified load condition (force acting on the lower bearing surface and forces - the load of the “bearings” acting in the holes for the pin), it was found that the maximum von Mises stress reaches a value of about 30 MPa for AlSi10Mg material, which corresponds to a safety factor greater than 8. Stress analysis was performed in Autodesk Fusion 360 for material property database values. The results of the stress analysis revealed that the

potential for savings in body weight and topology optimisation existed, and therefore the conditions for designing a new body pattern using a generative design module in the same software environment were defined.



Figure 4. Assembly of the final casting

Generative design steps

The first step in the definition is to determine which parts of the geometry are retained. The connection surfaces of the body must always be retained in the model - in this case, these were the hole for a screw and the holes for pins.

Constraints and body loads are then applied to the surfaces to be preserved which, together with other parameters of the model, can significantly affect the result of the generative design. The obstacles are then determined, i.e. areas in which the pattern of the generated body must not encroach under any circumstances. It is always necessary to carefully consider whether there will be any moving parts near the body, or whether the body itself would be mobile in the operating state. These motion envelopes must then be considered when setting up the study. The definition of the initial shape of the component (like topological optimization) is optional, however, this option was not used in this case. The generated models may be asymmetrically shaped with respect to the load case used in the study. Symmetry can therefore be enforced by selecting the planes of symmetry. Fig. 5 shows the final definition of the geometry, including the planes of symmetry and load. The next step is to define the goal and limits of the design, which specify the results we wish to achieve in generative design. In addition to the standard weight minimization or stiffness maximization (with the definition of the safety factor value and the required final weight), the maximum deformation value (either total or in components of the coordinate system), the buckling safety factor, or even the minimum required value of the first mode frequency can also be specified.

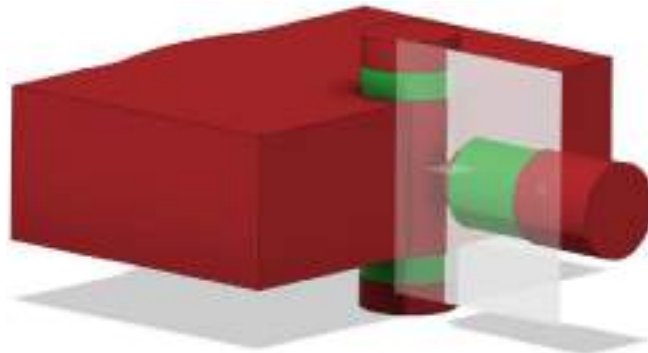


Figure 5. Assembly of the final casting

For the case described in this article, weight minimization was chosen with a minimum safety factor of 2. The designation of the anticipated methods of production of the generated shape is an essential part of the setup. Fusion 360 allows the selection of several production methods: additive (3D printing), 2.5D-5D milling, 2-axis cutting, and currently for die-casting technology only.

In addition to the production methods, it is also possible to specify the “unrestricted” method, which is suitable for assessing which variants meet the specified criteria, but without respecting the technological conditions of specific production methods. In this case, regarding the subsequent choice of 3D printing of the model and casting into shells on a combustible model, the “unrestricted” method was selected.

The calculation of a generative study is a relatively time-consuming process that entirely takes place in the Fusion 360 application in the cloud environment. Depending on the number of studies and combinations of their parameters, several hundred to thousands of results can be generated, and these may be compared and filtered based on various criteria (usually e.g. according to studies, material, production method, or defined parameters - safety factors, weight, etc.). The possibility to filter by visual similarity is also very appealing. It is possible, depending on the definition of the production method, the materials used and the number of manufactured pieces, to make an approximate estimate of future production costs from the results of generative design. Figure 6 shows an overview of the results from the generative design.



Figure 6. Overview of part of the GD results

A design variant was selected for the final verification using FEM and for subsequent production based on the evaluation of the shape of the part and the comparison of the dependence of the calculated safety factor on the weight of the design. (Figure 7). This figure also compares the generated design with the original variant, with the original weight reduced by almost 67% from 1.277 kg to 0.425 kg.

As mentioned above, current versions of GD have limited options when it comes to choose of production technology. We will encounter, with increasing frequency, geometries that are particularly suited to 3D metal printing, or for hybrid technologies. If the product is required as a casting, at least the basic aspects of the technological design need to be verified. At this point, the know-how of the technologist, who again has several virtual tools at his disposal, comes into play. This aids him in the identification of critical points of the design regarding the manufacturability and soundness of the casting.

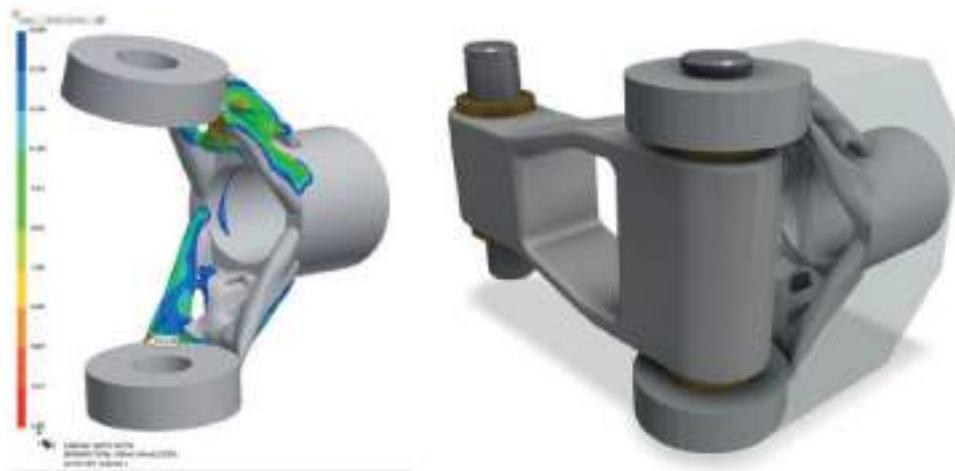


Figure 7. Final verification of the safety factor and the final design in the overall composition

Virtual manufacturing - effective tools in the hands of the technologist

In addition to the designers, technologists also have computer support at their disposal, allowing them to work with a virtual model.

The great advantage of GD is that the user can select any export format (*.igs, *.stp, *.stl, etc.), which will allow the direct testing of the submitted design, or the direct 3D printing of the model if necessary. The tool of choice in this study was the ProCAST simulation program and its special Co-Design module.

The Co-Design module is a tool for assessing the design of a component in terms of the manufacturability of casting technologies. The application consists of three basic steps:

- assessment of the part geometry
- simulation of solidification
- analysis of results

Assessment of the part geometry

The optimized construction of the hinge component does not consider its production technology. One should look at the part from the point of view of its manufacturability, in our case for the precision casting method. The user of the Co-Design module has the option to perform an analysis of the thickness of the component's wall (Fig. 8), on the basis of

which it is possible to decide on a design change, or on the location of notches and other technological elements.



Figure 8. Visualization of design local thicknesses

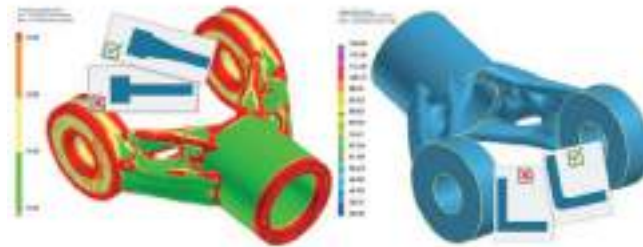


Figure 9. Wall transition analysis

Simulation of solidification and analysis of results

This is followed by a simplified simulation of the solidification of the casting in the shell. The volume of the shell is created around the casting automatically based on the choice of its thickness. All process conditions, such as the transition between the casting and the shell, or from the shell to the surroundings, are created automatically. The user only enters the materials of individual domains and their initial temperatures. The calculation itself takes a few minutes and its aim is to look at the method of solidification, the formation of separate hot spots, the time to solidification, prediction of shrinkage and micro porosity and other basic types of results.

The largest hot spots in the hinge knuckles were assessed to be suitable places for the connection of the inlet system, also from the feeding of hot spots by liquid metal during solidification point of view. Separate solidification points were detected in the casting around the shaft connection to the hinge arms, which is evident from the display of the solid phase progress on Figure 10. Based on the results, it was decided to construct a casting by blinding the arm opening in connection with the central nozzle. Regarding the transition of the geometry, the radius in connection with the hinge knuckle was increased. The changes were discussed with the designer and modified to variant 2 (Figure 11).

In the next step, an inlet system was created taking into consideration the subsequent production options. Regarding the results of the calculation in the Co-Design module, the notches of the inlet system were connected to the hinge knuckles at the sites of the largest hot spots.

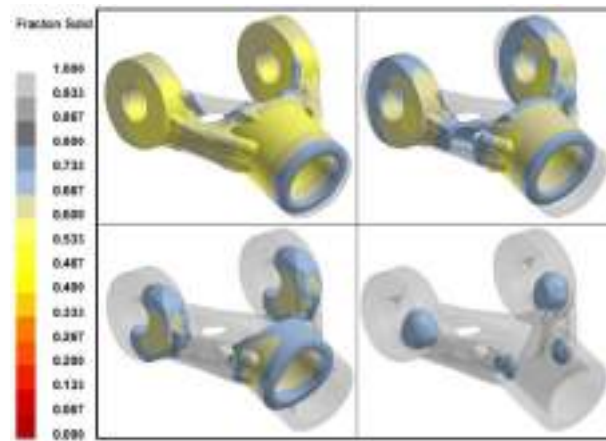


Figure 10. Solid fraction progression

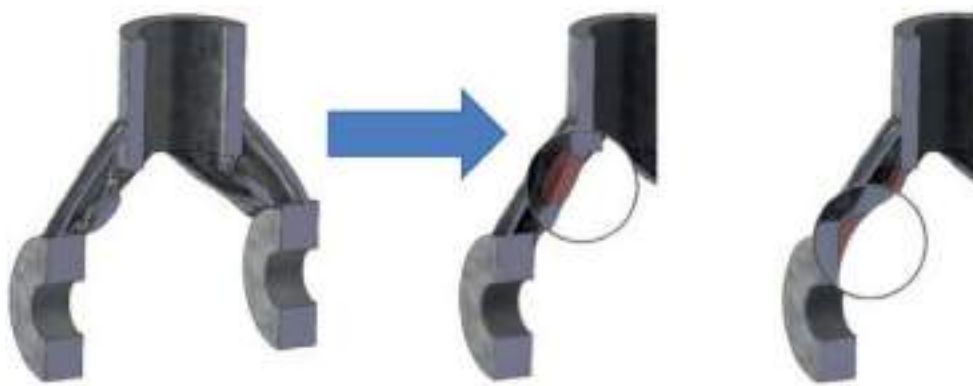


Figure 11. Geometric modification before manufacturing

The position of the casting in relation to the inlet system took into account the actual moulding of the casting, the stability of the gating system on the casting bed and also the direction of solidification from the colder subsurface in the direction of the inlet system (Figure 12). As this is only a case study, the production of a prototype and an outline of the individual steps, the optimal distribution of multiple castings on the inlet sprue and some other production aspects associated with the use of metal were not addressed.



Figure 12. Shell geometry and position of the casting on the gating system

The design of the technology was verified by a final simulation of the entire process, including the phase of moving the shell from the annealing furnace to the casting bed (pre-heating), the flow of metal while filling the shell from the casting ladle and solidification of

the casting in the shell. The results confirmed the correctness of the structural modifications of the casting. Solidification begins at the underside of the hinge sleeve from the casting bed and proceeds through the casting in the direction of the inlet system from which the metal is poured into the casting (Figure 13). In terms of shrinkage, the casting is predicted to be “sound”.

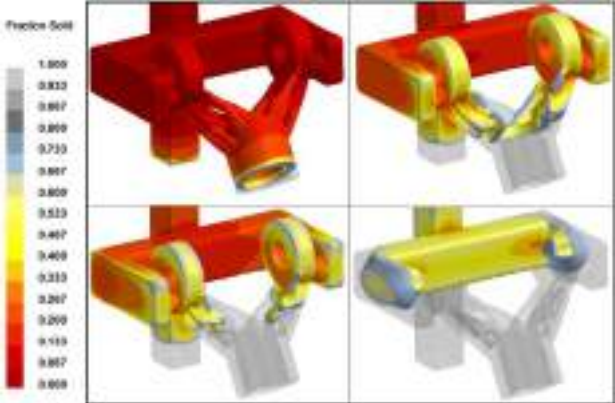


Figure 13. Fraction solid on model with gating system after design modification

Rapid production of a prototype casting

The technology of casting into a ceramic shell was selected as the production method in the case study, regarding the complicated shape of the part and the required speed of production. This means the use of “hybrid” technology [8], where the printed model replaces the expensive and, especially, time-consuming production of a metal parent mold. Regarding the time frame of the project, the Fused Filament Fabrication method from PLA material was chosen. The printing was done on a Prusa i3 MK3S printer with an ultra-detail resolution of 0.07 mm and the printing time total 18 hours. Figure 14 shows the printout of the model, including supports and fillings used for the model.

The geometry of the component itself, including the inlets, was exported from the numerical simulation, and loaded-in in the *.stl format.

Subsequent production of the shell took place in the development workshop at LANIK s.r.o. and VUT Brno under working name “LaBUT”. This workshop contains state-of-the-art technology for the rapid production of ceramic shells on Cyclone equipment by MK Technology.



Figure 14. 3D printing of model from PLA material

This device speeds up the production of shells from a few days to a few hours. The drying system is based on a fast and turbulent air flow that removes moisture. Infrared light balances cools and maintains a stable shell temperature at $\pm 1^\circ\text{C}$. The mirror inside the chamber reflects infrared light so it acts evenly on all parts of the shell. The continuous rotation of the cluster assembly ensures very gentle and even drying, which is also helped by pre-dried air, which further speeds up the process [9]. In our project, a ceramic water-based suspension and PrimeCoat binder was used, and molten SiO_2 (-200 mesh) was used to produce the shell. Zirconium sand (50/80) was used as the first grit and molochite (16/30) was used for back/up coatings. The shell consists of six layers and the total production time of the shell was 5 hours on a Cyclone device. Figure 15 documents the production of the shell on the device.

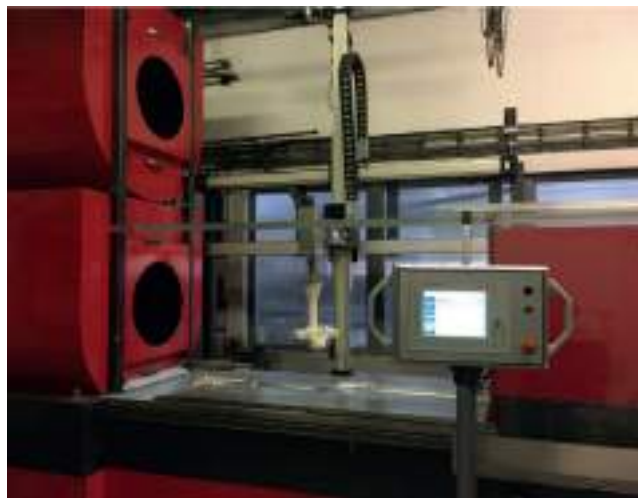


Figure 15. Production of a shell at VUT Brno on a Cyclone device

In the next step, the model was fired in a resistance furnace with an afterburner chamber, at a temperature of 800°C . After cooling, the shell was rinsed with water, then annealed again at 550°C and cast at a pouring temperature of 720°C . Figure 16 shows a cast prototype of a hinge made of AlSi10Mg material, which was cast in the BUT school foundry in Brno.



Figure 16. Prototype casting of the hinge after removal of the gating system

CONCLUSION

The final project represents modern procedures and benefits resulting from open cooperation between designers and technologists on an aluminum hinge project. We have

attempted to present the involvement of new construction tools, which we will increasingly encounter in the future. The focus by GD on “light weighting”, i.e. maximum weight reduction, led to a 67% reduction in component weight compared to the original design. Table 1. summarizes the time required for the steps used in this study.

Requirements to reduce the overall weight of components will continue to grow, especially in the automotive and aerospace industries. The use of optimisation techniques is therefore gaining in importance.

Table 1. Time needed for basic operations

Process	net time [h]
Assessment of the original design - FEM analysis	1
Generative design - optimisation	8
CAD + re-design	0.75
Co-Design	1
FEM simulation of casting and solidification - final verification	2
3D model printing	18
Shell production	5

There is also a growing need for effective communication between the customer, the designer, and the technologist, from the very first steps in the design of individual components upwards. Reductions in development times, the number of re-designs, and the number of critical points in the casting, as well as other technological interventions, will be critical in the field of cost reduction. We will be able to produce several pattern designs aimed at minimizing weight only with the involvement of additive technologies, whether it be model printing, mold printing, or 3D metal printing. In order to keep up with the competition, it will be necessary to introduce these technologies as one of the production alternatives, or it will be necessary to forge links with companies that provide such services, and thus offer customers comprehensive services in the form of final product delivery.

REFERENCES

- [1] D. Nagy, D. Zhao, D. Benjamin, Nature-Based Hybrid Computational Geometry System for Optimizing Component Structure, Springer, Singapore, 2018.
- [2] Demystifying Generative Design, Autodesk, [online]. [cit. 2020-10-27].
- [3] J. Rohrmann, Design optimization in early project stages, master thesis, Technical University of Munich, Munich, 2019.
- [4] Autodesk, The Next Wave of Intelligent Design Automation, Harvard Business review, June 04, 2018, [online]. [cit. 2020-10-27].
- [5] M. Mcknight, Generative Design: What it is? How is it being used? Why it's a game changer. KnE Engineering, 2(2017)2, pp. 176-181.
- [6] M. Smell, D. Weinberg, Generative design with autodesk nastran topology optimization, Autodesk presentation, [online]. [cit. 2020-10-28].
- [7] M. Marinov, Generative design conversion to editable and watertight boundary representation, Computer-Aided Design, 2019(115), pp. 194-205.

- [8] P. Kumar, I. P. S. Ahuja, R. Singh, A Framework for Developing a Hybrid Investment Casting Process. Asian Review of Mechanical Engineering., 2(2013)2, pp. 49-55., ISSN 2249-6289.
- [9] M. Kügelgen, From 7 days to 7 hours - Investment casting parts within the shortest time, 68th World Foundry Congress, 7.-10.02.2008, pp. 147-151.



POSSIBILITY OF ENERGY EFFICIENCY IMPROVING OF THE MELTING FURNACE IN SECONDARY ALUMINIUM PRODUCTION

Ladislav Lazić¹, Martina Lovrenić-Jugović^{1*}, Lorena Mrkobrada², Željko Grubišić¹, Damijan Cerinski¹

¹ University of Zagreb Faculty of Metallurgy, Sisak, Croatia

² Master degree student at University of Zagreb Faculty of Metallurgy, Sisak, Croatia

Oral presentation
Original scientific paper

Abstract

The type of a rotary furnace is often used in secondary aluminium processes. The furnace is charged with the scrap feed, which rotates to be melted under a salt layer. The furnace drum rotation enables more effective heat transfer from the hot refractory to the charge. The rotary furnace under consideration is fired by natural gas with the built-in oxy-fuel burner. Achieved higher temperatures of combustion gases allow heat transfer intensification and shortening the melting period. This paper identifies cost-effective energy savings that can be achieved through performance improvement of combustion processes in the industrial furnaces. The operating conditions having the greatest impact on the energy efficiency in an open-flame furnace are specified and the effect of oxygen-enriched air combustion on the combustion efficiency was particularly analysed. Particular attention is paid to the effect of temperature of exhaust gasses and excess oxygen on the combustion efficiency as well as the specific fuel consumption.

Keywords: *secondary aluminium process, rotary furnace, oxy-fuel burner, energy efficiency, combustion efficiency*

*Corresponding author (e-mail address): mlovrenic@simet.unizg.hr

INTRODUCTION

Aluminium (Al) as the second most numerous metallic element on Earth is one of the youngest industrial metals. Due to its good properties such as lightweight, high corrosion resistance, good conductivity, good formability, and non-toxicity, aluminium has been the fastest-growing metallic material in the past hundred years. Currently, aluminium is the most widely used non-ferrous metal in the world, with wide use in construction, transportation, packaging, electricity, and medicine. The necessity for better mechanical

properties and new applications causes the continuous development of new types of Al alloy [1, 2].

Aluminium recycling has many key economic and environmental benefits. With energy and cost savings in mind, many manufacturers are now aiming to increase the usage of secondary materials. Compared to other high volume materials, aluminium production has one of the largest energy differences between primary and secondary production: about 190 MJ/kg for primary compared to no larger than 20 MJ/kg for secondary [3].

Secondary aluminium production is increasing very rapidly in recent years and it will keep a steady growth in the future. Scrap is the raw material of Al recycling. An exhaustive classification of the aluminium scrap is described since 2003 in the European standards (EN 12258 and EN 13920). European standards cover all aluminium scrap types present in the practice where the characteristics, the chemical compositions, and the metal yield are provided for each category [2, 4].

In the metallurgical industry, the melting process is of central importance to foundries. This is a physical process that results in the complete transition of a substance from solid to liquid [5]. The scrap feed is charged into the melting furnaces. The melting of scraps is usually performed in rotary, reverberatory or crucibles furnaces. In a rotary furnace, the scrap feed is melted and mixed under a salt layer. The main functions of the salt layer are: act as a barrier between the liquid aluminium and the oxygen of the atmosphere, diminishing the process of superficial oxidation of aluminium, and remove impurities in the molten scrap [6]. Figure 1 shows the stages of the aluminium secondary process after scrap collecting [7].

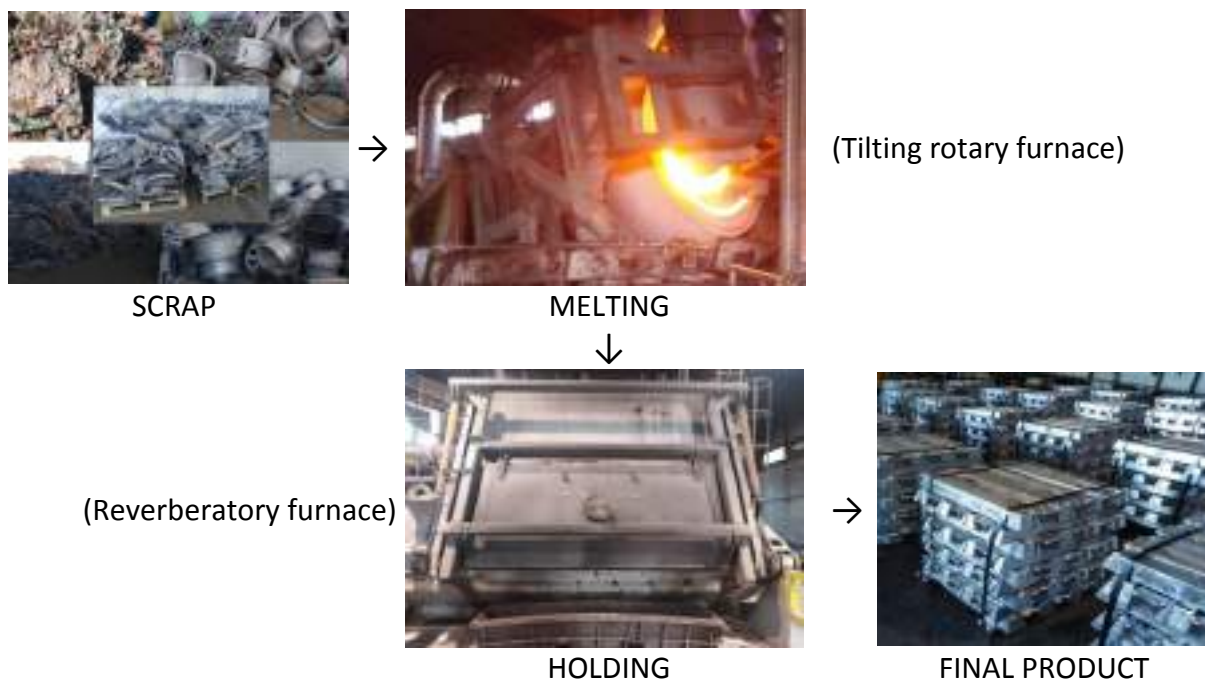


Figure 1. Scheme of stages of the aluminium secondary process

After melting, the molten metal is transferred to the holding furnaces for further refining processes such as degassing, reduction of magnesium content and adding alloying elements. Typically, the holding process is performed in reverberatory or crucible furnaces where the temperature of molten metal is maintained or increased and its composition is adjusted for the casting process. From the holding furnaces, molten metal is either tapped to the casting

unit to produce ingot or slabs or into crucibles for liquid aluminium delivery [6].

This paper identifies cost-effective energy savings that can be achieved through performance improvement of combustion processes at the rotary melting furnace in the Croatian secondary aluminium industry. Particular attention is paid to the effect of temperature of exhaust gasses and excess oxygen on the combustion efficiency as well as the specific fuel consumption.

TILTING ROTARY MELTING FURNACE WITH OXY-FUEL BURNER

The key equipment for the metallurgical processing of aluminium scrap is melting furnaces. Since a Croatian secondary aluminium company uses a rotary melting furnace, its operating mode is described in this section. The furnace consists of the single-ended steel drum in the rigid support cradle and the hydraulic tilting system. The hydraulic tilting system maximizes the charge volume with a 10° back tilt (Figure 2a) and provides controlled pouring with about 40° uptilt. The aluminium scrap is charged into a rotary furnace, which is suited to processes many different types of aluminium scrap [8]. To prevent the oxidation of aluminium in the furnace, contaminated aluminium scrap is melted by covering the melt with salt (NaCl and CaCl). The furnace drum rotates completely about the centre axis throughout the full range of tilt angle. The rotating action of the furnace results in the metal charge being heated from above by flame radiation and from below by the heated refractory. The rotation enables the hot refractory to pass under the metal charge, thus transferring heat more effectively to metal. Typical melting temperatures are in the interval from 700 to 800 °C [4]. Complex phenomena in a rotary furnace are shown in furnace cross-section in Figure 2b.

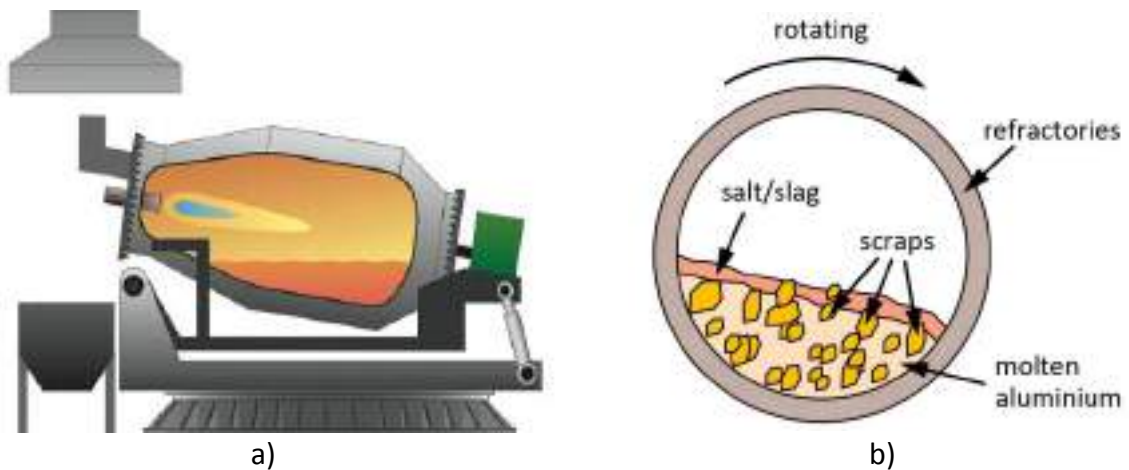


Figure 2. Tilting rotary melting furnace: a) schematic representation of lateral view [9] and b) draft of furnace cross-section

Due to the rotation of furnace drum, heat transfer to metal is more effective. The efficiency of the furnace can be increased by optimising existing combustion process, as it will be shown in the further analysis. As heat source in the rotary furnaces is burning of natural gas with oxygen. The oxy-fuel burner (Figure 3a) is used for distribution and injection of pure oxygen and fuel. The use of oxy-fuel combustion naturally fits high efficiency because the

higher available energy from oxy-fuel combustion can be more efficiently transferred to the melt in a rotary furnace [10]. The direction of the flame is parallel to the axis of the furnace. The burner creates a flame-curved shape corresponding to the cylindrical geometry of the furnace, thereby achieving uniform heat transfer from the flames and combustion gases to the aluminium scrap, and as well as the furnace wall. The better efficiency of the combustion system can be achieved with flue gas backflow through the furnace workspace, i.e. double pass firing scheme of the heating system. The scheme of the heating system of the analyzed rotary furnace is shown in Figure 3b.

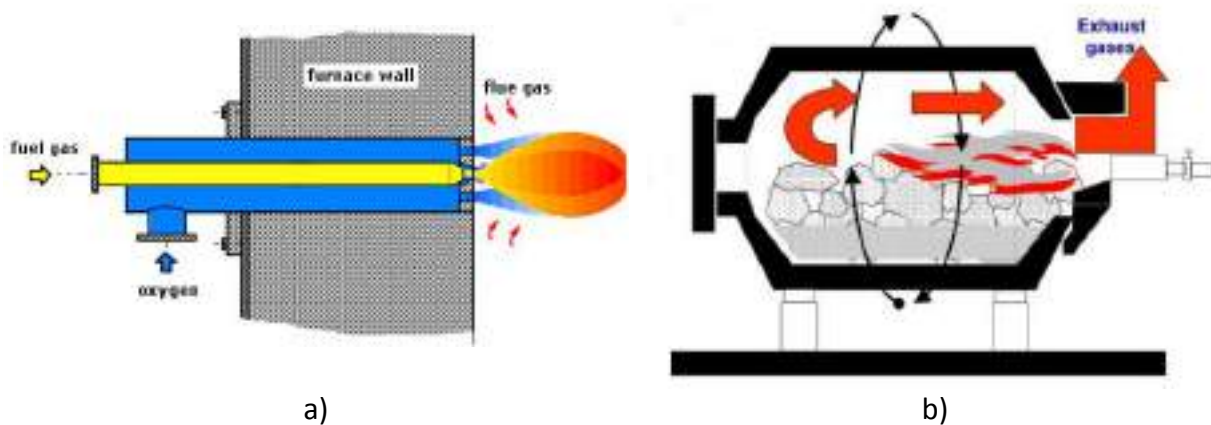


Figure 3. a) Oxy-fuel burner [11] and b) Rotary furnace – double pass [12]

Effects of oxygen on the combustion process are manifested through [13]:

- increased flame temperature and consequent more intense heat transfer by radiation;
- increased furnace production;
- improved energy efficiency and reduced specific fuel combustion;
- improved product quality;
- increased burning velocity;
- decreased ignition temperature,

but also has an impact on the composition and quantity of flue gases, as it can be seen from the stoichiometric equations presented in the next section.

Operating parameters of the tilting rotary furnace in the Croatian secondary aluminium company are presented in Table 1.

Table 1. Operating parameters of a tilting rotary furnace

Furnace capacity	10 000 kg
Duration of heating	4–5 h
Temperature of melt	700 – 750 °C
Flue gas temperature at the exit of the furnace	900 – 1000 °C

The total annual consumptions of combustion components for aluminium smelting in the rotary furnace in 2018 were as follows: 3483.53 m³ of natural gas and 6938.86 m³ of oxygen. The ratio of oxygen/natural gas was 1.99.

CALCULATION OF COMBUSTION EFFICIENCY

Stoichiometric equations of methane combustion at the excess air $\lambda = 1$:

- Stoichiometric combustion of methane with air:
 $1 \text{ CH}_4 + 2 \text{ O}_2 + 2 \cdot 3.76 \text{ N}_2 \rightarrow 1 \text{ CO}_2 + 2 \text{ H}_2\text{O} + 2 \cdot 3.76 \text{ N}_2$
The composition of the flue gases: 9.5 % CO_2 , 19 % H_2O , 71 % N_2
The amount of flue gas: $10.52 \text{ m}^3 \text{ flue gases/m}^3 \text{ CH}_4$
- Stoichiometric combustion of methane with oxygen:
 $1 \text{ CH}_4 + 2 \text{ O}_2 \rightarrow 1 \text{ CO}_2 + 2 \text{ H}_2\text{O}$
The composition of the flue gases: 33.3 % CO_2 , 66.7 % H_2O
The amount of flue gas: $3 \text{ m}^3 \text{ flue gases/m}^3 \text{ CH}_4$

According to the above equations, the influence of oxygen on the combustion process is as follows:

- Increased CO_2 and H_2O concentrations which result in the higher flame emissivity and consequently more intense heat transfer by radiation;
- Reduced exhaust mass flow rate, for 3 and a half times, and consequent improvement in thermal efficiency.

Calculations are based on combustion of natural gas of the following composition:

97 % CH_4 , 2.06 % C_2H_6 , 0.80 % N_2 , 0.14 % CO_2 , the net heat value of $H_i = 34.18 \text{ MJ/Nm}^3$ and at the excess air $\lambda = 1$.

The *combustion efficiency* (η_f) is defined as [14]:

$$\eta_f = \frac{h_{\text{fuel (NHV)}} + h_{\text{air}} - h_{\text{flue gas (inlet)}}}{h_{\text{fuel (NHV)}}} \quad (1)$$

where $h_{\text{fuel (NHV)}}$ is the net heat value of the fuel, h_{air} is the enthalpy of the preheated combustion air, and $h_{\text{flue gas (inlet)}}$ is the enthalpy of the gas at the inlet of the recuperator. Its physical meaning is identical to the available heat, i.e. to the percentage of the gross energy input which is available to heat the load and energy oriented to the furnace superstructure.

As can be seen from the expression (1) the enthalpy, i.e. the mass flow rate of flue gases leaving the furnace has the greatest impact on reducing the combustion efficiency, which is highlighted above.

RESULTS AND DISCUSSION

The paper analyzes the combustion efficiency for the use of air-fuel, oxy-fuel, and oxygen-enriched air-fuel burner for different flue gas temperatures (Figure 4).

From Figure 4 it can be seen that the available heat for the oxy-fuel technology is higher than that for air-fuel technology for the same temperature of exhaust, for example, at the temperature of exhaust flue gases of $1000 \text{ }^\circ\text{C}$ the available heat for air-fuel combustion (21 % O_2) has the value of 55 %, and for oxy-fuel combustion 84 %. The difference in available

heat increases as the exhaust temperature increases. The values of the available heat for oxygen enhanced combustion are in between these two technologies.

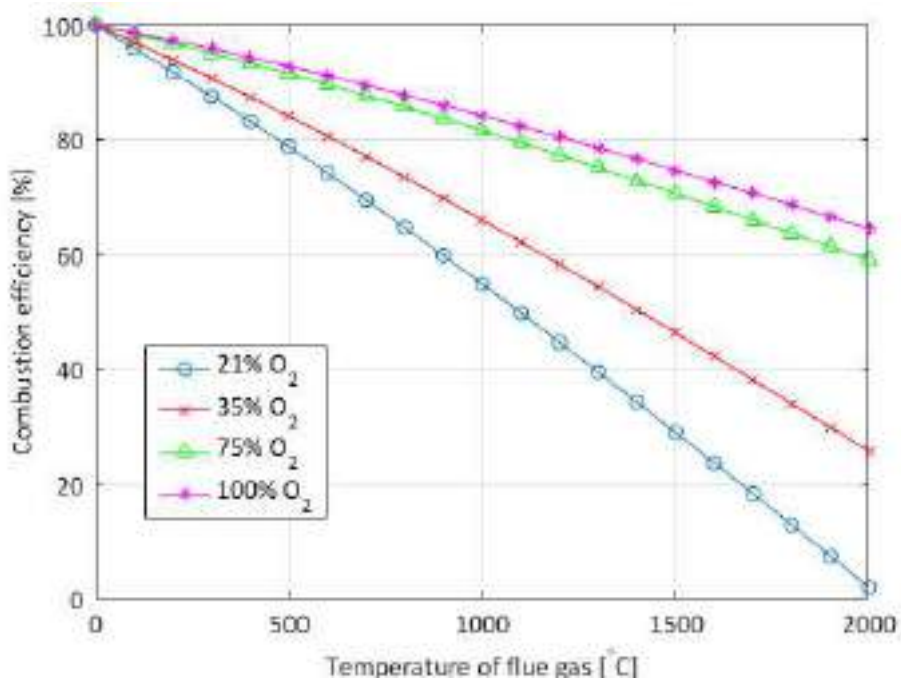


Figure 4. Combustion efficiency vs. flue gas temperature for different oxygen contents in the air

The rotary furnace used oxy-fuel burner for distribution and injection of pure oxygen and fuel. For this purpose, the effect of flue gas outlet temperature and excess oxygen ($\lambda \geq 1$) on the combustion efficiency (η_f) is calculated and shown in the form of a diagram (Fig. 5).

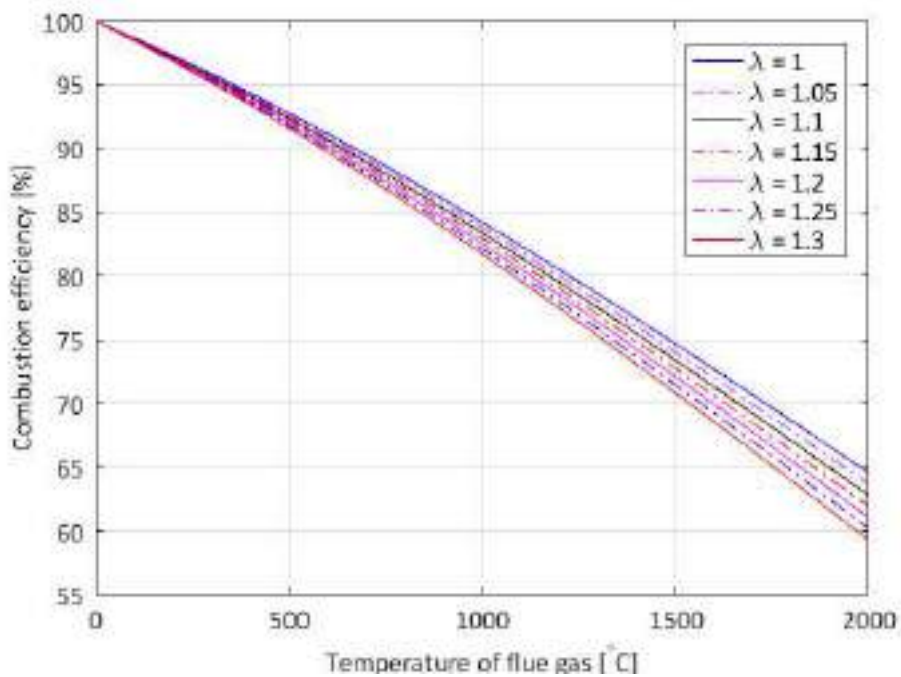


Figure 5. Combustion efficiency vs. flue gas temperature for different excess of oxygen

Based on the data in the diagram, the effect of combustion efficiency on oxygen consumption and operating costs for different excess of oxygen can be determined. With an assumed flue gas temperature at the furnace exit of 1200 °C and with an excess of oxygen of $\lambda = 1$, the combustion efficiency is 82 %, while with the excess of oxygen of $\lambda = 1.3$, the combustion efficiency is 77 %. From the above data it follows that by increasing the excess of oxygen (λ), from values 1 to 1.3, the combustion efficiency is reduced by 5 %. This also means increased fuel and oxygen consumption by 5 %.

Since the heating value of the supplied natural gas varies within 10 %, there is a need for continuous control of the oxygen concentration in the exhaust flue gases so that the oxygen/natural gas ratio can be controlled promptly. An oxygen probe installation may be recommended from the available oxygen concentration measuring devices.

Economic analysis of consumption

According to the data presented in the second section, the annual consumptions in 2018 were as follows: 6 938.86 m³ of oxygen and 3 483.53 m³ of natural gas. Taking into account the market price of oxygen in the amount of 1.68 €/kg O₂, and the price of natural gas in the amount of 0.71 €/kg, the annual consumptions of natural gas and oxygen as well as their costs were increased by 5 % [7]. The obtained data are shown in Table 2.

Table 2. Natural gas and oxygen consumption and a 5 % increase in consumption

	Annual consumption [m ³]	Annual costs [€]
Natural gas ($\lambda=1$)	3 483.53	2473.30
Natural gas ($\lambda=1.3$)	3 657.71	2596.97
Difference	174.18	123.67
Oxygen ($\lambda=1$)	6 938.86	11 657.28
Oxygen ($\lambda=1.3$)	7 285.80	12 240.14
Difference	346.94	582.86

With a 5% increase in consumption, the consumption of oxygen was increased by 346.94 m³ annually (582.86 €), and natural gas by 174.18 m³ (123.67 €). The total annual expenses were increased by 706.53 €.

CONCLUSIONS

The paper analyzes the energy efficiency of the tilting rotary furnace used in secondary aluminium production that is designed to have high energy efficiency. The reasons for achieving high energy efficiency are as follows:

- more effective heat transfer from refractory to the aluminium scrap due to rotation of the furnace drum,
- increasing the volume of aluminium scrap due to its 10° back tilt,
- use of oxygen-fuel burner,
- flue gas backflow through the furnace workspace, i.e. double pass of flue gases.

To achieve the optimal efficiency of tilting rotary furnace in realistic conditions, it is important to maintain the correct oxygen/fuel ratio by applying adequate controls. Because of variation in the heating value of the supplied natural gas, it is recommended to install an oxygen probe to ensure timely control of the oxygen concentration in the exhaust flue gases.

REFERENCES

- [1] U. M. J. Boin, M. Bertram, Melting standardized aluminum scrap: A mass balance model for Europe, *Jom*, 57(2005)8, pp. 26-33.
- [2] S. Capuzzi, G. Timelli, Preparation and melting of scrap in aluminium recycling: A review, *Metals*, 8(2018)4, 249, pp. 1-24.
- [3] G. Gaustad, E. Olivetti, R. Kirchain, Improving aluminum recycling: A survey of sorting and impurity removal technologies, *Resources, Conservation and Recycling*, 58(2012), pp. 79-87.
- [4] B. Zhou, Y. Yang, M. A. Reuter, U. M. J. Boin, Modelling of aluminium scrap melting in a rotary furnace, *Minerals Engineering*, 19(2006), pp. 299-308.
- [5] A. Bacchetti, S. Bonetti, M. Perona, N. Saccani, Investment and management decisions in aluminium melting: A total cost of ownership model and practical applications, *Sustainability*, 10(2018)3342, pp. 1-36.
- [6] M. Y. C. Garcia, Numerical analysis of melting and holding furnaces in secondary aluminium production, PhD Thesis, Universidad Zaragoza, Spain, 2014.
- [7] L. Mrkobrada, Energijska učinkovitost peći za taljenje i držanje aluminija, Master Thesis (in Croatian), University of Zagreb Faculty of Metallurgy, Sisak, 2019.
- [8] K. Boeckenhauer, T. Kaczmarczyk, Modern furnaces for aluminum scrap recycling, Accessible on Internet: <https://www.secowarwick.com/wp-content/uploads/2017/03/MODERN-FURNACES-FOR-ALUMINUM-SCRAP-RECYCLING-AP.pdf>, (15.01.2020.)
- [9] Industrial Heating: Minimizing Melt Loss in Aluminum Recycling, Accessible on Internet: <https://www.industrialheating.com/articles/91516-minimizing-melt-loss-in-aluminum-recycling>, (10.12.2019.)
- [10] A. Sane, S. Gangoli, X. He, M. Lawrence, R. Hewertson, Effective use of oxy-fuel combustion in aluminum reverberatory furnaces, *Light metal age: The International magazine of the light metal industry*, 2018, pp. 36-38.
- [11] M. Flamme, Low NOx combustion technologies for process heating: Two decades of R&D Activities at GWI. Proceedings of the 5th High Temperature Air Combustion and Gasification Conference, 28 – 31 October, Yokohama, Japan, 2002.
- [12] Accessible on Internet: <https://www.slideserve.com/steffi/international-secondary-lead-conference-1-sept-2009>, (22.01.2020.)
- [13] L. Lazić, D. Cerinski, J. Baleta, M. Lovrenić-Jugović, Improving fuel utilisation efficiency by oxygen-enriched air combustion. Proceedings of the 27th International Conference Ecological Truth & Environmental Research, 18-21 June, Bor, Serbia, 2019.
- [14] J. G. Wüning, Energy saving possibilities for gas-fired industrial furnaces, *Heat Treating Progress*, 7(2007)6, pp. 382-385.



19th INTERNATIONAL FOUNDRYMEN CONFERENCE
Humans - Valuable Resource for Foundry Industry Development
Split, June 16th-18^h, 2021
<http://www.simet.hr/~foundry/>

PRODUCTION AND CASTING OF AlSi7MgLi ALLOY

Mitja Petrič^{*}, Batri Zeka, Tilen Balaško, Primož Mrvar, Boštjan Markoli

University of Ljubljana Faculty of Natural Sciences and Engineering, Ljubljana, Slovenia

Oral presentation
Original scientific paper

Abstract

Presented paper describes the effect of lithium addition to AlSi7Mg cast alloys on solidification, microstructure development and mechanical properties. Mentioned alloy was produced in induction furnace with inert gas atmosphere and cast in various mould materials to study the suitability of mould material for casting Al-Li alloys. Thermal analysis was performed and compared to thermodynamic calculations of phase diagrams. Microstructure was analysed by optic and Scanning Electron Microscopy (SEM) equipped with Energy Dispersive Spectroscopy (EDS). X-ray Diffraction Analysis (XRD) was used to confirm microstructural constituents. Solidification path is changed at addition of lithium and first phase to precipitate is AlLiSi, followed by α_{Al} , iron rich phases, β_{Si} and Mg_2Si . Micro hardness of alloy containing Li is about 20 % higher and the most suitable moulding materials are steel and graphite.

Keywords: Al-Li alloys, casting, mechanical properties, solidification

*Corresponding author (e-mail address): mitja.petric@omm.ntf.uni-lj.si

INTRODUCTION

Al-Li base alloys have low density, high elastic modulus and high strength properties which make these alloys attractive for aerospace applications. The high strength is produced by the process of precipitation hardening. The addition of elements can form incoherent dispersoid or semi coherent precipitates and change the microstructure and mechanical properties of alloys [1-5]. Al-Li alloys use in aircraft applications, where the weight savings effected by using these low-density alloys greatly reduce the vehicle fuel costs and increase performance of parts such as: Aircraft parts such as leading and trailing edges, access covers, seat tracks; military and space applications such as main wing box, centre fuselage, control surfaces are made by Al-Li alloys. Al-Li alloys are used as substitute for conventional aluminium alloys in helicopters, rockets and satellite systems [5-7].

The precipitates of Al-Li alloys are in several metastable and stable phases which can be present in Al-Li alloys, depending on the alloying elements. The metastable precipitates in

this section are δ' (Al_3Li), while the stable phase discussed is δ (AlLi). The precipitation, in turn, depends upon chemistry, grain structure, and total thermomechanical history. In Al-Li alloys, the strengthening from Li additions is due to both solid solution strengthening and precipitation hardening [1-13]. The precipitation hardening is primarily due to the metastable strengthening phase, δ' (Al_3Li), which forms spherical, coherent, and ordered precipitate particles having a cube-on-cube orientation relationship with the aluminium matrix [13-16]. At equilibrium, and at its simplest in binary Al-Li alloys, the only phases present are the aluminium-rich solid solution and the δ (AlLi) phase [16].

The melting and casting of aluminium alloys with lithium has proven to be problematic, due to the high reactivity of lithium with oxygen and nitrogen. Lithium reacts with dry oxygen to form Li_2O at temperatures as low as 100 °C. Similarly, it reacts with water vapour to form Li_2O and H_2 . Although MgO has been reported to be thermodynamically more stable than Li_2O , the higher mobility and higher atomic fraction of Li favours the early formation of Li_2O compared to other compounds in Al-Li-Mg alloys [1,17]. Possible reactions of Al-Li alloys are also reported in literature [18]. The mentioned reaction products are mainly oxides, hydroxides, and carbonates. The calculated free energies show that Li and Mg are reactive in contact with oxygen and water and form lithium aluminate and magnesium oxide, while lithium carbonate can be formed from Li or Li_2O in combination with CO_2 [18].

The goal of a paper is to understand the way how to produce Al-Li alloys, their solidification path, new possibilities in development of mechanical properties and selection of moulding materials to cast Al-cast alloys with Li additions.

MATERIALS AND METHODS

New aluminium cast alloy AlSi7MgLi was investigated experimentally. The thermodynamic calculations were performed with ThermoCalc software and the chemical compositions of alloys given in Table 1 were used in order to calculate phase diagrams of alloys. Samples were melted in an induction furnace in a graphite crucible using argon atmosphere. 1 wt.% Li was added into the melt. Melt was cast in different moulds made of steel, graphite, Croning process and CO_2 process. Thermal analysis was performed as well. After data acquisition their numerical data, cooling curves and their derivatives were plotted, and characteristic temperatures determined. Differential scanning calorimetry was performed, and sample prepared for microstructural investigation with optic microscope and scanning electron microscope with EDS to determine the phases present in alloy AlSi7Mg . Vickers Hardness test was used to determine mechanical properties in period of 30 days after casting.

RESULTS AND DISCUSSION

Thermodynamic calculation

Thermodynamic description of system AlSi7MgLi cast alloys was constructed using ThermoCalc software. From the chemical composition in Table 1 the solidification and equilibrium phases were calculated for experimental alloy. It is seen that the amount of Li is 0,80 wt.%. According to the thermodynamic equilibrium calculation we have predicted solidification of the primary AlLiSi phase followed by the α_{Al} , β_{Si} and iron bearing phase β -

AlFeSi, Mg₂Si and π- AlMgFeS phases should precipitate from solid solution at temperatures around 475 °C (Figure 1).

Table 1. Chemical composition of alloy in wt.%

Alloy	Al	Si	Fe	Cu	Mg	Zn	Ti	Li
AlSi7Mg	Rest	6.7	0.44	0.01	0.35	0.01	0.01	-
AlSi7MgLi	Rest	7.05	0.10	0.05	0.36	0.02	0.09	0.80

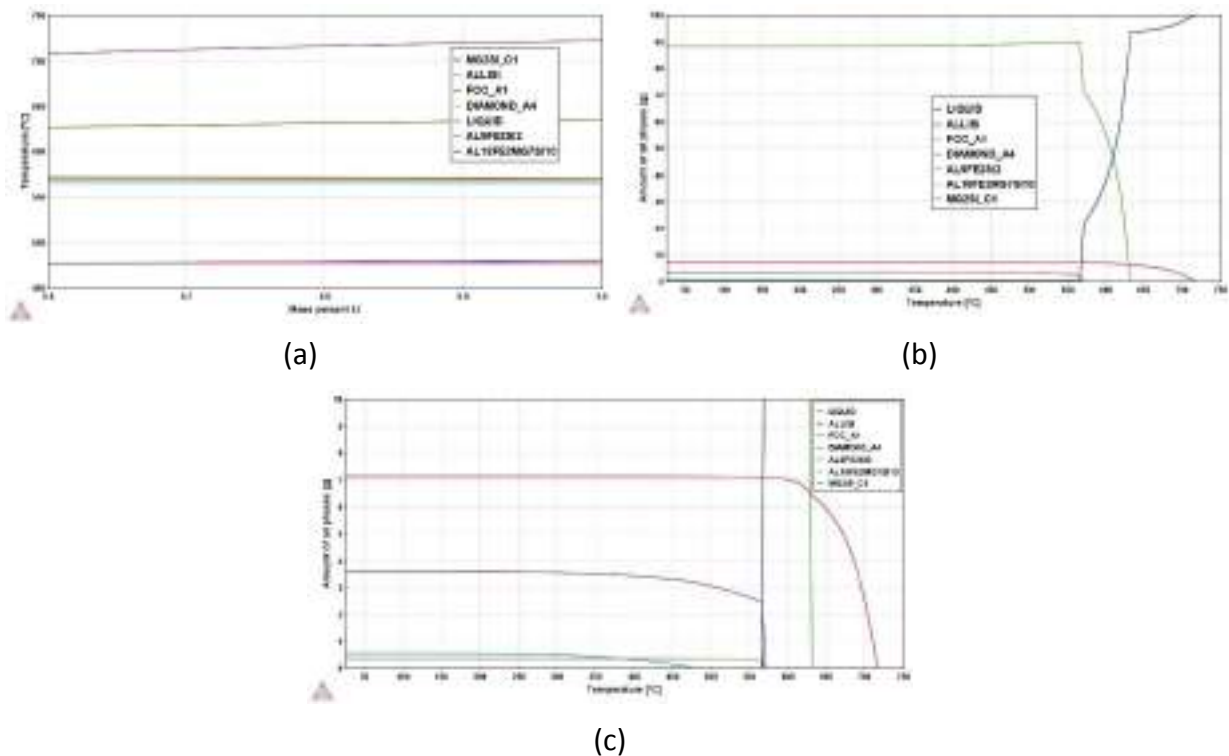


Figure 1. Thermodynamic calculation of: a) phase diagram of experimental alloy AlSi7MgLi, b) amount of phases of alloy during solidification and c) enlargement of b)

Thermal Analysis

Solidification process was analysed by thermal analysis on the samples cast in the steel mould and Croning mould, each sample subjected to the solidification by cooling in the air. After the data acquisition their numerical and graphical processing with the marked temperatures of the phase transformations was performed. The cooling and differentiated curves of AlSi7Mg alloy with Li addition from casting temperature 730 °C in steel mould and Croning mould are shown in Figure 2. Diagram with cooling curves in the fig. 2 indicates interactive significant deviation in values of the characteristic temperatures of the solidification, according to calculation and diagram of cooling curves at 730 °C with solidification start phases at approximately 658 °C in both cases. Solidification interval ended between 550 and 570 °C.

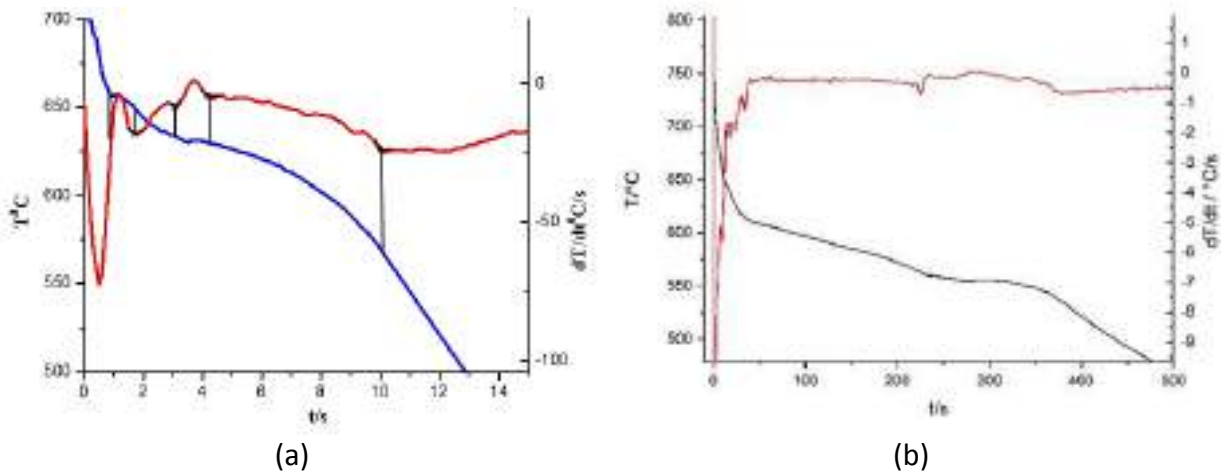
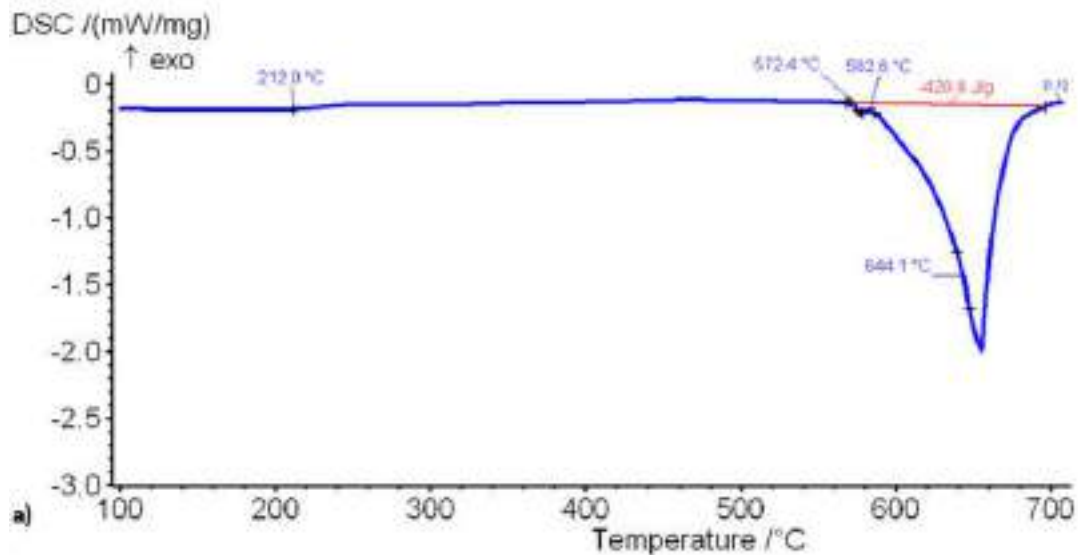
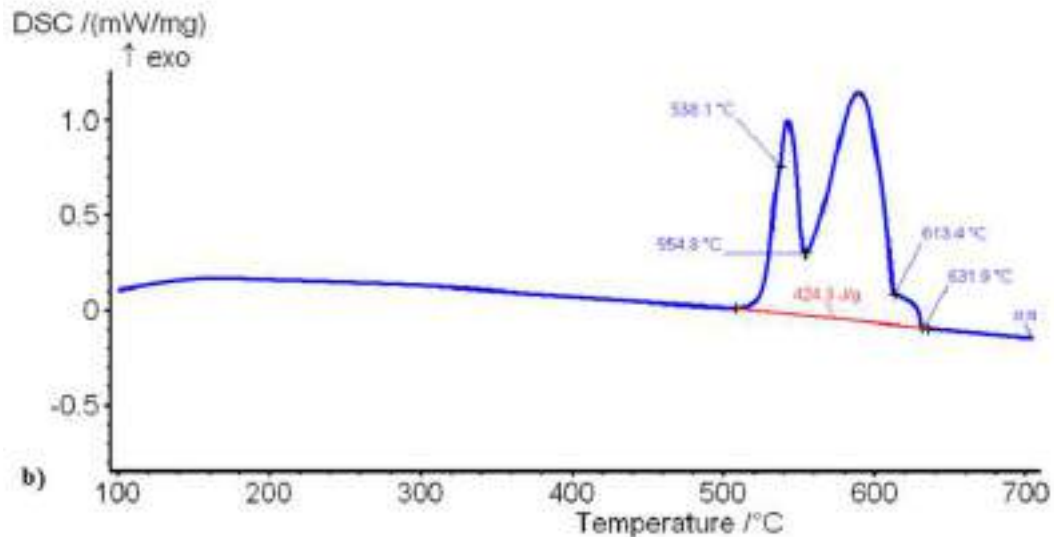


Figure 2. The cooling curves and differentiated curves of AlSi7MgLi alloy from: a) steel mould and b) from Croning mould.

The heating curve of the DSC analysis indicates melting start at 572 °C and the curve changes after 582.6 °C and continued with evaluation of phase at 644.1 °C, furthermore small peaks at 212 °C indicates precipitation process. Differential scanning calorimetry analysis was performed on the sample part from the sample poured in the steel mould and resulted in diagrams of the heating and cooling curves shown in the Figure 3a and 3b. Diagrams in the Figure 3 resulted in values of significant temperatures of the phase transformations. The temperature of the solidification starts (liquidus temperature) at 659.8 °C with AlLiSi phase at 620.6 °C, the $\alpha_{Al}+AlLiSi$ should solidify according to ThermoCalc at 607.8 °C, followed by iron bearing phase $\beta-AlFeSi$ at 565.2 °C, $\beta-Si$ and Mg_2Si at 547.7 °C.



(a)



(b)

Figure 3. Heating DSC curve (a) and cooling DSC curve (b) of AlSi7MgLi alloy

Microstructure Analysis

After analysis of solidification by thermal analysis technique samples were prepared for metallographic investigation. According to micrographs presented in Figure 4 and XRD analysis presented in Figure 5 the microstructure consists of α_{Al} phase, AlLiSi phase, π -AlMgFeSi phase, Mg_2Si which are confirmed by EDS and XRD analysis. With SEM we observed phases which are formed with Li addition. From Figure 4 it can be concluded that new phase AlLiSi appears. According to ThermoCalc calculation the elemental composition of AlLiSi phase should be 33.3 at.% for each element which was also confirmed by the XRD analysis. At SEM - EDS analysis only Al and Si were confirmed in 1 : 1 ratio since Li cannot be detected in EDS analysis. Furthermore, microstructure in the alloy with Li addition consists also of β -AlFeSi, π -AlMgFeSi and Mg_2Si confirmed by the EDS and they appear in the microstructure during solidification which is not in accordance with ThermoCalc calculations and is the result of non-equilibrium conditions of solidification.

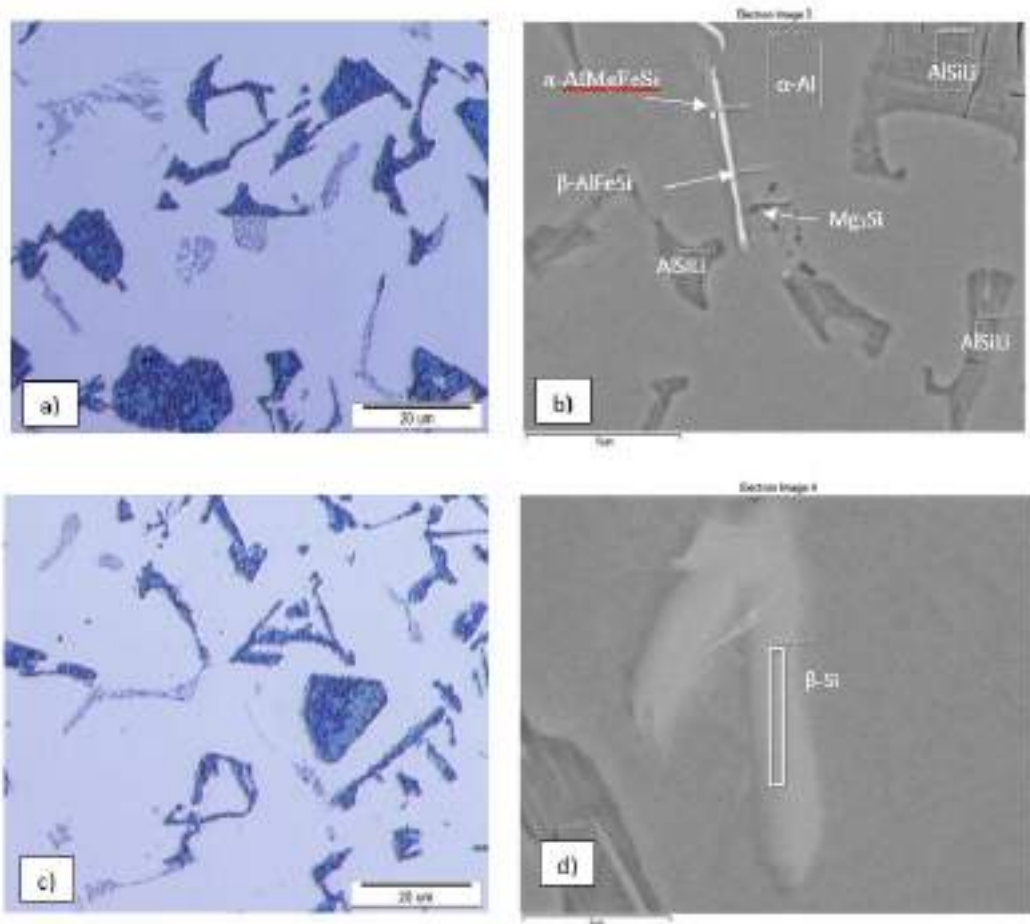


Figure 4. Optical (a, c) and SEM micrographs (b, d) of AlSi7MgLi

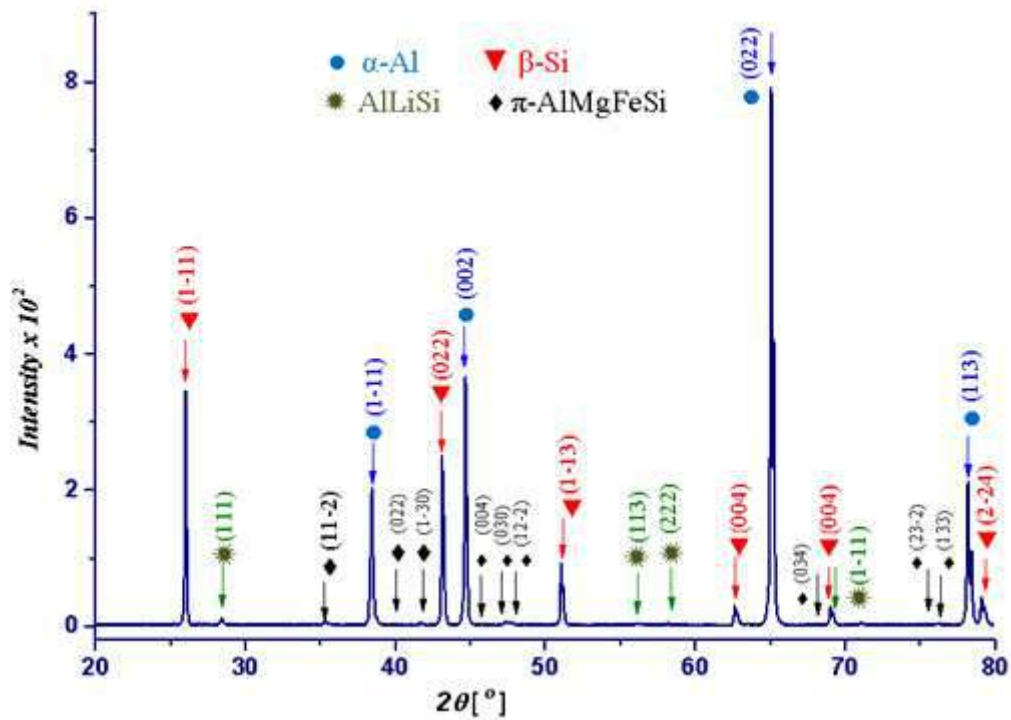


Figure 5. XRD pattern of AlSi7MgLi

Mechanical Properties

The samples were age-hardened for 30 days where 8 micro hardness measurements were performed at room temperature in 30 days and average values were calculated.

Hardness of AlSi7Mg alloy on first day was 66 HV. For 2-4 days, values showed a linear increase of hardness from 66 HV to 73 HV. It can be concluded that peak hardness was achieved after 7 days. Hardness of AlSi7MgLi alloy showed the hardness for first day was 89 HV in as cast state. After 24 hours of ageing, the hardness of sample dropped until 87 HV and after 2 to 7 days it increased gradually from 87 HV to 96 HV where plateau is reached at 96 HV. It can be concluded that peak hardness was achieved after 30 days reaching 102 HV. According to results of both alloys, the Li addition to AlSi7Mg alloy has great influence on increasing hardness compared to AlSi7Mg.

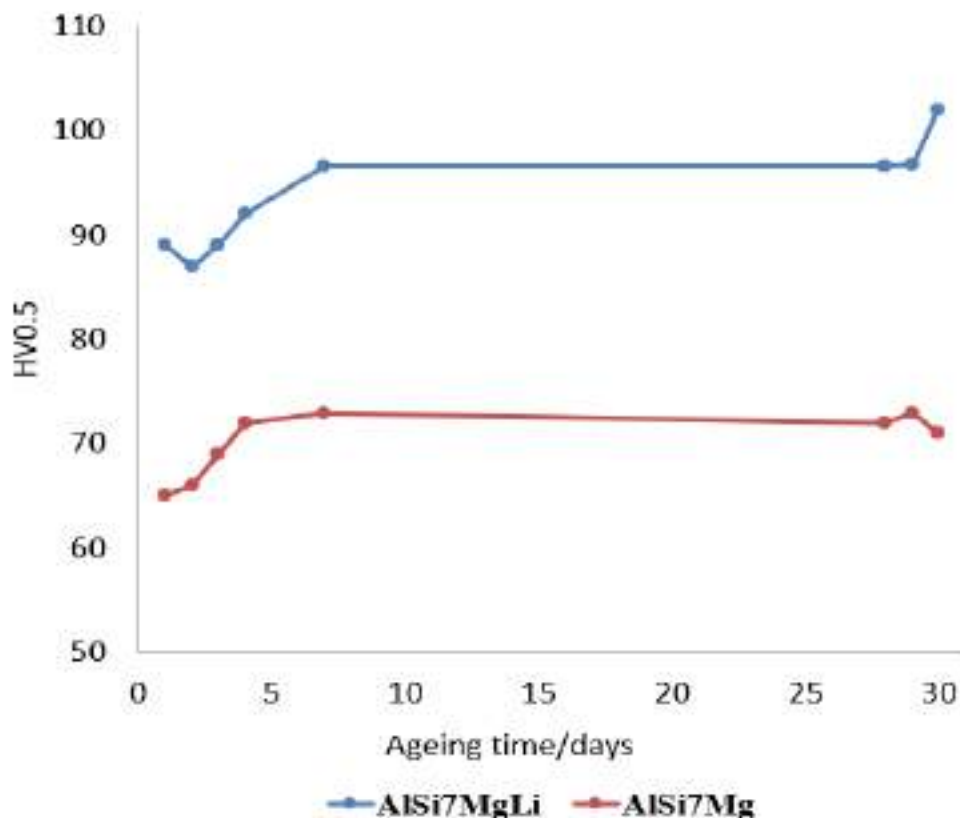


Figure 6. Hardness for natural ageing of AlSi7Mg and AlSi7MgLi

Moulding materials

Melt was poured in different moulding materials and reaction products between castings and moulds were analysed and casting quality assessed. Figure 7 displays casting quality and the best casting quality is obtained from steel mould and from graphite mould. Other moulding materials resulted in very porous castings which are the products of Li reacting with melt and the air. Also, reaction products on the surface of the castings were analysed by XRD analysis in cases of Croning mould and CO₂ mould. Steel mould and graphite mould do not show significant amounts of reaction products. Figure 8 is presenting XRD patterns, and one can see that reaction products consist of different oxides and carbonates.



Figure 7. Castings from: Croning mould (a), CO₂ mould (b), graphite mould (c) and steel mould (d)

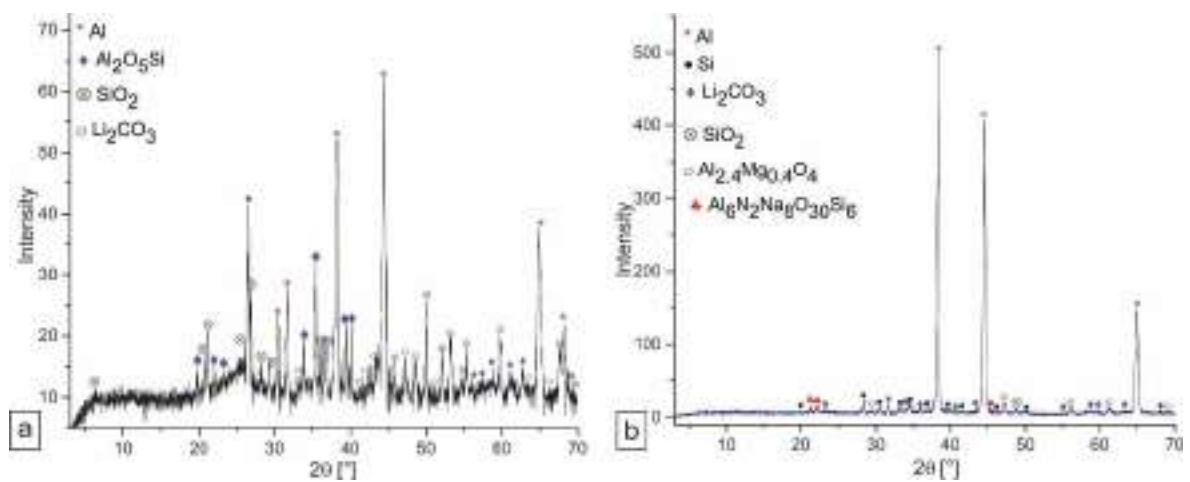


Figure 8. XRD patterns of reaction products from Croning mould (a) and CO₂ mould (b)

CONCLUSIONS

New alloy with Li addition to AlSi7Mg alloy was studied. For this purpose, 0.8 wt. % Li was added to designed AlSi7MgLi alloy containing 0.36 wt. % Mg and 7.05 wt. % Si. It was found that Li combination with AlSi7Mg resulted in different solidification path, development of new microstructure and creation of new phase AlLiSi. Li has influence to increase the mechanical properties in as cast state in comparison to AlSi7Mg. Li is very reactive metal and when added to Al alloy reacts with conventional moulding materials and air. Results are oxides and carbonates formed on casting surfaces and gaseous products in form of gas porosity in the castings. Higher cooling rates and steel or graphite moulding materials prevent reactions and give better castings quality.

REFERENCES

- [1] E. N. Prasad, A. Gokhale, R. J. H. Wanhill, Aluminium-lithium alloys, Butterworth-Heinemann, Oxford, 2014.
- [2] I. Polmear, D. StJohn, J. F. Nie, M. Qian, Light alloys-metallurgy of the light metals, Butterworth-Heinemann, Oxford, 2017.
- [3] J.R. Brown, Foseco non-ferrous foundryman's handbook, Butterworth-Heinemann: Oxford, 1999.
- [4] ASM Metals Handbook, Vol 02, Properties and Selection: Nonferrous alloys and special-purpose materials, ASM International, 1990.
- [5] I. Polmear, Light Alloys: From traditional alloys to nanocrystals, Butterworth-Heinemann: Oxford, 2006.
- [6] L. Backerud, G. Chai, J. Tamminen, Solidification characteristics of aluminium alloys, vol 2, Amer Foundry Society, 1990.
- [7] I. Polmear, S. P. Ringer, Evolution and control of microstructure in aged aluminium alloys, J. Japan Inst. Light Metals, 50(2000)12, pp. 633.
- [8] C. Baker, P. J. Gregson, S. J. Harris, Aluminium-Lithium Alloys III. Proceedings of 3rd International Conference on Aluminium-Lithium Alloys. The Institute of Metals, (C.J. Peel) 1986, London, UK, pp. 509-515.
- [9] C. M. Adam, Aluminium-Lithium Alloys, AIME, New York, 1981.
- [10] P. N. Anyalebechi, Analysis of the effects of alloying elements on hydrogen solubility in liquid aluminum alloys, Scripta Met. Mater., 33(1995)8, pp. 1209-1216.
- [11] R. F. Ashton, D. S. Thompson, E. A. Starke Jr., F. S. Lin, F. S., Processing Al-Li-Cu-(Mg) alloys, Aluminium-Lithium Alloys III. Proceedings of 3rd International Conference on Aluminium-Lithium Alloys. The Institute of Metals, (C.J. Peel) 1986, London, UK, pp. 66-77.
- [12] W. A. Averill, D. L. Olsen, D. K. Matlock, G. R. Edwards, Lithium reactivity and containment, Proceedings of the First International Aluminium-Lithium Conference, The Metallurgical Society of AIME, (Sanders, T.H., Starke, E.A.) 1981, Warrendale, PA, pp. 9-28.
- [13] W. A. Cassada, G. J. Shiflet, E. A. Starke, The effect of Germanium on the precipitation and deformation behaviour of Al-2Li alloys, Acta Metall., 34(1986)3, pp. 367-378.

- [14] C. R. Chakravorty, V. Singh, A. A. Gokhale, Melting and casting of aluminium-lithium alloys, Proceedings of the 36th Annual Convention of Institute of Indian Foundrymen, The Institute of Indian Foundrymen, 1987, Calcutta, India, pp. 135-140.
- [15] A. B. De Ross, L. F. Mondolfo, Metallurgical aspects of casting aluminium alloys, Aluminium Transformation Technology, ASM, Metals Park, 1980.
- [16] A. P. Divecha, S. D. Karmarkar, Casting problems specific to aluminium-lithium alloys, Aluminium-Lithium Alloys I, AIME, New York, 1981.
- [17] L. V. Tarasenko, O. E. Grushko, V. A. Zasytkin, L. A. Ivanova, Phase composition of surface films on aluminium alloys with lithium, Russ. Metall., 2(1980), pp. 174-77.
- [18] P. G. Partridge, Oxidation of aluminium-lithium alloys in the solid and liquid states, Int. Mater. Rev., 35(1990)1, pp. 37-58.



19th INTERNATIONAL FOUNDRYMEN CONFERENCE
Humans - Valuable Resource for Foundry Industry Development

Split, June 16th-18th, 2021

<https://ifc.simet.hr/>

**NUCLEATION AND GRAPHITE GROWTH IN NODULAR CAST IRON - AN
OVERVIEW**

Barbara Tubić Bulat^{1*}, Zdenka Zovko Brodarac¹, Primož Mrvar²

¹ University of Zagreb Faculty of Metallurgy, Sisak, Croatia

² University of Ljubljana Faculty of Natural Sciences and Engineering, Ljubljana, Slovenia

Oral presentation

Subject review

Abstract

The term nodular iron cast refers to a group of iron alloys with a maximum carbon content of 4 wt.% and silicon from 1.7 wt.% to 2.8 wt.%. This type of cast iron is characterized by the presence of carbon in the spherical or nodular form of graphite in a ferrite, pearlite or ferrite-pearlite matrix. Due to its better mechanical properties in relation to the other iron cast groups, it is widely used in production of gearboxes, crankshafts, turbine rotors, tanks, transportation industries, etc. Generally, size, distribution and shape of graphite nodules ensure a good toughness, high value of elongation and yield strength, castability and machinability.

The course of solidification and each parameter of the production and solidification process has a certain impact on the mechanical properties and microstructure of the final product. However, solidification and graphite growth mechanisms in nodular cast iron have not been fully explained in despite to a large amount of research on the subject. Different experiments have led to the creation of different theories about the solidification process which aim to enable the creation of models for predicting the solidification process and the growth of graphite nodules. Predicting the development of microstructure and defining optimal parameters of the production process could prevent casting and microstructural defects thus ensuring desired properties of the casting.

This paper provides an overview of several studies regarding the nucleation and graphite growth mechanism theories and experiments.

Keywords: *casting, nodular iron, solidification, nucleation, graphite growth, overview*

*Corresponding author (e-mail address): tubicb@simet.unizg.hr

INTRODUCTION

Prior to the use of steel in construction industry, cast iron was the most common material for such application. Continuous progress of research, casting industry development and lower production cost led to the revival of iron castings as desirable construction materials [1]. Microstructure is a significant element of physical metallurgy of iron alloys and

represents the relationship between chemical composition, production processes, microstructure and mechanical properties.

The Fe-Fe₃C diagram (Figure 1) shows a map of the phases present in iron alloys under equilibrium conditions relating the ratio of carbon content to the temperature. Equilibrium assumes that there is enough time available to achieve the right chemical compositions for phases to form [2]. Silicon is used in the industrial production of ferrous alloys to achieve the so-called carbon equivalent which is calculated according to equation 1.

$$CE = \% C + 1/3 \% Si + 1/3 \% P \quad (1)$$

Carbon equivalent defines a type of alloy. Thus eutectic alloy's CE equals 4.3 % while hypereutectic alloys have CE above 4.3 or CE lower than 4.3 for hypoeutectic alloys respectively [3].

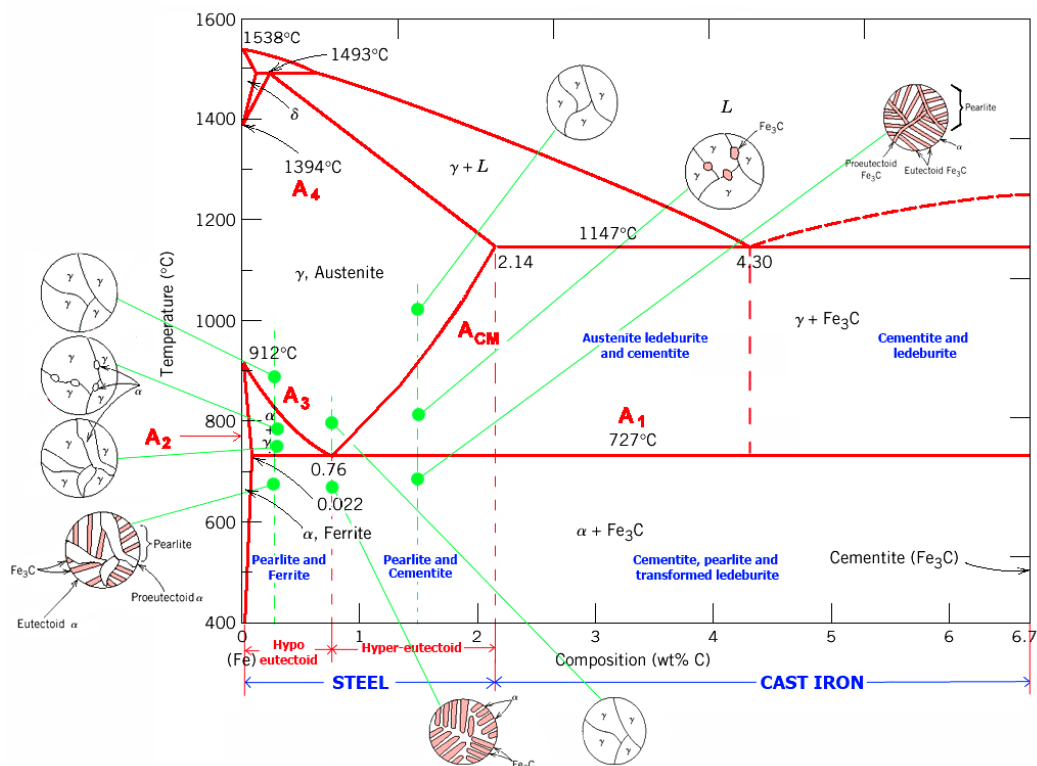


Figure 1. Iron- carbon phase diagram [4]

Nodular cast irons are a group of iron alloys containing a maximum 4 wt.% of carbon and 1.7 to 2.8 wt. % of silicon. Such alloys are characterized by the presence of carbon in spherical or nodular form of graphite in the ferrite, pearlite or ferrite-pearlite metal matrix [1]. The nodular form of graphite is achieved by magnesium and rare earth elements (RE) addition to the liquid iron before or during casting process [5]. This contributes to the improvement of mechanical properties such as strength, castability and toughness of cast iron. Nodular iron has mechanical properties comparable to those of some high-carbon steels achieved at lower production cost. Due to its better mechanical properties in relation to the other iron cast groups, it is widely used in production of gearboxes, crankshafts, turbine rotors, tanks, transportation industries, etc. [6]. Figure 2 shows the interdependence of the relative mass(a) and the relative production cost (b) of different materials products with tensile

strength in the product. Nodular cast iron has a very favorable ratio of price and mechanical properties in comparison to other metal materials which discloses its' significant application.

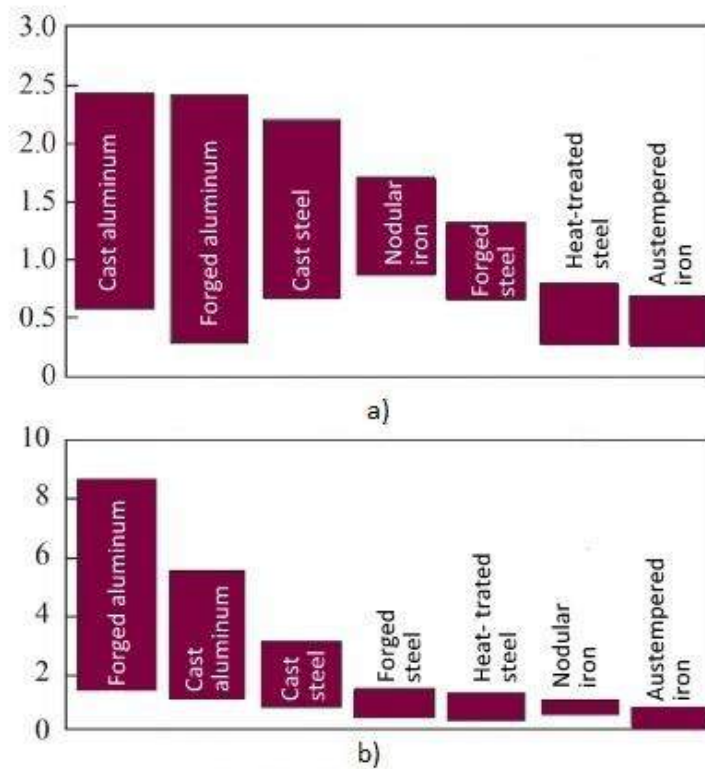


Figure 2. Comparison of
a) weight of different materials in relation to strength
b) relative cost of different materials in relation to strength [7]

Nodular iron castings are iron alloys used industrially in parts that require moderate plasticity without sacrificing mechanical resistance, such as valves, hardware elements, and auto parts. Studies focused on nodular iron castings have become important in recent years due to its extensive use and the growing trend of replacing forged steels due to lower production costs [8]. The improvement of the mechanical properties of ductile iron castings is achieved by alloying, which enables the replacement of cast and forged steel with nodular cast irons in various applications. In order to achieve further improvements in the quality of ductile iron casting parts, the physical mechanisms that make up the solidification process have to be explained. The mechanical properties of ductile iron castings are influenced by the metal matrix and morphology of graphite nodules [8, 9]. The solidification process of ductile iron starts at a temperature of 1147 °C (Figure 1), which makes it difficult to collect experimental data on the solidification sequence. The latter is therefore described assuming the cooling process in the liquid state of a well-insulated casting takes place in equilibrium conditions where the cooling rate is equal to zero. The first solid phase developed in hypereutectic (carbon equivalent CE = 4.5%) is a graphite cluster phase [8, 10]. Clusters are graphite particles that grow by binding carbon atoms from the melt until the temperature reaches the eutectic reaction temperature. Then in areas with low carbon concentration austenite is formed which then surrounds the graphite nodules. During eutectic solidification, only austenite is in direct contact with the melt. The further growth of graphite nodules takes place through austenite by carbon diffusion [11, 12]. After solidification ends, carbon diffusion continues toward the graphite nodules as the solubility of carbon in the

austenite decreases with temperature [8, 12]. This is followed by eutectoid transformation, where austenite is converted to pearlite and multiple carbon atoms diffuse into nodules. Finally, depending on the amount of carbon (CE), the metal base of ductile iron can be ferritic, pearlite or a mixture of ferrite and pearlite. Some assumptions of the solidification process can be found due to the research of the microstructure obtained by quenching of nodular cast iron melt at different temperatures [8, 9]. The importance of nodular cast iron utilization is the result of a wide range of different qualities. Quality can be varied by combining different chemical compositions, melt treatments (inoculation, nodulation, alloying), different cooling rates leading resulting in variations of shape, size and number of graphite nodules [10, 11].

Extensive research of the cast iron microstructure development led to the creation of different theories about the solidification process. The aim is to enable the creation of models for prediction of the solidification process and the mechanism of the graphite nodule growth. The following two models attempt to explain the solidification process of nodular cast iron with the eutectic composition (CE = 3.4 %). These models are called uninodular (Figure 3 a) [8, 13, 14] and multinodular (Figure 3 b) theory [8, 15]. Uninodular theory assumes that graphite clusters nucleate in the melt and are separately surrounded by round austenitic shells. In this case both phases grow by diffusing carbon from the liquid into graphite clusters until the end of solidification, creating nodules. However, this form of graphite growth is difficult to explain theoretically due to the time required for carbon diffusion through austenite, as well as because of the pressures that should occur in the austenite shell when the graphite nodule grows.

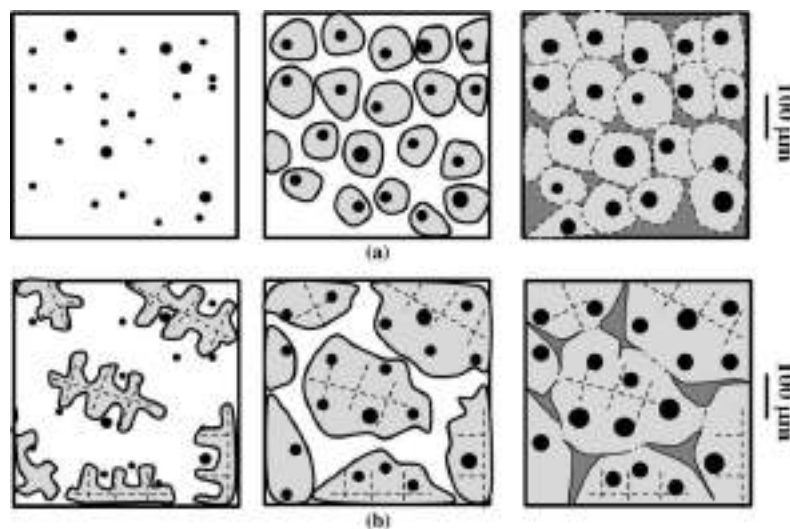


Figure 3. Microstructural evolution according to the a) uninodular b) multinodular theories[14]

The multinodular theory [8, 14, 15] suggests that both phases nucleate independently in the melt. This theory is based on the assumption that austenite grows in dendritic form and with continued solidification, dendritic branches surround graphite nodules [15]. Uninodular and multinodular models are described in more detail in the literature [15, 16]. One of the most important mechanical properties of nodular iron castings is its ductility which is achieved by the nodular form of graphite present in the metal matrix [8]. The growth of nodular graphite is limited due to the carbon diffusion through the austenite during the solidification process.

This limitation leads to the creation of preferential growth directions which obtain the shape similar to the rose lettuce. The final shape of the graphite mainly depends on the rate at which the austenite wraps around the nodule. This rate depends on the undercooling of the casting, which is also affected by the amount of magnesium present in the melt [11, 12].

Theoretically three types of austenite encapsulation (surrounding the nodule with an austenitic envelope) can be distinguished: fast, slow, and non-existent encirclement [17]. If there is a rapid nodule encirclement, then the graphite has the same radii for carbon diffusion from all directions, resulting in round graphite. If wrapped slowly, the nodule will have an area of preferred growth, reducing the final nodularity. And finally, if there is no wrapping of the nodule with an austenitic sheath, the final geometry will correspond to lamellar graphite [17, 18]. Although the multinodular theory is based on experimental findings of austenite dendrites in the microstructure of the eutectic composition alloy, more research has focused on simulating the solidification of nodular iron castings according to uninodular theory [12, 16, 19, 20] versus multinodular theory [8, 17, 18]. Existing solidification sequence prediction models assume that nucleation and growth of graphite will lead to the formation of a complete sphere, which is a theoretical and ideal behavior that does not occur in real production conditions [8, 13, 18].

The achievement of the required properties in nodular iron casting is depending on the mechanisms of solidification as well as inoculation, modification and degeneration within different solidification conditions [11, 12, 19]. Efforts are made in order to explain the nucleation process in iron-carbon alloys with graphite. A number of theories have been developed over the years. Nevertheless, significant questions remain unanswered. The reason lays in the wide variety of conditions, such as temperature range in which the nuclei are formed, the complexity of reactions that take place in the melt, the chemical composition of the nucleus, etc. It is difficult to give a clear and simple answer to the question of the course and mechanism of nucleation.

NUCLEATION THEORIES

The graphite nucleation mechanisms in the melt can generally be explained according to one of two theories. The first is the theory of homogeneous nucleation on a carbon-enriched cluster or on a particle of undissolved / residual graphite (single-phase nucleation) [12, 19]. The second is the theory of heterogeneous nucleation (single- or multi-phase nucleation). Even though the graphite-enriched particles are not considered homogeneous nuclei, they are taken into the account as homogeneous particles because they have the same chemical composition as the graphite phase growing on them. Both theories view residual graphite as the ideal nucleant for graphite formation during solidification [20, 21, 22]. The heterogeneous nucleation theory also points to the importance of the certain inclusions present in the melt as possible sites for heterogeneous nucleation of the graphite. Heterogeneous nucleation taking place in the real production conditions depends on the purity of the base metal, retention time, temperature and the melt processing. The inoculation is a melt treatment technique that manages the development of a microstructure which works by introducing particles into the melt. Those particles stimulate the accumulation of the suitable particles for the nucleation of graphite clusters. The commercial inoculants are based on a ferro-silicon master alloy containing the small amounts of elements such as Ca, Ba, Sr, Al, Zr, and rare earth elements [22, 23]. The significance of these elements is in their strong affinity for oxygen and sulfur in the melt.

When combined, those elements form complex oxides and sulfides which then act as the nucleation sites of graphite. Theories of heterogeneous nucleation developed in the recent history have mainly focused on non-metallic inclusions present in all commercial iron castings. The special requirements that the elements in the inoculant must meet in order to act as the potential nucleation sites in the melt are good crystallographic compatibility, small lattice irregularity, fine dispersion in the melt and high stability at elevated temperatures [19, 24]. Some of the most important theories of heterogeneous nucleation are mentioned below.

The gas bubble theory is based on the claim that tiny gas bubbles in the melt are ideal sites for the formation of nuclei on which the graphite particles can grow. According to this theory, the direction of growth of graphite is radially from the outside to the inside of the bubble. Gas bubble theory is in principle based on the presence of carbon monoxide in the melt. However, under industrial conditions of ductile iron melt production, strong deoxidants are added to remove dissolved oxygen. It is unlikely that the graphite cluster will expand in the direction of the internal volume of the gas bubble, because such growth would involve the diffusion of carbon through the graphite shell [19,25].

The graphite or carbon-rich cluster theory was introduced as a form of homogeneous nucleation. According to this theory, graphite grows from a small particle of crystalline graphite that is already present in the melt [16, 19, 26]. However, when the melt is treated with a ferro-silicon master alloy, Si promotes nucleation of the graphite. Since the dissolution time for the ferro-silicon master alloy in the melt is a few seconds, the theory assumes the formation and retention of particles in the melt. The condition for the retention of graphite clusters is that Ba or Sr are present in the melt in sufficient quantities to prevent the dissolving and to promote the formation of carbon clusters containing approximately 15 atoms. Therefore, in this theory, clusters of C_n or $(Fe_3C)_n$ exist in dynamic equilibrium in molten iron alloys with graphite and serve as sites for graphite nucleation [19]. Recent research has shown that in low-carbon gray cast irons, graphite nucleates at the austenite-liquid interface without the presence of foreign inclusions, which supports the theory of graphite nucleation on carbon-rich clusters [16, 26].

The silicon carbide theory is based on the presence of silicon carbide (SiC) crystals and an increased amount of graphite particles near the dissolving ferro-silicon master alloy has been observed [19, 27]. Because of this phenomenon, a theory of graphite nucleation and the mechanism of SiC particle fading has been created. The theory is based on the assumption that there is a local supersaturation of C and Si in the melt after dissolution of SiC, which gives the necessary driving force for homogeneous nucleation of graphite. The effect of fading is explained by the homogenization of C and Si in the melt through convection and diffusion [28]. However, the critical role of elements such as Ca, Sr, and Ba in the inoculant cannot be explained by this theory [19, 27, 28].

The silicate theory is based on the fact that the most inclusions in nodular cast iron are the primary or secondary product of magnesium melt processing [13, 19]. Hexagonal nuclei are composed of two-layer compounds of Mg or Ca sulfides composition surrounded by MgO, SiO_2 and $2MgO \times SiO_2$ with an epitaxial mechanism of graphite on oxide growth [22]. The hypothesis was supported by multiple studies that attempted to identify the chemical composition of the graphite nodule nucleus [19,.21, 22, 28].

The sulfide/oxide theory was developed when studies have suggested that sulfides, oxides, or nitrides, formed after inoculant addition, act as nucleation sites during graphite solidification [19, 28, 29]. The theory has been confirmed by research [30] which has indicated the importance of non-metallic inclusions. It was found that most graphite clusters in cast iron are associated with non-metallic inclusions, mainly magnesium and calcium sulfides. Graphite nucleation clusters for lamellar and spheroidal graphite are composed of complex oxides and sulfides. The spacing within the lattice for oxy-sulfide particles coincides with the spacing of the graphite lattice thus providing a suitable substrate for graphite growth [20, 28, 30].

GRAPHITE GROWTH

Favorable technological properties and relatively low production costs result in the increasingly frequent use of nodular cast iron in many industries [3, 5]. The properties of nodular cast iron are mainly influenced by cooling rate of products, addition of alloying elements, different casting technology application and cooling grate which can affect the shape of graphite and the formation of metal matrix [8, 10, 11]. Solidification process and the mechanism of graphite growth in nodular cast iron have not been fully understood despite a number of studies [12, 14, 18, 25]. Graphite crystallizes from the melt in different forms depending on the chemical composition of the melt and the solidification conditions (cooling rate). Basic morphologies of graphite present in iron cast alloys are: lamellar (LG), vermicular (CG) and nodular (SG) graphite. This transition is also based on changing of the growth direction of the graphite aggregate from the a- to c-direction, or from c- to a-direction. Chunky graphite is a highly branched, interconnected form of graphite, and it is considered degenerated form of spheroidal graphite [13, 22, 25]. The transition from lamellar to vermicular and from vermicular to nodular can be achieved by adding small amounts of Mg, Ce or lanthanide to the low-sulfur iron melt. This means that the process can be carried out in the opposite direction by adding sulfur or losing magnesium by evaporation and/or oxidation. The transition from vermicular to lacquered graphite is subject to the influence of certain elements used for production on melt processing [13, 25, 32]. Graphite forming in the shape of nodules attributes to high value of elongation and yield strength, good castability, machinability and toughness [22, 31]. The study has been done on the problem of trace elements and their influence on the development and shape of graphite nodules [25, 32]. It was discovered that magnesium and rare earth elements stabilize the precipitation of oxides and sulfides by stimulating the growth of graphite nodules as shown in Figure 4.

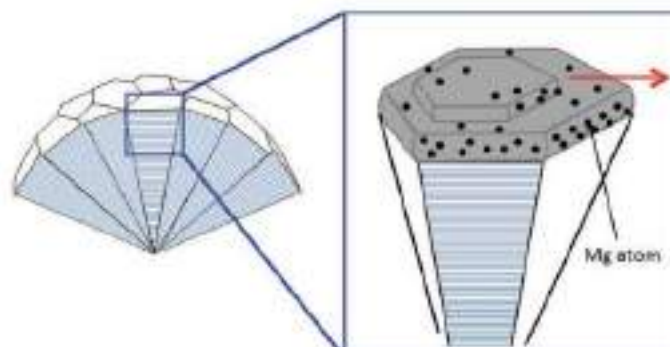


Figure 4. Schematic of spheroidal graphite growth [33]

Of all the elements present (except carbon) in nodular cast iron, silicon has the greatest influence on the carbon content in eutectic [24]. Today there are several nodular cast iron production processes. The base for all production processes is the modification of graphite form in the primary melt by modifiers (ferro-silicon master alloys) to obtain the characteristic spheroidal form of graphite [22, 27]. The commonly used modifiers are magnesium-based alloys that have a high affinity toward oxygen and sulfur in reference to the sulfide/oxide theory [19, 28]. This leads to the formation of stable oxides and sulfides which stimulate the growth of graphite nodules as shown in Figure 4 [32].

Alloying elements and cooling rate are the main factors influencing the formation of ferrite and pearlite as metal matrix [8]. Elements that promote the formation of pearlite are copper, chromium and manganese, but they also lower the temperature of eutectoid reaction and the rate of ferrite formation [19, 20]. With a proper content of elements that promote the formation of pearlite, nucleation will be possible at the boundaries of austenitic grains and at the interface of ferrite / austenite of graphite / austenite [21, 22].

Research on samples from thin-walled castings revealed that during high-temperature phase transformation in the solid state, nodules in the cast material have a dual microstructure [3, 23, 34]. In this case, graphite nodules consist of inner zone with disoriented graphite and the outer zone where the crystallization takes place properly. The disoriented zone is going to occur due to mechanical shrinkage deformation during solidification in a metastable system [34].

It is generally accepted that spheroidal graphite growth can be affected by surface-active impurities adsorbing on the unsaturated edges of graphite platelet leading to the change of preferred growth direction thus creating degenerated graphite nodules [13, 25, 35].

The sequence of solidification and the subsequent sequence of phase transformations in the solid state significantly affect the microstructure and mechanical properties of iron castings [19, 36]. It has been found that eutectoid transformation is a diffusion-controlled process and can be divided into two phases: ferrite formation (stable phase) and pearlite formation (metastable phase) from austenite [22, 36]. In the case of a low cooling rate, after solidification of the equilibrium phase there will be austenite and nodular graphite. The temperature decrease leads to the graphite nodules continuous growth due to carbon rejection by austenite [20, 36].

A review of the literature shows that the graphite growth and the course of solidification have significant impact on the microstructural and mechanical properties of nodular cast iron. However, the formation mechanism and thus the technology for degeneration prevention is still unknown.

CONCLUSIONS

The nucleation process and the mechanism of graphite growth in nodular cast iron have not been fully determined despite a large amount of research on the subject. Different experiments have led to the creation of theories about the solidification process and it is generally known that the sulfide/ oxide theory has been confirmed by research. It was found that most graphite clusters in cast iron are associated with non-metallic inclusions, mainly magnesium and calcium sulfides and that graphite nucleation clusters for lamellar and

spheroidal graphite are composed of complex oxides and sulfides. It is still uncertain what causes the changing of the growth direction of the graphite aggregate from the a- to c-direction, or from c- to a-direction. This change of growth direction causes graphite form degeneration which negatively affect mechanical properties of the cast. The aim of the future research should be the creation of models for prediction of the solidification process and the growth of graphite nodules in order to define optimal parameters for the nodular cast iron production process and help to achieve the desired properties of the casting.

Acknowledgements

This work was supported by the research topic “Design and Characterization of Innovative Engineering Alloys”, Code: IP-124- 2020-ZZB funded by University of Zagreb, Ministry of Science and Education and Infrastructural scientific projects: Center for Foundry Technology SIMET, Code: KK.01.1.1.02.0020 and VIRTULAB - Integrated Laboratory for Primary and Secondary Raw Materials, Code: KK.01.1.1.02.0022 funded by European Regional Development Fund, Operational Programme Competitiveness and Cohesion 2014. - 2020.

REFERENCES

- [1] A. Pereira, M. Costa, C. Anflor, J. Pardal, R. Leiderman, Estimating the effective elastic parameters of nodular cast iron from micro-tomographic imaging and multiscale finite elements: Comparison between numerical and experimental results, *Metals*, 2018, (8), 695
- [2] G. Krauss, *Physical metallurgy of steels: an overview*, Automotive steels, Elsevier Ltd. 2017, pp. 95-111.
- [3] X-R. Chen, Q-J. Zhai, H. Dong, B-H. Dai, H. Mohrbacher, Molybdenum alloying in cast iron and steel, *Advances in Manufacturing*, 2020, 8, pp. 3-14.
- [4] Accessible on internet: https://www.tf.unikiel.de/matwis/amat/iss/kap_6/illustr/s6_1_2.html (19.3.2021.)
- [5] M. Lekuhi, M. Kuna, G. Hütter, Characterising fatigue behaviour of nodular cast iron using micromechanical simulations, *MATEC Web of Conferences* 300, ICMFF12, 2019, 13002
- [6] J. Tang, Y. Shen, X. Yao, The mechanical model of refinement mechanisms of graphite particle of nodular cast iron during the fraction stir processing, *Materials Research Express* 6, 2019, p. 126573.
- [7] J. R. Keough, K. L. Hayrynen, *Designing with austempered ductile iron (ADI)*, AFS Proceedings, American Foundry Society, Schaumburg, IL USA, 2010
- [8] S. C. Murcia, E. A. Ossa, D. J. Celentano, Nodule evolution of ductile cast iron during solidification, *Metallurgical and Materials Transactions*, , 45(2014)2, pp. 707-718.
- [9] A. Basso, J. Sikora, Review on Production Processes and Mechanical Properties of Dual Phase Austempered Ductile Iron, *International Journal of Metalcasting*, 2012, vol. 6, pp. 7-14.
- [10] V. D. Shinde, B. Ravi, K. Narasimhan, Solidification behaviour and mechanical properties of ductile iron castings with varying thickness, *International Journal of Cast Metals Research*, 25(2012)6, pp. 364-373.

- [11] D. M. Stefanescu: Science and Engineering of Casting Solidification, Springer, New York, 2008
- [12] D.M. Stefanescu, Solidification and modeling of cast iron- A short history defining moments, Materials Science and Engineering, 2005, pp. 322-333.
- [13] M. I. Onsoien, O. Gundersen, O. Grong, T. Skaland, A process model for the microstructure evolution in ductile cast iron: Part I. the model, Metallurgical and Materials Transactions A, V 30, 1999, pp. 1053-1068.
- [14] G. Rivera, R. Boeri, J. Sikora, Revealing and characterising solidification structure of ductile cast iron, Materials Science and Technology, 18:6, 2002, pp. 691-697.
- [15] F. D. Carazo, P. M. Dardati, D. J. Celentano, L. A. Godoy, Stable Eutectoid Transformation in Nodular Cast Iron: Modeling and Validation, Metallurgical and Materials Transactions A, V 48A, 2017, pp. 63-75.
- [16] D. M. Stefanescu, ASM Handbook, Fundamentals of the Metallurgy of Cast Iron, V1A Cast Iron Science and Technology, 2017, ASM International
- [17] J. Zhou, Colour Metallography of Cast Iron, China Foundry 8, V6, 2011, pp. 447-462.
- [18] J. Qing, V. L. Richards, D. C. Van Aken, Examination of Spheroidal Graphite Growth and Austenite Solidification in Ductile Iron, Metallurgical And Materials Transactions A, V 47a, 2016, pp. 6197- 6213.
- [19] G. Alonso, P. Larranaga, D. M. Stefanescu, E. De la Fuente, A. Natxiondo, R. Suarez, Kinetics of nucleation and growth of graphite at different stages of solidification for spheroidal graphite iron, International Journal of Metalcasting, 11(2017)1, pp. 14-26.
- [20] D. M. Stefanescu, G. Alonso, P. Larranaga, R. Suarez, On the stable eutectic solidification of iron-carbon-silicon alloys, Acta Materialia, 2016, 103, pp. 103-114.
- [21] D. M. Stefanescu, R. Huff, G. Alonso, P. Larranaga, E. De la Fuente, R. Suarez, On the crystallisation of compacted and chunky graphite from liquid multicomponent iron-carbon-silicon based melts, Metallurgical and materials transaction, 2016, 47(2016)8, pp. 4012-4023.
- [22] D. M. Stefanescu, R. Huff, G. Alonso, P. Larranaga, E. De la Fuente, R. Suarez, Reexamination of crystal growth theory of graphite in iron-carbon alloys, Acta Materialia, 2017, 139, pp. 109-121.
- [23] S.N. Lekakh, B. Hrebec, Solidification kinetics of graphite nodules in cast iron and shrinkage porosity, International Journal of Metalcasting, 2016, 10(2016)4, pp. 389-400.
- [24] L. Laffont- Dantras, R. Jday, J. Lacaze, An electron microscopy study of graphite growth in nodular cast irons, Metallurgical and Materials Transactions A, 2018, (vol 49), pp. 1287-1294.
- [25] S. I. Karsay, Ductile Iron, The state of the art. Uitgave QIT, 1980.
- [26] G. A. Feest, G. McHugh, D. O. Morton, I. S. Welch, I. A. Cook, Proceedings of Solidification Technology in the Foundry and Casthouse, 1983.
- [27] A. Tadesse, H. Fredriksson, The effects of carbon on the solidification of nodular cast iron- its study with the help of linear variable differential transformer and microstructural analysis, International Journal of Cast Metals Research, 2017.
- [28] H. M. Muhmond, On the Inoculation and Graphite Morphologies of Cast Iron, Doctoral Thesis Stockholm, Sweden, 2014.
- [29] M. A. Gadd, G. H. J. Bennett, 3rd International Symposium on the Physical Metallurgy of cast Iron, Stockholm, 1984.

- [30] T. Kusakawa, S. Okimoto, K. Kobayashi, K. Ide, H. Okita, *The Casting Research Laboratory*, Waseda University, Tokyo, 1988.
- [31] C. Fragassa, G. Minak, A. Pavlovic, Tribological aspects of cast iron investigated via fracture toughness, *Tribology in Industry*, 38(2016)1, pp. 1-10.
- [32] J. Lacaze, Trace elements and graphite shape degeneracy in nodular graphite cast irons, *International Journal of Metalcasting*, 11(2017), pp. 44-51.
- [33] J. Lacaze, J. Bourdie, M. J. Castro-Román, A 2-D nucleation-growth model of spheroidal graphite, *Acta Materialia*, 134 (2017), pp. 230-235.
- [34] G. Gumienny, L. Klimek, B. Kurowska, Effect of annealing temperature on the microstructure and properties of ausferritic nodular cast iron, *Archives of Foundry Engineering*, vol. 16, 3/2016, pp. 43-48.
- [35] H. Megahed, E. El-Kashif, A. Y. Shash, M. A. Essam, Effect of holding time, thickness and heat treatment on microstructure of compacted graphite cast iron, *Journal of Materials Research and Technology*, 2019, 8(1), pp. 1188-1196.
- [36] K. Theuwissen, L. Laffont, M. Veron, J. Lacaze, Crystallography of graphite spheroids in cast iron, *International Journal of Cast Metals Research*, 29(2016)1-2, pp. 12-16.



19th INTERNATIONAL FOUNDRYMEN CONFERENCE
Humans - Valuable Resource for Foundry Industry Development

Split, June 16th-18th, 2021

<https://ifc.simet.hr/>

**THE COPPER ADSORPTION ON ZEOLITE NaX - THE IMPELLER LOCATION
IMPACT**

Anita Bašić^{*}, Mario Nikola Mužek, Marija Ćosić, Sandra Svilović

University of Split Faculty of Chemistry and Technology, Split, Croatia

Poster presentation
Original scientific paper

Abstract

Copper is a metal that naturally exists as a mineral in rocks, soil, plants, animals, and water but, it is also an essential trace element required to maintain a good health. Considering that copper is easily shaped, molded, or it may be combined with other metals, it is commonly used to make electrical wiring, pipes, valves, fittings, coins, cooking utensils, building materials, and household plumbing materials. The copper level in surface and groundwater is generally very low. However, higher levels may get into the environment through farming, mining, manufacturing processes, and municipal or industrial wastewater releases into rivers and lakes. Additionally, copper pipes can corrode and release copper into drinking water to a level that can affect its quality and safety. Since copper can be removed from water by applying various adsorbents, it is important to know the copper adsorption process as much as possible. The impact of hydrodynamic conditions in a batch reactor on the copper adsorption from solutions containing Cu^{2+} ions on zeolite NaX particles with a size of 0.063 to 0.090 mm was investigated. The aim of this research was to examine the influence of impeller location inside the batch reactor on Cu^{2+} adsorption on just suspended NaX zeolite, in baffled and unbaffled reactor. First, test suspended impeller speed were determined for further kinetic examination. During examination, beside solution concentration the power consumption at a constant suspension temperature was measured as well. The Blanchard model, Mixed surface reaction and diffusion controlled adsorption kinetic model and Weber-Morris model were used for the kinetic analysis of the experimental data. According to AARD values the reaction is kinetic controlled and follows the kinetics of the second order. It was also evident that the increase in the turbine location height results in the power consumption increase.

Keywords: *copper, zeolite NaX, kinetic models, impeller location*

*Corresponding author (e-mail address): abasic@ktf-split.hr

INTRODUCTION

Copper is an essential trace element required to maintain a good health that naturally exists as a mineral in rocks, soil, plants, animals, and water. As it is easily shaped, molded, or it may be combined with other metals, it is commonly used to make electrical wiring, pipes, valves, fittings, coins, cooking utensils, building materials, and household plumbing materials [1].

The copper level in surface and groundwater is generally very low. However, higher levels may get into the environment through farming (fertilizers), mining, manufacturing processes, and municipal or industrial wastewater released into rivers and lakes. Additionally, copper pipes can corrode and release copper into drinking water to a level that can affect its quality and safety [2, 3].

Adsorption is a highly effective physicochemical process for removing heavy metals from wastewater, especially at low initial metal concentrations. As copper can be removed from water by applying various adsorbents [4-12], it is important to know the copper adsorption process and parameters that affect it as much as possible.

When ion adsorption is carried out batch wise, mass transfer between solid and solution, definitely depends on mixing performance in the reactor. In this case mixing needs to ensure suspension of adsorbent particles and improve as much as possible the transport phenomenon from the liquid to the solid phase.

The aims of this research were to estimate the impeller location impact in the baffled and unbaffled batch reactor on the kinetics of copper ions adsorption at the state of complete suspension of NaX zeolite particles.

MATERIALS AND METHODS

Fraction of NaX zeolite (Alfa Aesar) particles in range between 0.063 and 0.090 mm was used as the adsorbent for the removal of copper ions from copper solutions which were previously prepared by dissolving the weighed amounts of $\text{Cu}(\text{NO}_3)_2 \cdot 3\text{H}_2\text{O}$ (Kemika) in ultrapure water.

Perkin Elmer Lambda 25 UV/Vis spectrophotometer was used to determine the exact concentrations of copper solutions at any given time t , during the adsorption process at the corresponding wavelength of 810 nm.

A glass batch reactor was used in all the experiments conducted. The liquid height, H , of 0.14 m equaled internal reactor diameter, d_T . Four baffles, whose width, R_v , was equal to $1/10 d_T$, were placed at 90° around the reactor periphery in baffled systems. The suspension inside the reactor consisted of 10.50 g of NaX zeolite mixed with 2.10 L of the copper solution and was agitated by the turbine impeller with four blades inclined at 45° , so called pitch blade turbine (PBT). Impeller with diameter, D , of 0.045 m was placed at 0.10 (Figure 1) and 0.50 off-bottom clearances (Figure 2), respectively.

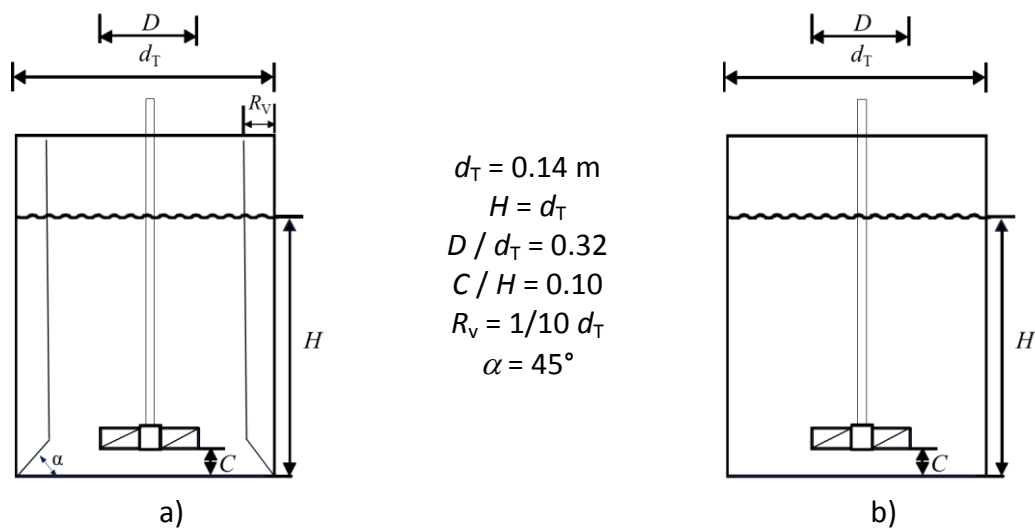


Figure 1. Batch reactor equipped with turbine impeller located at 0.10 off-bottom clearance in a) a baffled system and b) an unbaffled system.

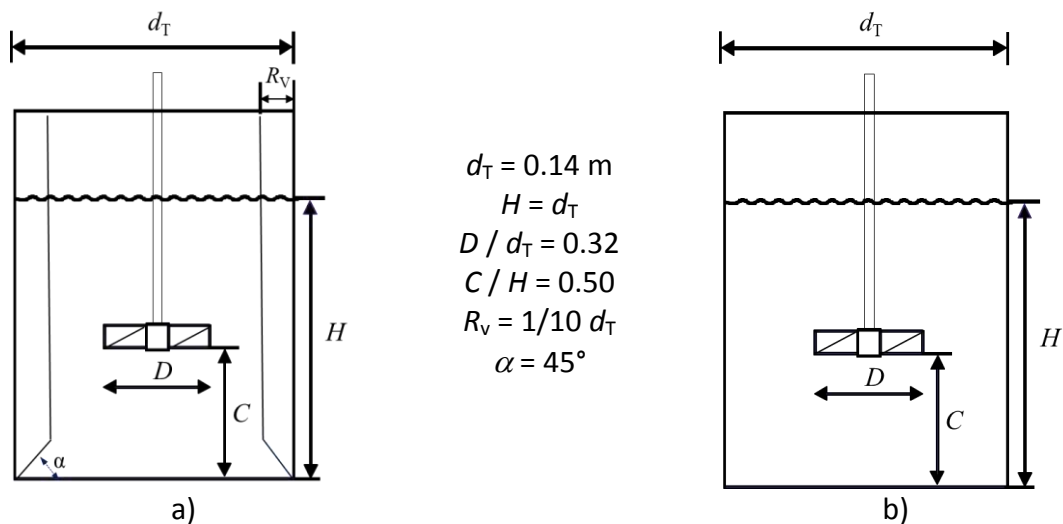


Figure 2. Batch reactor equipped with turbine impeller located at 0.50 off-bottom clearance in a) a baffled system and b) an unbaffled system.

Zwietering's visual method 1 s was used to determine the state of complete zeolite suspension achieved at critical impeller speed, N_{JS} [13]. To define this impeller speed at which no solid particle remained on the bottom longer than 1 second the reactor was illuminated from all directions and the bottom was observed using a mirror. For each impeller system design used for agitating the prepared NaX zeolite suspension, the impeller speed was progressively increasing to the one at which a complete suspension state was achieved by the given criteria. The measurements were repeated ten times, and the average value was taken as the impeller speed for further kinetic experiments.

The torque, M (N cm), for each impeller was measured at average N_{JS} by Lightnin LabMaster LB2 and the mixing power consumption at complete suspension state, P_{JS} (W), was calculated as:

$$P_{JS} = 2 \cdot \pi \cdot M \cdot N_{JS} \quad (1)$$

All kinetic experiments were performed at the previously determined N_{JS} which is a function of the turbine impeller location and presence of baffles. Suspension temperature (300 K) and initial concentration (6.480 mmol/L) were kept constant. The suspension samples were taken from the reactor at specific time periods, centrifuged and filtrated. The copper concentration in the suspension samples was determined by UV/Vis spectrophotometer to calculate the amount of copper retained on the zeolite, q_t (mmol/g) using equation (2):

$$q_t = \frac{(c_0 - c_t)V}{m} \quad (2)$$

where c_0 is the initial copper concentration in the solution (mmol/L), c_t is the copper concentration in the solution at time t (mmol/L), V is the initial solution volume (L), and m is the initial mass of NaX zeolite (g).

Experimentally obtained adsorption rate data were fitted using Blanchard model, Mixed surface reaction and diffusion controlled adsorption kinetic model and Weber-Morris model. The Blanchard model is reaction based model expressed as [14,15]:

$$q_t = \frac{q_e^2 k_2 t}{1 + q_e k_2 t} \quad (3)$$

where q_t is amount of copper ions adsorbed at time t (mmol/L), q_e is the amount of copper ions adsorbed at equilibrium (equilibrium capacity) (mmol/g), k_2 is the rate constant (g/mmol min) and t is time (min).

The Mixed surface reaction and diffusion controlled adsorption kinetic model is expressed as [16]:

$$q_t = q_e \frac{e^{(a t + b t^{1/2})} - 1}{u_e e^{(a t + b t^{1/2})} - 1} \quad (4)$$

where $u_e = 1 - \frac{c_e}{c_0}$, $a = k c_0 (u_e - 1)$, $b = 2 k c_0 \tau^{1/2} (u_e - 1)$, c_e is the equilibrium concentration, τ defines the contribution of a diffusion process on the rate of the adsorption; if $\tau > 0$ diffusion affects the kinetics.

The Weber-Morris is a diffusion based model [17,18] defined as:

$$q_t = k_d t^{1/2} + I \quad (5)$$

where k_d is the intraparticle diffusion rate constant (mmol/g min^{1/2}), t is time (min), and I is the intercept of the vertical axis (mmol/g). At $I > 0$ both film and intraparticle diffusion are considered as rate-limiting steps. Intraparticle diffusion is considered as the rate-limiting step if $I = 0$ [18,19].

Average absolute relative deviation AARD (%) was used for fitting estimation of the selected kinetic models to experimental data obtained. For AARD values are under 5 % the models are considered to be acceptable while above 10 % indicate a poor agreement of model predicted values [20]:

$$AARD = \frac{1}{n} \sum_{i=1}^n \left[\left| \frac{q_{t_i} - qt_model_i}{q_{t_i}} \right| 100 \right] \quad (6)$$

where q_t is the experimentally determined value, while qt_model is the calculated value of q_t , respectively.

RESULTS AND DISCUSSION

Critical impeller speed ensures the state of complete suspension of zeolite particles inside the batch reactor. Values of N_{JS} , determined according to Zwietering's criteria, are presented in Figure 3.

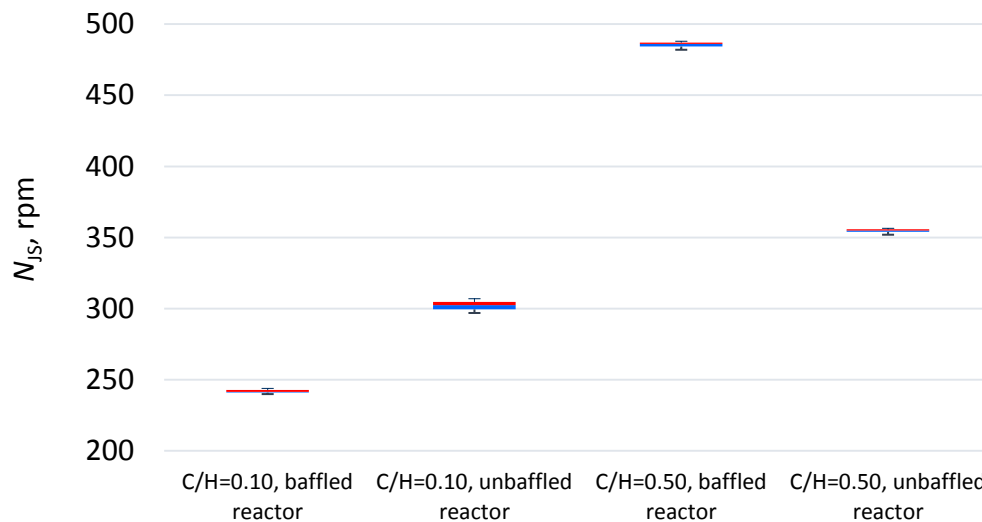


Figure 3. Critical impeller speed at different pitched blade turbine impeller location in baffled and unbaffled system

The values of the critical impeller speed increase as impeller distance from the vessel bottom increases in both reactors; baffled and unbaffled. Since these values were obtained at the constant mass of NaX zeolite, mean particle size, and concentration of heavy metal in the suspensions, the results obtained may be attributed to the flow characteristics of the suspension.

In this work mixing was performed by PBT impeller which flow is characterized as mixed axial-radial flow. In baffled reactor, when PBT impeller is at standard position ($C/H = 0.3$) impeller discharge the flow towards the corner formed between vessel wall and bottom. From this corner fluid flows towards liquid surface forming one, top to the bottom, circulation loop called the primary flow. Below the impeller simultaneously is formed another circulating loop in reverse direction, from the corner to the impeller, called secondary flow [21]. This flow near the vessel bottom is responsible for settling zeolite particle suspension. Suspension will be carried out when fluid velocities near the bottom become high enough to lift the particle from the surface. By increasing impeller distance from the bottom lower loop became broader but weaker. This is the reason why complete suspension of zeolite particles at this position, defined by ratio $C/H = 0.5$, has just been achieved at higher impeller speed. On the other hand, in the same reactor when the impeller is located closer to the bottom ($C/H = 0.1$), secondary flow has higher impact on settled particles and complete suspension has been achieved at lower impeller speed.

In the unbaffled reactor, fluid flow formed by PBT impeller is characterized by swirling motion. However, in this system obviously fluid velocity is higher in the impeller region. This is the reason why impeller near the bottom needed lower rotational speed for settled particles complete suspension.

Figure 4 presents values of mixing power consumption at complete suspension state with respect to the impeller location and baffle presence.

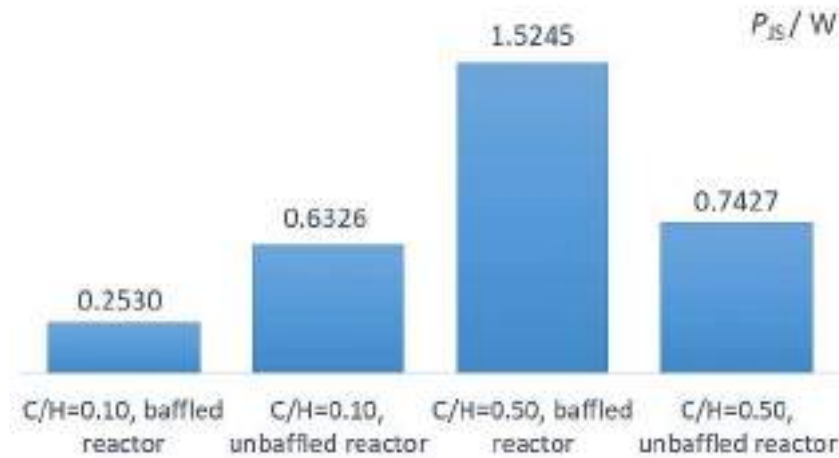


Figure 4. Power consumption at different impeller location in a baffled and unbaffled reactor

The values of P_{js} are higher at higher impeller location, and vice versa. But, the lowest mixing power consumption is observed at lower impeller location in baffled reactor. This leads to the conclusion that positioning the impellers at a lower location in a baffled system is more energy efficient than at a higher location in both; baffled and unbaffled reactor.

Adsorption kinetics on NaX zeolite was also studied and the results are shown in Figure 5.

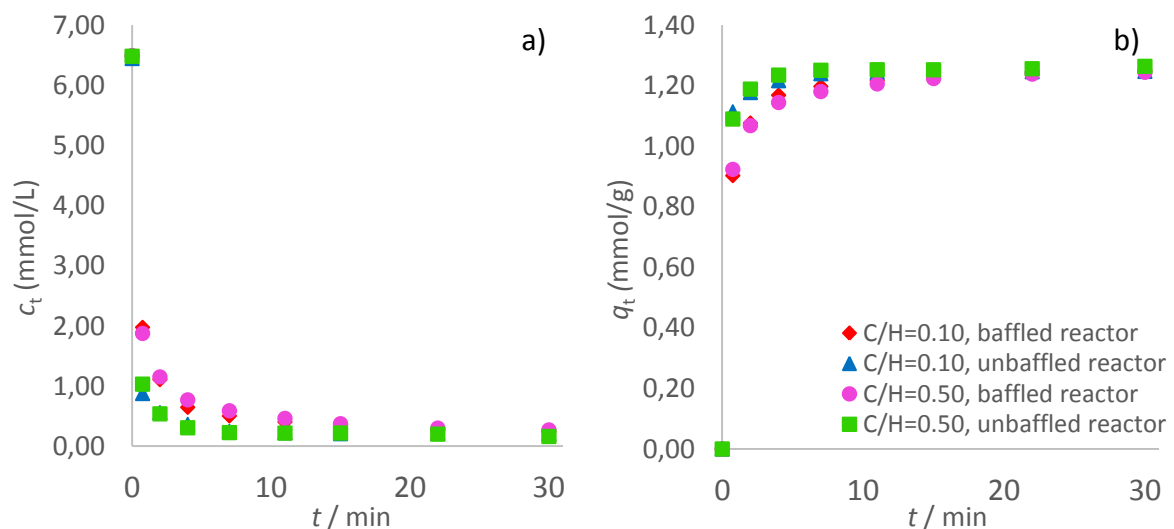


Figure 5. Dependence of copper ions concentration (a) and amount of copper retained on the NaX zeolite (b) over process time - comparison of data obtained for pitched blade turbine impeller placed at different location in baffled and unbaffled system

The copper concentration decreases rapidly in the initial minutes of kinetic experiments leading to the gradual equilibrium formation, as seen from Figure 5 a). Nevertheless, the adsorption of copper ions on the NaX zeolite is happening quickly at the beginning of the

adsorption process until a certain time at which equilibrium is established (Figure 5 b). It is evident from the shown changes of the concentration and the amount of copper ions retained on zeolite over time, at examined conditions that the obtained values are approximately the same and the curves almost match after time of 25 minutes if baffled and unbaffled system are observed separately. Also, equilibrium is established a bit earlier (2 to 3 minutes) in an unbaffled system.

Nonlinear and linear regression analysis of kinetic experimental data obtained for Blanchard, Mixed surface reaction and diffusion-controlled adsorption kinetic model (Mixed kinetic model), and Weber-Morris model (Figures 6 to 8) was performed using software Matchad 14. The goal of the kinetic analysis is to find a kinetic model that best describes the experimental data and to determine the kinetic parameters of the model with the highest accuracy. AARD was calculated to estimate the agreement of selected models with the experimental data obtained. All estimated kinetic parameters and statistical indicators of agreement of the models with the experimental data are presented in Table 1.

Table 1. Model parameters

MODEL	Impeller blade location	0.10		0.50	
	Baffles	Yes	No	Yes	No
	N_{JS} (rpm)	242	302	486	355
Experimental data	$q_{e,exp}$ (mmol/g)	1.251	1.248	1.245	1.264
	$u_{e,exp}$	0.963	0.968	0.958	0.975
Blanchard model	q_e (mmol/g)	1.254	1.251	1.240	1.267
	k (g/mmol min)	2.651	8.184	2.928	6.447
	AARD (%)	0.596	0.448	1.177	0.283
Mixed surface reaction and diffusion controlled adsorption kinetic model	q_e (mmol/g)	1.258	1.252	1.240	1.259
	k (L/mmol min)	0.425	1.367	0.515	0.892
	τ (min)	$8.6 \cdot 10^{-3}$	$5.8 \cdot 10^{-3}$	$2.5 \cdot 10^{-3}$	$20.0 \cdot 10^{-3}$
	u_e	0.998	0.999	0.998	0.963
	AARD (%)	0.402	0.333	0.917	0.236
Weber-Morris model	k_d (mmol/g min ^{1/2})	0.161	0.142	0.160	0.145
	l (mmol/g)	0.596	0.699	0.595	0.696
	AARD (%)	12.475	12.913	12.436	12.966

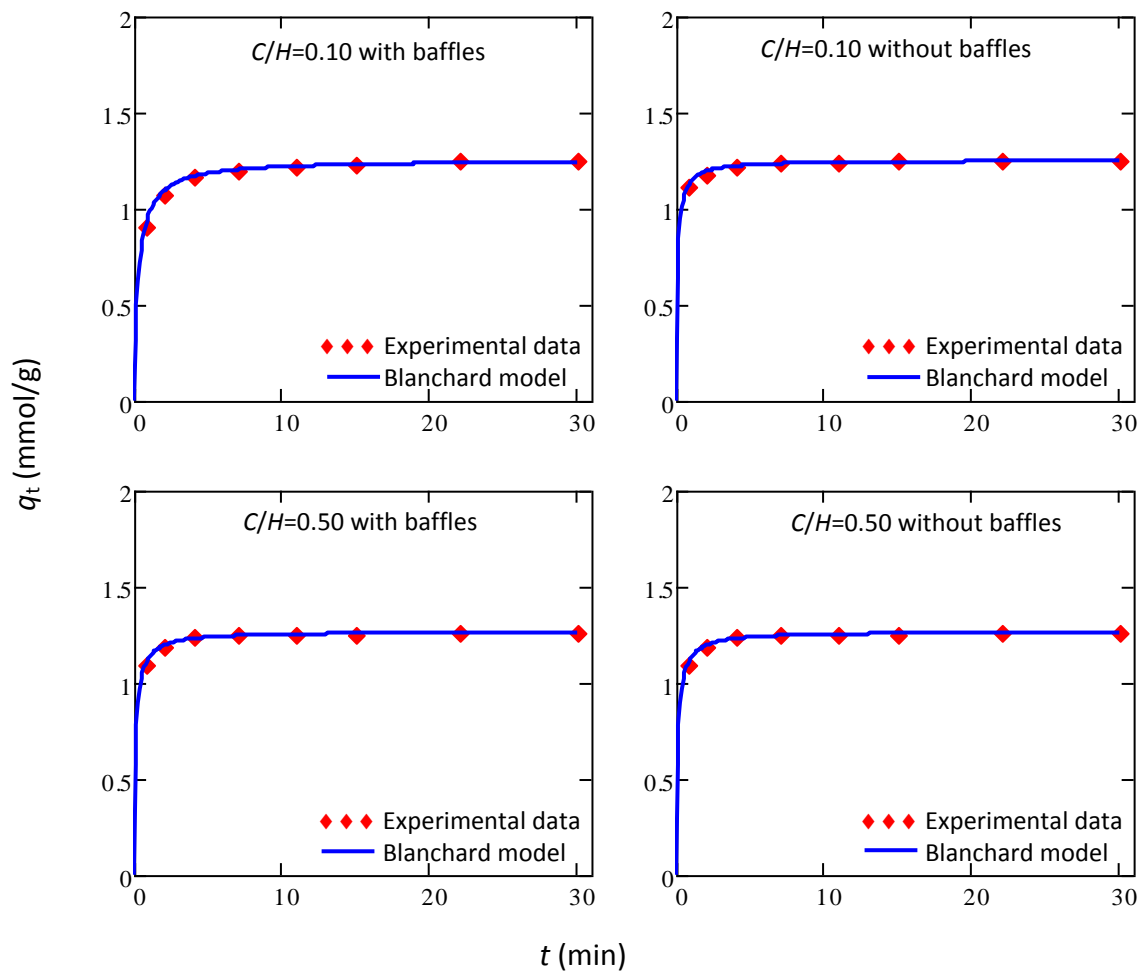


Figure 6. The agreement of Blanchard model with the experimental data for different pitched blade turbine impeller location in baffled and unbaffled system

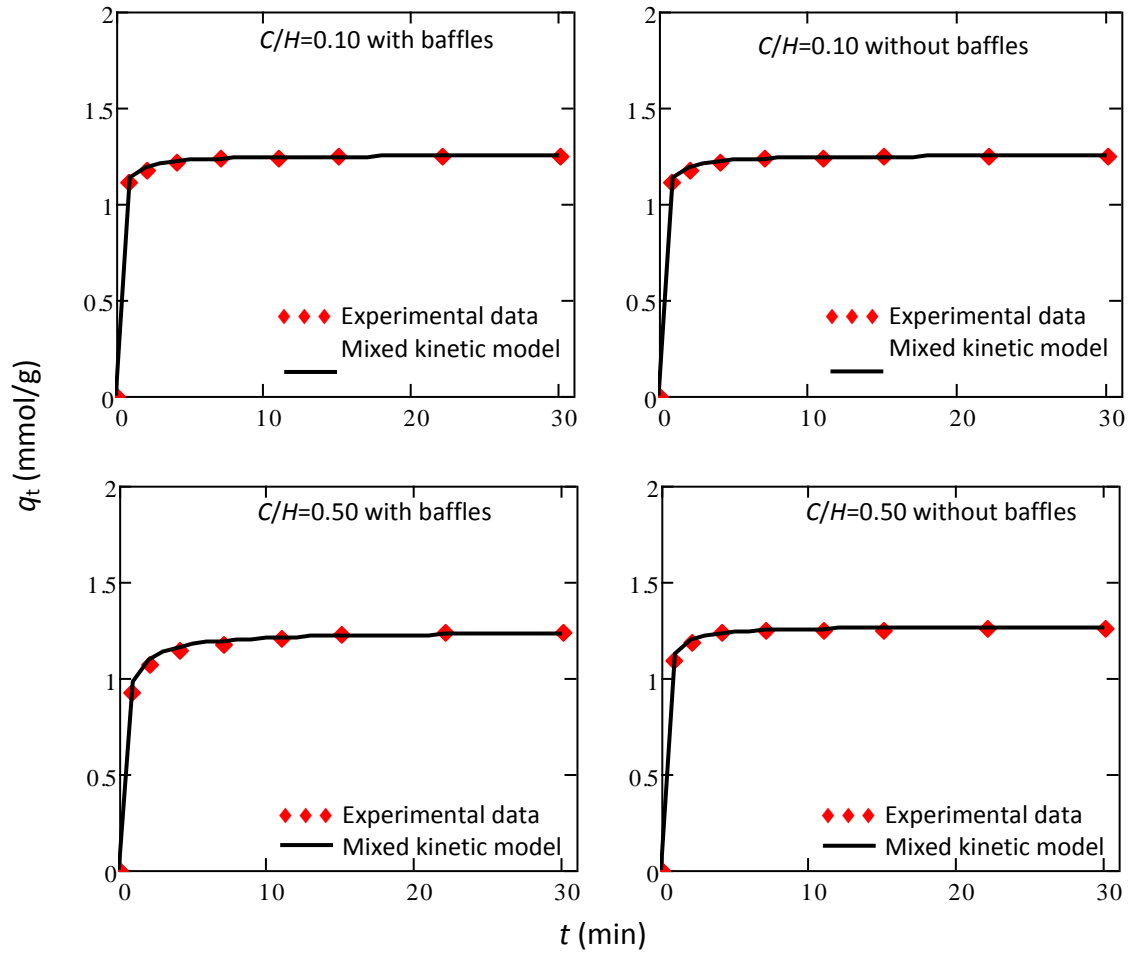
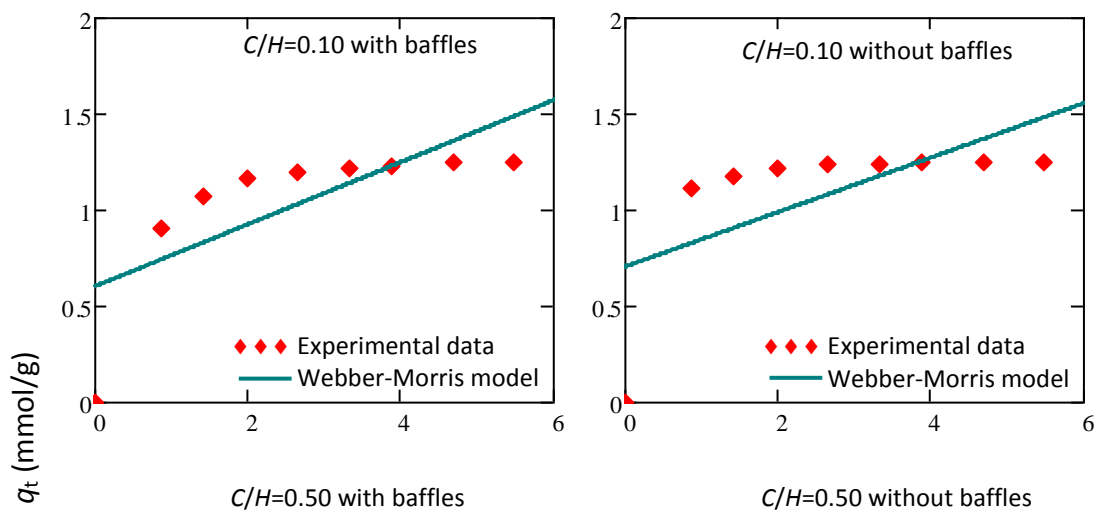


Figure 7. The agreement of Mixed surface reaction and diffusion controlled adsorption kinetic model with the experimental data for different pitched blade turbine impeller location in baffled and unbaffled system



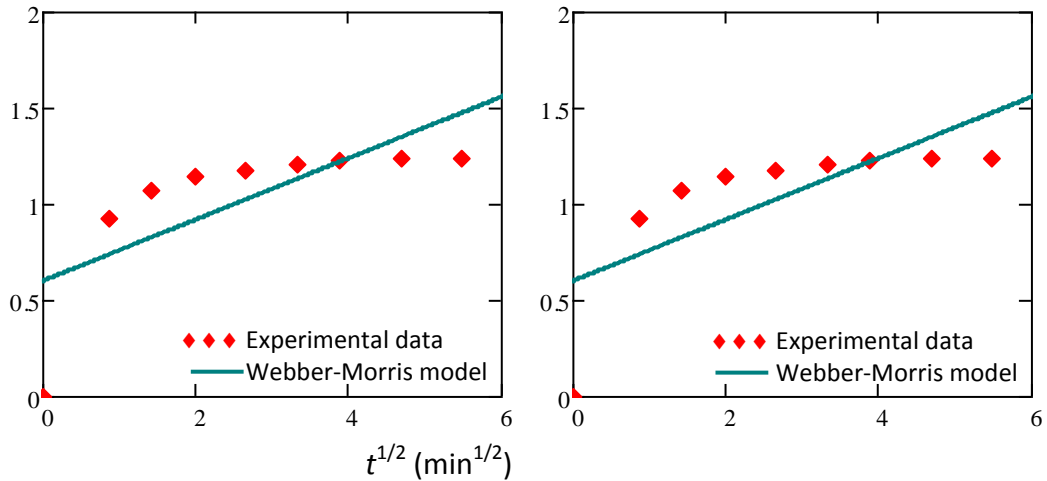


Figure 8. The agreement of Weber-Morris model with the experimental data for different pitched blade turbine impeller location in baffled and unbaffled system

The AARD values indicate the good agreement of the experimentally obtained data with the Blanchard model and Mixed kinetic model under the given operating conditions. These findings were confirmed by the graphical representations given in Figures 6 to 7. Nevertheless, the Blanchard model and Mixed kinetic model show similar equilibrium capacity values as the experimentally obtained ones for both impeller locations used in this work regardless of whether it is baffled or unbaffled system. All this points out that the adsorption of copper ions on NaX zeolite is controlled by surface reaction. These findings are confirmed by the τ values of the Mixed kinetic model which are approximately zero. Comparison of the rate constants of the chemical reaction leads to the conclusion that the fastest reaction occurs when the impeller is closer to the vessel bottom in unbaffled system for the process studied.

Figure 8 shows the poor agreement of the Weber-Morris model with the obtained experimental data confirming that the adsorption of copper ions on NaX zeolite is controlled only by surface reactions, thus the presence of diffusion can be neglected for the selected experimental conditions.

CONCLUSIONS

By decreasing the impeller position, the critical mixing speed required to achieve a state of complete suspension of NaX zeolite decreases in baffled and unbaffled systems. The same trend was observed for the mixing power consumption. The copper ions adsorption is prompt in the initial minutes of the experiment, i.e. the increase in the amount of copper retained on the zeolite is initially fast and then gradual until equilibrium is reached. The equilibrium capacity is almost equal for all system designs used in this work but, but rate is higher in the reactor without baffles which is characterized by higher impeller speeds. This fact implies that fluid velocity in the systems investigated influences the rate of equalization of Cu^{2+} ions concentration in the system and transport phenomenon on the zeolite - liquid interface. The obtained experimental data match very well with Blanchard's kinetic model and Mixed kinetic model. The rate of adsorption defines the total reaction rate, i.e. the rate is kinetic controlled. Copper adsorption on NaX zeolite is a second-order reaction regardless

of the impeller location and baffle presence, if the process is conducted at N_{JS} . In this case, it is more energy efficient to use an impeller closer to the reactor bottom and, if the kinetic is taken into account, to use reactor without baffles.

REFERENCES

- [1] Accessible on Internet: https://ww2.health.wa.gov.au/Articles/A_E/Copper-in-drinking-water, (20.11.2020.)
- [2] V. Geetha Varma, A. K. Misra, Copper contaminated wastewater – An evaluation of bioremedial options, *Indoor and Built Environment*, 27(2018)1, pp. 84-95.
- [3] Accessible on Internet: https://www.who.int/water_sanitation_health/dwg/chemicals/copper.pdf, (20.11.2020.)
- [4] M. N. Mužek, S. Svilović, J. Zelić, Fly ash-based geopolymetric adsorbent for copper ion removal from wastewater, *Desalination and Water Treatment*, 52(2014), pp. 2519-2526.
- [5] V. Krstić, T. Urošević, B. Pešovski, A review on adsorbents for treatment of water and wastewaters containing copper ions, *Chemical Engineering Science*, 192(2018), pp. 273-287.
- [6] S. Svilović, M. N. Mužek, I. Nuić, P. Vučenović, Taguchi design of optimum process parameters for sorption of copper ions using different sorbents, *Water Science and Technology*, 80(2019), pp. 98-108.
- [7] S. Meseldzija, J. Petrovic, A. Onjia, T. Volkov-Husovic, A. Nestic, N. Vukelic, Utilization of agro-industrial waste for removal of copper ions from aqueous solutions and mining-wastewater, *Journal of Industrial and Engineering Chemistry*, 75(2019), pp. 246-252.
- [8] R. Fernández-González, M. A. Martín-Lara, G. Blázquez, G. Tenorio, M. Calero, Hydrolyzed olive cake as novel adsorbent for copper removal from fertilizer industry wastewater, *Journal of Cleaner Production*, 268(2020), 121935.
- [9] A. Chaturbedi, S. Patil, R. Ramachandran, N. C. Shapley, Adsorption of positively and negatively charged heavy metal ions from wastewater by heteroaggregates of biopolymer particles, *Colloids and Surfaces A: Physicochemical and Engineering Aspects*, 602(2020), 124789.
- [10] Y. Chu, M. A. Khan, M. Xia, W. Lei, F. Wang, S. Zhu, X. Yan, Synthesis and micro-mechanistic studies of histidine modified montmorillonite for lead(II) and copper(II) adsorption from wastewater, *Chemical Engineering Research and Design*, 157(2020), pp. 142-152.
- [11] M. Shahrashoub, S. Bakhtiari, The efficiency of activated carbon/magnetite nanoparticles composites in copper removal: Industrial waste recovery, green synthesis, characterization, and adsorption-desorption studies, *Microporous and Mesoporous Materials*, 311(2020), 110692.
- [12] M. Bashir, S. Tyagi, A. P. Annachatre, Adsorption of copper from aqueous solution onto agricultural adsorbents: Kinetics and isotherm studies, *Materials Today: Proceedings*, 28(2020)3, pp. 1833-1840.
- [13] T. N. Zwietering, Suspending of solid particles in liquid by agitators, *Chemical Engineering Science*, 8(1958)3-4, pp. 224-253.

- [14] Y.-S Ho, Review of second-order models for adsorption system, *Journal of Hazardous Materials B*, 136(2006)3, pp. 681–689.
- [15] O. Hamdaoui, Common mistake in adsorption papers: The Blanchard et al.'s pseudo-second order kinetics model equation, *Process Engineering Journal*, 1(2017), pp. 29–30.
- [16] M. Haerifar, S. Azizian, Mixed surface reaction and diffusion – controlled kinetic model for adsorption at the solid/solution interface, *The Journal of Physical Chemistry C*, 117(2013), pp. 8310–8317.
- [17] H. Qiu, L. Lv, B. Pan, Q. Zhang, W. Zhang, Q. Zhang, Critical review in adsorption kinetic models, *Journal of Zhejiang University SCIENCE A*, 10(2009)5, pp. 716-724.
- [18] I. Tsibranska, E. Hristova, Comparison of different kinetic models for adsorption of heavy metals onto activated carbon from apricot stones, *Bulgarian Chemical Communications*, 43(2011)3, pp. 370–377.
- [19] S. Svilović, D. Rušić, R. Stipišić, Modeling batch kinetics of copper ions sorption using synthetic zeolite NaX, *Journal of Hazardous Materials*, 170(2009) pp. 941–947.
- [20] A. Bašić, S. Svilović, Effect of geometrical and operating mixing parameters on copper adsorption on zeolite NaX, *Desalination and Water Treatment*, 209(2021) pp. 197-203.
- [21] M. Ćosić, A. Kaćunić, N. Kuzmanić, The investigation of the influence of impeller blade inclination on borax nucleation and crystal growth kinetics, *Chemical Engineering Communications*, 203(2016)11, pp. 1497–1506.



19th INTERNATIONAL FOUNDRYMEN CONFERENCE
Humans - Valuable Resource for Foundry Industry Development

Split, June 16th-18th, 2021

<https://ifc.simet.hr/>

**CORROSION RESISTANCE OF CEMENTING STEEL X19NiCrMo4
IN MEDIUM OF 5 % NaOH AND 5 % H₂SO₄**

Sandra Brajčinović^{*}, Anita Begić Hadžipašić

University of Zagreb Faculty of Metallurgy, Sisak, Croatia

Poster presentation
Original scientific paper

Abstract

This paper presents the results of testing the corrosion behavior of X19NiCrMo4 cementing steel in 5 % NaOH and 5 % H₂SO₄ solution. Electrochemical measurements were performed by measuring the open circuit potential, determining the corrosion parameters using electrochemical impedance spectroscopy (EIS) and Tafel extrapolation. The corrosion rate, which was determined by Tafel extrapolation method, was lower in 5 % NaOH solution than that in 5 % H₂SO₄ solution. The obtained results were confirmed by the method of electrochemical impedance spectroscopy, which showed a higher value of charge transfer resistance of the tested steel in an alkaline medium, which proves higher corrosion resistance.

Metallographic analysis were performed on a sample previously etched in nital and on a sample after polarization measurements. Images of the electrode surface after polarization measurements in 5 % H₂SO₄ medium showed a completely corroded steel surface indicating dissolution of the oxide layer due to acid exposure. No changes were observed on the sample surface in the alkaline medium.

Keywords: *cementing steel, corrosion rate, impedance, charge transfer resistance, microstructure*

*Corresponding author (e-mail address): smitic@simet.unizg.hr

INTRODUCTION

Cementing steel marked X19NiCrMo4 (DIN 17350) is classified in the group of special steels, i.e. tool steels intended for cold work. For tool steels, it is necessary to meet certain requirements in their production. Top requirements are easy workability, good polishing and stability measures during the heat treatment, surface resistance to pressure and wear [1]. The primary use of X19NiCrMo4 steel is in the tool industry for the production of plastic molds and rollers for cold rolling of profiles. However, the application of tool steels is diverse and due to their mechanical properties they are also used for other purposes. Due to the above, cementing steel can come into contact with various aggressive agents and coolants,

which due to their properties can act aggressively and gradually destroy the surface layer of the metal [2].

Due to the variety of applications, the aim is to achieve good corrosion resistance of the material in various conditions of production and use. For this purpose, anti-corrosion protection methods are applied, such as: coating, electrochemical protection methods, use of corrosion inhibitors or alloying of steel with chromium and nickel. Studies based on testing the stability of metals in solutions of different pH values are important in selecting the appropriate inhibitor. Also, the influence of microstructure and selection of appropriate alloying elements greatly contributes to the quality of steel and thus to corrosion resistance in certain media [3].

The aim of this paper is to investigate the corrosion intensity of cementing steel in acidic and alkaline media. Sulfuric acid and sodium hydroxide were used for the study. Sulfuric acid is a strong acid. In aqueous solution, it completely dissociates into hydrogen ions (H^+) and sulfate ions (SO_4^{2-}). In extreme conditions, metals in contact with acids or alkalis are susceptible to corrosion. Sulfuric acid is used for the synthesis of various organic compounds, for the production of paints, in metal processing and is found in acid rains. It has multiple effects, in addition to acting as an acid, it can be an oxidizing, dehydrating or hygroscopic agent [4,5]. Sodium hydroxide is considered to be the most commonly used hydroxide in the chemical industry. Due to its alkalinity it is used as a pH regulator. It is used in the production of soap, in the textile industry, for aluminum processing or metal cleaning [6].

Tool materials are components of certain machines in industrial plants and can easily come into contact with acids and alkalis. The obtained corrosion parameters after testing in the mentioned media enable better recognition of the quality of materials, but also easier selection of anticorrosive agents and their application in industrial plants.

MATERIALS AND METHODS

A sample marked X19NiCrMo4 (DIN 17350) was used to test the influence of media and microstructure on the corrosion resistance of cementing steel. The chemical composition of the tested steel is shown in Table 1. Solutions of 5 % NaOH and 5 % H_2SO_4 were used as working medium during electrochemical tests.

Table 1. Chemical composition of X19NiCrMo4 steel (in weight percentage)

C	Si	Mn	P	S	Cr	Mo	Ni	Fe
0.170	0.27	0.41	0.009	0.002	1.18	0.19	3.90	balance

According to the table of chemical composition, it can be seen that the tested steel contains alloying elements chromium, manganese, molybdenum and nickel. In addition to nickel, all of the above alloying elements in combination with carbon form carbides. Nickel does not produce carbides, but it increases the corrosion resistance of steel. The content of phosphorus and sulfur is low, and the overall chemical composition meets the quality according to the prescribed production values. The addition of a controlled amount of selected alloying elements makes it possible to achieve stability of the surface oxide layers formed on the surface of the material. Improved corrosion resistance is most often achieved by adding chromium (up to 12 % Cr) [7].

SAMPLE PREPARATION

Samples of X19NiCrMo4 cementing steel were cut into cubes and prepared by pressing into a conductive mass using a hot sample pressing device (SimpliMet® 1000). After that, they were machine sanded with waterproof sandpaper of grade No. 240, 400, 600 and 800 and polished (Al_2O_3 suspension in water) on an automatic grinding and polishing device (Bühler). They were washed in distilled water and degreased in ethanol. One prepared sample was set aside for etching in the nital to highlight the microstructure [8]. The second sample was prepared for the purpose of electrochemical tests.

ELECTROCHEMICAL TESTS (E_{CORR} , EIS, TAFEL)

To obtain data on the corrosion behavior of samples, the method for determining the corrosion potential E_{corr} , electrochemical impedance spectroscopy (EIS) and Tafel extrapolation method were used. The sample represented a working electrode was immersed in a working medium in a three-electrode glass cell containing a saturated calomel electrode-SCE as a reference electrode and a Pt-grid as a counter-electrode [9].

Measurements were performed using a computer-controlled potentiostat/galvanostat (Parstat 2273). Electrochemical tests were performed in solutions of 5 % NaOH and 5 % H_2SO_4 , and the sample area was 0.98 cm^2 .

Determination of corrosion potential E_{corr}

Before starting the polarization measurement, it is necessary to stabilize the metal-electrolyte system. This means that after immersion in the electrolyte, the electrical circuit between the working and counter electrode is kept open, and the potential difference between the working and reference electrode is monitored as a function of time. Stabilization of the open circuit potential OCP was performed at room temperature $T = (19 \pm 2) \text{ }^\circ\text{C}$ using a computer-controlled potentiostat/galvanostat (Parstat 2273) and for 1800 seconds. By monitoring the time changes of the stationary open circuit potential OCP , data on the corrosion behavior of the sample in the tested medium were obtained [9].

Determination of corrosion parameters using electrochemical impedance spectroscopy (EIS)

In order to investigate the electrode/electrolyte phase boundary, impedance measurements are performed in the frequency range from 100 kHz to 10 mHz with a sinusoidal voltage amplitude of 5 mV. The impedance parameters were analyzed using ZSimpWin 3.60 software using the appropriate electrical circuit $R(Q(R(QR)))$. This method is based on the application of alternating current, and is based on the response of the circuit to alternating voltage or current as a function of frequency [10].

Determination of corrosion parameters using the Tafel extrapolation method

Corrosion parameters (corrosion potential E_{corr} , corrosion rate v_{corr} , anode slope b_a and cathode slope b_c) were determined by PowerCorrTM software using the Tafel extrapolation method and Faraday's laws. The Tafel extrapolation method was performed using

potentiodynamic polarization in the potential range from -250 mV to +250 mV vs E_{corr} , with a potential change rate of 1 mV/s [9].

METALLOGRAPHIC TESTS

An optical microscope with a digital camera (Olympus GX 51) and an automatic image processing system (AnalySIS® Materials Research Lab) was used for metallographic testing. Metallographic tests were performed on a sample previously etched in 0.5 % nital. Nital is a mixture of alcohol and nitric acid suitable for etching carbon steels for the purpose of recognizing their microstructure [8].

The second prepared sample was used for electrochemical tests, and after each measurement was observed using an optical microscope before and after exposure to the media.

RESULTS AND DISCUSSION

In order to prove the acidity or alkalinity of the medium, the pH values of the solution were measured before and after the electrochemical measurements with a pH meter. The obtained pH results are shown in Figure 1.

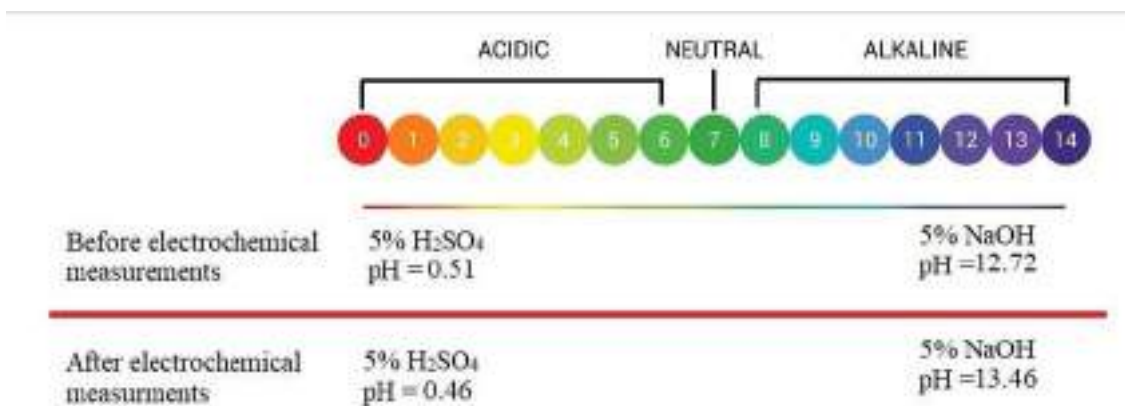


Figure 1. Measured pH values of 5% H₂SO₄ and 5% NaOH solutions

Figure 2 shows the time dependences of the open circuit potential for the tested sample of cementing steel in solutions of 5 % NaOH and 5 % H₂SO₄. It can be determined that after about one minute, a fairly stable *OCP* value is reached. According to the obtained curves, it can be seen that the sample weighs more negative potential values in the 5% H₂SO₄ solution than is the case for the NaOH solution. Sulfuric acid was corrosive to the metal, i.e. it caused the faster dissolution of metal.

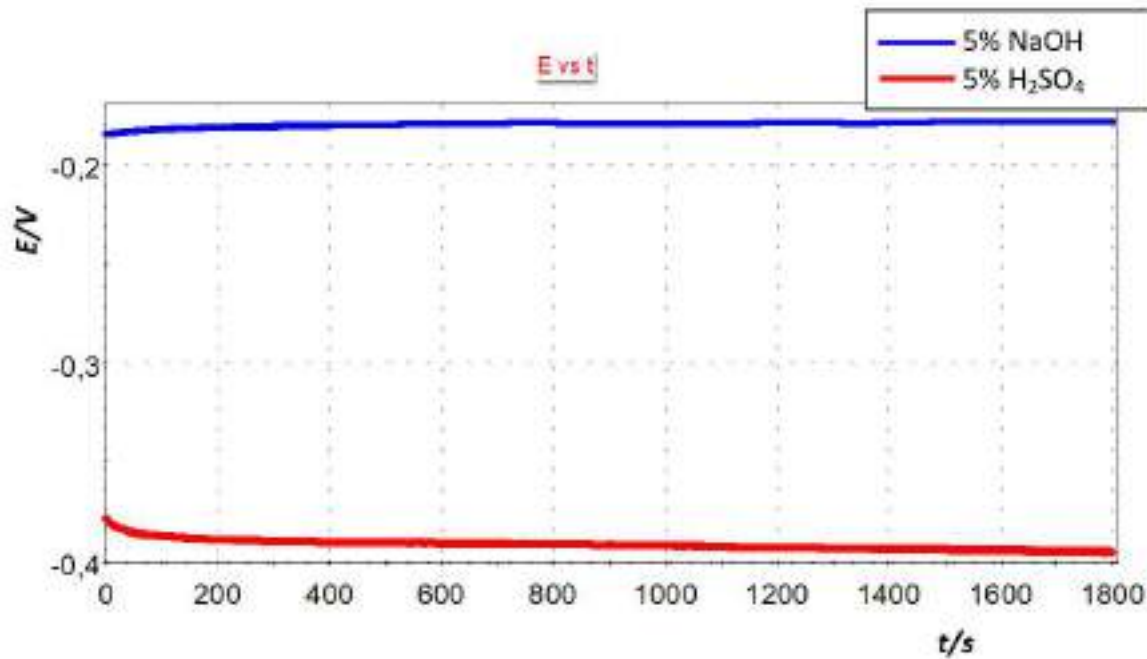


Figure 2. Time dependence of open circuit potential for X19NiCrMo4 steel in medium of 5% NaOH and 5 % H₂SO₄

The result of electrochemical impedance spectroscopy is shown by Nyquist diagram before (Figure 3) and after electrical circuit modeling (Figure 4 and 5). Table 2 shows the obtained impedance parameters: electrolyte resistance R_{el} , oxide layer resistance R_{ox} , constant phase element of the two-layer Q_{dl} , measure of surface heterogeneity n and charge transfer resistance R_{ct} .

The obtained Nyquist EIS spectra show the dependence of the imaginary impedance on the real impedance, and their analyzes were performed using the model of the electrical circuit $R(Q(R(QR)))$.

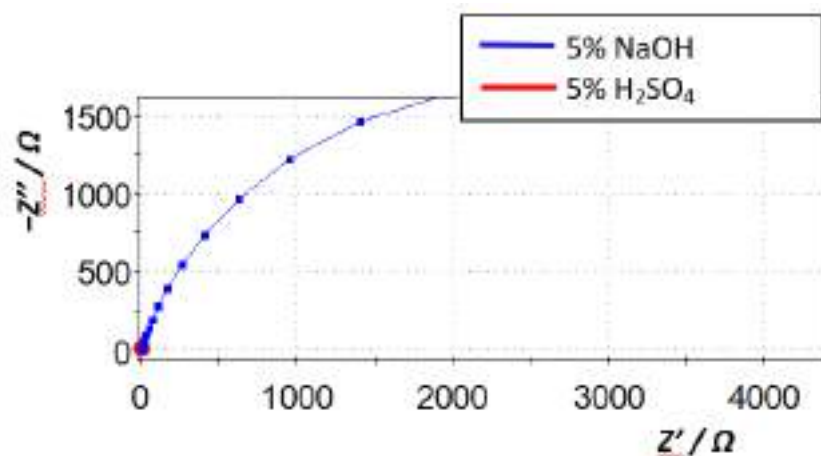


Figure 3. The comparative view of Nyquist's EIS diagrams obtained for X19NiCrMo4 steel in solution of 5 % NaOH and 5% H₂SO₄

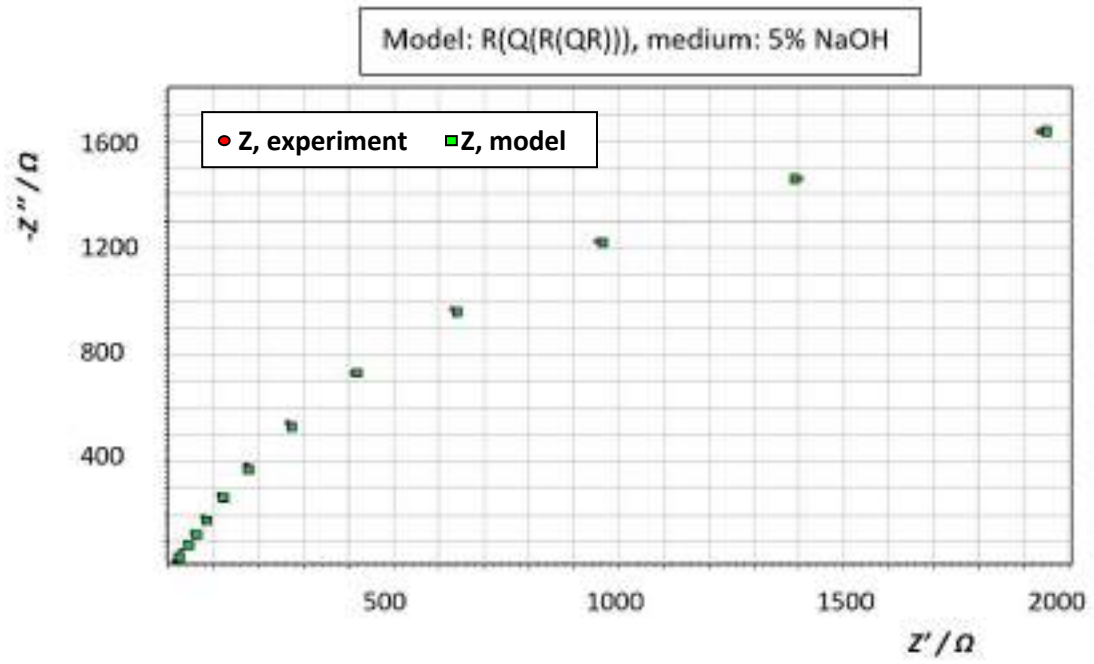


Figure 4. The comparative view of Nyquist's EIS diagrams obtained for X19NiCrMo4 steel in solution of 5 % NaOH

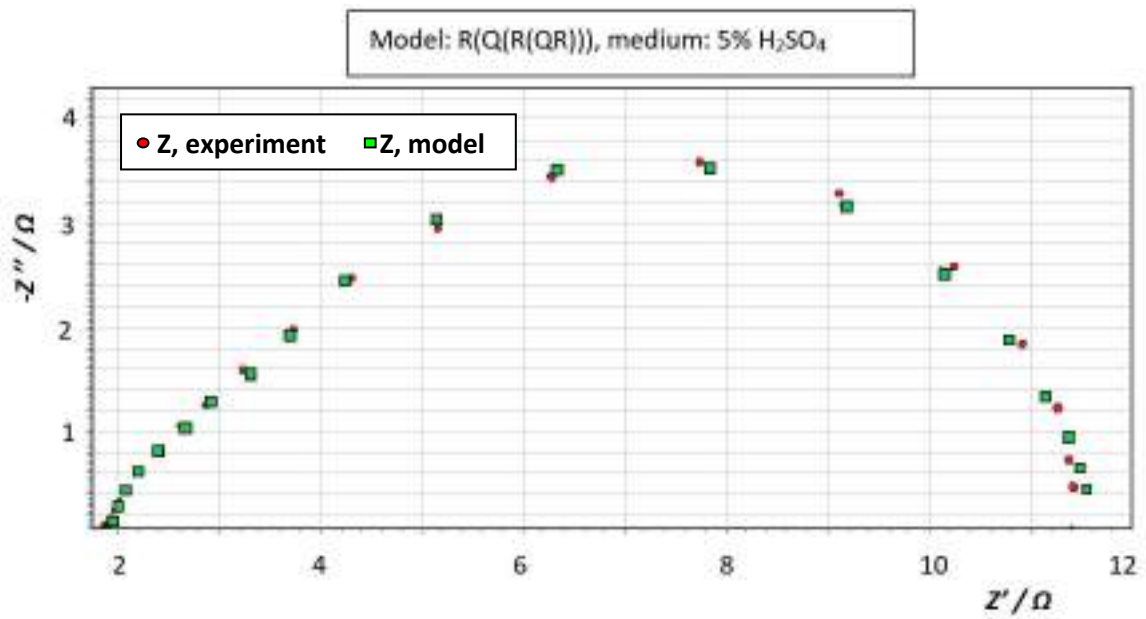


Figure 5. The comparative view of Nyquist's EIS diagrams obtained for X19NiCrMo4 steel in solution of 5 % H_2SO_4

Table 2. Impedance parameters of tested X19NiCrMo4 steel

Medium	E_{corr} vs. SCE	R_{el}	$Q_{dl} \times 10^3$	n	R_{ox}	$Q_{dl} \times 10^3$	n	R_{ct}
	mV	Ωcm^2	$\Omega^1 \text{s}^n \text{cm}^{-2}$		Ωcm^2	$\Omega^1 \text{s}^n \text{cm}^{-2}$		Ωcm^2
5% NaOH	-178	1.986	0.197	0.20	5.174	2.201	0.81	7793
5% H ₂ SO ₄	-395	1.873	2.351	0.80	3.562	2.531	0.94	6.259

The Nyquist impedance representation of the sample in 5 % H₂SO₄ solution is in the form of a semicircle which is characteristic of solid electrodes, and in 5 % NaOH solution it is in the linear form. The obtained diagrams are characteristic for certain configurations of electrical equivalent circuits, and are ideally composed of semicircles and straight lines. The appearance of the equivalent circuit by which the observed system can be described depends on a number of factors: electrode type, electrolyte type and composition, potential, temperature, pH.

From the data in Table 2 it can be seen that the tested steel in 5 % NaOH solution showed higher oxide resistance R_{ox} and charge transfer resistance R_{ct} . Namely, during the exposure of the sample in 5 % NaOH solution, an oxide layer of greater thickness was formed on the sample surface, which slowed down the corrosion processes. In contrast, the obtained parameters for the sample in 5 % H₂SO₄ solution indicate low values of charge transfer resistance. The acid with an extremely low pH value acts very aggressively, whereby the created oxide layer is quickly destroyed and allows further penetration of aggressive ions from the solution. Due to the dissolution of the sample, a more negative electrode potential was recorded in the acid.

The polarization curves of the tested sample of cementing steel in 5 % NaOH solution and 5 % solution H₂SO₄ are shown in Figure 6. Table 3 shows the values of corrosion parameters (corrosion potential E_{corr} , corrosion rate v_{corr} , anode slope b_a and cathode slope b_c).

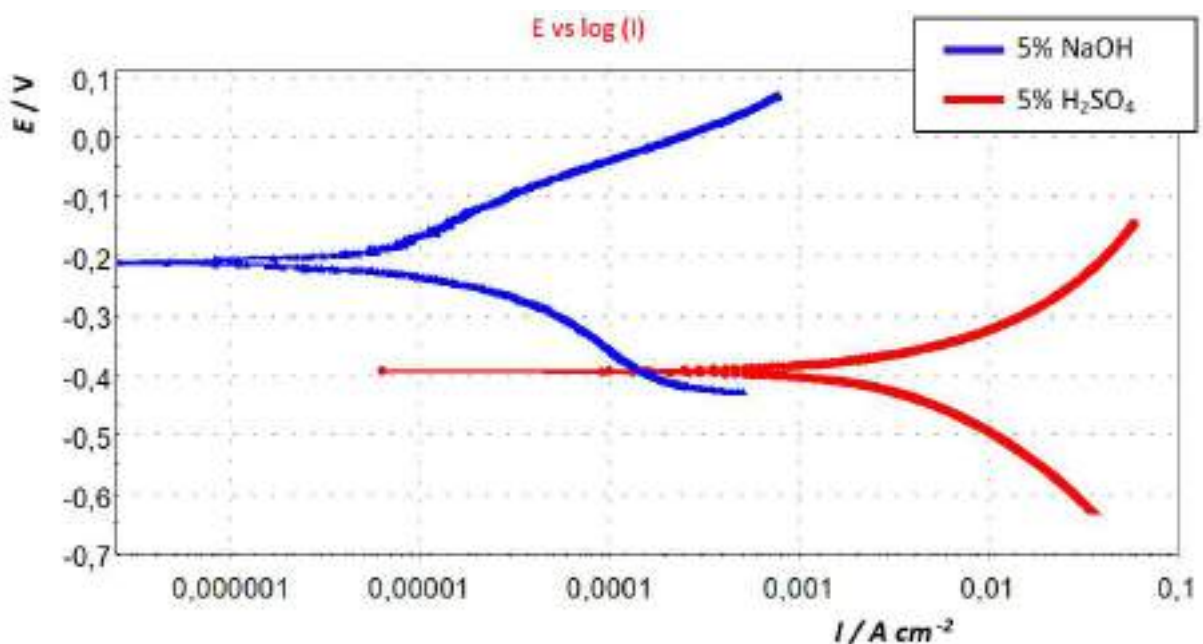


Figure 6. Polarization curves of tested X19NiCrMo4 steel in solution of 5 % NaOH and 5 % H₂SO₄

Table 3. Corrosion parameters of tested X19NiCrMo4 steel in solution of 5 % NaOH and 5 % H₂SO₄

Medium	E_{corr} vs. SCE	b_a	b_c	v_{corr}
	mV	mV dec ⁻¹	mV dec ⁻¹	mm yr ⁻¹
5% NaOH	-210.18	142.19	124.78	0.075
5% H ₂ SO ₄	-392.56	227.79	317.14	73.02

The results obtained from the impedance and polarization measurements are in good agreement. A large difference was observed in the obtained values after testing the steel in the 5 % NaOH and 5 % H₂SO₄ solutions. The corrosion rate of steel in 5 % H₂SO₄ is far higher than the corrosion rate in 5 % NaOH. Also, the electrode potential is more negative, and the amounts of cathode and anode slope are higher than the results in the solution of 5 % NaOH. These results lead to the conclusion that the cathode and anode iron dissolution reactions are more pronounced in the case of sample exposed in 5 % H₂SO₄ solution.

For the purpose of analyzing the microstructure of the tested tool steel, the sample was observed using an optical microscope after etching in nital (Figure 7). The microstructure of the tested steel after electrochemical tests in solutions of 5 % NaOH and 5 % H₂SO₄ is shown in Figure 8.

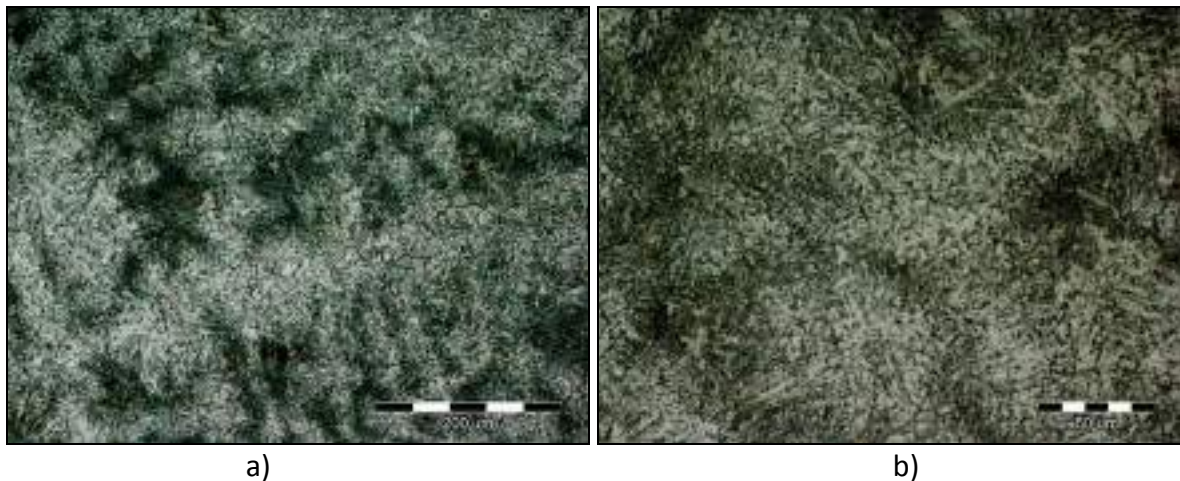


Figure 7. Microstructure of X19NiCrMo4 steel after etching in nital: a) magnification 200x and b) magnification 500x

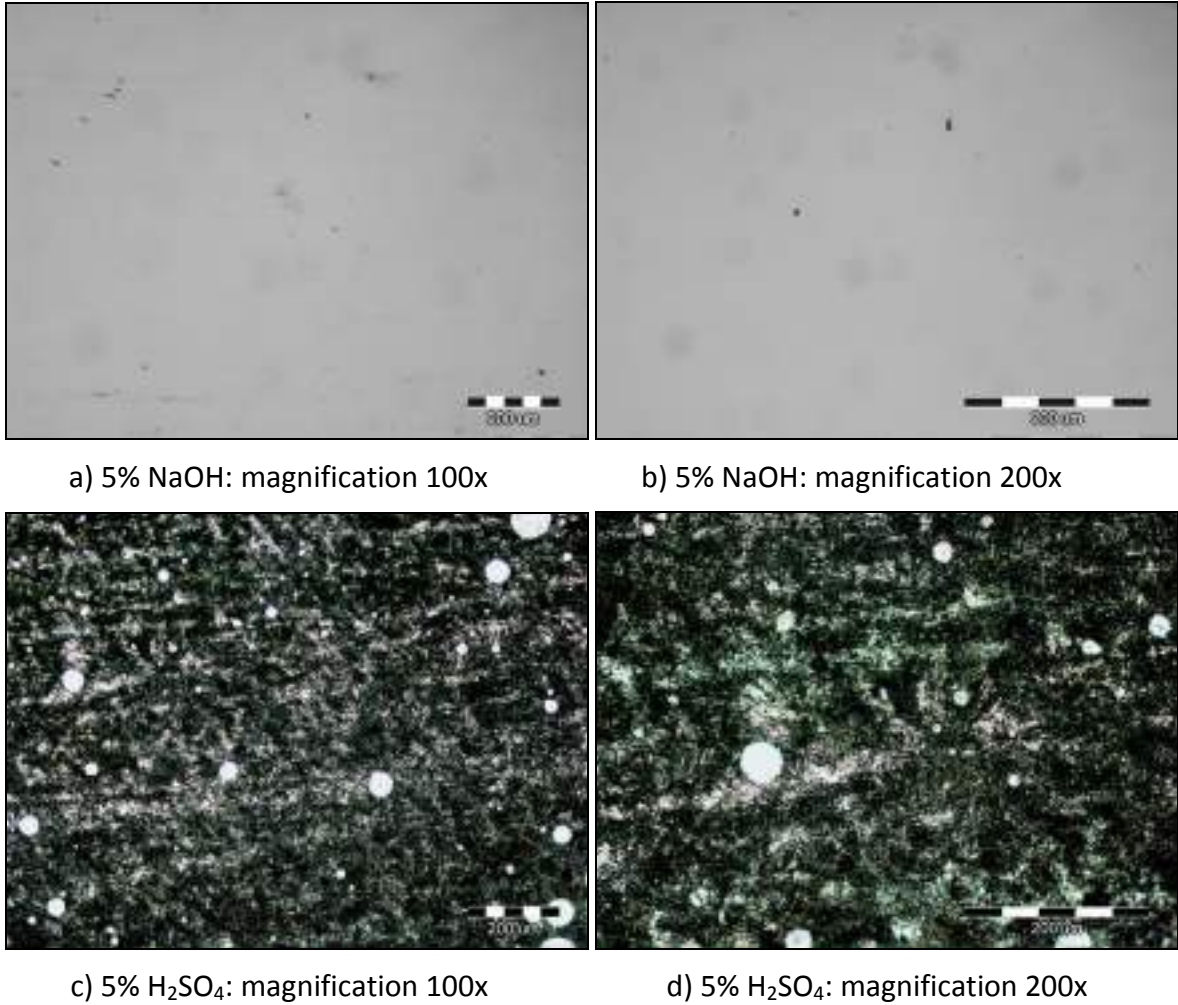


Figure 8. Microstructure of X19NiCrMo4 steel in solution of 5 % NaOH and 5 % H₂SO₄

According to the analysis of the microstructure after etching in the nital, it can be seen that the cementing steel marked X19NiCrMo4 consists of a martensitic phase.

After electrochemical measurements in alkaline medium (5 % NaOH) no changes were observed on the sample surface. The condition of the surface remained the same as before the electrochemical tests.

In the case of testing in an acid medium, the surface of the sample is completely covered by corrosion products. The corrosion in this case is of high intensity and occurred very quickly. The sample surface is completely corroded and parts of the martensite stand out with the separation of carbides. After the steel is immersed in the acid, the acid first dissolves the oxide layer that formed naturally on the steel, followed by a rapid attack on the metal base itself. The obtained results correspond to the registered higher corrosion rate and lower charge transfer resistance.

CONCLUSIONS

- By monitoring the changes in the open circuit potential E_{ocp} , data on the corrosion behavior of the tested sample in a medium of 5 % NaOH and 5 % H₂SO₄ were obtained. Extremely negative OCP values obtained for the sample in acid indicate instability and dissolution of the sample. Although negative OCP values were also observed in the case of sample immersed in the alkaline solution, it is assumed that in that case a thicker oxide layer was formed on the electrode surface in time. This prevented further penetration of ions from the solution and the development of corrosion on the electrode.
- The potentiodynamic polarization method showed that the corrosion rate of the tested sample after exposure to 5 % H₂SO₄ was higher than in the case when the sample was exposed to 5 % NaOH solution. Also, higher values for b_a and b_c were recorded after the sample was immersed in the acid. This means that in the case of steel in an acid medium, the reactions at the anode and cathode are more pronounced than in the case of steel immersed in alkaline media.
- The results obtained by the method of electrochemical impedance spectroscopy confirmed the higher corrosion resistance of the sample after testing in alkaline solution. The tested steel in 5 % NaOH solution showed higher resistance of oxide layer R_{ox} and charge transfer resistance R_{ct} , which again indicates the formation of a thicker oxide layer on the sample surface. Unlike alkaline medium, the acid acted very aggressively on the tested steel. The passive layer on the sample surface was not compact enough which allow aggressive ions to penetrate from the solution.
- The consequences of the action of aggressive H⁺-ions were established by metallographic analysis of the tested steel surface after corrosion in H₂SO₄ solution. Namely, aggressive H⁺-ions contributed to the destruction of the passive layer on the surface of the material and thus deteriorated the martensitic microstructure of steel.
- From the above tests it can be concluded that the tested steel proved to be a bad material for use in operating conditions where it can come into contact with acid. The chemical composition of X19NiCrMo4 steel did not show satisfactory quality in acidic medium, despite a favorable combination of alloying elements. Further alloying can improve corrosion resistance of steel; for instance corrosion resistance of steel increase with increase in chromium content as the addition of chromium results in the formation of a passive oxide film.
- The performed tests can serve as a basis for finding inhibitors that might be suitable for preventing the development of corrosion on steels.

Acknowledgements

Investigations were performed within the research topic "Design and Characterization of Innovative Engineering Alloys", Code: FPI-124-2019-ZZB funded by University of Zagreb and infrastructural scientific project: Center for Foundry Technology, Code: KK.01.1.1.02.0020 funded by European Regional Development Fund.

REFERENCES

- [1] W. E. Bryson, Heat treatment, selection and application of tool steels, 2nd Edition, Hanser Publications, Cincinnati, 2013.
- [2] J. Szumera, The tool steel guide, First edition, Industrial Press, Inc., New York, 2003.
- [3] D. C. Silverman, R. B. Puyear, Effects of environmental variables on aqueous corrosion, ASM Handbook, Volume 13, USA, 1987, pp. 71-88.
- [4] R. W. Revie, H. H. Uhlig, Corrosion and corrosion control: An introduction to corrosion science and engineering, Fourth edition, A John Wiley & Sons, INC., Publication, New Jersey, 2008.
- [5] Z. Panossian, N. Lira de Almeida, R. M. Ferreira de Sousa, Gutemberg de Souza Pimenta, L. B. Schmidt Marques, Corrosion of carbon steel pipes and tanks by concentrated sulfuric acid: A review, Corrosion Science, 58(2012), 1-11.
- [6] M. Ahmadi, S. H. Seyedin, Investigation of NaOH properties, production and sale mark in the world, Journal of Multidisciplinary Engineering Science and Technology (JMEST) ISSN: 2458-9403, 6(2019)10, 10809-10813.
- [7] D. W. Shoesmith, Effects of metallurgical variables on aqueous corrosion, ASM Handbook, Volume 13, USA, 1987, pp. 89-98.
- [8] Buehler® SumMet™, A Guide to Materials Preparation & Analysis, Fourth Edition, 2007, USA, Accessible on Internet:
<http://www.trimid.rs/upload/documents/buhler/Buehler%20Summet.pdf>,
(15.11.2020)
- [9] S. Brajčinović, A. Begić Hadžipašić, J. Medved, S. Kožuh, Influence of medium on corrosion and microstructural properties of HTCS-130 tool steel for hot work, Proceedings of 18th International Foundrymen Conference, (N. Dolić, Z. Zovko Brodarac, A. Begić Hadžipašić, Edts.), University of Zagreb Faculty of Metallurgy, 15-17.05.2019, Sisak, Croatia, pp. 188-205.
- [10] A. Lasia, Electrochemical impedance spectroscopy and its applications, Modern aspects of electrochemistry, (B. E. Conway, J. Bockris, and R. E. White, Edts.), Kluwer Academic/Plenum Publishers, 32(1999), New York, pp. 143-248.



19th INTERNATIONAL FOUNDRYMEN CONFERENCE
Humans - Valuable Resource for Foundry Industry Development
Split, June 16th-18th, 2021
<https://ifc.simet.hr/>

INHIBITORY EFFECT OF COMMERCIAL INHIBITOR VCI 379/611 ON CORROSION BEHAVIOR OF X153CrMoV12 TOOL STEEL FOR COLD WORK

Sandra Brajčinović, Anita Begić Hadžipašić*, Franjo Kozina

University of Zagreb Faculty of Metallurgy, Sisak, Croatia

Poster presentation
Original scientific paper

Abstract

In this paper, the influence of water and the influence of the commercial inhibitor VCI 379/611 on the corrosion processes of X153CrMoV12 tool steel for cold work were investigated. The research was carried out by electrochemical methods: by measuring the potential of an open circuit, by determining the corrosion parameters using the method of electrochemical impedance spectroscopy (EIS) and method of Tafel extrapolation. After each measurement, the sample surface was analyzed using an optical microscope. The obtained corrosion parameters showed a high efficiency of the applied inhibitor in the protection of tool steels for cold work from corrosion. For the sample that was exposed to distilled water medium with the addition of inhibitor, a significantly lower corrosion rate was registered and no damage to the sample surface was visible. Metallographic images of the electrode surface after polarization measurements in tap water indicate the occurrence of pitting corrosion.

Keywords: *tool steel for cold work, electrochemical techniques, corrosion parameters, inhibitor, microstructure*

*Corresponding author (e-mail address): begic@simet.unizg.hr

INTRODUCTION

Tool steels are integral parts of industrial machines. They are most often used to make tools with which metal or non-metal products are processed or shaped. Also, tool steels are produced for engine parts, bearings and springs due to very good mechanical properties. They are mainly used in the heat-treated condition and are delivered in the form of bars, strips or plates [1]. They are important for the modern development of the industry and are indispensable in production. Modern materials are obtained by optimizing the composition and microstructure of the material according to the desired properties. Depending on their purpose, the goal is to achieve the most favorable properties of tool steels. The most wanted properties are hardness, wear resistance, high toughness, yield strength and

corrosion resistance [2]. Corrosion is the undesirable wear of metals caused by mechanical, biological or chemical action of the environment [3]. Previous research has shown that electrochemical corrosion can occur in water, aqueous solutions of acids, alkalis and salts. The intensity of corrosion depends on the chemical composition and microstructure of the steel, the type of medium, the pH value of the medium, the presence of ions or various other factors that adversely affect the material [4]. One of the commonly used methods of protecting steel from corrosion can be achieved by changing the corrosion environment, i.e. by removing activators or adding inhibitors. In industrial plants, inhibitors are most often used as liquid emulsion concentrates that are diluted in a certain ratio with water. Inhibitors in the form of powders, greases and oils are also used. The prepared agent with the addition of inhibitor provides adequate protection of metallic materials, especially in warehouses where the presence of moisture is unavoidable [5, 6].

The mechanism of inhibitor action is based on the creation of a barrier, i.e. a thin film on the metal surface. Inhibitors are substances that are added in very small concentrations in order to reduce the corrosion rate, and according to the mode of action are divided into anodic, cathodic and mixed (anodic-cathodic) [7]. In this paper, the influence of water and commercial inhibitor VCI 379/611 on the corrosion and microstructural properties of X153CrMoV12 tool steel for cold work marked as K110 was studied. By applying electrochemical tests in the mentioned media and by applying metallographic analysis of the tested sample before and after corrosion, corrosion parameters were obtained which provide insight into the corrosion behavior of the tested sample of tool steel.

MATERIALS AND METHODS

To test the influence of medium and microstructure on corrosion resistance, a sample of tool steel for cold work X153CrMoV12 according to DIN/EN 1.2379, internal code K110 was selected. The chemical composition of the tested sample is shown in Table 1. Chromium is the main alloying element in this type of steel, and in combination with carbon it forms carbides of the Cr₂₃C₆ and Cr₇C₃ type. It is known from the literature that corrosion resistance increases with increasing chromium content, especially if the content is higher than 12% [8]. The addition of vanadium results in the grain refinement of the primary austenitic grain. Molybdenum influences the formation of fine-grained structure of steel and most often produces carbides of the Mo₂C type [9].

Table 1. Chemical composition of tested tool steel K110 (in weight percent)

C	Si	Mn	Cr	Mo	Ni	V	W	Co	Fe
1.55	0.30	0.30	11.30	0.75	-	0.75	-	-	balance

Samples of tool steel for cold work marked as K110 were prepared by pressing into a conductive mass using a device for hot pressing of samples (SimpliMet® 1000). Machine grinding and polishing was performed on an automatic grinding and polishing device (Bühler). Machine grinding was performed with waterproof sandpaper of grade No. 240, 400, 600 and 800, and polishing with a suspension of Al₂O₃ in water. The samples were then washed in distilled water and degreased in ethanol. One prepared sample was used for electrochemical measurements, while the other sample was used for etching in 0.5 % nital

(mixture of alcohol and nitric acid) [10]. Tap water and VCI 379/611 inhibitor concentrate mixed with distilled water were used as the working medium during the electrochemical tests. For the purpose of testing the effectiveness of the inhibitor, the solution was prepared as follows: the industrially prepared concentrate was diluted with distilled water in a ratio of 1:1. The sample thus prepared was mixed with distilled water in a ratio of 1%. The inhibitor concentrate was formulated on the basis of thixotropic calcium sulfonate inhibitors. The water-based corrosion inhibitor is intended as an additive for the conservation of metal elements in covered warehouses. The inhibitor agent leaves a very thin transparent, dry film on the metal surface.

Electrochemical tests (E_{corr} , EIS, Tafel)

The E_{corr} corrosion potential determination method, electrochemical impedance spectroscopy (EIS), and the Tafel extrapolation method were used to obtain data on the corrosion behavior of the samples. Measurements were performed in a three-electrode glass cell in which the working electrode, counter electrode and reference electrode were placed. The working electrode was a test sample of tool steel immersed in the working medium. The Pt electrode was used as the counter electrode, and the saturated calomel electrode was used as the reference electrode [11]. All electrochemical measurements were performed using a computer-controlled potentiostat / galvanostat (Parstat 2273) at room temperature (19 ± 2).

Before performing the measurements, a test of the time dependence of the corrosion potential was performed. Stabilization of the potential in the open circuit E_{ocp} was performed in a time period of 1800 seconds.

Electrochemical impedance spectroscopy was performed in the frequency range from 100 kHz to 10 mHz with a sinusoidal voltage amplitude of 5 mV. Impedance parameters were analyzed using ZSIMPWin 3.60 software using appropriate R (Q(R(QR))) circuit models.

The Tafel extrapolation method was performed using potentiodynamic polarization in the potential range from -250 mV to +250 mV vs E_{corr} , with a potential change rate of 1 mV/s, and the corrosion parameters were determined by PowerCorr™ software using a Tafel extrapolation method and Faraday's laws [10]. One series of electrochemical measurements (E_{corr} , EIS, Tafel) lasted about 60 minutes.

Metallographic tests

Metallographic tests on sample K110 after etching in nital were performed in order to determine the microstructure, while metallographic tests on sample K110 for electrochemical measurements were performed in order to register the condition of the sample surface before and after corrosion. Metallographic images were obtained using an optical microscope with a digital camera (Olympus GX 51) and an automatic image processing system (AnalySIS® Materials Research Lab) [10].

RESULTS AND DISCUSSION

Figure 1 shows the time dependences of the potential in the open circuit for the tested sample marked as K110 in tap water and distilled water with the addition of inhibitor.

According to the figure it can be seen that the sample is prone to dissolution in tap water, i.e. the electrode potential is expressed in negative values. The tested tool steel in distilled water with the addition of inhibitor proved to be more stable, because the electrode potential tends to more positive values. The results of electrochemical impedance spectroscopy is shown by the Nyquist diagram (Figure 2). Modeling of the EIS diagram was performed using the appropriate model of the equivalent electrical circuit R (Q(R(QR))), after which the impedance parameters were obtained: electrolyte resistance R_{el} , oxide layer resistance R_{ox} , constant phase element of double layer Q_{dl} , surface heterogeneity measure n and charge transfer resistance R_{ct} (Table 2). By modeling, it was found that the experimental values match well with the modeled ones with a registered deviation of the order of 10^{-3} .

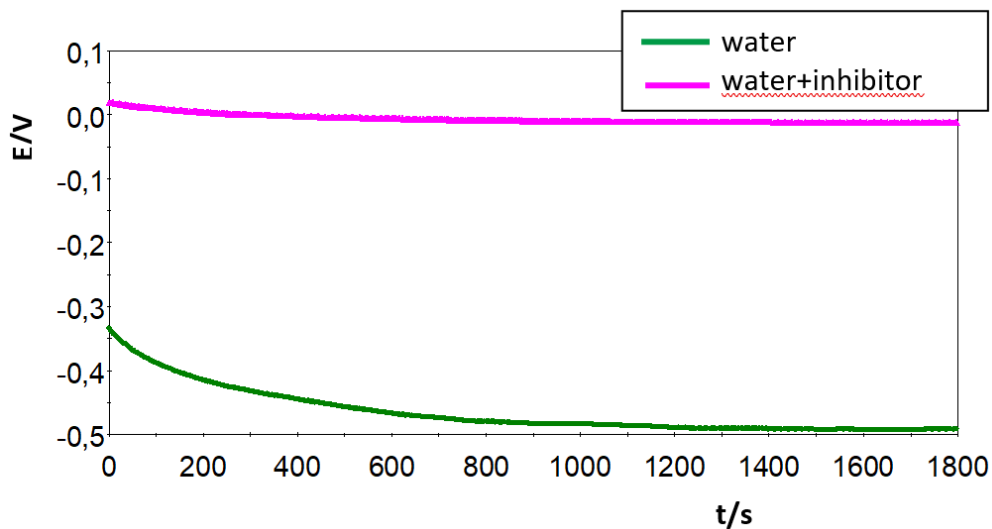


Figure 1. Time dependence of the open circuit potential for tool steel K110 in tap water and the concentrate of the inhibitor solution mixed with distilled water

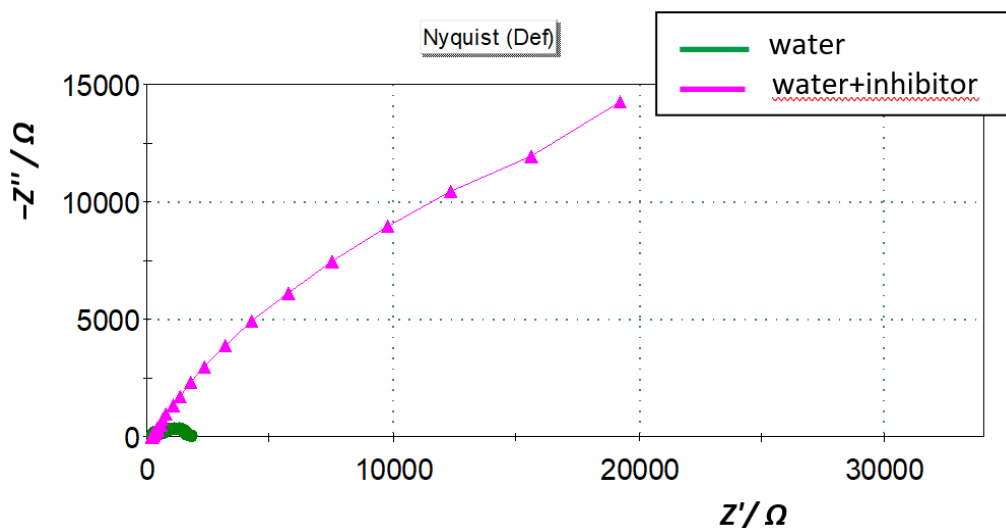


Figure 2. Comparative presentation of Nyquist EIS diagrams obtained for tool steel K110 in tap water and concentrate of inhibitor solution mixed with distilled water

Table 2. Impedance parameters of tested K110 tool steel

Medium	E_{corr} vs. SCE	R_{el}	$Q_{dl} \times 10^6$	n	R_{ox}	$Q_{dl} \times 10^6$	n	R_{ct}
	mV	Ωcm^2	$\Omega^1 \text{s}^n \text{cm}^{-2}$		Ωcm^2	$\Omega^1 \text{s}^n \text{cm}^{-2}$		Ωcm^2
Tap water	-492	277.0	10.67	0.8	315.9	429.6	0.6	1230
Distilled water + inhibitor	-12.7	229.4	135.5	0.7	27210	276.8	0.6	75160

It can be seen from Figure 2 that the Nyquist impedance representation of the sample in tap water is in the form of a depressive semicircle, and such a result is characteristic for solid electrodes. However, the tested sample in distilled water medium with the addition of inhibitor showed a tendency to form a semicircle of wider scale. This points to the fact that the addition of inhibitor can slow down corrosion processes, because a thicker protective layer is formed on the steel surface. This is confirmed by the data in Table 2, which shows that the tested tool steel in distilled water medium with the addition of inhibitor showed far higher oxide layer resistance R_{ox} and charge transfer resistance R_{ct} than that in tap water. The higher amount of charge transfer resistance indicates that a thicker surface layer has formed on the sample to protect the sample from further corrosion attack. In contrast, the tested tool steel showed a higher value of Q_{dl} in tap water. This can be explained by the fact that the passive layer growing on the surface of the K110 tool steel is not compact enough and there is an increase in capacity on the metal/oxide layer interface or inside the passive layer.

Figure 3 shows the polarization curves of the tested sample of tool steel K110 in tap water and distilled water with the addition of inhibitor. The results are presented graphically in semi - logarithmic form ($E - \log I$) where the corrosion current density logarithm is on the x - axis and the potential is on the y - axis.

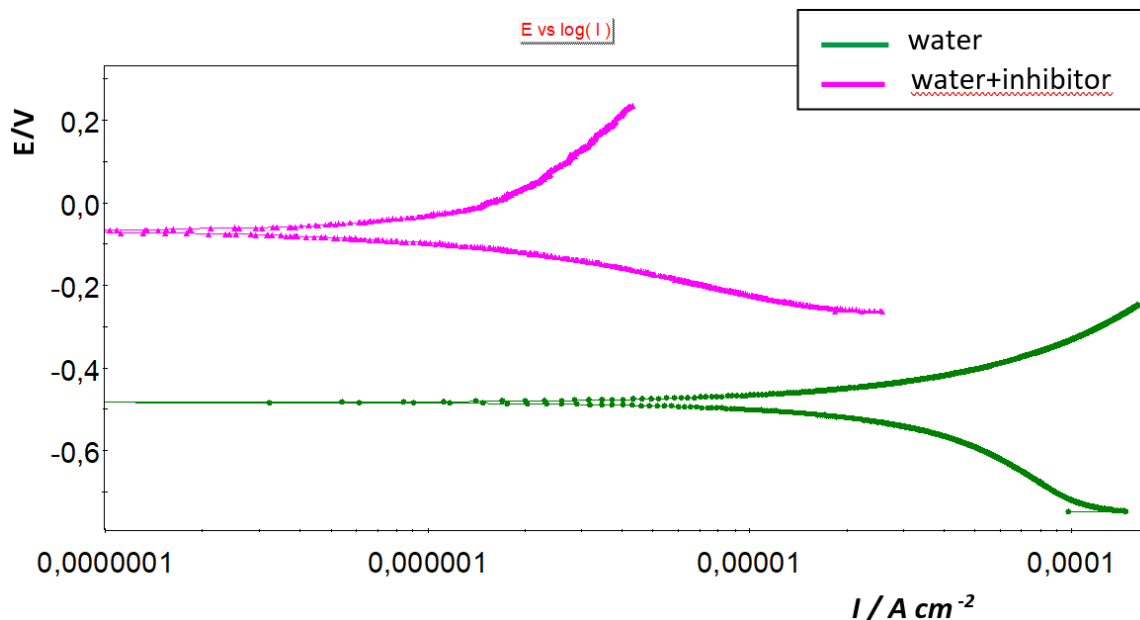


Figure 3. Polarization curves of the tested tool steel K110 obtained in tap water and concentrate of inhibitor solution mixed with distilled water

Potentiodynamic polarization was performed for the purpose of determining corrosion parameters (corrosion potential E_{corr} , corrosion rate v_{corr} , anodic slope b_a and cathodic slope b_c), and the obtained results are given in Table 3. According to the Tafel extrapolation method, a significantly lower corrosion rate was registered in distilled water with the addition of inhibitor. In order to determine the effectiveness of the inhibitor, the coefficient of effectiveness of the inhibitor Z [12] was calculated, in the amount of 0.98, which means that the effectiveness of the inhibitor at this added concentration is 98 %. This means that the added amount of inhibitor in the distilled water was sufficient to prevent the formation of corrosion products on the test sample. With the addition of inhibitor, the corrosion potential shifts towards more positive values, which reduces the corrosion current density, but also the corrosion rate.

Table 3. Corrosion parameters of tested K110 tool steel

Medium	E_{corr} vs. SCE	b_a	b_c	v_{corr}
	mV	mV dec ⁻¹	mV dec ⁻¹	mm yr ⁻¹
Tap water	-483.30	855.0	3824.7	2.115
Distilled water + inhibitor	-68.54	1277.8	215.7	0.028

For the purpose of analyzing the microstructure of tool steel marked as K110, the microstructure was observed using an optical microscope after etching in nital (Figure 4). It is known from the literature that after etching with nital, the distribution of carbides in tool steel is achieved in such a way that the carbides are highlighted in white and the matrix is dark [13]. Tool steel for cold work marked as K110 belongs to the group of ledeburite steels which, after hardening and low yielding, achieve the structure of martensite + secondary carbides.

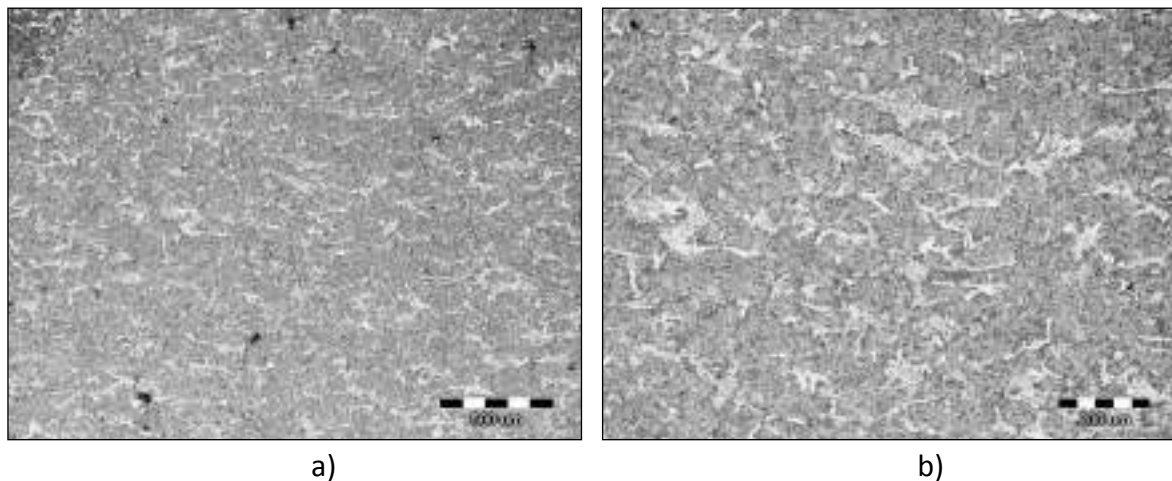
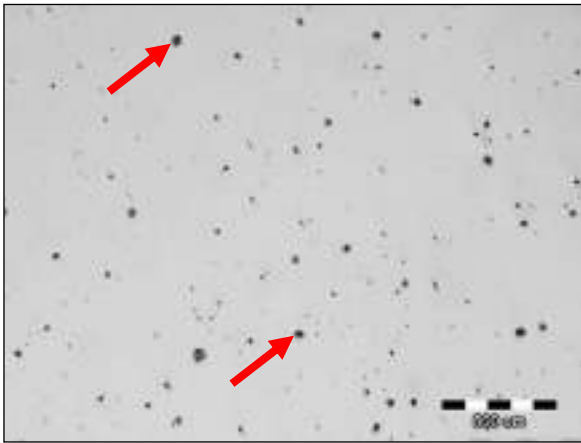
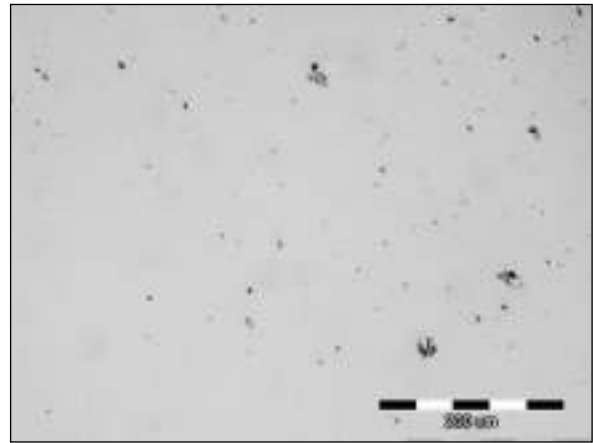


Figure 4. Microstructure of K110 tool steel for cold work after etching in Nital:
a) magnification 50x and b) magnification 100x

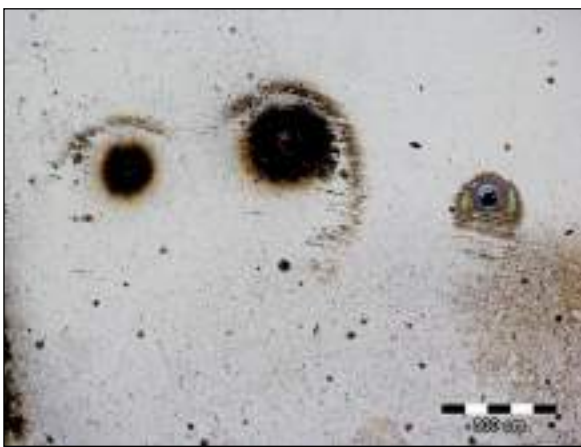
Figure 5 shows the microstructures recorded using an optical microscope after electrochemical measurements in tap water and distilled water with the addition of inhibitor.



a) no media: magnification 50x



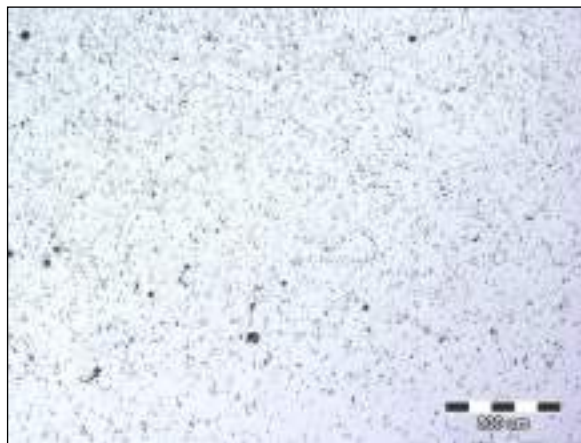
b) no media: magnification 200x



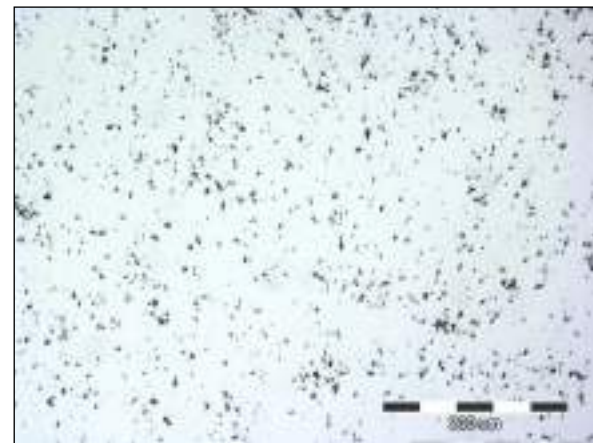
c) tap water: magnification 50x



d) tap water: magnification 100x



e) distilled water + inhibitor:
magnification 50x



f) distilled water + inhibitor:
magnification 200x

Figure 5. Microstructure of K110 tool steel for cold work: no media, in water, water and 1% inhibitor

The recorded microstructures of the sample before exposure in the media indicate the presence of inclusions. The inclusions are evenly distributed throughout the cross section. After electrochemical tests in tap water, pits were observed on the sample, i.e. the

occurrence of pitting corrosion was detected at the sites of inclusions. The behavior of steel in aqueous solutions depends on the natural oxide layer. It is very important to what extent a thin protective layer of oxide will be formed which will prevent further electrochemical reactions and protect the material from aggressive corrosive media [14]. Local inhomogeneities in the structure of the material can affect the occurrence of pitting corrosion. The formation of hydrated iron oxides depends on the anodic reaction. Namely, the less noble parts of the surface are the anodes where the metal melts due to the action of an aggressive medium. Excess released electrons travel to the nobler parts of the surface that represent the cathodes that bind to oxidants from the environment [10,15].

No surface damage was observed after testing in distilled water with the addition of a commercial VCI inhibitor. The inhibitor used is water-soluble and forms a water-transparent coating that can be observed in the form of uniformly distributed particles on the sample surface.

CONCLUSIONS

Using electrochemical tests, the results were obtained which indicate that the sample of tool steel for cold work marked as K110 in contact with water is subject to corrosion. However, after testing in a solution of distilled water with the addition of a commercial inhibitor VCI 379/611, a significantly lower corrosion rate v_{corr} and a significantly higher charge transfer resistance R_{ct} were registered. The obtained electrochemical and impedance parameters, as well as the inhibitor efficiency coefficient of 98% indicate that the commercial inhibitor VCI 379/611 is highly effective and is fully applicable in corrosion protection of X153CrMoV12 tool steel intended for cold work. The addition of inhibitors enabled the formation of a barrier on the surface, i.e. the anodic reaction of metal ionization was slowed down. The results obtained by electrochemical tests coincide with the results of metallographic analysis. Metallographic images on a sample that was exposed only to tap water indicate pitting corrosion. After the use of the commercial inhibitor, no corrosion products were observed on the steel surface, because the applied water-soluble inhibitor was adsorbed on the sample surface in the form of uniformly distributed particles. The coating thus formed reduces the number of potential sites on the sample surface for active penetration of the aggressive medium and increases the corrosion resistance of the tested tool steel for cold work.

Acknowledgements

Investigations were performed within the research topic "Design and Characterization of Innovative Engineering Alloys", Code: FPI-124-2019-ZZB funded by University of Zagreb and infrastructural scientific project: Center for Foundry Technology, Code: KK.01.1.1.02.0020 funded by European Regional Development Fund.

REFERENCES

- [1] R. Sunulahpašić, M. Oruč, *Alatni čelici i ostali alatni materijali*, Univerzitet u Zenici Metalurško-tehnološki fakultet, Zenica, 2019.
- [2] W. E. Bryson, *Heat treatment, selection and application of tool steels*, 2nd Edition, Hanser Publications, Cincinnati, 2013.
- [3] E. Stupnišek-Lisac, *Korozija i zaštita konstrukcijskih materijala*, Sveučilište u Zagrebu Fakultet kemijskog inženjerstva i tehnologije, Zagreb, 2007.
- [4] D. C. Silverman, R. B. Puyear, *Effects of environmental variables on aqueous corrosion*, ASM Handbook, Corrosion, United States of America, 13(1987), pp. 71-88.
- [5] R. W. Revie, H. H. Uhlig, *Corrosion and corrosion control: An introduction to corrosion science and engineering*, Fourth edition, A John Wiley & Sons, INC., Publication, New Jersey, 2008.
- [6] C. G. Dariva, A. F. Galio, *Corrosion Inhibitors – Principles, mechanisms and applications*, *Developments in Corrosion Protection*, 16(2014), pp. 365-379.
- [7] I. Esih, *Osnove površinske zaštite*, Sveučilište u Zagrebu, Fakultet strojarstva i brodogradnje, Zagreb 2010.
- [8] C. R. Sohar, *Lifetime controlling defects in tool steels*, Doctoral thesis, University of Technology, Vienna, Austria, 2011.
- [9] G. Roberts, G. Krauss, R. Kennedy, *Tool steels*, 5th edition, ASM International, Materials Park, 1998.
- [10] S. Brajčinović, A. Begić Hadžipašić, Lj. Slokar Benić, *Influence of medium on corrosion and microstructural properties of K110 tool steel for cold work*, *Metal 2020*, 29th International conference on metallurgy and materials, Conference Proceedings, Tanger Ltd., May 20th-22nd 2020, Brno, Češka, pp. 816-821.
- [11] M. Mobin, *Electrochemical studies on the corrosion behavior of carbon steel in presence of Cu and Ni*, *Portugaliae Electrochimica Acta*, Volume 26/5(2008), pp. 449-457.
- [12] A. Begić Hadžipašić, J. Malina, D. Petrović, *Primjena Aloe vere kao "zelenog" inhibitora u zaštiti konstrukcijskog čelika od korozije*, *Proceedings book of International Conference on materials, tribology, recycling, MATRIB 2014*, (editors: S. Šolić, M. Šnajdar Musa), Croatian Society for Materials and Tribology, 26.-28.06.2014., Vela Luka, Korčula, Croatia, pp. 40-51.
- [13] Accessible on Internet: <https://www.struers.com/en/Knowledge/Materials/Tool-steel#preparation-method>, (12.03.2021.)
- [14] D. Gassama, A. Aziz Diagne, I. Yade, M. Fall, S. Faty, *Investigations on the corrosion of constructional steels in different aqueous and simulated atmospheric environments*, *Bulletin of the Chemical Society of Ethiopia*, 29(2015), pp. 299-310
- [15] G. S. Frankel, *Pitting corrosion*, *Corrosion: Fundamentals, testing, and protection*, ASM Handbook, ASM International, 13A(2003), pp. 236-241.



19th INTERNATIONAL FOUNDRYMEN CONFERENCE
Humans - Valuable Resource for Foundry Industry Development

Split, June 16th-18th, 2021

<https://ifc.simet.hr/>

**ACTIVITY ASSESSMENT OF PHOTSENSITIVE DYES ANTHOCYANIN,
RHODAMINE B, RUTHENIUM N3 AND RHODAMINE B+ANTHOCYANIN
MIXTURE FOR APPLICATION IN SOLAR CELLS**

Anđela Čović^{*}, Pero Dabić, Damir Barbir

University of Split Faculty of Chemistry and Technology, Split, Croatia

Poster presentation
Original scientific paper

Abstract

The activity of photosensitive dyes such as anthocyanin, ruthenium N3, rhodamine B and anthocyanin + rhodamine B mixture was analyzed for potential use in solar cells based on nanostructured porous TiO₂ and ZnO films. Anthocyanin was extracted from a dry hibiscus (*Hibiscus sabdariffa*) flower in ethanol. The commercial light-sensitive dye N3 is an organometallic ruthenium complex, while rhodamine B is an indicator used in chemical laboratories. The UV-Vis spectrum of extracted anthocyanin, selected dyes and their combinations (anthocyanin + rhodamine B) were determined. The photoanodes were prepared by depositing an oxide layer based on TiO₂ and ZnO nanoparticles and were heated in furnace for a total of 40 minutes at different temperatures. The graphite film was applied to the conductive side of the solar cells by spray method, and the cathodes were dried at 80 °C for 1 hour to remove the organic solvent and then heated in furnace at 250 °C for 30 minutes. The graphite films and oxide layers were analyzed by digital microscope. From the microscopic images, it can be seen that the TiO₂ film is not compact and has visible cracks, while the ZnO film is also incompact, thinner and with smaller visible cracks. The solar cell efficiency of the open-circuit voltage (V_{oc}) and short-circuit current density (J_{sc}) were measured under simulated light (60 W) to obtain values of fill factor (FF) and conversion efficiency (η). Considering all the calculated parameters, the N3 dye is the most suitable for use in solar cells. In general, the TiO₂ layer gave better results than the ZnO layer.

Keywords: solar cells, photosensitive dyes, TiO₂ and ZnO nanoparticles, conversion efficiency, fill factor

*Corresponding author (e-mail address): ac6352@ktf-split.hr

INTRODUCTION

New generation of solar cells called dye-sensitized solar cells (DSSC) have been widely researched over the last decades. They are extremely suitable for laboratory research for their simple, short-time and low-cost fabrication procedure, wide range of materials, environmental friendliness, and high efficiency [1, 2]. Generally, DSSC consist of two transparent conductive glass plates where one is photoanode, coated with porous oxide layer of a wide band gap semiconductor, which is sensitized for visible light by an absorbed dye and other side as photocathode, with platinum or carbon layer. The space between the two electrodes is filled with an electrolyte containing a redox couple, such as iodide (I^-)/triiodide (I_3^-) [3-5]. DSSCs were first researched by M. Gratzel et al. who has developed special solar cells with nanocrystalline TiO_2 layer that achieved 7 % efficiency. They were named Gratzel solar cells [6]. Important parameters that affect the efficiency of DSSCs are the quality of oxide layer applied on the surface of the conductive glass as well as the bonding of the photosensitive dye to that surface. TiO_2 , ZnO , SnO_2 and Nb_2O_5 [7] are usually used as a oxide photoanode layers. TiO_2 is highly preferable oxide layer because of its adequate surface area and chemical affinity for dye adsorption as well as its suitable energy band potential for charge transfer with dye and electrolytes. As an alternative for TiO_2 -based DSSCs, ZnO nanoparticles have become intensively used thanks to the facts that ZnO have similar electron affinities and almost the same band gap energies as TiO_2 (≈ 3.2 eV). It is a low-cost material, it has a large excitation binding energy (60 eV) and it is stable against photocorrosion [1, 2, 8-10]. Many disadvantages can change the surface quality, such as formation of microcracks or agglomeration of nanoparticles during the paste preparation. To prevent those problems various nonionic dispersants are added (e.g. PEG, Triton X-100) [11, 12]. A dye that acts as an efficient photosensitizer should show excellent absorption in the visible range (400 nm to 700 nm), should be well absorbed to the semiconductor oxide surface, should have a high extinction coefficient and be stable in its oxidized form allowing it to be reduced by an electrolyte. In general, those dyes can be divided in two main classes: inorganic dyes which include metal complexes (polypyridyl complexes of ruthenium and osmium, metal porphyrin, phthalocyanine) and organic dyes which include natural and synthetic organic dyes [13, 14]. The ruthenium complexes have been reported as dye with current maximum efficiency of 11 % [15, 16]. Due to the high cost of inorganic dyes and the difficulty of purification, organic dyes started to be used more often. Anthocyanins are the largest group of water-soluble pigments founded in plants. They are responsible for red, purple or blue colors in many fruits and purple-red color of autumn leaves [17]. *Hibiscus sabdariffa*, commonly known as Roselle, is rich in anthocyanins. Previous research [18-22] based on using different methods of dye extraction or different solvents in extraction are very relevant in studies about improving the efficiency of DSSCs.

The aim of this work is to determine the solar cell efficiency in terms of adsorption of the dyes used on two different oxide surfaces. Four different dye solutions were used on two different oxide layers, TiO_2 and ZnO .

MATERIALS AND METHODS

Photovoltaic cell fabrication process

A series of eight photovoltaic cells were prepared: four with a porous TiO_2 layer and four with a porous ZnO layer. At first, all conductive glass plates (2.5 cm x 2.5 cm) were cleaned in

detergent solution, rinsed in distilled water and ethanol solution, and completely dried. The Conductive side of the glass was determined by multimeter. Also, the measurement of surface resistance was introduced as a value for quality assessment of conductive glass for solar cells. The unit for surface resistance is Ω/\square (read: Ohms per square). This corresponds to the resistance between two opposite angles of the square on the surface of the material, which is measured, where the measuring square can be of any size. If a known current flows through the film between the external contacts and the voltage is measured between the internal contacts, then the surface resistance is calculated according to equation 1:

$$\rho_s = \frac{V}{I} \cdot \frac{\pi}{\ln 2} \quad (1)$$

Where is: ρ_s = surface resistance, [Ω / \square], V = direct voltage, [V], I = direct current, [A] [23] These values were determined using the laboratory device shown in the Figure 1. The results obtained results can be seen in Table 1.

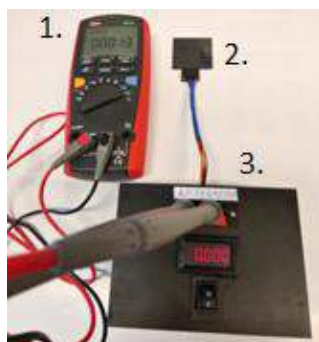


Figure 1. Laboratory device for voltage and current measurements to determine surface resistivity- 1. ampermeter, 2. four-contact probe, 3. source of constant voltage and current

After the glasses were selected for use, pastes and photosensitive dye solutions were prepared according to the procedures. Adhesive tape was used to limit and shape the TiO_2 and ZnO area for 2 cm x 2 cm.

Preparation of photosensitive dyes

Four solutions were prepared-solution of anthocyanin, Rhodamine B and N3 dyes. Anthocyanin and Rhodamine B were mixed in the ratio of 1:1. Five grams of dried Hibiscus flower (*Hibiscus sabdariffa*) were placed in a mortar and grounded in smaller pieces. Thus prepared sample was poured into 50 mL of 60% ethanol solution slightly acidified with 0.3% hydrochloride acid and kept in a dark and cool place for 24 hours. After that time, extraction was performed in an ultrasonic bath (Digital ultrasonic cleaner) for 540 sec at 60°C and solution was filtered with filter paper. The obtained dark red solution was stored in appropriate bottle without direct exposure to sunlight. Without subsequent purification it was used as a photosensitive dye in solar cells [24]. 50 mL of 0.5 mM solution of Rhodamine B ($\text{C}_{28}\text{H}_{31}\text{ClN}_2\text{O}_3$; Alfa Aesar Germany) and 50 mL of 0.5 mM solution of N3 (cis-Bis (isothiocyanato) bis (2,2'-bipyridyl-4,4'-dicarboxyalato)ruthenium(II); Sigma Aldrich Germany) dye were prepared by dissolving a sample in 50 mL of 96% ethanol solution. The obtained solutions were stored in appropriate bottle without direct exposure to sunlight.

Electrode preparation

The commercial TiO₂ (P25 nanopowder, Sigma Aldrich Germany, 21 nm primary particle size) powder (1 g), dilute acetic acid solution (0.5 mL), Triton X-100 (0.5 mL) and deionized water (2.5 mL) were mixed and continuously grinded for 2 hours in mortar to obtain TiO₂ [24]. Then the TiO₂ paste was uniformly coated on conductive side of glass by plastic plate, air-dried for 20 min, then dried at 60 °C for 20 min and at 130 °C for 20 min and then heated in furnace at 350 °C for 10 min, at 450 °C for 15 min and at 500 °C for 15 min. TiO₂ photoanode was obtained and immersed in prepared dyes for 24 hours under darkness. The same procedure was followed to prepare ZnO photoanodes (particle size <50 nm; Sigma Aldrich Germany). The only difference was that instead of dilute acetic acid, 70 % ethanol solution was used. They were also immersed in prepared dyes for 24 hours under darkness (Figure 2. a)) [25]. For preparation of counter electrode, graphite in spray form (CRC Industries Europe BVBA, Belgium) was used. Graphite was applied by spray technique uniformly, on the conductive side of glass, air-dried for 20 min and then in dryer at 80 °C for 1 hour, and at 250 °C for 30 min (Figure 2. b)) [4].

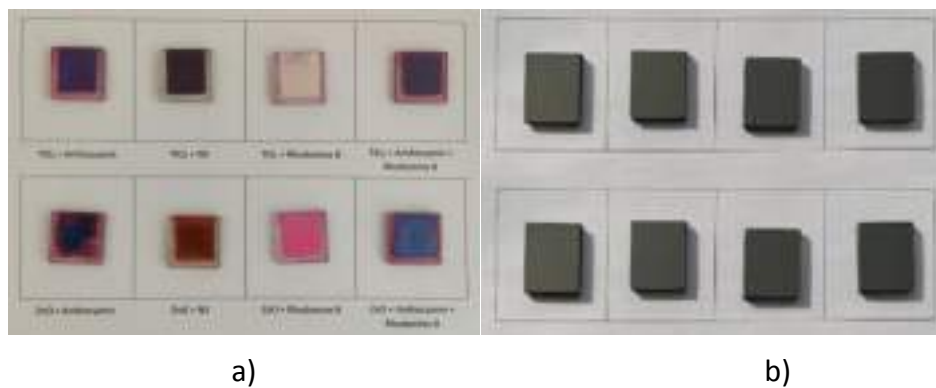


Figure 2. Prepared electrodes a) Photoanodes with TiO₂ and ZnO layer b) Graphite photocathodes

When all components were finished, the last step was to unite the active electrode substrate with counter electrode, using a binder clip with 0.5 cm offset at each end of the substrate (Figure 3). KI electrolyte was immersed in the gap between the two electrodes through dropper. Electrolyte distributed through entire porous layer.



Figure 3. Assembled solar cells

DSSC performance of the open-circuit voltage (V_{oc}), and short-circuit current density (J_{sc}) were measured under simulated sunlight (60 W) on effective area (2 cm x 2 cm) to calculate the fill factor (FF) and solar conversion efficiency (η).

TiO₂ and ZnO surfaces were analyzed using a digital microscope (MXFMS-BD, Ningbo Sunny Instruments Co, China) at two magnifications, 40 and 100X. In order to determine the wavelength range of absorption of prepared dyes solutions, ultraviolet and visible radiation absorption of the prepared dyes was measured using the UV-Vis spectrophotometer (Specord® 200 Plus, Analytik Jena, Germany). The measurements were performed in the wavelength range of 250-750nm.

I-V curve

The cell was illuminated by a 60W lamp 5 cm away from cell surface. Full current-voltage (I-V) curves were measured using 500- Ω potentiometer as a variable load as shown in Figure 4.

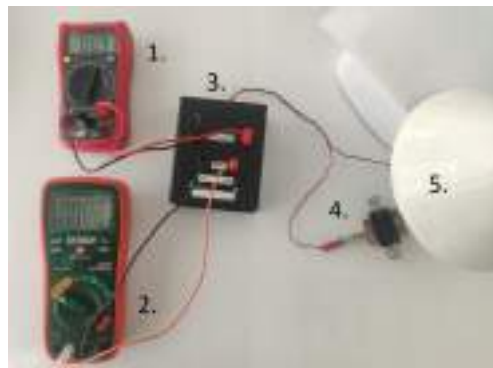


Figure 4. Demonstration of determining the values needed to calculate the efficiency of solar cells; 1.voltmeter (mV), 2. ampermeter(μ A), 3. electronic circuit with 500- Ω potentiometer as a variable load, 4. prepared solar cell, 5. 60W lamp

Output of the current and voltage was noted and then the fill factor (FF) and solar conversion efficiency (η) were calculated using the following equations (2-3) [15, 17, 26]:

$$FF = \frac{V_{max} \cdot I_{max}}{V_{oc} \cdot J_{sc}} \cdot 100\% \quad [\%] \quad (2)$$

$$\eta = \frac{P_{out}}{P_{in}} = \frac{FF \cdot V_{oc} \cdot J_{sc}}{I_r \cdot A} \cdot 100\% \quad [\%] \quad (3)$$

V_{max} = maximum voltage (mV), I_{max} = maximum current (mA),

V_{oc} = open-circuit voltage (mv), J_{sc} = short-circuit current density (mA),

P_{out} = output power (W), P_{in} = input power (W),

I_r = light intensity (W), A = DSSC area

Results are shown in Table 3 and 4.

RESULTS AND DISCUSSION

Current (mA) and voltage (mV) values were determined on commercial conductive glass plates to calculate the surface resistance. The results are shown in Table 1. The measurements were performed in such manner that the contacts of the device are in contact with the surface of the conductive glass.

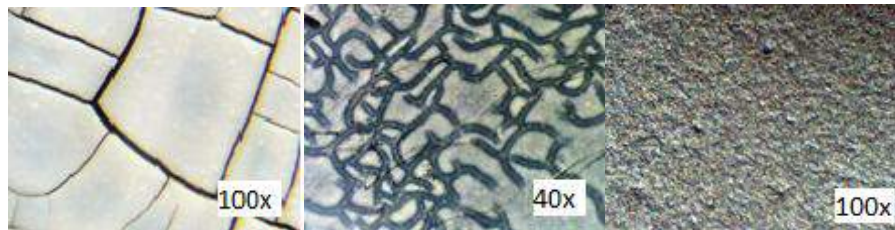
Table 1. The results of surface resistance determination

Commercial conductive glass		Voltage, (mV)	Current, (mA)	Surface resistance, ρ_s , (Ω / \square)
Glass plates used for graphite layer	1	235	71.5	14.89
	2	248	73.3	15.34
	3	275	80.2	15.55
	4	253	73.0	15.71
	5	276	77.2	16.20
	6	277	76.0	16.52
	7	279	71.3	17.73
	8	273	61.3	20.18
Glass plates used for TiO ₂ or ZnO layer	1	188	81.8	10.42
	2	236	87.2	12.27
	3	301	108.0	12.63
	4	250	81.9	13.84
	5	239	77.9	13.90
	6	230	74.7	13.96
	7	219	70.4	14.09
	8	271	84.6	14.52

Microscopic analysis of prepared photoanodes and graphite photocathodes

Microscopic analysis of the surface of titanium dioxide heated up to 500 °C shows that TiO₂ films don't have a compact surface, the thickness isn't the same along the entire surface and microcracks were formed (Figure 5. a)). The cracks are possibly a result of the shrinkage of the nanocrystalline TiO₂ film due to the drying process and the temperatures up to 500 °C. The accumulation of TiO₂ grains is visible in some places. After the preparation, the paste was quite viscous and seemingly homogeneous, but after recording under magnification a larger number of accumulations were observed that weren't homogeneously distributed in the paste. Figure 5. b) shows ZnO film after the heating process. That surface under magnification has the same appearance as TiO₂ surface only with more visible tiny cracks. Microscopic analysis of the graphite surface heated up to 250 °C is shown in Figure 5. c). The

graphite layer is compact, surface of the glass was well covered, and it has a seemingly fine-grained structure. It adheres well to the surface of the glass and doesn't come off with touch. The image isn't of distinct resolution due to the reflection of light from the surface of the graphite, so the analysis was performed in the dark to minimize the impact of the reflection.



a) b) c)
 Figure 5. Microscopic images of prepared films a)TiO₂surface b) ZnO surface
 c) Graphite surface

UV-Vis of dye solutions

Figure 6. a-d) shows the UV-Vis absorption spectrum of used dyes.

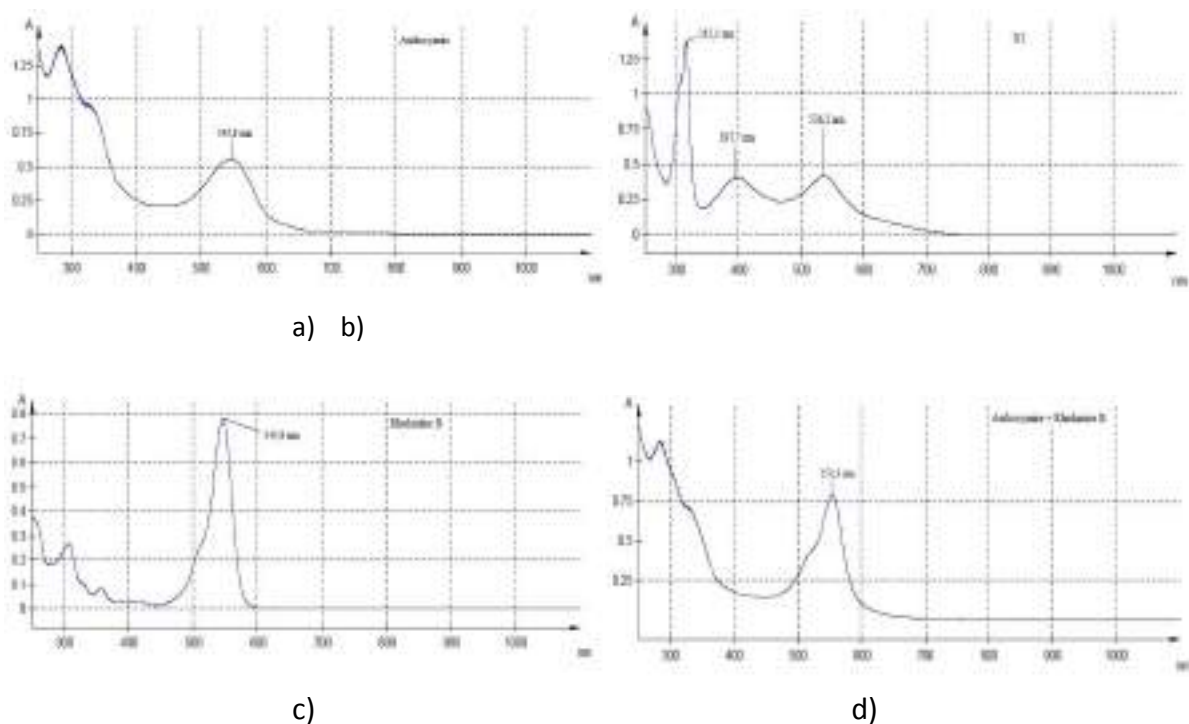


Figure 6. UV-Vis absorption spectrum of a) Anthocyanin dye b) N3 dye c) Rhodamine B dye
 d) Anthocyanin + Rhodamine B dye

The widest wavelength range has a dye solution N3 whose wavelength values range from 400 to 600 nm with an absorption maximum at 536.2 nm. Anthocyanin and Rhodamine B show a narrower absorption range of approximately 480 nm to 600 nm. Since they show almost the equal values of the maximum absorption band, their combination also gives the same value. Because N3 has a wider absorption wavelength range than other dyes and

achieves an absorption maximum at lower values, it will absorb more energy. Therefore, the conversion efficiency of solar cells with N3 is higher, which will be confirmed by the following results.

DSSC Performance analysis

Photoinduced voltage measurement

The photoinduced voltage under artificial lighting was measured on prepared solar cells for 14 days. After 8 days of measurements, a new amount of electrolyte solution was added to the prepared cells, and the measurements were continued for another 7 days. The obtained results are shown in Figure 7. a-d).

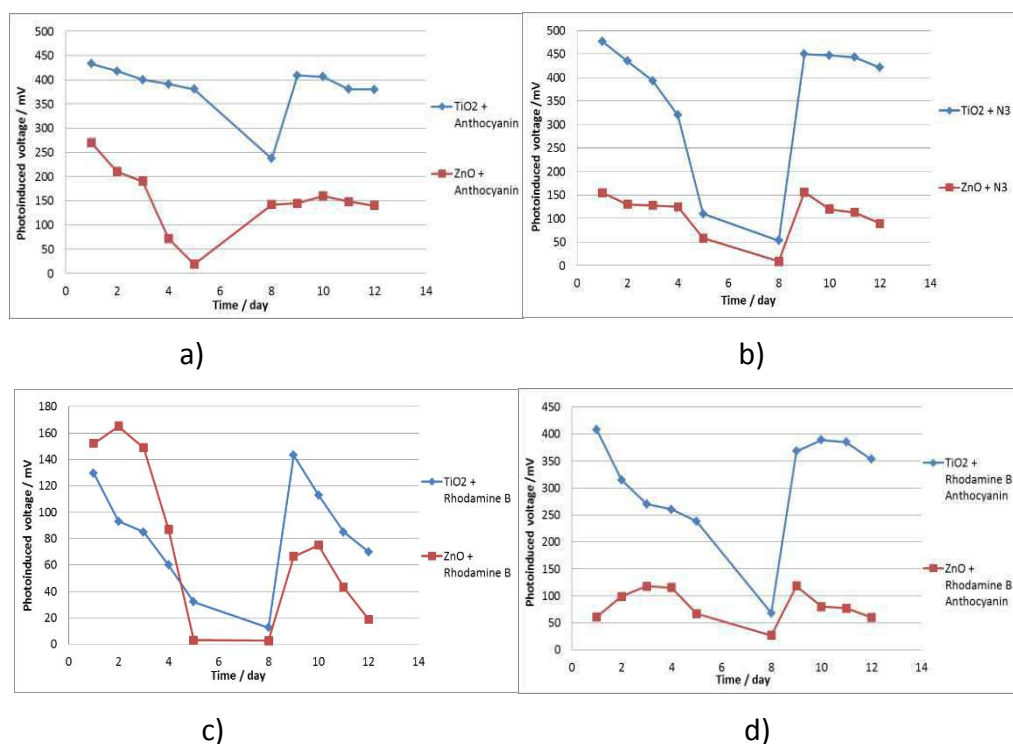


Figure 7. Comparison of photovoltage for two oxide layers with a) Anthocyanin dye b) N3 dye c) Rhodamine B dye d) Rhodamine B + Anthocyanin dye

The values of photoinduced voltage measured on the first day, shortly after the construction of solar cells were in the range from 100 to 500 mV for the titanium dioxide layer and in the range from 30 to 300 mV for the zinc oxide layer. Obtained values depend on several factors such as the type, thickness and quality of the applied oxide layer, the porosity of the applied layer, and the characteristics of used photosensitive dye. Solar cells prepared on the TiO₂ layer gave higher values of the photoinduced voltage compared to those on the ZnO layer. Solar cell with a porous layer of TiO₂ and anthocyanin dye gave satisfactory voltage values (433 mV), while solar cell which contains the ZnO layer with anthocyanin dye gave a significantly lower voltage value (270 mV) (Figure 7. a)). The reason for this may be the characteristics of the ZnO layer itself, its thickness, porosity, as well as the quality of preparation. As can be seen in the microscopic figures, the ZnO layer is significantly thinner than the titanium dioxide layer, and these results of photoinduced voltage may confirm the impact of paste preparation on cell efficiency. Also, during the preparation, the anthocyanin

solution is slightly acidified with 0.3 % hydrochloric acid, and since the ZnO layer has a tendency to slightly dissolve and form complexes with dye molecules in an acidic environment, it is possible that during the contact between ZnO layer and slightly acidified solution of anthocyanin, the layer dissolved and formed a complex with the dye molecules, resulting in lower values of the photoinduced voltage [27]. The same problem occurs in solar cell with ZnO layer and mixture of anthocyanin and Rhodamine B dyes (Figure 7. d)). A significant difference in the values of photoinduced voltage can be noticed in the case of using N3 dye, which shows a satisfactory value of 470 mV on the TiO₂ layer, while on ZnO is half less of that (Figure 7. b)). A comparison of cells with Rhodamine B dye on a first sight shows a difference in dye absorption (Figure 2. a)). In the case of the TiO₂ layer, absorption almost didn't occur, compared to a cell prepared with ZnO. This comparison is also confirmed by the obtained values of the photoinduced voltage.

Over the 8 days, the values of photoinduced voltages decreased slightly, and the reason for this was the drying and evaporation of the electrolyte, which caused a decrease in its efficiency. Eighth day of measurement, a larger drop in photoinduced voltage was observed, especially in solar cells 3, 6 and 7, for which the values of photoinduced voltage dropped to very low values (in the range 0-15 mV). Therefore, a new amount of electrolyte solution was added to all solar cells, and the values of the photoinduced voltage before and after the addition of a new amount of electrolyte solution were compared. According to the obtained results shown in Figure 7, the new addition of a small amount of electrolyte solution, leads to an increase in the value of photoinduced voltage in every cells, especially in solar cells prepared with anthocyanin and N3 dyes (Table 2.).

Table 2. Results obtained by measuring photoinduced voltage before and after electrolyte addition (8th day of measurement)

Cell	Oxide layer	Photosensitive dye	Before electrolyte addition (mV)	After electrolyte addition (mV)
1.	TiO ₂	Anthocyanin	237.0	410
2.		N3	53.0	465
3.		Rhodamine B	12.6	240
4.		Rhodamine B + Anthocyanin	68.0	400
5.	ZnO	Anthocyanin	142.0	310
6.		N3	8.6	150
7.		Rhodamine B	2.6	116
8.		Rhodamine B + Anthocyanin	26.5	130

This can confirm one of the main functions of the electrolyte in solar cells which is the regeneration of lost electrons from the used photosensitive dyes that can extend the life of solar cells. The problem of electrolyte drying in practice can be solved by hermetically closing the solar cell and using electrolyte in the form of a gel. The highest value of photoinduced voltage during 14 days of measurement was recorded in solar cell with oxide layer TiO₂ and N3 as dye, which was 477 mV. While Rhodamine B dye on TiO₂ layer gave the lowest results.

Generally, TiO₂ paste gave better results and the drop in photoinduced voltage is narrower than in solar cells prepared with ZnO paste.

DSSC performance test

Table 3. summarizes specifications of prepared DSSC solar cells, where two types of photocathode have been made using different types of photosensitive dyes. After the DSSCs have been assembled, voltage (mV) and current (mA) were measured. An example of determining the required values from the graph is shown in the Figure 8.

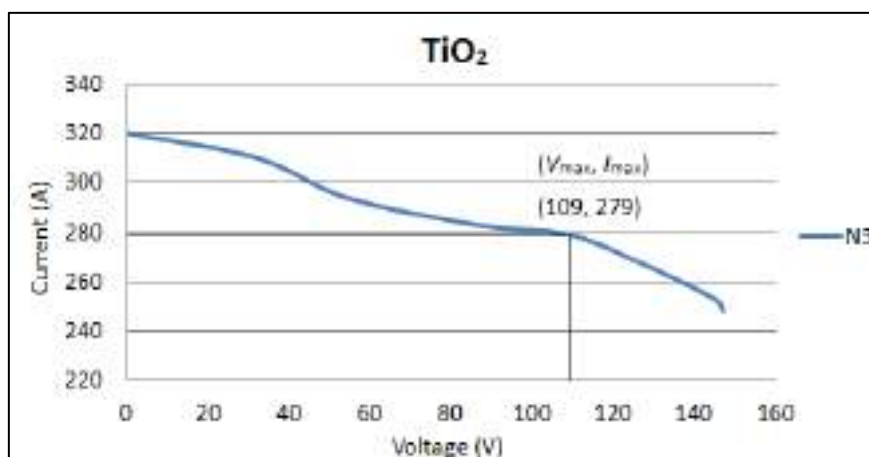


Figure 8. Current-voltage (I-V) curve of DSSC solar cell

Table 3. Results of V_{oc} , J_{sc} , FF and η obtained the 2nd day after the construction of solar cells

Oxide layer	Photosensitive dye	V_{oc} (mV)	J_{sc} (mA/cm ²)	FF (%)	η (%)
TiO ₂	Anthocyanin	92.0	0.169	13.39	1.13
	N3	147.0	0.320	64.64	12.66
	Rhodamine B	0.8	0.003	40.17	3.75×10^{-4}
	Rhodamine B + Anthocyanin	24.0	0.059	51.23	0.30
ZnO	Anthocyanin	3.6	0.007	52.78	5.15×10^{-3}
	N3	36.7	0.102	62.74	0.98
	Rhodamine B	50.1	0.120	24.55	0.62
	Rhodamine B + Anthocyanin	12.9	0.027	60.02	0.09

We have noted that the DSSC solar cells using N3 dye gave the highest values for solar conversion efficiency, e.g. on TiO₂ layer were 12.66 % and on ZnO 0.98 %. Rhodamine B dye still gives the lowest results on TiO₂ layer, but in general, all values on TiO₂ layer were higher than those on ZnO layer.

Table 4. Results of V_{oc} , J_{sc} , FF and η obtained after electrolyte addition (8th day of measurement)

Oxide layer	Photosensitive dye	V_{oc} (mV)	J_{sc} (mA/cm ²)	FF (%)	η (%)
TiO ₂	Anthocyanin	6.0	0.124	90.92	0.26
	N3	86.0	0.350	82.41	8.51
	Rhodamine B	8.2	0.331	88.37	0.99
	Anthocyanin + Rhodamine B	45.9	0.078	93.14	1.36
ZnO	Anthocyanin	50.5	0.001	96.63	0.03
	N3	16.7	0.071	87.69	0.44
	Rhodamine B	19.0	0.026	94.13	0.19
	Anthocyanin + Rhodamine B	1.8	0.034	47.96	0.01

After electrolyte addition (Table 4.) on TiO₂ layer with anthocyanin and N3 dye a decrease in values of solar conversion efficiency (η) is noted. In both cases, Rhodamine B was used. Because it wasn't well absorbed on the surface, as the time passed the oxide layer have dissolved and only electrolyte could give a respond to the measuring instrument. That is especially possible for solar cells with ZnO layer [27]. Another two dyes on TiO₂ layer note an increase in values. A possible reason for this is the electrolyte response.

CONCLUSIONS

The aim of this research is to determine the efficiency of the solar cells considering the absorption of used dyes on two different oxide surfaces. Four different dye solutions and two oxide layers were used. The UV-Vis spectrum of photosensitive dyes shows that N3 dye had a widest range of absorption. Microscopic images of the photoanode surfaces show the presence of cracks on both surfaces so regard to such results solar cells prepared with TiO₂ layer for all dyes had better results, than those on ZnO layer. The highest value of solar conversion efficiency was for N3 dye on TiO₂ layer. Otherwise, Rhodamine B dye, singly or in the mixture, showed the worst results on both surfaces.

REFERENCES

- [1] M. N. Fajar, Endarko, Study on conventional carbon characteristics as counter electrode for dye sensitized solar cells, IOP Conf. Series, Journal of Physics, Conf. Series 853, 2017, 012044
- [2] Y. Chiba, A. Islam, Y. Watanbe, R. Komiya, N. Koide, L. Han, Dye-Sensitized Solar Cells with Conversion Efficiency of 11.1%, Japanese Journal of Applied Physics, 45(2006)25, pp. L638-640.

- [3] A. Hagfeldt, G. Boschloo, L. Sun, L. Kloo, H. Pettersson, Dye-sensitized solar cells, *Chem. Rev.* 110(2010), pp. 6595-6664.
- [4] P. Joshi, X. Yu, J. Mwaura, M. Ropp, D. Galipeau, Q. Qiao, Dye-Sensitized Solar Cells based on carbon counter electrode, 33rd IEEE Photovoltaic specialists conference PVSC; 11 - 16 May 2008, San Diego, California, USA, pp. 1-4.
- [5] A. Kay, M. Gratzel, Low-cost photovoltaic modules based on dye sensitized nanocrystalline titanium dioxide and carbon powder, *Solar Energy Materials and Solar Cells*, 44(1996), pp. 99-117.
- [6] B. O'Regan, M. Grätzel, A low-cost, high efficiency solar cell based on dye sensitized colloidal TiO₂ film, *Nature*, Volume 353(1991), pp. 737-740.
- [7] S. C. T. Lau, J. Dayou, C. S. Sipaut, R. F. Mansa, Development in photoanode materials for high efficiency dye-sensitized solar cells, *International journal of renewable energy research*, Volume 4(2014), No. 3
- [8] A. Al-Kahlout, Thermal treatment optimization of ZnO nanoparticles-photoelectrodes for high photovoltaic performance of dye-sensitized solar cells, *Journal of the Association of Arab Universities for Basic and Applied Sciences*, Volume 17(2015)1, pp. 62-77.
- [9] J. Bandara, U.W. Pradeep, R.G.S.J. Bandara, The role of n-p junction electrodes in minimizing the charge recombination and enhancement of photocurrent and photovoltage in dye sensitized solar cells, *Journal of Photochemistry and Photobiology A: Chemistry*, Volume 170(2005), pp. 273-2782.
- [10] Y. K. Gan, N. F. Zakaria, I. S. Mohamad and M. N. Norizan, The effect of ZnO photoanode solution ageing to the performance of dye-sensitized solar cell (DSSC), *AIP Conference Proceedings*, Volume 2203(2020)1, p. 020048.
- [11] Y. Zhang, N. Cai, Y. Zhao, D. W. Zhao, G. L. Liu, W. W. Ji, R. X. Yang, Influence of Triton X-100 on the performance of dye-sensitized solar cell, Volume 26(2008), Issue 2, pp. 125-130.
- [12] Y. Kurokawa, D. T. Nguyen, K. Taguchi, Optimum conditions for titanium oxide thin film on dye-sensitized solar cells using organic dye sensitizer-MK2, *International Journal of Chemical Engineering and Applications*, Volume 9(2018)6, pp. 200-205.
- [13] A. Andualem, S. Demiss, Review on Dye-Sensitized Solar Cells (DSSCs), *Edelweiss Applied Science and technology*, Volume 2(2018)1, p. 6.
- [14] N. Sekar, V. Y. Gehlot, Metal complex dyes for dye-sensitized solar cells: recent developments, *Resonance* 9(2010)15, pp. 819-831.
- [15] K. Sharma, V. Sharma, S. S. Sharma, Dye-Sensitized Solar Cells: Fundamentals and current status, *Nanoscale Research Letters*, Volume 13(2018), p. 381.
- [16] S. Shalini, R. Balasundaraprabhu, T. Satish Kumar, N. Prabavathy, S. Senthilarasu, S. Prasanna, Status and outlook of sensitizers/dyes used in dye sensitized solar cells (DSSC): a review, *Int. J. Energy Res.* Volume 40(2016), pp. 1303-1320.
- [17] D. Rizali, H. Suryanto, S. Sukarni, The effect of Chlorophyll concentration from papaya leaves on the performance of dye-sensitized solar cell, Volume 3(2019)2, pp. 59-69.
- [18] A. Boyo, O. Paul, I. Abdulsalami, O. Surukite, H. O. Boyo, H. Boyo, Application of Hibiscus Sabdariffa and leaves of Azadirachta Indica calyxes as sensitizers in Dye-sensitized solar cells, Volume 8(2013)12, pp. 38-42.
- [19] D. Eli, M. Ahmad, I. Maxwell. D. Ezra, A. Francis, S. Sarki, Dye-sensitized solar cells using natural dyes extracted from Roselle (*Hibiscus sabdariffa*) flowers and Pawpaw (*Carica*

- Papaya) leaves as sensitizers, Journal of energy and natural resources, Volume 5(2016), pp. 11-15.
- [20] S. Shalini, R. Balasundaraprabhua, T. Satish Kumar, N. Muthukumarasamy, S. Prasanna, K. Sivakumaran, M. D. Kannan, Enhanced performance of sodium doped TiO₂ nanorods based dye sensitized solar cells sensitized with extract from petals of *Hibiscus sabdariffa* (Roselle), Elsevier Material letters, 221(2018), pp. 192-195.
- [21] N. A. Norhisamudin et al., The effect of different solvents in natural dyes from Roselle (*Hibiscus sabdariffa*) and green tea leaves (*Camelia Sinensis*) for dye-sensitizer solar cells, J. Phys., Conf. Ser. 1755(2021), p. 012024.
- [22] I. J. Junger, S. V. Homburg, H. Meissner, T. Grethe, A. Schwarz Pfeiffer, J. Fiedler, A. Herrmann, T. Blachowicz, A. Ehrmann, Influence of the pH value of anthocyanins on the electrical properties of dye-sensitized solar cells, AIMS energy, Volume 5(2017)2, pp. 258-267.
- [23] W. A. Maryniak, T. Uehara, M. A. Noras, Surface resistivity and surface resistance measurements using a concentric ring probe technique, Advanced energy, Volume 1005(2003), pp. 1-4.
- [24] P. Gu, D. Yang, X. Zhu, H. Sun, P. Wangyang, J. Li, H. Tian, Influence of electrolyte proportion on the performance of dye-sensitized solar cells, AIP, Advances 7(2017), pp. 105219 .
- [25] A. Syukron, R. A. Wahyuono, D. Sawitri, D. D. Risanti, The effect of paste preparation and annealing temperature of ZnO photoelectrode to dye-sensitized solar cells (DSSC) performance, Advanced Materials Research, Volume 896(2014), pp. 183-186.
- [26] M. Alhamed, A. S. Issa, A. W. Doubal, Studying of natural dyes properties as photo-sensitizer for dye sensitized solar cells(DSSC), Journal of Electron Devices, Volume 16(2012), pp. 1370-1383.
- [27] R. Vittal, Zinc oxide based dye-sensitized solar cells: A review., Renewable and sustainable energy reviews, Volume 70(2016), pp. 920-935.



19th INTERNATIONAL FOUNDRYMEN CONFERENCE
Humans - Valuable Resource for Foundry Industry Development

Split, June 16th-18th, 2021

<https://ifc.simet.hr/>

**PREPARATION AND CHARACTERIZATION OF POROUS ALUMINA CERAMICS
USING WASTE COFFEE GROUNDS (WCG)**

Ivana Gabelica^{1*}, Lidija Ćurković^{1*}, Vilko Mandić², Mihone Kerolli Mustafa³

¹ University of Zagreb Faculty of Mechanical Engineering and Naval Architecture, Zagreb, Croatia

² University of Zagreb Faculty of Chemical Engineering and Technology, Zagreb, Croatia

³ International Business College Mitrovica, Mitrovica, Kosovo

Poster presentation

Original scientific paper

Abstract

Different methods have been used to produce porous ceramics for various applications. The generation of pores in ceramic samples offers a new range of different properties. Moreover, that porosity can be achieved using all kinds of various waste such as industrial, agricultural, domestic etc. One example being the process of coffee brewing which produces a large amount of waste, that was therefore used as a pore-forming agent in the production of porous ceramics.

Suspensions of 60 wt.% alumina with different amount of waste coffee grounds were prepared. Viscosity of all suspensions was determined by means of rotational viscometer. Green bodies were prepared by slip casting in plaster mold. DTA/TGA analysis of waste coffee grounds revealed multistep endothermic and exothermic events related with release and burning of the precursor materials accompanied with mass loss. The sintering regime was determined according to the DTA/TGA analysis of thermal decomposition of waste coffee grounds. Density of the obtained sintered samples was investigated and calculated.

Keywords: *alumina, porous ceramics, coffee, density, slip casting*

*Corresponding authors (*e-mail address*): ivana.gabelica@fsb.hr, lidija.curkovic@fsb.hr

INTRODUCTION

Porous alumina ceramics have been widely manufactured for various applications such as filters and membranes [1], catalyst supports [2], refractory materials [3], construction materials [4] thermal insulators [5] and many other. This wide application scope is attributed to achieve bodies with high porosity, high surface area, low density, high thermal and chemical resistance as well as corrosion resistance. Manufacturing of porous ceramics can be executed with a number of different methods such as precipitation [6], replica technique

[2], sacrificial template [7], with a pore-forming agent [8–10], uniaxial pressing [4] and isostatic pressing [8].

With the decrease in non-renewable resources, the interest in using waste materials in production of new and improved ones has been rapidly growing. Waste is generated in all branches of society, from small households to large industry plants. Different kinds of waste are being used as pore forming agents in manufacturing porous ceramics. Liu et al. [8] used walnut shell powder as pore-forming agent combined with alumina sol impregnation for fabricating porous alumina ceramics with enhanced crushing strength and thermal insulation performance. Graphite waste, primarily from batteries, was used by Ali et al. [9] as pore-forming agent to fabricate porous alumina ceramics using a fugitive material technique. The increasing porosity decreased mechanical strength but improved deformation tolerance, resulting in higher strain at break. The same authors also used commercial rice husk ash via solid-state technique to obtain a porous ceramic composite [11]. Mechanical properties were improved for composites with higher ratios of rice husk ash. Eliche-Quesada et al. used various industrial wastes to produce ceramic bricks with improved thermal insulation properties [12]. Paper waste, corn starch and sawdust were used to manufacture low-cost porous ceramics by Salman et al. [10]. The paper waste was the most suitable pore-forming agent because it allowed preparing of porous ceramics displaying good mechanical properties, porosity and permeability.

Since coffee is one of the most popular and often consumed beverages in the world, huge amounts of coffee waste are produced during the brewing process [13]. This coffee waste can also be used as pore-forming agent in production of porous ceramics. Sena da Fonseca et al. studied the influence of coffee waste in structural ceramics for construction [4]. They concluded that coffee waste can be used as a secondary clay raw material to produce bricks with improved thermal insulation properties. The use of coffee waste for preparation of macroporous alumina ceramics resulted in high open porosity of the ceramic material as well as good mechanical strength performed by Alzukaimi and Jabrah [7]. Furthermore, spent coffee grounds were also used as filler for the formulation of lightweight clay ceramic aggregates by Andreola et al. [14]. Their results showed that the obtained material has an interesting set of properties that make it possible to use it in both urban and agricultural purposes.

In this paper, waste coffee grounds were used to produce porous alumina ceramics by slip casting method [15]. The preceramic suspensions containing different amounts of waste coffee grounds were described by rheological measurements, while sintering regime was discussed on behalf of achieved densities study and DTA-TGA analysis of thermal decomposition of coffee grounds.

MATERIALS AND METHODS

Alumina suspensions were prepared with 60 wt.% of alumina powder. High-purity Al_2O_3 powder was used, with the average particle size of 300-400 nm (Alcan Chemicals, USA). Dolapix CE64 (Zschimmer & Schwarz Chemie GmbH, Germany) was used as a dispersant to stabilize highly concentrated alumina suspensions. Polyvinyl alcohol, PVA (Sigma Aldrich, USA) was added to the suspension as a binder. Different amounts (1 and 5 wt.%) of waste coffee grounds (WCG), obtained from a household coffee machine with a grinder, were added to alumina suspensions as a pore-forming agent.

Suspension preparation

0.2 wt.% of dispersant and 0.5 wt.% of binder were mixed with deionized water and placed in the grinding jar of the planetary ball mill. 60 wt.% of dry monolithic alumina powder was mixed with different amounts of waste coffee grounds (WCG) and added into the grinding jar. Ten alumina balls were used for the mixture homogenization, which lasted for 90 minutes at a speed of 300 rpm. Alumina balls were separated from the suspension after the homogenization using a sieve. The suspension underwent an ultrasonic treatment for 15 min in an ultrasonic bath – BRANSONIC 220 (Branson Ultrasonics Corp., USA) to remove air bubbles and achieve better homogeneity. Afterwards, suspensions were poured into plaster moulds to produce a ceramic green body.

Determination of rheological properties

Rheological properties of prepared ceramic suspensions were determined using a rotational viscometer ViscoQCTM300 (Anton Paar, Graz, Austria) in a measuring cup C-CC12 with a measuring bob B-CC12. The shear rate was gradually increased from 0.1 to 180 s⁻¹, and then reduced back to 0.1 s⁻¹ divided into 50 equal time frames. Rheological parameters were recorded just before each shear rate change.

Sintering of green bodies

The obtained green bodies were sintered in an electric furnace (Nabertherm P310, Bremen, Germany) according with the course of thermal decomposition of waste coffee grounds, which was determined by Differential Thermal Analysis (DTA) and Thermo-Gravimetric Analysis (TGA) using a simultaneous DTA/TGA device STA409 (Netzsch, Selb, Germany). Density of the sintered alumina samples was measured using Archimedes' principle on a laboratory scale by Mettler-Toledo while the density of samples with the addition of waste coffee grounds was calculated theoretically.

RESULTS AND DISCUSSION

Rheological measurements

Rheological properties were examined using rheological flow curves which show the dependence of shear rate ($\dot{\gamma}$) on viscosity (η). They are used to predict the nature of interactions between particles in the suspension. Flow curves for alumina suspension without the addition of waste coffee grounds (WCG) as well as alumina suspensions with the addition of 1 and 5 wt.% of WCG are shown in Figure 1.

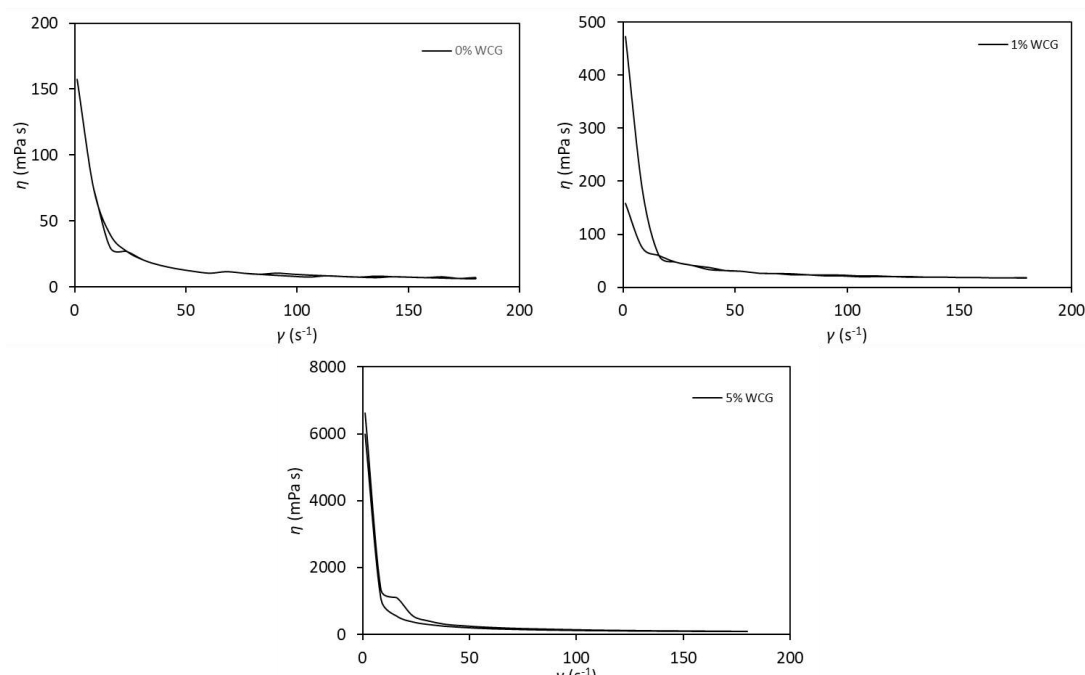


Figure 1. Rheological flow curves of prepared alumina ceramic suspensions with 0, 1 and 5 wt.% of waste coffee grounds (WCG)

The obtained results show that the suspension viscosity decreases with an increase of the shear rate, that is, all suspensions show typical pseudoplastic behaviour, characteristic of non-Newtonian fluids.

Suspension stability was estimated by the viscosity measurements at two shear rates, 50 and 100 s⁻¹. The shear rate of 50 s⁻¹ is the exact shear rate usually achieved during gravity slip casting while the shear rate of 100 s⁻¹ was chosen in purpose of better comparison. The obtained viscosity values of prepared alumina suspensions with the addition of waste coffee grounds (WCG) are shown in Table 1. Viscosity of prepared suspensions increased with the addition of waste coffee grounds.

Table1. Measured viscosity for prepared ceramic suspensions

w (WCG in powder mixture), %	η (mPa s)	
	$\gamma, 50 \text{ s}^{-1}$	$\gamma, 100 \text{ s}^{-1}$
0	11.78	8.87
1	29.44	19.22
5	241.40	143.40

Differential Thermal Analysis (DTA) and Thermo-Gravimetric Analysis (TGA)

DTA/TGA analysis (Figure 2) of waste coffee grounds revealed a single endothermic event up to 100 °C related with evaporation of the moisture accompanied with ~0.5 % of mass loss. After that, up to 200 °C another single endothermic event related with release of chemisorbed moisture accompanied with ~0.25 % of mass loss. Above 200 °C to about 450 °C from the DTA a single broad exothermic event related with burning of the organic material accompanied with TGA mass loss in what appears to be a three-step process; one from 200 °C to about 320 °C, second from 320 °C to about 390 °C, and the third from 390 °C to about 450 °C. From 400 °C to about 750 °C the DTA signal is dominated by broad

endothermic envelope attributed to the subsequent release of the decomposition residuals. At 800 °C ambiguous overlapped endothermic and exothermic effects with small intensity are observed without mass loss. Above 900 °C carbonaceous residuals burn out and gas out which slightly increases mass loss.

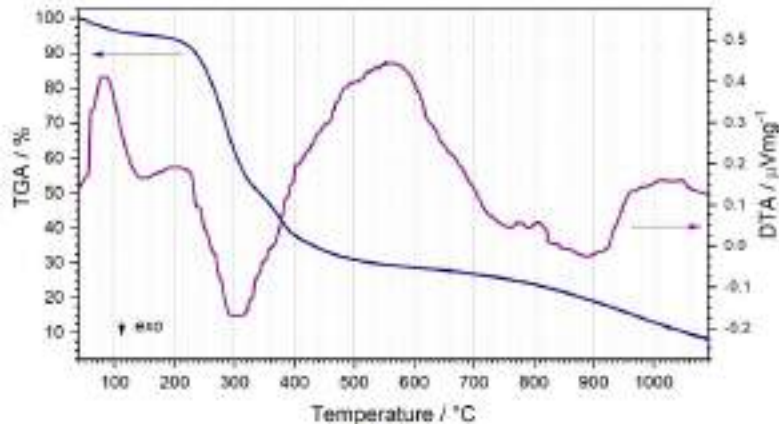


Figure 2. Differential Thermal Analysis (DTA) and Thermo-Gravimetric Analysis (TGA) curves of the waste coffee grounds

According to DTA/TGA curves, a sintering process was defined, as shown in Figure 3.

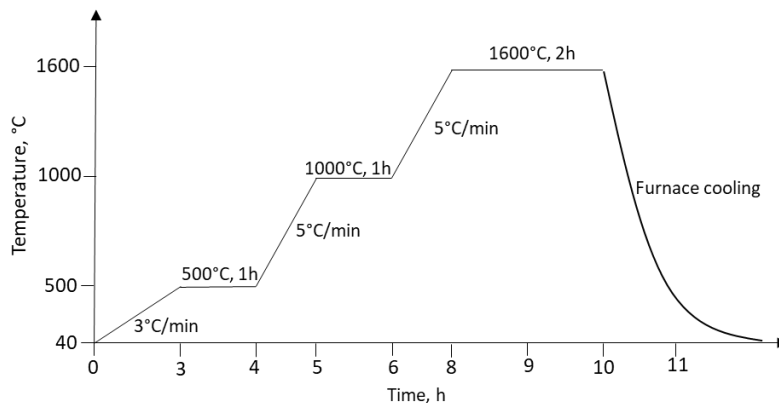


Figure 3. Scheme of sintering regime of alumina ceramics with the addition of waste coffee grounds

Firstly, heating to 500 °C with heating rate of 3 °C/min and 1 h holding time at 500 °C to enable the organic material to burn out. Next, the samples were heated to 1000 °C with heating rate of 5 °C/min and 1 h holding time at 1000 °C for carbonaceous residuals burn out and gas out. Afterwards, the samples were heated to the sintering temperature of 1600°C with heating rate of 5 °C/min and 2 h holding time at 1600 °C. After the cooling of the furnace, sintered samples were taken out for further characterization.

Density of pure alumina samples was measured using Archimedes' principle on analytical balance by Mettler-Toledo. Density of samples with the addition of waste coffee grounds was calculated theoretically using the following equation:

$$\rho = \frac{m}{V} \quad (1)$$

Where m (g) is mass of the sintered sample, and V (cm³) is volume of the sintered sample. The obtained density values are shown in Table 2.

Table 2. Measured and calculated density of sintered ceramic samples

w (WCG in powder mixture), %	Density, g/cm ³
0	3.759
1	3.089
5	2.496

The results of density measurements showed that the density decreased with an increase of the amount of waste coffee grounds added. This trend could indicate the formation of pores in sintered ceramic samples due to the burn out of waste coffee grounds. For confirmation of pore formation, further characterization is planned in form of pore size analysis by means of Brunauer-Emmett-Teller (BET) theory from absorption-desorption isotherms.

CONCLUSIONS

Porous alumina ceramic samples were successfully prepared with the addition of waste coffee grounds as a pore-forming agent. Highly concentrated alumina suspensions were prepared with 1 and 5 wt.% of waste coffee grounds. Viscosity of the prepared ceramic suspensions decreased with an increase of the shear rate, while an increase in the amount of waste coffee grounds leads to an increase of viscosity.

DTA/TGA analysis of waste coffee grounds revealed multistep endothermic and exothermic events related with evaporation and release of the moisture, burning of the organic material and subsequent release of the decomposition residuals as well as carbonaceous residuals burn outs accompanied with mass loss. According to DTA/TGA measurements, a suitable course of thermal treatment for sintering was implemented. Density of obtained sintered ceramic samples was measured and calculated. With an increase in the amount of waste coffee grounds, the density decreased which indicated the possible generation of pores during burn out of waste coffee grounds during the sintering process. Further characterization is necessary for confirmation of abovementioned conclusions regarding pore formation.

Acknowledgements

This work has been fully supported by the Croatian Science Foundation within the project IP-2016-06-6000: Monolithic and Composite Advanced Ceramics for Wear and Corrosion Protection (WECOR).

REFERENCES

- [1] K. K. O. S. Silva, C. A. Paskocimas, F. R. Oliveira, J. H. O. Nascimento, A. Zille, Development of porous alumina membranes for treatment of textile effluent, Desalination and Water Treatment, 57(2016), pp. 2640-8.

- [2] Z. Švigelj, V. Mandić, L. Ćurković, M. Biošić, I. Žmak, M. Gaborardi, Titania-Coated alumina foam photocatalyst for memantine degradation derived by replica method and sol-gel reaction, *Materials*, 13(2020)
- [3] J. Wang, J. Zhao, Investigating the effect of SPRM on mechanical strength and thermal conductivity of highly porous alumina ceramics, *Ceramics International*, 43(2017), pp. 16430-5.
- [4] B. Sena Da Fonseca, A. Vilão, C. Galhano, J. A. R. Simão, Reusing coffee waste in manufacture of ceramics for construction, *Advances in Applied Ceramics*, 113(2014), pp. 159-66.
- [5] Z. P. Wei, S. Li, Y. Li, X. S. Li, R. Xiang, N. N. Xu, Porous alumina ceramics with enhanced mechanical and thermal insulation properties based on sol-treated rice husk, *Ceramics International*, 44(2018), pp. 22616-21.
- [6] G. Xu, J. Li, H. Cui, Q. He, Z. Zhang, X. Zhan, Biotemplated fabrication of porous alumina ceramics with controllable pore size using bioactive yeast as pore-forming agent, *Ceramics International*, 41(2015), pp. 7042-7.
- [7] J. Alzukaimi, R. Jabra, The preparation and characterization of porous alumina ceramics using an eco-friendly pore-forming agent, *International Journal of Applied Ceramic Technology*, 16(2019), pp. 820-31.
- [8] J. Liu, W. Huo, B. Ren, K. Gan, Y. Lu, X. Zhang, et al., A novel approach to fabricate porous alumina ceramics with excellent properties via pore-forming agent combined with sol impregnation technique, *Ceramics International*, 44(2018), pp. 16751-7.
- [9] M. S. Ali, M. A. Azmah Hanim, S. M. Tahir, C. N. A. Jaafar, M. Norkhairunnisa, K. A. Matori, Preparation and characterization of porous alumina ceramics using different pore agents, *Journal of the Ceramic Society of Japan*, 125(2017), pp. 402–12.
- [10] M. M. Salman, N. S. Radhi, O. H. Sabr, H. T. Nhabih, Utilization of diverse cheap materials as pore generating agent to manufacture low-cost porous ceramic, *Ceramica*, 66(2020), pp. 179-85.
- [11] M. S. Ali, M. A. Azmah Hanim, S. M. Tahir, C. N. A. Jaafar, M. Norkhairunnisa, K. A. Matori, The Effect of Commercial Rice Husk Ash Additives on the Porosity, Mechanical Properties, and Microstructure of Alumina Ceramics, *Advances in Materials Science and Engineering*, 2017.
- [12] D. Eliche-Quesada, C. Martínez-García, M.L. Martínez-Cartas, M.T. Cotes-Palomino, L. Pérez-Villarejo, N. Cruz-Pérez, et al., The use of different forms of waste in the manufacture of ceramic bricks, *Applied Clay Science*, 52(2011), pp. 270-6.
- [13] R. Campos-Vega, G. Loarca-Piña, H.A. Vergara-Castañeda, B. Dave Oomah, Spent coffee grounds: A review on current research and future prospects, *Trends in Food Science and Technology*, 45(2015), pp. 24-36.
- [14] F. Andreola, A. Borghi, S. Pedrazzi, G. Allesina, P. Tartarini, I. Lancellotti, et al., Spent coffee grounds in the production of lightweight clay ceramic aggregates in view of urban and agricultural sustainable development, *Materials*, 12(2019)
- [15] H. Le Ferrand, Magnetic slip casting for dense and textured ceramics: A review of current achievements and issues, *Journal of the European Ceramic Society*, 41(2021), pp. 24-37.



19th INTERNATIONAL FOUNDRYMEN CONFERENCE
Humans - Valuable Resource for Foundry Industry Development

Split, June 16th-18th, 2021

<https://ifc.simet.hr/>

RAPID MICROWAVE-ASSISTED SYNTHESIS OF Fe₃O₄/SiO₂/TiO₂ CORE-SHELL NANOCOMPOSITE

Ivana Gabelica^{1*}, Lidija Ćurković^{1*}, Ivana Panžić²

¹ University of Zagreb Faculty of Mechanical Engineering and Naval Architecture, Zagreb, Croatia

² University of Zagreb Faculty of Chemical Engineering and Technology, Zagreb, Croatia

Poster presentation
Original scientific paper

Abstract

Magnetic nanomaterials have been getting a lot of attention lately due to their specific physical properties and various applications in medicine and biomedicine as well as support for photocatalyst in advanced oxidation processes for degradation of organic micropollutants. Magnetic behaviour of nanomaterials greatly depends on their particle size. Such behaviour enables a facile extraction of the magnetic nanoparticles from matrix or solution using an external magnetic field.

In this paper, magnetic nanoparticles were successfully prepared via rapid microwave-assisted synthesis. They were subsequently coated with a layer of silica (SiO₂) as a protective layer for magnetite and after that with titania (TiO₂) to photocatalytically degrade micropollutants from wastewater. The prepared nanocomposites were characterized by Fourier-transform infrared spectroscopy (FTIR) and X-ray diffraction (XRD), on behalf of which the core-shell configuration and chemical distribution of iron oxide, silica and titania chemical species was discussed.

Keywords: *microwave synthesis, magnetite, silica, titania, core shell nanocomposite*

*Corresponding author (e-mail address : ivana.gabelica@fsb.hr, lidija.curkovic@fsb.hr)

INTRODUCTION

Due to their various applications and specific physical properties, magnetic nanomaterials are a constant topic of scientific research. Magnetic properties of materials change significantly when the size of each particle is reduced to nanoscale compared to bulk materials [1]. Magnetite is one of the most famous iron oxides with inverse spinel structure B(AB)O₄. A and B ions in parentheses occupy octahedral sites, while the rest of the B ions occupy tetrahedral sites [2]. This specific structure gives the magnetite ferrimagnetic ordering. However, when the size of each particle is reduced to nanoscale, precisely 15 – 20 nm, they will exhibit magnetic moment as a single domain under external magnetic field which behaves as superparamagnet [3], whereas in the absence of magnetic field they will

have zero average residual magnetization [4]. In that case, magnetic behaviour is determined by magnetic anisotropy energy of each particle and the magnetic dipole-dipole interaction between the particles. For the particle to exhibit superparamagnetic behaviour the magnetic anisotropy energy must be greater than the dipole-dipole interaction [1].

This behaviour allows fast, easy, reversible and selective magnetic separation of the particles from matrix or solution using an external magnetic field. Another advantage of magnetite nanoparticles is their non-toxicity compared to other magnetic nanoparticles such as Nickel and Cobalt [5, 6]. Due to that and their low cost, they have a wide range of medical and biomedical applications such as drug delivery system [7], magnetic imaging [8], as a contrast agent for MRI [9]. They are also used for magnetic hyperthermia applications [10], heavy metal detection [11], as anode material for lithium-ion batteries [12] as well as a promising antibacterial agent [13]. In addition to the (bio)medical applications, magnetic nanoparticles have been used as support for photocatalyst in processes of photodegradation of various dyes [14–19], herbicides [20] in wastewater, in the treatment of drinking water supplies [21], and removal of pharmaceuticals [22–24].

Magnetic nanoparticles can be synthesized using various physical methods such as gas-phase deposition, electron beam lithography, pulsed laser ablation, laser-induced pyrolysis, power ball milling, combustion and chemical methods such as co-precipitation, thermal decomposition, reverse microemulsion method, hydrothermal, solvothermal and lately microwave assisted synthesis [3]. In comparison to other abovementioned methods, microwave synthesis is based upon the interaction of microwaves with the material, resulting in heat generation within the material itself (Figure 1). During synthesis, a lot of energy is produced offering higher heating rates and yields as well as precise heating control which enables early phase formation and monodisperse particle size distribution [25,26].

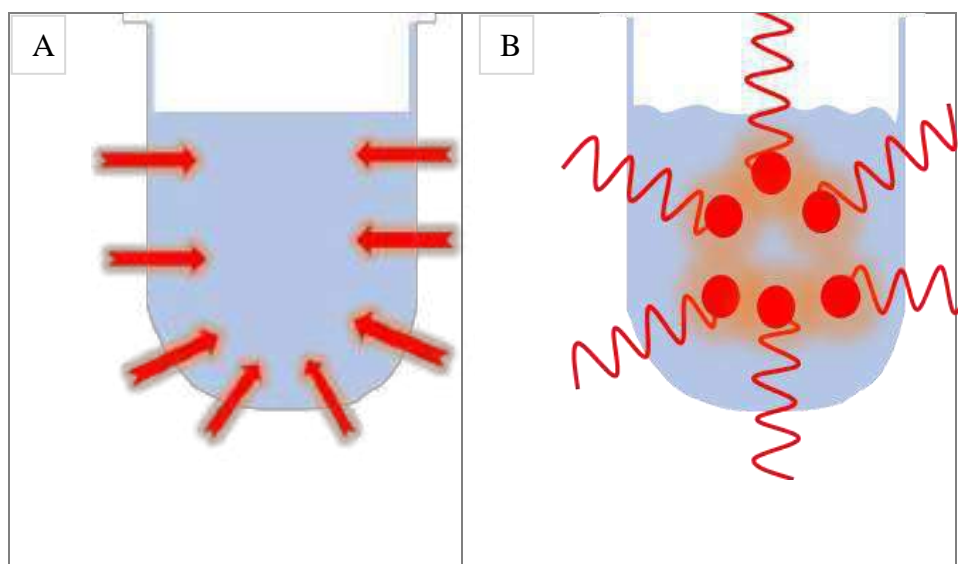


Figure 1. Heat distribution in (A) conventional and (B) microwave sintering

In this paper magnetite (Fe_3O_4) nanoparticles were prepared by rapid microwave-assisted synthesis. The obtained particles were coated with SiO_2 , and subsequently with TiO_2 to produce core shell nanoparticles. SiO_2 layer prevents iron leaching and oxidation, while TiO_2 layer can be used for degradation of various organic micropollutants from wastewater. The

obtained core-shell nanocomposite was characterized in each stage via Fourier-transform infrared spectroscopy (FTIR) and X-ray diffraction (XRD).

MATERIALS AND METHODS

For the synthesis of magnetic nanoparticles (Fe_3O_4), the chemicals $\text{FeCl}_3 \times 6\text{H}_2\text{O}$ (VWR chemicals, Germany), $\text{FeSO}_4 \times 7\text{H}_2\text{O}$ (Alfa Aesar, Germany), NaOH (Grammol, Croatia) and deionized water were used. Aqueous solutions of $\text{FeCl}_3 \times 6\text{H}_2\text{O}$ (0.4M) and $\text{FeSO}_4 \times 7\text{H}_2\text{O}$ (0.2M) were mixed after which 2M water solution of NaOH was added. The solution was then placed in microwave (Anton Paar monowave 600) and irradiated for 5 minutes at 100 °C under stirring. The obtained dark precipitate (Fe_3O_4) was separated and washed several times with deionized water and dried at 80 °C for 2 hours.

For the SiO_2 coating, Ethanol-Et 96% p.a. (Grammol, Croatia), Ammonia- NH_3 (25%) and tetraethyl orthosilicate-TEOS (Merck, Germany) were used.

0.5g of dried magnetite particles was dispersed in solution of ethanol, deionized water and ammonia. The suspension was ultrasonicated for 15 minutes. After ultrasonication, TEOS was added dropwise to the solution with magnetite and stirred for 24 hours. Molar ratio of used chemicals was: TEOS:Et:DI: NH_3 = 1:100:32:0.003 [27]. The particles ($\text{Fe}_3\text{O}_4 @ \text{SiO}_2$) were then separated and washed several times with deionized water and dried at 40 °C for 3 hours.

For the TiO_2 coating, TiO_2 sol was prepared by mixing Titanium (IV) isopropoxide-TIP (Sigma-Aldrich, USA) as a precursor, 2-propanol-PrOH alcohol (Grammol, Croatia) as a solvent, acetylacetone-AcAc (Honeywell, USA) as a chelating agent and nitric acid as a catalyst.

0.5g of dried $\text{Fe}_3\text{O}_4 @ \text{SiO}_2$ particles were dispersed in ethanol and ultrasonicated for 15 minutes. Pr-OH, AcAc, TIP and 0.5M HNO_3 were mixed properly in molar ratio: TIP:PrOH:AcAc:HN = 1:35:0.63:0.015 [28] and left covered until the next day. The next day TiO_2 sol was added dropwise to the solution with magnetic particles under vigorous stirring. The suspension was stirred for 15 minutes and transferred in microwave for 10 minutes at 200 °C. The obtained $\text{Fe}_3\text{O}_4 @ \text{SiO}_2 @ \text{TiO}_2$ particles were separated and washed several times with deionized water and dried at 60 °C for 3 hours.

All the particles, Fe_3O_4 , $\text{Fe}_3\text{O}_4 @ \text{SiO}_2$ and $\text{Fe}_3\text{O}_4 @ \text{SiO}_2 @ \text{TiO}_2$ were characterized via Fourier-transform infrared spectroscopy (FTIR) and X-ray diffraction (XRD).

Fourier-transform infrared spectroscopy (FTIR) measurements were performed using IRSpirit (Shimadzu) equipped with Single-Reflection ATR accessory in the wavenumber range of 400 to 4000 cm^{-1} .

X-ray diffraction (XRD) was performed on XRD-6000 (Shimadzu) using $\text{CuK}\alpha$ radiation at the accelerating voltage of 40 kV and current of 30 mA. All samples were analysed in the range 5 - 75° 2 θ in a continuous mode with 0.02° 2 θ step and a scan rate of 0.6s.

RESULTS AND DISCUSSION

Figure 2 shows the FTIR spectra for Fe_3O_4 , $\text{Fe}_3\text{O}_4 @ \text{SiO}_2$ and $\text{Fe}_3\text{O}_4 @ \text{SiO}_2 @ \text{TiO}_2$ particles. The main band for magnetite nanoparticles is observed at around 550 cm^{-1} and is assigned to Fe–O stretching vibration [1]. The spectra for $\text{Fe}_3\text{O}_4 @ \text{SiO}_2$ particles showed an absorption band at around 1100 cm^{-1} which is assigned to Si–O–Si asymmetric stretching vibration. The band

at around 800 cm^{-1} is caused by the deformation vibration of Si-O bonds [29] while the band at 950 cm^{-1} is assigned to the asymmetric bending and stretching vibration of Si-OH [30]. $\text{Fe}_3\text{O}_4@\text{SiO}_2@\text{TiO}_2$ spectra shows several bands. The band at around $400 - 450\text{ cm}^{-1}$ is due to stretching vibration of Ti-O-Ti [31]. The absorption bands in the range of $2800 - 3800\text{ cm}^{-1}$ are due to the stretching vibrations of OH groups, probably from adsorbed water but could also be from the OH groups bonded to Si and Ti (Ti-OH and Si-OH). A small peak is observed at around 960 cm^{-1} and is assigned to Si-O-Ti stretching vibration which indicates a bond between silica and titania layers [19].

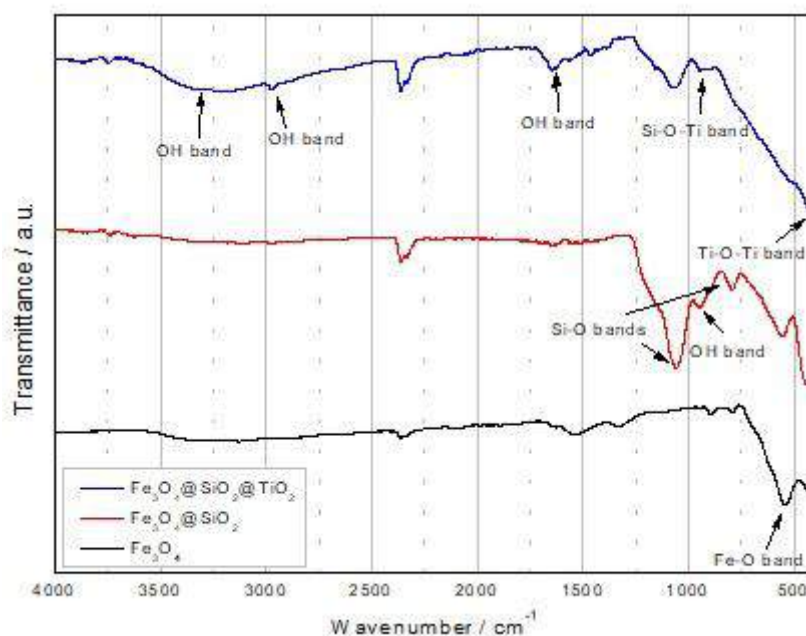


Figure 2. Fourier-transform infrared spectroscopy (FTIR) scans of Fe_3O_4 (black line), $\text{Fe}_3\text{O}_4@\text{SiO}_2$ (red line) and $\text{Fe}_3\text{O}_4@\text{SiO}_2@\text{TiO}_2$ (blue line) particles

XRD analysis (Fig 3) shows magnetite (ICDD PDF#19-0629) as the main crystalline phase in all samples. Samples thermally treated at lower temperatures (1 and 1.1) also show barely noticeable traces of goethite $\text{FeO}(\text{OH})$, (ICDD PDF#29-0713). For samples with silica coating, a silica based crystalline pattern was not observed, however, an amorphous hump centred around $26^\circ 2\theta$ was visible indicating presence of the SiO_2 -based amorphous phase. Magnetite intensity was not significantly reduced. Samples additionally coated with TiO_2 show anatase as main phase (ICDD PDF#21-1272), while magnetite is a minor phase. Such reduction of magnetite intensity points out to magnetite core and titania shell. Diffraction results are in agreement with FTIR results and confirmed the successful synthesis of the $\text{Fe}_3\text{O}_4@\text{SiO}_2@\text{TiO}_2$ composites.

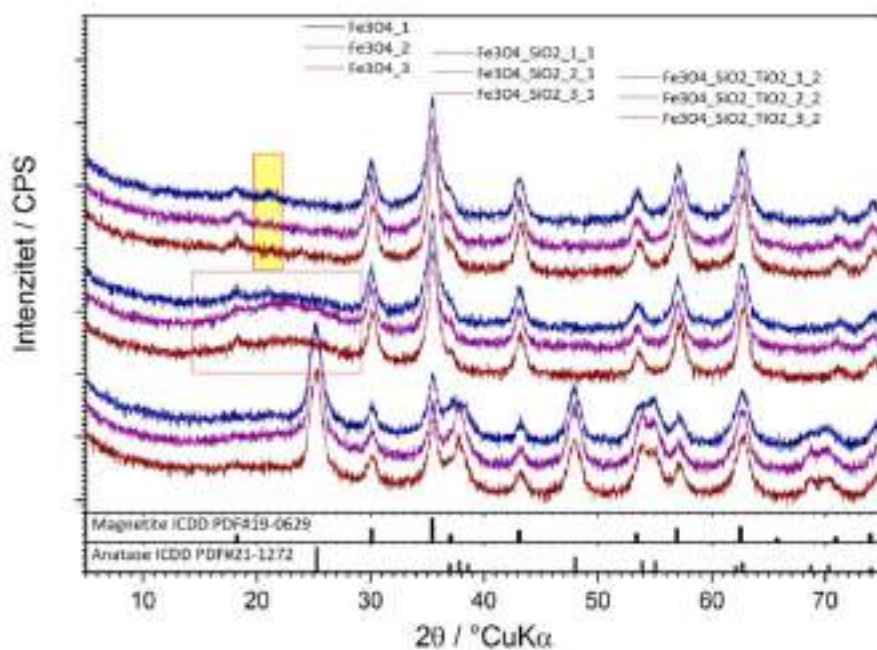


Figure 3. Diffractograms of Fe_3O_4 , $\text{Fe}_3\text{O}_4@\text{SiO}_2$ and $\text{Fe}_3\text{O}_4@\text{SiO}_2@\text{TiO}_2$ samples thermally treated at different temperatures; 100 °C – blue line, 150 °C – violet line and 200 °C – brown line.

CONCLUSIONS

Magnetite nanoparticles with SiO_2 and TiO_2 coating were successfully prepared by microwave assisted rapid synthesis. Fourier-transform infrared spectroscopy (FTIR) scans showed characteristic bands for Fe_3O_4 , SiO_2 and TiO_2 . Diffraction confirmed the successful preparation of the $\text{Fe}_3\text{O}_4@\text{SiO}_2@\text{TiO}_2$ core-shell composite.

REFERENCES

- [1] S. S. Pati, S. Kalyani, V. Mahendran, J. Philip, Microwave assisted synthesis of magnetite nanoparticles, *Journal of Nanoscience and Nanotechnology*, 14(2014), pp. 5790-7.
- [2] C. N. Lininger, C. A. Cama, K. J. Takeuchi, A. C. Marschlok, E. S. Takeuchi, A. C. West, et al., Energetics of Lithium Insertion into Magnetite, Defective Magnetite, and Maghemite, *Chemistry of Materials*, 30(2018), pp. 7922-37.
- [3] A. V. Samrot, C. S. Sahithya, J. Selvarani A, S. K. Purayil, P. Ponnaiah, A review on synthesis, characterization and potential biological applications of superparamagnetic iron oxide nanoparticles, *Current Research in Green and Sustainable Chemistry*, 4(2021), pp. 100042.
- [4] E. M. Kostyukhin, L. M. Kustov, Microwave-assisted synthesis of magnetite nanoparticles possessing superior magnetic properties, *Mendeleev Communications*, 28(2018), pp. 559-61.
- [5] F. Farahbakhsh, M. Ahmadi, S. H. Hekmatara, M. Sabet, E. Heydari-Bafrooei, Improvement of photocatalyst properties of magnetic NPs by new anionic surfactant,

- Materials Chemistry and Physics, 224(2019), pp. 279-85.
- [6] R. M. Patil, N. D. Thorat, P. B. Shete, P. A. Bedge, S. Gavde, M. G. Joshi, et al., Comprehensive cytotoxicity studies of superparamagnetic iron oxide nanoparticles, *Biochemistry and Biophysics Reports*, 13(2018), pp. 63-72.
- [7] S. O. Aisida, P. A. Akpa, I. Ahmad, T. kai Zhao, M. Maaza, F. I. Ezema, Bio-inspired encapsulation and functionalization of iron oxide nanoparticles for biomedical applications, *European Polymer Journal*, 122(2020), pp. 109371.
- [8] T. A. Lastovina, A. P. Budnyk, S. P. Kubrin, A. V. Soldatov, Microwave-assisted synthesis of ultra-small iron oxide nanoparticles for biomedicine, *Mendeleev Communications*, 28(2018), pp. 167-9.
- [9] D. Ling, N. Lee, T. Hyeon, Chemical synthesis and assembly of uniformly sized iron oxide nanoparticles for medical applications, *Accounts of Chemical Research*, 48(2015), pp. 1276-85.
- [10] L. Ansari, B. Malaekheh-Nikouei, Magnetic silica nanocomposites for magnetic hyperthermia applications, *International Journal of Hyperthermia*, 33(2017), pp. 354-63.
- [11] S. S. Li, W. J. Li, T. J. Jiang, Z. G. Liu, X. Chen, H. P. Cong, et al., Iron Oxide with Different Crystal Phases (α - and γ -Fe₂O₃) in Electroanalysis and Ultrasensitive and Selective Detection of Lead(II): An Advancing Approach Using XPS and EXAFS. vol. 88. 2016.
- [12] Z. Zeng, H. Zhao, J. Wang, P. Lv, T. Zhang, Q. Xia, Nanostructured Fe₃O₄@C as anode material for lithium-ion batteries, *Journal of Power Sources*, 248(2014), pp. 15-21.
- [13] S. O. Aisida, N. Madubuonu, M. H. Alnasir, I. Ahmad, S. Botha, M. Maaza, et al., Biogenic synthesis of iron oxide nanorods using *Moringa oleifera* leaf extract for antibacterial applications, *Applied Nanoscience (Switzerland)*, 10(2020), pp. 305-15.
- [14] E. Alzahrani, Photodegradation of Binary Azo Dyes Using Core-Shell Fe₃O₄/SiO₂/TiO₂ Nanospheres, *American Journal of Analytical Chemistry*, 08(2017), pp. 95-115.
- [15] D. F. F. Brossault, T. M. McCoy, A. F. Routh, Self-assembly of TiO₂/Fe₃O₄/SiO₂ microbeads: A green approach to produce magnetic photocatalysts, *Journal of Colloid and Interface Science*, 584(2021), pp. 779-88.
- [16] Q. Jiang, J. Huang, B. Ma, Z. Yang, T. Zhang, X. Wang, Recyclable, hierarchical hollow photocatalyst TiO₂@SiO₂ composite microsphere realized by raspberry-like SiO₂, *Colloids and Surfaces A: Physicochemical and Engineering Aspects*, 602(2020), pp. 125112.
- [17] S. Narzary, K. Alamelu, V. Raja, B.M. Jaffar Ali, Visible light active, magnetically retrievable Fe₃O₄@SiO₂@g-C₃N₄/TiO₂ nanocomposite as efficient photocatalyst for removal of dye pollutants, *Journal of Environmental Chemical Engineering*, 8(2020), pp. 104373.
- [18] P. R. Matli, A. M. A. Mohamed, R. R. Rajuru, Microwave Fast Sintering of Double Perovskite Ceramic Materials. IntechOpen, 2015.
- [19] Z. Bo, R. Dong, C. Jin, Z. Chen, High photocatalytically active cocoons-like TiO₂/SiO₂ synthesized by hydrothermal process and subsequent calcination at 900 °C, *Materials Science in Semiconductor Processing*, 72(2017), pp. 9-14.
- [20] T. Suwannaruang, K. Kamonsuangkasem, P. Kidkhunthod, P. Chirawatkul, C. Saiyasombat, N. Chanlek, et al., Influence of nitrogen content levels on structural properties and photocatalytic activities of nanorice-like N-doped TiO₂ with various calcination temperatures, *Materials Research Bulletin*, 105(2018), pp. 265-76.
- [21] S. Sultana, A. Amirbahman, C. P. Tripp, A method to produce robust magnetic particles

- coated with TiO₂ nano particulates, *Applied Catalysis B: Environmental*, 273(2020), pp. 118935
- [22] L. Fernández, M. Gamallo, M.A. González-Gómez, C. Vázquez-Vázquez, J. Rivas, M. Pintado, et al., Insight into antibiotics removal: Exploring the photocatalytic performance of a Fe₃O₄/ZnO nanocomposite in a novel magnetic sequential batch reactor, *Journal of Environmental Management*, 237(2019), pp. 595-608.
- [23] S. Sohrabnezhad, A. Pourahmad, M.F. Karimi, Magnetite-metal organic framework core@shell for degradation of ampicillin antibiotic in aqueous solution, *Journal of Solid State Chemistry*, 288(2020), pp. 121420.
- [24] M. Stan, I. Lung, M. L. Soran, C. Leostean, A. Popa, M. Stefan, et al., Removal of antibiotics from aqueous solutions by green synthesized magnetite nanoparticles with selected agro-waste extracts, *Process Safety and Environmental Protection*, 107(2017), pp. 357-72.
- [25] T. A. Lastovina, A. P. Budnyk, M. A. Soldatov, Y. V. Rusalev, A. A. Guda, A.S. Bogdan, et al., Microwave-assisted synthesis of magnetic iron oxide nanoparticles in oleylamine–oleic acid solutions, *Mendeleev Communications*, 27(2017), pp. 487-9.
- [26] C. Li, Y. Wei, A. Liivat, Y. Zhu, J. Zhu, Microwave-solvothermal synthesis of Fe₃O₄ magnetic nanoparticles, *Materials Letters*, 107(2013), pp. 23-6.
- [27] R. E. Kalan, S. Yaparathne, A. Amirbahman, C. P. Tripp, P25 titanium dioxide coated magnetic particles: Preparation, characterization and photocatalytic activity, *Applied Catalysis B: Environmental*, 187(2016), pp. 249-58.
- [28] L. Čurković, D. Ljubas, S. Šegota, I. Bačić, Photocatalytic degradation of Lissamine Green B dye by using nanostructured sol-gel TiO₂ films, *Journal of Alloys and Compounds*, 604(2014), pp. 309-16.
- [29] H. Zhang, S. Sun, H. Ding, T. Deng, J. Wang, Effect of calcination temperature on the structure and properties of SiO₂ microspheres/nano-TiO₂ composites, *Materials Science in Semiconductor Processing*, 115(2020)
- [30] S. C. Feifel, F. Lisdat, Silica nanoparticles for the layer-by-layer assembly of fully electro-active cytochrome c multilayers, *Journal of Nanobiotechnology*, 9(2011), pp. 1-12.
- [31] A. H. Shah, M. A. Rather, Effect of calcination temperature on the crystallite size, particle size and zeta potential of TiO₂ nanoparticles synthesized via polyol-mediated method, *Materials Today: Proceedings*, 2020.



IMPACT OF FeSi FERROALLOY CASTING CONDITIONS ON THEIR STRUCTURE AND GRAIN SIZE AFTER CRUSHING PROCESS

Stanisław Gil^{1*}, Wojciech Bialik¹, Bolesław Machulec¹,
Agnieszka Tomaszewska¹, Sławomir Kozłowski²

¹ Silesian University of Technology Faculty of Materials Engineering and Metallurgy,
Katowice, Poland

² Re Alloys Ltd., Łaziska Górne, Poland

Poster presentation
Original scientific paper

Abstract

In the article, the effects of FeSi75 ferroalloy casting conditions on the finished product size distribution after the crushing process have been presented. Liquid metal is cast into horizontal ingot molds or iron boxes that constitute a separate space in the casting hall. The casting method used in the process affects the alloy cooling, which determines segregation of elements in the cross-section of the layer and grain growth in the crystallizing material. These phenomena strongly affect heterogeneity of the chemical composition and phase transformations occurring in the solid state. The grain size and structure of the alloy determine its mechanical properties, which transfer into the crushing process and the resulting size distribution. For commercial purposes, it is desirable to obtain the largest amount of 10 ÷ 50 mm size pieces; therefore, it is important to determine the optimal casting conditions for FeSi.

Keywords: *ferroalloys, crushing process, casting FeSi alloys, FeSi structure*

*Corresponding author (e-mail address): stanislaw.gil@polsl.pl

INTRODUCTION

Industrial FeSi ferroalloys are mainly used in steelmaking processes for alloy deoxidation. Some of them can also be used for production of special steels with a great Si content. A ferroalloy that is provided to a purchaser should feature not only a proper chemical composition, but also appropriate granulation. In the process of production, the FeSi ferroalloy is poured from a ladle into ingot molds or foundry boxes that constitute a separate space in the casting hall. A casting method determines alloy cooling conditions that affect on-going phase transformations, the final structure of the alloy and segregation of elements in the cross-section of the layer. These parameters influence the process of mechanical

crushing of the alloy tiles and chunks derived from ingots and layers in the boxes. A local reduction in the alloy silicon content along with increased fractions of other components, such as calcium, aluminium and phosphorus, trigger disintegration of alloy granules. These phenomena have been described in more detail in [1÷3].

MELT CASTING AND CRUSHING - RESULTS AND DISCUSSION

During furnace tapping, the FeSi alloy is collected into a tapping ladle and further transferred to the casting hall where it is poured into foundry boxes or ingot molds. The casting process employs pig iron molds that are shallow, rectangular baths with rounded edges. A mold of a working volume $V=0.25 \text{ m}^3$, with a fixing system to facilitate transportation, is presented in Figure 1. Figure 2 illustrates the process of FeSi alloy casting into a foundry box using a gantry.



Figure 1. Ingot mold, volume $V=0.25 \text{ m}^3$



Figure 2. The process of alloy casting into a foundry box

During the furnace tapping, the temperature of liquid metal is approx. $1675 \text{ }^\circ\text{C}$. After the filling process, the ladle is transferred to a weighbridge and transported to the cast house within approx. $6 \div 7$ minutes. Meanwhile, the alloy slightly cools down so its temperature is 1888 K during the casting process. The metal temperature drop during the cooling process is illustrated in Figure 3. For research purpose, the ingot molds were filled with the alloy up to two levels. In Figure 4, temperature decrease on the cooling metal surface in an ingot mold designed for 5 cm and 10 cm thick ingots is shown. Table 1 presents the average chemical composition of the alloy as per the casting method.

Table 1. The average chemical composition of the alloy

	Component, mass %							
	Si	Fe	Al	Mn	Cr	Ti	Ca	P
Ladle	76.6	19.74	1.13	0.17	0.03	0.14	0.33	0.025
Ingot mold 5 cm	67.83	29.74	0.9	0.22	0.04	0.14	0.31	0.021
Ingot mold 10 cm	70.22	26.48	1.04	0.2	0.04	0.13	0.73	0.023
Box	75.53	22.15	1.11	0.18	0.03	0.14	0.28	0.023

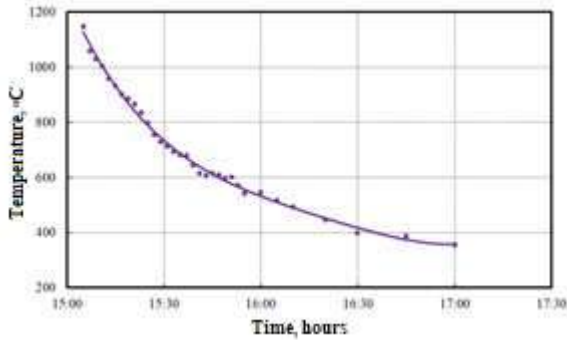


Figure 3. Temperature drop of metal cast in the box under cooling

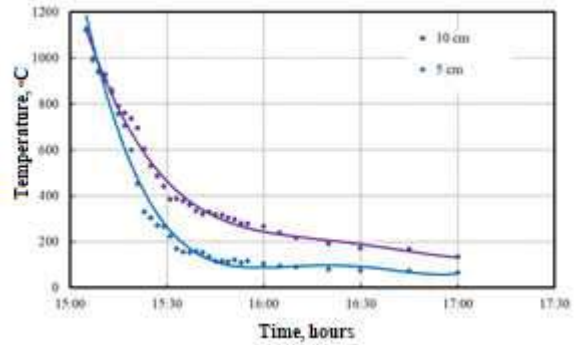


Figure 4. Temperature drop of metal cast in the ingot mold under cooling

Different metal cooling parameters affect the resulting crystal structure which is highly influenced by the cooling rate within the temperature range from the pouring temperature up to approx. 600 °C. Regarding the range considered, the slowest cooling process is observed for metal in the box where the rate is 11.2 °C/min, and the most rapid process – in the ingot mold with the rate of 37.1°C/min. For the 10 cm layer, the rate is also high: 29°C/min. To assess the alloy structures, tests were performed using the Nikon SMZ 745T stereomicroscope and the Nikon Eclipse MA200 light microscope with bright field. For a precise analysis of the microstructural constituents, images were enlarged at various levels, and selected ones of the same size are presented in Table 2. An additional analysis was performed using the Hitachi S-3400N scanning electron microscope with the EDS for the qualitative assessment of the chemical composition.

The light microscope images revealed sizes and distribution of pores. With the magnification applied, the highest amounts of macropores (dark phase) were observed in the 10 cm-thick specimen from the ingot mold. They were spherical- to bottle-like, open, unevenly arranged pores. The 5 cm-thick specimen featured slightly different pore structure with fewer pores of symmetrical shape and a smaller total surface area. A similar analysis of the structure was performed by Ott and Arnberg [3]: the least porosity was seen in a specimen from a foundry box where cracks throughout the whole surface were observed.

To perform a more detailed analysis of the structure, the specimens were studied using the scanning microscope with an additional point analysis of the chemical composition. For all specimens, the images revealed a biphasic structure and small amounts of precipitates. The EDS was used to analyse the chemical composition and to identify phases and precipitates. The analysis showed that phase 1 (dark grey) was composed of 100% Si while phase 2 (light grey) consisted of approx. 52% Fe, 48% Si and small amounts of Al (up to 0.6%). In addition, certain differences in morphology and amounts of the silicon phase were detected on specimens from the ingot mold and the foundry box. In the specimen from the box, there were more Si precipitates and silicon was more evenly arranged compared to the specimens from the mold.

A detailed analysis of the FeSi48 phase morphology revealed a network of microcracks that were probably induced by crystallographic strains generated in the crystal structure and resulting from the volumetric changes of phases during transformation. This is confirmed by observations of other authors in the area of interest [4]. Moreover, the structure analysis showed two types of precipitates. The first ones, seen as light points, contained Ti (up to 27

%), P (up to 7 %), Mn (up to 1.4 %) and Al (up to 0.6 %) in addition to Si and Fe, while the latter ones were darker fractions consisting of 30% Si, Al and Ca on average. Selected images of the specimens discussed along with the chemical analyses are presented in Table 3.

Table 2. Microscopic images of the FeSi alloy

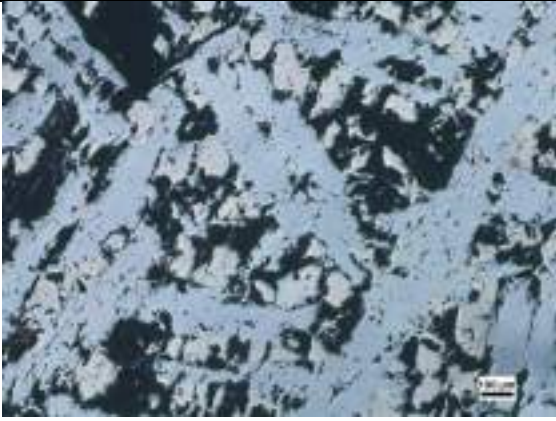
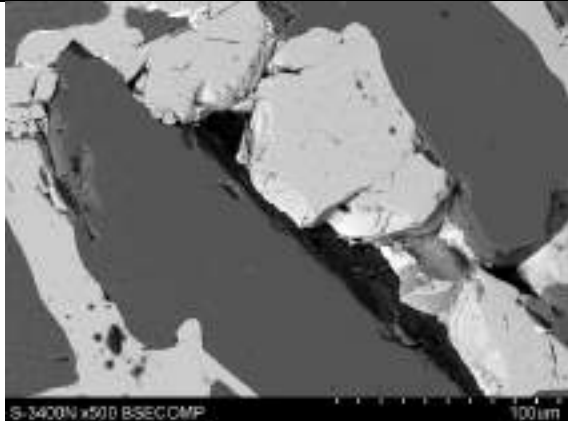
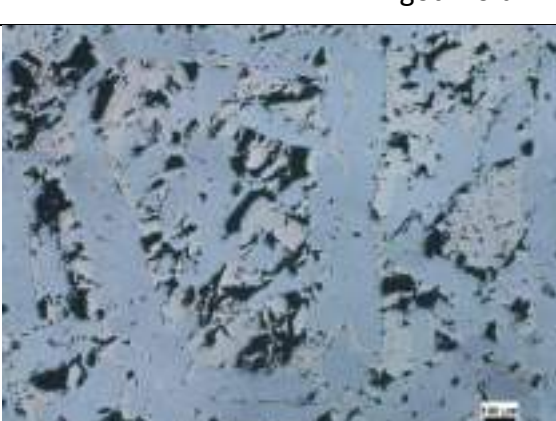
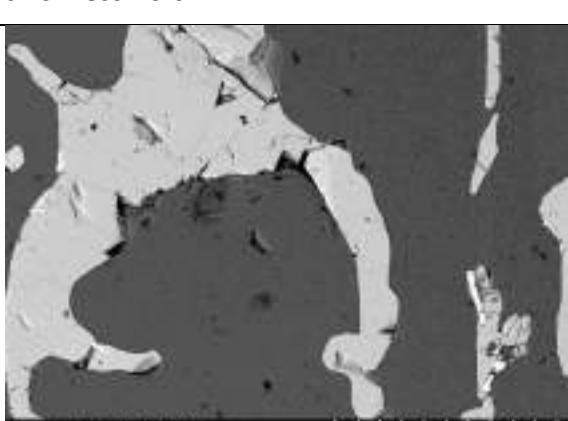
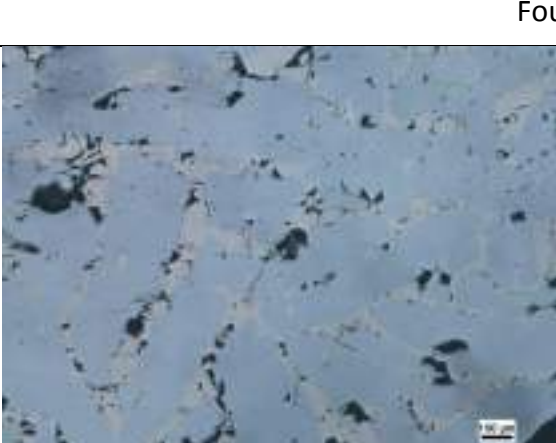

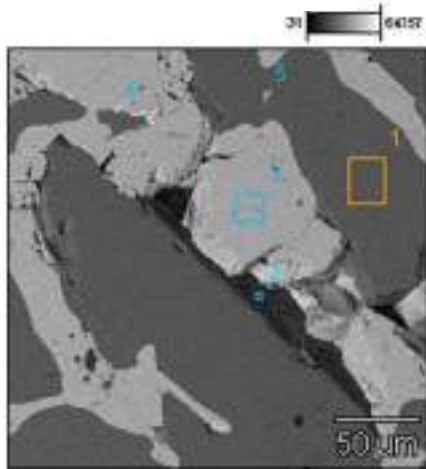
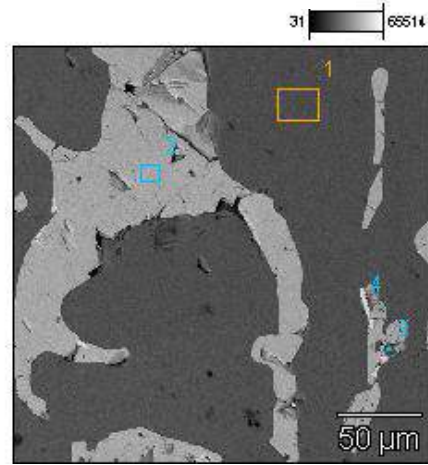
Stereoscopic microscope Nikon SMZ 745T	Scanning microscope Hitachi S-3400N
Ingot mold - ingot thickness 5 cm	
	
Ingot mold - ingot thickness 10 cm	
	
Foundry box	
	

Table 3. Microscopic images of the FeSi alloy with the point analysis of chemical composition using the EDS

Ingot mold -5-1(2)



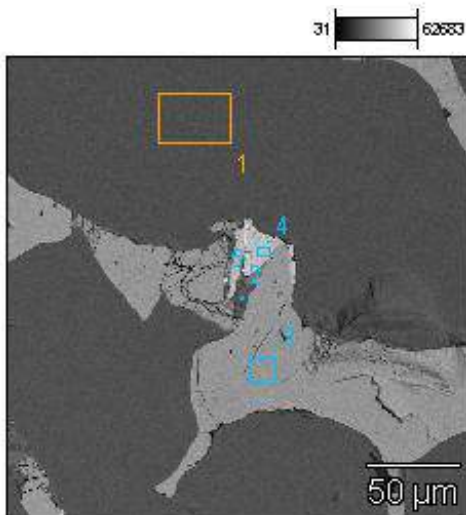
Ingot mold -10(4)



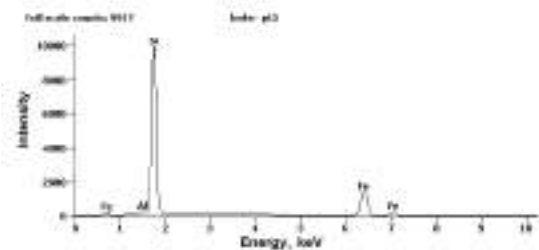
	Element content, mass %					
	Al-K	Si-K	Ca-K	Ti-K	Mn-K	Fe-K
Pt 1	-	100.0	-	-	-	-
Pt 2	-	97.2	-	-	-	2.8
Pt 3	0.2	47.8	-	-	-	52.0
Pt 4	0.5	28.6	-	27.5	1.2	42.2
Pt5	0.5	39.8	0.2	20.9	1.1	37.5

	Element content, mass %						
	Mg-Al-K	Si-K	Ca-K	Ti-K	Mn-K	Fe-K	P-K
Pt 1	-	100.0	-	-	-	-	-
Pt 2	0.6	48.0	-	-	-	51.4	-
Pt 3	26.0	37.9	29.8	1.1	-	4.4	0.9
Pt 4	0.8	28.7	0.2	26.4	1.4	42.6	-

Box – center (2)



	Element content, mass %						
	Mg-Al-K	Si-K	Ca-K	Ti-K	Mn-K	Fe-K	P-K
Pt 1	-	100.0	-	-	-	-	-
Pt 2	28.6	35.4	32.7	-	-	1.2	2.1
Pt 3	0.3	48.1	-	-	-	51.6	-
Pt 4	0.6	28.5	-	28.5	1.2	36.9	4.3
Pt 5	12.6	41.0	6.2	-	-	40.2	-



Analysis of the chemical composition for the box - point No. 3

Low cooling rate leads to the growth of ferrosilicon grains and distinct height-dependent diversification of the silicon content. Layers that contain less silicon but large grains of leboite (FeSi_2) have a far greater tendency to disintegrate and to generate higher amounts of fine fractions during the crushing process. The reason is a transformation of the high-temperature FeSi_2 to the low-temperature form along with a change in volume, which generates further strains in the alloy. Additionally, unfavourable effects are seen with higher contents of additives, such as Al, P, Ca, As, in the areas of lower Si contents [5].

Pre-broken ingots are directed to a two-stage crushing line. The stages consist of two METSO MINERALE crushers (Figure 5) of different sizes and a three-top sieving device. The line processes the alloy material into a commercial product containing $10 \div 50$ mm and $10 \div 80$ mm grains [6]. The process also gives subgrains sizes in brackets which decrease amounts of commercially valuable material. The grain distribution is highly affected by the charge material structure which derives from the alloy composition as well as the method of casting and its cooling. Effects of the crushing process are illustrated in Figure 6. Slower cooling of material in the foundry box clearly favours generation of higher amounts of subgrain sized $3 \div 10$ mm, leading to reduced amounts of commercially valuable material.



Figure 5. METSO MINERALE Crusher

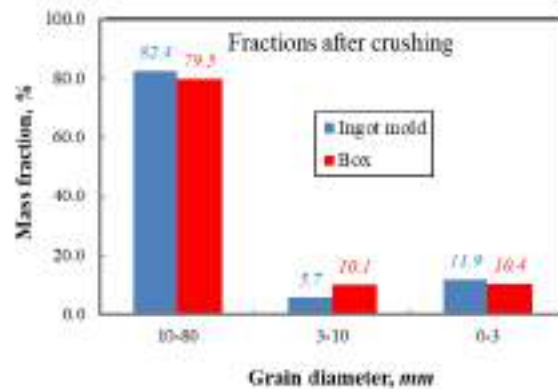


Figure 6. Fractions after crushing as a function of grain diameter

CONCLUSIONS

1. In order to reduce amounts of subgrain emerging in the process of crushing, a proper alloy structure and a limited impact of atmospheric conditions (moisture in particular) on pre-fragmented material should be achieved.
2. It is possible to gain the most valuable, fine-grain alloy structure through its rapid cooling down to approx. $650 \div 700$ °C if:
 - the alloy is poured as thin, 4 cm-thick layers into boxes
 - details of the box-casting schedule, ensuring a completely cooled layer from the previous casting process, are developed
 - a sufficient number of ingot molds is provided to ensure the assumed liquid metal level of maximum 4 cm
 - layer cooling is intensified, e.g. with water mist.

3. The amounts of emerging subgrain can be reduced in the alloy by decreasing the contents of unfavourable Al, P, Ca, As additives through raw material selection [7].
4. The pouring should start at the lowest temperature possible that does not exceed 1500 °C because this shortens the time to reach the solidification temperature of the melt.

REFERENCES

- [1] A. J. Schei, J. Kr. Tuset, H. Tveit, Production of High Silicon Alloys. Trondheim, 1998.
- [2] R. G. Zakharova, Effect of the Structure of Ferrosilicon on Its Desintegration, Russian Metallurgy, 2014.
- [3] E. Ott, L. Arnberg, Controlled solidification of ferrosilicon, Tenth International Ferroalloys Congress, 2004.
- [4] C. Guéneau, C. Servant, C. and F. Manier, Relationships between the grinding behaviour and the microstructure of ferro-silicon alloys with 65 wt. % silicon, Infacon VII 1995, pp. 673-681.
- [5] N. F. Yakushevich, A. A. Maksimov, A. Yu. Pronakin and O. A. Polyakh, Theoretical foundations of ferrosilicium disintegration, IOP Conference Series: Materials Science and Engineering, Volume 150 (2016) 012007, XIX International Scientific Conference on Metallurgy: Technologies, Innovation, Quality (Metallurgy 2015) 15–16 December 2015, Novokuznetsk, Russia, doi:10.1088/1757-899X/150/1/012007.
- [6] A. Wyrobek, Analiza pracy linii kruszenia żelazostopów i zaproponowanie rozwiązań technicznych mających na celu poprawę uzysków na kruszeniu, Raport wewnętrzny, (praca niepublikowana)
- [7] B. Machulec, W. Bialik, S. Gil, Application of the mining industry wastes as raw material for melting of the complex FeSiAl ferroalloys, Archives of Metallurgy and Materials 63(2018)2, pp. 975-979.



19th INTERNATIONAL FOUNDRYMEN CONFERENCE
Humans - Valuable Resource for Foundry Industry Development

Split, June 16th-18th, 2021

<https://ifc.simet.hr/>

IMPROVING THE MICROSTRUCTURE AND MECHANICAL PROPERTIES OF EN AC 43200 CAST ALUMINUM ALLOY MODIFIED WITH ZIRCONIUM

Peter Hajduch¹, Mile B. Đurđević¹, Srećko Manasijević^{2*}

¹ Nematik Linz GmbH, Linz, Austria

² Lola Institut Ltd., Belgrade, Serbia

Poster presentation
Original scientific paper

Abstract

Understanding the effect of alloying elements on the melt quality is of vital importance for foundryman. Therefore, the impact of primary and especially minor alloying elements need to be well known. The impact of the small addition of Zr into commercial EN AC 43200 cast alloy on its structural and mechanical properties in as-cast and heat-treated conditions was investigated to be better understood. It has been found that addition of Zr up to 0.24 wt.% reduce the grains size (from 3.5 mm to 1.2 mm) significantly, SDAS (from 57.3 μm to 50.4 μm) and porosity (from 19 % to 5 %), leading to the production of sound cast parts. The addition of Zr increases the hardness of investigated alloy in as-cast (from 71 to 77 HB) and heat-treated conditions (reaching 85 HB). An increase in the hardness after various solid solutions times correlate very well to the formation of small needle-like coherent Al_3Zr particles.

Keywords: EN AC 43200 alloy, zirconium, cast microstructure, hardness

*Corresponding author (e-mail address): srecko.manasijevic@li.rs

INTRODUCTION

The commercial EN AC 43200 (AlSi10MgCu) alloys have been widely used for the production of cast engine parts such as cylinder heads and engine blocks. To improve the properties of these alloys, it has been considered their additional alloying with Zr. Limited data exist in the available literature regarding the impact of Zr on the solidification path, structural, mechanical, and thermophysical properties of as-cast and heat-treated EN AC 43200 alloys. According to F. Wang et al [1] addition of Zr up to 0.2 wt.% change considerably primary morphology of $\alpha\text{-Al}$ from columnar to equiaxed grains (from 1150 μm to 500 μm). Any further addition of Zr up to 0.5 wt.% leads to the gradual decrease of grain size (from 500 μm to 350 μm). According to Elizondo [2], Superband [3], and Mahmudi [4] minor addition of Zr to AlSi6Cu4 alloys have a beneficial impact on the grain refinement of investigated alloys.

Recently, Vončina et al. [5–7], indicated in their works that the addition of 0.202 wt.% Zr to AlSi9Cu3(Fe) alloy did not considerably refine the grain size of this alloy. Superband et al., have shown in their work [3] that Zr added to the Al–Si–Mg cast alloys (up to 0.3 wt.%) precipitate during solid solution treatment in the small and coherent Al₃Zr phase. Due to low Zr diffusivity and limited solubility in the aluminum matrix, these fine particles are stable during solid solution and resistant to coarsening, increasing, therefore, the hardness and strength of cast EN AC 43200 alloys [9]. According to the literature [5–9], the Zr concentration in the investigated alloys needs to be between 0.08 wt.% [5] and 0.24 wt.% [9]. The higher level of Zr into Al–Si alloys (more than 0.20 wt.%), according to the literature [5] leads to precipitation coarse primary Al₃Zr phase, which considerably reduces the mechanical properties of the treated alloy.

Additionally, mechanical properties of these alloys can be improved through various thermal treatments such as solid solution and aging. During the solid solution, the alloys are exposed to the maximal elevated temperature defined by their lower melting point to dissolve soluble phases into the α -Al matrix [9]. The strengthening of these alloys is achieved during artificial and/or natural aging by precipitation of small, fine, and coherent metastable phases. Thus, it looks that still is not clear what is the optimal added concentration of Zr to EN AC 43200 alloys necessary to improve their structural and mechanical properties. Therefore, the main aim of this study was to investigate the impact of the small addition of Zr on the solidification paths and their structural as well as hardness properties of hypoeutectic EN AC 43200 alloys in as-cast and after certain heat treatment and find its optimal concentration.

MATERIALS AND METHODS

The material used in this work was hypoeutectic EN AC 43200 commercial alloy without and with Zr addition. The chemical composition of the alloy is presented in Table 1. A series of EN AC 43200 alloys with increased Zr contents (0.0, 0.08, 0.14 and 0.24 wt.%) were cast by adding master Al-10wt.% Zr alloy into the melt. The commercial alloy was melted in the 800 kg capacity electric resistance furnace. The melt was 15 minutes with nitrogen gas treated. To determine the solidification paths of investigated alloys, the cooling curve analyses have been run. The liquid test samples with masses of approximately 250±10 g were poured into preheated steel test cups (high 60mm, diameter 50mm) coated with Colin. Two calibrated N-type thermocouples were inserted into the melt at the constant height, 30 mm from the bottom of the crucible, and temperatures between 700–400 °C were recorded. The National Instrument Data Acquisition System linked to a personal computer was used to collect the data (temperature versus time) during all experiments. In total, eight experiments have been run for four investigated alloys (each cooling curve analysis has been performed twice). Standard metallographic techniques (sample preparation, LOM, and SEM) have been applied to analyze the macro and microstructure of collected thermal analysis test samples.

Table 1. Chemical composition of investigated EN AC 43200 alloy (wt.%)

Alloy	Si	Fe	Cu	Mg	Mn	Zn	Ti	Sr	Ni
AlSi10MgCu+Zr	9.19	0.38	0.27	0.39	0.31	0.13	0.13	0.015	0.008

The rest of the melt was poured into a steel mould to produce rounded samples with a diameter of 25mm and length of 100mm. These samples have been cut in small pieces and used for hardness measurement. As-cast samples have been solution treated at 530°C at various times up to 24 hours in an electric furnace and quenched in water at 60°C temperature. The hardness of as-cast and heat-treated samples has been measured using Brinell hardness tester QNEES 3000 with a load of 250 kN and a 5.0 mm diameter ball. From each specimen (25mm in diameter and 25 mm in high), at least three measurements have been taken, and the average hardness value has been calculated.

RESULTS AND DISCUSSIONS

The as-cast microstructure of EN AC 43200 alloy, as Figure 1 illustrates, is characterized by the presence of primary α -Al phase, modified Al-Si eutectic (Al-Si) distributed between primary α -Al dendrites as well as Mg_2Si and Zr-Ti rich phases.

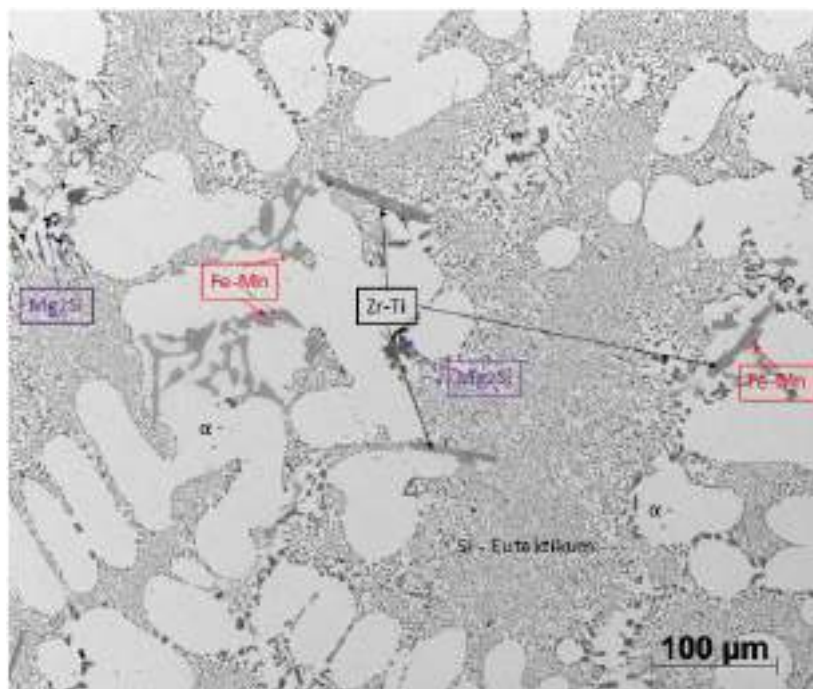


Figure 1. The microstructure of as-cast EN AC 43200 alloy (sample with 0.14 wt.% Zr) obtained using a light optical microscope

As Figure 2 illustrates, the Zr-Ti rich phase generally shows a plate-like form. Literature [4] has documented that the addition of 0.15 wt.% Zr into A319 alloy (AlSi5Cu3.8Mg0.26) does not change significantly the as-cast microstructure of investigated alloy except reduction in the size of SDAS caused by grain refinement effect of Zr.

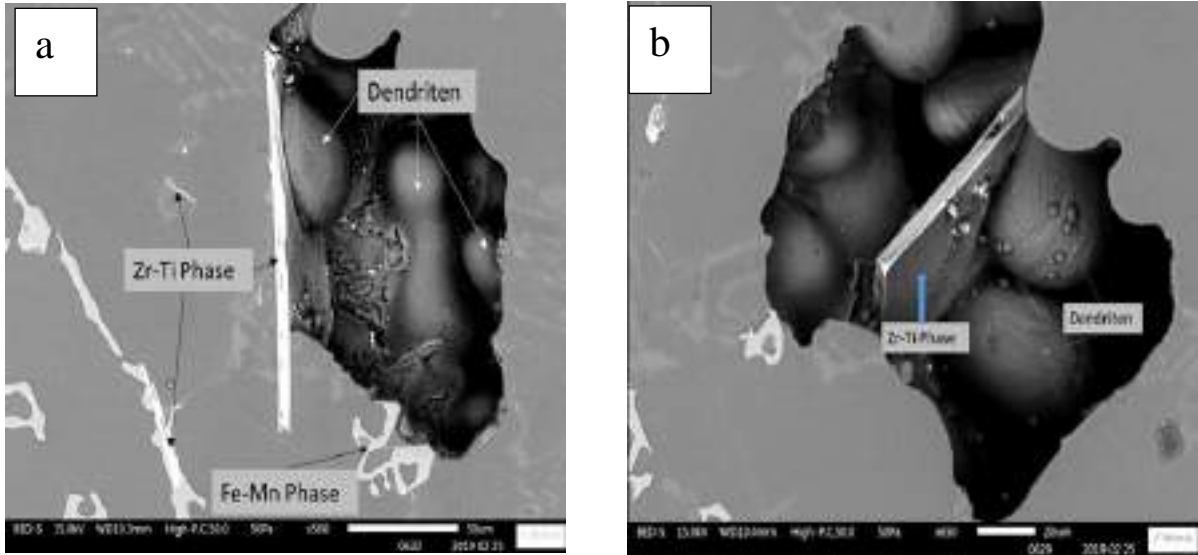


Figure 2. The microstructure of Zr-Ti rectangular phases in as-cast conditions (sample with 0.14 wt.% Zr) obtained using a scanning electron microscope

Figure 3 shows the results of the cooling curve analysis. The values of characteristic solidification temperatures (T_{LIQ} and T_{DCP}) have been plotted as a function of Zr content. Increase in the Zr content up to 0.14 wt.% increase the liquidus temperature from 588.7 °C up to 593.6 °C as well as the dendrite coherency temperature from 585.5 °C up to 587.5 °C, allowing earlier precipitation of primary α -Al dendrites. The addition of 0.24 wt.% of Zr leads to a decrease of both liquidus and dendrite coherency temperatures down to 591.2 °C and 586.5 °C, respectively. The addition of Zr into EN AC 43200 alloy significantly reduces the primary (ΔT) undercooling (already by 0.14 wt.% Zr $\Delta T=0.2$ °C), indicating strong grain refining potential of Zr addition.

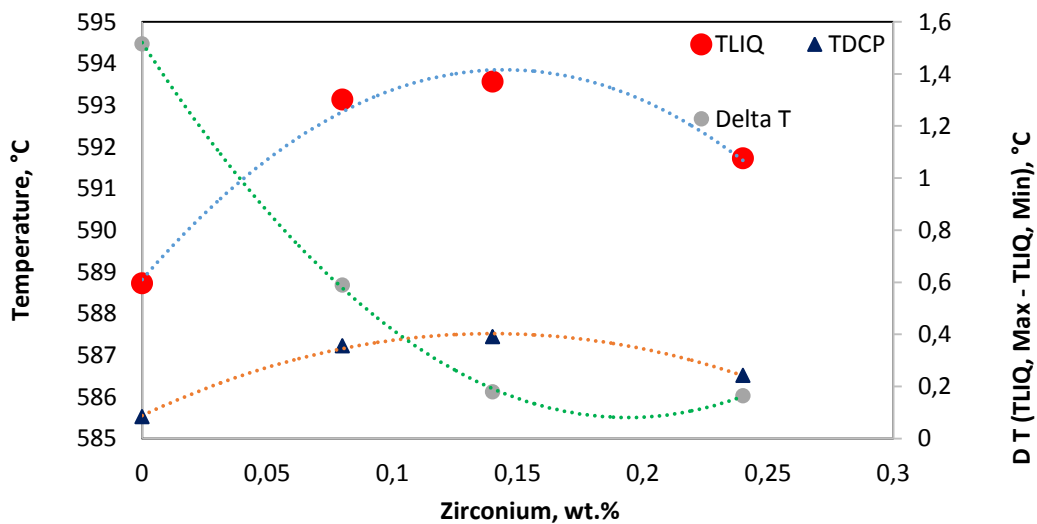


Figure 3. Influence of Zr addition into EN AC 43200 alloys on the T_{LIQ} and T_{DCP} as well as on the undercooling (ΔT) during solidification of primary α -Al dendritic structure (average cooling rate, CR was 0.15 °C/s; $CR = (T_{LIQ} - T_{SOL}) / (t_{SOL} - t_{LIQ})$).

As-cast EN AC 43200 alloy during primary solidification developed the primary and secondary dendritic structure (SDAS). The cooling rate, mould temperature, pouring melt temperature, and alloy compositions are major factors that determine the size of SDAS. As Figure 4 illustrates, the addition of Zr has an impact on the size of SDAS, reducing them significantly from 57.25 μm to 50.37 μm . This effect is related to the grain refinement effect of Zr as well as its small solubility in the $\alpha\text{-Al}$ matrix.

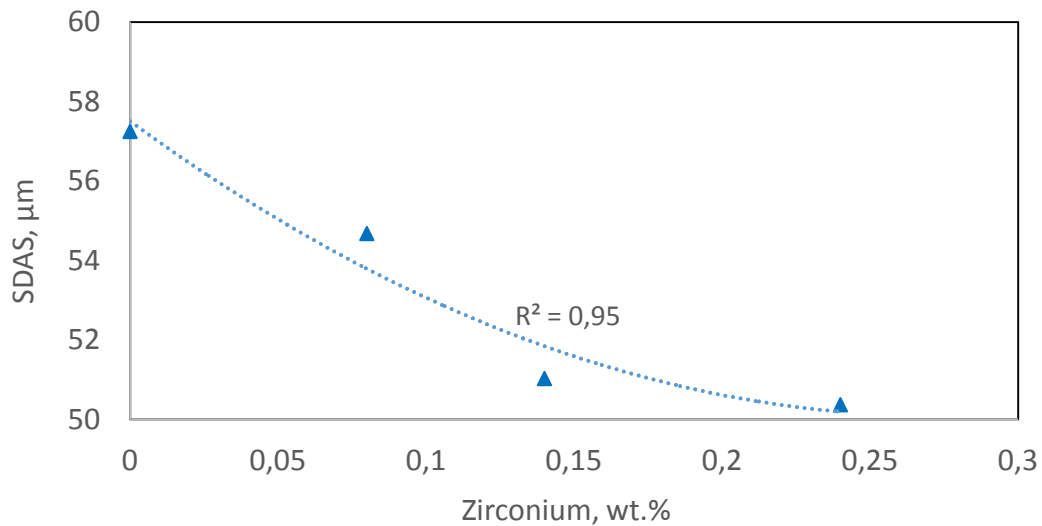


Figure 4. The effect of the various Zr content on the size of the SDAS in as cast EN AC 43200 alloy

The EN AC 43200 alloy has a small proportion of primary aluminum grains in their microstructure, which needs to be also, refined. Generally, finer grains are, for most applications, preferable to coarse grains. Grain refinement during solidification can be accomplished by rapid cooling, melt stirring, or by addition of certain alloying elements (Ti, B, Zr, and so on) to the melt promoting nucleation (chemical grain refinement). Chemical grain refinement is the most widely practiced, and most guaranteed method of grain refinement. According to Figures 3 and 5, it is obvious that the addition of Zr into EN AC 43200 melt caused the decrease of ΔT parameter and leads to the refinement of the as-cast structure of this alloy. As can be seen in Figure 5, the addition of 0.24 wt.% Zr decreases the grain size of the investigated alloy from 3.5 mm down to 1.17 mm. It can be recognized that the first addition of 0.08 wt.% Zr reduces the grain size by approximately 0.7 mm. Further addition of 0.06 wt.% Zr (in total 0.14 wt.% Zr) decrease the grain size considerably by around 1.6 mm. Finer grains of as-cast structure will lead to better feeding and filling ability of this alloy as well as improving its mechanical properties.

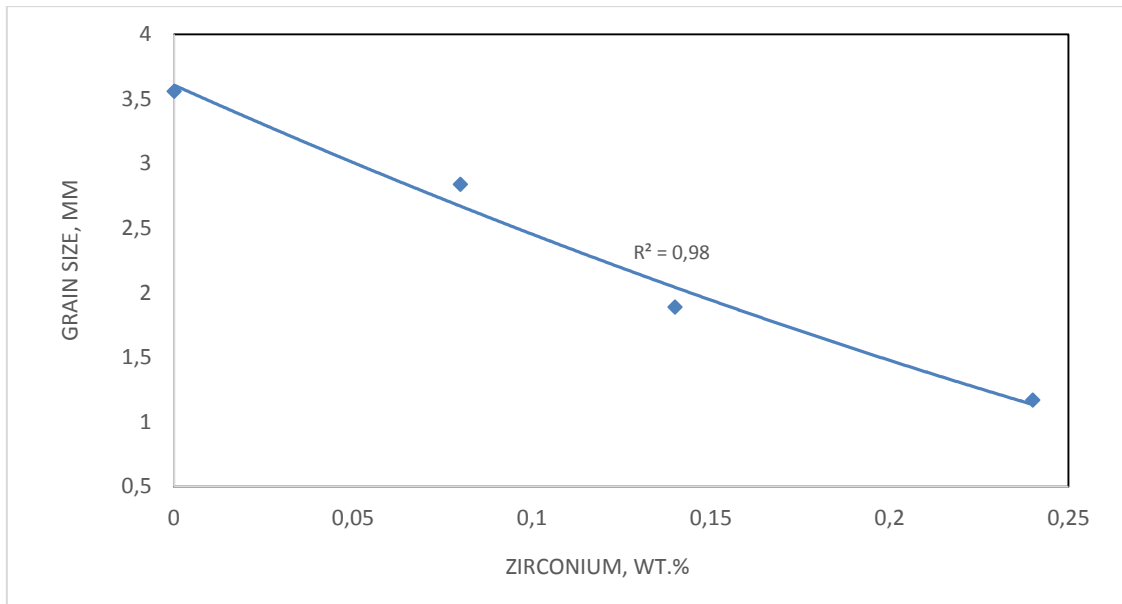


Figure 5. Impact of Zr on the grain size of as-cast EN AC 43200 alloy. The samples for grain size analysis have been taken from the bottom part of thermal analysis test samples (average cooling rate ~ 0.15 °C/s).

It is well known that the quality of as-cast alloys can be improved by grain refinement, which reduces the size of primary α -Al grains causing at the same time reduction of porosity. The present results indicate (Figure 6) that the addition of Zr exceeding a lower limit of about 0.08 wt.% is enough to trigger the reduction of porosity in EN AC 43200 alloy. The porosity reduction seems well connected with the decrease of the SDAS and grain size (Figures 4 and 5). Both microstructural parameters are strongly dependent on the presence of Zr into EN AC 43200 melt.

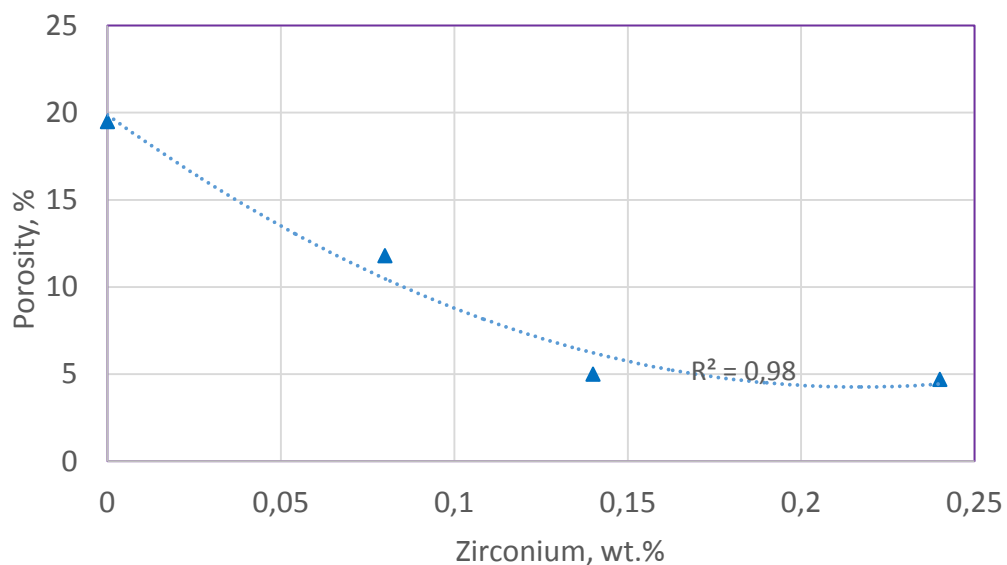


Figure 6. Impact of Zr on the porosity of as-cast EN AC 43200 alloy. The samples for porosity analysis has been taken from vertical cross-sections of thermal analysis test samples (average cooling rate ~ 0.15 °C/s).

The measured values of the Brinell hardness of investigated samples in as-cast conditions are presented in Figure 7. It can be noticed that the hardness of investigated alloys increases by increasing Zr content up to 0.14 wt.%. Further addition of Zr, up to 0.24 wt.% into EN AC 43200 alloy, decrease hardness of this alloy. According to Mahmudi [4] and Superband [3] minor addition of Zr (up to 0.15 wt.%) to AlSi6Cu4 alloy results in an 8% to 10% increase in hardness in all investigated alloys in both as-cast and heat-treated conditions. Vončina et al. [5-7], found that the addition of 0.202 wt.% Zr to AlSi9Cu3(Fe) alloy did not impact considerably the hardness of the diecast alloys (hardness barely increase after addition of Zr from 84 to 85 HV). Based on our investigation presented in Figure 7, it is worth noting to add at least 0.14 wt.% Zr into as cast EN AC 43200 alloy to improve its hardness.

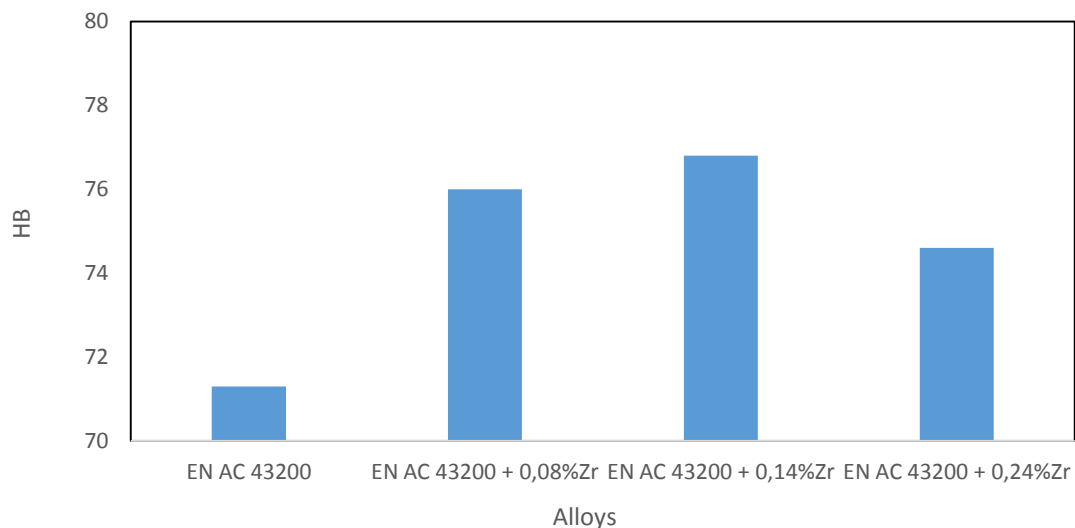


Figure 7. Impact of Zr content on the hardness of as-cast EN AC 43200 alloy

Alloys may not possess all the desired properties in as-cast conditions. Therefore, heat treatment, as a standard foundry procedure, is mostly used to improve their properties. In heat treatment, the microstructures of alloys are modified, resulting in improved mechanical properties like strength, ductility, toughness, hardness and wear resistance. To improve the hardness properties of EN AC 43200 + Zr as-cast structure, selected samples have been thermally treated applying a solid solution process.

A recent study by Seperband et al. [3] showed a small addition of Zr change the optimum solid solution time of the AlSi5Cu3.8Mg0.28 (A319) and AlSi5Cu3.8Mg0.28Zr0.15 (A319+Zr) alloys. Both alloys were solid solution treated at 503 °C from 4 to 36 hours. As Figure 8 shows, the hardness of two alloys with and without Zr drop down deeply with increasing solid solution time up to 8 hours.

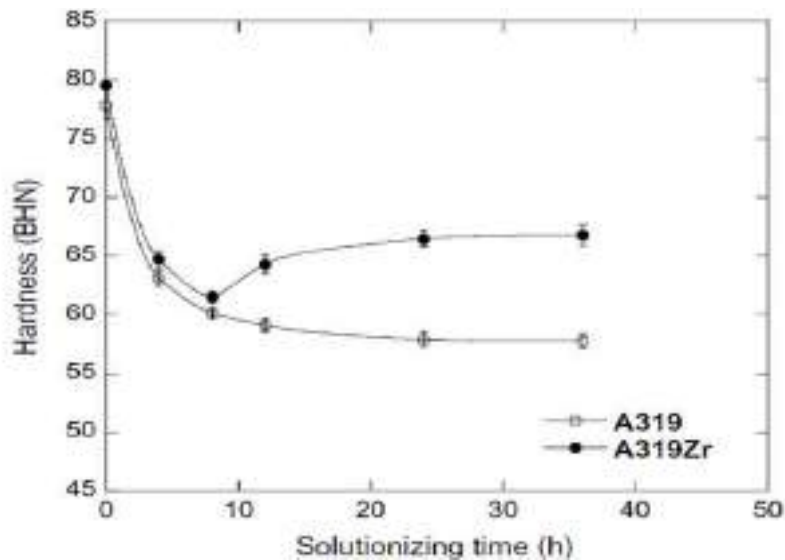


Figure 8. The hardness of the A319 and A319Zr alloys after different time of solid solution [3]

Longer solutionising time has a different impact on those two alloys. At standard A319 (AlSi5Cu3.8Mg0.26) alloy longer solid solution time decrease slightly hardness while A319 alloys with Zr content (0.15 wt.% Zr) gain hardness. The authors concluded that the observed decrease in the hardness by A319 alloys without Zr could be attributed to the dissolution of precipitates formed during solidification. An increase in the hardness of A319 alloys with Zr is related to the optimal solid solution temperature range for the formation of fine Al_3Zr phase as well as the longer period of soaking time may lead to the creation of this coherent phase, resulting in the higher hardness of investigated alloys.

The present work was aimed at determining the optimal solid solution time for EN AC 43200 alloy with (0.14 wt.% Zr) and without Zr (0 wt.%) addition that would generate the development of increased hardness. Solid solution time was scheduled to be: 0, 5.5, 7.0, 8.5, 10.0, 11.5, and 24 hours at 530 °C. Figure 9 shows the impact of Zr and selected solid solution times on the hardness of the EN AC 43200 and EN AC 43200 + Zr alloys.

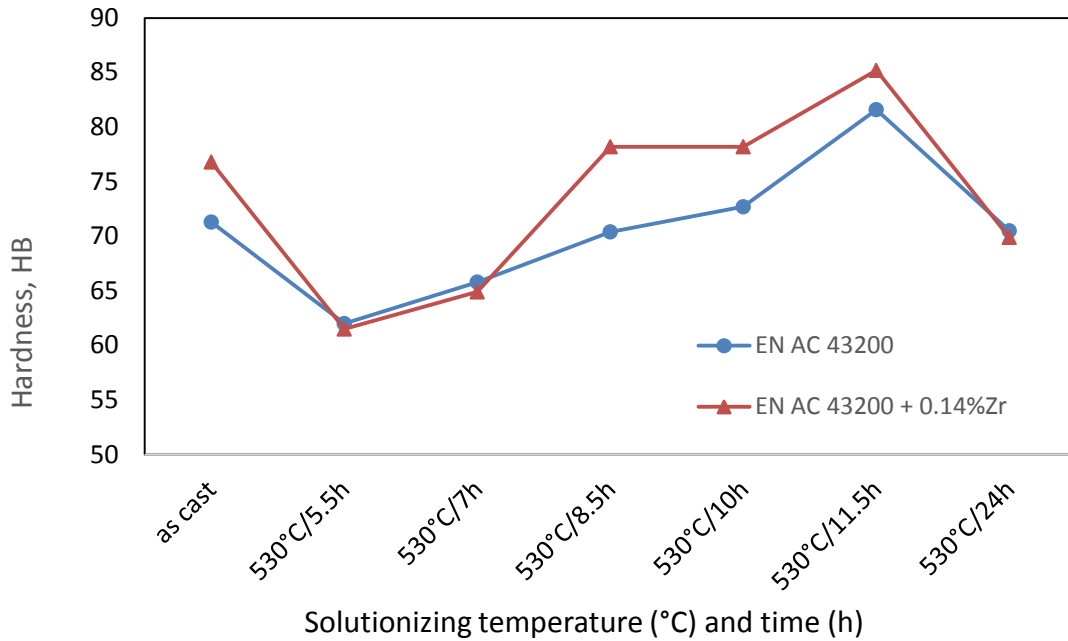


Figure 9. Effect of Zr (0 and 0.14 wt.%) and various solid solution time on the hardness of EN AC 43200 alloys [7]

According to Figures 7 and 9, the small addition of Zr (0.14 wt.%) increases the hardness of EN AC 43200 alloys in as-cast conditions. As Figure 9 indicated, the hardness of both materials, with and without Zr, firstly drop with increasing solution time up to 5.5 hours. The decrease of hardness for both alloys is significant (20% for EN AC 43200 + Zr alloy and 14% for EN AC 43200 alloy), being slightly stronger for the alloy with Zr. By longer solution time (up to ~ 24 hours), however, alloys with and without Zr show a similar trend and slightly different behavior. The hardness of alloy with Zr shows a stronger increase reaching the highest value of 85HB, while material without Zr reaches a maximal value of 82 HB after 11.5 hours solid solution time. The detected effect seems to correlate very well with the formation of coherent small Al_3Zr intermetallics. Due to low interface energy with a matrix of $\alpha\text{-Al}$, slow diffusion coefficient, and low solubility. The additional hardening effect of Al_3Zr has been recognized after 7 hours of solid solution treatment. As Figure 9 indicates, the longer solid solution time than 11.5 hours (up to 24 hours) resulted in a completely different trend decreasing the hardness of both alloys significantly. The hardness of both alloys (with and without Zr) after 24 hours solid solution treatment reached almost the same value of 70 HB. The main reason for such behavior can be found in different diffusion coefficients of Mg and Zr elements into the aluminum matrix. Mg has the higher diffusion coefficient compare to Zr ($\text{Mg} = 10^{-7} \text{ cm}^2/\text{s}$; $\text{Zr} = 10^{-19} \text{ cm}^2/\text{s}$ at $\sim 660 \text{ }^\circ\text{C}$) [9]. Therefore, it is clear that Zr needs more time to be dissolved during a solid solution treatment in the $\alpha\text{-Al}$ matrix. During longer solid solution time (up to 11.5 hours), Zr is precipitating in the small Al_3Zr particles (in nanoscale $\sim 48\text{nm}$) [9], which caused the slightly higher hardness of thermally treated alloy with Zr. The hardness of alloy without Zr increases due to precipitation of Ti_3Al particles. At longer solid solution time (>11.5 hours) the coarsening of both precipitated particles (Al_3Zr and Ti_3Al) is one of the reasons that in both observed alloys hardness decreased. The second reason for hardness decrease can be attributed to the coarsening effect of silicon particles. As Figure 10 illustrates, it is evident that at longer solid solution time, silicon particles are

getting coarser causing the decrease in the hardness value by both alloys [9]. Note the presence of Zr-Ti rich phases after various solid solution time without any considerable changes.

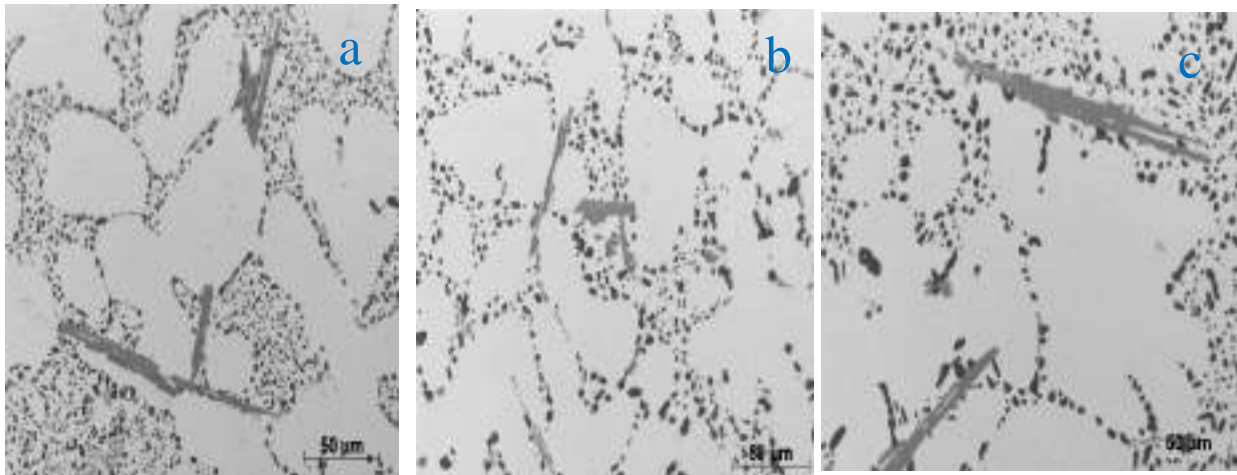


Figure 10. Coarsening silicon parties as a function of various solid solution time: a) 7 h, b) 10h and c) 24h

CONCLUSIONS

In this paper, experiments have been carried out to observe the effect of the small addition of Zr (0–0.24 wt.%) into the EN AC 43200 alloy on the structural and mechanical (hardness) properties. It was found that the addition of Zr up to 0.24 wt.% has significantly changed the as-cast structure of investigated alloy precipitated in the form of Zr-Ti rich intermetallics. Microstructural parameters such as SDAS, grain size and porosity and strongly influenced by the addition of Zr into AlSi10MgCu alloy. Added Zr into AlSi10MgCu melt slightly increase the liquids and dendrite coherency temperatures, while the effect of Zr on different characteristic solidification temperature is insignificant. The small increase in the liquidus and dendrite coherency temperature wide the mass feeding range, may origin better feeding and less porosity formation in as-cast structure. By alloying the standard commercial alloy with Zr, the rich Zr-Ti intermetallic phase has been formed nearby Fe-Mn rich phases. The small addition of Zr to AlSi10MgCu cast alloy improves the hardness in both as-cast and as thermally treated conditions. The optimal hardness of as-cast AlSi10MgCu alloy has been achieved by adding 0.14 wt.% Zr. Combined Zr addition (0.14 wt. %) and thermal treatment (solid solution 530°C/11.5 hours) are needed to achieve the maximal increase in the hardness of investigated alloys. The optimal hardness increases by approximately 18 % in comparison to the base alloy without Zr and thermal treatment. Longer solid solution time leads to a decrease in the hardness of alloys with and without Zr content due to the coarsening of fine precipitated phases (Al_3Zr and Mg_2Si) as well as silicon phases. During solid solution time, up to 24 hours, it has not been recognized any significant changes in the shape and form of the Zr-Ti rich phases.

REFERENCES

- [1] F. Wang, D. Qiu, Z. Liu, J. A. Taylor, M. A. Easton, M. Zhang, The grain refinement mechanism of cast aluminum by zirconium, *Acta Materialia*, 61(2013)15, pp. 5636–5645.
- [2] G.H.G., Elizondo, Effect of Ni, Mn, Zr and Sc additions on the performance of AlSiCuMg, Ph.D., UNIVERSITÉ DU QUÉBEC À CHICOUTIMI, Canada, April 2016.
- [3] P. Seperband, R. Mahmudi, F. Khomamizadeh, Effect of Zr addition on the aging behavior of A319 aluminum cast alloy, *Scripta Materialia*, 52(2005), pp. 253–257.
- [4] R. Mahmudi, P. Sepehrband, H.M. Ghasemi, Improved properties of A319 aluminum casting alloy modified with Zr, *Materials Letters*, 60(2006), pp. 2606–2610.
- [5] M. Vončina, S. Kores, M. Ernecl, J. Medved, The role of Zr and T6 heat treatment on microstructure evolution and hardness of AlSi9Cu3(Fe) diecasting alloys, *Journal of Mining and Metallurgy B*, 53(2017)3, pp. 423–428.
- [6] M. Vončina, J. Medved, S. Koresb, P. Xiec, P. Schumacher, J. Lic, Precipitation microstructure in Al-Si-Mg-Mn alloy with Zr additions, *Materials Characterization*, 155 (2019) 109820.
- [7] J. Medved, S. Kores, M. Vončina, Development of Innovative Al–Si–Mn–Mg Alloys with High Mechanical Properties, In book *Light Metals 2018*, DOI: 10.1007/978-3-319-72284-9_50, pp. 373–380.
- [8] T. Wang, Z. Jin, J. Zhao, Thermodynamic assessment of the Al-Zr binary system, *Journal of Phase Equilibria*, 22(2001)5, pp. 544–551.
- [9] P. Hajduch, M. B. Djurdjevic, D. Bolibruchova, Z. Simicevic, Effect of Zirconium on the solidification path and structural properties of commercial AlSi10MgCu alloys, *Archives of Metallurgy and Materials* 64(2019)3, pp. 1107–1110.



19th INTERNATIONAL FOUNDRYMEN CONFERENCE
Humans - Valuable Resource for Foundry Industry Development
Split, June 16th-18th, 2021
<https://ifc.simet.hr/>

**INFLUENCE OF COLD REDUCTION ON THE STRUCTURE AND HARDNESS OF
COLD DRAWN COPPER WIRE**

Ivan Jandrlić^{1*}, Franjo Kozina¹, Tin Brlić¹, Milica Vučenović²

¹ University of Zagreb Faculty of Metallurgy, Sisak, Croatia

² Student at University of Zagreb Faculty of Metallurgy, Sisak, Croatia

Poster presentation
Original scientific paper

Abstract

The production of copper wires involves the application of various processing operations that lead to certain structural changes. The electrical properties of wire depend on certain structural changes. Research was carried out on copper wire produced by the UPCAST process. Copper wire was subsequently subjected to the cold drawing through the dies in multiple passes. The structural changes in the process of cold drawing of Cu-wire were observed. During the cold drawing of Cu-wire through dies, a significant change in deformed structure occurred in relation to the initial cast structure. The microstructure analysis and hardness values of the deformed sample indicated that during the initial reduction the majority of the deformation was performed at the surface area of the Cu-wire that was in contact with the die. The initial equiaxed grains at the surface of the Cu-wire elongated in the drawing direction as a consequence of the deformation degree increase.

Keywords: *cold drawing, copper wire, microstructure, hardness*

*Corresponding author (e-mail address): ijandrli@simet.unizg.hr

INTRODUCTION

Today, copper is used as a technical metal in various technologies. In addition to silver and aluminium, copper is most frequently used as an electrical conductor and according to the electric conductivity it is right behind the silver. Copper wire manufacturing is a complex process that involves several parts of production. The quality of the produced copper wire depends on numerous production parameters, such as raw material purity, the technological process of production, thermomechanical processing, etc. [1,2].

Over the past few decades, copper wire production processes have significantly improved, while the energy consumption was reduced by the development of continuous processes. Some processes, such as Contirod, Dip forming, south wire procedure, etc., require heat treatment [3-5].

The UPCAST process is specific because it does not require heat treatment of cast wire [5,6]. Copper wire with a certain cross-section is obtained with the UPCAST process by continuous casting. After casting, Cu-wire is wound on coils and cooled on air. After cooling, the continuously cast wire is subjected to the cold drawing through the dies. Deformation and reduction of the wire's cross-section is achieved by the reduction in the cross-section of the die opening during cold drawing. The 99,90 % pure copper, i.e. Electrolytic-Tough Pitch (ETP) Cu is used for the production of copper wire. In more demanding cases, such as the modern electronic circuits, a 99,95 % pure copper, i.e. copper without oxygen content (Oxygen Free, OF-Cu), is used.

George Ellwood Dieter (1988) argues that the mechanical and electrical properties of materials are affected by modifications that occur in metals during the cold deformation drawing process. Microstructure changes of the metal, caused by the drawing process, occur due to the material hardening phenomenon. Therefore, it is necessary to carry out heat treatment to improve the electrical conductivity of Cu [2].

It is necessary to take care that the conductors have the lowest possible specific resistance in the production of electrical conductors. Higher specific resistance means higher electricity consumption, i.e. certain energy loss during transmission of electricity. Therefore, the numerous studies have been conducted on the influence of deformation and subsequent heat treatment on Cu specific resistance [7–10].

The hardening effect of Cu during cold deformation is a consequence of grain size reduction. The subsequent heat treatment leads to the processes of recovery and recrystallization improving the mechanical properties of the cold drawn Cu-wire.[9-10].The heat treatment of cold drawn Cu-wire will result in a hardness decrease, but the electrical conductivity will be increased, respectively [7, 9].

Research on cold-drawn wire shows inhomogeneous deformation through the cross section and more pronounced deformation in the edge parts of the wire [10]. They associate this with inhomogeneous recrystallization. In order to avoid inhomogeneity, it was concluded that higher reduction degrees have to be used for drawing [8, 10].

Other research [11] states that the conductivity of a copper alloy wire with 3 % of Zr increases with a certain reduction degree. This is associated with the formation of a fine not – like deformed microstructure. The microstructure orientation in drawing direction enables the acquirement of harder wire with good conductivity.

The aim of this paper is to explain the structural changes that occur in the cold drawing process of copper wire during plastic deformation. Special attention was placed to the influence of the reduction degree on copper wire microstructure changes. The tests were performed in perpendicular cross-section and longitudinal cross-section with respect to the direction of wire drawing. In order to show the effect of the reduction degree on the changes in Cu-wire hardness, the hardness measurements were performed through the cross sections.

MATERIALS AND METHODS

In the experimental part, continuously cast Cu-wire (99 % Cu) with a diameter of 8,00 mm obtained by the UPCAST method was used. Drawing through the dies with two reduction degrees, 23 % and 46 % with respect to the initial cross section, was carried out. During the second reduction, the deformation was stopped in order to take a sample from the deformation zone within the drawing die.

Sampling for structural tests and hardness measurements was performed in as cast state, after each reduction, and from deformation zone during second pass. Samples were prepared from perpendicular cross-section and longitudinal cross-section with respect to the direction of wire drawing. For the longitudinal cross-section, samples about 2 cm long were taken in all three states. They were then cut in half lengthwise and embedded in a conductive mass. After standard metallographic preparation of grinding and polishing, the samples were etched in a Behar's etching solution containing 200 g CrO₃, 20 g NaSO₄, 17 ml HCl and 1000 ml H₂O.

Microstructure analysis of the samples was performed using Olympus GX51 metallographic microscope with a DP 70 digital camera. After structural testing, on all sample's hardness measurement by the Vickers method was carried out on Mitutoyo hardness testing machine. The test conditions were: loading time of 15 s, load of 100 N and the tests were performed according to the given scheme, Figure 1.

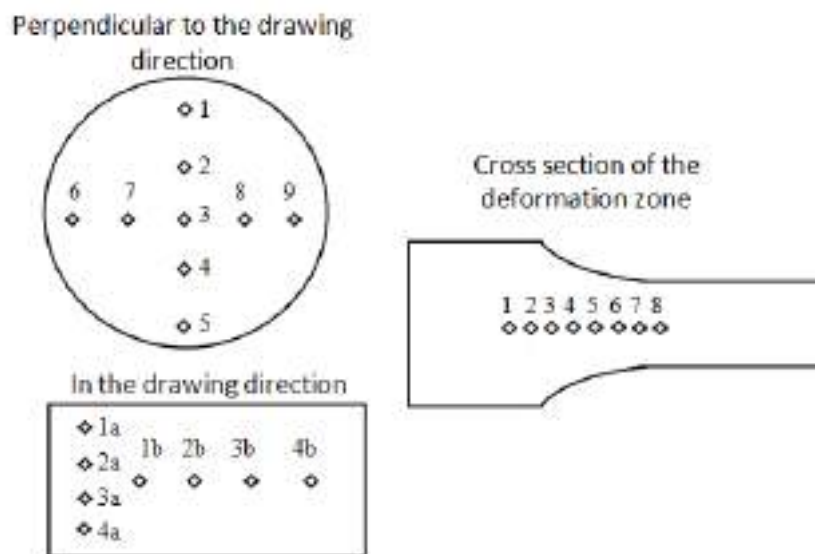
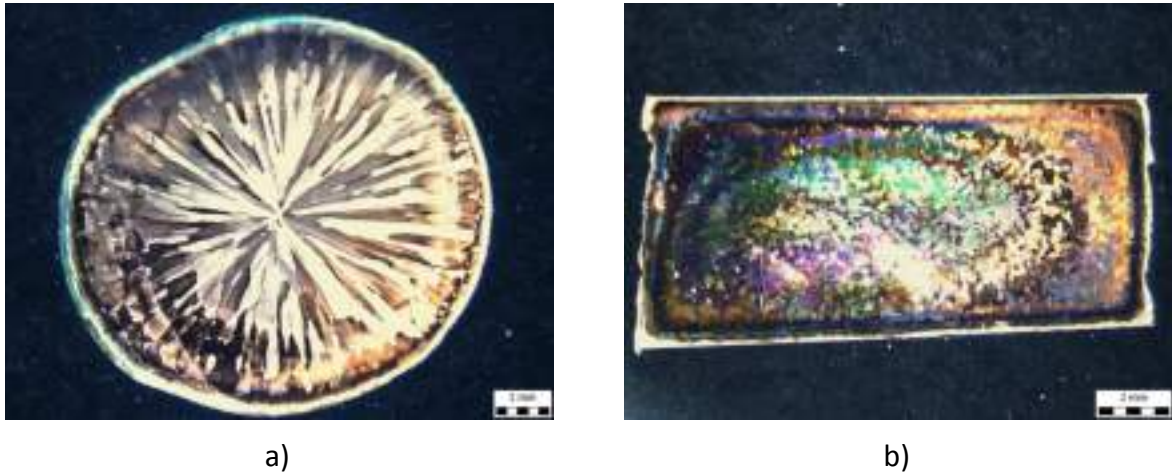


Figure 1. Scheme of hardness measurement on the samples

The results of the microstructure analysis and hardness measurements enabled the impact assessment of the structure changes on mechanical properties. The structure changes occurred during the manufacturing process by wire drawing through the dies.

RESULTS AND DISCUSSION

The macrostructure analysis of the sample in as cast condition indicates a typical macrostructure for the continuously cast copper wire, Figure 2.



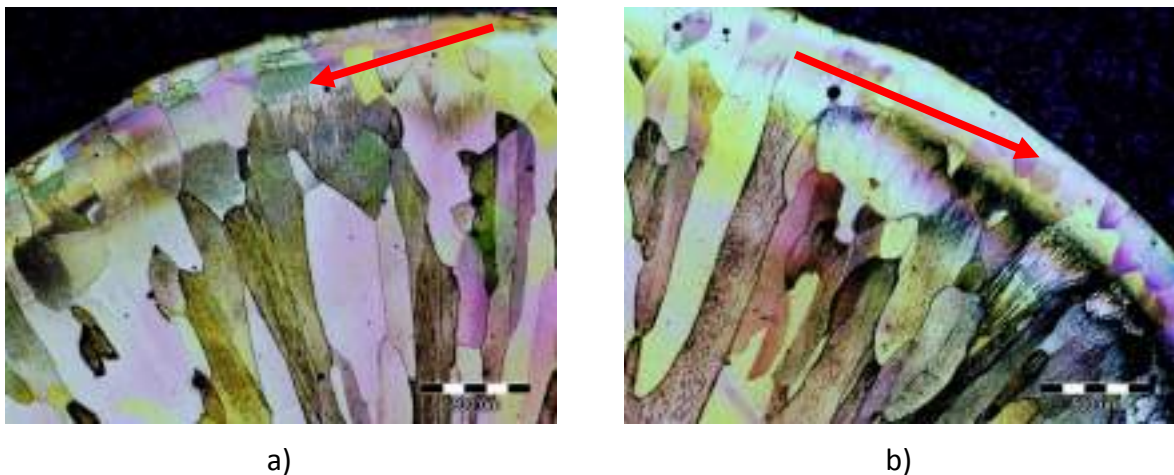
a)

b)

Figure 2. The macrostructure of the sample in as cast condition:
a) perpendicular to the casting direction
b) longitudinal to the casting direction

In the macrostructure of the copper wire sample taken perpendicular to the casting direction, three zones are observed, Figure 2. The edge of the cross-section consists of the chill crystals zone, followed by the columnar crystals zone and the equiaxed grains in the central zone, Figure 2 a). The macrostructure of the wire, longitudinal to the casting direction consists of fine equiaxed grains, Figure 2 b).

The cross-sectional microstructure of the continuously cast wire is shown in Figure 3.



a)

b)

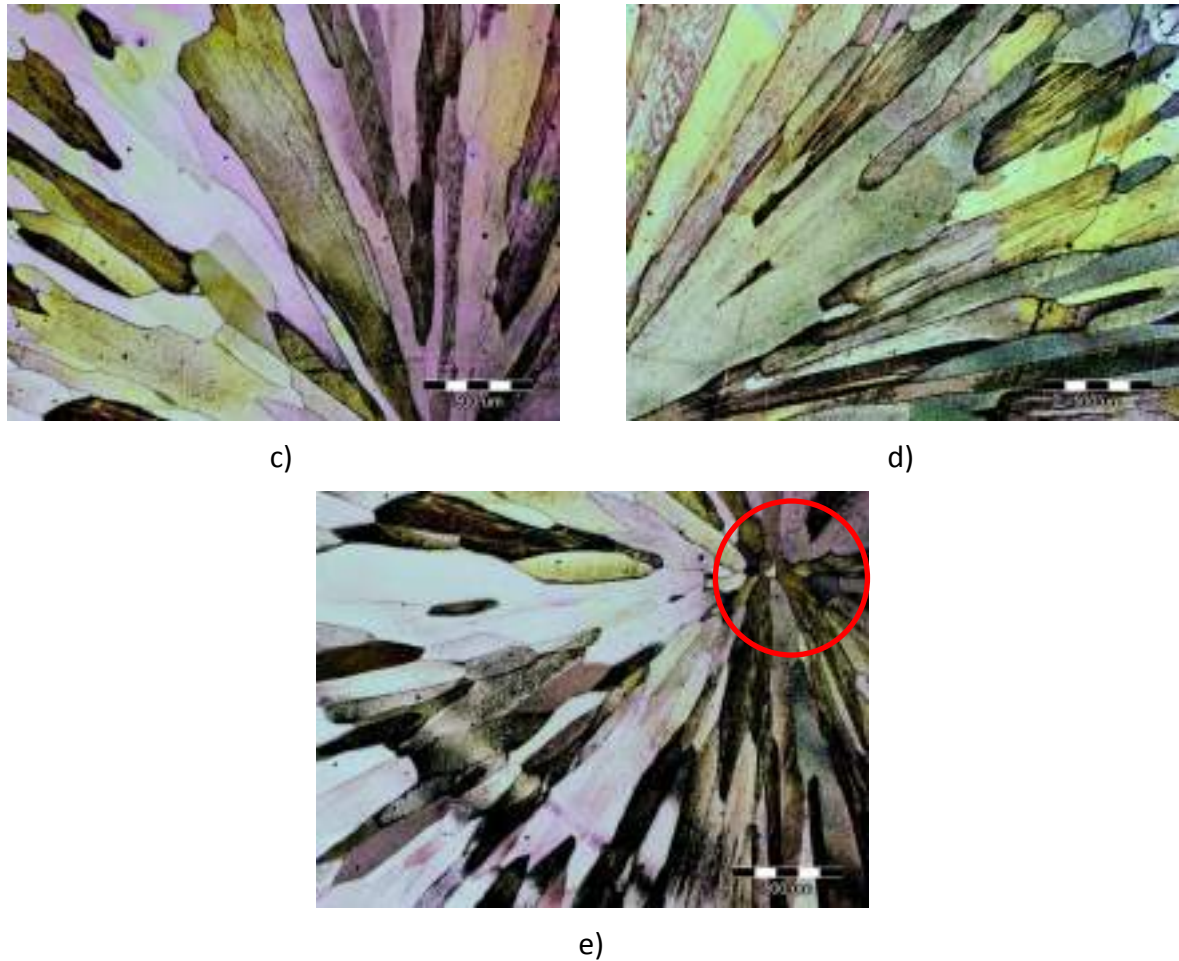


Figure 3. Microstructure of the as cast copper wire perpendicular to the casting direction:

- a) left edge part of the wire
- b) right edge part of the wire
- c) left middle part of the wire
- d) right middle part of the wire
- e) the central part of wire

The external edges of the as cast sample consist of the chill crystal zone (Figure 3 a and 3 b indicated by the arrow) that is formed due to the high cooling rate. The high cooling rate is ensured through the contact between the melt and graphite mould. The chill crystal zone is followed by the columnar crystal zone, Figure 3 c and d. The columnar crystals extend from the edge zone of the frozen crystals to the centre of the continuously cast wire. The equiaxial crystals (Figure 3 e - marked with a circle) are observed in the centre of the wire's cross section.

The microstructure of the deformed Cu-wire after first reduction of 23 %, is given in Figure 4.

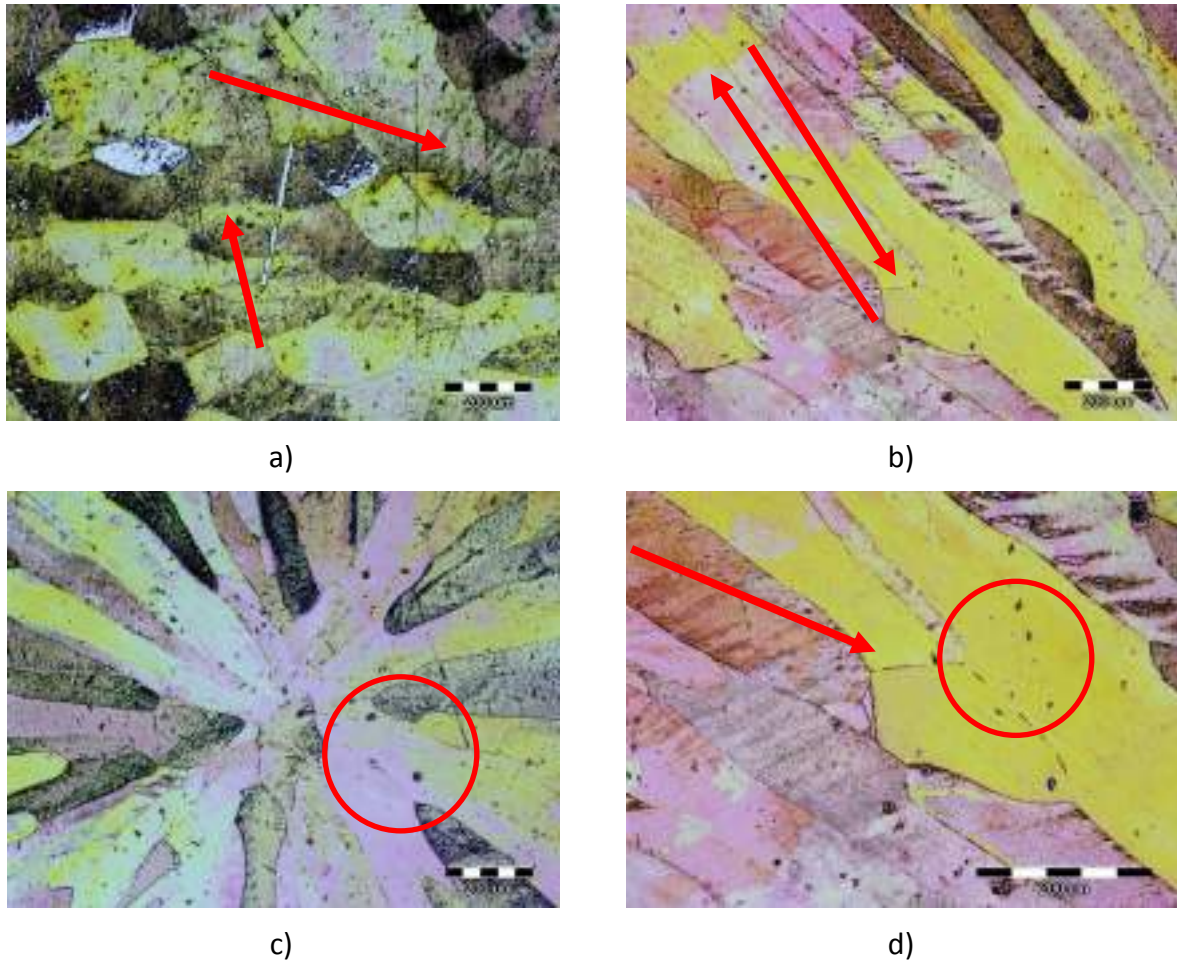


Figure 4. Microstructure of the copper wire sample after 23 % of reduction

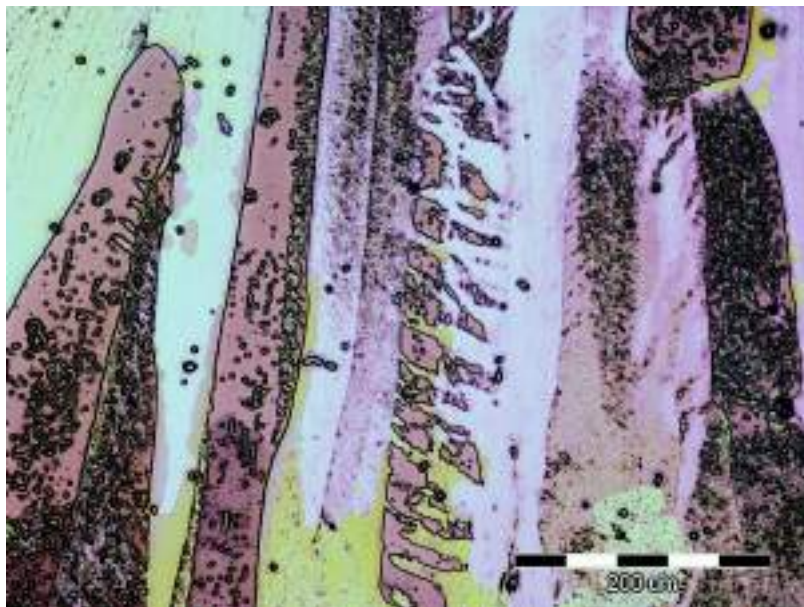
- a) microstructure on cross section in the drawing direction
- b) and c) microstructure in cross section perpendicular to the drawing direction
- d) microstructure perpendicular to the drawing direction, grain fracture

After reduction, dislocations are visible in the microstructure, indicated by arrows in Figure 4. The appearance of dislocations is clearly visible in the edge region of the wire, i.e. in the chill crystals zone, Figure 4 a. It is visible that the one part of the elongated grains broke due to the deformation, Figures 4 b and 4 d.

The microstructure after second reduction (46 % of relative reduction) is shown in Figure 5. A significant grain orientation in the wire drawing direction is observed. This is especially visible at the edge of the wire in the area where the chill crystals were initially observed.



a)



b)

Figure 5. Microstructures after 46 % of reduction

a) the surface part

b) the central part of the sample

The microstructure shows the initial elongated columnar crystals fracture during plastic deformation due to stresses after second pass, Figure 5 b. There is a greater number of dislocations in the cross section of the Cu-wire (Figure 5 b) as the deformation degree increases. Given that, the increase in hardness values is expected. The orientation in the drawing direction is clearly visible from the macrostructure of the sample taken from part of the wire that was in the deformation zone during second pass, Figure 6.

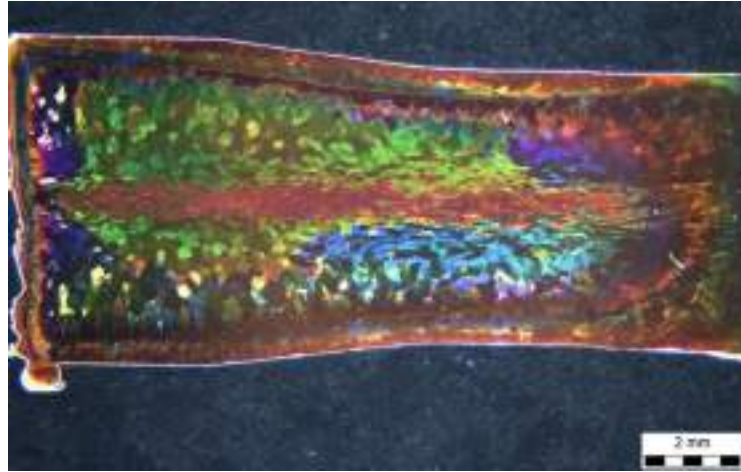


Figure 6. Macrostructure of the deformation zone during second pass

It can be seen that in the deformation zone during drawing, the structure is oriented in the drawing direction, and at the same time the equiaxial grains elongate in the direction of deformation and pass into the elongated grains.

Table 1 shows the measured hardness values along the cross section of the continuously cast Cu - wire, according to the given scheme, Figure 1.

Table 1. Measured hardness values in as cast state, HV10

	Perpendicular to the casting direction		Longitudinal to the casting direction
1.	66.0	1.a)	79.2
2.	69.4	2.a)	73.7
3.	64.9	3.a)	73.0
4.	69.3	4.a)	70.5
5.	71.8	1.b)	73.0
6.	79.5	2.b)	69.6
7.	69.3	3.b)	63.7
8.	65.2	4.b)	70.3
9.	78.0		

Table 2. Measured hardness values after 23 % and 46 % of reduction. HV10

23 % of reduction				46 % of reduction			
	Perpendicular to the drawing direction		Longitudinal to the drawing direction		Perpendicular to the drawing direction		Longitudinal to the drawing direction
1.	97.5	1.a)	83.6	1.	113.1	1.a)	112.6
2.	90.3	2.a)	87.2	2.	110.8	2.a)	107.4
3.	90.9	3.a)	90.3	3.	102.7	3.a)	110.1
4.	89.4	4.a)	94.7	4.	104.3	4.a)	109.5
5.	91.4	1.b)	89.5	5.	114.4	1.b)	108.7
6.	92.0	2.b)	91.3	6.	113.6	2.b)	104.2
7.	87.0	3.b)	91.8	7.	110.9	3.b)	108.7
8.	91.8	4.b)	92.8	8.	109.3	4.b)	104.1
9.	84.1			9.	109.2		

The measured hardness amounts show their uniform distribution across the wire cross section in the as cast state. Table 1. Slightly higher amounts were measured in the chill crystals area in the edge part of the wire (Figures 3a and 3b).The hardness measurements indicate an increase in the hardness of the Cu wire after each drawing. This is particularly evident from the measured hardness values through the deformation zone during second pass. Table 3.

Table 3. Measured hardness amounts through the deformation zone during second pass

Measurement position	1	2	3	4	5	6	7	8
Measured hardness. HV10	89.4	89.5	90.3	98.4	99.5	107.0	106.6	105.8

The measured hardness values after second pass indicate a more pronounced hardening in the edge of wire that is in contact with the die during drawing. It was noticed that in this part. There is a greater directed orientation in the wire microstructure. Figure 5 a.

It can be concluded. by comparing hardness and microstructure changes that during Cu-wire drawing hardening occurs due to grain refinement. increased dislocation density and directed orientation of microstructure. The hardness increase is more pronounced with an increase in the reduction degree. Directed microstructure with the finer grains formed by refinement of the initial elongated grains is observed. Figure 5.

CONCLUSIONS

The aim of the paper was to establish the impact of macrostructure and microstructure changes during cold drawing of continuously cast Cu-wire on the hardness. The conducted research shows the following:

- The macrostructure analysis of the sample in as cast condition indicates a typical macrostructure for the continuously cast copper wire consisting of chill crystal zone followed by columnar crystal zone and equiaxed zone.
- Significant changes in the microstructure in the form of grain refinement occur due to the Cu-wire deformation by drawing through the dies.
- The increase in the deformation degree caused columnar crystal fracture and microstructure orientation in drawing direction.
- The equiaxial grains elongate in the deformation direction and turn into elongated - grains as the deformation increases.
- The grain refinement caused by the cold deformation caused increase in hardness values.

Acknowledgements

This work was supported by the Institutional project FPI-124-2020-IJ.

REFERENCES

- [1] S. K. Ganguli. Power Cable Technology. CRC Press. Boca Raton. 2016.
- [2] G. E. Dieter. Mechanical Metallurgy. 3rd ed.. Mc Graw-Hill Book Co.. New York 1986.
- [3] D. Gusković. S. Marjanović. S. Stević. Copper rod production and environmentpollution reduction. Proceedings of Ecological Truth-Ekoist. Kladovo. Srbija. 2009.
- [4] Accessible on Internet: <https://energy-utilities.com/contirod-continuous-casting-plant-prod1240803.html>. (14.06.2020.)
- [5] V. Stoiljkovic. M. Arsenovic. L. Stoiljkovic. N. Stojanovic. Determination of the optimal parameters of castin a copper wire by the application of neural networks. In: E. Kuljanic (eds). Advanced Manufacturing Systems and Technology. International Centre for Mechanical Sciences (Courses and Lectures). vol 372. Springer. Vienna. 1996.
- [6] Accessible on Internet: <https://upcast.com/upcast-continuous-casting-technology/>. (10.06.2020.)
- [7] K. Rajan. R. Petkie. Microstructure and anisotropy in wire drawn copper. J. Mat. Sci. Eng. A. 257(1998). p. 185.
- [8] L. Zhang. L. Meng. Microstructure. mechanical properties and electrical conductivity of Cu–12 wt.% Ag wires annealed at different temperature. Materials Letters. 8(2004). p. 3888.
- [9] M. Zidani. S. Messaoudi. F. Dendouga. T. Baudin. C. Derfouf . A. Boulagroun. M. H. Mathon. Study of the relation between microstructure and properties (Mechanical/Electrical) of copper wire drawing and annealed. Proceedings of the 2nd International Congress APMAS2012. April 2629. 2012. Antalya. Turkey. pp. 470-473.

- [10] A. Akbari . G. H. Hasani. M. Jamshidi Jami. An experimental investigation on the effect of annealing treatment on strain inhomogeneity in the cross-section of drawn copper wires. Department of Material Science and Engineering. Department of Metallurgical and Material Engineering. Iran. Roznov pod Radhostem. Czech Republic. EU. 2010.
- [11] N. Al- araji . H. M. AL-Tamimi. W. T. Alshammari. The role of cold drawing on electrical and mechanical properties of copper cables. International Journal of Advanced Technology and Engineering Exploration. 2(2015)8. pp. 122-125.



19th INTERNATIONAL FOUNDRYMEN CONFERENCE
Humans - Valuable Resource for Foundry Industry Development
Split, June 16th-18th, 2021
<https://ifc.simet.hr/>

PREPARATION AND CHARACTERIZATION OF ARTIFICIAL PATINA ON BRONZE

Angela Kapitanović, Lana Brkić, Helena Pintarić, Dajana Mikić, Helena Otmačić Ćurković*

University of Zagreb Faculty of Chemical Engineering and Technology, Zagreb, Croatia

Poster presentation
Original scientific paper

Abstract

Numerous bronze objects and works of art are exposed to outdoor atmosphere that causes the formation of patina. Patina creates a protective layer that slows down further corrosion processes. The composition of patina will determine its protective properties as well as its color. The formation of natural patina can take years, but also it can be formed artificially, by chemical and thermal treatment of the surface. Therefore, the application of artificial patina has become a very common form of protection of bronze artefacts.

The aim of this work was to examine morphological and electrochemical properties as well as chemical composition of artificial patina formed on CuSn6 alloy. Chemical patina was formed by using sulfide solution to induce corrosion processes, while electrochemical patina was synthesized by polarization of bronze electrodes in an artificial rain solution. The samples were exposed either to urban outdoor atmosphere or artificial rain solution, after which the composition and structural properties were investigated by attenuated total reflectance Fourier transform infrared spectroscopy (ATR-FTIR), optical microscopy (OM) and scanning electron microscopy (SEM). Electrochemical properties were examined by electrochemical impedance spectroscopy (EIS). The results showed an increase in the impedance modulus with the exposure time, i.e., higher corrosion resistance, which confirms the protective effect of the patina. Morphological results show that the surface of the chemical patina obtained by spraying method is the most homogeneous.

Keywords: *artificial patina, bronze, atmospheric corrosion, electrochemical methods*

*Corresponding author (e-mail address): helena.otmacic@fkit.hr

INTRODUCTION

When exposed to atmosphere, water or soil, copper and copper-based alloys form a thin surface layer of corrosion products called patina. The naturally formed patina has complex composition which depends on several parameters, such as alloy composition, metallurgical features and environmental conditions in which patination occurred [1, 2]. In a clean atmosphere, water and many types of soil, a carbonate patina occurs in form of malachite

$\text{Cu}_2\text{CO}_3(\text{OH})_2$ or azurite $\text{Cu}_3(\text{CO}_3)_2(\text{OH})_2$. In seawater and saline soil a chloride patina is formed, whose composition often corresponds to atacamite $\text{Cu}_2\text{Cl}(\text{OH})_3$. Industrial and urban atmosphere containing sulphates causes the formation of sulphate patina in a form of brochantite $\text{Cu}_4(\text{SO}_4)(\text{OH})_6$ or posnjakite $\text{Cu}_4(\text{SO}_4)(\text{OH})_6 \cdot \text{H}_2\text{O}$ [3]. Duration of patination process on unprotected bronze depends mainly on atmosphere. It can take up to 100 years in clean air, or much less in a polluted atmosphere due to the presence of various corrosive compounds such as SO_2 , NO_2 and CO_2 [3, 4]. Therefore, patination process will last 20-100 years in rural areas, up to 10 years in urban areas, and the fastest patination will take place in marine environments. However, even in the most aggressive environments, patination remains a slow process, which is why the preparation of artificial patina is preferred not only to enhance the aesthetic of art objects, but also to protect the substrate metal from further corrosion [4,5]. Artificial patina is formed by treating the surface of bronze objects with specific chemicals or solutions at room temperature and/or by heating (flame, torch or oven) according to recipes. A wide range of chemicals, both household and commercial, can give a variety of patinas. Patina composition varies depending on the reagents used and it will determine the color of the patina. For works of art, patination is intentionally accelerated by heating. Colors range from sandstone yellow to distinct blue, red and various blacks, sometimes with a surface gloss enhanced by wax for works of art exhibited indoors. Since the composition and protective properties of patina formed on bronze artefacts are usually not examined by practitioners, more studies have been conducted to reveal patina composition, its protective properties and stability [3, 6].

In this work two types of artificial patinas were prepared: chemical sulphide patina and electrochemical patina. After preparation samples were exposed to urban outdoor atmosphere as well as to an artificial rain solution. The composition and structural properties of the patinas were investigated by attenuated total reflectance Fourier transform infrared spectroscopy (ATR-FTIR), optical microscopy (OM) and scanning electron microscopy (SEM). Electrochemical properties were examined by electrochemical impedance spectroscopy (EIS).

MATERIALS AND METHODS

Sample preparation

Studies were conducted on the CuSn6 bronze. Two sizes of bronze samples, bigger with 50 x 50 mm surface and small with 10 x 10 mm surface and 10 mm thickness. Smaller samples were embedded into an epoxy resin in order to serve as electrodes for electrochemical measurements. Samples were grinded with 80, 800, 1200 and 2500 grade SiC paper. Afterwards, samples were washed with redistilled water, degreased with ethanol in ultrasonic bath, then again washed with redistilled water and wiped with paper towel at the end.

Patina formation – chemical synthesis

The solution required for chemical patina was prepared by dissolving 10 g potassium polysulfide in 0.5 L distilled water by heating the solution to 80 °C.

Chemical patination was conducted in two ways. In the first method, the samples were immersed in the solution, kept in it for 3-4 minutes, then removed from the solution, washed with tap water and polished with a sponge. This procedure was repeated 5 times,

until the formation of a stable patina that was not easily removed with a sponge (Figure 1a). In the second case, the previously prepared solution was placed in a spray bottle. The bronze plates were heated on a burner and the solution was sprayed on the hot plates. The samples were then washed with tap water, polished with a sponge and the procedure was repeated until the patina on the samples was stable enough (Figure 1b).

Eventually, the samples were placed in outdoor atmosphere, except for some resin-embedded samples that were immersed in artificial rain with pH is 6.5. The artificial rain solution was prepared by dissolving 0.2 g/L Na_2SO_4 , 0.2 g/L NaHCO_3 i 0.2 g/L NaNO_3 in distilled water, and its pH was adjusted with $0.5 \text{ mol/dm}^3 \text{ H}_2\text{SO}_4$ solution.

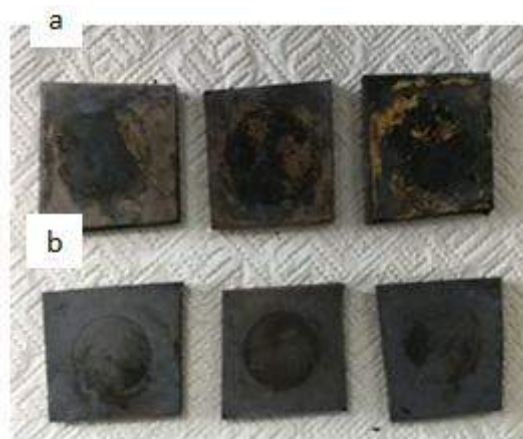


Figure 1. Chemical patina formed by a) immersion and b) spraying

Patina formation – electrochemical synthesis

The artificial rain solution, with pH = 8.8, was used as the electrolyte during the electrochemical synthesis. The patina formation was performed in a three-electrode system. The working electrodes were bronze samples connected in series, the reference was saturated calomel electrode and the counter electrode was stainless steel wire. Patina was formed by polarization of bronze (Figure 2) in following step according to the procedure adopted from literature [6]:

1. at -0.20 V vs. open circuit potential (E_{OCP}) during 60 s;
2. at $+0.14 \text{ V}$ vs. E_{OCP} during next 48 h;
3. at $+0.12 \text{ V}$ vs. E_{OCP} during another 48 h.

Eventually, half of the samples was placed in outdoor atmospheric conditions and half in artificial rain with pH = 6.5.

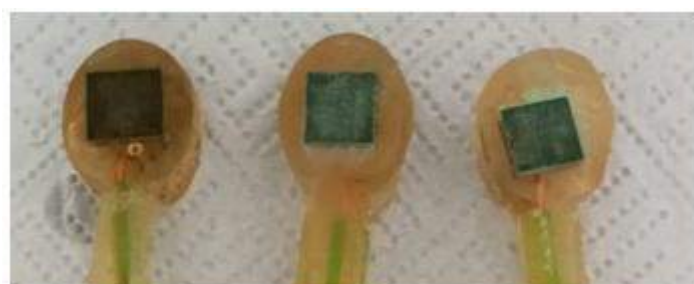


Figure 2. Electrochemical patina

Electrochemical measurements

The electrochemical characterization of bronze samples was conducted by using EIS. EIS was measured by using two different electrolytes: agar based electrolyte or artificial rain solution (pH = 6.5). The measurement was performed in a three-electrode system. Artificial rain was used to study chemically and electrochemically patinated samples embedded in resin. In the rain system, the samples (1 cm²) were the working electrode, the saturated calomel was reference and graphite was the counter electrode. Agar based electrolyte was used in the three-electrode system with larger samples as working electrodes. Agar was prepared by dissolving 0.5 g of powdered agar in 20 mL of an artificial rain solution (pH = 6.5). The solution was then stirred and heated in a microwave oven until agar was fully dissolved. The clear solution was poured into a prepared mold with the reference and counter electrode made of stainless steel wires, and was refrigerated until the formation of hardened gel. The working surface of such agar gel was 4.91 cm². The setup was adopted from literature [7,8]. Studies were conducted in a frequency range from 100 kHz to 10 mHz with 10 mV amplitude at open circuit potential (E_{oc}).

Spectroscopic and microscopic characterization

Composition of the patina was examined by the use of ATR-FTIR using a Shimadzu IRTracer-100, with the scan range from 4000 – 400 cm⁻¹, having a resolution of 0.5 cm⁻¹, and the results shown in this paper are averages of 45 scans.

OM was conducted by using Dino-Lite optical microscope with 50x magnification.

SEM was conducted by using EDS analysis was performed with VEGA 3 SEM TESCAN equipped with X-ray energy-dispersive spectroscopy SEM imaging at an acceleration voltage of 10 kV.

RESULTS AND DISCUSSION

Morphological and structural characterizations

Morphology of artificial patina was examined by SEM and elemental composition was identified at different positions on the patina surface. ATR-FTIR analysis was performed to identify the composition of the patina.

Chemical patina

Figure 3 shows SEM and OM images showing the surface layer of a chemical patina formed by immersion in a potassium polysulfide solution. An inhomogeneous surface with cracks can be observed. Figure 3b confirms unevenly distributed patina due to which the bronze surface is not well protected. Elemental composition, determined by EDX is shown in Table 1. At positions 1 and 3 a sulfide patina was formed, at position 1 traces of oxide were determined. At position 2 there is no indication of patina, but high amounts of Ca indicate a scale formation, most likely during the rinsing of the sample with tap water.

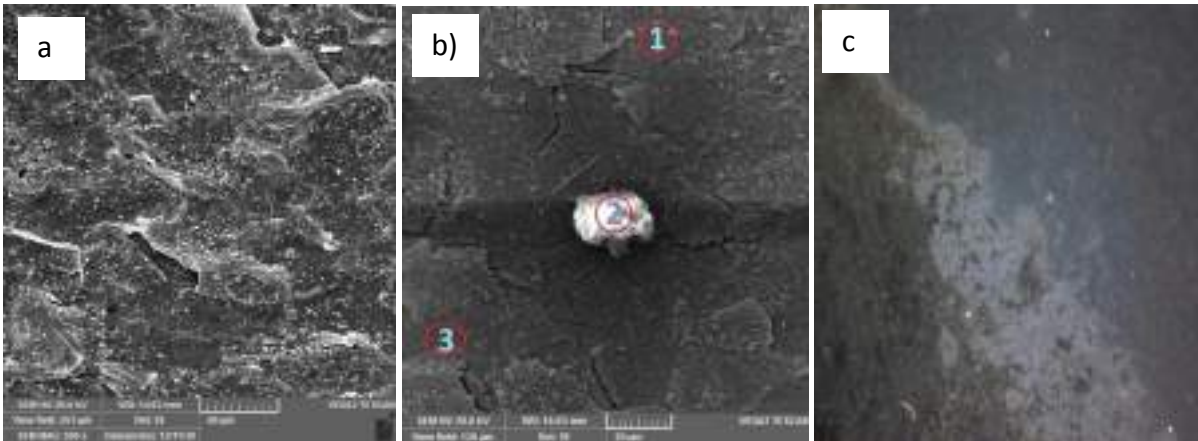


Figure 3. SEM (a, b) and OM (c) images of the chemical patina formed by immersion

Table 1. Elemental composition of the artificial patina chemically obtained by immersion at different positions according to Figure 3b

Wt. %	Cu	S	Sn	O	Ca	Mg	C	Al
Point 1	76.5	10.3	11.9	1.3	-	-	-	-
Point 2	4.7	-	-	18.5	63,8	8.1	4.1	0.8
Point 3	77.8	5.3	16.9	-	-	-	-	-

Figure 4 shows SEM and OM images of a chemical patina formed by spraying the surface of bronze samples with a potassium polysulfide solution. Homogeneous surface with more even patina can be observed. EDX analysis of the surface area shown in Figure 4b, shown in Table 2, reveals that only copper sulfides are present on the surface, and the absence of tin indicates that a thick layer of patina is formed.

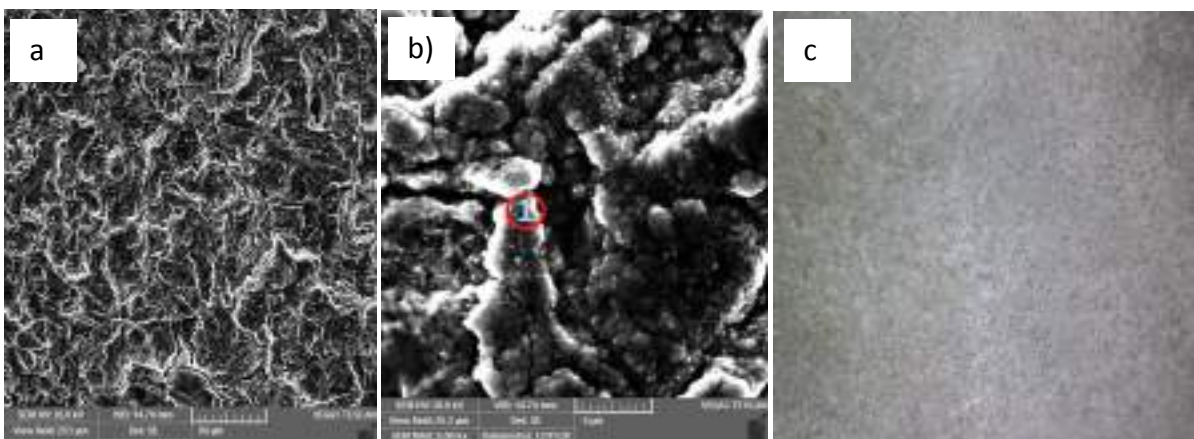


Figure 4. SEM (a, b) and OM (c) images of the chemical patina formed by spraying

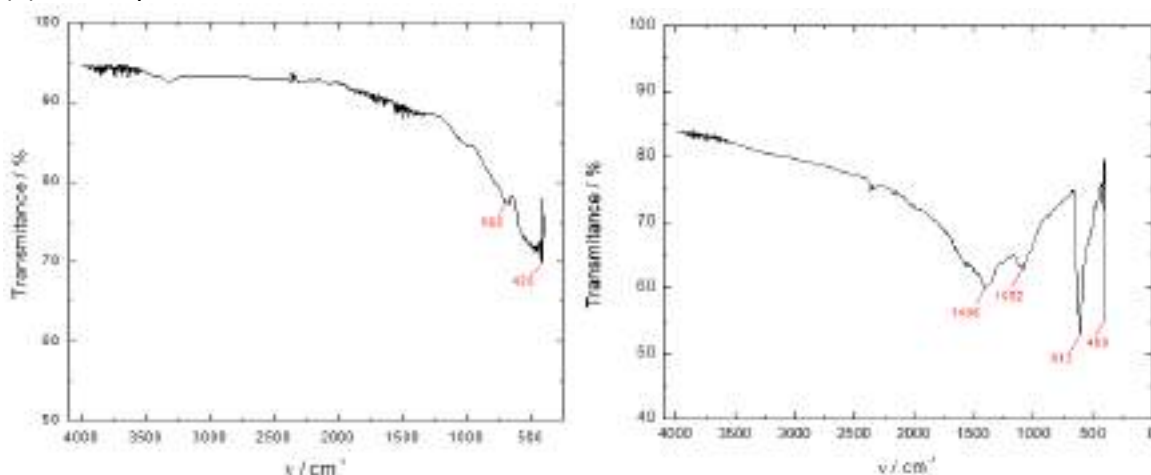
Table 2. Elemental composition of the artificial patina chemically obtained by spraying at position 1 according to Figure 4b

Wt. %	Cu	S
Point 1	84.5	15.5

FTIR spectra of two samples of chemically obtained patina after atmospheric exposure for 36 and 7 days are shown in Figure 5a. First spectrum (36-day exposure) shows two bands at 420 and 688 cm^{-1} that indicate presence of sulfides. Second spectrum (7-day exposure) shows four bands, two strong bands at 400 and 613 cm^{-1} and two at 1082 and 1406 cm^{-1} . This spectrum can be identified as malachite, $\text{Cu}_2\text{CO}_3(\text{OH})_2$.

FTIR spectrum of chemical patina after 50 days of exposure to an artificial rain solution is shown in Figure 5b. It shows one band at 418 cm^{-1} , indicating the presence of sulfides.

(a) Atmosphere



(b) Artificial rain solution

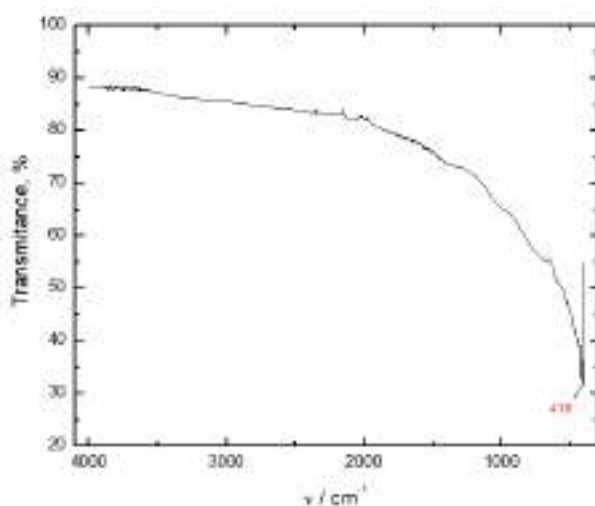


Figure 5. FTIR spectra recorded on the chemically obtained patina after exposure to atmosphere for 36 and 7 days (a) and to an artificial rain solution for 50 days (b)

Electrochemical patina

OM image (Figure 6c) shows that the patina is not formed over entire surface. SEM images (Figure 6a and Figure 6b) also show inhomogeneity of patina. In some parts of the sample, there was almost no patina formed (Figure 6b position 5) and in position 4 of the same image a thick layer of carbonate patina was formed.

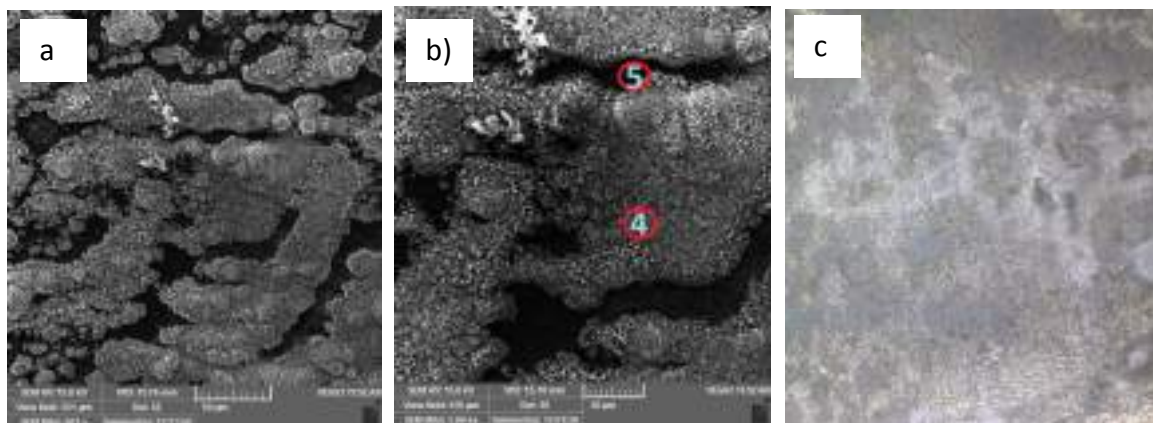


Figure 6. SEM (a, b) and OM (c) images of the electrochemical patina

Table 3. Elemental composition of the artificial patina electrochemically obtained by polarization of bronze samples at different positions according to Figure 6b

Wt. %	Cu	Sn	C	O
Point 4	85.6	-	1.6	12.8
Point 5	90.3	9.0	0.7	-

Conducted ATR-FTIR measurements reveal the patina composition. The ATR-FTIR spectrum shows bands with peaks at 1363, 1049 and 827 cm^{-1} which are characteristic of carbonate patina, namely malachite [9]. The FTIR spectrum also shows bands with peaks at 441 and 401 cm^{-1} which are present due to the formed oxides (Figure 7).

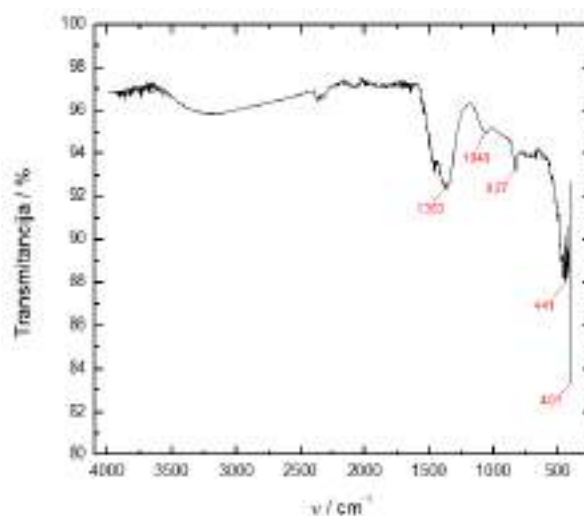


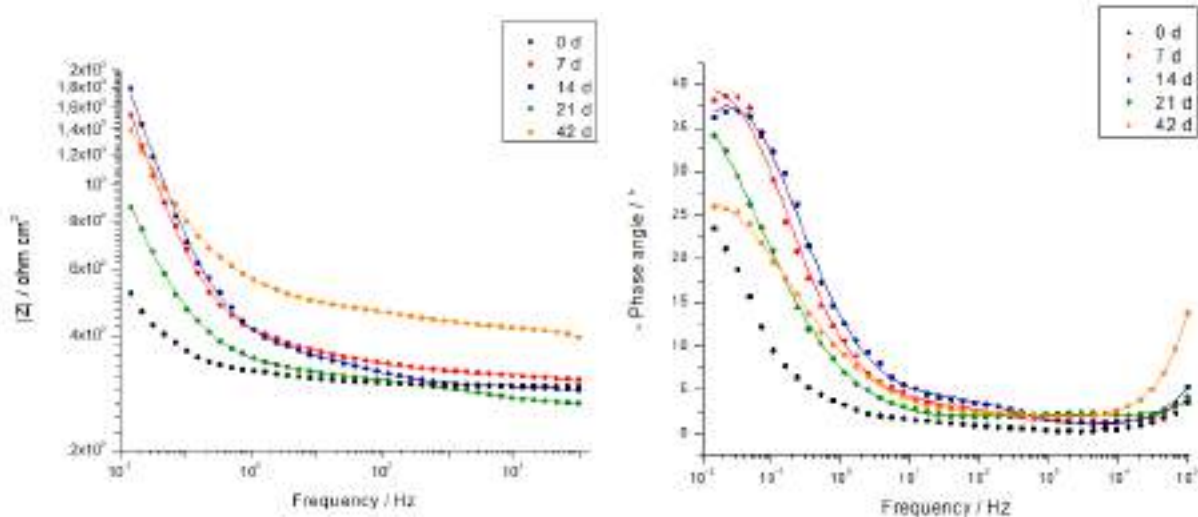
Figure 7. FTIR spectrum and characteristic bands for electrochemical patina

Electrochemical analysis

Chemical patina

Figure 8 shows the EIS spectra of a chemical patina formed by immersion exposed to atmosphere (a) and to an artificial rain solution (b). An increase in the impedance modulus, at the lowest frequencies, in time can be observed for both samples. For an atmosphere-stabilized patina, the highest impedance values are observed after 14 days of exposure while the highest impedance modulus for a chemical patina stabilized in an artificial rain solution is observed after 42 days. EIS measurements for both types of samples were performed in an electrochemical cell with an artificial rain solution pH = 6.5 as electrolyte. Recently, a new approach has been developed where electrochemical cells with gel electrolytes are used for EIS measurement on bronze objects exposed to atmosphere [8]. The results of measurements in an electrochemical cell with gel electrolytes based on agar are shown in Figure 9. A similar trend of increase of the impedance modulus with exposure time can be observed.

(a) Atmosphere



(b) Artificial rain solution

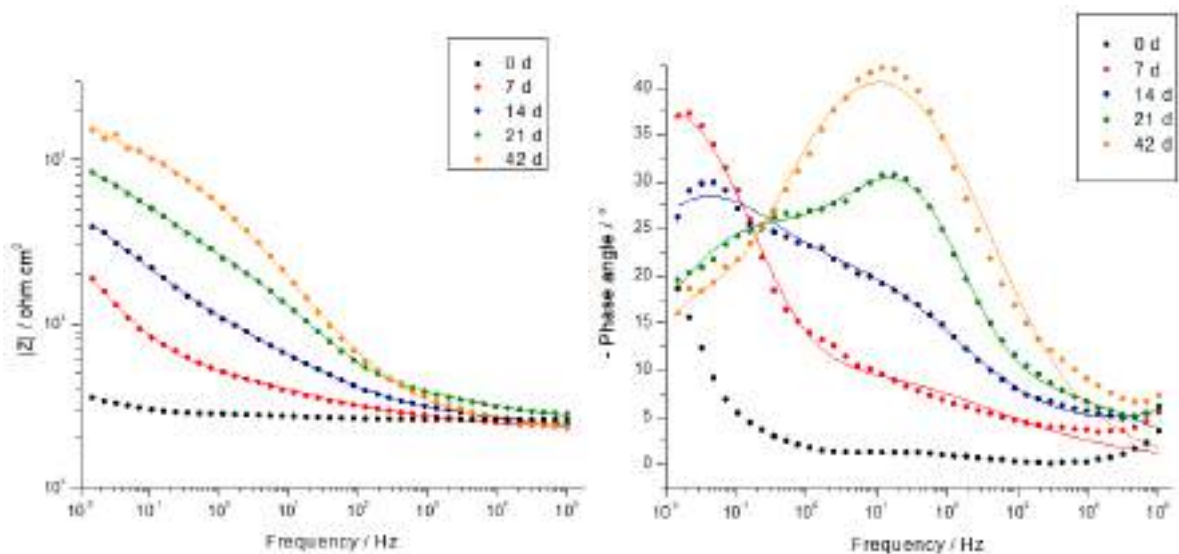


Figure 8. Electrochemical impedance spectra obtained on the chemical patina exposed to (a) atmosphere and (b) to an artificial rain solution

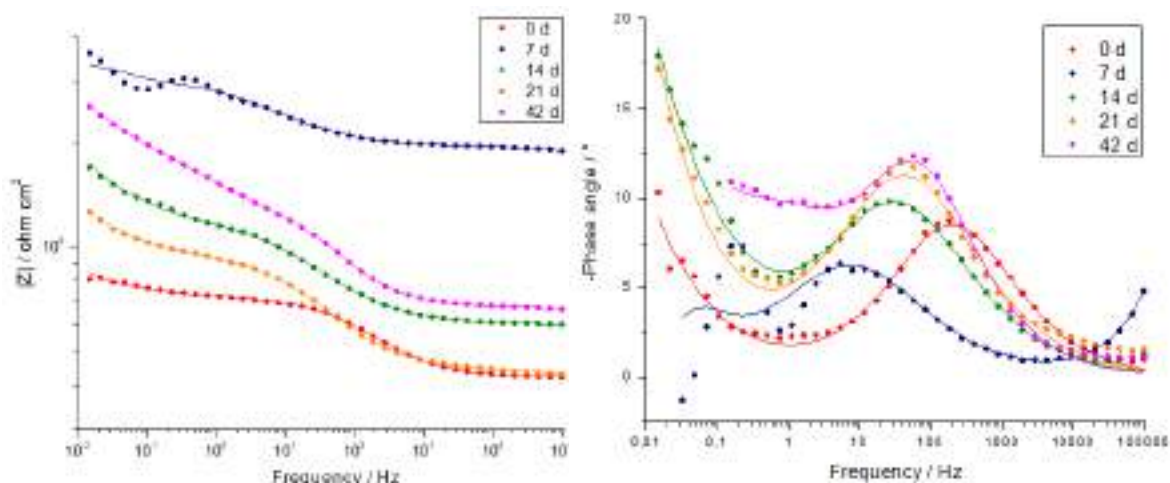
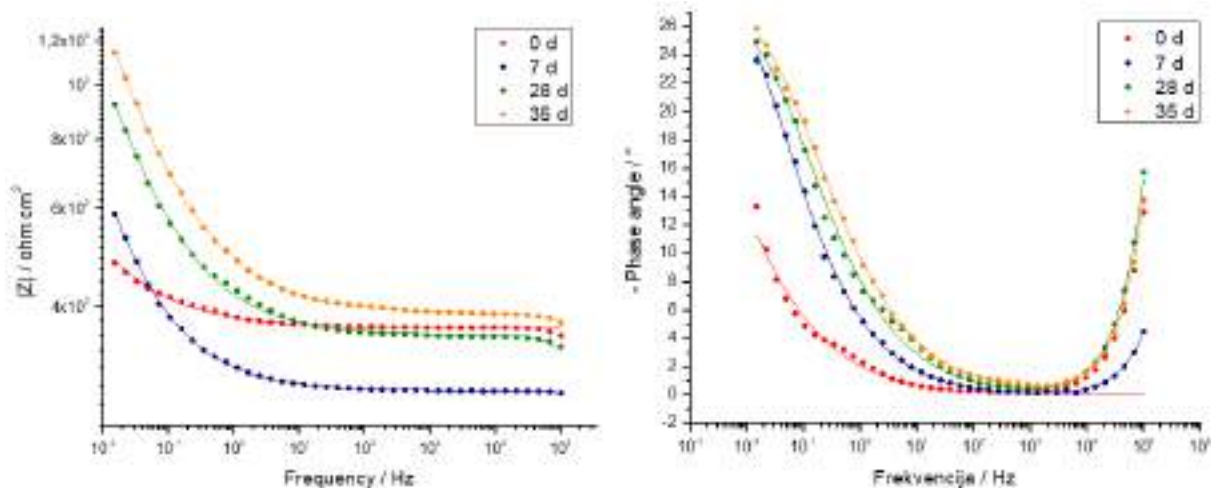


Figure 9. Electrochemical impedance spectra obtained on the chemical patina exposed to atmosphere measured in electrolytical cell with gel electrolyte based on agar

EIS measurements were also performed on samples of chemical patina formed by spraying method. EIS spectra obtained on samples exposed to the atmosphere and in artificial rain solution are shown in Figure 10. An increase in the impedance modulus with the exposure time can be observed, indicating patina stabilization and good protection of the bronze surface from further corrosion. Comparison of EIS spectra given in Figure 8 and Figure 10 reveals that for both types of types of chemical patina, continuous exposure to artificial rain solution results in faster and bigger increase of impedance of patinated samples than exposure to outdoor atmosphere. This implies that during continuous immersion patina layer is gradually transformed and becomes more protective, while the transformation of patina during atmospheric exposure, with occasional exchange of wet and dry conditions, is much slower.

(a) Atmosphere



(b) Artificial rain solution

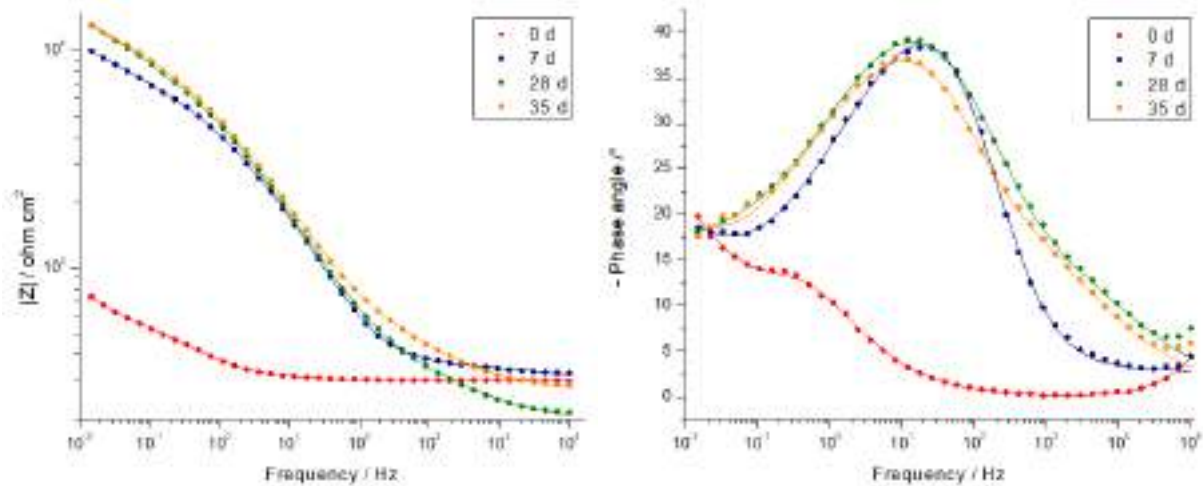


Figure 10. Electrochemical impedance spectra of chemical patina obtained by spraying after exposure to atmosphere

EIS spectra given in Figure 8 and Figure 10 were additionally analyzed by using equivalent electrical circuit models in order to obtain characteristic impedance parameters. For samples exposed to atmosphere, EIS spectra reveal two phase angle maxima. However, for EIS spectra of patina formed by immersion it was necessary to use model with three time constants while for patina formed by spraying model with two time constants was sufficient. These models are presented in Figure 11a and Figure 11b. In these models R represents resistive elements, Q represents constant phase element describing non-ideal capacitive behavior determined by coefficient n . R_{el} is electrolyte resistance, R_F - Q_F couple describes non-reactive patina layer behavior, R_{ct} - Q_{dl} describes bronze surface behavior, while R_F - Q_F couple describes reactive patina layer. Results of the regression calculation of the impedance data obtained on the chemical patina after atmospheric exposure are shown in Table 4, while Table 5 shows EIS parameters for the chemical patina after exposure to an artificial rain solution. Data for the first day of immersion, are not provided as for most of the samples it was not possible to obtain a good match experimental and fitted data.

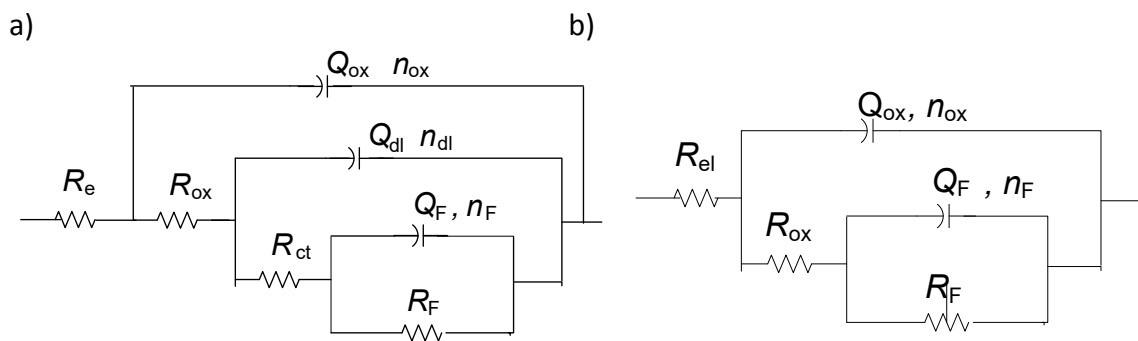


Figure 11. Electrical equivalent models used to fit EIS spectra

Table 4. EIS data for the chemical patina exposed to atmosphere

t/day	$Q_f / \mu S s^n$ cm^{-2}	n_f	R_f / Ω cm^2	$Q_{dl} / \mu S$ $s^n cm^{-2}$	n_{dl}	R_{ct} / Ω cm^2	$Q_F / \mu S$ $s^n cm^{-2}$	n_F	R_F / Ω cm^2
Immersion									
7	0.048	0.64	317.0	1016	0.52	89.3	2243	0.71	8098
14	0.0032	0.86	293.2	506	0.59	87.1	2181	0.67	5203
21	0.0003	1.0	255.7	526	0.38	69.0	5415	0.60	19050
42	0.0016	0.96	409.1	513	0.43	90.1	246.6	0.54	4921
Spraying									
7	0.0015	1.0	154.8				9316	0.53	3634
28	0.0025	1.0	255.9				4620	0.50	3777
35	0.0097	0.97	389.2				3340	0.47	6154

Table 5. EIS data for the chemical patina exposed to an artificial rain solution

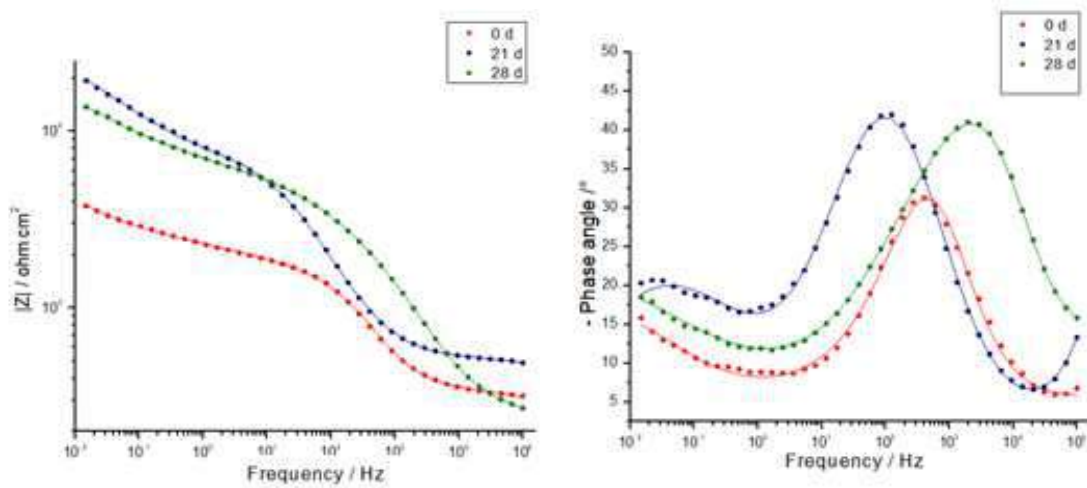
t/day	$Q_f / \mu S s^n$ cm^{-2}	n_f	R_f / Ω cm^2	$Q_{dl} / \mu S$ $s^n cm^{-2}$	n_{dl}	R_{ct} / Ω cm^2	$Q_F / \mu S s^n$ cm^{-2}	n_F	$R_F / k\Omega$ cm^2
Immersion									
14	8.13	0.33	272.3	323.3	0.44	1641	417.6	0.53	11.7
21	63.8	0.46	222.0	16.8	0.73	2773	225.5	0.50	11.34
42	50.6	0.57	1391	796.4	0.78	7857			
Spraying									
0	0.005	0.99	287.5	2494	0.67	327.6	14760	0.70	1.34
7	70.3	0.41	99.5	7.81	0.84	9767	951.3	0.55	277.6
28	39.8	0.52	356.0	12.6	0.68	8060	280.0	0.39	28.6
35	59.0	0.49	1269	3.49	0.83	11300			

Impedance parameters presented in Tables 4 and 5 show that capacitance of the reactive patina layer decreases while the resistance of reactive patina increases in time for all studied samples but this change is more pronounced for samples exposed to artificial rain solution than for samples exposed to outdoor atmosphere.

Electrochemical patina

Figure 12 and Table 6 show the EIS results on electrochemical patina and reveal that the impedance modulus increases both for the patina exposed to atmospheric conditions and the patina exposed to artificial rain. Impedance spectra for both systems are very similar, which confirms that electrochemical patina stabilizes already after 21 days of exposure to corrosive medium, which is also evident from the increase of R_{ct} and R_f in time (Table 6).

a)



b)

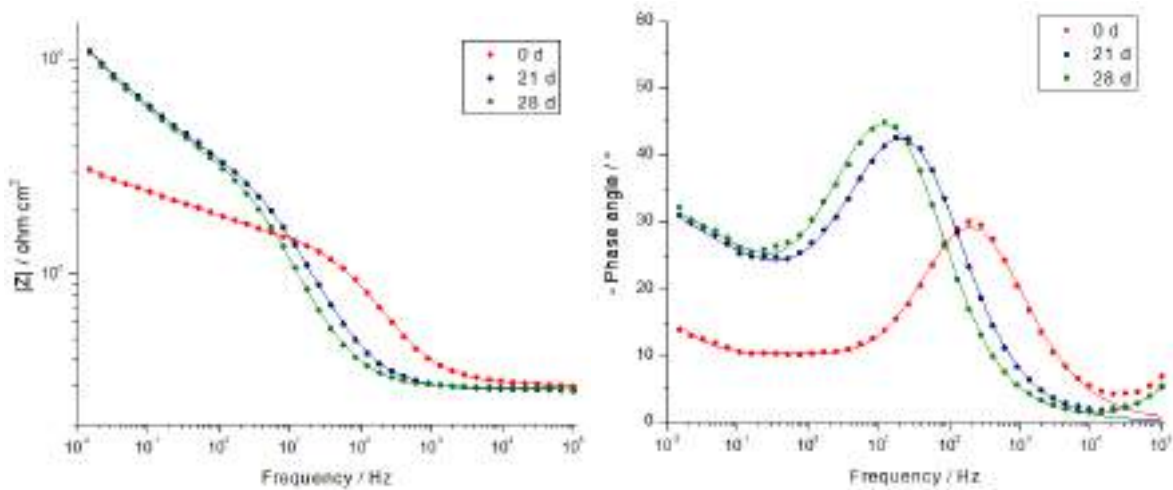


Figure 12. Electrochemical impedance spectra obtained on the electrochemical patina a) exposed to atmosphere and b) exposed to artificial rain solution

Table 6. EIS parameters calculated according to the model, in acid rain at pH = 6.5 for an electrochemical patina exposed to the atmosphere

t/day	$Q_f / \mu S s^n cm^{-2}$	n_f	$R_f / \Omega cm^2$	$Q_{dl} / \mu S s^n cm^{-2}$	n_{dl}	$R_{ct} / \Omega cm^2$	$Q_F / \mu S s^n cm^{-2}$	n_F	$R_F / \Omega cm^2$
0	86.4	0.21	381.6	1.26	0.86	2559	14760	0.70	1341
21	0.0063	0.84	523.5	4.04	0.76	5574	951.3	0.55	277600
28	72.3	0.47	307.1	0.14	0.86	5605	280.0	0.39	28620

CONCLUSIONS

Chemical patina was formed in two ways: by immersion and by spraying. EIS results show an increase in the impedance modulus with the exposure time, i.e., higher corrosion resistance, which confirms the transformation of patina in time. Slightly higher corrosion resistance is

observed for samples of chemical patina formed by spraying. Results obtained by measurements in electrochemical cell with gel electrolyte based on agar show the same trend of impedance increase. The results of morphological characterization showed a more homogeneous surface without cracks for patina formed by spraying. The surface composition consists only of copper sulfides.

The electrochemical patina was formed by polarization of the bronze electrodes in the electrolyte pH = 8.8. EIS results show an increase in impedance modulus with exposure time for both samples exposed to an artificial rain solution or to atmosphere. Microscopy of the electrochemical patina showed uneven morphology. EDX analysis and ATR-FTIR indicate dominate formation of carbonate patina.

From the results obtained it can be concluded that chemically formed patina shows greater stability than electrochemical patina and provides good protection of bronze from further corrosion.

Acknowledgements

This work was full supported by the Croatian Science Foundation under the project IP-2019-04-5030.

REFERENCES

- [1] M. Wadsak, I. Constantinides, G. Vittiglio, A. Adriaens, K. Janssens, M. Schreiner, F. C. Adams, P. Brunella, M. Wuttmann, Multianalytical Study of Patina Formed on Archaeological Metal Objects from Bliesbruck-Reinheim, *Mikrochim. Acta* 133(2000), pp. 159-164.
- [2] G. Di Carlo, C. Giuliani, C. Riccucci, M. Pascucci, E. Messinaa, G. Fierro, M. Lavorgnac, G. M. Ingoet, Artificial patina formation onto copper-based alloys: Chloride and sulphate induced corrosion processes, *Appl. Surf. Sci.* 421(2017), pp. 120-127.
- [3] M. Markusi, Zaštita brončane kulturne baštine ekološki prihvatljivim inhibitorima korozije, Fakultet kemijskog inženjerstva i tehnologije, Sveučilište u Zagrebu, Zagreb, 2015.
- [4] T. Kosec, A. Legat, I. Milošev, The comparison of organic protective layers on bronze and copper, *Progress in Organic Coatings* 69(2010), pp. 199-206.
- [5] R. Bureš, M. Klajmon, J. Fojt, P. Rak, K. Kristýna Jílková, J. Stoužil, Artificial Patination of Copper and Copper Alloys in Wet Atmosphere with Increased Content of SO₂, *Coatings* 9 (2019) pp. 837.
- [6] A. Marušić, H. Otmačić-Čurković, Š. Horvat-Kurbegović, H. Takenouti, E. Stupanišek-Lisac, Comparative studies of chemical and electrochemical preparation of artificial bronze patinas and their protection by corrosion inhibitor, *Electrochimica Acta* 54(2009), pp. 7106-7113.
- [7] B. Ramírez Barat, E. Cano, P. Letardi, Advances in the design of a gel-cell electrochemical sensor for corrosion measurements on metallic cultural heritage, *Sens. Actuators B* 261(2018), p. 572.
- [8] B. Ramírez Barat, E. Cano, The use of agar gelled electrolyte for in situ electrochemical measurements on metallic cultural heritage, *Electrochim. Acta* 182(2015), p. 751.
- [9] N. V. Chukanov, *Infrared spectra of mineral species*, Springer, New York, London, 2014.



19th INTERNATIONAL FOUNDRYMEN CONFERENCE
Humans - Valuable Resource for Foundry Industry Development

Split, June 16th-18th, 2021

<https://ifc.simet.hr/>

**MAKING PROTOTYPE CASTING USING 3D PRINTING AND INVESTMENT
CASTING**

Sebastjan Kastelic^{1,2*}, Almir Mahmutović², Matic Žbontar¹, Primož Mrvar¹, Mitja Petrič¹

¹ University of Ljubljana Faculty of Natural Sciences and Engineering, Ljubljana, Slovenia

² TC Livarstvo d.o.o., Ljubljana, Slovenia

Poster presentation

Expert work

Abstract

In this paper a production of a prototype casting made by using 3D printing technology, numerical calculation and investment casting technology is described. The 3D printing parts for investment casting were made using Fused Deposition Modelling (FDM) 3D technique using a Polylactic Acid (PLA) material. PLA is used due to low expansion during the burning the printed model out of a ceramic shell. Printed models were prepared in such a way that the printed layers did not have an effect on the surface roughness regarding the layer tolerance.

To design and check the proper gating system for investment casting technology the numerical calculation was used. After selecting the proper gating system and casting parameters the gating system was printed and final casting with gating system was assembled.

On the assembled casting finally, the ceramic shell was made. Before pouring the aluminum alloy the PLA model is burnt out using electrical furnace. Before pouring the ceramic shell is sintered and heated up.

To produce the final prototype only six days was needed.

Keywords: *3D printing, numerical calculation, investment casting, prototype casting*

Corresponding author: sebastjan.kastelic@ntf.uni-lj.si

INTRODUCTION

3D printing is more and more used technology for production of various parts from various materials. This technology can be much faster at small batch series than conventional technologies. It is often used for production of prototype parts. There are many 3D technologies known and the most used materials are different polymers. Recently also metal powders can be used for 3D printing, but with limited capabilities due to material properties such as contraction factors leading to distortions and stresses, phase transformations, etc [1].

One option to use 3D printing technology is in the field of investment casting. Conventional investment casting technology uses wax patterns assembled together in a tree to produce ceramic shells used for casting. One of the commonly used material for patterns is PLA. Using PLA for investment casting has its advantages in the low thermal expansion of PLA, what has its benefits during the burn out process. Due to low thermal expansion, there is minimal risk for ceramic shell to crack during the burn out [2, 3]. PLA printed patterns with FDM technology is relative fast and the costs of such patterns is very low. Also, the printers with adequate accuracy are at affordable price for every foundry shop.

For fast prototype production it is also suitable to use numerical calculations to prepare the optimal foundry technology for the prototype casting. With proper optimization of casting parameters and gating system we can avoid to make prototype castings with undesired defects.

MATERIALS AND METHODS

For production of prototype water tap made from aluminum alloy the final 3D model of water tap is made from two parts, which are presented on Figure 1.

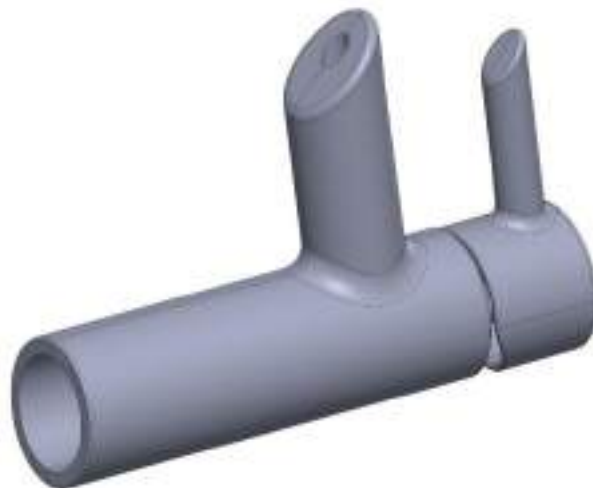


Figure 1. 3D water tap made from two parts

The PLA patterns for investment casting were printed using printer based on FDM printing method. The printer used was Prusa i3 MK3S+. For printing, each prepared 3D model was sliced on three parts. Slicing was done to get flat surface, to be able to start printing on the printer bead without the support. When printing starts on flat surface the proper sticking of printed model on print bed is achieved and the printed part is more stable. Additional slicing was done to avoid roughness due to finite layer accuracy. With proper slicing the changing of printing orientation was achieved. With changing printing orientation the roughness because of the layer height was eliminated. The sliced models prepared for printing are presented on Figure 2 and 3.



Figure 2. Water tap part 1 sliced and prepared for printing

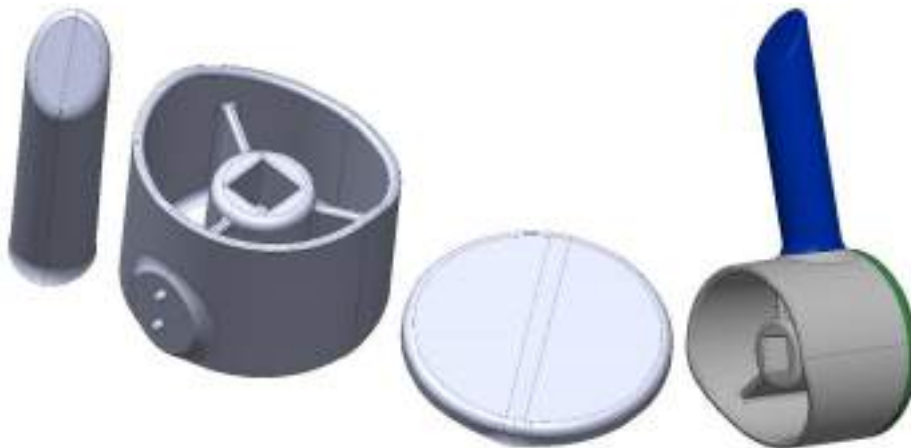


Figure 3. Water tap part 2 sliced and prepared for printing

Sliced model were prepared for printing using PrusaSlicer-2.3.0. To prepare the printed file for printing several settings had to be defined. In our case the layer height was set to 0.2 mm, and the wall thickness was set to 0.8 mm (two passes). To provide additional surface for first layer a 5 mm brim was set. Five parts were printed without support material, because the slicing of the parts was done optimal. For one part the printing could not be done without printing additional support due to geometrical restriction of part[4]. The infill was set to 15% using gyroid pattern. The visualization of prepared printing paths is shown on Figure 4. Printing time for one set was 13 hours.

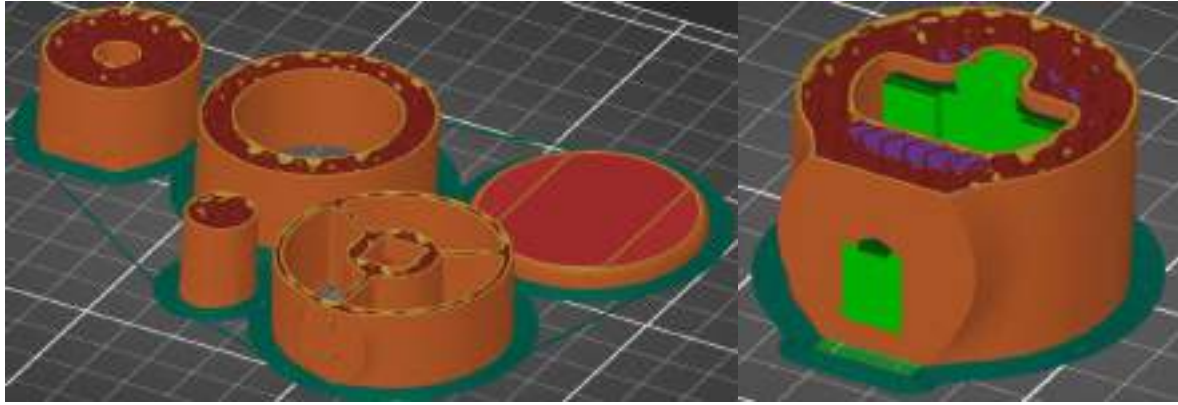


Figure 4. Cross-section of layers prepared for printing using PrusaSlicer

Three sets were prepared and printed for casting. Considering that, the proposed gating system with feeders were implemented. Proposed gating system was tested with numerical calculation using ProCAST software. Casted alloy was AlSi10Mg with pouring temperature 700 °C. The shell was preheated to 200 °C before pouring. The shell thickness used in simulation was 7 mm. On Figure 5 are presented areas where porosity can be expected based on the numerical calculation analysis. The porosity location was outside of the casting when proposed gating system was used. Due to the proposed gating system was approved for final prototype production.

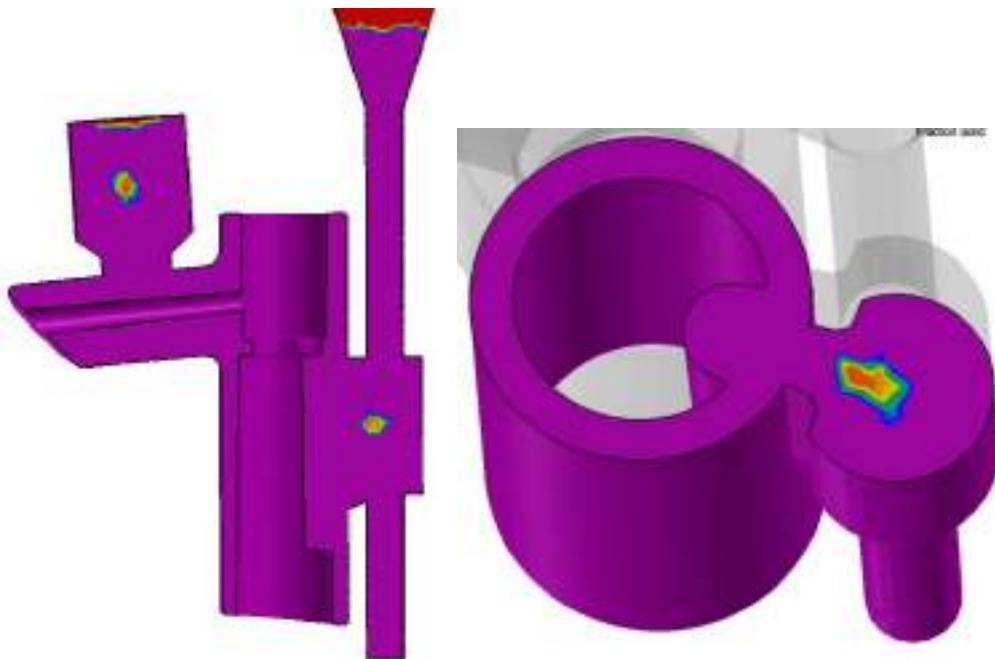


Figure 5. Calculated porosity

For final pattern preparation the gating system and the feeders were printed with same parameters as they were used for printing water tap parts. Assembling PLA parts together was done using a Loctite Super Attak glue which is commonly used for assembling PLA printed parts. When assembling the tree pattern some PLA filaments was added to provide venting of casting cavity. Also, some wax was used to provide additional vent on the feeders. Final assembled pattern is presented on Figure 6.

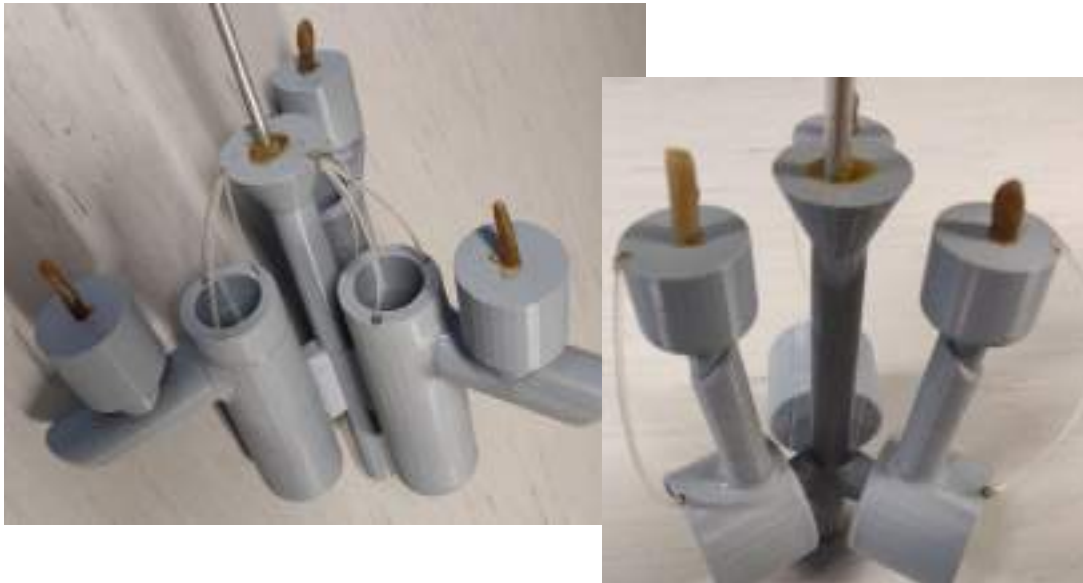


Figure 6. Final model prepared for shelling.

Models were prepared for shelling. Shelling was done using slurry based on fused-silica. Model was dipped into the slurry and then covered with the fused silica sand. First two layers fine sand was used, following four layers the sand was coarser. With six layers the shell wall thickness was between 6 and 10 mm. The drying of each layer was up to a few hours in well ventilated room. After last layer was done, the shells were put into the electric oven, set to 200 °C for two hours to burn out the PLA models. For PLA burn out it is better to use gas furnace so flue gasses can burn out. When PLA burned out the empty shells were transferred into another electric furnace for sintering at 900 °C for another two hours. Finished sintered shells are presented on Figure 7.

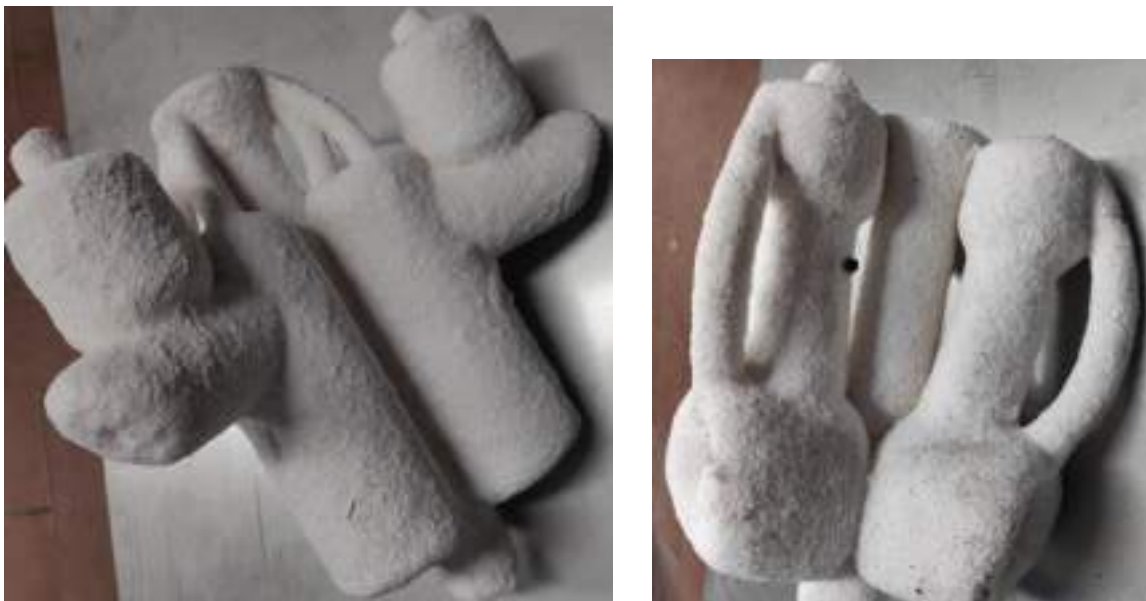


Figure 7. Shells prepared for casting

RESULTS AND DISCUSSION

Aluminum alloy AlSi10Mg was prepared for casting at induction furnace with purring temperature 700 °C and shells heated up to 200 °C. The final castings after the shell was removed are presented on Figure 8.



Figure 8. Casted water tap using 3D printed patterns and investment casting technology

As it can be seen on Figure 8 the surface on casting is exact copy of surface on printed parts from PLA on Figure 6. All the surface details and errors are visible including the printed layers.

The printed surface can be improved with decreasing the layer height – with the used printer the layer height can be 0,07 mm. Also the settings for exporting 3D model from the CAD program was not set proper, due to some surfaces were distorted. Considering this the final casting could be done with higher accuracy in areas where details are required.

The whole process from preparing the model for slicing to final casting took 6 days.

CONCLUSIONS

Prototype casting was done using a 3D printing technology and investment casting process. Final prototype was developed in six days with suitable accuracy. For higher accuracy one should invest more time into model preparation and 3D printing.

REFERENCES

- [1] B. Krizmanić, Tehnologija 3D tiskanaprototipa, diploma thesis, 2018.
- [2] M. Petič, R. Cerc Korošec, M. Vončina, P. Mrvar, S. Kastelic, Suitability of 3D printed polymer patterns for investment casting technology, *Livarskivestnik*, 67/2020 št.1, pp. 43-49.

- [3] T. Rogers, Everything You Need To Know About Polylactic Acid (PLA), Accessible on Internet: <https://www.creativemechanisms.com/blog/learn-about-polylactic-acid-pla-prototypes>, (15.04.2021.)
- [4] I. Shishkovsky, New Trends in 3D Printing, Intech Open, July 2016.



19th INTERNATIONAL FOUNDRYMEN CONFERENCE
Humans - Valuable Resource for Foundry Industry Development

Split, June 16th-18th, 2021

<https://ifc.simet.hr/>

**ANALYSIS OF THE CRACK FORMATION IN ASIS M2 HIGH-SPEED TOOL STEEL
DURING UTILIZATION**

Franjo Kozina^{1*}, Zdenka Zovko Brodarac¹, Ivan Jandrić¹, Renato Jagustović²

¹ University of Zagreb Faculty of Metallurgy, Sisak, Croatia

² DIV GRUPA d.o.o., Samobor, Croatia

Poster presentation

Expert work

Abstract

Tool steels are carbon, alloyed or high-speed steels, produced and processed under the tool steel manufacturing practices to meet special requirements. The advancements in tool steel engineering properties enabled work efficiency improvements in industrial applications. The high-speed tool steels (HSS) are complex iron-based alloys containing carbon, chromium, vanadium, molybdenum, tungsten or substitutional amount of cobalt. The chemical composition of HSS is designed to achieve the highest attainable hardening response, high wear resistance, high resistance to softening effect at elevated temperatures, and good toughness necessary for effective use in industrial cutting operations. The ASIS M2 is a molybdenum-based medium alloyed HSS with good machinability. Favorably designed chemical composition and adequately performed heat treatment assure good combination of toughness, wear resistance and hardness enabling its utilization as twist drills, taps, milling cutters, saws, and knives. It is also commonly used as cold work punches. The research was performed on two samples of ASIS M2 punches to estimate the cause of the shorter service life. In sample 1 the crack nucleation occurred after 50.000 punched marks, while in sample 2 cracking initiated after 20.000 punched marks. To indicate the cause of sample 2 shorter service life, the results of chemical composition analysis, metallographic analysis, and microhardness measurements were compared. The higher amount of carbide forming elements in sample 2 led to the solidification of higher number of eutectic carbides and precipitation of secondary carbides in intercellular regions. The microstructure analysis indicated significantly higher number of carbide particles in sample 2. The presence of carbide particles led to the texture development and impacted crack propagation direction. Higher amount of carbide particles in sample 2 caused higher crack dissipation and material layering with a decrease in crack propagation depth and shorter service life.

Keywords: ASIS M2, high-speed tool steels, cracking, service life, microstructure, carbides

*Corresponding author (e-mail address): fkozin@simet.unizg.hr

INTRODUCTION

The industrial utilization of tool steels with improved engineering properties, such as high-speed tool steels (HSS), enabled work efficiency improvement [1]. Tool steels are carbon, alloyed or high-speed steels, produced and processed under the tool steel manufacturing practices to meet special requirements. This type of steels is used in hand tools or in mechanical fixtures to cut, shape, form, or blank materials at room or elevated temperatures. Based on their final application tool steels can be classified as hot work tool steels, cold work tool steels, plastic mold steels, and HSS [2]. Due to their ability to machine materials at high cutting speeds [3], HSS are commonly used to manufacture broaches, drills, millings, cutters, tool bits, gear cutters, saw blades, jointers and planar blades[4]. The HSS are complex iron-based (Fe) alloys containing carbon (C), chromium (Cr), vanadium (V), molybdenum (Mo), tungsten (W) and in some steel types a substitutional amount of cobalt (Co). The chemical composition is designed to achieve highest attainable hardening response, high wear resistance, high resistance to softening effect at elevated temperatures, and good toughness necessary for effective use in industrial cutting operations[5].The American Iron and Steel Institute (AISI) established an HSS classification system based on chemical composition[6]. That system consists of a letter and numerical designation. The letter designation can be either T or M. The T designation is provided for HSS containing W as one of the primary alloying elements (12 wt.% to 20 wt.% W),while M refers to steels containing higher amounts of Mo (3.4 wt.% to 10 wt.% Mo). The numerical designation is used to distinguish between the classes based on the presence of other major alloying elements [7]. The C, Cr, V and Co are considered to be other major alloying elements in HSS [8]. The M class of HSS has higher absorption resistance, better dimensional stability during heat treatment and are less expensive compared to T class [6].The most important and closely controlled alloying element is C. Although, C content in any type of HSS is fixed within the narrow limits, variations within those limits can cause important changes in the mechanical properties and steel's cutting ability. Increase in C content increases working hardness, elevated temperature hardness, and wear resistance. This increase in mechanical properties, especially hardness, is a consequence of eutectic carbide solidification and precipitation of secondary carbides during heat treatment [6].The MC, M₂C, M₆C and M₇C₃(M refers to the strong carbide forming elements) are coarse and blocky carbides that solidify during eutectic reaction[9]. The solidification of austenite (γ_{Fe}) and eutectic carbides is a consequence of reduced solid solubility of C in ferrite (α_{Fe}) solid solution. While MC type of eutectic carbides mostly solidifies inside the solidification cells, the M₂C, M₆C and M₇C₃ form network in the intercellular regions[10]. The secondary carbides precipitate because of the eutectic carbide decomposition during heat treatment. Decomposition of eutectic M₂C carbide comprehends peritectoid and eutectoid precipitation of MC and M₆C secondary carbides[11]. While the primary function of eutectic carbides is to increase the wear resistance, secondary carbides improve strength at elevated temperatures. However, the thermal fatigue and fracture toughness cannot be influenced by eutectic to secondary carbide decomposition because MC and M₆C carbides retain M₂C eutectic carbide morphology. The W, Mo and V are strong carbide forming elements [12]. In all T types of HSS W is the major alloying element, and it is present in all M types of HSS as auxiliary element, except in M10 with regular or high C content. By forming hard complex W₂C, Fe₃W₃C and Fe₄W₂C carbides[13], W contributes to wear resistance, elevated temperature hardness and causes secondary hardening [14]. The M types of steels with higher Mo content have lower

melting points and require lower hardening temperatures. Consequently, they have more narrow hardening range compared to T types of HSS. Like W, the Mo forms simple Mo_2C [15] and complex $\text{Mo}_3\text{Fe}_3\text{C}$ and $\text{Mo}_4\text{Fe}_2\text{C}$ carbides [16]. Since the Mo ($A_r(\text{Mo}) = 95.939 \text{ g/mol}$ [17]) has half atomic weight of W ($A_r(\text{W}) = 183.85 \text{ g/mol}$ [18]), the preferred formation of Mo-based carbides is expected. Therefore, the M types of HSS have higher toughness and lower elevated temperature hardness. The improvement in elevated temperature stability can be addressed through the additions of W or V [6]. The V additions promote the formation of very hard, stable VC carbides [19] that increase wear resistance and elevated temperature hardness[6].The object of heat treatment is to transform a fully annealed HSS microstructure consisting of α_{Fe} and eutectic M_xC_y carbides into a hardened and tempered martensitic microstructure (α_{Fe}') containing secondary carbides that provide required properties. The HSS heat treatment can be divided into preheating, austenitizing, quenching and tempering. The preheating reduces thermal shock, carburization/decarburization and increases productivity with no direct influence on hardening reactions. The austenitizing is the second step in HSS heat treatment enabling dissolution of eutectic carbides and property development [20]. The eutectic carbide dissolution occurs at the temperatures between $1150 \text{ }^\circ\text{C}$ and $1290 \text{ }^\circ\text{C}$ with a holding time of 2 min to 6 min, depending upon HSS type, tool configuration and cross-section size[6]. The quenching or rapid cooling is designed to transform γ_{Fe} into a hard α_{Fe}' microstructure. The cooling rate is dictated by the type of steel and is strictly controlled. After quenching steel is in a highly stressed condition and susceptible to cracking [21]. To relieve stress, increase toughness and provide secondary hardening the HSS is tempered. The tempering involves reheating the steel to an intermediate temperature (below the critical transformation temperature), soaking and air cooling. The secondary hardening is obtained by the transformation of retained γ_{Fe} into α_{Fe}' and precipitation of complex secondary carbides. This subsequent transformation and precipitation require multiple tempering procedures specific to a particular HSS type [22]. The heat treatment of ASIS M2 with regular C comprehends preheating at the temperatures between $732 \text{ }^\circ\text{C}$ and $843 \text{ }^\circ\text{C}$ followed by austenitization at $1227 \text{ }^\circ\text{C}$. The austenitization of ASIS M2 with high C is performed at lower temperature ($1216 \text{ }^\circ\text{C}$). The ASIS M2 can be tempered at $538 \text{ }^\circ\text{C}$ or $552 \text{ }^\circ\text{C}$. If the ASIS M2 is tempered at $538 \text{ }^\circ\text{C}$ the tempering needs to be repeated four times with a soaking time of 2 h. Tempering at $552 \text{ }^\circ\text{C}$ is repeated two times with a soaking time of 2h [7].

The goal of this paper is to analyze the cause of the crack formation in ASIS M2 high speed tool steel punchers during utilization. The research was performed on two samples (sample 1 and sample 2). The crack formation in sample 1 was observed after 50.000 punched marks. Contrary, in sample 2 the cracks initiated after only 20.000 punched marks. By comparing the results of chemical composition analysis, metallographic analysis, and microhardness measurements the cause of the sample 2 shorter service life was indicated.

MATERIALS AND METHODS

The chemical composition of the ASIS M2 samples was determined spectroscopically using Optical emission spectrometer Analytical Instruments Group (GNR) S7 metal Lab Plus (MLP).The chemical composition of ASIS M2 HSS according to ASTM A 600 – 92a is given in Table 1.

Table 1. The Chemical composition of HSS M2 according to ASTM A 600 – 92a, wt.% [7]

HSS		C	Mn	P	S	Si	Cr	V	W	Mo	Co
M2 regular C	min	0.78	0.15	/	/	0.20	3.75	1.75	5.50	4.50	/
	max	0.88	0.40	0.03	0.03	0.45	4.50	2.20	6.75	5.50	/
M2 high C	min	0.95	0.15	/	/	0.20	3.75	1.75	5.50	4.50	/
	max	1.05	0.40	0.03	0.03	0.45	4.50	2.20	6.75	5.50	/

Based on the chemical composition ASIS M2 is divided into two subcategories: ASIS M2 with regular C (0.78 wt.% - 0.88 wt.% C) and ASIS M2 with high C (0.95 wt.% - 1.05 wt.% C) (Table 1). The difference in the content of other alloying elements cannot be observed (Table 1).

The metallographic analysis was performed to determine macrostructure and microstructure of the samples in polished and etched conditions. The metallographic analysis in polished condition was performed to assess the crack nucleation and progression as well as the occurrence of additional defects in the samples of HSS. The macrostructure analysis in the etched condition was used to indicate the influence of tool production and heat treatment on the structure development, while the microstructure analysis enabled phase identification and homogeneity assessment of the affected area.

The sampling for metallographic analysis is given in Figure 1.



Figure 1. Sampling for metallographic analysis: a) sample 1, b) sample 2

In both samples' cracks can be observed on the tools' surface at the sharp transition between the outer edge and the contact surface (Figure 1). When marking the screw, the outer edge of the tool serves to position and hold the screw while the contact surface marks the screw's head. Cracks in sample 1 occurred after 50.000 punched marks while in sample 2 they occurred after 20.000 punched marks.

The sampling was performed perpendicular to the cracks' propagation direction (Figure 1). The samples were etched after standard metallographic preparation comprehending grinding and polishing. Two different solutions were used for etching:

1. The 2% Nital (the 2 % solution of nitric acid (HNO₃) in ethyl alcohol (C₂H₅OH))
2. The Marshall's reagent consisting of two different solutions:
 - a. Solution containing 5 ml of sulfuric acid (H₂SO₄), 8 g of oxalic acid (C₂H₂O₄) and 100 ml of water (H₂O)
 - b. 30 % aqueous solution of hydrogen peroxide (H₂O₂).

The 2 % Nital was used as a general-purpose etchant for macrostructure and microstructure analysis. The Marshall's reagent is obtained by mixing equal parts of solution a and b immediately before etching. The Marshall's reagent was used for qualitative and quantitative phase analysis. The qualitative analysis comprehended the phase identification based on coloring. The quantitative analysis involved determining the amount of the identified phases and the phase classification with concerning the particle size. The identified phases were distributed into 5 classes: Class 1 (0.5-4.40 μm²), Class 2 (4.40-8.30 μm²), Class 3 (8.30-12.20 μm²), Class 4 (12.20-16.10 μm²), Class 5 (16.10-20.0 μm²). Besides phase analysis, the Marshall's etching solution enabled observation of the apparent austenitic grain boundaries in the martensitic matrix. The austenitic grain size was measured using the Linear intercept method according to ASTM E 112-10. The Linear intercept method implies drawing the reference line with the length (L) and counting the cross-section of the line and the grain boundaries (P_i). The line is drawn so that a single grain is intersected only once. After calculating the number of intersections per mm of the reference line (P_L), the apparent size of the austenitic grain (G) is determined based on the equation 1:

$$G = - 3.2877 + 6.6439 \log_{10} P_L \quad (1)$$

Where G is the ASTM grain size number and – 3.2877 and 6.6439 are constants relating P_L and magnification to G.

The macrostructure analysis of the samples was performed on the Olympus SZ11 stereo microscope equipped with a Promicra digital camera and the Quick PHOTO CAMERA 3.1 image processing software. Microstructure analysis was performed on the Olympus BX51 inverted metallographic microscope equipped with a DP70 digital camera and the AnalySIS Materials Research Labsoftware.

The microhardness measurements were performed after metallographic analysis. The microhardness was measured in the area of the defect and in non-affected area of the samples 1 and 2. The Vickers method with a load of 9.81 N on a Leica VMHT device was used to measure the microhardness.

RESULTS AND DISCUSSION

Results of chemical composition analysis

The results of chemical composition analysis are given in Table 2.

Table 2. The chemical composition of the samples 1 and 2

Sample	C	Mn	P	S	Si	Cr	V	W	Mo	Co	Fe
1	0.864	0.305	0.022	<0.001	0.235	4.076	1.697	6.295	4.890	0.640	Balance
2	0.855	0.349	0.029	0.002	0.434	4.374	1.841	6.618	5.245	0.727	Balance

The chemical composition of both samples (Table 2) is in accordance with ASTM A 600 – 92a Standard Specification for Tool Steel High Speed (Table 1). Based on the slightly higher C content, better hardenability of sample 1 is expected (Table 2). The higher amount of carbide forming elements suggests higher share of carbides in sample 2 (Table 2).

Results of macrostructure analysis

The macrostructure of the sample 1 in polished and etched condition is given in Figure 2 a and b. The details for subsequent microstructure analysis in polished end etched conditions are indicated in Figure 2 a.

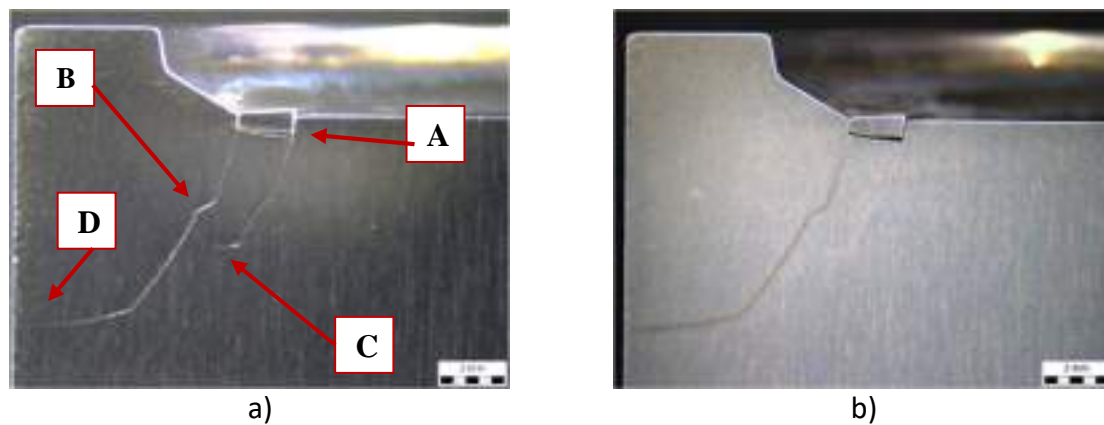


Figure 2. Macrostructure of the sample 1 in: a) polished condition with indicated details (A, b, C, and D) for subsequent microstructure analysis, b) etched condition

Two cracks are present in the macrostructure of the sample 1. Cracks initiate on the surface at the sharp transition between the outer edge and the contact surface of the tool (Figure 2). The cracks propagate perpendicular to the contact surface to a depth of 6.43 mm (Figure 2, crack left) and 4.14 mm (Figure 2, crack right). After that, the cracks change direction and progress parallel to the contact surface. The crack to the left propagates outside of the tool (Figure 2 a). In the area between the cracks, the surface layer is separated (Figure 2). After etching the texture can be observed in the macrostructure of the sample 1. The texture is perpendicular to the surface of the tool (Figure 2 b). Although the structure is not homogeneous, no significant difference between the surface and central part of the tool can be observed (Figure 2 b).

The *Multiple Image Alignment* (MIA) of the sample 1 in polished and etched condition is given in Figure 3.

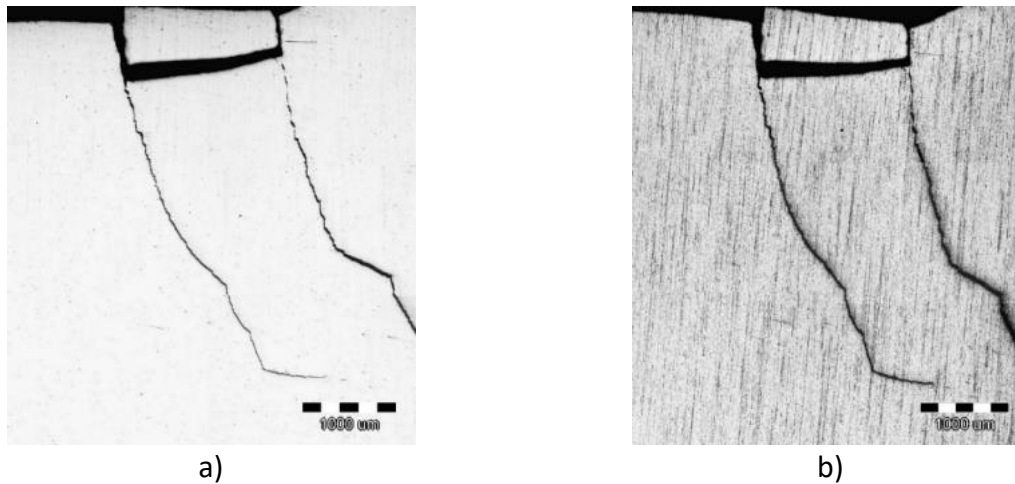


Figure 3. The MIA of the sample 1 in: a) polished, b) etched condition

Apart from the cracks and the separation of the surface layer between the cracks, there are no other visible defects present in the macrostructure of the polished sample (Figure 3 a). After etching, the texture can be observed in the microstructure of the sample 1 affecting the crack propagation direction. The texture affects the crack propagation direction. No other heterogeneities of macrostructure can be detected in the macrostructure of the area of the defect (Figure 3 b).

The macrostructure of the sample 2 in polished and etched condition with indicated details for subsequent microstructure analysis are given in Figure 4.

Three cracks can be seen in the macrostructure of sample 2. Cracks nucleate at the marking grooves of the contact surface. The cracks progress perpendicular to the tool's contact surface to a depth of 3.21 mm (crack left) and 3.24 mm (crack right), respectively. After that, the cracks change direction and progress parallel to the contact surface (Figure 4 a). The cracks on the left at a depth of 1.75 mm merge into one crack and propagate towards the center of the tool (Figure 4 a). At the depth of 3.67 mm crack on the right and crack on the left merge and propagate parallel to the contact surface of the tool (Figure 4 a). After etching the texture can be observed in the macrostructure of the sample 2. The texture is perpendicular to the surface of the tool (Figure 4 b).

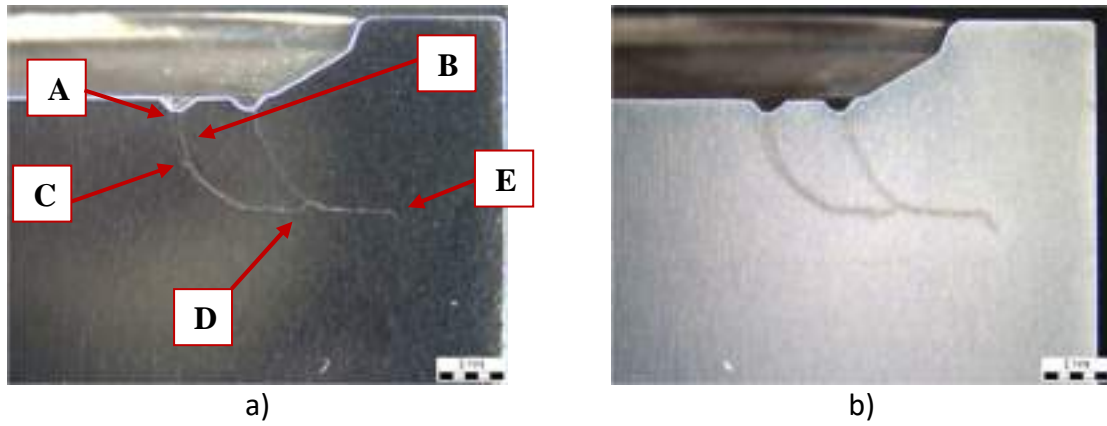


Figure 4. Macrostructure of the sample 2 in: a) polished condition with indicated details for subsequent microstructure analysis, b) etched condition

The MIA of sample 2 in polished and etched condition is given in Figure 5.

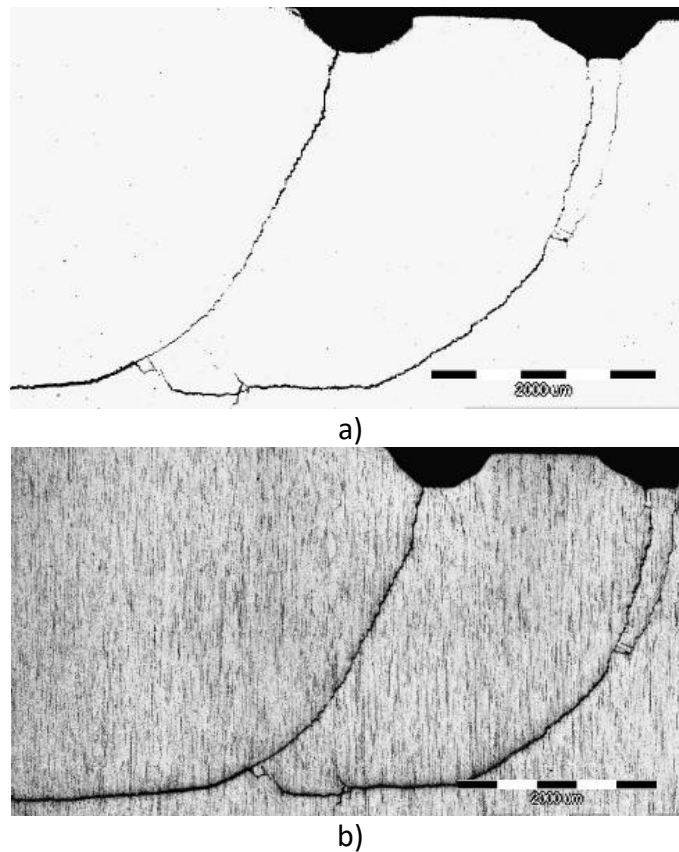


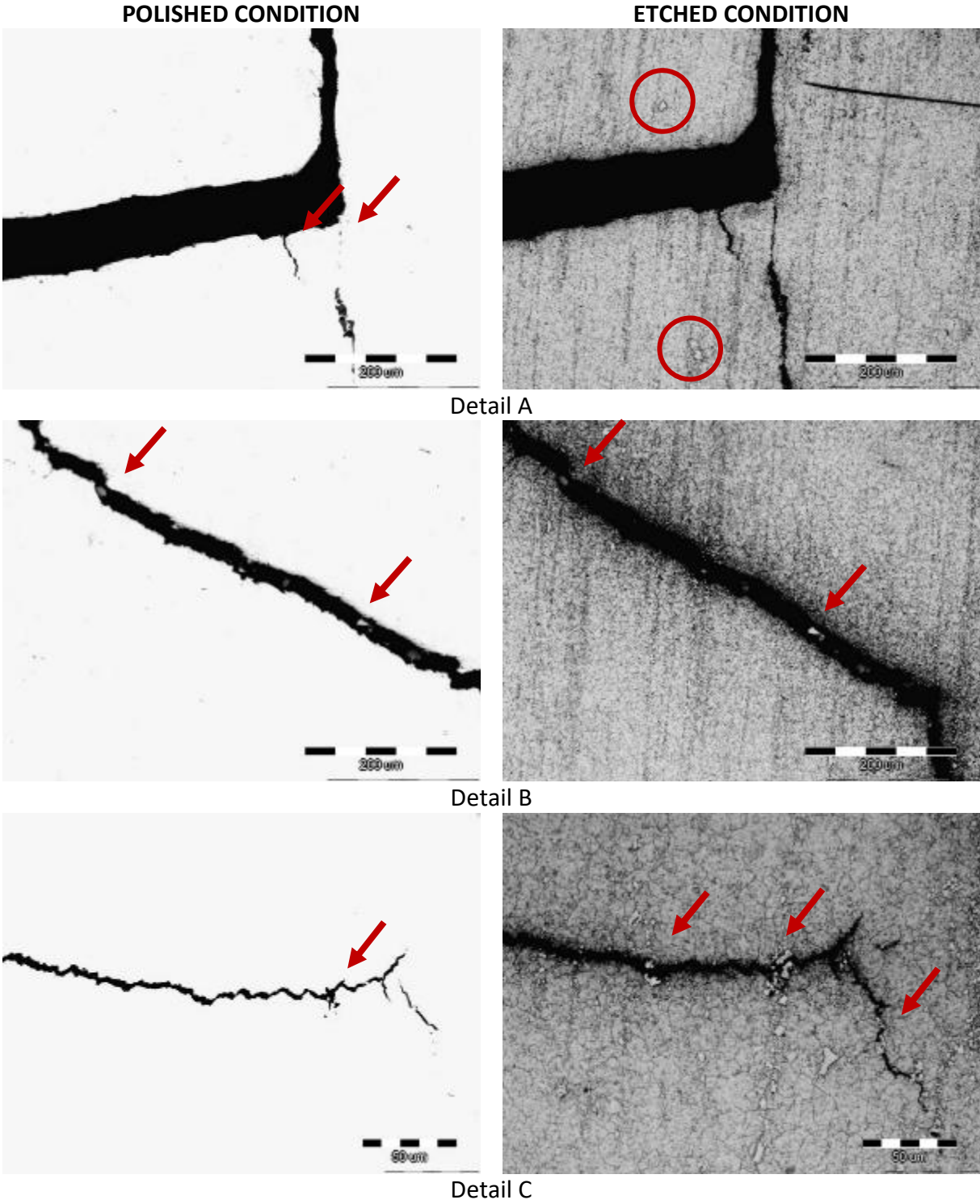
Figure 5. The MIA of the sample 2 in: a) polished, b) etched condition

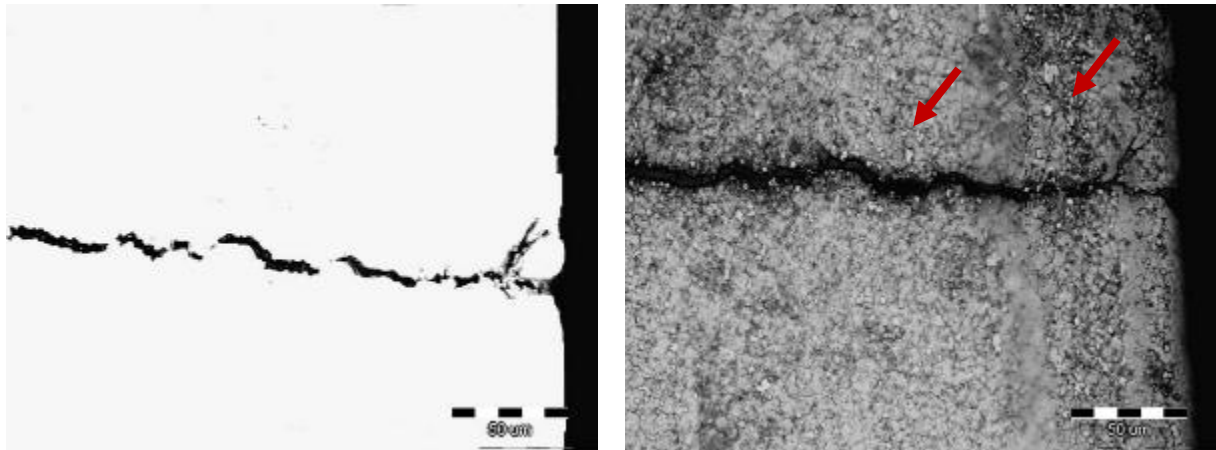
In contrary to the sample 1, the cracks in sample 2 show a greater tendency towards branching and material layering (Figure 5 a). Due to the energy dissipation, the crack propagation in the sample 2 is not as deep as in sample 1. Apart from the crack, there are no other visible defects in the macrostructure of sample 2. Etching of the sample revealed a

texture affecting the crack propagation direction. No other heterogeneities are observed in the macrostructure of the sample 2 (Figure 5 b).

Results of microstructure analysis

The microstructure of the sample 1 in polished and etched conditions is shown in Figure 6. The details for microstructure analysis were indicated in Figure 2 a.



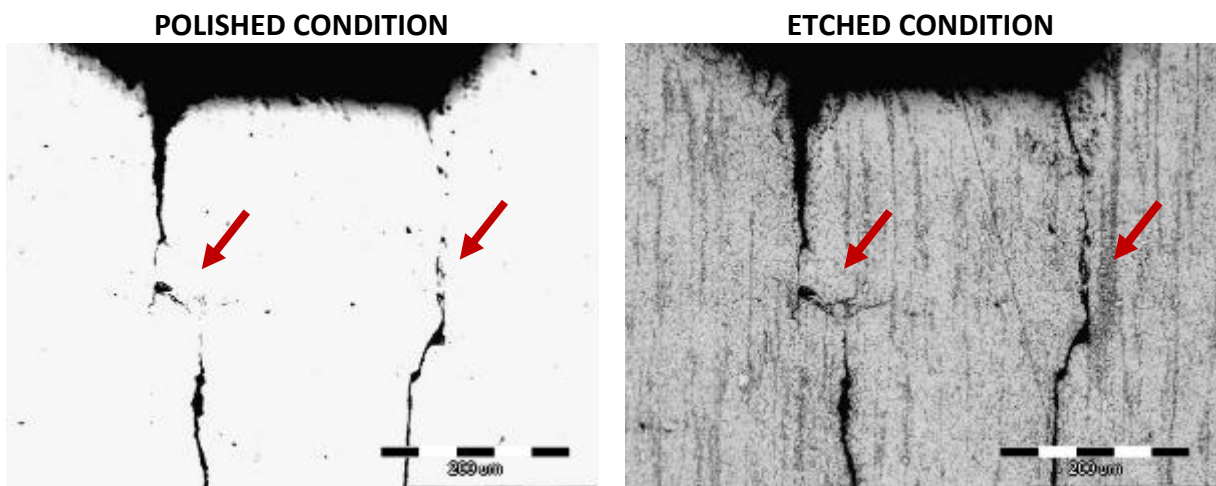


Detail D

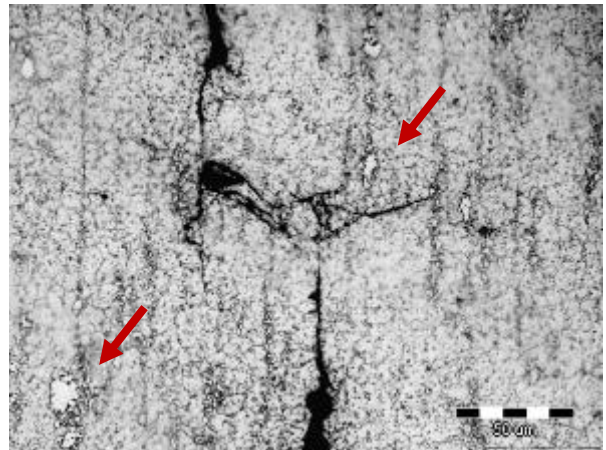
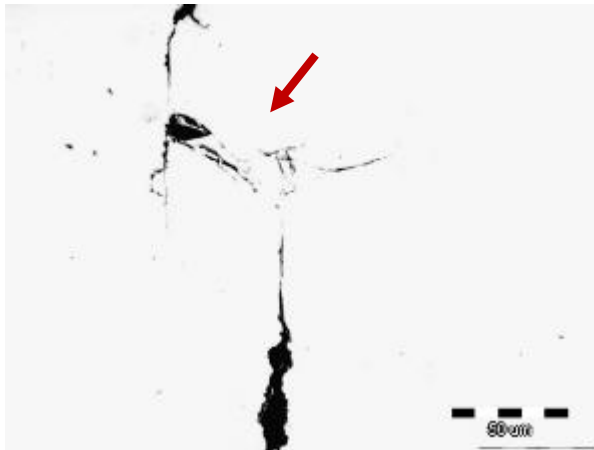
Figure 6. Microstructure of sample 1 in the area of the defect

The branching of the cracks occurs in the area of the surface layer separation. The crack branches propagate perpendicular to the work surface of the sample (Figure 6 detail A, polished condition). The matrix is martensitic with the particles located in the intercellular regions (Figure 6, etched condition). Besides particles with fine morphology, coarse particles are also present in the microstructure of sample 1. The nucleation and growth of these particles is associated with texture formation (Figure 6, etched condition). These particles can be observed near (Figure 6 detail A, etched condition) and inside the cracks (Figure 6 details B, C, D, polished and etched condition) influencing their propagation direction. The presence of the particles inside the cracks indicates intercrystal crack propagation (Figure 6).

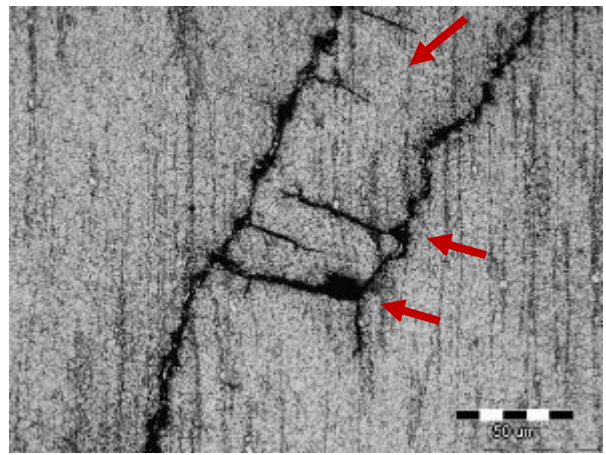
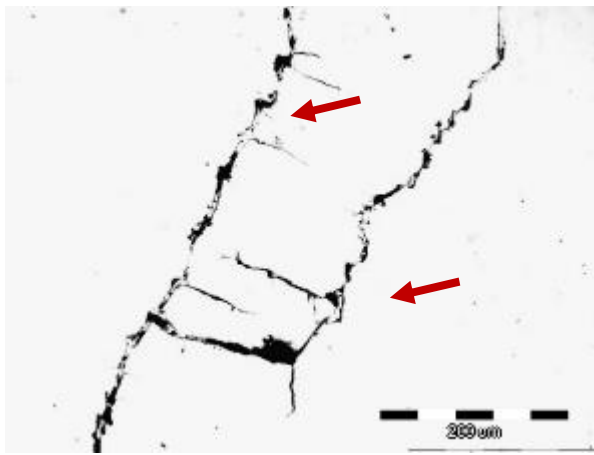
The microstructure of the sample 2 in polished and etched condition is shown in Figure 7. The details for microstructure analysis are indicated in Figure 4 a.



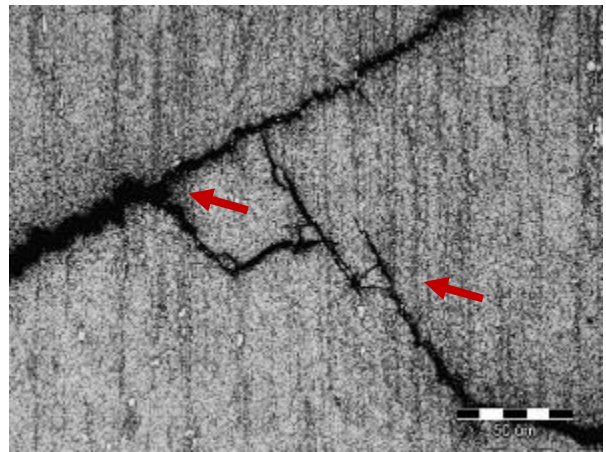
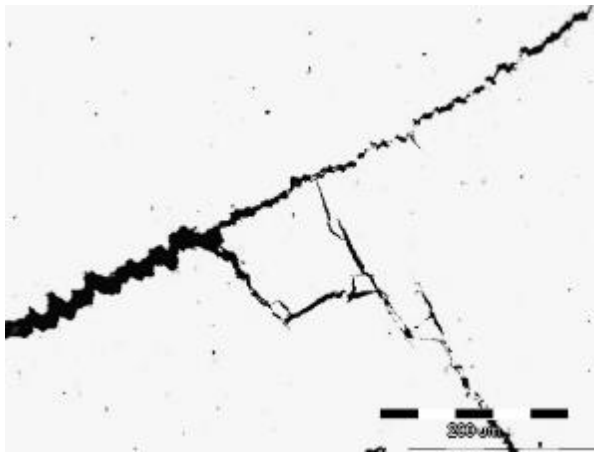
Detail A



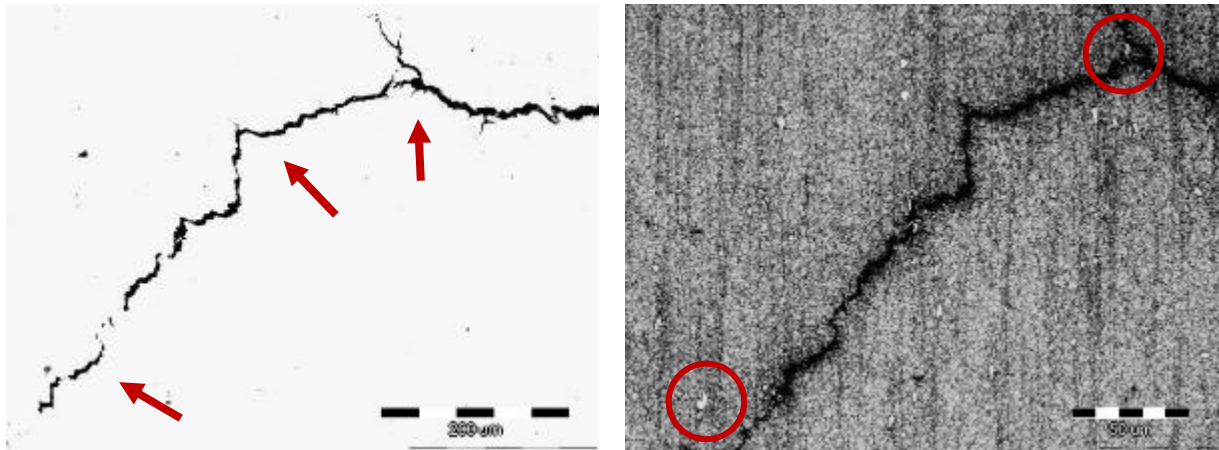
Detail B



Detail C



Detail D

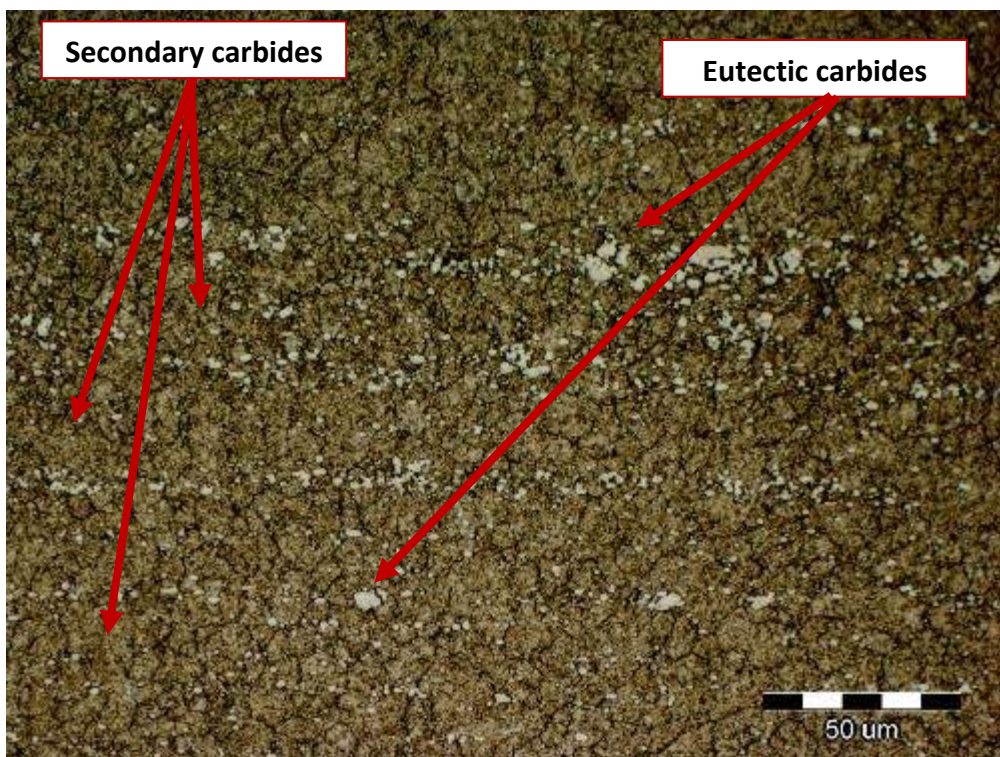


Detalj E

Figure 7. Microstructure of sample 2 in the details indicated in Figure 4 a

In sample 2, the crack nucleates at the work surface of the tool and progresses parallel to the texture direction. The material layering and cavity formation can be observed near the surface of the sample (Figure 7, polished condition). In this area, the existing crack dissipates followed by the nucleation of new cracks. The matrix of sample 2 is martensitic with fine particles located in the intercellular regions (Figure 7, etched condition). The nucleation and growth of coarse particles is connected to the texture development. In contrast to sample 1, cracks in sample 2 show a greater tendency towards branch and material layering (Figure 7 detail C, D, E, polished state). Initial cracks and branches of initial cracks propagate through the grain boundaries (Fig. 8 detail C, D, E, corroded state).

The microstructure of the sample 1 and 2 after etching with Marshall's etching solution is given in Figure 8.



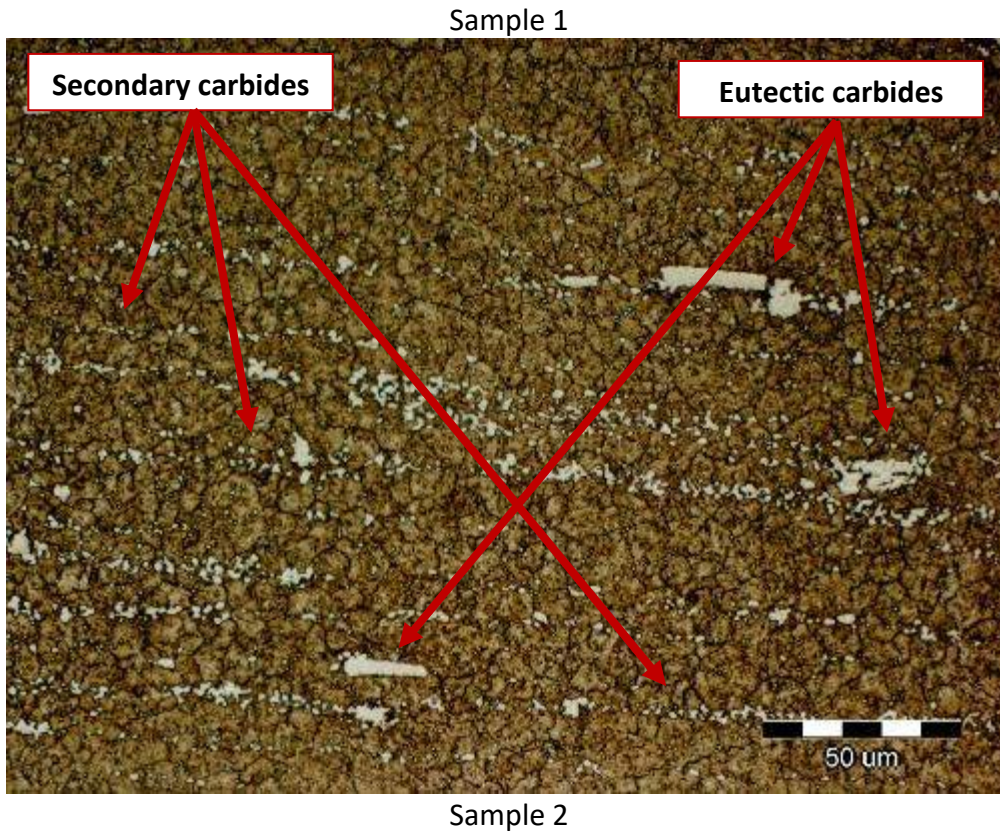


Figure 8. The microstructure of sample 1 and 2 after etching with Marshall's etching solution.

The use of Marshall's etching solution enabled identification of coarse particles as eutectic carbides. The fine particles precipitated at the apparent austenite grain boundaries are secondary carbides. Both primary and secondary carbides have preferred orientations (Figure 8). The matrix of both samples is martensitic with indicated apparent austenite grain boundaries (Figure 8.). The results of quantitative carbide particle analysis, performed on five different micrographs, are shown in Table 3.

Table 3. The amount of carbide particles in the microstructure of sample 1 and 2

Sample	Content of carbide particles, %		
	Number of measurements	Mid value, %	Standard deviation
1	5	7.90	1.21
2		12.93	6.51

The amount of carbide particles is higher in sample 2 (12.93 %) compared to sample 1 (7.90 %). In table 4 the carbide particles are classified with respect to the particle size.

Table 4. The classification of particles with respect to the particle size

Particle class	Sample 1			Sample 2		
	Number of particles	Total surface, μm^2	The share of particle class in the total number of particles	Number of particles	Total surface, μm^2	The share of particle class in the total number of particles
1	901	1052.78	0.95	1108	1556.13	0.91
2	41	227.85	0.04	76	451.90	0.06
3	4	40.02	0.004	25	246.04	0.02
4	0	0.00	0.00	10	134.28	0.008
5	0	0.00	0.00	5	87.41	0.005

The total area of detected particles is significantly higher in sample 2 ($2476.76 \mu\text{m}^2$) compared to sample 1 ($1320.65 \mu\text{m}^2$). The area occupied by particles of individual classes is also higher in sample 2 (Table 4). The 946 particles with a total surface area of $1320.65 \mu\text{m}^2$ were detected in sample 1. From the total number of detected particles, most of them were distributed in the first class (901 particles) with an area less than $4.40 \mu\text{m}^2$. In the second class ($4.40\text{-}8.30 \mu\text{m}^2$) 41 particles were distributed, and in the third class (area $8.30 - 12.20 \mu\text{m}^2$) only 4 particles. The particles from the fourth and fifth particle classes were not detected (Table 4). In sample 2 the 1224 particles with a total area of $2476.76 \mu\text{m}^2$ were detected. Of the total number of detected particles, 1108 were distributed in the first class. The 76 particles were distributed in the second class, 25 particles in the third class, 10 particles in the fourth class and 5 particles in the fifth class (Table 4).

The average particle size was calculated by dividing the total area occupied by particles of each class by the number of detected particles. The sample 1 has the largest amount of first class particles (0.95) with an average particle size of $1.2 \mu\text{m}^2$. The amount of larger class particles (classes between 2 and 5) is significantly lower. The amount of second class particles is 0.04 with an average particle size of $5.6 \mu\text{m}^2$, while the amount of third class particles is 0.004 with an average particle size of $10.0 \mu\text{m}^2$. The highest proportion of first class particles (0.91) with an average particle size of $1.4 \mu\text{m}^2$ was also detected in sample 2. The amount of larger particle class (classes between 2 and 5) is higher compared to sample 1. The amount of second-class particles is 0.06, and the average particle size is $5.9 \mu\text{m}^2$. The average particle size of the third class is $9.8 \mu\text{m}^2$ and the amount is 0.02. The amount of fourth grade particles with an average size of $13.4 \mu\text{m}^2$ is 0.008, while the amount of fifth grade particles is 0.005 and the average size is $17.5 \mu\text{m}^2$.

The results of the apparent austenitic grain size are given in Table 5.

Table 5. The apparent austenite grain size of the samples 1 and 2 according to ASTM E 112-10

Sample	Length of the reference line (L), mm	Number of intersects (P_i)	Average grain size, μm^2	Apparent austenite grain size (G) number
1	265,9	75	0.224	9
2	345,3	55	0.184	9

The results of the grain size measurements indicate that both samples have fine grade microstructure with the G of 9. The sample 1 has slightly higher grain size (0.224 μm^2) compared to sample 2 (0.184 μm^2).

The results of microhardness measurements

The results of microhardness measurements of samples 1 and 2 are given in Table 6.

Table 6. The results of microhardness measurements

Sample	Number of measurements	Microhardness, HV			
		The area of the defect		Non-affected area	
		Mid value, HV	Standard deviation	Mid value, HV	Standard deviation
1	3	696.6	9.99	700.1	8.35
2		741.1	1.76	741.2	2.8

In sample 1 higher hardness was measured in the non-affected area (700.1 HV) in relation to the area of the defect (696.6 HV), while in sample 2 almost the same value of hardness was measured in the area of the defect (741.1 HV) and non-affected area (741.2 HV). At both measurement locations, the microhardness of sample 2 is higher compared to the microhardness of sample 1. The higher microhardness of sample 2 is a consequence of higher amount of carbide particles.

CONCLUSIONS

The research was performed on two samples of ASIS M2 high-speed tool steel punchers to estimate the cause of the shorter service life of sample 2 compared to sample 1. The cracking occurred after 50.000 punched marks (sample 1) and 20.000 punched marks (sample 2).

The results of chemical composition analysis, metallographic analysis and microhardness measurements led to the following conclusions:

The higher amount of carbide forming elements in sample 2 led to the solidification of higher number of eutectic carbides and precipitation of secondary carbides in intercellular regions. The quantitative microstructure analysis indicated significantly higher number of carbide particles in sample 2 (2476.76 μm^2) compared to the sample 1 (1320.65 μm^2). The area occupied by carbide particles of individual particle classes is also higher in sample 2. The presence of carbide particles led to the texture development. Since texture orientation is perpendicular to the work surface of the samples, it influenced crack propagation direction. Higher amount of carbide particles in sample 2 caused higher crack dissipation and material layering with a decrease in crack propagation depth.

Acknowledgments

The investigation was performed within the research topic “Design and Characterization of Innovative Engineering Alloys”, Code: FPI-124- 2019-ZZB funded by University of Zagreb within the Framework of Financial Support of Research, scientific-research project within Croatian-Slovenian collaboration “Design and Characterization of Innovative Aluminum - Magnesium - Lithium alloy” (2018-2019) funded by Ministry of Science and Education and Infrastructural scientific projects: Center for Foundry Technology, Code: KK.01.1.1.02.0020 and VIRTULAB - Integrated Laboratory for Primary and Secondary Raw Materials, Code: KK.01.1.1.02.0022 funded by European Regional Development Fund, Operational Programme Competitiveness and Cohesion 2014 - 2020.

Personal gratitude to colleagues from DIV GRUPA d.o.o. for the given samples and enabled publication of the analysis results.

REFERENCES

- [1] M. Cabibbo, N. Clemente, F. Musharavati, S. Spigarelli, Thermal plasticity index of nanostructured N-based coatings on HSS 6-5-2 (1.3343) tool steel, *Material Science Forum*, 879(2017), pp. 262-267, 2017.
- [2] R. Agnelli Mesquita, *Tool Steels: Properties and Performance*, CRC Press, Boca Raton, 2016.
- [3] P. L. C. Serra, R. R. M. Sousa, J. R. Barros Neto, M. S. Libório, M. C. Feitor, T. H. C. Costa, Application of nitriding and duplex treatment on steel drills-HSS, *J Journal of Multidisciplinary Engineering Science*, 7(2020)4, pp. 11699-11708.
- [4] S. Kalyanakumar, C. Munikumar, S. Govind Nair, S. Shaju, Application of multi response optimization of drilling setting main process parameter using VIKOR approach, *Materials Today: Proceedings.*, In press(2020).
- [5] J. Jiang, W. Bao, Z. Y. Peng, X. H. Dai, Creep Property of TMCP High-Strength Steel Q690CFD at Elevated Temperatures, *Journal of Materials in Civil Engineering*, 32(2020)2.
- [6] A. M. Bayer, B. A. Becherer, T. Vasco, *Bulletin: High Speed Tool Steels, Latrobe Specialty Steel*, 16(1989), pp. 10-11.
- [7] ASTM A 600 - 92a (Reapproved 2004), *Standard Specification for Tool Steel High Speed*.
- [8] P. Jovicevic-Klug, B. Podgornik, Comparative study of conventional and deep cryogenic treatment of AISI M3:2 (EN 1.3395) high-speed steel, *Journal of Materials Research and Technology*, 9(2020)6, pp. 13118-13127.
- [9] M. M. Serna, E. R. B. Jesus, E. Galego, L. G. Martinez, H. P. S. Corrêa, J. L. Rossi, An Overview of the Microstructures Present in High-Speed Steel -Carbides Crystallography, *Materials Science Forum*, 530–531(2006), pp. 48-52.
- [10] T. Maurizi Enrici, A. Mertens, M. Sinnaeve, J. T. Tchuindjang, Elucidation of the solidification sequence of a complex graphitic HSS alloy under a combined approach of DTA and EBSD analyses, *Journal of Thermal Analysis and Calorimetry.*, 141(2020)3, pp. 1075-1089.
- [11] K. C. Hwang, S. Lee, H. C. Lee, Effects of alloying elements on microstructure and fracture properties of cast high speed steel rolls part I: Microstructural analysis, *Materials Science and Engineering: A*, 254(1998)1-2, pp. 282-295.
- [12] Y. Luan, N. Song, Y. Bai, X. Kang, D. Li, Effect of solidification rate on the morphology

- and distribution of eutectic carbides in centrifugal casting high-speed steel rolls, *Journal of Materials Processing Technology*, 210(2010)3, pp. 536-541.
- [13] M. Madej, High speed steel based composites with iron additions, *Kovové Materiály*, 50(2012)4, pp. 235-241, 2012.
- [14] T. Kivak U. Şeker, Effect of cryogenic treatment applied to M42 HSS drills on the machinability of Ti-6Al-4V alloy, *Materials and Technology*, 49(2015)6, pp. 949-956.
- [15] Y. Luan, N. Song, X. Kang, D. Li, A study of the carbides in high-speed steel rolls, *Materials Science Forum*, 638-642(2010)January, pp. 3356-3361.
- [16] D. W. Hetzner, W. Van Geertruyden, Crystallography and metallography of carbides in high alloy steels, *Materials Characterization*, 59(2008)7, pp. 825-841.
- [17] Atomic Weight of Molybdenum | Commission on Isotopic Abundances and Atomic Weights." <https://ciaaw.org/molybdenum.htm> (accessed Apr. 07, 2021).
- [18] Atomic Weight of Tungsten | Commission on Isotopic Abundances and Atomic Weights." <https://ciaaw.org/tungsten.htm> (accessed Apr. 07, 2021).
- [19] J. Tchoufang Tchuindjang, M. Sinnaeve, J. Lecomte-Beckers, Influence of High Temperature Heat Treatment on in situ Transformation of Mo-rich Eutectic Carbides in HSS and Semi-HSS Grades, *Proceedings of the international conference Abrasion 2011*, (J. Lecomte-Beckers, J. T. Tchuindjang), ULg-Service MMS, 21.-24.8., 2011, Liege, Belgium
- [20] A. Çiçek, T. Kivak, E. Ekici, Optimization of drilling parameters using Taguchi technique and response surface methodology (RSM) in drilling of AISI 304 steel with cryogenically treated HSS drills, *Journal of Intelligent Manufacturing*, 26(2015)2, pp. 295-305.
- [21] M. Kuřík, J. Lacza, T. Vlach, J. Sobotová, Study of the properties and structure of selected tool steels for cold work depending on the parameters of heat treatment, *Materials and Technology*, 51(2017)4, pp. 585-589.
- [22] S. A Afolalu, O. P. Abioye, E. Y. Salawu, I. P. Okokpujie, A. A Abioye, O. A. Omotosho, O.O. Ajayi Impact of heat treatment on HSS cutting tool (ASTM A600) and its behaviour during machining of mild steel (ASTM A36), *AIP Conference Proceedings*, (P. L. Verma, V. B. Tungikar and Y. J. Bhalerao), 5-6 July, 2018, Maharashtra, India



19th INTERNATIONAL FOUNDRYMEN CONFERENCE
Humans - Valuable Resource for Foundry Industry Development
Split, June 16th-18th, 2021
<https://ifc.simet.hr/>

MICROSTRUCTURE AND MICROHARDNESS OF Cu-Al-Mn-Zr ALLOYS BEFORE AND AFTER HEAT TREATMENT

Stjepan Kožuh^{1*}, Ivana Ivanić¹, Semir Oraščanin², Aleš Nagode³, Ladislav Vrsalović⁴

¹ University of Zagreb Faculty of Metallurgy, Sisak, Croatia

² Student at University of Zagreb Faculty of Metallurgy, Sisak, Croatia

³ University of Ljubljana Faculty of Natural Sciences and Engineering, Ljubljana, Slovenia

⁴ University of Split Faculty of Chemistry and Technology, Split, Croatia

Poster presentation
Original scientific paper

Abstract

In this work preliminary results of the heat treatment effect on microstructure and microhardness of Cu-8.5Al-10Mn-(0.25-1.00)Zr alloys were presented. Ingots (8 mm in diameter and 15 mm in length) were produced by melting and casting process. Production of investigated alloys was performed in laboratory electric arc furnace. Melting was carried out using the heat produced by electric arc and by a water-cooled, specially constructed copper anode that also served as a casting mould. The samples were analysed in as-cast state and after heat treatment at 900 °C/15 min/water. Microstructural analysis was performed by optical microscopy (OM), scanning electron microscopy (SEM) equipped by device for energy dispersive spectroscopy (EDS). Preliminary optical microscopy analysis of investigated alloys confirmed that microstructure was consisted of martensite only in Cu-8.5Al-10Mn-0.25Zr alloy in as-cast and heat treated state. SEM analysis show the start of martensite formation in some places at all investigated alloys in both, as-cast and heat treated state. A microhardness measurement was performed by Vickers method. Microhardness values of Cu-8.5Al-10Mn-(0.25-1.00)Zr alloys were up to 215.8 HV1 after casting and up to 224.5 HV1 after heat treatment.

Keywords: *Cu-Al-Mn-Zr alloy, microstructure, heat treatment, microhardness*

*Corresponding author (e-mail address): kozuh@simet.unizg.hr

INTRODUCTION

Shape memory alloys (SMA) can be categorized in a group of functional and smart materials which characterized the property of remembering the shape they had before pseudoplastic deformation. Primarily, shape memory properties are functions of microstructures i.e. grain size, texture and presence of precipitates. The presence of martensitic phase as main microstructural constituent is absolutely necessary at shape memory alloys. The martensitic

transformation exhibited from β phase during the cooling process of shape memory alloys and this alloys can contained two types of thermal induced martensites, β_1' and γ_1' respectively. Martensites which will be formed depending on alloy composition and heat treatment [1].

Shape memory alloys on Cu-base are commercially attractive mainly for their low cost as compared with other family of shape memory alloys. Usually, Cu-based shape memory alloys can be grouped into three main categories: Cu-Zn, Cu-Al and Cu-Sn [2]. However, a third (e.g. Ni, Mn, Zn etc.) and fourth (e.g. Zr, Ag, Ti etc.) alloying elements can be added to improve upon the properties and remove drawbacks [3-5]. So, for improvement and achieving high ductility Cu-Al-Mn shape memory alloys are developed. In this alloys can be added zirconium as fourth microalloying element in order to refine the grain size. Chen at al. [6] have developed a new shape memory alloys with compositions Cu-11.91Al-2.48Mn-0.1Zr (wt.%) and concluded that this alloy exhibits a good resistance to irreversible martensite stabilization and has a high martensite start temperature of 210 °C.

In this work a Cu-SMA with composition of Cu-8.5Al-10-Mn-(0.25-1.00)Zr (wt.%) is investigated and the preliminary results of microstructure and microhardness analysis are included. This alloy was selected because it has potential to be used as high-temperature smart material for many applications, mostly sensors.

MATERIALS AND METHODS

The Cu-Al-Mn-Zr alloys were prepared from the pure metals with purity 99.99 % Cu (pellets 6x6 mm), 99.8 % Mn (flakes < 4 mm), 99.99 % Al (granules 2-10 mm) and 99.8 % Zr (granules 1-3 mm). The pure metallic components were smelted by laboratory vacuum electro-arc furnace at high current of 112 A (Fig. 1) used vacuuming and protection by argon. After vacuuming the argon was introduced in chamber in duration of 15 minutes. The alloys were smelted three times in protective argon atmosphere. The smelted alloys were poured into Cu-moulds with diameter of 8 mm and 12 mm high.

The target chemical compositions of produced alloys and marks of samples are shown in Table 1. Microstructure and hardness of investigated samples was examined after casting in Cu-moulds and after the heat treatment at 900 °C/15 min/water. Samples for microstructural analysis were prepared by mechanical grinding. Grinding was performed with paper No. 240-1200 and polishing with 0.3 μm Al_2O_3 . After that, the samples are etcher in 2.5 g FeCl_3 + 48 ml methanol + 10 mL HCl solution during 5 s.

The microstructure characterization was carried out by optical microscope (OM) and scanning electron microscope (SEM) equipped with energy dispersive spectroscopy (EDS). Microhardness was tested by Vickers method at load 9.804 N for 10 s.



Figure 1. The laboratory electro-arc furnace used for smelting and casting in Cu-mould

Table 1. List of marks and target chemical composition of investigated samples Cu-Al-Mn-Zr alloys

Mark of sample	Cu, wt.%	Al, wt.%	Mn, wt.%	Zr, wt.%
1	81.25	8.5	10	0.25
2	81.00	8.5	10	0.50
3	80.75	8.5	10	0.75
4	80.50	8.5	10	1.00

RESULTS AND DISCUSSION

This paper presents preliminary investigation results of the effect of zirconium additions on microstructure and microhardness of Cu-Al-Mn shape memory alloy. Figs. 2 and 3 shows micrographs obtained by optical microscopy of the investigated Cu-Al-Mn-Zr alloys after casting and after heat treatment at 900 °C/15 min/water. A more detailed analysis of micrographs obtained by optical microscopy in the as-cast state of Cu-Al-Mn-Zr alloys shows that only in case of the alloy that has 0.25 wt.% of Zr (sample 1) can be observed the martensite phase (Fig. 2). Other investigated alloys show dual-phase microstructure without martensite, probably β and γ_2 . After heat treatment optical microscopy micrographs show similar behaviour (Fig. 3). According to the literature [4] the eutectic reaction takes place at 1037 °C and 8.5 % Al and at 565 °C and 11.8 % Al and β phase is transformed in the γ_2 phase.

During cooling at non-equilibrium conditions β phase can be replaced by a martensite phase β_1' . The shape memory alloys can show the next ordering transitions: $\beta(A2) \rightarrow \beta_2(A2) \rightarrow \beta_1(L2_1)$ and after that the thermoelastic martensitic transformation has occurred as $\beta_1(L2_1) \rightarrow \beta_1'$ (9R or 18R). The type β_1' martensite formed in the typical zig-zag morphology, while the γ_1' mainly appears as coarse variants.

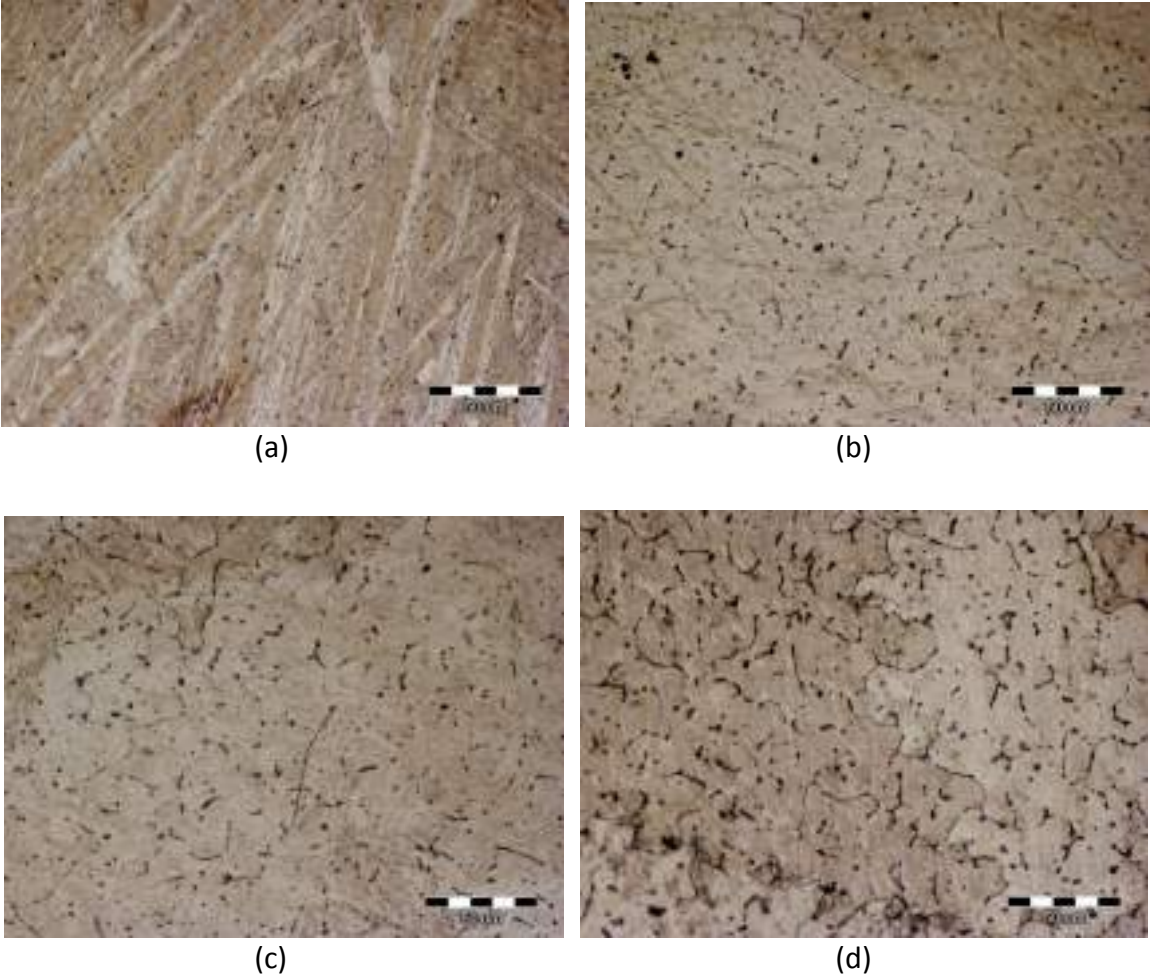
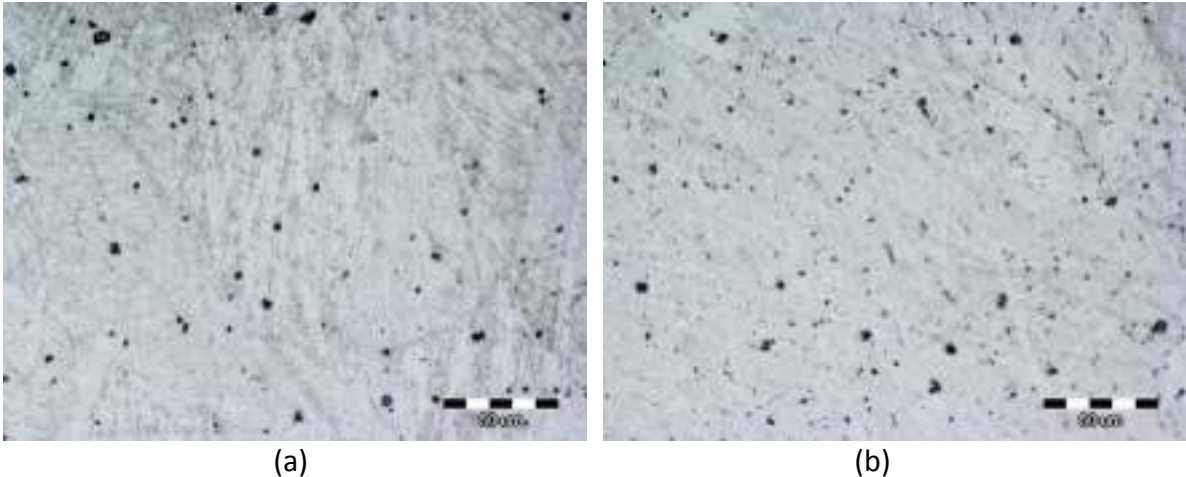
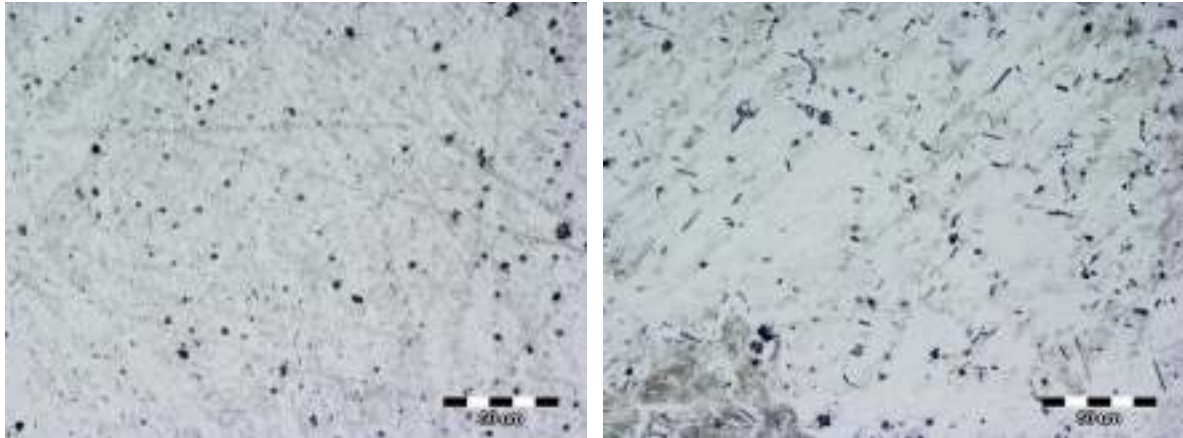


Figure 2. Optical micrographs of sample 1 (a), sample 2 (b), sample 3 (c) and sample 4 (d) after casting in Cu-mould; magnification 500X





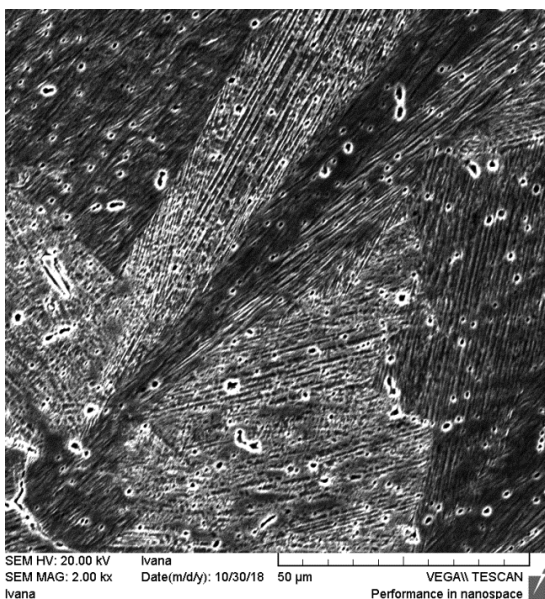
(c)

(d)

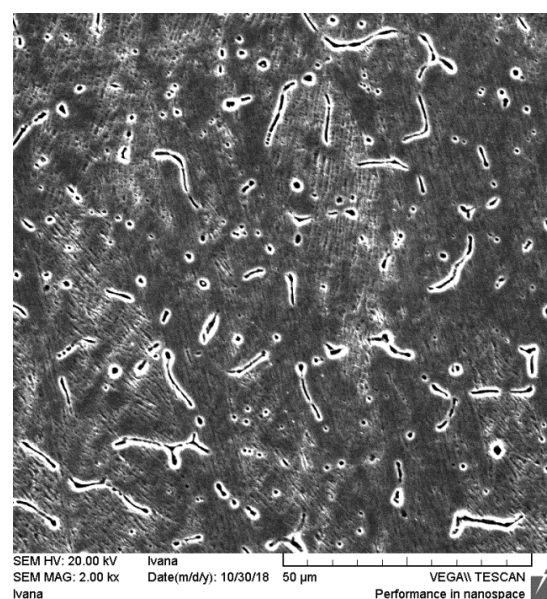
Figure 3. Optical micrographs of sample 1 (a), sample 2 (b), sample 3 (c) and sample 4 (d) after heat treatment 900 °C/15 min/water; magnification 500X

SEM micrographs of as-cast state sample 1 (alloy with 0.25 wt. % Zr) show presence of martensite, which was also observed on optical micrographs. However, at the higher magnifications by SEM analysis can be observed the start of martensite formation in some places in the other investigated alloys (Figs. 4 and 5). From the results of EDS analysis (Table 2) it can be seen that there is no significant difference in chemical composition in all investigated positions. Only at some places incompletely dissolved particles of zirconium were observed. After the heat treatment SEM micrographs show the presence of martensite but with more particles of γ_2 phase precipitates (Figs. 5 and 6). Results of EDX analysis performed after heat treatment (Table 3) show similar content of Cu, Al, Mn and Zr as in investigated position on sample after casting (Table 2).

Chen et al. [6] mentioned that parent phase of the Cu-11.9Al-2.48Mn-0.1Zr alloy is stable and does not decompose easily during aging. This can be caused by Mn addition to Cu-Al system which stabilizes the β phase and makes β phase region wider. Also, they concluded that as results of this process can be present a small quantity of γ_2 precipitates.



(a)



(b)

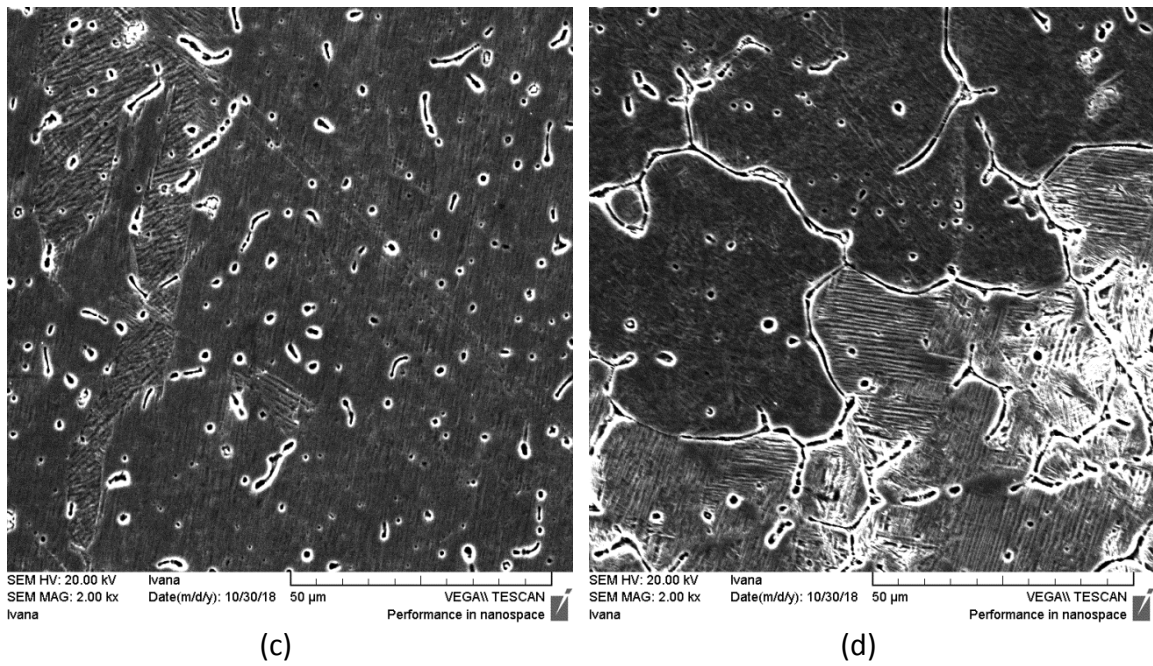


Figure 4. SEM micrographs of sample 1 (a), sample 2 (b), sample 3 (c) and sample 4 (d) after casting in Cu-mould

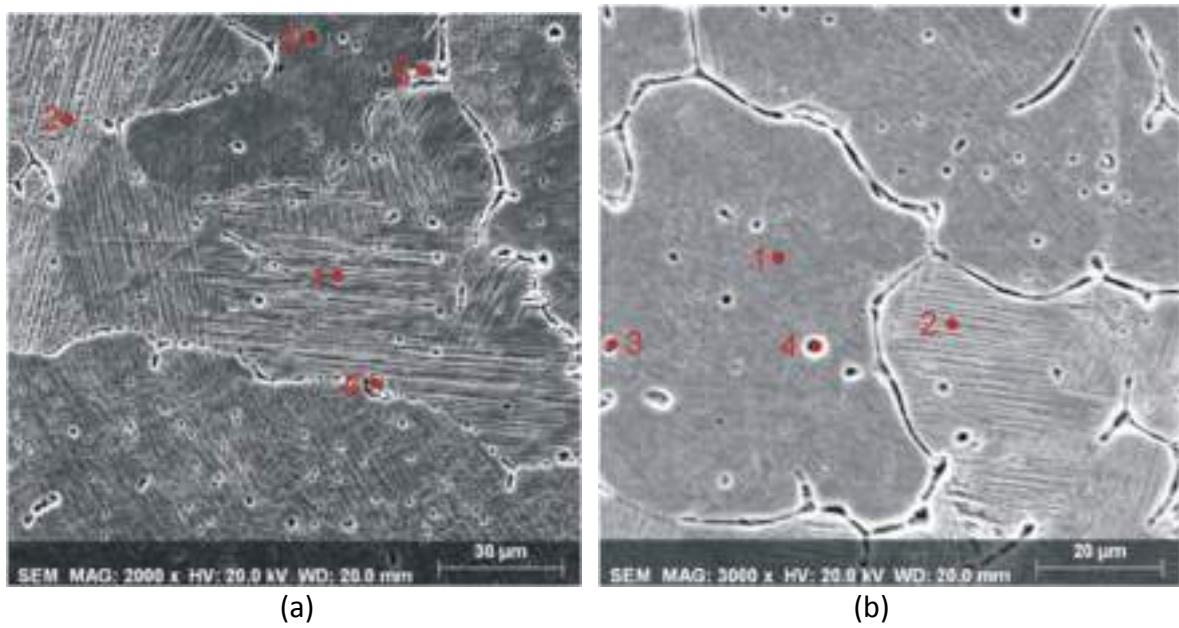
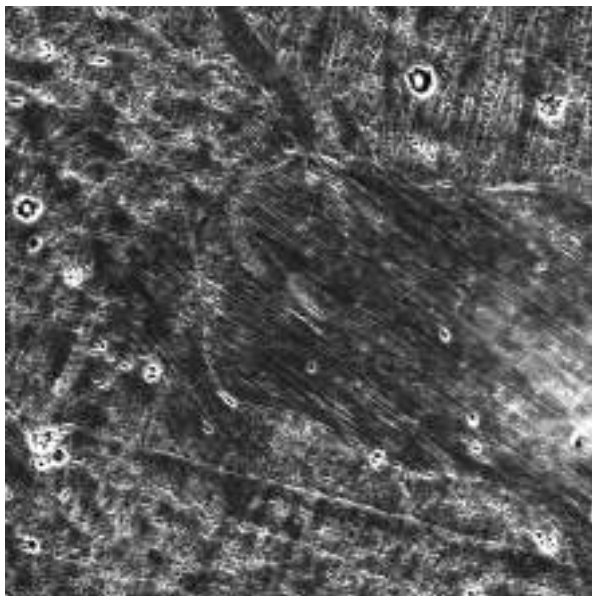


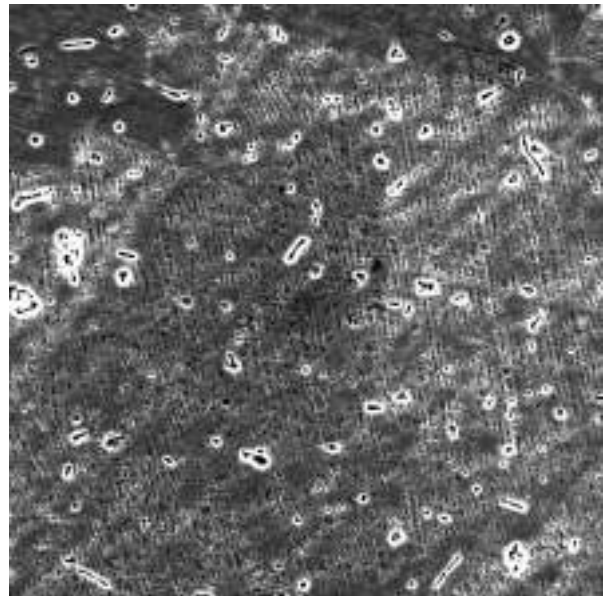
Figure 4. SEM micrographs of sample 1 (a) and sample 4 (b) after casting with marked positions for EDS analysis

Table 2. Results of EDS analysis of sample 1 (a) and sample 4 (b) after casting; positions marked at the Fig. 4

Sample	Position	Chemical composition, wt.%			
		Cu	Al	Mn	Zr
1	1	82.53	7.70	9.23	0.54
	2	82.34	8.04	9.01	0.61
	3	82.75	7.58	9.28	0.39
	4	80.75	7.61	9.17	2.47
	5	84.02	6.22	9.34	0.42
4	1	82.79	7.31	9.43	0.47
	2	83.07	6.87	9.75	0.31
	3	80.74	9.05	9.44	0.77
	4	82.87	7.22	9.38	0.53



(a)



(b)

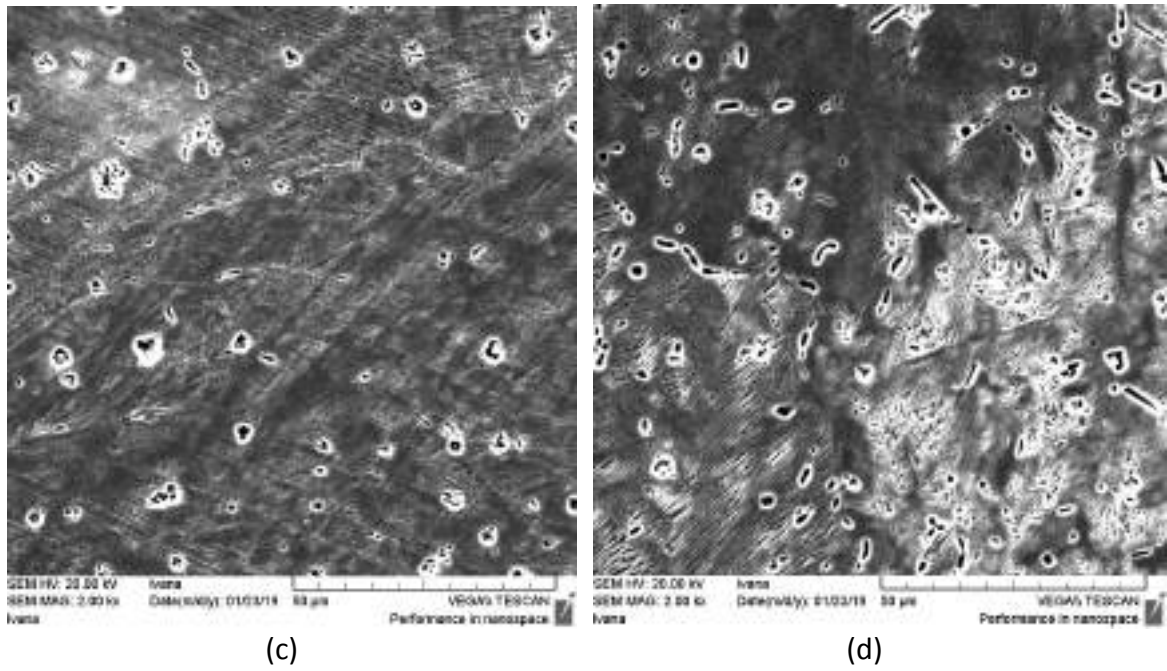


Figure 5. SEM micrographs of sample 1 (a), sample 2 (b), sample 3 (c) and sample 4 (d) after heat treatment 900 °C/15 min/water

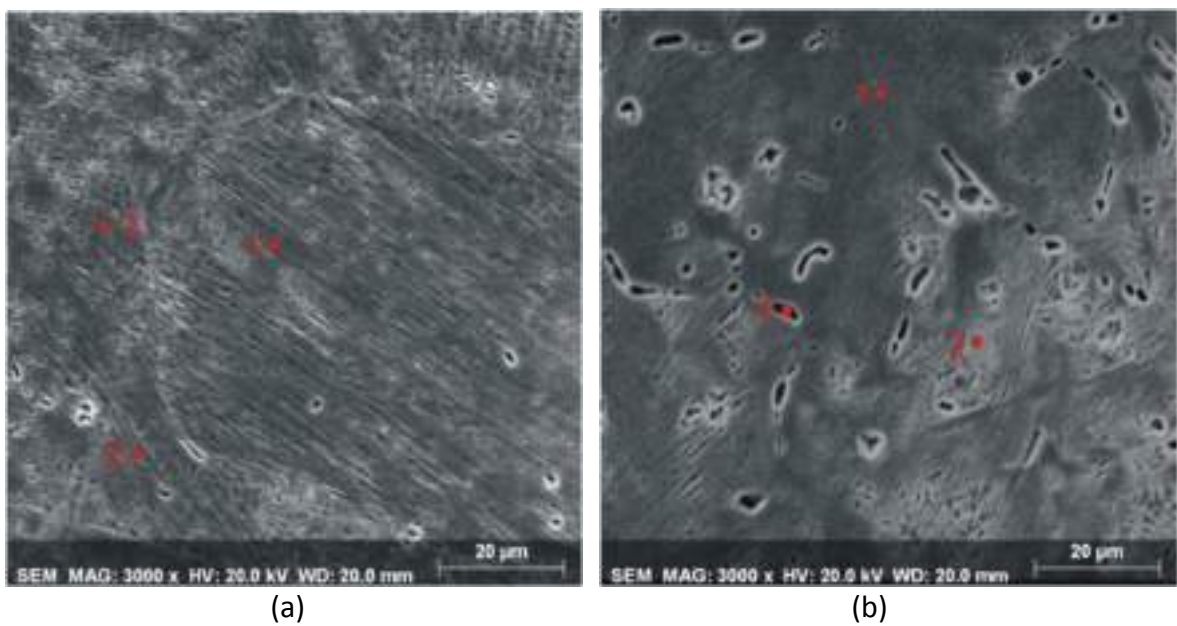


Figure 6. SEM micrographs of sample 1 (a) and sample 4 (b) after heat treatment 900 °C/15 min/water with marked positions for EDS analysis

Table 3. Results of EDS analysis of sample 1 (a) and sample 4 (b) after heat treatment 900 °C/15 min/water; positions marked at the Fig. 6

Sample	Position	Chemical composition, wt. %			
		Cu	Al	Mn	Zr
1	1	82.71	7.14	9.68	0.47
	2	82.56	7.51	9.50	0.43
	3	82.68	6.92	9.90	0.50
4	1	82.97	6.89	9.78	0.36
	2	82.63	7.40	9.34	0.63
	3	82.75	7.03	9.82	0.40

In Fig. 7 it can be seen that the as-cast state of the investigated Cu-Al-Mn-Zr alloys has the lowest microhardness values (188.4-215.8 HV1), in comparison with microhardness values of samples after heat treatment (212-224.5 HV1). However, these differences are negligible and can be related to small changes in microstructure and to the error of the measurement.

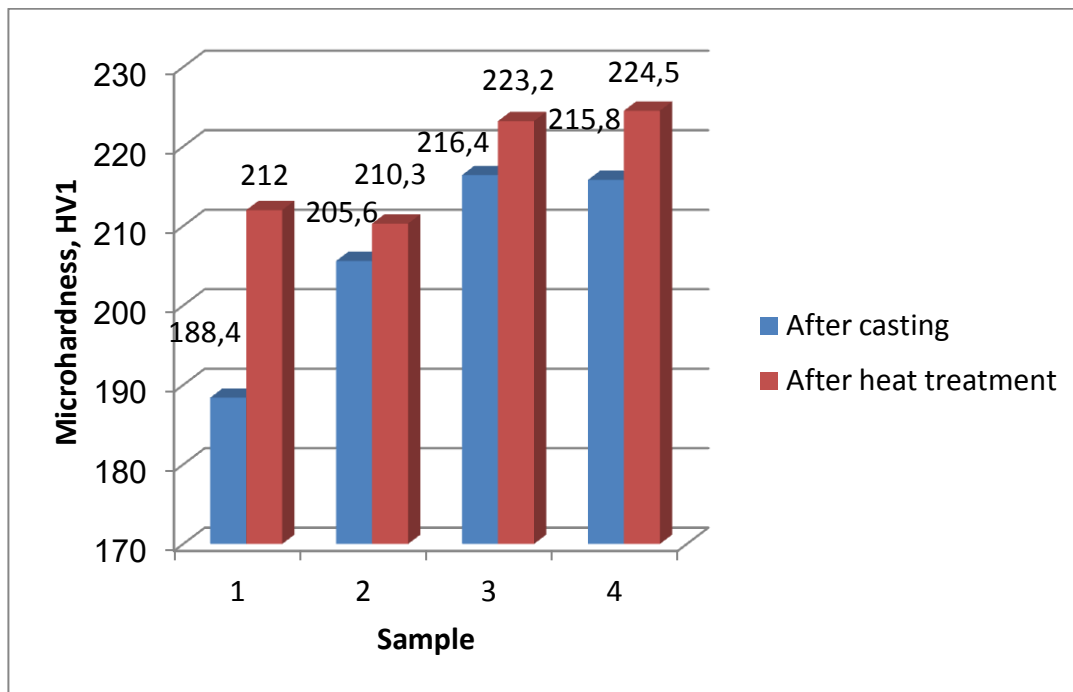


Figure 7. Microhardness values after casting and heat treatment 900 °C/15 min/water

CONCLUSIONS

The microstructural analysis with microhardness testing were carried out on laboratory produced ingots ($\phi 8 \times 12$ mm) of Cu-Al-Mn-Zr alloys before and after heat treatment (900

°C/15min/water). From the obtained preliminary results, we can draw the following conclusions:

- Optical microscopy in the as-cast state of investigated alloys shows that only in sample 1 (alloy with 0.25 wt.% Zr) can be clearly observed the martensite phase. Other investigated alloys show dual-phase microstructure without martensite, probably β and γ_2 . After heat treatment optical microscopy micrographs show similar behaviour.
- SEM micrographs before and after heat treatment of the sample 1 (alloy with 0.25 wt.% Zr) show clear presence of martensite, but because possibility of scanning at the higher magnifications by SEM analysis it is visible the start of martensite formation in some places in the other investigated alloys.
- EDS analysis shows that before and after heat treatment there is no significant difference in chemical composition in all investigated positions.
- Microhardness values before heat treatment were slightly lower (188.4-215.8 HV1), in comparison with microhardness values of samples after the heat treatment (212.0-224.5 HV1).

Acknowledgements

This work was supported by the institutional project of University of Zagreb Faculty of Metallurgy "Properties of metallic materials" (FPI-124-2020-MG).

REFERENCES

- [1] U. Arlic, H. Zak, B. Weidenfeller, W. Riehemann, Impact of alloy composition and thermal stabilization on martensitic phase transformation structures in CuAlMn shape memory alloys, *Materials Research* 21(2018)2, pp. 1-6.
- [2] R. Dasgupta, A look into Cu-based shape memory alloys: Present scenario and future prospects, *Journal of Materials Research* 29(2014)16, pp. 1681-1698.
- [3] Y. Sutou, R. Kainuma, K. Ishida, Effect of alloying elements on the shape memory properties of ductile Cu-Al-Mn alloys, *Materials science and Engineering A* 273-275(1999), pp. 375-379.
- [4] U. S. Mallik, V. Sampath, Influence of quaternary alloying additions on transformation temperatures and shape memory properties of Cu-Al-Mn shape memory alloys, *Journal of Alloys and Compounds* 469(2009), pp. 156-163.
- [5] S. N. Saud, E. Hamzah, T. Abubakar, H. R. Bakhshedhi-Rad, Correlation of microstructural and corrosion characteristics of quaternary shape memory alloys Cu-Al-Ni-X (X=Mn or Ti), *Trans. Nonferrous Met. Soc. China* 25(2015), pp. 1158-1170.
- [6] J. Chen, Z. Li, Y. Y. Zhao, A high-working-temperature CuAlMnZr shape memory alloy, *Journal of Alloys and Compounds* 480(2009), pp. 481-484.



19th INTERNATIONAL FOUNDRYMEN CONFERENCE
Humans - Valuable Resource for Foundry Industry Development
Split, June 16th-18th, 2021
<https://ifc.simet.hr/>

CHARACTERIZATION OF WELDED DUPLEX STAINLESS STEEL AFTER ANNEALING

Stjepan Kožuh^{1*}, Domagoj Kovačević², Ivana Ivanić¹, Borut Kosec³, Mirko Gojić¹

¹ University of Zagreb Faculty of Metallurgy, Sisak, Croatia

² Student at University of Zagreb Faculty of Metallurgy, Sisak, Croatia

³ University of Ljubljana Faculty of Natural Sciences and Engineering, Ljubljana, Slovenia

Poster presentation
Original scientific paper

Abstract

In this work microstructure analysis and microhardness testing was carried out on duplex stainless steel X2CrNiMoN22-5-3 after welding and annealing. Investigated stainless steel was welded using two welding procedures. The root of weld joint was performed with TIG process and for filling SMAW process was used. Analysis of microstructure and microhardness was carried out before and after annealing. Annealing of welded joint was performed at temperature of 850 °C in duration for 60 minutes followed by cooling in air. After annealing, the samples were metallographic prepared. Optical microscopy and scanning electron microscopy with energy dispersive spectrometer were used for characterization of microstructure. Results shows that before annealing microstructure was consisted of ferrite and austenite, and after annealing presence of sigma phase was determined in weld metal. Microhardness values of samples before and after annealing was determined by Vickers method. A significant increase in microhardness values was observed in weld metal after annealing (from 294.9 HV1 to 357.0 HV1).

Keywords: duplex stainless steel, microstructure, microhardness, welding, annealing

*Corresponding author (e-mail address): kozuh@simet.unizg.hr

INTRODUCTION

Stainless steel is steel which has a resistance to staining, rusting, and pitting in the air. Generally, stainless steels define a chromium content higher from 11 % but less than 30 % [1]. They can be produced, with specific restriction in certain types, in conventional ways, and used in the as-cast condition. All the stainless steels types can be classified into five major classes: ferritic, austenitic, duplex, martensitic, and precipitation hardened. The structure of duplex stainless steels is a structure which contain of ferrite and austenite, that is roughly half ferrite and half austenite [2]. The ratio of ferrite and austenite has an important effect on properties of these steels.

At annealing from 1000 °C to 1150 °C only austenite and ferrite are present in microstructure of duplex stainless steels. If temperature of annealing decrease below 1000 °C the duplex stainless steels are not more stable and other phases are formed, like carbides, chromium rich phases etc. The sigma phase is chromium rich intermetallic phase which most often occurs, and its compositions is the most Fe-Cr. Intermetallic sigma phase is hard and brittle phase which significantly affected on properties i.e. reduce impact energy, ductility and corrosion resistance of stainless steels [3,4].

Duplex stainless steels can be welded, and weld metal also contains a mixture of austenite and ferrite [5-8]. The solidification of weld metal occurs as ferrite and no austenite forms at the end of solidification process. The ferrite is stable in the solid state at elevated temperatures, and transformation to austenite carried out below the ferrite solvus. During transformation the austenite first formed along grain boundaries of ferrite [2]. Also, Folkhard [9] mentioned that the precipitation of sigma phase starts in weld metal after about 10-15 minutes after exposure to elevated temperatures 650 – 950 °C.

The aim of this study is microstructural characterization of a welded joint made from duplex stainless steel of grade X2CrNiMoN22-5-3 as well as analysis of annealing effect on microstructure and microhardness.

MATERIALS AND METHODS

Welding of duplex stainless steel (AISI/ASTM 2205, W.Nr. 1.4462, EN X2CrNiMoN22-5-3) was performed by TIG process for root of welded joint, and for filling by SMAW process on a 16 mm thick of plates, Fig. 1. The chemical composition of investigated steel was determined on an MA-ARL 8660 optical emission quantometer and presented in Table 1. The BOHLER CN 22/9 N-IG electrodes was used as filler material for TIG process while BOHLER FOX CN22/9 N-B electrodes was used for SMAW process, Table 2.

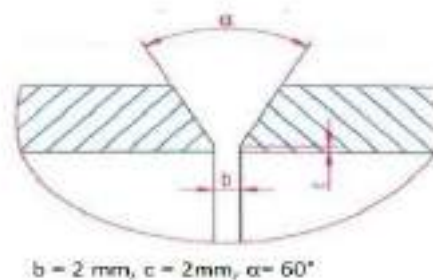


Figure 1. Schematic illustration of joint preparation

Table 1. Chemical composition of investigated duplex stainless steel plates (determined by optical emission quantometer), wt.%

C	Mn	Si	Cu	V	Mo	Al	Cr	Ni	N
0.03	1.52	0.36	0.26	0.02	3.15	0.005	22.21	5.27	0.171

Table 2. Chemical composition of BOHLER CN 22/9 N-IG and BOHLER FOX CN22/9 N-B electrodes, wt.% [10]

	C	Si	Mn	Cr	Ni	Mo	N
BOHLER CN 22/9 N-IG	<0.015	0.4	1.7	22.5	8.8	3.2	0.15
BOHLER FOX CN 22/9 N-B	<0.03	0.5	1.1	22.6	8.8	3.1	0.16

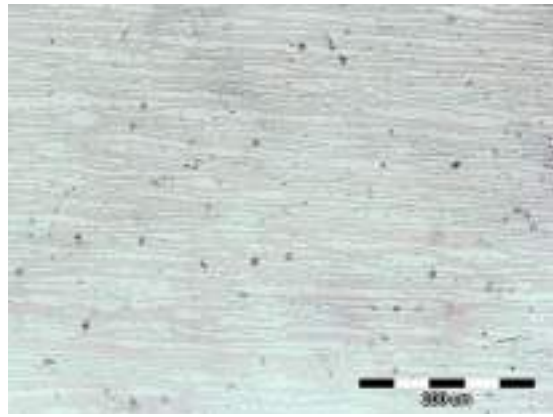
Annealing of welded duplex stainless steel X2CrNiMoN22-5-3 was performed in the electric resistance chamber furnace. The welded joint was annealed at 850 ° C for 60 minutes and then cooled in air.

Metallographic preparation for microstructural characterization was performed by grinding and polishing. The grinding was performed by a Phoenix Beta Buehler device with constant water cooling (papers 240, 400, 600 and 800), and polishing was performed with water solution 0.3 µm alumina (Al₂O₃). The samples were electrolytically etched with an etching solution consisting of 60 mL HNO₃ and 40 mL H₂O (1V for 20 seconds) to detect austenite. A solution consisting of 56 g KOH and 100 mL H₂O (2V for 10 seconds) was used to detect the sigma phase. Optical microscopy was performed on the Olympus GX51 at different magnification. Scanning electron microscopy (SEM) was performed on Tescan Vega 5136MM device equipped with an energy dispersive X-ray spectrometer (EDS).

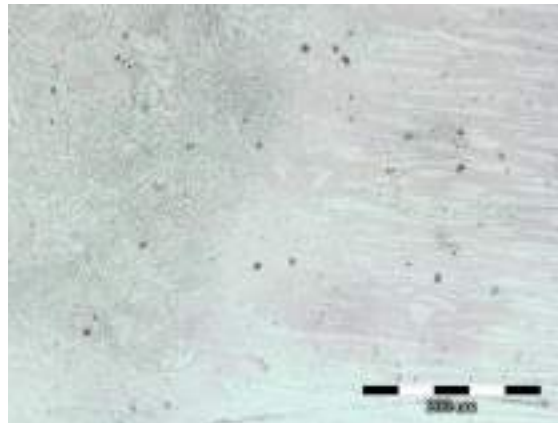
The microhardness of the welded duplex stainless steel samples was measured by the Vickers method on Leica VHMT device, and the injection force was 9.804 N over a period of 10 seconds.

RESULTS AND DISCUSSION

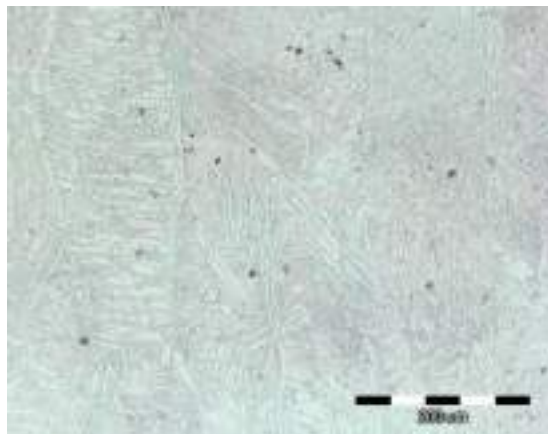
Microstructural analysis of the welded duplex stainless steel was performed by optical and scanning electron microscopy. Optical microscopy of the base material (BM), weld metal (WM) and heat affected zone (HAZ) were investigated in detail, Figs. 2 and 3. By analysis of the optical micrographs can be observed the existence of two-phase duplex microstructure i.e. the presence of ferrite and austenite in microstructure. Also, it can be obtained that the ferrite is elongated in the rolling direction during the production of the plates of investigated stainless steel. After annealing at 850 °C, the microstructure is still mostly two-phase (ferrite and austenite), but sporadically some precipitates are observed in weld metal. The composition of these precipitates therefore needed to be determined by SEM and EDS analysis.



(a)

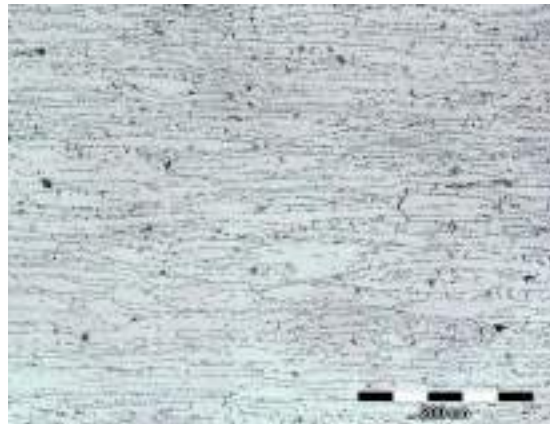


(b)

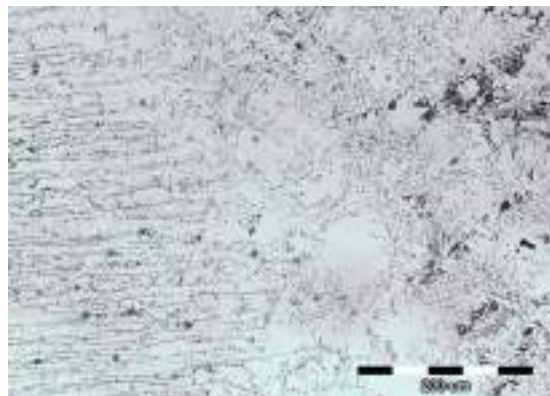


(c)

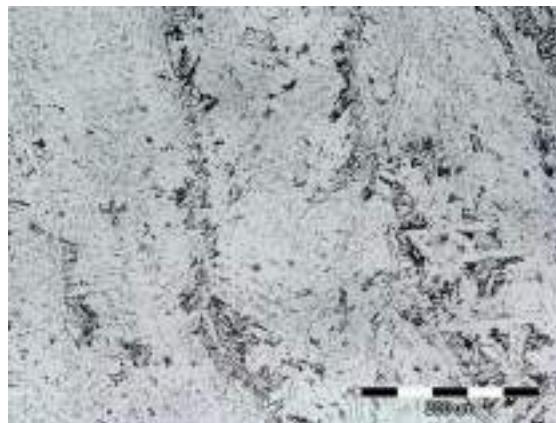
Figure 2. Optical micrographs of welded duplex stainless steel
X2CrNiMoN22-5-3
a) base material; b) heat affected zone; c) weld metal; *magnification 200X*



(a)



(b)

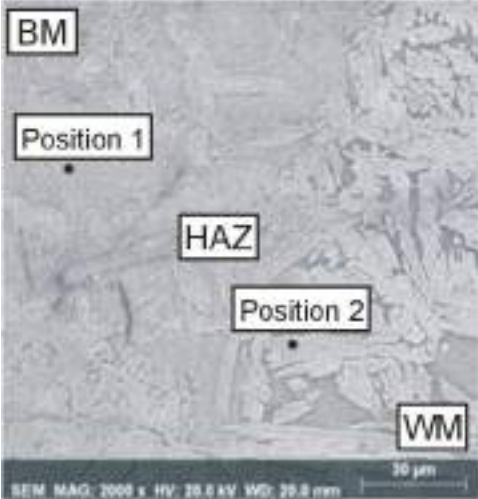


(c)

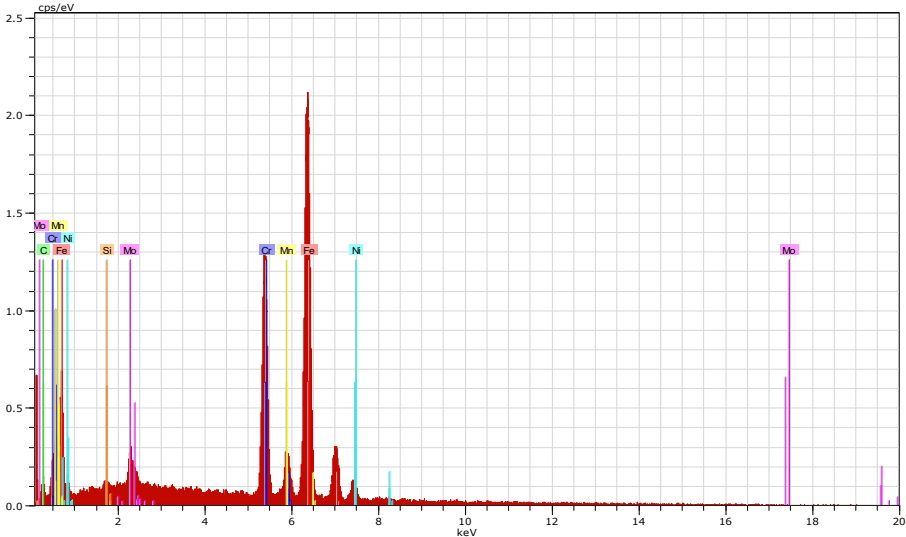
Figure 3. Optical micrographs of welded duplex stainless steel X2CrNiMoN22-5-3 after annealing 850°C/60`/air
 a) base material; b) heat affected zone; c) weld metal; *magnification 200X*

Fig. 4a shows a SEM micrograph of the sample before annealing and this image includes the base material, the heat affected zone and the weld metal. On Fig. 4a are marked the positions for chemical composition testing by EDS analysis. Fig. 4b shows the EDS spectrum obtained for position 1. The chemical composition of the analyzed positions is given in Table 3. By analysis of data in Table 3 can be seen that the chemical composition of position 1 was 65.31 % Fe, 22.01 % Cr, 1.69 % C, 4.78 % Ni, 2.81 % Mn, 3.42 % Mo and 0.2% Si (in wt.%). The

chemical composition of position 2 was 63.31 % Fe, 21.77 % Cr, 1.72 % C, 7.43 % Ni, 2.56 % Mn, 3.15 % Mo, 0.24 % Si (in wt.%). In SEM micrograph (Fig. 4a) the presence of precipitates was not observed and can be concluded that before annealing the only existed phases in microstructure were austenite and ferrite.



(a)



(b)

Figure 4. SEM micrograph (a) and EDS spectrum of position 1 (b) of the welded duplex stainless steel X2CrNiMoN22-5-3
BM - base material; HAZ - heat affected zone; WM - weld metal

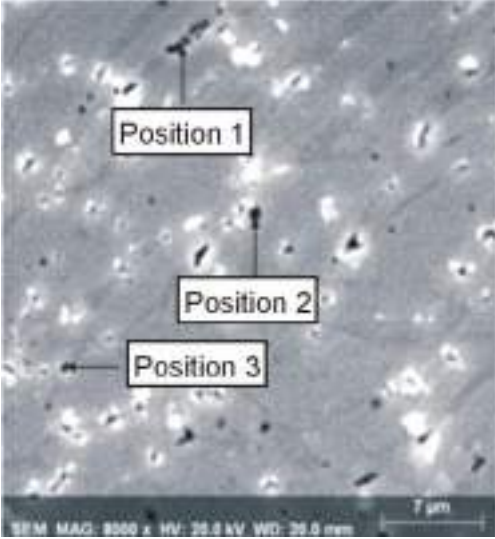
Table 3. Results of EDX analysis of the welded duplex stainless steel X2CrNiMoN22-5-3, wt. % (positions marked at Fig. 4a)

Position	Chemical composition, wt.%						
	Fe	Cr	C	Ni	Mn	Mo	Si
1	65.31	22.01	1.69	4.78	2.81	3.42	0.20
2	63.31	21.77	1.72	7.43	2.56	3.15	0.24

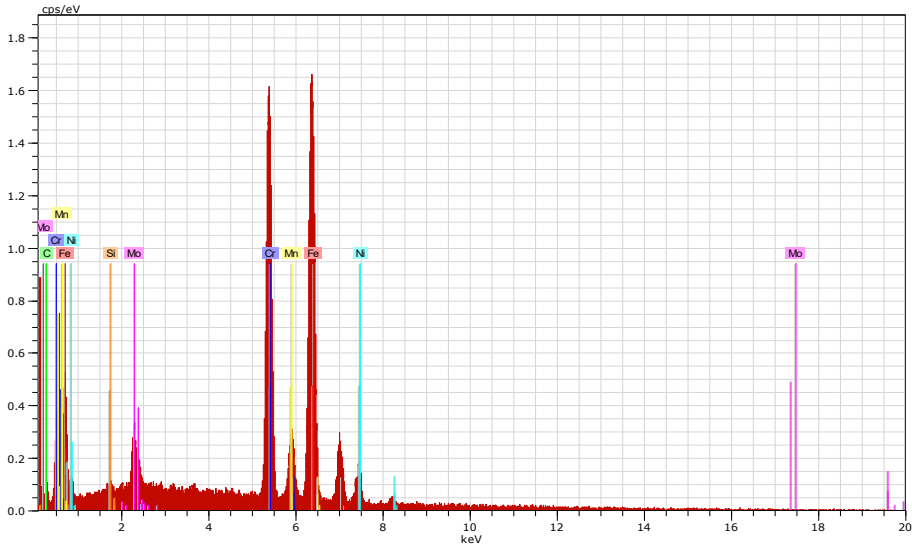
SEM analysis carried out after annealing confirmed the presence of the two-phase microstructure (ferrite and austenite), and existence of some precipitates but only in weld metal. Fig. 5a shows a SEM micrograph of the weld metal after annealing with marked positions for EDS analysis. Fig. 5b shows the EDS spectrum for the analyzed position 1. The chemical composition of the investigated positions is given in Table 4. By analysis of data in Table 4 can be obtained that the chemical composition of the position 1 was 55.39% Fe, 29.79 % Cr, 1.35 % C, 6.27 % Ni, 3.10 % Mn, 4.05 % Mo and 0.05 % Si (in. wt.%). The chemical composition of position 2 was 50.65 % Fe, 25.97 % Cr, 1.28 % C, 7.12 % Ni, 12.47 % Mn, 2.51 % Mo, 0.01 % Si, and the chemical composition of position 3 was 63.80 % Fe, 25.24 % Cr, 0.7 % C, 5.60 % Ni, 2.73% Mn, 1.91% Mo, 0.01 % Si. By detailed analysis of the chemical composition of all three investigated positions can be noticed an increase in content of chromium (25, 24-29.79 % Cr). Therefore, it can be concluded that the precipitates formed in the weld metal after annealing represent the intermetallic sigma phase. In stainless steels during welding or prolonged exposure to elevated temperatures can appear intermetallic phases. The sigma phase is most often formed intermetallic phase which occur in the weld metal. The sigma phase is a chromium-rich, hard and brittle non-magnetic intermetallic phase that has a tetragonal body centered crystal structure and its composition in high-alloy steels is often changed. There are about 50 different sigma phases, but the best known is the iron-chromium (Fe-Cr) sigma phase. When the chromium content in steel is less than 14-15%, the sigma phase does not occur if molybdenum, titanium or vanadium are not present [1]. The composition of the sigma phase can also be represented as $(FeNi)_x(CrMo)_yFeCr$ or $(FeNi)_x(CrMo)_y$. Its formation requires the diffusion of numerous elements and is favored by the presence of ferrite forming elements. The tendency to form the sigma phase increases with increasing chromium and molybdenum content, and molybdenum has 4 to 5 times stronger effect than chromium. In contrast, nickel, cobalt, aluminum, carbon, and nitrogen makes sigma phase precipitation difficult. The sigma phase is formed by the eutectoid transformation of δ -ferrite ($\delta \rightarrow \sigma + \gamma$). The sigma phase primarily occurs at the δ -ferrite/austenite phase boundaries and further expands into δ -ferrite [1, 4, 11-13]. In order for the sigma phase to occur, a local increase in the chromium content is required. Since chromium is more soluble in ferrite than in austenite, the precipitation and growth of the sigma phase in δ -ferrite first occur.

The precipitation of the sigma phase in duplex steel, which contains a relatively high chromium content and a low nickel content, is much faster than that of austenitic and ferritic steels. Hrivnak [4] mentioned that in duplex steels the sigma phase mainly contains 29-34 % Cr, and 3-5 % Mo which is similar to the composition of the sigma phase obtained by EDS analysis of the weld metal after annealing in this investigation (Table 4). Jimenez et

al. [14] concluded that in duplex stainless steel the formation of the sigma phase from δ -ferrite takes place in two stages, i.e. first the sigma phase with a high content of chromium and molybdenum is formed, and then austenite is formed from the remaining δ -ferrite enriched with iron and nickel.



(a)



(b)

Figure 5. SEM micrograph (a) and EDS spectrum of position 1 (b) of the duplex stainless steel X2CrNiMoN22-5-3 weld metal after annealing 850°C/60`/air

Table 4. Results of EDX analysis of the duplex stainless steel X2CrNiMoN22-5-3 weld metal after annealing 850 °C/60`/air, wt. % (positions marked at Fig. 5a)

Position	Chemical composition, wt.%						
	Fe	Cr	C	Ni	Mn	Mo	Si
1	55.39	29.79	1.35	6.27	3.10	4.05	0.05
2	50.65	25.97	1.28	7.12	12.47	2.51	0.01
3	63.80	25.24	0.70	5.60	2.73	1.91	0.01

From the detailed analysis of measured values of microhardness can be observed that after annealing there is an increase in microhardness, Fig. 6. The largest increase in microhardness values is obtained in weld metal. Before annealing, the microhardness of the weld metal was 294.9 HV1 and after annealing was 357.0 HV1. This increase in microhardness may be associated with the formation of the sigma phase in microstructure.

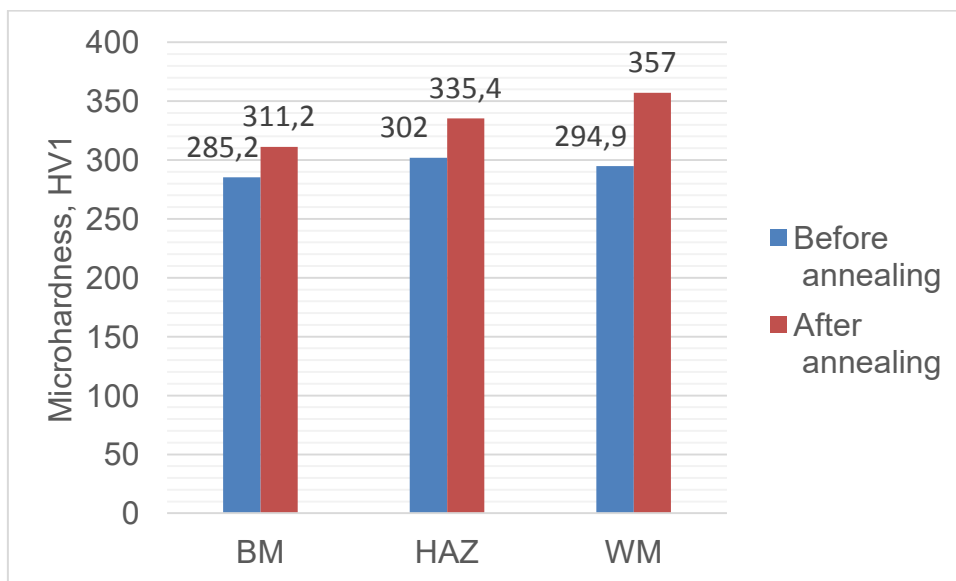


Figure 6. Average values of microhardness of the welded duplex stainless steel X2CrNiMoN22-5-3 before and after annealing 850°C/60`/air
BM – base material, HAZ – heat affected zone, WM – weld metal

CONCLUSIONS

On the basis of the microstructural characterization and the microhardness analysis of the welded duplex stainless steel X2CrNiMoN22-5-3 before and after annealing (850 °C/60`/air), the following can be concluded:

- The microstructure of the base material, the heat affected zone and the weld metal before annealing consisted of ferrite and austenite.

- Optical microscopy analysis showed that after annealing precipitates were sporadically observed in the weld metal.
- SEM analysis confirmed the presence of precipitates in the weld metal after annealing. EDS analysis showed that the precipitates formed in the weld metal represent the intermetallic sigma phase. The composition of the sigma phase was: 50.65-63.80 % Fe, 25.24-29.79 % Cr, 5.60-7.12 % Ni, 2.73-12.47 % Mn and 1.91- 4.05 % Mo.
- The microhardness of the base material, the heat affected zones and the weld metal were similar (285.2-302 HV1) before annealing. After annealing, the microhardness values increases. The higher increase was obtained in the weld metal (from 294.9 to 317.0 HV1), and this can be caused with the formation of the sigma phase.

Acknowledgements

This work was supported by the institutional project University of Zagreb Faculty of Metallurgy "Properties of metallic materials" (FPI-124-2020-MG).

REFERENCES

- [1] R. A. Lula, Stainless steel, American Society for Metals, Metals Park, Ohio, 1986.
- [2] J. C. Lippold, D. J. Kotecki, Welding metallurgy and weldability of stainless steels, John Wiley & Sons, New Jersey, 2005.
- [3] Y. Song, N. A. McPherson, T. N. Baker, The effect of welding process on the chi phase precipitation in as-welded 317L weld metal, ISIJ International 36(1996)11, pp. 1392-1396.
- [4] I. Hrivňák, Metallography of austenitic and dual phase stainless steels, Acta Metallurgica Slovaca 10(2004), pp. 91-102.
- [5] E. Margnardt, G. S. Halle, Welding of thin sheets of duplex steel, Welding&Cutting 52(2000) 3, E56-E58.
- [6] I. Juraga, I. Stojanović, B. Ljubenkov, Experimental research of the duplex stainless steel welds in shipbuilding, Brodogradnja/Shipbuilding 65(2014)2, pp. 73-85.
- [7] A. Vinoth Jebaraj, L. Ajaykumar, C.R. Deepak, K.V.V. Aditya, Weldability, machinability and surfacing of commercial duplex stainless steel AISI 2205 for marine application – A recent review, Journal of Advanced Research 8(2017), pp. 183-189.
- [8] T. Pickle, N. Henry, P. Morris, L. Tennis, D. Wagner, R.E. Baumer, Root pass microstructure in super duplex stainless steel multipass welds, Welding Research 98(2019), pp. 123-134.
- [9] E. Folkhard, Welding Metallurgy of Stainless Steels, Springer-Verlag, Wien, 1988.
- [10] Welding Guide, Böhler Welding, Technical Handbook of Böhler Welding Products, Böhler Schweißtechnik Austria GmbH, 2001.
- [11] V. Rede, S. Šolić, Utjecaj sigma faze u dupleks čeliku na otpornost na abrazijsko trošenje, Zbornik 10. Savjetovanja o materijalima, tehnologijama, trenju i trošenju, MATRIB`05, HDZMT, Vela Luka, 23.-25. lipanj 2005., pp. 321-328.
- [12] D.-Y. Lin, G.-L. Liu, T.-C. Chang, H.-C. Hsieh, Microstructure development in 24Cr-14Ni-2Mn stainless steel after aging under various nitrogen/air ratios, Journal of Alloys and Compounds 377(2004)1/2, pp. 150-154.

- [13] J. Barcik, The Kinetics of σ phase precipitation in AISI 310 and AISI 316 steels, Metallurgical Transactions A 14A(1983)4, pp. 635-641.
- [14] J. A. Jimenez, M. Carsi, O. A. Ruano, Characterization of a δ/γ duplex stainless steel, Journal of Materials Science 35(2000), pp. 907-915.



19th INTERNATIONAL FOUNDRYMEN CONFERENCE
Humans - Valuable Resource for Foundry Industry Development
Split, June 16th-18th, 2021
<https://ifc.simet.hr/>

**RHEOLOGICAL PROPERTIES OF WATER-BASED ALUMINA SUSPENSIONS IN
RECYCLING WASTE ALUMINA POWDER**

Filipa Krželj, Irena Žmak^{*}, Milan Vukšić, Lidija Ćurković

University of Zagreb Faculty of Mechanical Engineering and Naval Architecture, Zagreb, Croatia

Poster presentation
Original scientific paper

Abstract

Waste, i.e. secondary alumina (Al_2O_3) ceramic powder is produced when green bodies are machined prior to the sintering of ceramic products. This industrial waste, although non-hazardous, has to be disposed of using the legally adequate methods. Typically, landfills are used for this purpose, which presents additional manufacturing costs. This paper focuses on how to recycle waste alumina by slip casting of alumina water-based suspensions. Slip casting process requires limited suspension viscosity. When virgin alumina powder is substituted with waste alumina powder, the suspension viscosity increases.

This paper presents the results of studying the influence of adding commercially available dispersant on apparent viscosity of suspensions with 60 wt.% of solid loading. There were three different solid samples studied: 30, 45 and 60 wt.% of waste alumina, as expressed by total dry weight.

The water-based Al_2O_3 suspension were homogenized by a planetary ball mill, after which the suspension stability was tested to rheological properties. The tests have showed that in aqueous ceramic suspensions with up to 60 dry wt.% solid component it is possible to achieve favorable viscosity for slip casting when 0.06 dwb.% of the dispersant Tiron is added. The increase in waste alumina content caused a gradual increase in the apparent viscosity. Suspensions with more than 60 : 40 ratio of waste to virgin alumina powder become unusable for slip casting due to too high viscosity.

Keywords: *recycling, waste, alumina, rheology, viscosity*

*Corresponding author (e-mail address): irena.zmak@fsb.hr

INTRODUCTION

Technical ceramics is a modern material which is often used in mechanical [1], chemical, electrical engineering, as well as in stomatology and medicine [2], due to its favorable properties, for example: low density, chemical resistance to many aggressive media and biocompatibility, high hardness and wear resistance, stability of mechanical properties at high temperatures, etc. [3].

In industrial production of technical ceramics, the generation of non-hazardous ceramic waste inevitably occurs after processing of raw material into ceramic green bodies. This waste powder is not dangerous for the environment, i.e. "Absolute Non-hazardous" as per European List Of Waste [4], but it should be disposed of in a legally prescribed manner in regulated landfills, which is an additional cost. Possible recycling of waste alumina powder could lead to the creation of new products, i.e. added value of new ones. Waste alumina residue is legally allowed to be deposited on landfills in EU, whether by using wet or dry methods, depending on each country, and wet disposal is more economical [5]. The concept of Zero Waste is also applied in alumina production industries, where responsible production and consumption is encouraged by the reuse, recycling, or recovery of waste materials.

One of the simplest procedures for making ceramic products is slip casting, where it is very important to achieve the stability of the aqueous suspension, i.e. to prevent deposition. Numerous dispersants are used to achieve suspension stability, for example polyacrylic acid ammonium salt [6], sodium dodecyl benzene sulfonate for alumina nanofluids [7], or N, N-dimethylacrylamide, a monomer with low toxicity [8]. One of commercially available dispersants is dispersant Tiron (4,5-Dihydroxy-1,3-benzenedisulfonic acid disodium salt monohydrate), which was used in this paper.

In the slip casting process, the apparent viscosity of the suspension is important for the correct filling of the mold. Rheological measurements are a primary source of information when estimating the suspensions prior to slip casting [9]. Several methods may be used to determine the dispersion stability, like initial dispersion pH-value, or the zeta-potential (i.e. mobility) of the dispersion [10]. Often, the problem of the optimum amount of dispersant must be determined, and the best combination of amounts of different additives added to the same suspension has to be studied [11]. Additives contribute by improving the highest possible amount of solid load. The higher the solid load, the higher the density of the green body and consequently of the sintered ceramics. At the same time, a higher solid load leads to increased viscosity, which negatively affects the viscosity of the suspension, hence the slip casting is either more difficult or impossible.

In recent years different approaches have been made towards a more circular economy in technical ceramics manufacturing industry. Alumina waste was used for fabrication of geopolymer [12], extraction of nano alumina powder [13], as clay replacement in the production of unfired bricks [14], road building technologies [15], etc.

This research was focused on the possibilities of using waste alumina for preparing stable water-based suspensions by replacing a part of the new alumina powder with waste alumina powder. As stable and low viscosity suspensions are required for slip casting, the influence of added amount of the dispersant Tiron on the viscosity of the aqueous suspension with different proportions of waste ceramic powder was studied.

MATERIALS AND METHODS

Samples of raw ceramic material were obtained by the process of casting aqueous suspensions. Suspensions were prepared by mixing primary (i.e. virgin) and secondary (i.e. waste) Al₂O₃ powder, and distilled water. Secondary alumina powder was generated as waste by applying the machining of green ceramic bodies during the production of technical ceramics in a company named Applied Ceramics, Sisak, Croatia. Primary alumina powder is of high purity, average particle size 300-400 nm, from the American manufacturer Alcan

Chemicals, USA. Chemical composition of the primary Al₂O₃ powder used is shown in Table 1.

Table 1. Chemical composition of the used primary Al₂O₃ powder

Component	Al ₂ O ₃	MgO	Fe ₂ O ₃	SiO ₂	Na ₂ O	CaO
wt%	99.83	0.066	0.015	0.020	0.050	0.01
	4					5

A commercial dispersant Tiron, manufactured by Sigma-Aldrich Chemie GmbH, Germany was used to examine the influence of additives on the stability of prepared aqueous suspensions. In the first experiment, a suspension was prepared with 70 wt% of dry alumina powder (consisting of 60 wt% of waste and 40 wt% of primary powder, typically abbreviated as dwb% as per “dry weight basis”) and 30 wt% of distilled water. For an optimal suspension homogenization in the ball-mill, eight 10 mm diameter ceramic balls were used. For preventing the suspension contamination, the mixing balls were made from alumina as well. The suspension was subjected to homogenization in a planetary ball mill PM 100 (Retsch GmbH, Germany) at a speed of 300 rpm for 60 min. After the homogenization process, the mixing balls could not be separated from the suspension by a sieve due to the very high viscosity of the suspension, as shown in Figure 1.



Figure 1. 70 wt% of dry alumina water-based suspension after homogenization

This preliminary test showed a too high viscosity for slip casting. Therefore, it was decided to reduce the total amount of dry alumina powder in the aqueous suspension, from 70 wt% to 60 wt%. Three suspensions with different proportions of primary and secondary powder were prepared. Suspensions were made with 64 mL of distilled water using different amounts of the dispersant Tiron as well as without any dispersant.

Homogenization was performed in the same way as with the preliminary 70 wt% of powder and 30 wt% of distilled water, but this time with the powder to water ratio set to 60:40. After suspension ball-milling for 60 min at a speed of 300 rpm, formation of air bubbles usually takes place. Therefore, the prepared suspension was placed in an ultrasonic bath Branson 220, Branson Ultrasonics Corporation, USA for 10 minutes.

The viscosity of the prepared suspensions was determined using a DV-III Ultra rotary viscometer (Brookfield Engineering Laboratories, Inc., USA).

The apparent viscosity was read at defined shear rates, at exactly 50 equal intervals, with the shear rate increasing from 0.1 s^{-1} to 180 s^{-1} . Measurements were performed for three different suspensions with:

- a) 30 dwb% of waste alumina powder
- b) 45 dwb% of waste alumina powder
- c) 60 dwb% of waste alumina powder, as shown in Table 2.

Each suspension was prepared with different amounts of the dispersant Tiron: 0.03 %, 0.06 %, 0.09 %, 0.12 %, 0.15 % and 0.2 %, calculated based on total dry weight content (dwb%) of the primary and the secondary alumina powder.

RESULTS AND DISCUSSION

Based on the performed rheological tests, conclusions were obtained on the resistance of the ceramic suspensions to flow and information on the interaction between the particles within the suspension as well. Rheological diagrams typically show the dependence of the apparent viscosity, η on the shear rate, $\dot{\gamma}$.

Suspension 1

Suspension 1 consisted of 70 dwb% of primary and 30 dwb% of secondary powder in an aqueous suspension of 60 wt%. Examinations were performed on samples without the addition of the dispersant Tiron and with 0.03 %, 0.06 %, 0.09 %, 0.12 %, 0.15 % and 0.2 % of the dispersant Tiron, all in expressed as dry weight contents. As the dispersant content increased, the measurements became more stable, Figure 2. The sample that did not have any dispersant Tiron addition at all had a very high viscosity compared to the samples with the addition of the dispersant Tiron.

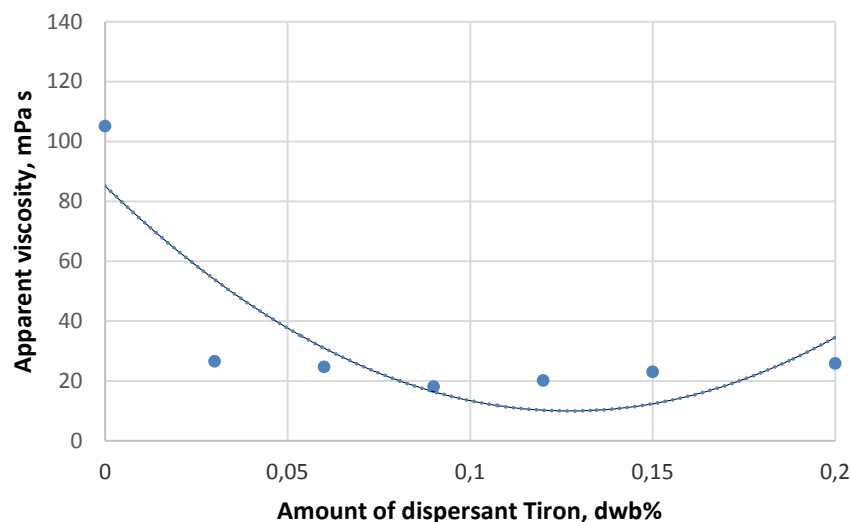


Figure 2. Influence of dispersant amount on apparent viscosity of Suspension 1

Suspension 2

Water-based Suspension 2 consisted of 55 dwb% of primary and 45 dwb% of secondary alumina powder, which resulted in 60 wt% of alumina suspension. Examinations were performed on samples without the addition of the dispersant Tiron, and with 0.03 %, 0.06 %, 0.09 %, 0.12 %, 0.15 % and 0.2 % of the dispersant Tiron.

0.09 %, 0.12 %, 0.15 % and 0.2 % of the dispersant Tiron, also in dry weight contents. Figure 3 shows the dependence of the apparent viscosity of Suspension 2 on the amount of added dispersant.

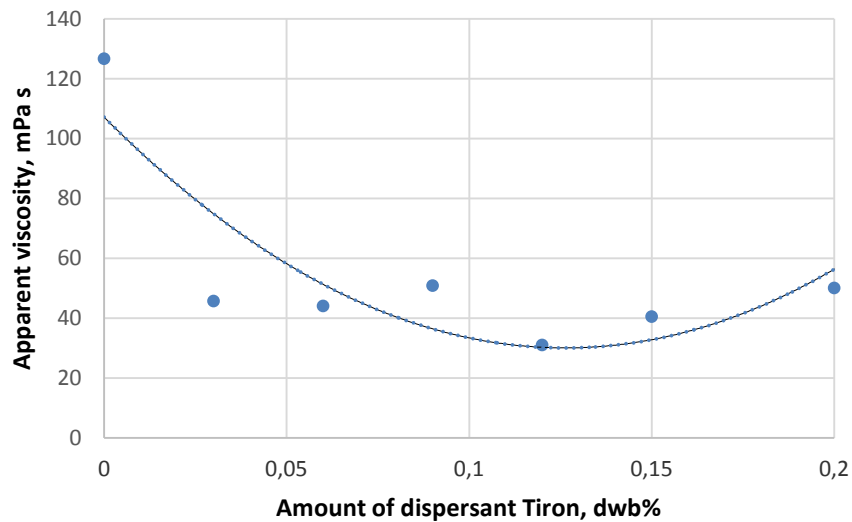


Figure 3. Influence of dispersant amount on apparent viscosity of Suspension 2

As the content of the dispersant Tiron increased, the decrease in viscosity of prepared alumina suspensions became more obvious, as it was presented in Figure 3.

Suspension 3

Suspension 3 consisted of 40 dwb% of primary and 60 dwb% of secondary powder producing 60 wt% of water-based ceramic suspension. Examinations were performed on samples without the addition of the dispersant Tiron, with 0.03%, 0.06%, 0.09%, 0.12%, 0.15% and 0.2% of the dispersant Tiron expressed on dry weight basis of alumina powders.

For the results obtained for 60 dwb% of secondary powder, it was noticeable that the scatter values are lower, which can be attributed to higher proportions of additives (dispersants) and higher proportions of secondary powder, Figure 4. The results, like in the previous two scenarios, show a decrease in the apparent viscosity with increasing shear rate.

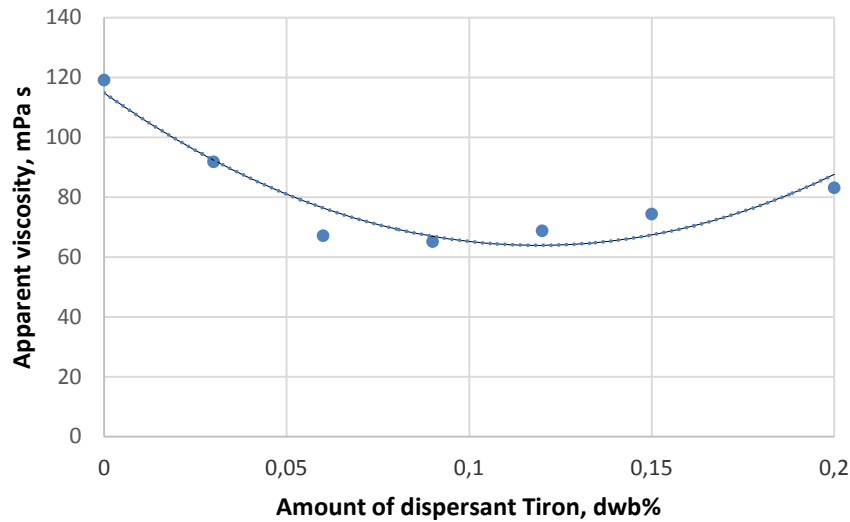


Figure 4. Influence of dispersant amount on apparent viscosity of Suspension 3

When all three data sets with different ratios of virgin to waste alumina are compared, Figure 5, it can be concluded that the higher replacing amount of the primary powder with the secondary alumina powder results in the more negative effect on the flow properties of aqueous ceramic suspensions.

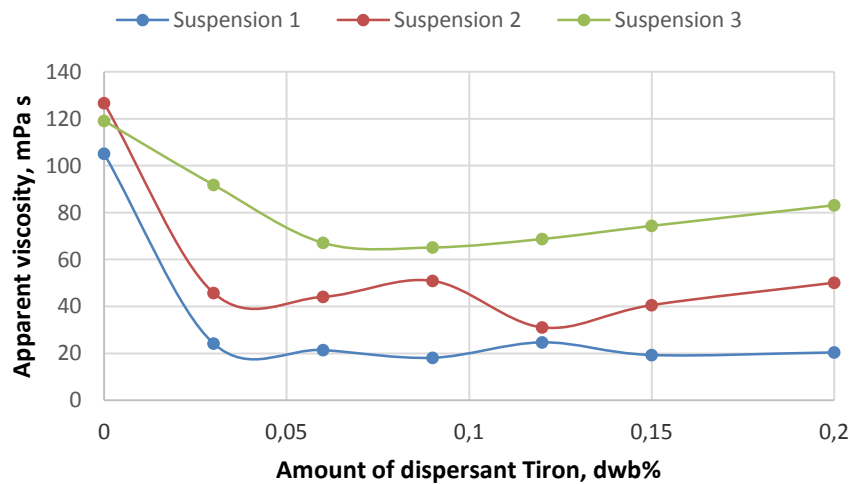


Figure 5. Comparison of rheological measurement results for all suspensions

The diagram in Figure 5 shows the dependence of the apparent viscosity on the proportion of the dispersant Tiron for each individual group of suspensions. The above diagram depicts the value of the apparent viscosity measured at a shear rate of 51.44 s^{-1} , which was selected from the measurement results as the closest to a speed of 50 s^{-1} , which corresponds to gravitational casting.

The diagram in Figure 6 indicates that for the same proportion of the dispersant Tiron (in this representation, of 0.06 dwb% of the dispersant Tiron), the viscosity increases with increasing secondary (waste) alumina powder content. The diagram applies to the value of the apparent viscosity measured at a shear rate of 51.44 s^{-1} .

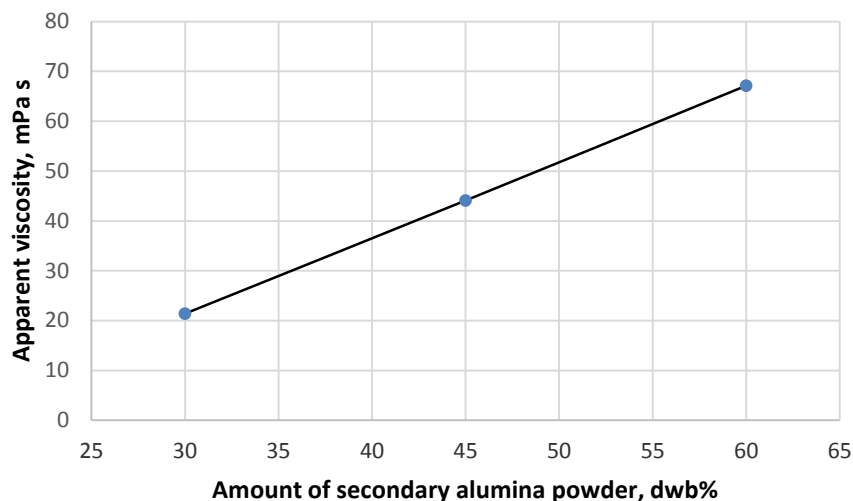


Figure 6. Influence of secondary (waste) alumina powder content on apparent viscosity of prepared suspensions with same proportion of dispersant Tiron (0.06 dwb%)

For Suspension 3, which consists of 60 dwb% of secondary powder and 40 dwb% of primary powder, the viscosity is very high and not suitable for slip casting process. In general, the slip casting method requires the suspensions of up to 60 mPa s apparent viscosity measured at low shear rates.

CONCLUSIONS

Based on the performed examinations of the rheological properties of the ceramic suspensions, the following conclusions are made on the preparation of a 60 wt% of stable virgin Al_2O_3 –waste Al_2O_3 suspension with the addition of the dispersant Tiron.

By replacing substantial amount of virgin alumina powder with waste alumina powder, it is possible to obtain an aqueous ceramic suspension up to 60 wt% of solid loading using the dispersant Tiron to achieve favorable viscosity for slip casting of alumina ceramic suspensions.

By increasing the waste alumina content, the apparent viscosity of prepared alumina suspensions gradually increases. If the ratio of waste powder to the proportion of the virgin alumina powder is increased to 60 : 40, the suspension becomes unusable for casting due the too high viscosity. Further research should examine the addition of other additives, such as binders and grain growth inhibitors, which, when combined with the dispersant, might have a different influence on viscosity of aqueous ceramic suspensions.

Acknowledgements

This work was supported by the Croatian Science Foundation project IP-2016-06-6000 “Advanced monolithic and composite ceramics for wear and corrosion protection” (WECOR).

REFERENCES

- [1] C. Piconi, S. G. Condo, T. Kosmač, *Advanced Ceramics for Dentistry*, Butterworth-

- Heinemann, Oxford, 2014.
- [2] T. J. Webster, E. S. Ahn, Nanostructured biomaterials for tissue engineering bone, in *Advances in Biochemical Engineering/Biotechnology*, 103(2006), 2006, pp. 275-308.
 - [3] A. Ruys, *Alumina Ceramics*, Woodhead Publishing, Woodhead Publishing, Cambridge, 2018.
 - [4] Eurostat, Guidance on classification of waste according to EWC-Stat categories, 2010. Accessible on Internet: <https://ec.europa.eu/eurostat/documents/342366/351806/Guidance-on-EWCStat-categories-2010.pdf/0e7cd3fc-c05c-47a7-818f-1c2421e55604>, April 4th, 2021.
 - [5] V. Dentoni, B. Grosso, G. Massacci, Environmental Sustainability of the Alumina Industry in Western Europe, *Sustainability*, 6(2014)12, pp. 9477-9493.
 - [6] M. Naito, Y. Fukuda, N. Yoshikawa, H. Kamiya, J. Tsubaki, Optimization of Suspension Characteristics for Shaping Processes, *Journal of the European Ceramic Society*, 17(1997)2, pp. 251-257.
 - [7] A. Gallego, K. Cagua, B. Herrera, D. Cabaleiro, M. M. Piñeiro, L. Lugo, Experimental evaluation of the effect in the stability and thermophysical properties of water-Al₂O₃ based nanofluids using SDBS as dispersant agent, *Advanced Powder Technology*, 31(2020)2, pp. 560-570.
 - [8] S. Yin, L. Pan, L. Guo, Y. Liu, Y. Feng, T. Qiu, J. Yang, Fabrication and properties of porous Si₃N₄ ceramics by aqueous gelcasting using low-toxic DMAA gelling agent, *Ceramics International*, 44(2018)7, pp. 7569-7579.
 - [9] G. Tari, J. M. F. Ferreira, O. Lyckfeldt, Influence of the Stabilising Mechanism and Solid Loading on Slip Casting of Alumina, *Journal of the European Ceramic Society*, 18(1998)5, pp. 479-486.
 - [10] P. Mikkola, P. Ylhä, E. Levänen, J. B. Rosenholm, Effect of impurities on dispersion properties of alpha-alumina powder, *Ceramics International*, 30(2004)2, pp. 291-299.
 - [11] A. Tsetsekou, C. Agrafiotis, I. Leon, A. Miliadis, Optimization of the rheological properties of alumina slurries for ceramic processing applications Part II: Spray-drying, *Journal of the European Ceramic Society*, 21(2001)4, pp. 493-506.
 - [12] P. Chawakitchareon, P. Kingthong, Utilization of alumina waste and silica waste for geopolymer production, *Engineering Journal*, 20(2016)4, pp. 51-57.
 - [13] N. M. Khalil, Exploitation of the ceramic wastes for the extraction of nano aluminum oxide powder, *Journal of Industrial and Engineering Chemistry*, 20(2014)5, pp. 3663-3666.
 - [14] L. Miqueleiz, F. Ramirez, J. E. Oti, A. Seco, J. M. Kinuthia, I. Oreja, P. Urmeneta, Alumina filler waste as clay replacement material for unfired brick production, *Engineering Geology*, 163(2013), pp. 68-74.
 - [15] I. Shepelev, N. Bochkov, A. Zhyzhaev, Study of composition and morphology features of alumina producing waste for its application in road building technologies, AIP Conference Proceedings 1698, (S. V. Starenchenko, Y. V. Soloveva, N. O. Kopanitsa), AIP Publishing, October 6th-9th, 2015, Tomsk, Russia, pp. 1-5.



19th INTERNATIONAL FOUNDRYMEN CONFERENCE
Humans - Valuable Resource for Foundry Industry Development
Split, June 16th-18th, 2021
<https://ifc.simet.hr/>

SIMULATION MODEL OF CONVENTIONAL SOLID STATE SINTERING OF Al₂O₃ CERAMICS

Darko Landek^{*}, Lidija Ćurković, Ivana Gabelica

University of Zagreb Faculty of Mechanical Engineering and Naval Architecture, Zagreb, Croatia

Poster presentation
Original scientific paper

Abstract

The paper presents a finite element method (FEM) of solid state sintering of aluminum oxide ceramics in an electric furnace. Alumina green bodies were prepared by slip casting of stable 70 wt.% Al₂O₃ aqueous suspension in a plaster (gypsum) mold. Dispersant Dolapix CE-64 was used for stabilization of highly concentrated alumina suspension. Sintering of green bodies was performed at temperatures of 1600 °C, 1625 °C and 1650 °C for 2 h, 4 h and 6 h. The FEM model was solved as a nonlinear thermo-mechanical problem with the heating, sintering and cooling phases in the FEM program Comsol Multiphysics. The density of the sintered samples was determined by the Archimedes method and compared with the density predicted by FEM simulations. The concordance of numerically predicted and measured density amounts, for the same sintering parameters is 86 %.

Keywords: *aluminum oxide ceramics, sintering, Archimedes density, FEM model*

**Corresponding author (e-mail address): dlandek@fsb.hr*

INTRODUCTION

Aluminum oxide (Al₂O₃) is the most common representative of oxide ceramics in industrial applications. Its main properties are high hardness and compressive strength, resistance to elevated temperatures, wear resistance and resistance to corrosion at elevated temperatures [1–3]. The most thermodynamically stable phase of alumina is hexagonal α -alumina (Figure 1) with lattice parameters of $a = 4.758 \text{ \AA}$ and $c = 12.991 \text{ \AA}$ [4]. Gibbsite (Al(OH)₃) and boehmite (AlOOH) are the most used precursors for the preparation of α -Al₂O₃ [5]. From different precursors (gibbsite, boehmite, bayerite) can transform to following metastable crystalline structures by calcination: α , χ , η , δ , κ , θ , γ , ρ (Figure 1).

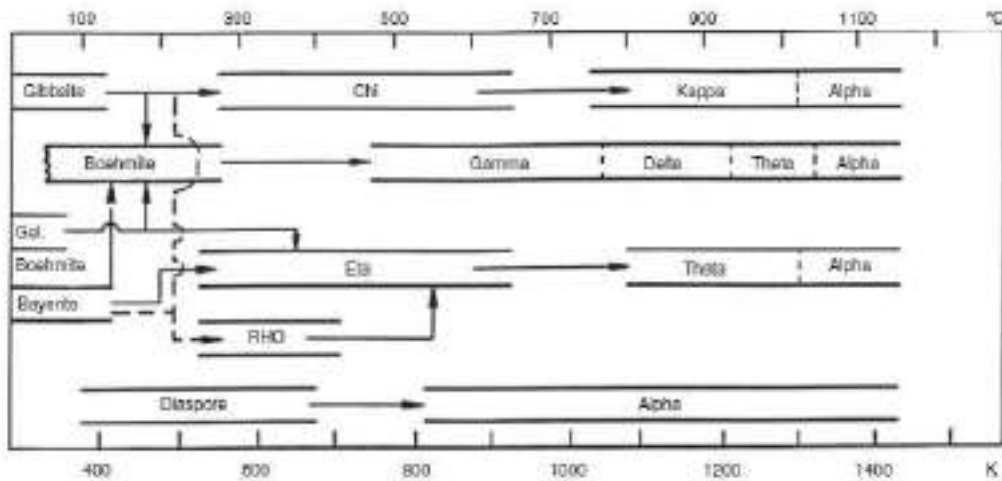


Figure 1. Transformation sequences form different precursors α - Al_2O_3 [6]

The first step in production of aluminum oxide ceramic parts is green body formation by (i) powder compaction (dry pressing, hot pressing, cold isostatic pressing, hot isostatic pressing), (ii) casting (slip casting, gel casting), (iii) plastic forming (extrusion, injection). The final properties of ceramics materials depend on the microstructure obtained after sintering process. The sintering process is usually accompanied by some desirable and some undesirable changes within the material. The largest changes occur in strength, elastic modulus, hardness, fracture toughness, electrical and thermal conductivity, permeability to gases and liquids, average grain size and shape, distribution of grain size and shape, average pore size and shape, distribution of pore size and shape, chemical composition and crystal structure [7]. The typical temperatures used for sintering alumina ceramics (α - Al_2O_3) are between 1600 °C and 1800 °C. Sintering of aluminum oxide ceramics is carried out by reactions in the solid state, which leads to an increase in density (densification), a decrease in porosity and an increase in the strength and hardness of the ceramic material. These processes lead to shrinkage of sintered product up to 20% [8-10]. The kinetics of sintering processes and the properties of sintered ceramic material also significantly depend on the type and concentration of impurities, shape and size of powder particles, uniformity of raw material density and technological parameters of sintering: heating rate (°C/s, K/s), heating methods (conventional, microwave, etc.), heating mode (single stage, two stage), sintering time and cooling rate of sintered product.

It was found that small amount of MgO (0.25 wt%) as additives in Al_2O_3 allow the achievement of fine-grained material at full density. Without doubt, MgO is the most intensively studied of the additives that promote the sintering of alumina to high densities. MgO inhibits the discontinuous grain growth. It was found that grain boundaries do not break away from the pores, which prevents the inclusion of pores trapped inside new large grains, with slow and long diffusion paths for densification [9-11]. The majority of MgO doped into Al_2O_3 resides at the grain boundaries, because the dissolution of MgO in Al_2O_3 is small, about 300 ppm. This is due to the relatively large difference in ionic radius: 0.72Å for Mg^{2+} and 0.53Å for Al^{3+} [11-13]. The paper presents a mathematical model of conventional solid state sintering of aluminum oxide ceramics in an electric furnace, which will analyze the influence of sintering time on the density and shrinkage of test samples. Simulation-modeled solid state sintering is performed without the presence of a liquid phase. Numerical

simulations of heating, sintering and cooling models will be performed by the finite element method in the computer program Comsol Multiphysics.

MATERIALS AND METHODS

The mathematical model of heating, single-stage dry sintering and cooling of single-phase aluminum oxide ceramics includes interconnected thermal, diffusion and mechanical processes. Influencing factors on the density and shrinkage of the sintered sample originating from the raw material properties, characteristics of the electric furnace and sintering parameters are shown in Figure 2. Sintering reduces the free energy of the system "starting powder-additives-moisture" which turns into a thermodynamically more stable solid with less free energy accumulated in the volume and surface area of the grain. The presence of at least one of the three main driving forces is necessary for the beginning of sintering: increased pressure, increased free energy of the grain surface or the occurrence of chemical reactions. Heat supply activates chemical reactions and increases free energy in the volume and on the grain surface [14, 15].

In the FEM modeled dry sintering process of single-phase aluminum oxide ceramics, the action of only one sintering driving force is assumed, increased free energy of the grain surface, which is jointly affected by heat input, atomic diffusion between starting powder grains and nucleation of new grains. The pressure in the electric furnace is constant and equal to the standard atmospheric pressure. The single-phase composition of the dried raw material composed of the starting powder $\alpha\text{-Al}_2\text{O}_3$ only, does not undergo polymorphic changes or chemical reactions are carried out in it.

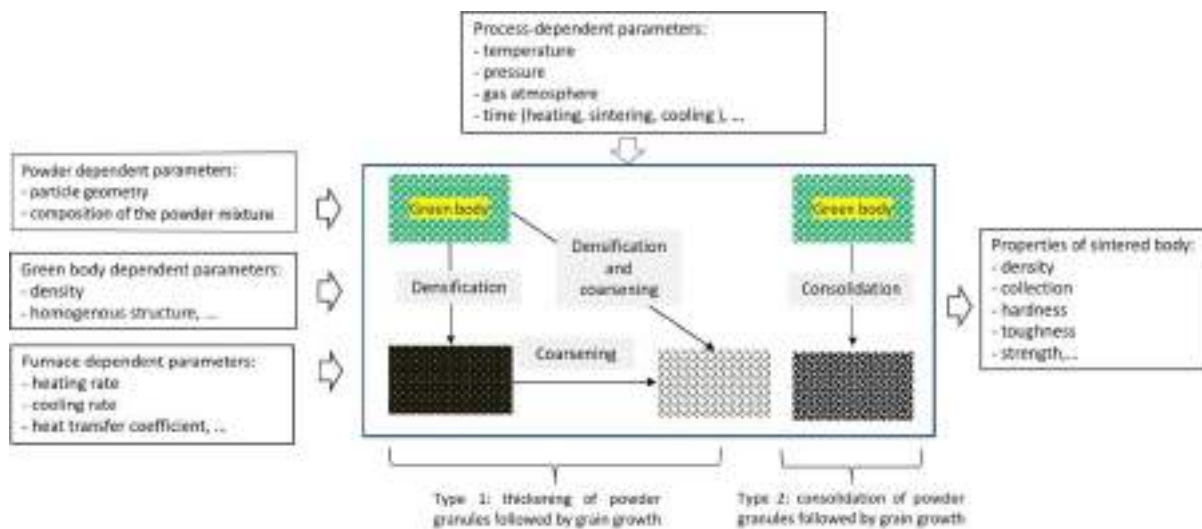


Figure 2. Influencing factors on shrinkage and density of dry sintered samples and main sintering mechanisms: densification, consolidation, and coarsening

During dry sintering, the starting grains of $\alpha\text{-Al}_2\text{O}_3$ do not melt but only densificate and aggregate through the processes of diffusion, evaporation and condensation, creep, and viscous flow. In the densification process, the powder particles are compressed and glued to form the starting grains of the sintered material. The elevated temperature encourages diffusion along the grain boundaries, creep, and viscous flow of material from the grain

boundary to the neck and porosity between the grains, allowing the starting grains to continue to grow and coarsen. In the processes of consolidation, large grains grow at the expense of small ones, and there is no significant densification. Consolidation is influenced by evaporation and condensation processes and surface and volume diffusion. In these processes, the transfer of matter is directed from the surface to the neck of the grain [14]. The mechanisms of densification and coarsening are opposed to each other, so the density and shrinkage of the sintered material depends on which mechanism was more dominant. When the densification mechanism dominates, the pores become smaller over time and may disappear completely, resulting in uniform shrinkage in all directions and achieving a theoretical density. When the grain coarsening mechanism is faster, grains and pores between grains grow. The action of densification and coagulation mechanisms is influenced by the temperature, grain size, pressure, and gas atmosphere in the furnace. The rate of densification and coarsening can be increased by increasing the sintering temperature or decreasing the size of the initial grain. The densification process can be stimulated by increasing the pressure in the sintering furnace or by applying unconventional sintering methods [14, 15].

During the sintering process, three basic phases are observed in which different mechanisms of substance transfer appear [6]: initial phase (which includes regrouping of particles and formation of contacts between grains), intermediate phase (which includes grain growth and grain boundary formation and further contact growth and thickening) and the final phase (which includes the reduction and closure of pores and the growth of new grains). The dependence of the density of the sintered material on the sintering time is shown in Figure 3. By heating the green material to the sintering temperature, several isolated pores are formed which need to be removed in the final stage. Removing isolated pores in the final stage is a lengthy process and requires most of the sintering time. For the successful elimination of pores in the final stage, there must be a transfer of the substance into the pores, and the gases that have hitherto filled the pores must come to the surface. Removing the isolated pores reduces the volume of the workpiece and increases the density.

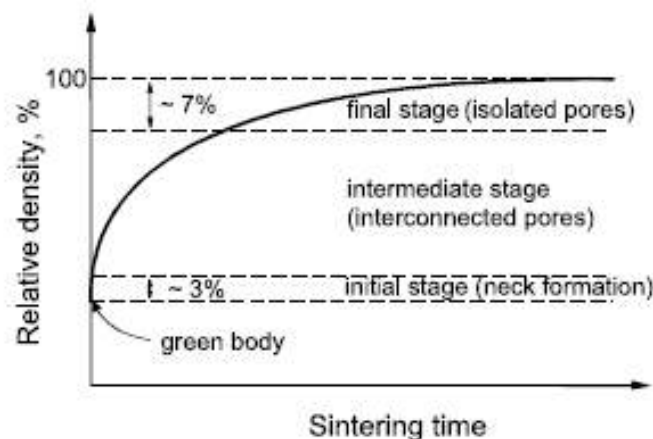


Figure 3. The densification curve of the green body as a function of the phases and duration of sintering [15]

The paper mathematically models the conventional solid state sintering of single - phase aluminum oxide ceramics with the aim of predicting the density of sintered samples. The chemical composition of the high purity starting powder (manufactured by Alcan Chemicals, USA) is listed in Table 1. The mean diameter of Al_2O_3 grains was 983 ± 120 nm. 70 wt.%

aqueous suspension of Al₂O₃ was prepared for casting in gypsum molds with the content of Dolapix CE-64 dispersant in the amount of 0.2 wt.%. The suspension was homogenized in a planetary ball mill for 90 min and an ultrasonic bath BRANSONIC 220 for 15 minutes at a frequency of 50 kHz and a power of 120 W. After homogenization, the suspension was poured into gypsum molds and dried at room temperature for 24 hours. After drying and machining of the green bodies to the dimensions of 20×20×20 mm, a conventional single-stage sintering was performed in an electric furnace Nabertherm P310 without a protective atmosphere.

Table 1. Chemical composition of Al₂O₃ powder

Component	MgO	Fe ₂ O ₃	SiO ₂	Na ₂ O	CaO	Al ₂ O ₃
w, wt. %	0.066	0.015	0.020	0.050	0.013	the rest

Heating to sintering temperature was performed at a rate 3 °C/min, 5 °C/min, and 7 °C/min. Sintering temperatures were 1600 °C, 1625 °C and 1650 °C. The isothermal holding time at the sintering temperature was 2 h, 4 h and 6 h. For each combination of sintering temperature and time, sintering of three test specimens was performed. The cooling rate of the sintered samples to room temperature was 11 °C/min. The density of sintered samples was determined by means of Archimedes method using a Mettler Toledo JP703C analytical balance. The density of test specimens is determined from the expression:

$$\rho = \frac{m_z}{m_z - m_m} (\rho_{H_2O} - \rho_{air}) + \rho_{air} \quad (1)$$

where m_m , mass of the sample in the medium, [g], m_z , mass of the sample in air, [g], ρ_{H_2O} , density of the medium, [g/cm³], ρ_{air} , density of the air, at room temperature, $\rho_{air} = 0.0012$ g/cm³. The density of green bodies was determined as ratio of mass and volume of green body, the mean density of the ceramic green body was 2.924 ± 0.053 g/cm³. To set up a mathematical model for sintering single-phase aluminum oxide ceramics, the temperature-dependent thermal properties listed in Figure 4 and the mechanical properties listed in Table 2 were applied.

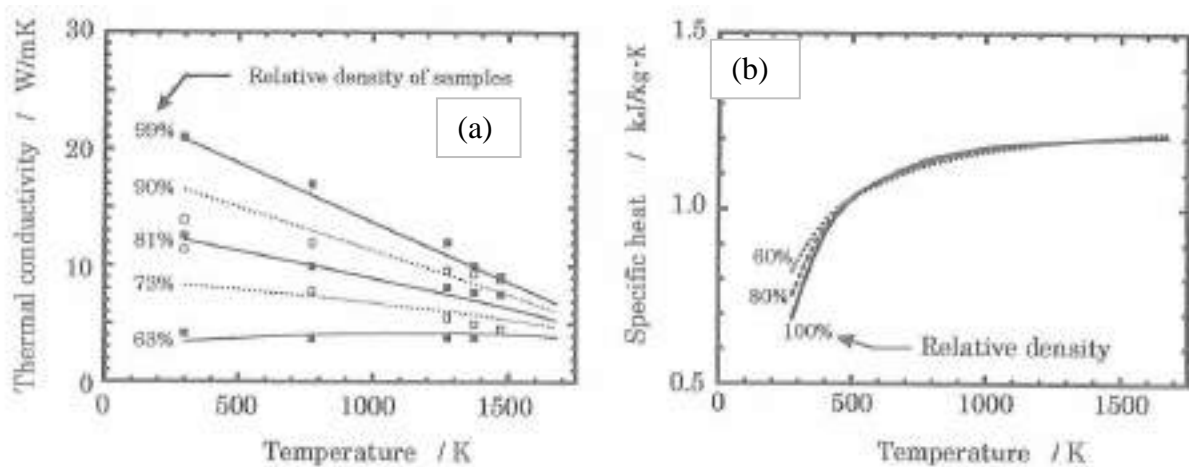


Figure 4. Thermal properties of raw materials of temperature dependent Al₂O₃ ceramics [17]: (a) thermal conductivity, (b) specific heat capacity

Table 2. Thermal and mechanical properties of polycrystalline Al₂O₃ [8, 14]

Property	Value	
Thermal expansion coefficient of the polycrystalline Al ₂ O ₃	from 25 °C to 100 °C, K ⁻¹	7.9 · 10 ⁻⁶
	from 25 °C to 200 °C, K ⁻¹	6.5 · 10 ⁻⁶
	from 25 °C to 800 °C, K ⁻¹	7.8 · 10 ⁻⁶
	from 25 °C to 1200 °C, K ⁻¹	8.3 · 10 ⁻⁶
Density, g/cm ³	3.960	
Young's modulus, GPa	from 25 °C to 100 °C	386
	from 25 °C to 1200 °C	286
Poisson's ratio	0.27	

The heating of the ceramics green body in an electric furnace is modeled as a three-dimensional thermal-mechanical problem by simultaneously solving the differential equations of heat conduction and the creation of thermal stresses and deformations.

$$\rho c \left(\frac{\partial T}{\partial t} + \vec{u} \cdot \nabla T \right) + \nabla \cdot \vec{q} = -\alpha T \frac{dS}{dt} \quad (2.a)$$

$$\vec{q} = -\lambda \nabla T \quad (2.b)$$

$$\varepsilon = \varepsilon_{el} + \varepsilon_{th} = \varepsilon_{el} + \alpha(T - T_0) \quad (2.c)$$

$$\vec{\sigma} = [D](\varepsilon - \varepsilon_{th}) \quad (2.d)$$

The meaning of the variables in the mathematical model of heat conduction in the sintered ceramics is as follows: ρ [kg/m³] is the density, c [J/kgK] is the thermal capacity, λ [W/mK] is the thermal conductivity, α [1/K] is the thermal coefficient expansion, q [W/m²] is the heat flux density vector, S [Pa] is the Piola Kirchhoff stress tensor, u [m/s] is the raw material deformation rate vector, ε_{el} is the elastic strain tensor, ε_{th} is the heat-induced strain tensor stresses, T_0 [K] is the reference temperature, σ [Pa] is the stress vector, $[D]$ is the elastic matrix. The differential equation of heat conduction was solved under the initial condition $\vartheta(x, y, z, 0) = 20$ °C. On the lower side of the sintered specimen leaning on the floor of the furnace, the boundary condition of the second type $q(x, y, 0, t) = 0$ is given. On the other sides of the sintered body, the boundary condition of the third type is given:

$$\alpha_{furnace}(T_{furnace} - T) = -\lambda \nabla T \quad (3)$$

in which $\alpha_{furnace}$ [W/m²K] is the heat transfer coefficient in the furnace, and T [K] is the surface temperature of the sample. The system of equations (2) - (3) represents a nonlinear and nonstationary thermo-mechanical problem which solves using the finite element method and iterative algorithms in the computer program Comsol Multiphysics. The corrections of values of thermal and mechanical properties and displacements of network nodes were done at the end of each time step. The geometric domain of the sintered specimen with initial dimensions of 20×20×20 mm was discretized with 16179 tetrahedral finite elements that make up a network with 72692 nodes with the greatest distance between two adjacent nodes being less than 2 mm. A regression model of the dependence of the density of sintered Al₂O₃ ceramics on the heating rate and temperature and sintering time was applied to model the change in density during sintering. The regression model was determined in the computer program Design - Expert 11 based on the results of the experimental implementation of the Box-Behnken experimental plan and ANOVA analysis of

changes in the density of sintered samples. The model validation range includes heating rates up to 7 K/min, sintering temperatures from 1600 °C to 1650 °C and sintering times from 2 h to 6 h:

$$\rho = 8.46634 - 2.865 \cdot 10^{-3} \cdot \vartheta - 1.87 \cdot 10^{-4} \cdot v_h - 1.10713 \cdot t_s + 6.9 \cdot 10^{-4} \cdot \vartheta \cdot t_s \quad (4)$$

In equation (4), the meaning of the notation is as follows: ρ [g/cm³] is the density of the sintered material, v_h [°C/min] is the heating rate, ϑ [°C] is the sintering temperature, t_s [h] is the sintering time. Based on equation (4), equations for deriving the dependence of density and shrinkage coefficient α_s depending on the sintering temperature of Al₂O₃ for a given heating rate and sintering time are derived. The shrinkage coefficient during sintering was determined under the assumption of isotropic shrinkage of green body weighing 0.023392 kg dried in a gypsum mold to form a sample with dimensions 20×20×20 mm. According to the results of the pre-experiments, the average decrease in the mass of the sintered sample by 0.90% in relation to the mass of the green body was determined. The shrinkage coefficient of the raw material during sintering is determined by equation (5):

$$\alpha_s = \frac{\sqrt[3]{\frac{m_s - L_0}{\rho}}}{(T - 293.15)L_0} \quad (5)$$

in which $m_s = 0.02318$ kg is mass of sintered sample, ρ [kg m³] is density of sintered sample determined according to equation (4), $L_0 = 0.02$ m length of raw material and T [K] temperature. The algorithm of the FEM model separately simulates the heating of the raw material, holding at the sintering temperature and cooling of the sintered sample. The density of the green body at room temperature was 2924 kg/m³. The increase in density as a function of sintering time, at a given temperature, was determined by Equation (4). The density of sintered Al₂O₃ ceramics depending on the value of absolute temperature during cooling was mathematically modeled by expression (6) taken from the database on material properties in the computer program Comsol Multiphysics.

$$\rho = 4003.559 - 0.02402771 \cdot T - 9.208687 \cdot 10^{-5} \cdot T^2 + 4.559764 \cdot 10^{-8} \cdot T^3 - 9.102231 \cdot 10^{-12} \cdot T^4 \quad (6)$$

Equations (4) to (6) modeled the change in density and coefficient of thermal expansion of Al₂O₃ in the FEM simulation in the temperature range from 1600 °C to 1650 °C for sintering times up to 6 hours, thus initiating a change in material properties caused by sintering. The dependence of the change in thermal conductivity and specific heat capacity on the sintering temperature in the FEM program was introduced by tabular values defined based on the data read from Figure 4.

RESULTS AND DISCUSSION

Computer simulations of sintering performed in the FEM program Comsol Multiphysics included solving the problem of heat conduction to the raw material during heating in an electric chamber furnace, the occurrence of thermal stresses and deformations and predicting changes in density and dimensions of the sintered sample in the form of a cube. A series of FEM simulations with different network densities of tetrahedral finite elements

with assumed sintering temperatures: 1600 °C, 1625 °C and 1650 °C and assumed sintering times between 2 to 6 hours were performed.

Figure 5a shows the change in the density of sintered Al₂O₃ ceramics depending on the temperature and sintering time determined based on computer simulations. From the course of the density change curves, a slower increase in density at a sintering temperature of 1600 °C is predicted by computer simulation. At sintering temperatures of 1625 °C and 1650 °C, a faster increase in density in the initial sintering phase and a slower growth in the final phase are observed. After 6 hours of sintering, the FEM simulation predicts the achievement of a density close to the theoretical value, i.e. a relative density of about 97%. Figure 5b and Table 3 show a comparison of the density determined based on computer simulation of sintering and the density determined in sintering experiments for the same sintering conditions (heating rate, temperature, and sintering time). The correlation coefficient of the calculated and experimentally determined densities is $R^2 = 0.86$. This value of the correlation coefficient indicates that the FEM sintering model qualitatively describes the kinetics of the sintering process, but the model has not yet fully covered the complex interaction of sintering parameters.

According to [14, 15], the initial phase of Al₂O₃ sintering begins at temperatures above 1200 °C, while at 1500 °C the intermediate phase already occurs. When heating at lower speeds up to 3 K/min, it can be assumed that the initial sintering phase was completed before heating the raw material to 1600 °C. When heating at speeds higher than 7 K/min, it can be assumed that the initial sintering phase will be prolonged to higher temperatures at which isothermal holding is performed. Due to the above, the calculated density at a shorter time and lower sintering temperature deviates from the experimentally determined one. The model predicts well the densities formed after sintering longer than 4 h at temperatures higher than 1625 °C.

Table 3. The measured and calculated density of sintered Al₂O₃ ceramics

Temperature, °C	Heating rate, °C/min	Sintering time, h	Measured density, g/cm ³	Calculated density, g/cm ³
1600	3	4	3.854	3.8693
1600	5	2	3.879	3.8751
1600	5	6	3.869	3.8626
1625	3	6	3.891	3.8949
1625	7	6	3.893	3.8941
1625	3	2	3.833	3.8384
1650	5	2	3.758	3.8009
1650	7	4	3.887	3.8633
1650	3	4	3.885	3.8640

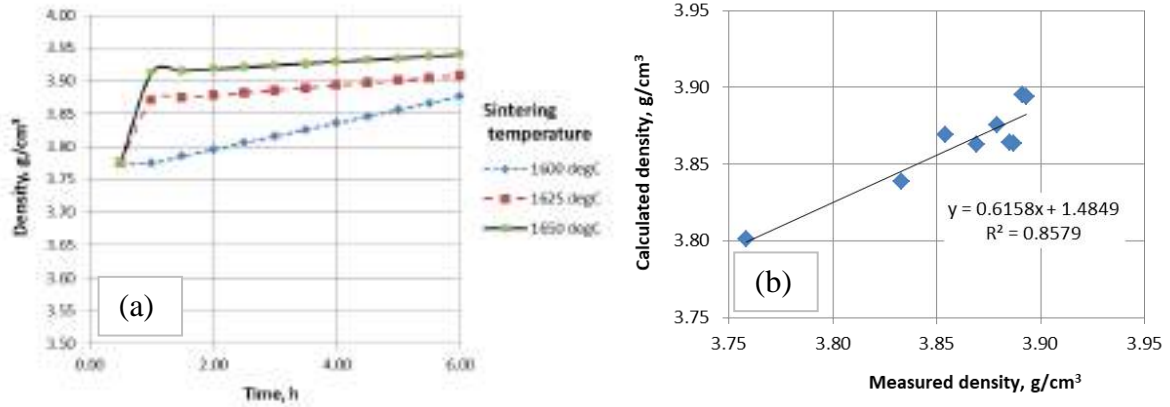


Figure 5. Density of sintered Al_2O_3 : (a) Density determined based on FEM simulations for heating rate $3\text{ }^\circ\text{C}/\text{min}$, (b) Comparison of calculated and measured densities for the same sintering conditions

Figure 6 a-b shows an example of a FEM simulation of sample collection after heating at $3.5\text{ }^\circ\text{C}/\text{min}$ and sintering at $1625\text{ }^\circ\text{C}$ for 2 hours and 6 hours. The shrinkage value is expressed as an absolute value as a function of sintering time. The 3D views in Figure 6.c-d show the areas of the same shrinkage amount. From their shape, a greater shrinkage at the edges relative to the center of the sample is observed.

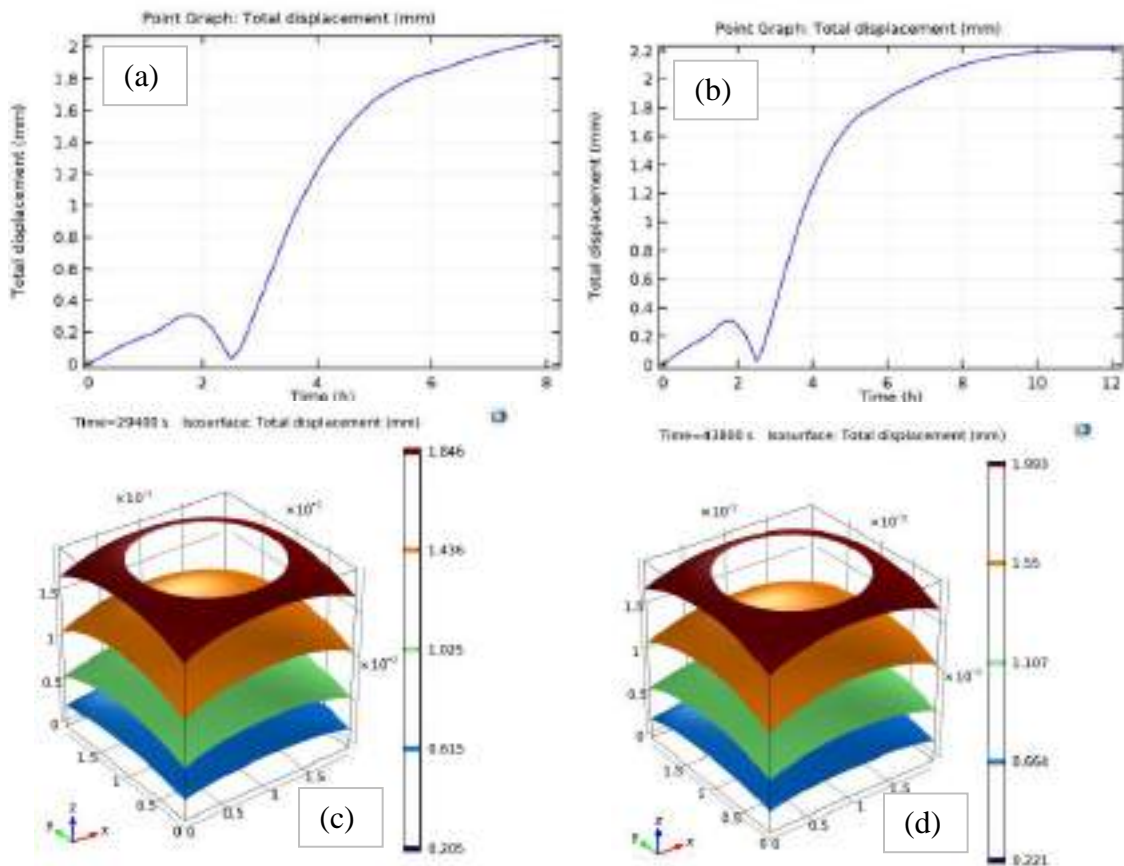


Figure 6. Prediction of the amount and form of shrinkage of the sintered sample after heating at a speed of $3.5\text{ }^\circ\text{C}/\text{min}$ to a sintering temperature of $1600\text{ }^\circ\text{C}$ and sintering for the duration of: a) 2 hours, b) 6 hours

Figure 7 shows the predicted relative linear shrinkage of dry sintered samples as a function of sintering temperature and time. The predicted shrinkage is less for a lower solid state sintering temperature (1600 °C) compared to for a higher sintering temperature (1655 °C). The predicted course of the shrinkage curves indicates the possible occurrence of grain growth during sintering at a lower temperature for more than 4 hours. When sintering at a higher temperature (1650 °C), simultaneous thickening and coarsening of the grain is expected, regardless of the selected sintering time.

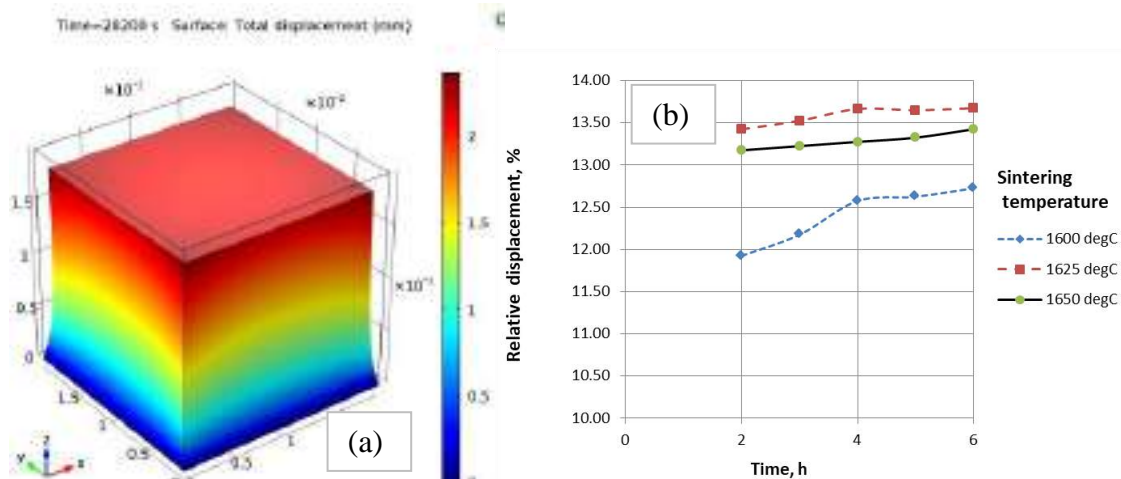


Figure 7. The shrinkage of the Al_2O_3 sample after heating to a sintering temperature at a rate of $3.5\text{ }^\circ\text{C}/\text{min}$ was determined by FEM simulation:
a) relatively linear shrinkage; b) shrinkage after sintering at $1625\text{ }^\circ\text{C}/4\text{ h}$

CONCLUSIONS

Computer simulation in the FEM program Comsol Multiphysics can predict well the change in density and shrinkage of solid state sintered aluminum oxide ceramics at the macroscopic level of the process description. The numerical model of the sintering process is solved as a nonlinear thermo-mechanical problem with the heating, sintering, and cooling phases of the sample. Validation of the model was performed by determining the density of sintered samples by the Archimedean method, which in comparison with the calculated values show a concordance of 86%.

The FEM model predicts the highest density of Al_2O_3 ceramics, in the amount of $3.895\text{ g}/\text{cm}^3$ after sintering at $1625\text{ }^\circ\text{C}$ or $1650\text{ }^\circ\text{C}$ for more than 5 hours. In sintering experiments, the highest density value, in the amount of $3.891\text{ g}/\text{cm}^3$, was achieved by sintering at $1625\text{ }^\circ\text{C}$ for 6 hours, with a heating rate of $3\text{ }^\circ\text{C}/\text{min}$. In computer simulations and experimental validation of the model, the heating rate on the sintering temperature did not show a significant influence on the final density.

Acknowledgements

The research was conducted with the financial support of the Croatian Science Foundation on the project IP-2016-06-6000 Advanced monolithic and composite ceramics for wear and corrosion protection (WECOR).

REFERENCES

- [1] L. Ćurković, M. Fudurić Jelača, Dissolution of alumina ceramics in HCl aqueous solution, *Ceram. Int.* 35(2009), pp. 2041-2045.
- [2] L. Ćurković, M. Fudurić Jelača, S. Kurajic, Corrosion behavior of alumina ceramics in aqueous HCl and H₂SO₄ solutions, *Corros Sci.* 50(2008), pp. 872-878.
- [3] L. Ćurković, I. Kumić, K. Grilec, Solid particle erosion behaviour of high purity alumina ceramics, *Ceram Int.*, 37(2011), pp. 29-35.
- [4] J. F. Shackelford, R. H. Doremus, *Ceramic and Glass Materials: Structure, Properties and Processing*, Springer, New York, NY, USA, 2008.
- [5] C. Legros, C. Carry, P. Bowen, H. Hofmann, Sintering of a transition alumina: effects of phase transformation, powder characteristics and thermal cycle, *J. Eur. Ceram. Soc.* 19(1999), pp. 1967-1978.
- [6] K. Wefers, C. Misra, *Oxides and Hydroxides of Aluminium Alcoa Technical Paper N°19*, Aluminium Company of America Pittsburgh, PA, 1987.
- [7] T. Shirai, H. Watanabe, M. Fuji, M. Takahashi, *Structural Properties and Surface Characteristics on Aluminum Oxide Powders*, Ceramics Research Lab, 2009 (9).
- [8] *Technical Ceramics*, Association of the German Ceramics Industry, Fahner Druck GmbH, Lauf, 2004.
- [9] P. Boch, J.C. Niepce, *Ceramic Materials: Processes, Properties, and Applications.*, John Wiley & Sons, 2010.
- [10] A. T. Ring, *Fundamentals of ceramic powder processing and synthesis*, Academic Press, 1996.
- [11] Z. Zhilui, L. Nan, R. Guozhi, Effect of polymorphism of Al₂O₃ on sintering and grain growth of magnesia aluminate spinel, *Sci. Sintering*, 39(2007), pp. 9-15.
- [12] M. Sathiyakumar, F. D. Gnanam, Influence of additives on density, microstructure and mechanical properties of alumina, *J. Mater. Processing Technol.*, 133(2003), pp. 282-286.
- [13] S. Pal, A. K. Bandyopadhyay, S. Mekherjee, B. N. Samaddar, P. G. Pal, Function of magnesium aluminate hydrate and magnesium nitrate as MgO addition in crystal structure and grain size control of α -Al₂O₃ during sintering, *Bull. Mater. Sci.*, 33(2010), pp. 55-63.
- [14] M. N. Rahman, *Ceramic processing and sintering*, Marcel Dekker, 2nd ed., Inc, New York, 2007.
- [15] L. Kang Suk-Joong, *Sintering densification, grain growth and microstructure*, Elsevier Butterworth-Heinemann, Oxford 2005.
- [16] C. A. Harper (editor), *Handbook of ceramics, glasses and diamonds*, McGraw-Hill Co. Inc, New York, 2001.

- [17] N. Miyata, T. Shiogai, C. Yamagishi, Y. Matsuo, Development of simulation model for normal sintering of Al_2O_3 by finite element method, Journal of the Ceramic Society of Japan, 106(1998), pp. 565-569.



IMPACT OF MOULD POWDER ON PHYSICOCHEMICAL PROPERTIES OF SLAG IN THE CONTINUOUS CASTING PROCESS

Vaso Manojlović^{1*}, Željko Kamberović¹, Miroslav Sokić², Branislav Marković², Milorad Gavrilovski³, Slobodan Radosavljević²

¹ University of Belgrade Faculty of Technology and Metallurgy, Belgrade, Serbia

² Institute for Technology of Nuclear and Other Mineral Raw Materials, Belgrade, Serbia

³ University of Belgrade Faculty of Technology and Metallurgy, Innovation center, Belgrade, Serbia

Poster presentation
Original scientific paper

Abstract

Mould powder is essential for the reliable operation of the continuous casting system and the quality of the cast steel. The very responsible roles of mould powder are fulfilled by selecting combinations of components that affect physicochemical properties of the resulting liquid slag, which lubricate the walls among the crystallizer and slab. The contribution of mould powder refers to the range of melting temperature and speed and the viscosity of glassy or crystalline slag and formation temperature. These connections are the research subject in this paper, emphasizing the functional dependence of viscosity and liquidus temperature of mould powder with its material composition. This research investigates the impact of basicity, alkali oxides (Na_2O and K_2O), and carbon-free content on viscosity and liquidus temperature of mould powder in the continuous casting process. The liquidus temperature of mould powder was obtained empirically after a year of experimental examination, and viscosity was determined using several models. Based on experimental investigation, we show empirical parameters for equitation of liquidus temperature of mould powder. Also, using established equations, we presented isolines for viscosity and liquidus temperature with experimental parameters.

Keywords: casting powder, continuous casting, viscosity, liquidus temperature

*Corresponding author (e-mail address): v.manojlovic@tmf.bg.ac.rs

INTRODUCTION

Mould powder is a synthetic product vital for a successful continuous casting process, minimizing defects and process problems. The basic functions of mould powder are:

- Protection of liquid steel from oxidation or nitration by forming liquid slag pool;
- Thermal insulation of liquid steel, preventing freezing of the steel meniscus;

- Formation of slag that lubricates the walls of the crystallizer and slab;
- Ensure even heat dissipation from the slab to the walls of the crystallizer;
- Dissolve inclusions and gas bubbles from the liquid steel;
- Control melting speed through lubrication of the formed steel shell and control of heat transfer;
- Provide formation of glassy or crystalline slag;
- Reduce scale formation [1-9].

Numerous parameters influence the properties of the mould powder, so optimization of its composition is based on empirical rules and plant data. Such parameters are chemical, mineral, granulometric composition, the surface-to-volume ratio of particles, and thermal conductivity. Main powder components are mineral components (oxides and fluorides) and carbon particles. The mineral component will form the mould slag and slag film, while carbon particles control the melting rate of the powder, meeting the requirements of liquid slag. Viscosities of mould powder and formed slag influence many parameters, such as powder consumption, brake (solidification) temperature, slag entrapment, lubrication supplied to the mould, and fraction crystal in the slag film (the ability of slag to dissolve inclusions). The slag viscosity increases with network forming components (e.g., SiO_2 and Al_2O_3) and decreases by introducing network breaking oxides (e.g., CaO) or fluxes (e.g., Na_2O , K_2O , and CaF_2) [1-9].

This research investigates the impact of basicity, alkali oxides (Na_2O and K_2O), and carbon-free content on viscosity and liquidus temperature of mould powder in a continuous casting process. The liquidus temperature of mould powder was obtained empirically after a year of experimental examination, and viscosity was determined using several models. As a result of this paper, we show a method for predicting different parameters, and we obtain novel equations within the proposed boundaries of the powder composition. Based on experimental investigation, we get empirical parameters for equitation of liquidus temperature of mould powder.

MATERIALS AND METHODS

The experiments are done and verified in industrial conditions in continuous steel casting local plant for over one year. The mould geometry is designed for continuous casting of the carbon (0.06-0.20%C) steel slabs.

Tables 1 show the matrix of the experiment for pseudo components (relative contents) and actual values of examined components: X_1 - (CaO/SiO_2); X_2 - ($\text{Na}_2\text{O}+\text{K}_2\text{O}$); X_3 – Carbon-free, in mas.%. The method of simplex lattice plan, lattice type {3,2}, for the second-degree model, for three - component systems was used to perform the planned experiment. Following the chosen model, the number of experimental points there were seven, including a control point (point 7) for checking the adequacy of the obtained mathematical models (Figure 1).The chemical composition of mould powder is shown in Table 2; the amount of Fe_2O_3 was constant to avoid its impact on observed models.

The coefficients of the regression equation were determined based on the general, canonical form of polynomials of the second degree for three-component systems, in the coordinates of the pseudo components, according to equation [3]:

$$y = \beta_1 z_1 + \beta_2 z_2 + \beta_3 z_3 + \beta_{12} z_1 z_2 + \beta_{13} z_1 z_3 + \beta_{23} z_2 z_3 \quad (1)$$

Where y is optimization parameter; β_i, β_{ij} are regression equation coefficients; z_i are pseudo components. The objectives (y_i) of the research are viscosity and liquidus temperature of mould powder. The viscosity was calculated using *Riboud, Lida, and K. Mills* models [2, 8, 9]. Liquidus temperatures were obtained experimentally in plant conditions using a thermo-microscope (E. Leitz Wetzlar, max. temperature 1450 °C, with a constant heat rate of 10 °C/min).

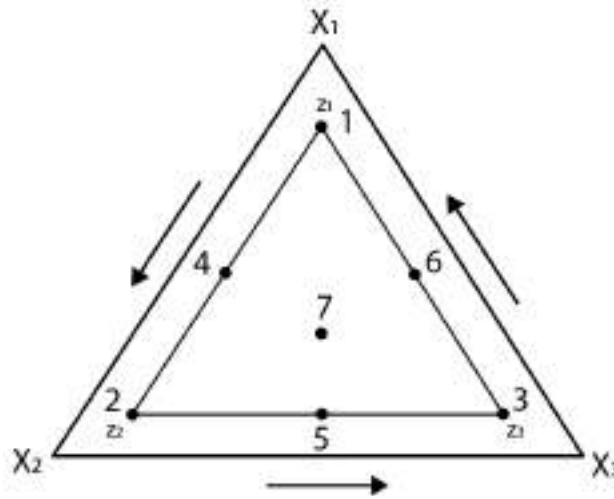


Figure 1. Experimental planning area and position of experimental points

Table 1. Matrix of the experiment for pseudo and examined components

Point of experiment	Pseudo components			The actual value of studied components		
	Z_1	Z_2	Z_3	X_1	X_2	X_3
1	1	0	0	1.2	6.5	7.5
2	0	1	0	0.7	9	7.5
3	0	0	1	0.7	6.5	10
4	0.5	0.5	0	0.95	7.75	7.5
5	0	0.5	0.5	0.7	7.75	8.75
6	0.5	0	0.5	0.95	6.5	8.75
7	0.33	0.33	0.33	0.86	7.32	8.32

Table 2. Chemical composition of mould powder, mas.%

Point of experiment	SiO ₂	CaO	Al ₂ O ₃	CaF ₂	Na ₂ O	K ₂ O	Fe ₂ O ₃	CO ₂	C-free
1	22.23	26.78	7.00	5.61	6.04	0.46	2.63	21.76	7.5
2	28.01	19.72	5.00	6.71	5.72	3.28	2.63	21.43	7.5
3	28.16	19.82	5.00	6.68	6.20	0.30	2.63	21.21	10
4	24.78	23.55	4.33	5.50	5.01	2.74	2.63	23.96	7.5
5	28.1	19.79	5.00	6.75	5.00	2.75	2.63	21.23	8.75
6	24.86	23.62	7.09	6.34	5.88	0.62	2.63	20.21	8.75
7	25.94	22.33	4.82	4.93	5.85	1.83	2.63	22.43	8.325

Phase compositions of the mould powder was determined using XRD (PHILIPS PW-1710) with a graphite monochromator, using Cu-K α radiation. The sample 7, in Table 2, was used

for XDR characterization. The granulometric composition of sample 7 was (in mm): -0,06 = 74 mas. %; -0.09 +0.06 = 11 mas. %; -0.2 +0.09 = 12 mas. %; -0.5 +0.2 mas. %; and +0.5 = 1 mas. %.

RESULTS AND DISCUSSION

The XRD analysis of the mould powder before melting showed that the basic components of the powder are: cuspidine, wollastonite, CaF_2 , CaCO_3 , Na_2CO_3 .

Water will be removed above 100 °C, crystalline water and hydroxides at about 450 °C, carbon combust above 500 °C, and dissociation of carbonates with releasing of CO_2 , above 650 °C.

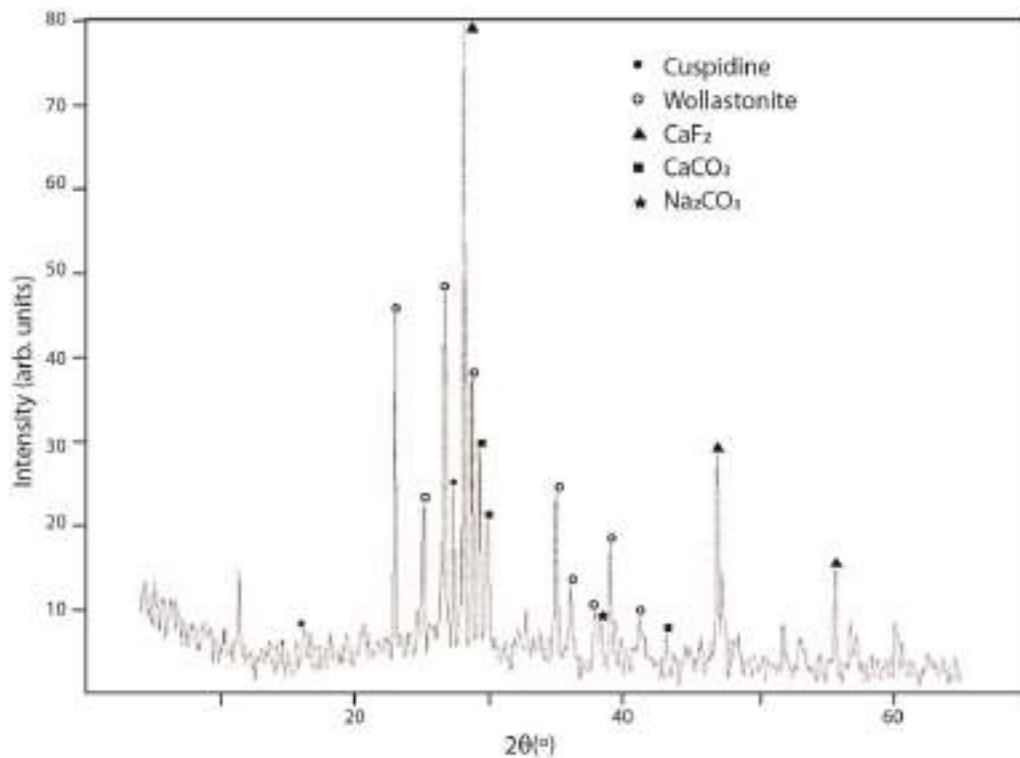


Figure 2. XRD analysis of the sample at point 7 (Table2)

The results of determining the values of regression equation coefficients for η and T_{liq} are given in equations 2 and 3. Table 3 shows calculated and actual values of liquidus temperature of mould powder for a given set of experiments. Since the *Lida* model corresponds best to the experimental data, we used this model to calculate the regression equation coefficients.

$$\eta = 1.679z_1 + 2.559z_2 + 3.484z_3 - 1.605z_1z_2 - 0.205z_1z_3 + 0.289z_2z_3 \quad (2)$$

$$T_{liq} = 1210.3z_1 + 1353.5z_2 + 1388.1z_3 + 0.001935z_1z_2 + 0.01476z_1z_3 + 57.90z_2z_3 \quad (3)$$

Table 3. Comparative values of experimental data and calculated values

Point	Viscosity, η [dPas]				Liquidus temperature, T_{liq} [°C]	
	Riboud	Lida	Mills	Calc.	Experiments	Calc.
1	1.79	1.68	2.04	1.68	1210	1210
2	3.02	2.56	8.65	2.56	1353	1353
3	3.85	3.48	12.04	3.48	1388	1388
4	1.98	1.72	2.27	1.72	1282	1282
5	3.53	3.09	11.06	3.09	1385	1385
6	2.82	2.53	5.52	2.53	1299	1299
7	2.32	2.38	3.56	2.38	1310	1310

Figures 3 and 4 show isolines at different basicity for liquidus temperature and viscosity of mould powder using equations 2 and 3, respectively.

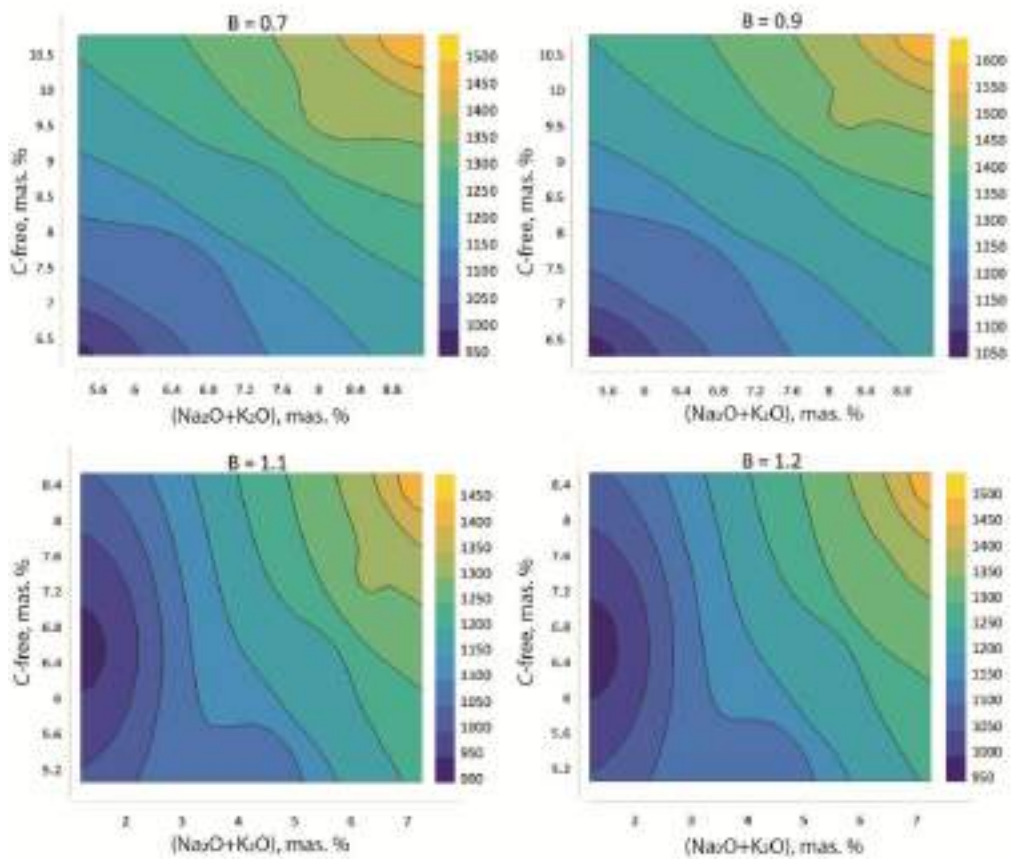


Figure 3. Liquidus temperature profiles (in °C)

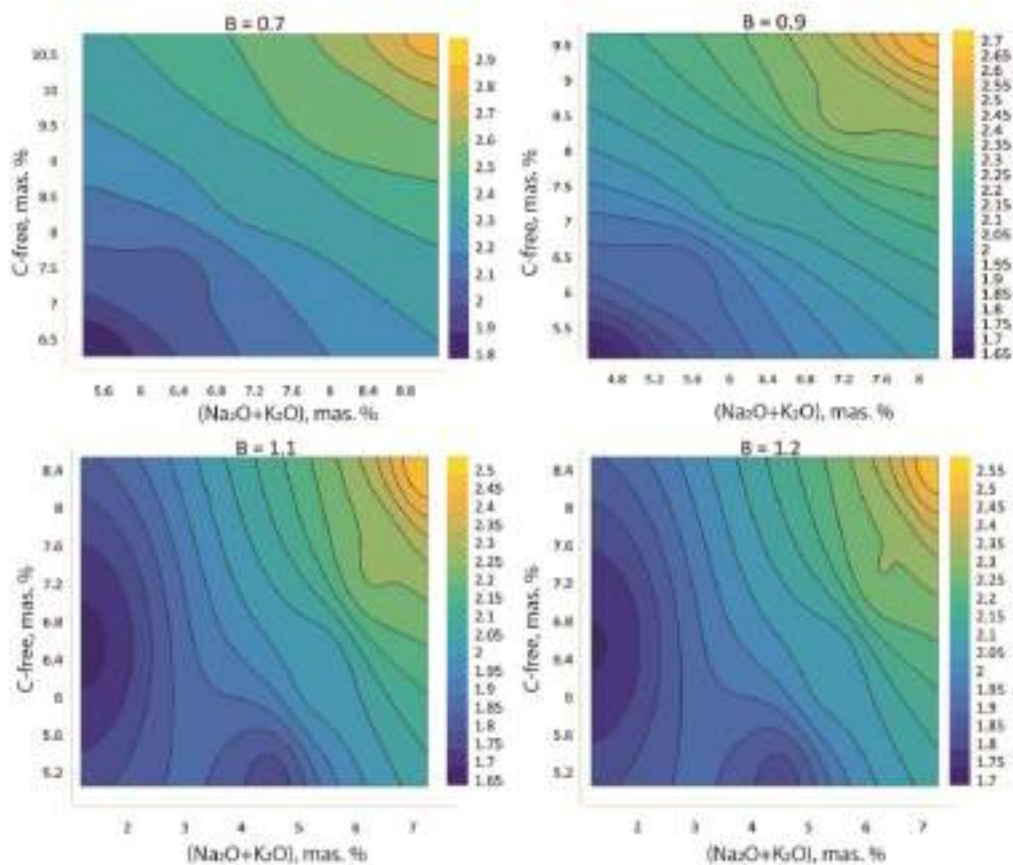


Figure 4. Viscosity profiles (in *dPas*)

Figure 4 shows appears of two local minimums, at middle of ranges of C-free and (Na₂O+K₂O) content, and higher values of basicity. One could note that effect of Na₂O and K₂O is synergetic, as we observed the sum of those components; however, the effect of Na₂O is much higher than K₂O, as it is shown in literature [1, 2]. The content of Al₂O₃ was in the range in the 4.3 to 8 mas. %, we did not examine its impact. Though, it would be very interesting to find correlation of this component, due to its dual and complex nature: it is capable to form or break oxygen networks.

CONCLUSIONS

In the presented work we presented method for getting regression equation coefficients for viscosity – η , and liquidus temperature – T_{liq} , of mould powder. The obtained equation could be used for a given range of chemical composition of mould powder. Also, using obtained equations we show isolines for viscosity and liquidus temperature with experimental parameters. Those results are very important for industrial application, due to influence of viscosity and liquidus temperature on many parameters, such as melting speed, consumption of powder (increases with increasing viscosity), slag entrapment, lubrication supplied to the mould, and fraction crystal in the slag film (the ability of slag to dissolve inclusions).

Acknowledgments

This work was supported by the Ministry of Education, Science and Technological Development of the Republic of Serbia (Contract No. 451-03-9/2021-14/200135).

REFERENCES

- [1] K. C. Mills, C. A. Däcker, *The casting powders book*, Chapter 9, Springer, Switzerland, 2017.
- [2] K. C. Mills, S. Karagadde, P. D. Lee, L. Yuan, F. Shahbazian, Calculation of physical properties for use in models of continuous casting process-part 1: mould slags, *ISIJ international*, 56(2016)2, pp. 264-273.
- [3] D. Gavrilovski, M. Gavrilovski, Determination of the chemical stability of glass-ceramic enamels, *Proceedings of XLVI ETRAN Conference*, (Ninoslav Stojadinović), The Society for Electronic, Telecommunications, Computers, Automation and Nuclear Engineering, Vol. IV, June 4-7, 2002, Banja Vrućica – Teslić, Serbia, pp. 250-252.
- [4] B. Arh, F. Tehovnik, F. Vode, Change of mould flux properties during continuous casting of ferritic stainless steel, *Metalurgija*, 56(2017)1-2, pp. 40-42.
- [5] A. Kamaraj, N. Haldar, P. Murugaiyan, S. Misra, High-Temperature simulation of continuous casting mould phenomena, *Transactions of the Indian Institute of Metals*, 73(2020)8, pp. 1-7.
- [6] E. Brandaleze, G. Di Gresia, L. Santini, A. Martín, E. Benavidez, Chapter 7, Mould fluxes in the steel continuous casting process, *Science and technology of casting processes*, IntechOpen, BoD–Books on Demand, 2012.
- [7] J. A. Kromhout, R. C. Schimmel, Understanding mould powders for high-speed casting, *Ironmaking & Steelmaking*, 45(2018)3, pp. 249-256.
- [8] P. V. Riboud, Y. Roux, L. D. Lucas, H. Gaye, Improvement of continuous casting powders, *Fachber, Huttenprax Metallweiterverarb*, 19(1981), p. 859.
- [9] I. Takamichi, H. Sakai, Y. Kita, K. Murakami, Equation for estimating viscosities of industrial mold fluxes, *High Temperature Materials and Processes*, 19(2000)3-4, pp. 153-164.



19th INTERNATIONAL FOUNDRYMEN CONFERENCE
Humans - Valuable Resource for Foundry Industry Development

Split, June 16th-18th, 2021

<https://ifc.simet.hr/>

**POSSIBILITIES OF ONLINE LABORATORY PRACTICALS IN TEACHING OF
CASTING COURSES**

Daniel Novoselović^{1*}, Štefanija Klarić², Francois Botha², Saša Gojković¹

¹ University of Slavonski Brod Mechanical Engineering Faculty, Slavonski Brod, Croatia

² Charles Darwin University, Casuarina, Australia

Poster presentation

Expert work

Abstract

Due to the pandemic, reconfiguration of teaching and operating approaches during 2020 became a reality for universities (as well as all other sectors). There was a need to adjust the delivery for students, whom were now not able to attend laboratory practicals, in order to provide them with a learning experience as close as possible to real laboratory conditions and allow them to achieve planned learning outcomes. This paper describes some adjustments to a casting laboratory practical for a Manufacturing Course (introductory and more advanced level).

Keywords: *casting laboratory practicals, online delivery, education*

*Corresponding author (e-mail address): dnovoselovic@unisb.hr

INTRODUCTION

Online delivery has been a reality in learning and teaching for over 20 years now. The development and application of learning management systems and implementation of e-learning allowed accessibility and flexibility in learning and obtaining degrees. Considering an organization and setup of delivery of online learning can be either synchronous (i.e. live teaching using conferencing video tools) or asynchronous (or hybrid) [1]. As in other areas, in general, implementation of digital technologies provides many benefits to education systems [2].

Due to well-known limitations of online teaching (i.e. isolation, lack of teacher – students and student-student interactions, possible motivation loss) traditional teaching in classroom (face-to-face F2F) remained present, especially for delivery in areas reliant on “hands-on” and practical learning [3, 4].

In order to exploit the flexibility of online teaching, with benefits of F2F delivery where appropriate, a blended learning (BL) model can be used [3].

Prior to COVID 19, engineering courses at Charles Darwin University were offered to internal and external students combining online delivery (synchronous through online collaboration systems, asynchronous using learning management system and providing students with learning materials and videos) and F2F delivery. Internal students would have classroom activities and laboratory practicals and external students would attend online classes and visit campus once a semester to cover practical parts of their courses in laboratories.

In the Mechanical Engineering Faculty of Slavonski Brod delivery in casting related subjects was F2F with lectures in classrooms, laboratory practicals in the Casting Laboratory and calculation and simulation tutorials in computer classrooms where students had full versions of software installed on the computers. Online learning management system was used only for assessments, development and submission (projects and reports).

In 2020 and 2021 adjustments had to be made to the delivery method as all teaching activities had to be offered online. This required the adjustment of teaching in laboratory practicals.

Providing laboratory experience as an online practice was a topic of a research for over a decade but its importance has grown in the last year [5-8]. In this paper the adjustment of an introductory laboratory practical in Casting is presented. In the development of an online version of this Casting practical principles (stages) of teacher professional development model (Determining the purposes, Creating the content, Self-paced learning, Discussing and Sharing, Reflecting and Mentoring and coaching) [3] were considered.

Another aspect of delivery that needed to be adjusted due to COVID 19 in subjects covering casting technology is application of software simulations. Simulations in casting can be used for solving problems with existing castings or development of the new casting systems, as they are important tool for [9]:

- visualisation and planning of mould filling,
- solidification and cooling of castings
- prediction of internal defects and their location,
- limitations related to mechanical properties, dimensional and surface accuracy etc.

PURPOSE OF CASTING PRACTICAL IN MANUFACTURING COURSE

At Charles Darwin University, the Manufacturing course introduces students to the basic principles of production, providing elementary information on processes like casting, forging, welding, material removal, additive manufacturing etc. The course is taught in the first/ third semester of Undergraduate Certificate Introduction to Science, Engineering and Technology and in the mechanical stream of Undergraduate Engineering programs.

Casting laboratory practical is the first assessment item in the unit. The purpose is to:

- introduce students to safety requirements of laboratory conditions, casting process and in manufacturing in general,

- demonstrate elementary principles, equipment and techniques of casting process
- offer considerations of casting conditions (parameters) and their influence on casting quality (casting defects).

In order to achieve these outcomes, and gain hands-on experience in casting, students would do casting in the laboratory by themselves and write a report, taking into consideration information provided from theory (lectures, tutorials and textbook [10]) and observations from the practical.

Prior to COVID 19, internal and external students would do this practical in the laboratory conditions at CDU Campus. Due to COVID and traveling and social distancing restrictions there was a need to adjust this practical for online delivery. In 2021 the practical was offered in a laboratory for internal students in Darwin and online for external students.

CREATING CONTENT FOR ADJUSTED CASTING LABORATORY PRACTICAL

For internal students, practical information: equipment list, personal protective equipment requirements and step by step task description are provided a few weeks prior the practical. Instructions also included a content guideline for the report and discussion questions that required observations of casting conditions (pouring temperature, measurement setup), cast quality (details of finished castings, casting defects, cast dimensions) and safety requirements.

For external students content needed to be adjusted to allow the same observations and analysis of the casting process online (*self-paced learning*). This included:

- adjusting the online resources and guidelines (Figure 1),
- development of the video materials (Figure 2) ,
- providing photos of temperature measurements and finished castings for the analysis
- setting the online class for students to provide additional clarifications and task description and answer questions around practical (*discussing and sharing*),
- setting a short online quiz to evaluate understanding of the task (*reflecting and evaluating*).


Title:
Casting practical

Overview:
Make sure it is very hot and very close vertical bars, please follow all safety guidelines and instructions

This is a practical session where some people, depending on what material casting is done to demonstrate the basic techniques of metal casting.

- The main objective is to consider the casting conditions (parameters) and their influence on the product quality and possible product defects.
- We will also consider work safety requirements in manufacturing.

Resources:
Read right through these instructions before you start.


 Casting Prac. Description subeet

Instructions:
Your job in this practical is to analyse the findings during the casting experiment and observation skills, and do calculations.

To complete this practical you should:
 If you are **internal student**: come to the lab on 10:00 (during the lab hours). If you don't attend practical session in the lab your report will be marked as 0.
 If you are **external student**: watch the recording of this practical on the LMS. The recording of this practical will appear under this item in Assessment Center in Faculty of the metal.


Submission requirements:
Submit your work when you have finished via the 'Add Content' link.

Grading and Feedback:
Marking rubric provided.

 EMQ215 Casting marking rubric subeet

Practical 1, Casting - Videos and Data for external students

Part 1 - Intro



CASTING

4


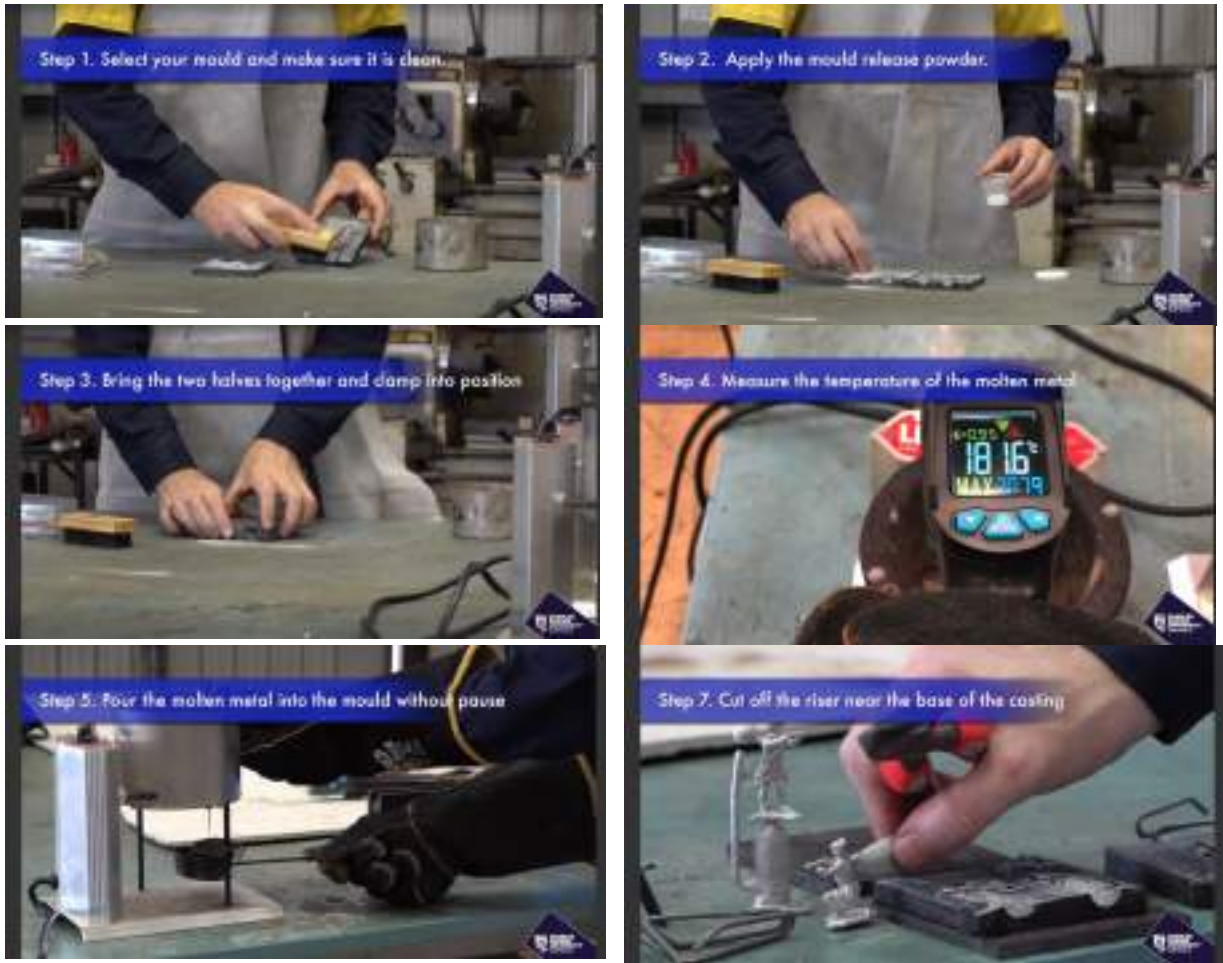


Figure 1. Online content adjusted to internal and online students



a)

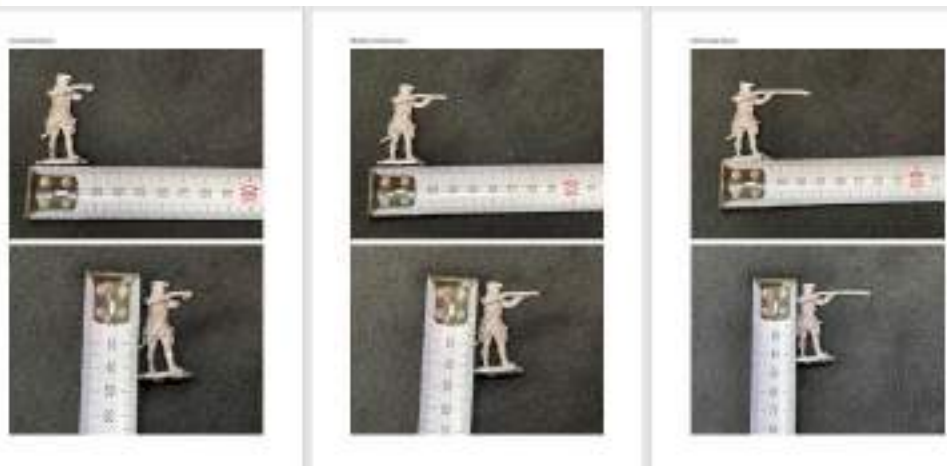
Practical 1 Casting
Temperature
Low:



Medium:



High:



b)

Figure 2. a) Sequences from the video of the casting practical and b) photos of finished castings

EXAMPLE OF SIMULATIONS IN AN ADVANCED CASTING COURSE

In the Mechanical Engineering Faculty of Slavonski Brod casting technology content is covered in two core subjects: Production processes I, on undergraduate level and in the subject of Casting, offered on postgraduate level (in the Technology stream).

In Production processes I, students are provided with basic knowledge of casting technology and they are introduced to different casting processes, basic technology possibilities of product forming by casting and simulation methods to define technology process parameters. As a part of this subject, mould production techniques, melting of metal and cast defects are presented as well.

In Casting, students are introduced to casting technology and casting as a production area and topics related to technology processes in casting facilities are covered.

Tutorials and practicals in Casting cover:

- visit to casting facilities in the area (Đuro Đaković Trade d. o. o.– Slavonski Brod, Saint Jean Industries doo – Slavonski Brod, Plamen doo - Požega),
- calculation and dimensioning of gating system,
- modelling of gating system in AutoDesk Inventor [11],
- calculations and simulations in NovaFlow&Solid software [12].

Taking into consideration COVID and transitioning to online delivery of teaching, lectures are provided in Learning Management System through webinars (Figure 3) while tutorials are modified:

- visits to casting facilities in the area and their production program are performed through a review of the content on their web pages,
- calculation and dimensioning of gating system is done as independent individual student work with support of available prepared content and consultations with the lecturer,
- modelling of gating system in student version of AutoDesk Inventor software,
- calculations and simulations that were conducted on computers in university classrooms where the software was installed are adjusted due to COVID and students are running simulations on Demo version of the software.



Figure 3. Web interface for Casting unit in Learning Management System

CALCULATIONS AND SIMULATIONS IN ONLINE DELIVERY

Calculation simulations imitate real events through a sequence of mathematical equations implemented in the software. For simulations to be useful, major influencing parameters need to be defined.

The Simulation of casting technology is well developed, and it is a basic tool for solving problems related to defects in casting production. This allows high quality and efficiency without additional casting attempts and failures and significantly reduce time to produce the first cast sample free of defects.

Taking into consideration limited availability of the full software licence for students, this part of the tutorials is adjusted to a Demo version of the Nova Flow & Solid software (Nova Flow & Solid CV Demo 4.60 r6), figure 4.



Figure 4. Interface of Demo version of simulation software NovaFlow & Solid CV Demo 4.60 r6 [12]

The demo version has the same options as the full version of the software, except that the Demo version doesn't allow simulation development on own castings but only on readily available casting models shown on Figure 5.

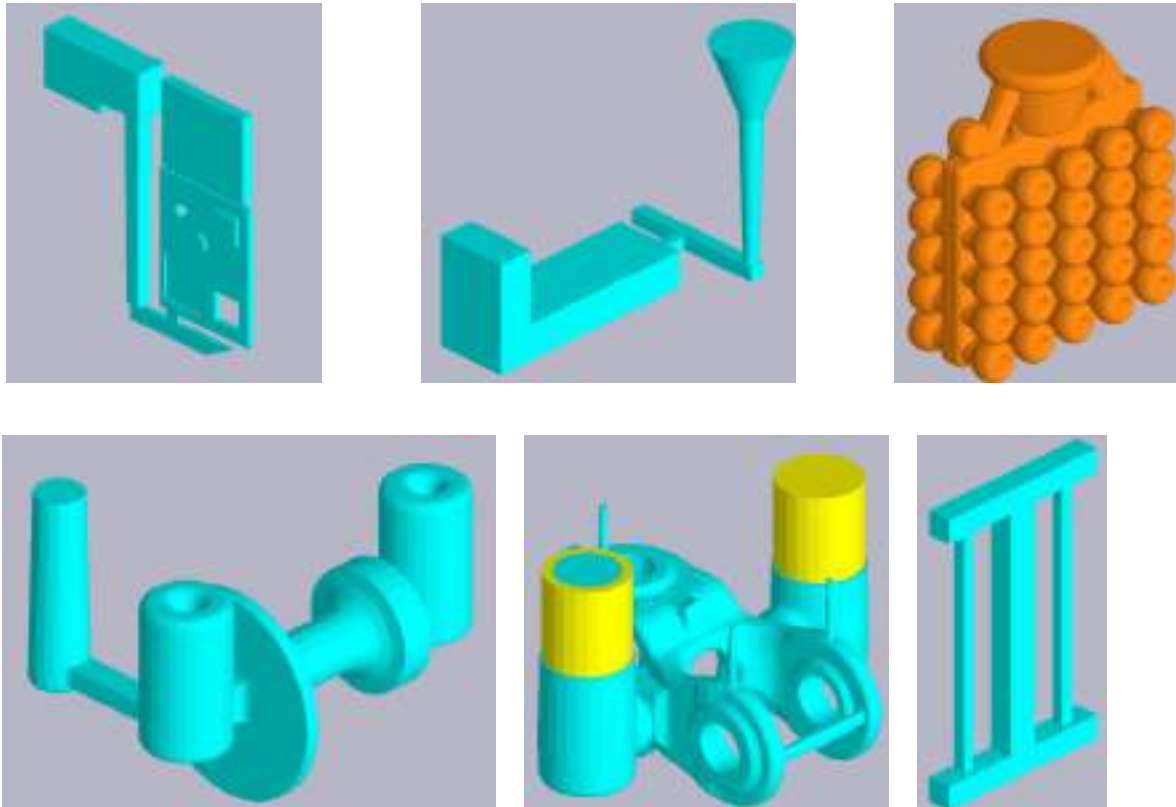


Figure 5. Available models for simulation in NovaFlow & Solid CV Demo 4.60 r6 [12]

Students are divided into teams and different technology parameters are given for simulation on the defined casting. After simulation students are supposed to submit a report (online submission, Figure 6) and provide analysis of their work through online presentation (example on Figure 7).

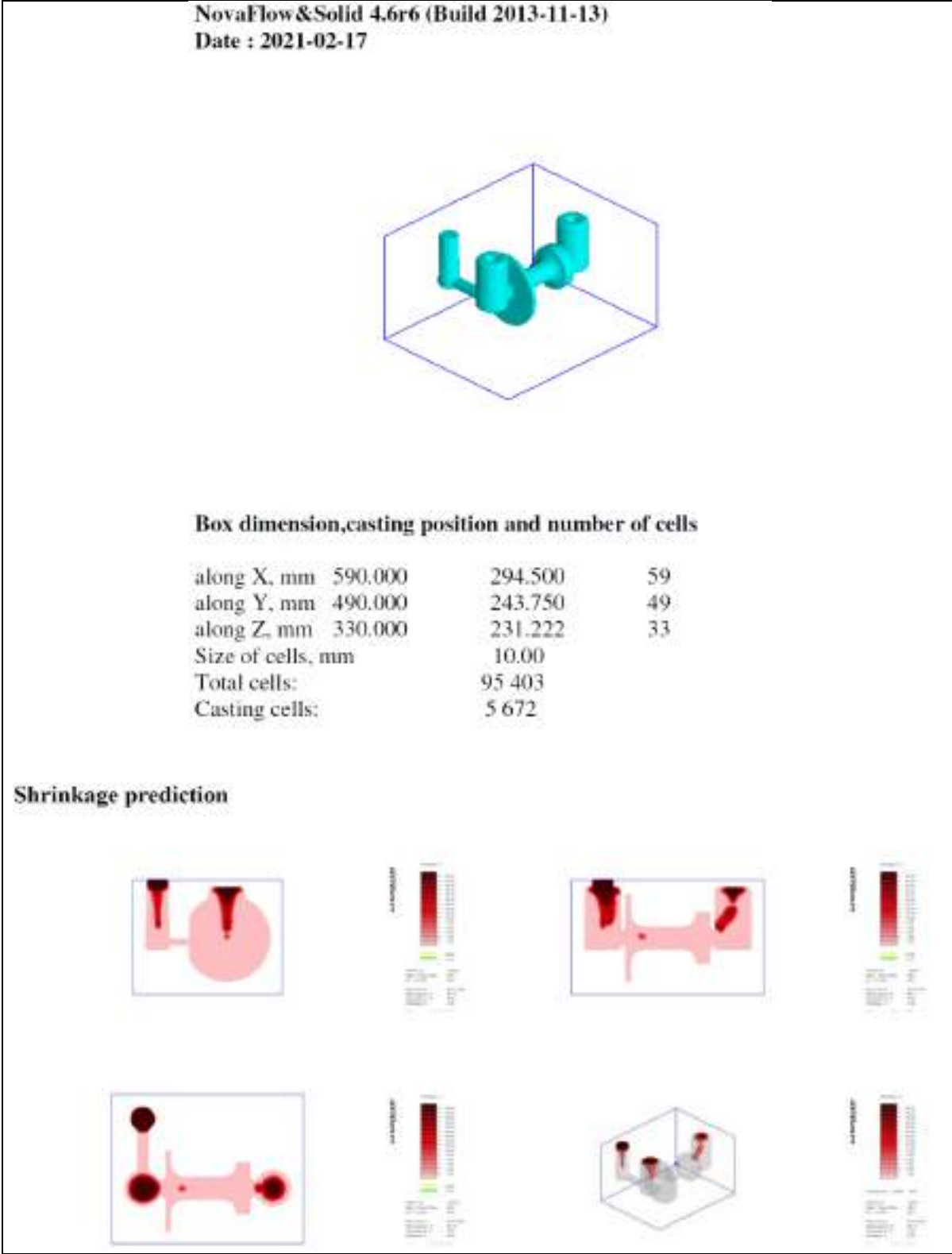


Figure 6. Report on casting simulation [11]

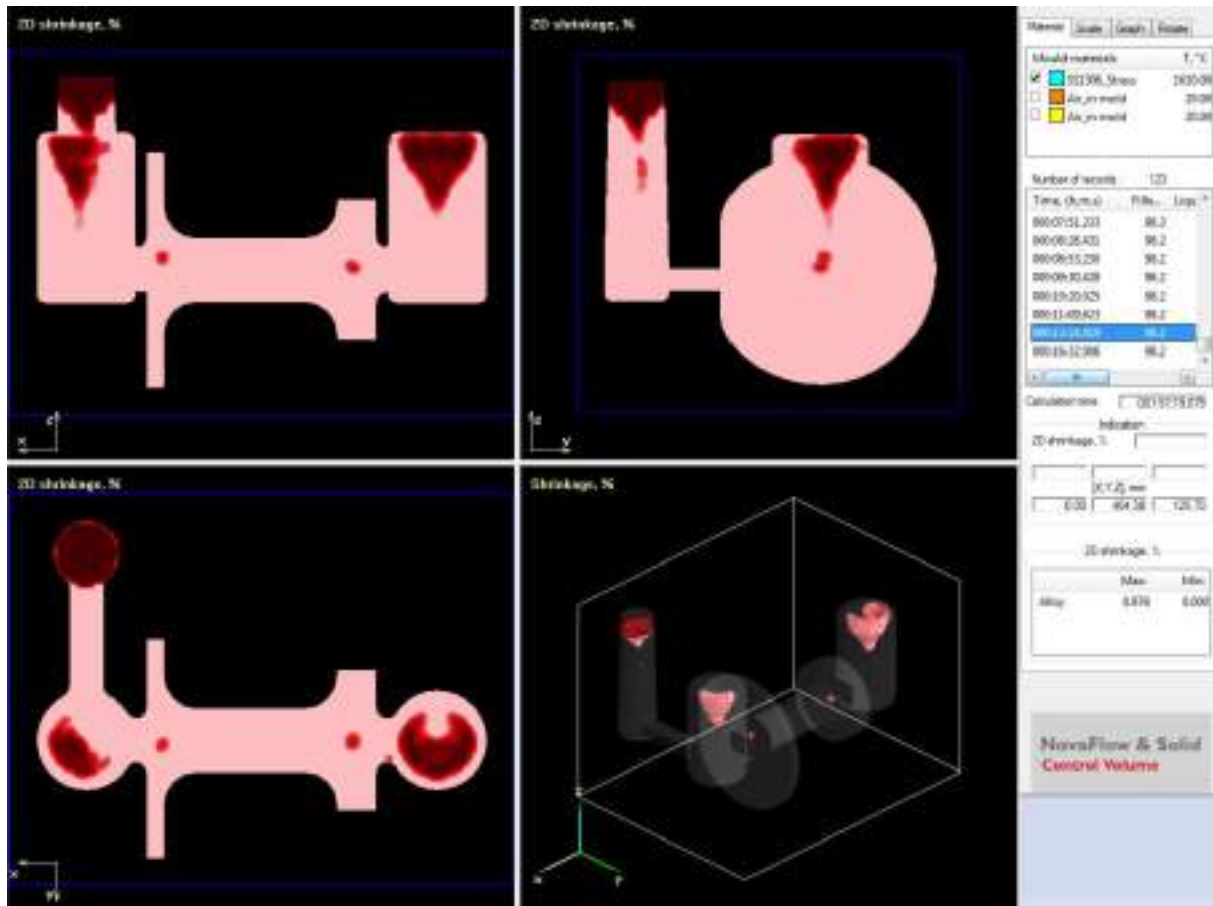


Figure 7. Presentation of the defect cause analysis in the casting [12]

CONCLUSIONS

Faced with the impossibility of offering lectures, tutorials and lab practicals from the subjects of metal casting in normal conditions, the authors of this paper presented ways for practical parts and tutorials to be adapted for the COVID situation.

Laboratory practicals were delivered online and by video recordings where previously, students had the opportunity to experience the influence of casting parameters on casting defects for themselves.

In an advanced level of course study, students did calculations, dimensioning and modelling of casting system for defined casting. Conduction and analysis of simulations are planned as teamwork where teams did analysis of influence of technological parameters on casting defects and provided analysis of results after simulations.

Keeping in mind that not all knowledge of casting technology can be learned from textbooks, the goal was to attempt to make the maximum changes to the online delivery method current circumstances would allow, trying to provide students with insight into casting technology as well as into problems that could occur during casting.

REFERENCES

- [1] T. Mladenova, Y. Kalmukov, I. Valova, Covid 19 - A major cause of digital transformation in education or just an evaluation test, TEM Journal, Volume 9(2020)3, pp. 1163-1170.
- [2] M. A. Camilleri, A. C. Camilleri, Digital learning resources and ubiquitous technologies in education, Tech Know Learn, 22(2017), pp. 65-82.
- [3] V. T. Ho, Y. Nakamori, T. B. Ho, C. P. Lim, Blended learning model on hands-on approach for in-service secondary school teachers: Combination of E-learning and face-to-face discussion, Educ Inf Technol, 21(2016), pp. 185-208.
- [4] L. Gaille, 20 Advantages and Disadvantages of Online Classes, Accessible on Internet: <https://vittana.org/20-advantages-and-disadvantages-of-online-classes>, (25.03.2021.)
- [5] M. T. Restivo, J. Mendes, A. M. Lopes, C. M. Silva, F. Chouzal, A remote laboratory in engineering measurement, 56(2009)12, pp. 4836-4843.
- [6] D. May, Cross reality spaces in engineering education - online laboratories for supporting international student collaboration in merging realities, iJOE, 16(2020)03
- [7] M. D. R. Uribe, A. J. Magana, J. H. Bahk, A. Shakouri, Computational Simulations as Virtual Laboratories for Online Engineering Education: A Case Study in the Field of Thermoelectricity, Computer Applications in Engineering Education, Volume 24(2016)3, pp. 428-442.
- [8] M. Lashley, R. McCleery, Intensive laboratory experiences to safely retain experiential learning in the transition to online learning, Ecology and Evolution, 10(2020), pp. 12613-12619.
- [9] B. Ravi, Casting simulation and optimisation: benefits, bottlenecks, and best practices, Indian Foundry Journal, 2008, Special Issue
- [10] S. Kalpakjian, S. R. Schmid, Manufacturing engineering and technology, Pearson, Singapore, 2014.
- [11] ..., Autodesk - Student and education software, Accessible on Internet: <https://www.autodesk.com/education/edu-software/>, (20.4.2021.)
- [12] ..., NovaCast Systems AB, NovaFlow&Solid, Accessible on Internet: <https://www.novacast.se/going-further/university/>, (20.4.2021.)



19th INTERNATIONAL FOUNDRYMEN CONFERENCE
Humans - Valuable Resource for Foundry Industry Development

Split, June 16th-18th, 2021

<https://ifc.simet.hr/>

**DETERMINATION OF RESIDUAL STRESSES IN STRESS LATTICE WITH
SIMULATION SOFTWARE**

**ODREĐIVANJE ZAOSTALIH NAPREZANJA U REŠETKASTOJ PROBI POMOĆU
RAČUNALNIH SIMULACIJA**

Daniel Novoselović¹, Štafanija Klarić², Josip Cumin¹, Saša Štrbac¹

¹ University of Slavonski Brod, Mechanical Engineering Faculty, Slavonski Brod, Croatia

² Charles Darwin University, Casuarina, Australia

Poster presentation

Preliminary work

Abstract

Residual stresses take place mainly due to unequal changes of volume and non-simultaneous phase and structural changes in different parts of the casting. If stresses exceed tensile strength of the component in production or service, deformation or cracking of the casting will happen. To avoid casting defects, it is necessary to know how big the residual stresses are and if they surpass the allowed values. In this paper determination of residual stresses in stress lattice with simulation software device are presented. These simulations confirm previous researches on the influence of mold thickness on the occurrence of residual stresses in the stress lattice. From the representation of the dependence of residual stresses on the thickness of the mold, it can be concluded that with increasing thickness of the mold, the residual stresses decrease. The greater the thickness of the mold causes a slower cooling which results in less residual stresses in the stress lattice.

Keywords: *residual stresses, stress lattice, software simulation*

*Corresponding author (e-mail address): dnovoselovic@unisb.hr

Sažetak

Zaostala naprezanja uglavnom se pojavljuju zbog nejednakih volumenskih promjena i neistovremenih faznih i strukovnih promjena u različitim dijelovima odljevka. Ukoliko su naprezanja veća od vlačne čvrstoće, u proizvodnji ili uporabi, pojavit će se iskrivljenje ili pucanje odljevka. Da bi se izbjegle greške na odljencima potrebno je znati kolika su zaostala naprezanja te da li ona prelaze dopuštena naprezanja. U radu je prikazano određivanje zaostalih naprezanja u rešetkastoj probi pomoću računalnih simulacija. Simulacije potvrđuju prethodna istraživanja o utjecaju debljine kalupa na nastanak zaostalih naprezanja u rešetkastoj probi. Iz prikaza ovisnosti zaostalih naprezanja o debljini kalupa može se zaključiti da se s povećanjem debljine kalupa zaostala naprezanja smanjuju. Veća

debljina kalupa uzrokuje sporije hlađenje što utječe na manja zaostala naprezanja u rešetkastoj probi.

Ključne riječi: zaostala naprezanja, rešetkasta proba, računalne simulacije

UVOD

Dobro je poznata činjenica da zaostala naprezanja u kombinaciji s opterećenjem konstrukcije te drugim eksploatacijskim uvjetima mogu dovesti do prijevremenog otkaza, ali isto tako da je u proizvodnoj praksi gotovo nemoguće proizvesti/obraditi komponentu, uključujući odljevke bez zaostalih naprezanja [1, 2].

Upravo zbog toga zaostala naprezanja predstavljaju važnu stavku pri planiranju proizvodnih postupaka (npr. naknadna strojna obrada), te imaju utjecaj na životni vijek proizvoda te pouzdanost konstrukcije [3, 4].

Temperaturni gradijent te fazne transformacije tijekom formiranja (hlađenja) odljevka razlog su pojave zaostalih naprezanja [3, 5]. Skupljanje, djelovanje kalupa te promjene volumena prilikom hlađenja posebice pri kompleksnoj geometriji odljevaka također mogu biti uzrok zaostalim naprezanjima [3]. Ukoliko zaostala naprezanja premašuju vrijednost vlačne čvrstoće u odljencima će doći do plastičnih deformacija ili razdvajanja materijala – napuklina [5].

Zbog gore navedenog, od velikog je značaja u praksi pravilno odrediti veličinu te uzrok zaostalim naprezanja u odljencima. Ovisno o mogućnostima, mjerenje zaostalih naprezanja u biti se bazira se na pristupima sa ili bez razaranja odljevka [6].

METODE MJERENJA ZAOSTALIH NAPREZANJA

Općenito gledajući, postoji nekoliko zahtjeva u vezi mjerenja zaostalih naprezanja [1]:

- mjerenje se obavlja na samoj konstrukciji,
- uređaji za mjerenje su prikladni za teren (jednostavni za primjenu i omogućuju primjenu u dijelovima konstrukcije sa otežanim pristupom),
- vanjski utjecaji (promjena temperature, vlažnosti i sl.) su eliminirani odabirom mjerne metode.

Metode određivanja zaostalih naprezanja mogu se podijeliti s obzirom prema stupnju oštećenja konstrukcije/odljevka na: nerazarajuće, djelomično razarajuće te razarajuće metode. Odabir metode ovisit će također i o potrebnom stupnju penetracije te radi li se o mikro ili makro zaostalim naprezanjima [7].

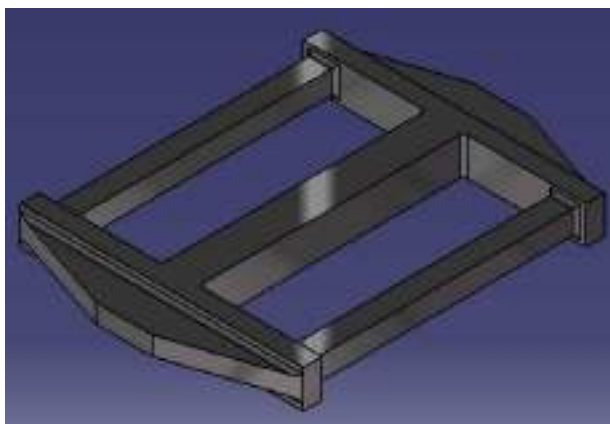
Mikro zaostala naprezanja obično se mjere nerazarajućim metodama (npr, difrakcija rendgenskog zračenja) [7]. Primjena ultrazvuka, mjerenje promjene magnetskih svojstava konstrukcijskog materijala nastalih zbog naprezanja i sl. Također se primjenjuju za nerazarajuće mjerenje zaostalih naprezanja [7, 1].

Djelomično razarajuće metode u praksi uzrokuju vrlo mala oštećenja konstrukcija. Među djelomično razarajućim metodama, metoda bušenja provrta spada u najrašireniju, relativno jeftinu metodu mjerenja zaostalih naprezanja [4].

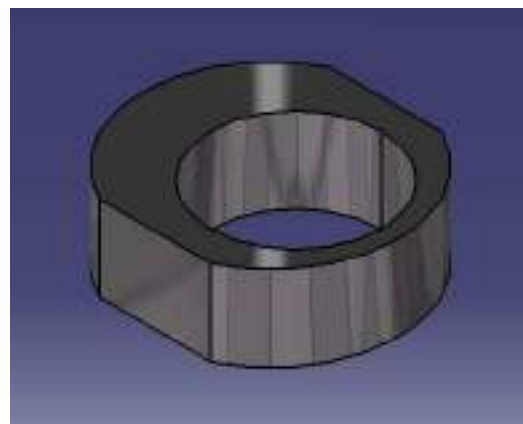
Razarajuće metode kojih se konstrukcija/odljevak potpuno uništi obično se prakticiraju u ljevačkoj praksi na tehnološkim probama projektiranim sa geometrijom koja sadrži tanke i masovne profile u svrhu namjernog unošenja naprezanja (slika 1 a i b). Ipak, moguća je i primjena na konkretnim odljencima [8]. Rezanje (razaranje) odljevka je obično popraćeno „relaksacijom“ te se ove metode se još nazivaju i relaksacijske.

Postoje dvije najčešće tehnološke probe i to :

- rešetkasta tehnološka proba (slika 1a)
- tehnološka proba prema Thomasu (slika 1b).



a) rešetkasta tehnološka proba



b) tehnološka proba prema Thomasu

Slika 1. Tehnološke probe [5]

RAČUNALNE SIMULACIJE

Računalne simulacije postale su važan dio matematičkog modeliranja realnih sustava iz područja fizike, kemije, biologije, socioloških znanosti, ekonomije, inženjerskih procesa kojima se nastoji steći dublji uvid u načine funkcioniranja takvih sustava. Tradicionalni pristup formalnom modeliranju sustava podrazumijeva dobivanje matematičkog modela, na temelju kojeg se nastoji dobiti analitičko rješenje problema koje omogućuje predviđanje ponašanja sustava s obzirom na parameter sustava i početne uvjete. Razvoj računalnih simulacija odvijao se paralelno s ubrzanim razvojem računala. Računalne simulacije često se koriste kao pomagalo ili kao zamjena u postupku modeliranja sustava kod kojih je teško doći do konačnog analitičkog rješenja. Primjeri računalnih simulacija u praksi su npr.: simulacija strujanja fluida, simulator leta aviona, zagađenost zraka (npr. u tunelu), simulacija utjecaja buke, meteorologija, simulacija zaostalih naprezanja, te u različitim područjima znanosti, tehnologije i zabave [9].

Simulacija je proces oponašanja stvarnih-realnih pojava pomoću niza matematičkih jednadžbi implementiranih u računalne programe. Moderna proizvodnja dimenzijski točnih

odljevaka zahtjeva usku suradnju konstruktora i ljevača s ciljem smanjenja troškova, dodatne obrade i mase. Treba iskoristiti sve mogućnosti koje nudi proces lijevanja, a kroz simulaciju lijevanja možemo optimirati sam proces lijevanja te smanjiti vjerojatnost pojave grešaka [10].

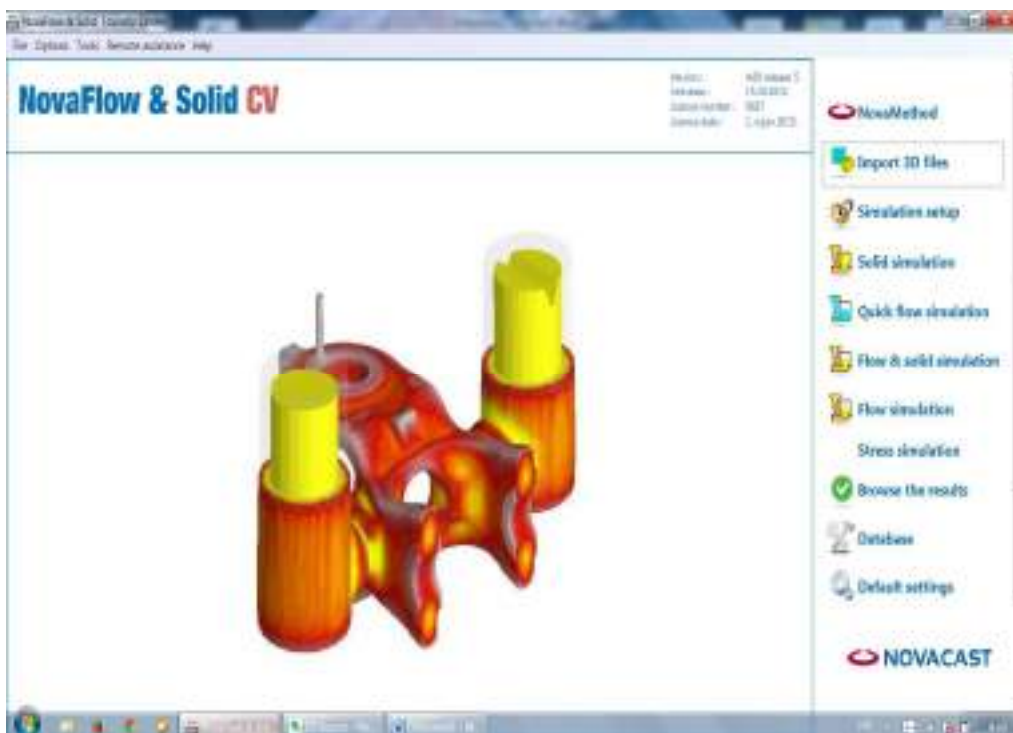
Rastući zahtjevi kvalitete u proizvodnji odljevaka čine upotrebu simulacijskih metoda neophodnim alatom za rješavanje problema prilikom lijevanja. Predviđanje mogućih grešaka prilikom lijevanja pomoću računalnih simulacija postalo je neophodan proces koji omogućavaju kvalitativno i kvantitativno lociranje mogućih problema [10].

Softver za simulaciju lijevanja koristiti 3D modele odljevaka sa uljevnim sustavom. Na taj način omogućava direktnu komunikaciju ljevača, konstruktora te kupca razmjenjujući informacije o postupku lijevanja mogućim greškama te mogućim izmjenama na odljevku i samom procesu.

Tri glavne primjene računalnih simulacija su mogućnost predviđanje grešaka pri lijevanju, optimizacija postupka lijevanja kroz različite parametre lijevanja te poboljšanje konstrukcije odljevka prilagodbom tehnologiji lijevanja. Prednosti računalnih simulacija može se vidjeti u smanjenje učestalosti metode pokušaja i pogrešaka kao dosadašnjem načinu rješavanja problema te sticanjem znanja o korištenju i upotrebi računalnih simulacija. Nedostaci računalnih simulacija prvenstveno su visoka cijena nabavke i upotrebe, potrebna kvalificirana radna snaga te potreba za 3D modeliranjem [10].

ODREĐIVANJE ZAOSTALIH NAPREZANJA SIMULACIJSKIM SOFTVEROM

Za određivanje zaostalih naprezanja u odljevcima korišten je simulacijski softver NovaFlow&Solid. Računalne simulacije provedenu su na Strojarskom fakultetu u Slavonskom Brodu, u Laboratoriju za Ljevarstvo na NovaFlow & Solid CV 4.6r5 64-bit verziji 4.6 r5 . Broj licence 9027Softver NovaFlow&Solid podijeljen je u izbornike, kako je prikazano slici 2.namijenjen je za simulacije postupaka lijevanja u pijesak i lijevanja u metalni kalup (kokilni lijev) [11].



Slika 2. Početno sučelje NovaFlow & Solid CV [11]

Softver simulira proces punjenja kalupa i skrućivanja litine za sve tehnologije i metale koji se koriste u ljevačkoj proizvodnji, koristeći numeričku metodu simulacije (metoda kontrolnih volumena). Nakon provedenih simulacija omogućen je grafički prikaz rezultata iz kojih se mogu vidjeti kritična područja koja je potrebno korigirati, da bi se izbjegle moguće greške na odljevku.

PLAN I PROVOĐENJE RAČUNALNIH SIMULACIJA

Usvojen je općeniti faktorski plan pokusa 2^3 . To znači da se tri tehnološka parametra (*A*, *B* i *C*) istražuju na dvije razine. Istraživani utjecajni tehnološki parametri i njihove granice prikazani su u Tablici 1. Plan provedbe simulacija prikazan je Tablici 2.

Tablica 1. Utjecajni parametri i njihove granice

Utjecajni parametar	Oznaka utjecajnog parametra	Razina utjecajnog parametra	
		-1	+1
Vrste sivog lijeva	A	EN-GJS 400	EN-GJS 700
Vrsta pijeska	B	Olivinski	Kvarcni
Debljina kalupa, mm	C	20	40

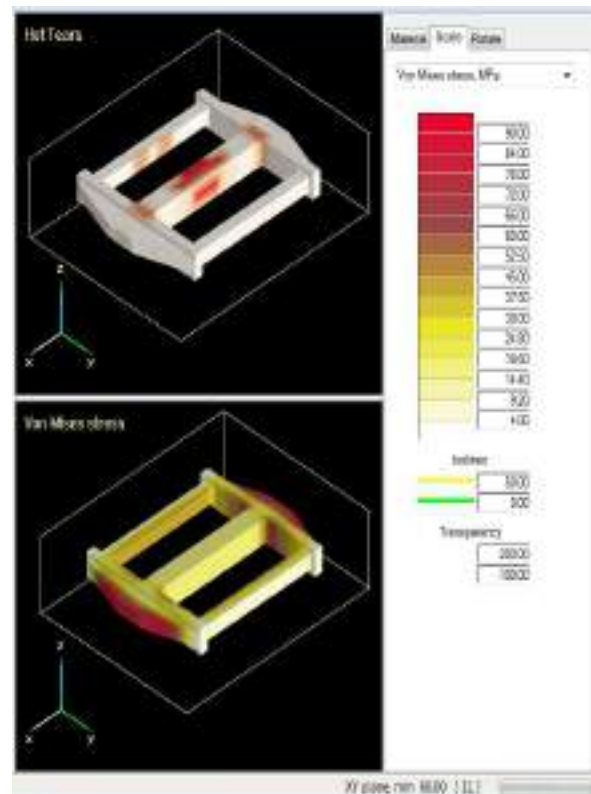
Tablica 2. Plan provedbe simulacija

Simulacija	Vrsta sivog lijeva	Vrsta pijeska	Debljina kalupa,mm
S01	EN-GJS 400	Olivinski	20
S02	EN-GJS 700	Olivinski	20
S03	EN-GJS 400	Kvarcni	20
S04	EN-GJS 700	Kvarcni	20
S05	EN-GJS 400	Olivinski	40
S06	EN-GJS 700	Olivinski	40
S07	EN-GJS 400	Kvarcni	40
S08	EN-GJS 700	Kvarcni	40

Parametri simulacija i rezultati prikazani su na slikama 3-10 [12].

Simulacija S01 (slika 3):

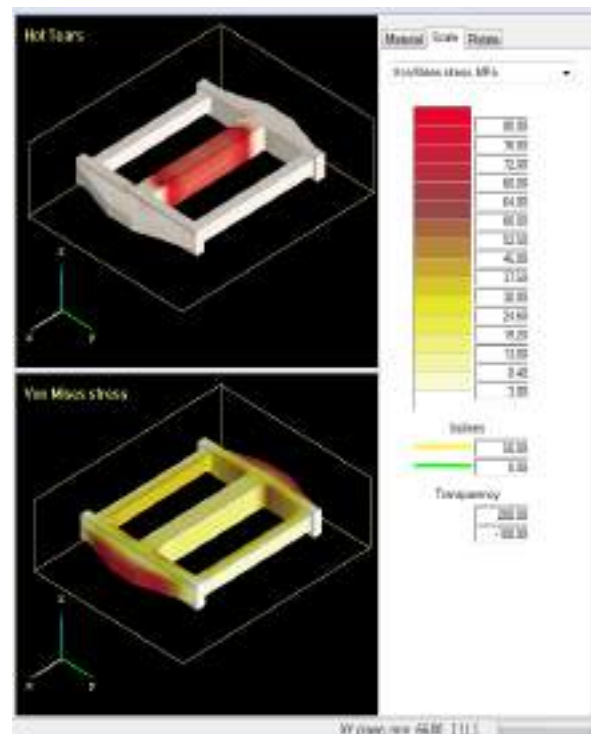
- Sivi lijev: EN-GJS 400
- Temperatura: 1380°C, ohlađeno na 20 °C
- Vrijeme hlađenja: 19 min
- Gustoća EN-GJS 400: 6807,303 kg/m³
- Materijal kalupa: Olivinski pijesak
- Debljina kalupa: 20 mm
- Dimenzije lijeva: 200 x 150 x 20 mm
- Dimenzija ćelije: 6 mm
- Ukupan broj ćelija: 12800
- Ćelije lijeva: 1432



Slika 3. Rezultati simulacije S01

Simulacija S02 (slika 4):

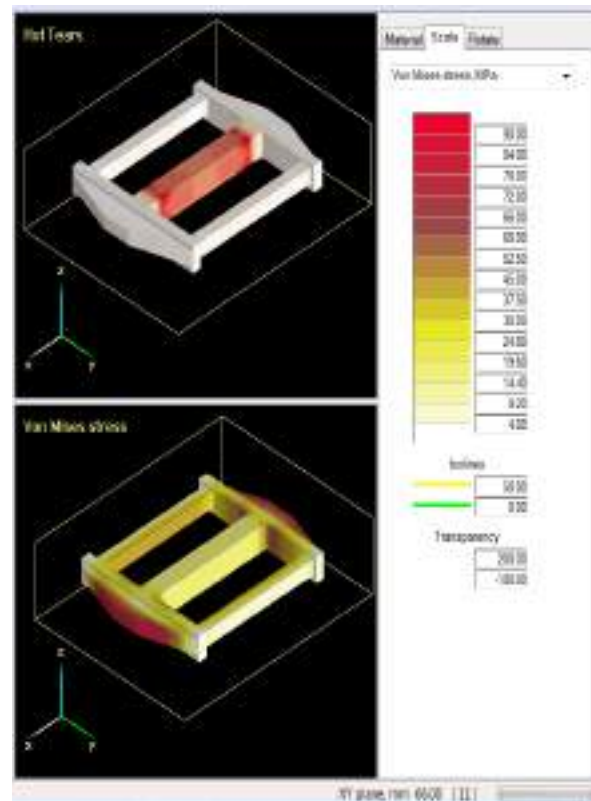
- Sivi lijev: EN-GJS 700
- Temperatura: 1270°C, ohlađeno na 20 °C
- Vrijeme hlađenja: 54 min
- Gustoća EN-GJS 700: 6802,209 kg/m³
- Materijal kalupa: Olivinski pijesak
- Debljina kalupa: 20 mm
- Dimenzije lijeva: 200 x 150 x 20 mm
- Dimenzija ćelije: 6 mm
- Ukupan broj ćelija: 12800
- Ćelije lijeva: 1432



Slika 4. Rezultati simulacije S02

Simulacija S03 (slika 5):

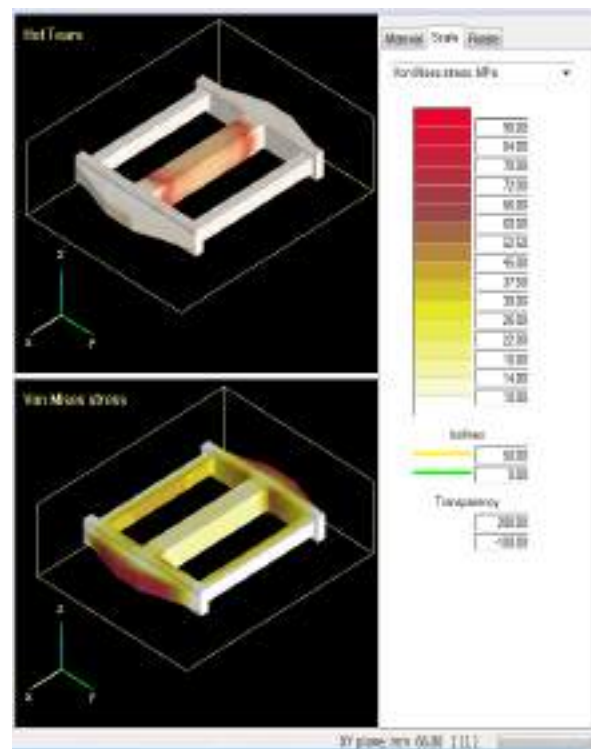
- Sivi lijev: EN-GJS 400
- Temperatura: 1380°C, ohlađeno na 20 °C
- Vrijeme hlađenja: 20 min
- Gustoća EN-GJS 700: 6807,303 kg/m³
- Materijal kalupa: Kvarcni pijesak
- Debljina kalupa: 20 mm
- Dimenzije lijeva: 200 x 150 x 20 mm
- Dimenzija ćelije: 6 mm
- Ukupan broj ćelija: 12800
- Ćelije lijeva: 1432



Slika 5. Rezultati simulacije S03

Simulacija S04 (slika 6):

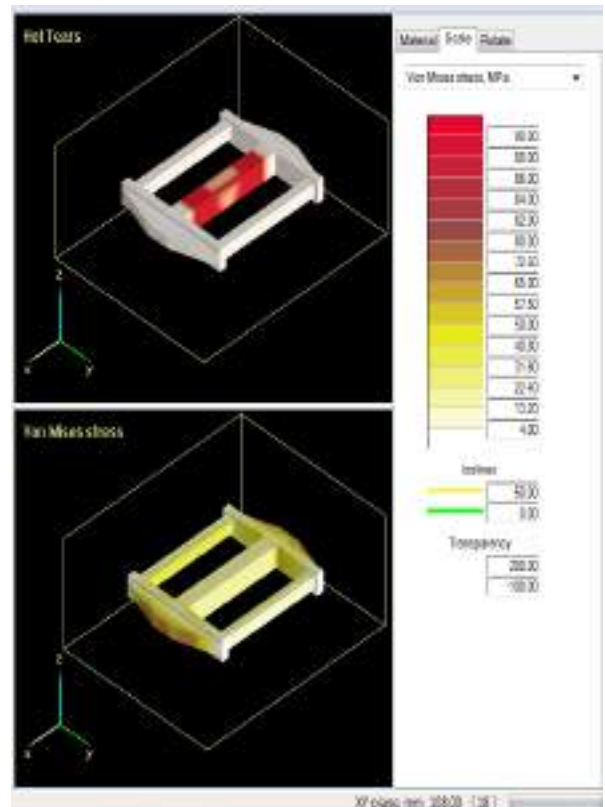
- Sivi lijev: EN-GJS 700
- Temperatura: 1270°C, ohlađeno na 20 °C
- Vrijeme hlađenja: 15 min
- Gustoća EN-GJS 700: 6802,209 kg/m³
- Materijal kalupa: Kvarcni pijesak
- Debljina kalupa: 20 mm
- Dimenzije lijeva: 200 x 150 x 20 mm
- Dimenzija ćelije: 6 mm
- Ukupan broj ćelija: 12800
- Ćelije lijeva: 1432



Slika 6. Rezultati simulacije S04

Simulacija S05 (slika 7):

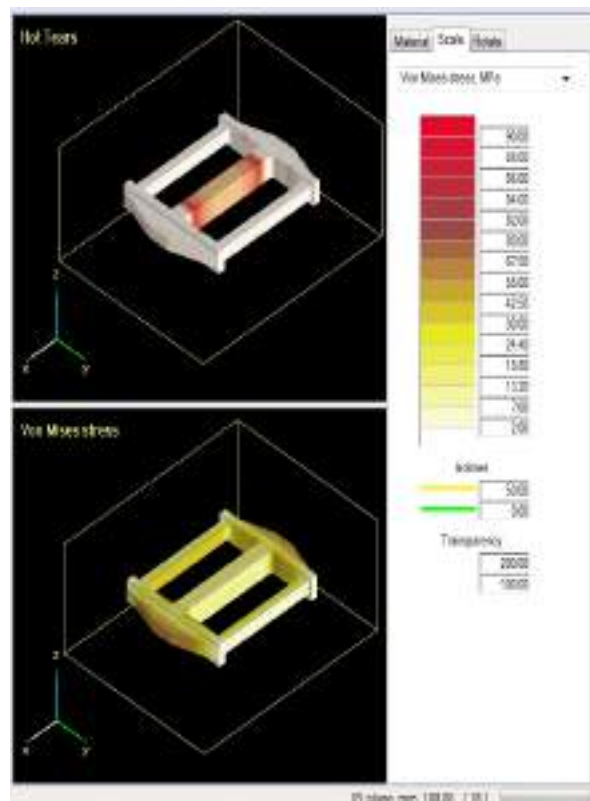
- Sivi lijev: EN-GJS 400
- Temperatura: 1380°C, ohlađeno na 20 °C
- Vrijeme hlađenja: 34 min
- Gustoća EN-GJS 700: 6807,303 kg/m³
- Materijal kalupa: Olivinski pijesak
- Debljina kalupa: 40 mm
- Dimenzije lijeva: 200 x 150 x 20 mm
- Dimenzija ćelije: 6 mm
- Ukupan broj ćelija: 30362
- Ćelije lijeva: 1571



Slika 7. Rezultati simulacije S05

Simulacija S06 (slika 8):

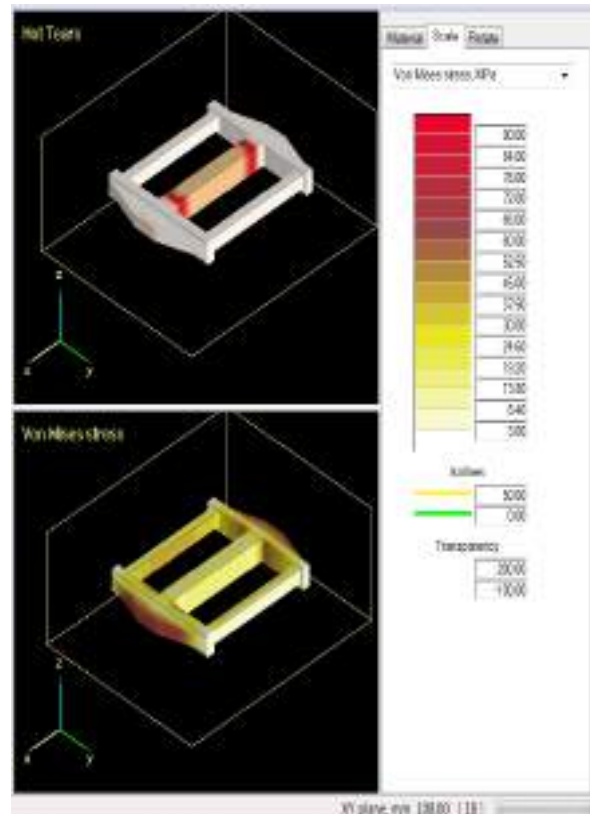
- Sivi lijev: EN-GJS 700
- Temperatura: 1270°C, ohlađeno na 20 °C
- Vrijeme hlađenja: 27 min
- Gustoća EN-GJS 700: 6802,209 kg/m³
- Materijal kalupa: Olivinski pijesak
- Debljina kalupa: 40 mm
- Dimenzije lijeva: 200 x 150 x 20 mm
- Dimenzija ćelije: 6 mm
- Ukupan broj ćelija: 30362
- Ćelije lijeva: 1571



Slika 8. Rezultati simulacije S06

Simulacija S07 (slika 9):

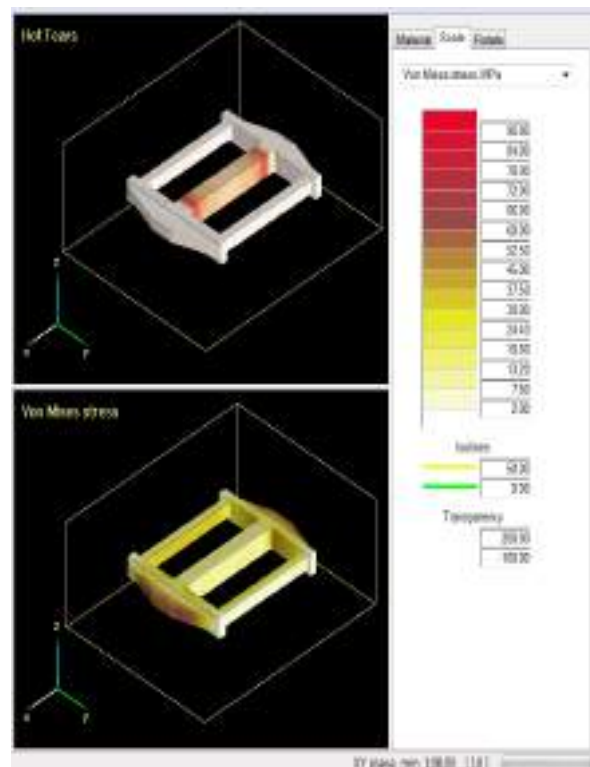
- Sivi lijev: EN-GJS 400
- Temperatura: 1380°C, ohlađeno na 20 °C
- Vrijeme hlađenja: 34 min
- Gustoća EN-GJS 700: 6807,303 kg/m³
- Materijal kalupa: Kvarcni pijesak
- Debljina kalupa: 40 mm
- Dimenzije lijeva: 200 x 150 x 20 mm
- Dimenzija ćelije: 6 mm
- Ukupan broj ćelija: 30362
- Ćelije lijeva: 1571



Slika 9. Rezultati simulacije S07

Simulacija S08 (slika 10):

- Sivi lijev: EN-GJS 700
- Temperatura: 1270°C, ohlađeno na 20 °C
- Vrijeme hlađenja: 27 min
- Gustoća EN-GJS 700: 6802,209 kg/m³
- Materijal kalupa: Kvarcni pijesak
- Debljina kalupa: 40 mm
- Dimenzije lijeva: 200 x 150 x 20 mm
- Dimenzija ćelije: 6 mm
- Ukupan broj ćelija: 30362
- Ćelije lijeva: 1571



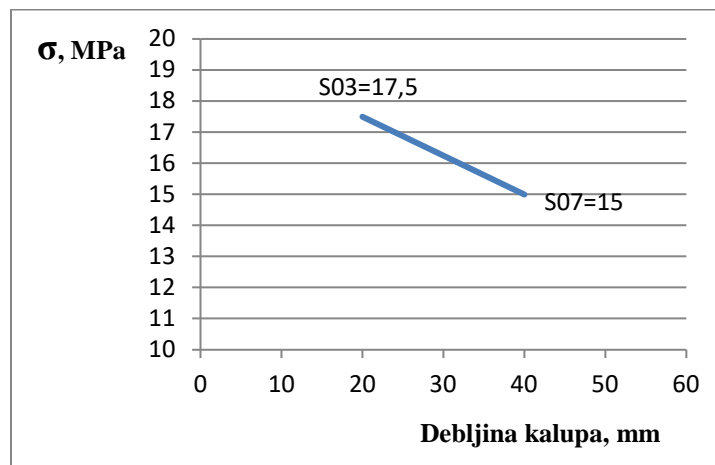
Slika 10. Rezultati simulacije S08

Iz provedenih simulacija prema bojama na rešetkastoj probi i mjernoj ljestvici može se očitati iznos zaostalih naprezanja u pojedinim dijelovima odljevka. Očitane vrijednosti zaostalih naprezanja prikazane su u tablici 3. Iznosi zaostalih naprezanja očitani su s ljestvice prema bojama u odabranom području.

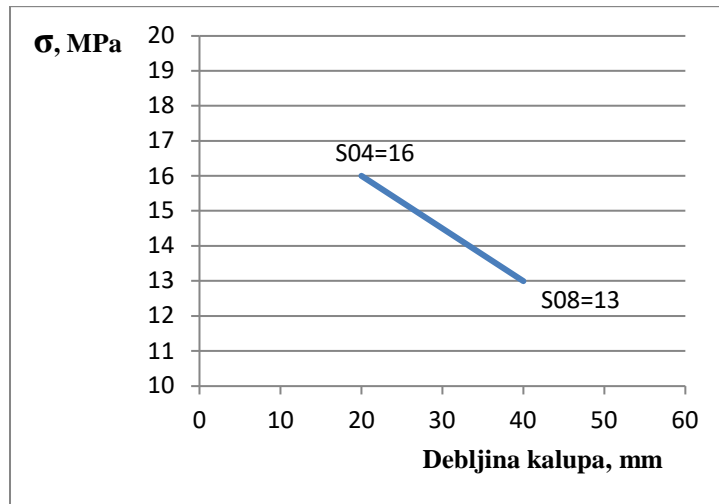
Tablica 3. Očitana ekvivalentna zaostala naprezanja u odljencima [12]

Simulacija	Von Mises, MPa srednja šipka	Von Mises, MPa vanjska šipka
S01	$\sigma_{SR} = 18,5$	$\sigma_{SR} = 45$
S02	$\sigma_{SR} = 15$	$\sigma_{SR} = 57$
S03	$\sigma_{SR} = 17,5$	$\sigma_{SR} = 36$
S04	$\sigma_{SR} = 16$	$\sigma_{SR} = 57$
S05	$\sigma_{SR} = 15$	$\sigma_{SR} = 20$
S06	$\sigma_{SR} = 12$	$\sigma_{SR} = 22$
S07	$\sigma_{SR} = 15$	$\sigma_{SR} = 52$
S08	$\sigma_{SR} = 13$	$\sigma_{SR} = 35$

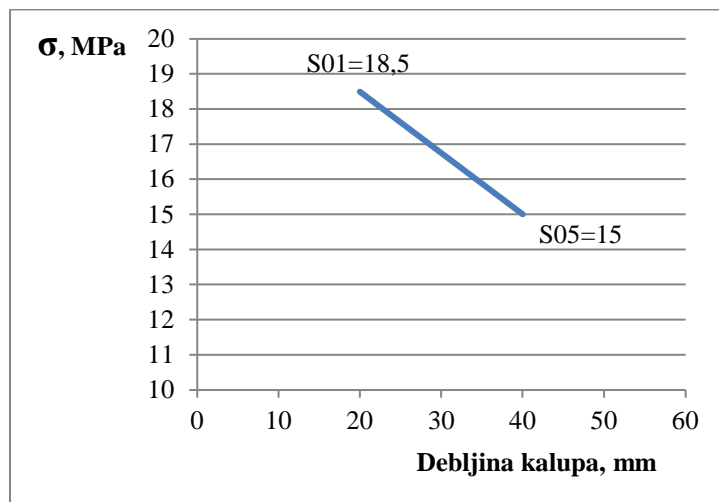
Na osnovi rezultata dobiveni su sljedeći dijagrami ovisnosti naprezanja o debljini kalupa slike 11-14.



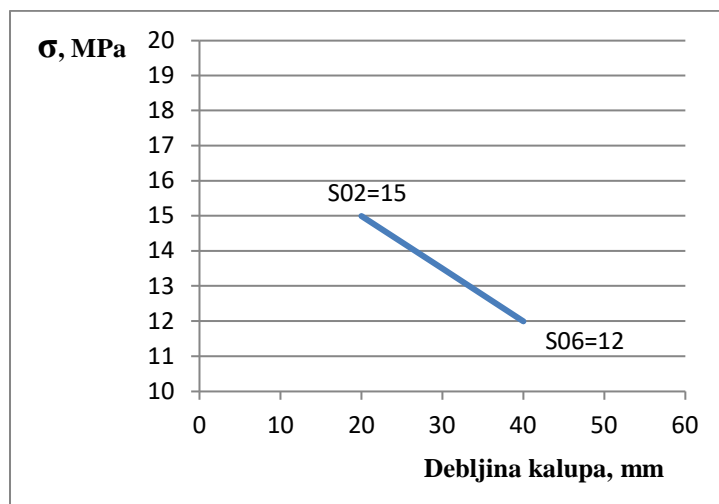
Slika 11. EN-GJS 400 i kvarcni pijesak [12]



Slika 12. EN-GJS 700 i kvarcni pijesak [12]



Slika 13. EN-GJS 400 i olivinski pijesak[12]



Slika 14. EN-GJS 700 i olivinski pijesak[12]

Iz dijagrama se vidi da s povećanjem debljine kalupa zaostala naprezanja se smanjuju. Veća debljina kalupa uzrokuje je sporije hlađenje što utječe na nastanak zaostalih naprezanja.

Naprezanja u odljencima javljaju se u procesu hlađenja odljevka u kalupu pri neravnomjernom rasporedu temperature i raznovremenim faznim promjenama. To znači ne samo u različitim, međusobno vezanim dijelovima odljevka, nego u svakoj stijenci odljevka kod kojih se skupljanje vrši uz međusobno suprotstavljanje [13].

Kod rešetkaste probe jedan je masivniji i sporije se hladi, a drugi je tanji i brže se hladi. temperatura u debljem i tanjem dijelu u različitim vremenima prelaze granicu plastičnih i elastičnih područja, te na taj način uzrokuju naprezanja u odljencima. U debljim stijenka odljevaka javlja se istezanje, a u tanjim dijelovima odljevka pojavljuju se naprezanja uslijed skupljanja. Ukoliko u odljencima s različitim debljinama stijenke pri hlađenju konstrukcija ne dopušta izvitoperenje dolazi do pojave naprezanja. U odljencima čija konstrukcija nije kruta pojavljuje se samo izvitoperenje odljevka [13].

ZAKLJUČAK

Naprezanja u odljencima pojavljuju se kod neravnomjernog hlađenja odljevka. Naprezanja ostaju u njima i poslije izjednačavanja temperature po volumenu odljevka. Ona se tijekom vremena mijenjaju, pri čemu njihova preraspodjela može izazvati plastičnu deformaciju odljevka.

Računalne simulacije pomažu da se potencijalne greške uoče i uklone u početnoj fazi razvoja proizvoda te u procesu proizvodnje odljevaka. Na taj način se skraćuje vrijeme potrebno za razvoj novog proizvoda. Simulacijski softver služi konstruktorima odljevaka kao alat za poboljšanje konstrukcije, a ljevačima za optimizaciju proizvodnog procesa.

Nakon provedenih računalnih simulacija možemo zaključiti da simulacije potvrđuju prethodna istraživanja o utjecaju debljine kalupa na nastanak zaostalih naprezanja u rešetkastoj probi. Može se zaključiti da se s povećanjem debljine kalupa zaostala naprezanja smanjuju. Veća debljina kalupa uzrokuje sporije hlađenje što utječe na manja zaostala naprezanja u rešetkastoj probi.

LITERATURA

- [1] I. Heidl, M. Husnjak, Tenzometrija, Tehnička enciklopedija 12, Leksikografskog zavoda "Miroslav Krleža", str. 688-690, 1987.
- [2] P. J. Withers, H. K. D. H. Bhadeshia, Residual stress. Part 2 - Nature and origins, Materials Science and Technology, 17:4, 2001, str. 366-375.
- [3] A. A. Keste, S. H. Gawande, C. Sarkar, Design optimization of precision casting for residual stress reduction, Journal of Computational Design and Engineering, 3(2016), pp. 140-150.
- [4] J. E. Wyatt, J. T. Berry, A. R. Williams, Residual stresses in aluminum castings, Journal of Materials Processing Technology 191, 2007, pp. 170-173.

- [5] B. Kočovski, Teorija livarstva, Izdavačko grafički zavod, Beograd, 1972.
- [6] H. Farhangi, S. Norouzi, M. Nili-Ahmadabadi, Effects of casting process variables on the residual stress in Ni-base superalloys, *Journal of Materials Processing Technology* 153-154, 2004, pp. 209-212.
- [7] J. E. Wyatt, J. T. Berry, A new technique for the determination of superficial residual stresses associated with machining and other manufacturing processes, *Journal of Materials Processing Technology* 171, 2006, pp. 132-140.
- [8] S. Kianfar, E. Aghaie, J. Stroh, D. Sediako, J. Tjong, Residual stress, microstructure, and mechanical properties analysis of HPDC aluminum engine block with cast-in iron liners, *Materials Today Communications* 26, 2021, 101814.
- [9] V. Čerić, Simulacijsko modeliranje, Zagreb, Školska knjiga, 1993.
- [10] B. Ravi, Casting Simulation and Optimisation: Benefits, bottlenecks, and best practices, *Indian Foundry Journal*, 54, 2008., Accessible on Internet: http://efoundry.iitb.ac.in/TechnicalPapers/2008/2008IFJ_CastingSimulation.pdf, (09.04.2021.)
- [11] NovaCast Systems AB, NovaFlow&Solid, Accessible on Internet: <https://www.novacast.se/going-further/university/>, (20.4.2021.)
- [12] S. Štrbac, Računalne simulacije zaostalih naprezanja, diplomski rad, Strojarski fakultet u Slavonskom Brodu, Slavonski Brod, 2015.
- [13] B. Kočovski, Praktikum iz teorije livarstva, Naučna knjiga, Beograd, 1981.



19th INTERNATIONAL FOUNDRYMEN CONFERENCE
Humans - Valuable Resource for Foundry Industry Development

Split, June 16th-18th, 2021

<https://ifc.simet.hr/>

**CHEMICAL LEACHING OF SUBBITUMINOUS COAL FROM THE BOGOVINA -
EAST FIELD (BOGOVINA BASIN, SERBIA) USING HYDROCHLORIC ACID**

**Katarina Pantović Spajić^{1*}, Branislav Marković¹, Miroslav Sokić¹,
Mladen Bugarčić¹, Gvozden Jovanović¹, Vaso Manojlović², Ksenija Stojanović³**

¹ Institute for Technology of Nuclear and Other Mineral Raw Materials, Belgrade, Serbia

² University of Belgrade Faculty of Technology and Metallurgy, Belgrade, Serbia

³ University of Belgrade Faculty of Chemistry, Belgrade, Serbia

Poster presentation

Original scientific paper

Abstract

All over the world, huge amounts of coal are available and it is utilized in large quantities for different purposes. The coal combustion causes environmental problems, such as the release of toxic metals and other pollutants into wastewaters, emission of noxious gases, produce of ash dumps, etc. One of the solutions for the reduction of environment pollution, caused by coal combustion, is demineralization and desulphurization of coal. In that sense, treatment of coal by different chemical reagents becomes important. A subbituminous coal, used in this study was taken from the Bogovina - East field (Lower Miocene \approx 20-16 Ma) of the Bogovina Basin, which is located in Eastern Serbia. The sample was selected based on the previous studies of Bogovina - East field which indicated a high amount of sulphur, relatively high percent of mineral matter and considerably amount of liptinites for humic coal, which represent the most reactive maceral group. The aim of the study was an attempt to reduce the amount of ash and sulphur in coal, keeping the organic matter unaltered as possible, using simple and cheap method e.g. treatment with hydrochloric acid (HCl). Ash and total sulphur content was determined before and after HCl leaching. In addition characteristics of initial and treated coal were tracked by X-ray diffraction (XRD) analysis and Fourier-transform infrared (FTIR) spectroscopy. The obtained results showed that the high percentage of deashing (\approx 80 %) was achieved with cheap hydrochloric acid. XRD analysis of ash before and after sample treatment provides more information about mineral phases in coal and effects of chemical leaching. FTIR analysis indicates almost no changes in structure of coal organic matter after treatment by HCl, which is important for further coal usage (e.g. combustion). On the other hand, the applied chemical leaching with HCl had low impact on the sulphur content in Bogovina coal (desulphurization percentage \approx 8 %). Therefore, in future research other reagents for efficient desulphurization should be investigated.

Keywords: coal, acid, demineralization

*Corresponding author (e-mail address): k.pantovic@itnms.ac.rs

INTRODUCTION

Coal may be defined as a sedimentary rock containing usually less than 50 % of mineral matter [1]. Coal is composed of organic, combustible phase and inorganic, mineral matter [1]. The inorganic mineral matter of coal can have various forms such as: coal discrete crystalline particles, amorphous mineral parts, inorganic elements chemically bonded to the organic phase and compounds dissolved in water absorbed by the coal pores [2]. Complex organic matter of coal is mainly composed of insoluble part (kerogen), whereas content of soluble (extractable) organic matter (bitumen) is commonly less than 5 %.

During the consumption of coal, i.e. coal combustion, byproducts that have damaging environmental effects are released. One of the ultimate environmental “culprits” in coal is sulphur. During coal combustion, sulphur causes gases, SO_2 and SO_3 to be released into the atmosphere together with ash and soot [3, 4]. In addition, the higher sulphur content in coal is considered to be harmful because sulphuric gases can cause corrosion and other consequences that require more frequent equipment maintenance [4].

Therefore investigations concerning demineralization (deashing) and desulphurization of coal have the substantial importance. These processes can be carried out by physical treatment, chemical treatment and microbial treatment [5].

For bioleaching of coal, in order to decrease the amount of sulphur, different microorganisms are used. In study of Mishra et al. (2018) [3] lignite was treated with *Leptospirillum ferriphilum* resulting in percent of desulphurization of 56 %, whereas small amounts of added surfactant, Span 80 decreased sulphur content for 61 %. The studies of coal desulphurization were conducted also with cultures of *A. ferrooxidans*, *A. thiooxidans*, *Sulfolobus acidocaldarius*, *Pseudomonas putida* and *Pseudomonas aeruginosa* [4].

Physical treatment of coal such as electrostatic separation resulted in decrease of ash content from 43 % to 18 % [6].

Chemical treatment for producing cleaner coal could be carried out by using acid solutions, alkali solutions, combine treatment of coal with acids and alkalis, oxidizing agents, chelating agents, and stepwise washing by acids [5]. In one of the studies, the removal of 70% of the organic sulphur was achieved when hydroiodic acid was applied as a single reagent. Applying of coal stepwise acid leaching (HCl and HNO_3) resulted in the ash and sulphur content decrease from 7.9 % to 0.6 % and from 2.6 % to 1.4 %, respectively [7]. An important oxidizing agent for chemical treatment of coal is H_2O_2 . In study of Vasilakos and Clinton [8], 90 % of pyritic sulphur was removed from coal using $\text{H}_2\text{O}_2/\text{H}_2\text{SO}_4$ solution. Use of alkali solutions (5 % NaOH) decreased ash content from 28.2 % to 1.6 %, and from 7.0 % to 0.9 % in two studied coals samples [9]. The combined acid and alkali solutions for leaching coal were also applied for coal demineralization. Treatment of coal with NaOH followed by acid solution leaching under the pressure, resulted in demineralization percent of 90 % [10].

Results of coal leaching depend on coal composition, particle size, reaction time, temperature, and reagent (solution) concentration.

MATERIALS AND METHODS

A subbituminous coal, used in this study was taken from the Bogovina - East field (Lower Miocene \approx 20-16 Ma) of the Bogovina Basin (Eastern Serbia). The sample was selected based on the previous studies [11] of Bogovina - East field which indicated high amount of sulphur,

relatively high percent of mineral matter and considerably amount of liptinites for humic coal, which represent the most reactive maceral group.

The sample was air-dried and ground to the particle size < 200 μm . Initial coal sample was characterized by a standard proximate analysis method. Proximate analysis included determination of analytical moisture, volatile matter, ash and fixed carbon. The analysis was performed according to ASTM-D-3172 standard. The results are shown in table 1, along with total sulphur content, which was determined by the Eschka method.

The coal sample was treated with hydrochloric acid (10 % solution) in a glass beaker for 30 minutes at three different reaction temperatures, while stirred at 250 rpm. Experiments were performed at 30 $^{\circ}\text{C}$ (A-1), 60 $^{\circ}\text{C}$ (A-2), and 90 $^{\circ}\text{C}$ (A-3). At the end of the reaction period the treated mixture was vacuum filtered. After filtration, the treated coal was washed with hot distilled water (until pH=7) and firstly was dried at room temperature, then was dried at 105 $^{\circ}\text{C}$.

X-ray diffraction (XRD) analysis was used to determine and monitoring the mineral composition of the samples' ashes. Prior to XRD analysis, samples were subjected to low temperature ashing (LTA) process. XRD analysis was carried out on a Philips X-ray diffractometer model PW-1710.

Fourier-transform infrared (FTIR) analysis of untreated and treated coal samples was performed on a Thermo Fisher Scientific Nicolet IS-50. Recording was done by ATR (Attenuated Total Reflectance) technique in the range from 4000 cm^{-1} to 400 cm^{-1} , and 32 scans at resolution 4.

Table 1. Characteristics of initial Bogovina coal sample

Parameter	Content (wt. %)	Proximate analysis of coal sample
Moisture	16.82	
Volatile meters	38.44	
Ash	17.52	
Fixed carbon	27.22	
Total sulphur	6.03	

RESULTS AND DISCUSSION

The results of the acid leaching of coal sample at different temperatures are presented in Table 2.

Table 2. Ash and total sulphur content in initial coal and leached coal samples after treatment by HCl solution (10 %) at different temperatures for 30 minutes

Sample	Temperature ($^{\circ}\text{C}$)	Content of ash in sample (wt. %)	Content of total sulphur in sample (wt. %)
Initial coal sample	/	17.52	6.03
A-1	30	3.65	5.58
A-2	60	3.62	5.51
A-3	90	3.68	5.53

The content of ash decreased significantly ($\approx 80\%$) by HCl treatment, while the content of total sulphur decreased only slightly ($\approx 8\%$). The obtained results (Table 2) indicate that temperature does not affect deashing and desulphurization of Bogovina coal by HCl. Ash and sulphur removal slightly increased by heating from $30\text{ }^{\circ}\text{C}$ – $60\text{ }^{\circ}\text{C}$, and then insignificantly decreased in the temperature range $60\text{ }^{\circ}\text{C}$ – $90\text{ }^{\circ}\text{C}$. The optimal temperature for both processes is $60\text{ }^{\circ}\text{C}$. Negligible impact of HCl on desulfurization, associated by absence of pyrite in XRD spectrum of coal sample (Figure 1a) may imply that majority of sulphur is associated with organic matter. Therefore, other reagents for desulphurization of Bogovina coal should be investigated. Deashing efficiency at $30\text{ }^{\circ}\text{C}$ (7.46%) and $60\text{ }^{\circ}\text{C}$ (8.62%) was rather similar, and consequently, energy consumption for heating from 30°C to 60°C in such case is not reasonable.

Changes in qualitative composition of mineral matter caused by chemical leaching are followed by XRD, performed on LTA of the initial and treated coal (Figure 1). LTA of initial Bogovina coal dominates by amorphous matter, whereas other constituents are quartz (Q), olivine (O), calcite (C) anhydrite (A), mica (M) and unidentified phase (U) (Figure 1a). Amorphous matter also dominates in LTA of leached coal (Figure 1b). As expected, treatment with HCl resulted in removal of calcite, anhydrite and mica, as well as unidentified phase. Scarce distribution of minerals in LTA of leached coal, represented mostly by resistant quartz, is consistent with efficient deashing ($\approx 80\%$). In addition to quartz, the coal residues obtained by HCl treatment contains low amount of olivine (Figure 1b), which is also relatively prone to acidic dissolution resulted from ion-exchange reaction between $\text{Mg}^{2+}/\text{Fe}^{2+}$ ions and H^{+} ions [12].

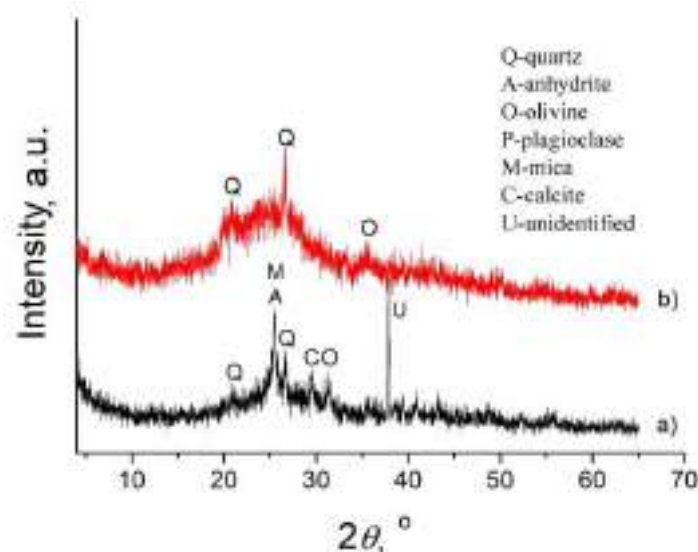


Figure 1. XRD spectra of (a) initial Bogovina coal sample and (b) coal sample after leaching with 10 % HCl at $60\text{ }^{\circ}\text{C}$ (A-2)

FTIR spectra indicate almost no change in structure of coal organic matter caused by HCl treatment (Figure 2) that is important for further utilization of coal (e.g. combustion).

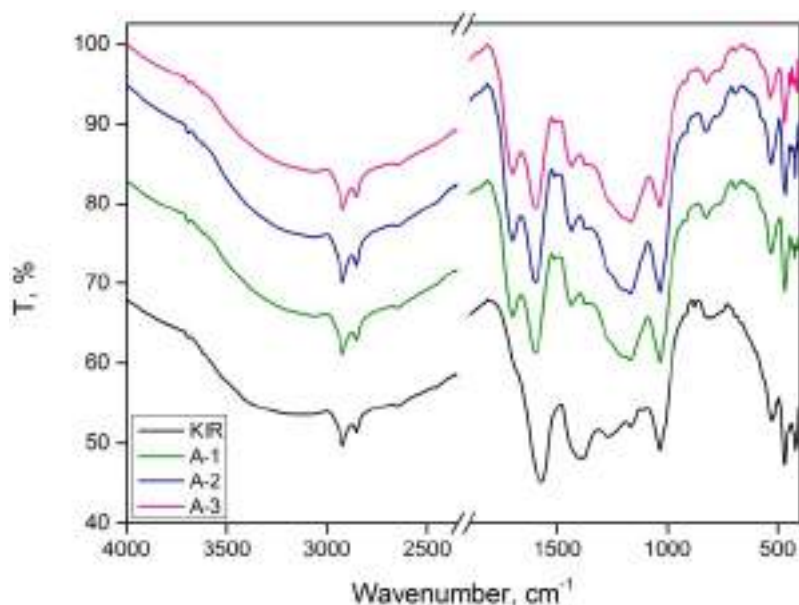


Figure 2. FTIR spectra of initial coal sample (KIR) and treated coal samples (A-1 – A-3)

CONCLUSIONS

The current study concerns an investigation of demineralization (deashing) and desulphurization of Lower Miocene subbituminous coal originating from the Bogovina - East field (Bogovina Basin, Eastern Serbia) by treatment with 10 % HCl solution at different temperatures (30 °C, 60 °C and 90 °C) for 30 minutes. The content of ash decreased significantly ($\approx 80\%$) by HCl treatment, while the content of total sulphur decreased only slightly ($\approx 8\%$). Therefore in future research other reagents for desulphurization should be investigated. The obtained results indicate that temperature does not affect deashing and desulphurization of Bogovina coal by HCl. XRD data showed that by acidic leaching with HCl complete removal of calcite, anhydrite and mica from LTA of the initial coal is achieved, resulting in very scarce distribution of minerals in LTA of the treated coal, represented by resistant quartz and low amount of olivine, only. The FTIR spectra signify that the structure of coal organic matter did not change substantially after HCl treatment. Accordingly, we can assume that the calorific value of coal remained unaltered after used acidic leaching.

Acknowledgements

The authors are grateful to the Ministry of Education, Science and Technological Development of the Republic of Serbia (Contract number: 451-03-9/2021-14/200023 and Contract number: 451-03-9/2021-14/200168) for the financial support of this investigation.

REFERENCES

- [1] D. Vitorović, B. Jovančičević, *Osnovi organske geohemije*, Beograd: Hemijski fakultet Univerziteta u Beogradu, Beograd, 2005.

- [2] K. Ceylan, Effects of treatments on the mineral matter and acidic functional group contents of Turkish lignites, *Fuel*, 74(1995)7, pp. 972-977.
- [3] S. Mishra, A. Akcil, S. Panda, C. Erust, Biodesulphurization of Turkish lignite by *Leptospirillum ferriphilum*: Effect of ferrous iron, Span-80 and ultrasonication, *Hydrometallurgy*, 176(2018), pp. 166-175.
- [4] P. A. Çelik, D. Ö. Aksoy, S. Koca, H. Koca, A. Çabuk, The approach of biodesulfurization for clean coal technologies: a review, *International Journal of Environmental Science and Technology*, 16(2019)4, pp. 2115-2132.
- [5] H. Dhawan, D. K. Sharma, Advances in the chemical leaching (inorgano-leaching), bio-leaching and desulphurisation of coals, *International Journal of Coal Science & Technology*, 6(2019)2, pp. 169-183.
- [6] R. K. Dwari, K. H. Rao, Tribo-electrostatic behaviour of high ash non-coking Indian thermal coal, *International Journal of Mineral Processing*, 81(2006)2, pp. 93-104.
- [7] K. M. Steel, J. Besida, T. A. O'Donnell, D. G. Wood, Production of Ultra Clean Coal - Part II - Ionic equilibria in solution when mineral matter from black coal is treated with aqueous hydrofluoric acid. *Fuel Processing Technology*, 70(2001)3, pp. 193-219.
- [8] N. P. Vasilakos, C. S. Clinton, Chemical beneficiation of coal with aqueous hydrogen peroxide/sulphuric acid solutions, *Fuel*, 63(1984)11, pp. 1561-1563.
- [9] P. Baláž, R. B. LaCount, D. G. Kern, L. Turčániová, Chemical treatment of coal by grinding and aqueous caustic leaching, *Fuel*, 80(2001)5, pp. 665-671.
- [10] A. B. Waugh, K. McG. Bouling, Removal of mineral matter from bituminous coals by aqueous chemical leaching, *Fuel Processing Technology*, 9(1984)3, pp. 217-233.
- [11] N. Vuković, D. Životić, J. G. Mendonça Filho, T. Kravić-Stevović, M. Hámor-Vidó, J.O. Mendonça, K. Stojanović, The assessment of maturation changes of humic coal organic matter – insights from closed-system pyrolysis experiments, *International Journal of Coal Geology*, 154-155(2016), pp. 213-239.
- [12] V. Prigiobbe, M. Mazzotti, Dissolution of olivine in the presence of oxalate, citrate, and CO₂ at 90 °C and 120 °C, *Chemical Engineering Science*, 66(2011), pp. 6544-6554.



19th INTERNATIONAL FOUNDRYMEN CONFERENCE
Humans - Valuable Resource for Foundry Industry Development

Split, June 16th-18th, 2021

<https://ifc.simet.hr/>

**PRELIMINARY STUDY ON TEMPERATURE DISTRIBUTION PATTERNS IN PEM
FUEL CELLS**

Anamarija Stoilova Pavasovic^{1,2,3*}, Frano Barbir^{1,2}

¹ Centar of Excellence for Science and Tehnology, Split, Croatia

² University of Split Faculty of Electrical Engineering, Mechanical Engineering and Naval Arhitecture, Split, Croatia

³ University of Split Faculty of Chemistry and Technology, Split, Croatia

Poster presentation
Original scientific paper

Abstract

This work presents a preliminary study on the degradation effects of low-temperature polymer electrolyte membrane (PEM) fuel cells caused by locally elevated temperature inside the membrane electrode assembly (MEA), where electrochemical reaction takes place. Overheated spots arise as a result of insufficient heat removal generated within a fuel cell. This study aims to investigate the performance resistivity of PEM fuel cells, due to effects of unsteady local temperature distribution on heat flow patterns, in order to optimize operating conditions and improve internal heat management. Local current and local temperature distribution in a PEM fuel cell has been mapped experimentally by using a specially designed segmented S ++[®] measurement sensor composite plate. An array of 121 individual conductive segments collected the current distribution measurements, while the temperature distribution measurements were obtained across 36 segments array. Furthermore, time-dependent current and temperature parameter changes were observed during the experimental study, together with their variations on the cathode side under different humidity conditions at three operating points, which includes the lowest and highest current density possible to achieve. The obtained preliminary results give the first insight into the thermal distribution phenomena within the observed fuel cell. Overall, a given approach could contribute to the deeper understanding of the local current and temperature distributions effects, in order to identify the local maximum temperature within the catalyst layer, as a possible local cell degradation spot, and it could be a helpful indicator to improve a design process of the fuel cell components.

Keywords: *current distribution, heat flow patterns, temperature distribution, PEM fuel cell*

*Corresponding author (e-mail address): astoilov@fesb.hr

INTRODUCTION

Over the past fifteen years, advances in fuel cell technology have spurred an enormous wave of interest in its potential energy applications, particularly for the transportation sector. Energy conversion through electrochemical devices such as fuel cells plays an essential role in developing long-term energy sustainability. Through an electrochemical rather than combustion process, fuel cell efficiently converts green hydrogen energy to electrical energy. One of the most promising clean energy power sources in various applications are polymer electrolyte membrane (PEM) fuel cells due to their high efficiency, relatively low-temperature operation (60 °C - 80 °C), and low/zero emission level. However, considering the operating cell temperature, it could be locally significantly different within the fuel cell. Some measurements show that the temperature in the bipolar plates can be 20°C cooler than that adjacent to the electrode itself [1]. Non-uniform temperature and current distribution can often cause starvation or localized corrosion of the membrane-electrode assembly (MEA) on the cathode side, potentially initiating and/or enhancing irreversible degradation affecting the lifetime of the cell. Also, insufficient heat removal from the electrochemical reaction places can often result in locally elevated temperatures inside the cathode catalyst layer (CL), potentially causing morphological changes of the polymer membrane. Since the operating environment inside the CL is specific – thickness of ca. 10 micrometers, it is impossible to measure or monitor the local temperature distributions on such a small scale with intrusive methods due to significant alteration of the local operating conditions. Therefore, the aim of this study is to determine the local maximum temperature within the catalyst layer with preliminary results obtained using S++[®] segmented plate.

MATERIALS AND METHODS

The heart of a PEM fuel cell is Membrane Electrode Assembly (MEA) which consists of a polymer electrolyte membrane (usually Nafion[®]) sandwiched between two electrodes anode and cathode. Nafion[®], based on perfluorosulfonic acid (PFSA), provides multiple functions, including proton conduction, separation of reactant gases, and prevents electron transport. Its hydrophobic perfluorinated backbone provides mechanical support and chemical stability, while the hydrophilic sulfonated side chains promote water absorption forming hydrated clusters. Electrodes comprise the Catalyst Layer (CL), the Microporous Layer (MPL), and the Gas Diffusion Layer (GDL). The major components of a PEM fuel cell are shown on figure 1.

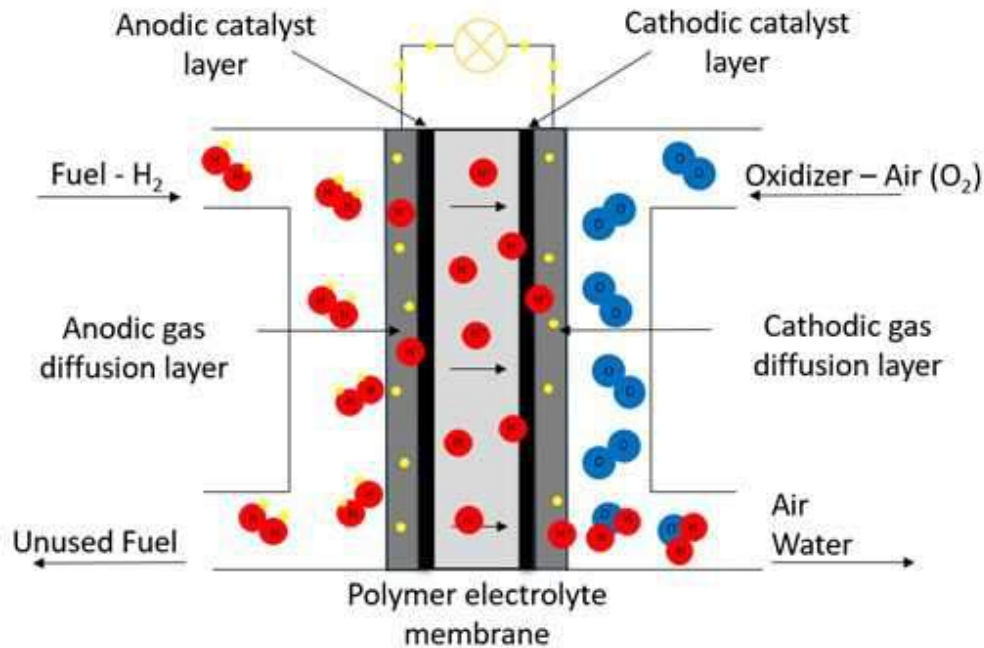


Figure 1. Main components of Polymer electrolyte membrane fuel cell

The place where hydrogen oxidation reaction (HOR) and oxygen reduction reaction (ORR) take place is so-called triple-phase boundary, and its located in the anode and cathode CLs, respectively. The measurements for preliminary study were performed with the Scribner Associates 890CL Teledyne Medusa fuel cell test station on an air-cooled single PEM fuel cell hardware from Fuel Cell Technologies in co-flow configuration with graphite four-channel serpentine cathode flow field and single-channel anode flow field and with a 50 cm² active area MEA (Nafion 212). Silicone gaskets (415 μm thickness) were employed for both electrodes to provide the required compression ratio. A specially designed segmented sensor, commercially made by the S++[®], sandwiched between the bipolar plate and the current collector plate, was used to map the local current and temperature distribution on the cathode side. The sensor plate consists of 11 x 11 segments for current and 6 x 6 segments for temperature distribution measurements, Figure 2. During each operating point, current and temperature distribution data were collected every 0.5 seconds for two hours. The measurements were recorded at different currents and different inlet relative humidities (100 % and 50 %) for both hydrogen on the anode and air (oxygen) on the cathode side. The operation temperature of the cell was held at 80 °C. Reactant flows were set at a constant stoichiometry of two on the anode and four on the cathode, while the backpressures were the same for both compartments and a 0.2 bar(g). The operating conditions from above were also kept during the polarization curves measurements, which were recorded in descending direction with the best time of 1 min at each point.

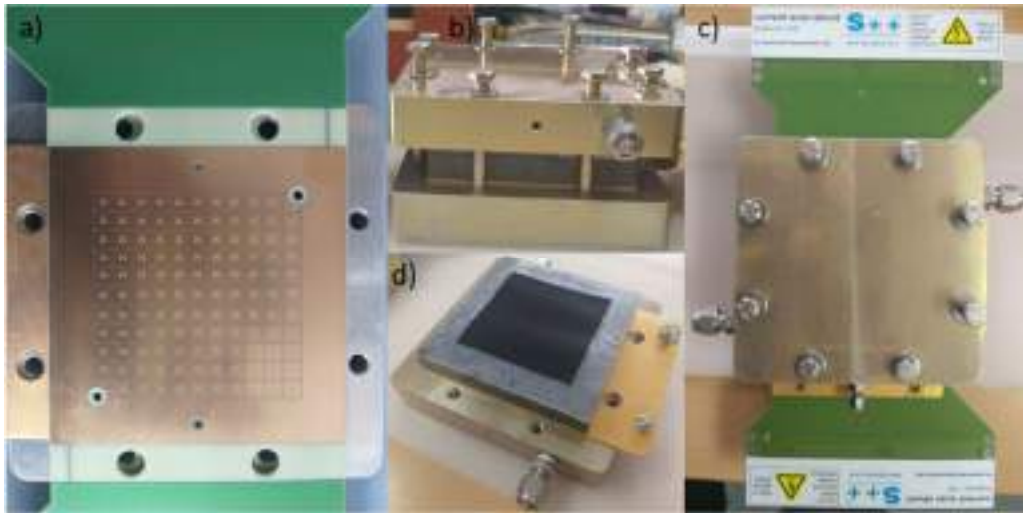


Figure 2. Disassembly of the cell: a) sensor plate, b) fuel cell layers, c) single cell with inserted S++ sensor plate, d) membrane-electrode assembly within the fuel cell

RESULTS AND DISCUSSION

The polarization curves measurements at the beginning of life of the observed cell were carried out for both testing cases (100% and 50% relative humidity; RH) after membrane break-in procedure, conditioning phase and right before each current and temperature distribution measurements. As it was expected, higher relative humidity results in better fuel cell performances, figure 3.

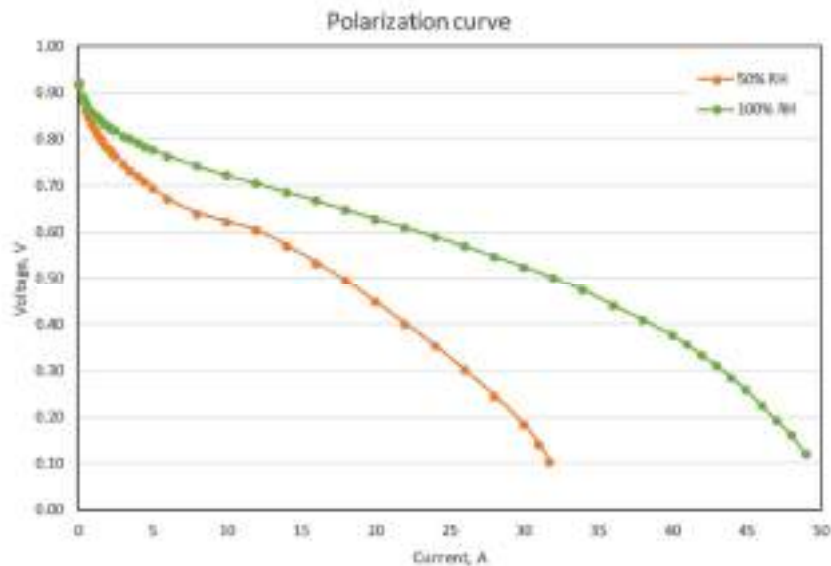


Figure 3. Polarization curve for both testing cases

Current and temperature mapping

Combined current and temperature distribution mapping was performed in two regimes of operation based on 'low' and 'high' average current densities during operation at two different relative humidity conditions, figure 4.

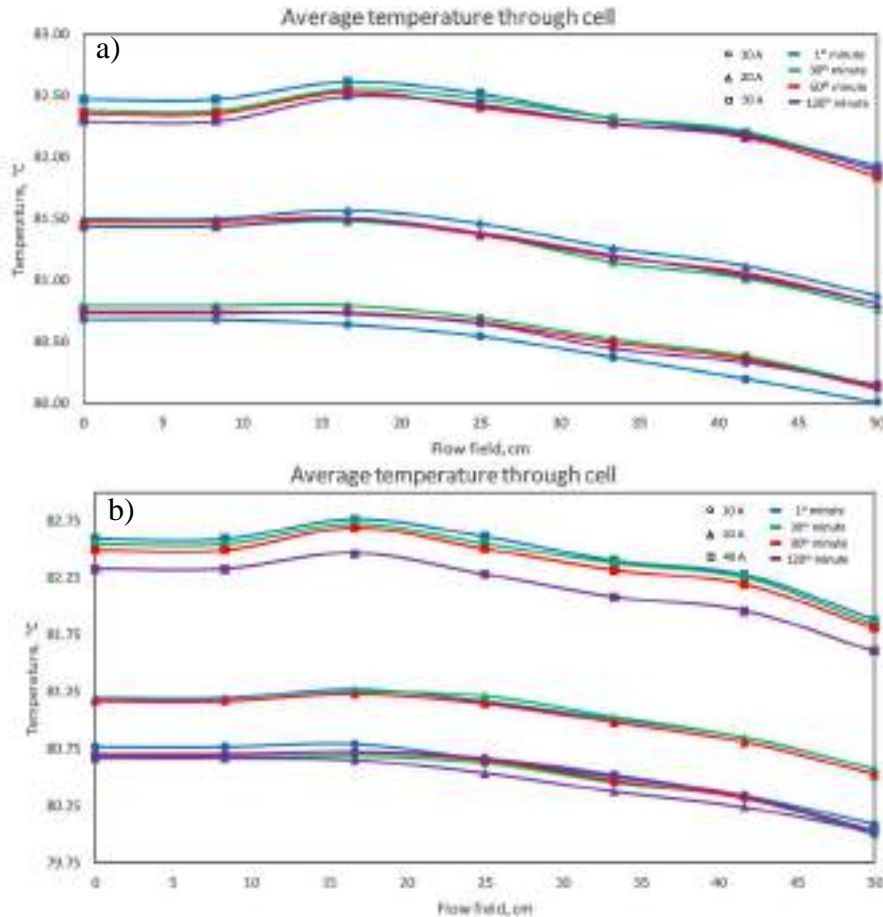


Figure 4. Average temperature distribution through cell at: a) 50% RH; b) 100% RH

Current and temperature mapping in the low current density regime

In order to gain insight into the temperature distribution inside the cell, numerical results obtained under various conditions by S++ segmented sensor plate were analyzed and shown in figures 5-8. It was noticed that temperature distribution follows a similar path which implies lower temperature near air inlet and outlet with a slight increase in the middle of the cell. The temperature measured during the experiment differs from the set cell temperature (80°C). However, every mapped temperature is maintained within the $\pm 25\%$ range of operation temperature. The temperature difference is more negligible at higher currents due to more released heat during the electrochemical reaction. Released heat during the experiment gathers more and more, impacting the increase of temperature. As a consequence, in natural convection conditions, at some point, the maximum temperature will exceed the set cell temperature even between the bipolar plate and current collector plate. The lack of instrumentation limits our comprehension, so at this point, we can only logically assume that the reaction site's temperature will be significantly higher.

The current density at first rashly decreases with temperature subsequently increases approximately linearly with increasing temperature in every cell segment, figure 11. That is an example of the coupled effect of current and temperature distribution. The higher relative humidity at the inlet produces a better performance environment with higher polymer electrolyte conductivity, leading to improved performance despite the hot spots that arise due to uneven cooling of the PEM fuel cell.

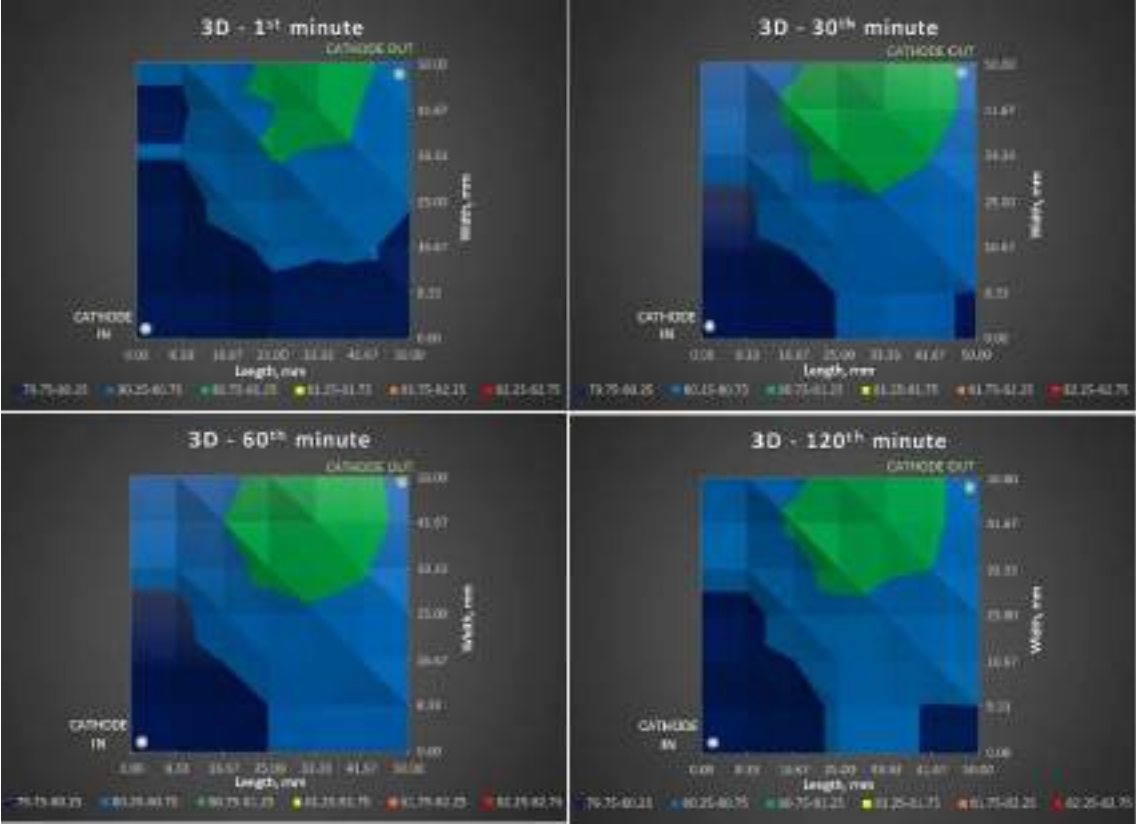


Figure 5. A three-dimensional plot of local temperature profile at 10A and 50%RH

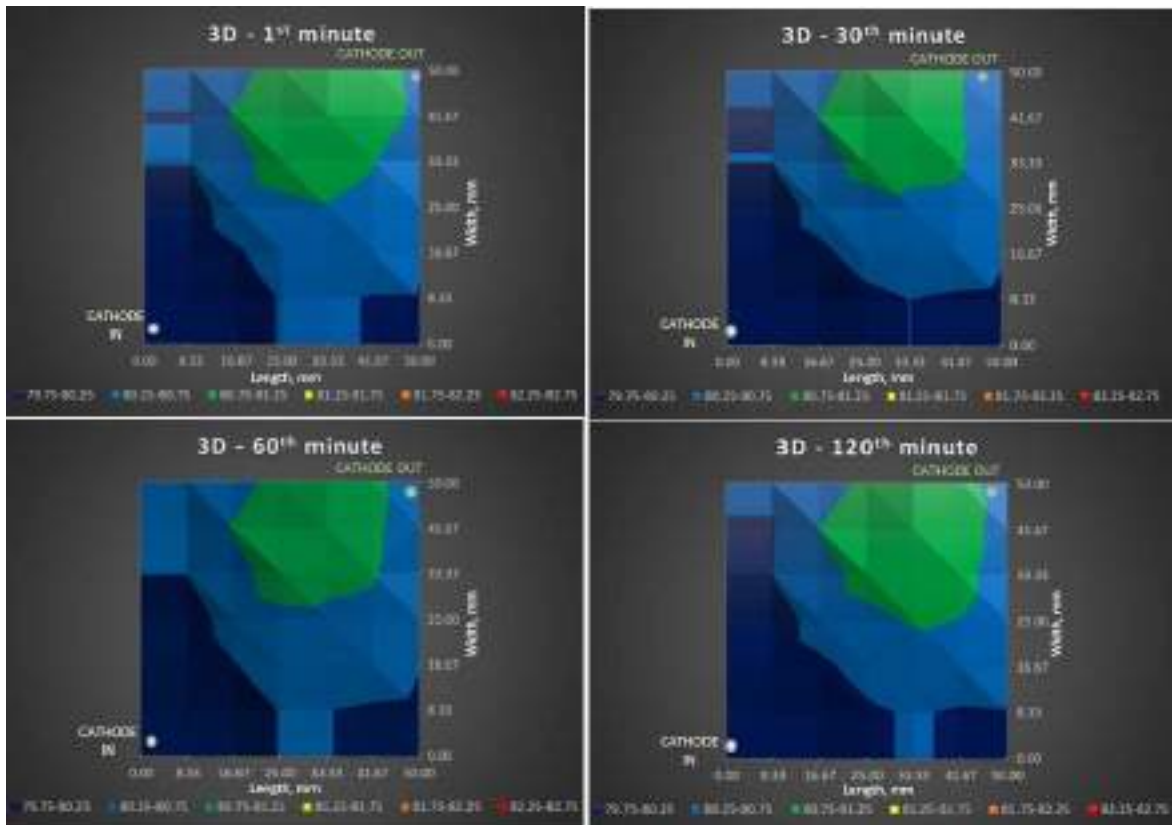


Figure 6. A three-dimensional plot of local temperature profile at 10A and 100%RH

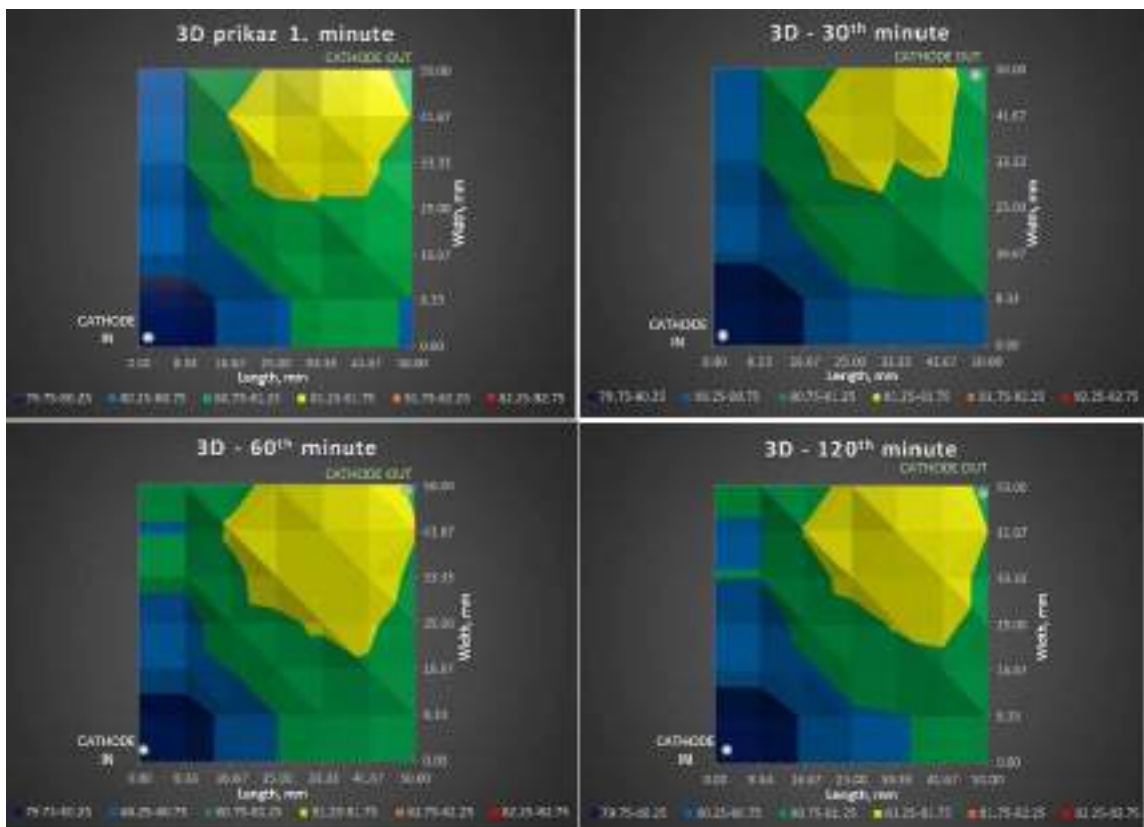


Figure 7. A three-dimensional plot of local temperature profile at 20A and 50%RH

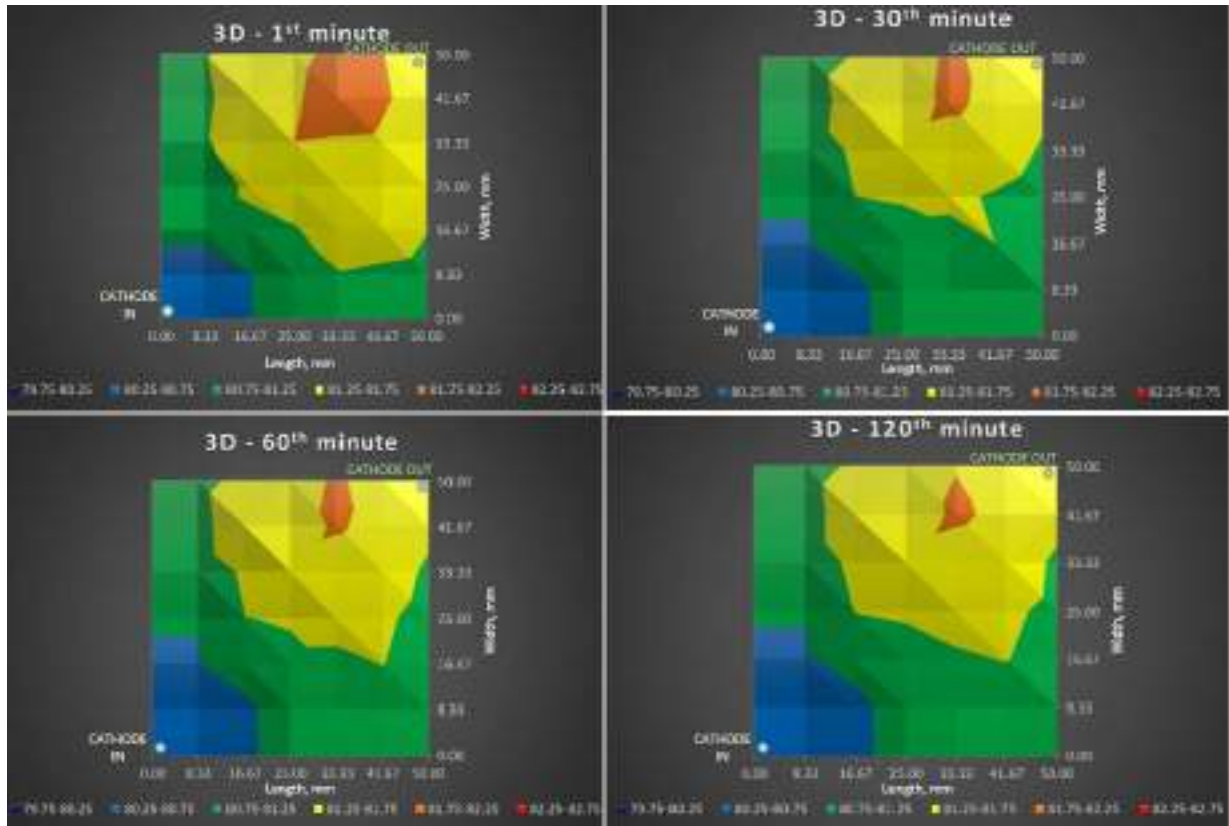


Figure 8. A three-dimensional plot of local temperature profile at 20A and 100%RH

Therefore, it can be concluded that the heat dissipation potential of air, natural convection cannot match the cooling demands of a single PEM fuel cell. In other words, a PEM fuel cell cannot be cooled appropriately by natural convection. It will result in overheating spots of the fuel cell electrode, which is even more evident in the high current density regime.

Current and temperature mapping in the high current density regime

At a high current exceeding 30 A, local temperature redistribution was observed (figures 9 and 10), with substantially elevated temperature occurring in both the x- and y-axis. It can be noticed that the temperature is even more than 83° C in some segments. Elevated temperature turns up as a consequence of the increased current which accelerating the rate of the electrochemical reaction. Furthermore, as expected, the local temperature is higher at higher loads and higher humidification level of the membrane comparing the results at the same segments. In addition, some disturbances during the experiment are probably related to the humidification level. A high humidification level can lead to disturbances during measurements due to the immense amount of water droplets irregularly distributed on the cathode side. In contrast, lower humidification level values affect the membrane resistance due to dehydration under these conditions affecting the fuel cell's long-term performance. Therefore, this result highlights the coupled nature of current, temperature, and relative humidity in figure 12. and stresses that all need to be considered to understand performance completely.

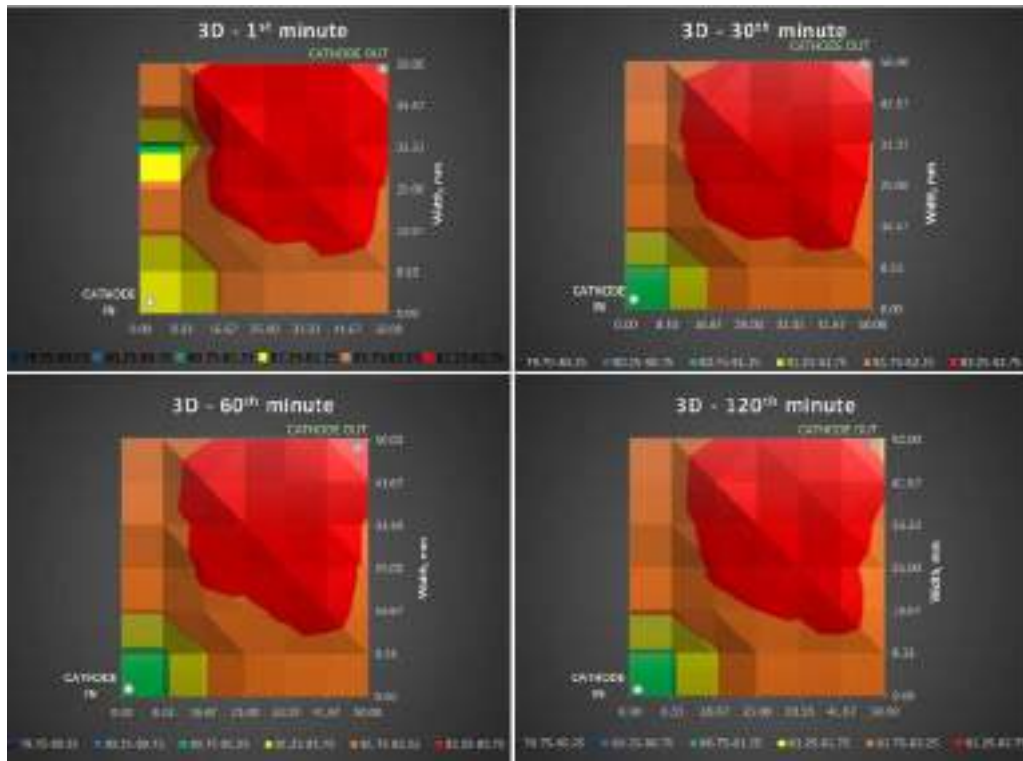


Figure 9. A three-dimensional plot of local temperature profile at 40A and 100%RH

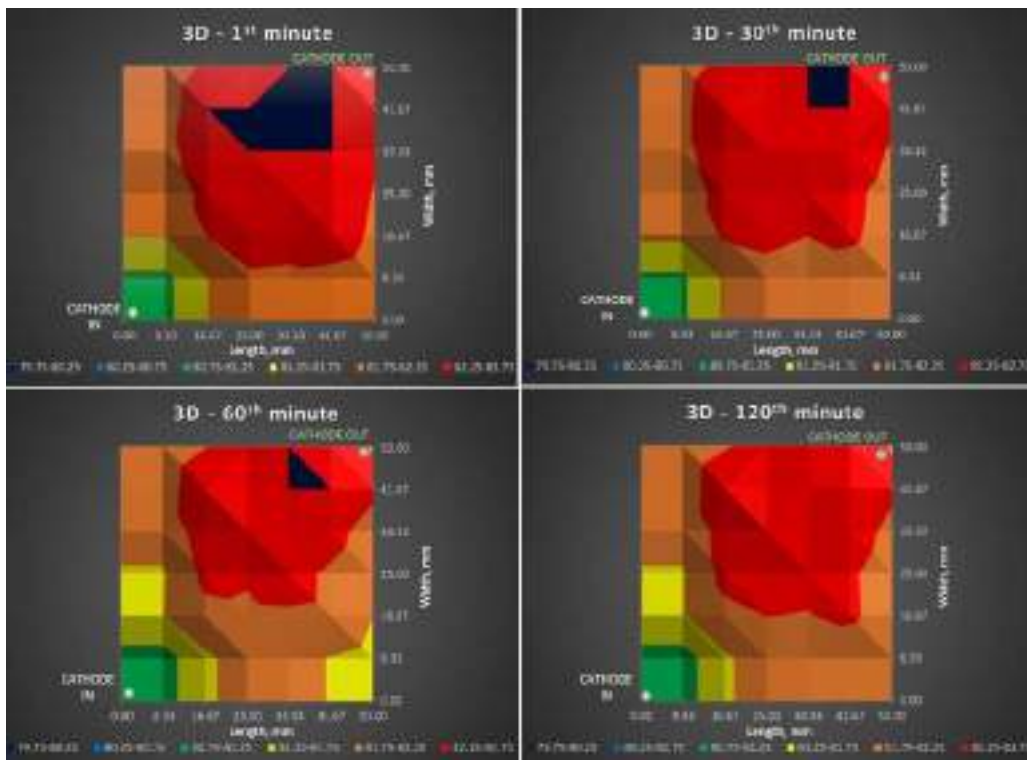


Figure 10. A three-dimensional plot of local temperature profile at 40A and 100%RH

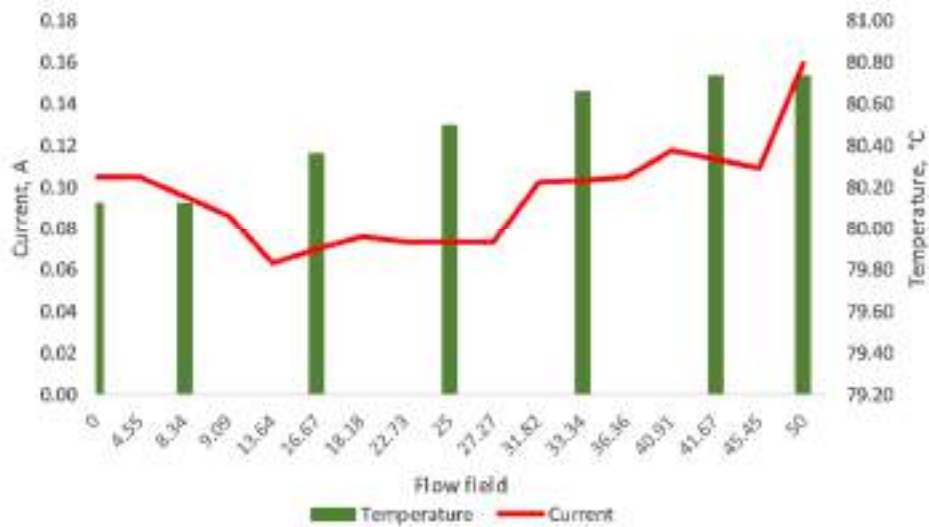


Figure 11. Average current and temperature distribution in low current density regime at 50% RH

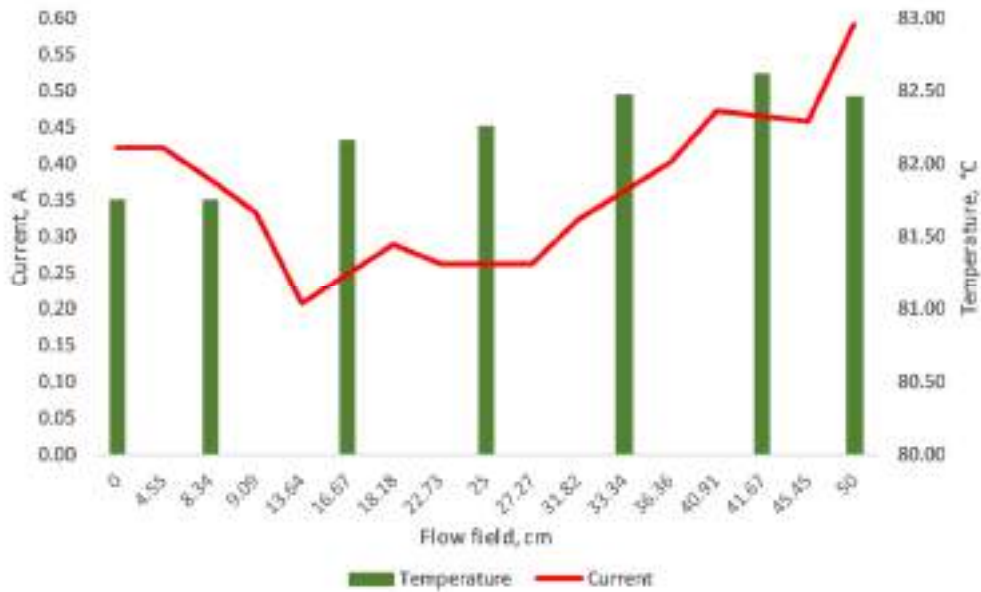


Figure 12. Average current and temperature distribution in low current density regime at 100% RH

CONCLUSIONS

The experimental investigation of the local temperature distributions inside the cathode catalyst layer of the PEM fuel cell was obtained using the S++[®] segmented sensor plate at different operating currents and humidification levels. It has been shown that under observed conditions, the cell was no isothermal even when both end plates were held at a constant temperature. Also, PEM fuel cell cannot be cooled appropriately by natural convection. The heat released during the electrochemical reaction will result in overheating

spots inside the fuel cell, contributing to the local degradation of the membrane. The influence of different pressures and states of water and its phase change within the fuel cell should be further explored. A preliminary study showed that understanding the temperature distribution inside the cell could be crucial to predicting long-term degradation and enhancing the system's lifetime.

Acknowledgements

This research was partially supported under the project STIM – REI, Contract Number: KK.01.1.1.01.0003, a project funded by the EU through the European Regional Development Fund – the Operational Programme Competitiveness and Cohesion 2014-2020 (KK.01.1.1.01).

REFERENCES

- [1] J. G. Pharoah and O. S. Burheim, “On the temperature distribution in polymer electrolyte fuel cells,” *J. Power Sources*, 195(2017)16, pp. 5235–5245.



19th INTERNATIONAL FOUNDRYMEN CONFERENCE
Humans – Valuable Resource for Foundry Industry Development

Split, June 16th-18th, 2021

<https://ifc.simet.hr/>

EVALUATION OF INFRARED DRIED SOLVENT-BORNE COATINGS

Ivan Stojanović¹, Ivan Cindrić^{1*}, Lara Janković¹, Daniela Rakela Ristevski²

¹ University of Zagreb Faculty of Mechanical Engineering and Naval Architecture, Zagreb, Croatia

² Končar Steel Structures Inc., Zagreb, Croatia

Poster presentation

Original scientific paper

Abstract

Accelerated infrared (IR) drying of coatings is increasingly used in the industry. Drying is performed via IR emitters, powered by gas or electricity. The main advantage of using IR drying is drying time reduction and higher production rate. Another advantage is burning the harmful VOCs (Volatile organic compound) from the coatings, therefore the environmental impact of this drying method is very low. In this study, solvent-borne coating systems were applied and dried by infrared as well as in atmospheric conditions. Catalytic IR emitters were used for accelerated drying of the coatings. The purpose of the investigation was to show how much time can be saved by using IR technology and to compare the protective properties of differently dried coatings. After the coatings were cured, chambers for accelerated corrosion testing were used. The succeeding steps were the adhesion and the hardness measurements, which were evaluated using Pull-off and Pencil test. The results have shown the same or even better properties of IR-dried coatings, along with the significant drying time reduction. This study is part of the project “Smart plant for drying liquid coatings” (reference code: KK.01.2.1.02.0030) which is co-financed by the European Union from the European Regional Development Fund.

Keywords: *IR drying, corrosion, solvent-borne coatings, drying properties, testing*

*Corresponding author (e-mail address): icindric@fsb.hr

UVOD

Korozija je spontani proces kojim se, uslijed prirodne ravnoteže, materijali vraćaju u svoje prvobitno stanje. Kao fenomen negativno utječe na mnoge materijale zbog čega je svijest o koroziji kao izrazito razornoj i štetnoj pojavi sve jača. S obzirom na to, primjena metoda zaštite od korozije postaje sve jača kao i razvoj novih načina za njeno usporavanje, smanjivanje i suzbijanje.

Organske prevlake imaju nezamjenjivu ulogu u zaštiti metalnih konstrukcija od korozije. Pritom, učinkovitost zaštite ne ovisi isključivo samo o svojstvima prevlake već i o karakteru

same metalne osnove, pripremi površine, tehnologiji nanošenja i sušenja prevlake. U praksi je stoga neophodno uzeti u obzir cijeli sustav i tehnologiju izvođenja zaštite uključujući i najčešće kompliciran sastav same prevlake [1].

Premazi se obično suše na temperaturi koja odgovara trenutnoj mikroklimi u lakirnici (atmosfersko sušenje) ili u konvekcijskoj peći prijenosom vrućeg zraka. Zbog konvencionalnih metoda sušenja tekućih premaza, tvrtke se suočavaju s mnogim ograničavajućim aspektima koji se odnose na vremenska, ekološka, energetska, prostorna, zdravstvena, ekonomska i tehnička ograničenja. Međutim, tehnologijama poput infracrvenog (IC) grijanja nastoji se eliminirati ili ublažiti ograničenja prouzročena konvencionalnim metodama.

Infracrveno zračenje u industrijskom sektoru nalazi se od kasnih 1930-ih, u početku koristeći komercijalne žarulje za osvjetljenje opremljene posebnim vanjskim reflektorima. Tehnika se pokazala vrlo uspješnom za pečenje prevlaka prevučenih na karoserije automobila pri povišenim temperaturama i uspješno je prebačena na proizvodnu liniju. U Drugom svjetskom ratu, infracrveno zračenje postalo je šire prepoznato kao tehnika za ubrzavanje završne obrade metala, posebno za vojnu opremu i, iako su žarulje koje su se koristile bile izrazito niskih intenziteta snage prema današnjim standardima, nudili su mnogo brže sušenje i otvrdnjavanje od konvekcijskih peći tog vremena. Sredinom 1950-ih industrija motornih vozila je opet bila pokretačka snaga iza sve većeg broja infracrvenih instalacija, ali stare su žarulje sada bile zamijenjene novim kvarcnim cijevima, koje su mnogo manje i nudile su mnogo veći intenzitet zračenja [2].

Danas su infracrvene lampe/emiteri dostupni u najrazličitijim oblicima i konfiguracijama, a uključuju keramičke emitere, emitere s metalnom oblogom i lampe s ugljičnim vlaknima, iako su najpopularniji i dalje oni kvarcni. Međutim, najvažniji napredak u infracrvenoj tehnologiji vjerojatno je bio način na koji su iskorištene razne korisne valne duljine infracrvenog zračenja da bi njihova primjena bila maksimalna [2].

IC sušenje podrazumijeva sušenje IC zrakama koje prenose toplinu kroz zrak izravno na svaku molekulu u premazu. Na taj način toplina iz IC zračenja apsorbiranjem kroz sloj mokre boje i refleksijom od metala vrši sušenje. Primjenom IC tehnologije za sušenje premaza samo manji dio IC zraka će se reflektirati od površine premaza dok će se veći dio IC zraka apsorbirati kroz mokri premaz te konačno reflektirati od površine metala koja će se zagrijati. Na taj se način premaz suši iznutra prema van, odnosno od vanjske površine premaza do površine metala i obrnuto čime se postiže izuzetno brzi prijenos zaostalih otapala te brze kemijske reakcije koja odgovara zadnjem stupnju polimerizacije. Dakle, premazi sušeni na ovaj način postižu stupanj umreženja kada je moguće obojani predmet odmah staviti u funkciju primjene odnosno eksploatacije [3].

U ovom radu je korištena infracrvena tehnologija za sušenje sustava premaza na bazi otapala. Cilj je bio dokazati koliko se vremena može uštediti upotrebom IC zračenja i usporediti zaštitna svojstva premaza osušenih IC-om u odnosu na atmosferski sušene premaze. Primijenjena su dva sustava premaza, koja su uključivala epoksi ili cink-epoksi (eng. Zn rich) temeljni premaz, zatim epoksidni međusloj i poliuretanski završni premaz. Zaštitna svojstva procjenjena su u 3%-tnoj otopini NaCl primjenom EIS metode te u vlažnom okolišu ispitivanjem u vlažnoj komori. Za procjenu fizikalnih svojstava provedena su ispitivanja tvrdoće i adhezije.

MATERIJALI I METODE

U eksperimentalnom dijelu rada ispitivani su sustavi premaza koji su se sastojali od dvokomponentnih (2K)epoksi temelja sa i bez cinka, zatim međusloja epoksida te završnog poliuretana. Pola uzoraka sušeno je atmosferski, a druga polovica IC zračenjem. Priprema površine uzoraka je provedena mlazom abraziva kako bi se postigla potrebna čistoća i hrapavost za nanošenje premaza. Sačmarenjima su na kvalitetu čistoće Sa 2,5 te je postignut srednji stupanj hrapavosti (*medium*, „M“). Učinjen je test prašine te Bresle test. Uzorci su čelične pločice dimenzija 150x120x8mm. U tablici 1. prikazani su aplicirani sustavi premaza proizvođača Hempel s obzirom na način sušenja i vrstu temeljnog sloja.

Tablica 1. Aplicirani sustavi premaza s obzirom na način sušenja i vrstu temeljnog premaza

Br. Uzorka	Način sušenja	Sustav		
		Temelj	Međusloj	Završni sloj
A1	atm.	cink-epoksi	epoksi	PUR
A2	IC	cink-epoksi	epoksi	PUR
B1	atm.	epoksi	epoksi	PUR
B2	IC	epoksi	epoksi	PUR

Zn-rich epoksidni premazi smanjuju učinak korozije i pružaju izvrsnu galvansku zaštitu. Koriste se kao temeljni premazi koji imaju izvrsnu mehaničku čvrstoću, također i u cikličkim temperaturama, uz poboljšanu toleranciju na velike debljine filma zahvaljujući visokoj fleksibilnosti i samozacjeljujućem učinku. Imaju izvrsnu toleranciju na visoku relativnu vlažnost tijekom nanošenja. Otvrdnjavanje je do -10°C. Čestice cinka aktivnije su od čelika i djeluju kao žrtvovana anoda u premazu koji korodira umjesto čelika kada je on izložen vodi, kisiku i/ili kloridima. Djelovanje galvanskog članka ovisi o pripremi podloge, jer i najmanja nečistoća prekida električni krug zaštite i dezaktivira sistem [4].

Epoksidni premazi općenito pružaju dobro prijanjanje na površinu, kemijsku postojanost i dobra fizička svojstva. Odlična su zaštita u korozivnim sredinama te se zbog toga učestalo upotrebljavaju u rafinerijama, na naftnim platformama, mostovima, kemijskim postrojenjima itd. Jedan od novijih vrsta epoksida koji su se pojavili posljednjih godina su epoksidni mastici koji sadrže manji udio otapala. Potrebna im je slabija priprema površine, mogu se stvrdnuti na temperaturama do -10 °C, te tvore vrlo homogene prevlake [5].

Poliuretanski premazi štite osnovni materijal od korozije, vremenskih utjecaja, ultraljubičastih (UV) zračenja i abrazije. Poliuretanska prevlaka može biti sjajna ili mat te neprozirna ili prozirna. Prema fizikalnim svojstvima je vrlo tvrda i čvrsta, pružajući iznimnu otpornost na habanje. S druge strane postoje mekše i žilavije, tako da se osnovni materijal može rastezati bez uništavanja premaza. Poliuretanski premazi nisu zapaljivi, pa se mogu koristiti i u okruženjima gdje dolazi do izgaranja. Imaju dobru sposobnost prijanjanja na širok raspon materijala, jednostavno se nanose te nemaju stroge zahtjeve na određenu temperaturu [5].

Ispitivanje korozije u vlažnoj atmosferi

Ispitivanjem u vlažnoj komori simulira se ponašanje materijala u vlažnoj i toploj atmosferi uz kondenziranje vode. Ispitivanje je provedeno u Laboratoriju za zaštitu materijala na Fakultetu strojarstva i brodogradnje, sukladno normi HRN EN ISO 6270-1:2017. Temperatura

ispitivanja je 40 ± 3 °C, a relativna vlažnost zraka je oko 100 % s orošavanjem uzoraka. Ispitivanje je provedeno u vlažnoj komori proizvođača C&W, *Humidity Cabinet Model AB6* te je zajedno s ispitivanim uzorcima prikazana na slici 1. Uzorci su u vlažnoj komori ispitivani 336 sati i potom su podvrgnuti analizi i ispitivanju fizikalnih svojstava.



Slika 1. Ispitivanje uzoraka u vlažnoj komori

Elektrokemijska impedancijska spektroskopija

Elektrokemijska impedancijska spektroskopija provedena je na uređaju VersaSTAT 3, proizvođača AMTEK, USA, upravljani računalom i software-om VersaSTUDIO v2.44. Za impedancijsko ispitivanje korištene su ugljikova te zasićena kalomel elektroda (ZKE), gdje je ugljikova predstavljala protuelektrodu, ZKE referentnu elektrodu, a mjerni uzorak radnu elektrodu. Za elektrolit je korištena 3 %-tna otopina NaCl. Ispitivanje je provedeno prema normi HRN ENISO 16773-2:2016, a parametri ispitivanja prikazani su u tablici 2.

Tablica 2. Parametri ispitivanja

Parametri	Vrijednost parametra
Frekvencija, raspon	0,1 – 100000 Hz
Amplituda	100-200mV
Površina ispitivanja	19,6 cm ²
Gustoća materijala	7,86 g/ml
Ekvivalentna masa	27,92 g
Vrijeme izlaganja	336 h

Ispitivanja fizikalnih svojstava

Provedena su ispitivanja tvrdoće i adhezije premaza. Tvrdoća se određivala Buchholz metodom (HRN EN ISO 2815:2003). Adhezija premaza ispitivana je Pull-off testom prema normi HRN EN ISO 4624:2016.

REZULTATI I DISKUSIJA

Uzorci navedeni u tablici 3. su pokazali mala odstupanja što se tiče debljine suhog filma, s izmjerenim srednjim vrijednostima 193 i 198 μm za sustave premaza s cink-epoksi temeljom i 231 μm za sustave bez cinka u temelju. Prema HRN EN ISO 12944 za C5-M traženi DSF-ovi za sustave s cink-ričetemeljem su 200 μm , a za sustave bez cinka su 240 μm . Vremena sušenja znatno su manja kod IC sušenih uzoraka gdje je aplikacija troslojnog sustava moguća u jednoj radnoj smjeni (8 h) dok se isti sustav atmosferski morao sušiti tri dana. Uzorci sušeni IC zračenjem se po završetku sušenja smatraju kemijski umreženima te se odmah mogu ispitivati njihova svojstva. Za uzorke sušene na sobnoj temperaturi prošlo je dva tjedna prije nego što se krenulo s korozivskim i fizikalnim ispitivanjima. Prije izlaganja u vlažnoj komori, na uzorcima je napravljen Pull-off test koji je pokazao zadovoljavajuće rezultate za oba slučaja, s većim vrijednostima kod IC sušenih premaza. Izlaganje uzoraka u vlažnoj komori u periodu od 336 h (14 dana) nije pokazalo nikakve znakove mjehuranja, hrđanja, pucanja i ljuštenja prema normi HRN EN ISO 4628. Uzorci su i nakon izlaganja u vlažnoj komori pokazali dobru prionjivost s rezultatima Pull-off testa od 10 MPa na više. Usporedba parametara između dva načina sušenja premaza kao i ocjene njihova stanja nakon izlaganja u vlažnoj komori prikazana su u tablicama 3, 4 i 5.

Tablica 3. Usporedba vremena sušenja i DSF-ova atmosferski i IC sušenih premaza

Način sušenja	Br. uzorka	Ukupno vrijeme sušenja sustava [h]	DSF [μm]
atm.	A1	72 h	193,9
	B1	72 h	231,45
IC	A2	1 h i 40 min	198,15
	B2	2 h i 15 min	231,15

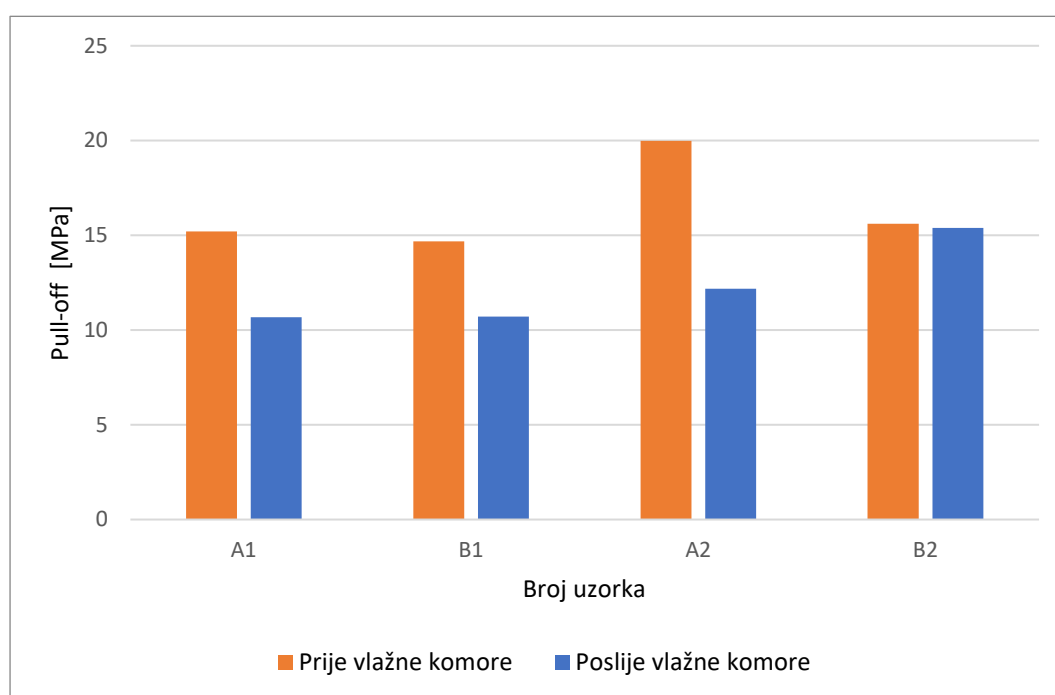
Tablica 4. Rezultati ispitivanja fizikalnih svojstava prije i poslije vlažne komore

Način sušenja	Br. uzorka	Prije vlažne komore			Poslije vlažne komore		
		Pull-off [MPa]	Buchholz		Pull-off [MPa]	Buchholz	
			l [mm]	α		l [mm]	α
atm.	A1	15,2	1,702	58,75	10,67	1,96	51,02
	B1	14,68	1,323	75,59	10,71	1,87	53,48
IC	A2	19,97	1,09	91,74	12,18	1,637	61,09
	B2	15,61	1,238	80,78	15,38	1,335	74,93

Tablica 5. Ocjena premaza nakon ispitivanja u vlažnoj komori

Br. uzorka	HRN EN ISO 4628-2	HRN EN ISO 4628-3	HRN EN ISO 4628-4	HRN EN ISO 4628-5
	Mjehuranje	Hrđanje	Pucanje	Ljuštenje
A1	0(S0)	Ri 0	0(S0)	0(S0)
A2	0(S0)	Ri 0	0(S0)	0(S0)
B1	0(S0)	Ri 0	0(S0)	0(S0)
B2	0(S0)	Ri 0	0(S0)	0(S0)

Vrijednosti Pull-off testa prije i nakon izlaganja u vlažnoj komori grafički su prikazani na slici 2. U ovom slučaju više vrijednosti imaju uzorci koji su sušeni IC zračenjem.

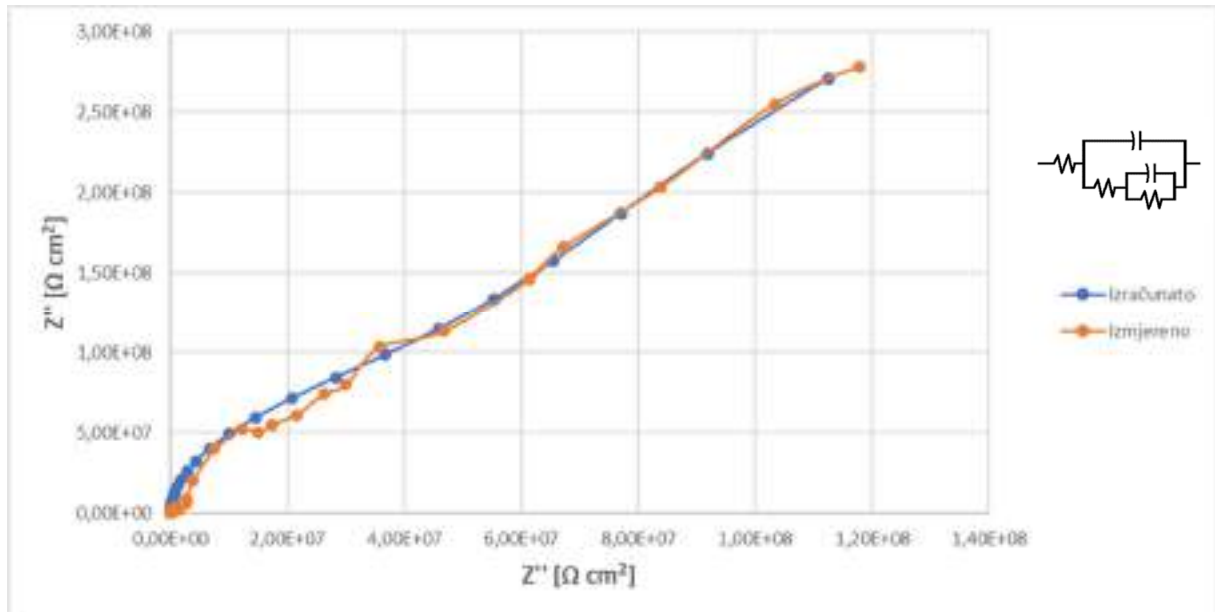


Slika 2. Usporedba prionjivosti prije i nakon ispitivanja u vlažnoj komori

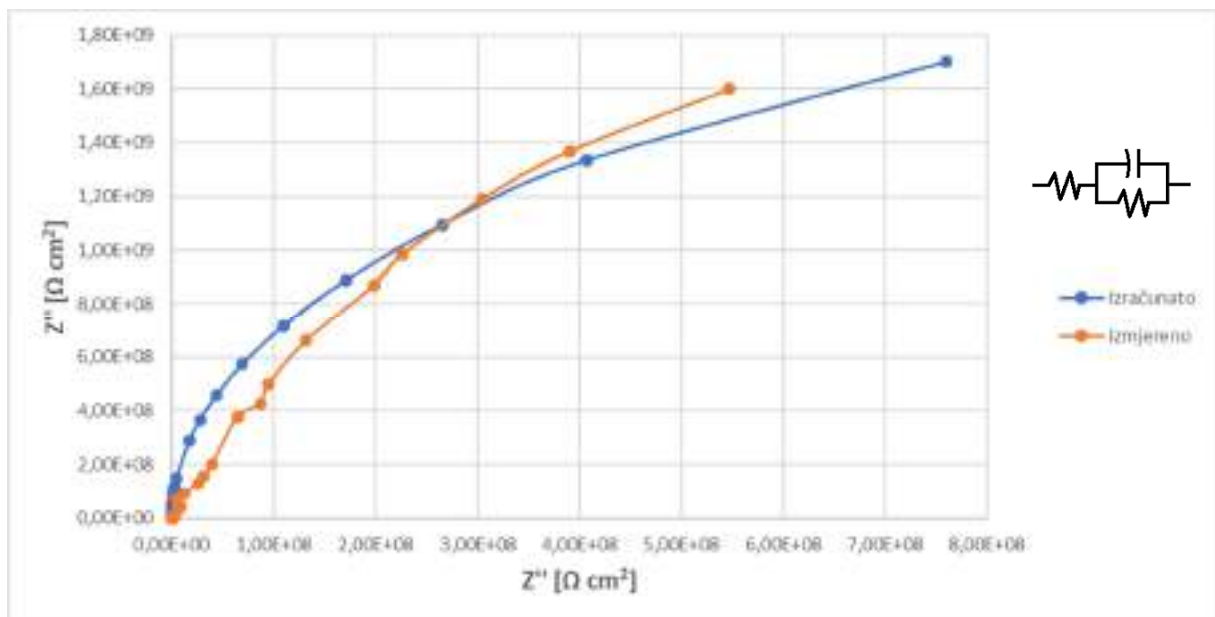
Usporedbom različitih načina sušenja uočljivo je da su postignuta značajno manja vremena sušenja s IC izvorom zračenja, a prilikom čega nije došlo do pada svojstva prionjanja. Štoviše, rezultati svih provedenih ispitivanja pokazuju da IC sušeni sustavi premaza imaju nešto bolja svojstva od atmosferski sušenih uzoraka.

U nastavku su prikazani Nyquistovi dijagrami (slika 3.-6.) ispitivanih uzoraka dobivenih elektrokemijskom impedancijskom spektroskopijom nakon 336 sati izlaganja u elektrolitu (3%-tna otopina NaCl). Za uzorke B1, B2 i A1 koristio se model ekvivalentnog strujnog kruga koji se koristi za opisivanje poroznog premaza, odnosno u slučaju kada je elektrolit došao do podloge. Za uzorak A2 odabran je Randelsov strujni krug kojim se tumači da još uvijek nije došlo do prodora elektrolita kroz prevlaku. Za sve uzorke izmjerene vrijednosti otpora sustava premaza pri 0,1 Hz iznosile su preko $10^8 \Omega \text{cm}^2$. Iz Bodeovog dijagrama na slici 7.

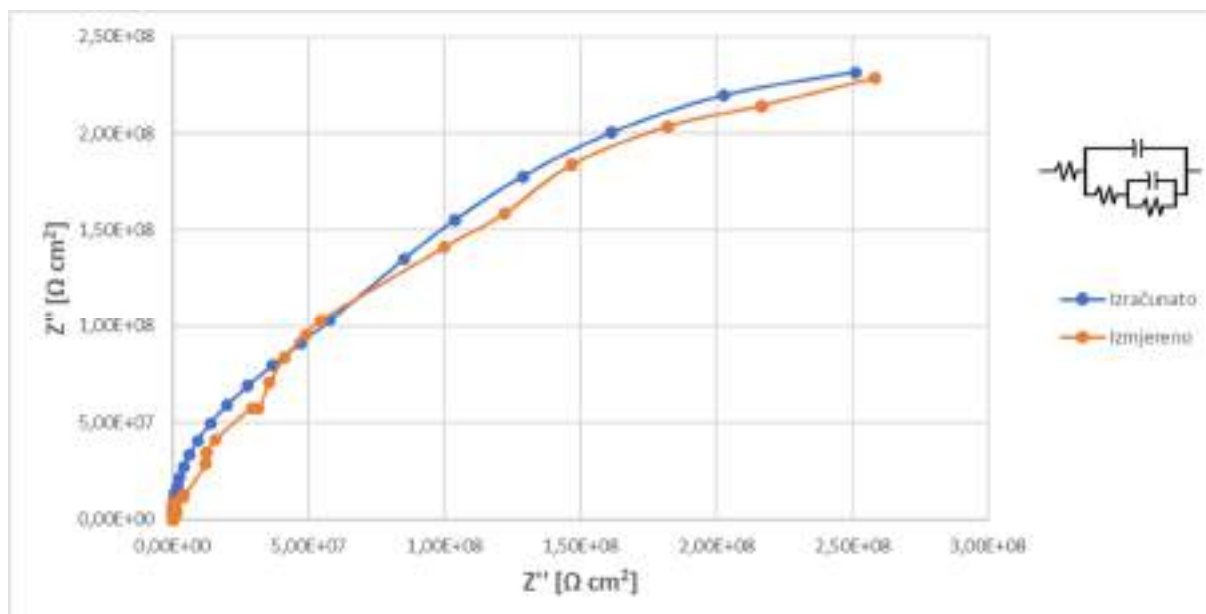
vidljivo je da uzorci sušeni IC zračenjem pokazuju veće vrijednosti otpora od atmosferski sušenih uzoraka.



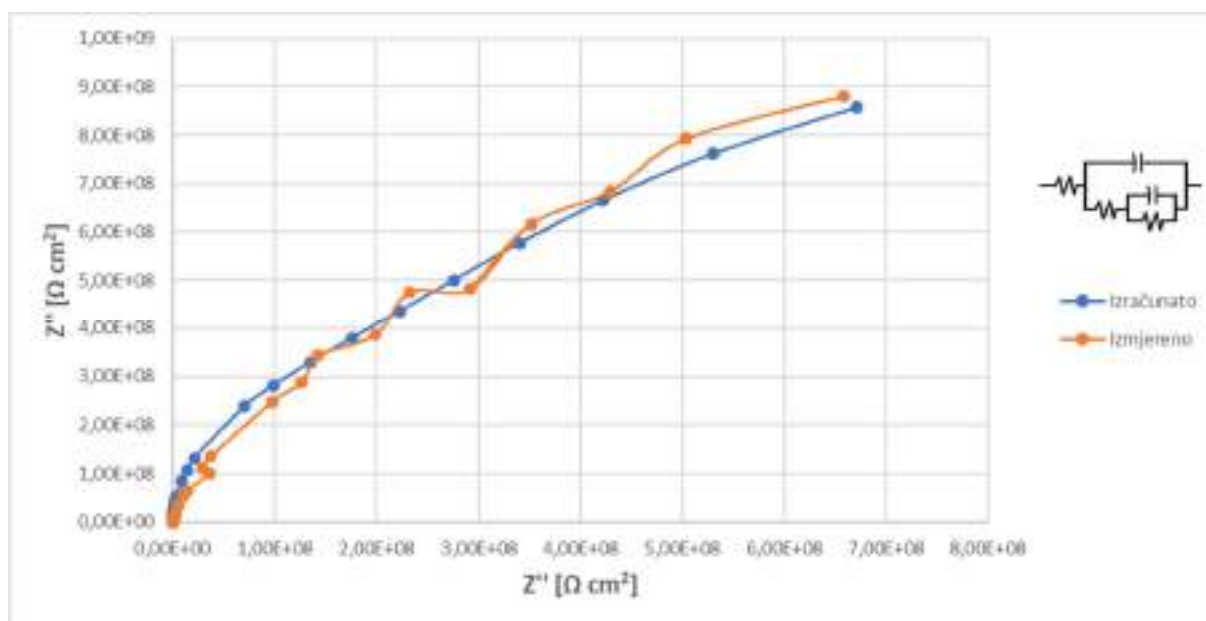
Slika 3. Nyquistov dijagram uzorka A1 nakon 336 h izlaganja u 3 %-tnoj otopini NaCl



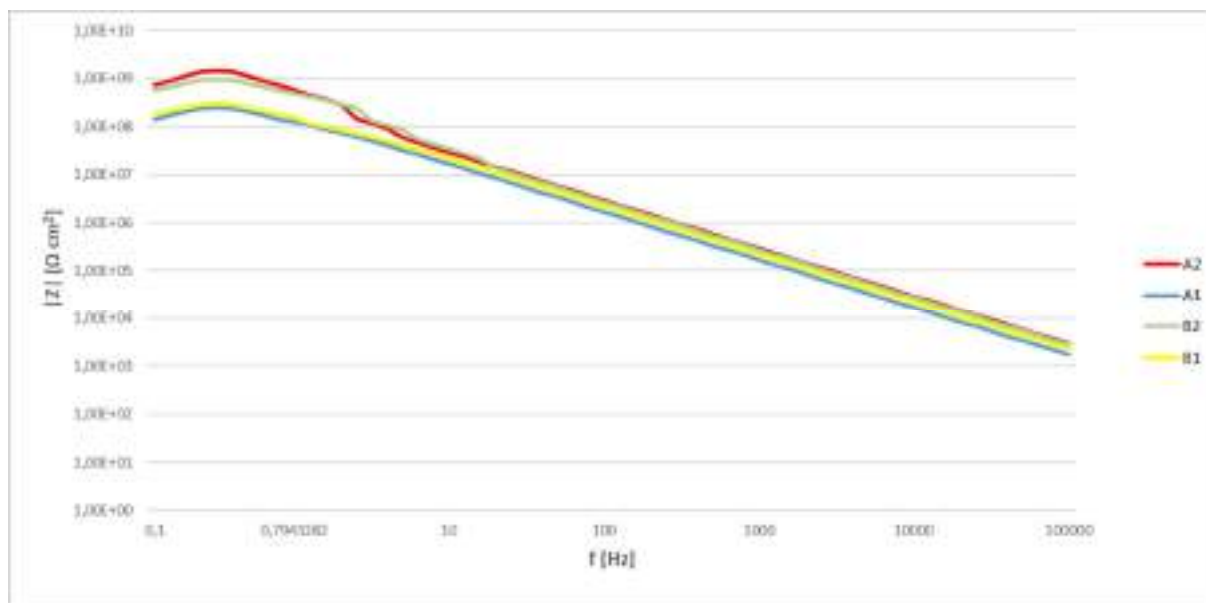
Slika 4. Nyquistov dijagram uzorka A2 nakon 336 h izlaganja u 3 %-tnoj otopini NaCl



Slika 5. Nyquistov dijagram uzorka B1 nakon 336 h izlaganja u 3 %-tnoj otopini NaCl



Slika 6. Nyquistov dijagram uzorka B2 nakon 336 h izlaganja u 3 %-tnoj otopini NaCl



Slika 7. Usporedni prikaz Bodeovih dijagrama ispitivanih uzoraka

ZAKLJUČAK

Rezultati istraživanja u ovom radu pokazuju da IC sušeni premazi drastično smanjuju međupremazni interval između nanošenja dva sloja. Aplikacija čitavog sustava premaza moguća je unutar jednog radnog dana, nakon čega se on smatra potpuno umrežen te ga je moguće odmah staviti u eksploataciju. Tu činjenicu potvrđuju korozijska i fizikalna ispitivanja provedena na IC premazima. Sustavi s cink-epoksi i epoksi temeljem su sušeni na sobnoj temperaturi i IC zračenjem te su u oba slučaja dobiveni rezultati svih provedenih ispitivanja bili bolji kod IC sušenih uzoraka. Svojstva prionjivosti premaza su nakon izlaganja u vlažnoj komori pala, no i dalje su sve dobivene vrijednosti zadovoljavajuće. Što se tiče mjerenja tvrdoće po Buchholzu, također su zabilježene lošije vrijednosti tj. veće otisne površine uslijed omekšavanja premaza u vlažnoj komori. Uspoređujući sustave, bolja svojstva prije izlaganja u vlažnoj komori pokazuju uzorci s cink-epoksi temeljem, dok su se nakon izlaganja otporniji pokazali uzorci bez cinka. Nakon ispitivanja u vlažnoj komori ni na jednom uzorku nije zamijećeno hrđanje, pucanje, ljuštenje ili mjehuranje.

Prema dostupnoj literaturi [6] rezultati elektrokemijske impedancijske spektroskopije svih ispitanih sustava su, analizom izmjerenih otpora, pokazali dobra zaštitna svojstva. Pritom, IC premazi imaju veći otpor od premaza koji su atmosferski sušeni. Ispitivanjima je dokazano da IC tehnologija sušenja skraćuje vrijeme i poboljšava svojstva zaštite od korozije.

Zahvala

Ovi materijali temelje se na radu koji je sufinancirala Europska unija iz Europskog fonda za regionalni razvoj pod referentnim brojem KK.01.2.1.02.0030.

LITERATURA

- [1] I. Juraga, V. Alar, I. Stojanović, Korozija i zaštita premazima, Sveučilište u Zagrebu, Fakultet strojarstva i brodogradnje, Zagreb, 2014.
- [2] I. Bartley, Coating curing – the role of infrared, Pigment & Resin Technology, 28(1999), pp. 233-237.
- [3] Heraeus: Infrared emitters dry water based coating sefficiently, Accessible on Internet: https://www.heraeus.com/media/media/hng/doc_hng/industries_and_applications_1/infrared_heat_1/pdfs/inrared_for_wet_coating.pdf, (29.03.2021.)
- [4] K. Riggs Larsen, Zinc-rich epoxy primer uses glass spheres zinc activator to enhance corrosion resistance, Materials Performance, 54(2015), pp. 16-23.
- [5] Z. Ahmad, Principles of Corrosion Engineering and Corrosion Control, Butterworth-Heinemann, Oxford, 2006.
- [6] A. Lasia, Electrochemical Impedance Spectroscopy and its Applications, Springer-Verlag New York, 2014.



19th INTERNATIONAL FOUNDRYMEN CONFERENCE
Humans - Valuable Resource for Foundry Industry Development

Split, June 16th-18th, 2021

<https://ifc.simet.hr/>

**TESTING OF ANTICORROSIVE PROPERTIES OF ELECTROSTATIC POWDER
COATING ON DIFFERENT TYPES OF ELECTRIC RESISTANCE WELDS**

**ISPITIVANJE ANTIKOROZIVNOSTI PRAŠKASTOG ELEKTROSTATSKOG PREMAZA
NA RAZLIČITIM TIPOVIMA ELEKTRO-OTPORNIH ZAVARA**

Ivan Stojanović, Anna Poropat*

University of Zagreb Faculty of Mechanical Engineering and Naval Architecture, Zagreb, Croatia

Poster presentation
Original scientific paper

Abstract

Corrosion of metal surfaces is inevitable, so it is needed to be prevented by a proper corrosion protection method. Powder coatings are effective way to prevent corrosion in metal parts. Critical areas on the structures are welded joints which can have negative effect on the coating durability due to different weld geometry and deformations. The aim of this work was to investigate the corrosion resistance of several electro-resistant weld types. Coating was performed at an electrostatic powder coating plant. All samples were treated under the same coating parameters, the difference is the chemical pre-treatment (phosphate and zirconium) and shape (appearance) of the welds. Namely, three weld types participated in the testing: 1. welds with minimal or no deformation, 2. welds with a slight degree of deformation, while the 3. weld type had significant and very significant deformations (needles, protrusion, foamy deformations). Research included salt spray test, microscopic analysis, and electrochemical impedance spectroscopy. Results of this work showed that phosphate conversion coating under epoxy-polyester coating is better for anticorrosion durability of spot-welded wire products that have significant weld deformations.

Keywords: *powder coating, corrosion, organic coatings, chemical pre-treatment, salt spray chamber, electric resistance spot weld*

*Corresponding author (e-mail address): Anna.Poropat@fsb.hr

Sažetak

Korozija metalnih površina je neizbježna, pa je potrebno spriječiti odgovarajućom metodom zaštite od korozije. Praškaste prevlake učinkovit su način sprječavanja korozije metalnih dijelova. Krična područja na konstrukcijama su zavareni spojevi koji mogu imati negativan utjecaj na trajnost prevlaka zbog različite geometrije zavara i deformacija. Cilj ovog rada bio je istražiti otpornost na koroziju

nekoliko vrsta elektrootpornih zavara. Prevlačenje je izvedeno u postrojenju za elektrostatsko nanošenje praškastih boja. Svi uzorci tretirani su pod istim parametrima, razlika je u kemijskoj predobradi (fosfat i cirkonij) i obliku (izgledu) zavara. Naime, u ispitivanju su sudjelovala tri tipa zavara: 1. zavari s minimalnom ili nikakvom deformacijom, 2. zavari s blagim stupnjem izbačaja materijala, dok je tip 3 zavara imao značajne i vrlo značajne (igle, izbočina, pjenaste deformacije). Istraživanje je uključivalo test slanim raspršivanjem, mikroskopsku analizu i elektrokemijsku spektroskopiju impedancije. Rezultati ovog rada pokazali su da je fosfatna konverzijska prevlaka u kombinaciji sa epoksidno-poliesterskom prevlakom bolja za antikorozivnu trajnost proizvoda zavarenih žicom koji imaju značajne deformacije zavara.

Ključne riječi: praškasti premaz, korozija, organske prevlake, kemijska predobrada, slana komora, elektrootporni točkasti zavar

UVOD

Metalni, a posebno čelični predmeti, zaštićuju se nanašanjem praškastih organskih praškastih prevlaka u kabinama za elektrostatsko nanašanje. Industrijski je to najisplativiji postupak zbog smanjenog utjecaja na okoliš u odnosu na prevlake koje sadrže otapala ili hlapljive komponente. Osim toga postupak elektrostatskog nanašanja praškastih prevlaka i financijski je jeftiniji. Također, postupak može biti uz regeneraciju praha koji tada ulazi u sustave za obnavljanje te se može ponovno koristiti [1]. Od ključne su važnosti elektrostatske sile o kojima uvelike ovisi debljina i ujednačenost pokrivanja površine praškom prevlakom. Praškaste prevlake koje se tako nanose najčešće su organskog kemijskog sastava i to na bazi epoksi-poliestera [2]. Thomas i dr., u svojem radu o klasifikaciji praškastih prevlaka po sposobnosti prevlačenja, došli su do zaključka kako za učinkovito nanašanje treba voditi računa o stupnju fluidizacije praha i njegovoj formulaciji, odnosno prisutnosti različitih aditiva u njegovom sastavu. Sukladno tome za pojedini prah odgovaraju određeni parametri struje i napona u kabini za elektrostatsko nanašanje praškastih boja [1]. Prilikom prolaska kroz mlaznicu pištolja prah se elektrostatički nabije i takav dolazi u koliziju sa uzemljenim predmetom na lancu (transporteru). Nakon elektrostatskog nanašanja tako deponirani prah na površini metalnog predmeta mora proći kroz proces polimerizacije (umrežavanja) u peći. Vizualne i mehaničke (adhezija, čvrstoća, otpornost na habanje) karakteristike praškastih prevlaka ovise o temperaturi i vremenu u peći prilikom polimerizacije. Bitan je i sastav praha. Svaki praškasti sustav namijenjen prevlačenju mora proći kroz polimerizaciju čiji su uvjeti zadani od strane proizvođača. M. Barletta i dr. u svojem u radu istražili su odnos vremena i temperature u peći za polimerizaciju koji bi se smanjio potrošnju energije na proizvodnju topline s jedne strane i dosegno potrebni stupnju umrežavanja prevlake s druge strane [3].

Prah organske prevlake nanosi se postupkom koji se naziva elektrostatsko nanošenje raspršivanjem kako bi se stvorio nanos praha na metalnoj podlozi. Nakon nanošenja praškaste prevlake slijedi zagrijavanje u peći omogućavajući premazu da kemijski reagira i tvori dugu molekularnu visoko umreženu polimernu strukturu - polimerizacija [4]. U praškastoj prevlaci, pripremljeni prah za nanošenje u čvrstom obliku taloži se izravno na podlogu. Ovo je ekološki prihvatljiv postupak u usporedbi s metodama premazivanja tekućim premazima, jer ne koristi otapalo, stvara malo otpadnih materijala ili opasnih kemikalija. Za istraživanje se često koristi elektrokemijska impedancijska spektroskopija kojom se na elektrodu dovodi izmjenično promjenjiv potencijal male amplitude i širokog opsega

frekvencija (1 mHz do 1 MHz). Motri se odziv strujnoga kruga na izmjenični napon ili struju kao funkciju frekvencije, odnosno amplituda i fazni pomak [5]. Korozija počinje na mjestu popuštanja prevlake. Zaffaroni i dr. su u svom istraživanju djelotvornost prevlake između ostalog karakterizirali pomoću mikroskopskih metoda [4]. U radu se u svrhu utvrđivanja dvaju sustava površinske zaštite uspoređuju svojstva iste epoksi-poliesterske prevlake sa fosfatnom i cirkonijevom konverzijskom prevlakom. Konverzijske prevlake služe kao kemijska priprema površine kako bi se poboljšala adhezija organskih prevlaka. Konverzijske se prevlake nanose prskanjem otopine na površinu metala koja se namjerava zaštititi, a organska se prevlaka (u ovom slučaju epoksi-poliester) nanosi u kabini za elektrostatsko nanašanje praškastih boja. Motivacija za odabir upravo tih materijala za površinsku zaštitu proizlazi iz njihove česte uporabe u završnom stadiju proizvodnje u industrijskim pogonima metaloprerađivačke industrije. Kako isti proizvod (zbog brzine proizvodnje u fazi zavarivanja) često ima različite vrste elektro-otpornih zavara potrebno je utvrditi koja je kombinacija površinske zaštite najpouzdanija kako bi se garantirala trajnost proizvoda od točkasto zavarene niskouglične čelične žice.

MATERIJALI I METODE

Metode ispitivanja ovog rada sastoje se od elektrokemijske impedancijske spektroskopije, stereomikrografske analize elektro-otpornih zavara i ispitivanja u slanoj komori.

Za ispitivanje su se koristili uzorci u obliku žice i uzorci od točkasto elektro-otporno zavarenih žica. Metodom elektrokemijske impedancijske spektroskopije usporedila su se svojstva dviju vrsta kemijske pripreme površine (na bazi fosfata i cirkonija). Konverzijske se prevlake nanose mokrim postupcima (upotrebom otopina i prskanjem), a služe kako bi se na površini metala stvorio sloj kristalne strukture koji pospješuje prianjanje naknadno nanosene organske prevlake. Sama konverzijska prevlaka ne pruža u dovoljnoj mjeri antikorozivnu zaštitu tako da nije uobičajeno zaštićivati metalne proizvode samo konverzijskom prevlakom.

Nanošenje fosfatne prevlake

Fosfatiranje je provedeno pod odgovarajućim parametrima na postrojenju u dvije faze (odmašćivanje površine uzoraka sa istovremenim fosfatiranjem i ispiranje neizreagirano fosfata sa površine). Radni ciklus započinje postavljanjem proizvoda na lanac (transporter), proizvodi se kreću prema tunelu za prvu fazu kemijske pripreme. U toj se fazi istovremeno odvija odmašćivanje i fosfatiranje. Druga faza je ispiranje čistom vodom iz mreže čime je kemijska priprema površine fosfatnom konverzijskom prevlakom završena. Potom slijedi sušenje u peći tijekom 10 minuta pri 90-100 °C. Fosfatna prevlaka nanijela se na jedan uzorak sa 81 zavarom za test u slanoj komori i jednu žicu za test elektrokemijske impedancijske spektroskopije. Zatim se nanijela organska prevlaka elektrostatskim putem.

Za postupak fosfatiranja koristile su se dvije kade. U prvu kadu unosi se sredstvo za odmašćivanje i konverziju željeznih fosfata. Otopinu iz kade pumpe vode do mlaznica u tunelu gdje se prskanjem nanosi na površinu čeličnog komada. U konkretnom slučaju sredstvo za odmašćivanje i konverziju željeznog fosfata je BONDERITE M-FE F-814, koncentracije 20-40 g/l pri temperaturi 35 do 55 °C. pH otopine iznosio je 5,5 (dopušteni raspon iznosi 5,2 do 5,8), dok vrijeme obrade prskanjem traje 1,5 do 3 min, pod tlakom

prskanja 1,5 do 2,5 bar. Nakon toga površina se isprala vodom na sobnoj temperaturi. Voda za ispiranje se kontinuirano dolijevala uz kontrolu protoka otpadne vode.

Nanošenje cirkonijeve prevlake

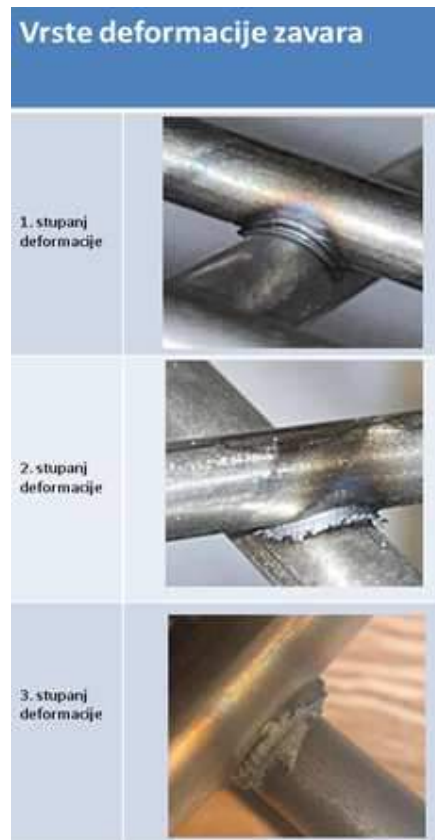
Nanošenje cirkonijeve konverzijske prevlake izvodi se postupkom prskanja u postrojenju koje se sastoji od (u ovom slučaju 6 kabina) ispod kojih se nalaze kade sa odgovarajućom otopinom koja se prskalicama nanosi na proizvode/uzorke. Proces je tunelskog tipa i sastojao se od 6 faza: odmaščivanje, ispiranje, ispiranje demineraliziranom vodom, cirkoniranje, ispiranje neizreagiranog cirkonija s površine i ispiranje demineraliziranom vodom. Potom je uslijedilo sušenje u peći tijekom 10 minuta pri 90-100 °C. Procesni parametri bili su: pH vrijednosti 5,0, koncentracija cirkonija 0,1, vrijeme prskanja otopine sa cirkonijem 60 sekundi (preporučeni raspon 20 – 120 s), temperatura 40°C. Cirkonijeva prevlaka nanijela se na jedan uzorak sa 81 zavarom za test u slanoj komori i jednu žicu za test elektrokemijske impedancijske spektroskopije. Zatim se nanijela organska prevlaka elektrostatskim putem pod istim uvjetima kao i uzorci sa fosfatnom konverzijskom prevlakom. Nanošenje cirkonijeve konverzijske prevlake u odnosu na fosfatnu je ekološki prihvatljiviji postupak jer nije potrebno zagrijavanje otopine i nema zaostalog mulja zbog čega je i ekonomičniji od fosfatnog postupka.

Ispitivani uzorci s elektro-otpornim zavarima

Uzorci od elektro-otporno zavarenih niskougličnih čeličnih žica korišteni su za stereomikrografsku analizu prevlake na mjestu zavara. U sklopu ovog rada koriste se uzorci od 81 elektro-otpornog zavara zavareni tako da uzorak sadrži tri vrste zavara po stupnju deformacija i to: s minimalnim deformacijama, s nešto više deformacija i sa znatnim deformacijama u obliku pjenjenja i iglica. Analiza izgleda svake vrste provedena je stereomikrografski po poprečnom presjeku zavarenog spoja. Napravljen je presjek zavara na uzorku na koji je prethodno nanosena konverzijska prevlaka i organska (epoksi-poliesterska) prevlaka. Pretpostavka je da zavari sa većim deformacijama zahtijevaju kvalitetniju površinsku zaštitu budući da su različitih mikrostruktura.

Tablica 1. prikazuje tri vrste zavara ispitivanih uzoraka podijeljene u 3 stupnja po deformacijama. Prvi stupanj karakteriziran je kao elektro-otporni zavar s minimalnim deformacijama bez značajnih protruzija, pjenastih dijelova i iglica. Takav je dizajn (geometrija) podloge najpogodniji za učinkovitost površinske zaštite zavara jer omogućava dobru zalivenost i pokrivenost metalne površine prevlakom. Drugi stupanj deformacije okarakteriziran je kao dizajn zavara s postojećim, ali ne značajnim odstupanjima od prvog stupnja. Takva je površina nepravilnija, nema ujednačenu strukturu i sadrži deformativne oblike na mikro razini što može utjecati na način depozicije praškaste prevlake prilikom elektrostatskog nanošenja. Treći tip zavara prikazan u tablici 1. ima značajne deformacije površine te je takav oblik zavara rizičan u pogledu potpunog prekrivanja prevlakom. U ovom se radu izraz deformacija odnosi na izbačaj materijala koji nastaje prilikom elektro-otpornog zavarivanja.

Tablica 1. Usporedni prikaz tri vrste ispitanih zavara



Elektrokemijska impedancijska spektroskopija

Test elektrokemijske impedancijske spektroskopije izvršen je radi usporedbe utjecaja fosfatne i cirkonijske konverzijske prevlake ispod iste vrste epoksi-poliesterske prevlake na svojstva površinske zaštite. Mjerenje svojstva otpornosti prevlake provedeno je na dva uzorka žice. Optimalno bi bilo da je u medij uronjeno područje zavara no za ovo testiranje odabrana je žica jer je nužno imati podatak točne površine u kontaktu sa medijem u koji je uronjena dok za drugi oblik uzorka izračunavanje točne površine nije moguće bez dodatnih alata. Test je proveden na jednom uzorku prethodno tretiranom fosfatnom konverzijskom prevlakom i jednom prethodno tretiranom cirkonijskom konverzijskom prevlakom. Oba su uzorka imala epoksi-poliestersku organsku prevlaku. Ispitivanje se obavilo na Katedri za zaštitu materijala Fakulteta strojarstva i brodogradnje na uređaju VersaSTAT 3, proizvođača AMTEK, USA, upravljanom softverom VersaSTUDIO v2.44. Ispitivanje je provedeno u troelektrodnoj ćeliji (slika 1) koja se sastoji od radne elektrode, referentne elektrode i protuelektrode. Ispitivani uzorak na kojem se nalazi prevlaka je radna elektroda, kao referentna elektroda bila je zasićena kalomelova elektroda, dok je kao protuelektroda korištena grafitna elektroda. Uzorci prethodno nisu bili izlagani agresivnim uvjetima. Mjerenje elektrokemijske impedancije provedeno je u mediju 3 %-tne otopine NaCl pri sobnoj temperaturi. Površina radne elektrode iznosila je 1,192 cm² za sustav fosfatna konverzijska prevlaka + organska prevlaka te 1,256 cm² za sustav cirkonijska konverzijska prevlaka + organska prevlaka. Ispitivanje je provedeno prema normi ISO 16773-2:2016. Tablice 2 i 3 prikazuju parametre ispitivanja EIS.



Slika 1. Troelektrodna ćelija za ispitivanje elektrokemijskom impedancijskom spektroskopijom

Tablica 2. Parametri ispitivanja EIS na sustavu fosfatna konverzijska prevlaka + organska prevlaka

Parametri	Vrijednost parametara
Frekvencija, raspon	0,1-100000 Hz
Amplituda	50 mV
Površina ispitivanja	1,192 cm ²
Gustoća materijala	7,86 g/ml
Ekvivalentna masa	27,92 g

Tablica 3. Parametri ispitivanja EIS na sustavu cirkonijeva konverzijska prevlaka + organska prevlaka

Parametri	Vrijednost parametara
Frekvencija, raspon	0,1-100000 Hz
Amplituda	50 mV
Površina ispitivanja	1,256 cm ²
Gustoća materijala	7,86 g/ml
Ekvivalentna masa	27,92 g

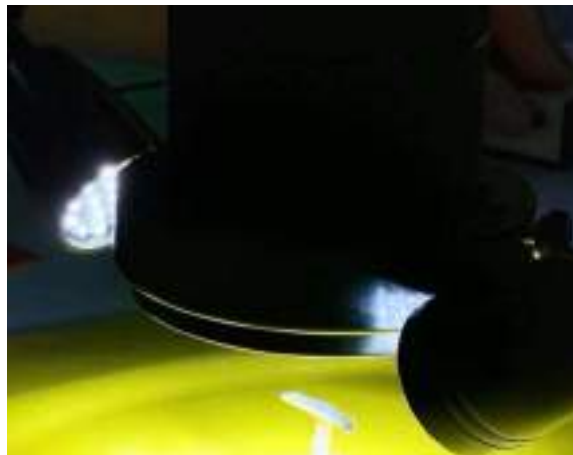
Stereomikroskopija prevlake na zavarima

Ispitni uzorci su načinjeni tako da su iz mreže od 81 zavora izrezana i strojno obrađena tri različita zavora te su na njima provedena stereomikroskopska ispitivanja korištenjem stereomikroskopa Leica MZ6, slika 2. Ova analiza provedena je u Laboratoriju za zaštitu materijala Fakulteta strojarstva i brodogradnje. Slika 3 prikazuje izgled poprečnog presjeka

uzorka dviju elektro-otporno zavarenih žica u području zavora u trenutku snimanja stereomikroskopije.



Slika 2. Stereomikroskop Leica MZ6, Laboratorij za zaštitu materijala FSB-a

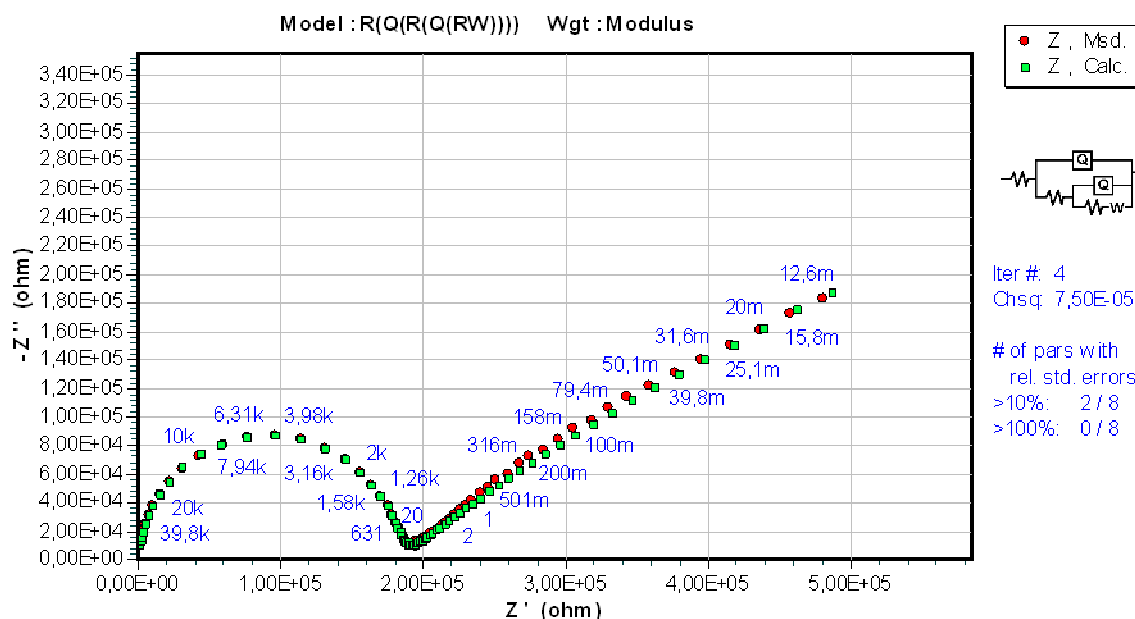


Slika 3. Postav uzorka presjeka zavora prilikom stereomikroskopije

Slana komora

Ispitivanje u slanoj komori koristi se za utvrđivanje otpornosti različitih metala i prevlaka na koroziju, za mjerenje napredovanja korozijskog djelovanja prevlake, za evaluaciju korozijske otpornosti u morskim uvjetima (vlaga, temperatura, slana maglica). Ispitivanja u slanoj komori provode se prema normi HRN EN ISO 9227.

Na slici 4 prikazana je skica uzorka za testiranje u slanoj komori. Uzorak je podijeljen na 9 zasebnih skupova. Na uzorku se pojavljuju tri vrste (stupnja) elektro-otpornog zavora. U slanoj komori ispitana su dva uzorka. Jedan je uzorak sa sustavom fosfatne, a drugi s cirkonijevom konverzijskom prevlakom. Oba uzorka imaju isti tip organske prevlake (epoksid-poliesterska praškasta boja nanescena elektrostatskim putem).



Slika 6. Eksperimentalni podaci za EIS za sustav prevlaka cirkonijeva konverzijska prevlaka + organska prevlaka

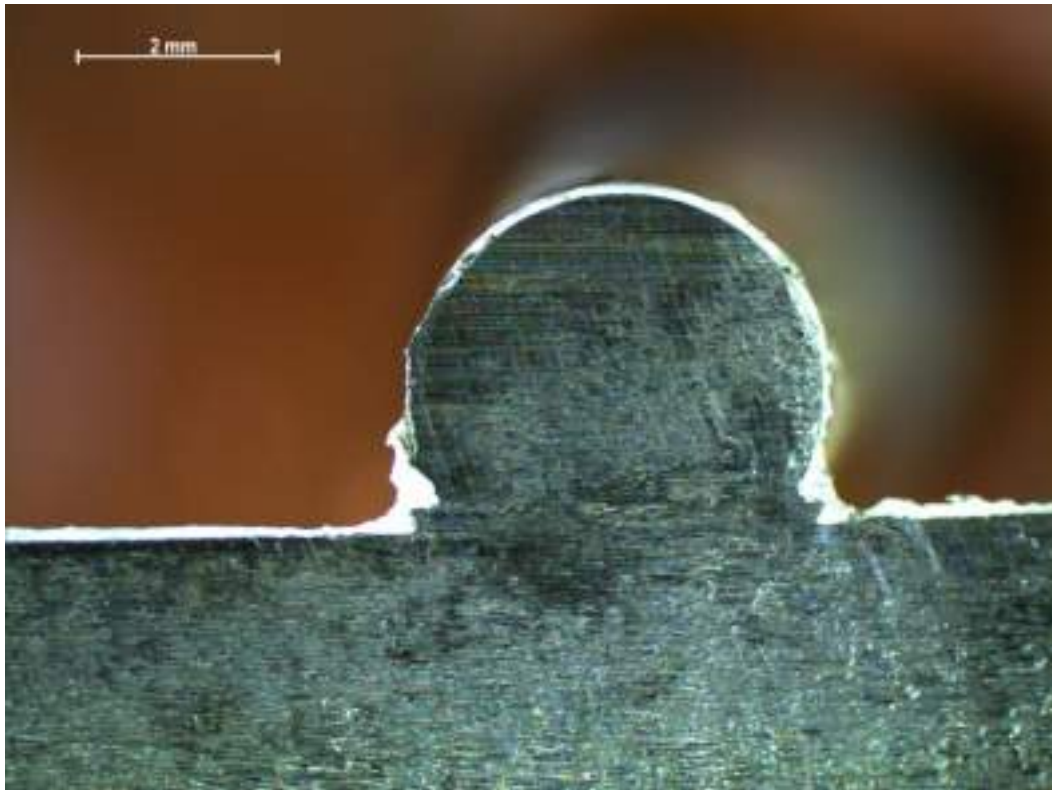
Ekvivalentni strujni krug prikazan na slici 5 najprikladniji je za podatke dobivene za sustav s fosfatnom konverzijskom prevlakom. Strujni krug opisuje model za sustav prevlaka u kojem je vidljiv otpor elektrolita, otpor organske prevlake, otpor konverzijske prevlake i otpor metala.

Ekvivalentni strujni krug prikazan na slici 6 najviše se podudara sa podacima dobivenih za sustav s cirkonijevom konverzijskom prevlakom. Strujni krug služi da bi se opisao model za sustav prevlaka u kojem eksperimentalni podaci ukazuju na difuziju medija kroz organsku prevlaku. Opisivanje rezultata pomoću strujnog kruga uobičajena je metoda prikaza rezultata elektrokemijske impedancijske spektroskopije.

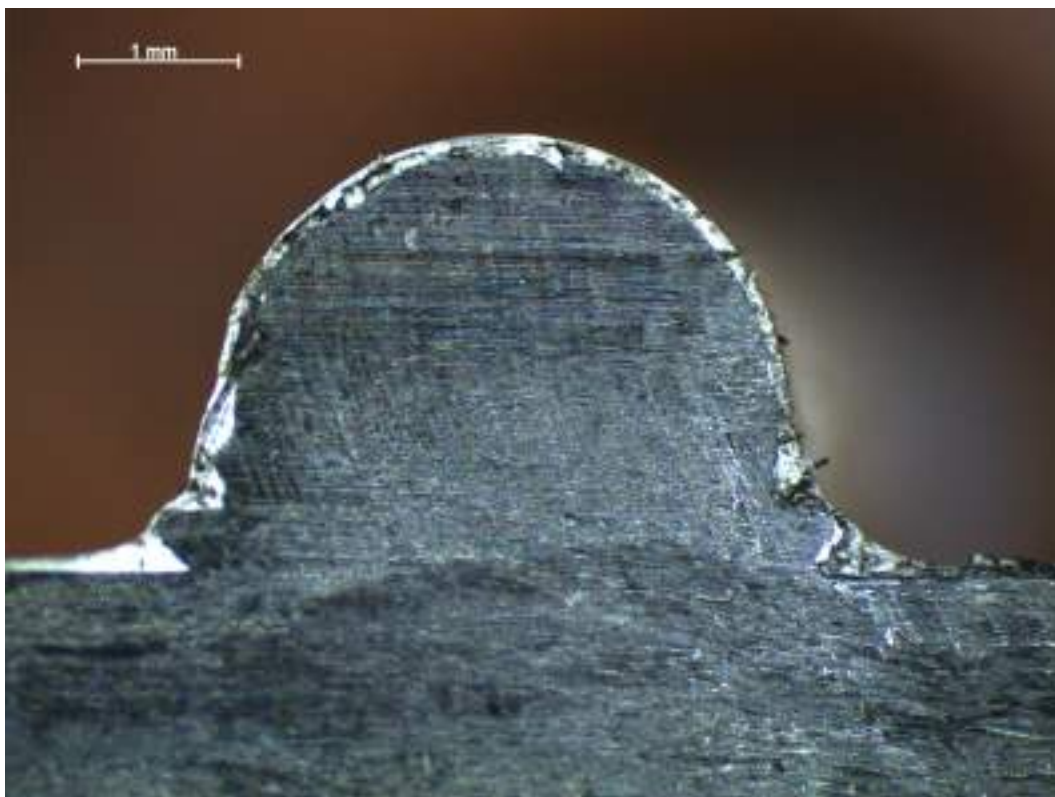
Rezultati ne pokazuju značajnije odstupanje vrijednosti otpora površinske zaštite s fosfatnom i cirkonijevom konverzijskom prevlakom.

Stereomikrografija zavara

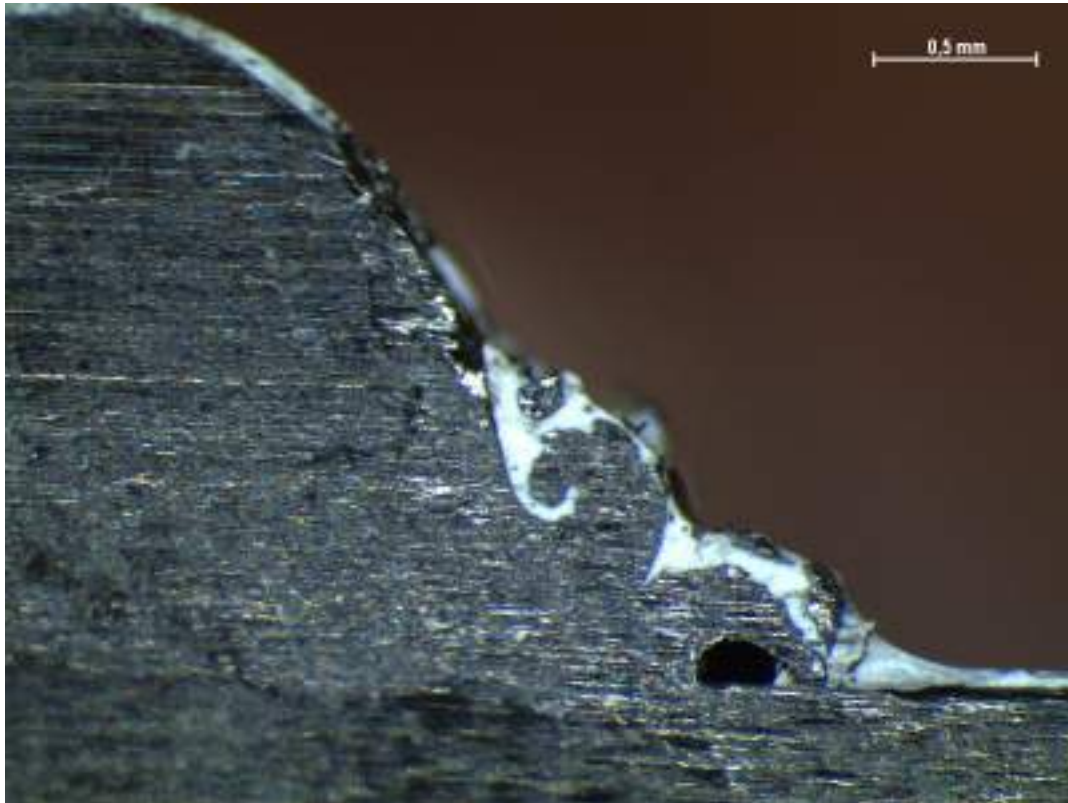
Rezultati provedenih vizualnih pregleda i stereomikroskopskih ispitivanja zbirno su prikazani za svaki ispitni uzorak elektro-otpornih zavara na slikama 7 do 9. Na slikama je vidljivo oblikovanje i način prijanjanja prevlake za strukturu zavara. Iz prikaza se može zaključiti kako kompliciraniji dizajn zavara može biti uzrok neravnomjernoj debljini prevlake što mjesto zavara čini kritičnim mjestom za pojavu korozije na metalnim proizvodima.



Slika 7. Stereomikroskopski prikaz zavora 1. stupnja deformacije



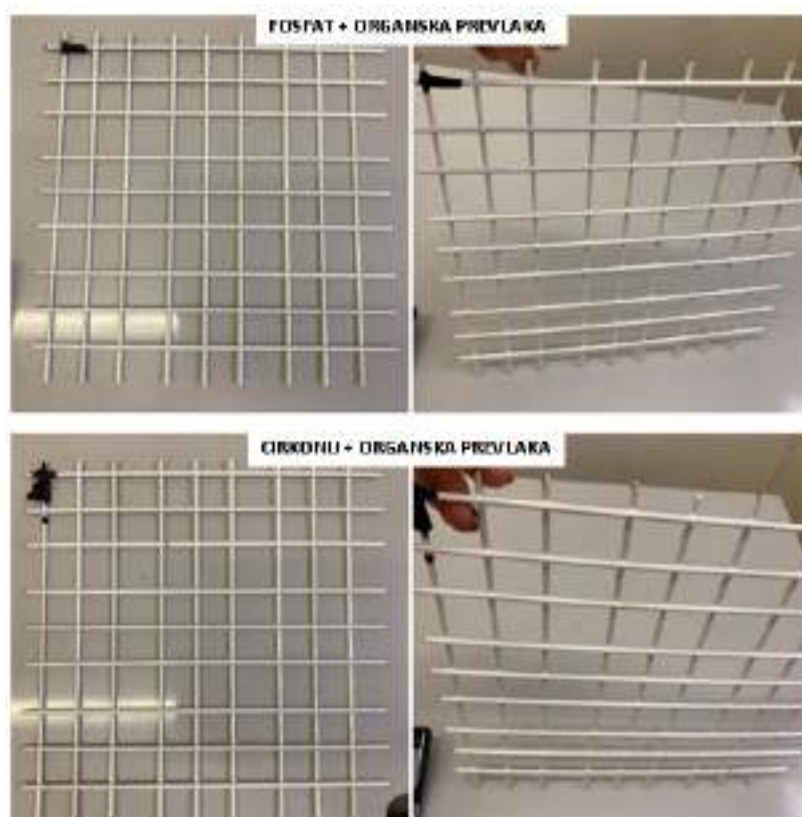
Slika 8. Stereomikroskopski prikaz zavora 2. stupnja deformacije – vidljiva neravnomjerna debljina prevlake



Slika 9. Stereomikroskopski prikaz 3. stupnja deformacije – vidljiva nepokrivena površina metala u području zavora

Slana komora

Izlaganje agresivnoj slanoj atmosferi trajalo je 168 sati. Na slici 10 su fotografije uzoraka nakon provedenog ispitivanja, a u tablici 4 prikazani su rezultati korodiranih zavora na uzorcima. Uzorak sa fosfatnom konverzijskom prevlakom u slanoj komori nije imao niti jedan korodirani zavar, dok je uzorak sa cirkonijevom konverzijskom prevlakom na kraju testiranja imao 6 korodiranih zavora (jedan zavar u kategoriji sa minimalnim izbačajima materijala koji su nastali prilikom zavarivanja i 5 zavora u kategoriji sa značajnim izbačajima materijala).



Slika 10. Prikaz uzoraka nakon 168 sati u slanoj komori

Tablica 4. Rezultati slanog testa s brojem korodiranih elektro-otpornih zavora unutar iste vrste (stupnja)

SUSTAV PREVLAKA	1. vrsta	2. vrsta	3. vrsta
FOSFAT + ORGANSKA PREVLAKA	0	0	0
CIRKONIJ + ORGANSKA PREVLAKA	1	0	5

ZAKLJUČAK

Rezultati elektrokemijske impedancijske spektroskopije ne pokazuju bolje performanse u korist ni jednog ispitanog sustava prevlaka u 3 %-tnoj otopini NaCl. Fotografije stereomikroskopske analize pokazuju kako je s povećanjem izbačaja materijala nastalog prilikom zavarivanja (deformacija) pokrivenost površine prevlakom neravnomjernija, odnosno pouzdanost prevlake u njezino antikoroziivno djelovanje smanjuje se s povećanjem stupnja deformacije. Ispitivanje u slanoj komori pokazalo je veću antikoroziivnu postojanost sustava prevlaka s fosfatnom konverzijskom prevlakom.

LITERATURA

- [1] A. Thomas, K. Saleh, P. Guigon, C. Czechowski, Characterisation of electrostatic properties of powder coatings in relation with their industrial application, *Powder Technology*, 190(2009), pp. 230-235.
- [2] K. Pélissier, D. Thierry, Powder and high-solid coatings as anticorrosive solutions for marine and offshore applications, A Review, *Coatings*, 10(10) (2020) 916
- [3] A. S. H. Makhoulf, Y. Gajarla, Chapter 8 - Advances in smart coatings for magnesium alloys and their applications in industry, *Advances in Smart Coatings and Thin Films for Future Industrial and Biomedical Engineering Applications*, Elsevier (2020), 245-261
- [4] G. G. B. Zaffaroni, V. C. Gudla, R. Ud Din, R. Ambat, Characterization of blisters on powder coated aluminium AA5006 architectural profiles, *Engineering Failure Analysis*, 103(2019), pp. 347-360.
- [5] Norma HRN EN ISO 9227, Korozijska ispitivanja u umjetnim atmosferama – Ispitivanja u slanoj komori



19th INTERNATIONAL FOUNDRYMEN CONFERENCE
Humans - Valuable Resource for Foundry Industry Development

Split, June 16th-18th, 2021

<https://ifc.simet.hr/>

**EFFECT OF BINDER ADDITION ON THE RHEOLOGICAL BEHAVIOUR OF
ALUMINA SUSPENSIONS**

Zrinka Švagelj*, Vera Rede, Ivana Gabelica, Lidija Čurković

University of Zagreb Faculty of Mechanical Engineering and Naval Architecture, Zagreb, Croatia

Poster presentation
Original scientific paper

Abstract

The aim of this research was to prepare a stable and highly (65 wt.%) loaded aqueous alumina suspension and to investigate the influence of binder addition on the rheological properties of the prepared suspensions. For that purpose, alumina suspensions with dispersant concentration from 0.3 to 0.7 wt.% were prepared and their viscosities were analysed. Also, suspensions with optimal dispersant concentration and polyvinyl alcohol (PVA) based binder with different amount, from 1 to 4 wt.%, were prepared and their rheological behaviour was analysed. It was found that concentration of 0.4 wt.% dispersant is optimal for preparation of 65 wt.% alumina suspension. Also, addition of PVA binder into stable alumina suspension affect rheological properties, i.e. increases viscosity and shear stress.

Keywords: *alumina suspension, dispersant, binder, polyvinyl alcohol, rheological behaviour*

*Corresponding author (e-mail address): zsvagelj@fsb.hr

INTRODUCTION

Highly concentrated ceramic suspensions are essential ingredients for engineering ceramic shaping processes such as casting (slip, tape or gel), electrophoretic deposition and additive manufacturing. This complex colloidal system directly affects the ceramic product properties and therefore it has been extensively studied over the past decades [1].

In colloidal suspensions particle size is less than 1 μm which contributes to the good properties of ceramic products. On the other hand, such small particles together with required high concentration of ceramic suspension show tendency to agglomerate, due to greater interactions between particles [2–4]. Therefore, various additives such as dispersants and binders have to be incorporated in suspension for stabilisation and adjustment of rheological properties.

Electrostatic, steric or electrosteric stabilization can be achieved by choosing appropriate dispersant. Among these mechanisms, the electrosteric stabilisation using a polyelectrolyte

dispersant proved to be very effective. Basically, this mechanism implies covering particle surface with polyelectrolyte molecules creating enough potential difference and, consequently, causing repulsion between particles [5,6].

Beside dispersant, many ceramic fabrication techniques require addition of binder. Various organic compounds have been used as binders including polyvinyl alcohol, cellulose derivatives, natural gums, starches, etc. These binder compounds increase a green body strength enabling a high density ceramic production. Properties such as polarity, affinity with processing liquid, interaction with the particulate material and especially compatibility with the dispersant should be considered while choosing an appropriate binder. The organic binder addition causes a suspension viscosity increment and changes inflow characteristics [7–10]. Therefore, carefully selection of additives and their quantities is required to obtain good quality ceramic body [11].

In this research, optimization of the highly (65 wt.%) concentrated alumina suspension with a polyelectrolyte dispersant was conducted and the effect of the PVA binder addition on rheological behaviour was investigated.

MATERIALS AND METHODS

In this investigation, commercial alumina (Al_2O_3) powder CT3000 SG (Almatis GmbH, Germany) with 99.78% purity and declared average particle size (D_{50}) 0.5 μm was used. Commercially available additives, a carbonic acid based polyelectrolyte dispersant Dolapix CE 64 and a polyvinyl alcohol (PVA) based binder (Optapix PAF 35), were provided by Zschimmer& Schwarz Chemie GmbH, Germany.

Suspension preparation

Two sets of experiment were conducted, as shown in Table 1. Firstly, optimal dispersant amount for stabilization of highly concentrated aqueous alumina suspension was investigated. After that, 65 wt.% alumina suspensions with optimal amount of dispersant and different amounts of binder were prepared. All suspensions were prepared by homogenization (90 min, 300 rpm) of alumina powder, deionized water and dispersant in the planetary ball mill (PM 100, Retsch, Germany) using ten balls and grinding jar, both made of alumina. In experiment 2, after homogenization, PVA binder was added and suspensions were further stirred for 30 min using a magnetic stirrer.

Table 1. Composition of investigated suspensions

Experiment	Al_2O_3 (wt.%)	H_2O (wt.%)	Dispersant Dolapix CE 64 (wt.%) *	Binder PVA (wt.%) *
1	65	35	0.3	-
			0.4	
			0.5	
			0.7	
2	65	35	Optimal from the experiment 1	1
				2
				4

* weight percent based on dry alumina powder

Rheology measurements

The rheological behaviour of the prepared suspensions was determined using the rotational viscometer (Brookfield DV-III Ultra, USA) and small sample chamber with spindle SC4-18 at constant temperature of $23 \pm 1^\circ\text{C}$. Prior to rheological measurements all suspensions were ultrasonically treated in an ultrasonic bath for 5 min to remove air bubbles. The suspensions were pres heared at 100 s^{-1} for 2 min. Measurements were performed by increasing shear rate from 0.1 to 180 s^{-1} with fifty equal intervals and then reducing it back to 0.1 s^{-1} with the same number of intervals. The obtained data was analysed using software Rheocalc V3.3.

RESULTS AND DISCUSSION

Dispersant optimization

In order to determine optimal dispersant concentration, rheological measurements were conducted and viscosity at shear rate of 50 s^{-1} against dispersant concentration is presented in Figure 1. Dispersant concentration that gives the lowest viscosity is considered as the optimal concentration which ensures effective particles separation and high fluidity[12].

As can be seen from Figure 1, at the lowest dispersant concentration (0.3 wt.% based on dry alumina powder) viscosity is relatively high indicating that the alumina surface is not fully covered by dispersant. With increasing dispersant concentration to 0.4 wt.%, the viscosity decreased significantly and it remains almost constant by further increasing the dispersant concentration (0.5 and 0.7 wt.%). In summary, once an optimal concentration of dispersant is exceeded (in this case 0.4 wt.%), influence of dispersant concentration on alumina suspension viscosity is low. That is typical for an alumina powder with mono-modal particle size distribution such as CT 3000 SG alumina powder used within this research. Finally, aqueous alumina suspension containing 65 wt.% solid loading and 0.4 wt.% was considered stable and used further for investigation of the PVA based binder addition on rheological properties.

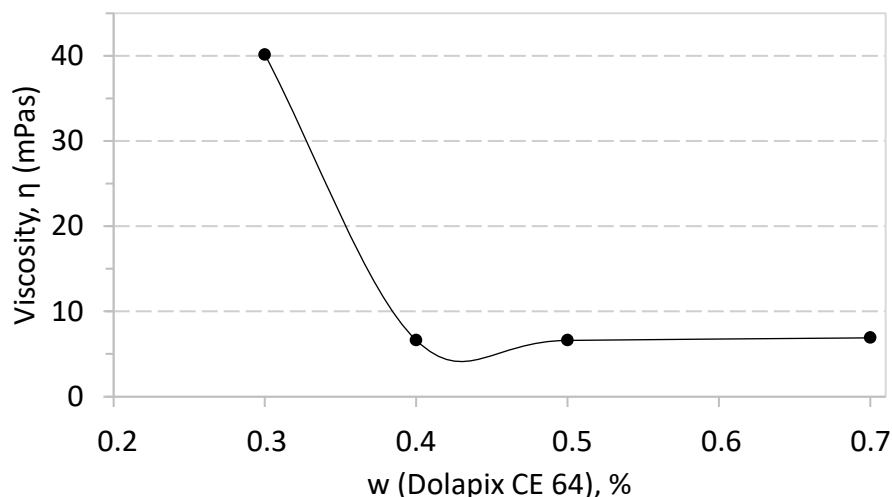


Figure 1. Viscosity of 65 wt.% alumina suspensions as a function of the dispersant concentration

Influence of binder amount on the rheological behaviour

Alumina suspensions with 65 wt.% solid loading, optimal dispersant concentration (0.4 wt.%) and different amounts of PVA based binder were prepared. The recorded rheological flow curves for the suspension without binder (0 PVA) and those with 1, 2 and 4 wt.% (based on dry alumina powder) PVA binder are shown in Figure 2. As can be seen in Figure 2, with increasing shear rate from 0.1 to 180 s⁻¹ the viscosity of all prepared suspensions decreases (A) and the shear stress increases (B), indicating the shear-thinning (pseudoplastic) behaviour, characteristic for the non-Newtonian fluids. The apparent viscosity at shear rate of 50 s⁻¹ for suspensions containing 0, 1, 2 and 4 wt.% PVA binder was 4.77, 6.39, 8.08 and 16.93 mPa·s, respectively. The flow curves show only slightly difference among 0 to 2 wt.% PVA binder addition. However, the addition of 4 wt.% PVA binder resulted in noticeable increment of viscosity (and shear stress) over the whole investigate shear rate range.

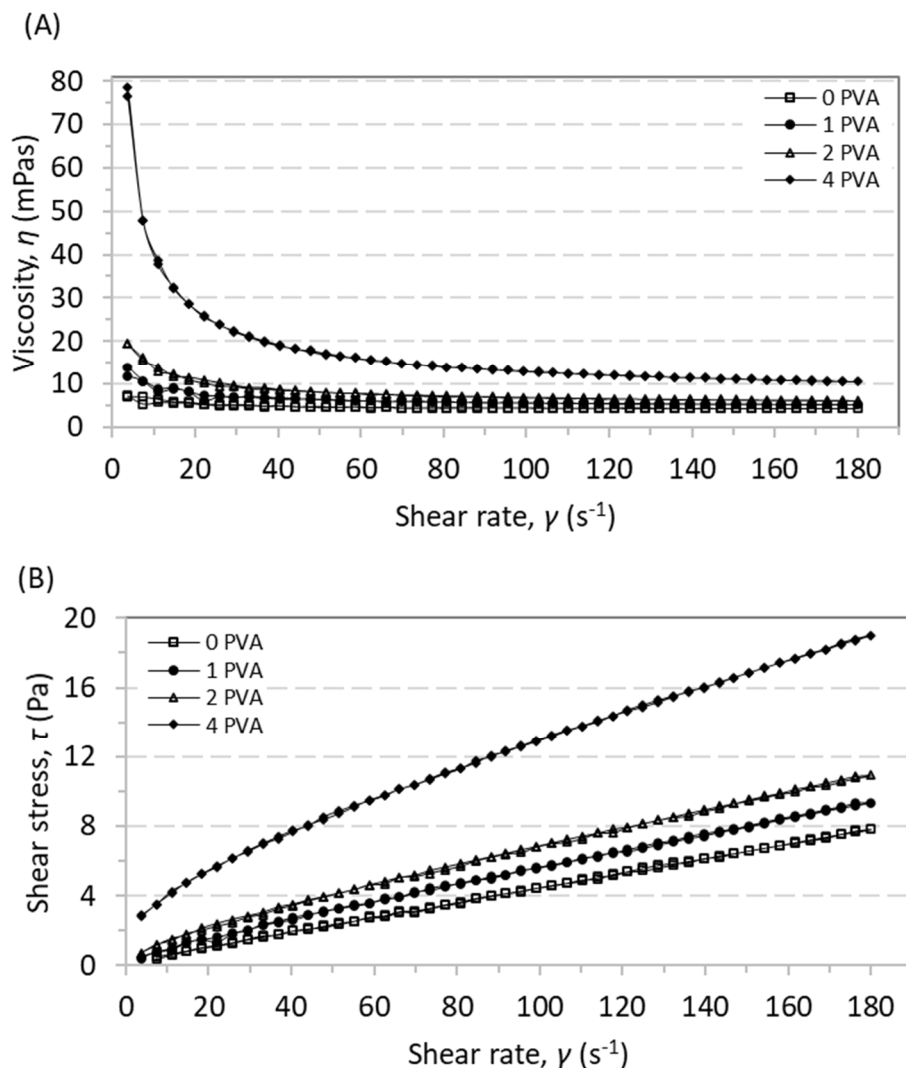


Figure 2. Flow curves for alumina suspensions containing 0.4 wt.% dispersant and different amount of PVA: (A) viscosity vs. shear rate and (B) shear stress vs. shear rate

Figure 3 shows the dependence of the apparent viscosity on the PVA addition at three shear rates 10, 50 and 150 s⁻¹. It is shown that viscosity increases with increasing PVA binder

amount and this trend is more pronounced at the lower shear rate. As expected, the largest viscosity increment was recorded for suspension containing 4 wt.% PVA binder.

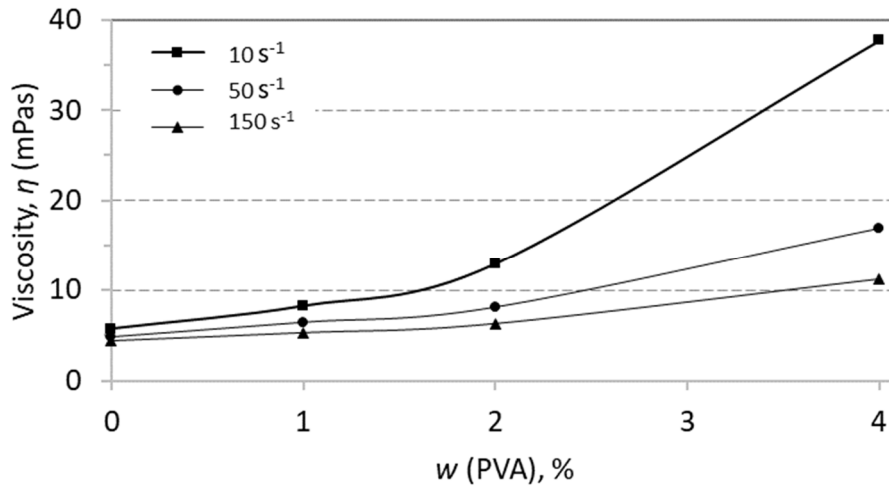


Figure 3. Dependence of the apparent viscosity on the PVA binder addition

To evaluate obtained results, experimental data were fitted using three common flow models [2]:

$$\text{Power law: } \tau = k\gamma^n \quad (1)$$

$$\text{Herschel-Bulkley: } \tau = \tau_0 + k\gamma^n \quad (2)$$

$$\text{Bingham: } \tau = \tau_0 + \rho\gamma \quad (3)$$

where τ (Pa) is shear stress, k is consistency index, γ (s^{-1}) is shear rate, n is flow index, τ_0 (Pa) is yield stress and ρ (Pa·s) is plastic viscosity. Obtained values of this parameters are presented in Table 2.

Table 2. Rheological parameters of alumina suspensions according to flow models

w (Al ₂ O ₃), %	w (PVA), %	Power law			Herschel-Bulkley				Bingham		
		k	n	R ²	τ ₀	k	n	R ²	τ ₀	ρ	R ²
65	0	7.5	0.89	0.978	0.02	4.65	0.98	1	0.02	4.23	0.983
	1	14.9	0.79	0.971	0.03	8.91	0.89	0.999	0.06	4.94	0.957
	2	26.0	0.71	0.973	0.05	13.5	0.84	0.999	0.11	5.58	0.951
	4	116.5	0.53	0.963	0.20	36.9	0.74	1	0.40	8.67	0.956

According to obtained correlation coefficients (R^2) it can be stated that all applied models are appropriate for describing prepared suspensions, but the Herschel-Bulkley model showed the best fit to the experimental data. The flow index (n) from the Herschel-Bulkley and Power law models is below 1 for all prepared suspensions, confirming the shear-thinning behaviour. According to the Herschel-Bulkley and Bingham models, yield stress (τ_0) increases with increasing amount of PVA binder.

CONCLUSIONS

Alumina suspensions containing 65 wt.% solid loading were prepared and rheological measurements were conducted. The optimal dispersant concentration was determined by varying its amount in alumina suspension from 0.3 to 0.7 wt.%. It was found that dispersant concentration of 0.4 wt.% is optimal for stabilisation of this particular suspension (i.e. ceramic powder type and amount).

PVA based binder was added in the stabilised alumina suspension in amount of 1, 2 and 4 wt.% and its effect on rheological properties was analysed. All prepared suspensions show shear-thinning behaviour. It has been shown that with increasing PVA amount, viscosity and yield stress also increase, especially when higher amount of binder was added (i.e. 4 wt.%).

Power law, Herschel-Bulkley and Bingham mathematical models was used to describe the rheological behaviour of prepared suspensions. The best fit to experimental data was obtained by Herschel-Bulkley model which indicate that all suspensions can be categorised as yield-stress materials which flow under sufficient applied stress.

Acknowledgements

This work was supported by the Croatian Science Foundation under the project IP2016-06-6000: Monolithic and composite advanced ceramics for wear and corrosion protection (WECOR).

REFERENCES

- [1] L. C. Guo, Y. Zhang, N. Uchida, K. Uematsu, Adsorption effects on the rheological properties of aqueous alumina suspensions with polyelectrolyte, *Journal of the American Ceramic Society*, 81(1998)3, pp. 549-556.
- [2] M. Majić Renjo, M. Lalić, L. Ćurković, G. Matijašić, Rheological properties of aqueous alumina suspensions, *Materialwissenschaft Und Werkstofftechnik*, 43(2012)11, pp. 979-983.
- [3] O. Akhlaghi, O. Akbulut, Y. Z. Menceloglu, Extensional rheology and stability behavior of alumina suspensions in the presence of AMPS-modified polycarboxylate ether-based copolymers, *Colloid and Polymer Science*, 293(2015)10, pp. 2867-2876.
- [4] A. Tsetsekou, C. Agrafiotis, I. Leon, A. Miliadis, Optimization of the rheological properties of alumina slurries for ceramic processing applications Part II: Spray-drying, *Journal of the European Ceramic Society*, 21(2001)4, pp. 493-506.
- [5] I. Sever, I. Žmak, L. Ćurković, Z. Švagelj, Stabilization of highly concentrated alumina suspensions with different dispersants, *Transactions of Famena*, 42(2018)3, pp. 61–70.
- [6] P. Tomasik, C. H. Schilling, R. Jankowiak, J. C. Kim, The role of organic dispersants in aqueous alumina suspensions, *Journal of the European Ceramic Society*, 23(2003)6, pp. 913-919.
- [7] A. U. Khan, N. Mahmood, P. F. Luckham, Rheological Characterization of Alumina Ceramic Suspensions in Presence of a Dispersant and a Binder, *Journal of Dispersion Science and Technology*, 33(2012)8, pp. 1210-1217.

- [8] A. U. Khan, B. J. Briscoe, P. F. Luckham, Interaction of binders with dispersant stabilised alumina suspensions, *Colloids and Surfaces A: Physicochemical and Engineering Aspects*, 161(2000)2, pp. 243-257.
- [9] C. Billotte, E. R. Fotsing, E. Ruiz, Optimization of Alumina Slurry for Oxide-Oxide Ceramic Composites Manufactured by Injection Molding, *Advances in Materials Science and Engineering*, 2017(2017), pp. 1-9.
- [10] K. Lebreton, J. M. Rodríguez-Parra, R. Moreno, M. I. Nieto, Effect of additives on porosity of alumina materials obtained by freeze casting, *Advances in Applied Ceramics*, 114(2015)5, pp. 296-302.
- [11] A. Zupancic, R. Lapasin, A. Kristoffersson, Influence of Particle Concentration on Rheological Properties of Aqueous α -Al₂O₃ Suspensions, *Journal of the European Ceramic Society*, 18(1998)5, pp. 467-477.
- [12] L. Palmqvist, O. Lyckfeldt, E. Carlström, P. Davoust, A. Kauppi, K. Holmberg, Dispersion mechanisms in aqueous alumina suspensions at high solids loadings, *Colloids and Surfaces A: Physicochemical and Engineering Aspects*, 274(2006)1-3, pp. 100-109.



19th INTERNATIONAL FOUNDRYMEN CONFERENCE
Humans - Valuable Resource for Foundry Industry Development

Split, June 16th-18th, 2021

<https://ifc.simet.hr/>

CORROSION STUDY OF CuAlNi ALLOY IN STIRRED H₂SO₄ SOLUTION

Ladislav Vrsalović^{1*}, Senka Gudić¹, Verena Šučurović¹, Ivana Ivanić², Stjepan Kožuh², Mirko Gojić², Borut Kosec³

¹University of Split Faculty of Chemistry and Technology, Split, Croatia

²University of Zagreb Faculty of Metallurgy, Sisak, Croatia

³University of Ljubljana Faculty of Natural Science and Engineering, Ljubljana, Slovenia

Poster presentation

Original scientific paper

Abstract

CuAlNi alloy has been evaluated for its corrosion behaviour in the 0.5 mol dm⁻³ H₂SO₄ stirred solution at the rotation rate of magnetic stirrer of 150 and 450 rpm, at 20 and 40 °C. Investigations were performed using open circuit potential measurements, linear and polarization measurements. After polarization measurements corroded surfaces were evaluated using light microscopy analysis. It was found that increasing in electrolyte temperature leads to higher corrosion damages of alloy while increase in rotation rate of stirrer has smaller impact on corrosion. The presence of intergranular corrosion on the electrode surfaces was clearly seen with optical microscope.

Keywords: CuAlNi alloy, corrosion, polarization, optical microscopy

*Corresponding author (e-mail address): ladislav@ktf-split.hr

INTRODUCTION

CuAlNi alloys belong to the group of functional smart materials called shape memory alloys (SMAs) because of its unique properties of “remembering” and recover their original shape [1-3]. In physical sense, this effect is due to the reversible phase transformation of austenite into martensite. Such a phase transformation can be achieved by mechanical (loading) or thermal methods (heating and cooling) [4, 5]. In recovering their shape these alloys can produced a displacement or a force, and in many alloys both combination is possible. So, these alloys can change shape, position, pull, compress, expand or turn with changing the temperature. The main types of these alloys are nitinol (Ni-Ti), Cu-based, and Fe-based alloys. During last decades, practical application of shape memory alloys increased almost exponentially in various applications such as sensors, actuators, robotics, automotive and airplanes industry, electronics, structural and medical applications [2, 3, 6-8]. NiTi alloys are

the most widely used due to its unique superplastic properties, high corrosion resistance, biocompatibility, fatigue life and ductility [9, 10].

Their disadvantages lies in high production costs and low transformation temperatures (-100 to 100 °C) which is why they are often replaced by cheaper Cu-SMA alloys in less demanding applications [11,12]. Cu-Al-Ni alloys have low production cost, better machinability, better work/cost ratio, they are easier to manufacture, and have a higher range of potential transformation temperatures [12-14].

Most of the research papers deals with the microstructure, mechanical and shape memory properties and possible practical applications of Cu-SMA while the corrosion behaviour of these alloys has been significantly less studied despite of the importance for their practical application [2-4, 6, 7, 12-15]. Aluminium has a positive effect on corrosion stability of alloy because of its higher affinity towards oxygen then copper and higher stability of Al_2O_3 then Cu_2O . Some researchers attributed the enhancement of corrosion resistance to the formation of surface duplex layer of oxide compounds composed of $\text{Cu}_2\text{O}\times\text{Al}_2\text{O}_3\times\text{XH}_2\text{O}$ [16]. Nickel play important role in the passivation of CuNi alloys because of its incorporation in the Cu(I) oxide, which is formed on the corroded surface of the alloy and reduce the number of cation vacancies that normally exist in Cu(I) oxide [16-18]. As the chloride ions are the most common corrosive agents, the most investigations have been performed in chloride solutions [12-14, 16, 17].

The present investigations were undertaken with the main aim of studying the corrosion behaviour of CuAlNi alloy in H_2SO_4 solution with an emphasis on the influence of the motion velocity of the solution and the temperature of the electrolyte.

MATERIALS AND METHODS

All electrochemical measurements were conducted with a PAR 273A potentiostat/galvanostat. A conventional three-electrode glass electrochemical cell was used with a platinum sheet counter electrode and saturated calomel reference electrode (SCE) along with CuAlNi working electrode. Electrochemical cell was connected with a Huber Kiss thermostatic bath to provide measurements at constant temperatures.

Working electrode was made by soldering cylindrical specimens of CuAlNi alloy (Cu – 12.8 % Al – 4.1 % Ni) to the copper wires and isolated by Polirepar S polyacrilate resin, leaving cylindrical base of a surface area of 0.5 cm^2 to contact with the solution. Before each experiment, the working electrode was grinding mechanically using successive grades of emery paper up to 1500 grit and then polished with alumina ($0.5 \mu\text{m}$). The electrode was then ultrasonically clean with ethanol and deionized water and transferred quickly to the cell.

Investigations were performed in deaerated $0.5 \text{ mol dm}^{-3} \text{ H}_2\text{SO}_4$, stirred with a magnetic stirrer (rotation rate of 150 and 450 rpm), at 20 and 40 °C. Open circuit potential measurements (in a time period of 90 min), linear and potentiodynamic polarization measurements were used in this study. Linear polarization measurements were performed in a potential range of $\pm 15 \text{ mV}$ around open circuit potential (E_{OCP}) with the scanning rate of 0.2 mVs^{-1} . Potentiodynamic polarization was carried out by sweeping a potential range from -250 mV (vs. SCE) to 1.2 V with a scan rate of 0.5 mVs^{-1} .

After polarization measurements electrode corroded surfaces were evaluated using light microscopy.

RESULTS AND DISCUSSION

Figure 1 a) and b) shows the open circuit potential E_{OCP} measurements for the CuAlNi alloy in $0.5 \text{ mol dm}^{-3} \text{ H}_2\text{SO}_4$ solution at different temperature and rotation speed of magnetic stirrer. Immediately after immersion in the solution E_{OCP} was shifted towards negative potential due to the adsorption of the sulphate ions on the electrode surface. Badawy and associates have explained this shift of the potential of the CuAlNi alloy towards more negative values in the presence of sulphate anions by the selective leaching of the active components from the alloy surface [18]. From the Figure 1 it can be seen that a steeper drop in potential values of CuAlNi alloy is indicated in a higher mixing rate of the solution. An increase in temperature leads to potential stabilization at slightly more negative values. From the Figure 1 it is also evident that stable potential values were achieved within 90 minutes of measurements.

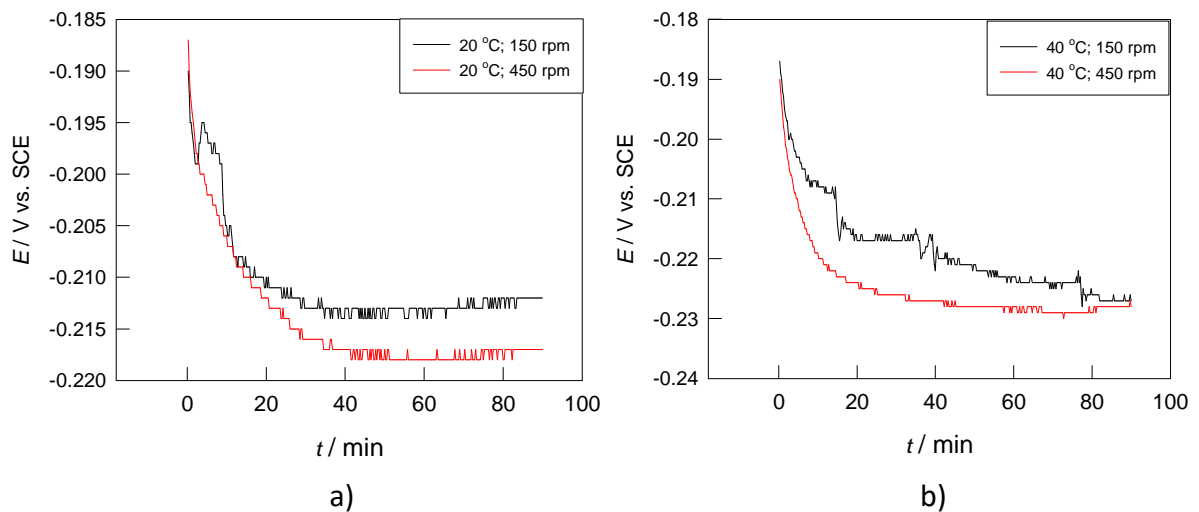


Figure 1. Variation of the open circuit potentials with time for the CuAlNi alloy in deaerated $0.5 \text{ M H}_2\text{SO}_4$ solution a) at $20 \text{ }^\circ\text{C}$ and different rotation speed of magnetic stirrer; b) at $40 \text{ }^\circ\text{C}$ and different rotation speed of magnetic stirrer

Linear polarization measurements were performed immediately after open circuit potential measurements in a narrow area of potential around E_{OCP} and measurement results are presented in Figure 2.

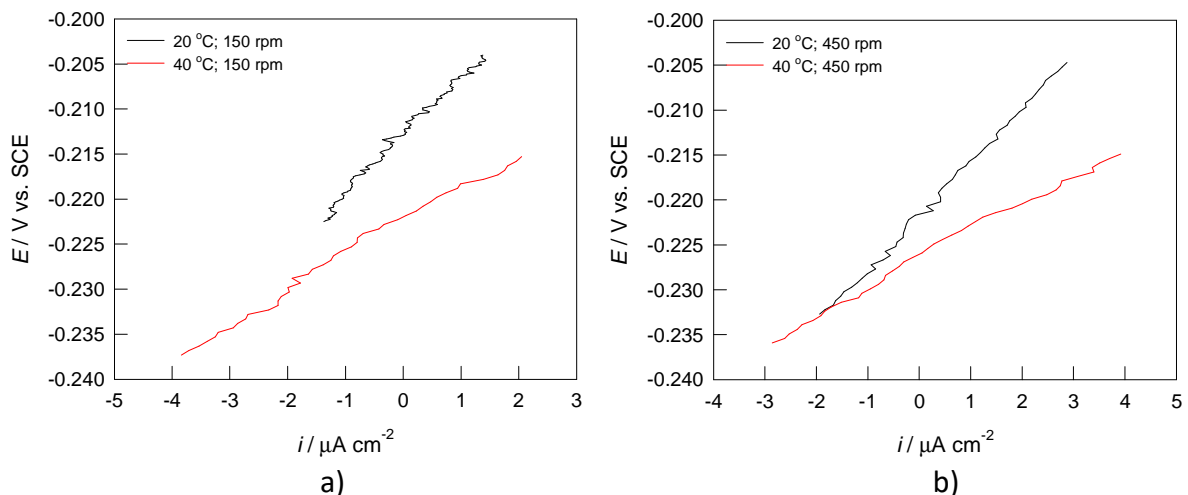


Figure 2. Linear polarization curves for the CuAlNi alloy in deaerated $0.5 \text{ M H}_2\text{SO}_4$ solution a) at 150 rpm and different temperatures; b) at 450 rpm and different temperatures of electrolyte.

From the Figure 2 it can be seen that increasing the temperature of the electrolyte leads to the decrease in slope of the linear parts of curves. As the polarization resistance (R_p) of a material is defined as a slope of the potential-current density (dE/di) curve in the vicinity of the open circuit potential, this means decreasing the values of polarization resistance. Values of polarization resistance are also affected by the rotation speed of magnetic stirrer but in a lesser extent with respect to temperature rise. The values of polarization resistance are presented in Table 1.

Potentiodynamic polarization measurements were conducted in the broad potential area in order to determine the cathodic and anodic behaviour of the alloy in H_2SO_4 solution, and the results have been presented on Figure 3 and the obtained corrosion parameters in Table 1.

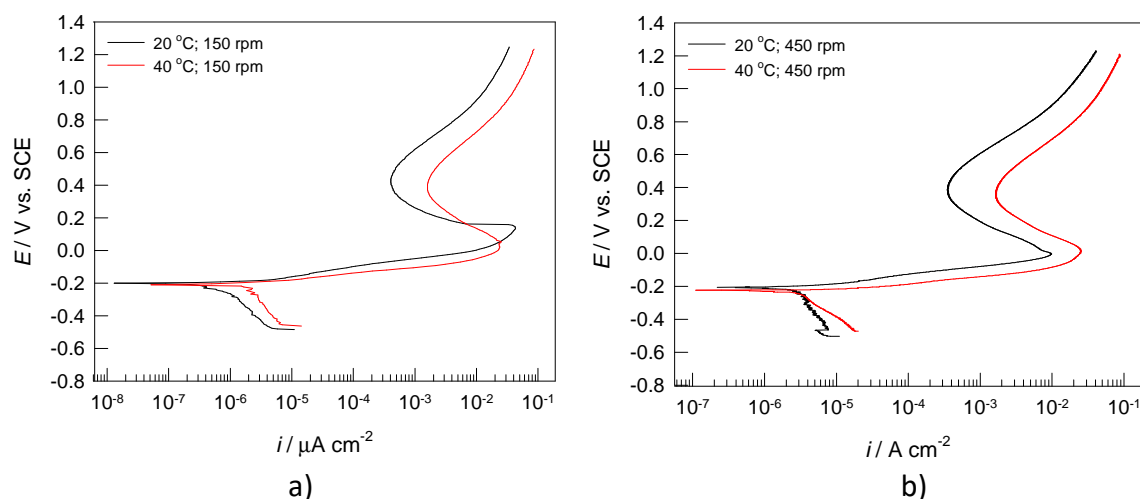


Figure 3. Potentiodynamic polarization curves for the CuAlNi alloy in deaerated 0.5 M H_2SO_4 solution a) at 150 rpm and different temperatures; b) at 450 rpm and different temperatures of electrolyte

Table 1. Corrosion parameters obtain by the polarization measurements

T (°C)	f (rpm)	R_p ($k\Omega\text{ cm}^2$)	i_{corr} ($\mu\text{A cm}^{-2}$)	E_{corr} (V)
20	150	6.436	1.55	-0.208
20	450	5.906	2.26	-0.215
40	150	3.828	3.16	-0.217
40	450	3.025	4.45	-0.233

The influence of electrolyte temperature on the anodic and cathodic current densities is clearly seen from the Figure 3. At 40 °C anodic and cathodic parts of the curves have higher values of current density which means that increase in temperature accelerates the anodic and cathodic reactions. Increasing the rotation speed of stirrer also have negative impact on corrosion stability of the alloy but to a lesser extent.

From the Table 1 it can be seen that by increasing the rotation speed of a stirrer as well as by increasing the electrolyte temperature, the values of polarization resistance decrease and the corrosion current density increases, which indicates a higher corrosion attack on CuAlNi alloy.

After polarization measurements, electrodes were cleaned ultrasonically in deionized water, dry and their surfaces were examined by light microscope with the magnification of 100 times (Figure 4).

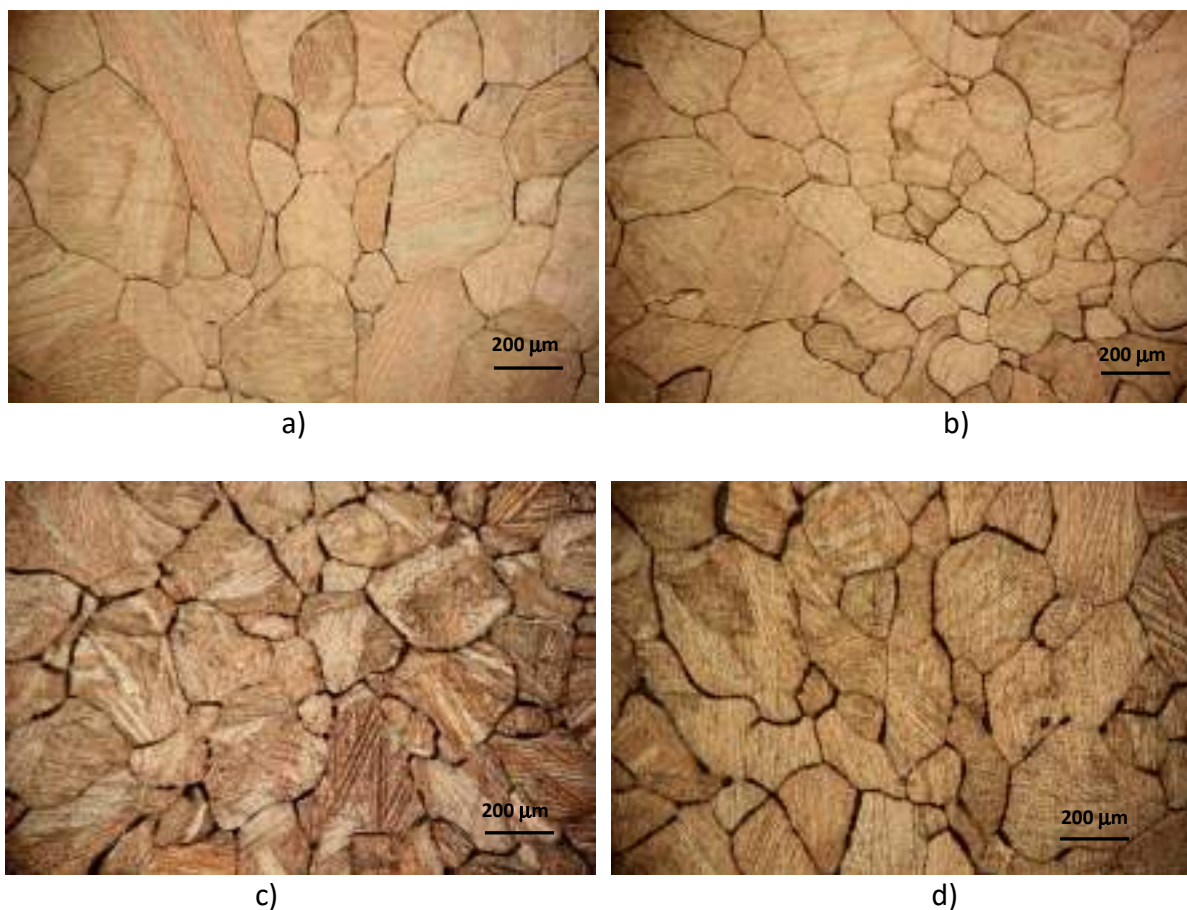


Figure 4. Optical micrographs for the CuAlNi alloy after potentiodynamic polarization in deaerated 0.5 M H₂SO₄ solution a) at 20 °C and 150 rpm; b) at 20 °C and 450 rpm c) at 40 °C and 150 rpm and d) at 40 °C and 450 rpm

From the Figure 4 it is evident that grain boundaries of the CuAlNi alloy suffer intergranular corrosion. This type of corrosion is an important mode of environmental attack on polycrystalline metallic materials. The reason for its appearance can lie in chemical inhomogeneity, such as segregation, precipitation and impurity at a grain boundary, but another reason why the grain boundary might be a site of preferred attack is that the structure of the region is less regular than those of matrix and possesses additional energy. Therefore the structure or energy of a grain boundary is considered to be one of the crucial factors which control the susceptibility to intergranular corrosion [19]. Kuo and associates [20] reported appearance of intergranular corrosion in similar corrosion investigations on Cu-Al alloy in 0.5 mol dm⁻³ H₂SO₄ and have shown that addition of small concentration of beryllium can prevent this type of corrosion.

In our investigation the intensity of the attack rises with the increase of the electrolyte temperature, while stirring velocity has a minor effect on the intensity of intergranular corrosion.

CONCLUSIONS

Investigation of corrosion behaviour of CuAlNi shape memory alloy in deaerated 0.5 mol dm⁻³ H₂SO₄ solution, stirring with magnetic stirrer at rotation rate of 150 and 450 rpm, at 20 °C and 40 °C have revealed the following:

- Increasing in electrolyte temperature and stirring of solution have negligible effect on the values of open circuit potential of CuAlNi alloy.
- Increasing in electrolyte temperature and stirring speed, the corrosion current density increases and the polarization resistance value decreases which indicate higher corrosion attack on the alloy surface.
- Dominant form of corrosion on the electrode surfaces was intergranular corrosion. Intensity of corrosion depends of temperature while solution stirring velocity has minor effect on the intensity of intergranular corrosion.

REFERENCES

- [1] I. Ivanić, M. Gojić, S. Kožuh, Slitine s prisjetljivosti oblika (I. dio): najznačajnija svojstva, *Kem. Ind.*, 63(2014)9-10, pp. 323-330.
- [2] L. Mikova, S. Medvecka-Benova, M. Kelemen, F. Trebuna, I. Virgala, Application of shape memory alloy (SMA) as actuator, *METABK*, 54(2015)1, pp. 169-172.
- [3] R. Dasgupta, A look into Cu-based shape memory alloys: Present scenario and future prospects, *J. Mater. Res.*, 29(2014)16, pp. 1681-1698.
- [4] S. Kožuh, M. Gojić, I. Ivanić, T. Holjevac-Grgurić, B. Kosec, I. Anžel, The effect of heat treatment on the microstructure and mechanical properties of Cu-Al-Mn shape memory alloy, *Kem. Ind.*, 67(2018)1-2, pp. 11-17.
- [5] M. Kelemen, I. Virgala, E. Prada, T. Ilić, Experimental verification of the shape memory alloy (SMA) spring actuator for application on in-pipe machine, *METABK*, 54(2015)1, pp. 173-176.
- [6] I. Ivanić, M. Gojić, S. Kožuh, Slitine s prisjetljivosti oblika (II. dio): podjela, proizvodnja i primjena, *Kem. Ind.*, 63(2014)9-10, pp. 331-344.
- [7] D. C. Lagoudas, *Shape memory alloys, modelling and engineering applications*, Springer, New York, USA, 2008.
- [8] J. M. Jani, M. Leary, A. Subic, M. A. Gibson, A review of shape memory alloy research, applications and opportunities, *Mater. Des.*, 56(2014), pp. 1078-1113.
- [9] Y. Jiao, H. Zhang, T. Zhang, Effect of Al content and annealing temperature on cold workability of CuAlMn alloys, *IOP Conf. Ser.: Mater. Sci. Eng.*, 381(2018), 012153 doi:10.1088/1757-899X/381/1/012153
- [10] T. Kanemura, K. Yokoyama, J. Sakai, Effects of acid type on corrosion and fracture behavior of Ni-Ti superelastic alloy under sustained tensile load in physiological saline solution containing hydrogen peroxide, *Corros. Sci.*, 50(2008), pp. 2785-2795.
- [11] S. N. Saud, E. Hamzah, T. Abubakar, H. R. Bakhsheshi-Rad, Microstructure and corrosion behaviour of Cu-Al-Ni shape memory alloys with Ag nanoparticles, *Mater. Corros.*, 66(2014), pp. 527-534.
- [12] M. Gojić, L. Vrsalović, S. Kožuh, A. Kneissl, I. Anžel, S. Gudić, B. Kosec, M. Kliškić, Electrochemical and microstructural study of Cu-Al-Ni shape memory alloy, *J. Alloy. Compd.*, 509(2011), pp. 9782-9790.

- [13] L. Vrsalović, I. Ivanić, S. Kožuh, S. Gudić, B. Kosec, M. Gojić, Effect of heat treatment on corrosion properties of CuAlNi shape memory alloys, *Trans. Nonferrous Met. Soc. China*, 28(2018), pp. 1149-1156.
- [14] M. Čolić, R. Rudolf, D. Stamenković, I. Anžel, D. Vučević, M. Jenko, V. Lazić, G. Lojen, Relationship between microstructure, cytotoxicity and corrosion properties of Cu-Al-Ni shape memory alloy, *Acta Biomater.*, 6(2010), pp. 308-317.
- [15] R. Bogue, Shape memory materials: a review of technology and applications, *Assem. Automat.*, 29(2009), pp. 214-219.
- [16] W. A. Badawy, M. M. El-Rabiee, N. H. Helal, H. Nady, Synergistic effects of alloying elements in Cu-ternary alloys in chloride solutions, *Electrochim. Acta*, 120(2014), pp. 39-45.
- [17] H. Nady, N. H. Helal, M. M. El-Rabiee, W. A. Badawy, The role of Ni content on the stability of Cu-Al-Ni ternary alloy in neutral chloride solution, *Mat. Chem. Phys.*, 134(2012), pp. 945-950.
- [18] W. A. Badawy, R. M. El-Sherif, H. Shehata, Electrochemical stability of Cu-10Al-5Ni alloy in chloride-sulphate electrolytes, *Electrochim. Acta*, 54(2009), pp. 4501-4505.
- [19] M. Yamashita, T. Mimaki, S. Hashimoto, S. Miura, Intergranular corrosion of copper and α -Cu-Al alloy bicrystals, *Phylos. Mag.*, 63(1991)4, pp. 695-705.
- [20] H. H. Kuo, W. H. Wang, Y. F. Hsu, C. A. Huang, The corrosion behaviour of Cu-Al and Cu-Al-Be shape memory alloys in 0.5 M H₂SO₄ solution, *Corros. Sci.*, 48(2006), pp. 4352-4364.



19th INTERNATIONAL FOUNDRYMEN CONFERENCE
Humans - Valuable Resource for Foundry Industry Development

Split, June 16th-18th, 2021

<https://ifc.simet.hr/>

**ELECTROCOAGULATION AUGMENTED WITH NATURAL ZEOLITE – THE NEW
HYBRID PROCESS FOR TREATMENT OF LEACHATE FROM COMPOSTING OF
BIOWASTE**

Nediljka Vukojević Medvidović^{1*}, Ladislav Vrsalović¹, Teo Ugrina², Ivona Jukić¹

¹ University of Split Faculty of Chemistry and Technology, Split, Croatia,

² Brodosplit d.d., Split, Croatia

Poster presentation
Original scientific paper

Abstract

The efficiency of electrocoagulation augmented with natural zeolite is tested on two leachate samples obtained from composting of biowaste. Electrocoagulation is conducted with aluminum electrode in duration of 60 min, at current intensity and applied voltage of $I = 0.1$ A, $U = 29.9$ V, respectively. Results show that addition of zeolite (at solid/liquid ratio of 20 g/L) influencing on neutralizing the final pH values in leachate solutions, while decreasing the el. conductivity (> 34 %), turbidity (> 99 %), COD (> 84 %) and total Kjeldahl nitrogen (> 81 %). Moreover, zeolite particles acted abrasively on the electrode and contributed to cleaning the electrode surface from oxides, corrosion products and organic mucous layer formed on anode by complexing aluminum with organic compounds in leachate. Beside aluminum dissolution from the anode, aluminum dissolution from the cathode is also recorded, confirming that both electrodes are influencing on forming floc of $Al(OH)_3$ during electrocoagulation. In addition, the overall operational costs of were evaluated and discussed. Results indicate that electrocoagulation augmented with zeolite can be considered as a cost-effective process for treatment of leachate from composting of biowaste.

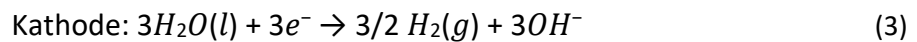
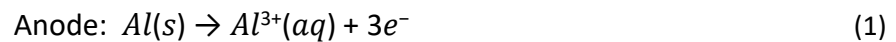
Keywords: *electrocoagulation, natural zeolite, hybrid process, treatment, leachate from composting of biowaste*

*Corresponding author (e-mail address): nvukojev@ktf-split.hr

INTRODUCTION

In order to meet water conservation requirements, there is a growing need to develop efficient and cost-effective wastewater treatment methods that can remove a wide range of pollutants from wastewater [1]. Compared to classical treatment methods, electrocoagulation (EC) provides a relatively compact and robust treatment alternative in which cations required for the process of coagulation/flocculation are released from the

sacrificial anodes in the reaction vessel under the influence of an electric field. The inherent advantage of EC is that no coagulants need to be added to the wastewater, and the salinity of the water does not increase after treatment [2]. Also, EC requires simple process equipment at smaller surface area, lower energy consumption and produces smaller amount of precipitate that is settled faster than conventional coagulation/flocculation. That is why EC is considered as a green technology. It is also environmentally compatible, high efficacy and safety because it operates at the ambient condition [3, 4]. In the EC treatment, aluminum or iron are usually used as a material for electrode. However, aluminum is more effective for elimination of soluble or insoluble organic pollutants (color, ammonia, turbidity and COD). Reactions on aluminum electrodes in the EC process are given by equations (1)-(3) [5]:



During floc generation, a number of monomeric and polymeric compounds such as $Al(OH)^{+}$, $Al(OH)^{2+}$, $Al_2(OH)_2^{4+}$, $Al(OH)_5^{4+}$ and $Al(OH)^{4-}$ are formed, in dependence of alkaline or acidic medium condition [6]. Electrolysis of water at the cathode generates hydroxide ions that combine dissolved aluminum from anode to form hydroxide precipitate at a suitable pH, and removing pollutant by a sweep-floc mechanism. Evolution of H_2 due to water electrolysis at cathode may promote flotation of some portion of coagulated pollutants to the surface [7]. A major problem that occurs with the application of EC is the occurrence of electrode passivation, which is reflected in the longevity of the process, due to the formation of deposits of calcium carbonate and magnesium hydroxide at the cathode and the oxide layer at the anode. Therefore, various methods for minimizing or preventing electrode passivation are proposed, such as electrode polarity change, hydromechanical electrode cleaning, mechanical electrode cleaning, and the introduction of inhibitory agents [2]. In this paper, a new hybrid process that integrates electrocoagulation with the addition of natural zeolite is proposed. Natural zeolites are aluminosilicate materials that show exceptional selectivity towards heavy metals, ammonia, radioactive ions, and their modified forms can also remove inorganic anions and microorganisms. Therefore, they are widely used in wastewater treatment and environmental remediation as ion exchangers, adsorbents and sieve molecules [8, 9]. As far as we know, only Hamid et al. (2020) [10, 11] have been applied combination of EC and natural zeolite in order to remove ammonia from landfills leachate, at solution/zeolite ratio of 1000 mL/120 g. In this paper, a significantly smaller amount of zeolite is used in integrated EC zeolite process (at solution/zeolite ratio of 250 mL/5 g) in order to investigate its effect on removal efficiency. The EC/Z will be tested on biowaste compost leachate in order to achieve more efficient wastewater treatment results.

MATERIALS AND METHODS

In this study, two leachate solutions from composting of biowaste were used for treatment. The biowaste consisted of onion peel, lettuce, cucumber, tomato, orange and coffee grounds mixed with straw as a structural material in an open container (biowaste A), and

mixed with sawdust as a structural material and placed in a rotating drum of a handmade composter (biowaste B). Since the formation of leachate during the composting process from the fourth day onwards was not recorded, two leachates were simulated from the compost mass sampled at 20th days of composting. The first leachate (mark as A₀) was simulated from composting mass in an open container and second from the rotary composter (mark as B₀). Procedure was consisted of passing distilled water through the compost mass of weight of 100 g, at a flow rate of 3.33 mL/min, in duration of 480 min and the obtained leachate volume was 1600 mL. The following water quality indicators were determined in leachate: pH value, electrical conductivity, turbidity, chemical oxygen demand (COD), biochemical oxygen demand (BOD), and Kjeldahl nitrogen.

The simulated leachate was treated by electrocoagulation, without and with the addition of zeolite. Zeolite from the deposit Vranjska Banja, Serbia, particle size 0.1-0.5 mm was used. The characterization of zeolites was previously published [12].

Electrocoagulation was performed in a cylinder glass beaker to which 250 ml of simulated leachate solution was added with immersed aluminum alloy electrodes. The dimensions of the electrodes were: height 5.9 cm, width 1.9 cm and thickness 0.6 cm. The electrodes were immersed in the solution to a height of 4.9 cm. The active surface of the electrode was 25.64 cm². The distance between the electrodes was 3 cm. Before and after immersion, the electrodes are weighed on an analytical balance. Between each experiment, the electrodes were grinding using grinding/polishing machine Metkon Forcipol 1V, with the emery paper 180, 400 and 600 grit, degreased ultrasonically in 70 % ethanol solution for a 5 minutes, washed with distilled water and immersed 60 sec in 0.1 mol/L HCl solution to remove impurities. Electrochemical treatment was performed under the conditions of $I = 0.1$ A, $U = 29.9$ V, contact time $t = 60$ min, with gentle stirring with a magnetic stirrer (Figure 1). In the EC experiments with addition of zeolite, the mass of added zeolite was 5 g per 250 mL of effluent (solid to liquid ratio 20 g/L).

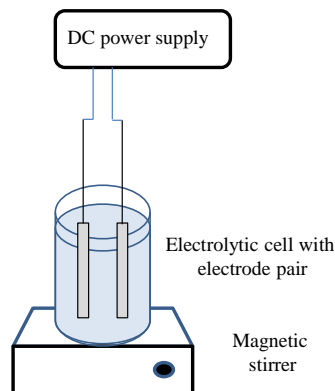


Figure 1. Experimental set-up for electrocoagulation process

During the electrocoagulation process, the pH value and electrical conductivity were monitored, and after the experiment, the pH value, electrical conductivity, turbidity, chemical oxygen demand (COD), biochemical oxygen demand (BOD), and total Kjeldahl nitrogen (TN_K) were determined. All experimental analysis were performed by Standard methods [13].

RESULTS AND DISCUSSION

Physico-chemical characterization of leachate

The results of physico-chemical characterization of leachate simulated from compost mass from an open container (marked A_o) and a rotary composter (marked B_o) are shown in Table 1. The results were compared with the limit values for pollutant emissions in wastewater prescribed by the Croatian regulation [14].

The resulting leachate was cloudy, dark brown color due to presence of colloidal particles. The turbidity values are in range from 48.5-87.5 NTU, and electrical conductivity in range from 759 - 838 $\mu\text{S}/\text{cm}$, which indicate general contamination with organic matter and increased presence of salts, anions and cations. The pH values are in range from 8.58-8.66, which is in accordance with the limit values prescribed by the Croatian regulation. The COD values indicate the presence of harmful substances subjected to oxidation, and they are in range from 557.20-606.95 $\text{mg O}_2/\text{L}$. The values are above the limit value prescribed by the Croatian regulation.

Five-day biological oxygen demand (BOD₅) is a measure of oxygen consumption during the biodegradation of organic compounds by microorganisms. The value of BOD₅ in range from 115.18 to 279.80 $\text{mg O}_2/\text{L}$ exceeds the limit value according to the Croatian regulation for discharge into surface waters (25 $\text{mg O}_2/\text{L}$), while the value for sample A exceeds and limit value for discharge into the public sewage system (250 $\text{mg O}_2/\text{L}$).

Table 1. Results of physico-chemical characterization of leachate

Parameter	Leachate simulated from compost mass A and B		Surface water	Public sewage system
	A _o	B _o		
pH	8.66	8.58	6.5-9.5	6.5 – 9.5
El. conductivity, $\mu\text{S}/\text{cm}$	838	759	-	-
Turbidity, NTU	87.5	48,5	-	-
COD, $\text{mg O}_2/\text{L}$	557.20	606.95	125	700
BOD ₅ , $\text{mg O}_2/\text{L}$	279.80	115.18	25	250
TN _k , $\text{mg N}/\text{L}$	47.62	44.82	15*	50*

Note: A_o - leachate from composting in an open container, B_o - leachate from composting in a rotary composter; Note * - values for total nitrogen are compared since values for Kjeldahl nitrogen are not specified in the Croatian regulation NN 26/20 [14]

The value of the BOD₅/COD ratio indicates the biodegradability of leachate formed during composting. BOD₅ / COD ratio for sample A is 0.502 and for sample B is 0.190. The value in sample A indicate the biodegradability of leachate, while in sample B this value is significantly lower and indicates the presence of less biodegradable organic components in leachate.

Ammonium nitrogen is toxic to microorganisms. The increased concentration of ammonium indicates the biodegradation of complex organic molecules and organic nitrogen, whereby

ammonium ions are formed by reduction. That is why Kjeldahl nitrogen (TN_K) is analyzed here since it includes organic and ammonium nitrogen. The obtained value is compared with the values for total nitrogen since the values for Kjeldahl nitrogen are not defined by Croatian regulation. It can be seen that TN_K values are higher than the limit value prescribed by the Croatian regulation for discharge into surface waters, but satisfactory for discharge into the sewage system.

Leachate treatment with electrocoagulation augmented with zeolite

The leachate was treated by electrocoagulation, without and with the addition of zeolite. Results of monitoring of pH and el. conductivity during the electrocoagulation process without and with the addition of zeolite are compared in Fig. 2.

During EC, the pH change curves show a slight and continuous increase in pH from the initial pH = 8.58 - 8.66 to values around pH = 10.27-10.70 for samples A and B. For samples with added zeolite, the increase in pH is smaller and reaches pH = 9.16-9.21. The slight increase in pH during electrocoagulation is due to the process of hydrolysis of water at the cathode, which produces OH^- ions and hydrogen gas, according to equation (3) [5].

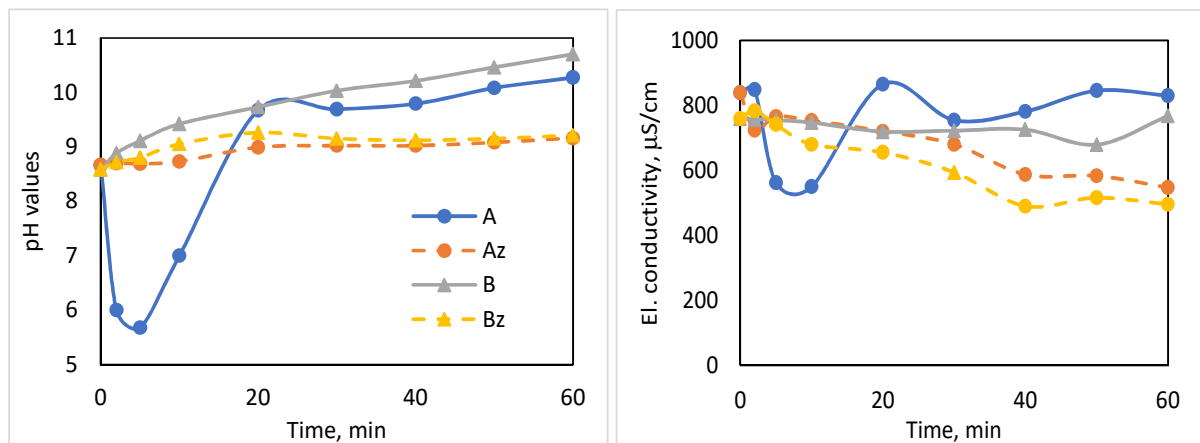


Figure 2. Comparison of pH and el. conductivity during the electrocoagulation process without (A, B) and with the addition of zeolite (Az, Bz)

The increase is less pronounced in samples with zeolite, which is attributed to the ability of zeolite to neutralize solutions [15]. From Fig 2a, pH values for the A sample in the initial times (up to 5 min) decreases significantly (as well as el. conductivity in Fig. 2b), and the reason for this is the formation of a layer on the electrode that causes passivation. No such effect was observed in samples with the addition of zeolite. Moreover, the addition of zeolite allowed the electrocoagulation process to take place continuously. Apparently, the zeolite particles acted abrasively on the electrodes and contributed to decreasing the effect of passivation.

Values of el. conductivity slightly oscillate during process with a slight downward trend. Decreasing of el. conductivity is more pronounced in samples with the addition of zeolite, which indicates that the zeolite binds part of the contaminants that contribute to el. conductivity.

Turbidity, COD and amonium Kjeldalh during leachate treatment with electrocoagulation processes augmented with zeolite

Results of turbidity, COD and TK_N of initial leachate, after treatment with electrocoagulation processes, and after treatment with EC augmented with zeolite are compared in Figure 3. Significant reduction in turbidity, COD and TK_N are evident in treated solution after applying electrocoagulation (EC) and electrocoagulation augmented with zeolite (EC/Z). It is also evident that EC/Z achieves better results. Turbidity is almost negligible (less than 0.31 NTU). COD values decreased below the limit value prescribed by the Croatian regulation for discharge into public sewage system. The TK_N vales also decreased significantly (below 8.4 mg N/L).

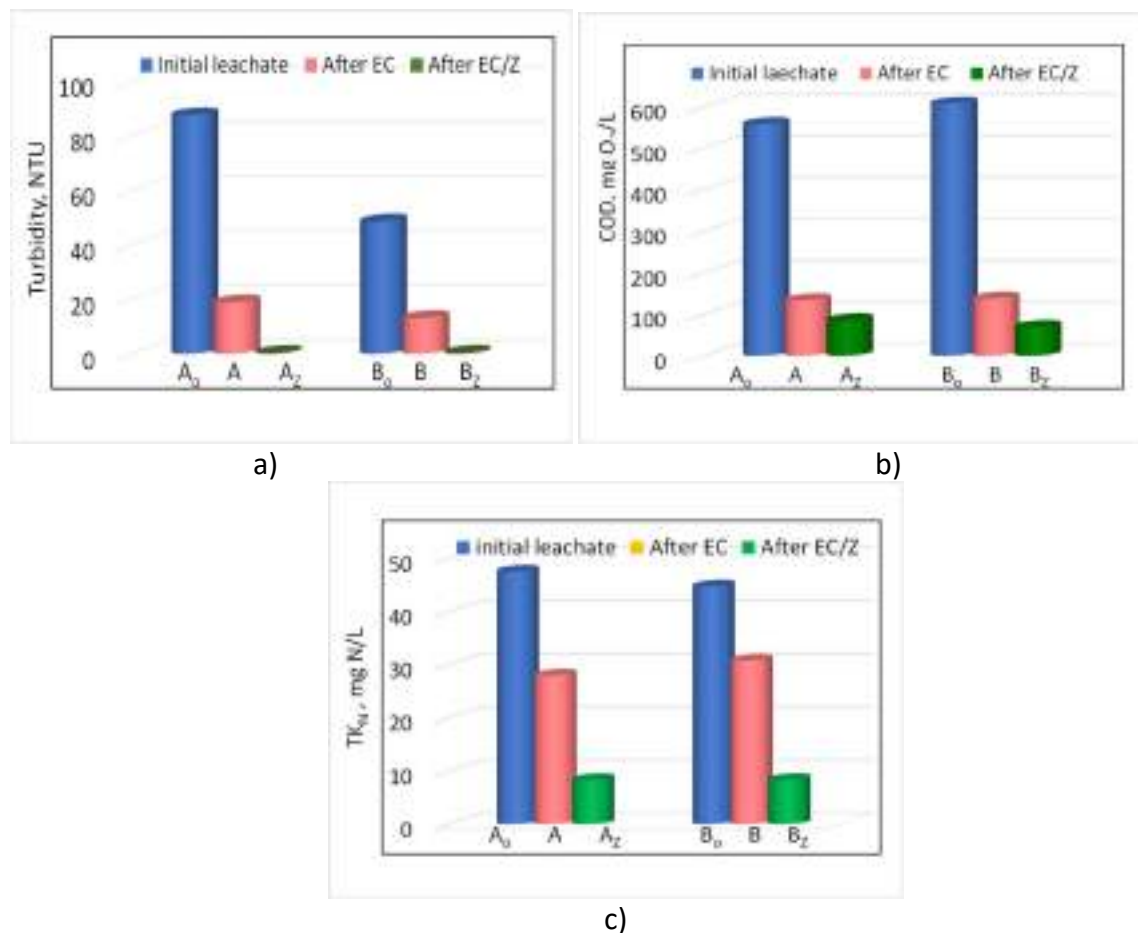


Figure 3. Comparison of turbidity, COD and TK_N in initial leachate, leachate after treatment with electrocoagulation (EC), and leachate after treatment with EC augmented with zeolite (EC/Z)

The removal efficiency based on electrical conductivity, turbidity, COD and Kjeldahl nitrogen were calculated according to equation (4) and results are shown in Table 2.

$$\text{Removal efficiency (in \%)} = [\text{initial values} - \text{final values}] \cdot 100 / \text{initial values} \quad (4)$$

The initial values correspond to the parameters of the initial solution, while the final values correspond to the parameters obtained in solution after application of EC or EC/Z.

Table 2. The removal efficiency α (%) based on electrical conductivity, turbidity, COD and TK_N

Parameter	Removal efficiency, %			
	After EC		After EC/Z	
	A	B	A _z	B _z
El. conductivity	0.95	-1.05	34.73	34.65
Turbidity	78.51	73.13	99.74	99.36
COD	76.07	77.38	84.64	88.52
TK_N	41.18	31.25	82.35	81.25

Table 2 indicate that better results of removal efficiency is achieved with application of EC/Z. Obtained el. conductivity is decreased for >34 %, turbidity for >99%, COD for >84 % and total Kjeldahl nitrogen for >81%, for both samples. Negative values of removal efficiency calculated for B sample after EC indicate that el. conductivity achieve slightly increased values. Our results confirm that EC process augmented with natural zeolite is more efficient for organic pollutant removal from biowaste compost leachate.

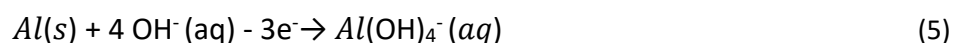
Comparison of the mass of Al electrodes consumed during the experiment

Before and after immersion, the electrodes are weighed on an analytical balance, and results are given in Table 3.

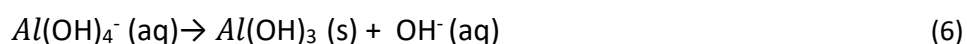
Table 3. Mass of Al electrodes consumed during the experiment

Experiment	Mass of Al electrodes consumed during the experiment, g	
	Anode	Kathode
A	0.0342	0.0076
A _z	0.0519	0.0083
B	0.0397	0.0044
B _z	0.0395	0.0048

The results confirm that Al was dissolved not only from anode but also from the cathode. These results are in agreement with reference [15]. Namely, mechanism of EC takes into account aluminum dissolution at cathode according to reaction (5):



Thus, aluminum dissolution at anode (reaction 1) and cathode (reaction 5) produces Al^{3+} and $Al(OH)_4^-(aq)$, respectively. In solution, Al^{3+} react with OH^- and forming floc $Al(OH)_3(s)$, but also contribute to with $Al(OH)_4^-$ to produce floc of $Al(OH)_3(s)$, according to reaction (6) [16]:



Estimation of operating costs of EC process with and without addition of zeolite

Performance of EC, depends on the electricity consumption, which directly affects the operating costs of the process. The operating costs of the EC process include material (mostly electrodes), electricity costs, as well as operation, maintenance and sludge disposal. In this paper, the operating costs of the EC reactor is calculated taking into account energy consumption, electrode material and zeolite consumption, according to equation (7):

$$\text{Operating cost} = a \cdot C_{\text{energy}} + b \cdot C_{\text{electrode}} + c \cdot C_{\text{zeolite}} \quad (7)$$

where a is average amount of electricity price of 0.95 HRK/kWh according to the valid HEP tariff models for entrepreneurship, b is the average market price of aluminum equals HRK 11.6 HRK/kg [17], and c is average price of natural zeolite equals 0.5 kn/kg [18].

Cost of electrical energy (kW/m³) and electrode (kg Al/m³) were calculated from the following equation:

$$C_{\text{energy}} = \frac{U \cdot I \cdot t}{V} \quad (8)$$

$$C_{\text{electrode}} = \frac{I \cdot t \cdot M}{z \cdot F \cdot V} \quad (9)$$

where U is cell voltage (V), t is the operating time (s), V is the treated leachate (m³), z is number of electron transfer ($z=3$), F is Faraday constant (96 485.33 C/mol), M is the molecular mass of aluminum (26.98 g/mol).

Considering the used values of operational parameters ($U = 29.9$ V, $I = 0.1$ A, $t = 3600$ s, $V = 0.25$ m³) material consumption of aluminum electrodes $C_{\text{electrode}}$ calculated according to equation (9) is equal 0.1342 kg/m³, which gives material cost of 1.56 kn/m³.

However, electrode consumption can be calculated also from the experimental data of electrode dissolution (Table 3) in dependence of process type (A, Az, B or Bz). Thus, material consumption of aluminum electrodes is in range 0.1672-0.2408 kg/m³, which gives material cost of 1.94-2.80 kn/m³.

Electricity consumption, C_{energy} calculated according to equation (8) equals 11.96 kWh/m³, while its cost equals 11.36 kn/m³. Natural zeolite consumption equals 20 kg/m³, while material cost equals 10 kn/m³. Considering the calculated unit values, the total operating cost for EC process calculated by equation (7) is in range of 13.30-13.41 kn/m³, while for EC/Z is in range of 23.41-24.16 kn/m³.

Obtained results of the total operating cost for EC process are in agreement with Lončar et al. [17]. Even those addition of zeolite increase the operational cost of EC/Z process, the advantage such as neutralizing final pH, significant decreasing of el. conductivity, turbidity, COD and TN_K, as well as influencing on diminishing the passivation effect, hybrid process based on electrocoagulation augmented with zeolite can be consider as a cost-effective for treatment of biowaste compost leachate. However, further studies of the influence of other process parameters (pH, electrolyte addition, zeolite addition, etc.) are needed in order to provide better insight into process efficiency and overall operating costs of electrocoagulation augmented with zeolite for leachate treatment from biowaste composting process.

CONCLUSIONS

The results of these studies are expanding the knowledge about the application and performance of electrocoagulation integrated with sorption on natural zeolite. Both technologies are recognized as green technologies, and their connection is expected to achieve better efficiency of real wastewater treatment while reducing the impact of electrode passivation, without the addition of electrolytes. The development of hybrid process EC augmented with zeolite would create the preconditions for more efficient treatment of leachate from composting and its reuse, which would reduce environmental pressures and contribute to the efficient management of water resources in the Republic of Croatia.

Acknowledgements

Many thanks to the executive director of the Sunce Association and the project manager of the "PAZI!" project, Gabrijela Medunić Orlić, as well as the management of the Faculty of Chemical Technology for financing the construction of a rotary pilot composter. Special thanks to students of the Faculty of Chemistry and Technology in Split, Zvonimir Jukić and Ante Čović Stanić, for construction of the rotary composter within the student project UniCompoST (<https://www.unicompost.com>).

REFERENCES

- [1] M. Tawalbeh, M. Al-Shannag, Z. Al-Anber, K. Bani-Melheme, Combined electrocoagulation processes as a novel approach for enhanced pollutants removal: A state-of-the-art review, *Sci. Total Environ.*, 744 (2020), p. 140806.
- [2] I. Kabdaşlı, I. Arslan-Alaton, T. Ölmez-Hancı, O. Tünay, Electrocoagulation applications for industrial wastewaters: a critical review, *Environ. Technol. Rev.* (2012), 1-44. <https://doi.org/10.1080/21622515.2012.715390>.
- [3] C. E. Barrera-Díaz, G. Roa-Morales, P. Balderas Hernández, C. M. Fernandez-Marchante, M. A. Rodrigo, Enhanced electrocoagulation: New approaches to improve the electrochemical process, *J. Electrochem. Sci. Eng.* 4 (4)(2014), pp. 285-296. <https://doi.org/10.5599/jese.2014.0060>.
- [4] L. Smoczyński, S. Kalinowski, H. Ratnaweera, M. Kosobucka, M. Trifescu, K. Pieczulis-Smoczyńska, Electrocoagulation of municipal wastewater – a pilot-scale test, *Desalin. Water Treat.*, 72(2017), pp. 162-168., <https://doi.org/10.5004/dwt.2017.20654>.
- [5] V. Oreščanin, R. Kollar, K. Nađ, Electrochemical treatment of wastewater from potato chips production, *Hrvatske vode*, 24(2016)95, pp. 129-142 (in Croatian)
- [6] D. Sharma, P. Kumar Chaudhari, S. Dubey, A. Kumar Prajapati, Electrocoagulation treatment of electroplating wastewater: A review, *J. Environ. Eng.* 146(2020), 03120009. [https://doi.org/10.1061/\(ASCE\)EE.1943-7870.0001790](https://doi.org/10.1061/(ASCE)EE.1943-7870.0001790).
- [7] I. D. Teglada, Q. Xu, K. Hu, G. Lv, J. Lu, Electrocoagulation processes: A general review about role of electro-generated flocs in pollutant removal, *Process Saf. Environ. Prot.*, 146(2021), pp. 169-189. <https://doi.org/10.1016/j.psep.2020.08.048>.

- [8] K. Margeta, N. Zabukovec Logar, M. Šiljeg, A. Farkas, Natural zeolites in water treatment - how effective is their use, Water treatment / Elshorbagy, Walid; Chowdhury, Rezaul Kabir (ur.). Rijeka: In Tech, 2013. pp. 81-112.
- [9] S. Wang, Y. Peng, Natural zeolites as effective adsorbents in water and wastewater treatment, Chem. Eng. J. 156(2010), 11-24. <https://doi.org/10.1016/j.cej.2009.10.029>.
- [10] M. A. A. Hamid, H. A. Aziz, M. S. Yusoff, S. Abdul Rezan, Clinoptilolite augmented electrocoagulation process for the reduction of high-strength ammonia and color from stabilized landfill leachate, Water Environ Res (2020) 1461. <https://doi.org/10.1002/wer.1461>.
- [11] M. A. A. Hamid, H. A. Aziz, M. S. Yusoff, S. Abdul Rezan, Optimization and analysis of zeolite augmented electrocoagulation process in the reduction of high-strength ammonia in saline landfill leachate, Water 12(2020), 247, <https://doi.org/10.3390/w12010247>.
- [12] N. Vukojević Medvidović, Lead removal on natural zeolite clinoptilolite – column process modelling, Doctoral thesis, Faculty of Chemistry and Technology in Split, Split, 2007.
- [13] Standard methods for examination of water and wastewater, 19th ed, A.D. Eaton, L.S. Clesceri, A.E. Greenberg (eds.), American Public Health Association, Washington, 1995.
- [14] Regulation on emission limits values in wastewater, NN 26/2020 (in Croatian)
- [15] N. Vukojević Medvidović, A. Daković, M. Ugrina, M. Trgo, I. Nuić, M. Marković, Evaluation of low-cost sorbents as potential materials for in situ remediation of water contaminated with heavy metals, Technologica acta, 10(2017)2, pp. 9-13.
- [16] D. Ghernaouta, B. Ghernaoutb, A. Boucherita, M. W. Naceura, A. Khelifaa, A. Kelli, Study on mechanism of electrocoagulation with iron electrodes in idealised conditions and electrocoagulation of humic acids solution in batch using aluminium electrodes, Desalin. Water Treat., 8 (2009) 91-99. <https://doi.org/10.5004/dwt.2009.668>.
- [17] G. Lončar, I. Halkijević, H. Posavčić, I. Ban, Application of electrocoagulation devices for reducing ammonium concentration, Hrvatske vode, 27(2019)108, 129-142 (in Croatian)
- [18] R. L. Virta, Zeolites, U. S. Geological survey - Minerals information, 1997, Accessible on Internet: <https://s3-us-west-2.amazonaws.com/prd-wret/assets/palladium/production/mineral-pubs/zeolites/zeomyb97.pdf>, (23.03.2021.)

University of Zagreb Faculty of Metallurgy, Sisak, Croatia

Organizer of the International Foundrymen Conference

Historical development of the University of Zagreb Faculty of Metallurgy and evolution of studies in the field of metallurgy should be considered in actual socio-economic situation and the status of the profession. Courses form the metallurgy begin within the High Technical College in 1919.

The city of Sisak has a long tradition in the field of metallurgy. Therefore, it is no coincidence that the study of metallurgy was first founded in Sisak, as a city of metallurgical industry of the 20th century. In the area of today's Sisak in Roman times, the city of Siscia grew, as one of the ten cities of the Roman Empire in which there was a mint. Sisak gained a new metallurgical role in 1939 by laying the foundations of metallurgical production, i.e. by founding the Caprag smelter, building of blast furnace with a daily capacity of 40 t of pig iron. In the middle of 1947, the Caprag smelter changed its name to the Željezara Sisak.

Rapid economic development in the middle of the 20th century imposed the need for faster training of highly qualified and specialized personnel in Croatia in the technical fields, including metallurgy. At that time, existing higher education institutions in the field of metallurgy in Ljubljana and Belgrade did not offer a sufficient number of metallurgical professionals. High education at the Department of the Faculty of Technology in Sisak began in 1960/61. After number of restructuring processes, in 1991 the Faculty of Metallurgy became an independent scientific and educational institution of the University of Zagreb for the following activities: Scientific and educational activities in the field of technical sciences (metallurgy); Scientific and research activities in the field of metallurgy, chemical engineering and other technical and technological areas relevant to the field of metallurgy; Auxiliary scientific and research activities.

Today, the Faculty of Metallurgy, University of Zagreb (hereinafter MF, Faculty) is the only scientific and educational institution in the Republic of Croatia that, respecting the culture of quality, provides undergraduate, graduate, postgraduate and professional education in metal materials and technology, metallurgical engineering. and industrial ecology, safety, occupational health and the working environment as well as foundry technology. By organizing conferences, seminars, workshops, public forums and lectures, it systematically implements a program of lifelong education and training and provides support to economic entities in the metallurgical, metalworking, shipbuilding and foundry industries. The Faculty of Metallurgy bases its activity on high academic and ethical values, contribution and responsibility towards society, world strengths and weaknesses, but also willing to solve difficulties.

The Faculty is a pivotal place of scientific research and publishing in the field of technical sciences - metallurgy, provides scientific and professional support to economic entities of metallurgical, metalworking, shipbuilding and foundry industries in the Republic of Croatia, which is especially important after the closure of relevant industrial institutes. The Faculty of Metallurgy of the University of Zagreb is the backbone and promoter of the metallurgical profession in the Republic of Croatia.

Scientific research activity at the Faculty of Metallurgy is carried out by proving projects at the National Science Foundation (HRZZ) and financial support for research at the University of Zagreb, bilateral projects or is initiated in direct contact with economic entities. The research is primarily focused on the production and processing of metallic and non-metallic materials, energy, ecology, protection and application of metals for the needs of the

metallurgical, metalworking and oil industries. Part of the scientific and professional potential of the Faculty of Metallurgy, in addition to teaching and scientific research activities, actively participates in solving practical technical and technological problems of existing companies, environment, etc.

Despite the hardships, wartime and destruction, and the post-war devastation of economic entities and the lack of a strategy for economic development of the Republic of Croatia, the Faculty of Metallurgy managed to preserve scientific and teaching potential, modernize studies, acquire modern and innovate part of existing scientific research equipment. In addition to the above, the implementation of an infrastructure project called Center for Foundry Technology - SIMET, highly positioned on the indicative list of the then Ministry of Science, Education and Sports, and funded by the European Regional Development Fund, Operational Program for Cohesion and Competitiveness 2014-2020; Strengthening of research, technological development and innovation; Investment Priority 1a - Improving the infrastructure and capacity for research and innovation (I&I) in order to develop I&I performance and promote competence centers, especially those of European interest, Specific objective 1a1 Increased research, development and innovation (IRI) capacity to conduct research top quality and meeting the needs of the economy. The project Center for Foundry Technology - SIMET (KK.01.1.1.02.0020), worth 40.401.494,36 HRK, is in the implementation phase, and is funded by the European Regional Development Fund, Operational Program for Cohesion and Competitiveness 2014- 2020 under the call "Investing in organizational reform and infrastructure in the research, development and innovation sector". This project includes the reconstruction and adaptation of existing scientific research infrastructure and the procurement of highly sophisticated equipment which will improve scientific excellence, research capabilities of scientific institutions, improve teaching methods using modern technologies and encourage strengthening links between the scientific research sector and the economy. At the same call, the project VIRTULAB - Integrated Laboratory for Primary and Secondary Raw Materials (KK.01.1.1.02.0022) worth 3.038.562,92 HRK was applied for, accepted and implemented. The project holder is the Faculty of Mining, Geology and Petroleum Engineering, and the Faculty of Metallurgy is one of the 6 partners from the University of Zagreb consortium.

Teaching, scientific research, professional and publishing activities, as well as the work of professional and administrative services of the Faculty of Metallurgy are based on the following values: personal approach to students and associates, openness, transparency, responsibility, ethics, communication, collegiality, efficiency, cooperation, interdisciplinary cooperation, improvement work based on the results of analyses and readiness to solve difficulties.

The metal industry in Croatia has a future, but it is necessary to concentrate on the trinity of competitiveness of the metal industry - modern technology, efficient production process and highly qualified workforce. A representative triangle of influential factors (Triple Helix) plays a key role in the development of scientific, teaching and professional activities of the Faculty of Metallurgy, but also in the development of the metal industry in the Republic of Croatia: business sector, scientific research capacities and public policy. In that sense, the Faculty of Metallurgy justifiably enjoys the recognition and evaluation of influential factors such as the University of Zagreb and the Sisak-Moslavina County as representatives of local and public policy. The cooperation resulted in support and partnership of both institutions with the efforts of the Faculty of Metallurgy to achieve excellence by investing in scientific research capacities and, consequently, to innovate the curricula.

The demands of students and employers and the economy market are changing faster than ever before and, although the goals of education remain constant, the ways in which they are achieved must be continuously changed, upgraded and improved through three basic groups of Metallurgical activities: teaching, research and professional work. These three groups of activities are systematically monitored by the quality assurance procedures which results in development of human, material and financial resources.

Socially responsible service to the community, as the goal of the Faculty of Metallurgy, is visible through a series of thoughtful and prepared activities in all five strategic directions, the outcomes of which are purposefulness and justification of existence by answering the common question WHY?. Only by thinking outside the comfort zone of reliable, small and current successes, it is possible to define a dominant and competitive parameter in the form of innovation in the field of teaching, research and professional activities in metallurgy and other related industries with the imperative to maintain quality standards. At the same time, with an inventive methodology and activities we answer the questions HOW? and WHAT?.

WWW: www.simet.unizg.hr

FB: www.facebook.com/pg/MFSISAK

IG: @metalurskifakultet

YT: Metalurški fakultet

Center for Foundry Technology – SIMET: <http://castingpoint.simet.hr>



University of Zagreb Faculty of Metallurgy, Sisak, Croatia

University of Split Faculty of Chemistry and Technology, Split, Croatia

Co-organizer and host of the International Foundrymen Conference

The Faculty of Chemistry and Technology in Split (FCT) was founded in 1960 in accordance with the need for the engineers in the field of chemical technology and chemistry, due to the intensive development of the chemical industry in Dalmatia. It is the oldest and the largest technological faculty outside the city of Zagreb. Until 1974, FCT was a part of the University of Zagreb. In 1974, it became a part of the University of Split (UNIST) as one of its founders. FCT is located at the University Campus Split, on address Ruđera Boškovića 35. The Faculty has 5058 m² of surface area, consists of 9 lecture halls, one amphitheater with the capacity of 250 seats, IT classroom, 28 student laboratories, 3 semi-industrial laboratories, 28 smaller science-research laboratories, 49 offices for teachers, 10 offices for the Faculty specialist services employees and Dean's Office, 2 IT offices, library, the Hall and 2 chemical warehouses.

The main activity of the FCT is higher education, scientific research and professional work in the scientific areas of: a) the technical sciences in the field of chemical engineering, b) the natural sciences in the field of chemistry and c) the biotechnical sciences in the field of food technology. The activity of FCT is evidenced by numerous competitive projects, in which FCT employees are the principal investigators or team members, collaborations with the domestic and foreign research and academic institutions, published scientific papers in distinguished scientific journals and participation in the organization of scientific congresses. Taking into account its area of interest, FCT develops both professional work and cooperation with the industry, through knowledge and technology transfer to the industry. With 97 full-time employees and over 700 students, FCT is a recognized scientific and educational institution that educates experts for the modern technologies, necessary for the development of society. Today, the FCT is a recognizable component of the University of Split with a wide range of study programs within the four scientific fields: undergraduate university studies (Chemistry, Chemical Technology and Food Technology) and graduate university studies (Chemistry, Chemical Technology and Food Technology), integrated undergraduate and graduate study of Pharmacy (in cooperation with School of Medicine in Split) and postgraduate university (doctoral) studies (Chemical Engineering in Materials Development and Environmental Protection and Chemistry of the Mediterranean Environment).

More than 2.500 students have graduated at the FCT. Many of them performed the responsible positions in the industry, science, schools, local and state administration bodies, hospitals, laboratories and numerous successful scientific domestic or foreign projects...

In accordance with the strategic program of scientific research, scientists are engaged in research of the following main scientific topics: Research and development of environmentally friendly materials and sustainable processes, Profiling and potential of natural organic compounds and Development of advanced methods of analysis. In the last five years, 217 papers in the WoSCC database and 231 papers in Scopus database have been published. The total number of FCT employees' citation was 9789 (WoSCC) and 14835 (Scopus).

60th anniversary of the Faculty of Chemistry and Technology in Split was celebrated in October 2020. On this occasion, Monography of the Faculty of Chemistry and Technology in Split as well as the special edition of the journal Chemistry in Industry were issued (<http://silverstripe.fkit.hr/kui/arhiva-brojeva/issue/178>). With its overall activity within the

last sixty years, FCT has significantly impacted the development of the City of Split, Dalmatia and Croatia and will continue to the same in the future.



South West side of Faculty building,
University of Split Faculty of Chemistry and Technology, Split, Croatia



19th INTERNATIONAL FOUNDRYMEN CONFERENCE

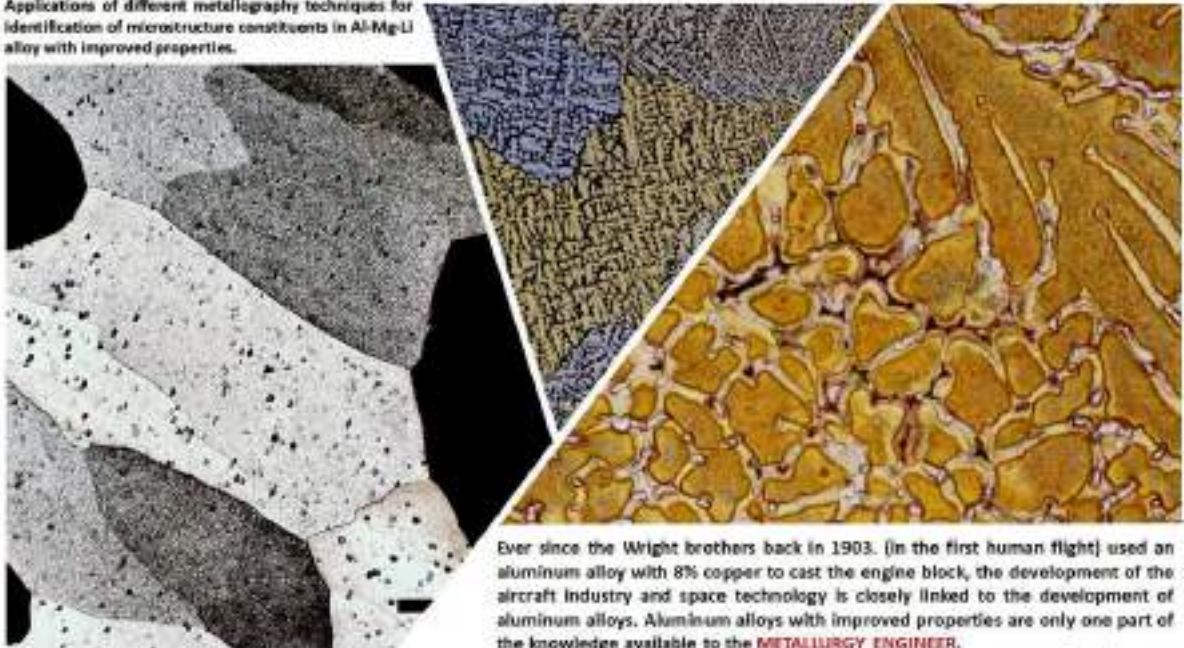
Humans - Valuable Resource for Foundry Industry Development

Split, June 16th-18th, 2021

<https://ifc.simet.hr/>

COMMERCIAL PAGES

Applications of different metallography techniques for identification of microstructure constituents in Al-Mg-Li alloy with improved properties.



Ever since the Wright brothers back in 1903. (in the first human flight) used an aluminum alloy with 8% copper to cast the engine block, the development of the aircraft industry and space technology is closely linked to the development of aluminum alloys. Aluminum alloys with improved properties are only one part of the knowledge available to the **METALLURGY ENGINEER**.

F. Kozina, Z. Zovko Brodarac, M. Petrić, Application of different metallography techniques for identification of microstructure constituents in Al-Mg-Li alloy with improved properties








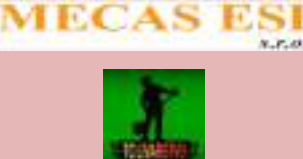




19th INTERNATIONAL FOUNDRYMEN CONFERENCE

Humans - Valuable Resource for Foundry Industry Development

Split, June 16th-18th, 2021

<https://ifc.simet.hr/>

SPONSORSHIP CATEGORY	COMPANY	COMPANY LOGO
CO-ORGANIZER	ELKEM ASA, Oslo (NO)	
GOLDEN SPONSOR	COMET d.o.o., Novi Marof (SI)	
	LABTIM ADRIA Ltd, Sesvete (HR)	
BRONZE SPONSOR	Kontroltest International d.o.o., Zagreb (HR)	
	EDC d.o.o., Zagreb (HR)	
	IDEF d.o.o., Zagreb (HR)	
	Tvornica gline Kutina d.o.o., Kutina (HR)	
	MECAS ESI s.r.o., Plzen (CZ) & TC LIVARSTVO Ltd, Ljubljana (SI)	
	LTH Metalni lijev d.o.o., Benkovac (HR)	
	Labeko d.o.o., Zagreb (HR)	



Five steps to high quality castings

1. Base iron preparation

2. Metal treatment of Grey Iron and Ductile Iron

3. Grey Iron and Ductile Iron Inoculation

4. Focus on ductile iron production

5. Optimisation of Cast Iron Production



Stable and well nucleated base iron

Production of sound and cost effective iron castings begins with the selection of good quality raw materials and additives. Yet the best materials can deliver a poor quality iron unless there is sufficient nucleation carried through the process to give the graphite morphology, chill control and mechanical properties required.

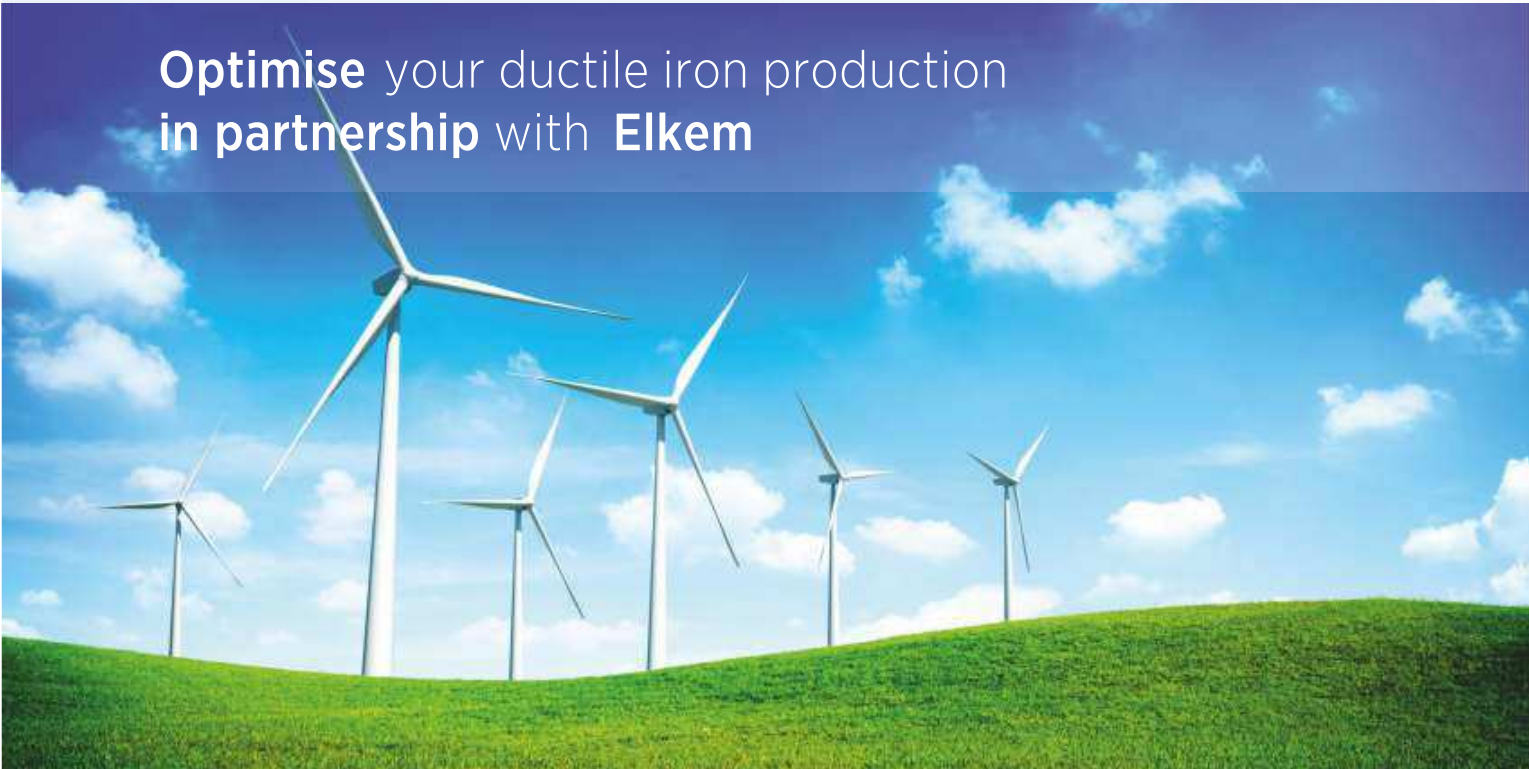
Preconditioning with a long-lasting material, such as Elkem's unique Preseed™ precondi-

tioner is the optimal way to ensure that the nuclei, once created in the melt, are stable enough to survive subsequent treatment processes prior to casting.

Essential to the process is a means of measuring the graphite activity with a melt and the thermal analysis system EPIC™ is able to quickly and accurately give an indication of whether the iron is suitable for pouring or requires correction.

www.elkem.com/foundry

Optimise your ductile iron production in partnership with Elkem



Business areas:

Silicon Materials

Silicones

Foundry Products

Carbon



Representative office:

Elkem ASA

J.J. Strossmayer 176, Sisak Croatia · Tel. +385/44/659-065 · Fax +385/44/659-067 · gordana.gojsevic@elkem.com · zoran.kovacic@elkem.com





Innovative Metal Treatment Solutions



More than 100 reasons
to have a partnership

Getting the best value from nodularising alloys can be a big saving for foundries. The trend towards low Mg alloys, which have lower reactivity and hence higher recovery, continues. Elkem's extensive range of over 100 MgFeSi chemistries, coupled with Topseed® cover alloy, means that together we can optimize your total treatment alloy package. Please contact your local Elkem representative for more details or visit us at www.elkem.com/foundry.



Conventional Mg Treatment



Topseed® cover alloy

Our Partner: **Ferrosad Low Carbon Steel Shot**

METALLTECHNIK SCHMIDT GMBH & CO. KG

FERROSAD
NISKOUGLIČNA SAČMA
STRAHL KRAFT

Representative office:

Elkem ASA

J.J. Strossmayer 176, Sisak Croatia · Tel. +385/44/659-065 · Fax +385/44/659-067 · gordana.gojsevic@elkem.com · zoran.kovacic@elkem.com



OFFERING WHOLE SPECTRUM OF CUSTOMIZED SOLUTIONS



TA Instruments offers high technology instruments/analyzers, such as: Dilatometers, Thermal Conductivity Meters, Mechanical Test Instruments and Dynamic Mechanical Analyzers for characterisation of steel and metal alloys composites.

www.tainstruments.com



Manufacturer and supplier of static tension and/or compression testing machines, designed to measure material's strength and performance.

www.tiniusolsen.com

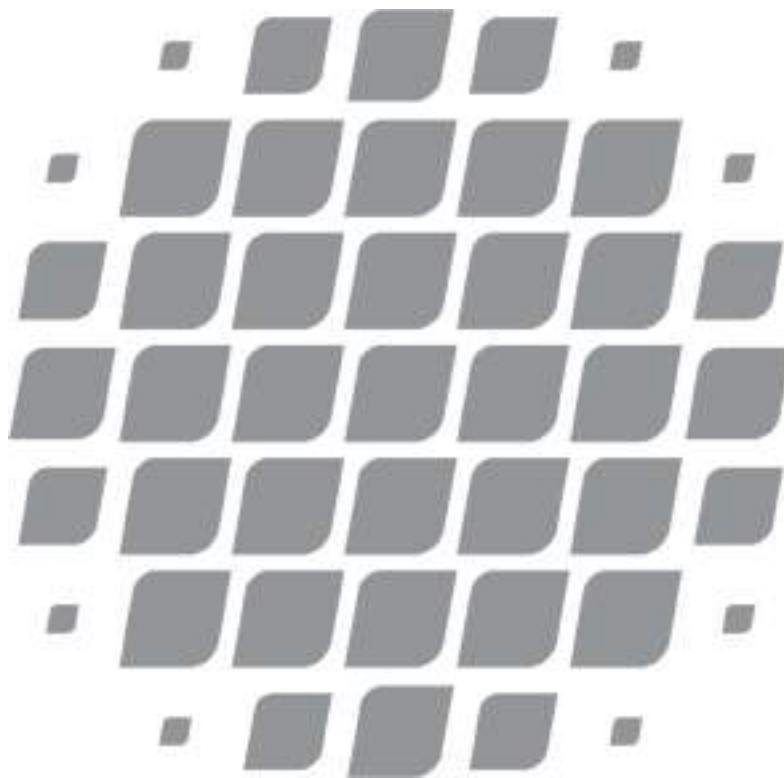


ATS Creep Testing Systems offers precision lever arm testers and also furnaces, customized to user's needs.

www.tiniusolsen.com

ZAGREB: Jaruščica 7/A, 10020 Zagreb, Hrvatska, +385 1 662 3883, info@labtim.hr

LJUBLJANA: Zihlerlova ulica 6, 1000 Ljubljana, Slovenija, +386 1 428 36 84, info@labtim.si



MCT LAB

Material Characterization and Testing Laboratory



Cooperation in the development and research projects of industrial partners in the field of materials science development.

Vision

To become a reliable and innovative analytical laboratory and to strengthen the position of a leading partner for the chemical development of companies.

Mission

Innovative sustainable economic development using state-of-the-art knowledge and approaches.

Values

Reliability, responsibility, professionalism and efficiency, innovation and creativity.

ZAGREB: Jaruščica 7/A, 10020 Zagreb, Hrvatska, +385 1 662 3883, info@labtim.hr

LJUBLJANA: Zihlerlova ulica 6, 1000 Ljubljana, Slovenija, +386 1 428 36 84, info@labtim.si



Vrhunski proizvodi za obradu metala

Karnasch
PROFESSIONAL TOOLS



FOUNDRY

WORK BETTER. FASTER. SAFER.

Visokokvalitetni proizvodi
za brušenje odljevaka.
Za najzahtjevnije zadatke.

www.weilerabrasives.com

WEILER

 Chicago
Pneumatic

CP3650

CP3850

CP3550

CP3119-12E1

POUZDANOST, MAKSIMALNA EFEKTIVNOST I SIGURNOST KLJUČNI SU FAKTORI
PERFORMANSI CHICAGO PNEUMATIC ALATA U NAJZAHTJEVNIJEM RADNOM OKRUŽENJU.

GENERALNI ZASTUPNIK
ZA HRVATSKU

 **COMET**

Varaždinska 40c, Novi Marof
www.comet.hr



19th INTERNATIONAL FOUNDRYMEN CONFERENCE

Humans - Valuable Resource for Foundry Industry Development

Split, June 16th-18th, 2021

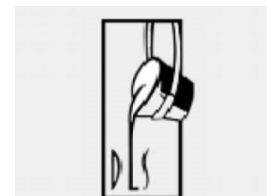
<https://ifc.simet.hr/>

SUPPORTING ASSOCIATION AND COMPANIES

Croatian Foundry Association, Zagreb (HR)



Slovenian Foundry Association, Ljubljana (SI)





19th INTERNATIONAL FOUNDRYMEN CONFERENCE

Humans - Valuable Resource for Foundry Industry Development

Split, June 16th-18th, 2021

<https://ifc.simet.hr/>

MEDIA COVERAGE

IRT 3000



Foundry Lexicon



Foundry Planet

